ENCYCLOPEDIA OF

POLYMER SCIENCE AND TECHNOLOGY

Fourth Edition

VOLUME 15

EDITORIAL STAFF

Executive Editor: **Arza Seidel**

Development Editor: **Mihai Peterca**

Production Manager: **Shirley Thomas**

Production Editor: **Kristen Parrish**

ENCYCLOPEDIA OF

POLYMER SCIENCE AND TECHNOLOGY

Fourth Edition

VOLUME 15

WILEY

Published by John Wiley & Sons, Inc., Hoboken, New Jersey.
Published simultaneously in Canada.

Library of Congress Cataloging-in-Publication Data:

Encyclopedia of polymer science and technology. – Fourth edition.
pages cm
An earlier edition was published under the title: Encyclopedia of polymer science and engineering.
Includes bibliographical references and index.
ISBN 978-1-118-63389-2 (volume 1: cloth)
1. Plastics–Encyclopedias.
2. Polymers–Encyclopedias.
3. Polymerization–Encyclopedias.
TP1110.E53 2014
668.903–dc23 2013037237

Printed in the United States of America.
10 9 8 7 6 5 4 3 2 1

CONTENTS

CONTRIBUTORS TO VOLUME 15

H. Ade, *North Carolina State University, Raleigh, North Carolina,* X-Ray Microscopy

R. Amin-Sanayei, *Atofina Chemicals Inc., King of Prussia, Pennsylvania,* Vinylidene Fluoride Polymers (PVDF)

Neil Ayres, *Department of Polymer Science, University of Southern Mississippi, Hattiesburg, Mississippi,* Water-Soluble Polymers

John K. Baird, *Kelco Division of Merck & Co., Inc.,* Xanthan

W. F. Beach, *Alpha Metals, Bridgewater, New Jersey,* Xylylene Polymers

D. E. Beyer, *The Dow Chemical Company,* Vinylidene Chloride Polymers (PVDC)

John C. Chadwick, *Dutch Polymer Institute, Eindhoven University of Technology, The Netherlands,* Ziegler-Natta Catalysts

John R. Christoe, *CSIRO Textile and Fibre Technology, Belmount, Victoria, Australia,* Wool

Ron J. Denning, *CSIRO Textile and Fibre Technology, Belmount, Victoria, Australia,* Wool

David J. Evans, *CSIRO Textile and Fibre Technology, Belmount, Victoria, Australia,* Wool

Patricia A. Heiden, *Michigan Technological University, Houghton, Michigan,* Wood Composites

B. A. Howell, *Central Michigan University,* Vinylidene Chloride Polymers (PVDC)

J. S. Humphrey, *Atofina Chemicals Inc., King of Prussia, Pennsylvania,* Vinylidene Fluoride Polymers (PVDF)

Mickey G. Huson, *CSIRO Textile and Fibre Technology, Belmount, Victoria, Australia,* Wool

Leslie N. Jones, *CSIRO Textile and Fibre Technology, Belmount, Victoria, Australia,* Wool

Peter R. Lamb, *CSIRO Textile and Fibre Technology, Belmount, Victoria, Australia,* Wool

Andrew B. Lowe, *Department of Chemistry and Biochemistry, University of Southern Mississippi, Hattiesburg, Mississippi,* Water-Soluble Polymers

Laurent M. Matuana, *Michigan State University, East Lansing, Michigan,* Wood Composites

Charles L. McCormick, *Department of Polymer Science, University of Southern Mississippi, Hattiesburg, Mississippi,* Water-Soluble Polymers

Matthew McGreer, *Atlas Material Testing Technology, LLC, Chicago, Illinois,* Weathering of Polymeric Materials

Gregory B. McKenna, *Texas Tech University, Lubbock, Texas,* Viscoelasticity; Yield and Crazing in Polymers

Keith R. Millington, *CSIRO Textile and Fibre Technology, Belmount, Victoria, Australia,* Wool

Paul A. O'Connell, *Texas Tech University, Lubbock, Texas,* Yield and Crazing in Polymers

David G. Phillips, *CSIRO Textile and Fibre Technology, Belmount, Victoria, Australia,* Wool

Anthony P. Pierlot, *CSIRO Textile and Fibre Technology, Belmount, Victoria, Australia,* Wool

John A. Rippon, *CSIRO Textile and Fibre Technology, Belmount, Victoria, Australia,* Wool

Ian M. Russell, *CSIRO Textile and Fibre Technology, Belmount, Victoria, Australia,* Wool

Norma D. Searle, *Consultant in Weathering of Materials,* Weathering of Polymeric Materials

Masato Suzuki, *Nagoya Institute of Technology, Nagoya, Japan,* Zwitterionic Polymerization

Allen Zielnik, *Atlas Material Testing Technology, LLC, Chicago, Illinois,* Weathering of Polymeric Materials

V

VINYLIDENE CHLORIDE POLYMERS (PVDC)

Introduction

Vinylidene chloride (VDC) copolymers were among the first synthetic polymers to be commercialized. Their most valuable property is low permeability to a wide range of gases and vapors (see BARRIER POLYMERS). From the beginning in 1939, the word Saran has been used for copolymers with high VDC content, and it is still a trademark of The Dow Chemical Co. in some countries. Sometimes the names Saran and poly(vinylidene chloride) (PVDC) are used interchangeably. This can lead to confusion because, although Saran includes the homopolymer, only copolymers have commercial importance. The homopolymer, ie, PVDC, is not commer-cially used because it lacks the thermal stability required for processing.

The principal solution to fabrication difficulties is copolymerization. Three types of comonomers are commercially important: vinyl chloride; acrylates, including alkyl acrylates and alkyl methacrylates; and acrylonitrile. When extrusion is the method of fabrication, other solutions include formulation with plasticizers, stabilizers, and extrusion aids plus applying improved extrusion techniques.

Monomer

Properties. Pure vinylidene chloride [75–35-4] (1,1-dichloroethylene) is a colorless, mobile liquid with a characteristic sweet odor. Its properties are summarized in Table 1. Vinylidene chloride is soluble in most polar and nonpolar organic solvents. Its solubility in water (0.25 wt%) is nearly independent of temperature at 16–90 °C (5).

Manufacture. Vinylidene chloride monomer can be conveniently prepared in the laboratory by the reaction of 1,1,2-trichloroethane [79–00-5] with aqueous alkali:

$$2CH_2ClCHCl_2 + Ca(OH)_2 \rightarrow 2CH_2 = CCl_2 + CaCl_2 + 2H_2O$$

Table 1. Properties of VDC Monomer[a, b]

Property	Value
Molecular weight	96.944
Odor	Pleasant, sweet
Appearance	Clear, liquid
Color (APHA)	0–10
Solubility of monomer in water at 25 °C, wt%	0.25
Solubility of water in monomer at 25 °C, wt%	0.035
Normal boiling point, °C	31.56
Freezing point, °C	– 122.56
Flash point, °C	
Tag closed cup	–28
Tag open cup	–16
Flammable limits in air (ambient conditions), vol%	6.5–15.5
Autoignition temperature, °C	513[b]
Latent heat of vaporization, ΔH°_{v}, kJ/mol[c]	
At 25° C	26.48 ± 0.08
At normal boiling point	26.14 ± 0.08
Latent heat of fusion at freezing point, ΔH_m, J/mol[c]	6514 ± 8
Heat of polymerization at 25 °C, ΔH_p, kJ/mol[c]	–75.3 ± 3.8
Heat of combustion, liquid monomer at 25 °C, ΔH_c, kJ/mol[c]	1095.9
Heat of formation	
Liquid monomer at 25 °C, ΔH_f, kJ/mol[c]	–25.1 ± 1.3
Gaseous monomer at 25 °C, ΔH_f, kJ/mol[c]	1.26 ± 1.26
Heat capacity	
Liquid monomer at 25 °C, C_p, J/(mol·K)[c]	111.27
Gaseous monomer at 25 °C, C_p, J/(mol·K)[c]	67.03
Critical temperature, T_c, °C	220.8
Critical pressure, P_c, MPa[d]	5.21
Critical volume, V_c, cm^3/mol	218
Liquid density, g/cm^3	
−20 °C	1.2852
0°C	1.2499
20°C	1.2137
Index of refraction, n_D	
10°C	1.43062
15°C	1.42777
20°C	1.42468
Absolute viscosity, mPa·s (= cP)	
−20 °C	0.4478
0°C	0.3939
x20° C	0.3302
Vapor pressure,[e] at T°C	$\log P_{kPa} = 6.1070 - 1104.29/(T = -237.697)$

[a]Refs. (2) and (3).
[b]Inhibited with methyl ether of hydroquinone.
[c]To convert J to cal, divide by 4.184.
[d]To convert MPa to atm, divide by 0.101.
[e]P measured from 6.7to104.7 kPa. To convert kPa to mm Hg, multiply by 7.5 (add 0.875 to the constant to convert $\log_{kPa}$ to $\log_{mmHg}$).

Other methods are based on bromochloroethane [25620–54-6], trichloroethyl acetate [625–24-1], tetrachloroethane [79–34-5], and catalytic cracking of trichloroethane (4). Catalytic processes produce hydrogen chloride as by-product, rather than less valuable salts, but yields of VDC have been too low for commercial use of these processes. However, good results have been reported with metal-salt catalysts ((5)–7).

Vinylidene chloride is prepared commercially by the dehydrochlorination of 1,1,2-trichloroethane with lime or caustic in slight excess (2–10%) (1,8). A continuous liquid-phase reaction at 98–99 °C yields ~90% VDC. Caustic gives better results than lime. Vinylidene chloride is purified by washing with water, drying, and fractional distillation. It forms an azeotrope with 6 wt% methanol (9). Purification can be achieved by distillation of the azeotrope, followed by extraction of the methanol with water. An inhibitor is usually added at this point. Commercial grades contain 200 ppm of the monomethyl ether of hydroquinone (MEHQ). Many other inhibitors for the polymerization of VDC have been described in patents, but MEHQ is the one most often used. The inhibitor can be removed by distillation or by washing with 25 wt% aqueous caustic under an inert atmosphere at low temperatures.

For many polymerizations, MEHQ need not be removed; instead, polymerization initiators are added. Vinylidene chloride from which the inhibitor has been removed should be refrigerated in the dark at –10 °C, under a nitrogen atmosphere, and in a nickel-lined or baked phenolic-lined storage tank. If not used within 1 day, more inhibitor should be added.

Health and Safety Factors. Vinylidene chloride is highly volatile and, when free of decomposition products, has a mild, sweet odor. Its warning properties are ordinarily inadequate to prevent excessive exposure. Inhalation of vapor presents a hazard, which is readily controlled by observance of precautions commonly taken in the chemical industry (3). A single, brief exposure to a high concentration of VDC vapor, eg, 2000 ppm, rapidly causes intoxication, which may progress to unconsciousness on prolonged exposure. The LC50/4 h in rats is 6350 ppm. However, prompt and complete recovery from the anesthetic effects occurs when the exposure is for short duration. A single, prolonged exposure and repeated short-term exposures can be dangerous, even when the concentration of the vapor is too low to cause an anesthetic effect. Such exposure may produce organic injury to the kidneys and liver. For repeated exposures, the vapor concentration of VDC should be much lower. The American Conference of Governmental Industrial Hygienists threshold limit value of 5 ppm has been established to provide an adequate margin of safety.

Vinylidene chloride is hepatotoxic, but does not appear to be a carcinogen (10–15). Pharmacokinetic studies indicate that the behavior of vinyl chloride and vinylidene chloride in rats and mice is substantially different (16). No unusual health problems have been observed in workers exposed to VDC monomer over varying periods (17). Because VDC degrades rapidly in the atmosphere, air pollution is not likely to be a problem (18). Worker exposure is the main concern. As such, personal monitoring can be done using passive dosimeters. Refer to the dosimeter supplier for collection and analysis details.

The liquid is irritating to the skin after only a few minutes of contact. The inhibitor MEHQ may be partly responsible for this irritation. Inhibited VDC is

moderately irritating to the eyes. Contact causes pain and conjunctival irritation, and possibly some transient corneal injury and iritis. Permanent damage, however, is not likely.

Peroxide Formation. In the presence of air or oxygen, uninhibited VDC forms a violently explosive complex peroxide at temperatures as low as 40° C. Decomposition products of VDC products are formaldehyde, phosgene, and hydrochloric acid. A sharp, acrid odor indicates oxygen exposure and probable presence of peroxides. This is confirmed by the liberation of iodine from a slightly acidified dilute potassium iodide solution. Formation of insoluble polymer may also indicate peroxide formation. The peroxide adsorbs on the precipitated polymer, and separation of the polymer may result in an explosive composition. Any dry composition containing more than ~15 wt% peroxide detonates from a slight mechanical shock or from heat. Vinylidene chloride that contains peroxides may be purified by being washed several times, either with 10 wt% aqueous sodium hydroxide solution at 25 °C or with a fresh aqueous solution of 5 wt% sodium bisulfite. Residues in vessels containing VDC should be handled with great care, and the peroxides should be destroyed with water at room temperature.

Copper, aluminum, and their alloys should not be used in handling VDC. Copper can react with acetylenic impurities to form copper acetylides, whereas aluminum can react with VDC to form aluminum chloralkyls. Both compounds are extremely reactive and potentially hazardous.

Polymerization

Vinylidene chloride polymerizes by both ionic and radical reactions. Processes based on the latter are far more common (19). Vinylidene chloride is of average reactivity when compared with other unsaturated monomers. The chlorine substituents stabilize radicals in the intermediate for an addition reaction. Because they are also strongly electron-withdrawing, they polarize the double bond, making it susceptible to anionic attack. For the same reason, a carbocation intermediate is not favored.

The 1,1-disubstitution of chlorine atoms causes steric interactions in the polymer, as is evident from the heat of polymerization (see Table 1) (20). When corrected for the heat of fusion, the heat of polymerization is significantly less than the theoretical value of −83.7 kJ/mol (−20 kcal/mol) for the process of converting a double bond to two single bonds. The steric strain apparently is neither important in the addition step because VDC polymerizes easily, nor is it sufficient to favor depolymerization. The estimated ceiling temperature for PVDC is about 400 °C.

Homopolymerization. The radical polymerization of VDC has been carried out by solution, slurry, suspension, and emulsion methods. Solution polymerization in a medium that dissolves both monomer and polymer has been investigated (21). Kinetic measurements lead to activation energies and frequency factors in the normal range for radical polymerizations of olefinic monomers. The kinetic behavior of VDC is abnormal when the polymerization is heterogeneous (22). Slurry polymerizations are usually used only in the laboratory. They can be carried out in bulk or in common solvents, eg, benzene. Poly(vinylidene chloride) is insoluble in these media and separates from the liquid phase as a crystalline

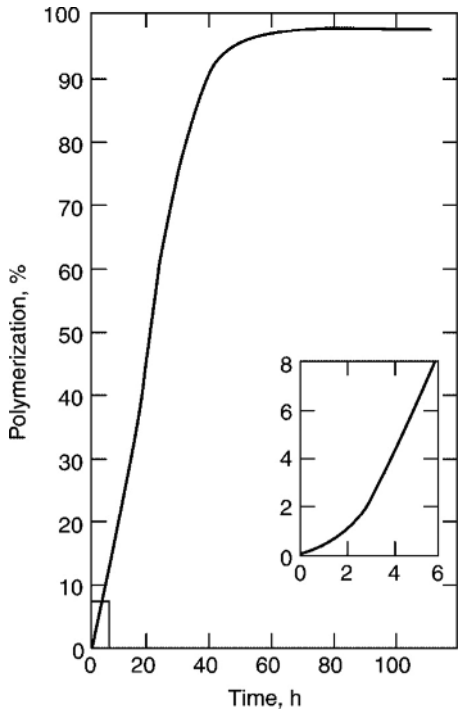

Fig. 1. Bulk polymerization of VDC at 45 °C, with 0.5 wt% benzoyl peroxide as initiator (25).

powder. The heterogeneity of the reaction makes stirring and heat transfer difficult; consequently, these reactions cannot be easily controlled on a large scale. Aqueous emulsion or suspension reactions are preferred for large-scale operations. Slurry reactions are usually initiated by the thermal decomposition of organic peroxides or azo compounds. Purely thermal initiation can occur, but rates are very low (23).

Bulk Polymerization. The spontaneous polymerization of VDC, so often observed when the monomer is stored at room temperature, is caused by peroxides formed from the reaction of VDC with oxygen. Very pure monomer does not polymerize under these conditions. Irradiation by either uv or γ rays (22,24) also induces polymerization of VDC.

The heterogeneous nature of the bulk polymerization of VDC is apparent from the rapid development of turbidity in the reaction medium following initiation. The turbidity results from the presence of minute PVDC crystals. As the reaction progresses, the crystalline phase grows and the liquid phase diminishes. Eventually, a point is reached where the liquid slurry solidifies into a solid mass. A typical conversion–time curve is shown in Figure 1 for a mass polymerization initiated by benzoyl peroxide. The first stage of the reaction is characterized by rapidly increasing rate, which levels off in the second stage to a fairly constant value. This is often called the steady-state region. Throughout the first two stages, monomer concentration remains constant because the polymer separates into another phase. In the third stage, there is a gradual decrease in rate to zero

as the monomer supply is depleted. Because the mass solidifies while monomer is still present (usually at conversions below 20%), further polymerization generates void space. The final solid, therefore, is opaque and quite porous. A similar pattern of behavior is observed when VDC is polymerized in solvents, eg, benzene, that do not dissolve or swell the polymer. In this case, however, the reaction mixture may not solidify if the monomer concentration is low.

Heterogeneous polymerization is characteristic of a number of monomers, including vinyl chloride and acrylonitrile. A completely satisfactory mechanism for these reactions has not been determined. This is true for VDC also. Early studies were not broad enough to elucidate the mechanism (22,26,27). Morphologies of as-polymerized poly(vinyl chloride) (PVC) and poly(acrylonitrile) (PAN) are similar, suggesting a similar mode of polymerization.

The morphology of as-polymerized PVDC is quite different (27). Nearly spherical aggregates form in the PVC and PAN systems, whereas anisotropic growth takes place in the PVDC case. The difference in morphology may be a consequence of the relative rates of polymerization and crystallization. Poly(vinylidene chloride) is unique because polymerization and crystallization probably occur nearly simultaneously. It has been reported that the average lifetime of a growing radical (τ_s) is between 0.1 and 10 s (28). The half-time (t_{y2}) for crystallization of PVDC copolymers in monomer was measured to be about 1 s at 60 °C and about 0.01 s at 90 °C (29). This information is important for developing an understanding of a mechanism that includes a contribution from a surface reaction which has the potential for autoacceleration.

Emulsion Polymerization. Emulsion and suspension reactions are doubly heterogeneous; the polymer is insoluble in the monomer and both are insoluble in water. Suspension reactions are similar in behavior to slurry reactions. Oil-soluble initiators are used, and so the monomer–polymer droplet is like a small mass reaction. Emulsion polymerizations are more complex. Because the monomer is insoluble in the polymer particle, the simple Smith–Ewart theory does not apply (30).

A kinetic model for the particle growth stage for continuous-addition emulsion polymerization has been proposed (31). Below the monomer saturation point, the steady-state rate of polymerization, R_p, depends on the rate of monomer addition, R_a, according to the following reciprocal relationship:

$$\frac{1}{R_p} = \frac{1}{K} + \frac{1}{R_a}$$

where K depends on the number of particles and the propagation rate constant. The kinetics of emulsion polymerization of nonswelling and swellable latex particles to define the locus of polymerization (33) have been examined. There are no significant differences between the behavior of swelling and nonswelling emulsion particles and neither polymerization follows Smith–Ewart kinetics. The results indicate strongly that polymerization takes place at the particle–water interface or in a surface layer on the polymer particle.

Redox initiator systems are normally used in the emulsion polymerization of VDC to develop high rates at low temperatures. Reactions must be carried out below ~80 °C to prevent degradation of the polymer. Poly(vinylidene chloride) in

Table 2. Reactivity of VDC (r_1) with Important Monomers (r_2)[a]

Monomer	r_1	r_2
Styrene	0.14	2.0
Vinyl chloride	3.2	0.3
Acrylonitrile	0.37	0.91
Methyl acrylate	1.0	1.0
Methyl methacrylate	0.24	2.53
Vinyl acetate	6	0.1

[a]Ref. (40).

emulsion is also attacked by aqueous base. Therefore, reactions should be carried out at low pH.

Ionic Mechanisms. The instability of PVDC is one of the reasons why ionic initiation of VDC polymerization has not been used extensively. Many of the common initiators are sufficiently basic so as to promote E2 elimination of hydrogen chloride as the polymer is being formed. For example, butyllithium polymerizes VDC by an anionic mechanism, but the product is a low molecular weight, discolored polymer having a low chlorine content (33). Cationic polymerization of VDC seems unlikely in view of its structure (34). Some available data, however, suggest the possibility. In the low temperature, radiation-induced copolymerization of VDC with isobutylene, reactivity ratios vary markedly with temperature, indicating a change from a radical reaction (35). Coordination complex catalysts may also induce polymerization of VDC by a nonradical mechanism. Again, this speculation is based on copolymerization studies. Poly(vinylidene chloride) telomers can be prepared by using chlorine as the initiator and chain-transfer agent (36,37). Plasma polymerization of VDC in a radio-frequency glow discharge yields cross-linked polymer, which is partially degraded (38).

Copolymerization. The importance of VDC as a monomer results from its ability to copolymerize with other vinyl monomers. The Q value for VDC is 0.22 and the e value is 0.36. It most easily copolymerizes with acrylates, but it also reacts, more slowly, with other monomers, eg, styrene, that form highly resonance-stabilized radicals. Reactivity ratios (r_1 and r_2) with various monomers are listed in Table 2. Many other copolymers have been prepared from monomers for which the reactivity ratios are not known. The commercially important copolymers include those with vinyl chloride (VC), acrylonitrile (AN), or various alkyl acrylates, but many commercial polymers contain three or more components, of which VDC is the principal one. Usually one component is introduced to improve the processibility or solubility of the polymer; the others are added to modify specific use properties. Most of these compositions have been described in the patent literature, and a list of various combinations has been compiled (39). A typical terpolymer might contain 90 wt% VDC, with the remainder made up of AN and an acrylate or methacrylate monomer.

Bulk copolymerizations yielding high VDC-content copolymers are normally heterogeneous. Two of the most important pairs, VDC–VC and VDC–AN, are heterogeneous over most of the composition range. In both cases and at either composition extreme, the product separates initially in a powdery form; however, for

intermediate compositions, the reaction mixture may only gel. Copolymers in this composition range are swollen but not completely dissolved by the monomer mixture at normal polymerization temperatures. Copolymers containing more than 15 mol% acrylate are normally soluble in the monomers. These reactions are therefore homogeneous and, if carried to completion, yield clear, solid castings of the copolymer. Most copolymerizations can be carried out in solution because of the greater solubility of the copolymers in common solvents.

During copolymerization, one monomer may add to the copolymer more rapidly than the other. Except for the unusual case of equal reactivity ratios, batch reactions carried to completion yield polymers of broad composition distribution. More often than not, this is an undesirable result.

Vinylidene chloride copolymerizes randomly with methyl acrylate and nearly so with other acrylates. Very severe composition drift occurs, however, in copolymerizations with vinyl chloride or methacrylates. Several methods have been developed to produce homogeneous copolymers regardless of the reactivity ratio (40). These methods are applicable mainly to emulsion and suspension processes where adequate stirring can be maintained. Copolymerization rates of VDC with small amounts of a second monomer are normally lower than its rate of homopolymerization. The kinetics of the copolymerization of VDC and VC has been studied (41–44).

Studies of the copolymerization of VDC with methyl acrylate (MA) over a composition range of 0–16 wt% showed that near the intermediate composition (8 wt%), the polymerization rates nearly followed normal solution polymerization kinetics (45). However, at the two extremes (0 and 16 wt% MA), copolymerization showed significant autoacceleration. The observations are important because they show the significant complexities in these copolymerizations. The autoacceleration for the homopolymerization, ie, 0 wt% MA, is probably the result of a surface polymerization phenomenon. On the other hand, the autoacceleration for the 16 wt% MA copolymerization could be the result of Trommsdorff and Norrish-Smith effects.

Copolymers of VDC can also be prepared by methods other than conventional radical polymerization. Copolymers have been formed by irradiation and with various organometallic and coordination complex catalysts (24,39,46–49). Graft copolymers have also been described (50–54).

Polymer Structure and Properties

Chain Structure. The chemical composition of PVDC has been confirmed by various techniques, including elemental analysis, x-ray diffraction analysis, degradation studies, and infrared (ir), Raman, and nuclear magnetic resonance (nmr) spectroscopy. The polymer chain is made upof VDC units added head-to-tail:

$$-CH_2CCl_2-CH_2CCl_2-CH_2CCl_2-$$

Because the repeat unit is symmetrical, no possibility exists for stereoisomerism. Variations in structure can occur only by head-to-head addition, branching, or degradation reactions that do not cause chain scission, including such

reactions as thermal dehydrochlorination, which creates double bonds in the structure to give, for example, $CH_2CCl_2CH = CClCH_2CCl_2$ and a variety of ill-defined oxidation and hydrolysis reactions that generate carbonyl groups.

The ir spectra of PVDC often show traces of unsaturation and carbonyl groups. The slightly yellow tinge of many of these polymers comes from the same source; the pure polymer is colorless. Elemental analyses for chlorine are normally slightly lower than the theoretical value of 73.2%.

The high crystallinity of PVDC indicates that no significant amounts of head-to-head addition or branching can be present. This has been confirmed by nmr spectroscopy (55). Studies of well-characterized oligomers having degrees of polymerization (DP) of 2–10 offer further nmr evidence (36), ie, a single peak from the methylene hydrogens. Either branching or another mode of addition would produce nonequivalent hydrogens and a more complicated spectrum. However, nmr cannot detect small amounts of such structures. The ir and Raman spectra can also be interpreted in terms of the simple head-to-tail structure (56,57).

Molecular weights of PVDC can be determined directly by dilute solution measurements in good solvents (58). Viscosity studies indicate that polymers having DP from 100 to more than 10000 are easily obtained. Dimers and polymers having DP < 100 can be prepared by special procedures (36,37). Copolymers can be more easily studied because of their solubility in common solvents. Gel-permeation chromatography studies indicate that molecular weight distributions are typical of vinyl copolymers.

Crystal Structure. The crystal structure of PVDC is fairly well established. Several unit cells have been proposed (59). The unit cell contains four monomer units with two monomer units per repeat distance. The calculated density, 1.96 g/cm^3, is higher than the experimental values, which are 1.80–1.94 g/cm^3 at 25 °C, depending on the sample. This is typically the case with crystalline polymers because samples of 100% crystallinity usually cannot be obtained. A direct calculation of the polymer density from volume changes during polymerization yields a value of 1.97 g/cm^3 (60). If this value is correct, the unit cell densities may be low.

The repeat distance along the chain axis (0.468 nm) is significantly less than that calculated for a planar zigzag structure. Therefore, the polymer must be in some other conformation (61–63). Based on ir and Raman studies of PVDC single crystals and normal vibration analysis, the best conformation appears to be $\theta_{\phi}\theta_{\phi}'$, where the skeletal angle θ is 120°, and the torsional angle ϕ(ϕ' of opposite sign) is 32.5°. This conformation is in agreement with theoretical predictions (64).

The melting temperature T_m of PVDC is independent of molecular weight above DP = 100. However, as shown in Figure 2, it drops sharply at lower molecular weights. Below the hexamer, the products are noncrystalline liquids.

The properties of PVDC (Table 3) are usually modified by copolymerization. Copolymers of high VDC content have lower melting temperatures than PVDC. Copolymers containing more than ~15 mol% acrylate or methacrylate are amorphous. Substantially more AN (25%) or VC (45%) is required to destroy crystallinity completely.

The effect of different types of comonomers on T_m varies. VDC–MA copolymers more closely obey Flory's melting-point depression theory than do copolymers with VC or AN. Studies have shown that for the copolymers of VDC with

Table 3. Properties of VDC Homopolymer

Property	Best value	Reported values
T_m, °C	202	198–205
T_g, °C	–17	–19 to –11
Transition between T_m and T_g, °C	80	
Density at 25 °C, g/cm^3		
Amorphous	1.775	1.67–1.775
Unit cell	1.96	1.949–1.96
Crystalline		1.80–1.97
Refractive index (crystalline), n_D	1.63	
Heat of fusion, ΔH_m, J/mol[a]	6275	4600–7950

[a]To convert J to cal, divide by 4.184.

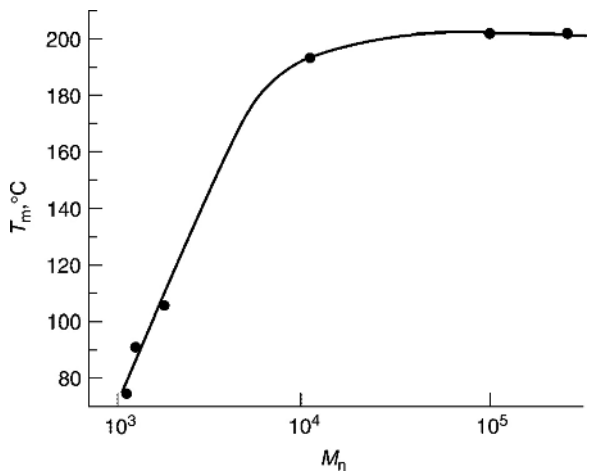

Fig. 2. Crystalline melting temperatures of PVDC (36).

MA, Flory's theory needs modification to include both lamellar thickness and surface free energy (65). The VDC–VC and VDC–AN copolymers typically display severe composition drift; therefore most of the comonomer units do not belong to crystallizing chains. Hence, they neither enter the crystal as defects nor cause lamellar thickness to decrease, and so the depression of the melting temperature is less than expected.

The glass-transition temperature T_g, of VDC copolymers has been studied extensively (66,67). The effect of various comonomers on the T_g is shown in Figure 3. In every case, T_g increases with the comonomer content at low comonomer levels, even in cases where the T_g of the other homopolymer is lower. The phenomenon has been observed in several other copolymer systems as well (68). In these cases, a maximum T_g is observed at intermediate compositions. In others, where the T_g of the other homopolymer is much higher than the T_g of PVDC, the glass-transition temperatures of the copolymers increase over the entire composition range. The T_g increases most rapidly at low AN levels but changes the slowest at low VC levels. This suggests that polar interactions affect the former, but the increase in T_g in the VDC–VC copolymers may simply

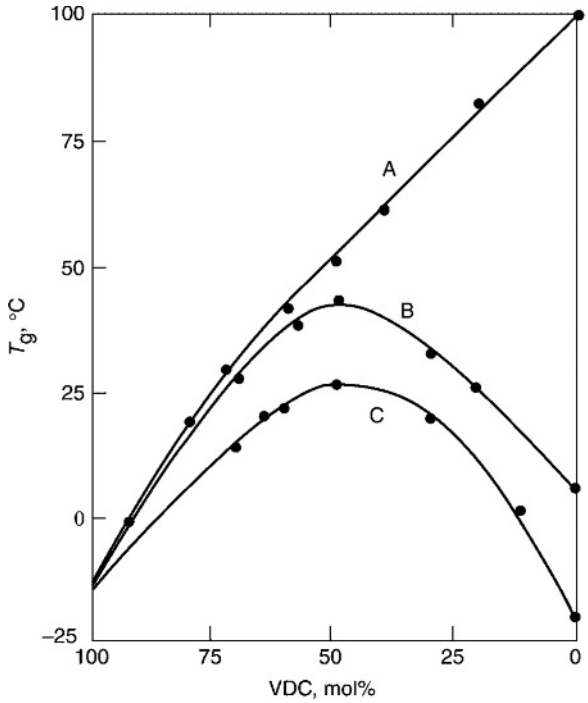

Fig. 3. Effect of comonomer structure on the glass-transition temperature of VDC copolymers (70), where A represents AN; B, MA; and C, EA.

result from loss of chain symmetry. Because of these effects, the temperature range in which copolymers can crystallize is drastically narrowed. Crystallization induction times are prolonged, and subsequent crystallization takes place at a low rate over a long period of time. Plasticization, which lowers T_g, decreases crystallization induction times significantly. Copolymers having lower glass-transition temperatures also tend to crystallize more rapidly (69).

Crystallization curves have been determined for 10 mol% acrylate copolymers of varying side-chain length. Among the acrylate copolymers, the butyl acrylate copolymer has a T_g of 8 °C; the octyl acrylate, –3 °C; and the octadecyl acrylate, –16 °C. The rates of crystallization of these copolymers are inversely related to the glass-transition temperatures. Apparently, the long alkyl side chains act as internal plasticizers, lowering the melt viscosity of the copolymer even though the acrylate group acts to stiffen the mainchain.

The maximum rates of crystallization of the more common crystalline copolymers occur at 80–120 °C. In many cases, these copolymers have broad composition distributions containing both fractions of high VDC content that crystallize rapidly and other fractions that do not crystallize at all. Poly(vinylidene chloride) probably crystallizes at a maximum rate at 140–150 °C, but the process is difficult to follow because of severe polymer degradation. The copolymers may remain amorphous for a considerable period of time if quenched to room temperature. The induction time before the onset of crystallization depends on

both the type and amount of comonomer; PVDC crystallizes within minutes at 25 °C.

Recrystallization of a copolymer having 15 wt% VC has been found to be nucleated by material that survives the melting process plus new nuclei (69). The maximum crystallization rate occurred at 100 °C; the maximum nucleation rate at 10 °C. Attempts to melt all the polymer led to degradation that interfered with recrystallization.

Orientation or mechanical working which accelerates crystallization has a pronounced effect on morphology. Crystals of uniaxially oriented filaments are oriented along the fiber axis (59). The long period (lamellar thickness), as determined by small-angle x-ray scattering, is 7.6 nm and decreases with comonomer content. The fiber is 43% crystalline and has a melting temperature of 195 °C and an average crystal thickness of 4.5 nm. The crystal size is not greatly affected by comonomer content, but both crystallinity and melting temperature decrease with increasing levels of comonomer.

Copolymerization also affects morphology under other crystallization conditions. Copolymers in the form of cast or molded sheets are much more transparent because of the small size of spherulites present. In extreme cases, crystallinity cannot be detected optically, but its effect on mechanical properties is pronounced. Before crystallization, films are soft and rubbery, with low modulus and high elongation. After crystallization, they are leathery and tough, with higher modulus and lower elongation.

Copolymers of VDC and MA have been studied by x-ray techniques (71). For example, the long period (lamellar thickness) for an 8.5 wt% MA copolymer was found to be 9.2 nm by small-angle x-ray scattering. The unit cell is monoclinic, with $a = 0.686$ and $c = 1.247$ nm by wide-angle x-ray scattering.

Significant amounts of comonomer also reduce the ability of the polymer to form lamellar crystals from solution. In some cases, the polymer merely gels the solution as it precipitates rather than forming distinct crystals. At somewhat higher VDC content, it may precipitate in the form of aggregated, ill-defined particles and clusters.

Morphology and Transitions. The highly crystalline particles of PVDC precipitated during polymerization are aggregates of thin lamellar crystals (72). The substructures are 5–10 nm thick and 100 or more times larger in other dimensions. Insome respects, they resemble the lamellar crystals grown from dilute solution (73–75). The single crystals are better characterized than the as-polymerized particles. They are highly branched, with branching angles of 65–70°; the angle appears to be associated with a twin plane in the crystal (76).

Melting temperatures of as-polymerized powders are high, ie, 198–205 °C as measured by differential thermal analysis (dta) or hot-stage microscopy (72). Two peaks are usually observed in dta curves: a small lower temperature peak and the main melting peak. The small peak seems to be related to polymer crystallized by precipitation rather than during polymerization.

As-polymerized PVDC does not have a well-defined T_g because of its high crystallinity. However, a sample can be melted at 210 °C and quenched rapidly to an amorphous state at < -20 °C. The amorphous polymer has a glass-transition temperature of –17 °C as shown by dilatometry (66). Glass-transition

temperature values of –19 to –11 °C, depending on both method of measurement and sample preparation, have been determined.

Once melted, PVDC does not regain its as-polymerized morphology when subsequently crystallized. The polymer recrystallizes in a spherulitic habit. Spherulites between crossed polarizing plates show the usual Maltese cross and are positively birefringent. The size and number of spherulites can be controlled. Quenching and low-temperature annealing generate many small nuclei that, on heating, grow rapidly into small spherulites. Slow crystallization at higher temperatures produces fewer but much larger spherulites. The melting temperature and degree of crystallinity of recrystallized PVDC is also dependent on crystallization conditions. The melting temperature increases with crystallization temperature, but the as-polymerized value cannot be achieved. There is no reason to believe that even these values indicate the true melting point of PVDC; it may be as high as 220 °C. Slow, high temperature recrystallization and annealing experiments are not feasible because of the thermal instability of the polymer (77). Other transitions in PVDC have been observed by dynamic mechanical methods.

Solubility and Solution Properties. Poly(vinylidene chloride), like many high melting polymers, does not dissolve in most common solvents at ambient temperatures. Copolymers, particularly those of low crystallinity, are much more soluble. However, one of the outstanding characteristics of VDC polymers is resistance to a wide range of solvents and chemical reagents. The insolubility of PVDC results less from its polarity than from its high melting temperature. It dissolves readily in a wide variety of solvents above 130 °C (77). However, it should be noted that significant degradation accompanies dissolution of the polymer in polar, aprotic solvents at these temperatures.

The polarity of the polymer is important only in mixtures having specific polar aprotic solvents. Many solvents of this general class solvate PVDC strongly enough to depress the melting temperature by more than 100 °C. Solubility is normally correlated with cohesive energy densities or solubility parameters. For PVDC, a value of 20 ± 0.6 $(J/cm^3)^{1/2}$ [10 ± 0.3 $(cal/cm^3)^{1/2}$] has been estimated from solubility studies in nonpolar solvents. The value calculated from Small's relationship is 20.96 $(J/cm^3)^{1/2}$ [10.25 $(cal/cm^3)^{1/2}$]. The use of the solubility parameter scheme for polar crystalline polymers such as PVDC has limited value. A typical nonpolar solvent of matching solubility parameter is tetrahydronaphthalene. The lowest temperature at which PVDC dissolves in this solvent is 140 °C. Specific solvents, however, dissolve PVDC at much lower temperatures. A list of good solvents is given in Table 4. The relative solvent activity is characterized by the temperature at which a 1 wt% mixture of polymer in solvent becomes homogeneous when heated rapidly.

Poly(vinylidene chloride) also dissolves readily in certain solvent mixtures (78). One component must be a sulfoxide or *N*,*N*-dialkylamide. Effective cosolvents are less polar and have cyclic structures. They include aliphatic and aromatic hydrocarbons, ethers, sulfides, and ketones. Acidic or hydrogen-bonding solvents have an opposite effect, rendering the polar aprotic component less effective. Both hydrocarbons and strong hydrogen-bonding solvents are nonsolvents for PVDC.

As-polymerized PVDC is not in its most stable state; annealing and recrystallization can raise the temperature at which it dissolves (74). Low crystallinity

Table 4. Solvents for VDC Homopolymer[a]

Solvents	T,[b] °C
Nonpolar	
1,3-Dibromopropane	126
Bromobenzene	129
1-Chloronaphthalene	134
2-Methylnaphthalene	134
o-Dichlorobenzene	135
Polar aprotic	
Hexamethylphosphoramide	–7.2
Tetramethylene sulfoxide	28
N-Acetylpiperidine	34
N-Methylpyrrolidinone	42
N-Formylhexamethyleneimine	44
Trimethylene sulfide	74
N-*n*-Butylpyrrolidinone	75
Diisopropyl sulfoxide	79
N-Formylpiperidine	80
N-Acetylpyrrolidinone	86
Tetrahydrothiophene	87
N, N-Dimethylacetamide	87
Cyclooctanone	90
Cycloheptanone	96
Di-*n*-butyl sulfoxide	98

[a]Ref. (77).
[b]Temperature at which a 1 wt% mixture of polymer in solvent becomes homogeneous.

polymers dissolve at a lower temperature, forming metastable solutions. However, on standing at the dissolving temperature, they gel or become turbid, indicating recrystallization into a more stable form.

Copolymers having enough VDC content to be quite crystalline behave much like PVDC. They are more soluble, however, because of their lower melting temperatures. The solubility of amorphous copolymers is much higher. The selection of solvents in either case varies somewhat with the type of comonomer. Some of the more common types are listed in Table 5. Solvents that dissolve PVDC also dissolve the copolymers at lower temperatures. The identification of solvents that dissolve PVDC at low temperatures makes possible the study of dilute solution properties. Both light-scattering and intrinsic-viscosity studies have been reported (58). Intrinsic viscosity–molecular weight relationships for the three solvents investigated ([η] in dL/g) are

$$[\eta] = 1.31 \times 10^{-4} M_{\omega}^{0.69} \ N\text{-Methylpyrrolidinone (MP)} \tag{1}$$

$$[\eta] = 1.39 \times 10^{-4} M_{\omega}^{0.69} \ \text{Tetramethylene sulfoxide (TMSO)} \tag{2}$$

$$[\eta] = 2.58 \times 10^{-4} M_{\omega}^{0.65} \ \text{Hexamethylphosphoramide (HMPA)} \tag{3}$$

Table 5. Common Solvents for VDC Copolymers

Solvents	Copolymer type	Temperature, °C
Tetrahydrofuran	All	<60
2-Butanone	Low crystallinity	<80
1,4-Dioxane	All	50–100
Cyclohexanone	All	50–100
Cyclopentanone	All	50–100
Ethyl acetate	Low crystallinity	<80
Chlorobenzene	All	100–130
Dichlorobenzene	All	100–140
Dimethylformamide	High acrylonitrile	<100

The relative solvent power (HMPA > TMSO > NMP) agrees with solution-temperature measurements. The characteristic ratio C_∞ is about 8 ± 1, which is slightly larger than that of a similar polymer, poly(isobutylene).

The dilute solution properties of copolymers are similar to those of the homopolymer. The intrinsic viscosity–molecular weight relationship for a VDC–AN copolymer (9 wt% AN) is $[\eta] = 1.06 \times 10^{-4} M_\omega^{0.72}$ (79). The characteristic ratio is 8.8 for this copolymer.

An extensive investigation of the dilute solution properties of several acrylate copolymers has been reported (76). The behavior is typical of flexible-backbone vinyl polymers. The length of the acrylate ester side chain has little effect on properties.

Intrinsic viscosity–molecular weight relationships have been obtained for copolymers in methyl ethyl ketone. The value for a 15 wt% ethyl acrylate (EA) copolymer is $[\eta] = 2.88 \times 10^{-4} M_\omega^{0.6}$.

The molecular weights of PVDC and VDC copolymers have been characterized by using the absolute viscosity of a 2 wt% solution in *o*-dichlorobenzene at 140° C. The exact correlation between this viscosity value and molecular weight is not known. Gel-permeation chromatography is the preferred method for characterizing molecular weight; studies of copolymers have been reported (80,81).

Mechanical Properties. Because PVDC is difficult to fabricate into suitable test specimens, very few direct measurements of its mechanical properties have been made. In many cases, however, the properties of copolymers have been studied as functions of composition, and the properties of PVDC can be estimated by extrapolation. Some characteristic properties of high VDC content, unplasticized copolymers are listed in Table 6. The performance of a given specimen is sensitive to morphology, including the amount and kind of crystallinity, as well as orientation. Tensile strength increases with crystallinity, whereas toughness and elongation decrease. Orientation, however, improves all three properties. The effect of stretch ratio applied during orientation on properties of VDC–VC monofilaments is shown in Table 7.

The dynamic mechanical properties of VDC–VC copolymers have been studied in detail. The incorporation of VC units in the polymer results in a drop in dynamic modulus because of the reduction in crystallinity. However, the

Table 6. Mechanical Properties of High VDC Content Copolymers

Property	Range
Tensile strength, MPa[a]	
Unoriented	34.5–69.0
Oriented	207–414
Elongation,%	
Unoriented	10–20
Oriented	15–40
Softening range (heat distortion), °C	100–150
Flow temperature, °C	>185
Brittle temperature, °C	–10 to 10
Impact strength, J/m[b]	26.7–53.4

[a]To convert MPa to psi, multiply by 145.
[b]To convert J/m to ft·lbf/in., divide by 53.38 (see ASTM D256).

Table 7. Effect of Stretch Ratio on Tensile Strength and Elongation of a VDC–VC Copolymer[a,b]

Stretch ratio	Tensile strength, MPa[c]	Elongation,%
2.50:1	235	23.2
2.75:1	234	21.7
3.00:1	303	26.3
3.25:1	268	33.1
3.50:1	316	19.2
3.75:1	330	21.8
4.00:1	320	19.7
4.19:1	314	16.2

[a]Ref. (82).
[b]Average of five determinations, using the Instron test at 5 cm/min.
[c]To convert MPa to psi, multiply by 145.

glass-transition temperature is raised; therefore, the softening effect observed at room temperature is accompanied by increased brittleness at lower temperatures. These copolymers are normally plasticized in order to avoid this. Small amounts of plasticizer (2–10 wt%) depress T_g significantly without loss of strength at room temperature. At higher levels of VC, the T_g of the copolymer is above room temperature and the modulus rises again. A minimum in modulus or maximum in softness is usually observed in copolymers in which T_g is above room temperature. A thermomechanical analysis of VDC–AN and VDC–MMA (methyl methacrylate) copolymer systems shows a minimum in softening point at 79.4 and 68.1 mol% VDC, respectively (82).

In cases where the copolymers have substantially lower glass-transition temperatures, the modulus decreases with increasing comonomer content. This results from a drop in crystallinity and glass-transition temperature. The loss in modulus in these systems is therefore accompanied by an improvement in low temperature performance. However, at low acrylate levels (<10 wt%), T_g increases with comonomer content. The brittle points in this range may therefore be higher than that of PVDC.

Table 8. Comparison of the Permeabilities of Various Polymers to Water Vapor[a]

	Density, g/mL		Permeability[b]	
Polymer	Amorphous	Crystalline	Amorphous	Crystalline
Ethylene	0.85	1.00	200–220	10–40
Propylene	0.85	0.94	420	
Isobutylene	0.915	0.94	90	
Vinyl chloride	1.41	1.52	300	90–115
Vinylidene chloride	1.77	1.96	30	4–6

[a]Refs. (40),(84) and (85).
[b]In g/(h·100 m^2) at 7.1 kPa (53 mm Hg) pressure differential and 39.5 °C for a film 25.4 μm (1 mil) thick.

The long side chains of the acrylate ester group can apparently act as internal plasticizers. Substitution of a carboxyl group on the polymer chain increases brittleness. A more polar substituent, eg, an *N*-alkylamide group, is even less desirable. Copolymers of VDC with *N*-alkylacrylamides are more brittle than the corresponding acrylates even when the side chains are long (83). Side-chain crystallization may be a contributing factor.

Barrier Properties. Vinylidene chloride copolymers are unique in that they have low permeability to a wider range of gases and liquids than other polymers. VDC copolymers are "barrier polymers" in a broad sense. Historically, the operating definition of a barrier polymer meant having an oxygen permeability less than 1.0 (cm^3(STP)·mil)/(100 $in.^2$·day·atm) [2.0 nmol/(m·s·GPa)]. A more useful descriptor for a barrier polymer is related to the application. A barrier polymer would have a set of permeabilities for important molecules sufficiently low to satisfy the containment needs. Some polymers have low permeability to gases. Others have low permeability to water. Still other polymers have low permeability to flavor/aroma/solvent (F/A/S) molecules. However, only rarely does a single polymer have low permeability in more than one category. VDC copolymers have low permeability in all three categories (see BARRIER POLYMERS).

The good barrier properties of VDC copolymers are a consequence of crystallinity and low free volume in the amorphous phase. The symmetric nature of the VDC unit in the polymer leads to nested packing that is adequate for crystallization and that leaves very little "dead" volume in the amorphous phase. Both polyisobutylene and PVDC have unusually low permeability to water compared to their monosubstituted counterparts, polypropylene and PVC (84). The values listed in Table 8 include estimates for the completely amorphous polymers. The estimated value for highly crystalline PVDC was obtained by extrapolating data for copolymers.

The effect of copolymer composition on gas permeability is shown in Table 9. The inherent barrier in VDC copolymers can best be exploited by using films containing little or no plasticizers and as much VDC as possible. However, the permeabilities of even completely amorphous copolymers, eg, 60 wt% VDC–40 wt% AN or 50 wt% VDC–50 wt% VC, are low compared to that of other polymers. The primary reason is that the diffusion coefficients for molecules in VDC copolymers are very low. This factor, together with the high crystallinity and the low solubility coefficients for many gases in VDC copolymers, results in very low

Table 9. Effect of Composition on the Permeability of Various Gases through VDC Copolymers[a]

Polymer	Gas	T, °C	P, nmol/(m-s-GPa)[b]
PVDC	O_2	25	<0.04
	N_2	25	<0.02
	CO_2	25	<0.10
90/10 VC	He	25	2.23
	H_2	25	2.54
	O_2	25	0.14
	N_2	25	0.03
	CO_2	25	0.98
	H_2S	30	0.10
85/15 VC	He	34	10
	O_2	25	0.40
	CO_2	20	2.0
70/30 VC	O_2	25	0.36
50/50 VC	O_2	25	1.2
80/20 AN	O_2	25	0.14
	N_2	25	0.02
	CO_2	25	0.35
60/40 AN	O_2	25	0.71
	N_2	25	0.09
	CO_2	25	1.6

[a]Ref. (86).
[b]To convert nmol/(m·s·GPa) to (cm^2·cm)/(cm^2·s·kPa), divide by 4.46×10^2.

permeabilities. A change from PVDC to a copolymer containing 40 wt% AN or 50 wt% VC increases the permeability 10-fold but has little effect on the solubility coefficient.

The addition of a more polar comonomer, eg, AN, increases the water vapor transmission rate more than the addition of a less polar comonomer, eg, VC, when other factors are constant. For the same reason, AN copolymers are more resistant to penetrants of low cohesive energy density. All VDC copolymers, however, are very impermeable to aliphatic hydrocarbons. Comonomers that lower T_g and increase the free volume in the amorphous phase increase permeabilities more than other comonomers. Higher acrylates are examples of this phenomenon. Plasticizers increase permeabilities for similar reasons.

The effects of plasticizers and temperature on the permeabilities of small molecules in a typical VDC copolymer have been studied thoroughly. Data for oxygen permeability are contained in Figure 4. The oxygen permeability doubles with the addition of about 1.7 phr (parts per hundred of resin) of common plasticizers or a temperature increase of about 8 °C (87). The moisture (water) vapor transmission rate (MVTR or WVTR) doubles with the addition of about 3.5 phr of common plasticizers (88). The dependence of the WVTR on temperature is a little more complicated. Water vapor transmission rate is commonly reported at a constant difference in relative humidity and not at a constant partial pressure difference. Hence, WVTR is a mixed term that increases with increasing temperature because both the permeability and the partial pressure at constant

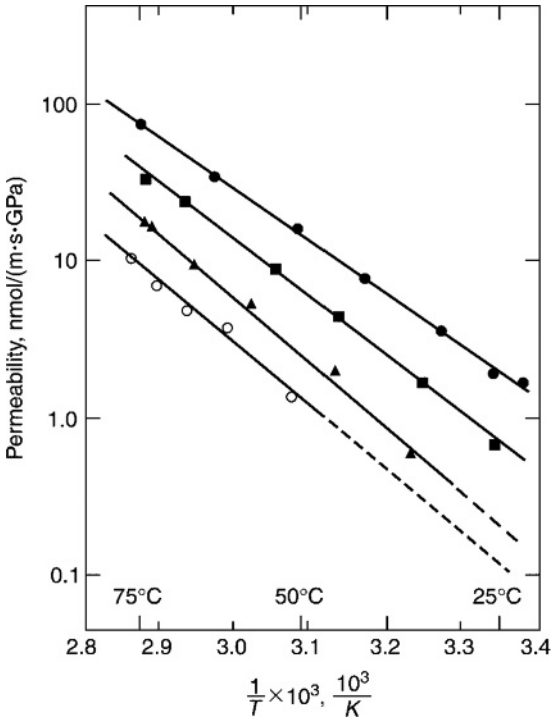

Fig. 4. Oxygen permeability in a VDC copolymer film at selected levels of plasticizer (Citroflex A-4). Plasticizer level in parts per hundred of resin (phr); ●, 7.2 phr; ■, 4.9 phr; ▲, 2.7 phr; and ○, 0.5 phr. To convert nmol/(m-s-GPa) to (cm^3-mil)/(100 $in.^2$-d-atm), divide by 2.

relative humidity increase. Carbon dioxide permeability doubles with the addition of about 1.8 phr of common plasticizers, or a temperature increase of 7 °C (89).

A comparison of the permeabilities of small molecules for several common polymers is presented in Table 10. The oxygen permeability is an important property for food packaging. In some cases the relative humidity is an important environmental variable. The oxygen permeability is not affected by humidity for VDC copolymers, nitrile barrier resins, poly(vinyl chloride), polystyrene, and polyolefins. The oxygen permeabilities of most nylons are increased modestly by increasing humidity, and the oxygen permeability of poly(ethylene terephthalate) is decreased modestly by increasing humidity. In contrast, the ethylene–vinyl alcohol copolymers (EVOH) are very sensitive to humidity. At low humidity, the oxygen permeabilities of EVOH are quite low. However, at the high humidity encountered in food packaging, the oxygen permeabilities of EVOH are much higher. Small changes in humidity can cause large changes in the oxygen permeabilities. Hence the data in tables need to be used carefully.

The data in Tables 11, 12, 13, describe VDC copolymers as good barriers for both gases and water. They are also good barriers to F/A/S molecules. This property for polymers has become more important since more sophisticated foods are

Table 10. Barrier Properties of Polymers[a]

Polymer	Gas permeability at 23 °C, nmol/(m·s·GPa)[b]			WVTR[c], nmol/(m-s)[d]
	O_2	N_2	CO_2	
High barrier vinylidene chloride copolymers	0.04–0.3	0.01–0.1	0.1–0.5	0.02–0.1
Nitrile barrier resin	1.6	—	6	1.0–1.2
Nylon-6,6; nylon-6	2–5	—	3–9	1.5–5.5
Polypropylene	300	60	1200	0.06–0.2
Poly(ethylene terephthalate)	10–18	2–4	30–50	0.4–0.7
Polylactide	90	—	375	5.1
Rigid poly(vinyl chloride)	10–40	—	40–100	0.2–1.3
High density polyethylene	300	—	1200	0.1
Low density polyethylene	500–700	200–400	2000–4000	0.2–0.4
Polystyrene	500–800	80–120	1400–3000	0.5–3.0
Ethylene vinyl alcohol				
32 mol% ethylene				
0% RH	0.02	0.002	0.09	0.9[e]
100% RH	2.3	—	—	—
44 mol% ethylene				
0% RH	0.18	0.015	0.8	0.3[e]
100% RH	1.3	—	—	—

[a]Refs. (90–92).
[b]To convert nmol/(m-s-GPa) to (cm -mil)/(100 in. -d-atm), divide by 2.
[c]WVTR = water vapor transmission rate at 90% RH and 38° C.
[d]To convert nmol/(m-s) to (g-mil)/(100 in. -d), multiply by 4.
[e]40 °C.

being packaged in plastics. The permeation of F/A/S molecules differs from the permeation of small molecules in some important ways. The diffusion coefficient D for F/A/S molecules is typically 10^2–10^5 times smaller. These molecules move slower because they need to find larger openings in the polymer. The solubility coefficient S is typically 10^2–10^6 times larger. This is related to higher boiling temperatures. Table 11 compares the D and S of large and small molecules in several polymers. A low D and a high S may mean that the principal mechanism for flavor loss is its being lost into the package wall (also known as scalping).

Humidity does not affect the permeability, diffusion coefficient, or solubility coefficient of F/A/S molecules in VDC copolymers. Results from studies using *trans*-2-hexenal and *d*-limonene are compared in Table 12. The transport in an EVOH copolymer is strongly enhanced by humidity plasticization.

Table 13 contains some representative data for the permeation of F/A/S molecules. VDC copolymers are good barriers to the migration of F/A/S molecules. Dry EVOH copolymers are also good barriers to the migration of F/A/S molecules. However, polyolefins are not good barriers to F/A/S molecules. The fact that most glassy polymers are good barriers to the migration of F/A/S molecules is not apparent from the data presented in this table.

Degradation Chemistry. Vinylidene chloride polymers are highly resistant to oxidation, permeation of small molecules, and biodegradation, which

Table 11. Diffusion Coefficients and Solubility Coefficients of Selected Penetrants in Polymers at 75°C[a]

Penetrant	Polymer	D, m^2/s	S, $kg/(m^3\text{-}Pa)$
Oxygen	Poly(ethylene terephthalate)	3×10^{-13}	9.8×10^{-7}
Oxygen	High density polyethylene	1.7×10^{-11}	6.6×10^{-7}
Oxygen	VDC copolymer	1.5×10^{-14}	3.5×10^{-7}
Carbon dioxide	Acrylonitrile copolymer	1.0×10^{-13}	1.6×10^{-6}
Carbon dioxide	Poly(vinyl chloride)	8.9×10^{-13}	3.4×10^{-6}
Carbon dioxide	VDC copolymer	1.4×10^{-14}	1.1×10^{-6}
d-Limonene	High density polyethylene	7.0×10^{-14}	0.3
d-Limonene	VDC copolymer	3.0×10^{-18}	0.6
Methyl salicylate	Nylon-6	2.1×10^{-17}	0.9
Methyl salicylate	VDC copolymer	5.8×10^{-16}	0.3

[a]Ref. (93).

Table 12. Transport of *trans*-2-Hexenal in Barrier Films at 75 °C

Film	Condition	Permeability P, MZU[a]	Diffusivity D, m^2/s
VDC copolymer[b]	Dry	4500	4.4×10^{-15}
VDC copolymer	90/0 [c]	4100	3.9×10^{-15}
EVOH[d]	dry	2300	1.6×10^{-14}
EVOH	90/0 [c]	98,000	7.2×10^{-13}

[a]To convert MZU (10^{-20} kg·m)/(m^2·s·Pa) to nmol/(m·s·GPa), divide by 9.8.
[b]Dow experimental resin XU32024.13.
[c]90% RH on the upstream side, 0% RH on the downstream side.
[d]44 mol% ethylene.

makes them extremely durable under most use conditions. However, these materials are thermally unstable and, when heated above about 120 °C, undergo degradative dehydrochlorination. Furthermore, the homopolymer degrades with rapid evolution of hydrogen chloride within a few degrees of its melting temperature (200 °C). For this reason, the superior characteristics of the homopolymer cannot be exploited. As a consequence, the copolymers of VDC with vinyl chloride, alkyl acrylates or methacrylates, acrylonitrile or methacrylonitrile, rather than the homopolymer, have come to commercial prominence. Such copolymers have often served as substrates for a study of the degradation reaction (99–102).

The thermal degradation of VDC copolymers occurs in two distinct steps. The first involves degradative dehydrochlorination via a chain process to generate poly(chloroacetylene) sequences (101,103). Subsequent Diels–Alder-type condensation between conjugated sequences affords a highly cross-linked network, which, upon further dehydrochlorination, leads to the formation of a large-surface-area, highly absorptive carbon (104). The initial dehydrochlorination occurs at moderate temperatures and is a typical chain process involving distinct initiation, propagation, and termination phases (103,105,106). Initiation is thought to occur via carbon–chlorine bond scission promoted by a defect structure within the polymer. An effective defect site in these polymers is unsaturation (103). Introduction of a random double bond produces an allylic dichloromethylene unit activated for carbon–chlorine bond scission. Initiation by the thermally

Table 13. Examples of Permeation of Flavor and Aroma Compounds in Selected Polymers[a] at 25°C[b], Dry[c]

Flavor/aroma compound	Permeability P, MZU[d]	Diffusivity D, m^2/s	Solubility S, kg/(m^3-Pa)
Vinylidene chloride copolymer			
Ethyl hexanoate [123–66-0] ($C_8H_{16}O_2$)	570	8.0×10^{-18}	0.71
Ethyl 2-methylbutyrate [7452–79-1] (C7H14 O2)	3.2	1.9×10^{-17}	1.7×10^{-3}
d-Limonene [5989–27-5] ($C_{10}H_{16}$)	32	3.3×10^{-17}	9.7×10^{-2}
Ethylene–vinyl alcohol copolymer			
Ethyl hexanoate	0.41	3.2×10^{-18}	1.3×10^{-3}
Ethyl 2-methylbutyrate	0.30	6.7×10^{-18}	4.7×10^{-4}
d-Limonene	0.5	1.1×10^{-17}	4.5×10^{-4}
Low density polyethylene			
Ethyl hexanoate	4.1×10^{6}	5.2×10^{-13}	7.8×10^{-2}
Ethyl 2-methylbutyrate	4.9×10^{5}	2.4×10^{-13}	2.3×10^{-2}
d-Limonene	4.3×10^{6}	—	—
High density polyethylene			
d-Limonene	3.5×10^{6}	1.7×10^{-13}	2.5×10^{-1}
Polypropylene			
Ethyl hexanoate	8.7×10^{4}	3.1×10^{-15}	2.8×10^{-1}
d-Limonene	1.6×10^{4}	7.4×10^{-16}	2.1×10^{-1}

[a]Refs. (94–98).
[b]Values for VDC copolymer and EVOH copolymer are extrapolated from higher temperatures.
[c]Permeation in the VDC copolymer and the polyolefins is not affected by humidity; the permeability and diffusion coefficient in the EVOH copolymer can be as much as 1000 times greater with high humidity.
[d]To convert MZU (10 kg·m)/(m·s·Pa) to nmol/(m·s·GPa), divide by molecular weight of permeant/10.

induced cleavage of this bond, followed by propagation by successive dehydrochlorination along the chain, ie, the so-called unzipping reaction, can then proceed readily (Fig. 5).

The thermal stability of these polymers is decreased by pretreatment with uv irradiation (107), electron-beam irradiation (108), and basic solvents or reagents (109,110); by an atmosphere of oxygen (107,111–114) or nitric oxide (107); and by the presence of peroxide linkages within the polymer (111,115), residues of emulsifying agents (111), organometallic initiator residues (111), ash from a previous decomposition (111), peroxide initiator residues (109)—(111,115–118), or metal ions (119). All the foregoing are sufficient to introduce random double bonds into the polymer structure. This can be demonstrated by examination of the treated sample by uv and ir spectroscopic methods (108). Prolonged treatment of the polymer with basic reagents leads to more extensive dehydrohalogenation (119–124). In fact, electrolysis of a solution of tetra(*n*-butyl)ammonium perchlorate in *N*,*N*-dimethylformamide generates a basic medium, presumably containing the formamide radical anion, capable of degrading the polymer (125). High energy radiation from a variety of sources may induce damage of several kinds, including carbon–carbon bond cleavage (107). A prominent radiation-induced process is carbon–chlorine bond scission followed by elimination of hydrogen

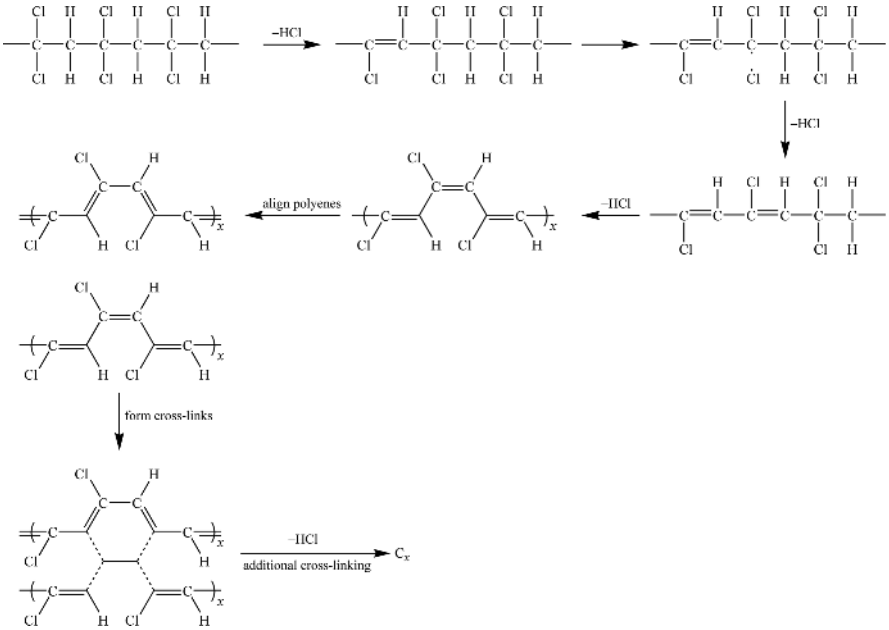

Fig. 5. Schematic of the degradation of PVDC to form carbon.

chloride (126,127). Property changes other than a decrease in thermal stability may arise as a consequence of high energy irradiation (128,129).

The principal steps in the thermal degradation of VDC polymers are formation of a conjugated polyene sequence followed by carbonization.

$$\left(CH_2 - CCl_2\right)_n \xrightarrow{\text{fast},\Delta} \left(CH = CCl\right)_n + n\text{HCl} \xrightarrow{\text{carbonization,show},\Delta} 2n\text{C} + n\text{HCl}$$

On being heated, the polymer gradually changes color from yellow to brown and finally to black. Early in the reaction, the polymer becomes insoluble, which indicates that cross-linking has occurred. The temperature of melting decreases, and the presence of unsaturation may be detected by spectroscopic (uv, ir, nmr) methods. The polymer eventually becomes infusible, and the crystal structure as detected by x-ray diffraction disappears even though the gross morphology is retained (130). The presence of carbon radicals can be detected by electron spin resonance (esr) measurements. If the temperature is raised substantially above 200 °C, aromatic structures are formed. Finally, at very high temperatures (>700 °C), complete carbonization occurs.

The first of these reactions, ie, the loss of the first mole of hydrogen chloride, has had the greatest impact on the end use of VDC polymers and has been the most studied and well characterized. The propensity of these polymers to undergo degradation is influenced by a wide variety of factors, including physical changes in the solid (annealing effects) and the method of preparation and purity of the polymer. The most stable polymers are those produced by bulk polymerization at low temperature with the use of a nonoxygen initiator. In general, the stability

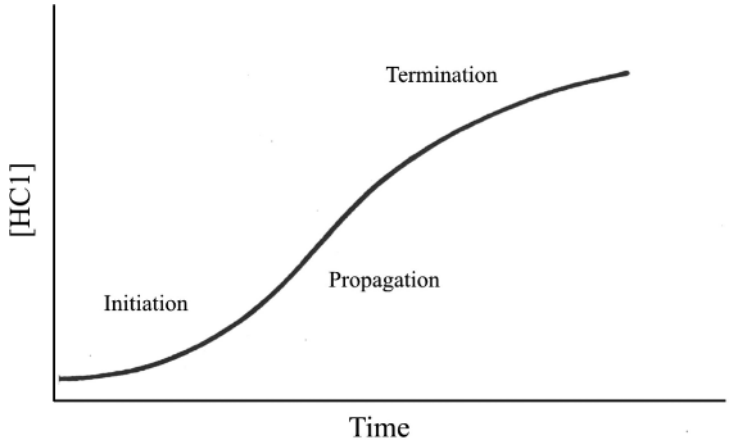

Fig. 6. Hydrogen chloride evolution for the thermal degradation of a typical VDC polymer.

of the polymer reflects the method of preparation, with bulk > solution > suspension >> emulsion (131). In the absence of elevated temperatures, suspending agents, polar solvents, redox initiators, etc, a more perfect polymer structure is formed, ie, one containing a minimum level of unsaturation.

The impact of a less defective structure may be seen in Figure 6, which depicts hydrogen chloride evolution for the thermal degradation of a typical VDC polymer. Initiation of degradation occurs at activated allylic sites within the polymer, but initiation does not occur simultaneously at all sites. Therefore, early in the reaction, hydrogen chloride evolution increases as a function of time as initiation occurs at more and more sites. In other words, unzipping is started in an increasing number of chain segments. This gives rise to the acceleratory induction period characteristic of VDC copolymer degradation. When a greater number of initiation sites are present within the polymer, ie, at higher levels of unsaturation, the rate of hydrogen chloride evolution during the initiation phase of the degradation is greater. After unzipping has begun in all chains containing defect structures, hydrogen chloride production is essentially first order until termination by completion or other means becomes a prominent reaction. Undoubtedly, some random double-bond initiation continues to occur during propagation. However, during this period termination is roughly in balance with initiation. As the rate of termination significantly exceeds that of initiation, deceleration of degradation is observed (103,106,107). An accurate representation of the dehydrochlorination reaction over the entire range of degradation may be achieved using a kinetic expression containing two constants (105,132).

Since the low temperature degradation, ie, that which occurs at process temperatures, involves only dehydrochlorination of VDC sequences, mass loss reflecting evolution of hydrogen chloride provides a convenient means of monitoring polymer decomposition. Thus, thermogravimetry analysis (TGA) is an appropriate method for assessing the degradation characteristics of VDC polymers (133,134). Rate constants may be obtained as the slopes of the appropriate linear portions of a plot of ln $[\omega_\infty - \omega_0)/(\omega_\infty - \omega_t]$ versus time. The variable ω_∞ is the

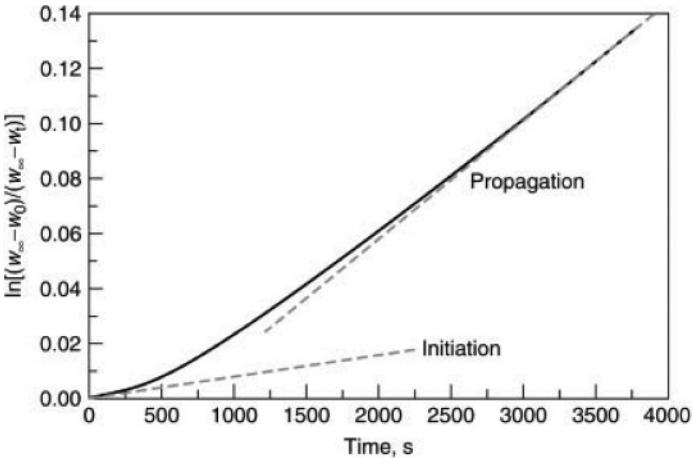

Fig. 7. Thermal degradation of a typical VDC polymer.

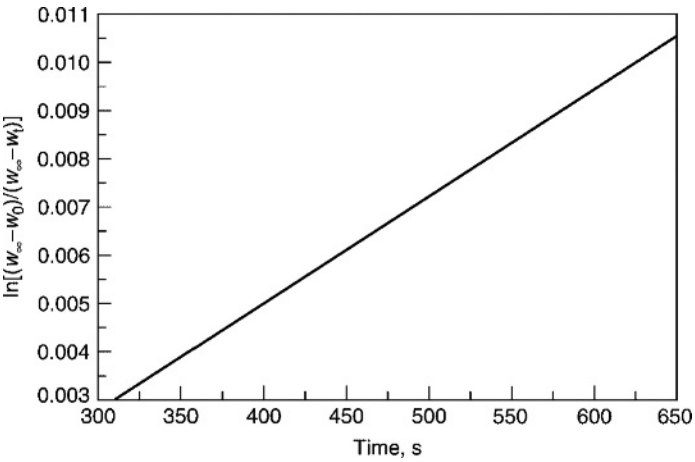

Fig. 8. Initiation rate constant (k_i) for the thermal degradation of a typical VDC polymer.

weight of the sample at infinite time (t_∞) taken as that weight which would remain after 37.62% of the initial VDC component weight (corresponding to the complete loss of 1 mole of hydrogen chloride per VDC unit in the copolymer). The variable w_0 is the weight at time zero (t_0), ie, the time at which the first point was recorded, and w_t is the weight at any time t during the run. This is illustrated for a typical VDC polymer in Figure 7. (135)

Initiation rate constants (k_i) for the degradation may be obtained by least-squares analysis of the linear segment of the early portion of this plot. Propagation rate constants (k_p) may be obtained in a similar manner from data obtained later in the run when propagation has become the dominant reaction. This is illustrated in Figures 8 and 9. Table 14 shows the rate constants obtained in this manner for the degradation of VDC/butyl acrylate copolymers.

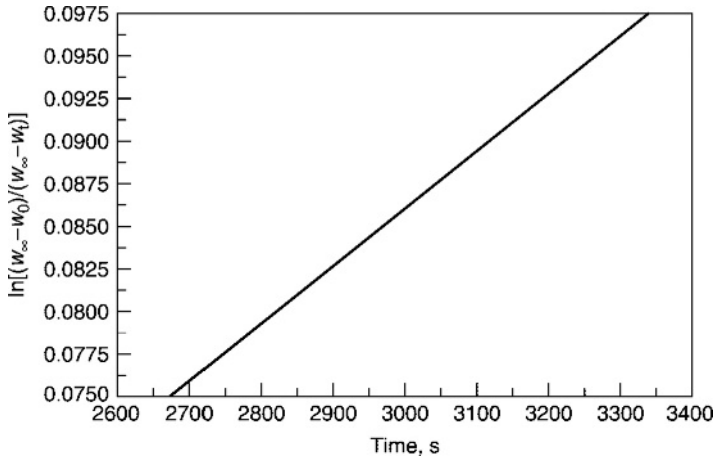

Fig. 9. Propagation rate constant (k_p) for the thermal degradation of a typical VDC polymer.

Table 14. Rate Constants for the Thermal Degradation of Vinylidene Chloride/Butyl Acrylate Copolymers at 180 °C

Butyl acrylate, wt%[a]	k_i, 10^{-5} s^{-1}[b]	k_p, 10^{-5} s^{-1}[b]
0	3.02 ± 0.09	8.75 ± 0.14
4	4.48 ± 0.004	8.34 ± 0.28
8	2.83 ± 0.25	6.73 ± 0.01
12	2.76 ± 0.03	5.35 ± 0.18
18	2.45 ± 0.25	4.08 ± 0.05
20	2.21 ± 0.005	3.74 ± 0.33

[a]Weight percent of monomer loaded.
[b]Averages of at least two determinations.

Much evidence has been accumulated to establish the radical nature of the degradation reaction. Prominent components of this include slight inhibition of the reaction by certain radical scavengers and changes in the esr spectrum of a sample undergoing degradation (136,137). Both suggest that radical intermediates are generated during the degradation. The exact nature of the chain-carrying species is made more apparent from the results of degradation in bibenzyl solution (101,103). Bibenzyl is an efficient radical scavenger that is converted to stilbene on interaction with a radical. Stilbene can be readily quantitated by gas–liquid partition chromatography. For the degradation of typical VDC polymers, the ratio of hydrogen chloride evolved to stilbene produced is approximately 35:1 (101,103). This is in sharp contrast to the 2:1 ratio expected for trapping of chlorine atoms with perfect efficiency and suggests that the propagating species is a radical pair that does not dissociate appreciably. Thus propagation most probably occurs by a radical chain process in which the chain-carrying species is a radical pair that decomposes to alkene and hydrogen chloride without dissociation.

To some extent, the stability of VDC polymers is dependent on the nature of the comonomer present. Copolymers with acrylates degrade slowly (138,139).

Apparent degradation propagation rates decrease somewhat as the acrylate content of the copolymer increases (138). The polyene sequences generated by dehydrochlorination are limited in size by the level of acrylate incorporation; that is, the acrylate molecules act as stopper units for the unzipping reaction. The impact of this chain-stopping is that the termination rate for higher acrylate content polymers is greater than for those containing smaller amounts of acrylate. Therefore, initiation and termination rates are in balance for a shorter portion of the overall reaction period. Despite the suggestion that the presence of a hydrogen-rich pendant might serve as a source of hydrogen atoms to disrupt degradation propagation (111), there is no apparent relationship between the degradation rate and the size of the alkyl portion of the acrylate comonomer (139,140).

Copolymers with AN or MA undergo degradation more readily. In addition, the degradation is more complex than that observed for acrylate copolymers. Acrylonitrile copolymers release hydrogen cyanide as well as hydrogen chloride; products of thermal degradation of MA copolymers contain methyl chloride in addition to hydrogen chloride (100,102,141,142). In both cases, degradation apparently begins in VDC units adjacent to comonomer units (141,142).

The degradation of VDC polymers in nonpolar solvents is comparable to degradation in the solid state (101,137,143,144). However, these polymers are unstable in many polar solvents (145). The rate of dehydrochlorination increases markedly with solvent polarity. In strongly polar aprotic solvents, eg, hexamethylphosphoramide, dehydrochlorination proceeds readily (143,146). This reaction is clearly unlike thermal degradation and may well involve the generation of ionic species as intermediates.

Polymers of high VDC content are reactive toward strong bases to yield elimination products and toward nucleophiles to yield substitution products. Agents capable of functioning as both a base and a nucleophile react with these polymers to generate a mixture of products (122,147–150). Weakly basic agents such as ammonia, amines, or polar aprotic solvents accelerate the decomposition of VDC copolymers. Amines function as bases to remove hydrogen chloride and introduce unsaturation along the polymer mainchain which may serve as initiation sites for thermal degradation. The overall effectiveness of a particular amine for dehydrohalogenation may be dependent on several factors, including inherent basicity, degree of steric hindrance at nitrogen, and compatibility with the polymer (152–155). Phosphines are more nucleophilic but less basic than amines. However, phosphines also promote dehydrohalogenation rather than displacement of allylic chlorine (156).

Amines can also swell the polymer, leading to very rapid reactions. Pyridine, for example, would be a fairly good solvent for a VDC copolymer if it did not attack the polymer chemically. However, when pyridine is part of a solvent mixture that does not dissolve the polymer, pyridine does not penetrate into the polymer phase (109). Studies of single crystals indicate that pyridine removes hydrogen chloride only from the surface. Kinetic studies and product characterizations suggest that the reaction of two units in each chain-fold can easily take place; further reaction is greatly retarded either by the inability of pyridine to diffuse into the crystal or by steric factors.

Aqueous bases or nucleophiles have little impacton VDC polymers, primarily because the polymer is not wetted or swollen by water. However, these

polymers do slowly degrade in hot concentrated aqueous sodium hydroxide solution (119).

Lewis acids, particularly transition-metal salts, strongly promote the thermal degradation of VDC polymers (119,137,157–168). The rate of initiation of degradation is greatly enhanced in the presence of metal ions (160). The metal ion (or other Lewis acid) coordinates chlorine atoms, making them much better leaving groups. This facilitates the introduction of initial double bonds, which act as defect sites from which degradative dehydrohalogenation may propagate. Care must be taken to avoid metal ions, particularly precursors of iron chloride, during the preparation and processing of VDC polymers.

Copolymers of VDC that are free of impurities do not degrade at an appreciable rate in the absence of light below 100 °C. However, when exposed to uv light, these polymers discolor (169). Again, the primary reaction seems to be dehydrochlorination. Hydrogen chloride is evolved and cross-linking occurs (107). Polyene sequences of narrow sequence length distribution are often formed (169–171). These function as initiation sites for subsequent thermal degradation (107). Laser-induced photochemistry may be used for the generation of polyene structures uncomplicated by cross-linking and graphitization (172,173). Laser-promoted dehydrohalogenation has some characteristics in common with the corresponding thermal process. Long-lived carbon radicals are formed, and the propagation of the dehydrochlorination reaction apparently proceeds via an allylic carbon radical, chlorine atom pair (173). Similar structures may be generated by chemical means (149,150,175). Other photodegradation processes, eg, hydroperoxide formation at the methylene groups, probably also occur but are less important for these polymers than is polyene formation (159).

Stabilization. The stabilization of VDC polymers toward degradation is a highly developed art and is responsible for the widespread commercial use of these materials. Although the mode of action is often not understood, some general principles of effective stabilization have been established (176). The ideal stabilizer system should

(1) absorb or combine with evolved hydrogen chloride irreversibly under conditions of use, but not strip hydrogen chloride from the polymer chain;
(2) act as a selective uv absorber;
(3) contain a reactive dienophilic moiety capable of preventing discoloration by reacting with and disrupting the color-producing conjugated polymer sequences;
(4) possess nucleophilicity sufficient for reaction with allylic dichloromethylene units;
(5) possess antioxidant activity so as to prevent the formation of carbonyl groups and other chlorine-labilizing structures;
(6) be able to scavenge chlorine atoms and other free radicals efficiently;
(7) chelate metals, eg, iron, to prevent chlorine coordination and the formation of metal chlorides.

Acid acceptors are of two general types: alkaline-earth oxides and hydroxides (177) or salts of weak acids, such as barium or calcium fatty acid

salts; and epoxy compounds, such as epoxidized soybean oil or glycidyl ethers and esters. Epoxidized oils are less effective for the stabilization of VDC polymers than for other halogenated polymers (161). The function of these materials as plasticizers and processing lubricants is probably responsible for modest improvements in processing stability. Effective light stabilizers have a chemical structure which imparts exceptional conjugative stability and very good uv absorption properties. The principal compounds of commercial interest are derivatives of salicylic acid, resorcylic acid, benzophenone, and benzotriazole. The typical hindered amine light stabilizers cannot be used in this application since they are sufficiently basic so as to promote dehydrohalogenation. This introduces allylic dichloromethylene units into the polymer mainchain, which act as initiation sites for thermal degradation. Consequently, satisfactory processing of the polymer in the presence of these additives is not possible. Examples of dienophiles that have been used are maleic anhydride and N-substituted maleimides (178,179).

Antioxidants are generally of two types: those that react with a radical to stop a radical chain, that is, to scavenge chlorine atoms or peroxy radicals; and those that reduce hydroperoxides to alcohols. Phenolic antioxidants, eg, 2,6-di-*tert*-butyl-4-methylphenol and substituted bisphenols, are of the first type. Because the chain-carrying species for the degradative dehydrochlorination is a tight chlorine atom, carbon radical pair that does not dissociate appreciably during the reaction, the effectiveness of these agents is limited (162). The second type is exemplified by organic sulfur compounds and organic phosphites. The phosphites, ethylene-diaminetetraacetic acid [60–00-4] (EDTA), citric acid [77–92-9], and citrates, can chelate metals. The ability of organic phosphites to function as antioxidants and as chelating agents illustrates the dual role of many stabilizer compounds. It is common practice to use a combination of stabilizing compounds to achieve optimum results (169). In addition, stabilization packages usually contain lubricants and other processing aids that enhance the effectiveness of the stabilizing compounds. The presence of these agents is particularly important to minimize the shearing component of degradation during extrusion and other processing steps (162).

Metal carboxylates have been considered as nucleophilic agents capable of removing allylic chlorine and thereby affording stabilization (163). Typical PVC stabilizers, eg, tin, lead, cadmium, or zinc esters, actually promote the degradation of VDC polymers. The metal cations in these compounds are much too acidic to be used with VDC polymers. An effective carboxylate stabilizer must contain a metal cation sufficiently acidic to interact with allylic chlorine and to facilitate its displacement by the carboxylate anion, but at the same time not acidic enough to strip chlorine from the polymer mainchain (164,168). Copper(II) carboxylates may have the balance of cation acidity and anion reactivity required to function as effective stabilizers for VDC polymers. This is reflected in Figure 10, which illustrates increasing stability of a typical VDC copolymer as it is aged at 150 °C in the presence of copper(II) formate.

Vinylidene chloride polymers containing stabilizing features have been prepared. More generally, these have been polymers containing comonomer units with functionality that can consume evolved hydrogen chloride such that good radical scavenging sites are exposed (165,166,180,181).

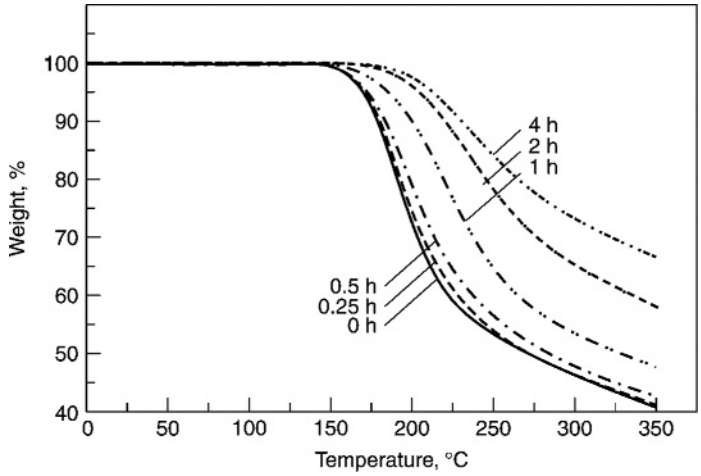

Fig. 10. Thermal degradation of a VDC/MPA (5 mol%) copolymer aged at 150 °C in the presence of 5 wt% copper(II) formate for 0.25, 0.50, 1.0, 2.0, and 4.0 h.

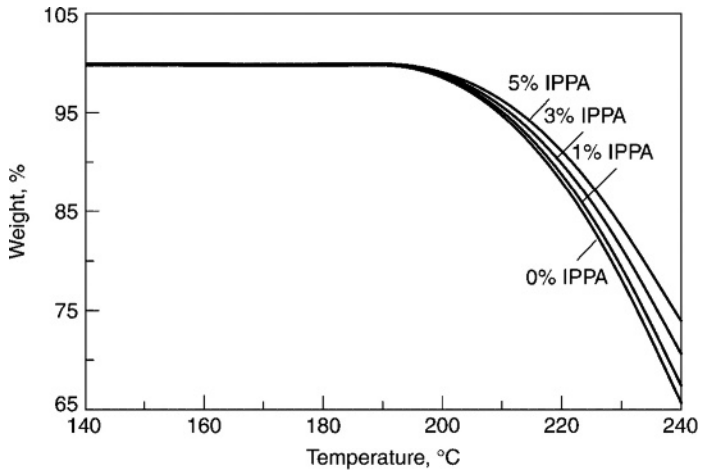

Fig. 11. Thermal degradation of vinylidene chloride/4-isopropylphenyl acrylate copolymers.

For example, copolymers containing 4-isopropylphenyl acrylate display greater thermal stability than do the corresponding polymers containing simple alkyl acrylates as comonomer (165). This is illustrated in Figure 11. Stability of the copolymer increases as the level of the comonomer containing the *t*-cumyl group, capable of scavenging chlorine atoms, increases. A more quantitative reflection of this effect is provided by the rate constants displayed in Table 15. It may be noted that the magnitude of the initiation rate constant k_i decreases by a factor of 2 as the isopropylphenyl acrylate content of the polymer is increased from 0 to 5 mol%.

Table 15. Rate Constants for the Degradation of Vinylidene Chloride/4-Isopropylphenyl Acrylate Copolymers at 140 °C

IPPA, mol%	k_i, 10^{-7} s^{-1} [b]	k_p, 10^{-7} s^{-1} [a]
0.0	3.02 ± 0.09	8.75 ± 0.14
1.0	4.48 ± 0.004	8.34 ± 0.28
3.0	2.83 ± 0.25	6.73 ± 0.01
5.0	2.76 ± 0.03	5.35 ± 0.18

[a] Averages of at least two determinations; average deviation ≤ = ±0.10.

Commercial Methods of Polymerization and Processing

Processes that are essentially modifications of laboratory methods and that allow operation on a larger scale are used for commercial preparation of VDC polymers. The intended use dictates the polymer characteristics and, to some extent, the method of manufacture. Emulsion polymerization and suspension polymerization are the preferred industrial processes. Either process is carried out in a closed, stirred reactor, which should be glass-lined and jacketed for heating and cooling. The reactor must be purged of oxygen, and the water and monomer must be free of metallic impurities to prevent an adverse effect on the thermal stability of the polymer.

Emulsion Polymerization. Emulsion polymerization is used commercially to make VDC copolymers. In some applications, the resulting latex is used directly, usually with additional stabilizing ingredients, as a coating vehicle to apply the polymer to various substrates. In other applications, the polymer is first isolated from the latex before use. When the polymer is not used in latex form, the emulsion/coagulation process is chosen over alternative methods. The polymer is recovered in dry powder form, usually by coagulating the latex with an electrolyte, followed by washing and drying. The principal advantages of emulsion polymerization are twofold. First, high molecular weight polymers can be produced in reasonable reaction times, especially copolymers with VC. The initiation and propagation steps can be controlled more independently than in the suspension process. Second, monomer can be added during the polymerization to maintain copolymer composition control.

The disadvantages of emulsion polymerization result from the relatively high concentration of additives in the recipe. The water-soluble initiators, activators, and surface-active agents generally cause the polymer to have greater water sensitivity, poorer electrical properties, and poorer heat and light stability. These agents promote degradative dehydrochlorination during polymerization.

A typical recipe for batch emulsion polymerization is shown in Table 16. A reaction time of 7–8 h at 30 °C is required for 95–98% conversion. A latex is produced with an average particle diameter of 100–150 nm. Other modifying ingredients may be present, eg, other colloidal protective agents such as gelatin or carboxymethylcellulose, initiator activators such as redox types, chelates, plasticizers, and stabilizers; and chain-transfer agents.

Commercial surfactants are generally anionic emulsifiers, alone or in combination with nonionic types. Representative anionic emulsifiers are the sodium

Table 16. Recipe for Batch Emulsion Polymerization[a]

Ingredient	Parts by weight
Vinylidene chloride	78
Vinyl chloride	22
Water	180
Potassium peroxysulfate	0.22
Sodium bisulfite	0.11
Aerosol MA,[b] 80 wt%	3.58
Nitric acid,60 wt%	0.07

[a]Ref. (182).
[b]Aerosol MA (American Cyanamid Co.) = dihexyl sodium sulfosuccinate.

alkylaryl sulfonates, the alkyl esters of sodium sulfosuccinic acid, and the sodium salts of fatty alcohol sulfates. Nonionic emulsifiers are ofthe ethoxylated alkylphenol type. Radical sources other than peroxysulfates may be used, eg, hydrogen peroxide, organic hydroperoxides, peroxyborates, and peroxycarbonates. Many of these are used in redox pairs, in which an activator promotes the decomposition of the peroxy compound. Examples are peroxysulfate or perchlorate activated with bisulfite, hydrogen peroxide with metallic ions, and organic hydroperoxides with sodium formaldehyde sulfoxylate. The use of activators causes the decomposition of the initiator to occur at lower reaction temperatures, which allows the preparation of a higher molecular weight polymer within reasonable reaction times. This is an advantage, particularly for copolymers of VDC with VC. Oil-soluble initiators are usually effective only when activated by water-soluble activators or reducing agents.

To ensure constant composition, the method of emulsion polymerization by continuous addition is employed. One or more components are metered continuously into the reaction. If the system is properly balanced, a steady state is reached in which a copolymer of uniform composition is produced (183). A process of this type can be used for the copolymerization of VDC with a variety of monomers. A flow diagram of the apparatus is shown in Figure 12; a typical recipe is shown in Table 17. The monomers are charged to the weigh tank A, which is kept under a nitrogen blanket. The emulsifiers, initiator, and part of the water are charged to tank B; the reducing agent and some water to tank C. The remaining water is charged to the reactor D, and the system is sealed and purged. The temperature is raised to 40 °C and one tenth of the monomer and initiator charges is added, and then one tenth of the activator is pumped in. Once the reaction begins, as indicated by an exotherm and pressure drop, feeds of A, B, and C are started at programmed rates that begin slowly and gradually increase. The emulsion is maintained at a constant temperature during the run by cooling water that is pumped through the jacket. When all components are in the reactor and the exotherm begins to subside, a final addition of initiator and reducing agent completes the reaction.

Suspension Polymerization. Suspension polymerization of VDC is used commercially to make molding and extrusion resins. The principal advantage of the suspension process over the emulsion process is the use of fewer ingredients

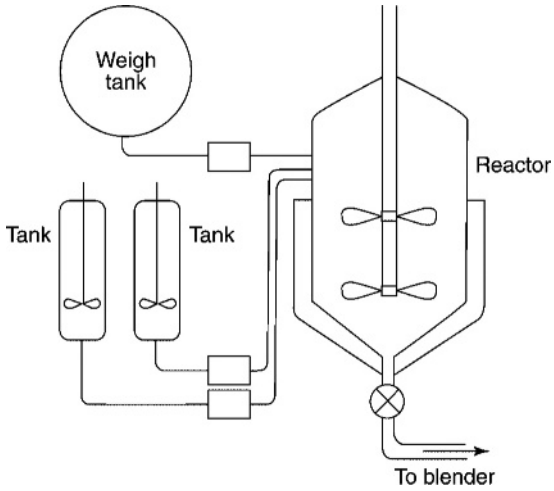

Fig. 12. Apparatus for continuous-addition emulsion polymerization of a VDC–acrylate mixture (183).

Table 17. Recipe for Emulsion Polymerization by Continuous Addition[a]

Ingredient	Parts by weight
Vinylidene chloride	468
Comonomer	52
Emulsifiers	
Tergitol[b] NP35	12
Sodium lauryl sulfate,25 wt%	12
Initiator ammonium peroxysulfate	10
Sodium metabisulfite ($Na_2S_2O_5$), 5 wt%	10
Water	436

[a]Ref. (183).
[b]Nonionic wetting agent produced by Union Carbide.

that might detract from the polymer properties. Stability is improved and water sensitivity is decreased. Extended reaction times and the difficult preparation of higher molecular weight polymers are disadvantages of the suspension process compared to the emulsion process, particularly for copolymers containing VC.

A typical recipe for suspension polymerization is shown in Table 18. At a reaction temperature of 60 °C, the polymerization proceeds to 85–90% conversion in 30–60 h. Unchanged monomer is removed by vacuum stripping; then it is condensed and reused after processing. The polymer is obtained in the form of small [150– 600 μm (30)–100 mesh)] beads, which are dewatered by filtration or centrifugation and then dried in a flash dryer or fluidbed dryer. Suspension polymerization involves monomer-soluble initiators, and polymerization occurs inside suspended monomer droplets, which form by the shearing action of the agitator and are prevented from coalescence by a protective surfactant. It is important

Table 18. Recipe for Suspension Polymerization[a]

Ingredient	Parts by weight
Vinylidene chloride	85
Vinyl chloride	15
Deionized water	200
400 mPa·s (= cP) methyl hydroxypropylcellulose	0.05
Lauroyl peroxide	0.3

[a]Ref. (184).

that the initiator be uniformly dissolved in the monomer before droplet formation. Unequal distribution of initiator causes some droplets to polymerize faster than others, leading to monomer diffusion from slow-polymerizing to fast-polymerizing droplets. The fast-polymerizing droplets form polymer beads that are dense, hard, glassy, and extremely difficult to fabricate because of their inability to accept stabilizers and plasticizers. Common protective surfactants that prevent droplet coalescence and control particle size are PVC, gelatin, and methylcellulose. Organic peroxides, peroxycarbonates, and azo compounds are used as initiators for VDC suspension polymerization.

The batch-suspension process does not compensate for composition drift, whereas constant-composition processes have been designed for emulsion or suspension reactions. It is more difficult to design controlled-composition processes by suspension methods. In one approach (185), the less reactive component is removed continuously from the reaction tokeep the unreacted monomer composition constant. This method has been used effectively in VDC–VC copolymerization, where the slower reacting component is volatile and can be released during the reaction to maintain constant pressure. In many other cases, no practical way is known for removing the slower reacting component.

Economic Aspects

Vinylidene chloride monomer is produced commercially in the United States by The Dow Chemical Co. and PPG Industries. The monomer is produced in Europe by Imperial Chemical Industries, Ltd. and Solvin. The monomer is produced in Japan by the Asahi Chemical Co., Kureha Chemical Industries, and Kanto Denka Kogyo Co. Commercial suppliers of VDC copolymers include The Dow Chemical Co. in the United States and Solvin in Europe. Asahi Chemical Co. and Kureha Chemical Industries are suppliers of VDC resins in Japan. Additional manufacturers of exclusively VDC latexes include W. R. Grace in the United States and Scott-Bader in Europe. Local suppliers of VDC resins have also been reported in Russia and the People's Republic of China.

Trademarks for VDC copolymers include SARAN and SERFENE (Dow Chemical) and DARAN (Owensboro Specialty Polymers) in the United States; DIOFAN and IXAN (Solvin) and POLIDENE (Scott-Bader) in Europe; and KUREHALON (Kureha) in Japan. In addition, The Geon Company (GEON) and Avecia (HALOFLEX) supply non-barrier VDC copolymers.

Applications

Melt Processing. Vinylidene chloride copolymers are melt processed via a variety of fabrication techniques. These include molding, monofilament fiber extrusion, monolayer blown film extrusion, multilayer cast- and blown-film extrusion, and multilayer sheet extrusion. There are a number of elements of melt processing and meltprocessing equipment that are common to all of these fabrication techniques (185–189). These include proper equipment design and materials of construction, proper and accurately controlled operating conditions, and a properly formulated resin.

Because of their high crystalline melting point, VDC copolymers are generally melt fabricated near their thermal stability limits. Products of degradation are corrosive to equipment and given sufficient time will generate a char or carbon. Also, at temperatures of about 130 °C and above, a number of metals, including iron, zinc, copper, and aluminum, catalyze the degradation of VDC resins. As a consequence the correct materials of construction are essential for melt processing VDC resins. High nickel alloys that are both corrosion resistant and do not catalyze resin degradation are preferred for all surfaces that are in direct contact with the polymer melt. For example, the extruder barrel liner may be made from Xaloy 306 or other high nickel, low iron containing alloy. Extruder screws may be made from Duranickel 301 with Colmonoy 56 flight lands. Other parts in direct contact with polymer melt should also be made out of Duranickel or similar material. Instruments such as melt thermocouples or pressure transducers could be Hastelloy C.

Degradation of VDC resins is a product of time at temperature. Both of these aspects should be controlled to optimize melt processing performance. Extruders in the range of 18:1 to 24:1 length-to-diameter ratio are commonly used. Melt channels should be designed with a smooth flow pattern to minimize dead spots where polymer may degrade excessively orpermit carbon buildup. The clearance between the screw tip and the extruder nosepiece should be minimized. Screen packs are also not recommended for melt-processing VDC resins. Proper instrumentation, including multiple melt thermocouples and pressure transducers, amperage or torque measurement for the extruder, and accurate screw speed measurement, is also critical.

Heat management is an important factor in melt-processing VDC resins. Screw design (190) and resin formulation combine to affect the amount of heat generated during melting and the eventual melt temperature. Vinylidene chloride polymer powders exhibit a relatively high level of frictional heating and also contain a large amount of entrained air (191). Screws are typically designed to be low work to minimize frictional and viscous heating. They must also be designed to eliminate air entrapment. Screws greater than 6.35-cm (2.5-in.) diameter for VDC resin processing also generally have two-zone cooling capability for further heat management.

Vinylidene chloride resins for melt processing are generally supplied formulated or unformulated. Formulated resins may be melt processed as supplied or with some additional additives. Unformulated resins require additives prior to melt processing. Processing additives for VDC resins include plasticizers, lubricants, and other process aids designed to control heat generation and residence

time in melt processing. Patent literature cites a wide variety of lubricants and processing aids, including acids, esters, amides, and metal salts of fatty acids; polyolefins or polyolefin waxes; and inorganic stabilizers such as magnesium hydroxide or tetrasodium pyrophosphate (192). Some of these processing aids are common to PVC melt processing as well. However, it should also be noted that some PVC melt-processing additives are incompatible with VDC resins and will actually degrade melt-processing performance.

Molding. Molded articles were among the earliest applications for VDC copolymers (186,193). Vinylidene chloride–vinyl chloride copolymers were originally developed for thermoplastic molding applications, and small amounts are still used for this purpose. When properly formulated with plasticizers and heat stabilizers, the resins can be fabricated by common methods, eg, injection, compression, or transfer molding. Conventional or dielectric heating can be used to melt the polymers. Rapid hardening is achieved by forming in heated molds to induce rapid crystallization. Cold molds result in supercooling of the polymer. Because the interior of the molded part remains soft and amorphous, the part cannot be easily removed from the mold without distortion. Mold temperatures of up to 100 °C allow rapid removal of dimensionally stable parts. The range of molding temperatures is rather narrow because of the crystalline nature of the resin and thermal sensitivity. All crystallites must be melted to obtain low polymer melt viscosity, but prolonged or excessive heating must be avoided to prevent dehydrochlorination.

The metal parts of the injection molder, ie, the liner, torpedo, and nozzle, that contact the hot molten resin must be of the noncatalytic, corrosion-resistant type previously described. The injection mold need not be made of noncatalytic metals; any high grade tool steel may be used because the plastic cools in the mold and undergoes little decomposition. However, the mold requires good venting to allow the passage of small amounts of acid gas as well as air. Vents tend to become clogged by corrosion and must be cleaned periodically.

Molded parts of VDC copolymers are used to satisfy the industrial requirements of chemical resistance and extended service life. They are used in such items as gasoline filters, valves, pipe fittings, containers, and chemical process equipment. Complex articles are constructed from molded parts by welding; hot-air welding at 200–260 °C is a suitable method. Molded parts have good physical properties but lower tensile strength than films or fibers, because crystallization is random in molded parts. Higher strength is developed by orientation in films and fibers. Physical properties of a typical molded VDC copolymer plastic are listed in Table 19.

Monofilament Fiber Extrusion. Monofilament fiber extrusion was another early application for VDC resins (186,193,195). Monofilament applications have included automotive seat covers, window screens, and upholstery fabrics, where the durability and ease of cleaning were important. Fabrics made from VDC copolymer monofilaments are still used today in applications such as filter fabrics, light screens, greenhouse covers, pool or bath fabrics, and shoe insoles (196). Such fabrics claim excellent resistance to flame, chemicals, uv light, moisture, and microbial attack.

Vinylidene chloride copolymer monofilaments typically range from 0.15- to 1.5-mm (0.006- to 0.06-in.) diameter. To produce these monofilaments, a molten

Table 19. Properties of Resin for Injection-Molding Applications[a]

Typical resin properties	Test method	Value
Ultimate tensile strength, MPa[b]	ASTM D638	24.1–34.5
Yield tensile strength, MPa[b]	ASTM D638	19.3–26.2
Ultimate elongation,%	ASTM D638	160–240
Modulus of elasticity in tension, MPa[b]		345–552
Izod impact strength, J/m[c] of notch	ASTM D256	21.35–53.38
Density, g/cm^3	ASTM D792	1.65–1.72
Hardness, Rockwell M	ASTM D785	50–65
Water absorption,% in 24 h	ASTM D570	0.1
Mold shrinkage, cm/cm (injection-molded)	ASTM D955	0.005–0.025
Limiting oxygen index,%	ASTM D2863	60.0 [d]
UL-94	UL-94 Test	V–O[d]

[a]Ref. (194).
[b]To convert MPa to psi, multiply by 145.
[c]To convert J/m to ft·lbf/in. of notch, divide by 53.38.
[d]The results of small-scale flammability tests are not intended to reflect the hazards of this or any other material under actual fire conditions.

VDC copolymer extrudate is quenched to about room temperature in a supercooling tank to produce an amorphous polymer strand (186,193,195). This strand is then wrapped several times around smooth take-off rolls, and then wrapped several times around orienting rolls, which operate at a higher speed than the take-off rolls. The difference in roll speeds produces mechanical stretching, orienting the filament along the longitudinal axis while the polymer is crystallizing. A typical stretch ratio for this process is about 400%. The orientation process increases the fiber strength from about 55 MPa (8000 psi) to as high as 414 MPa (60000 psi). Much of the increased tensile strength is obtained as the stretch ratio approaches 400%. Heat treatment may be used during or after stretching to affect the degree of crystallization and control the physical properties of the oriented filaments.

Monolayer Blown-Film Extrusion. One of the major applications for VDC resins is monolayer film produced via a blown-film extrusion process. Previously, VDC copolymer film extrusion was limited to just a few experts in the field. However, production of VDC-containing films has greatly expanded (197,198). Monolayer VDC copolymer blown-film lines are now commercially available from a number of manufacturers and a considerable number of lines have been installed around the world, particularly in the People's Republic of China.

A monolayer blown-film process for VDC resin is illustrated in Figure 13. In this process (187,199–202) a tube of molten VDC resin is extruded downward and is immediately quenched in a cold-water supercooling bath. This bath cools the polymer melt to create a leathery polymer tube which is essentially amorphous VDC copolymer. The low temperature of the bath also controls nucleation of the crystallites and thus impacts the subsequent film-formation processes. After the supercooling bath, the amorphous tube is passed through a warming or reheat bath. This bath increases the resin temperature, which in turn will make the film more pliable and increase the rate of crystallization propagation during the subsequent film-blowing process. Exiting the warming bath, the tube passes

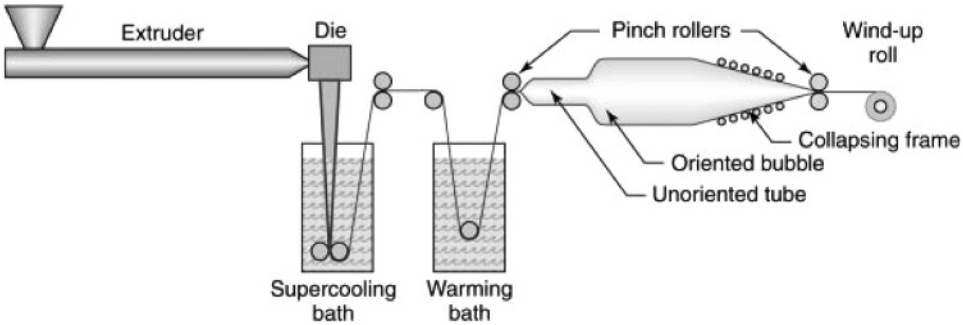

Fig. 13. Monolayer blown-film process for VDC resins (198).

through two sets of pinch rolls, which are arranged so that the second set of rolls travels faster than the first set. Between the two sets, air is injected into the tube to create a bubble that is entrapped by the pinch rolls. The entrapped air bubble remains stationary while the extruded tube is oriented as it passes around the bubble. In this manner, orientation is produced simultaneously in both the transverse and the longitudinal directions.

As the tube expands and orients, the amorphous polymer begins to crystallize rapidly, eventually limiting the diameter of the bubble. Adding additional air to the bubble at this point will only lengthen the bubble but will not change its overall diameter. Crystallization rate and thus bubble diameter or "blow up ratio" is controlled by a number of factors, including temperatures of the supercooling and warming baths, room temperature, polymer composition, and amount and type of plasticizer additives. These parameters as well as variables such as extrusion rate, die diameter, die gap, and drawdown ratio are combined to make a wide variety of film types and sizes. Films produced via this process generally have some shrink properties, which in many cases are advantageous. Where shrink is not desirable, films can be preshrunk via controlled heat application prior to the winding process.

Monolayer blown-film processes generally use a VDC–VC copolymer. Such resins have the combination of performance properties and optimum crystallization rate necessary for this process. Resins are generally formulated with plasticizers, lubricants, and other additives to affect performance during the extrusion process as well as in the final film applications.

Applications for VDC copolymer monolayer films fall into three major categories: household wrap, food and medical packaging, and industrial films. Food packaging includes packaging of processed meats, cheese and other dairy products, and bakery goods. Packaging types include film overwraps, shrinkable films, chub packaging, and unit packaging. Performance attributes of VDC copolymer films that are important to these applications include high barrier to oxygen, water, and other permeating molecules; clarity; resistance to fats and oils; dimensional stability; ability to be sealed and printed; and ability to withstand retort and microwave oven temperatures. Typical film properties are shown in Table 20.

Multilayer Cast- and Blown-Film Extrusion. A significant application for VDC copolymer resins is in the construction of multilayer film and sheet

Table 20. Physical Properties of PVDC Copolymer Films[a]

Properties[b]	Overwrap film	Chub packaging film A	Chub packaging film B	Unit packaging film A	Unit packaging film B	High barrier packaging film	Test methods
Average thickness, μm[c]	15	25	25	51	152	25	—
Yield, m^2 film/kg resin[d]	38	23	23	12	4	23	Calculated
Water vapor transmission rate at 90% RH and 38 °C, nmol/(m·s)[e]	0.09	0.09	0.1	0.06	0.06	0.01	Permatran W
Oxygen transmission at 100% RH and 23 °C, nmol/(m-s-GPa)[f]	2.6	2.6	3.8	2.9	2.9	0.16	ASTM D3985–81
Ultimate tensile strength, MPa[g]							ASTM D882–81
MD	76	97	83	111	111	83	
TD	124	138	117	133	95	128	
Ultimate elongation,%							ASTM D882–81
MD	75	90	90	95	80	100	
TD	55	60	75	80	70	50	
2% secant modulus, MPa[g]							ASTM D882–81
MD	690	690	607	690	655	1103	
TD	621	593	530	615	615	965	
Unrestrained shrink, 10 min at 100 °C in air,%							ASTM D1204
MD	16	16	20	8	12	6	
TD	9	9	11	4	7	4	
Haze,%	1	5	5	3	3	2.5	ASTM D1003–61 (77)
45° gloss	115	92	90	105	105	110	ASTM D2457–60 (77)
Clarity,%	86	65	52	73	73	80	ASTM D1746–70 (78)
Film block, unconditioned, g	114	—	—	—	—	—	ASTM D3354–89
Film cling, unstretched, g	65	—	—	—	—	—	ASTM D4649–87
Kinetic coefficient of friction, film-to-metal	—	0.29	0.30	0.30	0.30	—	ASTMD1894

[a]Ref. (203).
[b]MD is machine direction; TD is transverse direction.
[c]To convert μm to mil, divide by 25.6.
[d]To convert m^2 film/kg resin to $in.^2$ film/lb resin, multiply by 704.
[e]To convert nmol/(m·s) to (g·mil)/(100 $in.^2$·d), multiply by 4.
[f]To convert nmol/(m·s·GPa) to (cc·mil)/(100 in.·d·atm), divide by 2.
[g]To convert MPa to psi, multiply by 145.

Table 21. Physical Properties[a] of a Multilayer Barrier Film[b] and a Polyethylene Film[c]

Property[d]	Multilayer film	Polyethylene film	Test method
Yield tensile strength, MPa[e]			ASTM D882–61 T
MD	14	12.1	
TD	13	9.7	
Ultimate tensile strength, MPa[e]			ASTM D882–61 T
MD	24	20.0	
TD	17	17	
Tensile modulus, MPa[e]			ASTM D882–61 T
MD	170	180	
TD	150	180	
Elongation,%			ASTM D882–61 T
MD	400	325	
TD	400	550	
Elmendorf tear strength, g			ASTM D1922
MD	800	325	
TD	650	250	
Gas transmission at 24 °C, nmol/(m^2·s·GPa)[f]			ASTM D1434–63
Oxygen	6.6×10^4	1.6×10^7	
Carbon dioxide	11.1×10^4	10.0×10^7	
Nitrogen	0.8×10^4	0.8×10^7	
Water vapor transmission at 95% RH and 38 °C, nmol/(m·s)[g]	2000	6400	ASTM E96–63 T

[a]Refs. (204) and (206).
[b]0.05-mm total thickness with layers of polyethylene, adhesive, and vinylidene chloride copolymer.
[c]0.05-mm polyethylene, 0.921 g/cm^3 density.
[d]MD is machine direction; TD is transverse direction.
[e]To convert MPa to psi, multiply by 145.
[f]To convert nmol/(m^2·s·GPa) to cm^2/(100 $in.^2$ d·atm), divide by 7.9×10^4.
[g]To convert nmol/(m·s) to g/(100 $in.^2$·d), divide by 1×10^4.

(204,205). This permits the design of a packaging material with a combination of properties not obtainable in any single material. A VDC copolymer layer is incorporated into multilayer film for perishable food packaging because it provides a barrier to oxygen. A special high barrier resin is supplied specifically for this application. Typically, multilayer packaging films contain outer layers of a tough, low cost polymer such as high density or linear low density polyethylene with VDC copolymer as the core layer. Cast and blown films are produced on conventional film lines with one extruder and die designed to handle the heat-sensitive nature of VDC resin. The properties of a 0.05-mm (2-mil) multilayer cast film are listed in Table 21. Example properties of multilayer blown films are listed in Table 22. Films A to D in Table 22 illustrate the effects of thickness variation and variation of the specific grade of VDC copolymer used.

Multilayer films are produced by both cast- and blown-film coextrusion. One of the key enabling technologies in the manufacture of these multilayer films has been preencapsulation of the VDC resin (207). Preencapsulation means that the VDC resin extrudate is completely encapsulated with a more thermally stable

Table 22. Physical Properties of Multilayer Blown Coextruded Barrier Films

Property[a]	Film A	Film B	Film C	Film D	Test method
Thickness, mm	0.05	0.10	0.15	0.10	
Yield tensile strength, MPa[b]					ASTM D882–61 T
MD	12	12	16	15	
TD	12	13	16	14	
Ultimate tensile strength, MPa[b]					ASTM D882–61 T
MD	25	20	16	18	
TD	24	17	13	15	
Tensile modulus, MPa[b]					ASTM D882–61 T
MD	230	240	330	310	
TD	240	230	330	310	
Elongation,%					ASTM D882–61 T
MD	450	460	360	360	
TD	590	490	390	390	
Elmendorf tear strength, g					ASTM D1922
MD	480	950	270	60	
TD	210	610	320	190	
Oxygen transmission at 100% RH and 23 °C, nmol/(m-s-GPa)[c]	3.3×10^4	1.7×10^4	0.6×10^4	0.8×10^4	ASTM D3985–81
Water vapor transmission at 100% RH and 38 °C, nmol/(m·s)[d]	2900	1400	500	600	ASTM F1249

[a]MD is machine direction; TD is transverse direction.
[b]To convert MPa to psi, multiply by 145.
[c]To convert nmol/(m^2·s·GPa) to cm^3/(100 in.^{2} d·atm), divide by 7.9×10^4.
[d]To convert nmol/(m·s) to g/(100 in.^{2}·d), divide by 1×10^2.

polymer, such as an ethylene–vinyl acetate copolymer, prior to entering the coextrusion die. Using this technique, the VDC resin is not directly exposed to the large surface area of the multilayer extrusion die, eliminating a greater potential for carbon formation and subsequent problems. Upon entering the die the encapsulated VDC resin is combined with other polymer layers, including tie and skin layers, to create the multilayer film.

The application of encapsulation technology to flat dies and cast film coextrusion is fairly easy to envision. As shown in Figure 14, the encapsulating material completely surrounds the VDC resin. When the edges are trimmed, a flat film with a continuous barrier layer is produced.

Blown-film coextrusion presents the added difficulty of obtaining a continuous barrier layer. A die with a crosshead mandrel is preferred over a die with a spiral mandrel, because the spiral mandrel tends to lead to long residence time in the spirals. A standard crosshead mandrel, however, results in a weld line where the barrier layer is not continuous. As shown in Figure 15, this problem is solved by providing an overlap of the barrier layer at the weld line (208). Although the barrier layer is not continuous across the weld line, sufficient overlap will

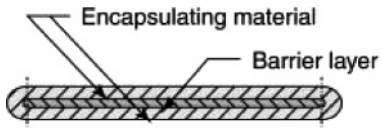

Fig. 14. Multilayer cast film showing a VDC copolymer barrier layer surrounded by a less thermally sensitive encapsulating material, such as ethylene–vinyl acetate (207). The edges are trimmed.

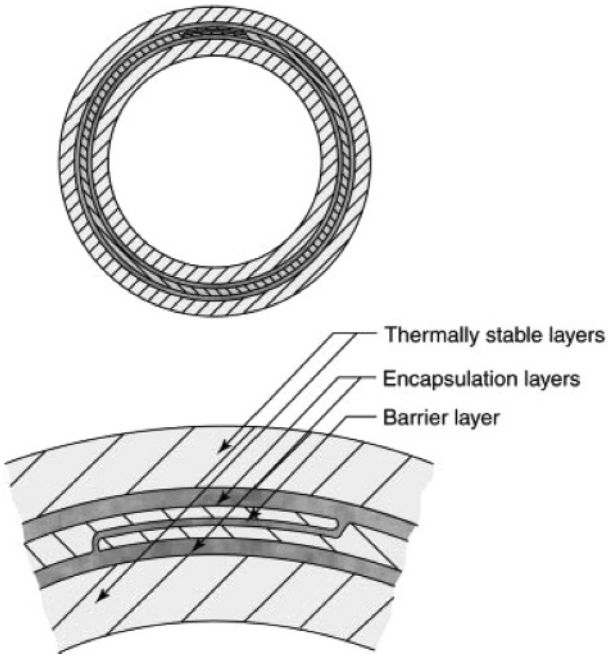

Fig. 15. Multilayer blown film with enlarged view showing overlap of barrier layer (208).

create a tortuous path for permeation, and the barrier properties will be maintained across the weld. This technology has only been recently applied to large blown-film dies. Five- to seven-layer blown-film dies up to 51-cm (20-in.) diameter have been demonstrated using this technology (209–212). These blown-film dies also incorporate temperature isolation techniques that allow VDC resins to be coextruded with resins such as nylon that require much higher melt temperatures. Similar to the monolayer films, multilayer films are used predominately in food packaging and medical applications.

Multilayer Sheet Extrusion. Rigid containers for food packaging can be made from coextruded sheet that contains a layer of a barrier polymer (213–215). A simple example is a sheet with five layers that has a total thickness of about 1.3 mm (50 mil). The outermost layers might be polypropylene, polyethylene, polystyrene, high impact polystyrene (HIPS), or other nonbarrier polymer having good mechanical properties. The innermost barrier layer is about 125 μm (5 mil) of a VDC copolymer. Adhesive layers connect the outer layers and the

barrier layer. This coextruded sheet can be formed into containers by any of several techniques, including solid-phase pressure forming and melt-phase forming. The final container has a total wall thickness of about 500 μm (20 mil) and a barrier layer that is about 50 μm (2 mil) thick. Such a container is capable of protecting oxygen-sensitive foods at ambient temperatures for a year or more. These containers are lightweight, microwavable, nonbreakable, and attractive. More sophisticated containers may have more than five layers and improved economics by including a layer of scrap or recycled polymers in the structure.

Lacquer Resins. Vinylidene chloride copolymers have several properties that are valuable in the coatings industry: excellent resistance to gas and moisture vapor transmission, good resistance to attack by solvents and by fats and oils, high strength, and the ability to be heat-sealed (216,217). These characteristics result from the highly crystalline nature of the very high VDC content of the polymer, which ranges from ~80 to 90 wt%. Minor constituents in these copolymers generally are vinyl chloride, alkyl acrylates, alkyl methacrylates, acryloni-trile, methacrylonitrile, and vinyl acetate. Small concentrations of vinyl carboxylic acids, eg, acrylic acid, methacrylic acid, or itaconic acid, are sometimes included to enhance adhesion of the polymer to the substrate. The ability to crystallize and the extent of crystallization are reduced with increasing concentration of the comonomers; some commercial polymers do not crystallize. The most common lacquer resins are terpolymers of VDC–MMA–AN (218,219). The VDC level and the MMA–AN ratio are adjusted for the best balance of solubility and permeability. These polymers exhibit a unique combination of high solubility, low permeability, and rapid crystallization (220).

Acetone, methyl ethyl ketone, methyl isobutyl ketone, dimethylformamide, ethyl acetate, and tetrahydrofuran are solvents for VDC polymers used in lacquer coatings; methyl ethyl ketone and tetrahydrofuran are most extensively employed. Toluene is used as a diluent for either. Lacquers prepared at 10–20 wt% polymer solids in a solvent blend of two parts ketone and one part toluene have a viscosity of 20–1000 mPa-s (= cP). Lacquers can be prepared from polymers of very high VDC content in tetrahydrofuran–toluene mixtures and can be stored at room temperature. Methyl ethyl ketone lacquers must be prepared and maintained at 60–70 °C or the lacquer forms a solid gel. It is critical in the manufacture of polymers for a lacquer application to maintain a fairly narrow compositional distribution in the polymer to achieve good dissolution properties.

The lacquers are applied commercially by roller coating, doctor and dip coating, knife coating, and spraying. Spraying is useful only with lower viscosity lacquers, and solvent balance is important to avoid webbing from the spray gun. Solvent removal is difficult from heavy coatings, and multiple coatings are recommended where a heavy film is desired. Sufficient time must be allowed between coats to avoid lifting of the previous coat by the solvent. In the machine coating of flexible substrates, eg, paper and plastic films, the solvent is removed by ir heating or forced-air drying at 90–140 °C. Temperatures of 60–95 °C promote the recrystallization of the polymer after the solvent has been removed. Failure to recrystallize the polymer leaves a soft, amorphous coating that blocks or adheres between concentric layers in a rewound roll. A recrystallized coating can be re-wound without blocking. Handling properties of the coated film are improved with small additions of wax as a slip agent and of talc or silica as an antiblock

agent to the lacquer system. The concentration of additives is kept low to prevent any serious detraction from the vapor transmission properties of the VDC copolymer coating. For this reason, plasticizers are seldom, if ever, used.

A primary use of VDC copolymer lacquers is the coating of films made from regenerated cellulose or of board or paper coated with polyamide, polyester, polypropylene, poly(vinyl chloride), and polyethylene. The lacquer imparts resistance to fats, oils, oxygen, and water vapor (221). These coated products are used mainly in the packaging of foodstuffs, where the additional features of inertness, lack of odor or taste, and nontoxicity are required. Vinylidene chloride copolymers have been used extensively as interior coatings for ship tanks, railroad tank cars, and fuel storage tanks, and for coating of steel piles and structures (222,223). The excellent chemical resistance and good adhesion result in excellent long-term performance of the coating. Brushing and spraying are suitable methods of application.

The excellent adhesion to primed films of polyester combined with good dielectric properties and good surface properties makes VDC copolymers very suitable as binders for iron oxide pigmented coatings for magnetic tapes (224–226). They perform very well in audio, video, and computer tapes.

Vinylidene Chloride Copolymer Latex. Vinylidene chloride copolymers can be made in emulsion, and then isolated, dried, and used as coating or extrusion resins. Stable latices have been prepared and can be used directly for coatings (227–232). The principal applications for these materials areas barrier coatings on paper products and, more recently, on plasticfilms. The heat-seal characteristics of VDC copolymer coatings are equally valuable in many applications. They are also used for paints and as binders for nonwoven fabrics (233). Special VDC copolymer latices are used for barrier laminating adhesives, and the use of VDC copolymers in flame-resistant carpet backing is well known (234–237). VDC latices can also be used to coat poly(ethylene terephthalate) bottles to retain carbon dioxide (238).

Poly(vinylidene chloride) latices can be easily prepared by the same methods but have few uses because they do not form films. Copolymers of high VDC content are film-forming when freshly prepared but soon crystallize and lose this desirable characteristic. Because crystallinity in the final product is very often desirable, eg, in barrier coatings, a significant developmental problem has been to prevent crystallization in the latex during storage and to induce rapid crystallization of the polymer after coating. This has been accomplished by using the proper combination of comonomers with VDC.

Most VDC copolymer latices are made with varying amounts of acrylates, methacrylates, and acrylonitrile, as well as minor amounts of vinylcarboxylic acids, eg, itaconic and acrylic acids. Low foam latices having high surface tension are prepared with copolymerizable sulfonate monomers (235,237–239). The total amount of comonomer ranges from about 8 wt% for barrier latices to as high as 60 wt% for binder and paint latices. The properties of a typical barrier latex used for paper coating are listed in Table 23. Barrier latices are usually formulated with antiblock, slip, and wetting agents. They can be deposited by conventional coating processes, eg, with an air knife (240,241).

Coating speeds in excess of 305 m/min can be attained. The latex coating can be dried in forced-air or radiant-heat ovens (242,243). Multiple coats are applied,

Table 23. Properties of a Typical Barrier Latex

Properties	Value
Total solids, wt%	54–56
Viscosity at 25 °C, mPa-s (= cP)	25
pH	2
Color	Creamy white
Particle size, nmv	ca 250
Density, g/cm^3	1.30
Mechanical stability	Excellent
Storage stability	Excellent
Chemical stability	Not stable to di- or trivalent ions

Table 24. Film Properties of VDC Copolymer Latex

Property	Value
Water vapor transmission at 38 °C and 95% RH, nmol/(m·s)[a]	0.012[b]
Grease resistance	Excellent
Scorability and fold resistance	Moderate
Oxygen permeability at 25 °C, nmol/(m·s·GPa)[c]	0.07
Heat sealability[d]	Good
Light stability	Fair
Density, g/cm^3	1.60
Color	Watery white
Clarity	Excellent
Gloss	Excellent
Odor	None

[a]To convert nmol/(m·s) to (g·mil)/(100 in.^{2}·d), multiply by 4.
[b]Values 0.37 g/(24 h·100 in.^{2}) for 0.5 mil.
[c]To convert nmol/(m·s·GPa) to (cm^3·mil)/(100 in.^{2}·d·atm), divide by 2.
[d]Face-to-face.

particularly in paper coating, to reduce pinholing (244). A precoat is often used on porous substances to reduce the quantity of the more expensive VDC copolymer latex needed for covering (245). The properties of a typical coating are listed in Table 24.

Vinylidene Chloride Copolymer Foams. Low density, fine-celled VDC copolymer foams can be made by extrusion of a mixture of VDC copolymer and a blowing agent at 120–150 °C (246). The formulation must contain heat stabilizers, and the extrusion equipment mustbemade ofnoncatalytic metalstoprevent accel-erated decomposition of the polymer. The low melt viscosity of the VDC copolymer formulation limits the size of the foam sheet that can be extruded.

Expandable VDC copolymer microspheres are prepared by a microsuspension process (247). The expanded microspheres are used in reinforced polyesters, blocking multipair cable, and in composites for furniture, marble, and marine applications (248–251). Vinylidene chloride copolymer microspheres are also used in printing inks and paper manufacture (252).

Vinylidene Chloride Copolymer Ignition-Resistant Applications. The role of halogen-containing compounds in ignition and flame suppression has been studied for many years (253–258). Vinylidene chloride copolymers are an abundant source of organic chlorine, eg, often above 70 wt%. Vinylidene chloride emulsion copolymers are used in a variety of ignition-resistant binding applications (259,260). Powders dispersible in nonsolvent organic polymer intermediates, eg, polyols, are used for both reinforcement and ignition resistanceinpolyurethane foams. Vinylidene chloride copolymer powder is also used as an ignition-resistant binder for cotton batt (261–263).

The halogenated polymers generate significantly more smoke than polymers that have aliphatic backbones, even though the presence of the halogen does increase the limiting oxygen index. Heavy-metal salts retard smoke generation in halogenated polymers (263,264). A VDC emulsion copolymer having a high AN graft can be used to make ignition-resistant acrylic fibers (265). A rubber-modified VDC copolymer combines good ignition resistance with good low temperature flexibility (266,267). The rubber-modified VDC copolymer has been evaluated in wire coating where better ignition resistance and lower smoke generation are needed.

Materials are also blended with VDC copolymers to improve toughness (267–270). Vinylidene chloride copolymer blended with ethylene–vinyl acetate copolymers improves toughness and lowers heat-seal temperatures (271,272). Adhesion ofa VDC copolymer coating topolyester can beachievedby blending the copolymer with a linear polyester resin (273).

BIBLIOGRAPHY

"Vinylidene Chloride Polymers" in *EPST* 1st ed., Vol. 14, pp. 540–579, by R. A. Wessling and F. G. Edwards, The Dow Chemical Company; in *EPSE* 2nd ed., Vol. 17, pp. 492–531, by R. A. Wessling, D. S. Gibbs, P. T. DeLassus, The Dow Chemical Company; B. A. Howell, Central Michigan University; in *EPST* 3rd ed., Vol. 4, pp. 458–510, by R. A. Wessling, D. S. Gibbs, B. E. Obi, D. E. Beyer, The Dow Chemical Company; P. T. DeLassus, Valparaiso University; B. A. Howell, Central Michigan University.

CITED PUBLICATIONS

1. P. T. DeLassus and D. D. Schmidt, *J. Chem. Eng. Data* **26**, 274 (1981).
2. *Vinylidene Chloride Monomer Safe Handling Guide*, No. 00–6339-88-SAI, The Dow Chemical Co., Midland, Mich., 1988.
3. L. G. Shelton, D. E. Hamilton, and R. H. Fisackerly, in E. C. Leonard, ed., *Vinyl and Diene Monomers, High Polymers*, Vol. **24**, Wiley-Interscience, New York, 1971, pp. 1205–1282.
4. U. S. Pat.2238020 (Apr. 8, 1947), A. W. Hanson and W. C. Goggin (to The Dow Chemical Co.).
5. U. S. Pat. 3760015 (Sept. 18, 1973), S. Berkowitz (to FMC Corp.).
6. U. S. Pat. 3870762 (Mar. 11, 1975), M. H. Stacey and T. D. Tribbeck (to Imperial Chemical Industries, Ltd.).
7. U. S. Pat. 4225519 (Sept. 30, 1980), A. E. Reinhardt III (to PPG Industries).
8. P. W. Sherwood, *Ind. Eng. Chem.* **54**, 29 (1962).

9. U. S. Pat. 2293317 (Aug. 18, 1942), F. L. Taylor and L. H. Horsley (to The Dow Chemical Co.).
10. P. L. Viola and A. Caputo, *Environ. Health Perspect.* **21**, 45 (1977).
11. C. C. Lee and co-workers, *J. Toxicol. Environ. Health* **4**, 15 (1978).
12. V. Ponomarkov and L. Tomatis, *Oncology* **37**, 136 (1980).
13. R. D. Short and co-workers, EPA Report, No. PB281713, Environmental Protection Agency, Washington, D. C., 1977.
14. T. R. Blackwood, D. R. Tierney, and M. R. Piana, EPA Report, No. PB80–146442, Environmental Protection Agency, Washington, D. C., 1979.
15. J. M. Norris, *personal communication*, The Dow Chemical Co., Midland, Mich., 1982.
16. M. J. McKenna, P. G. Watanabe, and P. J. Gehring, *Environ. Health Perspect.* **21**, 99 (1977).
17. M. G. Ott and co-workers, *J. Occup. Med.* **18**, 735 (1976).
18. J. Hushon and M. Kornreich, EPA Report, No. PB280624, Environmental Protection Agency, Washington, D. C., 1978.
19. G. Talamini and E. Peggion, in G. E. Ham, ed., *Vinyl Polymerization*, Vol. **1**, Marcel Dekker, Inc., New York, 1967, Part 1, Chapt. "5".
20. P. J. Flory, *Principles of Polymer Chemistry*, Cornell University Press, Ithaca, N.Y., 1953, Chapt. "6".
21. W. H. Stockmayer, K. Matsuo, and G. W. Nelb, *Macromolecules* **10**, 654 (1977).
22. J. D. Burnett and H. W. Melville, *Trans. Faraday Soc.* **46**, 976 (1950).
23. C. E. Bawn, T. P. Hobin, and W. J. McGarry, *J. Chem. Phys.* **56**, 791 (1959).
24. W. J. Burlant and D. H. Green, *J. Polym. Sci.* **31**, 227 (1958).
25. R. C. Reinhardt, *Ind. Eng. Chem.* **35**, 422 (1943).
26. W. I. Bengough and R. G. W. Norrish, *Proc. R. Soc. London, Ser. A* **218**, 149 (1953).
27. R. A. Wessling and I. R. Harrison, *J. Polym. Sci., Part A-1*, **9**, 3471 (1971).
28. G. Odian, *Principles of Polymerization*, John Wiley & Sons, Inc., New York, 1981, Chapt. "3".
29. B. E. Obi and co-workers, *J. Polym. Sci, Part B: Polyms. Phys.* **33**, 2019–2032 (1995).
30. J. L. Gardon, in C. E. Schildknecht, ed., *Polymerization Processes*, John Wiley & Sons, Inc., New York, 1977, Chapt. "6".
31. R. A. Wessling, *J. Appl. Polym. Sci.* **12**, 309 (1968).
32. R. A. Wessling and D. S. Gibbs, *J. Macromol. Sci., A: Chem.* **7**, 647 (1973).
33. A. Konishi, *Bull. Chem. Soc. Jpn.* **35**, 197 (1962).
34. A. Konishi, *Bull. Chem. Soc. Jpn.* **35**, 193 (1962).
35. A. P. Sheniker and co-workers, *Dokl. Akad. Nauk SSSR* **124**, 632 (1959).
36. D. R. Roberts and R. H. Beaver, *J. Polym. Sci., Polym. Lett. Ed.* **17** (3), 155 (1979).
37. B. A. Howell, A. M. Kelly-Rowley, and P. B. Smith, *J. Vinyl. Tech.* **11**, 159 (1989).
38. A. R. Westwood, *Eur. Polym. J.* **7**, 377 (1971).
39. J. F. Gabbett and W. Mayo Smith, in G. E. Ham, ed., *Copolymerization*, John Wiley & Sons, Inc., New York, 1964, Chapt. "10".
40. J. Brandrup and E. H. Immergut, eds., *Polymer Handbook*, 2 nd ed., John Wiley & Sons, Inc., New York, 1975.
41. K. Matsuo and W. H. Stockmayer, *Macromolecules* **10**, 658 (1977).
42. W. I. Bengough and R. G. W. Norrish, *Proc. R. Soc. London, Ser. A* **218**, 155 (1953).
43. C. Pichot, Q. T. Pham, and J. Guillot, *J. Macromol. Sci., Chem.* **12**, 1211 (1978).
44. C. Pichot and Q. T. Pham, *Eur. Polym. J.* **15**, 833 (1979).
45. B. E. Obi, *Technical data*, The Dow Chemical Company, Midland, MI, 1995.
46. N. Yamazaki and co-workers, *Polym. Prepr. (Am. Chem. Soc., Div. Polym. Chem.)* **5**, 667 (1964).

47. A. Konishi, *Bull. Chem. Soc. Jpn.* **35**, 395 (1962).
48. B. L. Erusalimskii and co-workers, *Dokl. Akad. Nauk SSSR* **169**, 114 (1966).
49. Brit. Pat. 1119746 (July 10, 1968) (to Chisso Corp.).
50. Can. Pat. 798905 (Nov. 12, 1968), R. Buning and W. Pungs (to Dynamit Nobel Corp.).xs
51. U. S. Pat. 3366709 (Jan. 30, 1968), M. Baer (to Monsanto Co.).
52. U. S. Pat. 3509236 (Apr. 28, 1970), H. G. Siegler, R. B. Oberlar, and W. Pungs (to Dynamit Nobel Aktiengeselfichaft Co.).
53. U. S. Pat. 3655553 (Apr. 11, 1972), R. C. DeWald (to Firestone Tire and Rubber Co.).
54. M. Pegoraro, E. Beati, and J. Bilalov, *Chim. Ind. Milan* **54**, 18 (1972).
55. T. Fisher, J. B. Kinsinger, and C. W. Wilson, *Polym. Lett.* **5**, 285 (1967).
56. M. Meeks and J. L. Koenig, *J. Polym. Sci., Part A-1* **9**, 717 (1971).
57. S. Krimm, *Fortschr. Hochpolym. Forsch.* **2**, 51 (1960).
58. K. Matsuo and W. H. Stockmayer, *Macromolecules* **8**, 660 (1975).
59. K. Okuda, *J. Polym. Sci., Part A* **2**, 1749 (1964).
60. E. J. Arlman and W. M. Wagner, *Trans. Faraday Soc.* **49**, 832 (1953).
61. M. M. Coleman and co-workers, *J. Macromol. Sci., Phys.* **15**, 463 (1987).
62. M. S. Wu and co-workers, *J. Polym. Sci., Polym. Phys. Ed.* **18**, 95 (1980).
63. M. S. Wu and co-workers, *J. Polym. Sci., Polym. Phys. Ed.* **18**, 111 (1980).
64. R. H. Boyd and L. Kesner, *J. Polym. Sci., Polym. Phys. Ed.* **19**, 393 (1981).
65. B. E. Obi, P. T. DeLassus, and E. A. Grulke, *Macromolecules* **27**, 5491–5497 (1994).
66. R. F. Boyer and R. S. Spencer, *J. Appl. Phys.* **15**, 398 (1944).
67. K. H. Illers, *Kolloid Z.* **190**, 16 (1963).
68. R. A. Wessling and co-workers, *Appl. Polym. Symp.* **25**, 83 (1974).
69. G. R. Riser and L. P. Witnauer, *Polym. Prepr.* **2**, 218 (1961).
70. N. W. Johnston, *Rev. Macromol. Chem. C* **14**, 215 (1976).
71. B. G. Landes, P. T. DeLassus, and I. R. Harrison, *J. Macromol. Sci. B* **22**, 735 (1984).
72. R. A. Wessling, J. H. Oswald, and I. R. Harrison, *J. Polym. Sci., Polym. Phys. Ed.* **11**, 875 (1973).
73. I. R. Harrison and E. Baer, *J. Colloid Interface Sci.* **31**, 176 (1969).
74. R. A. Wessling, D. R. Carter, and D. L. Ahr, *J. Appl. Polym. Sci.* **17**, 737 (1973).
75. A. F. Burmester and R. A. Wessling, *Bull. Am. Phys. Soc.* **18**, 317 (1973).
76. M. Asahina, M. Sato, and T. Kobayashi, *Bull. Chem. Soc. Jpn.* **35**, 630 (1962).
77. R. A. Wessling, *J. Appl. Polym. Sci.* **14**, 1531 (1970).
78. R. A. Wessling, *J. Appl. Polym. Sci.* **14**, 2263 (1970).
79. M. L. Wallach, *Polym. Prepr.* **10**, 1248 (1969).
80. A. Revillion, B. Dumont, and A. Guyot, *J. Polym. Sci., Polym. Chem. Ed.* **14**, 2263 (1976).
81. A. Revillion, *J. Liq. Chromatogr.* **3**, 1137 (1980).
82. G. S. Kolesnikov and co-workers, *Izu. Akad. Nauk SSSR Otd. Khim. Nauk* 731 (1959).
83. E. F. Jordan and co-workers, *J. Appl. Polym. Sci.* **13**, 1777 (1969).
84. S. W. Lasoski, *J. Appl. Polym. Sci.* **4**, 118 (1960).
85. S. W. Lasoski and W. H. Cobbs, *J. Polym. Sci.* **36**, 21 (1959).
86. H. J. Bixler and O. S. Sweeting, in O. J. Sweeting, ed., *The Science and Technology of Polymer Films*, Vol. **2**, Wiley-Interscience, New York, 1971, Chapt. "1".
87. P. T. DeLassus, *J. Vinyl Technol.* **1**, 14 (1979).
88. P. T. DeLassus and D. J. Grieser, *J. Vinyl Technol.* **2**, 195 (1980).
89. P. T. DeLassus, *J. Vinyl Technol.* **3**, 240 (1981).
90. *Introduction to Barrier Polymer Performance*, No. 190–333-1084, The Dow Chemical Co., Midland, Mich., 1984.
91. *Permeability of Polymers to Gases and Vapors*, No. P302–336-79, The Dow Chemical Co., Midland, Mich., 1979.

92. *Kuraray EVAL Resin*, No. 6–1000-605, Kuraray Co., Ltd., Osaka, Japan, 1986.
93. P. T. DeLassus, in Proceedings of COEX America, Scotland, 1986, p. 187.
94. P. T. DeLassus, in J. I. Kroschwitz, ed., *Kirk-Othmer: Encyclopedia of Chemical Technology*, 4th ed., Vol. **3**, John Wiley & Sons, Inc., New York, 1992, pp. 931–962.
95. G. Strandburg, P. T. DeLassus, and B. A. Howell, in S. A. Risch and J. H. Hotchkiss, eds., *Food and Packaging Interactions II* (ACS Symposium Series No. 473), American Chemical Society, Washington, D. C., 1991, pp. 133–148.
96. P. T. DeLassus and co-workers, in J. H. Hotchkiss, ed., *Food and Packaging Interactions* (ACS Symposium Series No. 365), American Chemical Society, Washington, D. C., 1988, Chapt. "2", pp. 11–27.
97. P. T. DeLassus, G. Strandburg, and B. A. Howell, *TAPPI J.* **71** (11), 177–181 (1988).
98. G. Strandburg, P T. DeLassus, and B. A. Howell, in W. J. Karos, ed., *Barrier Polymers and Structures* (ACS Symposium Series No. 423), American Chemical Society, Washington, D. C., 1990, pp. 333–350.
99. R. F. Boyer, *J. Phys. Colloid Chem.* **51**, 80 (1947).
100. G. M. Burnett, R. A. Haldon, and J. N. Hay, *Eur. Poly. J.* **4**, 83 (1968).
101. B. A. Howell and P. T. DeLassus, *J. Polym. Sci., Polym. Chem. Ed.* **25**, 1967 (1987).
102. U. S. Pat. 3321417 (May 23, 1967) (to Union Carbide Corp.); N. L. Zutty and F. J. Welch, *J. Polym. Sci., Part A* **1**, 2289 (1963).
103. B. A. Howell, *J. Polym. Sci., Polym. Chem. Ed.* **25**, 1981 (1987), and references cited therein.
104. R. R. Lagasse and J. L. Schroeder, *Mater. Res. Soc. Symp. Proc.* **371**, 432 (1995).
105. J. D. Danforth, *Polym. Prepr.* **21**, 140 (1980).
106. J. D. Danforth, in P. O. Klemchuk, ed., *Polymer Stabilization and Degradation*, American Chemical Society, Washington, D. C., 1985, Chapt. 20, and references cited therein.
107. D. H. Everett and D. J. Taylor, *Trans. Faraday Soc.* **67**, 402 (1971).
108. D. Vesely, *Ultramicroscopy* **14**, 279 (1984).
109. I. R. Harrison and E. Baer, *J. Colloid Interface Sci.* **31**, 176 (1969).
110. D. R. Roberts and A. L. Gatzke, *J. Polym. Sci., Polym. Chem. Ed.* **16**, 1211 (1978).
111. B. Dolezel, M. Pegoraro, and E. Beati, *Eur. Polym. J.* **6**, 1411 (1970).
112. T.-H. Hsieh, *Polym. J.* **31**, 948 (1999).
113. T.-H. Hsieh and K.-S. Ho, *J. Polym. Sic., Part A: Polym. Chem.* **37**, 2035 (1999).
114. R. J. Pasek, D. P. Y. Chang, and A. D. Jones, *Hazard. Waste Hazard. Mater.* **13** 23 (1996).
115. P. Pendleton, B. Vincent, and M. L. Hair, *J. Colloid Interface Sci.* **80**, 512 (1981).
116. R. D. Bohme and R. A. Wessling, *J. Appl. Polym. Sci.* **16**, 1961 (1972).
117. A. Crovato-Arnaldi and co-workers, *J. Appl. Polym. Sci.* **8**, 747 (1964).
118. G. M. Burnett, R. A. Haldon, and J. N. Hay, *Eur. Polym. J.* **3**, 449 (1967).
119. R. A. Wessling, *Am. Chem. Soc. Div. Org. Coat. Plast. Chem. Pap.* **34**, 380 (1976).
120. F. F. He and H. Kise, *J. Polym. Sci., Polym. Chem. Ed.* **21**, 1972 (1983).
121. D. H. Davies, *J. Chem. Soc. Faraday Trans. 1* **72**, 2390 (1976).
122. E. Tsuchido and co-workers, *J. Polym. Sci., Part A* **2**, 3347 (1964).
123. S. S. Barton and co-workers, *Trans. Faraday Soc.* **67**, 3534 (1971).
124. S. S. Barton, J. R. Dacey, and B. H. Harrison, *Am. Chem. Soc. Div. Org. Coat. Plast. Chem. Pap.* **31**, 768 (1971).
125. Y. V. Konotsur, G. S. Shapoval, and A. A. Pud, *Theor. Exp. Chem.* **33**, 150 (1997).
126. B. A. Howell, S. I. Ahmed, and D. E. Beyer, *Polym. Prepr.* **42**, 868 (2001).
127. A. L. Evelyn and co-workers, in J. L. Duggan and I. L. Morgan, eds., *Application of Accelerators in Research and Industry*, AIP Press, New York, 1997, pp. 933–936.
128. A. K. Srivastava and H. S. Virk, *Indian J. Pure Appl. Phys.* **37**, 713 (1999).

129. A. M. Shaban, *Mater. Lett.* **22**, 309 (1995).
130. A. Bailey and D. H. Everett, *J. Polym. Sci., Part A-2* **7**, 87 (1969).
131. B. A. Howell and co-workers, in Proceedings of 28th North American Thermal Analysis Society Meeting, 2000, p. 283–286.
132. R. Simon, *Polym. Degr. Stab.* **43**, 125 (1994).
133. B. A. Howell, *Thermochim. Acta* **148**, 375 (1989).
134. B. A. Howell, *Thermochim. Acta* **134**, 207 (1988).
135. B. A. Howell, *J. Therm. Anal. Cal*, **83**, 53 (2006).
136. G. M. Burnett, R. A. Haldon, and J. N. Hay, *Eur. Polym. J.* **3**, 449 (1967).
137. D. E. Agostini and A. L. Gatzke, *J. Polym. Sci., Polym. Chem. Ed.* **11**, 649 (1973).
138. B. A. Howell, P. T. DeLassus, and C. Gerig, *Polym. Prepr.* **28**, 278 (1987).
139. S. Collins and co-workers, *Polym. Degrad. Stab.* **66**, 87 (1999).
140. B. A. Howell, Z. Ahmed, and S. I. Ahmed, *Thermochim. Acta* **357**, 103 (2000).
141. P. L. Kumler and co-workers, *Macromolecules* **22**, 2994 (1989).
142. V. Rossbach and co-workers, *Angew. Makromol. Chem.* **40/41**, 291 (1974).
143. D. H. Grant, *Polymer* **11**, 581 (1970).
144. D. L. C. Jackson and W. S. Reid, *Nature* **162**, 29 (1948).
145. B. A. Howell and P. B. Smith, *J. Polym. Sci., Polym. Phys. Ed.* **26**, 1287 (1988).
146. D. H. Davies and P. M. Henheffer, *Trans. Faraday Soc.* **66**, 2329 (1970).
147. E. Tsuchida and co-workers, *J. Polym. Sci., Part A* **2**, 3347 (1964).
148. S. S. Barton and co-workers, *Trans. Faraday Soc.* **67**, 3534 (1971).
149. S. E. Evsyukov, S. Paasch, and B. Thomas, *Ber. Bunsen-Ges.* **101**, 837 (1997).
150. T. Danno, K. Murakami, and R. Ishikawa, in *AIP Conf. Proc.*, 1999, p. 486.
151. B. A. Howell and H. Liu, *Thermochim. Acta* **212**, 1 (1992).
152. B. A. Howell and F. M. Uhl, *Thermochim. Acta* **357**, 113 (2000).
153. B. A. Howell and F. M. Uhl, *Polym. Prepr.* **39**, 663 (1998).
154. B. A. Howell and P. B. Smith, *J. Therm. Anal. Cal.*, **83**, 71 (2006).
155. B. A. Howell and A. O. Odelana, *J. Therm. Anal. Cal.*, **89**, 373 (2007).
156. B. A. Howell and B. B. S. Sastry, in Proceedings of 22 nd North American Thermal Analysis Society Meeting, 1993, pp. 122–127.
157. U. S. Pat. 3852223 (Dec. 3, 1974), R. D. Bohme and R. A. Wessling (to The Dow Chemical Co.).
158. A. Ballistreri and co-workers, *Polymer* **22**, 131 (1981).
159. S. Gopalkrishnan and W. H. Starnes Jr., *Polym. Prepr.* **30**, 201 (1989).
160. B. A. Howell and J. R. Keeley, *Thermochim. Acta* **272**, 131 (1996).
161. B. A. Howell and co-workers, *Thermochim. Acta* **166**, 207 (1990).
162. B. A. Howell, M. F. Debney, and C. V. Rajaram, *Thermochim. Acta* **212**, 115 (1992).
163. S. R. Betso and co-workers, *J. Appl. Polym. Sci.* **51**, 781 (1994).
164. B. A. Howell and C. V. Rajaram, *J. Vinyl Tech.* **15**, 202 (1993).
165. B. A. Howell and co-workers, *Polym. Adv. Tech.* **5**, 485 (1994).
166. B. A. Howell and co-workers, *Thermochim. Acta* **272**, 139 (1996).
167. J. Ozaki, T. Watanabe, and Y. Nishiyama, *J. Phys. Chem.* **97**, 1400 (1983).
168. B. A. Howell and A. Q. Campbell, *Thermochim. Acta* **340**, 231 (1999).
169. L. A. Matheson and R. F. Boyer, *Ind. Eng. Chem.* **44**, 867 (1952).
170. G. Oster, G. K. Oster, and M. Kryszewski, *J. Polym. Sci.* **57**, 937 (1962).
171. M. Kryszewski and M. Mucha, *Bull. Acad. Pol. Sci. Ser. Sci. Chim. Geol. Geogr.* **13**, 53 (1965).
172. Y. Izumi, S. Kawanishi, N. Takagi, S. Honda, and T. Yamamoto, *Bull. Chem. Soc. Jpn.* **71**, 2459 (1998).
173. H. Niino and A. Yabe, *J. Polym. Sci., Part A: Polym. Chem.* **36**, 2483 (1998).
174. A. Yabe, *Phys. Chem. Mater. Low-Dimens. Struct.* **21**, 75 (1999).
175. R. R. Lagasse and J. L. Schroeder, *Mater. Res. Soc. Symp. Proc.* **371** 431 (1995).

176. U. S. Pat. 4418168 (Nov. 29, 1983), E. H. Johnson (to the Dow Chemical Co.).
177. B. A. Howell, F. M. Uhl, and D. Townsend, *Thermochim. Acta* **357**, 127 (2000).
178. B. A. Howell and J. Zhang, *Polym. Prepr.* **42**, 880 (2001).
179. B. A. Howell and J. Zhang., *J. Vinyl Addit. Technol.*, **12**, 88 (2006).
180. B. A. Howell, D. A. Spears, and P. B. Smith, *J. Therm. Anal. Cal.*, **85**, 115 (2006).
181. B. A. Howell and B. Pan, *Thermochim. Acta* **357**, 119 (2000).
182. U. S. Pat. 3033812 (May 8, 1962), P. K. Isacs and A. Trofimow (to W. R. Grace & Co.).
183. D. M. Woodford, *Chem. Ind. (London)* **8**, 316 (1966).
184. U. S. Pat. 2968651 (Jan. 17, 1961), L. C. Friedrich Jr., J. W. Peters, and M. R. Rector (to The Dow Chemical Co.).
185. U. S. Pat. 2482771 (Sept. 27, 1944), J. Heerema (to The Dow Chemical Co.).
186. W. C. Goggin and R. D. Lowrey, *Ind. Eng. Chem.* **34**, 327 (1942).
187. A. T. Widiger and R. L. Butler, in O. J. Sweeting, ed., *The Science and Technology of Polymer Films*, Wiley-Interscience, New York, 1971, pp. 333–339.
188. *Saran Polymers for Barrier Packaging*, Form No. 190–00445-992, The Dow Chemical Co., Midland, Mich., 1996.
189. Z. Li and Y. Peng, *Suliao* **27** (2), 40–43 (1998).
190. S. R. Jenkins and co-workers, in 1998 Polymers, Laminations and Coating Conference, Book 2, TAPPI Press, Atlanta, 1989, p. 501.
191. M. A. Spalding and co-workers, *Polym. Eng. Sci.* **35**, 1907 (1995).
192. U. S. Pat. 5006368 (Apr. 9, 1991), P. T. Louks (to The Dow Chemical Co.).
193. C. E. Schildknecht, *Vinyl and Related Polymers*, John Wiley and Sons, Inc., New York (1952).
194. *Saran Resins*, No. 190–289-79, The Dow Chemical Co., Midland, Mich., 1979.
195. E. D. Serdynsky, in H. F. Mark, S. M. Atlas, and E. Cernia, eds., *Man-Made Fibers: Science and Technology*, Vol. **3**, Wiley-Interscience, New York, 1968, pp. 317–322.
196. *Product Literature*, Fugafil-saran GmbH & Co., 2001.
197. S. Jenkins and J. Naumovitz, *Packed with Performance*, Vol. **3**, The Dow Chemical Co., Midland, Mich., May 1999.
198. D. Zuo, *Shanghai Chem. Ind.* **22** (6), 40–43 (1997).
199. W. R. R. Park, *Plastics Film Technology*, Van Nostrand Reinhold Company, Newy York, 1969.
200. J. H. Briston, *Plastics Films*, 3rd ed., Longman Scientific & Technical, Essex, England, 1988.
201. C. J. Benning, *Plastics Films for Packaging*, Technomic Publishing Co., Lancaster, Pa., 1989, p. 31.
202. H. Tamber, in PVDC Films, Plast-Ex '98 Technical Conference, 1998.
203. *Technical Datasheets*, Form No. 190-(00481 through 00487)-01, The Dow Chemical Co., Midland, Mich., 2001.
204. D. L. Roodvoets, in P. F. Bruin, ed., *Packaging with Plastics*, Gordon & Breach, New York, 1974, p. 85.
205. *SARANEX Barrier Medical Films*, Form No. 500–01814-1199, The Dow Chemical Co., Midland, Mich., 1999.
206. *SARANEX Coextruded Barrier Film*, Form No. 500–01923-0401, The Dow Chemical Co., Midland, Mich., 2001.
207. U. S. Pat. 4643927, (Feb. 17, 1987), R. A. Luecke (to The Dow Chemical Co.)
208. U. S. Pat. 4842791, (Jun. 27, 1989), G. E. Gould and R. A. Luecke (to The Dow Chemical Co.)
209. H. Tamber, in *Advanced Technology Seminar, Macro Engineering & Technology Inc.*, Mississauga, Ontario, Canada, Sept. 1999.
210. *Can. Plast.* **59** (9), 17 (2000).

211. H. Tamber, *"Barrier Films Containing PVDC/EVOH in Food & Medical Packaging Ap-plications," in Specialty Plastics Films 2000, 16th Annual World Congress, on Global Film Resins, Markets, Applications, Zurich, Macro Engineering & Technology Inc.*, 2000.
212. *Plast. Technol.* **47** (1), 13 (2001).
213. *Rigid Coextruded Plastic Barrier Containers for Unrefrigerated Foods*, Form No. 190–337-1084, The Dow Chemical Co., Midland, Mich., 1984.
214. W. J. Schrenk and S. A. Marcus, in K. M. Finlayson, ed., *Plastic Film Technology*, Vol. **1**, Technomic Publishing Co., Lancaster, Pa., 1989, pp. 1–11.
215. R. J. Macy, in Ref. (211), pp. 220–226.
216. S. F. Roth, in *American Chemical Society Chemical Marketing Economic Division Symposium (N.Y.)*, American Chemical Society, Washington, D. C., 1976, p. 29.
217. *Saran F Resin*, Technical Bulletin, The Dow Chemical Co., Horgen, Switzerland, 1969.
218. U. S. Pat. 3817780 (June 18, 1974), P. E. Hinkamp and D. F. Foye (to The Dow Chemical Co.).
219. U. S. Pat. 3879359 (Apr. 22, 1975), P. E. Hinkamp and D. F. Foye (to The Dow Chemical Co.).
220. U. S. Pat. 4097433 (June 27, 1978), W. P. Kane (to E. I. du Pont de Nemours & Co., Inc.).
221. U. S. Pat. 2462185 (Feb. 22, 1949), P. M. Hauser (to E. I. du Pont de Nemours & Co., Inc.).
222. W. W. Cranmer, *Corros. Houston* **8** (6), 195 (1952).
223. R. L. Alumbaugh, *Mater. Prot.* **3** (7), **34**, 39 (1964).
224. U. S. Pat. 3144352 (Aug. 11, 1964), J. P. Talley (to Ampex Corp.).
225. U. S. Pat. 3865741 (Feb. 11, 1975), F. J. Sischka (to Memorex Corp.).
226. U. S. Pat. 3894306 (July 1, 1975), F. J. Sischka (to Memorex Corp.).
227. L. J. Wood, *Mod. Packag.* **33**, 125 (1960).
228. R. F. Avery, *Tappi J.* **45**, 356 (1962).
229. A. D. Jordan, *Tappi J.* **45**, 865 (1962).
230. B. J. Sauntson and G. Brown, *Rep. Prog. Appl. Chem.* **56**, 55 (1972).
231. P. S. Bryant, in European Flexographic Technical Association Barrier Coatings and Laminations Seminar, Vol. 1, Manchester, U. K., 1977, p. 7.
232. G. H. Elschnig and co-workers, *Pop. Plast.* **17** (2), 19 (1972).
233. U. S. Pat. 3787232 (Jan. 22, 1974), B. K. Mikofalvy and D. P. Knechtges (to B. F. Goodrich Co.).
234. R. G. Jahn, *Adhes. Age* **20** (6), 37 (1977).
235. U. S. Pat. 3946139 (Mar. 23, 1976), M. Bleyle and co-workers (to W. R. Grace & Co.).
236. U. S. Pat. 3850726 (Nov. 26, 1974), D. R. Smith and H. Peterson (to A. E. Staley Co.).
237. U. S. Pat. 3617368 (Nov. 2, 1971), D. S. Gibbs and R. A. Wessling (to The Dow Chemical Co.).
238. P. T. DeLassus, D. L. Clarke, and T. Cosse, *Mod. Plast.* **60**, 86 (Jan. 1983).
239. Brit. Pat. 1233078 (May 26, 1971), H. Gould and J. A. Zaslowsky (to Alcolac Chemical Co.).
240. G. H. Elschnig and A. F. Schmid, *Pop. Plast.* **17** (3), 36 (1972).
241. G. H. Elschnig and A. F. Schmid, *Pop. Plast.* **17** (4), 17 (1972).
242. G. H. Elschnig and A. F. Schmid, *Pop. Plast.* **17** (6), 17 (1972).
243. G. H. Elschnig and A. F. Schmid, *Paintindia* **22** (6), 22 (1972).
244. F. C. Caruso, in Proceedings of Test. Pap. Synth. Conf., TAPPI, Atlanta, Ga., 1974, p. 167.

245. E. A. Chirokas, *Tappi J.* **50**, 59 A (1967).
246. U. S. Pat. 3983080 (Sept. 28, 1976), K. S. Suh, R. E. Skochdopole, and M. E. Luduc (to The Dow Chemical Co.).
247. U. S. Pat. 3615972 (Oct. 26, 1971), D. S. Morehouse and R. J. Tetreault (to The Dow Chemical Co.).
248. D. S. Morehouse and H. A. Walters, *SPE J.* **25**, 45 (1969).
249. T. E. Cravens, *Am. Chem. Soc. Div. Org. Coat. Plast. Chem. Pap.* **33**, 74 (1973).
250. R. C. Mildner and co-workers, *Mod. Plast.* **47** (5), 98 (1970).
251. T. F. Anderson, H. A. Walters, and C. W. Glesner, *J. Cell. Plast.* **6** (4), 171 (1970).
252. *Mater. Plast. Elastomer* **10**, 468 (Oct. 1980).
253. D. L. Chamberlain, in W. C. Kuryla and A. J. Papa, eds., *Flame Retardancy of Polymeric Materials*, Vol. **2**, Marcel Dekker, Inc., New York, 1973, pp. 109–168.
254. D. W. Van Krevelen, *Polymer* **16**, 615 (1975).
255. L. G. Imhoff and K. C. Stueben, *Polym. Eng. Sci.* **13**, 146 (1973).
256. E. R. Larsen, *J. Fire Flamm. Fire Ret. Chem.* **1**, 4 (1974).
257. E. R. Larsen, *J. Fire Flamm. Fire Ret. Chem.* **1**, **2**, 5 (1974).
258. R. C. Kidder, in *Proceedings of Fire Retardant Chemicals Association Semiannual Meeting*, 1977, pp. 45–51.
259. J. Knightly and J. C. Bax, in *Proceedings of the European Conference on Flammability Fire Retardance*, 1979, pp. 75–83.
260. J. R. Goots and D. P. Knechtges, *Polym. Plast. Technol. Eng.* **5**, 131 (1975).
261. C. V. Neywick, R. E. Yoerger, and R. F. Peterson, *J. Cell. Plast.* **16**, 171 (1980).
262. U. S. Pat. 4232129 (Nov. 4, 1980), D. S. Gibbs, J. H. Benson, and R. T. Fernandez (to The Dow Chemical Co.).
263. U. S. Pat. 4002597 (Jan. 11, 1977), E. D. Dickens (to B. F. Goodrich Co.).
264. U. S. Pat. 4055538 (Oct. 25, 1977), W. J. Kronke (to B. F. Goodrich Co.).
265. U. S. Pat. 4186156 (Jan. 29, 1980), D. S. Gibbs (to The Dow Chemical Co.).
266. *Plast. Technol.* **26** (1), 13 (1980).
267. U. S. Pat. 4206105 (June 3, 1980), O. L. Stafford (to The Dow Chemical Co.).
268. U. S. Pat. 4239799 (Dec. 16, 1980), A. S. Weinberg (to W. R. Grace & Co.).
269. U. S. Pat. 3840620 (Oct. 8, 1974), R. Gallagher (to Stauffer Chemical Co.).
270. U. S. Pat. 3513226 (May 19, 1970), T. Hotta (to Kureha Kagaku Kogyo Kabushiki Kalsha Co.).
271. U. S. Pat. 3565975 (Feb. 23, 1971), F. V. Goff, F. Stevenson, and W. H. Wineland (to The Dow Chemical Co.).
272. U. S. Pat. 3558542 (Jan. 26, 1971), J. W. McDonald (to E. I. du Pont de Nemours & Co., Inc.).
273. U. S. Pat. 3896066 (July 22, 1975), R. O. Ranck (to E. I. du Pont de Nemours & Co., Inc.).

B. A. HOWELL
Central Michigan University
D. E. BEYER
The Dow Chemical Company

VINYLIDENE FLUORIDE POLYMERS (PVDF)

Introduction

Poly(vinylidene fluoride) [24937-79-9] is the addition polymer of 1,1-difluoroethene [75-38-7], commonly known as vinylidene fluoride and abbreviated VDF or VF_2. The formula of the repeat unit in the polymer is $-[CH_2–CF_2]_n-$. The preferred acronym for the polymer is PVDF, but the abbreviation PVF_2 also is used frequently. (Note: PVF is the accepted acronym for poly(vinyl fluoride), $-[CH_2\text{-}CHF]_n-$.) The history and development of PVDF technology has been reviewed (1). This article deals only with *thermoplastic* VDF-based polymers having greater than 50 wt% VDF, and not *fluoroelastomeric* copolymer versions, which have significant levels of fluoro-comonomers to impart rubber-like properties and usually less than 50 wt% VDF. (see FLUOROCARBON ELASTOMERS).

Since the commercialization of this linear fluoropolymer in the mid-1960s, the applications have expanded until the production of the monomer VDF and polymer PVDF reached significant tonnages at the end of the twentieth century, albeit with essentially the same producers during the last decade. The worldwide PVDF market in 2000 was about 21,000 t according to several industry sources. PVDF usage is expected to grow at an average of about 6% for all fluoropolymers during the first decade of the twenty-first century (2). Several manufacturers (see Table 1) have announced that there would be significant capacity increases between 2000 and 2005. Applications are increasing rapidly in China and Southeast Asia as well as Japan and Korea with a high growth projection for the next few years in these areas.

The production of VDF and PVDF requires significant investment in corrosion-resistant pyrolysis reactors and low temperature distillation columns for the monomer; high pressure polymerization reactors and associated finishing equipment; and special environmental and waste handling processes. Raw material costs for the overall process of feedstock to monomer and polymer are high, depending upon the processes, but reflect to a large extent the pricing of anhydrous hydrogen fluoride, which is involved in the various manufacturing processes for VDF. Also the processes for the monomer and polymer are energy intensive. It is for these reasons that several manufacturers of PVDF have extra production capacity for VDF monomer to supply not only their internal PVDF polymer needs but also to provide the large quantities needed by the manufacturers of VDF-based fluoroelastomers.

The demand for PVDF has been driven by a number of factors: (*1*) a unique set of properties, (*2*) the ease and versatility in processing and fabricating, (*3*) over 30 years of proven performance under various and severe thermal, chemical, radiation, weathering environments and (*4*) the need for special attributes. For example, PVDF parts are subjected to superheated steam temperatures in some chemical processes. It is used also in strong acid, chlorine, bromine, and ultrapure water systems as well as in special applications where fire resistance is required. And PVDF has been used extensively during the last 30 years in nuclear radiation environments because unlike most plastics it cross-links, retaining mechanical integrity, rather than degrades. In one of the major applications

Table 1. Manufacturers of VDF and PVDF[a]

Producers and country of production	Trademarks
Alventia LLC–USA Joint venture – Solvay and Dyneon; VDF monomer only, starting 2000	
Atofina[b]–France, USA	KYNAR, KYNAR 500, KYNAR FLEX, KYNAR Superflex, KYNAR Powerflex, HYLAR
www.atofina.com (Paris) www.atofinachemicals.com (USA) Largest capacity VDF and PVDF producer; expansion underway 2002	
Ausimont–USA www.ausimont.com Large capacity VDF and PVDF	
Daikin–Japan Minimal production PVDF resins; VDF-based coating resins use trademark	NEOFLON
Dyneon–USA, Germany www.dyneon.com Not currently a PVDF producer; produces TFE-based polymers with VDF as comonomer at low content	DYNEON, HOSTAFLON
Creanova[c]–Germany www.creanovainc.com Very small amounts PVDF available	DYFLOR
Kirova–CHEPETSKY Khimichesky Kombinat–Russia Small capacity PVDF	FLUOROPLAST
Kureha Chemical Company–Japan www.kureha.co.jp Moderate PVDF capacity—expansion underway for 2001	KF POLYMER
Solvay–Belgium, USA www.solvay.com Large capacity Europe; USA production 2000	SOLEF VIDAR

[a]Locations and capacities of production sites may be found in the following reference: K.-L. Ring, A. Leder, M. Ishikawa- Yamaki, SRI International Chemical Economics Handbook Marketing Report, Dec. 1998; http://ceh.sric.sri.com/Reports/580.0700/index.html.
[b]Formerly Elf Atochem.
[c]Subsidiary of Degussa-Hüls, formerly Hüls America.

worldwide, there is now over 30 years exposure of thin PVDF-based paint coatings on monumental structures and skyscrapers documenting the durability of these coatings to protect metal from corrosion, retaining essentially the original appearance features.

During the 1990s, there has been much activity in polymerization, scientific studies, and application development related to PVDF. Many copolymer variations and compounds of PVDF have been introduced by the polymer

manufacturers and their immediate resin customers. This article will reference selected recent scientific and technology advances and focus upon property profiles and uses of the various PVDF grades available. A prior encyclopedia article (3) provides extensive references to the earlier studies. Detailed information on the properties and applications is given by the PVDF manufacturers at their websites. When the term *pvdf* is used to search the *Chemical Abstracts* databases from 1992, there are approximately 500 citations per year, about half of which are patents. Hence, the freedom to operate or utilize PVDF in any application by a new user should be verified by a careful check of the patent literature. In addition, producers of PVDF should be consulted regarding proposed medical applications, especially related to body invasive or implant technology.

PVDF is a partially crystalline, linear hydrofluorocarbon polymer that contains 59.4 wt% fluorine and 3 weight percent hydrogen. The high level of intrinsic crystallinity, typically near 60%, confers stiffness and tough, creep resistant properties. Incorporation of various fluorinated comonomers at low levels, typically about 5–10 wt% but as much as 20 wt% in some cases, enhances the flexibility of PVDF by reducing the crystallinity, which, in general, also reduces the end use temperature ratings. Commercial processes involve polymerization in emulsion or suspension using free-radical initiators. The spatial arrangement of the alternating CH_2 and CF_2 groups along the polymer chain and the strong dipole moment of the CF_2 accounts for the unique polarity, unusually high dielectric constant, complex polymorphism, and high piezoelectric and pyroelectric activity of the polymer when processed appropriately (4–6).

PVDF has the characteristic resistance of fluoropolymers to harsh chemical, thermal, ultraviolet, weathering, and oxidizing or high energy, ionizing radiation environments. The chemical resistance of this hydrofluorocarbon polymer is not as broad as exhibited by perfluoropolymers because the somewhat acidic hydrogen atoms along the chain are reactive in strongly basic media, leading to the formation of fluoride salt by-products (7,8). This chemical susceptibility has, in fact, been turned to advantage in preparing PVDF samples for adherence to a variety of substrates as well as introducing reactive functionality for chemical grafting; the mechanism of the surface chemistry has been studied (9).

PVDF homopolymers and copolymers with various fluoroolefins have a wide range of applications including wire and cable products, electronic devices, chemical process equipment, use as a weather-resistant binder for exterior architectural finishes, and many specialized uses such as a stable binder for electroactive constituents in electrochemical cells. The polymer is readily melt-processed without processing aids or stabilizers using conventional molding or extrusion equipment; porous membranes are cast from solutions; and coatings are deposited from dispersions of PVDF using latent solvents, which solubilize the polymer at elevated temperatures, along with other additives to enhance the appearance, properties, and function. Certain grades of PVDF are used extensively for fluid handling components which convey high purity chemicals and ultrapure water because the resins may be fabricated easily into parts that have very low levels of extractable ionic or organic species and also very smooth surfaces that inhibit microbial fouling.

PVDF exhibits an unusual compatibility with other polymers having strong polar groups or carbonyl groups. This miscibility aspect has led to the

Table 2. Physical Properties of VDF, $CH_2{=}CF_2$

	Units/conditions	Value
Molecular weight	Da	64.038
Boiling point	°C	−84
Freezing point	°C	−144
Vapor pressure	kPa @ 21°C	3683
Critical pressure	kPa	4434
Critical temperature	°C	30.1
Critical density	kg/m^3	417
Explosive limits	vol% in air	5.8–20.3
Heat of formation	kJ/mol @ 25°C	−345.2
Heat of polymerization	kJ/mol @ 25°C	−474.21
Water solubility	cm3/100 g @ 25°C/10 kPa	6.3

development of many alloys and mixed systems for coatings, membranes, and extruded products.

In summary, PVDF fulfills special requirements in a variety of niche applications because of its unique characteristics. Hence, the broad and growing usage of this polymer is understandable. VDF usage also is increasing in other fluoropolymer and fluoroelastomer applications.

Monomer

Preparation. The principal industrial route to VDF involves dehydrochlorination of 1-chloro-1,1-difluoroethane (HCFC-142b) [75-68-3]. The principal producers are ATOFINA and Solvay in Europe and the United State and Ausimont and Alventia in the United States. Many patents exist for this and other similar preparative routes based upon dehydrohalogenation of various chlorofluorohydrocarbons or related compounds. Research efforts have escalated because the HCFC production will be curtailed in the mid-2000 period as a result of environmental concerns. Kureha (Japan) announced that their expansion would involve production of VDF from 1,1-difluoroethane (HFC-152a).

Properties. VDF is a colorless, flammable, and nearly odorless gas that has a very low boiling point like other small molecules with fluorine bonds. The physical properties are listed in Table 2. It is usually polymerized above its critical temperature and pressure, typically at pressures well above 3 MPa (30 atm), and approaching 10 MPa (100 atm) in some commercial processes; the polymerization is highly exothermic. Considering the flammability limits, caution must be exercised in any handling system.

Storage and Shipment. VDF (HFC-1132a) can be stored or shipped in gas cylinders or high-pressure tube trailers without polymerization inhibitors. Terpene and quinone inhibitors, however, may be used as a safety element where there might be uncertain environmental storage conditions. Liquid VDF can cause frostbite upon contact with the skin.

Health and Safety Factors. The combustion products are toxic. The OSHA website www.osha-slc.gov/ChemSamp_data/CH_275620.html provides the following information and full definitions of each classification code for environmental exposure and health factors as of year-end 2000.

Classification	Ratings	Comment
ACGIH TLV	500-ppm TWA	Not classifiable as a human carcinogen
NIOSH REL	1-ppm TWA; 5-ppm ceiling (15 min)	
IARC	Group 3	Not classifiable as to its carcinogenicity to humans

Uses. The variety of fluoropolymers and fluoroelastomers incorporating VDF in the main chain is extensive. The commercially important thermoplastic copolymers are based upon hexafluoropropylene HFP (10,11) chlorotrifluoroethylene (CTFE) (12,13) and co- or ter-polymers with tetrafluoroethylene (14). Telomerization of VDF to form fluorinated oligomers by radical addition has been reviewed (15).

Polymerization

VDF and other fluoromonomers are polymerized usually in aqueous medium in either emulsion or suspension. VDF polymerization in nonaqueous media is an active research area. VDF can copolymerize with fluorinated and some nonfluorinated monomers. Several aspects of VDF copolymerization with an array of fluorinated and nonfluorinated monomers have been reviewed (16,17); the reactivity ratios along with the Q and e parameters, which are measures of reactivity and polarity, respectively, have also been compiled. The interest in these copolymers centers upon introducing functionality in the PVDF chain for subsequent reactions.

Only emulsion and suspension polymerization of VDF are commercially practiced because water provides a sufficient heat sink for the large heat release associated with VDF polymerization. Only one VDF-copolymer with nonfluorinated comonomers, maleic monoesters, and allyl glycidal ethers has been commercialized for battery applications (18); all other reported VDF-copolymers with nonfluorinated olefins have been laboratory or patent examples (3).

Polymerization procedures, temperature, pressure, recipe ingredients, monomer feeding strategy, and post-polymerization processing are variables that influence product characteristics and quality (19–26). The variety of commercial VDF-copolymers has been reviewed (27). VDF–HFP copolymers having decreased extractable oligomers and improved solution clarity and processability, especially important to lithium ion battery applications, have been claimed (28).

The degree of polymerization of commercial PVDF ranges from 1000 to 2500 VDF units. During radical-initiated polymerization, the "head-to-tail" addition of monomer units predominates where the "head" is $-CF_2\cdot$ and the "tail" is $-CH_2\cdot$.

Reversed monomeric addition leading to "head-to-head" ($-CF_2-CF_2-$) and "tail-to-tail" ($-CH_2-CH_2-$) or so-called defect structures occurs. Commercial grades exhibit a wide range of 3–7 mol% defect structures as determined usually by nmr (29). The level increases with increasing polymerization temperature (30). The defect linkages affect significantly the crystallization processes and ultimate morphology (31,32).

In the emulsion process, a water-soluble *perfluorinated*-emulsifying agent is used to avoid radical scavenging reactions during polymerization and produce stable latex with a desired solid content. Typically, perfluoroalkylcarboxylate salts are cited in many VDF polymerization process patents. VDF can be polymerized without surfactant similar to conventional monomers (33,34), but only at low solid contents. Both inorganic peroxy compounds [eg, persulfates] and organic peroxides [eg, percarbonates (21)] may be employed as initiators. Other initiator systems such as a redox system (35) or a combination of fluoroaliphatic sulfinate and bromate (36) can also initiate VDF polymerization. Operating pressures can range from 1 to 20 MPa (10–200 atm) and temperature from 10 to 130°C. In a typical recipe, the polymer particles are solid and partial crystalline with diameters ranging from 100 to 250 nm depending upon the surfactant level. Particles are formed in the early stage by a homogeneous nucleation mechanism since VDF is in the vapor state. Various chain-transfer agents can be used such as chlorofluorohydrocarbons, fluorohydrocarbons, esters, and mercaptans.

VDF and suitable comonomers can be polymerized as a microemulsion where fluorinated oil-in-water microemulsion and fluorinated surfactant are present (37–39). The core-shell structure of these self-assembling systems and their distinctive polymerization features along with the range of particle size distribution have been reported (40).

Colloidal dispersants such as cellulose derivatives or vinyl alcohol are generally used in suspension polymerization of VDF to prevent coalescence and agglomeration of particles during polymerization. The polymerization pressure is similar to that of emulsion polymerization. Organic oil-soluble initiators such as peroxides, peroxycarbonates, or peroxypivalates are used depending upon polymerization temperature, which ranges from 20 to 110°C (41–46). The molecular weight is regulated using oil-soluble chain-transfer agents such as dialkyl ethers and dialkyl carbonates. The reactor product is a slurry of suspended particles, usually spheres 15 to 120-μm diameter (41,43).

A suspension polymerization can be carried out using a radical photoinitiator with uv–visible light. Thus, photogeneration of radicals allows a lowering of the polymerization temperature (40). Lowering the polymerization temperature reduces the number of defect structures in PVDF.

Alloys of PVDF and PVDF copolymers with acrylic polymers are produced by a multistage aqueous dispersion polymerization. These intimately mixed polymer particles have found various industrial applications; particularly, in the waterborne high performance coasting application. In the early stages of the polymerization, the fluoropolymer portion is produced under standard condition with 50- to 150-nm particles. In a later stage, acrylic monomers are added to the reactor in the presence of persulfates under atmospheric pressure. The final morphology of the alloy, which ranges from a core-shell to an inter-penetrated

structure to an intimate blend morphology, depends upon the composition of the fluoropolymer particles, the acrylic type, and the feed schedule (47–53).

The nonaqueous media used for VDF polymerization is either fluorocarbons or carbon dioxide under high pressure conditions. Fluorocarbons (54,55) and partially fluorinated hydrocarbons with no significant chain-transfer activities (56) are reported to be a suitable media for VDF polymerization.

VDF polymerization technology based upon super critical or liquid carbon dioxide as polymerization media has been reported (57–62). This technology offers an advantage in the polymer isolation step where a clean dry polymer is produced simply by depressurization. The residual monomer(s) and CO_2 can be recycled back to the reactor. PVDF is not soluble in CO_2 (58–60) and as a result, additional polymeric stabilizers are required to produce stable particles. Adequate CO_2 density for polymerization requires pressure significantly higher (typically >100 bar) than a conventional emulsion polymerization.

Telomerization of VDF in methanol with *tert*-butyl peroxide as the initiator is reported; polymerization kinetics along with telomer characterization are discussed (63). Microwave-stimulated, low pressure plasma polymerization of VDF gives a polymer film that is less than 10 μm thick (64). Highly regular PVDF polymer with minimized head-to-head addition was synthesized (65). Perdeuterated PVDF has also been prepared and described (66). The effectiveness of 1,1,1-trifluoro-2,2-dichloroethane (HCFC-123) as a chain transfer agent producing thermally stable PVDF in emulsion polymerization has been claimed (67).

Polymer Properties

Compared to the softer and mechanically less robust perfluorocarbon polymers, PVDF has high mechanical strength, abrasion resistance, and excellent resistance to both creep under long-term stress and fatigue upon cyclic loading (68,69). It also has excellent thermal stability and resists damage from most chemicals and solvents as well as from ultraviolet and high energy radiation. Typical design properties are shown in Table 3 for the homopolymers. The resin form is not hygroscopic and adsorption pickup is less than 0.05 wt% of surface water under ambient room conditions.

The properties of PVDF homopolymers and copolymers are sensitive to the chemical composition, molecular mass characteristics, and molecular architecture. These attributes are dictated by the polymerization method and ingredients, the method of isolation, and the thermal/mechanical history during isolation and subsequent processing.

From a composition viewpoint, the choice of initiator and chain-transfer agent determines end groups that affect thermal stability. These ingredients also dictate molecular mass characteristics involving the distribution of chain lengths and the molecular weight affecting processing and, ultimately, those properties related to the morphology of the solid polymer. The processing, morphology, properties, and end use performance are affected by the branching, cross-linking, differences in the content of defect structures, and other chain irregularities which exist in the PVDF polymers prepared under different conditions and ingredients. A 1999 study contrasts two commercial PVDF polymers based upon different

Table 3. Design Properties of PVDF Homopolymers[a]

Properties	Value or description
Appearance in film form	Transparent to translucent
Melting transitions, crystalline, °C	155–192
Specific gravity	1.75–1.80
Refractive index, n_D at 25°C	1.42
Mold shrinkage, average %	2–3
Flammability	Self extinguishing, no dripping
Tensile strength, MPa[b]	
25°C	42–58.5
100°C	34.5
Elongation at break, %	
25°C	50–100
100°C	200–500
Yield point, MPa[b]	
25°C	38–52
100°C	17
Creep % 25°C / 13.79 MPa[b], 10,000 h	2–4
Compressive strength, 25°C, MPa[b]	55–90
Modulus of elasticity, 25°C, GPa[c]	
In tension	1.0–2.3 (145–334 E3)
In flexure	1.1–2.5 (160–362 E3)
In compression	1.0–2.3 (145–334 E3)
Izod impact, 25°C, J/m[d]	
Notched	75–235
Unnotched	700–2300
Durometer hardness, Shore D scale	77–80
Heat distortion temperature, °C	
@ 0.455 MPa (psi)	140–168 (20.3–24.4 E3)
@ 1.82 MPa (psi)	80–128 (11.6–18.6 E3)
Abrasion resistance, Tabor CS-17 @ 0.5 kg load, mg/1000 cycles	17.6
Coefficient of sliding friction to steel	0.14–0.17
Thermal coefficient of linear expansion, °C	0.7–1.5 E −4
Thermal conductivity, 25–160°C, W/(m·K)	0.17–0.19
Specific heat, J/(kg·K)	1255–1425
Water absorption, %	0.04
Moisture vapor permeability @ 1 mm thickness, g/(24 h)(m^2)	2.2 E −2
Radiation resistance to Co^{60}, MGy	10–12
Speed of sound, m/s	
Longitundinal	1930
Shear	775
Dielectric constant, 23°C	
1 kHz	12.2
1 MHz	8.9
1 GHz	4.7

[a]Values are ranges for the variety of *commercially* available grades or representative single point values. The values for any given test reflect the specific polymerization process and subsequent thermal/mechanical history of the sample. To assure consistent results in some tests, it is essential to anneal the samples in order to approach a thermodynamically stable morphology. See Ref. 27 for a compilation of VDF-copolymer properties.
[b]To convert MPa to psi, multiply by 145.
[c]To convert GPa to psi, multiply by 145,000.
[d]To convert J/m to ft·lbf/in., divide by 53.38.

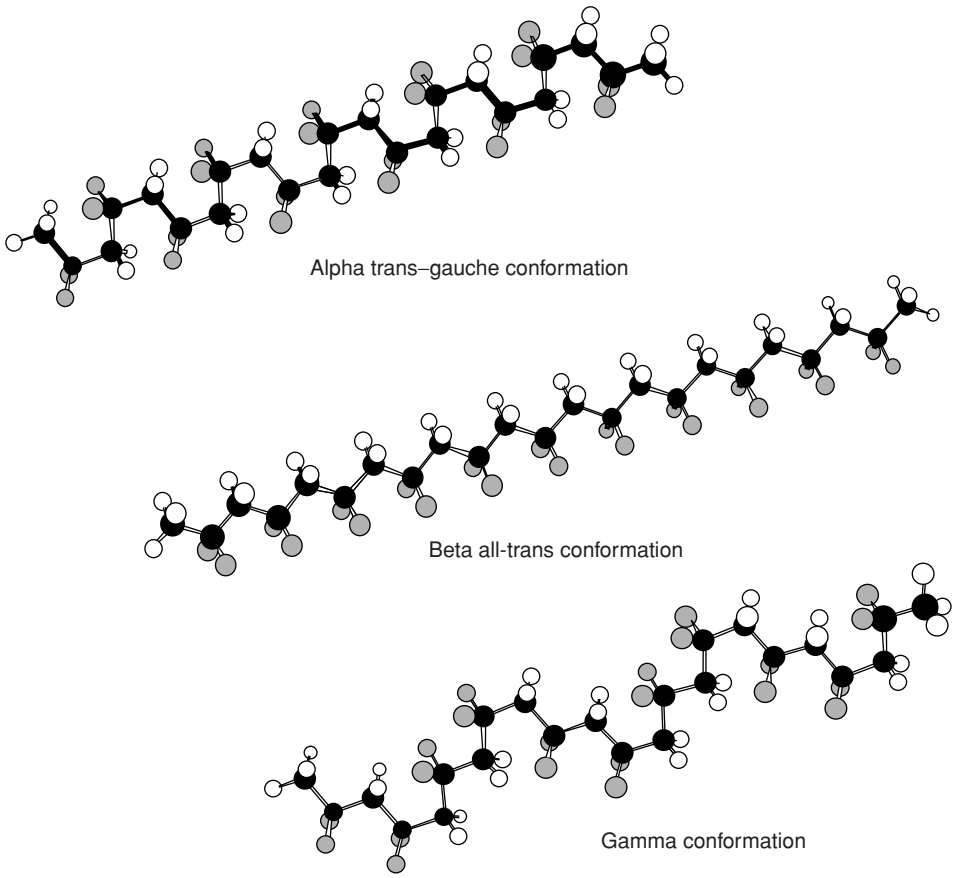

Fig. 1. Main polymorphs of PVDF.

polymerization chemistries (70), revealing differences in end groups and other properties related to composition.

Several of the key properties of PVDF homopolymers and copolymers depend upon the crystalline content and type of crystalline structure. The polymer chains involve long sequences of VDF units and can exist in several conformations. Figure 1 shows the alpha, beta, and gamma forms. The thermodynamically more stable alpha form involves a crankshaft configuration of the chain, which minimizes the steric interference between fluorine atoms along the chain. The beta form places the fluorines along one face of the chain, which is in a zigzag conformation. The gamma form is essentially a distortion of the alpha, where periodically one of the "cranks" is twisted out of the main chain geometry. Two other forms have been identified under very special conditions (71), but these so-called delta and epsilon forms are not typical of the structures existing in normal production or fabrication of parts. The effect of molecular weight and chain end groups on crystal forms of PVDF oligomers has been studied by several techniques (72) with interesting conclusions about the effect of the size of end groups

upon conformational disorder in the crystals. A complex morphology involving the alpha and gamma forms occurs and dominates the spherulitic characteristics of the PVDF when the melted polymer is allowed to solidify at temperatures near the melting point (73). The reorganization rate of metastable crystals in PVDF and HFP-copolymers is dependent upon molecular weight (74).

Amorphous PVDF regions have a density of 1.68 (75), the alpha and gamma polymorphs 1.92 and 1.93, respectively, and the beta polymorphs 1.97 g/cm^3 (76). The density of the homopolymer PVDF cooled quickly from the melt is 1.76–1.78 g/cm^3. The melt density of PVDF homopolymers and VDF/HFP-copolymers is approximately 1.45–1.48 g/cm^3 at 230°C and 1 bar (77), ie a volumetric shrinkage factor of almost 20% occurs in cooling from the melt to the solid.

Depending upon the conditions, the linear PVDF chain configurations crystallize into spherulites that are lamellae of polymer chain segments. The alpha configuration is the thermodynamically stable form and predominates in the solid when molten PVDF is cooled. The beta configuration occurs in mixtures with carbonyl functional polymers or when a PVDF film sample is stretched. The gamma form will develop when solid PVDF is exposed to certain chemicals. The heat of crystallization is high ranging from 50 to 58 J/g. The rates of crystallization are not only dependent upon backbone chain conformation dynamics, but also reflect the polymerization technique, which determines defect structures and end groups as well as molecular mass characteristics. PVDF crystallization may be nucleated by a variety of agents. In the absence of nucleating agents, emulsion PVDF samples show small crystallites developing slowly from the molten state compared to suspension polymer samples, which will show rapid development of very large crystallites under the same thermal conditions (rate of cooling and hold times at temperatures).

Many of the performance related properties (Table 3) in a given application (Table 4) depend upon the crystalline characteristics of the part. Interestingly, the content of defect structures determines the crystalline form; in the range of 11–14% levels, the beta form develops, whereas the alpha predominates at either extreme of this range (71,73,106). A detailed review of the effects of crystallization conditions upon the phases and morphology includes a summary of crystallographic, infrared, and thermal studies as well as related scanning electron microscopic evidence (5). The crystallization behavior of a mixture of PVDF samples, one with a low and the other a high content of defect structures, led to the interesting observation that the blended mixture crystallized faster than crystals formed in the individual samples (107), again emphasizing the importance of defect structures in affecting the properties of PVDF.

The complicated PVDF chain dynamics and the strong thermodynamic driving force to crystallize confer a complex set of intrinsic transitions as a function of temperature, which ultimately are reflected in the physical properties and behavior under various test conditions. The heat of fusion is approximately 100 J/g and depends upon the level of defects in the sample. Thermodynamic data for the amorphous and crystalline PVDF are tabulated at the website web.utk.edu/~athas/databank/vinyl/pvf2

The glass transition (T_g) of the amorphous PVDF regions is in the range of −40 to −30°C, depending upon the sample and test method. Other sub-T_g transitions have been studied recently by dielectric relaxation spectroscopy (108).

Table 4. Applications Profile for PVDF Homopolymers and Copolymers in Key Markets

Market applications	PVDF attributes	Comments
Coatings and paints	Solution characteristics are related to chemical composition and method of polymerization. Some processes utilize dispersions of PVDF particles with latent solvents to solubilize the PVDF at temperatures above ambient room conditions	Differences in solution behavior are exhibited by the various PVDF grades because of intrinsic chain composition (defect structures, end groups, comonomers, etc) and molecular mass characteristics
Binder for long lasting, weather resistant finishes for metals (primed galvanized steel, aluminum) used on sidings, roofing tiles, and other building components (78,79)	Photostability and resistance to radical attack. Film forming at reasonable temperatures. Long term weathering protection achieved at 25-μm film thickness.	These organosol paint formulations utilize inorganic pigments and < 30 wt% acrylic polymers, which enhance adhesion and confer other important attributes for a successful product. Major application worldwide. Thirty years of demonstrated weathering resistance (81). Often referenced as "architectural coatings"
	Formability of coated metal dependent upon coating application and storage conditions. (80)	Powder coating versions have been developed (82,83)
Decorative films for lamination to surfaces; automotive trim applications; aircraft interior surfaces in-mold lining processes (84)	Resistance to weather and chemicals; thermoformable; stain resistance; cleanability. Ability to solvent cast very thin, pigmented formulations onto carrier films, creating extremely smooth surfaces. Extruded films also	Becoming a major U.S. application. Two major film manufacturers. Both homopolymers and copolymer grades utilized to make films (85)
Corrosion resistant coatings tank liners (86)	Chemical resistant and ease of forming relatively thick coatings from liquid systems. Extruded PVDF tubing and sheet; easily thermoformed. Bead welding with PVDF rod to form seamless joints in liners	Primer coating and several applications of liquid system necessary to build to 1–2 mm thickness; drying temperatures around 250°C. Copolymer grades usually used for extruded tank lining sheets for lining tanks

Chemical processing equipment (25)	Note that PVDF may be adequate for high pH environments in applications where the surface degradation and fluoride leaching is not problematic, eg, alkaline waste streams (87)	Differences in chemical stress resistance are related to the different crystal structure of suspension and emulsion PVDF, the latter usually showing better performance
Flexible tubing for deep sea oil transport, (88)	Special PVDF grades are available (ATOFINA) having cold temperature flexibility important to installation conditions, high temperature chemical resistance	Major application. Hot, sulfurous oil at high pressure is a harsh chemical environment. Long service life requirement. Worldwide application
Packing for distillation towers	Chemical resistance, ease of molding complex shapes	Preferred over metal in many chemical processes because of corrosion issues with metals
High purity water systems; semiconductor facilities; pharmaceutical systems	Very low ionic and organic extractables; smooth surfaces inhibit microbial fouling. Operations at 90°C and in ozonated water (89)	Major application for special grades processed in special equipment to achieve low contamination resin
Piping for chemicals	Chemical resistance to strong acids and oxidizers; relatively high temperature stability	Pipe linings and solid pipe products. In one process, a solid PVDF tube with a wall thickness of several mm is hammered to a slightly smaller diameter than original, inserted into steel pipe, and allowed to relax to a tight fit, exemplifying the toughness of PVDF.
Pumps and instrument parts (90)	Chemical resistance at high temperatures Ease of molding complex shapes	Nonporous nature compared to PTFE parts High modulus reinforced compounds available from compounders

(*Continued*)

Table 4. (Continued)

Market applications	PVDF attributes	Comments
Fuel handling systems including underground storage tank systems and automotive fuel lines (91,92)	Very low permeation by hydrocarbons and oxygen containing additives achieved as a very thin barrier layer, typically about 50–250 μm	In general, these products are composites of less expensive polymers with the PVDF layer incorporated as an inner liner or embedded barrier
Electrical and Electronic	Note: High dielectric constant and dielectric loss factor are factors to be considered in any application	PVDF is not suitable as a primary insulation on AC power wiring because of absorption of the electromagnetic field and heating
Jacketing of cables for plenum areas including signaling, communication, and power lines	Flexible PVDF grades with additives as jackets on plenum cables have passed the severe UL910 modified Steiner tunnel test to qualify the products as low smoke and flame propagating assemblies meeting strict specifications	Another major application area for flexible PVDF copolymers only in the United State at this time. European and rest of the world specifications based upon fire testing may lead to further markets worldwide based upon this technology
Insulating compounds for jacketing wire and cable assemblies, cathodic protection, industrial power control systems, high temperature wiring	Radiation cross-linking improves toughness and abrasion resistance in these applications. PVDF copolymer responds readily to electron beam irradiation (93,94)	The compounds usually are mixtures of polymers and additives with PVDF being the major portion. It is the PVDF susceptibility to efficient cross-linking that allows economical processing rates
Speciality Applications		
Microporous membranes	PVDF is one of the few fluoropolymers that can be processed in solution. See Ref. 95 for a typical process and references to past technology	The technology involves casting a PVDF solution onto a surface covered with a nonsolvent, followed by special processing of the paper-like sheet. Extensive literature and patents
Toners	Triboelectric characteristics allowing charging of the carbonaceous powder. Thermoplastic nature important to fusion process. See Ref. 96 for a leading reference	PVDF is an essential ingredient at low levels in almost all commercial toners for photocopiers and many laser printers

Fishing lines and nets, Musical strings (97)	No water absorption; invisible in water; high knot strength; high specific gravity	Japanese application almost exclusively. Nylon monofilaments blended with PVDF have high knot strength and improved surface smoothness (98). Blends with polyethylene fibers (99)
Processing aid for polyolefins	PVDF copolymers at <1000 ppm in typical blown film applications is effective in reducing melt fracture and allowing increased extrusion rates	Developing market for PVDF in competition with established fluoroelastomer products
Monofilament for fabrics used in filtering wood pulp during bleaching	Chemical resistance to bleaching agents and other paper mill process chemicals	PVDF fabric replaced perforated stainless steel 25 years ago because of operational issues with metal corrosion
Lithium ion batteries; separators; electrode binder, (100–102)	Electrochemical stability at over 4 V is key property; high purity; solution casting; ability to cast thin electrodes from very high (>80%) carbon formulations	Relatively new application developing during late 1990s. Several hundred tons market in 2000, mainly in Japan
Piezo- and pyroelectric transducers for motion sensors, hydrophones, audio devices, etc; supercapacitors (103); electrolytic capacitors (104); aircraft interior sound control	Orientation under high electrical fields of the beta crystallites in thin films achieves high sensitivity to changes in shape because of pressure (piezo) or temperature (pyro). Considered a ferroelectric material because the remnant polarization is stable. Piezo film for active cancellation of noise in sound absorbing foam laminate	Very small volume application with significant impact over the years in the development of sensitive devices for military as well as security applications. Major research efforts since 1970s for this reason. Russian facilities had significant PVDF development efforts during the cold war “Foam-smart skin” concept (105)

These studies also indicate correlations with other techniques and identify a 50°C molecular chain transition as probably related to the amorphous region at the surfaces of crystals (109). Permeation characteristics are very sensitive to these transitions as well as the usual environmental parameters (110). Water molecules trapped in the amorphous regions are monomeric, not associated and clustered as in the liquid state (111).

The crystalline content in homopolymer PVDF samples that solidify quickly from the molten state is typically near 50%, increasing with time to higher levels approaching as a maximum 70%, again dependent upon the method of preparation and finishing. Because of the high crystallinity, the hardness or resistance to indentation of solid PVDF samples is retained up to within 10–15°C of the softening and melting transition region. Copolymers of VDF show lower levels of crystallinity (25–40%) depending upon the level of the comonomer and the method of preparation.

Unlike most crystalline polymers, PVDF exhibits thermodynamic compatibility with other polymers (112). Blends of PVDF and poly(methyl methacrylate) (PMMA), are miscible over a wide range of compositions (113–115). A variety of analytical techniques indicates specific hydrogen bonding between the oxygen of the carbonyl group and the acidic hydrogens along the PVDF chain (116). The same phenomenon explains the types of effective solvents for PVDF: cyclohexanone, dimethylsulfoxide, dimethylacetamide, phosphate esters, and other liquids with carbonyl functionality. Generally, the morphology of the polymer blends becomes even more complex than for the homopolymer PVDF because the polar or hydrogen-bonding interactions are not strong enough to overcome the strong thermodynamic driving force for PVDF crystallization. Studies indicate that the beta PVDF chain conformation develops in blends with acrylic polymers (116,117). Recently, blends with polymers containing imide moieties have been claimed (118). Ternary blends of PMMA, poly(vinyl acetate), and PVDF have been studied as a completely miscible system (119). Addition of 10–30 wt% PMMA improves the transparency of the PVDF films or coatings in the uv–visible spectrum. The relationship between the optical transmission and compatibility of PVDF/PMMA blends is reported (120); in general, films of the blends with at least 15 wt% PMMA are very transparent (>90% transmissivity).

Fabrication and Processing

PVDF is available commercially in a wide range of melt flow rates and with various additives to enhance processing or end use properties. A variety of forms are available—latex and fine powders from emulsion processes and granules from either suspension or emulsion processes.

In melting processes, it is essential to consider the full range of shear rate characteristics of the polymer. Moreover, polymerization techniques have been developed which make different versions of the same composition and polymerization ingredients behave rheologically differently. The rheological characteristics specified for a given commercial PVDF grade should be a consideration in developing a melt-based process to produce parts. Figure 2 shows the different shear

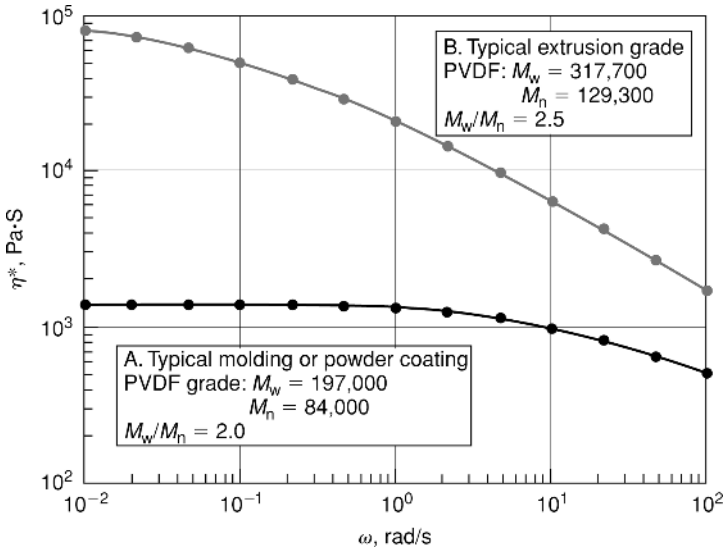

Fig. 2. Rheological profiles for two commercial PVDF grades. The melt rheology converges at high shear rates above 100 rad/s.

behavior of two homopolymer PVDF samples prepared by polymerization with different recipes. Hence, a process such as fusion of powders to a contiguous film requires Newtonian flow at zero shear conditions (curve A), which is achieved by a narrow molecular weight distribution and low molecular weight mass. A high speed extrusion generally would proceed with less surface fracture or melt instabilities given a broad molecular weight distribution or shear-thinning melt, which is sample B, having a high molecular weight mass.

Both homopolymers and copolymers may be shaped from the molten state without extrusion aids or thermal stabilizers. A broad operating window exists for melt processing between the points when crystallites begin to melt and the onset of thermal decomposition. Figure 3 superimposes the thermal gravimetric analysis (tga) curve and the differential scanning calorimeter (dsc) graph for the melting phenomenon. Conventional equipment is used in processing molten PVDF. Longevity of equipment can be extended with special alloys on surfaces that contact the melt, but usually are not necessary.

All the common extrusion and molding techniques can be used to process PVDF into shapes. Typical molding temperatures in the cylinder and nozzle are 180–240°C for injection types, and for molds are 50–90°C. As a crystalline polymer, it shows relatively high mold shrinkage of about 3%, reflecting the high degree of crystallization and the difference between the solid and molten densities as mentioned earlier. In most cases, it is prudent to develop appropriate post-forming annealing cycles, typically 15°C or more above the crystallization temperature (Table 3), to stabilize the parts. Hence, the design of molds requires careful considerations of final part tolerances before cutting metal.

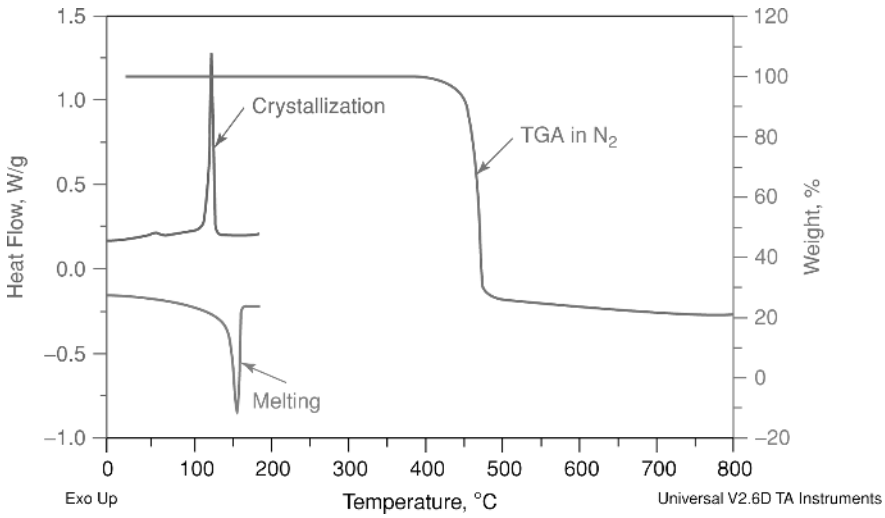

Fig. 3. Thermal gravimetric analysis and differential scanning calorimetry of a PVDF homopolymer.

PVDF is not hazardous under typical melt processing conditions. At temperatures approaching 300°C, the onset of a thermal degradation will be evident as a darkening of the resin. This discoloration arises from the dehydrofluorination reaction forming the conjugated polyene structures that absorb strongly in the visible spectrum. It is helpful, in fact, as a very sensitive indicator of overheating. Immediate remedial action should be taken to reduce the heat. At temperatures well above 300°C and approaching 350°C, thermal decomposition accelerates, leading to release of hydrogen fluoride. The tga curve (Fig. 3) shows that the decomposition is essentially quantitative with respect to carbonaceous residue and hydrogen fluoride evolution at about 400°C.

Before ingredients are added to PVDF to make compounds, a thorough laboratory study should be conducted in properly vented ovens at temperatures that might be encountered in the range of operating conditions. Certain additives such as titanates and silicates catalyze the thermal decomposition of molten PVDF at temperatures lower than typical for the natural resin, leading to dangerously high pressures in the equipment because of by-product gases. Generally, metal oxides catalyze degradation at high processing temperatures, eg, the oxides of titanium, manganese, and iron. Resin producers should be consulted for melt processing recommendations whenever additives are utilized in compounds. Frequently, the compounds include an acid-scavenging agent like zinc or calcium oxide to react with any hydrogen fluoride that might form during processing.

Coextrusion and lamination processes have been described extensively in the patent literature. The technology usually involves multilayer structures utilizing, as an adhesive layer, a compound of PVDF with another material, which provides the bonding to the substrate. In this way, the full benefits of a thin film of PVDF may be realized (121). Another approach using acrylic alloys with PVDF

sometimes achieves adherence to various substrates without the "tie layer" necessary for the pure PVDF film (122). The full breadth of options available by these technologies to protect surfaces with weatherable PVDF surfaces has been reviewed (123). Surface PVDF layers on polyolefins has been a particular technology of interest with respect to suitable finishes in cost effective parts for exterior automotive and agricultural equipment applications (124).

Powder grades usually are used whenever compounds are prepared in order to achieve homogeneity of the blends. Latex grades are utilized in some applications where it is possible to dry and fuse the material under conditions producing a coating upon the substrate, typically fabrics.

Solid PVDF parts may be joined by various fusion methods; the manufacturers should be consulted for recommendations. Fusion methods are preferred over solvent joints because the strength is much greater and for the ease in preparation. Vibration welding has been practiced. Because of the high dielectric loss, ie absorption of microwave electromagnetic radiation, rf-induction heating methods have been used to soften or melt PVDF parts. Welds may be particularly susceptible to stress cracking in strongly basic solutions where discoloration develops as a result of dehydrofluorination (7,8).

Economic Aspects

The extensive use of PVDF has developed in spite of the relatively high price and specific gravity compared to the commodity nonfluoroplastic polymers and the widely known thermoplastic engineering resins. Compared to all other common fluoropolymers, PVDF is the least expensive on a volume basis. Over the last decade the market pricing of standard PVDF grades has remained remarkably constant around $14–15/kg. See www.plasticstechnology.com for updated pricing comparisons.

Health and Safety Factors

PVDF is nontoxic, odorless, and has no taste. Extraction testing has led to a listing with the FDA as being suited to single use contact with food (125); this applies to both homopolymer and copolymers with low content of HFP (<20 wt%). Various manufacturers have qualified specific grades with appropriate agencies and standards organizations for a variety of applications including potable water systems, home construction, medical applications, food contact, and packaging. Some of the agencies or standards involved are the U.S. Department of Agriculture, 3A Sanitary Standards, Food & Drug Administration, National Sanitation Foundation, U.S. *Pharmacopeia* USP Class 6, and others. See the producers websites for specific applications having the appropriate approvals.

PVDF powders are not explosive, but the MSDS guidelines for personal protective equipment should be followed. The powder is not removed readily by dry cleaning; it should be brushed from dark clothing. Storage of large quantities of PVDF should adhere to local regulations regarding possible hazards in fire environments.

Uses

The major applications of PVDF are summarized in Table 4. Since the 1996 version of this encyclopedia series (3), an increasing interest has developed in the use of PVDF as a binder and polymeric separator in lithium ion batteries. The literature since 1998 also has numerous references to the use of PVDF in fuel cells, eg, in membranes (102) and electrodes (126); it is a technology anticipated to become a significant factor in electrical vehicles before 2010. These two technology areas, both of which reflect the electrochemical stability and chemical resistance attributes of PVDF, may lead to major applications for PVDF. In a related application area, the use of PVDF films for electrostatic capacitors is being investigated because it has a very high DC current breakdown voltage (770 MV/m) and a large maximum energy density capability (28.9 J/cm). Both attributes are related to the very high dielectric constant (Table 3) (103). Note that some PVDF grades are more suited to this application by virtue of purity than others are because ionic impurities lead to dielectric breakdown at relatively low voltages.

Several Japanese patent applications since 1992 discuss the processing technology necessary to manufacture monofilaments for fishing lines and nets or other monofilament applications, which must have extremely high tensile strength and knot strength (127). It is claimed that PVDF monofilaments are not visible to the fish in seawater (refractive index $\approx$ 1.31 compared to 1.42 for homopolymer PVDF).

Since the original Timmerman patent in 1964 (128) on the radiation response of PVDF, the use of PVDF in wire and cable applications has increased dramatically with electron beam irradiation as the key process step to cross-link the PVDF compounds for higher temperature capability (93,94). In general, the copolymers cross-link more efficiently than homopolymer grades. A certain PVDF homopolymer, which is polymerized at high temperatures with organic peroxides, seems to be an exception among the various homopolymer grades. Presumably, because of the particular polymerization process, this resin has been used as insulation on signal wiring since the late 1970s; it can be extruded at very high rates and cross-links more readily under ebeam irradiation than other homopolymer grades. PVDF polymers cannot be considered a generic grouping like polyethylene, which according to density or polymerization catalyst have essentially the same properties. PVDF properties and suitability for any given application are a sensitive function of the polymerization and isolation methods of the polymer, which differ for each producer.

Table 3 indicates the excellent radiation resistance to 61 Mev beta emissions from cobalt-60. A process to etch "tracks" of high energy, heavy nuclei in PVDF films has been developed in order to make nuclear track microfilters (129).

Another recent advance in PVDF technology involves coating applications using the acrylic–fluoropolymer lattices which are produced by sequential polymerizations (see as given earlier). Initial reports indicate improved paint properties than heretofore produced by mixing and blending techniques (130).

As space exploration, development of speciality military and oceanic equipment, and advances in telecommunication equipment and connection systems

evolve during the next millennium, the use of PVDF will expand because of its unique set of properties and useful functions in various designs. In addition, the ease of processing by a variety of techniques into complex shapes and relatively simple and straightforward fabrication methods will be significant factors in choosing PVDF for these future applications.

BIBLIOGRAPHY

"Vinylidene Fluoride Polymers" in *EPST* 1st ed., Vol. 14, pp. 600–610, by J. Dohany, A. A. Dukert, and S. S. Preston II, Pennwalt Corp.; in *EPSE* 2nd ed., Vol. 17, pp. 532–548, by J. E. Dohany and J. S. Humphrey, Pennwalt Corp.; in *EPST* 3rd ed., Vol. 4, pp. 510–533, by J. S. Humphrey and R. Amin-Sanayei, Atofina Chemicals Inc.

CITED PUBLICATIONS

1. J. E. Dohany in R. B. Seymour and G. S. Kirshenbaum, eds., *High Performance Polymers: Their Origin and Development*, Elsevier Science Publishing Co., New York, 1986, p. 287.
2. C. K. Brennen, in *Fluoropolymer 2000, Conference Sponsored by the ACS Division of Polymer Chemistry, Oct. 15–18, 2000.*
3. J. E. Dohany, in J. I. Kroschwitz, ed., *Encyclopedia of Chemical Technology*, 4th ed., Vol. **11**, Wiley-Interscience, New York, 1994 p. 694.
4. B.-J. Jungnickel, *Polymeric Materials Encyclopedia*, CRC Press, New York, Vol. **11**, 1996 pp. 7115–7127.
5. R. Gregório Jr. and co-workers, Ref. 4, pp. 7128–7138.
6. H. A. Nalwa, Inc., *Ferroelectric Polymers (Chemistry, Physics, and Applications)*, Marcel Dekker, Inc., New York, 1995.
7. P. Hinksman, D. H. Isaac, and P. Morrissey, *Polym. Degrad. Stab.* **68**(2), 299–305 (2000).
8. P. Maccone, G. Brianti, and V. Arcella, *Polym. Eng. Sci.* **40**(3), 761–767 (2000).
9. G. J. Ross and co-workers, *Polymer* **41**(5), 1685–1696 (2000).
10. U.S. Pat. 3178399 (Apr. 13, 1965), E. S. Lo (to 3M Co.).
11. Eur. Pat. Appl. 456019 (Nov. 13, 1991), L. A. Barber (to Elf Atochem North America, Inc.).
12. U.S. Pat. 4851479 (July 25, 1989), J. Blaise and P. Kappler (to Elf Atochem SA).
13. U.S. Pat. 4472557 (Sept. 18, 1984), C. Kawashima and T. Yasumura (to Central Glass Co., Ltd.).
14. Brit. Pat. 827308 (Feb. 3, 1960) (to 3M Co.).
15. B. Ameduri and B. Boutevin, *Organofluorine Chemistry: Fluorinated Alkenes and Reactive Intermediates*, Springer, Berlin, 1997, pp. 165–233; Top. Curr. Chem. Vol. **192**,
16. B. Ameduri and B. Boutevin, *J. Fluorine Chem.* **104**, P53–62 (2000)
17. B. Ameduri and co-workers, *Macromolecules* **32**, 4544–4550 (1999).
18. Eur. Pat. Appl. EP 751157 B1 (July 14, 1999), H. Ikashio, K. Horie, and F. Suzuki (to Kureha KKKK).
19. U.S Pat. 4076929 (Feb. 29, 1978), J. Dohany (to Pennwalt Corp.).
20. U.S Pat. 4128517 (Dec. 5, 1978), N. Kydonieus (to Pennwalt Corp.).
21. U.S Pat. 4360652 (Nov. 23, 1982), J. Dohany (to Pennwalt Corp.).
22. U.S Pat. 4569978 (Feb. 11, 1986), L. Barber (to Pennwalt Corp.).

23. World Pat. 9838242 (Aug. 3, 1998), R. Wille and M. Burchill (to Elf Atochem North America, Inc.).
24. Eur. Pat. Appl. 456019 (Nov. 13, 1991), L. Barber (to Atochem North America, Inc.).
25. D. A. Seiler, in J. Scheirs, ed., *Modern Fluoropolymers*, John Wiley & Sons, Inc., New York, 1997, p. 487.
26. G. Hougham, K. Johns, P. E. Cassidy, and T. Davidson, *Fluoropolymers: Synthesis and Properties*, Plenum Press, New York, 1999.
27. C. Tournut, in J. Scheirs, ed., *Modern Fluoropolymers*, John Wiley & Sons, Inc., New York, 1997, p. 577.
28. World Pat. WO 9838687 (Sept. 3, 1998), R. A. Wille and M. T. Burchill (to Elf Atochem North America, Inc.).
29. S. Russo and co-workers, *Polymer* **34**, 4777 (1993).
30. M. Gorlitz and co-workers, *Angew. Makromol. Chem.* **29/30**, 137 (1973).
31. K. Tashiro, in H. Nalwa, ed., *Ferroelectric Polymers (Chemistry, Physics, and Applications)*, Marcel Dekker, Inc., New York, 1995, pp. 97–99.
32. P. Maccone, G. Brinati, and V. Arcella, *Polym. Eng. Sci.* **40**, 761–767 (2000).
33. T. F. McCarthy and co-orkers, *J. Appl. Polym. Sci.* **70**, 2211–2225 (1998).
34. P. Bonardelli, G. Moggi, and S. Russo, *Makromol. Chem. Suppl.* **10**11, 11–23 (1985).
35. World Pat. 9717381 (June 15, 1997), T. F. McCarthy, Y. Chen, and E. J. Raional (to Allied Signal Inc.).
36. World Pat. 9702300 (July 23, 1997), W. B. Farnham and co-workers (to E. I. du Pont de Nemours and Co., Inc.).
37. Eur. Pat. 722882 (May 22, 1996), J. Abusleme and A. Chittofrati (to Ausimont S.P.A., Italy).
38. Eur. Pat. Appl. 816397 (Jan. 7, 1998), G. Brinati, P. Lazzari, and V. Arcella (to Ausimont S.P.A.).
39. Eur. Pat. 570762 (Nov. 24, 1993), V. Arcella and co-workers (to Ausimont S.P.A.).
40. E. Giannetti, A. Chittofrati, and A. Sanguineti, *Chim. Ind. (Milan)* **79**, 611–618 (1997).
41. Eur. Pat. 526216 (Feb. 3, 1993), H. Wakamori, F. Suzuki, and K. Horie (to Kureha Chemical Industry Co., Ltd.).
42. Eur. Pat. 423097 (April 17, 1991), Lasson (to Solvay et Cie.).
43. Eur. Pat. 417585 (Oct. 20, 1991), Lasson (to Solvay et Cie.).
44. Jpn. Pat. 87286707 (Nov. 12, 1987), K. Ihara, Y. Noda, and T. Amano (to Daikin Industries, Ltd.).
45. Eur. Pat. 215710 (Mar. 25, 1987), J. Blaise (to ATO CHEM SA).
46. Fr. Pat. 2542319 (Apr. 14, 1984), J. Dumoulin (to Solvay et Cie.).
47. Eur. Pat. 695766 (June 7, 1996), J. Abusleme, P.A. Guarda, and P.R. De (to Ausimont S.P.A.).
48. World Pat. 9921921 (May 6, 1999), N. Tsuda, and co-workers (to Daikin Industries, Ltd.).
49. World Pat. 9903900 (Jan. 28, 1999), S. Gaboury and X. F. Drujon (to Elf Atochem North America, Inc.).
50. Jpn. Pat. 08170045 (July 2, 1996), K. Nishiwaki, T. Shimizu, and M. Kato (to Japan Synthetic Rubber Co. Ltd.).
51. Eur. Pat. 360575 (Mar. 28, 1990), M. Kato and co-workers (to Japan Synthetic Rubber Co., Ltd.).
52. Ger. Pat. 2952457 (July 3, 1980), K. Kido, F. Suzuki, and K. Kushida (to Kureha Chemical Industry Co., Ltd.).
53. U.S Pat. 4141873 (Feb. 27, 1982), J. Dohany (to Pennwalt Corp.).

54. World Pat. 0047641 (Aug. 17, 2000), H. Saito and co-workers (to Daikin Industries, Ltd.).
55. Ger. Pat. 1806427 (May 16, 1969), D. P. Carlson (to E. I. du Pont de Nemours & Co., Inc.).
56. World Pat. 9948937 (Sept. 30, 1999), R. Kruger, G. Heilig, and C. Sommerfeld (to Bayer Aktiengesellschaft).
57. Eur. Pat. 964009 (Dec. 15, 1999), P. D. Brothers (to E. I. du Pont de Nemours & Co. Inc.).
58. P. A. Charpentier and co-workers, *Macromolecules* **32**, 5973–5975 (1999).
59. B. J. Briscoe and co-workers, *J. Polym. Sci., Part B: Polym. Phys.* **36**, 2435–2447 (1998).
60. C. A. Mertdogan, T. P. DiNoia, and M. A. McHugh, *Macromolecules* **30**, 7511–7515 (1997).
61. World Pat. 9628477 (Sept. 19, 1996), J. M. DeSimone and T. Romack (to University of North Carolina at Chapel Hill).
62. U.S. Pat. 5674957 (Oct. 7, 1997), J. M. Desimone and T. Romack, (to University of North Carolina at Chapel Hill).
63. B. Ameduri and co-workers, *Polym. Prepr. (Am. Chem. Soc., Div. Polym. Chem.)* **39**, 816–817 (1998).
64. Eur. Pat. 403915 (Dec. 27, 1990), J. Kammermaier and G. Rittmayer (to Siemens AG).
65. U.S. Pat. 4438247 (Mar. 20, 1984), R. E. Cais (to AT&T Technology).
66. R. E. Cais and J. M. Kometani, *Macromolecules* **17**, 1887 (1984).
67. Eur. Pat. Appl. EP 655468 (May 31, 1995), V. Arcella and co-workers (to Ausimont S.P.A.).
68. P. E. Bretz, R. W. Hertzberg, and J. A. Manson, *Polymer* **22**, 1272–1278 (1981).
69. S. Castagnet, J.-L. Gacougnolle and P. Dang, *Mater. Sci. Eng. A* **276**(1/2), 152–159 (2000).
70. S. M. Jo and co-workers *Polymer (Korea)* **23**, 800–808 (1999)
71. A. J. Lovinger, *Macromolecules* **15**, 40 (1982).
72. P. Herman and co-workers, *Polymer* **38**(7), 1677–1683 (1997).
73. R. Gregorio and R. C. Capitao, *J. Mater. Sci.* **35**, 299–306 (2000).
74. L. Judovits and S. M. Dounce, in *57th Annu. Tech. Conf.—Soc. Plast. Eng.*, Vol. 2, 1999, pp. 2334–2339.
75. K. Nakagawa and Y. Ishida, *Koloid Z. Z. Polym.* **251**, 103 (1973).
76. R. Hasagawa and co-workers, *Polym. J.* **3**, 600 (1972).
77. N. Mekhilef, *J. Appl. Polym. Sci.* **80**, 230–241 (2001).
78. R. A. Iezzi, *Modern Fluoropolymers*, John Wiley & Sons, Inc., New York, 1997, 271–299.
79. J. Scheirs, S. Burks, and A. Locaspi, *Trends Polym. Sci.* **3**(3), 74–81 (1995).
80. K. Kawanishi, *Hyomen Gijutsu* **48**(8), 811–814 (1997).
81. J. L. Perillion and E. J. Bartoszek, *Eur. Coatings J.* 277–283 (Apr. 1995).
82. U.S. Pat. 5739202 (Apr. 14, 1998), R. L. Pecsok (to Pennwalt Corp.).
83. U.S. Pat. 6063855 (May 16, 2000), R. L. Pecsok and J. E. Dohany (to Pennwalt Corp.).
84. Jpn. Pat. 09193237 A2 (July 29, 1997), M. Hattori, H. Yamada, and I. Ishii (to Mitsubishi Chemical Ind. Ltd.).
85. World Pat. WO 9640449 (Dec. 19, 1996), M. D. Flynn and K. Truog (to Avery Dennison Corp.).
86. G. A. Glein, in *Semicond. Pure Water Chem. Conf., 15th (UPW & Chemical Proceedings), Balazs Analytical Laboratory, 1996*, pp. 125–136.
87. P. Hinksman, D. H. Isaac, and P. Morrissey, *Polym. Degrad. Stab.* **68**, 299–305 (2000).
88. F. Dawans, J. Jarrin, T. Lefevre, and M. Pelisson, in *Proceedings of 1986 Offshore Technology Conference, Paper No.: OTC-5231, Houston, Tex. May 1986; API*

Recommended Practice 17B: Recommended Practice for Flexible Pipe, 2nd ed., Section 6.2.2, "Polymer Materials," American Petroleum Institute, Washington, D.C., 1998.
89. T. H. Meltzer, *Pharm. Technol.* **21**(3), 90–98 (1997).
90. D. Knight, *Chem. Eng.* **104**(4), 151 (1997).
91. Eur. Pat. Appl. EP 673762 A2 (Sept. 27, 1995), S. Roeber, H. Jadamus, and H. Ries (to Hüls Aktiengesellschaft).
92. EP 729830 (Sept. 4 1996), S. Roeber and H. Ries (to Hüls Aktiengesellschaft).
93. B. J. Lyons, in J. Scheirs, ed., *Modern Fluoropolymers*, John Wiley & Sons, Inc., New York, 1997, p. 335.
94. WO 2000017889 A1 (Mar. 30, 2000), G. H. Rodway (to Raychem Ltd.).
95. U.S. Pat. 6013688 (Jan. 11, 2000), M. M. Pacheco and J. F. Pacheco (to Corning Costar Corp.).
96. J. M. Crowley, C. Snelling, and D. Mashtare, *J. Imaging Sci. Technol.* **40**, 285–290 (1996).
97. JP 09146541 A2 (June 6, 1997), H. Ueba (to Kureha Gosen).
98. JP 10331033 (Dec. 15, 1998), Y. Yamamoto (to Furukawa Electric Co., Ltd.).
99. JP 2000017518 A2 (Jan. 18, 2000), T. Soga (to Mitsubishi Chemical Ind.).
100. U.S. Pat. 5540741 (July 30, 1996), A. Godz and co-workers (to Bell Communications Research, Inc.).
101. T. Nagatomo, C. Ichikawa, and O. Omoto, *J. Electrochem. Soc.* **134**, 305 (1987).
102. PSSA/PVDF Polymer Electrolyte Membranes for CH_3OH Fuel Cells, NASA Tech Briefs, June 1999, p. 54.
103. B. E. Conway, *Electrochemical Supercapacitors*, Kluwer Academic/Plenum Publishers, New York, 1999, p. 669.
104. M. Ishikawa, M. Morita, and Y. Matsuda, in *Proc.—Electrochem. Soc. 96-25 (Electrochemical Capacitors II)* 1997, pp. 325–335
105. C. Guigou and C. R. Fuller, in *Proc. SPIE-Int. Soc. Opt. Eng. (Industrial and Commercial Applications of Smart Structures Technologies) 3044,* pp. 68–78 (1997).
106. K. E. Cais and N. J. Sloane, *Polymer* **24**, 179 (1983).
107. J. Datta and A. K. Nandi, *Polymer* **39**, 1921–1927 (1998).
108. A. Korzhenko, F. Beaume, and B. Ernst, in *Proceedings of the 28th North American Thermal Analysis Society*, Oct. 2000, pp. 184–191.
109. Z. Liu, P. Marechal, and R. Jerome, *Polymer* **38**(19), 4925–4929 (1997).
110. S. Lee and K. S. Knaebel, *J. Appl. Polym. Sci.* **64**(3), 455–492 (1997).
111. H. Kusanagi, *Chem. Lett.* (7), 683–684 (1997).
112. D. R. Paul and J. W. Barlow, *J. Macromol. Sci., C: Rev. Macromol. Chem.* **18**, 109 (1980).
113. J. S. Noland and co-workers, *Adv. Chem. Ser.* **99**, 15 (1971).
114. J. Mijovic, H.-L. Luo, and C. D. Han, *Polym. Eng. Sci.* **22**, 234 (1982).
115. H. Yoshida, *J. Therm. Anal.* **49**(1), 101–105 (1997).
116. K. J. Kim, Y. J. Cho, and Y. H. Ho, *Vib. Spectrosc.* **9**(2), 147–59 (1995).
117. N. Tsutsumi, M. Terao, and T. Kiyotsukuri, *Polymer* **34**(1), 90–4 (1993).
118. U.S. Pat. 5959022 (Sept. 9, 1999), S.-C. Lin and S. J. Burks (to Ausimont Inc.).
119. Q. Guo, *Eur. Polym. J.* **32**, 1409–1413 (1996).
120. H. Horibe and F. Baba, *Nippon Kagaku Kaishi* **2**, 115–120 (2000).
121. U.S. Pat. 4317860 (Mar. 2, 1982), A. Strassel (to Atochem).
122. J. S. Humphrey and B. Simkin, in *Society of Plastics Engineers Vinyl RETEC 97*, Oct. 15, 1997.
123. D. Silagy, P. Bussi, and G. Marot, *J. Fluorine Chem.* **104**(1), 79–86 (2000).
124. Jpn. Pat. 08336937 A2 (Dec. 24, 1996), T. Ogura and co-workers (to Japan Synthetic Rubber Co. Ltd.).

125. *PVDF homopolymer: "Articles or component of articles intended for repeated use in contact with food", 21 CFR 177.2510; VDF copolymers: "Rubber articles intended for repeated use in food contact applications," 21 CFR 177.2600.*
126. U.S. Pat. 5783325 (July 21, 1998), I. Cabasso, Y. Yuan, and X. Xu (to The Research Foundation of New York).
127. Jpn. Pat. 9291215 (Mar. 24, 1990), Nishikawa, H. Nakada, and T. Sato (to Toray K.K.); Jpn. Pat. 10052199 (Feb. 24 1998), Y. Nakano, S. Ohira, and T. Mizuno (to Kureha Chem. Co.); Jpn. Pat. 11012850 (Jan. 19, 1999), K. Amano and M. Okano (to Toray Monofilament Co.); Jpn. Pat. 2000192327 (July 11, 2000), K. Amano and co-workers (to Toray Monofilament Co.).
128. U.S. Pat. 3142629 (July 28, 1964), R. Timmerman (to Radiation Dynamics).
129. C. D. Zhao, P. Vater, and R. Brandt, *Nucl. Tracks Radiat. Meas.* **19**, 829–832 (1991).
130. R. Iezzi, S. Gaboury, and K. Wood, *Acrylic—Fluoropolymer Mixtures and Their Use in Coatings*, Elsevier Science S. A., Ireland, 2000, pp. 1–4, 53–58. Progress in Organic Coatings, Vol. **40**.

J. S. HUMPHREY
R. AMIN-SANAYEI
Atofina Chemicals Inc.

VISCOELASTICITY

Introduction: Perspectives on the Fundamentals of Polymer Viscoelasticity

Viscoelasticity is a phenomenon that has been known since the middle of the nineteenth century when workers such as Weber (1), the Kohlrausches (2), and others were interested in using natural fibers, such as silk, to hold needles in measuring devices such as ammeters. They found hysteretic and time-dependent effects that were difficult to explain fully and to characterize. Later, Boltzmann (3) developed his superposition principle and linear viscoelasticity began to have a formal framework for understanding the phenomenology of the inelastic effects observed earlier (4). While other early pioneers such as Andrade (5) and Zener (6) observed anelasticity or viscoelasticity in metals, the real impetus for understanding viscoelasticity came with the commercial development in the middle of the twenieth century of high molecular weight polymers. One reason for this is that polymers exhibit non-Newtonian behavior in the melt state, which is attributable to both elastic effects and shear-rate-dependent viscosity. This leads to important time and rate effects during the processing of polymers. In addition, once processed, polymers are generally used at less than 200 K from the glass-transition temperature. Hence, even in the "solid-like" state, polymeric materials exhibit time- and frequency-dependent mechanical (and other) properties that have been categorized as viscoelastic. In the current work, the linear and nonlinear viscoelastic responses of polymers from both phenomenological and molecular

views are surveyed. An overview of the viscoelastic behavior of polymers in solution, melt, glassy, and semicrystalline states is provided.

Material Functions—Linear Viscoelasticity. One of the most important aspects of both the phenomenological and the molecular theories of viscoelasticity is the ability to characterize the *material functions*. The material functions are the properties that allow one to relate the stress response to a strain (deformation) history and vice versa through a *constitutive* equation. In linear viscoelasticity theory, generally isotropic descriptions are dealt with; that is, the properties are the same in all directions. However, a material may be anisotropic and still have properties that vary with the direction of the test (7). Here only the isotropic case is considered and it is recognized that straight forward extensions can be made to the anisotropic case. In addition, only homogeneous materials, for which the properties are the same at all points within the material, only are discussed.

Stress and Strain Definitions. As remarked, the material functions relate the stress and strain responses of the material through a constitutive equation. For the elastic material, there is no time dependence and the relationships are relatively simple. In the case of linear viscoelasticity, equations that take into account the time history of the stresses or strains are required. First, stress and strain are defined.

The infinitesimal strain tensor is defined in various ways; here the notation of Timoshenko and Goodier (8) is adopted in terms of the displacements u_i of a material element and as depicted in Figure 1a.

$$\varepsilon_{ij} = \frac{1}{2}\left(\frac{\partial u_i}{\partial x_j} + \frac{\partial u_j}{\partial x_i}\right) \tag{1}$$

and the full strain matrix in terms of the ε_{ij} is written as

$$\varepsilon_{ij} = \begin{bmatrix} \varepsilon_{11} & \varepsilon_{12} & \varepsilon_{13} \\ \varepsilon_{21} & \varepsilon_{22} & \varepsilon_{23} \\ \varepsilon_{13} & \varepsilon_{23} & \varepsilon_{33} \end{bmatrix} \tag{2}$$

Similarly, the stress tensor can be defined in terms of the forces acting on the faces of an element and these are given by the following expression (see Fig. 1b):

$$\sigma_{ij} = \begin{bmatrix} \sigma_{11} & \sigma_{12} & \sigma_{13} \\ \sigma_{21} & \sigma_{22} & \sigma_{23} \\ \sigma_{13} & \sigma_{23} & \sigma_{33} \end{bmatrix} \tag{3}$$

Note that when $i \neq j$, it is common to write the shear strain $\gamma_{ij} = 2\varepsilon_{ij}$ and shear stress $\tau_{ij} = \sigma_{ij}$. In addition, $\gamma_{ij} = \gamma_{ji}$ and $\tau_{ij} = \tau_{ji}$.

Elastic Material Functions. The material functions that are used here for an isotropic, elastic material are the shear modulus G, the extensional modulus E, the bulk modulus K, and the Poisson's ratio ν. However, any two of these provides the full set of information needed to describe such a material, as they are

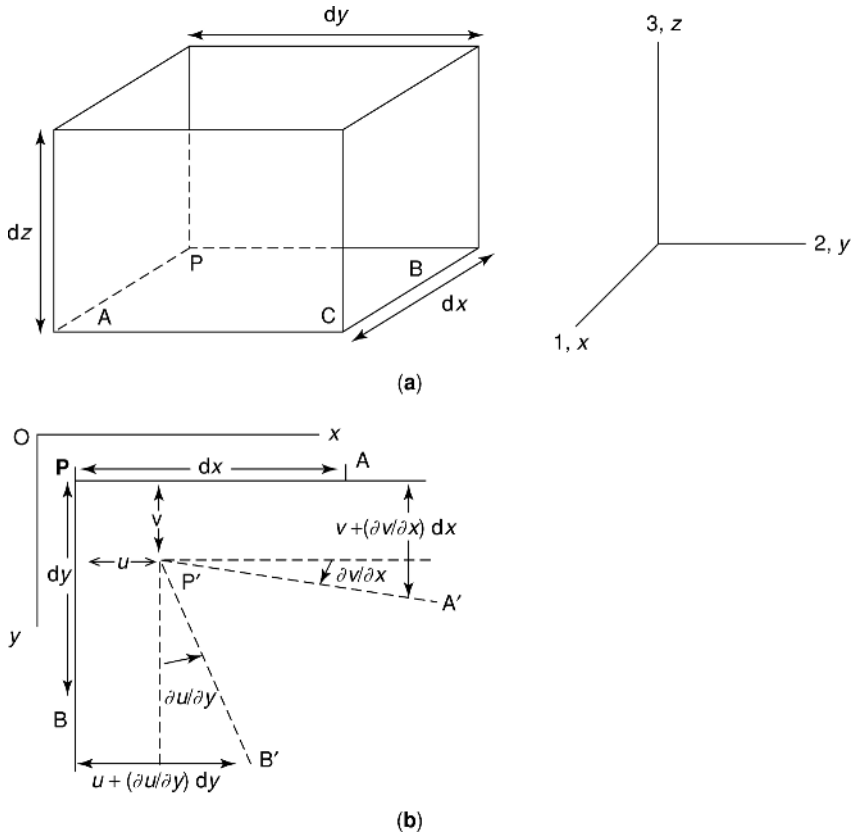

Fig. 1. (**a**) Three-dimensional depiction of elementary material point (dx, dy, dz) and the two-dimensional sketch of the displacements in the x and y directions of the cube that define the strains. The displacement of the point P has components u, v, w, and the displacement in the x direction of a nearby point A is $u + \partial u/x$; and the increase in length of PA due to a deformation would be $(\partial u/\partial x)$ dx, making the unit elongation in the x direction $\partial u/\partial x$. Similarly, unit elongations in the y and z directions would be given by $\partial v/\partial y$ and $\partial w/\partial z$. After Timoshenko (8). (**b**) Considering the distortions of the angular elements PA and PB in this two-dimensional depiction, the displacements of the point A in the y direction and of B in the x direction are given by $v + (\partial v/\partial)$ dx and $u + (\partial u/\partial y)$ dy, respectively. The small angles in the figure (distortion of the P′B′ and P′A′ relative to PB and PA) are given by $\partial v/\partial x$ and $\partial u/\partial y$. Hence, it is seen that the original right angle APB distorts to A′P′B′ by an amount $(\partial v/\partial x + \partial u/\partial y)$, which is the shearing strain between the planes xz and yz. After Timoshenko (8). (**c**) Representation of the components of stress acting on an elementary cube. After Timoshenko (8).

not all independent. For simple deformations, the definitions of these moduli are

$$\text{Extensional modulus: } E = \frac{\sigma_{11}}{\varepsilon_{11}}$$

$$\text{Bulk modulus: } K = \frac{P}{\varepsilon_v} \quad \textit{where} \quad P = \frac{\sigma_{11} + \sigma_{22} + \sigma_{33}}{3} \quad \text{and} \quad \varepsilon_v = \varepsilon_{11} + \varepsilon_{22} + \varepsilon_{33}$$

$$\text{Poisson's ratio: } v = \frac{\varepsilon_{11}}{\varepsilon_{22}} \tag{4}$$

And the relations between the moduli are

$$G = \frac{E}{2(1 + v)}$$
$$K = \frac{E}{(1-2v)} \tag{5}$$
$$E = \frac{9KG}{3K+G}$$

and one more constant referred to as the Lamé constant λ is defined as

$$\lambda = \frac{vE}{(1+v)(1-2v)} \tag{6}$$

The ways in which the moduli are obtained through experimental measurements are discussed subsequently. Still working with an elastic material, one can now define the relationships between the stresses and the strains. In this case, this is the linear elastic constitutive relation:

$$\sigma_{ij} = \lambda\delta_{ij}\varepsilon_{kk} + 2G\varepsilon_{ij} \tag{7}$$

where δ_{ij} is the Kronecker delta. For simple geometries of deformation, such as those used in experiments, equation 7 can be simplified as

$$\begin{aligned} \text{Simple extension:} \quad & \sigma_{11} = \lambda\varepsilon_{kk} + 2G\varepsilon_{11} = E\varepsilon_{11} \\ \text{Simple shear:} \quad & \sigma_{12} = \tau_{12} = \lambda\varepsilon_{kk}(0) + 2G\varepsilon_{12} = G\gamma_{12} \end{aligned} \tag{8}$$

Hence, one can relate the stresses to any applied state of strain. Furthermore, the strains can be determined as functions of the applied stresses. Note that, in general, the theory of elasticity does not demand the development of compliance functions, which relate strains to stresses, as they are the inverse of the moduli. In the case of viscoelasticity, this is not so, and both modulus and compliance functions are developed in the next section.

The Viscoelastic Material Functions. In linear viscoelasticity, the moduli discussed for the elastic case can be recast as time- or frequency-dependent functions. The same is true for the compliance functions that are discussed here. For simplicity, consider the shear modulus G which becomes $G(t)$ or $G^*(\omega)$ in the case of the viscoelastic material. An important point here is that the viscoelastic modulus functions all exhibit time (frequency) dependence. Hence, one will have functions for $K(t)$ and $E(t)$ [or, eg, $G(t)$ and $\nu(t)$] and these are required in the case of a three-dimensional strain or stress field.

The general approach to discussing linear viscoelasticity comes from the Boltzmann superposition principle represented as a *convolution* integral. For the shear stress as a function of shear strain, one obtains

$$\tau_{12}(t) = \int_0^t G(t-t')\frac{\mathrm{d}\gamma_{12}}{\mathrm{d}t'}\mathrm{d}t' \tag{9}$$

and for the strain as a function of the stress,

$$\gamma_{12}(t) = \int_0^t J(t-t')\frac{\mathrm{d}\tau_{12}}{\mathrm{d}t'}\mathrm{d}t' \tag{10}$$

Here it is emphasized that the definition of the elastic compliance $J = 1/G$ is not valid for the viscoelastic compliance $J(t)$ used in equation 10. Rather it is the complex compliance $J^*(\omega) = 1/G^*(\omega)$. In addition, all the linear viscoelastic functions can be related one to the other. Full discussion of these relationships can be found in Ferry (9) and Tschoegl. (10).

As shown above, the material functions and the constitutive equation determine the relationships between the stresses and the applied deformations or vice versa. Hence, understandings of both the material functions and the form of the constitutive law are important to successful use of our current knowledge of the viscoelastic behavior of polymers. The material functions alone can give much insight into molecular viscoelasticity and the general time-dependent behavior of the material. Combined with the constitutive laws (eqs. 9 and 10), the material functions give a predictive capability of material performance in arbitrary loading histories. The next section first discusses these aspects of the material functions, using simple mechanical analogues that give some sense of viscoelastic behavior. This is followed by examples of the Boltzmann superposition represented in equations 9 and 10. Finally, the meaning of linear viscoelastic behavior is discussed as a potential means to gain insight into molecular behavior in polymers.

Mechanical Analogues.

The Maxwell Model. In the above development, discussion moves from elastic behavior to viscoelastic descriptions of material behavior. In a simple sense, viscoelasticity is the behavior exhibited by a material that has both viscous and elastic elements in its response to a deformation or load. In early days, this was often represented by elastic or viscous mechanical elements combined in different ways (9–12). The simplest models are two element models that contain a viscous element (dashpot) and an elastic element (spring). The dashpot is assumed to follow a Newtonian fluid constitutive law in which the stress is related directly to the strain rate by the following expression:

$$\tau_{12} = \eta_0 \dot{\gamma}_{12} \tag{11}$$

and the spring is assumed to be linearly elastic:

$$\tau_{12} = G\gamma_{12} \tag{12}$$

and when they are combined in series to form a *Maxwell* model the response is the combined response of the two elements. The Maxwell model is represented in the insert in Figure 2.

Now, imagine deforming the Maxwell model by applying a constant strain to it at a time $t = 0$. The deformation is held constant and the stress is monitored. Figure 2 shows the mechanical response of the Maxwell model to an applied deformation. The first (early time) response is that the "material" responds only elastically because the viscous damper initially behaves rigidly (at infinite rate

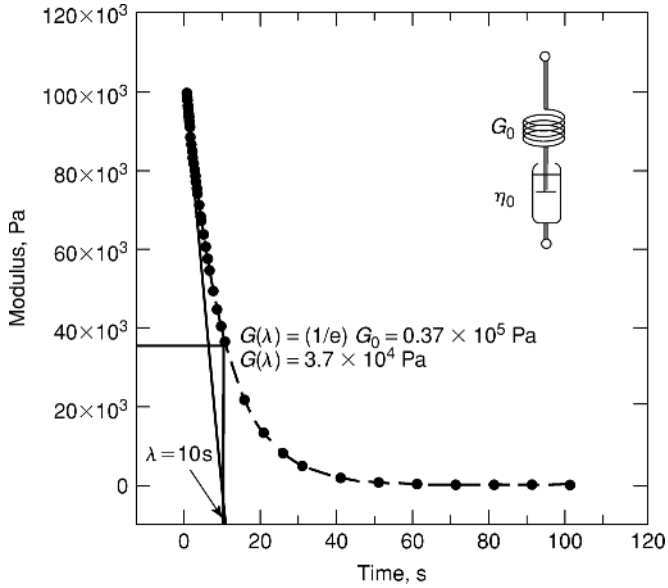

Fig. 2. Relaxation of the modulus in a stress relaxation experiment for a Maxwell element (insert). The construction shows two ways in which the relaxation time λ can be determined.

of strain). The total deformation of the element remains constant, but it redistributes itself between the spring and the dashpot. This results in *stress relaxation* that occurs exponentially with time:

$$G(t) = \frac{\tau_{12}(t)}{\gamma_{12}} = G\mathrm{e}^{-t/\lambda} \tag{13}$$

And the reader is reminded that the stress is relaxing at constant strain. Furthermore, equation 13 allows one to introduce the concept of a relaxation time

$$\lambda = \frac{\eta_0}{G} \tag{14}$$

that is, the characteristic time for the stress in the Maxwell element to decay to 1/e of its initial value (see Fig. 2). (Note the use of the symbol λ as the relaxation time and not the Lamé constant given previously. Also, τ is often used as the symbol to represent the relaxation time, but τ is used here for the shear stress.)

The Kelvin–Voigt Model. The other two-element mechanical model for viscoelasticity is the Kelvin–Voigt model in which the spring and dashpot are in parallel. In this model, the deformation or *creep* response to the imposition of a constant load is illustrated. In this instance a constant load is applied at $t = 0$ and the deformation is monitored. The Kelvin–Voigt model and its response are illustrated in Figure 3. The material property of interest in this case is the *creep compliance* $J(t)$ and it is written as

$$J(t) = \frac{\gamma_{12}(t)}{\tau_{12}} = \frac{1}{G}(1 - \mathrm{e}^{-t/\lambda}) \tag{15}$$

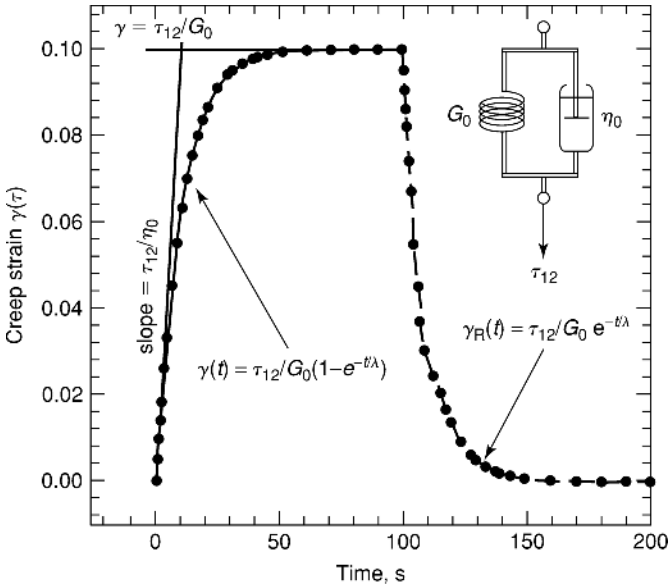

Fig. 3. Creep and recovery response for a Kelvin–Voigt model (insert).

And, now, the characteristic time λ is referred to as the *retardation time* because of the retarded elasticity of the material. That is, initially the load is carried by the viscous dashpot and then redistributes until, at long times, the load is carried fully by the elastic spring. Figure 3 shows the response to a loading history in which the load is applied for 100 s and then reduced to zero. Both the creep strain $\gamma(t)$ and the recoverable strain are depicted in the figure. The recoverable compliance would be obtained from the recoverable strain and the applied stress as $J_R(t) = \gamma_R(t)/\tau_{12}$, but only when the material has reached its equilibrium response is this a material property.

The Burgers Model. As a preview to the viscoelastic behavior of polymers, we next consider the four-element Burgers model that captures a "minimum" set of behaviors that is seen in polymeric materials and as discussed here (13). The insert in Figure 4 shows the Burgers model as a Maxwell model in series with a Kelvin–Voigt model. As shown in Figure 4, upon application of a constant stress τ_{12} for a time t_1 followed by its removal, the model captures the following aspects of polymer viscoelasticity:

(1) "Instantaneous" elasticity or elastic recovery (spring element G_1)
(2) Molecular "slip" (viscous element η_1)
(3) "Entropic" or rubbery elasticity (spring G_2)
(4) "Retarded" elasticity (Kelvin–Voigt element G_2 is retarded by η_2)

Polymers, as seen later, show more complex viscoelastic behaviors than does the Burgers model, but the essentials are in the Burgers model. The "instantaneous" elasticity can be thought of as the "glass-like" response; the molecular "slip" is the terminal response, as the long polymer molecules slide past each

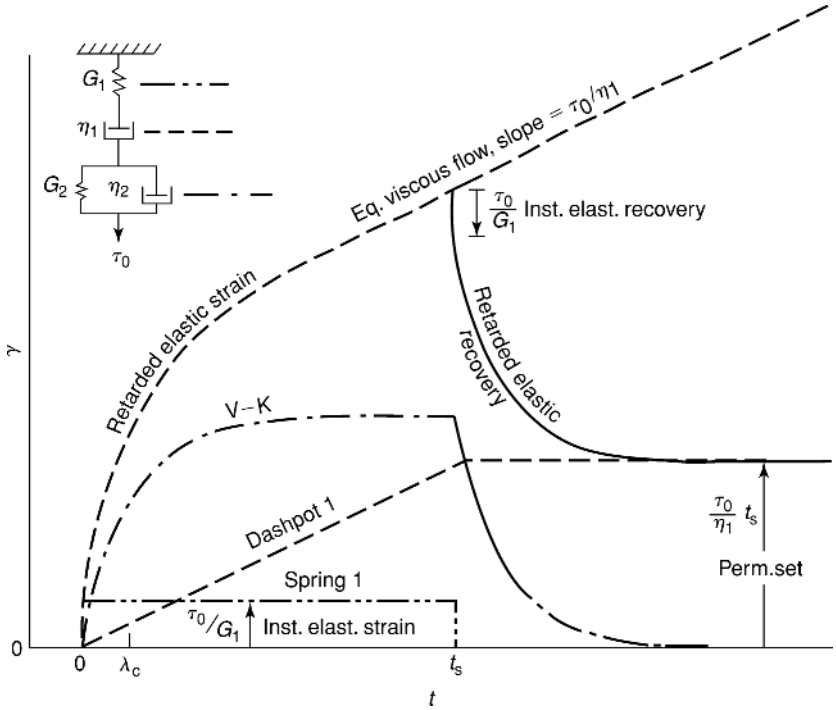

Fig. 4. Creep and recovery response for a Burgers model (insert), showing the four regions of "polymer-like" viscoelastic response as discussed in text. After Rosen (13), with permission.

other and disentangle; the entropic elasticity occurs because of the long chains being entangled like a three-dimensional network of "entropic springs"; and the retarded elasticity occurs because of the resistance of the polymer melt to the forces applied by the spring. The equation for the creep compliance of the Burgers model is

$$J(t) = \frac{1}{G_1} + \frac{1}{G_2}(1 - e^{-t/\lambda}) + \frac{t}{\eta_1} \tag{16}$$

where $\lambda = \eta_2/G_2$. Upon unloading, the *recoverable compliance* $J_R(t)$ is

$$J_R(t) = J(t) - \frac{t}{\eta} \tag{17}$$

Note that equation 17 is the general equation for the recoverable compliance regardless of the model. Figure 4 gives a simplified sense of what the various aspects of polymer viscoelastic behavior are, although the actual behavior is more complex.

General Models. Clearly, one can add up springs and dashpots in a great number of ways. It is common practice to use either a generalized Maxwell model or a generalized Kelvin–Voigt model. The generalized Maxwell model, which is

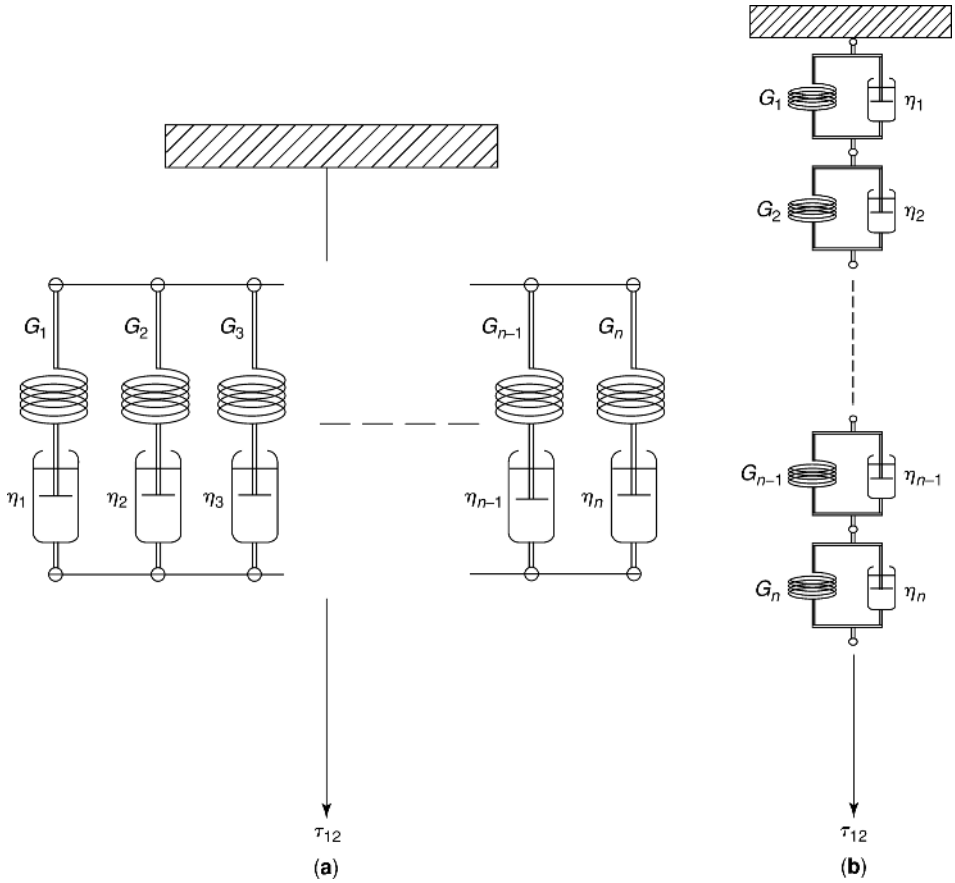

Fig. 5. (**a**) The generalized Maxwell model. (**b**) The generalized Kelvin–Voigt model.

simply a set of Maxwell elements in parallel, is shown in Figure 5a. The generalized Kelvin–Voigt model, which is a set of Kelvin–Voigt elements in series, is shown in Figure 5b. The choice of model is primarily a matter of convenience because it is possible to find a *conjugate* Maxwell model to any Kelvin–Voigt model and vice versa (10). However, the moduli are most easily described with the Maxwell model and the equations for these are

$$G(t) = G_0 + \sum_{i=1}^{N} G_i \mathrm{e}^{-t/\lambda_i}$$

$$G'(\omega) = G_0 + \sum_{i=1}^{N} \frac{G_i \omega^2 \lambda_i^2}{1+\omega^2 \lambda_i^2} \tag{18}$$

$$G''(\omega) = \sum_{i=1}^{N} \frac{G_i \omega \lambda_i}{1+\omega^2 \lambda_i^2}$$

and the compliances are most easily described using the generalized Kelvin–Voigt model:

$$J(t) = J_g + \sum_{i=1}^{N} J_i(1 - e^{-t/\lambda_i}) + \frac{t}{\eta_0}$$

$$J'(\omega) = J_g + \sum_{i=1}^{N} \frac{J_i \omega^2 \lambda_i^2}{1+\omega^2 \lambda_i^2} \tag{19}$$

$$J''(\omega) = \sum_{i=1}^{N} \frac{J_i \omega \lambda_i}{1+\omega^2 \lambda_i^2} + \frac{\eta_0}{\omega}$$

The equation sets 18 and 19 provide a means of fitting experimental data to an arbitrary accuracy. It is important to remark, however, that the problem of actual fitting of data, while easier today than in the past because of the prevalence of high speed personal computers and commercial software, is nontrivial, and the reader who is interested in details of the treatments should refer to the appropriate literature (14–19).

Interrelationships among the Viscoelastic Material Functions. There is a continuing disagreement within the molecular viscoelasticity community about which of the above methods should be used to characterize a material (20). In fact, if one can obtain the zero shear rate viscosity and any of the other functions, these methods are all equivalent. The issue, however, revolves around the fact that some features that appear in the dynamic modulus disappear if the compliance is used as the function to represent the data and vice versa. Also, some measurements are more or less dominated by the viscosity contribution. As a result, some problems of misinterpretation of data could be averted if workers who prefer modulus representations would calculate the compliances. In addition, those who measure the compliance should calculate the moduli in order to provide the data in the format that is more common in the field because of the large number of commercial instruments that obtain dynamic moduli. The advent of modern software packages that make the interrelationships easily calculated makes this dispute seem to go away. The pathways to determine the different material functions, one from the other, are shown in Figure 6.

Boltzmann Superposition and Linear Behavior.

The Phenomenology of the Linear Theory of Viscoelasticity. One of the powers of the linear viscoelasticity theory is that it is predictive. The constitutive law that comes from Boltzmann superposition theory requires simply that the material functions discussed above be known for a given material. Then, for an arbitrary stress or deformation history, the material response can be obtained. In addition, the *elastic–viscoelastic correspondence principle* can be used so that boundary value problems such as beam bending, for which an elastic solution exists, can be solved for linear viscoelastic materials as well. Both of these subjects are treated in this section.

Boltzmann Superposition and the Constitutive Law for Linear Viscoelasticity. The underlying assumption of the Boltzmann superposition principle is

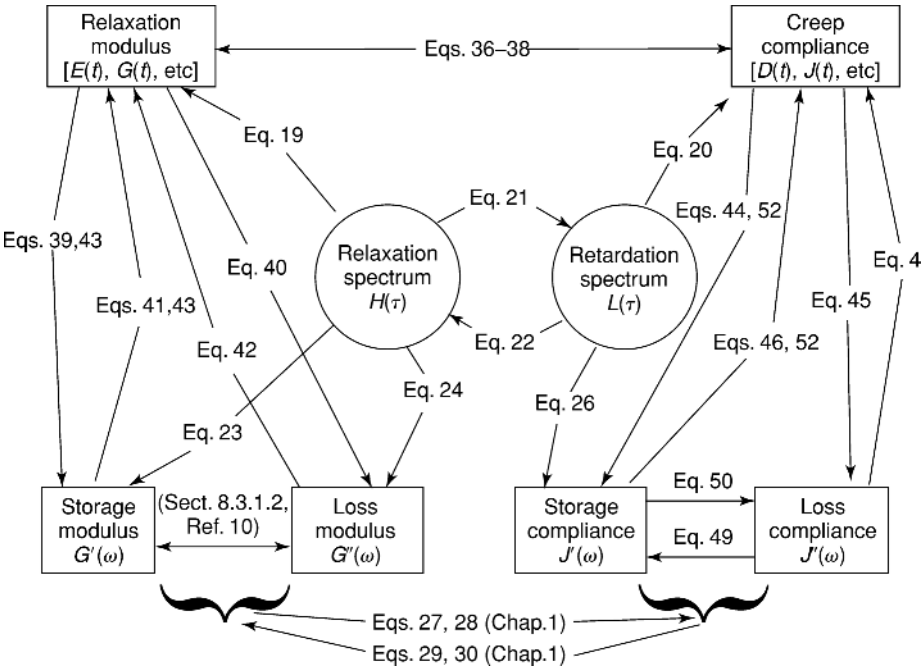

Fig. 6. Chart showing the paths to interrelate the linear viscoelastic material functions. Equation numbers refer to Chapter 3 of Ferry's book (9) unless otherwise indicated. Determination of $G'(\omega)$ from $G''(\omega)$ and $J'(\omega)$ from $J''(\omega)$ and vice versa comes from the Kramer–Kronig relation and is discussed in Tschoegl (10).

that responses to loads or deformations applied to a material at different times are linearly additive. This set of assumptions leads to the constitutive laws of linear viscoelasticity theory which can be considered as a linear response theory. For discussion purposes, consider a Maxwell material that is subjected to a two-step deformation history. The history is such that a deformation $\gamma_1 = \Delta\gamma_1$ is applied at a time $t = 0$ and an additional deformation $\Delta\gamma_2$ is applied at a time t_1 so that $\gamma_2 = \gamma_1 + \Delta\gamma_2$. This can be carried on for as many steps as desired, as depicted in Figure 7a. The stress response to this deformation history is written as

$$\tau(t) = \sum_{i=1}^{N} \Delta\sigma_i(t - t_i') = \sum_{i=1}^{N} \Delta\gamma_i G(t - t_i') \tag{20a}$$

For $N = 2$

$$\tau(t) = \Delta\sigma_1(t - t_1') + \Delta\sigma_2(t - t_2') \tag{20b}$$

but $t'_1 = 0$ and $t'_2 = t_1$; therefore

$$\begin{aligned}\tau(t) &= \Delta\sigma_1(t) + \Delta\sigma_2(t - t_1) = \Delta\gamma_1 G(t) + \Delta\gamma_2 G(t - t_1)\\ &= \gamma_1 G(t) + (\gamma_2 - \gamma_1) G(t - t_1)\end{aligned} \tag{20c}$$

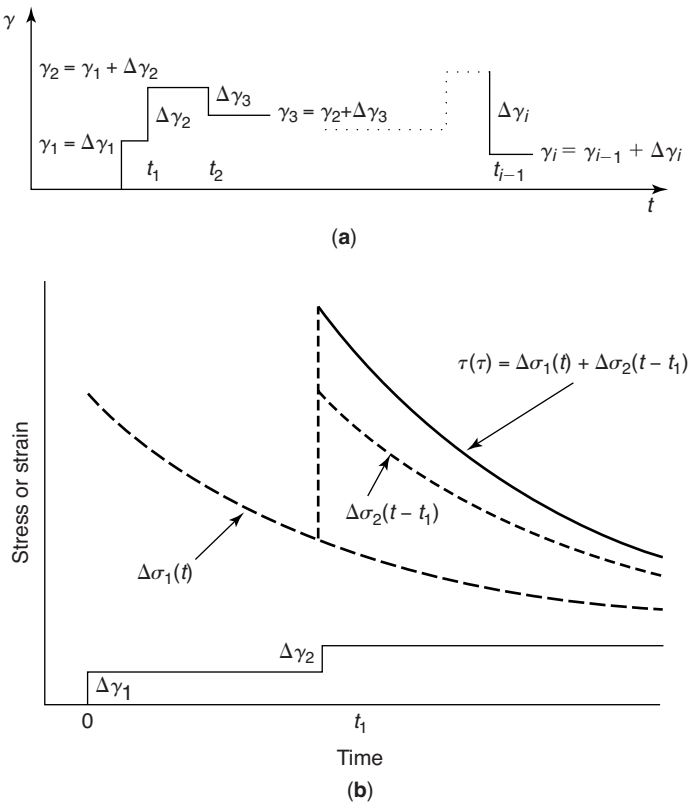

Fig. 7. (**a**) General step-strain deformation history relevant to Boltzmann-type linear superposition. (**b**) Schematic of stress additivity of responses for a Maxwell model in a two-step strain history (see text for discussion).

Figure 7b illustrates the way in which the responses add for a two-step history in which each step has the same magnitude. Equation 20a is the general form and is the discrete form of the linear superposition principle cast as a simple shear. It shows the simple linear additivity of the responses. A similar equation could be written for the strain response in terms of the stresses for a creep history. The equations can easily be generalized to include the full range of strains and stresses discussed in the next section. Furthermore, the responses can be written in terms of *convolution integrals*:

$$\tau(t) = \int_0^t G(t-t')\frac{\mathrm{d}\gamma}{\mathrm{d}t'}\mathrm{d}t' \tag{9}$$

$$\gamma(t) = \int_0^t J(t-t')\frac{\mathrm{d}\tau}{\mathrm{d}t'}\mathrm{d}t' \tag{10}$$

Equations 9 and 10 can be solved for arbitrary strain (stress) histories to obtain the material stress (strain) response. Solution for the step-deformations requires use of the "unit Heaviside function" and is discussed in detail by

Tschoegl (10) and by Findley, Onaran and co-workers. (21) Wineman and Rajagopal (22) deal with the step-strains, using Riemann–Stieltjes integrals. Other histories are more directly solvable. Also, in the linear theory the limits on the integral can be written from 0 to t rather than from $-\infty$ to t (9,10,21,22).

The final point of the current section is to illustrate that linear viscoelasticity can give rise to what looks like a "nonlinear" response. The typical example comes for a constant rate of deformation experiment. If a generalized Maxwell model is assumed, the material can be subjected to a constant rate of strain and a stress–strain curve can be plotted. As shown in Figure 8a, even though the theory behind equations 20a (or eqs. 9 and 10) is completely linear, one observes that the stress–strain response appears to be nonlinear. This is an illustration of the practicality of understanding viscoelasticity and of understanding the complex time-dependent behavior of polymeric materials. In addition, the linearity of the responses is illustrated in Figure 8b, where all the curves from Figure 8a collapse to a single curve when $\tau/(d\gamma/dt)$ vs $\gamma/(d\gamma/dt)$, (22) is plotted.

Elastic–Viscoelastic Correspondence Principle. One of the difficulties in working with time-dependent materials is solving for their response in actual conditions. For example, a composite aircraft wing might be considered as a viscoelastic beam subjected to bending moments (see Fig. 9). The problem can be solved by applying the viscoelastic constitutive equations to the problem, but in many instances this approach is tedious. Fortunately, it was shown that many classes of viscoelastic boundary-value problems can be solved if the elastic solution is known (23). This is referred to as the *elastic–viscoelastic correspondence principle*. One substitutes the Laplace transform of the viscoelastic material functions for their elastic counterparts into the elastic solution. Inversion of the Laplace transform gives the time-dependent response of the material. In the case of the pure bending of the beam just mentioned, the elastic solution for the displacements, stresses, and deflection can be written as follows (21):

$$\begin{aligned} \text{Strain:} \quad & \varepsilon(t) = -\frac{M(t)y}{E_e I} \\ \text{Stress:} \quad & \sigma(t) = -\frac{M(t)y}{I} \\ \text{Deflection:} \quad & \frac{d^2 w(x,t)}{dx^2} = \frac{M(t)}{E_e I} \end{aligned} \tag{21}$$

where $M(t)$ is the applied moment, y is the beam half thickness, I is the moment of inertia of the beam, and E_e is the elastic modulus. In the case of the viscoelastic beam, we first take the Laplace transform for the time-varying parameters and then substitute $s\hat{E}(s)$ for E_e. Then (see Ref. 21)

$$\begin{aligned} \text{Strain:} \quad & \hat{\varepsilon}(s) = -\frac{\hat{M}(s)y}{s\hat{E}(s)I} = -\frac{y}{I}\hat{J}(s)s\hat{M}(s) \\ \text{Stress:} \quad & \hat{\sigma}(s) = -\frac{\hat{M}(s)y}{I} \\ \text{Deflection:} \quad & \frac{d^2 w(x,s)}{dx^2} = \frac{\hat{M}(s)}{s\hat{E}(s)I} = \frac{\hat{J}(s)s\hat{M}(s)}{I} \end{aligned} \tag{22}$$

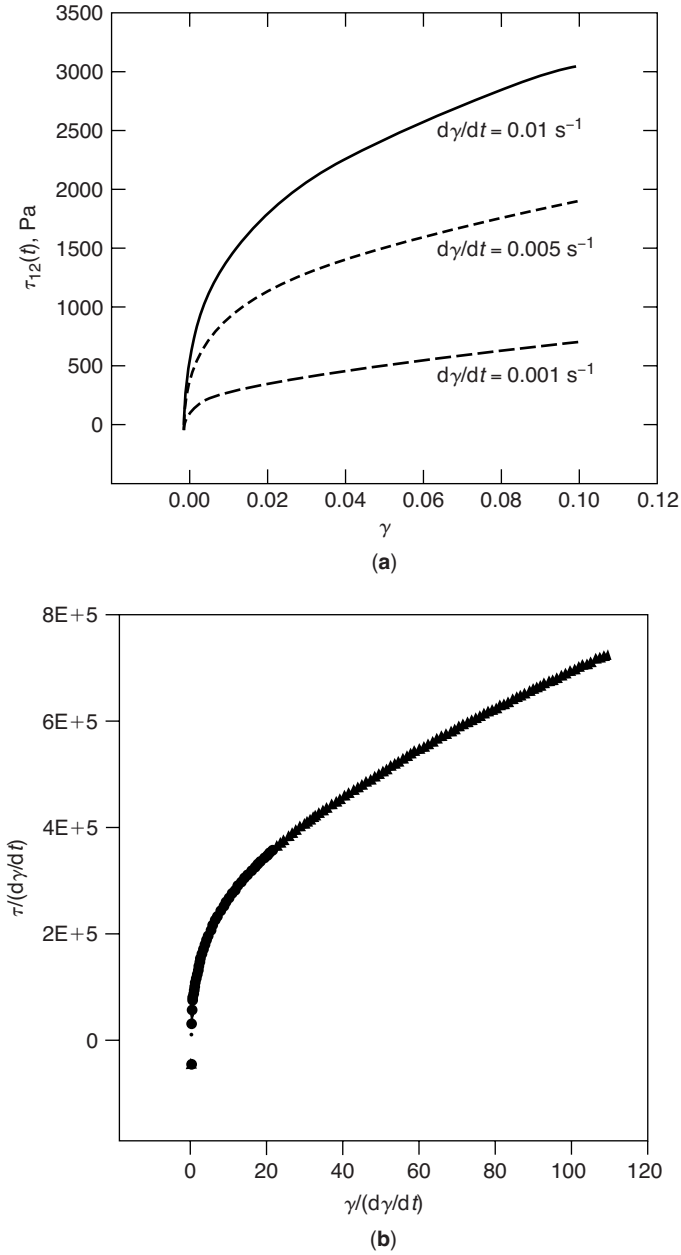

Fig. 8. (**a**) Stress–strain plot for a generalized Maxwell model to different strain rates, as depicted in figure. Plot shows "nonlinear" stress–strain behavior in spite of material model (Maxwell) following laws of linear viscoelasticity (see text). (**b**) Stress and strain data from different strain rates given in (**a**) divided by strain rate $d\gamma/dt$, demonstrating that material model follows linear viscoelasticity (see text).

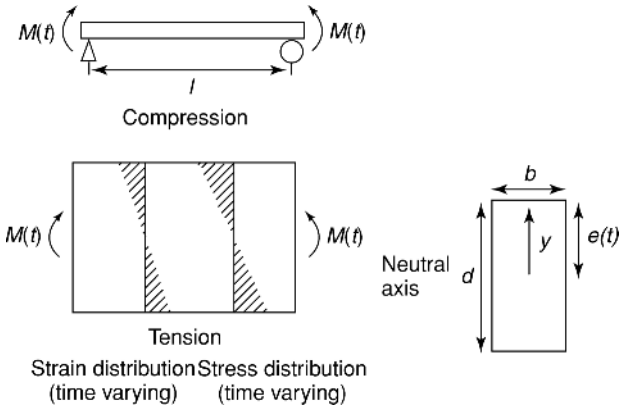

Fig. 9. Schematic of the beam-bending problem. After Findley et al. (21).

Note that the relationships between the viscoelastic compliance and the relaxation modulus are given by

$$s\hat{E}(s) = \frac{1}{s\hat{J}(s)} \tag{23}$$

Inversion of equation 22, using the convolution transform, gives

$$\begin{aligned} \varepsilon(t) &= -\frac{y}{I}\int_0^t J(t-t')\frac{\mathrm{d}M(t)}{\mathrm{d}t'}\mathrm{d}t' \\ \sigma(t) &= -\frac{M(t)}{I} \\ \frac{\mathrm{d}^2 w(x,t)}{\mathrm{d}x^2} &= \frac{1}{I}\int_0^t J(t-t')\frac{\mathrm{d}M(t)}{\mathrm{d}t'}\mathrm{d}t' \end{aligned} \tag{24}$$

And integration of the hereditary integrals for strain and deflection gives the solution to any applied history of the moment $M(t)$. A note of caution, however, arises for mixed conditions in which the interface between the stress and the displacement boundaries is not constant. In such cases the elastic–viscoelastic correspondence principle is not applicable and the solutions become more difficult (21).

Finally, this section concludes by noting that Schapery (7,24) has shown that when the material properties are changing very slowly, an approximate solution can be obtained by substituting the viscoelastic moduli for their elastic counterparts. This will be justified in some instances. The reader should examine the literature for further consideration of the limitations of these approaches. Also, the advent of commercial finite element codes that have linear viscoelastic material elements makes the solution of such problems more routine.

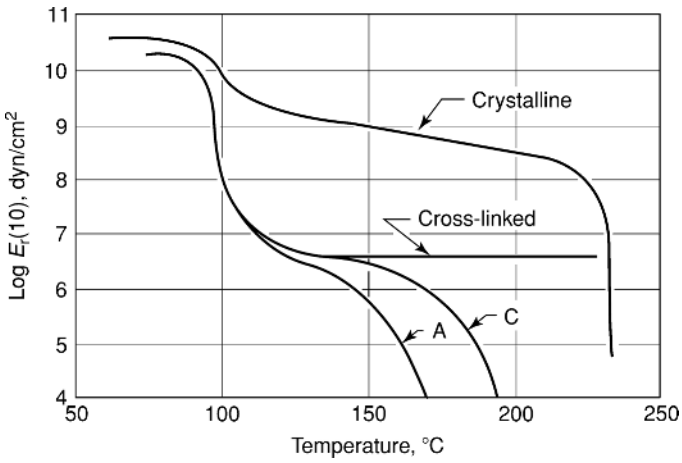

Fig. 10. The relaxation modulus (at 10 s) for a polymer measured as a function of temperature. Curves labeled A and C depict amorphous, linear polymers with the molecular weight of A being less than that of C. The cross-linked polymer is also amorphous, but cannot flow. The crystalline polymer behaves differently because it is "reinforced" by crystalline domains. After Tobolsky (25).

Linear Viscoelastic Behavior of Polymeric Materials

General Regimes of Response. Polymeric materials exhibit a very rich set of viscoelastic responses. The responses observed depend upon the state of the polymer and on its structure. The material can be in an amorphous state if it is a glass, a rubber, a melt, or a solution. In addition, the material can be semicrystalline in that crystallites partially fill or reinforce the otherwise amorphous material. Figure 10 illustrates a plot of the relaxation modulus vs T; it indicates schematically the sort of responses that are observed for an amorphous polymer as a function of temperature. Also shown is the sort of response to be obtained in a semicrystalline polymer over the same temperature range. At low temperatures, one observes a behavior that for both structures is the same as that of a high modulus material. As the glass temperature T_g is approached the amorphous material undergoes a dramatic drop in modulus by several orders of magnitude. The modulus of the semicrystalline material changes significantly, but not nearly as much. Following the modulus drop associated with the glass temperature, the amorphous polymer can exhibit a rubbery plateau due to the *entanglement network* formed by the long-chain molecules. If the molecules are not long enough the entanglement plateau will be weak or nonexistent. In the same temperature regime the semicrystalline polymer exhibits a long and slow reduction of modulus. As temperature increases, the amorphous polymer undergoes terminal flow due to the disentanglement of the molecules while the semicrystalline polymer continues changing slowly. Above the melting point of the semicrystalline polymer its modulus drops dramatically because the material has become an amorphous polymer at a temperature well above the terminal flow region. In the next sections these behaviors are discussed in more detail.

Behavior in the Amorphous State. Polymer behavior in the amorphous state can be divided into two categories: the glassy state and the fluid state. The former applies to polymers below the glass transition and is generally dominated by the segmental or local movements of the polymer chains. The fluid state of the amorphous polymer is dominated by long-range motions of the polymer chains and the eventual onset of entanglements that give rise to very interesting viscoelastic properties. This section first describes the viscoelastic behavior of the polymer in the glassy state and through the glass temperature. This is followed by a section on the fluid-state properties that are dominated by the long-chain nature of the polymer.

Time–Temperature Superposition. In Figure 10 one observes that the viscoelastic relaxation modulus at a single time or frequency (*isochrones*) shows dramatic changes as temperature increases (25). It turns out that such behavior can be described within the context of a model which is referred to as *time–temperature superposition* or *thermo-rheological simplicity* (9,10,25). The fundamental concept here is that the relaxation times introduced above for, eg, a generalized Maxwell model, all exhibit the same temperature dependence. When thermo-rheological simplicity is valid, one can replace each λ_i in equations 18 and 19 by $a_T\lambda_i$ where the *shift factor* a_T represents the amount that the relaxation time λ_i is changed in going from some reference temperature T_R to the current temperature T. That is

$$a_T = \frac{\lambda_i(T)}{\lambda_i(T_R)} \tag{25}$$

When equation 25 is valid, it is possible to make measurements of the viscoelastic functions over a range of, say four logarithmic decades of time (frequency), at multiple temperatures and use the data to create *reduced* or *master* curves that span many more decades in time (frequency). This is useful for determining the polymer's behavior at longer or shorter times (lower or higher frequencies or rates) that would be extremely difficult to do otherwise. This can be important in both processing applications where rates can be very high and in long-term durability applications where unreasonably long times might otherwise be required to obtain test data. Figure 11 shows the actual data that were obtained for a polymeric material over a limited time range, but at multiple temperatures (25). Figure 12 shows the data reduced to a master curve using time–temperature superposition. As discussed below, the reduced curve in Figure 12 can also be related to the observed temperature dependence of the modulus depicted schematically in Figure 10.

Figure 13 shows the data for the shift factors as log a_T vs T (26). The description of the shift factors as a function of temperature is very important both for ease of application of the method to actual material behavior and because it has implications for the physical understanding of the behavior of polymeric materials. In the next three sections, the temperature dependence of the viscoelastic properties is discussed by examining the temperature dependence of the shift factors.

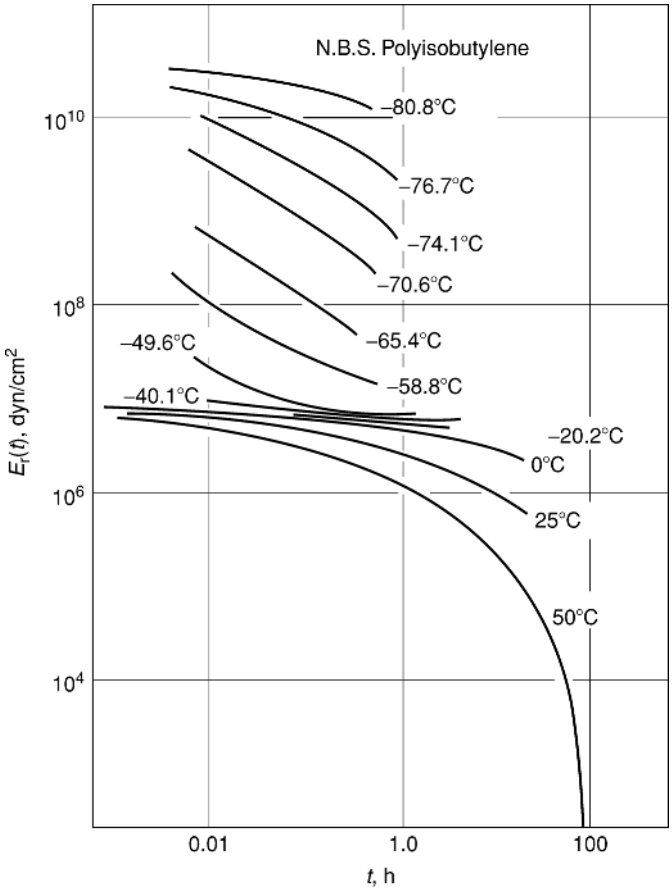

Fig. 11. Stress relaxation isotherms for a polyisobutylene amorphous polymer. After Tobolsky (25).

Properties near the Glass Temperature. In Figure 10 the curve for the amorphous polymer exhibits a behavior in which the modulus at low temperatures changes slowly as temperature increases. As the temperature approaches the glass temperature T_g, however, the modulus begins to change rapidly, dropping by up to 3 orders of magnitude, as the T_g is traversed. This is related to the changing relaxation times. Figure 12 shows a similar behavior, but now with time. At short times, the material response changes slowly and as a glass "transition" time is approached begins to drop rapidly by the same 3 orders of magnitude. In fact, the time–temperature superposition principle allows one to go from curves in temperature space to curves in time (or frequency) space and vice versa.

When the shift factors for the relaxation times are plotted as in Figure 13, an important type of behavior is seen. Here it is observed that the shift factors increase dramatically as the temperature decreases. In fact, if one extrapolates the behavior, there is a singularity point that is reached that is about 50 K below the nominal glass temperature determined from other test methods (such as dsc). This rapid increase of the material shift factor also corresponds (eq. 25) to

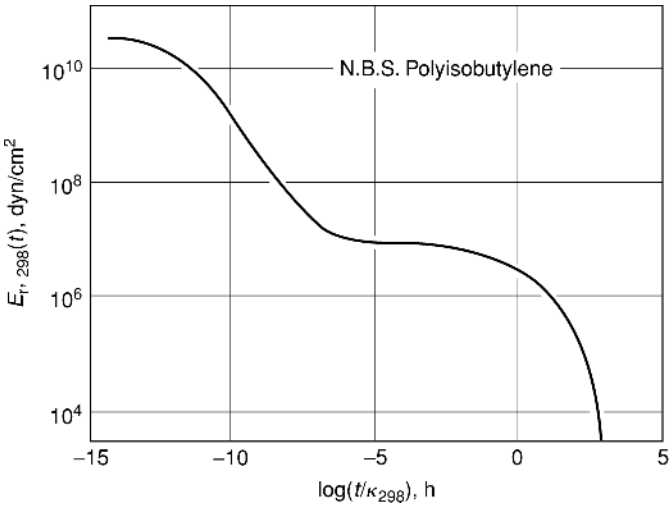

Fig. 12. Master curve generated by applying time–temperature shifting to the data given in Figure 11. (Note that $\kappa_{298} = 1/a_T$.) After Tobolsky (25).

a rapid increase in the relaxation times as the temperature is decreased. Hence, the glass temperature is approached because the mobility in the polymer becomes so slow that, in normal experimental time scales, the molecules cannot respond to the mechanical solicitation and the material exhibits nearly solid-like properties [imagine the glassy poly(methyl methacrylate) (PMMA) that makes up aircraft windows. The T_g of PMMA is about 110°C]. There are two equations that are commonly used to describe the shift factor behavior and these are discussed later. First the relationship between the viscosity and the shift factor is discussed.

The viscosity is related to the relaxation modulus through the following equation (9):

$$\eta_0 = \int_{-\infty}^{\infty} tG(t)\mathrm{d}\ln t \tag{26}$$

(for a Maxwell element, this would translate into $\eta_0 = G\lambda$). When the modulus is proportional to temperature T and density ρ (as in the case of rubber elasticity) the shift factor can be determined from viscosity measurements:

$$a_T = \frac{\eta_{0,T}\,\rho_{T_R} T_R}{\eta_{0,T_R}\,\rho_T\, T} \tag{27}$$

Hence, when the shift factor is increasing rapidly, this implies that the viscosity is also increasing rapidly.

One equation used to describe the rapid increase of the viscosity with decreasing temperature is the Vogel–Fulcher equation (27,28):

$$\eta_0 = A\mathrm{e}^{B/(T - T_\infty)} \tag{28}$$

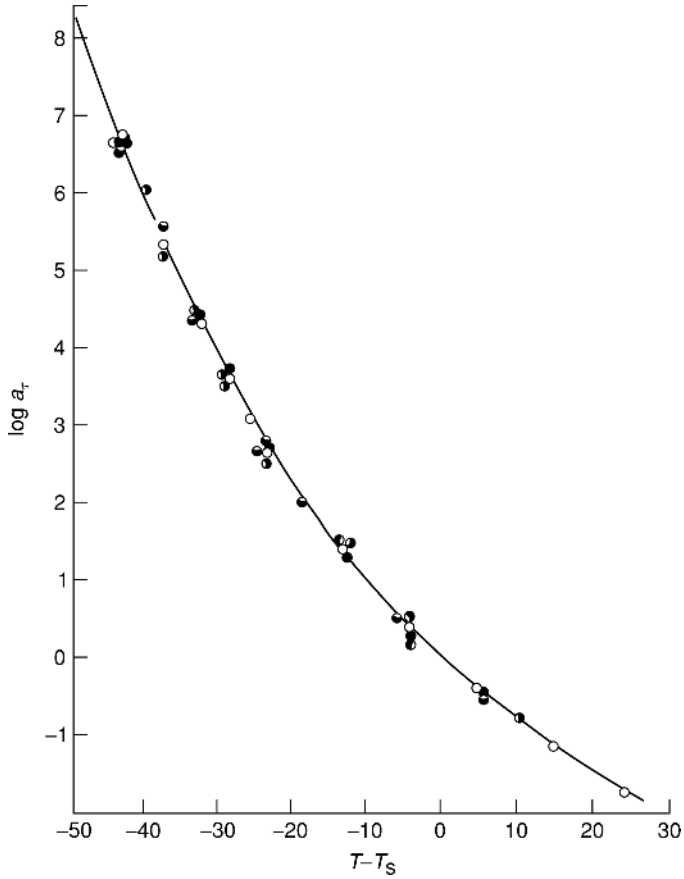

Fig. 13. Time–temperature shift factors for poly(α-methyl styrene). $T_{ref} = 204°C$. After Fujimoto et al. (26), with permission.

where A is a prefactor and T_∞ is the temperature at which the viscosity extrapolates to an infinite value. Note that when $T_\infty = 0$ K, equation 28 reverts to an Arrhenius form and B would have the meaning of an activation energy (E_a/R). Equations 28 and 27 can be used together to obtain the shift factor a_T. Also, a similar form to equation 28 can be used to represent the temperature dependence of the relaxation times.

The other equation that is often used to describe the dependence of the shift factors on temperature is the Williams, Landel, and Ferry (WLF) equation (29):

$$\log a_T = \frac{C_1(T - T_R)}{C_2 + T - T_R} \tag{29}$$

where C_1 and C_2 are constants. The singularity in the shift factor occurs when $C_2 = -(T - T_R)$, and when $T_R = T_g$ this value is approximately 50 K, ie, the singularity occurs some 50 K below the nominal glass temperature. When

$T_R = T_g$, the Vogel–Fulcher and WLF equations are related by the following expressions (9):

$$C_1 = \frac{B}{T_g - T_\infty}$$
$$C_2 = T_g - T_\infty \tag{30}$$
$$2.303 C_1 C_2 = B$$

Note that for many polymers the values of the WLF parameters are close to the so-called universal values, which are $C_1 = 17.44$ and $C_2 = 51.6$ K when $T_R = T_g$. (When no other information is available, the "universal" values for C_1 and C_2 can make useful approximations to actual behavior.)

In discussing the temperature dependence of the shift factors in polymers, it is essential that a distinction be made between the segmental relaxations and the terminal relaxations. The reason for this can be seen in Figure 10 where there are two regions of rapid change in properties. The first occurs in the vicinity of the glass temperature and is due to increasing segmental or local mobility. The second occurs after the rubbery plateau and is related to the terminal relaxations that occur because of chain disentanglement in the fluid state. These two processes are now known to generally show different temperature dependences and one should be clear which relaxations are relevant in any particular situation (30–32).

Figure 13 shows the rapid increase of the shift factors (or viscosity) as T_g is approached from above. As noted previously, the point of singularity is approximately 50 K below the T_g. However, as the glass temperature is traversed, the material response does not continue to follow the WLF curve, rather it falls away from it, as shown in Figure 14 (33–35). The reasons for this are involved with the nature of the glass-transition event and the fact that the molecular mobility has become extremely low in the vicinity of the glass temperature (9,25,28,36,37). As a result, as the temperature changes, the molecules do not have enough time to relax into their equilibrium state and a glass is formed. Glasses are nonequilibrium materials and the sub-T_g behaviors are determined very much by this (36–40). Regardless of this fact, the response below T_g does not follow the WLF behavior. It can, however, follow time–temperature superposition, but with a less dramatic dependence of the shift factors on the temperature, as is seen in Figure 14. In Figure 14 there are three lines for the shift factors below T_g. In this instance, it is due to the physical aging (40) that accompanies the evolution of the nonequlibrium glass toward its equilibrium state.

Viscoelastic Relaxation Properties far below the Glass Temperature. As one moves below the glass-transition temperature, the relaxation behavior of the amorphous polymer becomes more and more sluggish as the thermal energy available to stimulate molecular motion becomes smaller. This behavior is seen in the schematic of Figure 10. However, below the glass temperature, polymers often exhibit other relaxation responses that are referred to as sub-T_g relaxations (9,41–44). A typical example is shown in Figure 15 where the dynamic responses of a series of poly(n-alkyl methyl methacrylates) as a function of temperature are

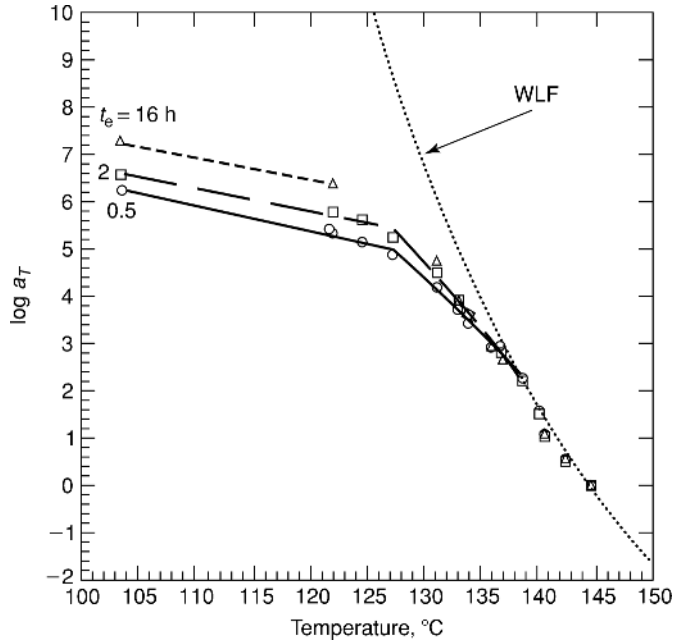

Fig. 14. Plot of shift factor (logarithm) vs T for polycarbonate, illustrating the change in behavior away from the WLF-type of temperature dependence as T_g is traversed. Also, because the glassy state is a nonequilibrium state, the material "ages." The curves at 0.5, 2, and 16 h represent the results at these aging times. After Pesce et al (33).

shown. The reader can see that G' ($\omega = 1$ Hz) shows a smeared out "step" in response at low temperatures (approximately 0°C in the PMMA). The PMMA shows a broad peak at the same temperature in tan δ. This relaxation is referred to as the β-relaxation (relative to the α-relaxation of the glass temperature). Some materials exhibit a γ-relaxation at even lower temperatures, as seen for the poly(n-butyl methacrylate) and poly(n-propyl methacrylate). The sub-T_g relaxations can affect other material properties, although the relationship between linear viscoelastic properties and, eg, failure is complicated and simple relationships not generally universal.

One important aspect of the sub-T_g relaxations is that they generally exhibit different temperature dependences than does the main glassy relaxation. The result is that time–temperature superposition is not usually valid when there is a strong sub-T_g relaxation in the polymer. An example of this is the behavior shown for poly(ethylene naphthalate) in Figure 16, where one can see that time–temperature shifting of creep data does not collapse the data to a single curve because this material has a strong β-relaxation that is not far from the glass temperature (45).

Finally, it is worth noting that the sub-T_g relaxations are often attributed to side-group motions on the polymer chain. A good example is the changing relaxation strength and position in the series of n-alkyl methacrylates that was presented in Figure 15 (44). There it is shown that both the α and the β

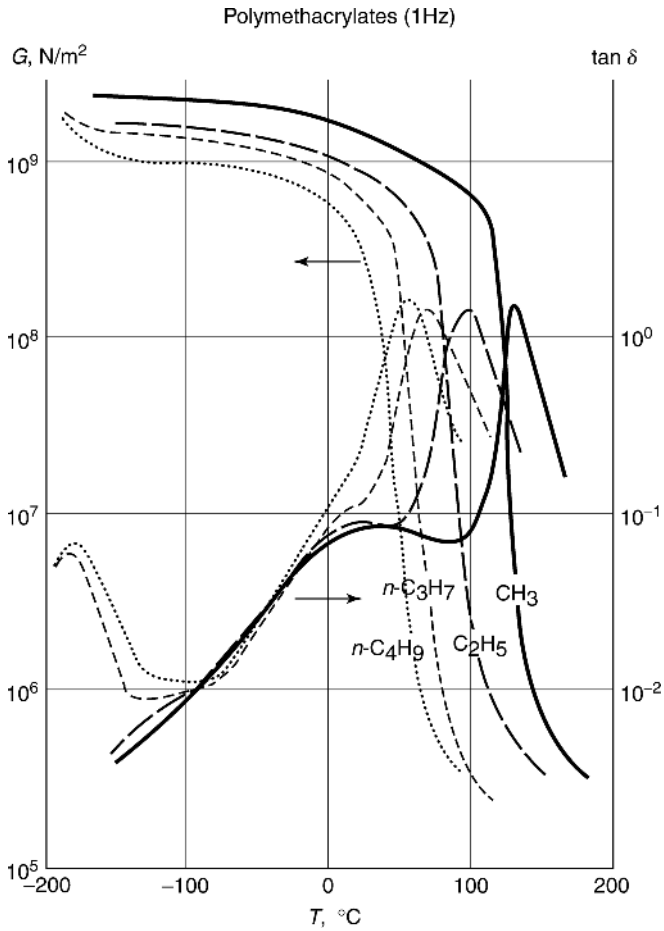

Fig. 15. Dynamic modulus and loss tangent (at 1 Hz) of a series of n-alkyl methacrylates showing how side groups change the α and β transitions. After Heijboer (44).

relaxations shift systematically as the side-chain length increases from $n = 1$ (methyl) to $n = 4$ (butyl). Note, however, that the α-relaxation shifts more strongly than does the β-relaxation with increasing side-group length.

Viscoelastic Response far above the Glass Temperature: T_g The Fluid State. From Figure 10 or Figure 12 one can see the fluid state response of the polymer. This is the portion of the curve at long times or high temperatures from the rubbery plateau to the end of relaxation where the polymer would take the shape of whatever container held it, ie, it is a liquid. There are several fundamental aspects to polymer behavior in this region. On the rubbery plateau, the polymer chains behave as if they were part of a three-dimensional network and their response can be described from modern rubber elasticity theories. This behavior is beyond the scope of the current review and the reader is referred to the literature for further information (46–50). At long enough times, however,

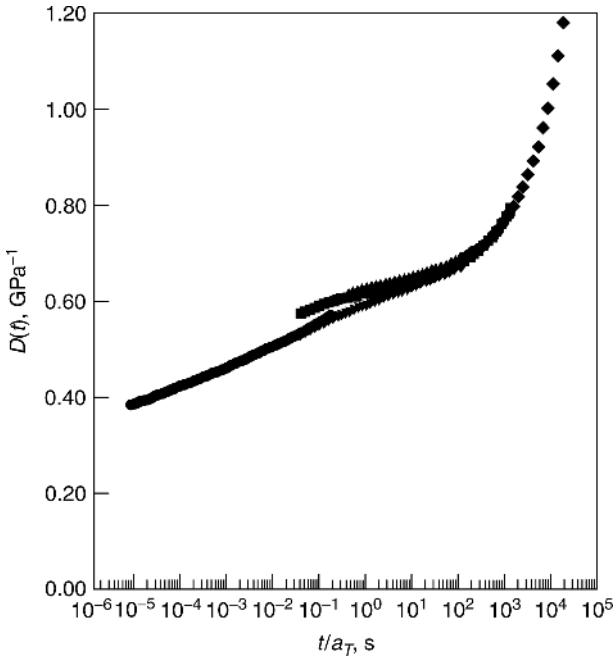

Fig. 16. Reduced curve of creep compliance vs time for PEN showing lack of time–temperature superposition (see text for discussion). • 30°C; ▼ 50°C; ■ 80°C; ◇ 100°C. After Cerrada and McKenna (45).

the polymer chains have the opportunity to slip out of the entanglement points and the relaxation behavior seen in the terminal response regime results. The current paradigm for the viscoelastic response of polymers in this terminal flow regime is the reptation theory given by de Gennes (51) and Doi and Edwards (52–56). According to this model, the entanglement field can be represented by a tube through which the chain "reptates" along the chain direction. This is schematicized in Figure 17, where one can see (a) the topology of a chain in a fixed network and (b) the primitive path defined by the tube.

Before describing the reptation theory quantitatively, we first examine part of the rich set of behaviors that any theory of polymer chain dynamics in the melt state needs to be able to describe. One of the most interesting aspects of polymer melt and solution behavior is that once the material is well entangled, the viscoelastic behavior is quasi-universal. First, the zero shear rate viscosity η_0 is observed to vary with the molecular weight to a very strong power (9,57):

$$\eta_0 = AM^{\alpha} \tag{31}$$

where A is an empirical prefactor and M is the molecular weight. In fact, the observed power law dependence seems to follow very well the weight average molecular weight. This power law exponent α is generally found to be approximately 3.4. The variation of viscosity with molecular weight is shown in Figure 18

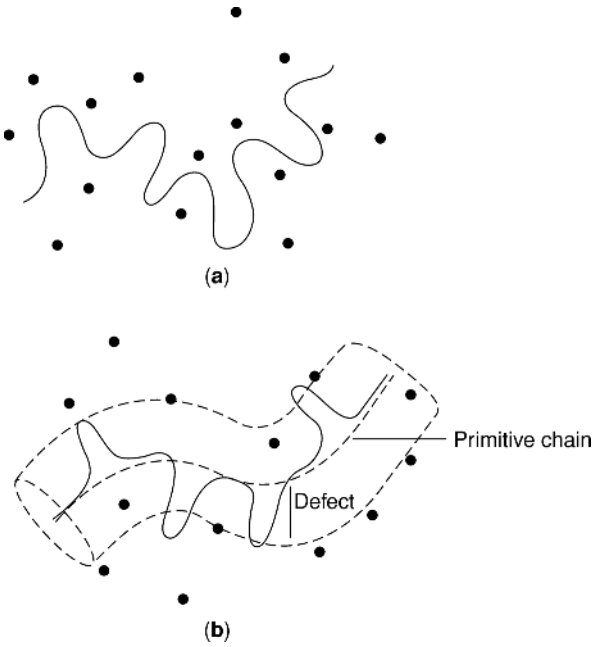

Fig. 17. Schematic of a polymer chain confined in (**a**) a fixed network of obstacles and (**b**) the primitive path representation of the same constraints as a tube. After Doi and Edwards (56), with permission.

for a number of polymers from the classic work of Berry and Fox (57). The molecular weight axis also includes the concentration effect discussed shortly. The very strong molecular weight dependence of the viscosity is still not fully understood, although reptation theory has provided a very large step toward understanding.

According to the reptation theory, the dramatic slowing down of the motion of long polymer chains can be considered as similar to the motion of a chain through a network, as represented by the tube in the Doi–Edwards (DE) model. The network chains of the tube walls prevent the polymer chain from lateral motion (or at least reduce lateral motion) with the result that the chain is forced to move along the contour of the tube. The chain's Brownian movement causes it to slide back and forth within the tube until it eventually disengages. Quantitative analysis of the chain's diffusive properties leads to the estimation that the viscosity-molecular weight exponent $\alpha = 3.0$ rather than the observed 3.4. The reasons for this have been variously attributed to different mechanisms such as "primitive path" fluctuations (58), "constraint release (59)," tube fluctuations (60), and others that provide a means for the viscosity to crossover from a 3.4 power law dependence on molecular weight to a purely reptative behavior at extremely high molecular weights (61–64). There is only one set of data currently available that really bears relevance to the question of such crossover behavior and that is based on a single data point that falls well off of the 3.4 line for a polybutadiene of 1.65×10^7 g/mol molecular weight (65).

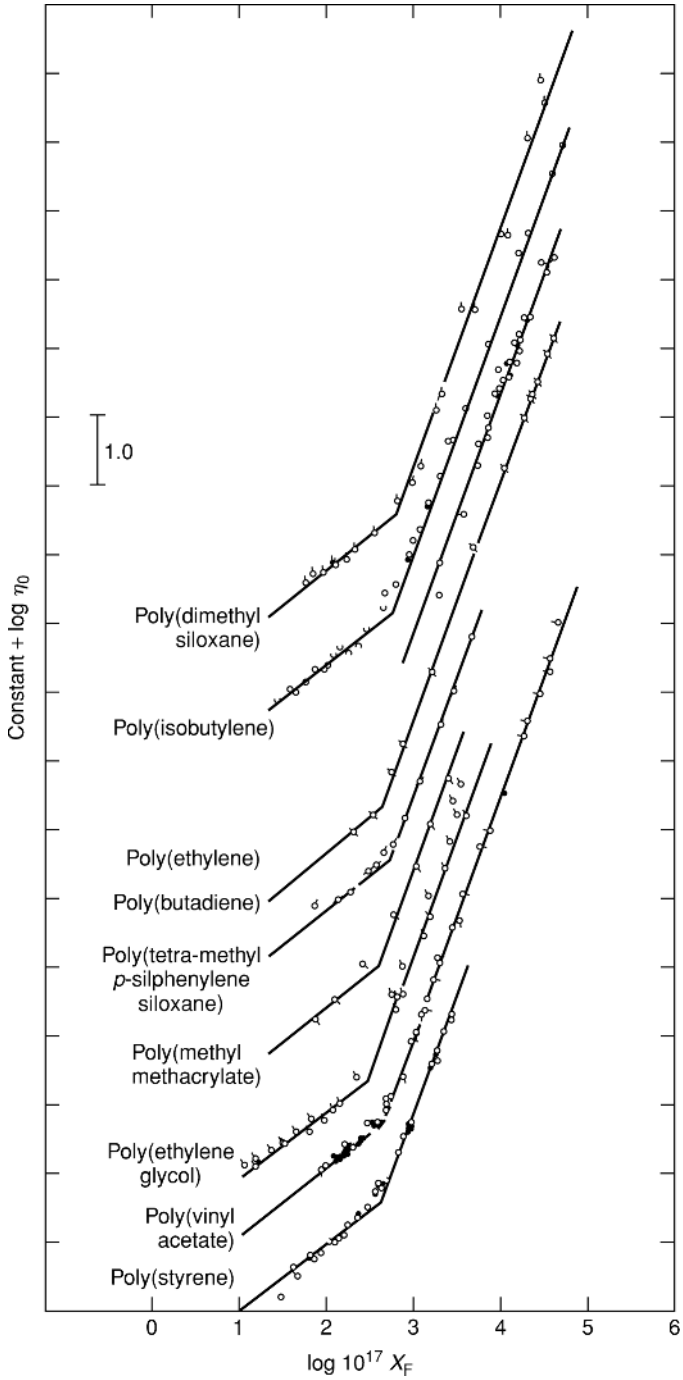

Fig. 18. Double logarithmic representation of the viscosity vs scaled molecular weight for a series of polymers, showing the change from a weak (nearly linear) dependence of viscosity on molecular weight to the entangled regime where $\eta_0 \propto M^{3.4}$. After Berry and Fox (57), with permission.

In addition to the large molecular weight dependence of the viscosity, another aspect of the chain dynamics of polymers in the terminal region is the observation that the relaxation spectrum is very broad. One measure of the breadth of the relaxation spectrum is the product of the rubbery plateau value G_N^0 and the steady-state recoverable compliance J_e^0. The predicted and observed values for polymer melts are

$$\begin{aligned} J_e^0 G_N^0 &\approx 2.0(\text{observed}) \\ J_e^0 G_N^0 &= 1.2(\text{reptation}) \end{aligned} \tag{32}$$

Hence, the reptation theory does not predict a broad enough relaxation spectrum and current modifications of the theory seem insufficient to describe the full range of observed viscoelastic behavior of polymer melts. Reptation theory is still the paradigm for polymer chain dynamics and provides tremendous insight into material behavior. However, as described, there are still pieces of the puzzle of polymer molecular viscoelasticity that remain to be elucidated.

Behavior of Concentrated Solutions. Another aspect of polymer chain dynamics that is important to their understanding is their behavior in entangled solution. This is particularly so because the reptation theory does not explicitly deal with the effects of concentration on the tube diameter and resulting chain dynamics. However, there are several aspects to the effects of the interactions between small molecule "solvents" or "plasticizers" that are important. The first effect is the observation that the glass-transition temperature of the material is changed, generally to lower temperatures (9,37). For the segmental relaxation, this can be reasonably well accounted for by a time–concentration superposition principle (9,66) similar to the time–temperature superposition discussed above. In the event that one is dealing with the plasticization and the segmental relaxation, the major effect is that the T_g is decreased. The other parameters in the WLF or Vogel–Fulcher equations are less impacted. The reader is directed to the extensive treatment of the problem by Ferry (9) in terms of the free-volume model of dynamics for further information.

On the other hand, the impact of the solvent as one moves into the entanglement regime is different from the simple shift in T_g, although this change is also important for understanding the behavior. The other factor that occurs is that the entanglement density decreases (perhaps the tube diameter gets larger) and the plateau modulus and steady-state recoverable compliance both change dramatically with concentration. When we work with the polymer concentration ϕ, we find that $G^0{}_N$ and $J^0{}_e$ vary as

$$G_N^0 \propto \phi^{2-2.25} \text{ and } J_e^0 \propto \phi^{-(2-2.25)} \tag{33}$$

In Figure 18 the viscosities were found to scale as approximately $\phi^{3.4}$—the same as the molecular weight. At the same time, it has been reported (67) that the viscosity can vary by as much as ϕ^5. This difference in apparent behavior depends somewhat on the polymer–solvent system, the temperature of test relative to T_g, and whether or not the data are corrected to a constant "distance" from the glass temperature. The reason stems from the simple relation between viscosity and

the relaxation modulus given in equation 26, which for a simple Maxwell model would be

$$\eta_0 = G_N^0 \lambda \tag{34}$$

Because the characteristic relaxation times λ_i vary in a way that is determined by the concentration dependence of the glass temperature, equation 34 combined with equation 33 indicates that the method of data analysis will determine the scaling behavior observed for the viscosity as a function of concentration. When one is well above the glass transition, the λ_i can follow a dependence as strong as ϕ^3, then equation 34 with equation 33 would give (68)

$$\begin{gathered} \eta_0 \propto G_N^0 \lambda \propto \phi^2 \phi^x \\ \text{For x} = 3{:}\eta_0 \propto \phi^5 \\ \text{For x} = 1.4{:}\eta_0 \propto \phi^{3.4} \end{gathered} \tag{35}$$

Hence, description of the dynamics of the polymer–solvent system demands complete specification of both the complex T_g–concentration relationship and the temperature(s) of test. Importantly, unlike the case of time–temperature superposition, the shift factors for the relaxation times and the viscosity will not be the same. The latter will scale, as does the viscosity, as in equation 35. However, the relaxation times themselves will scale with a much weaker concentration dependence.

Viscoelastic Response of Semicrystalline Polymers. Figure 10 illustrated the general response of the semicrystalline polymer as a function of temperature. For the amorphous polymer it was possible to show the response as a function of time (or frequency) as in Figure 12 because of time–temperature superposition principles. Unlike the amorphous polymer, the viscoelastic response of the semicrystalline polymers cannot generally be treated using time–temperature superposition. There are several reasons for this. First, the crystallites in the material may exhibit relaxations that have different temperature dependences than the amorphous phase. This would clearly lead to a breakdown of thermo-rheological simplicity. In addition, the amorphous phase in the semicrystalline polymer may be changed by the presence of the crystallites. This has been referred to as a rigid amorphous phase or a constrained phase. The impact of the constraint is to change the temperature dependence of the relaxation response of the constrained amorphous material relative to that of the unconstrained material. The result is that, again, time–temperature superposition does not describe the material. Figure 19 shows the viscoelastic behavior of a semicrystalline material at several temperatures (25). Tobolsky (25) made the important observation that these curves are not superimposable by simple shifting procedures. The result is that for the semicrystalline polymers, determination of the full thermo-viscoelastic response of the material can be a very time-consuming task because the ability to extrapolate outside the testing range of times or frequency is limited.

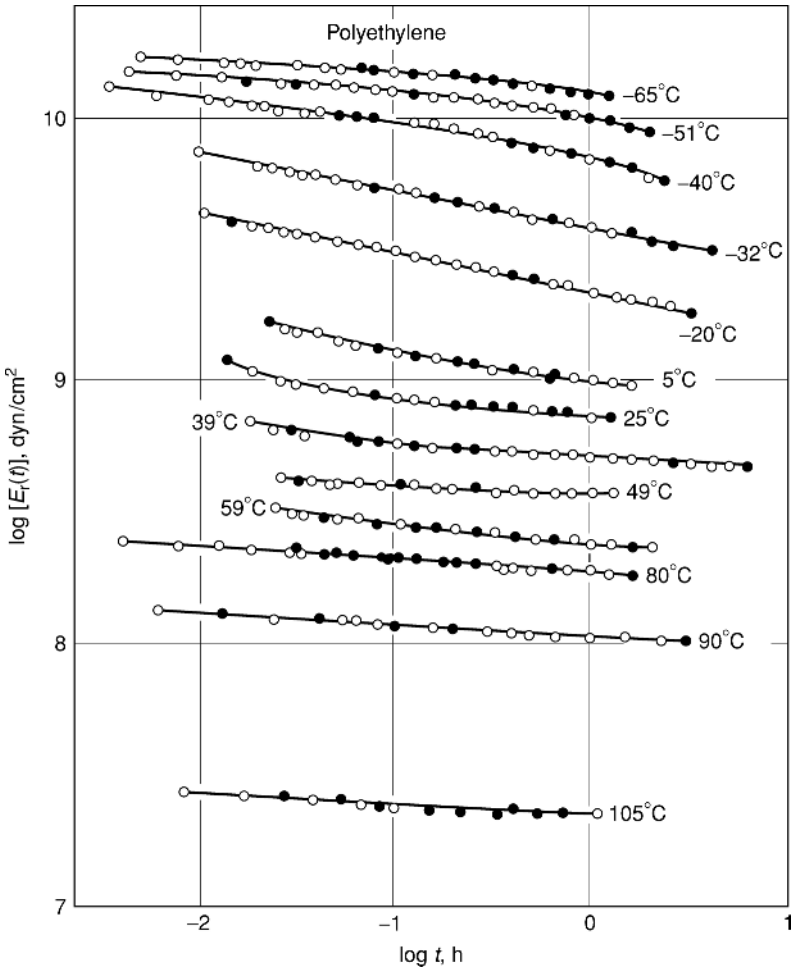

Fig. 19. Relaxation response of polyethylene in isothermal conditions, illustrating that time–temperature superposition does not generally describe the behavior of semicrystalline polymers. After Tobolsky (25).

Nonlinear Viscoelastic Behavior of Polymeric Materials

General Regimes of Response. The nonlinear viscoelastic response of polymers, of course, follows some of the same classifications as does the linear response. Hence, the behavior above the glass temperature and into the terminal zone is fluid behavior, and often follows time–temperature superposition. The phenomenology of polymer melts and solutions is commonly described by *constitutive laws* that relate the stress and strain histories to each other (59,69). A brief description of the K-BKZ model (70–72) is provided as it seems to capture most of the behaviors of polymer melts and solutions subjected to large deformations or high deformation rates. At the same time the nonlinear form of the reptation

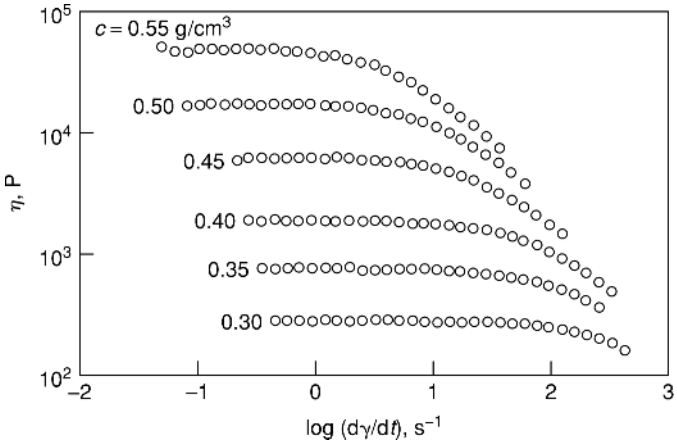

Fig. 20. Double logarithmic representation of viscosity vs. shear rate for polymer solutions having indicated concentrations. Plot illustrates shear thinning of entangled polymers as shear rate increases. After Graessley et al. (73), with permission. To convert Pa·s to P, multiply by 10.

model is introduced, which in early versions reduced to the K-BKZ constitutive law.

Below the glass temperature, the nonlinear viscoelastic response of polymeric materials has been much less widely studied than has the behavior of melts and solutions. One reason for this is the lack of an adequate theory of behavior. Therefore the discussion about amorphous materials below the glass temperature focuses on recent measurements of the nonlinear response as well as attempts to apply some of the formalisms that have been applied in the melt and solution states to the behavior of glassy polymers. Finally, the behavior of semicrystalline polymers can be even more complicated and this is discussed briefly.

Behavior of Entangled Polymer Melts and Solutions: Steady-State Behavior. Before discussing the constitutive law given by the K-BKZ theory, it is important to discuss the nonlinear behavior of polymers that is observed. One such behavior is that in steady state, ie, when the material response has quit changing after the application of a stress or deformation rate. For such a situation and recalling that a Newtonian fluid follows a viscosity law in which the stress is proportional to the strain rate

$$\tau = \eta_0 \, \dot{\gamma} \tag{36}$$

where η_0 is the viscosity coefficient. While many small molecule fluids follow expression 36 extremely well, polymeric liquids exhibit *shear thinning* behavior and the viscosity is a function of the shear rate. Typical behavior is exhibited in Figure 20, where viscosity is a function of the shear rate (73). At low shear rates, one observes a Newtonian plateau, followed by a powerlaw region. After the power law region, there is some evidence that at very high shear rates there is a second Newtonian plateau where the viscosity again becomes independent of the shear

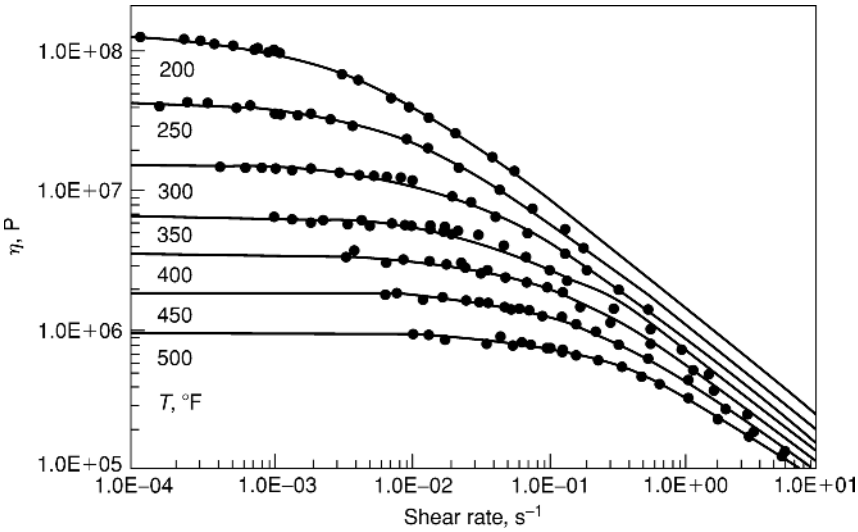

Fig. 21. Shear-rate dependence of the viscosity of a polyisobutylene material, illustrating the fit provided by equation 38. After Rosen (74), with permission. To convert Pa·s to P, multiply by 10.

rate. The power law regime can be described by an empirical equation (74):

$$\tau = K(\dot{\gamma})^n$$
$$\eta = \frac{\tau}{\dot{\gamma}} = K(\dot{\gamma})^{n-1} \tag{37}$$

A possibly better description of the behavior comes from the modified Cross equation (75), particularly if there is a second Newtonian plateau:

$$\eta(T, \dot{\gamma}) = \frac{\eta_0(T)}{1+[C\eta_0(T)\dot{\gamma}]^{1-n}} \tag{38}$$

This equation has the advantage of having the temperature dependence in it explicitly. When the shear-rate-dependent viscosity follows the same temperature dependence, such as WLF, as does the zero shear rate viscosity, then equation 38 is a reasonable approximation to the observed behavior. Otherwise, this is just an estimate. Figure 21 illustrates the fitting of equation 38 to some typical shear-rate-dependent data (74,76).

In addition to the observations in shear that have just been discussed, there is considerable interest in the elongational response in polymeric fluids. The elongational or Trouton viscosity η_E is three times the zero shear rate viscosity in the linear viscoelastic range. However, its behavior is more complex and, as shear rates get higher, the viscosity can even go through a maximum with increasing shear rate as illustrated in Figure 22 (77).

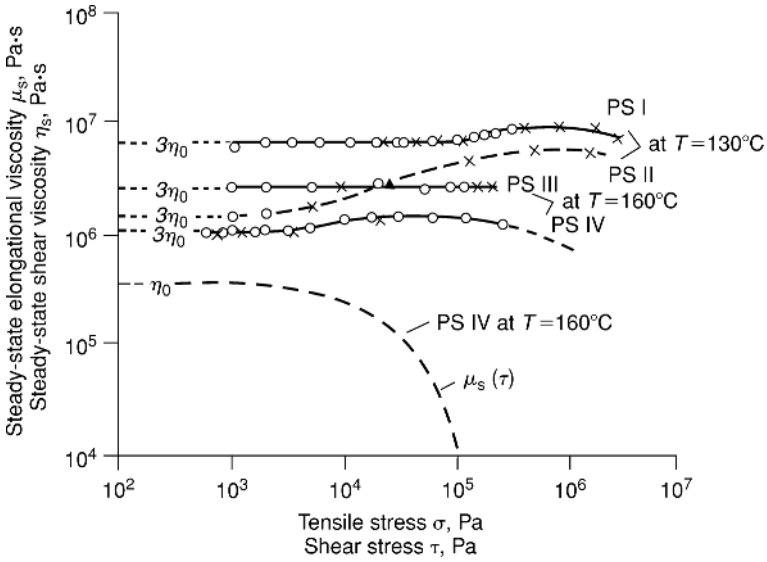

Fig. 22. Elongational viscosity as a function of shear rate for several polystyrene samples. O σ_0 = constant; X $\dot{\varepsilon}_0$ = constant After Münstedt (77), with permission.

Behavior of Entangled Polymer Melts and Solutions: Transient Response. While the steady-state response of polymers in shear and elongational flows is of much interest, there are also many instances in which the transient response is important because not all processes attain steady state. There are two important transient responses in the nonlinear regime of behavior. These are the stress relaxation response in which the deformation is held constant and the stress evolution with time is followed. This was discussed above for the linear viscoelastic case. In addition, the response to a constant rate of deformation can be an important transient response to study. Also note that creep experiments are sometimes used to characterize the nonlinear response of polymeric fluids and these will also be discussed briefly.

Transient Response: Stress Relaxation. In single-step stress relaxation experiments, the observation is that the response of a polymeric fluid becomes very deformation dependent, ie, it becomes nonlinear. Unlike the case of a linear viscoelastic response, the stress required to maintain a constant deformation is no longer simply proportional to the applied strain. Figure 23 shows the nonlinear response as log $G(\gamma, t)$ vs log t (78). As can be seen, when the strain is larger than about 0.50, the modulus begins falling onto different lines depending on the strain. In Figure 24 *isochronal* data are shown for a polymer solution as log τ_{12} vs log γ (79). If the material were linear, the plots at the different times (isochrones) would be straight with a slope of unity. This is the behavior that one observes in the limit of small strains, as indicated in the figure by the lines of slope unity at the lower deformation levels. Deviations from unity arise when the response is nonlinear; that is, the value of the modulus is a function of the strain. Finally, another way in which to consider the nonlinear behavior is to look at a plot of the relaxation modulus at different times vs the strain. A normalized form of such a

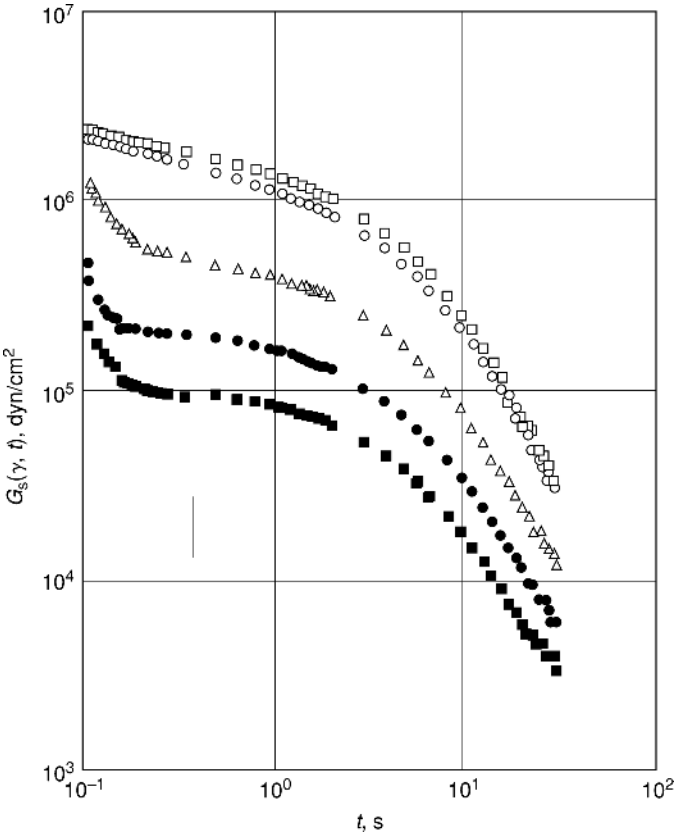

Fig. 23. Stress relaxation modulus of a concentrated polybutadiene solution subjected to increasing shear strains. From top to bottom: $\gamma = 0.333$, 0.667, 1.33, 2.00, and 2.67. After Vrentas and Graessley (78), with permission.

plot is shown for a polymer solution in Figure 25 (80). Here, were the material response linear, the data would collapse to a line that was a constant, independent of the strain magnitude. The actual nonlinear behavior that is observed is commonly described in terms of the damping function in the Doi–Edwards model and is described subsequently.

Transient Response: Constant Rate of Deformation. The constant rate of deformation response of the linear viscoelastic material was discussed above. From that discussion, the stress-deformation response looks nonlinear even when the material is linear viscoelastic. For the nonlinear material the response will not be simply described by the linear viscoelastic laws. However, the curves will look similar at low strain rates. At higher strain rates, a stress overshoot is observed, which cannot occur for the linear viscoelastic material. Figure 26 shows the effect of increasing the strain rate on the transient stress–time response (which is related to the strain) for a polymer solution (81). As seen, the stress overshoot becomes weaker with decreasing strain rates (when the material response may be linearly viscoelastic); however, as strain rate increases, there is an onset of

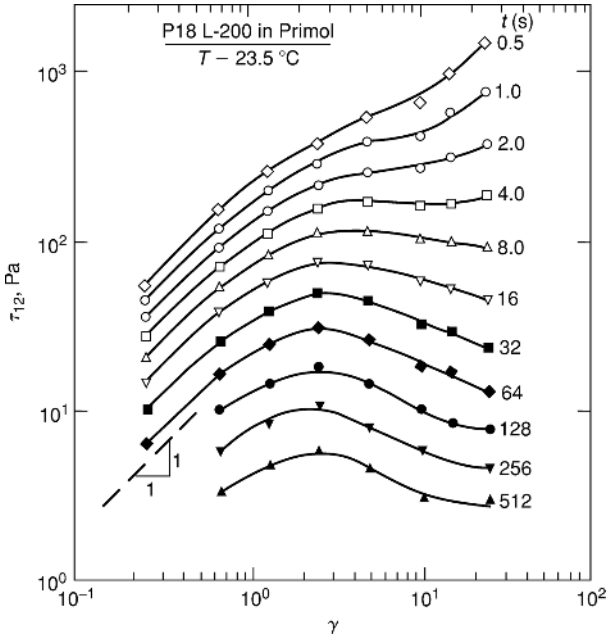

Fig. 24. Double logarithmic representation of the shear stress vs the shear strain for a polymer solution and for different isochrones, as indicated. After McKenna and Zapas (79).

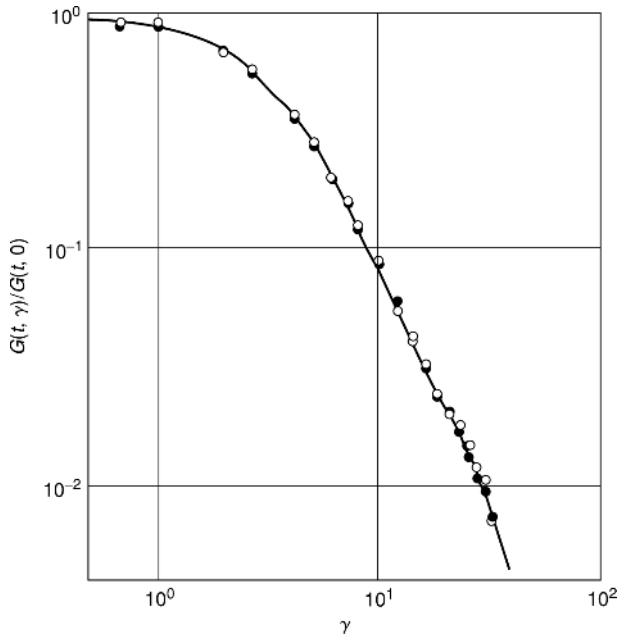

Fig. 25. Reduced nonlinear stress relaxation modulus as a function of strain for a polymer solution. This plot illustrates the strongly nonlinear or strain-dependent behavior of entangled polymers. After Osaki et al. (80), with permission.

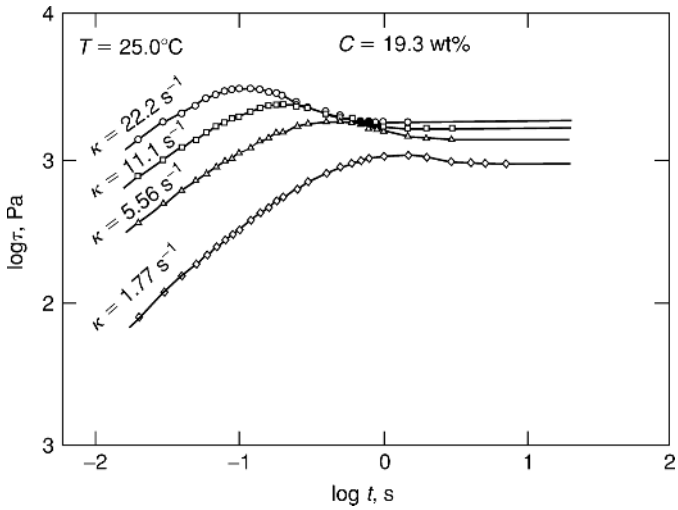

Fig. 26. Effect of strain rate on the stress-time (double logarithmic plot) behavior for a concentrated polymer solution, showing the increasing strength of the stress overshoot phenomenon with increasing strain rate. After Zapas and Phillips (81), with permission.

a stress overshoot where the early time stress goes through a maximum before settling down to its steady-state value (from which the strain-rate-dependent viscosity would be obtained).

Transient Response: Creep. The creep behavior of the polymeric fluid in the nonlinear viscoelastic regime has some different features from what were found with the linear response regime. First, there are no ready means of relating the creep compliance to the relaxation modulus as was done in the linear viscoelastic case. In fact, the relationship between the relaxation properties and the creep properties depends entirely on the exact constitutive relationship chosen for the response of the material, and numerical inversion of the specific constitutive law is ordinarily necessary to predict creep response from the relaxation behavior (or vice versa). For most cases, the material properties that appear in the constitutive equations are written in terms of the relaxation response. We discuss this subsequently in the context of the K-BKZ model.

Constitutive Description of Polymer Melt Behavior: K-BKZ and DE Descriptions. Although there are many nonlinear constitutive models that have been proposed, the focus here is on the K-BKZ model because it is relatively simple in structure, can be related conceptually to finite elasticity descriptions of elastic behavior, and because, in the mind of the current author and others (82), the model captures the major features of nonlinear viscoelastic behavior of polymeric fluids. In addition, the reptation model as proposed by Doi and Edwards provides a molecular basis for understanding the K-BKZ model. The following sections first describe the K-BKZ model, followed by a description of the DE model.

The K-BKZ Constitutive Model.

Finite Elasticity Theory: Classical Theory. The finite elasticity theories available today are very powerful and well developed from a phenomenological

perspective. Because the K-BKZ (70–72) has the form of a time-dependent finite elasticity (it was developed as a "perfect elastic fluid") it is useful to briefly outline the basics of finite elasticity theory here. In the initial sections of this article, the stress and strain tensors were discussed, and it was noted that the constitutive relationships that arise between the stress and the strain include material parameters called moduli. When a material is classified as *hyperelastic* then the moduli are related to derivatives of the free energy function (often the Helmholtz free energy) with respect to appropriate measures of the strains or deformations (83). Because here large deformations are discussed, there may be multiple possible choices for the actual deformation measurement used. In the discussion that follows, one uses the formalism developed in which the deformations are treated in the context of the Left Cauchy–Green deformation tensor B_{ij} and the free energy function $W(I_1, I_2, I_3)$ is treated as a function of the invariants of the deformation tensor. The material parameters are, then, written as derivatives of the free energy function (or strain energy density function) with respect to the invariants I_i of B_{ij}. The constitutive relationship between the stresses and deformations is then written in terms of these functions (83–86):

$$\sigma_{ij} = \frac{2}{I_3^{1/2}}\left[\left(\frac{\partial W}{\partial I_2} I_2 + \frac{\partial W}{\partial I_3} I_3\right) \Big/ + \frac{\partial W}{\partial I_1} B_{ij} - \frac{\partial W}{\partial I_2} I_3 B_{ij}^{-1}\right] \tag{39}$$

where I is the identity tensor. The invariants of B_{ij} are written in terms of the principal stretches $\lambda_i = 1 + \varepsilon_{ii}$ as

$$\begin{aligned} I_1 &= \lambda_1^2 + \lambda_2^2 + \lambda_3^2 \\ I_2 &= \frac{1}{\lambda_1^2} + \frac{1}{\lambda_2^2} + \frac{1}{\lambda_3^2} \\ I_3 &= \lambda_1^2 \lambda_2^2 \lambda_3^2 \end{aligned} \tag{40}$$

Note here that the λ_i's are stretches and not relaxation times as used previously. Also note that for polymer melts and solutions, the shear response function (shear modulus) is several orders of magnitude smaller than is the bulk modulus. Therefore, these materials can be treated as *incompressible*. For the linear case, the incompressibility assumption has $K \to \infty$ or $\nu \to 0.5$. Here, $I_3 = 1$ and the constitutive law for the incompressible material becomes

$$\sigma_{ij} = -p\delta_{ij} + \frac{\partial W}{\partial I_1} B_{ij} - \frac{\partial W}{\partial I_2} B_{ij}^{-1} \tag{41}$$

where p is an indeterminate hydrostatic pressure that arises because of the incompressibility condition and δ_{ij} is the Kronecker delta.

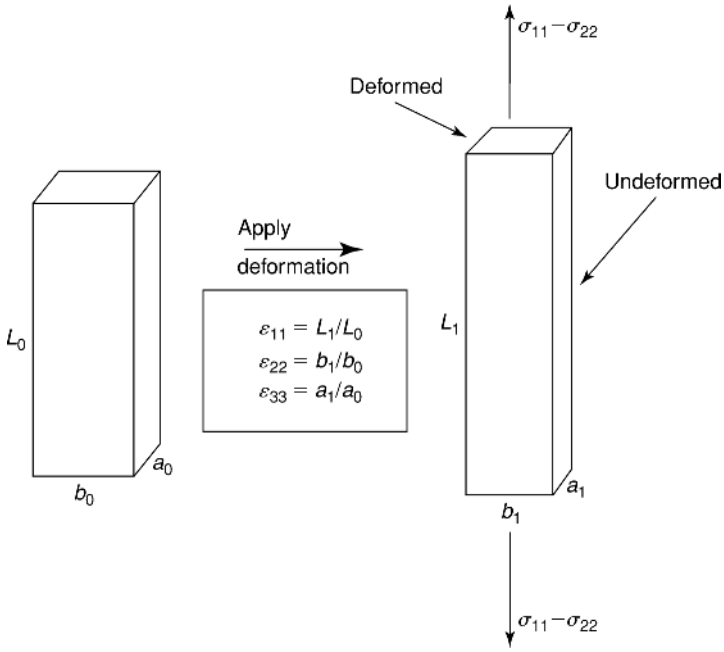

Fig. 27. Schematic of the simple extension geometry.

Referring to Figure 27, one can solve for the stresses in simple extension. First, the stretches are given by

$$\begin{aligned} \lambda_1 &= 1 + \varepsilon_{11} \\ \lambda_2 = \lambda_3 &= 1 + \varepsilon_{22} \\ \lambda_2 = \lambda_3 &= \frac{1}{\lambda_1^{1/2}} \text{ (because of incompressibility)} \end{aligned} \tag{42}$$

Because the material is incompressible, the stresses are only determined within an indeterminate pressure. Therefore, to represent the actual experimental conditions, it is recognized that the *principal stress difference* $\sigma_{11} - \sigma_{22}$ is being measured, and this is given as

$$\begin{aligned} \sigma_{11} - \sigma_{22} &= \frac{\partial W}{\partial I_1}(B_{11} - B_{22}) - \frac{\partial W}{\partial I_2}\left(B_{11}^{-1} - B_{22}^{-1}\right) \\ &= \frac{\partial W}{\partial I_1}\left(\lambda_1^2 - \lambda_2^2\right) - \frac{\partial W}{\partial I_2}\left(\lambda_1^{-2} - \lambda_2^{-2}\right) \\ &= \frac{\partial W}{\partial I_1}\left(\lambda_1^2 - \lambda_1^{-1}\right) - \frac{\partial W}{\partial I_2}\left(\lambda_1^{-2} - \lambda_1\right) \\ &= \left(\lambda_1^2 - \lambda_1^{-1}\right)\left(\frac{\partial W}{\partial I_1} + \frac{1}{\lambda_1}\frac{\partial W}{\partial I_2}\right) \end{aligned} \tag{43}$$

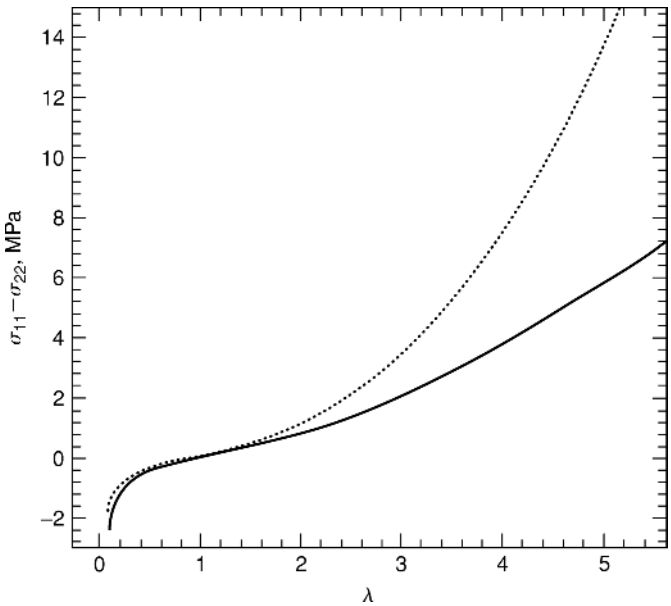

Fig. 28. Stress-stretch response for a Neo-Hookean rubber compared with that of a Mooney–Rivlin material. (———) Neo-Hookean: $C_1 = 0.24$ MPa; (- - - - -). Mooney–Rivlin: $C_1 = 0.16$ MPa, $C_2 = 0.08$ MPa.

The simple stress-deformation response given by equation 43 shows the strong nonlinearity that arises when the stress–strain curve for a typical rubber is plotted, even when the material is *Neo-Hookean* or *Mooney–Rivlin*, meaning that the values of $\partial W/\partial I_1 = W_1 = C_1$ and $\partial W/\partial I_2 = W_2 = C_2$ are constants. For the Neo-Hookean material, $W_1 = C_1$ and $W_2 = 0$. For the Mooney–Rivlin material (87,88), $W_1 = C_1$ and $W_2 = C_2$. Figure 28 shows plots of the stress-deformation behavior for a Neo-Hookean rubber and for a Mooney–Rivlin rubber. The figure shows that in spite of the fact that the material parameters are constants, there is a strong nonlinear response due to the geometry of deformation, ie, the $[\lambda^2 - \lambda^{-1}]$ and $1/\lambda$ terms in equation 43. Also, from equation 43 one can readily see from where the concept of the Mooney–Rivlin material arose. Dividing the equation by $[\lambda^2 - \lambda^{-1}]$, one obtains

$$\sigma_{\mathrm{R}} = \frac{\sigma_{11} - \sigma_{22}}{\lambda_1^2 - \lambda_1^{-1}} = \frac{\partial W}{\partial I_1} + \frac{1}{\lambda_1}\frac{\partial W}{\partial I_2} \tag{44}$$

where σ_{R} is referred to as the reduced stress. For Mooney–Rivlin behavior, a plot of σ_{R} vs $1/\lambda_1$ gives a straight line of slope C_2 and intercept C_1. Real rubber often shows near to Mooney–Rivlin behavior in extension, but deviates in compression. For the Neo-Hookean material, the reduced stress is a constant. Figure 29a shows the calculations for the general behavior of σ_{R} vs $1/\lambda_1$ for the Neo-Hookean and Mooney–Rivlin materials. Figure 29b shows experimental results for two typical cross-linked rubbers, and it is seen that neither the Neo-Hookean nor the

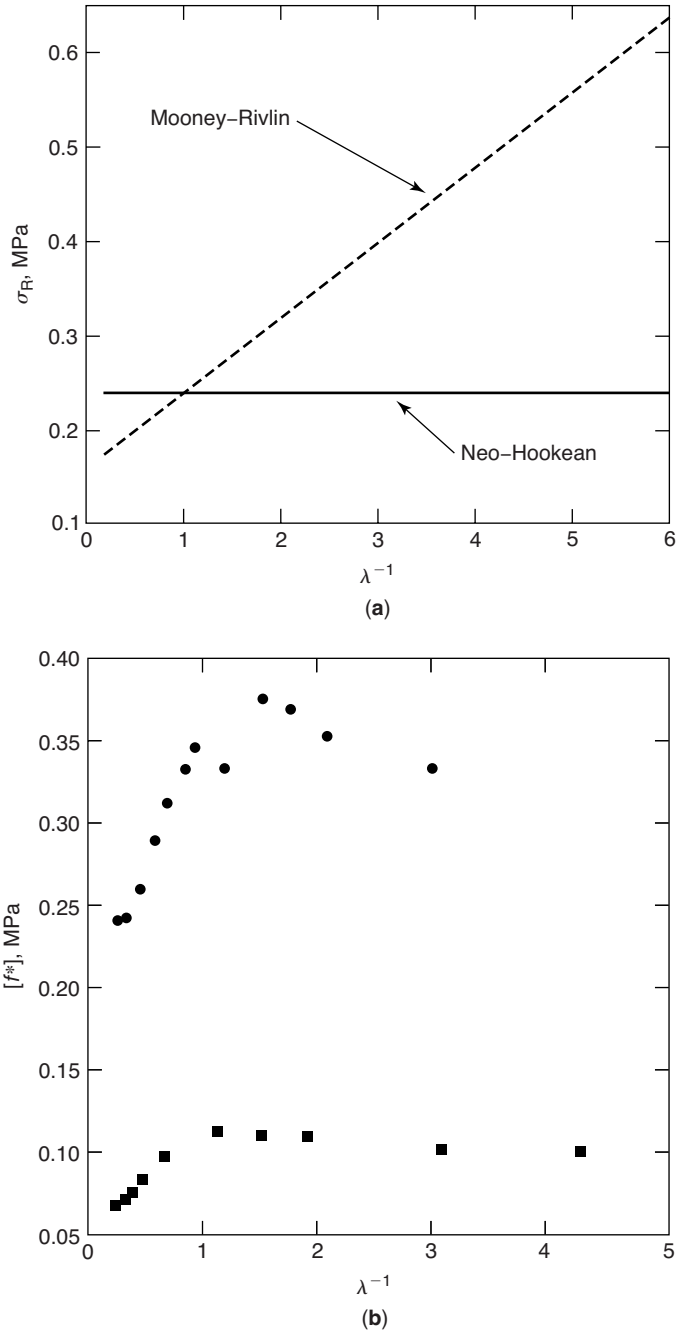

Fig. 29. (**a**) Reduced stress plot for the Neo-Hookean and Mooney–Rivlin materials of Figure 28. (**b**) Reduced stress plot for natural rubber and a polydimethylsiloxane (PDMS) rubber as indicated. Plot illustrates that actual rubber behavior may be Mooney–Rivlin-like in tension ($\lambda^{-1} < 1$), but not in compression. • Natural rubber; ■ PDMS. Plot from Han et al. (89), natural rubber data from Ref. 90, and PDMS data form reference 91.

Mooney–Rivlin model would describe the behaviors exhibited (89–91). The reader is referred to reviews of various proposed strain energy functions (89,92,93) for further information.

Another important aspect of finite elasticity theory is the ability to measure the strain energy function derivatives $W_1 = \partial W/\partial I_1$ and $W_2 = \partial W/\partial I_2$. Penn and Kearsley (94) showed how this is done using data from torsional experiments. An interesting aspect about torsion in finite deformations is that in order to maintain the cylinder at a constant length, it is necessary to apply normal forces at the ends of the cylinder. If the cylinder is left unrestrained, it will lengthen in an effect referred to as the Poynting (95) effect, first observed early in the last century in experiments with metal wires. When a cylinder of length L is twisted by an amount ψ per unit length ($\psi = \theta/L$, where θ is the angle of twist) the magnitude of the torque (moment) M and the normal force N are given by the following expressions:

$$T = 4\pi\psi \int_0^R (W_1 + W_2) r^3 \mathrm{d}r \tag{45}$$

$$N = -2\pi\psi^2 \int_0^R (W_1 + 2W_2) r^3 \mathrm{d}r \tag{46}$$

where R is the cylinder radius. By differentiating each expression with respect to the limits of integration after an appropriate variable change, Penn and Kearsley (90) showed that W_1 and W_2 can be expressed as simple algebraic expressions in the torques and normal forces measured at different angles of twist, ie, deformations:

$$W_1 + W_2 = \frac{1}{4\pi\psi R^4}\left(3T + \psi\frac{\mathrm{d}t}{\mathrm{d}\psi}\right) \tag{47}$$

$$W_1 + 2W_2 = \frac{-1}{\pi\psi^2 R^4}\left(N + \psi^2\frac{\mathrm{d}N}{\mathrm{d}\psi^2}\right) \tag{48}$$

Figure 30 shows typical torque and normal force measurements for a natural rubber sample as functions of the deformation (as ψR) in a double logarithmic plot (96). The data for T, N, and their derivatives can then be obtained and used in equations 47 and 48 to solve for W_1 and W_2. Figure 31 shows typical data for the values of W_1 and W_2 as functions of deformation for a cross-linked natural rubber obtained from such measurements (94,97). Importantly, these values are related to the *damping function* of the DE model discussed subsequently. They represent the deformation dependence of the shear modulus in this instance.

Finite Elasticity Theory: The VL Representation. While the above description of the finite deformation behavior of elastic materials is very powerful, the limitation on it is that the material parameters W_1 and W_2 need to be determined in each geometry of deformation of interest. Hence, the torsional measurements described above only give values of $W_1(I_1, I_2)$ and $W_2(I_1, I_2)$ for the condition of

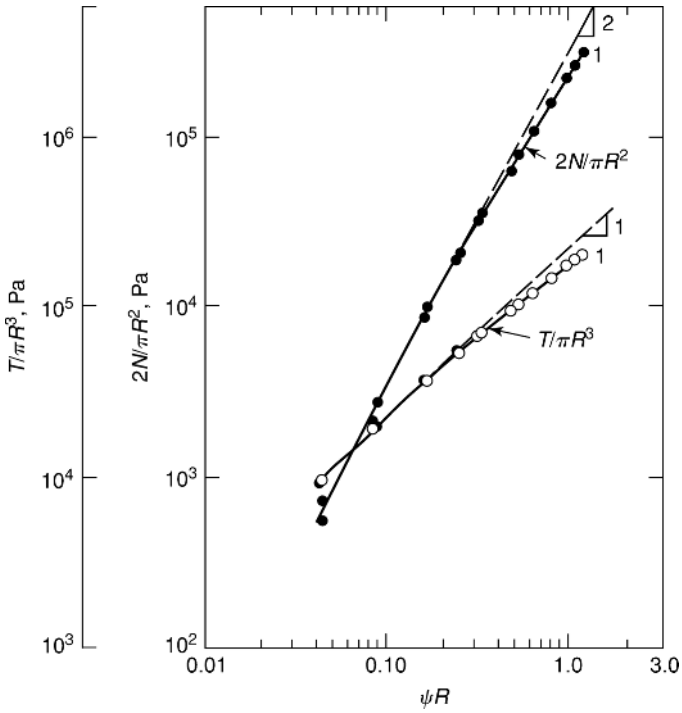

Fig. 30. Torque and normal forces (scaled by sample geometry) vs strain at outer edges of cylinder for a natural rubber sample subjected to torsional deformations. After McKenna and Zapas (96).

shear (torsion is a nonhomogeneous shear) and that condition is $I_1 = \mathrm{I}_2 = 3 + \gamma^2$. More measurements need to be made to obtain the parameters in extension, compression, etc. However, in 1967, Valanis and Landel (98) proposed a strain energy function that, rather than being a function of the invariants, is a function of the stretches λ_i. The function was assumed to be separable in the stretches as

$$\hat{w}(\lambda_1,\lambda_2,\lambda_2) = w(\lambda_1) + w(\lambda_2) + w(\lambda_3) \tag{49}$$

Then, for example, in simple extension, the stress–deformation relationship becomes

$$\sigma_{11} - \sigma_{22} = \lambda_1 w'(\lambda_1) - \lambda_2 w'(\lambda_2) \tag{50}$$

and it becomes a matter, for any deformation to determine the values of $w'(\lambda_i)$ and these can be obtained in any geometry of deformation. Thus, the inconvenience of performing large numbers of experiments in multiple geometries of deformation is avoided. There has been a considerable effort to establish the validity of the Valanis–Landel (VL) form of strain energy function (98–102) and it is generally found to be a very good representation of the material behavior, although some discrepancies have been observed. Some special forms of the VL function, such as

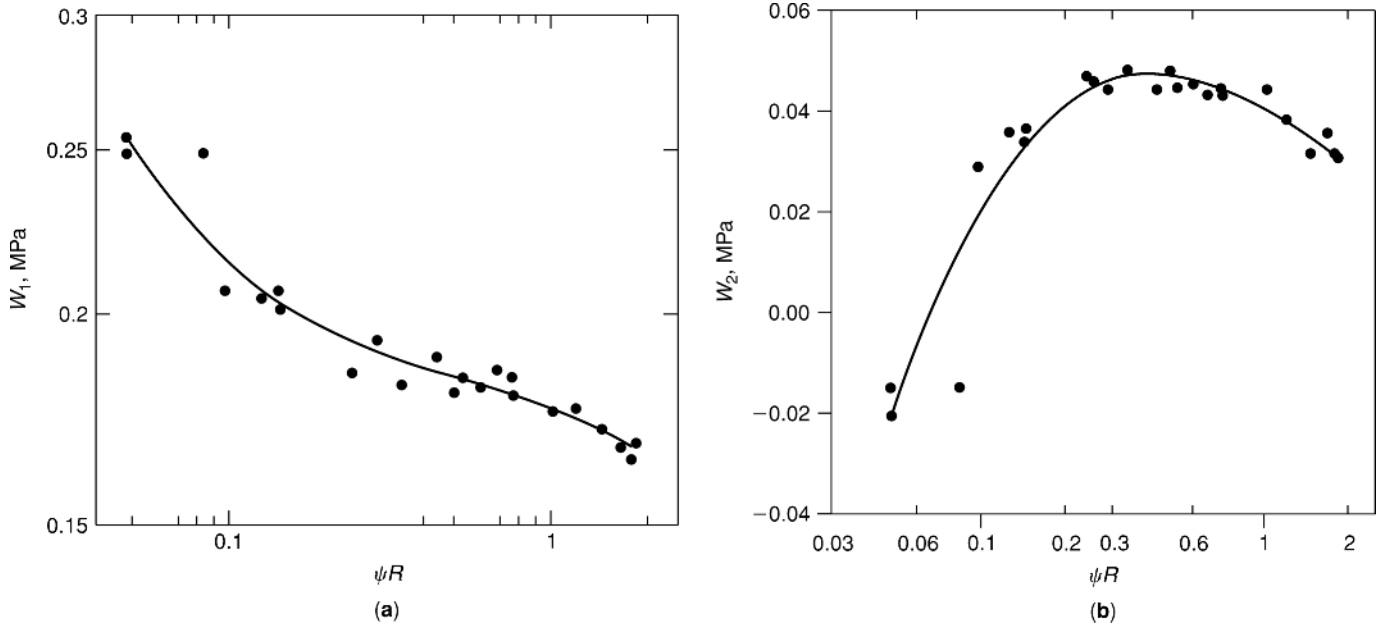

Fig. 31. (**a**) W_1 vs strain for a natural rubber material. (**b**) W_2 vs strain for a natural rubber material. Data of Penn and Kearsley (94) given in Kearsley and Zapas (97).

the Ogden model (103,104), have been found to be very useful and are commonly used in commercial finite element modeling of rubber behavior.

Because of this usefulness it is important to have relatively simple experiments available to obtain the VL function. Kearsley and Zapas (97) have shown that either simple extension combined with simple compression or torsion with normal force measurements can be used to obtain the VL function. Valanis and Landel (98) used pure shear measurements. The equations for the torsional measurements arise from the relationship between $w'(\lambda)$ and W_1 and W_2 given by

$$w'(\lambda) - \frac{w'(1)}{\lambda} = \frac{2}{\lambda}(\lambda^2 - 1)\left(W_1 + \frac{1}{\lambda^2}W_2\right) \tag{51}$$

and the values of λ are determined from the twists of the cylinder by

$$\text{For } \lambda > 1 : \lambda_{\max} = \frac{1}{2}[(\psi^2 R^2 + 4)^{1/2} + \psi R] \tag{52}$$

Thus, from torque and normal forces in torsional experiments, the VL function derivative can be obtained. Typical data for natural rubber are presented in Figures 30, 31, 32. The figures illustrate the sequence that would be used to obtain the VL function. First, obtain torque and normal force data (Fig. 30) and use equations 47 and 48 to obtain the strain energy function derivatives W_1 and W_2 (some typical results shown in Fig. 31). Finally, data of the sort shown in Figure 31 are used to obtain the VL function derivative $w'(\lambda)$. Figure 32 shows such data obtained from torsional measurements on natural rubber samples cross-linked to different extents (102).

In the case of extension and compression data, Kearsley and Zapas (97) developed a recursive method to determine the VL function from stress–strain data similar to those presented in Figure 28. The advantage in using extension and compression data rather than torsional data is that higher values of λ can be reached.

Finally, the power of finite elasticity theory is that once the material properties [W_1 and W_2 or $w'(\lambda)$] are known, the stresses in any deformation field can be calculated. There is an extensive literature on ways to represent the material functions and, in fact, commercial finite element codes use finite elasticity theory in calculations that can be important in applications that range from the stresses in automobile tires (105) to those in earthquake bearings for large buildings (106). One feature of the K-BKZ theory to be discussed next is that it retains the structure of finite elasticity theory and includes time-dependent properties of the viscoelastic materials that were discussed in the earlier sections of this article.

The K-BKZ Theory: Model. The K-BKZ model was developed in the early 1960s by two independent groups. Bernstein, Kearsley, and Zapas (70) of the National Bureau of Standards (now the National Institute of Standards and Technology) first presented the model in 1962 and published it in 1963. Kaye (71), in Cranfield, U.K., published the model in 1962, without the extensive derivations and background thermodynamics associated with the BKZ papers (82,107). Regardless of this, only the final form of the constitutive equation is of concern here.

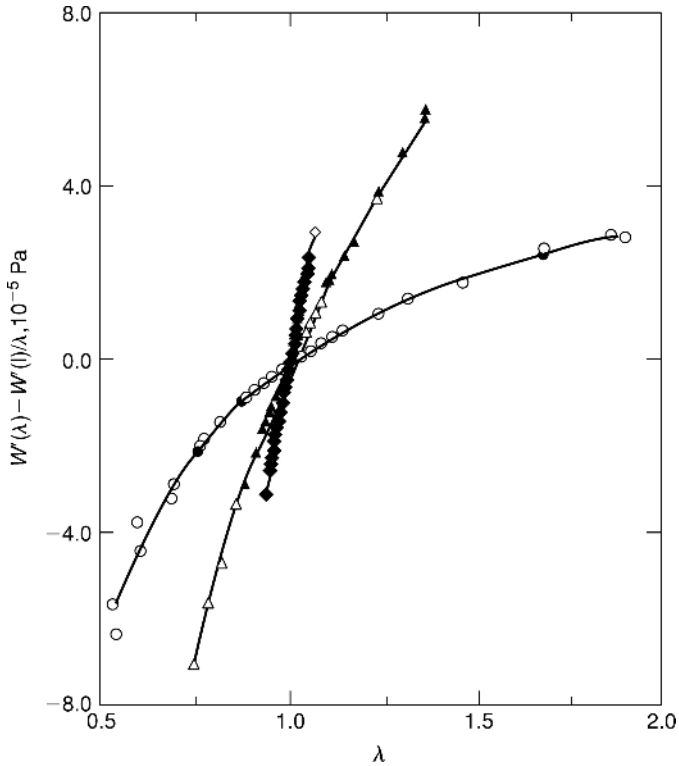

Fig. 32. The VL function (98) derivative vs stretch for natural rubber samples cured with 1, 5, and 15 parts per hundred dicumyl peroxide, as indicated. The VL function was obtained from torque and normal force measurements. ○ APHR1; △ APHR5; ◇ APHR15. After McKenna et al. (102).

Similar to the idea of finite elasticity theory, the K-BKZ model postulates the existence of a strain potential function $U(I_1, I_2, t)$. This is similar to the strain energy density function, but it depends on time and, now, the invariants are those of the *relative* left Cauchy–Green deformation tensor $\boldsymbol{B}_{t,ij}$. The relevant constitutive equation is

$$\sigma_{ij}(I_1,I_2,t) = -p\delta_{ij} + \int_{-\infty}^{t} \{U_1(I_1,I_2,t-t')B_{t,ij}(t,t') - U_2(I_1,I_2,t-t')B_{t,ij}^{-1}(t,t')\}\mathrm{d}t' \tag{53}$$

Also note that the hydrostatic pressure is indeterminate because the K-BKZ is an incompressible material model. As in finite elasticity theory, the material parameters need to be obtained and, in principle, the stress response to any deformation history can be obtained. Unlike linear viscoelasticity, the integration must be carried out from $-\infty$ to t, which can lead to difficulties in numerical computer codes. This aspect of the K-BKZ theory has been discussed by (62) Larson, among others.

The relative deformation tensor $\boldsymbol{B}_{t,ij}$ assumes that the current material *configuration* (the configuration at time t) is the reference configuration. This idea is important as it is common in fluid models because fluids have no natural

reference configuration while solids do. Hence, for example, the relative deformations in simple extension become

$$\lambda_{t,1} = \frac{\lambda_1(t)}{\lambda_1(t')}; \quad \lambda_{t,2} = \frac{\lambda_2(t)}{\lambda_2(t')}; \quad \lambda_{t,3} = \frac{\lambda_3(t)}{\lambda_3(t')} \tag{54}$$

and the invariants of $\boldsymbol{B}_{t,ij}$ are similar to those for the elastic material, but in terms of the relative deformations

$$\begin{aligned} I_1(t,t') &= \left[\frac{\lambda_1(t)}{\lambda_1(t')}\right]^2 + \left[\frac{\lambda_2(t)}{\lambda_2(t')}\right]^2 + \left[\frac{\lambda_3(t)}{\lambda_3(t')}\right]^2 \\ I_2(t,t') &= \left[\frac{\lambda_1(t')}{\lambda_1(t)}\right]^2 + \left[\frac{\lambda_2(t)}{\lambda_2(t')}\right]^2 + \left[\frac{\lambda_3(t)}{\lambda_3(t')}\right]^2 \\ I_3(t,t') &= 1 = \left\{\left[\frac{\lambda_1(t)}{\lambda_1(t')}\right]\left[\frac{\lambda_2(t)}{\lambda_2(t')}\right]\left[\frac{\lambda_3(t)}{\lambda_3(t')}\right]\right\}^2 \end{aligned} \tag{55}$$

The utility of the K-BKZ theory arises from several aspects of the model. First, it does capture many of the features, described below, of the behavior of polymeric melts and fluids subjected to large deformations or high shear rates. That is, it captures many of the nonlinear behaviors described above for steady flows as well as behaviors in transient conditions. In addition, unlike the more general *multiple integral* constitutive models (108,109), the experimental data required to determine the material properties are not overly burdensome. In fact, the information required is the single-step stress relaxation response in the mode of deformation of interest (72). If one is only interested in, eg, simple shear, then experiments need only be performed in simple shear and the exact form for $U(I_1, I_2, t)$ need not be obtained. Furthermore, because the structure of the K-BKZ model is similar to that of finite elasticity theory, if a full three-dimensional characterization of the material is needed, some of the simplifying aspects of finite elasticity theories that have been developed over the years can be applied to the behavior of the viscoelastic fluid description provided by the K-BKZ model. One such example is the use of the VL form (98) of the strain energy function discussed above (110). The next section shows some comparisons of the material response predicted by the K-BKZ theory with actual experimental data.

The K-BKZ Theory: Comparison with Experiment. The first data required to test the K-BKZ model is single-step stress relaxation data to determine the material parameters of interest. This is best seen from the following example for a simple shearing history. From equation 49, the shear stress for a simple shear deformation can be expressed as (see Ref. 72)

$$\sigma_{i,j}(t) = \int_{-\infty}^{t} -K_*[\gamma(t) - \gamma(t'), t - t']\mathrm{d}t' \tag{56}$$

where $\gamma(t) - \gamma(t')$ is the relative strain and K_* is the partial derivative of the relaxation function $K[\gamma(t) - \gamma(t'), t - t']$ with respect to the second (time) argument. For the single-step stress relaxation history in which $\gamma(t) = 0$ for $t < 0$ and $\gamma(t) = \gamma$

for $t > 0$, equation 52 reduces to

$$\sigma_{ij}(t) = \int_{-\infty}^{0} -K_*[\gamma, t - t']\mathrm{d}t' \tag{57}$$

Defining $\xi = t - t'$ and performing a change of variables, equation 57 can be evaluated as

$$\sigma_{ij}(t) = \int_{\infty}^{t} K_*(\gamma, \xi)\mathrm{d}\xi = K(\gamma, t) - K(\gamma, \infty) \tag{58}$$

and because the material is a fluid, $K(\gamma, \infty) = 0$. Therefore, the shear stess is simply equal to its relaxation function $K(\gamma, t)$ for an applied shear strain of γ. As suggested by equations 56, 57, 58, one need not actually determine the values of $U_i(I_1, I_2, t)$ when the experiments of interest are always of the same geometry.

Also, because of the structure of the K-BKZ theory, torsional measurements can also be analyzed in a fashion similar to equation 58. Recall Figure 24, which depicts the single-step stress relaxation responses for a concentrated polymer solution in a torsional (parallel plate) experiment as isochronal plots of stress vs strain on double-logarithmic axes. It is worth noting that in the moderate strain regime, these data look similar to the elastic data of Figure 30. But, at large strains the curves go through a maximum. This is undoubtedly because the solutions can be deformed to a much greater magnitude than can the cross-linked rubber.

Once the single-step data are known, then integration of equation 56 (or eq. 53) for different strain histories leads to predictions for the material response in any deformation history of interest. A very powerful method of evaluating constitutive equations is the double-step strain history in which the second-step response should be able to be predicted by the model in question. Figure 33 shows the set of two-step histories that is dealt with here and subsequently. Figures 34, 35, 36, 37, 38 show comparisons between K-BKZ predictions and the experimental data for two-step stress relaxation experiments (111), constant rate of loading and unloading experiments, creep and recovery experiments, relaxation after steady shearing flow at different shear rates, and superposition of small deformations on large ones; this last being a multiple-step experiment that could be treated as a three-step case (79) As seen, these experiments show excellent agreement between the theory and the experiment, indicating the power of the model. Another interesting aspect of the K-BKZ theory is the predictions it makes for the normal stress responses in the so-called *half-step deformation history* in which the second step is $\frac{1}{2}$ the magnitude of the first, as depicted in Figure 33c. For any two-step history, the shear and normal stress difference responses (or torque and normal force responses) can be written as (72,112–117)

$$\begin{aligned}
\sigma_{12}(t - t_1) &= K(\gamma_2, t) + K(\gamma_2 - \gamma_1, t - t_1) - K(\gamma_2 - \gamma_1, t) \\
\sigma_{22}(t - t_1) - \sigma_{22}(t - t_1) &= H_1(\gamma_2, t) + H_1(\gamma_2 - \gamma_1, t - t_1) - H_1(\gamma_2 - \gamma_1, t) \\
\sigma_{22}(t - t_1) - \sigma_{33}(t - t_1) &= H_2(\gamma_2, t) + H_2(\gamma_2 - \gamma_1, t - t_1) - H_2(\gamma_2 - \gamma_1, t)
\end{aligned} \tag{59}$$

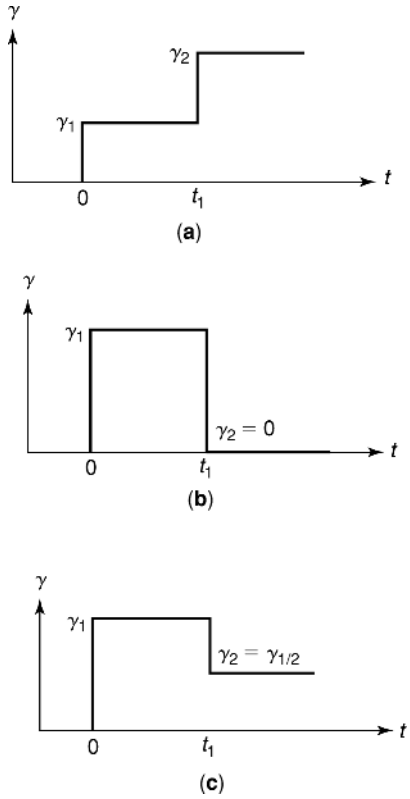

Fig. 33. Two-step strain histories. (**a**) Step-up, (**b**) step to zero deformation, and (**c**) half-step deformation histories.

where $K(\gamma, t)$ is the single-step stress relaxation response of the shear (or torque) and $H_i(\gamma, t)$ is that of the ith principal stress difference (or normal force). On substituting torque T and normal force N for a torsional experiment into equations 59, one would see that the torque response is an odd function of the strain $[T(-\gamma) = -T(\gamma)]$ and the normal force is an even function of strain $[N(-\gamma) = N(\gamma)]$. Then, for the special $\frac{1}{2}$-step history where $\gamma_1 = 2\gamma$, the torque and normal force responses become

$$\begin{aligned} T(\psi_2, t - t_1) &= 2K(\psi_2, t) - K(\psi_2, t - t_1) \\ N(\psi_2, t - t_1) &= H(\psi_2, t - t_1) \end{aligned} \tag{60}$$

which means that the torque response depends upon the full deformation history. On the other hand, the normal force response depends only upon the time after the first step $(t - t_1)$, ie, is independent of the duration of the first step and would be equal to the magnitude of the response to a single-step deformation to a torsion magnitude of ψ_2. Figure 39 provides the experimental evidence that this is, indeed, the behavior followed by a polyisobutylene solution. Subsequent

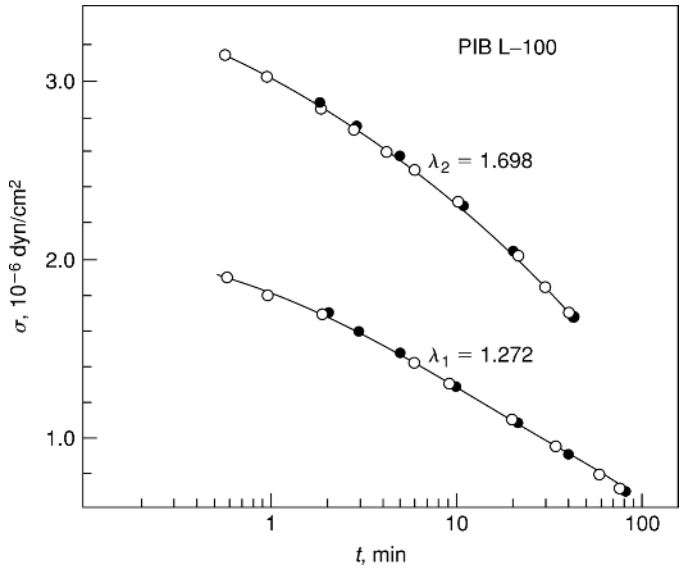

Fig. 34. Comparison of K-BKZ predictions (filled circles) with experimental data (open circles) for step-up experiment in uniaxial extension for a polyisobutylene material. After Zapas and Craft (111), with permission.

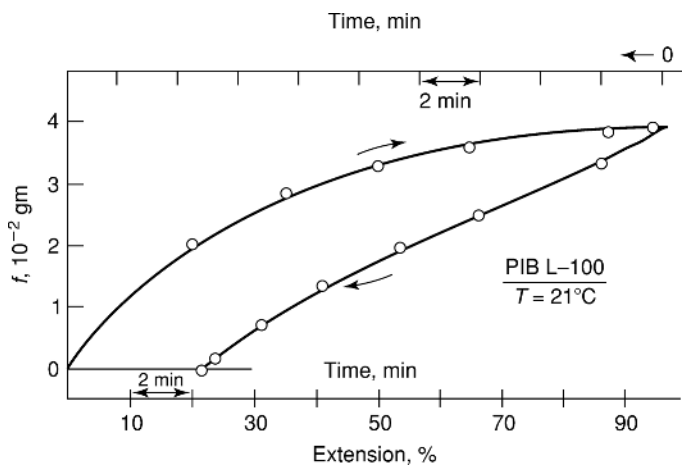

Fig. 35. Comparison of K-BKZ predictions (open circles) with experimental data (solid line) for a constant rate of strain (load–unload) history for a polyisobutylene material. After Zapas and Craft (111), with permission.

data, however, indicate that this may not be universally true (115–117). This is discussed subsequently.

The data shown thus far describing the success of the K-BKZ theory were, generally, such that the stress never changed sign. However, it turns out that in *stress-reversing* flows, the K-BKZ theory seems not to work as well (62,82,107,

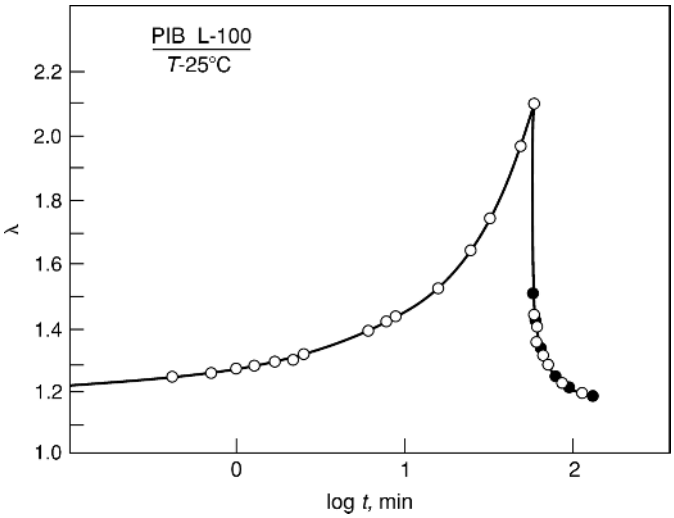

Fig. 36. Comparison of K-BKZ predictions (filled circles) with experimental data (open circles) for creep and recovery for a polyisobutylene material. After Zapas and Craft (111), with permission.

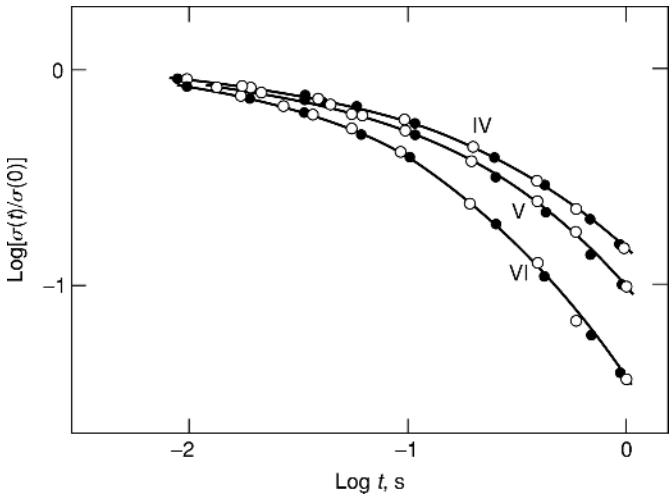

Fig. 37. Comparison of K-BKZ predictions (filled circles) with experimental data (open circles) for relaxation after a steady shearing flow. (IV) 0.177 s^{-1}; (V) 1.11 s^{-1}; (VI) 5.56 s^{-1}. After Zapas and Craft (111), with permission.

112,114,116,118). Figure 40 shows the shear stress response for a polyisobutylene solution in the half-step history just discussed. The response is clearly not in agreement with the K-BKZ theory prediction. Also, in some flows, predicting the pure shear behavior, which has an extensional component to it, is not consistent with the simple shear predictions (119).

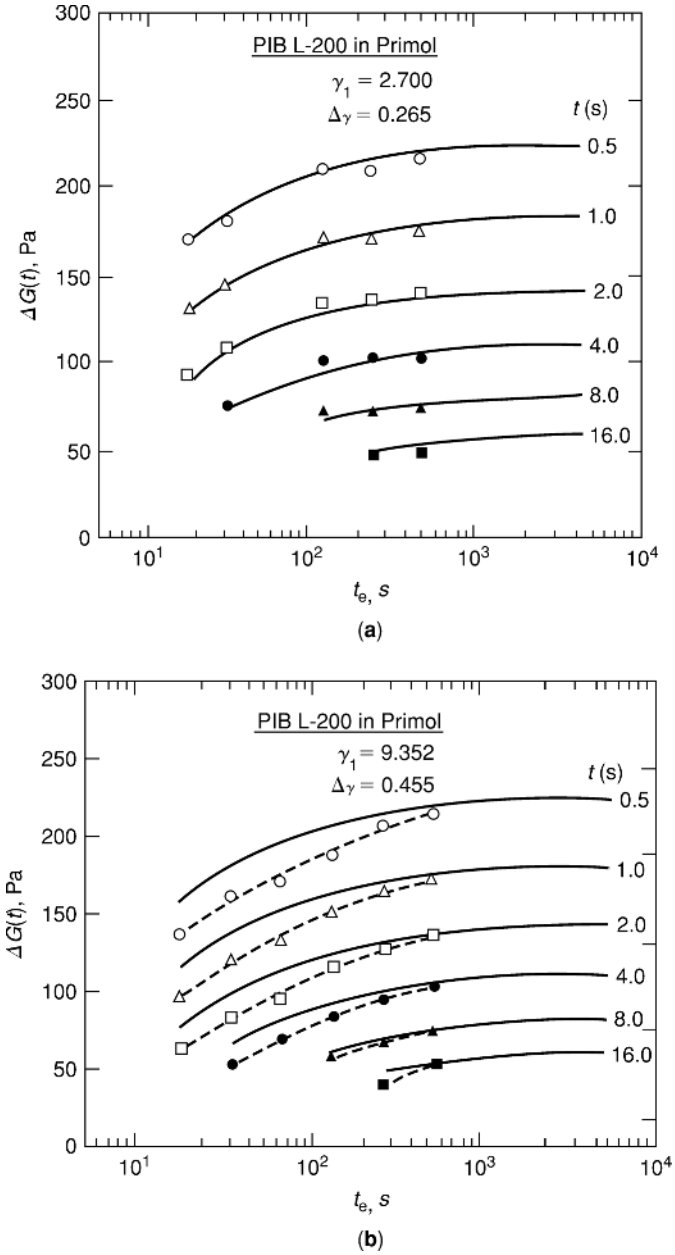

Fig. 38. Comparison of the K-BKZ predictions (lines) with data for the incremental modulus response to a small strain $\Delta\gamma$ superimposed on a large strain γ as a function of time t_e elapsed after the imposition of the large strain. Part (**a**) shows excellent agreement between the theory and experiment for $\gamma = 2.7$, while part (**b**) shows moderate deviations at small t_e values when $\gamma_1 = 9.4$. After McKenna and Zapas (79).

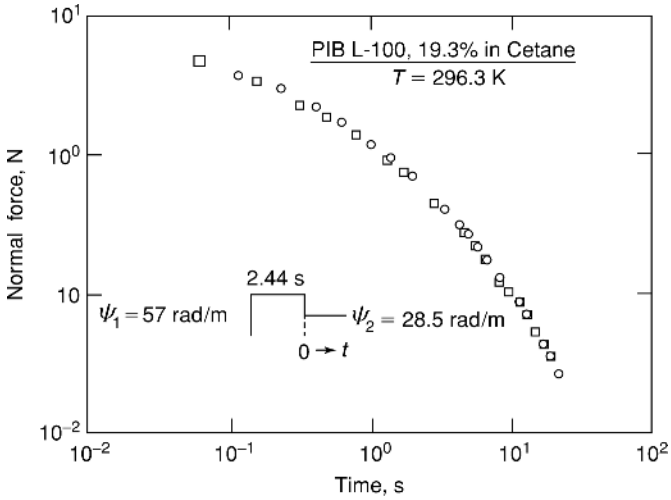

Fig. 39. Comparison of the K-BKZ prediction (squares) for the "half-step" normal stress response with the experimental behavior (open circles) for a polyisobutylene solution. After McKenna and Zapas (113).

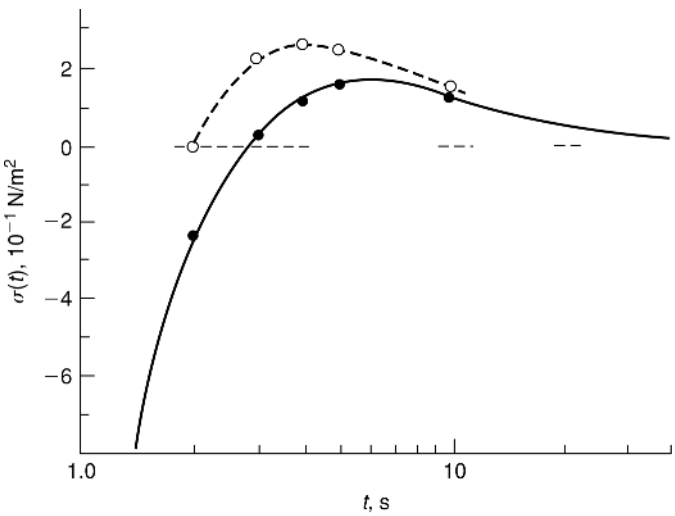

Fig. 40. Comparison of the "half-step" shear stress response predicted by the K-BKZ theory (open circles) with the experimental data (filled circles) for a polyisobutylene solution. After Zapas (118), with permission.

The Doi–Edwards Theory. Much of the excitement that came during the early years of the Doi–Edwards (DE) tube model (52–56) for reptation of polymer chains revolved about the fact that the use of the *independent alignment* assumption resulted in a special form of the K-BKZ model. Hence, much of the machinery that was developed in the 1960s and early 1970s to test the K-BKZ model could be implemented to test the DE model. The next sections discuss the

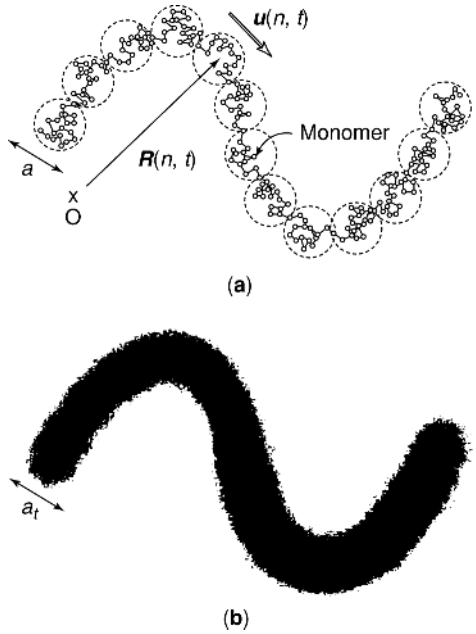

Fig. 41. Schematic representation of a real chain (**a**) and a coarse-grained chain (**b**). In the real chain depiction the small beads connected by rods are the monomeric segments and the circles represent the submolecules of the coarse-grained chain. Part (b) represents the hypothetical time-exposure photograph. After Watanabe (63), with permission.

molecular basis of the DE model, the independent alignment assumption, and how well monodisperse polymers follow the DE version of the K-BKZ model.

The Molecular Description. The fundamentals of reptation theory are best understood with the general *coarse-grained* models of a single polymer chain. If one considers the linear polymer chain to be composed of m monomers and also considers the *Rouse* approximation (120) that there are no hydrodynamic interactions [in concentrated solutions and melts this is a very good approximation (9,63)] and that the chain assumes a *Gaussian* conformation, the chain can be divided into N submolecules, each containing g monomers. The average size a of the submolecule in the Gaussian conformation is related to the step length b of the monomer (63):

$$a^2 = gb^2 \tag{61}$$

The real chain is coarse-grained in both time and space, by dividing it into submolecules. Figure 41a shows the Rouse chain and Figure 41b illustrates a hypothetical experiment (63) in which the molecule is photographed with an exposure time t_0. When the time t_0 is large, the chain looks like a fuzzy thread with a width a_t because of the chain motion in the time interval of the "photograph." The dynamics of this Rouse chain are considered as the motion of a string of Gaussian submolecules in a viscous medium. The friction coefficient ζ on the submolecule

or bead is given by

$$\zeta = g\zeta_0 \tag{62}$$

where ζ_0 is the monomeric friction coefficient. It is assumed that the force acting on a bead is represented by a Gaussian spring with a spring constant κ given by

$$\kappa = \frac{3k_B T}{a^2} \tag{63}$$

where k_B is the Boltzmann constant and T is the absolute temperature. The time-evolution of the position $\boldsymbol{R}(n,t)$ of the nth submolecule (bead) can be obtained by considering the forces acting on the the bead: frictional $\boldsymbol{F}_f$, elastic (entropic) $\boldsymbol{F}_e$, and Brownian $\boldsymbol{F}_B$. For large N (long chains) the equation can be written as (121)

$$-\zeta\left[\frac{\partial R(n,t)}{\partial t}\right] + \kappa\frac{\partial^2 R(n,t)}{\partial n^2} + F_B(n,t) = 0 \tag{64}$$

The first and second terms represent the frictional force $\boldsymbol{F}_f(n, t)$ and the elastic force $\boldsymbol{F}_e(n, t)$, respectively. The Brownian force $\boldsymbol{F}_B$ is modeled as white noise (56, 63).

Solution of equation 64 permits the determination of the dynamic properties of the chain (56,63). For this paper, the results are given for the polymer melt or concentrated solution, not for the single chain contributions to a dilute solution. The reader is referred to References 56 and 63 for more details. The properties of interest are

$$\text{Relaxation modulus: } G(t) = \frac{vk_B T}{N}\sum_{p=1}^{N}\exp\left(\frac{-2tp^2}{\lambda_{R,G}}\right) \tag{65}$$

where $\lambda_{R,G}$ is the longest relaxation time for the Rouse chain, given by

$$\lambda_{R,G} = \frac{\zeta a^2 N^2}{3\pi^2 k_B T} \tag{66}$$

Note that v is the number density of Rouse segments in chains of N segments in length and that are monodisperse. The index p is the eigenmode from the solution to the equation of motion. Furthermore, equation 65 is the equation for a special form of the generalized Maxwell model having constant coefficients $G_i = vk_B T$ (see eq. 18). The relaxation times are given by $\lambda_{R,G}/2p^2$.

The *zero shear rate viscosity* is calculated from (56)

$$\eta_0 = \frac{v\zeta\alpha^2 N}{36} \tag{67}$$

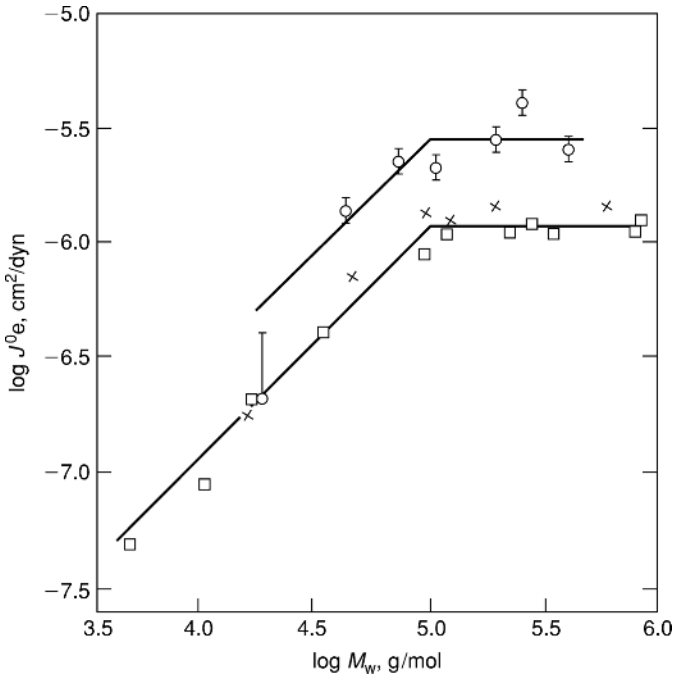

Fig. 42. Double logarithmic representation of the steady-state (recoverable) compliance as a function of molecular weight for linear (squares and crosses) and cyclic (circles) polystyrenes melts. After McKenna et al. (122).

and the *steady-state (recoverable) compliance* is calculated from

$$J_s = \frac{1}{\eta_0^2}\int_0^\infty tG(t)\mathrm{d}t = \frac{2}{5vk_\mathrm{B}T} = \frac{2M}{5\rho RT} \tag{68}$$

where ρ is the density and M is the molecular weight. Although the Rouse model was derived for dilute solutions in which there is no hydrodynamic interaction, it seems to best describe the behavior of concentrated solutions and melts that are disentangled. This is particularly so for the viscosity, which at low molecular weights seems to follow the first power prediction given by equation 67 (recall Fig. 18 at low molecular weights). Also, the equilibrium recoverable compliance of short-chain melts (both linear and cyclic) seems to follow the correct scaling with molecular weight, as shown in Figure 42. However, once the chains get long enough to be entangled, the Rouse-like behavior no longer holds. After entanglement begins, the viscosity follows the very strong $M^{3.4}$ behavior seen in Figure 18 and the steady-state (recoverable) compliance becomes constant as seen in Figure 42 (122). It is here that a model is needed that goes beyond the Rouse model and includes entanglement effects. As noted above, the reptation model of de Gennes (51) and Doi and Edwards (52–56) is the current paradigm for polymer dynamics in the entangled state. Essentially, the DE tube model of reptation is a Rouse chain that moves through a tube that acts as a mean field of constraint. Figure 43 illustrates the movement of the chain in a tube, where the Brownian dynamics

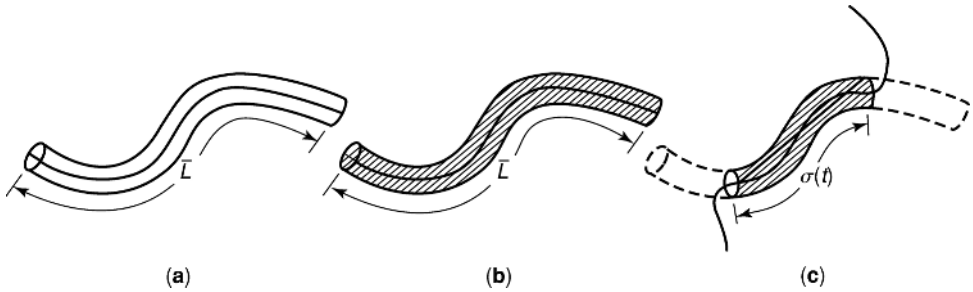

Fig. 43. Schematic of stress relaxation of a chain in the tube in the DE model for small deformations. (**a**) Prior to deformation, the tube has its equilibrium conformation. (**b**) Immediately after the deformation, the entire tube is deformed. At small strains, the contour length of the tube is unchanged. (**c**) At a later time t, the chain has partially escaped from the tube and remains partially confined by the deformed tube. The average of the contour length $\sigma(t)$ of this part of the tube is equal to $L\mu_{\mathrm{rep}}(t)$. After Doi and Edwards (56), with permission.

of the chain causes it to move about in the original tube until it completely disengages and the new surroundings form a new tube. Here we consider the model at length scales greater than the tube diameter a, which has been identified (57) with the (mean) distance between entanglements or a Rouse submolecule of the size of the entanglement spacing. The important parameters are the number of monomers m_{e} in the *entanglement segment*, the tube diameter, the friction coefficient ζ for the entanglement segment, and the number of segments in the chain N. The trajectory of bond vectors of the entanglement segments coincides with the tube axis that is referred to as the *primitive path*. These are related to the physical chain by (63)

$$\begin{aligned} \text{Tube diameter: } a &= m_{\mathrm{e}}^{1/2} b \\ \text{Friction factor: } \zeta &= m_{\mathrm{e}} \zeta_0 \\ \text{Number of segments: } N &= \frac{m}{m_{\mathrm{e}}} \end{aligned} \tag{69}$$

where b is the effective step length of the monomer, m is the number of monomers in the chain or the degree of polymerization, and ζ_0 is the monomeric friction factor. Note that, with the exception of N, the parameters in equation 69 are independent of chain length.

In the equilibrium conformation the centerline of the tube represents a random walk with a step length that corresponds to the tube diameter. If the tube is treated as a system of slip links through which the chain can pass, the mean field of the surrounding chains results in an equivalent tensile force $\boldsymbol{F}_{\mathrm{eq}}$ that acts on the chain ends (63,121):

$$F_{\mathrm{eq}} = \frac{3k_{\mathrm{B}}T}{a} \tag{70}$$

This force acts to constrain the lateral motion of the chains (tube constraints) and the average contour length of the tube coincides with the equilibrium tube length $\boldsymbol{L}_{\mathrm{eq}}$:

$$L_{\mathrm{eq}} = Na = \frac{R_{\mathrm{e}}^2}{a} \tag{71}$$

where $R_{\mathrm{e}}{}^2$ is the mean-square end-to-end distance of the unperturbed chain.

According to the DE model, the tube is fixed in space and, at equilibrium, the contour length is constant $L = L_{\mathrm{eq}}$. This results in all entanglement segments moving together back and forth within the tube and along the tube axis. Hence, the motion is equivalent to one-dimensional diffusion within the tube along the tube axis. If one defines the position along the tube as a segment number (given by s/a, where s is the segment position), one can write an equation for the evolution of the position $\boldsymbol{R}(n, t)$ and the unit bond vector of the nth entanglement segment $\boldsymbol{u}(n, t)$:

$$R(n,t+\Delta t) = R(n+\Delta n,t), u(n,t+\Delta t) = u(n+\Delta n,t) \tag{72}$$

where $\Delta \boldsymbol{n}$ is a normalized (by a) stochastic sliding distance and $\Delta \boldsymbol{t}$ is the time for the chain to slide this distance. Then, the Rouse chain in the tube has a curvilinear motion with a diffusion coefficient $\boldsymbol{D}_{\mathrm{c}}$ that is obtained from the stochastic sliding process (61):

$$\langle \Delta n \rangle = 0, \langle \Delta n^2 \rangle = \frac{2D_{\mathrm{c}}}{a^2}\Delta t, \text{ and } D_{\mathrm{c}} = \frac{k_{\mathrm{B}}T}{N\zeta} \tag{73}$$

The rapid motion of the entanglement segments at the chain (and tube) ends allows these to have their equilibrated configuration:

$$u = a\tilde{u}_{\mathrm{eq}} (\text{at the chain ends}) \tag{74}$$

where $\tilde{u}_{\mathrm{eq}}$ is an isotropically distributed unit vector.

The coarse-grained chain just discussed can be used to describe reptation dynamics at spatial scales $> a$ and time scales greater than the time $\Delta t^*(a)$ for the chain to move (reptate) a distance a (63):

$$\Delta t^*(a) = \frac{Na^2\zeta}{2k_{\mathrm{B}}T} \tag{75}$$

The dynamic properties for the reptation model just described are obtained by solving the equations 71, 72, 73, 74 and the linear viscoelastic properties are solved from the relationship between the stress and the chain orientation function (63). Without going into detail, the results for times longer than the tube equilibration time but shorter than the reptation time are

$$G(t) = G_{\mathrm{N}}\mu_{\mathrm{rep}}(t) \tag{76a}$$

where

$$G_N = \frac{4}{5} \upsilon N k_B T \tag{76b}$$

and

$$\mu_{rep} = \sum_{p=\text{odd}} \frac{8}{p^2 \pi^2} \exp\left(-\frac{tp^2}{\lambda_{rep}}\right) \tag{76c}$$

with

$$\lambda_{rep} = \frac{\zeta N^3 a^2}{\pi^2 k_B T} \tag{76d}$$

In equation 76a the reptation time λ_{rep} is the time for the chain to escape from the tube (orientation relaxation occurs from the end to the center of the chain). G_N is the entanglement plateau modulus (this value is slightly different from that implied from rubber elasticity of an entangled network) and $\mu_{rep}(t)$ is a normalized relaxation modulus for the reptation process. In this time regime, equation 76a implies that the modulus is separable into a time function and a modulus function. This becomes important in discussing the nonlinear response, which is done, in more detail, below. Some other viscoelastic functions from the DE tube model of reptation are

$$\eta_0 = \frac{\pi^2 G_N \lambda_{rep}}{12} \tag{77}$$

$$J_s = \frac{6}{5G_N} = \frac{6}{5} J_N \tag{78}$$

At this point the reptation theory makes some strong predictions about the viscoelastic response in the linear regime, viz, the viscosity varies as N^3 and the ratio of $J_s^0/G_N = 6/5 = 1.2$. Note that the molecular weight dependence of the viscosity has already been discussed above, and recall that, experimentally, the viscosity varies as $N^{3.4}$. In addition, the ratio J_s^0/G_N is observed experimentally to be in the range of 2–2.5. In spite of these failings, the reptation model is very powerful. The next section examines the stress response to deformation histories in the nonlinear range.

The DE Constitutive Equations. The DE model (52–56) made a major breakthrough in polymer viscoelasticity in that it provided an important new molecular physics based constitutive relation (between the stress and the applied deformation history). This section outlines the DE approach that built on the reptation-tube model developed above and gave a nonlinear constitutive equation, which in one simplified form gives the K-BKZ equation (70,71). The model also inspired a significant amount of experimental work. One should begin by

looking at the calculation of the stresses for a material at times longer than the time it takes for the tube to equilibrate, ie, times in the reptation regime.

Doi and Edwards (56) calculate the stress considering how the conformation of the primitive chain $\boldsymbol{R}(s, t)$ is changed by the macroscopic deformation. First, one needs to know the stress equation in terms of the chain conformation, and then how the chain conformation (orientations) changes with the macroscopic deformation field. The stress equation is developed as follows:

$$\sigma_{\alpha\beta}(t) = \frac{v}{N}\left\langle \int_0^L F(t)u_\alpha(s,t)u_\beta(s,t)\mathrm{d}s \right\rangle \tag{79}$$

where $\boldsymbol{u}(s, t) = \partial\boldsymbol{R}(s, t)/\partial s$ is the unit vector tangent to the primitive chain and $F(t)$ is the tensile force acting on the primitive chain. In the equilibrium state

$$F_{\mathrm{eq}} = \frac{3k_{\mathrm{B}}T}{Na^2}L \tag{80}$$

and in the nonequilibrium state

$$F(t) = \frac{3k_{\mathrm{B}}T}{Na^2}L(t) \tag{81}$$

where $L(t)$ is the tube contour at time t and L is its equilibrium value. From equations 79, 80, 81 the relationship between the stress, the contour length, and the changing chain orientation is obtained as

$$\sigma_{\alpha\beta} = \frac{3vk_{\mathrm{B}}T}{N^2a^2}\left\langle \int_0^{L(t)} L(t)\left[u_\alpha(s,t)u_\beta(s,t) - \frac{1}{3}\delta_{\alpha\beta}\right]\mathrm{d}s \right\rangle \tag{82}$$

It is now necessary to develop the equations for the relationship between the macroscopic deformations and the chain orientations. Doi and Edwards assume that the deformation is affine, ie, the primitive chain deforms in the same way as the macroscopic deformation field. Thus, a point $\boldsymbol{R}(s, -0)$ on the primitive chain is displaced as

$$R(s, -0) \rightarrow E{\cdot}R(s, -0) \tag{83}$$

where $\boldsymbol{E}$ is the deformation gradient tensor and its components are written as

$$E_{\alpha\beta} = \frac{\partial r'_\alpha}{\partial r_\beta} \tag{84}$$

where r′ is the coordinate in the deformed state and $\boldsymbol{r}$ is the coordinate in the undeformed state. (Note that this is similar to the definitions used earlier in defining the strains and relative deformations.)

Doi and Edwards then derive expressions for the changing contour length and change in the orientation of the primitive path. The development is beyond the scope of the current article. The important expression is that for the chain

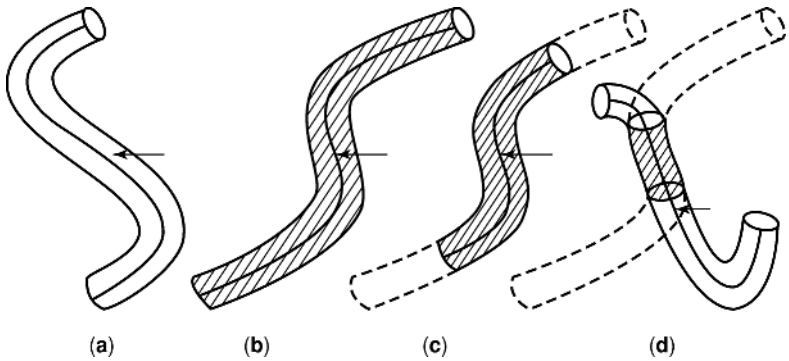

Fig. 44. Schematic of the stress relaxation process after a large step in deformation. (**a**) Equilibrium conformation of the tube prior to deformation. (**b**) Immediately after deformation, the primitive chain has been affinely deformed. (**c**) After the time λ_R, the primitive chain retracts along the tube and recovers its equilibrium contour length ($t \cong \lambda_R$). (**d**) After the time λd the primitive chain leaves the deformed tube by reptation ($t \cong \lambda_d$). After Doi and Edwards (56), with permission.

orientation tensor $\boldsymbol{Q}$ as a function of the macroscopic deformation gradient tensor:

$$Q_{\alpha\beta}(E) = \frac{\left\langle \frac{(E\cdot u)_\alpha (E\cdot u)_\beta}{|E\cdot u|} \right\rangle_0}{\langle |E\cdot u| \rangle_0} - \frac{1}{3}\delta_{\alpha\beta} \tag{85}$$

Then it is possible to determine the response of the "reptation" material to single-step stress relaxation strain histories at large deformations. The relaxation of the tube contour length $L(t)$ takes place on the time scale of the longest Rouse time of the chain in the tube and reorientation takes place over the reptation time scale λ_{rep} as the chain disengages from the tube. This is shown schematically in Figure 44. Therefore, the relaxation for times greater than the equilibration time (the Rouse time for a free chain) takes place in two steps. In the time scale during which the tube recovers its original contour length (contour length relaxation),

$$\begin{gathered} \sigma_{\alpha\beta}(t) = G_e\{1 + [\alpha(E) - 1]\exp(-t/\lambda_R)\}^2 Q_{\alpha\beta}(E),\ \lambda_e \le t \le \lambda_R \\ \text{where } G_e = \frac{15}{4} G_N \text{ and } \alpha(E) = \langle |E\cdot u| \rangle_0 \end{gathered} \tag{86}$$

For the time after the tube has regained its original contour length, the chain begins to disengage from the tube via the reptation mechanism. The relaxation response during this time is

$$\sigma_{\alpha\beta}(t) = G_e Q_{\alpha\beta}(E)\mu_{rep}(t),\ t > \lambda_R \tag{87}$$

where $\mu_{rep}(t)$ is given as the relaxation function for reptation in equation 76a. Combining equations 86 and 87 one obtains the relaxation function for the

two-step process:

$$\sigma_{\alpha\beta}(t) = G_e Q_{\alpha\beta}(E)\{1+[\alpha(E)-1]\exp(-t/\lambda_R)\}^2 \mu_{rep}(t),\ t>\lambda_e \tag{88}$$

For a simple shearing deformation, $\alpha(E) = \alpha(\gamma)$ and $Q_{\alpha\beta}(E) = Q_{\alpha\beta}(\gamma)$. In the linear (small deformation) regime one finds

$$\begin{aligned} \sigma(\gamma) &= \langle(1+2\gamma u_x u_y+\gamma^2 u_y^2)^{1/2}\rangle_0 = 1+\frac{2}{15}\gamma^2+O(\gamma^4) \\ Q_{xy}(\gamma) &= \frac{1}{\alpha(\gamma)}\left\langle\frac{(u_x+\gamma u_y)u_y}{(1+2\gamma u_x u_y+\gamma^2 u_y^2)^{1/2}}\right\rangle = \frac{4}{15}\gamma + O(\lambda^3) \end{aligned} \tag{89}$$

and the stress response (eq. 88) becomes

$$\sigma_{xy}(t) = \frac{4}{15}\gamma G_e \mu_{rep}(t) + O(\gamma^3) \tag{90}$$

which is the linear viscoelastic response to a single-step stress relaxation history.

For larger deformations, equation 88 is used. For convenience the nonlinear relaxation modulus is defined as

$$G(\gamma,t) = \frac{1}{\gamma}\sigma_{xy}(t,\gamma) \tag{91}$$

Then, equations 88 and 91 give the following expression for the nonlinear modulus:

$$\begin{aligned} G(\gamma,t) &= G_e \frac{Q_{xy}(\gamma)}{\gamma}\{1+[\alpha(\gamma)-1]\exp(-t/\lambda_R)\}^2 \mu_{rep}(t) \\ &= h(\gamma)G(t)\{1+[\alpha(\gamma)-1]\exp(-t/\lambda_R)\}^2 \end{aligned} \tag{92}$$

Here $G(t)$ is the linear viscoelastic modulus and $h(\gamma)$, the *damping function* in shear is introduced. For small γ, the linear response is recovered. As γ increases, we see another relaxation in $G(\gamma, t)$ at short times that corresponds to the relaxation of the contour length. Figures 45 and 46 show the expected relaxation behavior and that obtained experimentally for a high molecular weight polymer in solution. The theoretical curves show more nearly exponential decays for both mechanisms than is seen in the actual data, which has a broader relaxational behavior. This is a well-known weakness of the DE model that is related to the relaxation function being nearly exponential in nature (the longest relaxation time is widely separated from the next time which also has a lower intensity).

In examining the single-step stress relaxation behavior of the DE model, one can also look at the normal stress responses in shearing experiments. The first and second normal stress differences are $N_1(\gamma, t)$ and $N_2(\gamma, t)$ respectively.

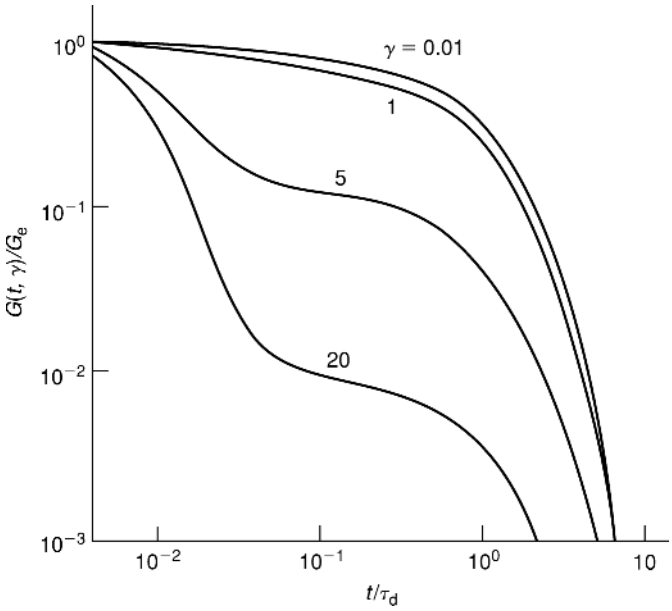

Fig. 45. Theoretical curve for the nonlinear relaxation modulus $G(t, \gamma)$ [$= G(\gamma, t)$] at different values of γ as indicated in the figure. The plot is for the case of $\lambda_d/\lambda_R = 100$. After Doi and Edwards (56), with permission.

The relevant equations are (56)

$$N_1(\gamma,t) = \frac{Q_{xx}(\gamma) - Q_{yy}(\gamma)}{Q_{xy}(\gamma)}\sigma_{xy}(\gamma,t)$$
$$N_2(\gamma,t) = \frac{Q_{yy}(\gamma) - Q_{zz}(\gamma)}{Q_{xy}(\gamma)}\sigma_{xy}(\gamma,t) \tag{93}$$

and since

$$Q_{xx}(\gamma) - Q_{yy}(\gamma) = \gamma Q_{xy}(\gamma) \tag{94}$$

$N_1(\gamma, t)$ can be written as

$$N_1(\gamma,t) = \gamma\sigma_{xy}(\gamma,t) \tag{95}$$

This relation, which also results from the K-BKZ model, is referred to as the Lodge–Meissner relationship (124) and results for materials with a finite elastic modulus at zero time.

The framework for examining arbitrary deformation histories for the "reptation" fluid has now been established and one can obtain a constitutive law for the stress response to arbitrary deformation histories. While the DE model can provide a more general constitutive equation than that to be developed now, the

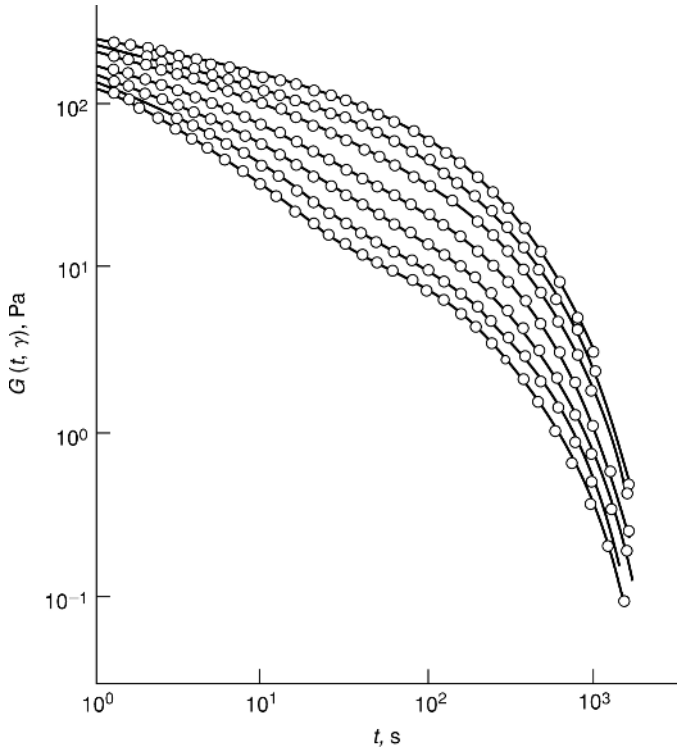

Fig. 46. Nonlinear relaxation modulus $G(t, \gamma)$ [$= G(\gamma, t)$] for a solution of polystyrene in chlorinated biphenyl ($\phi = 0.06$ g/cm^3) at 30°C. From top to bottom, shear strains γ are 0.57, 1.25, 2.06, 3.04, 4.0, 5.3, and 6.1. After Osaki et al. (123), with permission.

more general form requires numerical solution. The approximation known as the *independent alignment assumption* (IA) results in a closed form solution that gives a special case of the K-BKZ theory developed previously.

First, consider a simplification in which it is assumed that the contour length of the primitive chain remains at the equilibrium length L under the imposed deformation. This assumes an inextensible primitive chain and is seen as a reasonable approximation for slow flows or long times. Then, the deformation of the primitive chain is given by considering that the segment in the middle of the chain changes position affinely as

$$R'(0) = E \cdot R(0) \tag{96}$$

where $R(s)$ is the primitive chain conformation before deformation and $R'(s)$ is that after deformation. The primitive chain segments go from $-L/2$ to $L/2$; hence the middle is at 0.

Then the segment s' lies on the curve $E \cdot R(s)$ so that

$$R'(s') = E \cdot R(s) \tag{97}$$

s' is the contour length along the curve $E \cdot R(s'')$ from $s'' = 0$ to $s''=s$:

$$s' = \int_0^s |E \cdot u(s'')| \mathrm{d}s'' \tag{98}$$

Combination of equations 96, 97, 98 gives the transformation

$$u'(s') = \frac{E \cdot u(s)}{|E \cdot u(s)|} \tag{99}$$

Because s and s' are not equal to each other, the general constitutive equation becomes very complicated and requires numerical solution. The independent alignment approximation allows us to ignore this difference. Then, with $s' = s$ the transformation equation 99 becomes

$$u'(s) = \frac{E \cdot u(s)}{|E \cdot u(s)|} \tag{100}$$

The consequences of this approximation have been extensively investigated and the results are outlined here. In terms of the orientation tensor, the IA approximation in a single-step stress relaxation experiment in simple shear is given by

$$\begin{aligned} Q_{xy}^{\mathrm{IA}}(\gamma) &= \frac{1}{5}\gamma(\gamma \ll 1) \\ Q_{yy}^{\mathrm{IA}}(\gamma) - Q_{zz}^{\mathrm{IA}}(\gamma) &= -\frac{2}{35}\gamma^2(\gamma \ll 1) \end{aligned} \tag{101}$$

and the damping function is then given by

$$h^{\mathrm{IA}}(\gamma) = \frac{Q_{xy}^{\mathrm{IA}}(\gamma)}{\gamma/5} \tag{102}$$

which is not very different from the more general $h(\gamma)$ introduced earlier (eq. 91) over a wide range of γ (56).

Without derivation, note that Doi and Edwards developed expressions for the probability distribution function for the chain as well as the relationship between the stress and the chain orientations to arrive at an evolution equation for the stress to the chain orientation process, which is a function of the macroscopic deformations. The resulting constitutive equation is

$$\sigma_{\alpha\beta}(t) = G_{\mathrm{e}} \int_{-\infty}^{t} \left(\frac{\partial \psi(t-t')}{\partial t'} \right) Q_{\alpha\beta}^{\mathrm{IA}}[E(t,t')] \mathrm{d}t' \tag{103}$$

where $\psi(t) = \mu_{\mathrm{rep}}(t)$ is the DE relaxation function given previously. This equation is equivalent to a special form of the K-BKZ model discussed above. Note, however, that the deformation measure is somewhat different. [The reader should see Wagner and Schaeffer (125) for further discussion of the DE strain measures

relative to classic strain measures.] A relaxation function $\phi_{\alpha\beta}(t, E)$ can be defined as

$$\begin{aligned}\phi_{\alpha\beta}(E,t) &= G_e \int_{-\infty}^{0} \left(\frac{\partial \psi(t-t')}{\partial t'} \right) Q_{\alpha\beta}^{IA}(E) \mathrm{d}t' \\ &= G_e \psi(t) Q_{\alpha\beta}^{IA}(E)\end{aligned} \tag{104}$$

which is the single-step stress relaxation response to the deformation represented by $Q_{\alpha\beta}{}^{IA}(E)$. Then, the stress response to an arbitrary flow history is given by

$$\sigma_{\alpha\beta}(t) = \int_{-\infty}^{t} \left(\frac{\partial \phi(E, t-t')}{\partial t'} \right)_{E=E(t,t')} \mathrm{d}t' \tag{105}$$

This has the same form as the K-BKZ model described above and where the function $\phi(E, t)$ has the meaning of $K(I_1, I_2, t)$ for any given deformation (see eqs. 56, 57, 58, 59, 60). This result was a very important aspect of the DE model's success because of the broad success of the K-BKZ continuum model that had already been established. The next sections examines some of the data that were specifically generated to test the validity of the DE model constitutive equation.

Comparison with Experiment. Of particular importance in comparing the DE model with nonlinear rheological experiments is the fact, already noted above, that the relaxation function in the linear viscoelastic regime is not broad enough to capture the actual behavior of polymers. This resulted in two important trends in the experimental tests of the DE work. First, because the K-BKZ work, eg, in two-step deformation histories, had been mostly performed on commercial polymers of broad molecular weight distribution, the tests of DE focused primarily on monodisperse polymers that were anionically polymerized. (Later developments (15,18,126–128) lead to use of broader molecular weight distributions but these will not be treated here.) Hence, much work was done, particularly by Osaki (123,129–133) and co-workers, in different two-step deformation histories where both the shear and normal stress differences could be obtained. Also, more recent work by the Venerus and Burghardt groups (115–117,134,135) has further expanded on the Osaki work. The second development was that much effort was expended to compare the form of the damping function that was measured with that given by the DE model, part of which was discussed above.

Single-Step Stress Relaxation Experiments. The damping function of the DE equation has already been compared with some of the Osaki data (Figs. 45 and 46). Here two other aspects of the Osaki work are emphazied. At long times, when the material response is dominated by the chain disengaging from the tube, the DE model gives a response that is refered to as *time–strain separable*. The possibility of time–strain separability in the response of polymer relaxation behavior was originally used by Zapas and Craft (111). Empirically, time–strain separability can be expressed by the following (see also eqs. 76a and 90):

$$G(\gamma, t) = h(\gamma) g(t) \tag{106}$$

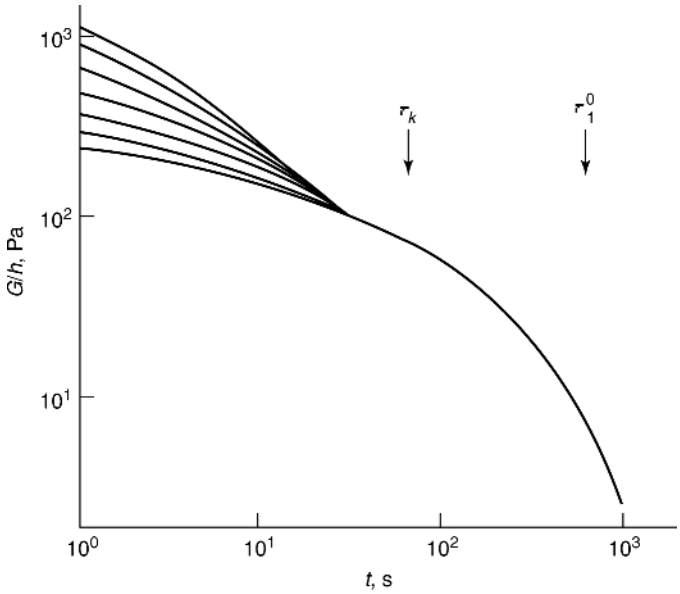

Fig. 47. Reduced relaxation modulus $G(t, \gamma)/h(\gamma)$ [$= G(\gamma, t)/h(\gamma)$] derived from data of Figure 46. The curves for $\gamma > 1.25$ shift vertically by an amount $-\log h(\gamma)$ so that they superpose in the long time regime. $\tau^0{}_1$ represents the longest relaxation time and τ_k represents the time below which superposition is not possible. After Osaki et al. (123), with permission.

where $h(\gamma)$ is referred to as the *shear damping function* discussed above and $g(t)$ would be a linear viscoelastic relaxation response. Osaki (123) showed that the time–strain separability appears to be valid after some characteristic time the called τ_k (now time and not stress). This is shown in Figure 47, which is a plot of $G(\gamma, t)/h(\gamma)$. If time–strain separability were valid over all times, the curves at different strains would have collapsed onto a single curve. In Figure 47 it is observed that the curves do not collapse until after the time τ_k. Unfortunately, it is not currently possible to uniquely attribute τ_k to any of the times discussed above for the tube model. It is, however, common to attribute τ_k to the finite time required for the molecule to retract along its contour length.

Another interesting aspect of the work done by Osaki was the demonstration that $h(\gamma)$ is not a universal function. Rather, it seems to depend on the number of entanglements M/M_e. The reptation theory expectation for the actual behavior in concentrated solution has been variously interpreted and there is not general agreement on the expected behavior. However, the data shown in Figure 48 are important for the understanding of polymer molecular viscoelasticity and were obtained within the important framework provided by the DE theory. From Figure 48 it is seen that the damping function depends on M/M_e and on concentration. Subsequently Osaki and co-workers (123) stated that "the quantity $h(\gamma)$ scarcely varies with molecular weight or concentration." A still later work by Osaki (136), however, again shows a disagreement between experimental data and the universal $h(\gamma)$ for polystyrene solutions. In addition, Wagner and Schaeffer

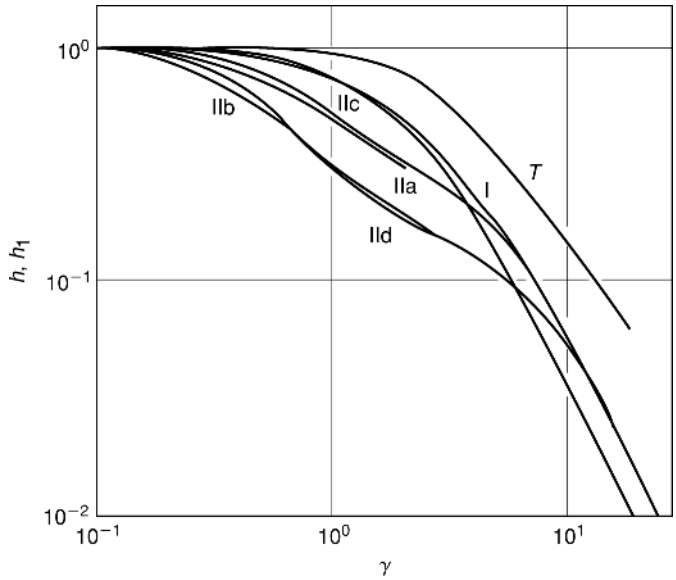

Fig. 48. Strain-dependent functions $h(\gamma)$ and $h_1(\gamma)$. The heavy line represents the DE damping function and the light lines represent experimental results $[h_1(\gamma)]$ for polystyrene solutions. For type I sample, $\phi\ M < 10^6$ (g·Da)/cm^3 and for type II samples $\phi\ M > 10^6$ (g·Da)/cm^3. For IIa, $M = 3.10 \times 10^6$ Da and $\phi = 0.329$ g/cm^3. For IIb, $M = 5.53 \times 10^6$ Da and $\phi = 0.221$ g/cm^3. For IIc and IId, $M = 7.62 \times 10^6$ Da and $\phi = 0.176$ and 0.221 g/cm^3, respectively. T is for a broad molecular weight distribution sample in which $M_w = 1.10 \times 10^6$ Da and $M_w/M_n = 4$ and $\phi = 0.21$ g/cm^3. After Osaki and Kurata (130), with permission.

(119,125,137) have extensively studied the form of the universal damping function and found that it is inadequate for the description of polydisperse polymer melts.

Two-Step Stress Relaxation Experiments. As discussed above in the context of the K-BKZ model, the two-step stress relaxation experiment is a very important tool in the assessment of constitutive relations. The same has been true in the use of the two-step experiment to assess the DE model. Here, the tests in the context of the independent alignment assumption are first examined. The important aspect of the experiments performed by Osaki and co-workers is that (123,129–133) the work was performed on monodisperse polymers. The work of Venerus and Burghardt, which is further built on the work of Osaki, will also be discussed. Finally, a proposed form of constitutive model that goes beyond the independent alignment assumption and gives a tractable set of predictions for the double-step experiments is examined.

Here three types of two-step experiment are viewed and the reader is asked to recall Figure 33. The figure shows the step-up (a), the step to zero (b), and the half-step (c) histories. Both the torque and normal force responses are examined. In addition, because much of the data in the literature include comparisons with the DE model both with and without independent alignment, the equations for the form of the DE model that Doi proposed by suppressing the independent alignment assumption are presented. Here the results are referred to as DE-NIA.

In this case for two-step stress relaxation histories recall equations 59 (DE-IA or K-BKZ)

$$\begin{aligned}
\sigma_{12}(t) &= K(\gamma_2, t) + K(\gamma_2-\gamma_1, t-t_1) - K(\gamma_2-\gamma_1, t) \\
\sigma_{22}(t)-\sigma_{22}(t) &= H_1(\gamma_2, t) + H_1(\gamma_2-\gamma_1, t-t_1) - H_1(\gamma_2-\gamma_1, t) \\
\sigma_{22}(t)-\sigma_{33}(t) &= H_2(\gamma_2, t) + H_2(\gamma_2-\gamma_1, t-t_1) - H_2(\gamma_2-\gamma_1, t)
\end{aligned} \tag{59}$$

and compare these with the DE-NIA equations:

$$\begin{aligned}
\sigma_{12}(t) &= A(\beta)K(\gamma_2, t) + K(\gamma_2-\gamma_1, t-t_1) - [A(\beta) + B(\alpha_2, \beta)]K(\gamma_2-\gamma_1, t) \\
\sigma_{22}(t)-\sigma_{22}(t) &= A(\beta)H_1(\gamma_2, t) + H_1(\gamma_2-\gamma_1, t-t_1) - [A(\beta) + B(\alpha_2, \beta)]H_1(\gamma_2-\gamma_1, t) \\
\sigma_{22}(t)-\sigma_{33}(t) &= A(\beta)H_2(\gamma_2, t) + H_2(\gamma_2-\gamma_1, t-t_1) - [A(\beta) + B(\alpha_2, \beta)]H_2(\gamma_2-\gamma_1, t)
\end{aligned} \tag{107}$$

where

$$\begin{aligned}
A(\beta) &= \frac{4\beta\cos(\frac{\pi\beta}{2})}{\pi(1-\beta^2)},\ B(\alpha_2,\beta) = \frac{\pi^2(1-\beta)^3}{12(\alpha_2-\beta)} \text{ for } \beta<1 \\
A(\beta) &= \frac{4\cos(\frac{\pi}{2\beta})}{\pi(1-\beta^{-2})},\ B(\alpha_2,\beta) = 0 \text{ for } \beta\geq 1 \\
\beta &= \left(\frac{3+\gamma_2^2}{3+\gamma_1^2}\right)^{1/2},\ \alpha_2 = [1 + (\gamma_1-\gamma_2)^2]^{1/2}
\end{aligned} \tag{108}$$

As seen in the next paragraphs, the DE-NIA equations sometimes do better and sometimes worse than the DE-IA or K-BKZ equations. Also note that in all instances the measured single-step relaxation function is used rather than the theoretical DE function, which as already discussed is too narrow to capture the full breadth of the relaxation response of entangled polymers.

Step-Up. Figure 49 shows the response for a two-step history in which the second step is approximately the same magnitude as the first step, ie, $\gamma_2 = 2\gamma_1$. The results are from Osaki's work (138) on polystyrene solutions and illustrate that both the shear stress response and the normal stress response are well represented with the DE independent alignment approximation (ie, the K-BKZ equations). This result is similar to what was found previously for the K-BKZ model (Fig. 34) (138).

Step to Zero Deformation. Figures 50 and 51 show the response for a two-step history in which one first applies a step strain γ_1 for some time t_1 and then returns the material to zero deformation, $\gamma_2 = 0$. The results are, again, from Osaki (138). Figure 50 shows the results when the first step duration $t_1 = 20$ s, and it is seen that both the shear and normal stress responses are poorly represented by either the DE model with independent alignment (solid lines) or the predictions without the independent alignment assumption (dashed lines). Figure 51

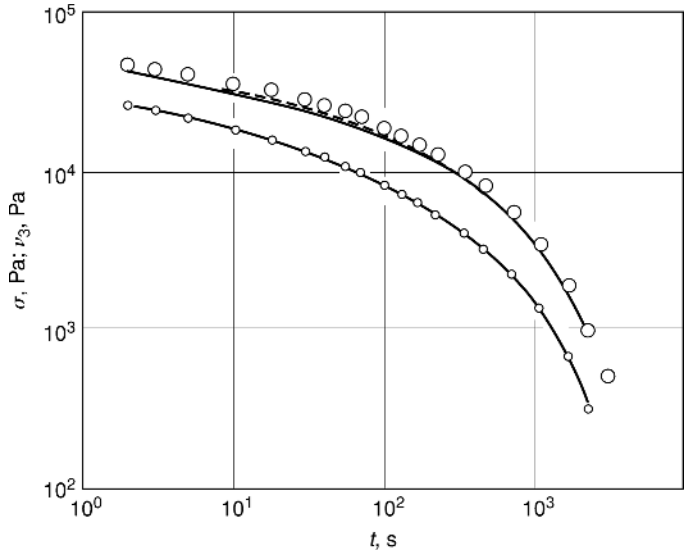

Fig. 49. Shear stress σ (○) and normal stress ν_3 (○) responses to a two-step "step-up" type of deformation history with $\gamma_1 = 1.47$ and $\gamma_2 = 2.90$ for a concentrated polystyrene solution. The solid lines are the predictions for the K-BKZ or DE-IA equations and the dashed lines are for the DE-NIA equations. After Osaki and et al. (138), with permission.

shows that when t_1 gets longer ($t_1 = 200$ s) the agreement between theory and experiment improves. Also, note that both theoretical curves also begin to approach each other, as might be expected because the models are fading memory models and at very long times, the step back to zero should become equivalent to the single-step response.

Half-Step Deformation. In the discussion of the K-BKZ model, the half-step deformation was covered. Here two sets of data that go beyond what was described above are discussed. First, in the Osaki data shown in Figure 52, it is seen that the DE model with independent alignment fits the shear stress response, but not the normal stress response. Also, the theory without the independent alignment assumption does not fit the shear data. The normal stress deviation from the model prediction is interesting, as this was a "special" history for which the K-BKZ and DE-IA models both predicted that the normal stress response is independent of the duration of the first step (and equal to a single-step experiment with magnitude $\gamma_2 = \gamma_1/2$). Figure 52 shows that for the polystyrene solution, the single-step response for the normal stress is only in agreement with the single-step response at long times. Interestingly, Osaki's data (138) showed that the normal stress response was independent of the duration of the first step, although not equal to the single-step response. Figures 53 and 54 show a set of half-step data from Burghardt and Brown (111). The shear stress theory is not shown for comparison, but it is seen that the shear stresses go negative and then become positive, going through a maximum before joining what would be the single-step relaxation at very long times. On the other hand the normal force responses for the different values of t_1 are very interesting because they seem to become

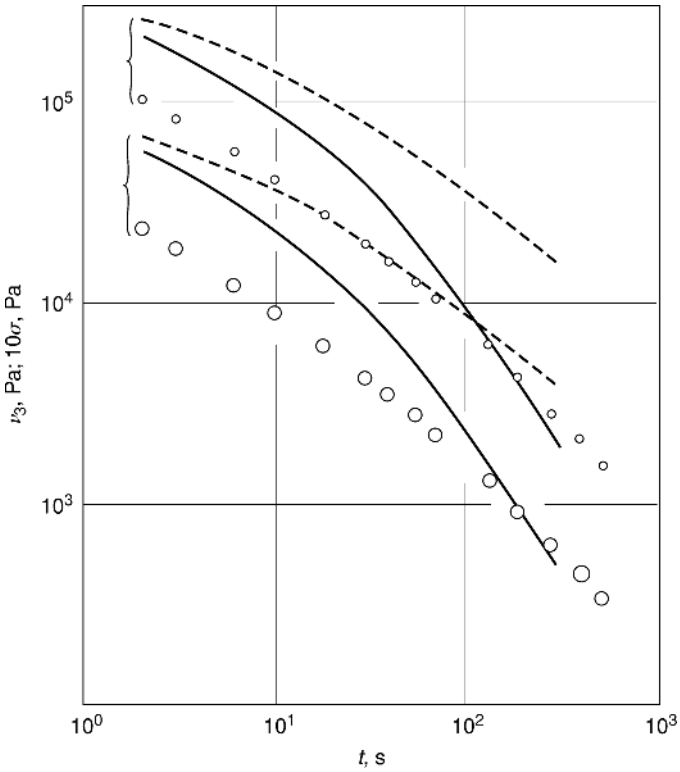

Fig. 50. Shear stress σ (○) and normal stress ν_3 (○) responses to a two-step "step to zero" type of deformation history with $\gamma_1 = 2.89$ and $\gamma_2 = 0$ for a concentrated polystyrene solution. Duration of the first step was $t_1 = 20$ s. The solid lines are the predictions for the K-BKZ or DE-IA equations and the dashed lines are for the DE-NIA equations. After Osaki et al. (138), with permission.

independent of the duration of the first step at a characteristic time. At short times, deviations occur. Hence, the original findings of McKenna and Zapas that the normal force response is independent of the duration of the first step, seems to only be confirmed for long times. Osaki associated this time with the value of τ_k discussed previously and where time-strain separability is applicable. An interesting aspect of this is that the observation that the normal stresses in the half-step history can independent of the duration of the first step is also observed for some polymer glasses (112–114), as discussed subsequently.

Nonlinear Viscoelastic Response of Solid-like Polymers. The study of the nonlinear viscoelastic response of solid or solid-like polymers is one that has been relatively neglected. One reason is that there is no real molecular framework for the description of these materials, particularly when they are amorphous. The other reason is that many workers in the field have adopted the framework of metal plasticity and then made modifications to try to adapt it to, for example, the fact that amorphous polymers do not readily admit to treatment with the physics of dislocations. In the case of semicrystalline polymers, the

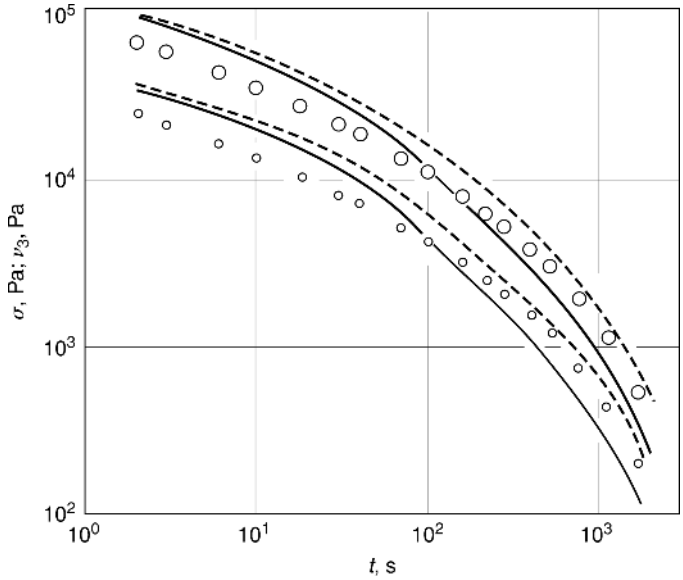

Fig. 51. Shear stress σ (○) and normal stress ν_3 (○) responses to a two-step "step-to zero" type of deformation history with $\gamma_1 = 2.89$ and $\gamma_2 = 0$ for a concentrated polystyrene solution. Duration of the first step was $t_1 = 200$ s. The solid lines are the predictions for the K-BKZ or DE-IA equations and the dashed lines are for the DE-NIA equations. After Osaki et al. (138), with permission.

crystalline phase may, in some instances, succumb to a plasticity treatment, (139) but the full description of the nonlinear response requires treatment of a two-phase system. The following sections treat the problem of nonlinear behavior of solid or solid-like polymers as a problem in viscoelasticity. Primarily amorphous, glassy polymers are chosen. There are several reasons for these choices. First, the semicrystalline polymers are very complicated, as discussed briefly above, and our physical understanding of their linear viscoelastic response is still somewhat limited because of the complex interactions between amorphous and crystalline phases. Hence, while some progress has been made in dealing with the yield response of polyethylene (140,141) it is unclear how general the models are to other materials. This leaves one with the amorphous, glassy polymers. Here, because the materials seem to follow time-temperature superposition in many instances, (9,33–35,40,142) there is a reasonable likelihood that a viscoelasticity framework is a good one with which to treat them. In addition, most work has focused on *post-yield* behavior, a regime to which plasticity in metals seems (inappropriately in this author's mind) applicable. With this in mind, therefore, it becomes important to investigate the *sub-yield* behavior of amorphous materials because it is the sub-yield behavior that is the precursor to yielding behavior. The latter cannot be understood until the former is. The following section deals with the K-BKZ framework and adapts it to the present investigations of the viscoelastic response of glassy polymers. Several other viscoelastic frameworks that have been, or are being, used in the study of amorphous polymers are also discussed.

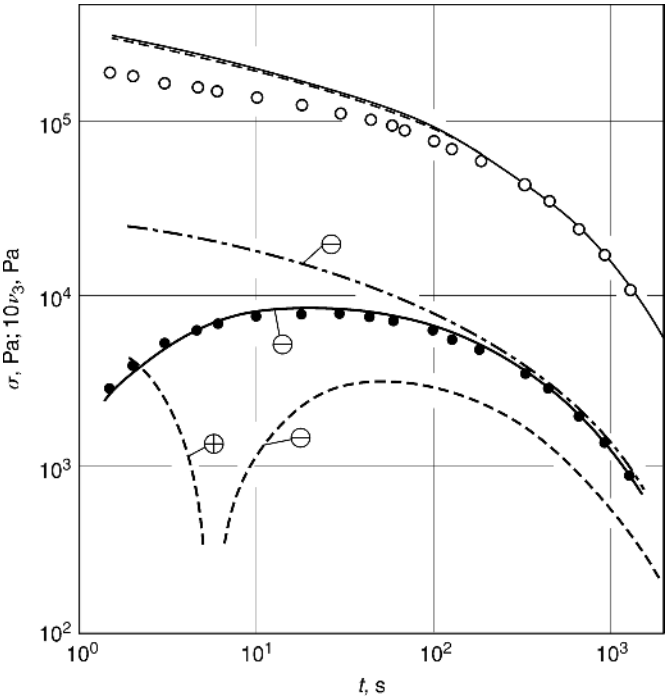

Fig. 52. Shear stress σ (○) and normal stress ν_3 (○) responses to a two-step "half-step" type of deformation history with $\gamma_1 = 2.89$ and $\gamma_2 = 1.45$ for a concentrated polystyrene solution. Duration of the first step was $t_1 = 20$ s. The solid lines are the predictions for the K-BKZ or DE-IA equations and the dashed lines are for the DE-NIA equations. Dashed-dotted line is the single-step shear stress response for $\gamma = 1.45$. After Osaki et al. (138), with permission.

The K-BKZ Framework. The above sections dealt with the K-BKZ framework for describing the nonlinear constitutive response of polymeric fluids. While the K-BKZ theory was developed for incompressible fluids, polymeric glasses are compressible in that the bulk modulus and the shear modulus are of the same order of magnitude. However, in the first work described here only torsional behavior is examined, which is nearly volume conserving (143–145). Hence, there may be reason to think that the incompressible framework is justifiable. Some aspects of compressibility are also examined and these are adapted to one instance of extension and compression behavior. Other constitutive models are also analyzed.

Torsional Experiments. The geometry and equations for torsion of an elastic cylinder are presented above. For the viscoelastic K-BKZ material, the equations look similar. For isochronal values of the strain potential function, one can define what looks like a time-dependent strain-energy function $W_i(I_1, I_2, t)$:

$$W_i(I_1,I_2,t) = \frac{\partial W(I_1,I_2,t)}{\partial I_i} = \int_{-\infty}^{t} \frac{\partial U(I_1,I_2,t-t')}{\partial I_i} \mathrm{d}t' \tag{109}$$

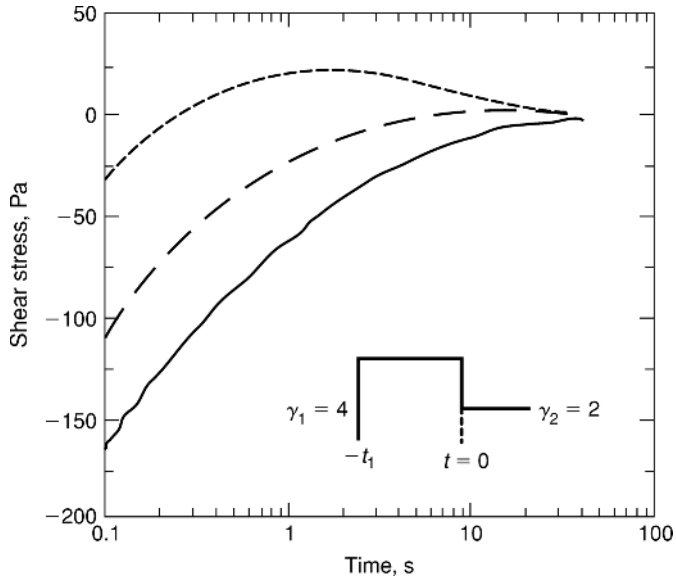

Fig. 53. Shear stress response to "half-step" type of deformation history for a concentrated polystyrene solution and for different values of the first step duration t_1. Dotted line; $t_1 = 1$ s; dashed line; $t_1 = 4$ s; solid line; $t_1 = 16$ s. After Brown and Burghardt (134), with permission.

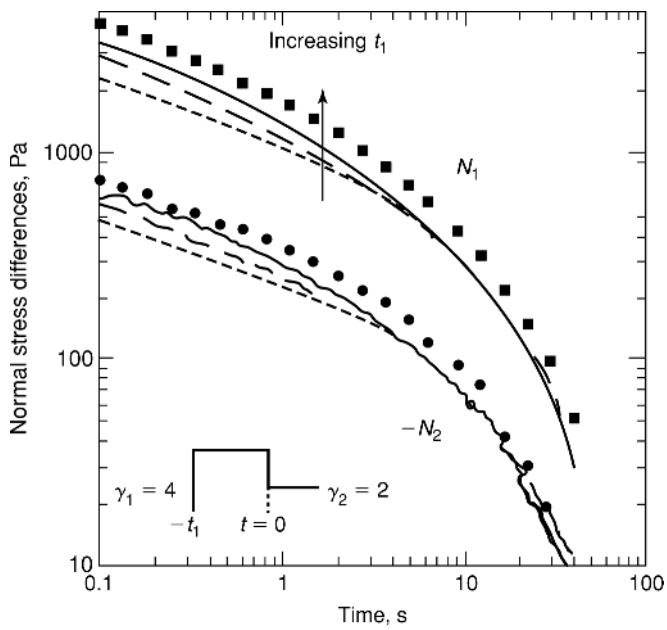

Fig. 54. Normal stress response to "half-step" type of deformation history for a concentrated polystyrene solution and for different values for the first step duration t_1. Dotted line: $t_1 = 1$ s; dashed line: $t_1 = 4$ s; solid line: $t_1 = 16$ s. Symbols represent single-step response for $\gamma = 2.0$. After Brown and Burghardt (134), with permission.

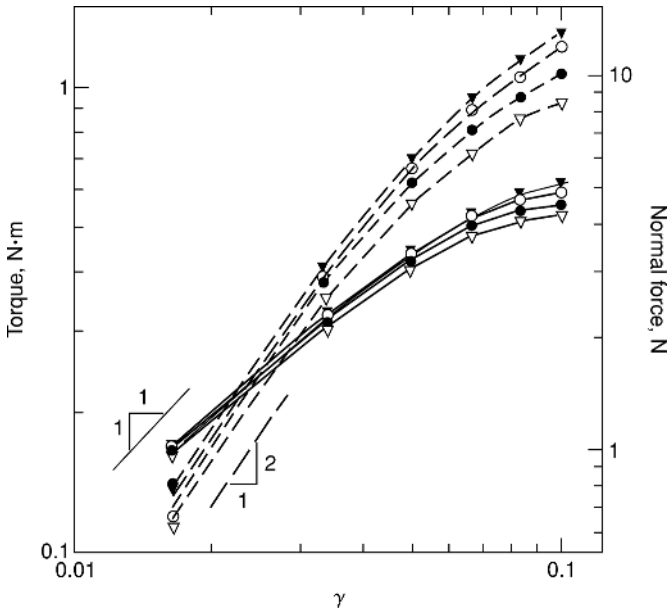

Fig. 55. Torque and normal force responses for a glassy polycarbonate material in stress relaxation conditions. *Isochrones*: ▼ 1 s; ○ 10 s; ● 100 s; ▽ 1000 s. After Pesce and McKenna (146).

Then, isochronal values $W_i(I_1, I_2, t)$ can be used to characterize the stress relaxation behavior of solid cylinders and, similar to the behavior found for rubber, the strain energy function derivatives can be determined for different materials. There is relatively little work in this area, but the results are intriguing. Figure 55 shows the isochronal torque and normal force responses for a polycarbonate material subjected to maximum strains of approximately 0.10 at the outside radius of the cylinder. This strain is just below the yield point of the polycarbonate in torsion. These data have a similar appearance to the rubber data shown in Figure 31 at small strains (the torque follows ψR and the normal force follows $\psi^2 R^2$), but as the strain increases toward $\psi R = 0.1$, there is a strong softening in the responses as yield is approached. In the case of the rubber samples, such softening does not occur even for strains as high as $\psi R = 2.0$. The time-dependent equivalent of equations 47 and 48 can be used to analyze the torque and normal forces so as to determine the values of $W_1(I_1, I_2, t)$ and $W_2(I_1, I_2, t)$. Such data are shown for a PMMA material in Figure 56 and for the polycarbonate in Figure 57. Figure 58 shows the isochronal VL function behavior for the polycarbonate as a function of the stretch λ. Clearly, the behavior is very different for the material below the glass transition, that is the solid-like or glassy polycarbonate, than it is for the rubbery material in Figure 32.

Although this approach seems useful, unlike the rubbery polymers, the glassy polymers are compressible materials in the sense that the ratio of the bulk and shear moduli is near unity, rather than being in the neighborhood of

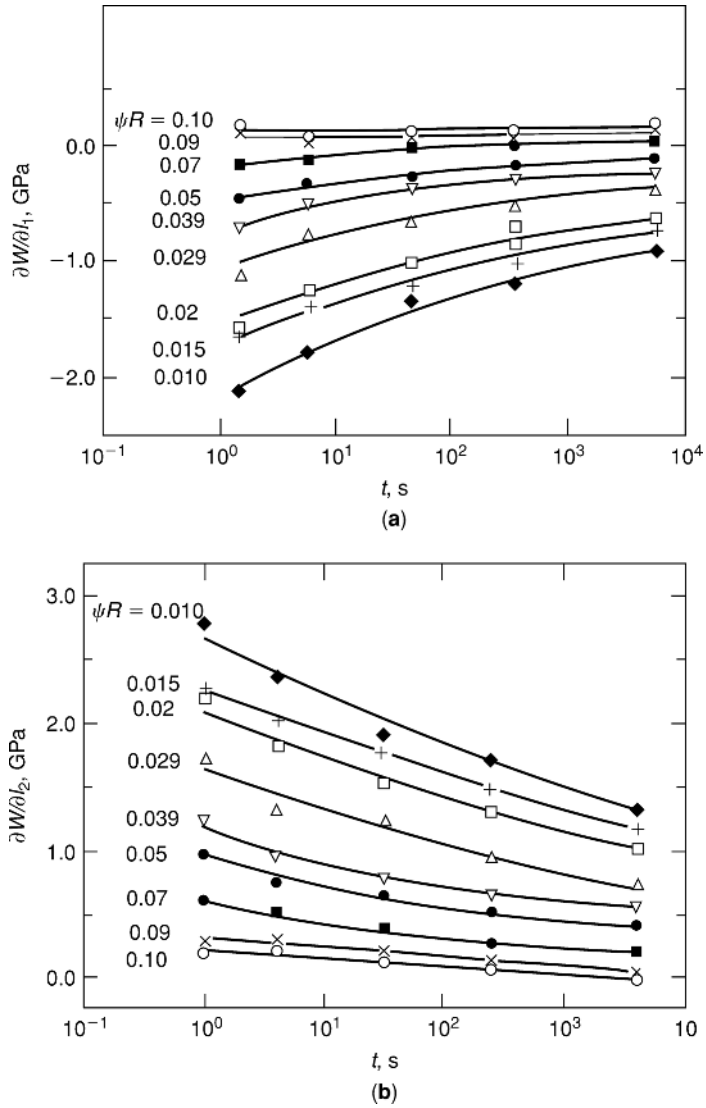

Fig. 56. Values of the time and strain-dependent strain energy function derivatives $\partial W/\partial I_1$ and $\partial W/\partial I_2$ for a glassy PMMA determined from torque and normal force measurements in single-step stress relaxation torsional experiments. After McKenna (114).

100–1000 for the rubber. This means that the forces to cause shape changes (distortions or shears) in the rubber are much smaller than those required to cause volume changes, while these forces are of approximately the same magnitudes in the glassy polymer. Hence, incompressible theory describes very well the behavior of the rubbery material, but does not obviously apply to the polymer glass. The next section examines the material compressibility issues and the extension of the VL function to the compressible case.

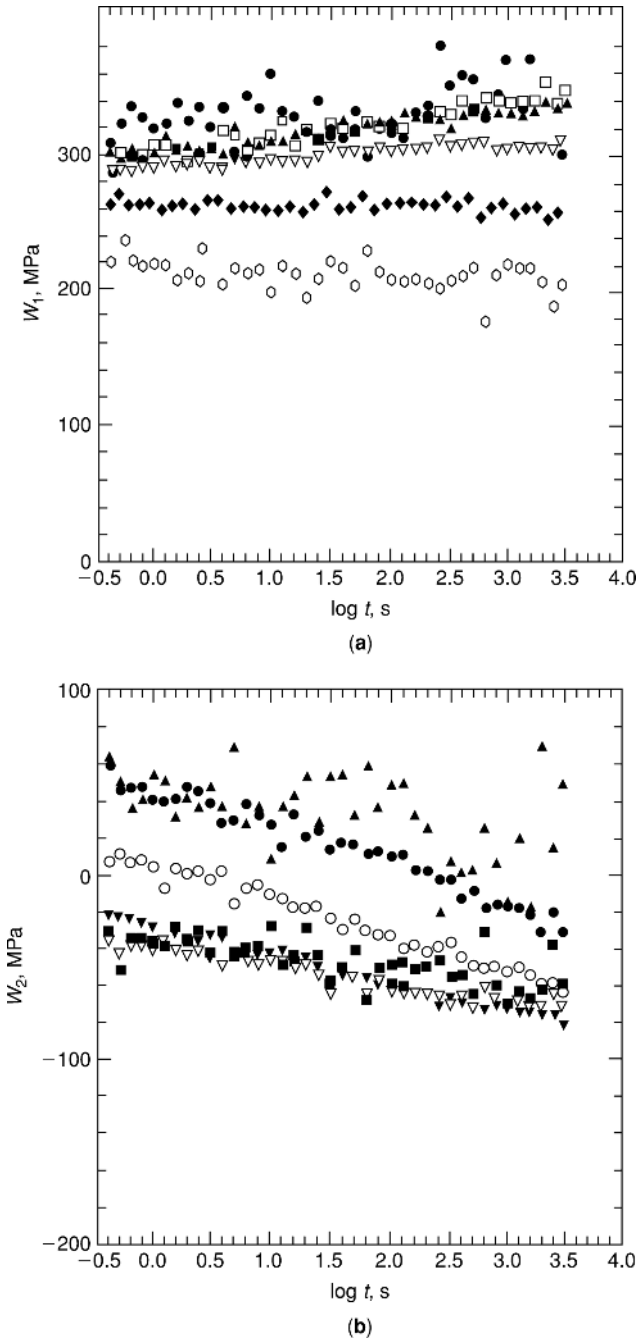

Fig. 57. Values of the time and strain-dependent strain energy function derivatives $W_1 = \partial W/\partial I_1$ and $W_2 = \partial W/\partial I_2$ for a glassy polycarbonate determined from torque and normal force measurements in single-step stress relaxation torsional experiments. (a) γ: ● 0.017; □ 0.033; ▲ 0.050; ▽ 0.067; ◇ 0.083; ○ 0.10. (b) γ: ▲ 0.017; ● 0.033; ○ 0.050; ▼ 0.067; ▽ 0.083; ■ 0.10. After Pesce and McKenna (146).

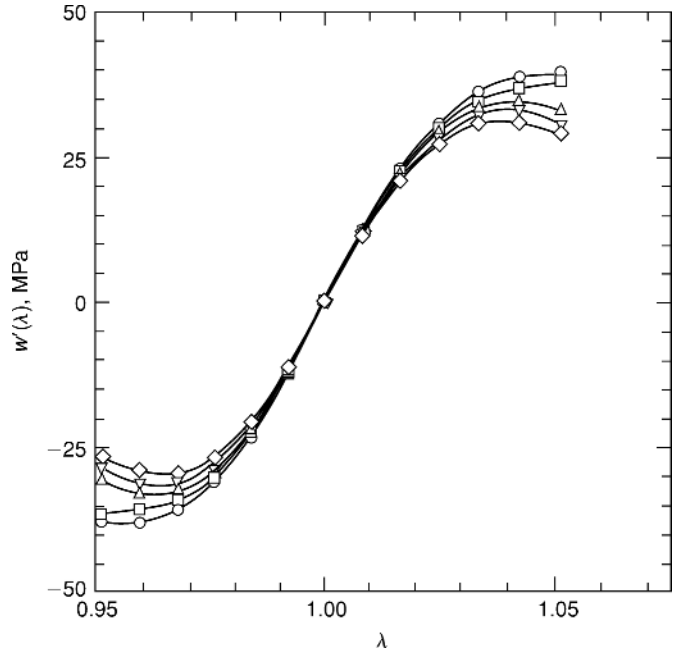

Fig. 58. The VL Valanis-Landel (98) function derivative as a function of deformation for polycarbonate as determined from data of Figures 55 and 57. ○ 0.3 s; □ 3.2 s; Δ 32 s; ∇ 320 s; ◇ 3000 s. After Pesce and McKenna (146).

Issues of Material Compressibility. There is a full theory of compressible and nonlinear viscoelastic materials that would be equivalent to the compressible finite deformation elasticity theory described above (eq. 39), but more complicated because of the need to develop an expansion of the time-dependent strain potential function as a series of multiple integrals (108,109). One such formalism is discussed briefly under Lustig, Shay and Caruthers Model. Here a simplified model that is based upon the K-BKZ framework with a VL-like kernel function (98) is examined.

One important issue in dealing with the nonlinear viscoelastic response of materials is the amount of data needed to determine the material parameters in the models. As noted above, even the general finite elasticity theory requires significant work to obtain the material parameters over the full three-dimensional deformation space. This is one reason that the VL framework is so attractive, when it works. Therefore, it is of interest to investigate whether or not the model can be extended to include compressibility. Pesce and McKenna (146) performed torsional tests on polycarbonate as described above. They then asked whether the VL function could be used to predict the tension and compression responses of the material. An important assumption in their approach was that the VL function determined from the torsional measurements using equations 45, 46, 47, 48, 49, 50, 51 (described immediately above) could be used to predict uniaxial data. When the incompressible equations 50 were applied to try to estimate the uniaxial stress-deformation data (isochronal), these equations did not work. However,

upon considering the compressibility of the material good agreement with the data could be obtained. Taking, now, the strain energy density function [assumed to be separable as in the VL function (98)], one obtains

$$\hat{w}(\lambda_1,\lambda_2,\lambda_3) = w(\lambda_1) + w(\lambda_2) + w(\lambda_3) + f(\lambda_1\lambda_2\lambda_3) \tag{110}$$

where the volume $v = \lambda_1\lambda_2\lambda_3$ and the function $f(\lambda_1\lambda_2\lambda_3)$ represents the extra volume-dependent term beyond that incorporated implicitly in the principal stretches. Writing the constitutive equation for the principal stress (here the stress differences are not used), one obtains

$$\sigma_i = \frac{1}{\lambda_j\lambda_k}\left\{\frac{\partial \hat{w}}{\partial \lambda_i}\right\} \tag{111}$$

For a uniaxial deformation (extension or compression) in direction 1 and under normal ambient conditions (where $\sigma_2 = \sigma_3 \approx 0$) one can write

$$\sigma_1 = \frac{1}{\lambda_2\lambda_3}\left[\frac{\partial w}{\partial \lambda_1}\left(\frac{\partial f}{\partial v}\right)\left(\frac{\partial v}{\partial \lambda_1}\right)\right] \tag{112a}$$

$$\sigma_2 = \frac{1}{\lambda_1\lambda_3}\left[\frac{\partial w}{\partial \lambda_2} + \left(\frac{\partial f}{\partial v}\right)\left(\frac{\partial v}{\partial \lambda_2}\right)\right] \approx 0 \tag{112b}$$

Solution of equation 112b gives the relation

$$\left(\frac{1}{\lambda_1\lambda_3}\right)\left(\frac{\partial w}{\partial \lambda_2}\right) = -\frac{\partial f}{\partial v} \tag{113}$$

which when substituted into equation 112b gives the following expression for σ_1, which is similar to the equation for the principal stress differences for the incompressible material:

$$\sigma_1 = \frac{1}{\lambda_2\lambda_3}w'(\lambda_1) - \frac{1}{\lambda_1\lambda_3}w'(\lambda_2) \text{ or } v\sigma_1 = \lambda_1\lambda_2\lambda_3\sigma_1 = \lambda_1 w'(\lambda_1) - \lambda_2 w'(\lambda_2) \tag{114}$$

Pesce and McKenna (140) applied equation 114 with the VL function obtained from torsional data and successfully described the uniaxial data for the same polycarbonate material to within approximately 15% up to the yield point (140). The results are shown in Figure 59. Importantly, the successful description required both a knowledge of $w'(\lambda)$ and the actual values of the lateral contraction of the material—the equivalent in the nonlinear range of the Poisson's effect in linear elasticity (or viscoelasticity).

Although the compressible VL function shows promise for the description of the response of glassy polymers in the nonlinear deformation regime, further work is required to establish the generality of the approach and how far it can be extended into the post-yield region.

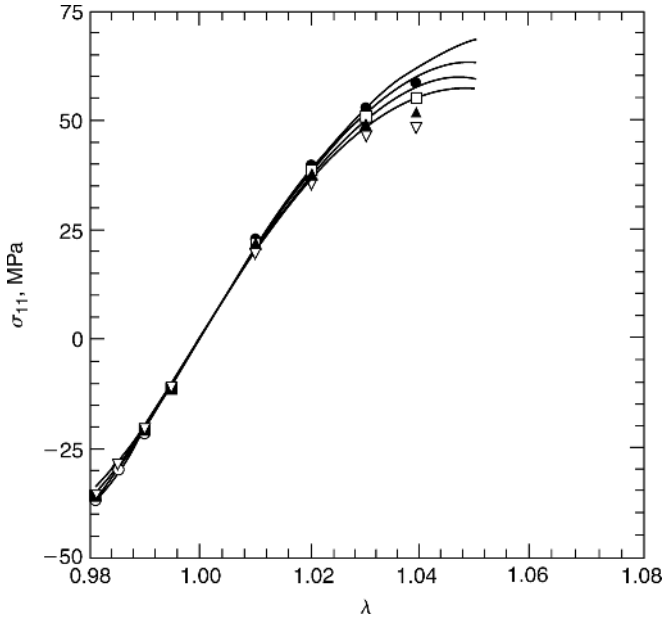

Fig. 59. Comparison between the experiment (points) and predictions (lines) from equation 114 for stress-deformation response of polycarbonate in uniaxial extension and compression. • 3.2 s; □ 32 s; ▲ 320 s; ▽ 3000 s. After Pesce and McKenna (146).

Other Constitutive Model Descriptions. The above work describes a relatively simple way to think of nonlinear viscoelasticity, viz, as a sort of time-dependent elasticity. In solid polymers, it is important to consider compressibility issues that do not exist for the viscoelastic fluids discussed earlier. In this penultimate section of the article, other approaches to nonlinear viscoelasticity are discussed, hopefully not abandoning all simplicity. The development of nonlinear viscoelastic constitutive equations is a very sophisticated field that we will not even attempt to survey completely. One reason is that the most general constitutive equations that are of the multiple integral forms are cumbersome to use in practical applications. Also, the experimental task required to obtain the material parameters for the general constitutive models is fairly daunting. In addition, computationally, these can be difficult to handle, or are very CPU-time intensive. In the next sections, a class of single-integral nonlinear constitutive laws that are referred to as reduced time or material clock-type models is disscused. Where there has been some evaluation of the models, these are examined as well.

The fundamental concept of the material clock or reduced time is similar to the principle described above in the discussion of time–temperature superposition. In the mechanical constitutive models, however, the change in the stress or deformation induces a shift in the material relaxation time. The fact that the time depends on the state of stress (or strain) or on its history leads to additional nonlinearities in behavior from what is expected with, eg, the K-BKZ model. Physical explanations for the shifting material time are often based on free-volume ideas that are often invoked to explain time–temperature superposition. In addition, entropy changes have been invoked as have stress-activated processes.

The Schapery Model. One of the earliest models of the nonlinear viscoelastic response of polymers to use the concept of a reduced time is due to Schapery (147–149). The model is based on thermodynamic considerations and has a form similar to the Boltzmann superposition principal described previously. The model time dependences, except for the shift factors, are the same as those obtained in the linear response regime. Hence, the model is relatively easy to implement and to determine the relevant material parameters. It results in a generalization of the generalized superposition principal developed by Leaderman (150).

While the model can be formulated for three-dimensional stresses and strain states, here only the uniaxial deformation is dealt with. It is important to add that the model has both a creep formalism and a relaxation formalism. The relevant equations are presented in the next paragraphs. In addition, although this is a nonlinear theory, it is a small strain theory.

In creep experiments the equation is given as

$$\varepsilon(t) = g_0 D_0 \sigma \quad + \quad g_1 \int_0^t \Delta D(\psi - \psi') \frac{\mathrm{d}g_2\sigma}{\mathrm{d}t} \mathrm{d}t' \tag{115}$$

where D_0 is the zero time compliance, ΔD is the time-dependent part of the compliance, and the g_i's are material parameters. The material clock arguments are written as

$$\psi = \int_0^t \frac{\mathrm{d}\varsigma}{a_\sigma[\sigma(\varsigma)]} \text{ and } \psi' = \int_0^{t'} \frac{\mathrm{d}\varsigma}{a_\sigma[\sigma(\varsigma)]} \tag{116}$$

where a_σ is the stress shift factor.

A similar set of equations describes the stress relaxation behavior (stress as a function of strain):

$$\sigma(t) = h_\mathrm{e} E_e \varepsilon \quad + \quad h_1 \int \Delta E(\phi - \phi') \frac{\mathrm{d}h_2\varepsilon}{\mathrm{d}t'} \mathrm{d}t' \tag{117}$$

Here E_e is the equilibrium modulus (infinite time modulus), ΔE is the time-dependent part of the model, and h_e and h_1 are material parameters. The reduced time arguments ϕ and ϕ' are written as

$$\phi = \int_0^t \frac{\mathrm{d}\varsigma}{a_\varepsilon[\varepsilon(\varsigma)]} \text{ and } \phi' = \int_0^{t'} \frac{\mathrm{d}\varsigma}{a_\varepsilon[\varepsilon(\varsigma)]} \tag{118}$$

Here, note, that a_ε is the strain shift factor.

Figure 60 illustrates two-step creep and recovery data at different stresses for a reinforced polymer along with the predictions from the Schapery creep formulation and those obtained from simply applying a modified form of the Boltzmann superposition principle. Without going into the details of the procedures of obtaining all the parameters, it is clear that the model captures much of the observed nonlinear response, while the modified Boltzmann rule does not. (Note that the modified Boltzmann rule simply assumes additivity of responses, but without the linearity assumptions.) Figure 61 shows the creep and recovery data

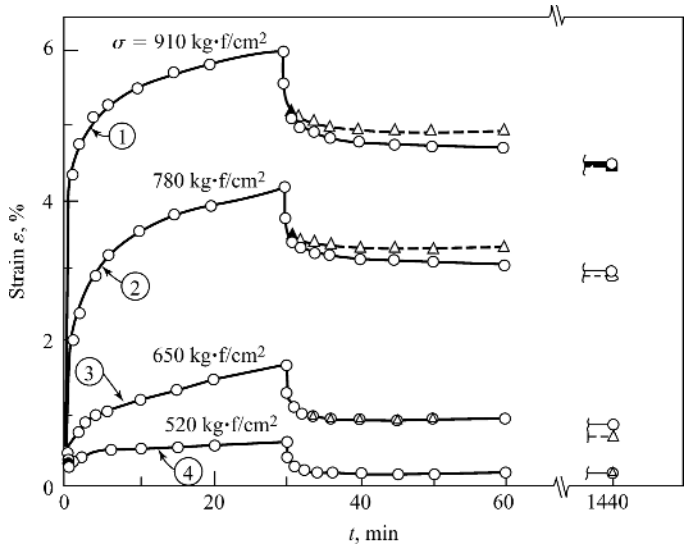

Fig. 60. Comparison of experimental (circles) creep and recovery behavior of a glass-reinforced phenolic resin with the predictions from the Schapery (147–149) nonlinear viscoelastic model. ○ Experimental Data; Δ Predicted Recovery Data (Nonlinear Theory). After Schapery (147), with permission.

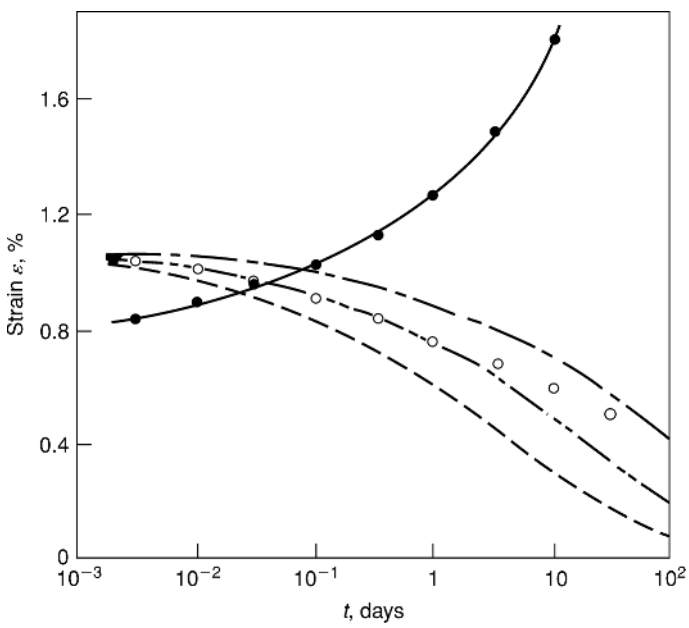

Fig. 61. Comparison of experimental (circles) creep and recovery behavior of a nitrocellulose material with the predictions from the Schapery (147–149) nonlinear viscoelastic model using different stress shift factors, as indicated. ●— Exp. Creep Strain; —○— Exp. Recovery Strain; ----- Case 1, $a_\sigma^{-1} = 1$; —-—Case 2, $a_\sigma^{-1} = 23.15$; -—Case 3, $a_\sigma^{-1} = 4.1$. After Schapery (147), with permission.

for a nitrocellulose film and with different values of the shift factor a_σ to try to describe the second (recovery) step. Here there is less of an agreement between the theory and the data, yet the trends are captured. In cases where materials, such as reinforced polymer matrix composites, exhibit strongly nonlinear behavior at very small strains, this set of models has been very useful (151–154). Also note that in certain deformation histories, the model can reduce to a K-BKZ type of expression and the data presented in Figure 34 was successfully described by the Schapery model (even though the deformations are fairly large).

The Zapas Strain-Clock Model and the Bernstein–Shokooh Stress-Clock Model. Although the K-BKZ theory has been highly successful, as discussed above, it also had some flaws, which lead to attempts to modify the model by incorporating material clock or reduced time concepts. In one form, Zapas introduced a strain-clock (118), ie, a change in the time scale that depended on the strain history. While the model is fully three-dimensional, for simplicity, consider only the equations for the simple shearing case:

$$\sigma_{12}(t) = \int \{[\gamma(t) - \gamma(t')]G_*[\gamma(t) - \gamma(t'), \Phi(t, t')]\}\dot{\Phi}[\gamma(t), \gamma(t'), t - t']\mathrm{d}t' \tag{119}$$

and the material time $\Phi(t, t')$ is written as

$$\Phi(t, t') = \Phi[\gamma(t), \gamma(t'), t - t'] = \int \dot{\Phi}[\gamma(t), \gamma(\xi), t - \xi]\mathrm{d}t' \tag{120}$$

The strain-clock term (eq. 120) is a function of the entire deformation history. McKenna and Zapas used the strain-clock formalism to describe the torsional response of a PMMA material in two-step strain histories (112). The difficulty arises because the determination of material parameters requires at least the data for both the first and second step responses. Furthermore, McKenna and Zapas also assumed that the clock-form for the torque response and for the normal force response was the same. Their results were consistent with this assumption, as shown in Figure 62. However, that work also indicates that considerable experimental data are required to use the model—a constant issue in nonlinear viscoelasticity. One other interesting thing that came from the work of McKenna and Zapas (112–114) was the verification of equation 60 for the normal force. This is seen in Figure 63, where the normal force response after the half-step history is plotted against the duration of the first step for two different isochrones. As seen, for times beyond 1677 s and for both short and long isochrones, the response is both independent of the duration of the first step and the same as if the material had been subjected to a step only to γ_2. The other point of import here is that, while the normal stress is following equation 60, the shear response is dramatically different. In fact, the strain-clock model fits the data, but the "reversing stress" nature of the deformation leads to a similar deviation from K-BKZ-type behavior as was seen in the polymer solution. This is shown in Figure 64. The reader is also reminded that polymer solutions seem to follow this response only at long times ($t > \tau_k$).

While the strain-clock version of the K-BKZ model seems capable of describing fairly complex nonlinear behavior, it is, at least, an inconvenient model to use. The stress-clock model of Bernstein and Shokool (155) has two features that could make it very useful. It takes less data to determine the material properties

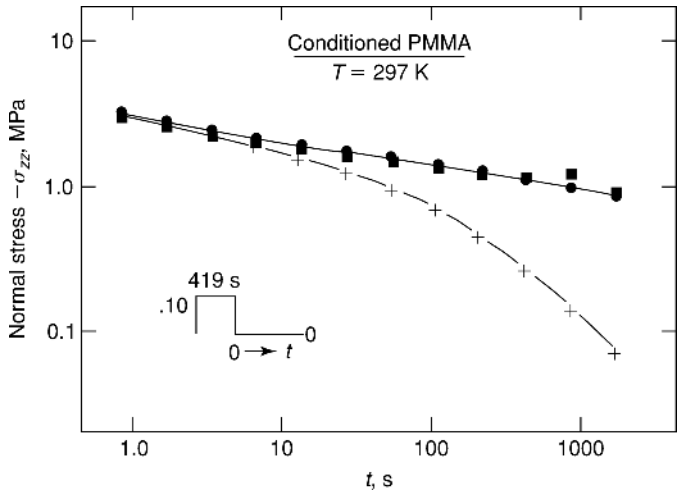

Fig. 62. Normal force response in "step to zero" type of deformation history for a PMMA polymer glass, showing the comparison between the experimental data (filled squares), the K-BKZ model predictions (crosses), and the predictions (filled circles) from the Zapas strain-clock model (118). Note that the clock terms for the normal force response were determined by fitting the shear stress response in the same experiment. After McKenna and Zapas (112).

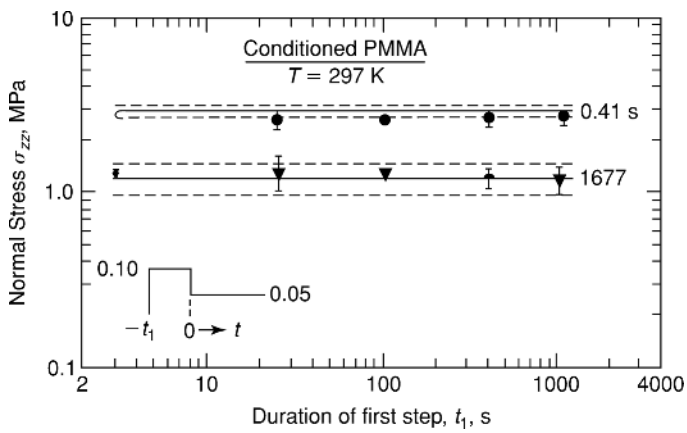

Fig. 63. "Half-step" normal force response in a PMMA polymer glass, showing that the normal force response is independent of the duration t_1 of the first step. Points are data from the second step response for $\gamma = 0.05$ after a step to $\gamma = 0.10$. Lines are data from a single-step experiment at $\gamma = 0.05$. (Solid lines: mean; dashed lines: single standard deviation). Time values of 0.41 and 1677 s are isochronal values after the imposition of the step in the deformation. After McKenna and Zapas (113).

(under certain conditions) and, in the relatively small deformation regime, it can be inverted between creep and stress relaxation.

The equations in simple shear can be written as

$$\sigma_{12}(t) = \int_{-\infty}^{t} \{G_*[\gamma(t) - \gamma(t'), \beta(t, t')] b_\sigma(t')\} \mathrm{d}t' \tag{121}$$

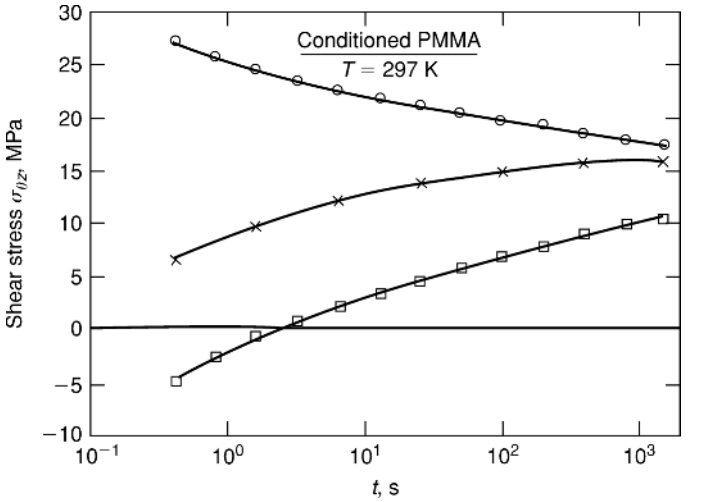

Fig. 64. "Half-step" shear stress response for a PMMA glass. Circles represent single-step stress relaxation response at $\gamma = 0.05$; crosses, K-BKZ prediction; and open squares, experimental data for second step of $\gamma = 0.05$ after a first step of $\gamma = 0.10$ having a duration $t_1 = 419$ s. After McKenna (114).

where b_σ is the stress shift factor. The reduced time $\beta(t, t')$ is written as

$$\beta(t, t') = \int_{t'}^{t} b_\sigma(s)\mathrm{d}s \tag{122}$$

An interesting aspect of the Bernstein–Shokooh model is that the structure of the nonlinear equations is somewhat different from either the Schapery model or the Zapas strain-clock model. In the Bernstein–Shokooh model, the nonlinearity is set up by having the stress response to a deformation history depend also on the stress through the stress shift factor b_σ. Hence, in equation 121 there are stress terms on both sides of the equation. For the other models, including those discussed subsequently, the stresses or deformations are isolated on either side of the equation. For example, in the Schapery stress relaxation formulation (eq. 117) the stress depends on the strain and a strain-dependent material clock. Examination of equations 115 and 119 provides a similar type of conclusion for the Schapery creep formulation or the K-BKZ strain-clock equation. Hence, one might expect that the stress-clock formulation of Bernstein and Shokooh might capture a different sort of material nonlinearity from the other models. To this author's knowledge, the only other set of equations that provides a similar type of nonlinear response comes in the field of *structural recovery or physical aging* of glassy materials. The so-called Tool–Narayanaswamy–Moynihan and Kovacs–Aklonis–Hutchinson–Ramos models have been very successful to describe the kinetics of structural recovery. (The reader is referred to the relevant literature for further examination of these equations (156–160). See also AGING, PHYSICAL).

There has been relatively little testing of the Bernstein–Shokooh model. Penn did some work to describe the nonlinear response of aluminum, but this, however, was not published (161). Pesce and McKenna did some two-step stress relaxation experiments in torsion (162) using polycarbonate as the material. The results, one of which is shown in Figure 65, indicated that the model is better

than the K-BKZ model, but does not perfectly describe the material response for polycarbonate.

The Knauss–Emri Model. There have been several works in the literature in which volume- or *free-volume*-dependent clocks were used to describe the nonlinear viscoelastic response of polymeric glasses. The chief success among these is the Knauss–Emri model (163) in which the reduced time was defined in terms of a shift factor that depended on temperature, stress, and concentration of small molecules in such a way that the responses depended on the free volume induced by each of these parameters. For an isothermal single phase and homogeneous material, the equations are

$$\begin{aligned} S_{ij} &= 2\int_{-\infty}^{t} G(Z-Z')\frac{\partial \varepsilon_{ij}}{\partial t'}\mathrm{d}t' \\ \kappa_{ii} &= 3\int_{-\infty}^{t} K(Z-Z')\frac{\partial \varepsilon_{\mathrm{v}}}{\partial t'}\mathrm{d}t' \end{aligned} \tag{123}$$

where Z is the reduced time, S_{ij} are the deviatoric stresses, κ_{ii} is the first stress invariant, $G(t)$ and $K(t)$ are material functions, and ε_v is the dilatational strain. The dilatational strain is related to the bulk creep compliance $M(t)$ and determines the reduced time as

$$\begin{aligned} Z(t)-Z(t') &= \int_{t'}^{t} = \frac{\mathrm{d}s}{\phi[\varepsilon_v(s)]} \\ \varepsilon_v(t) &= \frac{M(t)^{*}\mathrm{d}\kappa_{kk}}{3} \end{aligned} \tag{124}$$

where the asterisk denotes a Stieltjes convolution operation.

The Knauss–Emri model captures some of the nonlinear stress relaxation response of materials and looks like linear viscoelasticity in the reduced time variables, and hence is relatively straightforward to implement. However, the observation that material nonlinearities occur in shearing deformations as well as in compression, where the free-volume mechanisms predict decreasing mobility suggest that the model is limited in its usefulness (164,165).

The Lustig–Shay–Caruthers Model. In the past several years there has been a serious effort at the Purdue University School of Chemical Engineering under the direction of J.M. Caruthers (166–170) to adapt one such formalism to the problem of glassy materials. The formalism is that of Rational Mechanics (171) or Rational Thermodynamics, and here the Caruthers group's contributions in this area are examined briefly.

The thermoviscoelastic model is an extension of the original ideas of Coleman (171) and Noll (109) for a nonequilibrium thermodynamics referred to in the literature as *rational mechanics* or *rational thermodynamics*. Historically this approach has been controversial for a variety of reasons beyond the scope of this article. However, one very important issue in the development and uses of the rational mechanics framework has been the need to deal with multiple integral expansions of the relevant response functions and the inherent complexity that

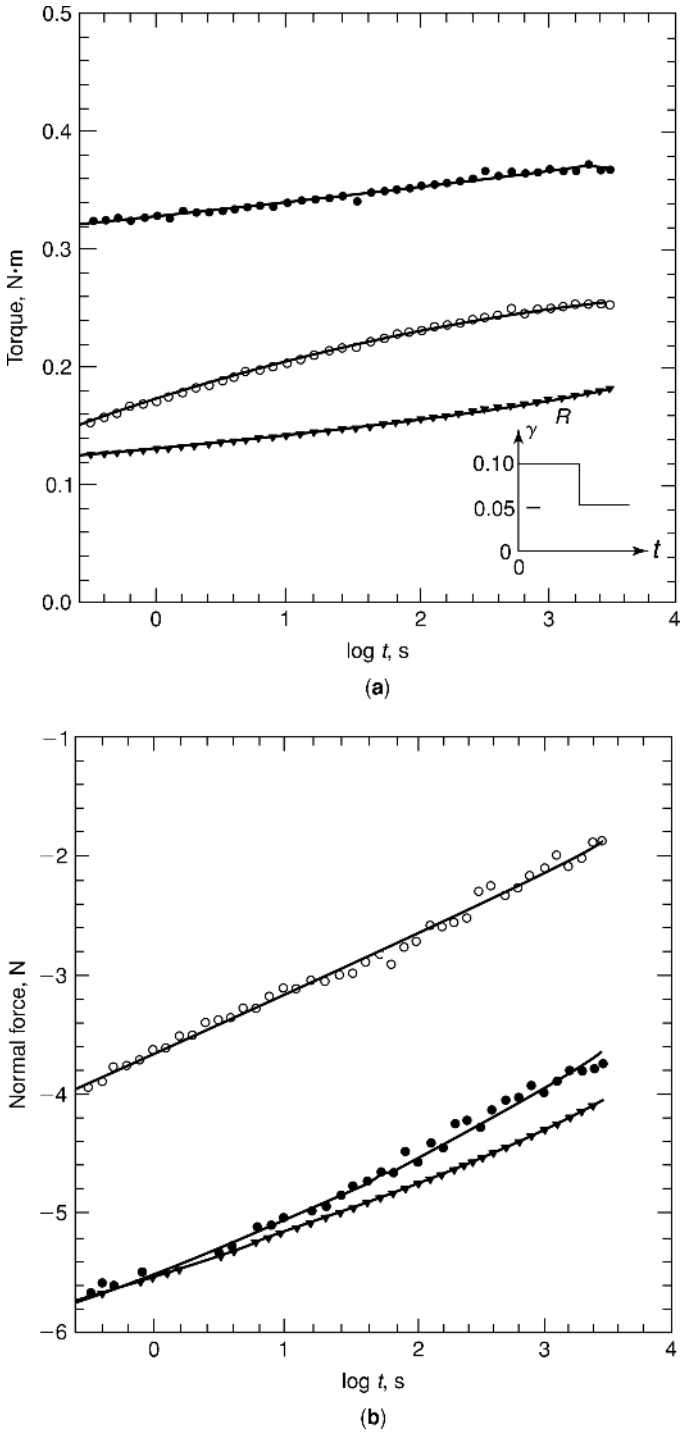

Fig. 65. "Half-step" torque (**a**) and normal force (**b**) responses for a polycarbonate glass comparing the experimental data (open circles) with the K-BKZ equation (closed circles) and the Bernstein–Shokooh stress-clock model (155) modified to an energy clock (inverted triangles) predictions. After Pesce and McKenna (162).

arrives in dealing with such representations. The advantage of Lustig–Shay–and Caruthers model (170) is its ability to truncate the multiple integrals and arrive at single integral representations of the material behavior. This leads to a very attractive and tractable set of equations for describing the material response. Because the single integral forms are of themselves insufficient to describe the observed nonlinear response of glass-forming materials, a reduced time much as used in the models presented above, that depends on the configurational entropy has been introduced (170). Hence, one starts with the assumption that there exists a free energy potential functional that is time-dependent. Appropriate differentiation of the functional results in volume, enthalpy, and mechanical responses that contain sufficient information to predict strongly nonlinear behavior from laboratory determined linear viscoelastic response functions.

The detailed development that is followed is beyond the scope of this article. Here simply note that they followed a rigorous approach, beginning with a representation of the time-dependent "free energy" function $\psi(t)$ and through appropriate simplifications and differentiations arrived at a set of equations for the entropy and stress as functions of the thermal and mechanical histories. The fluid form of the model through, single integral terms, is given by the following equations for the stress and entropy. Significantly, note that an important aspect of the model is that all the material parameters are related to response functions obtained from linear viscoelastic measurements, PVT measurements, and heat capacity measurements:

Stress:

$$\begin{aligned} T(t) = -P^{(\infty)}I \; + \; & \frac{\rho}{\rho_{\mathrm{R}}}\int_{-\infty}^{t} G_{\Delta}[I_3(t),\theta(t),t^*-\xi^*][\frac{\mathrm{d}C_t(\xi)}{\mathrm{d}\xi} - \frac{1}{3}I\frac{\mathrm{d}I_{t1}(\xi)}{\mathrm{d}\xi}]\mathrm{d}\xi \\ & + \frac{\rho}{\rho_R}I\int_{-\infty}^{t}\frac{1}{2}K_{\Delta}[I_3(t),\theta(t),t^*-\xi^*]\frac{\mathrm{d}I_{t1}(\xi)}{\mathrm{d}\xi}\mathrm{d}\xi \\ & + \frac{\rho}{\rho_{\mathrm{R}}}I\int_{-\infty}^{t} 2\rho_{\mathrm{R}}A_{\Delta}[I_3(t),\theta(t),t^*-\xi^*]\frac{\mathrm{d}\theta(\xi)}{\mathrm{d}\xi}\mathrm{d}\xi \end{aligned} \tag{125}$$

$$\begin{aligned} \eta(t) = \eta^{(\infty)}[I_3(t),\theta(t)] - & \int_{-\infty}^{t} A_{\Delta}[I_3(t),\theta(t),t^*-\xi^*]\frac{\mathrm{d}I_{t1}(\xi)}{\mathrm{d}\xi}\mathrm{d}\xi \\ & - \int_{-\infty}^{t} 2C_{\Delta}[I_3(t),\theta(t),t^*-\xi^*]\frac{\mathrm{d}\theta(\xi)}{\mathrm{d}\xi}\mathrm{d}\xi \end{aligned} \tag{126}$$

where P is the pressure and η is the entropy. The superscript ∞ implies the equilibrium value. ρ is the density and ρ_{R} is its value in the undeformed, reference state. I is the identity tensor, I_3 is the third absolute strain invariant of the deformation tensor (related to the volume change), $C_t(\tau)$ is the relative right Cauchy–Green strain tensor, and $I_{t1}(\tau)$ is the first relative strain invariant of $C_t(\tau)$. Note that in the Caruther's group the notation is that θ is the absolute temperature. The K_{Δ} term is the relaxation function for the bulk modulus, G_{Δ} is the shear modulus relaxation function, A_{Δ} is a constant volume thermal stress function, and C_{Δ} is the constant volume heat capacity divided by temperature. Finally, the

reduced time t^* is defined by

$$t^* = \int_0^t \frac{d\xi}{a(\xi)} \tag{127}$$

where $a(\xi)$ is a generalized shift factor that is taken to depend on the configurational entropy following the Adam–Gibbs (172) relationship:

$$loga = M\left[\frac{1}{\eta_c\theta} - \frac{1}{\eta_{cr}\theta_r}\right] \tag{128}$$

where M is a constant, η_c and η_{cr} are the configurational entropy in the current and reference states respectively, and θ and θ_r are the temperature and reference temperature respectively. The configurational entropy can be calculated from the experimental heat capacity data, assuming that it is approximately equal to the total. The reader is referred to McWilliams (169) for further discussion. Also, note that Hodge (160) has discussed this form of shift factor in the Tool–Narayanaswamy-Moynihan equations for enthalpy recovery.

The Lustig–Shay–Caruthers model has, to date, been primarily used to estimate volume and enthalpy responses in glassy materials (see AGING, PHYSICAL)—a subset of the viscoelastic behaviors seen in solid-like or glassy polymers and not covered in this article. However, recent work between the Purdue group and Sandia National Laboratories (173) has made great strides in implementing the model into finite element codes as well as defining limits on the forms of some of the functions. The model, when finally published, will require full evaluation. At this point, the current author thinks that it will be an important contribution to the understanding of the nonlinear viscoelastic behavior of polymeric glasses.

Plasticity and Viscoplasticity and Other Models. As discussed above, the alternative representation of the nonlinear viscoelastic response of polymers is that of plasticity and viscoplasticity. In some respects, these models could be recast as viscoelastic models and they would be equivalent to some of the models discussed above. However, the perspective that glassy polymers are really fluids and do follow time–temperature superposition is lost with these models. Hence, the physical interpretation of material parameters, in this author's opinion, becomes very questionable. Therefore, only references to the major papers on polymer plasticity and viscoplasticity are given (174–177).

In addition, there are other viscoelastic models that are not dealt with here. Again, the references are provided for the reader's information (178–184).

BIBLIOGRAPHY

"Viscoelasticity" in *EPST* 1st ed., Vol. 14, pp. 670–717, by J. D. Ferry, University of Wisconsin; in *EPSE* 2nd ed., Vol. 17, pp. 587–665, by F. R. Schwarzl, University of Erlangen – Nürnberg; in *EPST* 3rd ed., Vol. 4, pp. 533–628, by G. B. McKenna, Texas Tech University.

CITED PUBLICATIONS

1. W. Weber, Ueber die Elasticität der Seidenfäden *Pogg. Ann. Physik.* **4**, 247–257 (1835).

2. R. Kohlrausch, Theorie des Elektrischen Rückstandes in der Leidener Flasche *Annalen der Physik und Chemie von J. C. Poggendorff* **91**, 179–214 (1854); F. Kohlrausch, Ueber die elastische Nachwirkung bei der Torsion *Annalen der Physik und Chemie von J. C. Poggendorff* **119**, 337–369 (1863).
3. L. Boltzmann, Zur Theorie der Elastischen Nachwirkung *Sitzungsber. Akad. Wiss. Wien. Mathem.-Naturwiss. Kl.* **70**, 275–300 (1874).
4. H. Markovitz, Boltzmann and the Beginnings of Linear Viscoelasticity *Trans. Soc. Rheol.* **21**, 381–398 (1977).
5. E. N. da C. Andrade, A Theory of the Viscosity of Liquids. Part I *Phil. Mag.* **17**, 497–511 (1934); E. N. da C. Andrade, A Theory of the Viscosity of Liquids. Part II *Phil. Mag.* **17**, 698–732 (1934).
6. C. Zener, *Elasticity and Anelasticity of Metals*, University of Chicago Press, Chicago, 1948.
7. R. A. Schapery, in G. P. Sendeckyj, ed., *Composite Materials*, Vol. **2**: *Mechanics of Composite Materials* Academic Press, Inc., New York, 1974, Chapt. 4, pp. 85–168.
8. S. P. Timoshenko and J. N. Goodier, *Theory of Elasticity*, 3rd ed., McGraw-Hill, New York, 1970.
9. J. D. Ferry, *Viscoelastic Properties of Polymers*, 3rd ed., John Wiley and Sons, Inc., New York, 1980.
10. N. W. Tschoegl, *The Phenomenological Theory of Linear Viscoelastic Behavior*, Springer Verlag, Berlin, 1989.
11. A. J. Staverman and F. Schwarzl, in H. A. Stuart, ed., *Die Physik der Hochpolymeren. Vierter Band. Theorie und Molekulare Deutung Technologischer Eigenschaften von Hochpolymeren Werkstoffen*, Springer-Verlag, Berlin, 1956, Chapt. 1, pp. 1–125 (In English).
12. H. Leaderman, in F. R. Eirich, ed. *Rheology, Vol. 2: Theory and Applications*, Academic Press, Inc., New York, 1958, pp. 1–62.
13. S. L. Rosen, *Fundamental Principles of Polymeric Materials*, 2nd ed., Wiley-Interscience, New York, 1993.
14. H. H. Winter, Analysis of Dynamic Mechanical Data-Inversion into a Relaxation-Time Spectrum and Consistency Check *J. Non-Newt. Fl. Mech.* **68**, 225–239 (1997).
15. D. W. Mead, Determinations of Molecular Weight Distributions of Linear Flexible Polymers from Linear Viscoelastic Material Functions *J. Rheol.* **38**, 1797–1827 (1994).
16. G. A. Carri and H. H. Winter, Mapping of the Relaxation Patterns of Polymer Melts with Linear Flexible Molecules of Uniform Length *Rheol. Acta* **36**, 330–344 (1997).
17. M. Baumgaertel and H. H. Winter, Interrelation Between Continuous and Discrete Relaxation-Time Spectra *J. Non-Newt. Fl. Mech.* **44**, 15–36 (1992).
18. W. H. Tuminello, Molecular Weight Distributions of Tetrafluoroethylene-Hexafluoropropylene Copolymers *Polym. Eng. Sci.* **29**, 645–653 (1989).
19. S. W. Park and R. A. Schapery, Methods of Interconversion between Linear Viscoelastic material Functions. Part. I.–A Numerical Method Based on Prony Series *Int. J. Solids and Struct.* **36**, 1653–1675 (1999).
20. D. J. Plazek, Don't Cry for Me Charlie Brown or with Compliance Comes Comprehension *J. Rheol.* **44**, 831–841 (2000).
21. W. N. Findley, J. S. Lai, and K. Onaran, *Creep and Relaxation of Nonlinear Viscoelastic Materials with an Introduction to Linear Viscoelasticity*, North Holland, New York, 1976.
22. A. S. Wineman and K. R. Rajagopal, *Mechanical Response of Polymers*, Cambridge University Press, New York, 2000.
23. E. H. Lee, Stress Analysis in Viscoelastic Bodies *Quart. Appl. Math.* **13**, 183 (1955).

24. R. A. Schapery, Approximate Methods of Transform Inversion for Viscoelastic Stress Analysis in *Proc. 4th Int. Cong. Appl. Mech.*, Vol. 2, ASME, New York, 1962, p. 1075.
25. A. V. Tobolsky, *Properties and Structure of Polymers*, John Wiley and Sons, Inc., New York, 1967.
26. T. Fujimoto, M. Ozaki, and M. Nagasawa, Stress Relaxation of Monodisperse Poly-α-methylstyrene *J. Polym. Sci., Part A-2* **6**, 129–140 (1968).
27. H. Vogel, Das Temperaaturabhängigkeitsgesetz der Viskosität Flüssigkeiten *Phys. Z.* **22**, 645–646 (1921).
28. G. S. Fulcher, Analysis of Recent Measurements of the Viscosity of Glasses *J. Am. Ceram. Soc.* **8**, 339–355 (1925).
29. M. L. Williams, R. F. Landel, and J. D. Ferry, The Temperature Dependence of Relaxation Mechanisms in Amorphous Polymers and Other Glass-forming Liquids *J. Am. Chem. Soc.* **77**, 3701–3706 (1955).
30. D. J. Plazek, X. D. Zheng, and K. L. Ngai, Viscoelastic Properties of Amorphous Polymers. 1 Different Temperature Dependences of Segmental Relaxation and Terminal Dispersion *Macromolecules* **25**, 4920–4924 (1992).
31. P. G. Santangelo and C. M. Roland, Temperature Dependence of Mechanical and Dielectric-Relaxation in Cis-1,4-Polyisoprene *Macromolecules* **31**, 3715–3719 (1998).
32. R. Zorn, G. B. McKenna, L. Willner, D. Richter, Rheological Investigations on Polybutadienes with Different Microstructures over a Large Temperature Range *Macromolecules* **28**, 8552–8562 (1995).
33. J.-J. Pesce, J. M. Niemiec, M. Y. Chiang, C. L. Schutte, C. R. Schultheisz, and G. B. McKenna in M. Negahban, ed., Characterization of Polymers in the Glass Transition Range: Time-Temperature and Time-Aging Time Superposition in Polycarbonate in *Current Research in the Thermo-Mechanics of Polymers in the Rubbery–Glassy Range*, American Society of Mechanical Engineers, New York, AMD-Vol. **203**, 1995, pp. 77–88.
34. H. G. Merriman and J. M. Caruthers, Nonlinear Stress Relaxation of a Styrene-Butadiene Random Copolymer *J. Polym. Sci., Polym. Phys. Ed.* **19**, 1055–1071 (1981).
35. P. A. O'Connell and G. B. McKenna, Large Deformation Response of Polycarbonate: Time-Temperature, Time-Aging Time and Time Strain Superposition *Polym. Eng. Sci.* **37**, 1485–1495 (1997).
36. G. W. Scherer, *Relaxation in Glass and Composites*, Krieger Publishing Co., Malabar, Fla., 1992.
37. C. A. Angell K. L. Ngai, G. B. McKenna, P. F. McMilllan and S. W. Martin, Relaxation in Glassforming Liquids and Amorphous Solids *J. Appl. Phys.* **88**, 3113–3157 (2000).
38. A. J. Kovacs, Transition Vitreuse dans les Polyméres Amorphes. Etude Phénoménologique *Fortschritte der Hochpolymeren-Forschung* **3**, 394–507 (1963).
39. G. B. McKenna, in C. Booth and C. Price, eds., *Comprehensive Polymer Science, Vol. 2: Polymer Properties*, Pergamon Press, Oxford, 1989, pp. 311–362.
40. L. C. E. Struik, *Physical Aging in Polymers and Other Amorphous Materials*, Elsevier, Amsterdam, 1976.
41. L. P. Chen, A. F. Yee, and E. J. Moskala, The Molecular Basis for the Relationship Between the Secondary Relaxation and Mechanical Properties of a Series of Polyester Copolymer Glasses *Macromolecules* **32**, 5944–5955 (1999).
42. W. C. Child Jr. and J. D. Ferry, Dynamic Mechanical Properties of Poly-n-Butyl Methacrylate *J. Colloid. Sci.* **12**, 327–341 (1957).
43. A. K. Rizos, L. Petihakis, K. L. Nagi, J. H. Wu, and A. F. Yee, A Dielectric-Relaxation Study of the Gamma-Relaxation in Tetramethylbisphenol-A Polyearbonate Plasticized by Tris(2-Ethylhexyl) Phosphate *Macromolecules* **32**, 7921–7924 (1999).
44. J. Heijboer, in J. A. Prins, ed., *Physics of Non-Crystalline Solids*, North-Holland, Amsterdam, 1965, pp. 231–254.

45. M. L. Cerrada and G. B. McKenna, Stress Relaxation of Poly(ethylene Naphthalate): Isothermal, Isochronal and Isostructural Responses *Macromolecules* **33**, 3065–3076 (2000).
46. L. R. G. Treloar, *The Physics of Rubber Elasticity*, 3rd ed., Clarendon Press, Oxford, 1975.
47. J. P. Cohen Addad, ed., *Physical Properties of Polymeric Gels*, John Wiley and Sons, Inc., New York, 1996.
48. F. Horkay and G. B. McKenna, in J. E. Mark, ed., *Physical Properties of Polymers Handbook*, AIP Press, Woodbury, N. Y., 1996, pp. 379–400.
49. J. E. Mark and B. Erman, ed., *Elastomeric Polymer Networks*, Prentice Hall, Englewood Cliffs, N. J., 1992.
50. G. B. McKenna and J. A. Hinkley, Mechanical and Swelling Behavior of Well Characterized Polybutadiene Networks *Polymer* **27**, 1368–1376 (1986).
51. P. G. de Gennes, Reptation of a Polymer Chain in the Presence of Fixed Obstacles *J. Chem. Phys.* **55**, 572–579 (1971).
52. M. Doi and S. F. Edwards, Dynamics of Concentrated Polymer Systems Part 1. Brownian Motion in the Equilibrium State *J. Chem. Soc., Faraday Trans. 2* **74**, 1789–1801 (1978).
53. M. Doi and S. F. Edwards, Dynamics of Concentrated Polymer Systems Part 2.–Molecular Motion under Flow *J. Chem. Soc., Faraday Trans. 2* **74**, 1802–1817 (1978).
54. M. Doi and S. F. Edwards, Dynamics of Concentrated Polymer Systems Part 3.–The Constitutive Equation *J. Chem. Soc., Faraday Trans. 2* **74**, 1818–1832 (1978).
55. M. Doi and S. F. Edwards, Dynamics of Concentrated Polymer Systems Part 4,–Rheological Properties *J. Chem. Soc. Faraday Trans. 2* **75**, 38–54 (1979).
56. M. Doi and S. F. Edwards, *The Theory of Polymer Dynamics*, Oxford Science Publishers, Oxford, 1986.
57. G. C. Berry and T. G. Fox, The Viscosity of Polymers and Their Concentrated Solutions *Adv. Polym. Sci.* **5**, 261–357 (1968).
58. M. Doi and N. Y. Kuzuu, Rheology of Star Polymers in Concentrated Solutions and Melts *J. Polym. Sci., Polym. Lett. Ed.* **18**, 775–780 (1980).
59. W. W. Graessley, Entangled Linear, Branched and Network Polymer Systems *Adv. Polym. Sci.* **47**, 68–117 (1982).
60. M. Doi, Explanation for the 3.4 Power Law for Viscosity of Polymeric Liquids on the Basis of the Tube Model *J. Polym. Sci., Polym. Lett. Ed.* **19**, 265–273 (1981).
61. R. G. Larson, *The Structure and Rheology of Complex Fluids*, Oxford University Press, New York, 1999.
62. R. G. Larson, *Constitutive Equations for Polymer Melts and Solutions*, Butterworths, London, 1988.
63. H. Watanabe, Viscoelasticity and Dynamics of Entangled Polymers *Prog. Polym. Sci.* **24**, 1253–1403 (1999).
64. W. W. Graessley, The Entanglement Concept in Polymer Rheology *Adv. Polym. Sci.* **16**, 1–179, (1974).
65. R. H. Colby, L. J. Fetters, and W. W. Graessley, Melt Viscosity-Molecular Weight Relationship for Linear Polymers *Macromolecules* **20**, 2226–2237 (1987).
66. W. G. Knauss and V. H. Kenner, On the Hygrothermal Characterization of Polyvinyl Acetate *J. Appl. Phys.* **51**, 5131–5136 (1980).
67. T. W. Dewitt, H. Markovitz, F. J. Padden, Jr., and L. J. Zapas, Concentration Dependence of the Rheological Behavior of the Polyisobutylene-Decalin System *J. Colloid Sci.* **10**, 174–188 (1955).
68. R. W. Rendell, K. L. Ngai, and G. B. McKenna, Molecular Weight and Concentration Dependences of the Terminal Relaxation Time and Viscosity of Entangled Polymer Solutions *Macromolecules* **20**, 2250–2256 (1987).

69. C. W. Macosko, *Rheology: Principles, Measurements, and Applications*, VCH Publishers, New York, 1994.
70. B. Bernstein, E. A. Kearsley, and L. I. Zapas, A Study of Stress Relaxation with Finite Strain *Trans. Soc. Rheol.* **7**, 391–410 (1963).
71. A. Kaye, Non-Newtonian Flow in Incompressible Fluids. Part I. A General Rheological Equation of State, Note No. 134, College of Aeronautics, Cranfield, 1962, pp. 1–4.
72. B. Bernstein, Time Dependent Behavior of an Incompressible Elastic Fluid. Some Homogeneous Deformation Histories *Acta Mech.* **2**, 329–354 (1966).
73. W. W. Graessley, R. L. Hazleton, and L. R. Lindeman, The Shear Rate Dependence of Viscosity in Concentrated Solutions of Narrow Distribution Polystyrene *Trans. Soc. Rheol.* **11**, 267–285 (1967).
74. S. L. Rosen, *Fundamental Principles of Polymeric Materials*, 2nd ed., Wiley-Interscience, New York, 1993 pp. 252–253.
75. H. C. Tseng, C. A. Heiber, K. K. Wang, H. H. Chiang, and G. E. Grant, Analysis of Rheological Data from an Automated Injection-Molding Capillary Rheometer in *ANTEC '85*, Society of Plastics Engineers, 1985, pp. 716–719.
76. D. M. Best, *Prediction of Polymer Melt Processing Behavior*, Thesis, Carnegie Institute of Technology (now Carnegie Mellon Institution), 1969.
77. H. Münstedt, Dependence of the Elongational Behavior of Polystyrene Melts on Molecular Weight and Molecular Weight Distribution *J. Rheol.* **24**, 847–867 (1980).
78. C. M. Vrentas and W. W. Graessley, Study of Shear Stress Relaxation in Well-Characterized Polymer Liquids *J. Rheol.* **26**, 359–371 (1982).
79. G. B. McKenna and L. J. Zapas, The Superposition of Small Deformations on Large Deformations: Measurements of the Incremental Modulus for a Polyisobutylene Solution *J. Polym. Sci., Polym. Phys. Ed.* **23**, 1647–1656 (1985).
80. K. Osaki, N. Bessho, T. Kojimoto, and M. Kurata, Experimental Tests of a Few Constitutive Models for Polymer Solutions Based on Birefringence Data in Time-Dependent Fields *J. Rheol.* **24**, 125–144 (1980).
81. L. J. Zapas and J. C. Phillips, Nonlinear Behavior o Polyisobutylene Solutions as a Function of Concentration *J. Rheol.* **25**, 405–420 (1981).
82. R. I. Tanner, From A to (BK)Z in Constitutive Relations *J. Rheol.* **32**, 673–702 (1988).
83. D. C. Leigh, *Nonlinear Continuum Mechanics*, McGraw-Hill, New York, 1968.
84. W. Prager, *An Introduction to Mechanics of Continua*, Ginn and Co., Boston, 1961.
85. O. H. Varga, *Stress–Strain Behavior of Elastic Materials. Selected Problems of Large Deformation*, wiley-Interscience, New York, 1966.
86. A. S. Lodge, *An Introduction to Elastomer Molecular Theory*, Bannatek Press, Madison, Wis., 1999.
87. M. Mooney, A Theory of Large Elastic Deformation *J. Appl. Phys.* **11**, 582–592 (1940).
88. R. S. Rivlin, Large Elastic Deformations of Isotropic Materials. I. Fundametal Concepts *Phil. Trans. R. Soc. London, Ser. A*, **240**, 459–525 (1948).
89. W. H. Han, F. Horkay, and G. B. McKenna, Mechanical and Swelling Behaviors of Rubber: A Comparison of Some Molecular Models with Experiment *Math. Mech. Solids* **4**, 139–167 (1999).
90. R. S. Rivlin and D. W. Saunders, Large Elastic Deformations of Isotropic Materials. VII. Experiments on the Deformation of Rubber *Phil. Trans. R. Soc. London, Ser. A* **243**, 251 (1951).
91. H. Pak and P. J. Flory, Relationship of Stress to Uniaxial Strain in Corsslinked Poly(dimethyl siloxane) over the Full Range from Large Compression to High Elongation *J. Polym. Sci., Polym. Phys. Ed.* **17**, 1845 (1979).
92. M. Gottlieb and R. J. Gaylord, Experimental Tests of Entanglement Models of Rubber Elasticity: 1. Uniaxial Tension Compression *Polymer* 1644–1646 (1982).

93. M. Gottlieb and R. J. Gaylord, Experimental Tests of Entanglement Models of Rubber Elasticity: 2. Swelling *Macromolecules* **17**, 2024–2030 (1984).
94. R. W. Penn and E. A. Kearsley, The Scaling Law for Finite Torsion of Elastic Cylinders *Trans. Soc. Rheol.* **20**, 227–238 (1976).
95. J. H. Poynting, On the Changes in he Dimensions of a Steel Wire when Twisted, and on the Pressure of Distortional Waves in Steel *Proc. R. Soc. London, Ser. A* **86**, 534–561 (1912).
96. G. B. McKenna and L. J. Zapas, Experiments on the Small Strain Behavior of Crosslinked Natural Rubber. Part I. Torsion *Polymer* **24**, 1495–1501 (1983).
97. E. A. Kearsley and L. J. Zapas, Some Methods of Measurement of an Elastic Strain Energy Function of the Valanis–Landel Type *J. Rheol.* **24**, 483–500 (1980).
98. K. C. Valanis and R. F. Landel, A Strain Energy Function of a Hyperelastic Material in Terms of the Extension Ratios *J. Appl. Phys.* **38**, 2997–3002 (1967).
99. H. Vangerko and L. R. G. Treloar, The Inflation and Extension of Rubber Tube for Biaxial Strain Studies *J. Phys. D: Appl. Phys.* **11**, 1969–1978 (1978).
100. D. G. Jones and L. R. G. Treloar, The Properties of Rubber in Pure Homogeneous Strain *J. Phys. D: Appl. Phys.* **8** 1285–1304 (1975).
101. J. Glucklich and R. F. Landel, Strain Energy Function of Styrene Butadiene Rubber and the Effect of Temperature *J. Polym. Sci.* **15**, 2185–2199 (1978).
102. G. B. McKenna, K. M. Flynn, and Y.-H. Chen, Experiments on the elasticity of Dry and Swollen Networks: Implications for the Frenkel Flory-Rehner Hypothesis *Macromolecules* **22**, 4507–4512 (1989).
103. R. W. Ogden, Large deformation Isotropic Elasticity–On the Correlation of Theory and Experiment for Incopressible Rubberlike Solids *Proc. R. Soc. London, Ser. A* **326**, 565–584 (1972).
104. E. H. Twizell and R. W. Ogden, Non-Linear Optimization of the Material Constants in Ogden's Stress Deformation Function for Incompressible Isotropic Elastic Materials *J. Austral. Math. Soc., Ser. B* **24**, 424–434 (1983).
105. G. Karami, H. Zohari, and E. Setoudeh, Stress Disribution Change in Bias Tires Due to Changes in Cord Angle–A Finite Element Analysis *Kautsh. Gummi Kunstst.* **51**, 450–454 (1998).
106. G. L. Bradley, P. C. Chang, and G. B. McKenna, Rubber Modeling Using Uniaxial Test Data *J. Appl. Polym. Sci.*, **81**, 837 (2001).
107. R. I. Tanner, *Rheology: An Historical Perspective*, Elsevier, Amsterdam, 1998.
108. B. D. Coleman, Thermodynamics of Materials with Memory *Arch. Ration. Mech. Anal.* **17**, 1–46 (1964).
109. W. Noll, A Mathematical Theory of the Mechanical Behavior of Continuous Media *Arch. Ration. Mech. Anal.* **2**, 197–226 (1958).
110. V. Rouiller and G. B. McKenna, *Society of Plastics Engineers, in ANTEC '98, Vol. II*, 1998, pp. 2138–2143.
111. L. J. Zapas and T. Craft, Correlation of Large Longitudinal Deformations with Different Strain Histories *J. Res. Natl. Bur. Stand. (U.S.)* **69A**, 541–546 (1965).
112. G. B. McKenna and L. J. Zapas, Nonlinear Viscoclastic Behavior of Poly(methyl methacrylate) in Torsion *J. Rheol.* **23**, 151–166 (1979).
113. G. B. McKenna and L. J. Zapas, The Normal Stress Response in Nonlinear Viscoelastic Materials-Some Experimental Findings *J. Rheol.* **24**, 367–377 (1980).
114. G. B. McKenna, in K. L. Ngai and G. B. Wright, eds., Measurement of the Torque and Normal Force in Torsion in the Study of the Thermoviscoelastic Properties of Polymer Glasses in *Relaxations in Complex Systems*, U.S. Government Printing Office, NTIS, Springfield, Virginia, 1985, pp. 129–144.
115. D. C. Venerus and H. Kahvand, Doi Edwards Theory Evaluation in Double-Step Strain Flows *J. Polym. Sci., Part B: Polym. Phys.* **32**, 1531–1542 (1994).

116. D. C. Venerus and H. Kahvand, Normal Stress Relaxation in Reversing Double Step Strain Flows *J. Rheol.* **38**, 1297–1315 (1994).
117. D. C. Venerus, E. F. Brown, and W. R. Burghardt, The Nonlinear Response of a Polydisperse Polymer Solution to Step Strain Deformations *Macromolecules* **31**, 9206–9212 (1998).
118. L. J. Zapas, in H. H. Kausch, J. A. Hassell, and R. I. Jaffee, eds., Nonlinear Behavior of Polyisobutylene Solutions in *Deformation and Fracture of High Polymers*, Plenum, New York, 1974, pp. 381–395.
119. M. H. Wagner and J. Schaeffer, Assessment of Nonlinear Strain Measures for Extensional and Shearing Flows of Polymer Melts *Rheol. Acta* **33**, 506–516 (1994).
120. P. E. Rouse, A Theory of the Linear Viscoelastic Properties of Dilute Solutions of Coiling Polymers *J. Chem. Phys.* **21**, 1272–1980 (1953).
121. T. C. B. McLeish, in M. E. Cates and M. R. Evans, eds., Rheology o Linear and Branched Polymers in *Soft and Fragile Matter. Nonequilibrium Dynamics, Metastability and Flow*, Institue of Physics, London, 2000, pp. 79–111.
122. G. B. McKenna, B. J. Hostetter, A. Hadjichristides, L. J. Fetters and D. J. Plazek, A Study of the Linear Viscoelastic Properties of Cyclic Polystyrenes Using Creep and Recovery Measurements *Macromolecules* **22**, 1834–1852 (1989).
123. K. Osaki, K. Nishizawa, and M. Kurata, Material Time Constant Characterizing the Nonlinear Viscoelasticity o Entangled Polymer Systems *Macromolecules* **15**, 1068–1071 (1982).
124. A. S. Lodge and J. Meissner, On the Use of Instantaneous Strains, Superposed on Shear and Elongational Flows of Polymeric Liquids, to Test the Gaussian Network Hypothesis and to Estimate Segment Concentration and its Variation During Flow *Rheol. Acta.* **11**, 351–352 (1972).
125. M. H. Wagner and J. Schaeffer, Nonlinear Strain Measures for General Biaxial Extension of Polymer Melts *J. Rheol.* **36**, 1–27 (1992).
126. J. des Cloiseaux, Double Reptation vs. Simple Reptation in Polymer Melts *Europhys. Lett.* **5**, 437–442 (1988).
127. S. T. Milner, Relating the Shear-Thinning Curve to the Molecular Weight Distribution in Linear Polymer Melts *J. Rheol.* **40**, 305–315 (1996).
128. C. Tsenoglou, Molecular Weight Polydispersity Effects on the Viscoelasticity of Entangled Linear-Polymers *Macromolecules* **24**, 1762–1767 (1991).
129. K. Osaki, S. Kimura, and M. Kurata, Relaxation of Shear and Normal Stresses in Step-Shear Deformation of a Polystyrene Solution. Comparison with the Predictions of the Doi–Edwards Theory *J. Polym. Sci., Polym. Phys. Ed.* **19**, 517–527 (1981).
130. K. Osaki and M. Kurata, Experimental Appraisal of the Doi–Edwards Theory for Polymer Rheology Based on the Data for Polystyrene Solutions *Macromolecules* **13**, 671–676 (1980).
131. K. Osaki, Y. Einaga, M. Kurata, N. Yamada, and M. Tamura, Stress Relaxation of Polymer Solutions under Large Strain: Application of Double-Step Strain *Polym. J.* **5**, 283–287 (1973).
132. K. Osaki and M. Kurata, Stress Relaxation of a Polymer Solution in Double-Step Shear Deformations: A Separate Evaluation of the Stress Components due to Entangled Segments of Different Orientations *J. Polym. Sci., Polym. Phys. Ed.* **20**, 623–632 (1982).
133. Y. Einaga, K. Osaki, M. Kurata, S. Kimura, and M. Tamura, Stress Relaxation of Polymer Solutions under Large Strain *Polym. J.* **2**, 550–552 (1971).
134. E. F. Brown and W. R. Burghardt, First and Second Normal Stress Difference Relaxation in Reversing Double-Step Strain Flows *J. Rheol.* **40**, 37–54 (1996).
135. E. F. Brown, W. R. Burghardt, H. Kahvand, and D. C. Venerus, Comparsion of Optical and Mechanical Measurements of Second Normal Stress Difference Relaxation Following Step-Strain *Rheol. Acta* **34**, 221–234 (1995).

136. K. Osaki, H. Watanabe, and T. Inoue, Damping Function of the Shear Relaxation Modulus and the Chain Retraction Process of Entangled Polymers *Macromolecules* **29**, 3611–3614 (1996).
137. M. H. Wagner and J. Schaeffer, Rubbers and Polymer Melts: Universal Aspects of Nonlinear Stress-Strain Relations *J. Rheol.* **37**, 643–661 (1993).
138. K. Osaki, S. Kimura, and M. Kurata, Relaxation of Shear and Normal Stresses in Double-Step Shear Deformations. A Test of the Doi–Edwards Theory for Polymer Rheology *J. Rheol.* **25**, 549–562 (1981).
139. Z. Bartczak, A. S. Argon, and R. E. Cohen, Deformation Mechanisms and Plastic Resistance in Single-Crystal-Textured High Density Polyethylene *Macromolecules* **25**, 5036–5053 (1992).
140. N. W. Brooks, M. Ghazali, R. A. Duckett, R. A. Unwin, and I. M. Ward, Effects of Morphology on the Yield Stress of Polyethylene *Polymer* **40**, 821–825 (1999).
141. N. W. J. Brooks, R. A. Duckett, and I. M. Ward, Modeling of Double Yield Points in Polyethylene Temperature and Strain Rate Dependence *J. Rheol.* **39**, 425–436 (1995).
142. P. A. O'Connell and G. B. McKenna, Arrhenius-type Temperature Dependence of the Segmental Relaxation below T_g *J. Chem. Phys.* **110**, 11054–11060 (1999).
143. R. S. Duran and G. B. McKenna, A Torsional Dilatometer for Volume Change Measurements on Deformed Glasses: Instrument Description and Measurements on Equilibrated Glasses *J. Rheol.* **34**, 813–839 (1990).
144. T. T. Wang, H. M. Zupko, L. A. Wyndon, and S. Matsuoka, Dimensional and Volumetric Changes in Cylindrical Rods of Polymers Subjected to a Twist Moment *Polymer* **23**, 1407–1409 (1982).
145. R. Pixa, V. LeDû, and C. Wippler, Dilatometric Study of Deformation Induced Volume Increase and Recovery in Rigid PVC *Colloid Polym. Sci.* **266**, 913–920 (1988).
146. J.-J. Pesce and G. B. McKenna, Prediction of the Sub-Yield Extension and Compression Responses of Glassy Polycarbonate from Torsional Measurements *J. Rheol.* **41**, 929–942 (1997).
147. R. A. Schapery, On the Characterization of Nonlinear Viscoelastic Materials *Polym. Eng. Sci.* **9**, 295–310 (1969).
148. R. A. Schapery, A Theory of Nonlinear Thermoviscoelasticity Based on Irreversible Thermodynamics *Proc. 5th U.S. National Congress of Applied Mechanics*, ASME, New York, 1966, pp. 511–530.
149. R. A. Schapery, Further Development of a Thermodynamic Constitutive Theory: Stress Formulation, Report AA & ES 69–72, Purdue University, Lafayette, Ind., 1969.
150. H. Leaderman, *Elastic and Creep Properties of Filamentous Materials and Other High Polymers*, The Textile Foundation, Washington, D.C., 1943.
151. G. C. Papanicolaou, S. P. Zaoutsos, and A. H. Cardon, Prediction of the Nonlinear Viscoelastic Response of Unidirectional Fiber Composites *Compos. Sci. Technol.* **59**, 1311–1319 (1999).
152. M. E. Tuttle and H. F. Brinson, Prediction of the Long-Term Creep Compliance of General Composite Laminates *Exp. Mech.* **26**, 89–109 (1986).
153. H. Poon and M. F. Ahmad, A Finite-Element Constitutive Update Scheme for Anisotropic Viscoelastic Solids Exhibiting Nonlinearity of the Schapery Type *Int. J. Numer. Methods Eng.* **46**, 2027–2041 (1999).
154. R. A. Schapery, Nonlinear Viscoelastic Solids *Int. J. Solids Struct.* **37**, 359–366 (2000).
155. B. Bernstein and A. Shokooh, The Stress Function in Viscoelasticity *J. Rheol.* **24**, 189–211 (1980).
156. A. Q. Tool, Relation Between Inelastic Deformability and Thermal Expansion of Glass in Its Annealing Range *J. Am. Ceram. Soc.* **29**, 240–253 (1946); A. Q. Tool, Viscosity and the Extraordinary Heat Effects in Glass *J. Res. Natl. Bur. Stand. (U.S.)* **37**, 73–90 (1946).

157. O. S. Narayanaswamy, A Model of Structural Relaxation in Glass *J. Am. Ceram. Soc.* **54**, 491–498 (1971).
158. C. T. Moynihan, P. B. Macedo, C. J. Montrose, P. K. Gupta, M. A. DeBolt, J. F. Dill, B. E. Dom, P. W. Drake, A. J. Esteal, P. B. Elterman, R. P. Moeller, H. Sasabe, and J. A. Wilder, Structural Relaxation in Vitreous Materials *Ann. N.Y. Acad. Sci.* **279**, 15–35 (1976).
159. A. J. Kovacs, J. J. Aklonis, J. M. Hutchinson, and A. R. Ramos, Isobaric Volume and Enthalpy Recovery of Glasses. II. A Transparent Multiparameter Model *J. Polym. Sci., Polym. Phys. Ed.* **17**, 1097–1162 (1979).
160. I. M. Hodge, Enthalpy Relaxation and Recovery in Amorphous Materials *J. Non-Cryst. Solids* **169**, 211–266 (1984).
161. R. W. Penn, *National Bureau of Standards, unpublished*.
162. J. J. Pesce and G. B. McKenna, in M. C. Boyce, ed., *Mechanics of Plastics and Plastic Composites vols. MD–68 and AMD–215, 1995*, ASME, New York, pp 309–336 1995.
163. W. G. Knauss and I. J. Emri, Nonlinear Viscoelasticity Based on Free Volume Consideration *Comput. Struct.* **13**, 123–128 (1981).
164. G. B. McKenna, On the Physics Required for the Prediction of Long Term Performance of Polymers and Their Composites *J. Res. NIST* **99**, 169–189 (1994).
165. H. Lu and W. G. Knauss, The Role of Dilatation in the Nonlinearly Viscoelastic Behavior of Pmma under Multiaxial Stress States *Mech. Time-Dependent Matls.* **2**, 307–334 (1999).
166. J. M. Caruthers, *Ph.D. Dissertations, School of Chemical Engineering*, Purdue University, Lafayette, Ind.
167. S. R. Lustig, *A Continuum Thermodynamics Theory for Transport in Polymer/Fluid Systems*, Ph.D. Dissertation, School of Chemical Engineering, Purdue University, Lafayette, Ind., 1989.
168. D. M. Colucci, *The Effect of Temperature and Deformation on the Relaxation Behavior in the Glass Transition Region*, Ph.D. Dissertation, School of Chemical Engineering, Purdue University, Lafayette, Ind., 1995.
169. D. S. McWilliams, *Study of the Effect of Thermal History on the Structural Relaxation and Thermoviscoelasticity of Amorphous Polymers*, Ph.D. Dissertation, School of Chemical Engineering, Purdue University, Lafayette, Ind., 1996.
170. S. R. Lustig, R. M. Shay, and J. M. Caruthers, Thermodynamic Constitutive Equations for Materials with Memory on a Material Time Scale *J. Rheol.* **40**, 69–106 (1996).
171. B. D. Coleman, On Thermodynamics, Strain Impulses, and Viscoelasticity *Arch. Ration. Mech. Anal.* **17**, 230–254 (1964).
172. G. Adam and J. H. Gibbs, On the Temperature Dependence of Cooperative Relaxation Properties in Glass Forming Liquids *J. Chem. Phys.* **43**, 139–146 (1965).
173. J. M. Caruthers, *Purdue University and D. B. Adolf and R. S. Chambers of Sandia National Laboratories, unpublished*.
174. E. M. Arruda and M. C. Boyce, Evolution of Plastic Anisotropy in Amorphous Polymers during Finite Straining *Int. J. Plast.* **9**, 697 (1993).
175. C. G'Sell and J. J. Jonas, Yield and Transient Effects During the plastic Deformation of Solid Polymers *J. Mater. Sci.* **16**, 1956–1974 (1981); C. G'Sell, H. El Baril, J. Perez, J. Y. Cavaillé and G. P. Johari, Cavaillé and G.P. Johari, Effect of Plastic Deformation on the Microstructure and Properties of Amorphous Polycarbonate *Mater. Sci. Eng., A* **110**, 223–229 (1989).
176. E. Oleynik, S. N. Rudnev, O. B. Salamatina, and V. A. Topolkaraev, Stressed Polymer Glasses-Formation, Microstructure and Properties of Local Plastic Transformations *Makromol. Chem. Macromol. Symp.* **53**, 77–80 (1992).
177. M. C. Boyce, D. M. Parks, and A. S. Argon, Large Inelastic Deformation of Glassy Polymers, Part 1: Rate-Dependent Constitute Model *Mech. Mater.* **7**, 15–33 (1988).

178. T. A. Tervoort, E. T. J. Klompen, and L. E. Govaert, A Multi-Mode Approach to Finite, Three Dimensional, Nonlinear Viscoelastic Behavior of Polymer Glasses *J. Rheol.* **40**, 779–797 (1996).
179. A. I. Leonov, Nonequilibrium thermodynamics and rheology of viscoelastic polymer media *Rheol. Acta* **15**, 85–98 (1976).
180. E. Krempl and K. Ho, in R. A. Schapery, ed., An Overstress Model for Solid Polymer Deformation-Behavior Applied to Nylon-66 in *Time Dependent and Nonlinear Effects in Polymers and Composites*, ASTM STP-**1357**, W Conshohocken: American Society Testing and Materials (Series: American Society for Testing and Materials Special Technical Publication, Vol **1357**) 2000, pp. 118–137.
181. W. K. Waldron and A. S. Wineman, Shear and Normal Stress Effects in Finite Circular Shear of a Compressible Non-linear Viscoelastic Solid *Int. J. Nonlinear Mech.* **31**, 345–369 (1996).
182. K. S. Cho and S. Y. Kim, A Thermodynamic theory on the Nonlinear Viscoelasticity of Glassy Polymers, 1. Constitutive Equation *Macromol. Theory Simul.* **9**, 328–335 (2000).
183. Z. P. Bazant and C. Huet, Thermodynamic Functions for Ageing Viscoelasticity: Integral Form without Internal Variables **36**, 3993–4016 (1999).
184. A. Drozdov, On Constitutive Laws for Aging Viscoelastic Materials at Finite Strains *Eur. J. Mech. A—Solids* **12**, 305–324 (1993).

GREGORY B. MCKENNA
Texas Tech University

W

WATER-SOLUBLE POLYMERS

Introduction

Water-soluble macromolecules represent a diverse class of polymers ranging from biopolymers that mediate life processes to synthetic polymers of immense commercial utility. In this article water-soluble polymers have been grouped into the categories biopolymers, nonionic, ionic, and associative, based on key structural features. Recently developed controlled polymerization techniques imparting important technological features to water-soluble polymers are also discussed.

General Considerations

Structure. Solution properties and ultimate performance of water-soluble polymers are determined by specific structural characteristics of the hydrated polymer chain. Primary structure depends directly on the nature of the repeating units (bond lengths, valence bond angles) effective compositions, and locations along the backbone. The polymer structure may derive from a single monomer [ie, poly(ethylene oxide) or polyacrylamide] or from multiple monomers. These units may be placed to yield random, alternating, block, graft, or more intricate architectures such as stars or dendrimers (Fig. 1). Biopolymers such as proteins and polynucleotides have multiple repeating units specifically ordered by template polymerization.

Secondary structure in water-soluble polymers is related to configuration, conformation, and intramolecular effects such as hydrogen bonding and ionic interactions. Tertiary structure involves intermolecular and water-polymer interactions; quaternary structure requires multiple chain aggregation or complexation.

A large number of functional groups (Fig. 2) can impart water solubility in copolymers. The degree of solubility is dependent on the number, position, and frequency of these moieties. Hydration relies on interaction at polar (ionic and hydrogen bonding) sites.

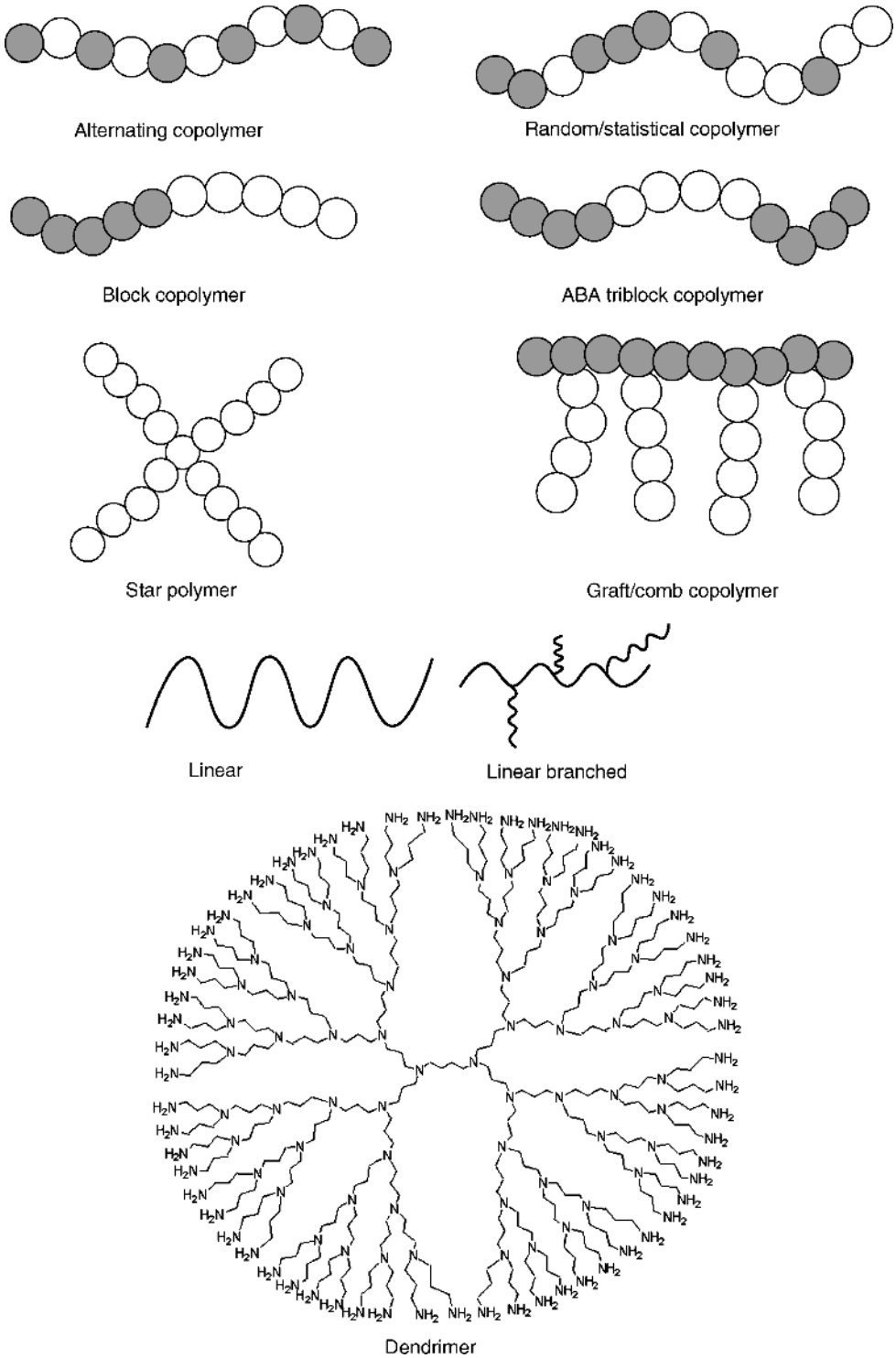

Fig. 1. Structural representation of polymer architectures (1).

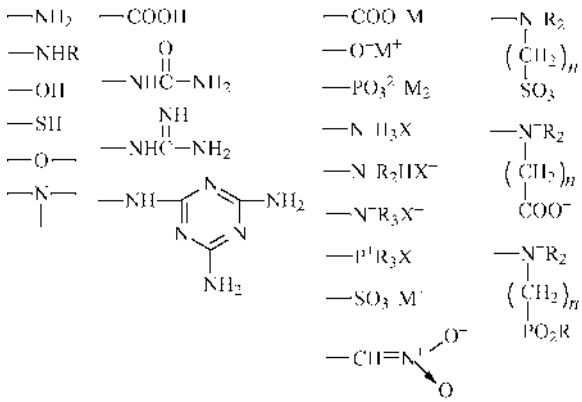

Fig. 2. Examples of functional groups imparting water solubility.

Hydrodynamic Volume. Polymers are often described in terms of hydrodynamic volume (HDV) or that volume occupied by the solvated chain. HDV and molecular shape, determined from light scattering measurements, may be used along with chemical microstructure to predict rheological behavior.

Theoretical attempts to relate dimensions of polymers to chemical structure were pioneered by Flory (2). Statistical macromolecular size in solution can be modeled from first principles by considering the number and length of bonds along with valence bond angles and conformational restrictions. Excluded volume, segmental interactions, specific intramolecular interactions, and chain solvation contribute to dimensions.

Ionic interactions (repulsive or attractive) can also dramatically affect HDV. For charged polymers, ionic effects often dominate behavior, especially in aqueous solutions. Theoretical treatments for predicting polyelectrolyte dimensions and phase behavior are discussed by Barrat and Joanny (3); scaling theory for charged polymers is reviewed by Dobrynin, Colby, and Rubinstein (4).

A number of synthetic strategies may be employed to increase macromolecular coil size (HDV) for water-soluble polymers. Monomers with water-soluble moieties may be polymerized to high molecular weight. Effective bond lengths along the backbone may be increased by introducing chain stiffening-elements. These include covalent rings (polysaccharides), charge–charge repulsions (polyelectrolytes), and helical segments (nucleic acids and proteins). The shape of the solvated coil is determined by placement of charged groups, hydrophobic moieties, hydrogen bonds, chiral centers, or restrictive rings along the molecular backbone. The native shapes of globular proteins, for example, are a result of water-induced organization of strategically placed hydrophilic and hydrophobic moieties.

Polymers dissolved in water can have structures (Fig. 3) ranging from random coils to microheterogeneous polymeric vesicles. Solution behaviors of the various types are quite diverse. Water-soluble random and extended coil polymers are often used for rheology control in various applications. Extended rods in aqueous solution may exhibit lyotropic liquid crystalline behavior. Amphiphilic molecules such as hypercoils, polymeric micelles, and vesicles are used in formulation, drug delivery, and phase-transfer catalysis.

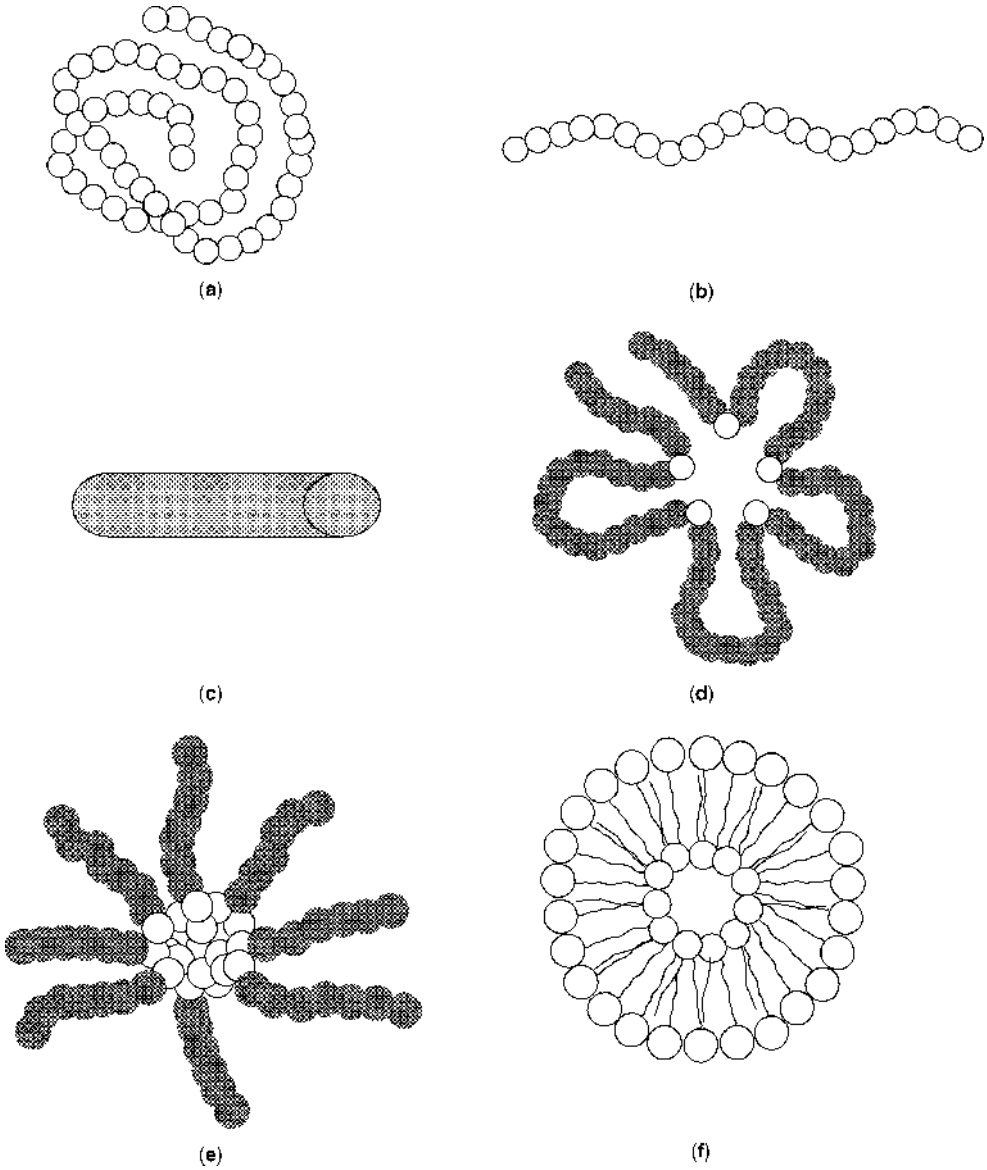

Fig. 3. Structural dependence of molecular shapes of copolymers in aqueous media. (**a**) Hydrated random coil; (**b**) hydrated extended coil; (**c**) rod-like polymer; (**d**) unimeric micelle; (**e**) multimeric micelle; (**f**) vesicle.

Role of Water in Solvation/Phase Behavior. Water plays an extremely important role in determining the properties and ultimate utility of polymers in solution. Solvation of polymer chains may involve simple interaction of ionic, polar, or hydrogen-bonded hydrophilic segments of linear chains with water (Figs. 3**a** and 3**b**) or more complex solvation of amphiphilic structures (Figs. 3**d**, 3**e**, and 3**f**). For amphiphilic polymers, water structure around the hydrophobic portion of

the chain is thought to be more ordered than in the bulk whereas hydrophilic portions disorder water structure. Amphiphilic macromolecules, including stimuli-responsive copolymers, have been studied in great detail and are the subject of several books and reviews (5–7). Although the precise nature of water structuring is the subject of continuing debate and extensive research, polymer solubility and phase behavior is rationalized in terms of entropy- or enthalpy-dominated events.

Some polymers such as poly(acrylic acid) or polyacrylamide precipitate from aqueous solutions when cooled (normal solubility behavior) whereas others such as poly(ethylene oxide), poly(propylene oxide), or poly(methacrylic acid) phase separate when heated (inverse solubility behavior). Solution turbidimetry is often used to obtain plots of phase-separation temperatures termed *cloud point* vs concentration for fixed solvent conditions. Changes in ionic strength, molecular weight, and addition of co-solvents or structure breakers affect the shapes of phase behavior curves. The important conclusion of such studies is that the total free energy of the polymer and water must be considered to predict phase behavior. The structure and dynamics of water surrounding polynucleotides, proteins, polysaccharides, and lipids are also major determinants of biological activity (8–10).

Viscosity and Rheology. Viscosity yields important information as to the disposition of the polymer chains in solution and is routinely used to evaluate polymers for particular applications. Dilute solution measurements can yield intrinsic viscosity $[\eta]$, which is a direct indication of the hydrodynamic volume of an isolated polymer chain. This fundamental parameter is related to molecular weight M through the Mark–Houwink–Sakurada (MHS) relationship (eq. 1):

$$[\eta] = KM^a \tag{1}$$

The parameters K and a are characteristics of a polymer chain under specific conditions of solvency and temperature. Values of a can be related to chain extension in dilute solution.

Flexible polyelectrolytes generally are more extended than nonionic polymers owing to charge–charge repulsions along the chain, particularly at low ionic strength. Estimates of $[\eta]$ under such conditions are made by the Fuoss (11) relationship (eq. 2) rather than the traditional Huggins relationship (eq. 3). η_{sp} is the specific viscosity, c is polymer concentration, B and k are characteristic constants. Alternatively, small-molecule electrolytes may be added in sufficient quantity to suppress the charge–charge interactions and equation 3 may then be used.

$$\frac{\eta_{sp}}{c} = [\eta]/(1 + B\sqrt{c}) \tag{2}$$

$$\frac{\eta_{sp}}{c} = [\eta] + kc \tag{3}$$

The MHS relationship (eq. 1) is often used in conjunction with experimentally determined values of molecular weight and intrinsic viscosity to determine

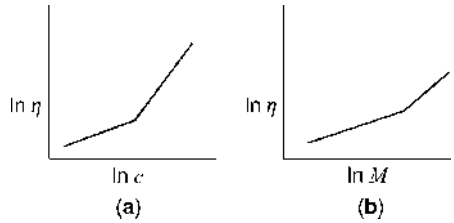

Fig. 4. Relationship between apparent viscosity and (**a**) concentration at constant molecular weight; (**b**) molecular weight at constant concentration.

chain stiffness indicated by values of a. Values can range from 0.5 for random coils in theta conditions to nearly 2.0 for extended rods.

In semidilute and concentrated solutions, polymer molecules are no longer isolated from one another. Chain–chain interactions at and above a critical concentration c^*, often termed the *overlap concentration*, lead to increased values of apparent viscosity η. Apparent viscosity can be related to concentration and molecular weight by equation 4, in which b and d are scaling constants.

$$\eta \propto c^b M^d \tag{4}$$

Usually plots of ln η vs ln c at constant molecular weight (Fig. 4**a**) or ln η vs ln M at constant concentration (Fig. 4**b**) are used to measure entanglement onset. Measurements are made at constant shear rate, temperature, and solvent conditions.

Rheological characteristics of aqueous solutions are dictated by molecular structure, solvation, and by inter- and intrachain associations. In many cases, segmental interactions must be accounted for in more rigorous terms than simple statistical encounters. Enthalpic interactions or entropically driven hydrophobic associations must be considered.

Rheological behavior is dependent on polymer type and can be clearly illustrated, providing appropriate interactive parameters of polymer concentration, ionic strength, pH, shear rate or shear stress, temperature, and time are taken into account. Representative plots are shown in Figure 5 for major behavioral patterns. Figure 5**a** illustrates the shear thickening (dilatant), Newtonian, and shear thinning (pseudoplastic) behavior. Figure 5**b** represents time dependence on viscosity for rheopetic and thixotropic polymers. Figure 5**c** illustrates the viscosity-concentration dependence in water for a polyelectrolyte and nonionic polymer in dilute solution.

Synthetic Methods. Water-soluble copolymers are prepared by step-growth or chain-growth mechanisms. Linear or branched systems may be formed from single monomers or from multiple monomers. Distribution of monomers, along the backbone or side chain, can be controlled in a number of ways. In nearly all cases, sequence selection is obtained by carefully controlling monomer reactivity, concentration, addition order, and reaction conditions. Most chain-growth, water-soluble polymers are prepared by classical free radical polymerization techniques.

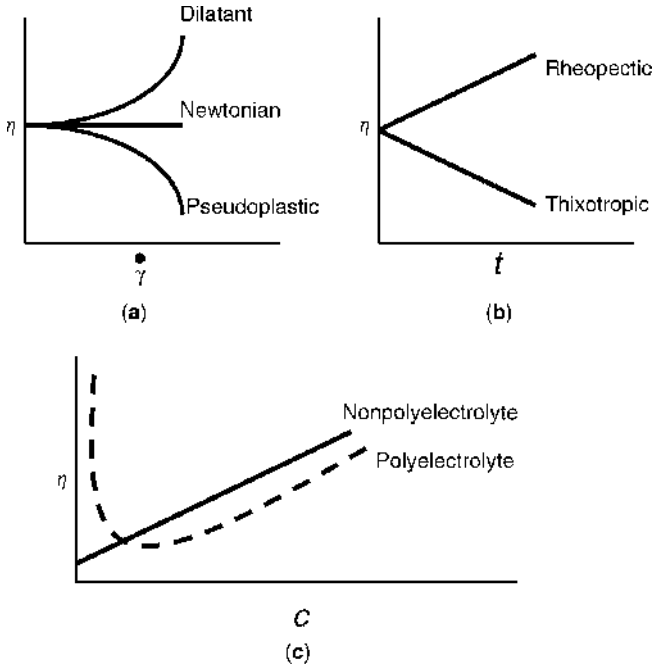

Fig. 5. Rheological characteristics of water-soluble polymers. All variables other than those on the axes are held constant. (**a**) Viscosity vs shear rate; (**b**) viscosity vs time; (**c**) viscosity vs concentrations below c^*.

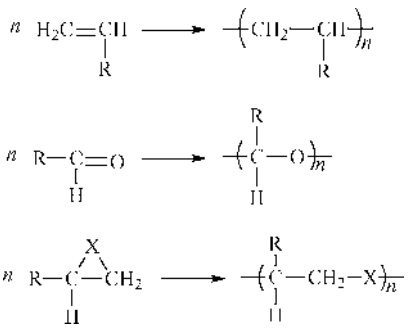

Fig. 6. Synthetic pathways to common water-soluble chain growth polymers.

Step-growth condensation reactions may be carried out in organic solvents, interfacially, in bulk, microheterogeneously, or on a solid support. Active esters are often employed in solution methods at relatively low temperatures to yield water-soluble polyesters or polyamides. Synthetic polypeptides, polynucleotides, and polysaccharides are commonly made by sequential addition of protected monomer units onto polymer supports.

Major commercial synthetic water-soluble polymers are made by chain-growth polymerization of functionalized alkenes, carbonyl monomers, or strained ring compounds, as illustrated in Figure 6. These may be initiated utilizing

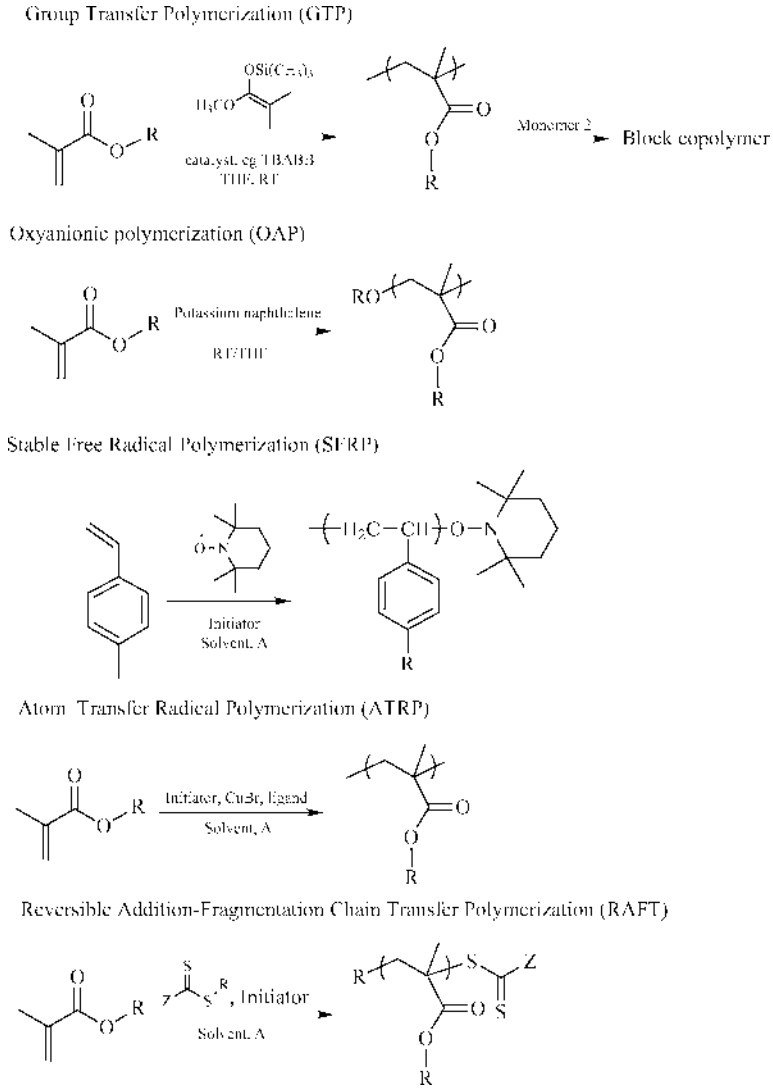

Fig. 7. Controlled or controlled/living polymerization techniques potentially applicable to synthesis of water-soluble or amphiphilic copolymers.

free radical, cationic, anionic or coordinated cationic initiators, depending on monomer structure. Of particular *commercial* interest are syntheses of water-soluble polymers in solutions, dispersions, suspensions, or emulsions. In cases where hydrophobic monomers are to be incorporated with hydrophilic species, microemulsions, or micellar polymerization methodologies are required.

During the last 10–20 years significant advances have occurred in polymer synthesis. Noteworthy is the development of less demanding living polymerization techniques, such as group transfer polymerization (GTP) (12,13) and oxyanionic polymerization (14,15). Most recently, rapid technological advances have been made in the so-called controlled/living free radical polymerizations

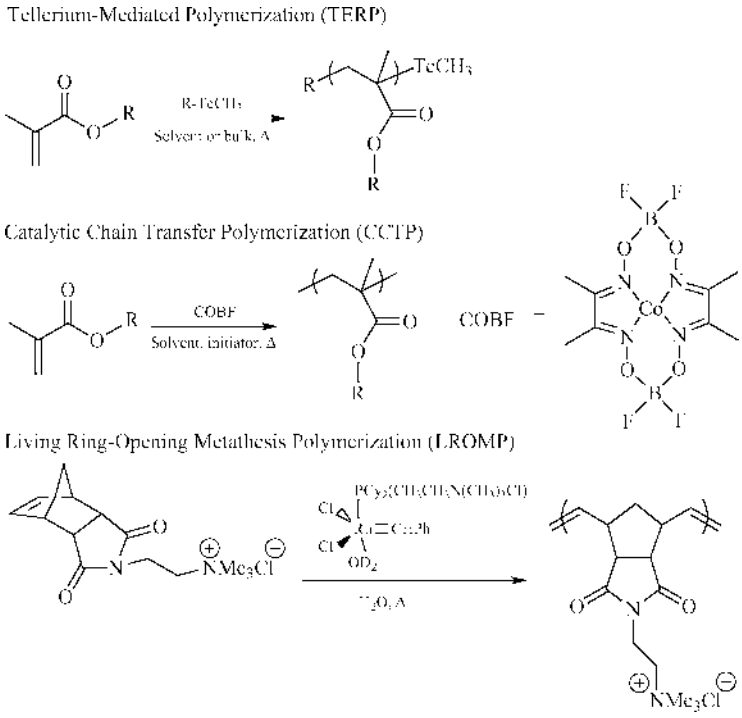

Fig. 7. (Continued.)

(CLRP), such as stable free radical polymerization (SFRP) (16,17), atom transfer radical polymerization (ATRP) (18–23), reversible addition-fragmentation chain transfer (RAFT) polymerization (24–27), and tellerium-mediated radical polymerization (TERP) (28–31). Additionally, catalytic chain transfer polymerization (CCTP) (32,33) and living ring-opening metathesis polymerization (LROMP) (34–37) have also been developed. All of these techniques, to some greater or lesser degree, have been employed for the synthesis of novel water-soluble (co)polymers (Fig. 7) with much of the research having been conducted in academic research laboratories (see ANIONIC POLYMERIZATION; LIVING RADICAL POLYMERIZATION).

Whereas each of these techniques has its merits, many have severe limitations either with respect to monomer choice or reaction conditions. The most versatile of the above techniques are arguably the CLRP techniques and have received the greatest attention, to date, with respect to the preparation of novel water-soluble (co)polymers (38,39). These techniques generally exhibit the versatility associated with conventional free radical polymerizations but simultaneously bear many of the characteristics associated with living polymerizations. They are highly tolerant of functional substituents with virtually all vinylic monomers being polymerized by one, or more, of the techniques; additionally, polymerization may be conducted under a wide range of conditions (bulk, solution, dispersion, emulsion etc). Also, molecular weights can be tuned via the monomer/initiator ratio; (co)polymers with narrow molecular weight distributions are typically produced and materials with complex architectures, such as

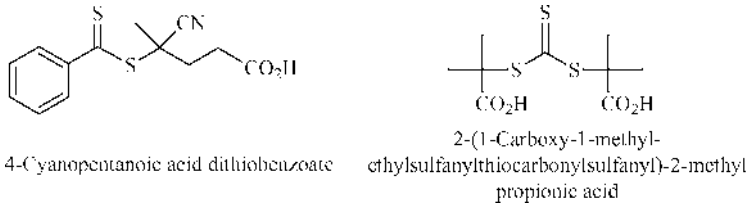

Fig. 8. Structures of chain transfer agents CTP and CTSP.

blocks or stars, can be obtained (40,41). With specific reference to the preparation of water-soluble polymers, ATRP and RAFT have been the most widely examined, with RAFT being the most versatile, at least with respect to monomer choice. For example, certain species such charged (meth)acrylamido monomers can, at present, *only* be polymerized in a controlled fashion by RAFT (42–45). Key to control in RAFT polymerizations is an appropriate thiocarbonylthio compound, called a chain transfer agent (CTA). While many have proven to be effective, such as the dithioesters, trithiocarbonates, xanthates, and dithiocarbamates (38,46,47), to conduct the polymerizations directly in water requires the use of a suitable water-soluble CTA. Of those reported to date, 4-cyanopentanoic acid dithiobenzoate (CTP) has proven to be the most generally effective (46–48), with others such as 2-(1-carboxy-1-methylethylsulfanylthiocarbonylsulfanyl)-2-methylpropionic acid (CTSP) (Fig. 8) also proving particularly effective for acrylamido and methacrylamido monomers (49,50).

Naturally Occurring Polymers

A large number of water-soluble polymers are derived from biological sources. Termed *biopolymers*, this class includes polynucleotides (qv), polypeptides and polysaccharides (qv). Because these polymers perform special biological functions, they have specific microstructures and are often perfectly monodisperse. In the following section the general structural features of major biopolymer types will be reviewed as related to water solubility.

Polynucleotides.

Structure. Nucleic acids (Fig. 9) are biopolymers that carry genetic information involved in the processes of replication and protein synthesis. The primary structural units of the nucleic acids, the mononucleotides, are composed of a 5-carbon cyclic sugar with a phosphate ester at the C-5 carbon. A heterocyclic amine base (purine or pyrimidine) is attached at C-1. RNA and DNA are terpolymers with sugar phosphate backbones (3′ and 5′ position) and pendent bases on the 1′ position. Deoxyribonucleic acids (DNAs) contain the deoxyribose sugar (no hydroxyl group at the 2′ position on the sugar ring). The usual bases substituted at the 1′ position are adenine (A), guanine (G), thymine (T), and cytosine (C). Ribonucleic acids contain a ribose sugar and the principal bases A, G, C, and uracil (U).

Studies of the structure of DNA by a large number of investigators led to the proposal by Watson and Crick (51) of the classic DNA double helix. Major

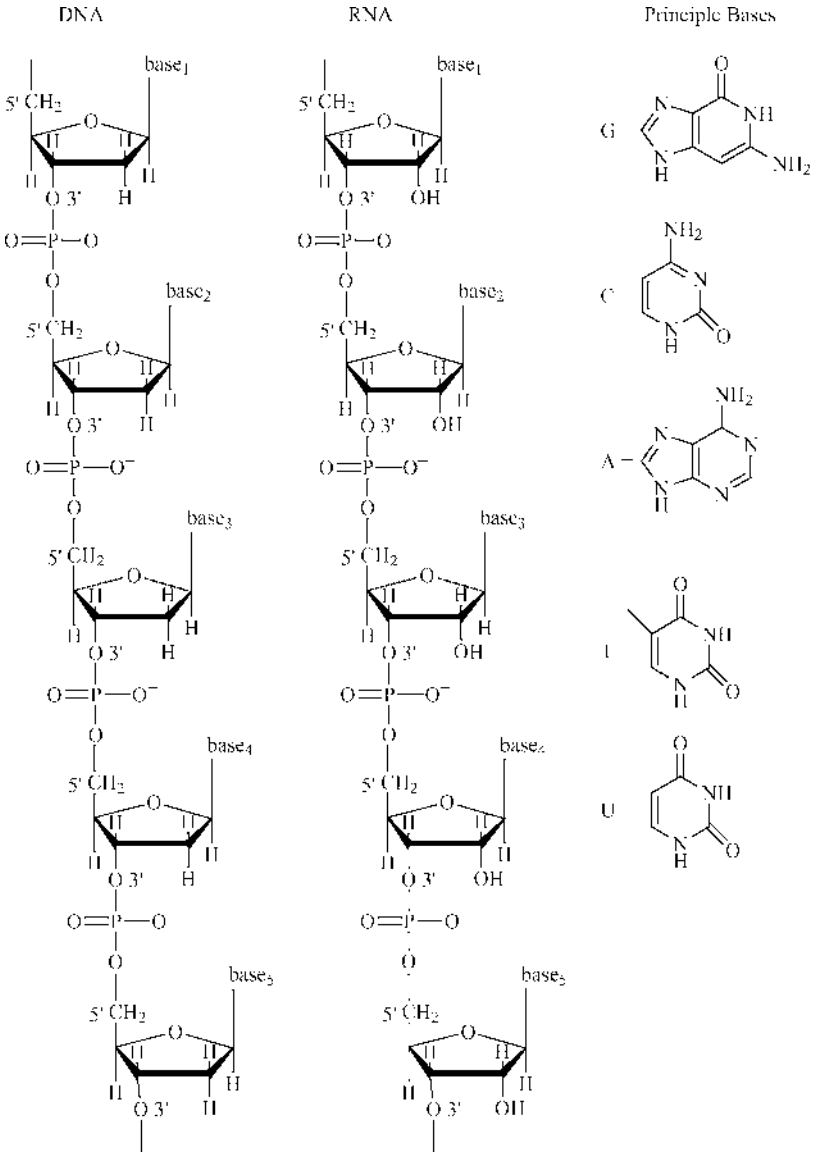

Fig. 9. Structural representations of DNA and RNA; principal bases present in nucleic acid. U,T, and C are the pyrimidines; A and G are the purines.

contributions as to base content and of X-ray structure were made by the groups of Chargaff (52) and Wilkins and co-workers (53). This proposal not only allowed explanation of DNA stability but also provided a framework for postulation of template polymerization during the replication and transcription processes.

The template synthetic process allows organization of the DNA helix into an assembly having two antiparallel strands of DNA (Fig. 10). The pendent bases on the strands are paired in such a manner that A is always paired with T and G with C. The strong hydrogen bonding of the complimentary pairs in hydrophobic

Fig. 10. DNA double-stranded helix (54).

regions orients the hydrophilic-charged phosphate groups outwardly. One negative charge per phosphate unit gives the DNA polyanionic character. The balance of hydrophilic and hydrophobic forces and the presence of divalent ions such as Mg^{2+} are also responsible for chain stability under physiological conditions. Three conformational variations of the double helix have been confirmed by X-ray diffraction—the A, B, and Z forms. Conformational variation, location of certain base-paired sequences, and specific modification (methylation for example) can lead to supercoiling, branching, and direct binding to other polynucleotides or to specific proteins. Such structural organization has major implications in gene regulation (transcription, silencing, etc).

The molecular weights of DNA, depending on the source, can be extremely large. For example, the recently sequenced human genome has been reported to have over 27,000 genes and 3 billion base pairs (55). By contrast, a simple bacterium such as *Escherichia coli* has 5 million (54) chromosomal base pairs. In addition, the latter contains cyclic DNA, called plasmids, which contain from 1000 to 10,000 base pairs. Recombinant DNA technology is routinely utilized to insert synthetic genes or genes from other species into such plasmids. The resultant recombinant DNA segments then serve as templates for synthesis of specific proteins with pharmacological, agricultural, or materials applications.

Ribonucleic acids are synthesized from the DNA template through transcription. The mononucleotides contain ribose. Unlike DNAs, RNAs are single stranded, although twisting may occur in a complementary fashion matching base pairs. RNAs are much lower in molecular weight than DNAs. The three major types—messenger RNA (mRNA), transfer RNA (tRNA), and ribosomal RNA (rRNA)—are involved in a multistep process of protein synthesis (56,57).

Beyond their well-established roles in protein synthesis, RNAs termed *ribozymes* have been shown to catalyze a number of biochemical reactions. Significantly, short hairpin sequences of RNA can hybridize with DNA to suppress (silence) gene expression (58). Alternatively, some of these short RNA sequences bind in a complementary fashion to mRNA resulting in destruction of the latter and preventing protein translation from that gene segment (58).

Synthesis. Recently, nucleic acids have been synthesized from mononucleotides, some with altered or substituted bases. Synthetic methods, along with nucleic acid sequencing methods, have allowed rapid advancement in identifying gene sequences responsible for specific protein synthesis. Kornberg and coworkers first prepared synthetic DNAs polymerized from mononucleotides using isolated enzymes, DNA polymerases (59). Likewise, RNA polymerases have been found for synthesis of oligomeric RNAs (60). DNA also can be made from RNA using reverse transcriptase enzymes. The resulting complementary DNA can be greatly amplified using the polymerase chain reaction process (PCR) (61). These are readily characterized and in many instances introduced into plasmids or other vectors for recombinant protein synthesis. Automated synthesis of single-stranded polynucleotides can be accomplished utilizing sequential protection/deprotection chemistry (62). Although entirely synthetic methods are quite slow compared to biosynthesis, designed oligonucleotides for targeting or diagnostic purposes (including micro arrays with variable sequences for rapid screening) can be readily produced. Post-reaction chemistry including ligation and PCR can then be utilized to produce significant quantities of desired oligonucleotides.

Polypeptides and Proteins. Most polypeptides and proteins are water-soluble or water-swellable. Enzymes are proteins that catalyze all chemical reactions of biological origin. Enzyme functions include oxygen transport, muscle movement, nerve response, nutrient digestion and storage, hormonal regulation, gene expression, and protein synthesis (63).

Structure. Despite the large number of functions, all proteins are similar with repeating structures along the backbone chosen from 20 amino acid monomers (Fig. 11). These polymers, the structures of which are assembled from a template coded by mRNA, are monodisperse. Each protein has a unique sequence and molecular weight. The 20 amino acids, capable of appearing in various microstructural combinations, sequence lengths, and total molecular lengths, allow assembly of a nearly unlimited number of distinct proteins with specific physical properties and behavioral characteristics.

Primary structure (covalent bond lengths and bond angles) is determined by the microstructure of the amino acid repeating units along the chain. Numerous procedures, including sequential degradation, gel electrophoresis, dye binding, and immunoassays, have been used to determine sequences (63).

Secondary structure of proteins is determined by configuration and conformation along the backbone of the polymer. The resistance to bond rotation of the C—N bond of the peptide unit, the configuration about the chiral carbon, and conformational restrictions to rotation by short-range charge–charge interactions or intramolecular hydrogen bonding play major roles in secondary structure.

The three-dimensional structure, or tertiary structure, depends strongly on primary and secondary structure with the added elements of long-range intramolecular hydrogen bonding, polar and ionic effects, and chain solvation. An

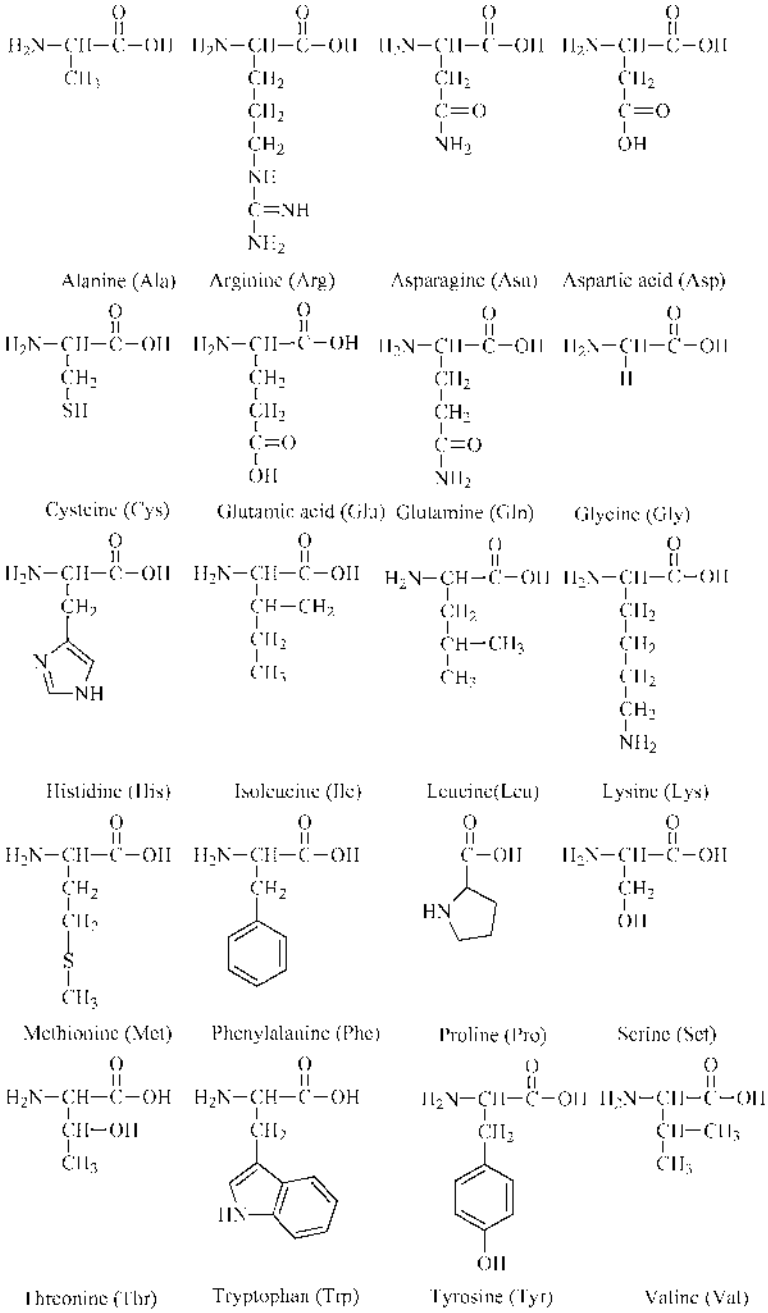

Fig. 11. Chemical structures of the 20 amino acids.

example of the three-dimensional structure of myoglobin is shown in Figure 12. The compact structure illustrates the hydrophobic interior, helical features from intramolecular hydrogen bonding and the L-amino acids, and polar external groups for hydration.

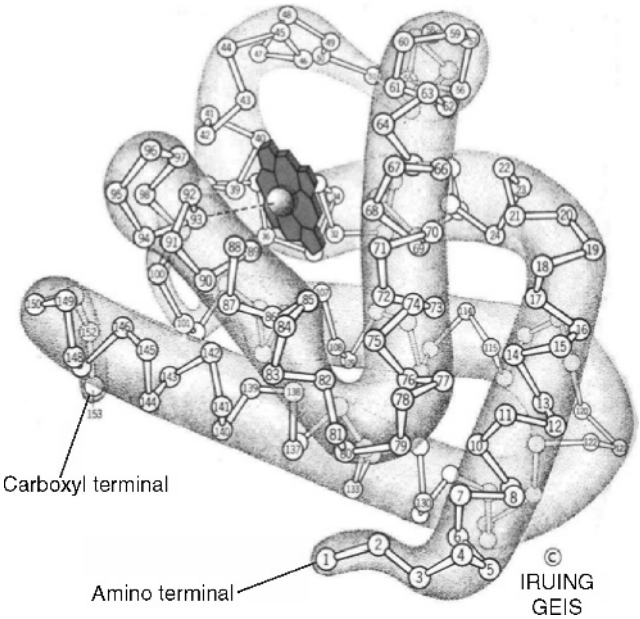

Fig. 12. Tertiary structure of myoglobin (64).

Many proteins exist in subunits of a composite structure. The organization of these subunits is termed the *quaternary structure* and is particularly important in enzyme-mediated reactions. The tertiary and quaternary structure of native protein in water can be disrupted by addition of electrolytes, alkali solutions, urea, or detergents, and by increasing temperature. The properties change markedly; eg, enzyme activity is often lost. In most cases this denaturation is not reversible. The solubilities of proteins vary considerably based on composition and conditions of ionic strength, pH, and concentration. Those with the highest density of polar groups or electrolyte character are most soluble. Therefore, solubility in water is lowest at the isoelectric point and increases with increasing basicity or acidity. A review of enzyme activity as related to protein structure is given by Fersht (65).

Protein Synthesis. Protein biosynthesis is complex, involving more than 300 macromolecules (63). Five stages can be identified involving (*1*) activation of amino acid monomers and transfer to ribosomes, (*2*) initiation of polymerization, (*3*) propagation, (*4*) termination and release, and (*5*) folding and processing. Ordering of the monomers is dictated by operation of the triplet code in which a sequence of three consecutive nucleotide units on mRNA positions a specific amino acid for polymerization.

Synthetic polypeptides can be made by sequential addition of protected amino acids onto a solid support. This procedure, pioneered by Merrifield (66,67) has been used to prepare hundreds of peptides of varying sizes and functions. A review of the technique and recent modifications are found in Reference 68.

The study of genes responsible for identifiable biological products and processes (genomics) (69) and the more ambitious study of translated proteins, their isoforms, modifications and interactions (proteomics) (70) has advanced at an

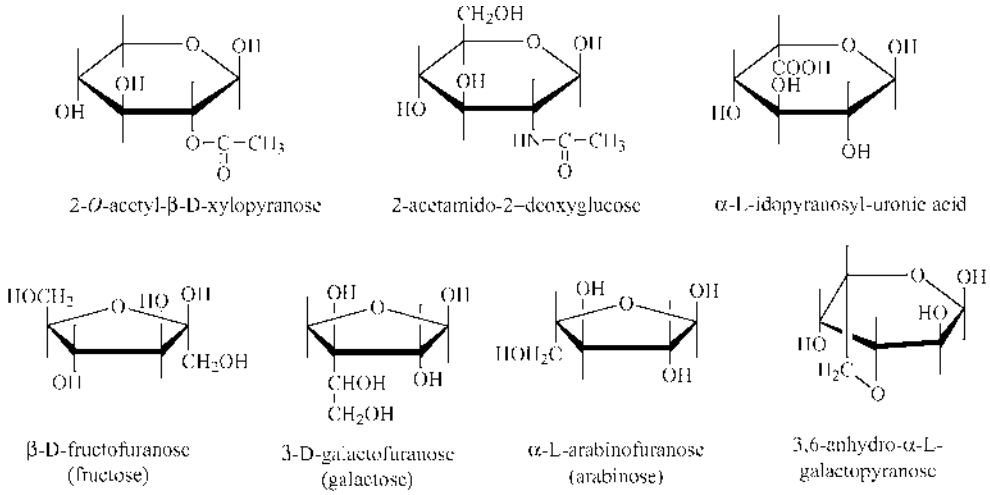

Fig. 13. Common structural units in naturally occurring polysaccharides (71).

incredibly fast pace during the last five years. In a very short time a number of genes have been targeted for recombinant expression in a variety of hosts to produce a wide range of new drugs and to develop new diagnostic markers.

Commercial Use. In addition to the rapid growth of genetically engineered enzymes and hormones for medical and agricultural applications, other water-soluble proteins are isolated from biological sources in a more traditional manner for commercial application. Enzymes are used as detergent additives, for hydrolyzing polysaccharides and proteins, to isomerize various glucose and sucrose precursors, for wine and beer making, for leather tanning, and for mineral recovery. Support-bound enzymes are becoming commercially significant for large-scale substrate conversion.

Polysaccharides

Water-soluble polysaccharides are a diverse class of biological macromolecules with a wide range of structural and behavioral characteristics. More than 100 sugars and sugar derivatives comprise the monomers available for polysaccharide synthesis (63). Covalent linkages between repeating units may occur at different ring positions; linear and branched structures with single or multiple monomers may be formed.

Industrial polysaccharides have traditionally been extracted from renewable resources in the plant and animal kingdom. Examples include starch and gums from plant seeds, pectin from fruits, and algin and carrageenan from algae. Recently, microbial sources have produced commercially useful polysaccharides such as dextran, curdlan, pullulan, xanthan, and pharmacologically active oligosaccharides.

Polysaccharides are cyclolinear or branched polymers formed by enzyme-directed step-growth condensation reactions of various activated sugar molecules (71). Some common monomer units are shown in Figure 13; other units include

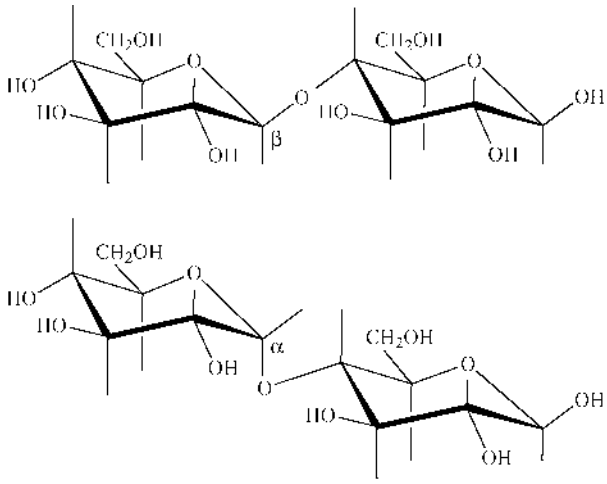

Fig. 14. Dimerization of glucopyranose units to yield α and β structures.

glycerol and other polyhydroxyalcohols, phosphate, sulfate, malonate, and pyruvate.

Aqueous solution properties, including solubility, phase behavior, and viscosity, are highly dependent on the macroscopic nature (linear, branched) of the chain as well as the chemical microstructure (polar characteristics, sequencing) of the repeating units. As with proteins, the presence of acidic or basic functionality causes pH, electrolyte, and temperature-dependent behavior. Degrees of polymerization may vary from 30 to 1×10^5. Of primary importance in the solution behavior of water-soluble polysaccharides are the configurations of asymmetric carbon atoms in the cyclic monomers and the ring conformations of the resulting covalent backbone units.

Dimerization of glycopyranose (Fig. 14) by condensation of the hydroxyl group at C-1 on one ring with C-4 on the other can lead to two isomers, depending on whether the reaction is equatorial–equatorial or axial-equatorial. The former linkage is designated β, the latter, α. Polymers formed by successive α-1 $\rightarrow$4 linkages, eg, amylose, have markedly different properties than polymers formed by successive β-1$\rightarrow$4 linkages, eg, cellulose.

Polysaccharides based on glucopyranose occur with backbones through carbons 1$\rightarrow$2, 1$\rightarrow$3, 1$\rightarrow$4, and 1$\rightarrow$6. The less-ordered structures are more water-soluble in general, with the α-1$\rightarrow$3 and the β-1$\rightarrow$6 forms exhibiting highest aqueous solubility; β structures often form strong inter- or intramolecular hydrogen bonds, making solubilization difficult.

Branched structures, especially for α linked polysaccharides, enhance solubility. Heterogeneity in types of repeating units, backbone linkages, and polar or charged functionality also imparts greater solubility. Excellent reviews of the effects of the structural conformation of monosaccharides are found in References 71 and 72.

Water-soluble polysaccharides can be classified according to structure and commercial applications. Classes include storage polysaccharides, pectins, plant gums, seed and bark mucilage, algal polysaccharides, bacterial and fungal

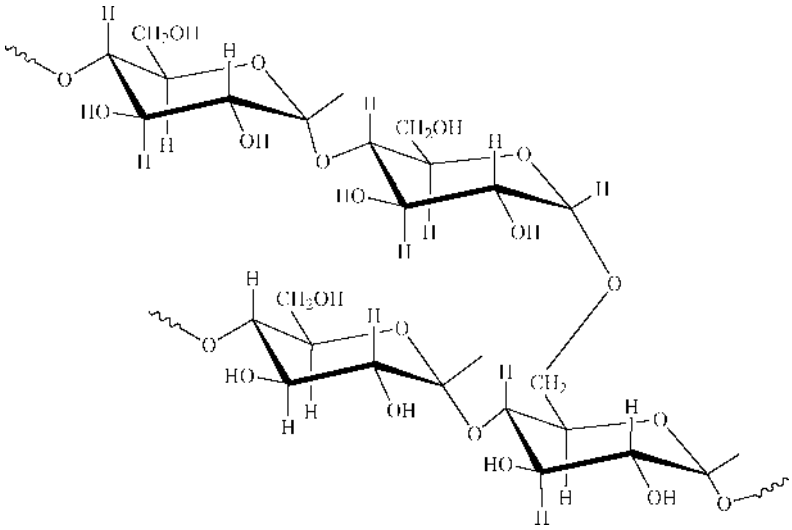

Fig. 15. Structure of amylopectin (73).

polysaccharides, mucopolysaccharides, and synthetically modified polysaccharides. For more detailed descriptions see References 72–75.

Storage Polysaccharides. *Starch and Starch Derivatives*. Amylose and amlyopectin are the major components of starch granules found in food reserves of all green plants. Commercial starch is obtained from sources such as corn, sorghum, rice, wheat, and potatoes. The compositions of the amylose and amylopectin vary with source.

Amylose is the linear polysaccharide of α-1$\rightarrow$4-D-glucopyranose having a molecular weight of $1.6 \times 10^5 - 2.6 \times 10^6$. Amylose is not water-soluble in an unmodified state but can be dispersed in water. In the solid state it is reported to exist as a left-hand six-fold helix; in solution it behaves like an extended helix (74). Shearing and heating of starch cause hydration and swelling termed *germination*. Gradually the amylose in this dispersion precipitates through association in a process called *retrogradation*.

Amylopectin (Fig. 15), the water-soluble portion of starch, is an α-1$\rightarrow$4-D-linked glucopyranose with α-1$\rightarrow$6-D-branches. Amylopectin is polydisperse with a molecular weight of $5 \times 10^7 - 4 \times 10^8$.

A number of starch derivatives (73,74) have been prepared in order to control solubility, viscosity, and phase behavior over a temperature range or under conditions of shear and added electrolytes. Major modifications include lowering molecular weight enzymatically or chemically, oxidation, forming derivatives, and cross-linking. Derivatives include starch esters, phosphates, sulfates, and ethers. Cationic, anionic, and amphoteric starches have been prepared as well as starch–graft copolymers, some with super absorbent properties.

Starch (qv) and starch derivatives have a number of applications in the food industry as viscosifiers, gelatinizers, fillers, and paste formers; in the textile and paper industries for coatings, sizing agents, rheology modifiers, and pigment binders; and in the medical area as surgical powders, absorbents, adhesives, and in pharmaceuticals.

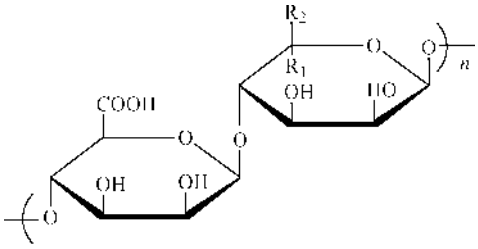

Fig. 16. Structure of β-D-mannuronic acid.

Glycogen. Glycogen is the storage polysaccharide in animals and is found in highest concentration in the liver and muscle tissues. The backbone of glycogen is α-1$\rightarrow$4-D-linked glucopyranose units with large numbers of α-1$\rightarrow$6-D-branch points.

Glucans. Algae form two types of storage polysaccharides. Starch type algal polysaccharides are α-D-glucans similar to those found in land plants, except they contain a small number of α-1$\rightarrow$3-D-linkages and are of lower molecular weight (76). Laminaran is the main carbohydrate food reserve of several green seaweeds and is a β-1$\rightarrow$3-D-linked D-glucan with β-1$\rightarrow$6-D-branches. Other sources include fungi, yeast, flagellates, and diatoms.

Laminaran has two forms distinguished by solubility in cold water. Differences are related to the degree of 1$\rightarrow$6 branching. Both are soluble in hot water and have molecular weights from 3500 to 5300. Laminaran has been used for surgical dusting powder and has been reported to have antitumor activity.

Algal Polysaccharide. *Alginic Acid*. Alginic acid represents the generic group of polymers (74) composed of D-mannuronic acid and L-guluronic acid extracted from brown algae (77). Alginic acid is not soluble in pure water, but easily dissolves in aqueous solutions of alkali metal hydroxides or carbonates. The structure (77) of alginic acid shown in Figure 16 is complicated with three types of segments: poly(β-1$\rightarrow$4-D-mannuronic acid); poly(α-1$\rightarrow$4-L-gluronic acid); and those in alternating patterns. The ionic forms of algins are polyelectrolytes with extended structures. The precise properties are determined by the structural disposition of these segments. Alginates are used as thickeners and stabilizers in the food industry, in pharmaceutical, cosmetic, and coating formulations, and as flocculants.

Sulfated Derivatives. Sulfated algal polysaccharides (78) are a class of heteropolymers with alternating α-1$\rightarrow$3-D- and β-1$\rightarrow$3-D- (carrageenan and furcellaran) or alternating α-1$\rightarrow$3-L- and β-1$\rightarrow$3-D- galactans (agar). Conformational differences have been shown between the nongelling λ carregeenan and gel-forming κ and ι forms (Fig. 17) (71). Molecular weights range from 1×10^5 to 1×10^6.

Carrageenan has diverse industrial applications including use in toothpaste, ice cream, chocolate milk, jellies, puddings, pet foods, pharmaceutical and industrial suspensions, antiulcer treatments, shampoos, creams, lotions, and oil/water and water/oil emulsions. Carrageenan reacts with denatured proteins and has been shown to exhibit properties similar to those of the animal mucopolysaccharides, such as anticoagulant activity and induction of growth of new connective tissue.

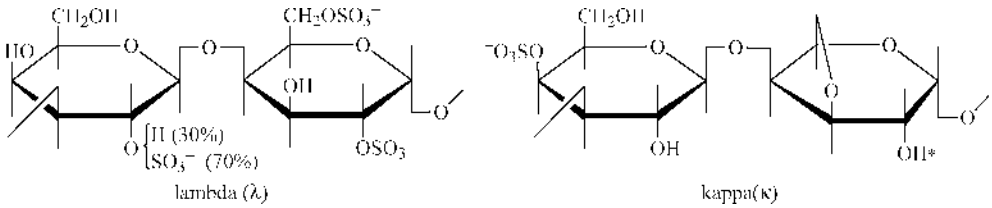

Fig. 17. λ and κ carrageenan. In ι carrageenan, OSO_3^- replaces OH* in the κ-form (72).

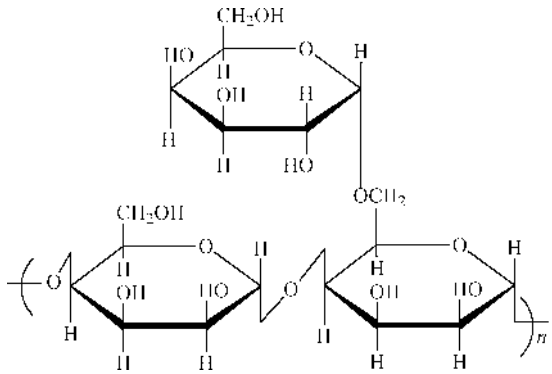

Fig. 18. Structure of guaran.

Pectins. Pectins (pectic and pectinic acids or their derivatives) are gel-forming water-soluble polysaccharides found in the primary cell walls and intercellular layers in land plants. They are found in abundance in apples, sugar beets, and the rinds of citrus fruits. Pectic acids are poly(α-D-galactopyranoslyuronic acids) with varying degrees of neutralization. Pectinic acids are also galactouronglycans but with significant quantities of methyl ester groups. Pectins are soluble in water and exhibit pseudoplastic behavior. When heated at appropriate pH, in the presence of divalent electrolytes and sugars, they form spreadable gels (74). For this reason pectins are used for making jams and jellies.

Plant Gums. Plant gums or exudate gums are formed spontaneously at sites of injury to the plant. The exudate is a viscous fluid consisting of complex, highly branched polysaccharides with residues of hexuronic acid and two or more neutral sugars. Many plant gums are used commercially as thickening agents or emulsion stabilizers. Commercially important are karaya gum, gum tragacanth, gum Arabic, and gum ghatti (76).

Seed Mucilages. Guaran is a purified polysaccharide from the guar plant seed. It is a linear chain of β-1→4-linked D-mannopyranosyl units onto which is linked an α-1→6-D-galactopyranosyl unit (Fig. 18). Molecular weights are estimated to be 2.2×10^5 (79). Guaran forms high viscosity, pseudoplastic solutions at low concentrations, is nonionic, and is little affected by electrolyte addition or pH changes. Guar easily forms gels with transition metal elements or borate ions and is therefore useful in drilling, cementing, and fracturing in oil-filed applications. It has also been used as a thickener and stabilizer in the manufacture of ice cream, cheese, pet foods, and deodorant gels.

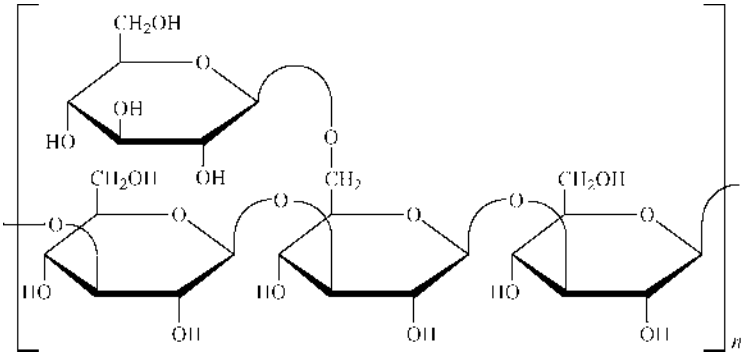

Fig. 19. Structures of scleroglucan and schizophyllan (75).

Extracellular Polysaccharides. One of the most important extracellular bacterial polysaccharides is dextran. Dextrans are high molecular weight α-1$\rightarrow$6-D-glucopyranose polymers with varying proportions of α-1$\rightarrow$4 and α-1$\rightarrow$3 branch linkages. Dextran is produced from sucrose by a number of bacteria from the family *Lactobacillaceae*. Dextran has a variety of commercial applications, including use as a plasma substitute, an anticoagulant, or in studies of cells, viruses, and proteins. Fractionated commercial dextrans are used as standards in various studies of the properties of water-soluble polymers. Dextran–graft copolymers have utility in viscosifications, superabsorbancy, and oil-field applications (80).

Bacterial and Fungal Polysaccharides. Microbes generate a large number of polysaccharides, many of which are not produced by the higher plants or animals. A large number of microbial polysaccharides are used in the food, cosmetic, and pharmaceutical industries. Particular polysaccharides, when isolated from the dried bacteria, have been shown to induce an immune response and generate antibodies in organisms exposed to them. Several of these capsular polysaccharides have been used to develop vaccines for various bacterial infections such as meningitis and typhoid fever (81).

Xanthan (qv) is an extracellular bacterial polysaccharide produced by *Xanthomonas campestris*. Xanthan is a branched polysaccharide with β-1$\rightarrow$4-D-glucopyranose units along the backbone. On every other unit the oxygen at C-3 is substituted with a trisaccharide unit. Approximately half the β-D mannose units have a pyruvic acid group linked as an acetal derivative. Molecular weight has been estimated to be 2×10^6.

The solutions are viscous as low polymer concentrations, pseudoplastics, and insensitive to salt, temperature, and pH over a wide range. Much controversy remains as to changes in the tertiary structure with changing solution conditions. Single, double, and even triple helical structures have been proposed as well as quaternary structures from side-by-side double helix dimers (72,75,82).

Other water-soluble microbial polysaccharides include the anionic polysaccharides gellan from *Pseudomonas elodea* and bacterial alginate from *Pseudomonas aeruginosa*, and the neutral polysaccharides scleroglucan, curdlan, and pullulan (72,75,76,83).

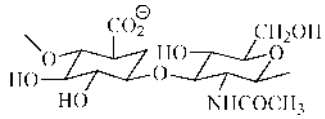

Fig. 20. Structure of hyaluronic acid.

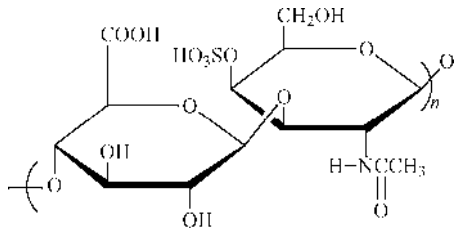

Fig. 21. Structure of chondroitin sulfate. In dermatan sulfate the —COOH group extends axially from the bottom face (77).

Scleroglucan and schizophyllan (Fig. 19) are examples of fungal polysaccharides (72,75,81,84). Their structures are identical except for the distribution of side chains along the polymer backbone. Both are rod-like macromolecules forming triple helices in aqueous solutions. They are used industrially as viscosifiers and in polymer flooding for enhanced oil recovery. They have also been shown to exhibit specific biological activity against cancers and infections.

Mucopolysaccharides of Higher Animals. Mucopolysaccharides of higher animals are generally found in the connective tissues. They form highly viscous aqueous solutions that gel readily. These polysaccharides consist of amino sugars (D-glucuronic acid or L-iduronic acid) and may have *N*-acetyl, *O*-sulfate, or *N*-sulfate groups. Their functions include induction of calcification; control of metabolites, ions, and water; and healing of wounds. Several of these polymers are under study for medical, cosmetic, and personal care applications.

Hyaluronic acid (Fig. 20) is a regularly alternating copolymer of D-glucuronic acid and 2-acetamido-2-deoxy-D-glucose (77). It is found in most connective tissues, especially in umbilical cord, vitreous tissue, joint fluid, and skin. It is synthesized by fibroblasts in the mesenchymal tissue and also by bacteria. Hyaluronic acid binds a large amount of water in the interstitial spaces and is thought to be involved with the control of permeability and thus resistance of the tissues to infection. Hyaluronic acid is involved in the wound-healing process and is produced in large amounts at the site of the wound in the days following the injury. Hyaluronic acid also serves as a lubricant in the joints. Commercially, hyaluronic acid has application in postoperative healing in eye surgery.

Chondroitin and chondroitin sulfates (Fig. 21) are found in cartilage, skin, cornea, sclera, and bone. They show high viscosity and water retention and play a role in the connective tissue similar to that of hyaluronic acid. Sulfate groups contribute additional ion-binding capacity.

Dermatan sulfate (β-heparin) is found in the skin, lungs, tendons, spleen, brain, and heart. Dermatan sulfate exhibits high water retention and acts in a way similar to the chondroitin sulfates. It is also an anticoagulant.

Heparin (85) is found in the heart, liver, lung, spleen, muscle, kidney, and blood. It is synthesized in the mast cells and has a molecular weight of

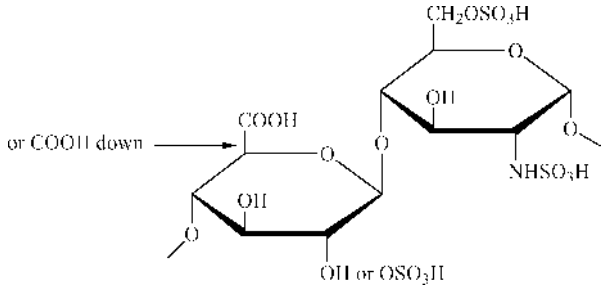

Fig. 22. Structure of heparin.

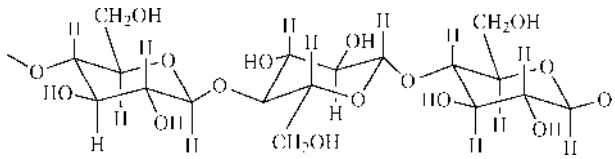

Fig. 23. Structure of cellulose.

5000–25,000. Heparin is a mixture of polysaccharide chains of varying lengths and heterogeneity. It consists of 2-acetamido-2-deoxy-α-D-glucopyranosyl, α-D-glucopyranosyluronic acid, and L-iduronic acid residues containing various proportions of *O*-sulfate, *N*-sulfate, and *N*-acetyl groups (Fig. 22). It is an anticoagulant and antilipemic agent and is widely used in cardiovascular surgery and therapy.

Synthetically Modified Polysaccharides. Water solubility can be conferred on a number of naturally occurring polysaccharides by synthetic derivations producing charged or polar functionality. Two of nature's most abundant polysaccharides, cellulose and chitin, have been synthetically modified in a multitude of ways to produce polymers with significant commercial utilization (86,87).

Cellulose Derivatives. Cellulose (qv) is a β-1$\rightarrow$4-D-anhydroglucopyranose copolymer (Fig. 23) that serves as the major structural component of plants. When the cellulose molecule is extended, it is a flat ribbon with hydroxyl groups protruding laterally and is capable of forming both intra- and intermolecular hydrogen bonds. This form allows the strong interaction with neighboring chains that makes dissolution difficult. In fact, strongly interactive solvents are necessary for solubilization. Molecular weights range from 5×10^5 to 1.5×10^6, depending on the source. Water-soluble cellulose ethers can be prepared by nucleophilic substitution, ring opening, or Michael addition mechanisms (72).

Carboxymethylcellulose (CMC) is usually prepared by the reaction of cellulose with the sodium salt of chloroacetic acid in aqueous alkaline organic slurries. The extent of substitution on C-2, C-3, and C-6 is related to the degree of disruption of hydrogen bonding, steric factors, and reaction conditions (72,87). The acid form of CMC is a polyelectrolyte with limited solubility and a pK_a of 4. The monovalent metal or ammonium salts are soluble; divalent cations result in borderline solubility; multivalent cations allow gel formation. Solutions of sodium CMC are pseudoplastic for high viscosity grades with degrees of substitution (DS) of 0.9–1.2. Solutions of less uniformly substituted, high molecular weight CMC with

low DS are thixotropic; CMC is stable over the pH range 4–10 (see CELLULOSE ETHERS).

CMC is used in sizing for textile and paper applications and as a thickener, stabilizer, suspending agent, or binder in foods, pharmaceuticals, and cosmetics. CMC is a fluid loss and rheology modifier in drilling muds.

Hydroxyethylcellulose (HEC) and hydroxypropylcellulose (HPC) are prepared by nucleophilic ring opening of ethylene oxide and propylene oxide, respectively, by the hydroxyl anions on the anhydroglucose ring of cellulose. Reactions are conducted commercially in caustic aqueous slurry processes (72). Laboratory methods recently have been reported for preparation of cellulose ethers, esters, and carbamates under homogeneous reaction conditions in organic solvents (88–91). Such solvents may lead to development of new commercial processes for cellulose derivatives with more uniform substitution.

HEC is a nonionic polymer with little surface activity in solution and is compatible with a wide range of surfactants and salts. Solutions are pseudoplastic at higher molecular weights and concentrations. Molecules behave as rigid rods in dilute aqueous solution. Commercial HEC has molar substitution (MS) between 1.8 and 3.5 degree of substitution of 0.8–1.8.

HPC is more hydrophobic than HEC owing to the presence of the methyl group on the side chain. The polymer is soluble in organic solvents but phase separates from water above 45°C. In concentrated solutions, HPC exhibits lyotropic liquid cryalline behavior (61). Commercial HPC has MS values between 3.5 and 4.5 and DS values of 2.2–2.8 (72,87).

HEC is used in coatings, cements, thickeners, pharmaceuticals, oil-well fracturing, cementing, and drilling applications, and in cosmetics, inks, paper finishes, lubricants, gels, and agricultural formulations. HPC is used for warp sizing, flocculations, wetting, thickening, binding, formulation of hair sprays, cosmetics, pharmaceuticals, and personal care items.

Methylcellulose is prepared commercially by reaction of the respective methyl chloride or dimethyl sulfate with alkali cellulose with organic slurry systems, batch methods, or continuous processes (72,87). The methyl ether derivatives have a DS range from 1.5 to 2.0, the uniformity of which depends on the heterogeneity of the reaction medium and other reaction conditions. Substitution occurs preferentially at the C-6 and C-2 positions. Methylcellulose exhibits both an upper and lower critical solution temperature as signified by gel formation on heating or cooling homogeneous solutions. Uses for methyl cellulose include gelling fluids, viscosifiers, pharmaceutical coatings, and food additives.

Hydroxypropylmethylcellulose (HPMC) is one of the many mixed ethers of cellulose. It is prepared by reactions of alkali cellulose with methyl chloride and propylene oxide in a slurry process. Reaction conditions may be varied to control compositions despite the greater reactivity of methyl chloride. HPMC is an extremely effective viscosifier compared to conventional cellulose ethers. Its microheterogeneous nature, phase behavior, and interaction with surfactants allow use in food, pharmaceutical, and coatings applications (72,87).

Cellulose sulfates and phosphates are water-soluble derivatives prepared by reactions of alcohol/water/organic diluent mixtures of sulfuric or phosphoric acids. Phosphate derivatives are flame retardant but have not been commercialized (72).

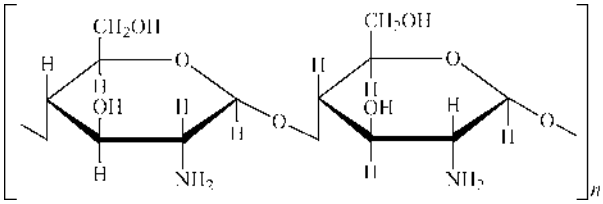

Fig. 24. Chitosan.

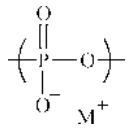

Fig. 25. Poly(phosphoric acid) salt.

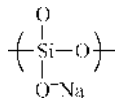

Fig. 26. Poly(silicic acid) salt.

Chitin Derivatives and Chitosan. Chitin (92) is a water-insoluble, high molecular weight polymer of 2-acetamido-2-deoxy-D-glucopyranosyl units linked through β-1$\rightarrow$4-D bonds. This most abundant skeletal material of invertebrates is recovered from shrimp, crab, or lobster waste materials. Fungi are also an important commercial source of chitin. Chitin may be converted to chitosan by partial or complete deacetylation. In the protonated form (Fig. 24), this cationic polyelectrolyte is water-soluble with a number of potential commercial uses including flocculation, viscosification, wound healing, medical dressing, pharmaceutical formulation, drug delivery, membrane technology, and animal nutrition.

Chitin can be derivatized (92–95) by reaction of the hydroxyl substituents on carbons 3 and 6 of the anhydroglucose ring. *N*-substituted derivatives at C-2 can be obtained from reactions on chitosan or partially deacetylated chitin. Hydroxyethylchitin and other water-soluble derivatives are useful wet-end additives in papermaking and flocculants for anionic waste streams (see CHITIN AND CHITOSAN).

Inorganic Water-Soluble Polymers

Poly(metaphosphoric acid) (96,97) (Fig. 25) is formed by controlled dehydration of NaH_2PO_4. The lower molecular weight sodium hexametaphosphate is available commercially. High molecular weight analogues can be prepared with various cations. The other widely abundant inorganic polymers, poly(silicic acid) (Fig. 26) and its sodium or potassium salts are highly branched, associated, high viscosity polymers. Aqueous solutions of silicates have been used as raw materials for centuries in window-glass formation and insulating-glass fibers (96).

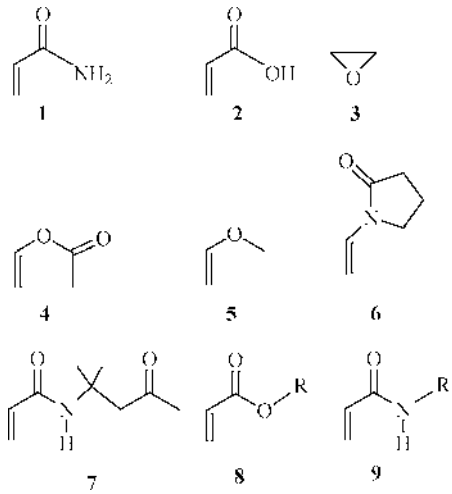

Fig. 27. Examples of uncharged monomers utilized in the synthesis of water-soluble, nonionic copolymers.

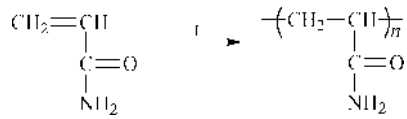

Fig. 28. Polymerization of acrylamide.

Nonionic Polymers

A number of commercially available and experimental nonionic monomers including those shown in Figure 27 have been utilized to prepare a large number of water-soluble (co)polymers. Water solubility is a result of a high concentration of polar or hydrogen-bonding functional groups on the repeating units. Major commercial polymers are based on acrylic, vinyl, oxide, or imine functionality.

Polyacrylamide. Acrylamide (AM) monomer **1** is polymerized by free-radical initiators, eg, azo compounds, redox, catalysts, light, and radiation (Fig. 28). This monomer is unique among vinyl and acrylic monomers because it can be polymerized to ultrahigh molecular weight (10^6–10^7). This extraordinary feature of acrylamide polymerization is attributed, in part, to the ease of purification of AM monomer and to the unusually high ratio of its propagation to termination rate constants (k_p/k_t). In fact, AM has the highest k_p/k_t of any free radically polymerizable monomer. Polyacrylamide (PAM) can be prepared via solution, inverse emulsion, inverse microemulsion, or precipitation techniques (98–100) (see ACRYLAMIDE POLYMERS).

Low temperature initiation, high monomer concentration, and a small amount of added 2-mercaptobenzimidazole, a radical scavenger, are reported to be the optimal reaction conditions for preparing high molecular weight, soluble polymers. High total solids concentrations usually result in intractably high solution viscosities. Inverse emulsion polymerization offers the opportunity for

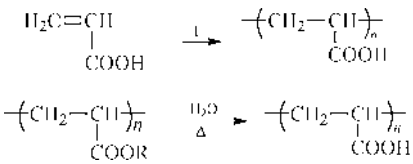

Fig. 29. Preparation of poly(acrylic acid) by direct polymerization or by hydrolysis of a polyacrylate.

lowered viscosities without compromising polymer molecular weights (101–103). Inverse microemulsion polymerization results in rates 10–200 times faster than conventional inverse emulsion systems (104). Precipitation polymerization can also be accomplished using a solvent (eg, *tert*-butyl alcohol) that dissolves the AM monomer but not the PAM (100).

Solution polymers are usually isolated by precipitation or dialysis/freeze drying. However, such solid products are hard to re-dissolve. Recently this problem was overcome by the discovery that water-in-oil (w/o) emulsions of polyacrylamide can be inverted by adding a water-soluble surfactant to produce an oil-in-water (o/w) emulsion. Thus a low HLB surfactant is used for polymerization and a high HLB surfactant is used for phase inversion (103). The resulting polymers re-dissolve easily. Inversion must be complete or polymer (activity) is lost.

AM is difficult to polymerize by any of the "controlled/living" polymerization techniques. However, McCormick and co-workers have recently made significant progress in this area by reporting the CLRP, via RAFT, of AM in both aqueous and organic media (47,49,50). To achieve "living" conditions, judicious choices must be made with respect to RAFT chain transfer agent (CTA) and polymerization conditions.

PAM has reported T_g values of 165 and 188°C. No matter which value is correct, it is clear that PAM remains glassy to relatively high temperatures. Although PAM is slow to dissolve, it is soluble in water in all proportions. However, PAM solution viscosities show a time dependence, attributed to intramolecular conformational changes (98). Because PAM can be polymerized to very high molecular weight, it is a highly efficient aqueous viscosifier. Solution viscosities of nonionic PAM are insensitive to changes in pH (between 1 and 10). Above pH = 10, it is subject to hydrolysis. Solutions of nonionic polyacrylamide are also tolerant of electrolytes (eg, NaCl). Viscosities increase with increasing molecular weights, according to equation 5.

$$[\eta] = 1.0 \times 10^{-2} M_w^{0.755} \text{ (water, 25°C)} \tag{5}$$

Polyacrylamides function as flocculating agents, in rheology control, and as adhesives.

Poly(acrylic acid). Poly(acrylic acid) (PAA) can be prepared by direct free-radical polymerization of **2** in aqueous solution (6) or by precipitation polymerization in benzene. Alcohols and mercaptans are commonly used chain-transfer agents for regulating polymer molecular weight. Alternatively, PAA can be prepared by hydrolysis of poly(alkyl acrylates) (6) (Fig. 29).

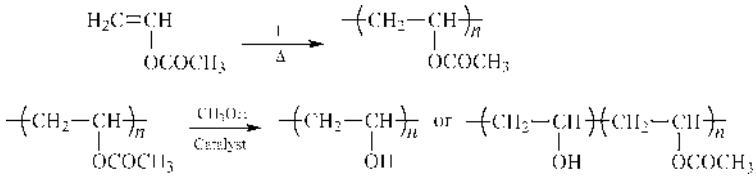

Fig. 30. Polymerization of vinyl acetate.

Both RAFT and NMP controlled/living techniques are suitable for the direct polymerization of acrylic acid. The RAFT polymerization of AA has been reported in DMF (24,105), various alcohols (106,107), water (108), and dioxane (109) employing a variety of RAFT CTAs including dithioesters, xanthates, dithiocarbamates and trithiocarbonates. AA is also susceptible to controlled polymerization by NMP (110,111).

The T_g of PAA has been variously reported as 75, 106, and 126°C, depending on the mode of measurement. However, the highest value is probably the most accurate. Solid polymers are hard, clear, brittle materials. In aqueous solutions, viscosity increases with increasing molecular weight. PAA undergoes a number of reactions in solution, ie, hydrolysis, esterification, dehydration, and complex formation with polyethers. PAA is an excellent thickener for lattices. PAA has been used in oil recovery, as a dispersant for inorganic pigments, as a flocculant, and as an adhesive.

Poly(ethylene oxide). Poly(ethylene oxide) (PEO) is prepared by ring-opening polymerization of the ethylene oxide monomer **3** (112,113). Polymers of molecular weight greater than 1×10^5 are prepared by heterogeneous catalysis (eg, alkaline earth carbonates) in low boiling aliphatic hydrocarbons. Few of the details of the commercial manufacture have been made public (see ETHYLENE OXIDE POLYMERS).

PEO is a white free-flowing powder with commercial grades from 100,000 to 5 million molecular weight (114). It has a T_m of about 65°C and a T_g of −45 to −53°C. Above the melting point it can be processed as a thermoplastic, ie molded or extruded. However, owing to its high melt viscosity, incorporation of plasticizer is often desired. PEO resins are completely soluble in water at room temperature, but show a lower critical solution temperature (LCST) near the boiling point of water. The LCST is lowered by the addition of inorganic salts according to the following order: $PO_4^{3-} > SO_4^{2-} > F^- > Cl^- > I^- > K^+ > Na^+ > Li^+$. Aqueous solutions of high molecular weight PEO show high extensional and shear viscosities and pseudoplastic rheology.

Poly(vinyl alcohol). Poly(vinyl alcohol) (PVA) is manufactured by alcoholysis/hydrolysis of poly(vinyl acetate), which is, in turn, produced by free-radical polymerization of vinyl acetate monomer **4** (114) (Fig. 30) (see VINYL ALCOHOL POLYMERS).

Polymerization of vinyl acetate monomer can be effected by bulk, solution, or emulsion techniques. The poly(vinyl acetate) formed is then dissolved in solvent (eg, CH_3OH) and alcoholized/hydrolyzed with acidic or basic catalysts. Vinyl acetate can also be polymerized in a controlled fashion via RAFT/MADIX (115). PVA is insoluble in CH_3OH and precipitates. It is isolated by filtration, washing, and drying.

Properties of PVA depend on the degree of alcoholysis/hydrolysis and polymer viscosity/molecular weight. Bulk/film properties (eg, tensile strength, tear resistance, elongation, and flexibility) of PVA increase with increasing extent of alcoholysis/hydrolysis and with increasing viscosity/molecular weight. The tensile strength is exceptional compared with other water-soluble polymers. Water solubility/sensitivity is at a maximum at 88% alcoholysis/hydrolysis. Beyond that level, polymer–polymer interactions via intramolecular H-bonding become so extreme that solvation of the polymer becomes difficult.

Other noteworthy properties of PVA are its film-forming ability, its barrier, adhesive, and emulsifier properties, and its grease, oil, and solvent resistance. PVA films and coatings do not require a curing cycle because tough films can be formed by evaporation. PVA film also has remarkable gas impermeability, forming barriers to oxygen, nitrogen, carbon dioxide, hydrogen, helium, and hydrogen sulfide. However, PVA does exhibit permeability to ammonia and water vapor. Its adhesive binding strength is attributable, in part, to its film-forming ability and its high strength. PVA has surface activity as an o/w emulsifier and/or protective colloid. Oil and solvent resistance increases with extent of hydrolysis.

Poly(vinyl alcohol) is used alone or combined with extenders, pigments, etc, in the preparation of high wet-strength adhesives for paper. It is an excellent binder for textiles and sizing agent for paper and can be used to emulsify a wide range of materials including vegetable oils, mineral oils, solvents, plastics, waxes, and resins. Its emulsifying, binding, film-forming, and thickening behaviors are useful in cosmetic formulation. PVA films can also be used for making oxygen tents.

Poly(methyl vinyl ether). Methyl vinyl ether (MVE) **5** is isomeric with PPO, but is significantly more water-soluble. Indeed, it is the methyl ether derivative of poly(vinyl alcohol). MVE is readily polymerized using carbocationic methods (116–118). This also facilitates the preparation of novel MVE-based block copolymers. Purification of homo polymers and copolymers prepared by the termination of living poly(methyl vinyl ether) (PMVE) with *n*-alcohols involves a combination of solvent removal, dialysis, and freeze drying (118).

MVE can also be polymerized under alternating free radical conditions with, for example, maleic anhydride to yield poly(9-methylvinylether-alt-maleic anhydride).

The T_g of PMVE is -34°C (119) and as such exists in a rubbery state at standard temperatures and pressures. PMVE exhibits broad solubility. Common solvents include benzene, halogenated hydrocarbons, ethanol, *n*-butanol, acetone, ethylacetate, cold water, heptane and cyclohexenes. Common nonsolvents include hexane, ethylene glycol, and dioxyl ether (119). PMVE is readily soluble in water, but like many nonionic water-soluble polymers, PMVE exhibits inverse temperature water-solubility. The cloud point varies over a broad range depending on MW. For example, low molecular weight PMVE with a D_p of 19 is reported to have a cloud point of 18°C while some commercial grades have significantly higher cloud points at ca 35°C (117).

Poly(*N*-vinylpyrrolidinone). *N*-Vinylpyrrolidinone (NVP) monomer **6** polymerizes under free-radical conditions via bulk, solution, and suspension methods (Fig. 32).

Azo initiators are preferred over persulfate initiators because the latter react with the monomer. One of the curious features of this polymerization is that

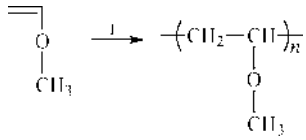

Fig. 31. Polymerization of methyl vinyl ether.

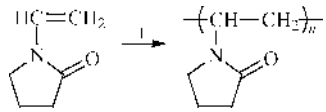

Fig. 32. Polymerization of *N*-vinylpyrrolidinone.

it has a maximum rate of polymerization in the presence of about 1 mol of water (120,121). Presumably, a specific complex forms between the monomer and a water molecule. NVP does not polymerize to particularly high molecular weight, in part because it is difficult to purify the monomer.

The T_g of PNVP is 175°C, but this value is reduced considerably by small amounts of water. Dry-cast films of PNVP are hard and transparent. However, the presence of strong intermolecular dipole–dipole interactions causes it to have a high processing temperature. Consequently, PNVP has never found acceptance for molded parts. PNVP has interesting solution properties. It is readily soluble in water and forms complexes with a wide variety of substances, eg, iodine, polyacids, phenolics. Solutions of PNVP are stable to electrolytes. Solution viscosities increase with increasing polymer molecular weight. PNVP (bulk or solution) is also characterized by high thermal or thermohydrolytic stability and chemical resistance. PNVP is also compatible with a wide range of hydrophilic and hydrophobic resins and modifiers.

PNVP has found applications in a wide variety of industries, including medicine, pharmaceuticals, cosmetics, textiles, beverages, adhesives, and paper (121,122). For example, PNVP was an early plasma and blood volume extender. It is used extensively in pharmaceutical tablets. Its complex with iodine is a germicide. It is used as a component in cosmetics, hair shampoos, and sprays and is a stabilizing agent for beer. PNVP also exhibits excellent adhesion to glass (see *N*-VINYLAMIDE POLYMERS).

Polyelectrolytes

Polyelectrolytes (qv) are polymers with charged functional groups attached along the chain. These polymers are usually classified as either polyanions (negative charges) or polycations (positive charges). Associated with the polyions are counterions or gegenions of the opposite charge in sufficient numbers to maintain electroneutrality (123).

Water-soluble polyelectrolytes exhibit a number of common traits with water-soluble nonionics. However, differences arise from the presence of charges on the macromolecular backbone and more mobile counterions electrostatically

bound to an extent determined by pK_a, solvent, and local dielectric effects. Generally, phase behavior and enhanced solubility result from increased segmental hydration and increased free energy of mixing.

The interactions between fixed charges on the polymer chain in dilute solution normally expand (repulsive) or contract (attractive) coil dimensions. Counterion binding also influences hydrodynamic volume and involves specific ion binding as well as atmospheric ion binding. Theoretical discussions of these effects can be found in References 123 and 124.

Polyelectrolytes with flexible chains and high charge density are more expanded in water than nonionic polymers, especially at low ionic strength. Determination of intrinsic viscosity is difficult in this regime (Fig. 5**c**). Electrostatic repulsions not only cause increases in hydrodynamic volume but also increases in shear sensitivity or non-Newtonian behavior.

The extent of ionization of polybases or polyacids depends on the relative base or acid strength, degree of solvation, and dielectric constant of the solvent. Poly(acrylic acid), for example, ionizes progressively in aqueous basic solution to yield a copolymer with ionized acrylate units and un-ionized acrylic acid units along the backbone; neighboring group hydrogen-bonding effects accelerate initial ionization. Eventually, however, ionization becomes more difficult owing to excessive buildup of charge along the backbone.

Polyelectrolytes have been studied extensively because molecular structures can be tailored to allow large conformational changes with pH, temperature, or added electrolytes. Molecular parameters that influence behavior include number, type, and distribution of charged repeat units on the chain, hydrophobic/hydrophilic balance, distance of charged moiety from the backbone, and counterion type. Solution properties including phase behavior, hydrodynamic volume, and binding can be altered, offering utilization in flocculation, adhesion, stabilization, compatibilization, viscosification, suspension, etc.

Anionic Polyelectrolytes. Anionic poly(acrylic acid) (PAA) can be synthesized in two ways, ie direct polymerization of **1A** (Fig. 33) or via hydrolysis of a suitable precursor polymer (6). In the direct method, salts of acrylic acid are homopolymerized or copolymerized by free-radical initiation in aqueous media. Usually the rate of polymerization of the ionic monomer is lower than the corresponding nonionic monomer, presumably owing to charge repulsion between the growing chain and the incoming ionic monomer. Direct polymerization of acrylic acid salt solutions has some commercial advantages because the nonvolatility of acrylic acid salts allows simultaneous polymerization and spray drying (or drum drying) to produce high molecular weight polymers directly. Hydrolysis (saponification) is the alternative method for producing anionic poly(acrylic acid) (Fig. 34). Hydrolysis of syndiotactic esters gives syndiotactic salt, and hydrolysis of isotactic esters gives isotactic salts.

The T_g of anionic poly(acrylic acid) [eg poly(sodium acrylate)] is substantially higher (251°C) than that of nonionic poly(acrylic acid) (102°C) because of the strong intermolecular forces due to ionomeric clustering. Physical/mechanical properties (eg, moduli) are also generally higher for salts vs free acids in the bulk phase. Atactic and syndiotactic salts of acrylic acid are water-soluble, but isotactic forms are not. Salts of poly(acrylic acid) show characteristic polyelectrolyte solution behavior (6).

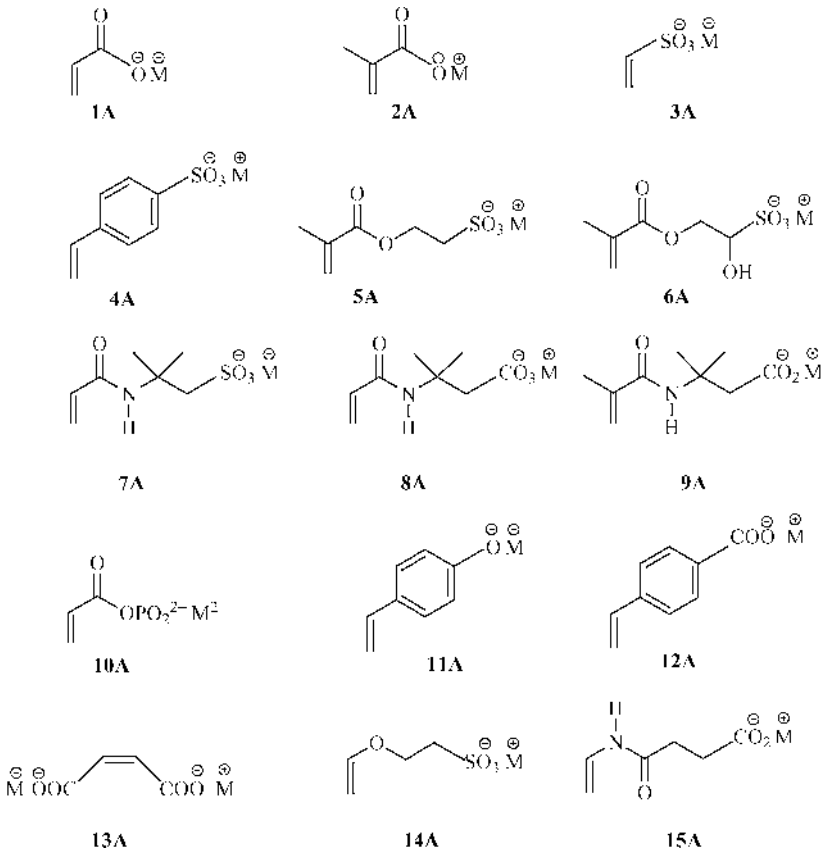

Fig. 33. Examples of monomers utilized in preparing anionic polyelectrolytes.

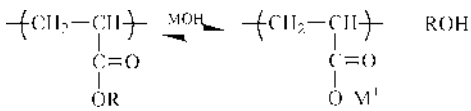

Fig. 34. Preparation of poly(acrylic acid) salts via hydrolysis of a precursors poly(alkyl acrylate).

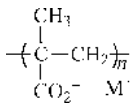

Fig. 35. Structure of poly(methacrylic acid) salt.

The applications of anionic poly(acrylic acid) include use as latex thickeners, oil-field chemicals, dispersants, and flocculants. In addition, poly(acrylic acids) containing small amounts of cross-linking agents are water-swellable polymers that have found use as superabsorbents.

Poly(methacrylic acid) and Its Salts. A wide variety of methods have been used to prepare poly(methacrylic acid) (PMAA) (6) (Fig. 35). Free-radical

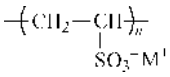

Fig. 36. Structure of poly(vinylsulfonic acid) salt.

polymerization by hydrogen peroxide, persulfate, or redox systems in aqueous solution yields atactic polymer with syndiotactic tendency. At higher pH, a higher syndiotactic content is produced. Stereoregularity can be obtained by hydrolysis of appropriate precursor polymers.

Controlled structure PMAA can be prepared by the deprotection of an appropriate precursor polymethacrylate which has itself been polymerized under living conditions. Both anionic polymerization and GTP have been used to prepare PMAA employing a variety of PMAA precursor monomers such as benzyl methacrylate (125), *tert*-butyl methacrylate (126), trimethylsilyl methacrylate (127) and 2-tetrahydropyranyl methacrylate (128,129). Removal of the protecting group yields the desired PMMA.

The sodium salt of methacrylic acid **2A** has also been polymerized directly in aqueous media via ATRP employing a PEO macro-initiator (130). Short chain, controlled structure oligomers of PMAA may also be prepared by CCTP (131).

Poly(methacrylic acid) in the nonionized form in solution has a compact conformation and low intrinsic viscosity. Upon ionization to the polyelectrolyte form, chain expansion occurs and viscosity increases. Unlike PAA, PMAA shows inverse solubility-temperature behavior. The presence of chain-stiffening methyl groups and their added hydrophobicity are responsible for the phase and viscosity behavior. Tacticity also plays an important role.

PMAA and its copolymers with acrylamide are used in viscosification and flocculation. Copolymers of MAA and its salts have been used as components of superabsorbents, coatings, adhesives, and in drilling operations.

Poly(vinylsulfonic acid) and Its Salts. Poly(vinylsulfonic acid) (PVSA) (Fig. 36) is prepared by polymerization of ethylenesulfonic acid or its sodium salt **3A** under free-radical conditions. It is purified precipitating aqueous solutions of the sodium salt form with methanol or dioxane.

The sodium and ammonium salts of PVSA are soluble in water but insoluble in organic solvents (6). The calcium salt is insoluble. Potentiometric titration studies indicate that PVSA is a strong acid that ionizes completely in water. Ion binding selectivity with alkali metals has been observed in viscosity and phase separation studies. Mark–Houwink–Sakurada (MHS) parameters of $K = 2.22$ and $\alpha = 0.65$ have been obtained for sodium PVSA in 0.5 M NaCl at 25°C.

Poly(styrenesulfonic acid) and Its Salts. Poly(styrenesulfonic acid) (PSSA) (6) (Fig. 37) may be prepared by free-radical polymerization of the monomer in solution using the free acid, sodium, or potassium salt **4A** form.

PSSA may also be prepared by sulfonation of polystyrene or by hydrolysis of poly(n-propyl p-vinylbenzenesulfonate). The latter cases allow preparation of tactic structures. Copolymers can also be prepared by free-radical copolymerization of appropriate monomers or post-reaction. Polymers are purified by precipitation of aqueous solutions with methanol, alkaline methanol, or other alcohols. Controlled structure PSSA homopolymers and block copolymers may also be prepared directly in aqueous media via RAFT using 4-cyanopentanoic acid dithiobenzoate

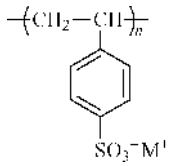

Fig. 37. Structure of poly(styrene sulfonate) salt.

as the CTA and V-501 as the radical source (48). NMP has been successfully employed in the preparation of near-monodisperse PSSA homo/copolymers. For example, PSSA homopolymer can be prepared in an ethylene glycol/water mixture (3:1 vol/vol) using TEMPO and sodium bisulfite/potassium persulfate as the redox initiating pair (132,133).

Atactic PSSA is soluble in water, methanol, and ethanol but insoluble in hydrocarbons. PSSA salts are insoluble in common organic solvents but soluble in water. Ultraviolet and fluorescence spectrometry measurements can yield information on features including local environment, neighboring groups, and tacticity. MHS values and solution properties are reviewed in Reference 56. Crosslinked PSSA has been used commercially as an ion-exchange resin and in heavy metal binding studies. Fractionated PSSA has been offered as a standard for aqueous gel-permeation chromatography.

Other Sulfonic Acids. Extensive development work has been conducted on acrylic sulfonate-containing monomers. 2-Sulfoethyl methacrylate (SEM) monomer **5A** has proved to be of limited commercial value owing to the hydrolytic instability of the ester linkage. However, recently well-defined homopolymers of 3-sulfopropyl methacrylate (SPMA) were prepared under aqueous RAFT conditions with 4-cyanopentanoic acid dithiobenzoate and V-501 as the CTA/initiator pair at 70°C (39). This same hydrolytic instability has been a serious problem with 3-sulfo-2-hydroxypropyl methacrylate. In contrast, 2-acrylamido-2-methylpropanesulfonic acid (AMPSA) **6A**, prepared by the reactions of SO_3 with isobutylene followed by the Ritter reaction with acrylonitrile (134), is quite hydrolytically stable.

AMPS or 2-acrylamido-2-methyl propanesulfonate **7A** is highly reactive in both homo- and copolymerizations and can be incorporated by homogeneous, solution, or emulsion polymerization techniques. With advances in CLRP, acrylamido monomers such as AMPS (specifically in its Na+ form) are now easily polymerized in a controlled manner, as homopolymers, statistical copolymers, or block copolymers. Indeed PAMPS and its copolymers may be prepared under facile conditions via RAFT, directly in water employing CTP and V-501 as the CTA/initiator pair (42,44,45). Applications include improving emulsion stability (135), flocculation (136), improving dry strength in paper (137), sludge dispersal in boiler-water treatment (138), and silt control in cooling water systems (139). Copolymers of the sodium salt of AMPS with acrylamide copolymers (140–142) and ampholytic terpolymers (143,144) have potential in oil-field applications and in superabsorbency, respectively.

Other Anionic Carboxylate Monomers. The anionic carboxylate monomers **8A** and **9A**, prepared by the Ritter reaction involving acrylonitrile or methacrylonitrile and 3,3-dimethylacrylic acid have been copolymerized in the

sodium salt form to yield calcium-tolerant copolymers with utility in enhanced oil recovery (145–148). Monomer **8A**, for example, has been copolymerized with **7A** under RAFT conditions to yield novel stimuli-responsive water-soluble polymers capable of reversible pH-induced micellization (42,44). Sodium 4-vinylbenzoate **12A** has also been polymerized under both NMP and ATRP conditions (133,149).

Other examples of specialty anionic monomers shown in Figure 33 include salts of vinylphosphonates **10A**, vinylphenolates **11A**, vinyl benzoate **12A**, maleic acid **13A**, 3-vinyloxypropane sulfonates **14A**, and *N*-vinylsuccinimidic acid **15A**.

Cationic Polyelectrolytes. Cationic polymers are a class of polyelectrolytes that derive their unique properties from the density and distribution of positive charges along a macromolecular backbone as well as molecular weight. Chain conformation and solubility depend on the extent of ionization and interaction with water. Cationic functional groups can strongly interact with suspended, negatively charged particles or oil droplets and are useful for many applications (76,150–153) including waste treatment and paper making. A number of the most common monomers utilized for preparation of cationic polyelectrolytes are shown in Figure 38.

Polymethacrylic Cationics.

Poly(2-(dimethylamino)ethyl methacrylate). 2-(Dimethylamino)ethyl methacrylate [DMAEMA, **1C** (Fig. 38)] is readily polymerized under a variety of conditions such as conventional free radical polymerization (154), living free radical polymerization, specifically ATRP and RAFT, anionic polymerization (155), group transfer polymerization (156) and oxyanionic polymerization (157,158). For example, conventional free radically prepared copolymers of **1C** with *N*-vinyl-2-pyrrolidone (159,160), *N*-phenylmaleimide (161), and ethylene (162) have been reported. While 1C is readily polymerized via both ATRP and RAFT, to date ATRP has received the most attention as a means of preparing controlled-structure homo- and copolymers of **1C** in both aqueous (163) and organic media (164,165) with Cu(I) species as the catalysts employing a variety of different ligands (166–169). It should be noted that under certain conditions **1C** may undergo a transesterification reaction when polymerized via ATRP in MeOH and MeOH/H_2O mixtures (170). It is also possible to directly polymerize quaternized versions of **1C** via aqueous or mixed H_2O/MeOH ATRP (171). **1C** has been successfully polymerized via RAFT in EtOAc with CTP and V-501 as the CTA/initiator pair (172), and also under bulk conditions with cumyl dithiobenzoate and AIBN (173).

Synthesis of Other Amine-Containing Polymethacrylates. Figure 38 shows the structures of other amine-containing methacrylic monomers. Like poly(2-dimethylamino)ethyl methacrylate) (PDMAEMA), the homopolymers of these monomers are water-soluble, albeit under somewhat more limiting conditions. The copolymerization of **2C** with methacrylic acid has been reported under conventional free radical conditions in methanol using AIBN as the initiator (174). The controlled polymerization of **2C**, **3C**, **4C**, and **5C** have been reported under GTP conditions (175–179) and oxyanionic conditions (15,180). Homopolymers of **2C** have also been prepared under ATRP conditions (181). Interestingly, **6C** can be polymerized in a controlled fashion by both oxyanionic and classical anionic techniques even though it contains a secondary amine species (180,182).

Aqueous Solution Characteristics. The behaviors of the polyamine methacrylates in aqueous media are both interesting and varied. The polymer

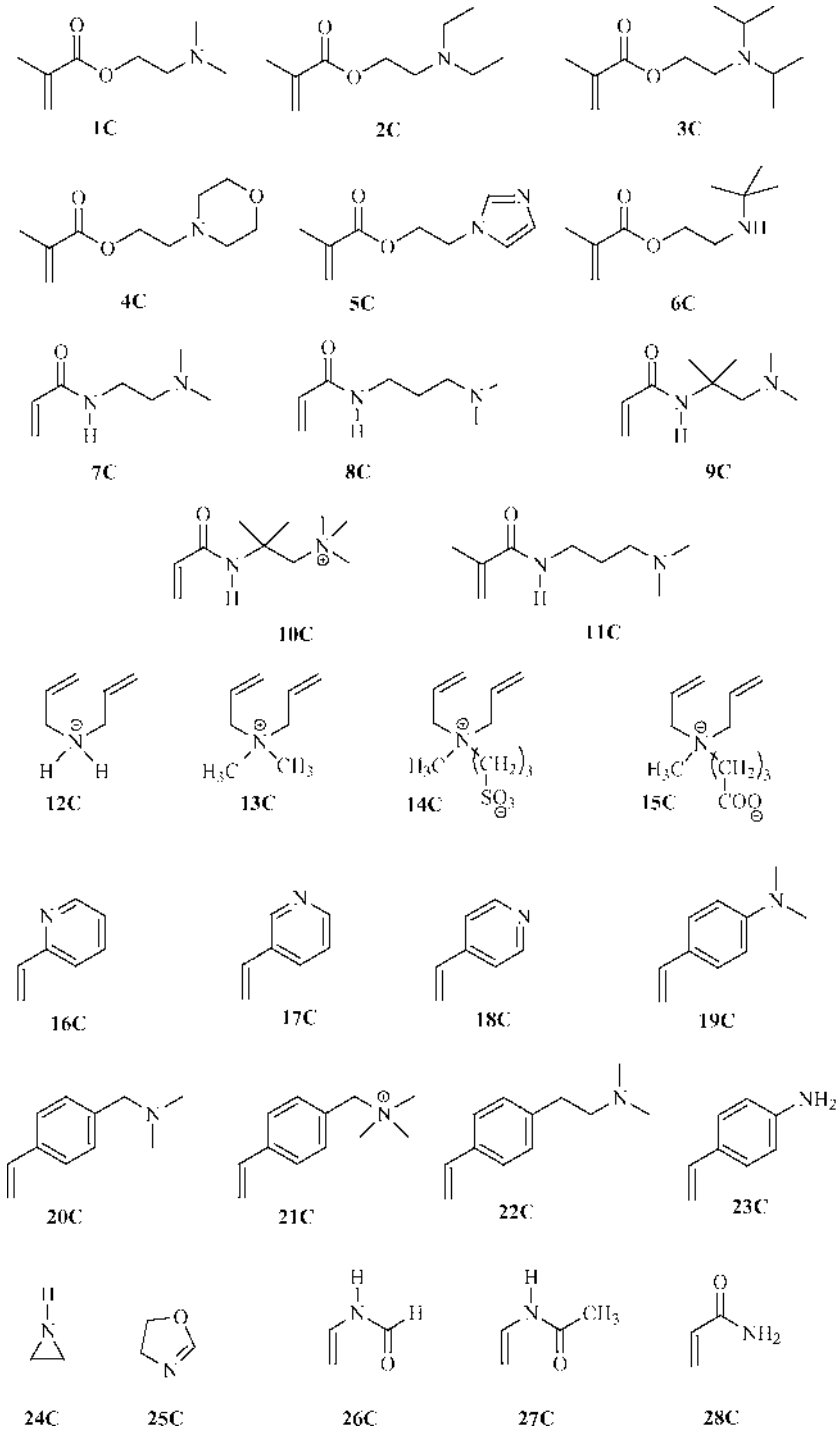

Fig. 38. Chemical structures of common amine-containing monomers (**1C–23C**) and reactive precursors (**24C–28C**) to amine-containing polymers.

from **1C** is a weak polybase which is soluble over most of the useful pH range. However, in its non ionized form, and like most nonionic water-soluble polymers, it shows inverse-temperature water-solubility. The neutral polymer has a lower critical solution temperature (LCST), or cloud-point (C_p), between ~32 and 47°C depending on its molecular weight. In its protonated form, however, it remains readily soluble up to 100°C.

The other "common" tertiary amine polymethacrylates, PDEAEMA, PDiPAEMA, and PMEMA from **2C** and **3C**, are also responsive to applied stimuli in aqueous solution. These are only soluble in aqueous media at low pH, ie under those conditions in which the tertiary amine residues are protonated and thus cationic. Under basic conditions, where the 3° amine groups are neutral both species are hydrophobic and thus phase separate. So, simply adjusting the pH of an aqueous solution for homopolymers derived from **2C** or **3C** results in phase separation. Polymers from **4C** and **1C** are soluble over the entire useful pH range, but do have an LCST in the range 34–54°C, the exact C_p being molecular weight dependent. However, the former is also susceptible to changes in electrolyte concentration. Certain salts such as sodium sulfate readily "salt out" this polymer inducing a phase change (183). These various responses to different applied stimuli have been exploited for the synthesis of novel self-assembled polymeric micelles.

Poly(meth)acrylamido Cationics. (Meth)acrylamido species are one of the most important commercial class of water-soluble monomers with wide-ranging applications. Cationic polyacrylamides are most often prepared by the normal free radical polymerization of the amine-containing monomer, and then most often in a copolymerization. For example, the protonated form of **9C** and the monomer **10C** are both readily copolymerized with **28C** to yield high molecular weight statistical copolymers in which the molar composition is virtually identical to the feed composition (184,185).

The controlled polymerization of amine-containing (meth)acrylamido monomers has, until recently, remained elusive. None of the classical living techniques can be employed and of the controlled free radical polymerization techniques only RAFT has the versatility required for this particular class of monomer. Even so, there is only one report of the controlled polymerization of an amine-containing monomer, namely *N*-[3-(dimethylamino)propyl] methacrylamide, **11C** (186). **11C** is readily homopolymerized in aqueous media (neutral pH) at 70°C using 4-cyanopentanoic acid dithiobenzoate as the RAFT CTA and V-501 as the azo initiator, at an initial molar ratio of 5/1. Under these conditions reasonable control was attained as evidenced by the molecular weight control and resulting polydispersities. Control over the RAFT polymerization of **11C** was attained by conducting the polymerizations in a buffered solution (pH = 5.0). Under these conditions possible side reactions such as monomer hydrolysis followed by aminolysis of the CTA is essentially eliminated (such side reactions have been previously shown to be significant in the homopolymerization of **28C**) (47,186).

Amine functionality can also be introduced into acrylamido polymers via post-polymerization modification of polyacrylamide from monomer **28C**. Strategies include the Mannich reaction (introduction of tertiary-amine functionality), Hofmann degradation (yields polyvinylamine residues) and transamidation reactions. The Mannich reaction is reversible; however, subsequent quaternization of the Mannich product prevents the reverse reaction (187).

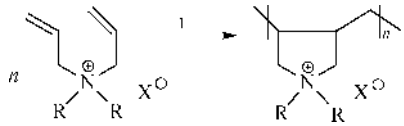

Fig. 39. Cyclopolymerization of diallyl ammonium monomers.

Polydiallylammonium Cationics. Diallyl ammonium monomers, such as **13C–15C** in Figure 38, can be polymerized via so-called cyclopolymerization (Fig. 39) (188).

DADMAC **13C**, for example, can be readily polymerized under these cyclopolymerization conditions to yield PolyDADMAC in which a structure composed of 5-membered *N*-heterocycles predominates. **13C** will readily polymerize at ~35°C employing ammonium persulfate as the initiator. **13C** is readily copolymerized with other diallyl monomers, with acrylamido monomers such as **28C** or diacetone acrylamide, or quaternized **1C**. Extensive reviews of cyclopolymerization and cyclocopolymerization can be found in Reference 188. Recent examples of cyclocopolymerization with sulfobetaine (**14C**) and carboxybetaine (**15C**) diallyl ammonium monomers are given in References (188–191).

Polyvinylpyridines

2-, 3- and 4-vinylpyridines (**16C**, **17C**, and **18C**) are all readily polymerized under normal free radical conditions. Of these species, **18C** has been the most widely studied. An extensively studied derivative of **17C** is 2-methyl-5-vinylpyridine (or 6-methyl-3-vinylpyridine) and its quats (192–195). For example, 1,2-dimethyl-5-vinylpyridinium methyl sulfate is readily polymerized in aqueous solution at room temperature with common free radical initiators such as AIBN or potassium persulfate. In fact it will spontaneously polymerize at concentrations in excess of ~75% (196).

It is also possible to prepare vinylpyridine-based (co)polymers in a controlled fashion with predetermined molecular weights and narrow molecular weight distributions. For example, the controlled polymerization of **16C** and **18C** is possible via anionic polymerization (197–201).

Also, **16C**, **17C**, and **18C** have been polymerized via nitroxide-mediated controlled radical polymerization employing a variety of different nitroxides (202–209). For example, **17C** may be polymerized under bulk or solution conditions (in ethylene glycol) employing 2,2,6,6-tetramethylpiperidin-1-oxyl (TEMPO) as the persistent free radical and benzoyl peroxide as the free radical initiator to yield controlled structure homopolymers with narrow molecular weight distributions (210). More recently, the controlled polymerization of **18C** using a β-phosphonylated nitroxide, namely *N-tert*-butyl-*N*-(1-diethylphosphono-2,2-dimethylpropyl) nitroxide, was reported and was shown to be extremely effective for the homopolymerization of **17C** as well as facilitating the synthesis of novel AB diblock copolymers (202).

The controlled polymerizations of **16C** and **18C** have also been reported using RAFT chemistry (211,212). Triblock copolymers of **17C** and styrene were prepared using dibenzyl trithiocarbonate as the RAFT CTA and AIBN as the azo

initiator. The RAFT polymerization of **16C** and **18C** has additionally been achieved using cumyl dithiobenzoate and AIBN as the CTA/initiator pair (212). Homopolymers of **16C** and **18C** were prepared under bulk conditions at 60°C. Excellent control over both the molecular weight and molecular weight distribution was observed with the polydispersity indices for the homopolymers all in the range 1.10–1.25. It was also shown that the corresponding AB diblock copolymers of **16C** with **18C** could be readily prepared using either homopolymer as the macro-CTA for the polymerization of the second block (212).

As well as NMP and RAFT, **16C** and **18C** have been polymerized via ATRP (213–215). For example, **18C** may be polymerized in a controlled fashion using 1-phenylethyl chloride as the initiator and CuCl/5,5,7,12,12,14-hexamethyl-1,4,8,11-tetraazamacrocyclotetradecane (Me_6[14]aneN_4) as the catalyst/ligand pair in propanol at 40°C (215).

Polymers from **16C** and **18C**, and presumably **17C**, may be hydrogenated to form the corresponding polyvinylpiperidines (6), or oxidized to the corresponding water-soluble *N*-oxide. The polyvinylpyridines may also be readily derivatized via quaternization with an appropriate alkylating agent, such as methyl iodide. The monomeric quats are readily water-soluble but can be prone to spontaneous polymerization above critical concentrations (216). The nature of the counterion can also affect the propensity of the quaternized monomers to autopolymerize.

Aqueous Solution Characteristics. The polymer from **16C** becomes water-soluble at a critical degree of ionization (protonation) of ca 30 mol% (217). In comparison, the polymer from **18C** only becomes water-soluble at an apparent degree of ionization of 70 mol%. The polymeric quats behave as strong polyelectrolytes and are readily water-soluble.

Amine-Containing Styrenic Monomers

Several amino-styrenic monomers are known; for example see **19C**–**23C** in Figure 38. The simplest of these, the primary amine species 4-vinylaniline (or 4-aminostyrene), **23C**, is susceptible to polymerization under conventional free radical conditions, as are **19C**–**22C**. For example, the UV-induced graft polymerization of **23C** from a Si surface was recently disclosed (218). These monomers tend to polymerize most effectively in aqueous media in their hydrochloride salt form. Given the reactive nature of the amine functionality in **23C** it is also a suitable precursor for the synthesis of novel amide-based styrenics (219). The controlled polymerization of **19C**, **20C**, and **22C**, under classical anionic conditions is also possible (220,221). For example, AB diblock copolymers of **22C** with styrene can be prepared at −78°C, in THF using cumyl potassium as the initiator with **22C** being polymerized first. Near-monodisperse *n*-butyl quats of **19C**, **20C**, and **22C** have also been reported. These were prepared by the post-polymerization modification of polymers from **19C**, **20C**, and **22C** with *n*-butyl bromide (220).

Homo and copolymers comprised of amine-containing styrenic monomers have also been reported by controlled free radical polymerization techniques. Both NMP and RAFT have been employed with varying degrees of success. For example, **20C** was block copolymerized with sodium 4-styrenesulfonate which was employed as a macro-initiator and had been prepared using TEMPO in a

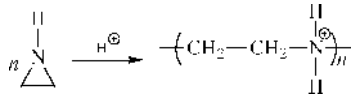

Fig. 40. Polymerization of ethyleneimine.

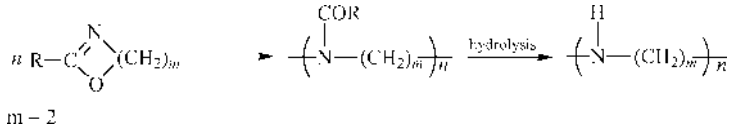

Fig. 41. Polymerization of substituted oxazolines.

3:1 ethylene glycol water mixture at 120°C with potassium persulfate as the initiator (133). More recently, McCormick and co-workers reported the synthesis of novel diamine AB diblock copolymers comprised of **21C** with the protonated form of **20C** (48). These were prepared directly in aqueous media using CTP as the RAFT CTA and V-501 as the azo initiator. Well defined block copolymers were obtained with excellent control over the molar mass and molar mass distribution. Also, new RAFT-synthesized AB diblock copolymers of *N*,*N*-dimethylacrylamide and **20C** have been reported (222). This work demonstrated the importance of blocking order in RAFT polymerizations when the two comonomers are from different monomer families. While highly efficient blocking was achieved when *N*,*N*-dimethylacrylamide was polymerized first, very poor crossover efficiencies were seen in the case of the styrenic-based macro-CTA.

Aqueous Solution Characteristics. The amine monomers tend to be water-soluble only in their protonated or quaternized forms. For example, homopolymers from **19C** are water-soluble at pH's below ~5.3; above this value they are hydrophobic and phase separate. This behavior is completely reversible and has been exploited by several researchers for the preparation of reversible pH-induced supramolecular nanoassemblies (48).

Poly(ethylene imine). Poly(ethylene amine) (PEI) is the simplest polybase. It can be prepared directly via the acid-catalyzed polymerization of ethyleneimine (aziridine, **24C**) (Fig. 40). **24C** may be prepared via a number of routes with ethanolamine being a convenient precursor (223). The cationic polymerization of **24C** is very rapid due to the release of the ring strain associated with the monomer. However, the synthesis of PEI under these conditions leads to highly branched structures due to chain transfer reactions involving the —NH— species in the polymer backbone. Cyclic products can also be produced under these conditions. Copolymerization with an appropriate comonomer can reduce the degree of chain branching (224).

The polymerization of suitable precursor monomers, with subsequent conversion to PEI, is the only route to truly linear products. The most common precursors studied are the substituted oxazolines (Fig. 41), with the 2-substituted-2-oxazolines **25C** being the most thoroughly investigated (225).

Polyvinylamine. Along with PEI, polyvinylamine (PVAm) prepared from **26C** is the simplest polybase, and is related to PEI in a similar manner to the relationship between PVOH and PEO, ie as constitutional isomers. Also like

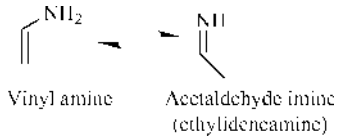

Fig. 42. Vinylamine tautomerization.

PVOH, PVAm cannot be prepared by the direct polymerization of the vinyl amine monomer because it very readily tautomerizes to acetaldehyde imine (Fig. 42).

As such, PVAm must be prepared by indirect methods employing protected monomers which, once polymerized, can be converted to PVAm. The most common employed precursors are the *N*-vinylamides (eg **26C** and **27C**) which after polymerization may be converted to PVAm via hydrolysis. For example, suitable precursors include poly(*N*-vinylacetamide) (PNVA) (226) and poly(*N*-vinylformamide) (PNVF) (227). PNVF is more readily hydrolyzed than other *N*-vinylamides. It is also possible to prepare PVAm via the Hofmann degradation of polyacrylamide prepared from **28C** (228). These precursor polymers are typically prepared using normal free radical polymerization chemistries and as such have broad molecular weight distributions. Recent advances in controlled radical polymerization methodologies, and especially the RAFT technology, should facilitate the synthesis of controlled-structure near-monodisperse PVAm. For example, it is now possible to polymerize **28C** in a controlled fashion under RAFT conditions (49,50). There is also at least one report detailing the RAFT polymerization of **26C** (229).

Miscellaneous Cationic Monomers

While the most common, amine-based species are not the only type of cationic monomers/polymers. There are several other functional species capable of yielding cationic species, namely the sulfonium (230), phosphonium (231,232), and pyrylium (233) species. Several examples of such species are shown in Figure 43.

For example, the statistical free radical polymerizations of **32C** and **33C** with *N*-isopropyl acrylamide were successfully conducted in DMSO employing AIBN at 50°C (234,235). This yielded readily water-soluble copolymers with a thermosensitive component. Such copolymers are also interesting since they can exhibit antibacterial properties against *Escherichia coli* and *Staphylococcus aureus* (234,236,237). Novel water-soluble sulfonium monomers such as **31C** can be polymerized and used as precursor polymers for the synthesis of light-emitting polymers such as poly(2,5-bis(trimethylsilyl)-1,4-phenylenevinylene (238).

Polyzwitterions. Amphoteric water-soluble polymers are polymeric systems containing both anionic and cationic charges. Such polyzwitterions may be subdivided into two major families, the *polyampholytes* and the *polybetaines* (239). Each of these groups may be further subdivided into specific types of each (see below). Figure 44 shows a number of monomers which have been used in pairs (cationic with anionic) to form polyampholytes.

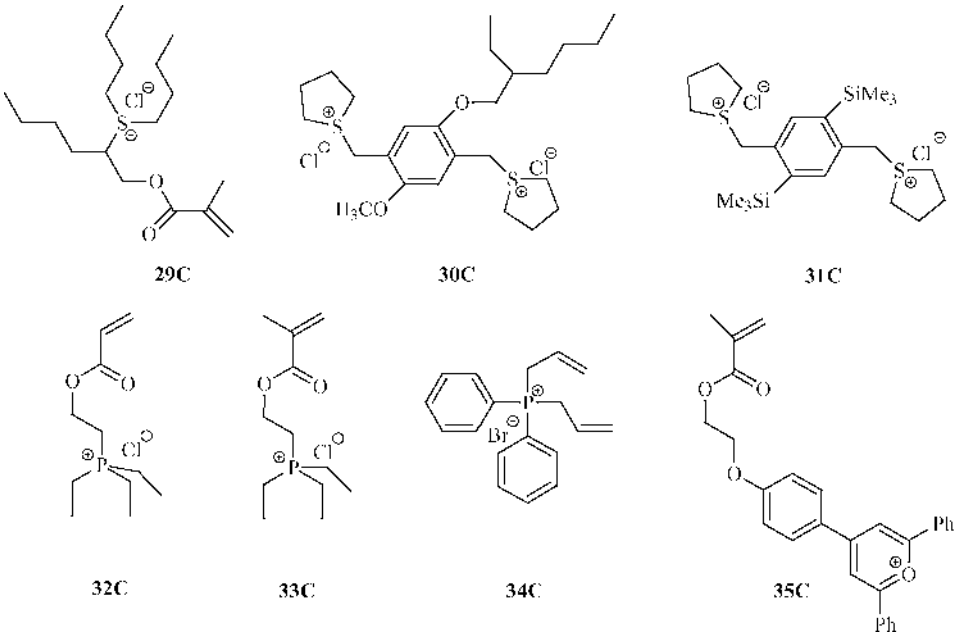

Fig. 43. Specialty cationic monomers.

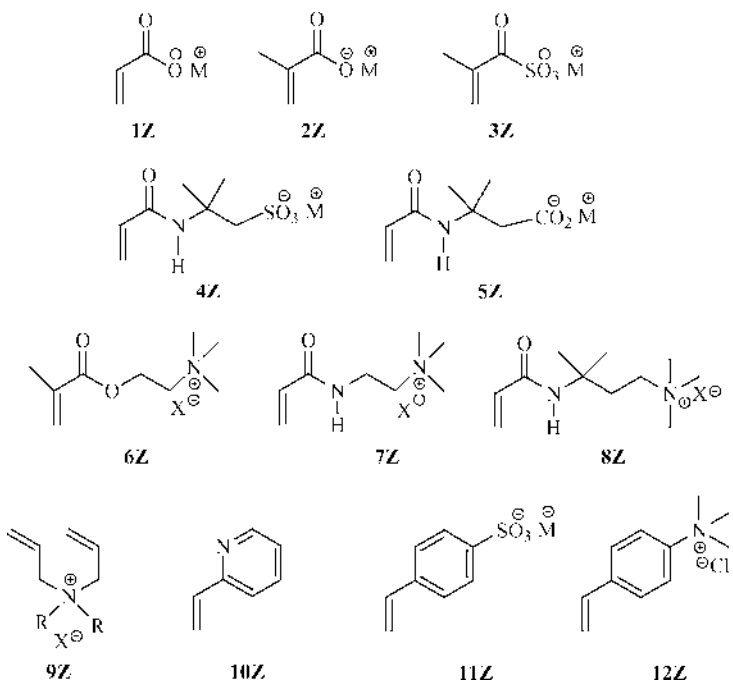

Fig. 44. Monomer pairs utilized in preparing polyzwitterions.

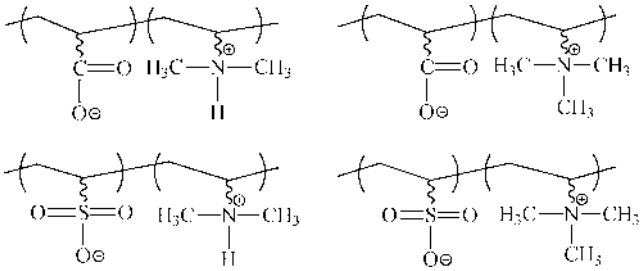

Fig. 45. Polyampholyte structures.

Polyampholytes. Polyampholytes are those materials in which the anionic and cationic charges reside on *different* mer units. Due to this, polyampholytes may be either charge balanced or unbalanced depending on the molar ratio of the anionic/cationic monomers. Polyampholytes may also be subdivided into four inherently different types. There are those in which the anionic and cationic residues may be neutralized, those where the cationic residue may be neutralized but the anionic residue is insensitive to changes in pH, those in which the anionic charges may be neutralized but the cationic residues are insensitive to pH changes, and finally those in which both the anionic and cationic residues are insensitive to changes in the pH (see Fig. 45).

Synthesis. Polyampholytes are most readily prepared by the direct statistical copolymerization of anionic and cationic monomers typically in aqueous media, via conventional free radical polymerization. Examples of such materials were first reported in the 1950s (240–244). Using this approach a wide range of copolymers and terpolymers, often with a neutral hydrophilic monomer such as acrylamide, have been reported. For example, early reports of statistical polyampholytes include the methacrylic acid-*stat*-2-(dimethylamino)ethyl methacrylate copolymers (245), from **1Z** and **2Z** with **6Z** and the *N,N*-diethylallylamine-*stat*-acrylic acid copolymers from **1Z** and **6Z** (246). More recently, synthesis and properties of novel polyampholytic terpolymers have been described (247–250). For example, the aqueous solution properties of novel ampholytic terpolymers of acrylamide, sodium 3-acrylamido-3-methylbutanoate **5Z** and 3-(acrylamidopropyl)trimethylammonium chloride **8Z** have been studied in detail (187).

It was not until the 1970s that the first block polyampholytes were reported (251,252). Anionic polymerization was used to prepare precursor AB diblock copolymers of 2-vinylpyridine **10Z** with trimethylsilyl methacrylate (TMSMA). The TMSMA residues were subsequently hydrolyzed to poly(methacrylic acid) residues to yield the corresponding AB diblock polyampholytes. Anionic polymerization has also been employed to prepare other block polyampholytes (253–258). GTP has also been successfully employed for the preparation of block polyampholytes. As with anionic polymerization, protected acid monomers must be employed since methacrylic acid (MAA) cannot be polymerized directly by this technique. A variety of protected monomers have been reported to be suitable as a means of introducing MAA residues, with 2-tetrahydropyranyl methacrylate being the most effective (Fig. 46).

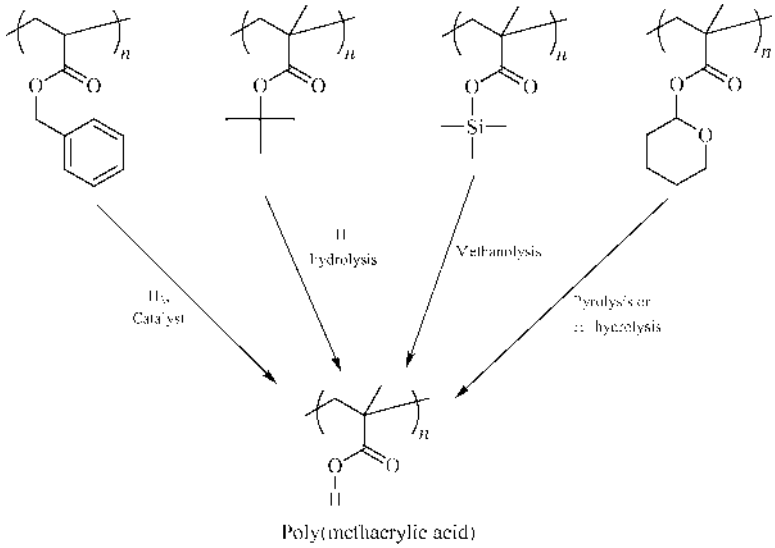

Fig. 46. Deprotection chemistry utilized to produce polymethacrylic acid or its salts.

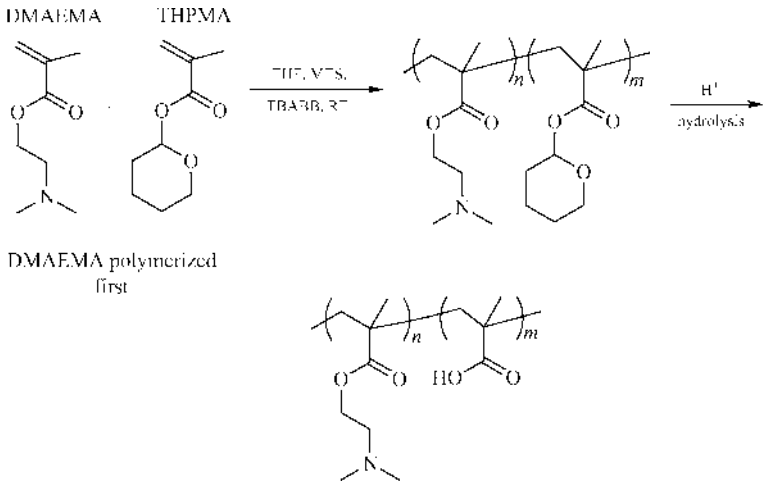

Fig. 47. GTP synthesis of AB diblock polyampholytes.

For example, AB diblock and ABC triblock polyampholytes comprised of basic DMAEMA **6Z** and acidic MAA residues, and hydrophobic methyl methacrylate residues in the case of the triblocks, have been reported (128,259–262).

While these living polymerization techniques do offer the ability to prepare block polyampholytes they are both synthetically demanding and somewhat limiting with respect to monomer choice for example. There are a handful of reports detailing the synthesis of block polyampholytes using controlled/living polymerization techniques discussed earlier (Fig. 47). For example, Gabaston and co-workers have described the TEMPO-mediated SFRP of block copolymers of sodium 4-styrenesulfonate **11Z** with 4-(dimethylamino)methyl styrene **12Z**

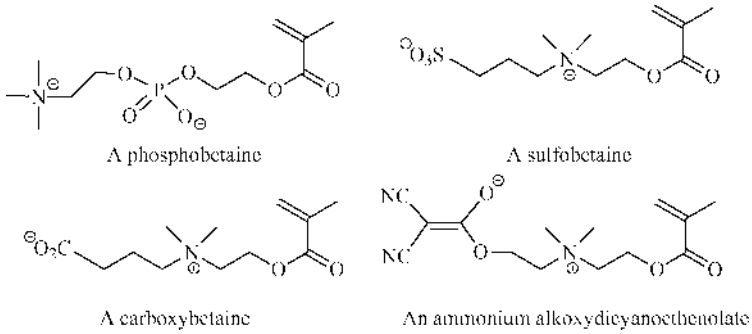

Fig. 48. General structures of selected methacrylic-based betaines.

(133), and several authors have reported the synthesis of block polyampholytes using ATRP although they still employed protecting group chemistry for the methacrylic acid residues (263–265).

Solution Properties. The aqueous solution behavior of polyampholytes is dictated by coulombic interactions between the basic and acidic residues. Polyampholytes have the ability to exhibit both polyelectrolyte and antipolylelectrolyte behavior in aqueous media. Which type of behavior is exhibited depends on factors such as solution pH, copolymer composition, the relative strengths of the acidic and basic residues, and the presence/absence of low molecular weight electrolyte (239). A feature of polyampholytes—in particular those comprised of weak acidic and basic residues—is the so-called *isoelectric point*, or IEP. This is simply defined as the solution pH at which the polyampholyte is electrically neutral. Statistical polyampholytes often remain soluble at and around the IEP whereas block polyampholytes tend to be soluble above and below but insoluble at this critical pH. The IEP may be determined either by titration or by measuring the reduced viscosity as a function of pH—the IEP also represents the point at which the polyampholyte chain is in its most compact conformation and thus corresponds to the minimum in reduced viscosity (239,266). With a knowledge of the respective pK_a's and copolymer composition it is also possible to predict the IEP (267).

Polybetaines. *Polybetaines* are materials in which the anionic and cationic functional species are part of the *same* mer unit (Fig. 48). Because of this the number of anionic, or potentially anionic, residues is always exactly equal to the number of cationic residues. The cationic residue in polymeric betaines is typically a quaternary ammonium species. The anionic functionality can vary and leads to the classification of polymeric betaines as sulfobetaines (sulfonate functional group), carbo or carboxybetaines (carboxylate functional groups), phosphobetaines (phosphate functional group), and etheneolatebetaines (dicyanoetheneolate functional group) (239).

Synthesis. Betaine monomers may be prepared in a number of different ways. For sulfobetaines, the most common, and easiest, method is to react a monomer containing a tertiary amine residue with either 1,3-propanesultone or 1,4-butanesultone (268). This is an extremely facile reaction and proceeds readily at RT in common solvents such as THF or CH_3CN to yield the

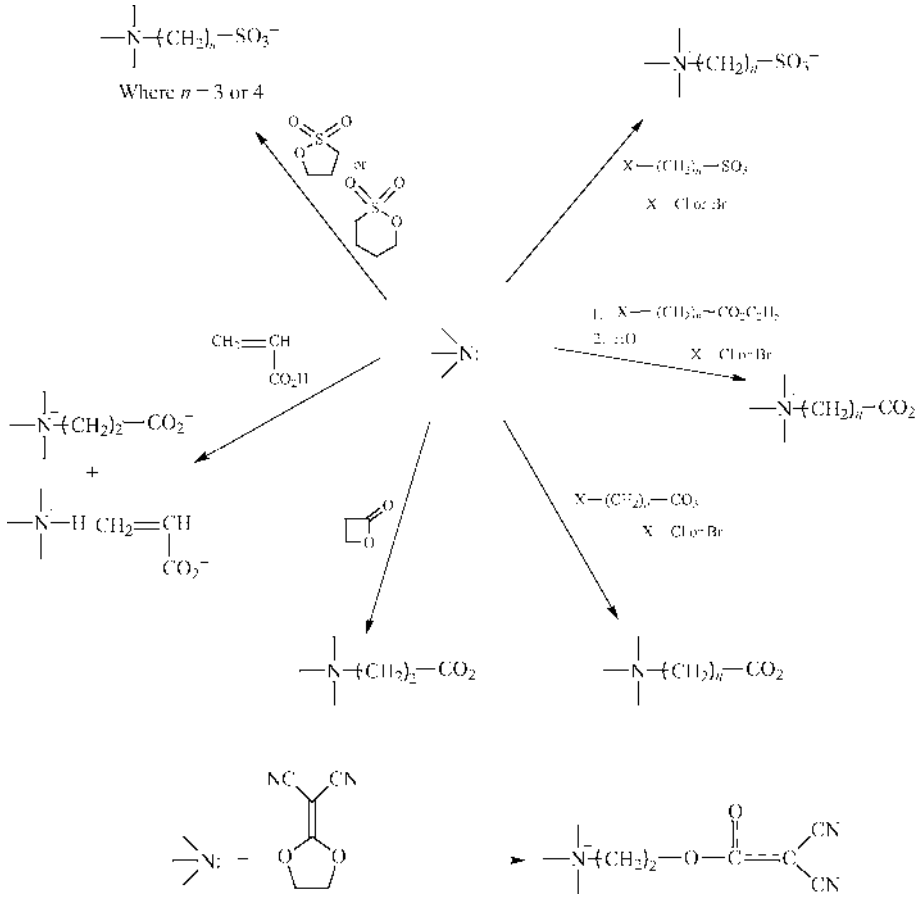

Fig. 49. General synthetic routes for sulfo/carboxybetaines.

corresponding sulfobetaine monomer. Alternatively, the tertiary amine functionality may be reacted with a haloalkylsulfonate species (269). Carboxybetaine monomers may be prepared via a number of different routes (Fig. 49). They may be obtained from the reaction of a suitable lactone (270) with a tertiary amine species, although this is somewhat limited to highly strained lactones to avoid competing nucleophilic attack at the carbonyl group. Alternatively they can be obtained from the Michael addition of a tertiary amine to acrylic acid (271), although again this route is prone to side reactions and simple salt formation. Perhaps the most versatile route for the preparation of carboxybetaines involves the reaction of a tertiary amine with a haloalkylcarboxylate to yield the carboxy betaine directly, or by reaction with the corresponding haloalkylester to yield the quaternized species followed by ester hydrolysis to yield the carboxybetaine (272,273).

Phosphobetaine monomers may also be prepared via a number of routes (239,274). Probably the most common phosphobetaine monomer is 2-(methacryloyloxy)ethyl phosphorylcholine (MPC), although other derivatives are also known (275–278). MPC is prepared from the reaction of 2-hydroxyethyl

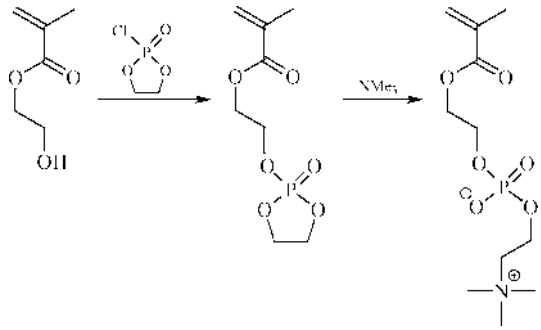

Fig. 50. Synthesis of MPC.

methacrylate with 2-chloro-2-oxo-1,3,2-dioxaphospholane, followed by ring opening of the intermediate phospholane with trimethylamine (Fig. 50). This is a general synthetic procedure which can be applied to any alcohol functional monomer. There are very few examples of the dicyanoetheneolate betaines. These particular species are prepared from the reaction of a tertiary amine monomer with 2,2-dicyanoketene-1,2-ethylene acetal (279–281).

Polymeric betaines are most readily prepared by the direct polymerization of the betaine monomers, typically in aqueous salt solution. Since their initial report in 1957, by Ladenheim and Morawetz (282), there have been a large number of polymeric betaines reported based on many different families of monomers (239). Polymeric betaines may also be prepared under condensation polymerization conditions thus yielding polymers in which the betaine functionality is attached directly to the (co)polymer backbone (283–285).

Controlled structure polymeric betaines were reported for the first time only recently (286). The first examples were those prepared from the post-polymerization modification of poly(2-(dimethylamino)ethyl methacrylate) (PDMAEMA), and its block copolymers, which had been prepared under GTP conditions (286,287). Initial reports detailed the modification of hydrophilic-hydrophobic block copolymers, but this was subsequently extended to the selective modification of diamino hydrophilic-hydrophilic block copolymers (276).

The *direct* polymerization of betaine monomers in a controlled fashion has been reported by ATRP (288–291), and, most recently, via RAFT (38,43,292,293). Methacrylic derivatives of carboxy-, sulfo-, and phosphobetaines have been prepared via ATRP, while RAFT is more versatile with respect to monomer choice, and examples of styrenic, methacrylic and acrylamido sulfobetaines have been disclosed.

Solution Properties. Zwitterionic polymers show interesting aqueous solution behavior. As a general rule, they are *insoluble* in pure water due to the formation on intra- and interchain ion contacts resulting in an ionically cross-linked network-type structure. Polyampholytes and polybetaines which are not soluble become soluble upon the addition of low molecular weight electrolytes, such as NaCl (Fig. 51). This dissolution process can best be understood in terms of the low molecular weight electrolyte penetrating the ionically cross-linked network whereupon the ions screen the net attractive interactions between the polymer

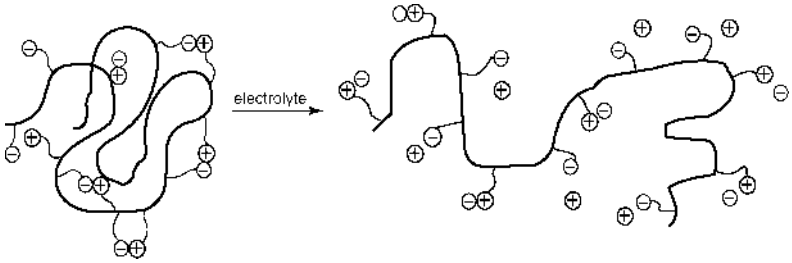

Fig. 51. Schematic illustration of polyampholyte response to added electrolyte.

chains and hence promote solubility. The addition of the salt also results in antipolylelectrolyte behavior, ie chain expansion upon the addition of the salt.

Applications of Polyzwitterions. Polyzwitterions have wide-ranging applications. For example, statistical polyampholytes comprised of 2-vinylpyridine **10Z** and acrylic acid **1Z** have been evaluated as desalination membranes, while others have been used in sewage treatment, flocculation, coagulation, drilling fluids, enhanced oil recovery, and drag reduction.

Polymeric betaines have applications in areas similar to those of the polyampholytes described above. Additionally, phosphobetaines in particular have found application in the biomedical field. (Co)polymers comprised of MPC and various alkyl methacrylates (294,295) for example have been shown to exhibit both good bio and hemocompatability and have found application as coatings for medical devices such as catheters or arterial stents as well as materials for contact lens application. The success of MPC-based materials, and other phosphobetaines, is attributed to their biomimetic characteristics, ie their structural and chemical similarity to naturally occurring phospholipids. Recently, sulfobetaine-based materials were also shown to exhibit similar properties indicating that these bio/hemocompatability characteristics may not be unique to polymer phosphobetaines but perhaps to polybetaines in general (296).

Stimuli-Responsive Amphiphilic Polymers

Amphiphilic copolymers with appropriate balance of hydrophilic and hydrophobic sequences along or pendent to the micromolecular backbone can self-organize in water (297). In principle, intramolecular (closed) or intermolecular (open) associations can result. Intramolecular self assembly can, for example, lead to unimeric or multimeric micelles (Fig. 52**a,b**) with solution behavior resembling that of small molecule surfactants above their critical micelle concentration. Intermolecular assembly (Fig. 52**c**) often results in network or associative thickening behavior. Judicious choice of polymerization methods and conditions, monomer selection, post reactions, etc allows molecular construction of a wide variety of systems capable of self-assembly. Strategic placement of functional groups along the macromolecular backbone can also lead to reversible association in response to external stimuli including pH (298,299), ionic strength (300), light (301–303), temperature (304), and shear stress (297,305).

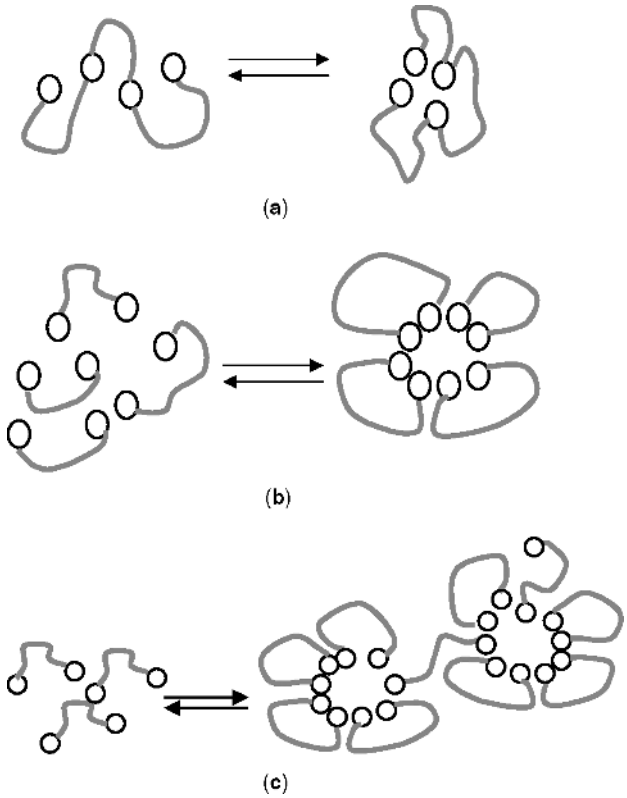

Fig. 52. Behavior of amphiphilic copolymers in response to stimuli.

The earliest synthetic polymeric micelles, often referred to as *polysoaps*, were prepared as biological protein mimics (306–308). Copolymers synthesized by partial *n*-dodecylation of poly(2-vinyl pyridine) or by hydrolysis of poly(maleic anhydride-*alt*-alkylvinyl ethers) possessed surfactant-like properties in water (309–312). The initial associative thickeners, on the other hand, were prepared by (*1*) substitution of water-soluble cellulose derivatives with long chain alkyl groups (153,313–317) (*2*) partial esterification of poly(styrene-*alt*-maleic anhydride) with nonionic surfactants (318–321), (*3*) step growth polymerization of hydrophobically modified diisocyanates with poly(oxyethylene glycols) (322), or (*4*) by statistical chain growth free radical polymerization of a variety of hydrophobic and hydrophilic monomers under heterogeneous reaction conditions including emulsion polymerization (323,324) and micellar polymerization (325–330).

Despite a number of successes in preparing polymers with aqueous solution behavior depicted in Figs. 21**a** and 21**c**, little understanding of the nature of associative polymer domains existed prior to 1990. As well, studies of block copolymer associations had been limited to phase behavior in selective organic solvents. Since then, rapid developments in characterization of reversible microdomains via static and dynamic fluorescence spectroscopy (331–351), NMR spectroscopy (345,352–359) light scattering (171,175,360–364), and rheological

techniques (365–370) have led to a better understanding of the structural parameters governing assembly/disassembly in water. Likewise, the development of facile controlled/living free radical polymerization techniques for preparing block copolymers with well-defined structures has led to better models for study.

It can be established that the extent of closed or open associations depends on the architectures of the macromolecular chains. Molecular parameters affecting such associative behavior include hydrophilic and hydrophobic block lengths, placement and molecular weight of the segments, polymer concentration, flexibility and spacer lengths side-chain functionality. Responsiveness to pH, electrolyte, and to temperature changes depends markedly on the nature of the functional groups (cations, anions, zwitterions), their proximity to hydrophilic or hydrophobic units, and the ionic strength of the surrounding aqueous media. Some theoretical models have been put forth that describe unimolecular micelle formation progressing to bridged micelles and eventually networks (371–373).

Statistical Amphiphilic Polymers

Statistical amphiphilic polymers with ionic charges along the macromolecular backbone represent most of the stimuli-responsive systems reported in the literature. In principle, hydrophilic monomers from Figures 27, 33, 38, 43, or 44 can be copolymerized with hydrophobic comonomers or macromonomers under conditions allowing sufficient incorporation of the latter. The most successful methods have been "micellar" polymerization (324,325,347,348) in which high concentrations of surfactants are added to solubilize the hydrophobic monomer in the aqueous phase or emulsion polymerization utilizing macromonomers having amphiphilic character (323,324). Table 1 gives examples of associative polymers and the type of responsiveness reported in the literature. A comprehensive review (305) presents details of the synthetic routes to and behavioral characteristics of associative polyelectrolytes as determined by a wide variety of analytical techniques.

Well-Defined Amphiphilic Copolymers. Well-defined, controlled structure amphiphilic copolymers may be prepared using a range of polymerization techniques that includes anionic, cationic, and controlled free radical approaches. The materials may be "simple" AB diblock copolymers or more structurally complex species such as ABA or ABC triblock copolymers for example.

Hydrophilic-Hydrophobic Block Copolymers. These materials represent the "simplest" type of amphiphilic block copolymer. Materials are comprised of one block which is inherently hydrophobic, such as polystyrene or poly(methyl methacrylate), and a second block which is hydrophilic such as poly(methacrylic acid). For example, anionic polymerization may be employed for the synthesis of AB diblock copolymers comprised of styrene with 2- (438) or 4-vinylyridine (439). In the case of the styrene-2-vinylpyridine copolymers, self-assembly, under appropriate aqueous conditions, leads to the formation of block copolymer micelles with styrene forming the hydrophobic core and the 2-vinylpyridine forming the stabilizing corona. These block copolymer micelles are highly stable in 0.1 *M* HCl. Similarly, styrene–acrylic acid block copolymers may likewise be prepared via anionic polymerization using *tert*-butyl acrylate as a protected precursor for the

Table 1. Copolymer Compositions[a] Responsiveness, and References for Stimuli-Responsive Polyelectrolytes

Polymer Composition	Response	Ref.
K-S	pH, salt	(312,374–380)
K-T	pH, salt, shear	(336,374,381–383)
E-H-Fl	pH, salt, shear	(374,384)
I-P	salt, shear	(374,385–388)
G-B-R	salt, shear	(374,389,390)
E-Q-B	pH, salt, shear	(374,391,392)
E-B-Fl	pH, salt, shear	(374,393)
B-R-D	pH, salt, shear	(365,366,374)
E-Q	shear	(327,328,374,393–404)
E-R	shear	(327,328,374,393–404)
E-S	shear	(327,328,374,393–404)
E-U	shear	(374,405,406)
E-B-U	pH, salt, shear	(374)
B-Q	pH, salt, shear	(305,407)
B-Fl	pH	(305,408,410)
A-S	pH, salt, shear	(305,411)
B-Fl	pH, salt, shear	(305,412)
B-Q	pH, salt, shear	(305,345,413)
A-R	pH, salt, shear	(305,363,364)
B-E-Q	pH, salt, shear	(305,404,414,415)
B-Fl	pH, salt, shear	(305,349,409)
C-F-Q	pH, salt, shear	(305,416)
Y	pH, salt, shear	(305,417)
Z	pH, salt, shear	(305,418)
Z-T	pH, salt, shear	(305,382)
Z-T-Fl	pH, salt, shear	(305,336,381)
I-P-Fl	pH, salt, shear	(305,385,419–422)
I-R	pH, salt, shear	(305,423–426)
I-R-P	pH, salt, shear	(305,427)
E-A-R	pH, salt, shear	(305,428)
E-I-R	pH, salt, shear	(305,429,430)
O-V	pH, salt, shear	(305,431–436)
U-M	pH, salt, shear	(276,305)
U-N	pH, salt, shear	(305,437)

[a]Letters refer to repeating units in Figure 53.

acrylic acid residues. Such block copolymers exhibit similar self-assembly behavior in aqueous media (440,441). Other examples of such hydrophilic-hydrophobic block copolymers capable of supramolecular self-assembly include the poly(2-(dimethylamino)ethyl methacrylate-*block*-methyl methacrylate) (442). and the poly(3-(*N*-2-methacroyloyethyl)-*N*,*N*-dimethylammonio)propanesulfonate-*block*-methyl methacrylate) copolymers (287,443). In both instances the block copolymers were prepared via group transfer polymerization. Cationic polymerization also offers a route to amphiphilic vinyl ether-based AB diblock copolymers. For example, the synthesis and micellization properties of isobutyl vinyl ether-*block*-methyl tri(ethyleneglycol) vinyl ether copolymers have been reported (444).

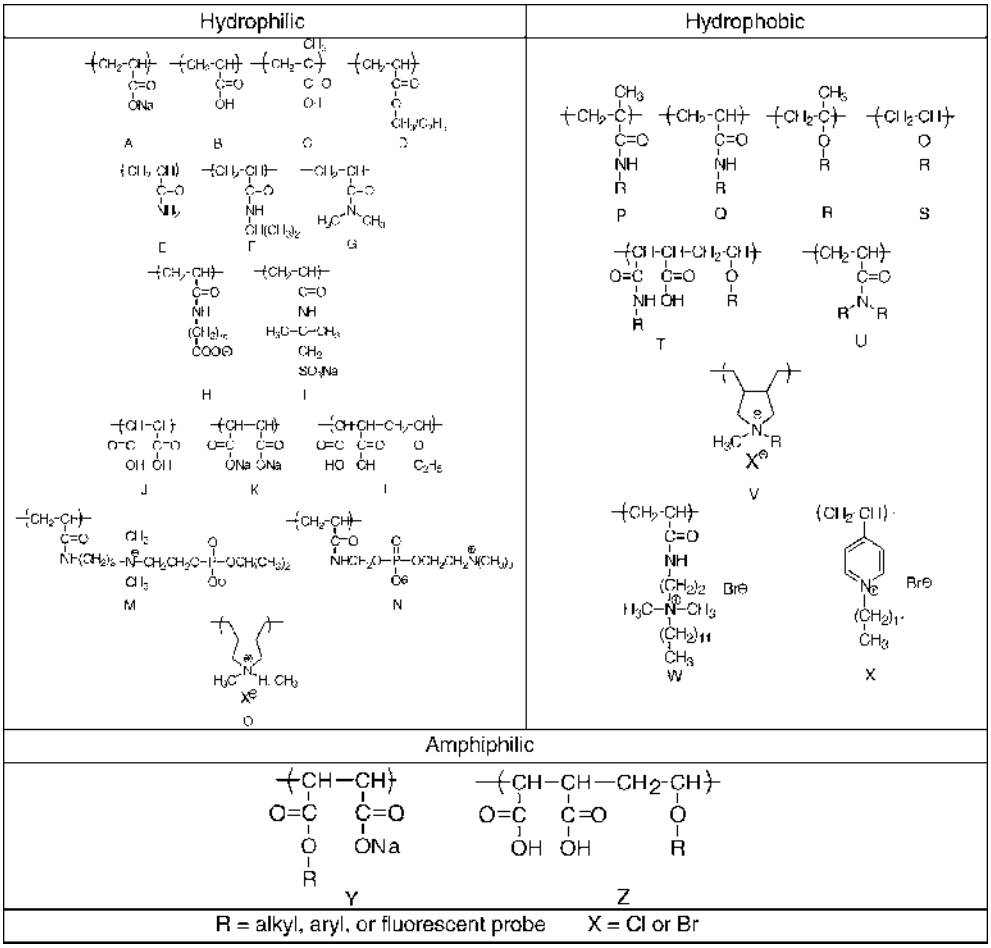

Fig. 53. Polymer segments utilized in statistical polymers with stimuli-responsive associative behavior in water. For polymers incorporating a fluorescent probe the letters Fl are used in Table 1.

Also the self-association of AB diblocks comprised of methyl tri(ethyleneglycol) vinyl ether (hydrophilic block) and benzyl vinyl ether (hydrophobic block) have been investigated (445). In water, micelles with hydrodynamic diameters in the range 10–26 nm were observed depending on the molar composition of the block copolymer.

Hydrophilic/Tunably Hydrophilic/Hydrophobic Block Copolymers. The next level of complexity for amphiphilic block copolymers are those comprised of one block which is permanently hydrophilic with the second block being tunably hydrophilic/hydrophobic, ie under a set of conditions A, the second block is readily water soluble and thus the block copolymer exists as unimers, but upon the application of a certain stimulus (change in pH or temperature for example) to condition B the second block becomes hydrophobic. Provided appropriate block copolymer compositions are employed this will lead to self-assembly. Additionally,

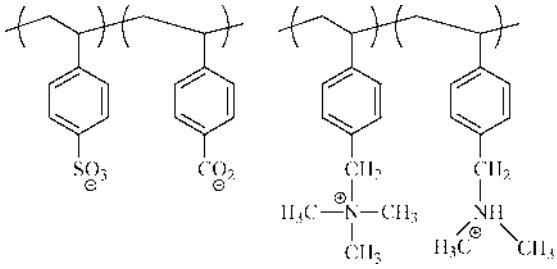

Fig. 54. Responsive AB block copolymers from ionic styrenic monomers.

such behavior is typically completely reversible. While there are now numerous examples of such "smart" self-assembly these types of systems have not been as thoroughly investigated as the inherently hydrophilic/hydrophobic species, with perhaps one notable exception being the PEO/PPO and PEO/PPO/PEO, PPO/PEO/PPO block copolymers.

Group transfer polymerization has proven to be an extremely useful technique for the synthesis of such AB diblock copolymers. For example, the synthesis of AB diblock copolymers in which the A block was 2-(dimethylamino)ethyl methacrylate (**1C** in Fig. 38) and the B block was either **2C** or **3C** in Figure 33 have been reported. **1C** is temperature responsive whereas **2C** and **3C** are both pH responsive. At low pH when both the tertiary amine blocks (**1C** + **2C** or **1C** + **3C**) are protonated the block copolymers are molecularly dissolved. Raising the solution pH above the p*K*a of tertiary amine residues for **2C** and **3C** renders these blocks hydrophobic and as such the block copolymers self-assemble to form micelles with the hydrophobic **2C** (or **3C**) residues in the core, stabilized by coronal chains of 1. Supramolecular self-assembly is completely reversible—lowering of the pH back below the respective p*K*a's results in molecular redissolution (183).

More recently controlled free radical polymerization methodologies have been employed for the preparation of novel "smart" AB diblock copolymers. Nitroxide-mediated polymerization was utilized for the synthesis of sodium 4-styrenesulfonate-block-sodium 4-vinylbenzoate block copolymer (133). These strong acid/weak acid species exhibit reversible pH-induced self-assembly, with the sodium 4-styrenesulfonate residues remaining ionized and thus permanently hydrophilic over the useful pH range whereas the sodium 4-vinylbenzoate block can be reversible protonated (the carboxylate residue has a $pK_a \sim 4.0$). The same block polymers can also be prepared via RAFT, albeit with somewhat more control. Other workers reported the preparation of such AB diblock copolymers as well as some analogous amine-based styrenic diblock copolymers, (48) shown in Figure 54.

Similarly, such AB diblocks may be prepared based on the acrylamido family of monomers. For example, the synthesis of novel AB diblock copolymers comprised of the two anionic monomers sodium 2-acrylamido-2-methylpropanesulfonate (AMPS) and sodium 3-acrylamido-3-methylbutanoate (AMBA) have been reported (42,44). By analogy with the styrenic block copolymers, these AMPS-AMBA species also exhibit reversible pH-induced self-assembly by virtue of the fact that the AMBA residues may be reversible

protonated, switching the residues from a hydrophilic (high pH) to a hydrophobic (low pH) state. Similar AB diblocks of AMPS with sodium 6-acrylamidohexanoate which also exhibit pH-induced micellization have been reported by Yusa and co-workers (45) RAFT has additionally proven very useful for the preparation of AB diblock copolymers comprised of blocks from different monomer families. For example, AB diblocks of *N*,*N*-dimethylacrylamide (DMA) with *N*,*N*-dimethylbenzyl vinyl amine (DMBVA) were recently disclosed. These particular blocks are also capable of undergoing reversible pH-induced micellization (222). The DMA residues are nonionic, permanently hydrophilic whereas the styrenic-based DMBVA block is water soluble in its protonated form, but hydrophobic in its nonionized state. As such, simply raising the pH of an acidic solution of the block copolymer results in self-assembly and the formation of aggregates with the hydrophobic DMBVA blocks residing in the core which is stabilized by the DMA block. RAFT has also been utilized for the preparation of AB diblocks in which one of the blocks is a salt-responsive specie (293). For example, AB diblocks of *N*,*N*-dimethylacrylamide with 3-[2-(*N*-methylacrylamido)-ethyldimethylammonio]propanesulfonate (MAEDAPS).

Doubly "Smart" Block Copolymers. Doubly "smart" or responsive copolymers are those in which *both* the blocks of the copolymer are tunably hydrophilic/hydrophobic. As such this potentially facilitates the preparation of both normal and inverse micelles in the *same* solvent (NB: normal and inverse micelles are well known but switching between the two often requires a change of solvent). Some authors have termed such materials *"schizophrenic" block copolymers*. At present these represent the least studied of the amphiphilic block copolymers. Examples of such materials include the poly(2-(*N*-morpholino)ethyl methacrylate-*block*-2-(diethylamino)ethyl methacrylate) (177, 446) and the poly(propylene oxide-*block*-2-(diethylamino)ethyl methacrylate) copolymers (447). A number of these types of block copolymers have been studied (263,264,448,449). As a representative example, a precursor poly(2-(dimethylamino)ethyl methacrylate-*block*-2-(*N*-morpholino)ethyl methacrylate) (DMAEMA-MEMA) copolymer was reacted with 1,3-propanesultone to yield the corresponding sulfopropylbetaine-MEMA block copolymer (Fig. 55) (448). At temperatures between 30 and 40°C a block copolymer comprised of an equimolar ratio of the two comonomers exists as molecularly dissolved unimeric chains. Upon raising the temperature above the cloud point of the MEMA block, the copolymer self-assembles forming polymeric micelles with the now-hydrophobic MEMA residues residing in the core with the sulfobetaine blocks in the corona.

Sulfobetaine-core micelles were obtained by lowering the solution temperature below 20°C at which point increased attractive electrostatic interactions result in phase separation of the sulfobetaine block and thus micelle formation. A similar doubly temperature responsive block copolymer, prepared via RAFT, was reported which was based on acrylamido monomers (292).

Shell and Core Cross-Linked Nanoassemblies. Shell or core cross-linked nanoassemblies represent a group of materials which can, in principle, be derived from any of the amphiphilic species described in the earlier sections. Clearly the self-assembled structures described above are dynamic species. However, one can envisage the need for "locked" structures for certain applications. One method to achieve this is via cross-linking of either the coronal or core chains. To facilitate

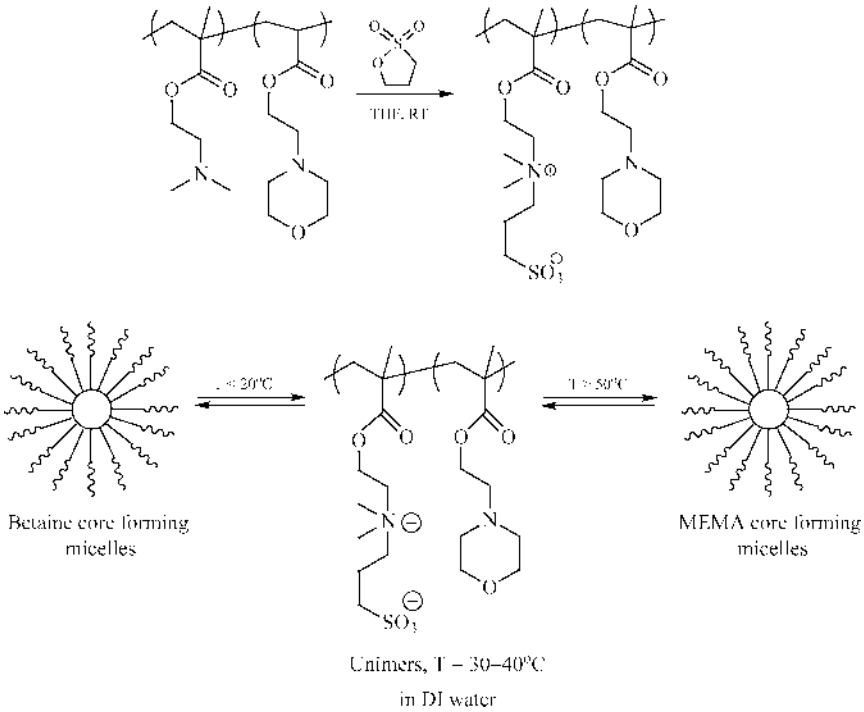

Fig. 55. An example of a "schizophrenic," methacrylic-based AB diblock copolymer and conditions leading to self-assembly.

either approach there must be a suitable reactive species in the core or corona susceptible to chemical modification after self-assembly.

Shell cross-linked micelles, also referred to as *knedel* or *SCK micelles*, were first reported in 1997 (450,451). For example, an amphiphilic AB diblock copolymer comprised of hydrophobic polystyrene with hydrophilic partially quaternized poly(4-vinylpridine) was prepared by the sequential living anionic polymerization of styrene and 4-vinyl pyridine followed by quaternization of some of the 4-vinylpyridine residues with 4-vinylbenzyl chloride. Micelles are prepared by dissolving the quaternized block copolymer in a mixture of water and THF. Finally, shell cross-linking is accomplished by polymerizing the styrenic residues in the shell (present as a result of the quaternization reaction) in the presence of a free radical initiator (452). Examples in which the micelle coronal shell consists of hydrophilic acrylic acid residues, with a variety of hydrophobic cores, may be conveniently shell cross-linked using 2,2′-(ethylenedioxy)bis(ethylamine). Thus, cross-linking is achieved via an amidation reaction using a bifunctional primary amine (453–457). Other examples of these novel nanomaterials include those with polysilane cores and partially cross-linked poly(methacrylic acid) coronas (458,459), and micelles in which the reactive, cross-linkable functionality is either methacrylic acid or DMAEMA residues, with the actual cross-linking being achieved with bis-(2-iodoethoxy)ethane (460–462). The effectiveness of bis-(2-iodoethoxy)ethane as a cross-linking agent is illustrated in Figure 56.

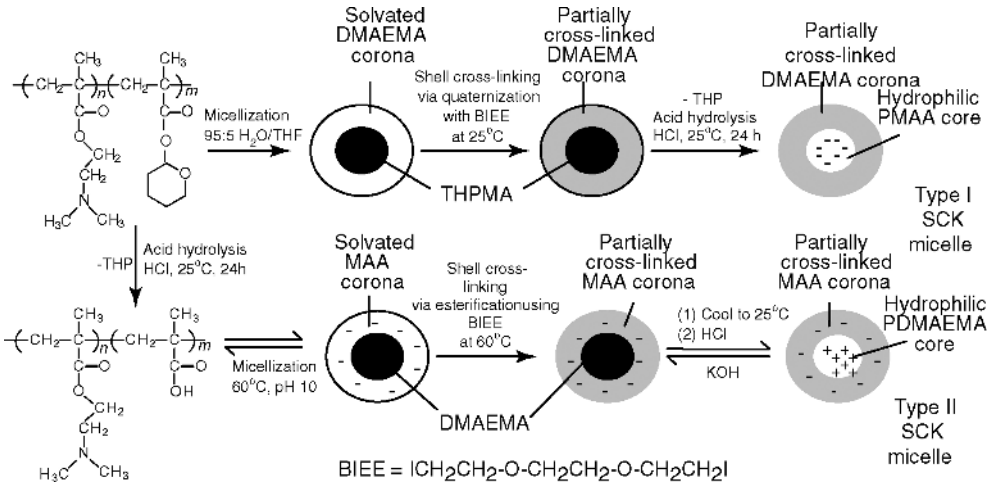

Fig. 56. An example of bis-(2-iodoethoxy)ethane as a cross-linking agent.

Here so-called Type I and Type II zwitterionic SCK micelles can be prepared from the hydrophilic-hydrophobic precursors poly(2-(dimethylamino)ethyl methacrylate-*block*-2-tetrahydropyranyl methacrylate) (DMAEMA-THPMA) copolymers prepared via group transfer polymerization (128,129,461). Micellization of the DMAEMA-THPMA block copolymers in a water/THF mixture (95:5) results in the formation of core-shell structures in which the hydrophobic THPMA species forms the core and the hydrophilic DMAEMA species the corona. The reactive tertiary amine residues in the coronal may be cross-linked using bis-(2-iodoethoxy)ethane in a *quaternization* reaction (Menshutkin Reaction). Subsequent hydrolysis of the micelles cores leads to the formation of the Type I SCK species. Alternatively, the DMAEMA-THPMA precursor block copolymers may be initially deprotected to form the block polyampholytes. Heating an aqueous solution of this block polyampholyte above the cloud point of the DMAEMA residues results in the formation of inverse micelles in which the now-hydrophobic DMAEMA residues form the micelle core and ionized poly(methacrylic acid) chains form the corona. These carboxylate coronal chains may also be cross-linked using bis-(2-iodoethoxy)ethane, in this instance via an esterification reaction.

A potential drawback of shell cross-linking is the need to perform such chemistries under relatively dilute conditions to avoid the occurrence of inter-particle cross-linking. However it was recently demonstrated that SCK micelles could be successfully prepared at high solids with ABC triblock copolymers in which the *C block* forms the *micelle core*, the *A block the outer coronal chains* and the *cross-linkable B block the inner coronal chains*. Here, the outer A block is effectively acting as a steric barrier to inter-particle cross-linking (463,464).

Most recently the core cross-linking approach was adopted for the preparation of novel nanoassemblies derived from pH-responsive AB diblock copolymers prepared via RAFT (222). Here the A block was the permanently hydrophilic DMA species with the tunably hydrophilic/hydrophobic DMBVA forming the B

block. In aqueous media, at high pH, these block copolymers form core-shell structures with the DMA residues forming the corona and the DMVBA chains in the core. Addition of a hydrophobic, difunctional, alkyl halide namely 1,4-bisbromomethylbenzene results in this species being sequestered into the hydrophobic core of the micelles where it reactions with the tertiary amine residues via the Menshutkin reaction to yield the core-cross-linked species. Successful core cross-linking was verified via NMR spectroscopy, dynamic light scattering and transmission electron microscopy.

Concluding Remarks

Water-soluble polymers are an extremely important class of materials that permeate every facet of our lives. This class of materials encompasses a wide range of interesting species ranging from naturally occurring proteins, peptides, RNA, DNA, and sugars (carbohydrates) to complex synthetic nanoassemblies such as the well-defined core-cross-linked AB diblock polymeric micelles.

Clearly there have been significant advances in the field of water-soluble polymers since the previous edition of this encyclopedia. Arguably the most important development in recent years has been the discovery and application of more facile controlled/living polymerization techniques for the synthesis of highly functional, well-defined, model, materials. Of these, the controlled/living free radical polymerization techniques, and especially reversible addition–fragmentation chain transfer (RAFT) are proving to be especially versatile.

It is likely that such developments will continue to revolutionize water-soluble polymer synthesis in the years to come with chemists taking up the challenge to prepare ever more complex structures capable of supramolecular self-assembly for a wide variety of specialized applications.

BIBLIOGRAPHY

"Water-Soluble Polymers" in *EPSE* 2nd ed., Vol. 17, pp. 730–784, by C. L. McCormick, University of Southern Mississippi; J. Bock and D. N. Schulz, Exxon Research; in *EPST* 3rd ed., Vol. 12, pp. 452–521, by C. L. McCormick, N. Ayres, and A. B. Lowe, University of Southern Mississippi.

CITED PUBLICATIONS

1. http://www.mathemagic.com/MOBM/fractals.html.
2. P. J. Flory, *Principles of Polymer Chemistry*, Cornell University Press, Ithaca, N.Y., 1953.
3. J.-L. Barrat and J.-F. Joanny, *Adv. Chem. Phys.* **94**, 1–66 (1996).
4. A. V. Dobrynin, R. Colby, and M. Rubinstein, *Macromolecules* **28**, 1859–1871 (1995).
5. F. Franks, ed., *Water: A Comprehensive Treatise*, Vol. 4, Plenum Press, New York, 1975.
6. P. Molyneaux, *Water-Soluble Synthetic Polymers*, Vols. 1 and 2, CRC Press, Inc., Boca Raton, Fla., 1984.
7. C. Tanford, *The Hydrophobic Effect: Formation of Micelles and Biological Membranes*, John Wiley & Sons, Inc., New York, 1973.
8. W. Saenger, *Annu. Rev. Biophys. Chem.* **16**, 93 (1987).

9. J. T. Edsal and H. A. McKenzie, *Adv. Biophys.* **16**, 53 (1978).
10. J. L. Finney, *J. Mol. Biol.* **119**, 415 (1978).
11. R. M. Fuoss, *J. Polym. Sci.* **3**, 603 (1948).
12. O. W. Webster, W. R. Hertler, D. Y. Cogah, W. B. Farnham, and T. V. TajanBabu, *J. Am. Chem. Soc.* **105**, 5706 (1983).
13. U.S. Pat. 4,417,034 (1984), O. W. Webster (to E. I. du Pont de Nemours & Co., Inc.).
14. Y. Nagasaki, Y. Sato, and M. Kato, *Macromol. Rapid Commun.* **18**, 827 (1997).
15. M. Vamvakaki, N. C. Billingham, and S. P. Armes, *Macromolecules* **32**, 2088 (1999).
16. G. Moad, D. H. Soloman, S. R. Johns, and R. I. Willing, *Macromolecules* **15**, 1188 (1982).
17. M. K. Georges, P. M. Veregin, P. M. Kazmeier, and G. K. Hamer, *Macromolecules* **26**, 2987 (1993).
18. M. Kato, M. Kamigaito, M. Sawamoto, and T. Higashimura, *Macromolecules* **28**, 1721 (1995).
19. M. Kato, M. Kamigaito, M. Sawamoto, and T. Higashimura, *Polym. Prep. Jpn.* **43**, 1792 (1994).
20. T. Ando, M. Kato, M. Kamigaito, and M. Sawamoto, *Macromolecules* **29**, 1070 (1996).
21. J.-S. Wang and K. Matyjaszewski, *Macromolecules* **28**, 7572 (1995).
22. J.-S. Wang and K. Matyjaszewski, *J. Am. Chem. Soc.* **117**, 5614 (1995).
23. T. E. Patten, J. Xia, T. Abernathy, and K. Matyjaszewski, *Science* **272**, 7970 (1996).
24. J. Chiefari, Y. K. Chong, F. Ercole, J. Krstina, J. Jeffrey, T. P. T. Le, R. T. A. Mayadunne, G. F. Meijs, C. L. Moad, G. Moad, E. Rizzardo, and S. H. Thang, *Macromolecules* **31**, 5559 (1998).
25. M. Desarac, D. Charmot, X. Franck, and S. A. Zard, *Macromol. Rapid Commun.* **21**, 1035 (2000).
26. R. T. A. Mayadunne, E. Rizzardo, J. Chiefari, Y. K. Chong, G. Moad, and S. H. Thang, *Macromolecules* **32**, 6977 (1999).
27. D. Charmot, P. Corpart, H. Adam, S. Z. Zard, T. Biadatti, and G. Bouhadir, *Macromol. Symp.* **150**, 23 (2000).
28. S. Yamago, K. Iida, and J.-I. Yoshida, *J. Am. Chem. Soc.* **124**, 2874 (2002).
29. S. Yamago, K. Iida, and J.-I. Yoshida, *J. Am. Chem. Soc.* **124**, 13666 (2002).
30. A. Goto, Y. Kwak, T. Fukuda, S. Yamago, K. Iida, M. Nakajima, and J. I. Yoshida, *J. Am. Chem. Soc.* **125**, 8720 (2003).
31. S. Yamago, K. Iida, M. Nakajima, and J.-I. Joshida, *Macromolecules* **36**, 3793 (2003).
32. D. M. Haddleton, E. Depaquis, E. J. Kelly, D. Kukulj, S. R. Morsley, S. A. F. Bon, M. D. Eason, and A. G. Steward, *J. Polym. Sci., Polym. Chem.* **39**, 2378–2384 (2001).
33. A. A. Gridnev and S. D. Ittle, *Chem. Rev.* **101**, 3611 (2001).
34. T. M. Trinka and R. H. Grubbs, *Acc. Chem. Res.* **34**, 18 (2001).
35. D. M. Lynn, B. Mohr, and R. H. Grubbs, *J. Am. Chem. Soc.* **120**, 1627 (1998).
36. D.-J. Liaw, C.-C. Huang, and P.-L. Wu, *Polymer* **42**, 9371 (2001).
37. E. Khosravi and Szymanska-T. Buzar, eds., *Ring Opening Metathesis Polymerization and Related Chemistry*, Kluwer Academic Publishers, Boston, Mass., 2002.
38. A. B. Lowe and C. L. McCormick, *Aust. J. Chem.* **55**, 367 (2002).
39. C. L. McCormick and A. B. Lowe, *Acc. Chem. Res.* **37**, 312 (2004).
40. K. Matyjaszewski, ed., *Controlled/Living Radical Polymerization*, Vol. 768, American Chemical Society, Washington, D.C., 2000.
41. K. Matyjaszewski, ed., *Advances in Controlled/Living Radical Polymerization*, Vol. 854., American Chemical Society, Washington, D.C., 2003.
42. B. S. Sumerlin, M. S. Donovan, Y. Mitsukami, A. B. Lowe, and C. L. McCormick, *Macromolecules* **34**, 6561 (2001).
43. M. S. Donovan, B. S. Sumerlin, A. B. Lowe, and C. L. McCormick, *Macromolecules* **35**, 8663 (2002).

44. B. S. Sumerlin, A. B. Lowe, D. B. Thomas, and C. L. McCormick, *Macromolecules* **36**, 5982 (2003).
45. S.-I. Yusa, Y. Shimada, Y. Mitsukami, T. Yamamoto, and Y. Morishima, *Macromolecules* **36**, 4208 (2003).
46. A. B. Lowe, B. S. Sumerlin, and C. L. McCormick, *Polymer* **44**, 6761 (2003).
47. D. B. Thomas, A. J. Convertine, R. D. Hester, A. B. Lowe, and C. L. McCormick, *Macromolecules* **37**, 1735 (2004).
48. Y. Mitsukami, M. S. Donovan, A. B. Lowe, and C. L. McCormick, *Macromolecules* **34**, 2248 (2001).
49. D. B. Thomas, A. J. Convertine, L. J. Myrick, C. W. Scales, A. B. Lowe, N. Ayres, and C. L. McCormick, *Macromolecules* **37**, 8941 (2004).
50. D. B. Thomas, B. S. Sumerlin, A. B. Lowe, and C. L. McCormick, *Macromolecules* **36**, 1436 (2003).
51. J. D. Watson and F. H. C. Crick, *Nature* **171**, 737 (1953).
52. E. Chargaff, *Experientia* **6**, 201 (1950).
53. M. H. F. Wilkins, A. R. Stokes, and H. R. Wilson, *Nature* **171**, 738 (1953).
54. D. L. Nelson and M. M. Cox, *Principles of Biochemistry*, 3rd ed., Worth Publishers, Inc., New York, 2000, p. 913.
55. D. Cooper, ed., *Nature Encyclopedia of the Human Genome*, Nature Publishing Group, London, 2003.
56. K. Itakura, J. J. Rossi, and R. B. Wallace, *Annu. Rev. Biochem.* **53**, 323 (1984).
57. D. Freifelder, *The DNA Molecule--Structure and Properties*, W. H. Freeman & Co., San Francisco, 1978.
58. V. Schranke and R. Allshire, *Science* **301**, 1069 (2003).
59. A. Kornberg, *DNA Replication*, W. H. Freeman & Co., San Francisco, 1980.
60. M. J. Chamberlin, *RNA Polymerasses: An Overview*, Cold Spring Harbor Laboratory, Cold Spring Harbor, N.Y., 1976.
61. N. Arnheim and H. Erlich, *Annu. Rev. Biochem.* **61**, 131 (1992).
62. M. E. Scott, *Am. Biotech. Lab.* **3**, 131 (1985).
63. D. M. Nelson, A. L. Lehninger, and M. M. Cox, *Principles of Biochemistry*, 3rd ed., Worth Publishers, Inc., New York, 2000.
64. A. L. Lehninger, *Principles of Biochemistry*, Worth Publishers, Inc., New York, 1982.
65. A. Fersht, *Protein Science: A Guide to Enzyme Catalysis and Protein Folding*, W. H. Freeman & Co., New York, 1999.
66. R. B. Merrifield, *J. Am. Chem. Soc.* **85**, 2149 (1963).
67. R. B. Merrifield, *Adv. Enzymol.* **32**, 221 (1969).
68. E. Gross and Meienhofer, eds., *The Peptides, Analysis, Synthesis, and Biology*, Academic Press, Inc., Orlando, Fla., 1979, pp. 43–48.
69. F. S. Collins, E. D. Green, A. E. Guthmacher, and M. S. Guyer, *Nature* **422**, 835 (2003).
70. R. S. Morrison, Y. Kinoshita, M. D. Honson, and T. P. Conrad, *Protein Chem.* **65**, 1 (2003).
71. A. G. Walton and J. Blackwell, *Biopolymers*, Academic Press, Inc., Orlando, Fla., 1973, pp. 12–13.
72. D. A. Brant and G. S. Buliga, in R. R. Colwell, ed., *Biotechnology of Marine Polysaccharides*, Hemisphere Publishers, Washington, D.C., 1985, pp. 30–73.
73. R. L. Whistler and E. F. Paschall, *Starch: Chemistry and Technology*, Academic Press, Inc., Orlando, Fla., 1965.
74. R. L. Whistler, *Industrial Gums*, 2nd ed. Academic Press, Inc., Orlando, Fla., 1973.
75. P. A. Sanford and A. Laskin, eds., *Extracellular Microbial Polysaccharides*, American Chemical Society, Washington, D.C., 1977.

76. R. L. Davidson, *Handbook of Water-Soluble Gums and Resins*, McGraw-Hill, Inc., New York, 1980.
77. P. M. Collins, ed., *Carbohydrates*, Chapman and Hall, London, 1987 p. 313.
78. R. F. Gould, ed., *Cabohydrate Sulfates*, American Chemical Society, Washington, D.C., 1978.
79. B. V. McCleary, A. H. Clark, I. C. Dea, and D. A. Rees, *Carbohydr. Res.* **139**, 237 (1985).
80. C. L. McCormick, in D. A. Brant and G. S. Buliga, eds., *Biotechnology of Marine Polysaccharides*, Hemisphere Publichers, Washington, D.C., 1985, pp. 232–245.
81. T. Bishop and H. J. Jennings, *The Polysaccharides*, Vol. I, Academic Press, Inc., Orlando, Fla., 1982, p. 291.
82. R. Moorhous, M. D. Walkinshaw, S. Arnott, ACS Symposium Series 45, American Chemical Society, Washington, D.C., 1977, pp. 90–98.
83. P. A. Sanford, *Pure Appl. Chem.* **56**, 879 (1984).
84. W. Pigman and D. Horton, eds., *The Carbohydrates*, Vols. IIA and IIB, Academic Press, Inc., Orlando, Fla., 1970.
85. E. Casu, in R. S. Tipson and D. Horton, eds., *Advances in Carbohydrate Chemistry and Biochemistry*, Academic Press, Inc., Orlando, Fla., 1985, p. 51.
86. T. P. Nevell and S. H. Zeronian, *Cellulose Chemistry and Its Applications*, John Wiley & Sons, Inc., New York, 1985.
87. R. Y. Lochhead, in R. Y. Lochhead, ed., *Encyclopedia of Polymers and Thickeners for Cosmetics*, Vol. 108, Allured Publishing Corp., 1993, pp. 95–135.
88. C. L. McCormick and P. A. Callais, *Polymer* **28**, 2317 (1987).
89. U.S. Pat. 4,278,790 (1981), C. L. McCormick.
90. U.S Pat. 4,024,335 (1977), M. D. Nicholson.
91. U.S. Pat. 3,447,939 (1969), D. L. Johnson.
92. R. A. A. Muzzarelli, *Carbohydr. Polym.* **3**, 53 (1983).
93. J. P. Zikakis, ed., *Chitin, Chitosan and Related Enzymes*, Academic Press, Inc., Orlando, Fla., 1984.
94. C. L. McCormick and D. K. Lichatowich, *J. Polym. Sci.* **17**, 479 (1979).
95. C. L. McCormick, D. K. Lichatowich, J. A. Pelezo, K. W. Anderson, and C. E. Carraher, eds., ACS Symposium Series 121, American Chemical Society, Washington, D.C., 1980, p. 371.
96. H. G. Elias, *Macromolecules* **2**, 1113 (1977).
97. Ref. 6, p. 31.
98. W. M. Kulicke, R. Kniewske, and J. Klein, *Prog. Polym. Sci.* **8**, 373 (1982).
99. R. A. M. Thomson, in C. A. Finch, ed., *Chemistry and Technology of Water Soluble Polymers*, Plenum Press, New York, 1983, pp. 31–70.
100. N. M. Bikales, in N. M. Bikales, ed., *Water Soluble Polymers*, Plenum Press, New York, 1973, pp. 213–225.
101. D. L. Visioli, M. S. El-Assar, and J. W. Vanderoff, *Polym. Prep. (Am. Chem. Soc., Div. Polym. Chem.)* **51**, 258 (1984).
102. J. M. Vanderhoff, D. L. Visioli, and M. S. El-Assar, *Polym. Prep. (Am. Chem. Soc. Div. Polym. Chem.)* **54**, 375 (1986).
103. U.S. Pat. 3,624,019, A. J. Frisque (to Nalco Chemical).
104. F. Candau, U. S. Leong, and R. M. Fitch, *J. Polym. Sci., Polym. Chem.* **23**, 167 (1984).
105. Y. K. Chong, T. P. T. Le, G. Moad, E. Rizzardo, and S. H. Thang, *Macromolecules* **32**, 2071 (1999).
106. C. Ladaviere, N. Dorr, and J. P. Claverie, *Macromolecules* **34**, 5370 (2001).
107. J. Loiseau, N. Doerr, J. M. Suau, J. B. Egraz, M. F. Llauro, C. Ladaviere, and J. Claverie, *Macromolecules* **36**, 3066 (2003).
108. D. Taton, Z.-Z. Wilczewska, and M. Destarac, *Macromol. Rapid Commun.* **22**, 1497 (2001).

109. N. Gaillard, A. Guyot, and J. Claverie, *J. Polym. Sci., Polym. Chem.* **41**, 684 (2003).
110. C. Burguiere, S. Pascual, C. Bui, J.-P. Vairon, B. Charleux, K. A. Davis, K. Mayjaszewski, and I. Betremieux, *Macromolecules* **34**, 4439 (2001).
111. L. Couvreur, C. Lefay, J. Belleney, B. Charleux, O. Guerret, and S. Magnet, *Macromolecules ASAP*, **36**, 8260 (2003).
112. R. H. Harding and J. K. Rose, in R. L. Davidson and M. Sittig, eds., *Water-Soluble Resins*, 2nd ed., Van Nostrand Reinhold, New York, 1982.
113. D. B. Braun, in R. L. Davidson, ed., *Handbook of Water-Soluble Gums and Resins*, McGraw Hill Book Co., Inc., New York, 1980.
114. W. H. Montgomery, in R. L. Davidson and M. Sittig, eds., *Water-Soluble Resins*, 2nd ed., Van Nostrand Reinhold, New York, 1962.
115. M. H. Stenzel, L. Cummins, G. E. Roberts, T. P. Davis, P. Vana, and C. Barner-Kowollik, *Macromol. Chem. Phys.* **204**, 1160 (2003).
116. C. Forder, C. S. Patrickios, N. C. Billlingham, and S. P. Armes, *Chem. Commun*. 883 (1996).
117. C. Forder, C. S. Patrickios, S. P. Armes, and N. C. Billingham, *Macromolecules* **29**, 8160 (1996).
118. C. S. Patrickios, C. Forder, S. P. Armes, and N. C. Billingham, *J. Polym. Sci., Polym. Chem.* **36**, 2547 (1998).
119. O. Fuchs, in J. Brandrup and E. H. Immergut, eds., *Polymer Handbook*, 3rd ed., Wiley-Interscience, New York, 1989, pp. vii–383.
120. S. R. Sandler and W. Karo, *Polymer Synthesis*, Vol. 2, Academic Press, Inc., New York, 1977.
121. L. Blecher, D. H. Lorenz, H. L. Lowd, A. S. Wood, and D. P. Wyman, in R. L. Davidson, ed., *Handbook of Water-Soluble Gums and Resins*, McGraw-Hill Book Co., Inc., New York, 1980.
122. J. L. Azorlosa and A. J. Martinelli, in W. H. Montgomery, R. L. Davidson, and M. Sittig, eds., *Water-Soluble Resins*, 2nd ed., Van Nostrand Reinhold, New York, 1962.
123. C. Tanford, *Physical Chemistry of Macromolecules*, John Wiley & Sons, Inc., New York, 1961.
124. G. S. Manning, *Annu. Rev. Phys. Chem.* **23**, 117 (1972).
125. J. Mykytiuk, S. P. Armes, and N. C. Billingham, *Polym. Bull.* **29**, 139 (1992).
126. S. P. Mannard, N. C. Billingham, S. P. Armes, and J. Mykytiuk, *Eur. Polym. J.* **29**, 407 (1993).
127. C. S. Patrickios, W. R. Hertler, N. L. Abbott, and T. A. Hatton, *Macromolecules* **27**, 930 (1994).
128. A. B. Lowe, N. C. Billingham, and S. P. Armes, *Chem. Commun*. 1035 (1997).
129. A. B. Lowe, N. C. Billingham, and S. P. Armes, *Macromolecules* **31**, 5991 (1998).
130. E. J. Ashford, V. Naldi, R. O'Dell, N. C. Billingham, and S. P. Armes, *Chem. Commun*. 1285 (1999).
131. D. M. Haddleton, E. Depaquis, E. J. Kelly, D. Kukulj, S. R. Morsley, S. F. A. Bon, M. D. Eason, and A. G. Steward, *J. Polym. Sci., Polym. Chem.* **39**, 2378 (2001).
132. B. Kesoshivianan, M. Georges, and D. Boils-Boissier, *Macromolecules* **28**, 6387 (1995).
133. L. J. Gabaston, S. A. Furlong, R. A. Jackson, and S. P. Armes, *Polymer* **40**, 4505 (1999).
134. U.S. Pat. 3,506,707 (1970), L. E. Miller and D. L. Murfin (to Lubrizol Corp.).
135. U.S. Pat. 3,332,904 (1967), E. M. LaCombe and W. P. Miller (to Union Carbide Corp.).
136. U.S. Pat. 3,692,673 (1972), D. I. Hoke (to Lubrizol Corp.).
137. U.S. Pat. 3,709,780 (1973), R. C. Slagel and G. D. Sinkovitz (to Calgon Corp.).
138. U.S. Pat. 3,709,816 (1973), J. E. Boothe III, and T. E. C. (to Calgon Corp.).
139. U.S. Pat. 3,709,816 (1973), J. L. Walker and J. E. Boother (to Calgon Corp.).
140. U.S. Pat. 3,679,000 (1972), P. R. Kaufman (to Lubrizol Corp.).

141. C. L. McCormick and G. S. Chen, *J. Polym. Sci. Chem.* **20**, 817 (1982).
142. C. L. McCormick and G. S. Chen, *J. Appl. Polym. Sci.* **29**, 713 (1984).
143. C. L. McCormick and C. B. Johnson, *Macromolecules* **21**, 694 (1988).
144. C. B. Johnson, Ph.D. dissertation, University of Southern Mississippi, Hattiesburg, Miss., 1987.
145. C. L. McCormick and K. P. Blackmon, *J. Polym. Sci. Chem. A* **24**, 2635 (1986).
146. C. L. McCormick, K. P. Blackmon, and D. L. Elliott, *J. Polym. Sci. Chem. A* **24**, 2619 (1986).
147. C. L. McCormick and K. P. Blackmon, *Macromolecules* **19**, 1512 (1986).
148. C. L. McCormick, K. P. Blackmon, and D. L. Elliott, *Macromolecules* **19**, 1516 (1986).
149. L. Shiyang and S. P. Armes, *Angew. Chem. Int. Ed.* **41**, 1413 (2002).
150. M. F. Hoover, *J. Macromol. Sci. Chem. A* **4**, 1327 (1970).
151. M. F. Hoover and G. B. Butler, *J. Polym. Sci., Polym. Chem.* **45**, 1 (1974).
152. E. W. Flick, *Water-Soluble Resins—An Industrial Guide*, Noyes, Park Ridge, N.J., 1986.
153. U.S. Pat. 4,663,159 (1987), G. L. Brode, R. L. Kreefer, D. Goddard, F. M. Merritt, and D. B. Braun, (to Union Carbide).
154. S. Wen, X. Yin, and W. T. K. Sevenson, *J. Appl. Polym. Sci.* **43**, 205 (1991).
155. S. Creutz, P. Tessie, and R. Jerome, *Macromolecules* **30**, 6 (1997).
156. F. L. Baines, N. C. Billingham, and S. P. Armes, *Macromolecules* **29**, 3416 (1996).
157. M. V. de Paz Banez, K. L. Robinson, and S. P. Armes, *Macromolecules* **41**, 451 (2000).
158. M. V. de Paz Banez, K. L. Robinson, M. Vamvakaki, S. F. Lascelles, and S. P. Armes, *Polymer* **41**, 8501 (2000).
159. K. Deboudt, M. Delporte, and C. Loucheux, *Macromol. Chem. Phys.* **196**, 279 (1995).
160. K. Deboudt, M. Delporte, and C. Loucheux, *Macromol. Chem. Phys.* **196**, 29 (1995).
161. M. Prady, J. Lokaj, M. Novotna, and S. Sevcik, *Makromol. Chem.* **190**, 2229 (1989).
162. T. Ohmae, S. Hosoda, H. Tanaka, H. Kihara, B. Jiang, Q. Ying, R. Qian, and T. Nakajima, *Pure Appl. Chem.* **65**, 1825 (1993).
163. F. Zeng, Y. Chen, S. Zhu, and R. Pelton, *J. Polym. Sci., Polym. Chem.* **38**, 382 (2000).
164. X. Zhang, J. Xia, and K. Matyjaszewski, *Macromolecules* **31**, 516 (1998).
165. X. Zhang and K. Matyjaszewski, *Macromolecules* **32**, 1763 (1999).
166. X. Zhang, J. Xia, and K. Matyjaszewski, *Macromolecules* **31**, 5167 (1998).
167. A. P. Narrainen, S. Pascual, and D. M. Haddleton, *J. Polym. Sci., Polym. Chem.* **40**, 439 (2002).
168. S. Liu, J. V. Weaver, M. Y. Tang, N. C. Billingham, and S. P. Armes, *Macromolecules* **35**, 6121 (2002).
169. L.-H. Gan, P. Ravi, B. W. Mao, and K.-C. Tam, *J. Polym. Sci., Polym. Chem.* **41**, 2688 (2003).
170. X. Bories-Azeau and S. P. Armes, *Macromolecules* **35**, 1024 (2002).
171. Y. Li, S. P. Armes, X. Jin, and S. Zhu, *Macromolecules ASAP* **36**, 8268 (2003).
172. J. Chiefari, Y. K. Chong, F. Ercole, J. Krstina, J. Feffery, T. P. T. Le, R. T. A. Mayadunne, G. F. Maijs, C. L. Moad, G. Moad, E. Rizzardo, and S. H. Thang, *Macromolecules* **31**, 5559 (1998).
173. A. B. Lowe and C. L. McCormick, Unpublished Results, 2003.
174. T. Alfrey, R. M. Fuoss, H. Morawetz, and H. Pinner, *J. Am. Chem. Soc.* **74**, 438 (1952).
175. V. Bütün, N. C. Billingham, and S. P. Armes, *Chem. Commun.* **7**, 671 (1997).
176. V. Bütün, C. E. Bennett, M. Vamvakaki, A. B. Lowe, N. C. Billingham, and S. P. Armes, *J. Mater. Chem.* **7**, 1693 (1997).
177. V. Bütün, N. C. Billingham, and S. P. Armes, *J. Am. Chem. Soc.* **120**, 11818 (1998).
178. M. R. Simmons and C. S. Patrickios, *Macromolecules* **31**, 9075 (1998).
179. M. R. Simmons and C. S. Patrickios, *J. Polym. Sci., Polym. Chem.* **37**, 1501 (1999).
180. M. V. de Paz Banez, K. L. Robinson, V. Bütün, and S. P. Armes, *Polymer* **42**, 29 (2001).

181. L.-H Gan, P. Ravi, B. W. Mao, and K.-C. Tam, *J. Polym. Sci., Polym. Chem.* **41**, 2688 (2003).
182. S. Creutz, P. Teyssie, and R. J. Jerome, *J. Polym. Sci., Polym. Chem.* **35**, 2035 (1997).
183. V. Bütün, S. P. Armes, and N. C. Billingham, *Polymer* **42**, 5993 (2001).
184. C. L. McCormick, K. P. Blackmon, and D. L. Elliott, *Polymer* **27**, 1976 (1986).
185. C. L. McCormick and L. C. Salazar, *J. Polym. Sci., Polym. Chem.* **31**, 1099 (1993).
186. D. B. Thomas, Ph.D. dissertation, University of Southern Mississippi, Hattiesburg, Miss., 2003.
187. M. J. Fevola, Ph. D. dissertation, University of Southern Mississippi, Hattiesburg, Miss., 2003.
188. G. B. Butler, *Cyclopolymerization and Cyclocopolymerization*, Marcel Dekker, Inc., New York, 1992.
189. R. S. Armentrout and C. L. McCormick, *Macromolecules* **33**, 419 (2000).
190. R. S. Armentrout and C. L. McCormick, *Macromolecules* **33**, 2944 (2000).
191. D. B. Thomas, *Macromolecules* **36**, 9710 (2003).
192. W. P. Shyluk, *J. Polym. Sci., Part A-2* **2**, 2191 (1964).
193. W. P. Shyluk, *J. Appl. Polym. Sci.* **8**, 1063 (1964).
194. W. P. Shyluk, *J. Polym. Sci., Part A-2* **6**, 2009 (1968).
195. W. P. Shyluk and R. W. Smith, *J. Polym. Sci., Part A-2* **7**, 27 (1969).
196. W. P. Shyluk, *J. Polym. Sci., Part A* **2**, 2191 (1964).
197. C. L. Lee, J. Smid, and M. Szwarc, *Trans. Faraday Soc.* **59**, 1192 (1963).
198. C. Tsitsiliani, G. A. Voyiatzis, and J. K. Kallitsis, *Macromol. Rapid Commun.* **21**, 1130 (2000).
199. N. Ekizoglou and N. Hajichristidis, *J. Polym. Sci., Polym. Chem.* **40**, 2166 (2002).
200. S. K. Varsheny, X. F. Zhong, and A. Eisenbert, *Macromolecules* **26**, 701 (1993).
201. F. Liu, Q. Wu, A. Eisenbert, 226th ACS National Meeting, American Chemical Society, New York, 2003.
202. T. Diaz, A. Fischer, A. Jonquieres, A. Brembilla, and P. Lochon, *Macromolecules* **36**, 2235 (2003).
203. Z. Chen, J. Cai, X. Jiang, and C. Yang, *Eur. Polym. J.* **37**, 33 (2001).
204. A. Fischer, A. Brembilla, and P. Lochon, *Eur. Polym. J.* **37**, 33 (2001).
205. M. Baumann and G. Schmidt-Naake, *Macromol. Chem. Phys.* **201**, 2751 (1999).
206. A. Fischer, A. Brembilla, and P. Lochon, *Macromolecules* **32**, 6069 (1999).
207. X. Z. Ding, A. Fischer, A. Brembilla, P. Lochon, *J. Polym. Sci., Polym. Chem.* **38**, 3067 (2000).
208. I. Chalari, S. Pispas, and N. Hadjichristidis, *J. Appl. Polym. Sci., Polym. Chem.* **39**, 2889 (2001).
209. J. Lokaj and P. Holler, *J. Appl. Polym. Sci.* **80**, 2024 (2001).
210. X. Ding, A. Fischer, and A. Brembilla, *J. Polym. Sci., Polym. Chem.* **38**, 3067 (2000).
211. J.-J. Yuan, R. Ma, Q. Gao, Y.-F. Want, S.-Y. Cheng, L.-X. Feng, A.-Q. Fan, and L. Jiang, *J. Appl. Polym. Sci.* **89**, 1017 (2003).
212. A. J. Convertine, B. S. Sumerlin, D. B. Thomas, and C. L. McCormick, *Macromolecules* **36**, 4679 (2003).
213. A. Ramakrishnan and R. Dhamodharan, *J. Macromol. Sci., Pure Appl. Chem. A* **37**, 621 (2000).
214. K. A. Davis and K. Matyjaszewski, *Macromolecules* **34**, 2101 (2001).
215. R. Yang, Y. Wang, X. Wang, W. He, and C. Pan, *Eur. Polym. J.* **39**, 2029 (2003).
216. G. B. Butler and N. Z. Zhang, in S. W. Shalaby, C. L. McCormick, and G. B. Butler, eds., *Water-Soluble Polymers Synthesis: Solution Properties, and Applications*, American Chemical Society, Washington, D.C., 1991, p. 37.
217. P. Molyeaux, *Water-Soluble Synthetic Polymers*, Vol. 2, CRC Press, Inc., Boca Raton, 1984, p. 50.
218. L. Y. Ji, E. T. Kang, K. G. Neoh, and K. L. Tan, *React. Func. Polym.* **46**, 145 (2000).

219. T. Ucchida, Furuzeno K. Ishihara, N. Nakabayashi, and M. Akashi, *J. Polym. Sci., Polym. Chem.* **38**, 3052 (2000).
220. K. Se, M. Kijima, R. Ohtomo, and T. Fujimoto, *J. Polym. Sci., Polym. Chem.* **35**, 1219 (1997).
221. K. Se, M. Kijima, and T. Fujimoto, *Polymer* **38**, 5755 (1997).
222. B. S. Sumerlin, A. B. Lowe, D. B. Thomas, A. J. Convertine, M. S. Donovan, and C. L. McCormick, *J. Polym. Sci., Polym. Chem. ASAP* **42**, 1724 (2004).
223. H. Wenker, *J. Am. Chem. Soc.* **57**, 2328 (1935).
224. D. Fischer, A. V. Harpe, K. Kunath, H. Peterson, Y. Li, and T. Kissel, *Bioconjugate Chem.* **13**, 1124 (2002).
225. G. Odian, *Principles of Polymerization*, 3rd ed. Wiley-Interscience, New York, 1991.
226. G. B. Butler and N. Z. Zhang, in S. W. Shalaby, C. L. McCormick, and G. B. Butler, eds., *Water-Soluble Polymers: Synthesis, Solution Properties and Applications*, ACS Symposium Series 467, American Chemical Society, Washignton, D.C., 1991, pp. 25–27.
227. K. Yamamoto, Y. Imamura, E. Nagatomo, T. Serizawa, Y. Muraoka, and M. Akashi, *J. App. Polym. Sci.* **89**, 1277 (2003).
228. Z. Hu, S. Zhang, and J. Yang, *J. App. Polym. Sci.* **89**, 3889 (2003).
229. L. Shi, T. M. Chapman, and E. J. Beckman, *Macromolecules* **36**, 2563 (2003).
230. D.-H. Hwang, J.-H. Chang, H.-K. Shim, and T. Zyung, *Syn. Met.* **119**, 393 (2001).
231. G. B. Butler, D. L. Skinner, W. C. Bond, and C. L. Rogers, *Polym. Prep.* **10**, 923 (1969).
232. G. B. Butler and N. Z. Zhang, *Water-Soluble Polymers: Synthesis, Solution Properties and Applications*, American Chemical Society, Washington, D.C., pp. 25–56.
233. C. C. Petropoulos, *J. Polym. Sci. A* **10**, 957 (1972).
234. T. Nonaka, L. Hua, T. Ogata, and S. Kurihara, *J. Appl. Polym. Sci.* **87**, 386 (2003).
235. T. Nonaka, H. Li, K. Makinose, T. Ogata, and S. Kurihara, *J. Appl. Polym. Sci.* **90**, 1139 (2003).
236. A. Kanazawa, T. Ikeda, and T. Endo, *J. Polym. Sci., Polym.Chem.* **31**, 335 (1993).
237. A. Kanazawa, T. Iked, and T. Endo, *J. Polym. Sci., Polym. Chem.* **31**, 3003 (1993).
238. D.-H. Hwang, I.-N. Kang, J.-I. Lee, L.-M. Do, H. Y. Chu, T. Zyung, Shim, and H.-K., *Polym. Bull.* **41**, 275 (1998).
239. A. B. Lowe and C. L. McCormick, *Chem. Rev.* **102**, 4177 (2002).
240. T. Alfrey, H. Morawetz, E. B. Fitzgerald, and R. M. Fuoss, *J. Am. Chem. Soc.* **72**, 1864 (1950).
241. T. Alfrey and H. Morawetz, *J. Am. Chem. Soc.* **74**, 436 (1952).
242. T. Alfrey, R. Fuoss, H. Morawetz, and S. H. Pinner, *J. Am. Chem. Soc.* **74**, 438 (1952).
243. T. Alfrey and S. H. Pinner, *J. Am. Chem. Soc.* **23**, 533 (1957).
244. A. Katchalsky and I. R. Miller, *J. Polym. Sci.* **14**, 57 (1954).
245. G. Ehrlich and P. Doty, *J. Am. Chem. Soc.* **76**, 3764 (1954).
246. F. Ascoli and B. Botre, *J. Polym. Sci.* **62**, S56 (1962).
247. C. L. McCormick and C. B. Johnson, *Macromolecules* **21**, 686 (1988).
248. C. L. McCormick and C. B. Johnson, *Macromolecules* **21**, 694 (1988).
249. C. L. McCormick and C. B. Johnson, *Polymer* **31**, 1100 (1990).
250. C. L. McCormick and C. B. Johnson, *J. Macromol. Sci. Chem. A* **27**, 539 (1990).
251. M. Kamachi, M. Kurihara, and J. K. Stille, *Macromolecules* **5**, 161 (1972).
252. M. Kurihara, M. Kamachi, and J. K. Stille, *J. Polym. Sci., Chem. Ed.* **11**, 587 (1973).
253. R. Varoqui, Q. Tran, and E. Pefferkorn, *Macromolecules* **12**, 831 (1979).
254. Y. Morishima, T. Hashimoto, Y. Itoh, M. Kamachi, and S. Nozakura, *J. Polym. Sci., Polym. Chem.* **20**, 299 (1982).

255. E. A. Bekturov, V. A. Frolova, S. E. Kudaibergenov, R. C. Schulz, and J. Zoller, *J. Makromol. Chem.* **191**, 457 (1999).
256. E. A. Bekturov, S. E. Kudaibergenov, R. E. Khamzamulina, V. A. Frolova, , E. E. Nurgalieva, R. C. Schulz, and J. Zoller, *J. Makromol. Chem. Rapid Commun.* **13**, 225 (1992).
257. S. Creutz, P. Teyssie, and R. Jerome, *Macromolecules* **30**, 6 (1997).
258. S. Creutz, J. V. Stam, F. C. D. Schryver, and R. Jerome, *Macromolecules* **31**, 681 (1998).
259. C. S. Patrickios, W. R. Hertler, N. L. Abbott, and T. A. Hatton, *Macromolecules* **27**, 930 (1994).
260. W. I. Chem, P. Alexandridis, C. K. Su, C. S. Patrickios, W. R. Hertler, and T. A. Hatton, *Macromolecules* **28**, 8604 (1995).
261. A. B. Lowe, N. C. Billingham, and S. P. Armes, *Macromolecules* **31**, 5991 (1998).
262. C. S. Patrickios, A. B. Lowe, N. C. Billingham, and S. P. Armes, *J. Polym. Sci., Polym. Chem.* **36**, 617 (1998).
263. S. Liu and S. P. Armes, *Angew. Chem. Int. Ed.* **41**, 1413 (2002).
264. S. Liu and S. P. Armes, *Langmuir* **19**, 4432 (2003).
265. S. Dai, P. Ravi, K. C. Tam, B. W. Mao, and L. H. Gan, *Langmuir* **12**, 5175 (2003).
266. F. Ascoli and C. Botre, *J. Polym. Sci.* **62**, S56 (1962).
267. C. S. Patrickios, *J. Colloid Interface Sci.* **175**, 256 (1995).
268. D. W. Roberts and D. L. Williams, *Tetrahedron* **43**, 1027 (1987).
269. U.S. Pat. 3,671,502 (1972), C. M. Samour and M. L. Flaxa (to The Kendall Co.).
270. M. Hahn, E. Gornitz, and H. Dautzenberg, *Macromolecules* **31**, 5616 (1998).
271. V. Barboiu, E. Streba, C. Luca, and C. I. Simionescu, *J. Polym. Sci., Polym. Chem.* **33**, 389 (1995).
272. N. Bonte and A. Laschewsky, *Polymer* **37**, 2011 (1996).
273. E. E. Kathmann, L. A. White, and C. L. McCormick, *Polymer* **38**, 879 (1997).
274. T. Nakaya and Y.-J. Li, *J. Prog. Polym. Sci.* **24**, 143 (1999).
275. K. Ishihara, T. Ueda, and N. Nakabayashi, *Polym. J.* **22**, 355 (1990).
276. Y. F. Wang, T. M. Chen, Y. J. Li, M. Kitamura, T. Nakaya, and I. Sakurai, *Macromolecules* **29**, 5810 (1996).
277. D. Hamaide, L. Germanaud, and P. L. Perchec, *Makromol. Chem.* **187**, 1097 (1986).
278. T. Nakaya, H. Toyoda, and M. Imoto, *Polym. J.* **18**, 881 (1986).
279. M.-L. Pujol-Fortin, and J.-C. Galin, *Polymer* **35**, 1462 (1994).
280. J.-C. Galin and M. Galin, *J. Polym. Sci., Polym. Phys.* **33**, 2033 (1995).
281. A. Biegle, A. Mathis, and J.-C. Galin, *Macromol. Chem. Phys.* **201**, 113 (2000).
282. H. Ladenheim and H. Morawetz, *J. Polym. Sci.* **26**, 251 (1957).
283. T. Umeda, T. Nakaya, and M. Imoto, *Makromol. Chem. Rapid Commun.* **6**, 285 (1985).
284. K. Sugiyama and T. Nakaya, *Makromol. Chem. Rapid Commun.* **7**, 679 (1986).
285. M. Yamada, Y.-J. Li, and T. Nakaya, *Macromol. Sci., Pure Appl. Chem. A* **32**, 1723 (1995).
286. A. B. Lowe, N. C. Billingham, and S. P. Armes, *Chem. Commun.* 1555 (1996).
287. Z. Tuzar, H. Posposil, J. Plestil, A. B. Lowe, F. L. Baines, N. C. Billingham, and S. P. Armes, *Macromolecules* **30**, 2509 (1997).
288. E. J. Lobb, I. Ma, N. C. Billingham, S. P. Armes, and A. L. Lewis, *J. Am. Chem. Soc.* **123**, 7913 (2001).
289. Y. Ma, S. P. Armes, and N. C. Billingham, *Polym. Mater. Sci. Eng.* **84**, 143 (2001).
290. I. Y. Ma, E. J. Lobb, N. C. Billingham, S. P. Armes, A. L. Lewis, A. Lloyd, and W. J. Salvage, *Macromolecules* **35**, 9306 (2002).
291. Y. Ma, Y. Tang, N. C. Billingham, S. P. A. L. Lewis, A. L. Lloyd, and J. P. Salvage, *Macromolecules* **36**, 3475 (2003).

292. M. Arotcarena, B. Heise, S. Ishaya, and A. Laschewsky, *J. Am. Chem. Soc.* **124**, 3787 (2002).
293. M. S. Donovan, A. B. Lowe, T. A. Sanford, and C. L. McCormick, *J. Polym. Sci., Polym. Chem.* **41**, 1262 (2003).
294. T. Ueda, H. Oshida, K. Kurita, K. Ishihara, and N. Nakabayashi, *Polym. J.* **24**, 1259 (1992).
295. K. Ishihara, *Trends Polym. Sci.* **5**, 401 (1997).
296. A. B. Lowe, M. Vamvakaki, M. A. Wassall, L. Wong, N. C. Billingham, S. P. Armes, and A. W. Lloyd, *J. Biomed. Mater. Res.* **52**, 88 (2000).
297. C. L. McCormick, ed. *Stimuli-Responsive Water Soluble and Amphiphilic Polymers*, ACS Symposium Series 780, American Chemical Society, Washington, D.C., 2000.
298. S. Y. Park and Y. H. Bae, *Macromol. Rapid Commun.* **20**, 269 (1999).
299. X. Qui, C. M. S. Kwan, and C. Wu, *Macromolecules* **30**, 6090 (1997).
300. M. Schops, H. Leist, A. DuChesne, and U. Wiesner, *Macromolecules* **32**, 2806 (1999).
301. I. Porcar, P. Sergot, and C. Tribet, *Stimuli-Responsive Water Soluble and Amphiphilic Polymers*, American Chemical Society, Washington, D.C., 2000, p. 82.
302. M. Irie and R. Iga, *Macromolecules* **19**, 2480 (1986).
303. H. Yamamoto, *Macromolecules* **19**, 2472 (1986).
304. Z. Tong, F. Zeng, X. Zheng, and T. Sato, *Macromolecules* **32**, 4488 (1999).
305. A. Hashidzume, Y. Morishima, and K. Szczubialka, in S. K. Tripathy, J. Kumar, and H. S. Nalwa, eds., *Handbook of Polyelectrolytes and Their Applications*, Vol. 2, American Chemical Society, Washington, D.C., 2002.
306. U. P. Strauss and E. G. Jackson, *J. Polym. Sci.* **6**, 649 (1951).
307. S. J. Assony and J. Layton, *J. Polym. Sci.* **9**, 509 (1952).
308. W. Kauzmann, ed., *Advances in Protein Chemistry*, Academic Press, Inc., Orlando, Fla., 1959.
309. P. Dubin and U. P. Strauss, *J. Phys. Chem.* **77**, 1558 (1973).
310. P. Dubin and U. P. Strauss, *J. Phys. Chem.* **71**, 2757 (1963).
311. P. Dubin and U. P. Strauss, *J. Phys. Chem.* **74**, 2842 (1967).
312. U. P. Strauss and G. Vesnaver, *J. Phys. Chem.* **79**, 1558 (1975).
313. U.S. Pat. 4,663,159, G. L. Brode and R. L. Kreeger (to Union Carbide Co.).
314. U.S. Pat. 4,352,916 (1982), L. M. Landoll.
315. U.S. Pat. 4,228,277 (1980), L. M. Landoll.
316. L. M. Landoll, *J. Polym. Sci., Polym. Chem.* **20**, 443 (1982).
317. U.S. Pat. 4,426,485 (1984), K. L. Hoy and R. C. Hoy (to Hercules, Inc.).
318. U.S. Pat. 3,779,970 (1973), S. Evani and R. H. Lalk (to Hercules, Inc.).
319. S. Evani and G. D. Rose, *Polym. Mater. Sci. Eng.* **57**, 477 (1987).
320. U.S. Pat. 3,963,684 (1976), S. Evani and E. P. Corson (to Union Carbide Co.).
321. U.S. Pat. 4,105,649 (1978), S. Evani and F. P. Corson (to Dow Chemical Co.).
322. J. E. Glass, *Polym. Mater. Sci. Eng.* **57**, 618 (1987).
323. U.S. Pat. 4,514,552 (1985), G. D. Shay, E. Eldridge, and J. E. Kail (to Dow Chemical Co.).
324. U.S. Pat. 4,600,761 (1986), C. G. Ruffner and J. M. Wilkerson (to Dow Chemical Co.).
325. J. Bock, D. B. D. N. Schulz, S. R. Turner, P. L. Valint, and S. J. Pace, *Polym. Mater. Sci. Eng.* **55**, 355 (1986).
326. U.S. Pat. 4,520,182 (1985), S. R. Turner, D. B. Siano, and J. Bock (to Exxon Research & Engineering Co.).
327. U.S. Pat. 4,528,348 (1985), S. R. Turner, D. B. Siano, and J. Bock (to Exxon Research & Engineering Co.).
328. C. L. McCormick and C. B. Johnson, *Polym. Mater. Sci. Eng.* **55**, 366 (1986).

329. C. L. McCormick and C. B. Johnson, T. Nonaka, *Polymer* **29**, 731 (1987).
330. C. B. Johnson, Ph.D. dissertation, University of Southern Mississippi, Hattiesburg, Miss., 1986.
331. S. A. Ezell and C. L. McCormick, *Macromolecules* **25**, 1881 (1992).
332. S. A. Ezell, C. E. Hoyle, and C. L. McCormick, *Macromolecules* **25**, 1887 (1992).
333. F. M. Winnik, M. A. Winnik, H. Ringsdorf, J. Venzmer, and S. E. Webber, *J. Phys. Chem.* **95**, 2583 (1991).
334. S. E. Webber, *Chem. Rev.* **90**, 1469 (1990).
335. H. Ringsdorf, J. Simon, and F. M. Winnik, *Macromolecules* **25**, 5353 (1992).
336. Y. Hu, M. C. Kramer, C. Boudreaux, and C. L. McCormick, *Macromolecules* **28**, 7100 (1995).
337. M. C. Kramer, J. A. Steger, Y. Hu, and C. L. McCormick, *Macromolecules* **29**, 1992 (1996).
338. Y. Morishima, *Prog. Polym. Sci.* **15**, 949 (1990).
339. Y. Morishima, T. Hashimoto, Y. Itoh, M. Kamaichi, and S. Nozakura, *J. Polym. Sci., Polym. Chem.* **20**, 299 (1982).
340. T. J. Martin and S. E. Webber, *Macromolecules* **28**, 8845 (1995).
341. S. Cruetz, J. V. Stam, S. Antoun, and R. Jerome, *Macromolecules* **30**, 4078 (1997).
342. C. K. Smith and G. Liu, *Macromolecules* **29**, 2060 (1996).
343. A. R. Eckert, T. J. Martin, and S. E. Webber, *J. Phys. Chem. A* **101**, 1646 (1997).
344. K. T. Wang, I. Illiopoulos, and R. Audibert, *Polym. Bull.* **20**, 577 (1988).
345. Y. Sato, A. Hashidzume, and Y. Morishima, *Macromolecules* **34**, 6121 (2001).
346. G. L. Smith and C. L. McCormick, *Macromolecules* **34**, 918 (2001).
347. G. L. Smith and C. L. McCormick, *Macromolecules* **34**, 5579 (2001).
348. G. L. Smith and C. L. McCormick, *Langmuir* **17**, 1719 (2001).
349. C. L. McCormick, C. E. Hoyle, and M. D. Clark, *Macromolecules* **23**, 3124 (1990).
350. C. L. McCormick and K. Kim, *J. Macromol. Sci., Chem. A* **25**, 285 (1988).
351. C. L. McCormick and K. Kim, *J. Macromol. Sci., Chem. A* **25**, 307 (1988).
352. F. Petit-Agnely, I. Iliopoulous, and R. Zana, *Langmuir* **16**, 9921 (2000).
353. F. Petit-Agnely and I. Iliopoulous, *J. Phys. Chem. B* **103**, 4053 (1999).
354. Z. Gao, A. Desjardins, and A. Eisenburg, *Macromolecules* **27**, 794 (1994).
355. J. K. Newman and C. L. McCormick, *Macromolecules* **27**, 5123 (1994).
356. H. Yamamoto and Y. Morishima, *Macromolecules* **32**, 7469 (1999).
357. M. Seki, Y. Morishima, and M. Kamachi, *Macromolecules* **25**, 6540 (1992).
358. Z. Gao, A. Desjardins, and A. Eisenberg, *Macromolecules* **25**, 1300 (1992).
359. K. Nagashima, V. Strashke, P. M. McDonald, R. D. Jenkins, and D. R. Bassett, *Macromolecules* **33**, 9329 (2000).
360. J. Selb and Y. Gallot, *Makromol. Chem.* **182**, 1491 (1981).
361. J. Selb and Y. Gallot, *Makromol. Chem.* **182**, 1513 (1981).
362. J. Selb and Y. Gallot, *Makromol. Chem.* **182**, 1775 (1981).
363. T. Noda, A. Hashidzume, and Y. Morishima, *Polymer* **42**, 9243 (2001).
364. T. Noda, A. Hashidzume, and Y. Morishima, *Langmuir* **17**, 5984 (2001).
365. V. Tirtaatmadja, K. C. Tam, and R. D. Jenkins, *Macromolecules* **30**, 1426 (1997).
366. V. Tirtaatmadja, K. C. Tam, and R. D. Jenkins, *Macromolecules* **30**, 3271 (1997).
367. S. Dai, K. C. Tam, R. D. Jenkins, and D. R. Bassett, *Macromolecules* **33**, 7021 (2000).
368. M. F. Islam and R. D. Jenkins, *Macromolecules* **33**, 2480 (2000).
369. S. Dai, K. C. Tam, and R. D. Jenkins, *Macromolecules* **33**, 404 (2000).
370. W. K. Ng, K. C. Tam, and R. D. Jenkins, *Polymer* **42**, 249 (2001).
371. P. G. deGennes, *Isr. J. Chem.* **35**, 33 (1995).
372. A. Halperin, *Macromolecules* **24**, 1418 (1991).
373. A. N. Semenov, J. Joanny, and A. Kholokov, *Macromolecules* **28**, 1066 (1995).

374. G. L. Smith, Ph.D. Dissertation, University of Southern Mississippi, Hattiesburg, Miss., 2001.
375. M. G. Baldwin, *J. Polym. Sci. A* **3**, 703 (1965).
376. W. Binana-Limele and R. Zana, *Macromolecules* **23**, 2731 (1990).
377. W. Binana-Limele and R. Zana, *Macromolecules* **20**, 1331 (1987).
378. U. P. Strauss and M. S. Schlesinger, *J. Phys. Chem.* **82**, 1627 (1978).
379. U. P. Strauss and M. S. Schlesinger, *J. Phys. Chem.* **82**, 571 (1978).
380. U. P. Strauss and G. Vesnaver, *J. Phys. Chem.* **79**, 2428 (1975).
381. C. L. McCormick and Y. Chang, *Macromolecules* **27**, 2151 (1994).
382. C. L. McCormick, C. E. Hoyle, and M. D. Clark, *Polymer* **33**, 243 (1992).
383. Y. Hu, M. C. Kramer, C. J. Boudreaux, and C. L. McCormick, *Macromolecules* **30**, 3526 (1997).
384. M. C. Kramer, C. G. Welch, J. R. Steger, and C. L. McCormick, *Macromolecules* **28**, 5248 (1995).
385. Y. Morishima, S. Nomura, T. Ikeda, M. Seki, and M. Kamachi, *Macromolecules* **28**, 2874 (1995).
386. Y. Morishima and M. Kamachi, *Proc. Am. Chem. Soc., Div. Polym. Mater. Sci. Eng.* **71**, 271 (1994).
387. Y. Morishima, in S. E. Webber, D. Tuzar, and P. Munk, eds., *Solvents and Self-Organization of Polymers*, Kluwer Academic Publishers, Dordrecht, the Netherlands, 1996, p. 331.
388. H. Yamamoto, M. Mizusaki, K. Yoda, and Y. Morishima, *Macromolecules* **31**, 3588 (1998).
389. F. Petit-Agnely and I. Iliopoulos, *J. Phys. Chem. B.* **103**, 4803 (1999).
390. L. Guillaumont, G. Bokias, and I. Iliopoulos, *Macromol. Chem. Phys.* **201**, 51 (2000).
391. C. L. McCormick, J. C. Middleton, and C. E. Grady, *Polymer* **33**, 4184 (1992).
392. K. D. Branham, Ph.D. dissertaion, University of Southern Mississippi, Hattiesburg, Miss., 1995.
393. K. D. Branham, C. L. McCormick, and G. S. Shafer, *Proc. Am. Chem. Soc. Div. Polym. Mater., Sci. Eng.* **71**, 423 (1994).
394. W. Peer, in J. E., Glass, ed., *Polymers in Acqueous Media: Performance Through Association*, Advances in Chemistry Series 223, American Chemical Society, Washington, D.C., 1989, p. 381.
395. S. A. Ezzell and C. L. McCormick, in W. Shalaby, C. L. McCormick, and G. B. Butler, eds., *Water Soluble Polymers, Synthesis, Solution Properties, and Applications*, ACS Symposium Series 467S, American Chemical Society, Washington, D.C., 1991, p. 130.
396. S. A. Ezzell and C. L. McCormick, *Macromolecules* **25**, 1881 (1992).
397. S. A. Ezzell, C. E. Hoyle, and C. L. McCormick, *Macromolecules* **25**, 1887 (1992).
398. U.S. Pat. 4,432,881 (1984), S. Evani (to Dow Chemical Co.).
399. C. L. McCormick, T. Nonaka, and C. B. Johnson, *Polymer* **29**, 731 (1988).
400. S. Biggs, A. Hill, J. Selb, and F. Candau, *J. Phys. Chem.* **96**, 1505 (1992).
401. C. Graillat, M. Lepais, and C. Pichot, *J. Dispersion Sci. Technol.* **11**, 455 (1990).
402. C. Holtzscherer and F. Candau, *J. Colloid Interface Sci.* **125**, 97 (1988).
403. F. Candau, Y. S. Leong, G. Pouyet, and S. Candau, *J. Colloid Interface Sci.* **101**, 167 (1984).
404. K. D. Branham, S. Snowden, and C. L. McCormick, *Macromolecules* **29**, 254 (1996).
405. E. Volpert, J. Selb, and F. Candau, *Macromolecules* **29**, 1452 (1996).
406. E. J. Regalado, J. Selb, and F. Candau, *Macromolecules* **32**, 8580 (1999).
407. C. Poncet, F. Tiberg, and R. Audebert, *Langmuir* **14**, 1697 (1998).

408. D. F. Anghel, V. Alderson, F. M. Winnik, M. Mizusaki, and Y. Morishima, *Polymer* **39**, 3035 (1998).
409. C. L. McCormick, C. E. Hoyle, and M. D. Clark, *Macromolecules* **24**, 2397 (1991).
410. C. J. Boudreaux, W. C. Bunyard, and C. L. McCormick, *J. Controlled Release* **40**, 223 (1996).
411. P.-L. Kuo, M.-N. Hung, and Y.-H. Lin, *J. Appl. Polym. Sci.* **47**, 1295 (1993).
412. C. J. Boudreaux, W. C. Bunyard, and C. L. McCormick, *J. Controlled Release* **44**, 171 (1997).
413. J. Chen, M. Jiang, Y. Zhang, and H. Zhou, *Macromolecules* **44**, 171 (1999).
414. R. Varadaraj, J. Bock, N. Brons, and S. Pace, *J. Phys. Chem.* **97**, 12991 (1993).
415. K. D. Branham, *Diss. Absstr. Int. B* **56**, 5518 (1996).
416. T. L. Lowe, J. Virtanen, and H. Tenhu, *Langmuir* **15**, 4259 (2000).
417. D. Tsiourvas, C. M. Paleos, and A. Malliaris, *J. Polym. Sci., Polym. Chem.* **31**, 387 (1993).
418. G. Akazome, S. Sakai, and K. Murai, *Kobunshi Kagaku* **17**, 618 (1960).
419. Y. Morishima, M. Kobayashi, and S. Nozakura, *Macromolecules* **20**, 1707 (1987).
420. Y. Morishima, T. Kobayashi, and S. Nozakura, *Polym. J.* **21**, 267 (1989).
421. Y. Morishima, Y. Tominaga, S. Nomura, and M. Kamachi, *Macromolecules* **25**, 861 (1992).
422. Y. Morishima, Y. Tominaga, S. Nomura, M. Kamachi, and T. Okada, *J. Phys. Chem.* **96**, 1990 (1992).
423. T. Noda and Y. Morishima, *Macromolecules* **32**, 4631 (1999).
424. A. Hashidzume, T. Noda, and Y. Morishima, in C. L. McCormick, ed., *Stimuli-Responsive Water Soluble and Amphiphilic Polymers*, ACS Series 780, American Chemical Society, Washington, D.C., 2001, p. 14.
425. T. Noda and Y. Morishima, *Macromolecules* **33**, 3694 (2000).
426. T. Noda, A. Hashidzume, and Y. Morishima, *Macromolecules* **34**, 1308 (2001).
427. S. Yusa, M. Kamachi, and Y. Morishima, *Langmuir* **15**, 6059 (1998).
428. J. C. Middleton, D. Cummins, and C. L. McCormick, *Polym. Prep. (Am. Chem. Soc., Div. Polym. Chem.)* **30**, 348 (1989).
429. J. C. Middleton, D. F. Cummins, and C. L. McCormick, in W. Shalaby, C. L. McCormick, and G. B., Butler, eds., *Water Soluble Polymers: Synthesis, Solution Properties, and Applications*, ACS Symposium Series 467S, American Chemical Society, Washginton, D.C., 1991, p. 338.
430. C. L. McCormick, J. C. Middleton, and D. F. Cummins, *Macromolecules* **25**, 1201 (1992).
431. Y. J. Yang and J. B. F. N. Egberts, *Recl. Trav. Chim. Pays-Bas* **110**, 384 (1991).
432. Y. J. Yang and J. B. F. N. Engberts, *J. Org. Chem.* **56**, 4300 (1991).
433. Y. J. Yang and J. B. F. N. Engberts, *Eur. Polym. J.* **28**, 881 (1992).
434. J. B. F. N. Engberts, *Pure Appl. Chem.* **64**, 1653 (1992).
435. G.-J. Wang and J. B. F. N. Engberts, *J. Org. Chem.* **59**, 4076 (1994).
436. G.-J. Wang and J. B. F. N. Engberts, *Langmuir* **10**, 2583 (1994).
437. Y.-F. Wang, T.-M. Chen, K. Okada, I. Sakurai, and T. Nakaya, *J. Polym. Sci., Part A: Polym. Chem.* **37**, 1293 (1999).
438. M. R. Talingting, P. Munk, S. E. Webber, and Z. Tuzar, *Macromolecules* **32**, 1593 (1999).
439. Z. Gao, S. K. Varshney, S. Wong, and A. Eisenberg, *Macromolecules* **27**, 7923 (1994).
440. L. Zhang and A. Eisenberg, *J. Am. Chem. Soc.* **118**, 3168 (1996).
441. L. Zhang and A. Eisenberg, *Macromolecules* **32**, 2239 (1999).
442. F. L. Baines, S. P. Armes, N. C. Billingham, and Z. Tuzar, *Macromolecules* **29**, 815 (1996).

443. A. B. Lowe, N. C. Billingham, and S. P. Armes, *Macromolecules* **32**, 2141 (1999).
444. C. S. Patrickios, C. Forder, S. P. Armes, and N. C. Billingham, *J. Polym. Sci., Polym. Chem.* **34**, 1539 (1996).
445. C. Forder, C. S. Patrickios, S. P. Armes, and N. C. Billingham, *Macromolecules* **30**, 5758 (1997).
446. V. Bütün, S. P. Armes, N. C. Billingham, Z. Tuzar, A. Rankin, J. Eastoe, and R. K. Heenan, *Macromolecules* **34**, 1503 (2001).
447. S. Liu, N. C. Billingham, and S. P. Armes, *Angew. Chem. Int. Ed.* **40**, 2328 (2001).
448. J. V. M. Weaver, S. P. Armes, and V. Bütün, *Chem. Commun.* **18**, 2122 (2002).
449. V. Bütün, M. Vamvakaki, N. C. Billingham, and S. P. Armes, *Polymer* **41**, 3173 (2000).
450. K. B. Thurmond, T. Kowalewski, and K. L. Wooley, *J. Am. Chem. Soc.* **119**, 6656 (1997).
451. H. Huang, T. Kowalewski, E. E. Remsen, R. Gertzmann, and K. L. Wooley, *J. Am. Chem. Soc.* **119**, 11653 (1997).
452. K. B. Thurmond, T. Kowalewski, and K. L. Wooley, *J. Am. Chem. Soc.* **118**, 7239 (1996).
453. Q. Zhang, E. E. Remsen, and K. L. Wooley, *J. Am. Chem. Soc.* **122**, 3642 (2000).
454. K. S. Murthy, W. Ma, C. G. Clark, E. E. Remsen, and K. L. Wooley, *Chem. Commun.* 773 (2001).
455. Q. Ma, E. E. Remsen, T. Kowalewski, J. Schafer, and K. L. Wooley, *Nano Lett.* **1**, 651 (2001).
456. J. Liu, Q. Zhang, E. E. Remsen, and K. L. Wooley, *Biomacromolecules* **2**, 362 (2001).
457. M. L. Becker, E. E. Remsen, and K. L. Wooley, *J. Polym. Sci., Polym. Chem.* **39**, 4152 (2001).
458. T. Sanji, Y. Nakatsuka, F. Kitayama, and H. Sakurai, *Chem. Commun.* 2201 (2000).
459. T. Sanji, Y. Nakatsuka, S. Ohnishi, and H. Sakurai, *Macromolecules* **33**, 8524 (2000).
460. V. Bütün, N. C. Billingham, and S. P. Armes, *J. Am. Chem. Soc.* **120**, 12135 (1998).
461. V. Bütün, A. B. Lowe, N. C. Billingham, and S. P. Armes, *J. Am. Chem. Soc.* **121**, 4288 (1999).
462. V. Bütün, and S. P. Armes, in C. L. McCormick, ed., *Stimuli Responsive Water Soluble and Amphiphilic Polymers*, American Chemical Society, Washington, D.C., 2000.
463. V. Bütün, W.-S. Wang, M. V. de Paz Banez, K. L. Robinson, N. C. Billingham, and S. P. Armes, *Macromolecules* **33**, 1 (2000).
464. S. Liu and S. P. Armes, *J. Am. Chem. Soc.* **123**, 9910 (2001).

CHARLES L. MCCORMICK
NEIL AYRES
Department of Polymer Science,
University of Southern Mississippi
ANDREW B. LOWE
Department of Chemistry and Biochemistry,
University of Southern Mississippi

WEATHERING OF POLYMERIC MATERIALS

Introduction

The resistance of polymeric materials to weathering is a very important consideration for their use in outdoor applications that depend on their durability. *Weathering* of a polymeric material may be defined as the irreversible changes in the material's chemical and physical properties in a direction that is usually to the detriment of its usefulness. Changes in appearance and mechanical properties result from modification of the chemical structure of the material by its complex interaction with the environmental elements, primarily solar radiation, heat/cold, moisture (solid, liquid, and vapor), oxygen, and pollutants. Although all weather factors play a very important role in the deteriorating effect of the environment on polymeric materials, the actinic radiation of the sun is the critical factor because it initiates the reactions that lead to degradation. Testing the weatherability of polymeric materials is an essential step in development of new and improved products and in ascertaining that production lots meet the specified requirements. Most polymeric products require stabilization against the effects of the environment to obtain reasonable serviceability. For some applications, polymeric materials are designed to degrade rapidly after their intended use in order to protect the environment. Weathering of "degradable" polymeric materials is not specifically addressed in this article, although much of the information on weatherability testing of polymeric materials is applicable.

The destructive effect of the weather varies with geographic location, season, time of day, cloud cover, and exposure orientation due to variations in the critical weather factors with these conditions as well as in individual years. Therefore, outdoor tests in one location during a specific time interval cannot be expected to provide information on either absolute durabilities or stability rankings of materials under all service conditions. To determine resistance to the worst conditions, tests are commonly carried out in environments that have the most severe conditions, such as subtropical or desert climates. As a result of the progressive improvement over the years in the durability of polymeric materials for outdoor applications, it is now impractical in many cases to screen potential new formulations by standard outdoor weathering tests, even those that provide severe environmental conditions. Therefore, accelerated outdoor weathering techniques and laboratory-accelerated weathering tests simulating the effects of natural weathering are required for development of weatherable formulations as well as for quality control and specification tests. Laboratory tests have the advantage of repeatability of test results and control of the three main test parameters, that is, radiation, heat, and moisture, for more consistent stability evaluations and for research studies on the effect of these parameters. Development of valid laboratory-accelerated tests requires measurement of the critical weather factors in the end use environment and determination of the effects of natural weathering on polymeric materials.

Weather Factors and Their Effect on Polymeric Materials.

Solar Radiation. Solar radiation on the earth's surface consists of energy received both directly from the solid angle of the sun's disk and diffusely reflected

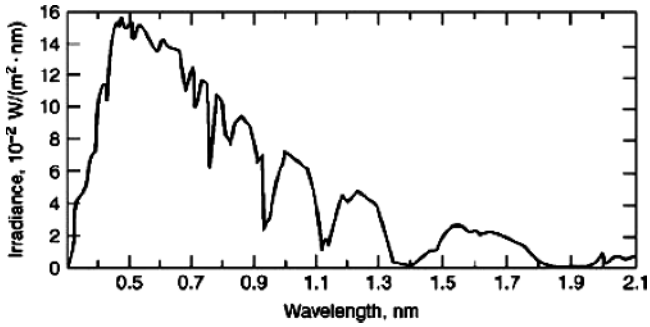

Fig. 1. Hemispherical solar spectral irradiance incident on a 37° sun-facing tilted surface (air mass of 1.5). Based on data in Table 2 of ASTM G173-08. Courtesy of ASTM International.

by the atmosphere. The diffuse component is strongly influenced by atmospheric conditions and is generally a large fraction of the total radiation, particularly in the UV region because of the greater scattering of the shorter wavelengths (1). For this reason, the spectral power distribution (SPD) of the diffuse component differs from that of the solar beam in that it contains a higher intensity of short wavelength radiation. Thus, the type of exposure that materials receive depends on their orientation. Samples positioned for maximum direct beam exposure receive less short wavelength radiation than those positioned for maximum exposure to sky radiation.

The hemispherical (direct plus diffuse) solar spectral irradiance incident on a 37°-tilted surface facing the equator at an air mass of 1.5, representative of average conditions in the 48 contiguous states of the United States, is shown in Figure 1 (2). It is referred to as "U.S. Standard Atmosphere." The spectral energy ranges from about 298 nm in the UV region to about 2500 nm in the near-infrared (NIR) region. Both the quantity and quality of solar radiation vary with time of day, season, altitude, geographical location, and atmospheric conditions. The shorter the wavelength, the more sensitive it is to these variables. The UV portion (298–400 nm), the portion that has the largest actinic effect on most materials, varies from less than 1% to about 5% of total solar radiation. Owing to the seasonal effect of the angle of the sun, at north latitude of about 41° the short wavelength cut-on of direct normal solar radiation shifts from below 300 nm in the summer to about 310 nm in the winter. At all latitudes, the altitude of the sun, and thus total solar irradiance, is highest at solar noon.

Because of the small percentage of UV present in the full solar spectrum, changes in this important component cannot be detected in measurements of total solar radiation. Therefore, commercial outdoor testing facilities measure and monitor the irradiance of the UV portion alone, both total UV and narrow spectral bands of the UV, in addition to total solar radiation. Total solar UV radiation (TUVR) is typically measured between 295 and 385 nm. Irradiance is reported in watts/square meter (W/m^2) and radiant exposure, ie, irradiance integrated over time, is reported in megajoules/square meter (MJ/m^2). The average

12-month TUVR radiant exposure is reported to be 308 MJ/m^2 at a 5° angle in a subtropical climate and 333 MJ/m^2 at latitude angle in a desert climate (3).

Spectral Effects of Solar Radiation: Activation Spectra. The wavelength-specific degradation of a material by the light source to which it is exposed is referred to as the activation spectrum. It is a graphical representation of the relative damage caused by individual spectral regions of the radiation source. Degradation is wavelength specific because both the absorption capability of the material for the incident radiation and the capability of the absorbed radiation to break some of the chemical bonds of the material, and thus initiate degradation, vary with wavelength. According to the first law of photochemistry, light must be absorbed by a material to have any effect on it. Since the energy of radiation is inversely proportional to its wavelength, the shorter the wavelength, the higher the energy of the photons associated with it. The shorter wavelengths also have a greater likelihood of being absorbed by materials. Therefore, the shorter the wavelength, the greater is its potential to break stronger and more types of chemical bonds. In order to be able to cleave specific chemical bonds, the radiation must contain wavelengths that have photon energies in excess of the binding energies of the chemical bonds. Thus, UV radiation generally has a greater deleterious effect on materials than visible radiation and the shorter the wavelength of UV, the more degradation it can be expected to cause. However, the wavelength-specific effectiveness of the light source in causing degradation also depends on the relative number of photons of each wavelength, ie, the wavelength-specific intensity of the radiation. Because the intensity of solar and solar-simulated UV radiation decreases nearly exponentially with decrease in wavelength, the shortest wavelengths cause less degradation than longer UV wavelengths in the majority of polymeric materials. Although the UV portion of solar radiation is mainly responsible for initiating weathering effects in polymeric materials, the visible and NIR portions also contribute to degradative processes. The damaging wavelengths of some colorless polymeric materials extend into the short wavelength visible region. Visible radiation absorbed by colored polymeric materials can cause photolytic bond cleavage of pigments followed by polymer degradation, initiated by the free radicals formed or due to charge-transfer processes. The absorbed visible radiation that does not have sufficient energy to cause bond cleavage and the NIR radiation absorbed by both colored and colorless polymeric materials raise the temperature of the materials and thus accelerate the chemical reactions initiated by the actinic wavelengths.

The activation spectra listed in Table 1 show that many polymeric materials are degraded to a greater extent by the longer UV wavelengths of simulated terrestrial solar radiation than by the shorter UV wavelengths. There are a number of reasons for this, including the fact that there are fewer photons associated with the shortest wavelengths of the light source. The activation spectra show that solar-simulated radiation shorter than 340 nm is responsible for the maximum amount of yellowing in less than half of the polymeric materials examined. The wavelengths listed represent just the peak(s) of the activation spectrum for each of the polymeric materials. Both longer and shorter wavelengths also cause degradation that decreases with both the increase and decrease in wavelength from the peak of the activation spectrum. In polymers

Table 1. Activation Spectra Based on Borosilicate Glass Filtered Xenon Arc Radiation

Polymeric Material	Type of Degradation	Mils	Wavelengths (nm) Causing Maximum Degradation (nm)
Acrylonitrile–Butadiene–Styrene (ABS)	Yellowing[a]	10	330
	Yellowing[b]	100	340–360
	Bleaching[a]	10	380–400
	Bleaching[b]	100	>380
	Impact strength	100	350–380[c]
	Impact strength	100	>380[d]
Nylon-6	UV, modulus	?	390, 450
Aromatic polyamides[e]	Yellowing and Tensile strength	?	360, 370, 414
Polyarylate	Yellowing[b]	3	350
	Yellowing[b]	60	385
Polycarbonate	Yellowing[a]	4.5	295, 310–340
	Yellowing[b]	28	<300, 310–340
Polyethylene	Yellowing[a]	4	310
	C=O increase[a]	4	340
Polyethylene-naphthalate	Yellowing, IR, modulus[a]	5	370–380
Polypropylene	C=O increase[a]	15	340–380
	C=O increase[b]	10	320
	Tensile strength[b]	60	320–350[c]
	Tensile strength[b]	60	360–380[d]
Polystyrene	Yellowing[a]	125	319
	Yellowing[b]	125	300–330
Polysulfone	Yellowing[a]	1	310–320
	Yellowing[b]	1	320
	C=O,OH increase	1	330
Aromatic polyurethane	Yellowing[a]	?	350–415[f]
Poly(vinyl chloride)	Yellowing[a]	2	308–325[f]
	Yellowing[b]	40	300–320

[a]Spectrographic technique.
[b]Sharp cut-on filter technique.
[c]Short exposure duration.
[d]Longer exposure duration.
[e]Films and fibers.
[f]Various samples.

such as acrylonitrile-butadiene-styrene (ABS), aromatic polyamides, polyarylate, polyethylenenaphthalate, and aromatic polyurethane, wavelengths longer than 340 nm are mainly responsible for yellowing. In all polymers, including those in which shortwavelength UV radiation causes yellowing, longwavelength UV is primarily responsible for degradation of physical properties, such as tensile strength

and impact strength. In some cases this extends into the visible region. The explanation for differences in damaging wavelengths with type of change lies in the differences in the wavelengths that affect the surface versus the bulk of the material. Short wavelengths, which are more strongly absorbed by most materials, have a greater effect on the layers close to the surface and cannot penetrate as far into the material as the longer wavelengths. Thus, the changes that occur in the surface layers, such as yellowing, opacity to UV radiation, and cracking and crazing, result from exposure to shorter wavelength radiation. Longer wavelengths penetrate more deeply into materials, where the physical property changes occur.

The activation spectra of ABS and polypropylene based on changes in impact strength and tensile strength, respectively, show a progressive shift to longer wavelength sensitivity with an increase in duration of exposure. It results from an increase in the absorption of longer wavelengths due to a progressive increase in chain length of the unsaturated conjugation species in aliphatic polymers and aliphatic portions of aromatic polymers. A similar shift to maximum degradation by longer wavelengths for extended exposures of polyethylene and poly(vinyl chloride) can be expected for the same reason. Pickett and co-workers (4) had shown that the yellowing of polycarbonate containing titanium dioxide is caused mainly by filtered xenon arc wavelengths shorter than 300 nm during initial exposure, but after a period of exposure the activation spectrum peaks at about 320 nm and identifies the 310–340 nm spectral region as being mainly responsible for yellowing. Damaging wavelengths vary with the thickness of aromatic-type polymers because of the shift in the tail end of the main absorption band to longer wavelengths with an increase in the thickness. For example, the activation spectra of two thicknesses of ABS and polyarylate show that the thicker specimens are degraded by the longer wavelengths of the light source. The activation spectrum of a polymeric material also depends on its formulation, particularly with the addition of UV absorbing components. Addition of a protective UV absorber will generally shift the damaging radiation to shorter wavelengths.

Photodegradations of polymeric materials are complex processes usually with many thermally dependent steps between absorption of the photons and the final products. Their wavelength sensitivities to a radiation source must be determined experimentally. The activation spectra cannot be determined by multiplication of the source-independent wavelength sensitivity (action spectrum) of the material by the emission spectrum of the light source at each wavelength (5). It also cannot be determined from the absorption spectrum of the material and the SPD of the light source, even if the chemical mechanism of degradation is known, as quantum efficiencies cannot be predicted from fundamental principles. The activation spectra shown in Table 1 are based on two techniques for obtaining activation spectra, the spectrographic and sharp cut-on filter techniques. They are described in the *Handbook of Polymer Degradation,* 2nd ed. (5), *ASTM G178* (6), and other publications (7–11).

Temperature. Elevated temperatures can significantly influence the destructive effects of light on polymeric materials by accelerating the rate of the secondary reactions and by altering the reaction processes following the primary photochemical step of bond breakage. For example, the increase with temperature of the rate of oxygen diffusion and rates of reactions of free-radical fragments

can alter the main mechanism of degradation. Therefore, temperature differences in various climatic zones of the earth are responsible to a large extent for the variations in weathering. The areas exposed to the greatest solar irradiance are also those exposed to the highest temperatures. Both are usually highest near the equator and decrease with increasing latitude. Because of differences among materials in the effect of temperature on the secondary reactions, the stability ranking of materials can change with increase in temperature.

Daily averages and extremes of air temperature are measured to quantify temperature conditions during exposure of specimens to natural weathering, but the temperatures that materials attain are higher than that of the surrounding atmosphere. The temperature of exposed materials depends on the amount of radiation absorbed, the emissivity of the specimen, thermal conduction within the specimen, and exchange of heat with the surroundings through conduction and convection. A large portion of the absorbed radiation is converted to heat, and the amount absorbed is closely linked to color, with white materials absorbing only about 20% of the incident energy and black about 90%. Thus, the darker the color the higher the temperature. Surface temperatures of exposed plastic specimens have been reported to reach 77°C (12), and specimens inside a closed automobile exposed to sunlight have been reported to reach 120°C (13). Because it is not practical to measure the surface temperature of individual test specimens, black panel and white panel temperature sensors are used to represent, respectively, the maximum and minimum temperatures attained by samples.

Temperature differences between the surface and bulk of polymeric materials, due to the low thermal conductivity and heat capacity of these materials, result in physical stresses. Daily and seasonal temperature cycling can cause mechanical stress in composite systems, such as between a coating and a substrate or between coating layers, because of mismatch in the thermal expansion coefficients. It often results in cracking and loss of adhesion of the coating. Temperature and its cycles can also affect the weathering of polymeric materials through its influence on the effect of moisture. An increase in the temperature accelerates hydrolysis reactions, whereas a reduction in the temperature results in condensation as dew on the material. Freeze/thaw cycling or thermal shocks due to cool rain hitting hot, dry surfaces induces mechanical stress that can cause structural failures in some systems, or accelerate degradation already initiated.

Moisture. Moisture is a critical variable for many polymeric materials. In combination with solar radiation, it can significantly contribute to the effect of weather, both by reacting chemically and by imposing mechanical stresses when it is absorbed or desorbed (14). It can also act as a solvent or carrier, for example, in leaching away plasticizers or in transporting dissolved oxygen. Examples of chemical reactions of moisture are hydrolysis of labile bonds in polymers such as polyesters, polyamides, and poly(ether)urethanes; the promotion of chalking of titanium dioxide (TiO_2) pigmented coatings; and chemical changes in building products exposed to solar radiation in a moist environment. Chalking results from the release of TiO_2 particles at the surface when the organic binder is degraded by the hydroxyl and perhydroxyl free radicals formed in the reaction between water, oxygen, and the titanium and hydroxyl ions produced on exposure of the pigment to UV radiation.

Compressive stresses on the surface and tensile stresses in the bulk of materials result from expansion of the volume of surface layers by absorbed moisture. During drying, reduction in volume of surface layers results in compressive stress in the bulk and surface tensile stress gradients. These stresses result in cracking and loss of adhesion of coatings. Solar radiation has a pronounced effect on the moisture-induced stresses because of the formation of hydrophilic groups, which increase the tendency of the material to absorb moisture. Also, embrittlement of the surface by solar radiation enhances the tendency to crack under tensile stresses during the drying period. High relative humidity levels in conjunction with heat, as, for example, in tropical and subtropical climates, often promote microbial growth, which can play a significant role in material degradation.

The form and amount of moisture vary widely, depending on the geographic area and ambient temperature. Moisture can take the form of humidity, dew, rain, frost, snow, or hail. Commercial exposure facilities typically measure two main types of moisture, relative humidity and wet time. The wet time is the amount of time during which liquid water is present on a material's surface due to condensation and precipitation. The span of time over which precipitation occurs and the time the sample surface is exposed to wetness are more important in weathering of materials than the total amount of precipitation. The penetration depth of moisture into the material, and thus the influence on weathering, is substantially greater when the total amount of precipitation is distributed over a longer time period.

Oxygen. Oxidative degradation of organic polymers is generally very slow at room temperature in the dark, but is greatly accelerated by solar radiation in the presence of oxygen. Photooxidation reactions account for most polymer failures that occur during outdoor exposure. The reaction products of oxygen with the free radicals formed as a result of bond cleavage by solar radiation propagate radical chain reactions that multiply the destructive effect of the radiation. Thus, the degradative effect of solar radiation and oxygen acting in combination with each other is synergistic, ie, it is considerably larger than the sum of both factors acting individually. Polymers containing carbon–carbon double bonds are most sensitive to oxidation, their sensitivity increasing with the degree of unsaturation. Saturated polymers are considerably less sensitive, particularly those having bulky side groups that interfere with the attack by oxygen. Tertiary carbon atoms are more susceptible to oxidation than secondary ones, unless they are shielded by bulky side groups, as in polystyrene. Polymers that contain activated carbon–hydrogen bonds, such as polyethers, polyesters, and polyamides, display a higher susceptibility to oxidation than other hydrocarbon polymers. Oxygen can also increase the amount of solar radiation absorbed by conjugated unsaturated hydrocarbons through formation of a complex with these structural components. The singlet state of oxygen formed by reaction of oxygen with sensitizers, such as ketones and certain dyes in the presence of solar radiation, is a very reactive form of the molecule. It is responsible for rapid deterioration of natural rubber and polymeric materials with conjugated unsaturation.

The importance of oxygen in the weathering process is evidenced by the fact that photooxidation in polymers, such as polyolefins, is significantly reduced toward the center of thick samples because of the limited supply of oxygen. The

penetration of oxygen into the polymer is a critical factor and is related to its rate of diffusion, which depends on the temperature, polymer type, and morphology. It has been shown that oxygen diffusion and not UV radiation becomes the rate-controlling process in photooxidation of polypropylene and polyethylene plaques at a depth at which the rate of oxygen consumption is greater than the rate at which it can be replenished from the environment (15–18).

Atmospheric Pollutants. Ozone is present in the earth's atmosphere both as a result of UV photolysis of oxygen in the upper atmosphere and as a result of reaction between terrestrial solar radiation and atmospheric pollutants such as nitrogen oxides and hydrocarbons from automobile exhausts. It is a powerful oxidant that can react rapidly with elastomers and other unsaturated polymeric materials to cause stiffening and cracking, particularly under mechanical stress. Other common air pollutants include sulfur oxides, hydrocarbons, nitrogen oxides, and particulate matter such as sand, dust, dirt, and soot. Some of these may react directly with organic materials, but have a much more severe effect in combination with other weather factors.

Acid rain is an important consequence of pollutants generated by modern industrial societies and has been shown to damage both organic and inorganic materials exposed to the environment. Dilute sulfuric acid is formed on the surface of materials from sulfur dioxide (SO_2) and water exposed to solar radiation. It causes rapid discoloration when it reacts with pigments and causes cross-linking (14) and embrittlement (19) of polymers. The results of the action of acidic pollutants and solar radiation on automotive coatings have been described (20).

Acid rain enhances hydrolytic degradation and thus is an important factor in weathering of polymeric materials in which the mechanism includes hydrolysis. Acids have also been shown to interfere with the use of hindered amine light stabilizers (HALS) to improve the light stability of acrylic urethane clearcoats. It is believed that acids may reduce the effectiveness of HALS by reacting to form salts, which are then washed out of the coating. While acids generally act synergistically with radiation to accelerate the effects of weathering, acid precipitations can also slow the aging processes in polymers (21).

Outdoor Weathering Tests. Outdoor weathering tests are commonly characterized as "natural" or "accelerated." Ideally, "natural" weathering would be the result of exposure of a material in its actual intended location and orientation. The term is, however, generally used for outdoor exposure on fixed angle racks in locations and orientations that maximize the effects of weathering components, particularly solar radiation. Since these exposures will generally produce higher degradation rates than the normal end-use environments, they are actually outdoor accelerated tests. In this article, "natural" exposures are divided into "static" exposure tests at fixed positions and "dynamic" exposure tests in which sample orientations are changed during the test, or in which the sun is tracked. "Accelerated" outdoor exposures include techniques that further increase either the temperature, solar irradiance, moisture, or some combination of these factors. Practices for natural and accelerated outdoor weathering of polymeric materials are described in ASTM D1435 (3), ASTM D4364 (22), and ISO 877 (23).

Most natural and accelerated outdoor weathering tests in the United States are carried out in either (or both) South Florida or CENTRAL Arizona. These have the two most important "benchmark" environments where materials typically fail fastest because of intensification of the weather elements responsible for degradation. South Florida has a subtropical climate with higher levels of the three critical weathering factors, solar radiation, temperature, and moisture, than are present in most end-use environments. The climate is particularly destructive to materials sensitive to moisture. A number of studies have shown that the South Florida climate has a twofold or higher weathering rate for coatings compared to that in central Europe. The CENTRAL Arizona desert has become a worldwide recognized standard exposure environment for testing in a climate typical of the hot and dry conditions of the desert, having summer solar radiant exposures and temperatures that are higher than those in South Florida. The large daily and summer-to-winter temperature swings also differentiate Arizona from South Florida environments. Other test sites are in tropical and temperate climates, industrial areas, and salt air locations. Often, the same materials are tested in several different climates.

Because of seasonal and year-to-year climatological variability of outdoor conditions, repeated testing during different seasons and over a period of at least 2 years is usually recommended. Results of tests conducted for less than 12 months will often depend on the particular season of the year in which they begin. To take into account the variability of weather, the performance of test materials should be evaluated by comparing their weatherability with that of one or more control materials of known performance exposed at the same time rather than in terms of absolute changes in the test materials. The use of a number of control materials of different durability and multiple replicate specimens of the test and control materials should be exposed for statistical evaluations of the test results.

Static Exposures. Outdoor static weathering tests can take numerous forms. Some of the variables include tilt angle, unbacked or backed exposure with various types of backing material, under glass exposure, additional wetting, and other special conditions, all of which have an impact on the critical weathering factors. The variables of static outdoor exposures are described in detail in ASTM G7 (24), ASTM G24 (25), and ISO 877 (23). The particular test variables chosen depend on the application of the material and should generally simulate the worst-case in-service conditions as closely as possible. Materials used with a backing should be exposed with a similar type backing to provide the higher temperatures and longer wetness times of typical in-use conditions. In some cases, the backing is painted black to increase surface temperature and degradation rates. Materials intended for applications indoors or in enclosures behind specific types of glass, such as in automotive interiors, require weathering tests simulating conditions found in their specific end-use environment. Because of variations in specimen temperature and time of wetness due to location of a specimen on the exposure rack and the type or color of adjacent specimens, control, and test specimens should be placed on a single test panel or on test panels adjacent to each other.

The direction and angle of the exposed samples, measured from the horizontal, influence the amount of total radiant energy received, the quality and

quantity of UV, the temperature, and time of wetness. The 45° angle facing toward the equator is the most widely used, probably because many of the early exposure tests were carried out at temperate latitudes at which this angle was considered to be the fixed angle for optimum solar radiation for the whole year. However, in both temperate and tropical zones, exposures at 0°–20° angles contain a higher proportion of the diffuse component of incident solar radiation and therefore higher annual doses of shortwavelength UV than exposures at higher angles of inclination (26,27). At 0° (horizontal) and 5° angles, samples are exposed to essentially the entire sky dome and experience higher temperatures and longer time of wetness and thus more rapid deterioration. The 5° angle is preferable because it provides for some drainage to reduce ponding and allows some of the dirt to be washed off by rain. It is used extensively by the automotive industry for exterior applications, such as surface coatings, and may be used as an alternate to horizontal exposures for items such as indoor–outdoor carpeting, artificial turf, and roofing materials.

Samples receive maximum annual total solar radiation at an angle equal to the latitude of the exposure station. At a more horizontal exposure angle, specimens are nearly perpendicular to the sun's radiation during the summer months when the UV content is highest (28). The 90° angle facing the equator is used to simulate in-service applications of construction materials such as sidings, windows, door profiles, and automotive components, eg., doors and seat backs. However, it provides significantly lower radiant exposure, temperature, and time of wetness than a 45° or smaller angle. Therefore, the rate of degradation is usually slower for many samples exposed at this than at other fixed angles. A 90° angle facing away from the equator is a common exposure angle for testing a material's resistance to mold/mildew in subtropical climates.

In applications of polymeric materials as building sealants, particularly for joint seals, a major stress factor acting synergistically with the critical environmental stress factors is mechanical movement. Both daily and annual cycles of expansion and contraction caused by variations in the temperature and moisture content of the sealants lead to premature cohesive and adhesion failure and thus to functional failure of the sealants. Studies have shown the importance of added cyclic movement during outdoor exposure in order to reliably assess the in-use performance of sealants as well as accelerate the test results (29). In the absence of mechanical cycling, only surface changes are accelerated, but periodic expansion and compression during weathering also accelerates deterioration in the bulk of the sealant. Specially designed exposure strain-cycling racks used to simultaneously subject sealants to cyclic movement and temperature change were shown to produce early failures similar to those that occur during in-service use (30).

Dynamic Exposures. While the incidence of critical weather parameters can be modified by the setting of the static exposure angle, at any one angle it is not optimum for all seasons. Several dynamic exposure techniques have been developed to further optimize the annual radiant exposure, temperature, and moisture delivery to specimens. One technique consists of changing exposure angle with seasonal changes of the sun's path. However, compared with fixed angle exposures of less than 90° in Florida and Arizona, the maximum increase in annual

solar radiant exposure is only about 12% (31). In a study using this technique applied to exposure of a coating in Florida, no appreciable acceleration in degradation was obtained compared with 5° south exposure (32).

Another type of dynamic exposure uses a motor-driven, follow-the-sun rack designed to maintain direct-normal conditions from sunrise to sunset by keeping the sample surface at a constant near-normal angle to the direct solar beam. It is often combined with variable angle exposure, but is mainly applicable to arid environments such as central Arizona where the direct beam component of solar radiation is high. Its efficiency is low in subtropical environments where the diffuse portion of solar radiation is a significant portion of the total irradiance. The option of adding water spray to this type of exposure provides a combination of three of the critical weather factors, increased radiant exposure, temperature, and moisture, which can significantly accelerate degradation rates of many materials over static exposures.

Accelerated Weathering Exposures. In spite of optimization of weather factors by site selection, type of backing, exposure angle, and follow-the-sun exposures, long periods of outdoor testing are required to establish the durability of modern materials. Options available to further accelerate degradation by natural weathering tests include black box enclosures for higher panel temperatures and longer wetness time than open or backed exposures and Fresnel reflectors for increased irradiance. Any major intensification of weather factors over those present under end-use conditions must be used with caution to avoid changing the types and mechanisms of degradation or altering stability rankings because of differences among materials in their response to intensified stress factors. This cannot be overemphasized.

Black-Box Exposures. The black box test was developed to simulate the air heatsink characteristics of an automotive body and thus provide the high temperatures encountered by the surface coatings and decorative trim on automobiles exposed to direct sunlight. Details of the black boxes and test procedures are given in ASTM G7 (24), ASTM D4141 (33), and SAE J1976 (34). The test panels form the top surface of an open aluminum box painted with flat black paint on the outside. The box is typically positioned at 5° from the horizontal, facing the equator, but can be positioned at any angle. Black-box exposures maintain surface condensation longer after daybreak and have elevated daytime temperatures, which extend longer into the evening, thus providing greater probability of interactions with the materials of the combined effects of irradiance, temperature, and moisture than in other types of exposures.

Black-Box under-Glass Exposures. These tests were designed specifically to simulate and accelerate the effect of interior automotive conditions. Air temperatures in the box may exceed 80°C under conditions of high outside ambient air temperature and solar irradiance. Exterior non-glass surfaces are painted flat black, and interior surfaces are left unpainted. The specimens, supported on a rack in a plane parallel to the glass cover at a distance of at least 75 mm (3 in.), can be unbacked or backed with either expanded aluminum or a solid backing such as plywood. Liquid water is prevented from accumulating on the specimen's surface by the cover glass, and blowers inside the box circulate enclosed air for better temperature distribution. The box is typically covered with

Fig. 2. Fresnel reflecting solar concentrators. Photo courtesy of Atlas Material Testing Technology LLC.

"single-strength" window glass that is 2–3 mm thick, although other types of glass more suitable to replicate the end-use application of the material exposed may also be used. Because of variability between different lots of glass, the relative performance of materials is best determined by testing them at the same time behind the same lot of glass.

Fresnel Reflector Solar Concentrator. The maximum acceleration of aging processes in outdoor weathering is obtained by exposure on a Fresnel-reflector panel rack that provides high intensity solar radiation of approximately eight suns to materials by following the sun and reflecting the sun's rays from an array of 10 flat mirrors onto a single target area. Figure 2 (35) is a photograph of a typical Fresnel reflector solar concentrator. These devices were originally developed at DSET Laboratories (part of the Atlas Weathering Services Group) in the mid 1960s. The device is a follow-the-sun rack with its axis oriented in a north–south direction. Mirrors are positioned as tangents to an imaginary parabolic trough. Test specimens are placed in frames and mounted on the target board on which the mirrors are focused. A blower forces air across the target to cool the test specimens and generally limits sample surface temperatures to about 5–15°C above the maximum temperature of equatorially mounted samples exposed to unconcentrated normal incidence radiation. Testing of samples exceeding 13 mm (0.5 in.) in thickness is not recommended because the cooling may not be sufficient for such samples. Oscillating or pulsing nozzles provide periodic spraying with deionized water to simulate the moisture conditions of conventional testing in semi-humid subtropical and temperate regions. Nighttime spray cycles simulate rain and dew. Special cycles have also been recently developed for more customization and to improve the similarity between moisture delivery on these devices and moisture processes that exist with natural weathering exposures. Tests carried out in the absence of a programmed moisture cycle are intended to simulate conventional exposure testing in desert, arid, and semiarid regions.

The test can be used to intensify either direct exposures or those behind glass. Descriptions of the device and guidelines for its use are given in ASTM G90 (36) and ISO 877 (23).

New features, related to temperature control, have been added to the Fresnel reflecting devices to improve repeatability and provide the capability to define specimen temperatures (37) These include (1) static temperature control to maintain a user-defined temperature of a reference specimen within device capability limits; (2) dynamic temperature control to match the temperature of a reference panel to the diurnal temperatures of a reference specimen exposed at the same time on a static exposure rack; and (3) control of nighttime heating of specimens to elevate low nighttime desert temperatures, especially in winter. This is useful for accelerating degradation as well as for matching the higher nighttime temperatures in Florida and other locations. The most recent development in acceleration of the effects of solar radiation is the "UV Concentrator," an ultraaccelerated device that provides up to 63× intensification of the UV and short wavelength visible portion of solar radiation while eliminating the NIR wavelengths that cause excessive specimen temperatures (38).

Because these devices only concentrate the direct rays of the sun and not the diffuse radiation, they require clear atmospheric conditions with little moisture, such as is prevalent in the Sonoran desert area of Central Arizona. Acceleration factors over conventional outdoor tests based on elapsed time to a predetermined change in property have been reported to vary from 2 to 11 using the basic Fresnel reflector solar concentrators for various polymer types and compositions (31). The acceleration factor varies with the material tested because the effect of increased irradiance and temperature on the degradation rate varies with the material and its formulation. Therefore, the stability rankings may differ from that of natural exposure. However, acceleration of degradation using Fresnel-reflector exposure can provide better correlation to natural exposures than laboratory-accelerated weathering due to the fact that the radiation source (the sun) does not contain any unnatural wavelengths of radiation. Good correlations as well as discrepancies have been reported between Fresnel-reflector exposures and standard outdoor tests based on stability ranking of polymeric materials (32,39–43).

Timing of Exposures. Methods of "timing" outdoor weathering tests include (1) chronological basis—exposure for a specified number of days, months, or years; (2) radiant exposure basis—exposure to a specified level of solar radiant energy in a specified wavelength region based on hemispherical radiation measurements at the same tilt and azimuth angle as the test specimens; and (3) property change in a weathering reference material (WRM)—exposure until a specified property change has occurred in a WRM exposed at the same time. Timing on a calendar basis has been the most widely used method of evaluating stabilities because of its simplicity, but it is subject to seasonal or year-to-year variations, especially for shorter weathering tests. Timing based on radiant exposure can reduce the seasonal and year-to-year variations in weathering due to inconsistent conditions of total solar and solar UV irradiance. Timing based on property change in a WRM can reduce variations in weathering also due to other weather factors, provided its response to all factors is similar to the response of the test materials.

Studies have shown that better correlations are obtained among exposures made at different times when timing is based on incident solar UV radiation rather than on incident total solar radiation (39,44–49). Timing based on only the portion of solar radiation that is responsible for the damage, that is, on the actinic portion identified by the activation spectrum of the material, should further improve correlations. Furthermore, since all actinic wavelengths are not equally destructive, the optimum method of timing should be on the basis of "effective" radiant exposure H_{Eff}. The latter can be determined by using the activation spectrum to weight the incident radiation in accordance with equation 1.

$$E_{\mathrm{Eff}}=\sum_{\lambda_1}^{\lambda_2} E_0(\lambda)\frac{[\Delta(\lambda)]}{[\Delta(\lambda_{\mathrm{max}})]} \tag{1}$$

where E_{Eff} is the effective irradiance, $E_0(\lambda)$ is the incident irradiance at a specified wavelength, $\Delta\ (\lambda_{\mathrm{max}})$ is the property change at the wavelength of the activation spectrum peak, and $\Delta\ (\lambda)$ is the property change at a specified wavelength.

The irradiance at the wavelength corresponding to the peak of the activation spectrum, $\Delta\ (\lambda_{\mathrm{max}})$, is normalized to 1.0, and irradiances at other wavelengths are multiplied by the fractional sensitivities obtained from the activation spectrum. The sum is the "effective" irradiance. The effective radiant exposure H_{Eff} is obtained by multiplying the total radiant exposure H_{Total} by the ratio of the effective irradiance divided by the total irradiance (eq. 2).

$$H_{\mathrm{Eff}}=\left[\frac{E_{\mathrm{Eff}}}{E_{\mathrm{Total}}}\right]H_{\mathrm{Total}} \tag{2}$$

Laboratory-Accelerated Weathering Tests. Laboratory-accelerated weathering devices have been used for nearly a century with increasing importance concomitant with the development of more weatherable materials and the need to determine in a short time the effects of natural exposures over prolonged periods. The importance of these devices lies in their ability to accelerate the weathering processes and provide variations of the individual weathering stresses for experimentation under controlled and consistent test conditions. They are particularly useful in research and development of new polymeric formulations and are also used for quality control and specification testing. Their application to prediction of service life under use conditions is continually improving as the technology of the instruments advances and new testing methodologies are developed (see the section Service Life Predictions).

These devices have the unique requirement of accelerating as well as simulating the effects of the natural environment. In some cases, simulation of a specialized environment is required as, for example, extreme climates or the miniclimate of the interior of an automobile. Appropriate acceleration techniques require knowledge of material-specific sensitivities to the weathering factors because the validity of the tests requires that the results correlate with the effects of natural exposure. Thus, the chemical and macroscopic changes induced in materials by laboratory-accelerated weathering and the relative stabilities of

the materials tested must be the same as those induced by natural weathering. These requirements can only be realized if the critical weather factors in the environment are appropriately intensified so that their complex interactions with the materials are reproduced. Although the variability of weathering factors in nature precludes an exact representation of the actual conditions, the least that should be achieved is simulation of the full spectral actinic radiation of sunlight by the laboratory test source and appropriate irradiance, temperature, and moisture conditions. The ability to closely control the conditions is now included in the basic design of most laboratory-accelerated weathering devices.

The single most important consideration when conducting laboratory-accelerated weathering tests is the SPD of the radiation source. Degradation is wavelength-specific because both absorption of the incident radiation and initiation of degradation, caused by bond breakage by the photon energies absorbed are wavelength-specific (see the section Spectral Effects of Solar Radiation: Activation Spectra). Therefore, simulation of the incident wavelengths and their relative intensities in terrestrial solar radiation is critical to simulation of the performance of polymeric materials under natural weather conditions. A close match to the short wavelength cut-on of solar radiation is essential when testing polymers such as polycarbonate or isophthalate-based esters and others that are particularly sensitive to small changes in radiation in this region. For polymeric materials that are degraded either mainly or to a large extent by the long wavelength UV of solar radiation and for colored materials, it is essential that the artificial source contains long wavelength UV and visible radiation in order to simulate the effects of natural weathering, Nevertheless, the SPD of some exposure sources commonly used in artificial weathering devices has very little resemblance to the SPD of hemispherical solar radiation on the earth's surface, referred to as "daylight." Users should directly measure the SPD or refer to the manufacturer of the artificial test device for specific information pertaining to the SPD produced by a particular light source with any additional optical filters.

Xenon Arc Devices. Laboratory-accelerated weathering tests advanced significantly with the introduction of xenon arc devices in the 1950s in Europe and in the 1960s in the United States. The properly filtered xenon arc more closely simulates terrestrial solar radiation in both the UV and visible regions than any other artificial test source. It has become established worldwide as the radiation source for optimum simulation of terrestrial solar radiation. Because the irradiance from the xenon arc can be adjusted and controlled, the SPD is presented in Figure 3 (50) in relation to that of daylight by normalization of the two at 560 nm. The filtered xenon arc emission closely matches the spectrum of terrestrial solar radiation in the region of the solar UV cut-on as well as in the full UV and visible spectral regions; the emission also contains NIR radiation. Coated NIR absorbing filters screen out about 50% of the 800- to 1000-nm radiation, thus reducing the excessive energy in this region of the xenon arc compared with daylight and reducing the heat it causes in materials that absorb this radiation. Other filters are used with the xenon arc to simulate exposure to daylight through window glass for applications in which this is required. Procedures for

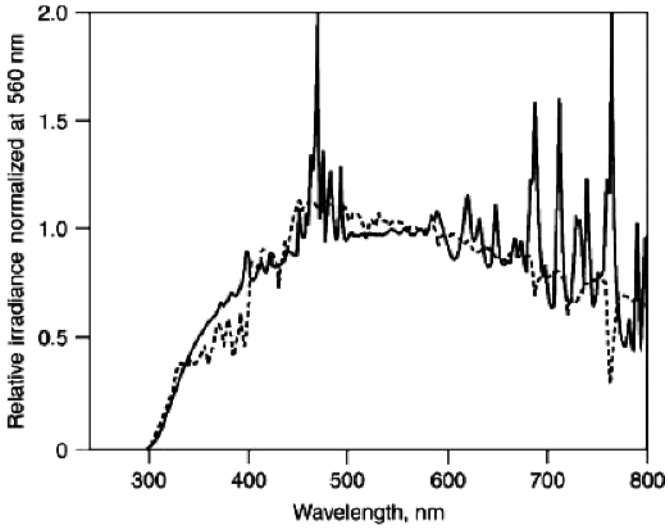

Fig. 3. Spectral power distributions of the water-cooled xenon arc with filters meeting ASTM and ISO requirements for daylight _____, and noon daylight in Miami, Fla. at 26° south exposure during the spring equinox _ _ _ _ _. Courtesy of Atlas Material Testing Technology, Reprinted from Ref. 5, copyright (2000) with kind permission from Marcel Dekker, Inc LLC.

exposure of polymeric materials in xenon arc weathering devices are given in ASTM Standards D2565 (51), D4459 (52) and G155 (53), and in the ISO 4892-2 (54) standard.

Photographs of the two different lamp/specimen configurations that have been developed for weathering tests using xenon arc exposure sources are shown in Figures 4 (55) and 5 (56). The most predominant of these incorporates a cylindrical specimen rack that rotates around a centrally located vertical xenon arc lamp. Larger instruments allow for placement of specimens on more than one tier, and these tiers are commonly inclined to provide uniform irradiance levels deposited onto the exposed specimens. The rack rotates around the light source for even more uniform irradiance and temperature distribution and to allow for periodic spraying, either on the front surface during exposure to radiation or on the back surface of the specimens during a dark period. Smaller, less expensive instruments place the xenon lamp horizontally over the specimens on a flatbed specimen tray, often tilted at 5° from the horizontal to facilitate water runoff during a water spray period. Irradiance and temperature uniformity is typically not as good as in rotating-rack instruments.

Two related xenon arc systems have been developed, air cooled and water cooled. The type of cooling has some influence on the overall design and on the optical filtering system but has a negligible effect on the SPD of the U/visible radiation. The irradiance in watts per square meter (W/m^2) in a specified spectral range is photometrically monitored, and the lamp power is automatically adjusted to maintain constant irradiance. It is commonly controlled at either 340 nm, referred to as "narrowband control," or over the full UV, 300–400 nm, referred to as "broadband control." In some cases, control includes the full UV and

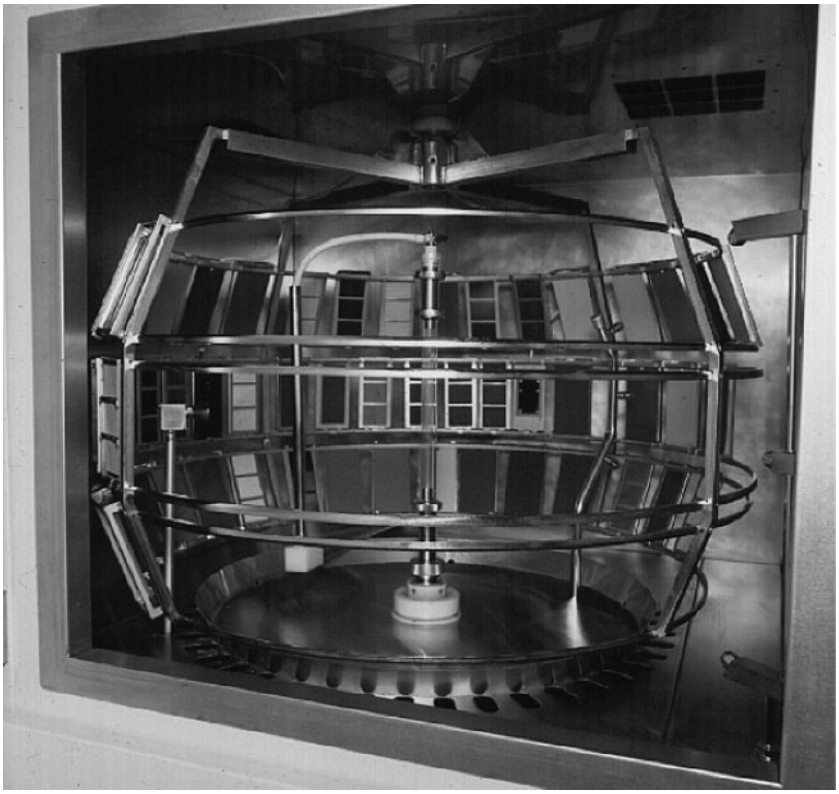

Fig. 4. Interior of a rotating-rack xenon-arc weathering instrument. Photo courtesy of Atlas Material Testing Technology LLC.

visible range, 300–800 nm. Most standard weathering tests currently specify an irradiance of 0.35 or 0.51 W/(m^2·nm) measured at 340 nm. The irradiance of 0.35 W/(m^2·nm) at 340 nm represents the daily average of irradiance measured at this wavelength over a full day in Miami, Florida, or Central Arizona at normal incidence under clear sky conditions during the spring equinox. It is half the peak irradiance of 0.68 W/(m^2·nm) at 340 nm measured at these locations at solar noon. The irradiance level of 0.51 W/(m^2 ·nm) at 340 nm is more representative of the type of exposures samples receive in Miami or Arizona for 2–3 h before and after solar noon and is equivalent to the irradiance setting used in ISO standards. Interest in using even higher irradiance is increasing because of the demands of the market for faster test results. This necessitates improved filter technology to better match the SPD of terrestrial solar radiation, in particular to restrict excessive heating of specimens by the xenon arc NIR radiation. The irradiance integrated over time is the radiant exposure in Joules per square meter, which may be automatically monitored. Test duration is often specified in terms of radiant exposure rather than in chronological time.

The UV radiation absorbed by any glass filters used with exposure sources cause "solarization" of the filters, resulting in a decrease in their UV transmission; the shorter the wavelength the greater the decrease. Deposition of some of

Fig. 5. Interior of a flat-bed xenon-arc weathering instrument. Photo courtesy of Atlas Material Testing Technology LLC.

the electrode material on the inside of the quartz envelope also decreases transmission. The automatic light monitoring and control systems of xenon arc devices can compensate for this to a large degree, but only at the wavelengths the device can monitor and control. Manufacturers of artificial testing instruments provide recommended lamp and filter replacement schedules, but these schedules are based on certain conditions. Lamp quality, water quality, irradiance levels, etc can cause aging to occur at higher or lower rates. The most effective way to know the appropriate time to replace these optical components is to measure the SPD directly, which has recently been made available. The criticality of an accurate SPD match as well as irradiance measurement and control of the actinic wavelengths in artificial weathering devices cannot be overemphasized, especially in connection with correlation studies and service life prediction methodologies. The use of an onboard spectroradiometer, such as the Full Spectrum Monitoring (FSM) system (57), permits continuous measurement and verification of the spectrum during exposure as well as irradiance control over the critical actinic wavelengths identified by the activation spectrum of the material.

Xenon arc devices have capabilities for temperature control as well. Standard test methods specify controlling the temperature of both the chamber air and a reference material (usually an insulated or uninsulated black metal panel). Specimens are heated to a large extent by the visible and NIR radiation they absorb but also by the heated air. Therefore, the specimen temperatures depend on the absorption properties of the materials as well as on the SPD and irradiance of the source. Generally, the black panel temperature specified is the maximum temperature that dark samples attain under use conditions, but it does not provide information on the temperature of actual test specimens of various colors

while on exposure. New technology has recently been developed for rotating-rack instruments incorporating a n-contact infrared pyrometer to measure temperatures of individual specimens as they rotate around the xenon arc lamp.

Moisture can be provided in xenon arc instruments in the form of water spray, condensation, immersion, or humidity. The type of moisture present can influence the type and rate of degradation. Many test procedures include more than one type of moisture. Commonly, the front surface of samples is periodically sprayed with cool, deionized water simultaneous with exposure to light. This imparts a thermal shock to the samples, but does not simulate natural weather conditions in which rain is unaccompanied by exposure to radiation. The formation of condensation on samples during the dark period is an effective means of simulating nighttime conditions in an environment with high moisture content, such as in South Florida. It is accomplished by providing high humidity conditions while cooling the back of the samples with ambient air or a water spray. High humidity can be as effective as liquid water. In many devices, during light or dark periods without water spray, relative humidity is automatically controlled to a specified level by moistening the air using either the evaporation or atomization technique. In devices in which wetting is by immersion, the sample is immersed in water while the surface is exposed to light.

The cycle that has been historically specified for wetting by water spray or immersion in most of the xenon arc test standards is 102 min light only followed by 18 min light plus wetting. Although it does not provide sufficient moisture to adequately represent the amount of moisture to which materials are exposed in humid climates, such as in Miami, Florida, it has been the main cycle used since the inception of laboratory-accelerated weathering tests. In the past few years, an alternate cycle providing more moisture has been included in test standards for sealants. It consists of 2 h light only followed by 2 h light plus wetting. Automotive weathering tests with xenon arc exposure use a cycle that also has equal periods of light and water spray, but most of the latter is during a dark period and includes condensation in an attempt to more closely simulate end-use conditions.

Fluorescent Ultraviolet Devices. Fluorescent UV lamps, similar in mechanical and electrical characteristics to fluorescent lamps used for residential and commercial lighting, have been developed with specific spectral distributions in the UV region. The emission properties of two most common types of fluorescent UV lamps, UVB-313 and UVA-340, are shown in Figure 6 (58) in comparison with the same daylight spectrum shown in Figure 3. Procedures for exposing polymeric materials in devices with fluorescent UV lamps are given in ASTM standards D4329 (59), D4587 (60), and G154 (61) and the ISO 4892–3 (62) standard.

In general, fluorescent UV devices produce moisture in the form of condensation during a dark period. The test surface is exposed to a heated, saturated mixture of air and water vapor. The relative humidity inside the chamber is approximately 100% during the dark cycle. The reverse side of the panel is exposed to room air that drops the panel temperature below the dew point, causing condensation (dew) on the exposed surface. The sequence and time intervals for both the UV exposure phase and condensation phase are programmable and

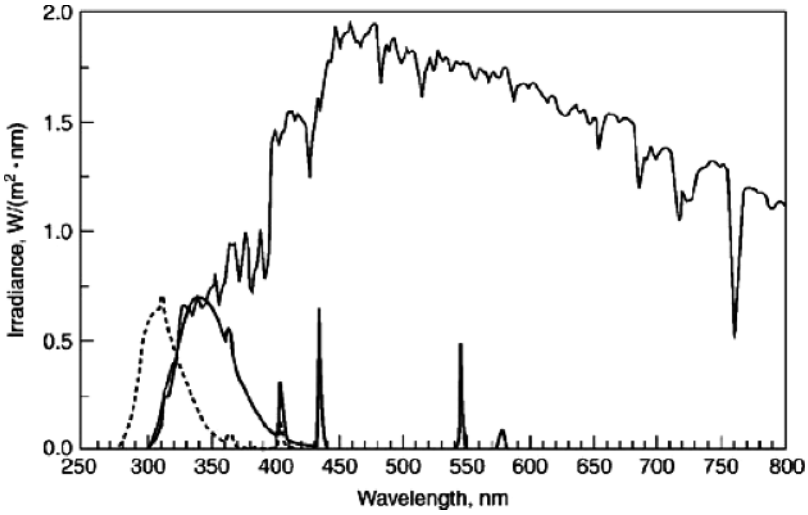

Fig. 6. Spectral power distributions of fluorescent UVB-313 lamps ……., fluorescent UVA-340 lamps,____, and noon daylight in Miami, Fla. at 26° south exposure during the spring equinox.____. Courtesy of Atlas Electric Devices, Reprinted from Ref. 5, copyright (2000) with kind permission from Marcel Dekker, Inc.

automatic. Spray cycles are commonly available as an option. Likewise, temperature can be controlled (within limits) during both the UV and condensation phases. Newer devices control irradiance at a wavelength appropriate for the type of fluorescent UV lamp used.

All fluorescent UV lamps are deficient in long-wavelength UV radiation and, except for a few mercury emission lines in the visible region, lack the visible and NIR energy present in daylight and xenon arc radiation. Thus, they are not suitable for testing materials that are sensitive to these spectral regions. Compared with stability ranking by daylight, reversals have been reported for materials exposed to these lamps as well as to the fluorescent UVA-351 lamps, which emit somewhat longer UV wavelengths (63). The UVB-313 lamps were previously commonly used because they provided rapid tests of the sensitivity of polymeric materials to UV radiation owing to the high flux of short wavelengths below the solar cut-on. However, because of the excessive short wavelength radiation, exposures to these lamps often caused reversals in stability rankings of polymers and errors in the performance of stabilizers compared with outdoor tests. These highly energetic wavelengths can initiate different mechanisms and types of degradation than the wavelengths present in solar radiation.

Because the UVB-313 type lamps generally cannot predict the outdoor performance of polymeric materials (64–66), the UVA-340 lamps are gradually replacing them in tests on polymers that are mainly sensitive to wavelengths in the 300- to 330-nm region. These lamps match the cut-on and short-wavelength spectral irradiance of solar radiation quite well in this region. However, in addition to the lack of actinic effects on materials sensitive to long wavelength UV and visible radiation, heating of colored materials by absorbed visible radiation is

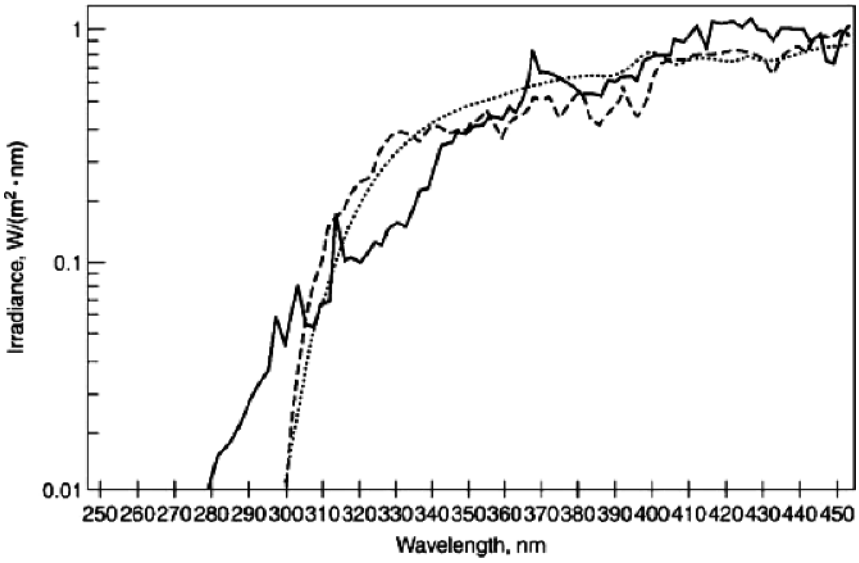

Fig. 7. Spectral power distributions of the water-cooled xenon arc with filters meeting "daylight" requirements ....., the filtered HMI metal halide lamp,____ and daily average of optimum daylight in Miami, Fla. measured at normal incidence during the spring equinox under clear sky conditions _ _ _ _ _. Courtesy of Atlas Material Testing Technology, Reprinted with kind permission from Hanser Gardner Publications, Inc.

absent. Therefore, in contrast to the temperature variations of differently colored materials exposed to a source that emits visible radiation, all materials attain the same (ambient) temperature. Thus, stability rankings will differ from those based on exposure to solar or solar-simulated radiation. Also, the mechanical stresses resulting from the heating and cooling of the absorbing surface layer are absent, resulting in reduced tendency to crack. For all these reasons, it is important to simulate the full SPD of the source to which the materials will be exposed under use conditions.

Metal Halide Lamps. The UV emission curve of the borosilicate-filtered menaury mercury medium-arc iodide (HMI) metal halide lamp is shown in Figure 7 (67) compared with the emission curves of daylight and filtered xenon arc radiation. It has a multiline spectrum, which can be considered to be a continuum for purposes of material testing. It gives a relatively good simulation of terrestrial solar radiation in the UV region above 300 nm but requires additional filtering of the short wavelength radiation for better simulation of daylight. Their high efficiency and low infrared output, which eliminates the need for water cooling, makes these sources ideally suited for use in large-scale multiple source arrays and are effective in thermal loading studies. However, metal halide lamps have technical problems that make them difficult to use in weathering systems. One is the dependence of the SPD of the radiation on the temperature of the lamp, thus requiring as constant a temperature as possible in the vicinity of the lamp.

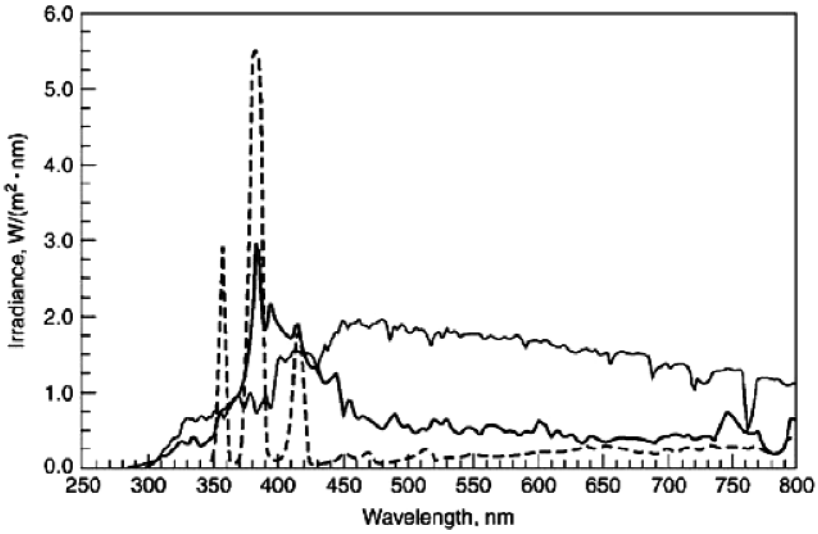

Fig. 8. Spectral power distributions of the enclosed carbon arc _____, the open flame carbon arc with Corex D filters _____, and noon daylight in Miami, Fla. at 26° south exposure during the spring equinox _____. Courtesy of Atlas Electric Devices, Reprinted from Ref. 5, copyright (2000), with kind permission from Marcel Dekker, Inc.

Because of the effect of temperature on the SPD, the latter changes with change in power. Therefore, the ability to alter the level of irradiance by changing the power is limited to about 5–10%. Reduction in irradiance is accomplished either by the use of close-meshed wire filters or by increase in the distance between the lamp and the sample. The other problem is the variation in SPD from one lamp to another of the same type. It is remedied by measuring the SPD of each lamp and selecting one that is applicable.

Carbon Arcs. Figure 8 (68) compares the representative UV/visible emission of two types of carbon arc radiation sources with daylight measured at noon at a 26°-tilt angle in Miami, FL during the spring equinox. The enclosed carbon arc uses both solid and cored electrodes burning within a semisealed borosilicate glass globe that provides optical filtering of the short wavelength UV radiation and an oxygen-deficient atmosphere to enhance the efficiency of the arc. The SPD differs significantly from that of terrestrial solar radiation in both the UV and visible regions. The enclosed carbon arc has a much weaker effect than solar radiation on materials that absorb only short wavelength UV radiation, but a stronger effect on materials that also absorb long wavelength UV radiation. Therefore, the stability ranking of materials that differ in the relative UV absorption characteristics in these regions can be expected to be distorted by this source compared with exposure to daylight. Procedures for using enclosed carbon arc devices for exposure of polymeric materials are given in ASTM standards D5031 (69), D6360 (70), and G153 (71).

The open-flame carbon arc device (also referred to as the Sunshine carbon arc) uses copper-coated electrodes operating in a free-flow of air in an open-flame

type lamp. The unfiltered arc emits a significant amount of short wavelength UV radiation below the solar cut-on. The SPD in Figure 8 represents the emission through Corex D borosilicate glass filters, commonly used to improve simulation to daylight in this region. Although the SPD of the radiation of the filtered open-flame carbon-arc is considerably improved over that of the enclosed carbon arc, it is still considered a poor match to terrestrial solar radiation. The open flame carbon arc used without the glass filters for faster testing, often produces reversals in stability rankings compared with outdoor testing because of the excessive amount of high energy radiation below the solar cut-on. It can also result in differences in degradation mechanisms and types of failure. Procedures for using the filtered open flame carbon arc devices for exposures of polymeric materials are given in ASTM standards D822 (72), D1499 (73), and G152 (74).

Both types of carbon arc devices have capabilities for periodic water spray on the samples and condensation during a dark period as well as for humidity and temperature control. The carbon arc devices typically require daily replacement of the carbon rods, cleaning of the filters or globes and periodic replacement of the latter because of changes in their transmission characteristics with exposure to UV radiation. There is a large volume of historical data using carbon arcs, and a number of test methods still specify their use; but this technology is largely being replaced with xenon arc systems.

Laboratory-Accelerated versus Natural Weathering. Laboratory-accelerated weathering tests have played an important role in development of polymeric materials with highly improved weatherability. However, because all types and modes of stresses present in an outdoor exposure cannot be simulated in a laboratory-accelerated test, the latter cannot replace natural exposure. It is a complimentary technique, the usefulness of which largely depends on how closely it reproduces the chemical and macroscopic changes in a material and the relative weatherabilities of materials under environmental conditions. Thus, correlation is a fundamental issue that must be considered when selecting a laboratory-accelerated weathering method. The critical weather factors, that is, the SPD of the radiation, temperature, and moisture, must be reasonably representative of those in the service environment and their effects accelerated without distorting the type of failure and mechanism of degradation as well as the stability ranking of the materials under natural exposure conditions. Higher irradiance than materials encounter under use conditions is very effective in accelerating degradation by laboratory weathering, but the irradiance must be below the level that distorts the degradation processes. Similarly, higher temperature is effective in accelerating the degradation reactions that follow bond breakage by the actinic radiation, but the temperature cannot exceed that which alters the degradation mechanism or distorts stability rankings. Acceleration of degradation must not interfere with good correlation with natural weathering (refer to the section on Correlation). Appropriate laboratory-accelerated tests that correlate with environmental effects have the potential of providing information to predict lifetimes of polymeric materials under natural weathering conditions. However, before drawing any final conclusions concerning the ability of a polymeric material to withstand the outdoor environment based on laboratory-accelerated weathering tests, it is necessary to validate the results by conducting outdoor exposure tests.

SPD of the Radiation Source. The SPD of the radiation source is the most critical weathering factor as degradation of polymeric materials, which is wavelength specific, is initiated by the actinic radiation absorbed. If the SPD of the radiation source used in the laboratory-accelerated test does not closely simulate the SPD of terrestrial solar radiation, the degradation mechanism and type of failure produced in materials can differ from those due to exposure to environmental conditions. The inability to simulate the degradation processes eliminates the possibility of predicting the service life of the materials based on laboratory-accelerated tests. Solar radiation on the earth's surface, shown in Figure 1, has a short wavelength UV cut-on of about 298 nm. The intensity is very weak at the shortest UV wavelengths and increases nearly exponentially to about 500 nm in the visible region. The intensity decreases from there, but the radiation continues into the NIR region. A close match to the cut-on wavelength and the SPD of the short UV wavelengths of solar radiation by the artificial source is important for tests of materials that are mainly degraded by these wavelengths. However, simulation of the SPD in the long wavelength UV and, at least, short wavelength visible regions is also essential for testing materials that are either solely or largely degraded by these regions (refer to Table 1). In a number of aromatic type polymers, different degradation mechanisms and type of degradation result from exposure to short versus long UV wavelengths. Absorption of short UV wavelengths results in photo-Fries rearrangements of the chemical structure, whereas absorption of longer UV wavelengths initiates photooxidation reactions involving free radicals. Therefore, the predominant mechanism of degradation of these polymeric materials is determined by the relative intensities of short-to-long wavelengths responsible for degradation and thus on the SPD of the radiation source. Some examples of differences in macroscopic changes in these polymers are bond scission versus cross-linking, chalking versus cracking and crazing of TiO_2-pigmented systems, and yellowing versus bleaching of the yellow color. The importance of simulating the SPD of the full solar spectrum is shown in Table 1 by the large differences in solar UV wavelengths to which different types of polymers are sensitive. Differences in the actinic wavelengths, that is, those responsible for degradation of a specific polymeric material, can be determined by comparison of the activation spectra of the material obtained using each of the radiation sources (refer to the section on Spectral Effects of Solar Radiation: Activation Spectra). Because of differences among polymeric materials in their absorption capabilities and in the effect of the absorbed radiation, the stability ranking of materials can vary with differences in emission properties of radiation.

Sources. The effectiveness of stabilizers, such as free radical scavengers and excited state quenchers, that act by interfering with the mechanism of degradation is dependent on the predominant mechanism of degradation and thus on the SPD of the radiation source to which the material is exposed. For example, HALS can only protect polycarbonate and aromatic polyurethane against the mechanism initiated by long wavelength UV. They are ineffective against the degradation caused by short wavelength UV. For this reason, evaluation of the performance of HALS in these polymers by exposure to a radiation source that primarily emits short UV wavelengths and lacks the long wavelength UV

radiation representative of solar radiation will give misleading information on their ability to protect the polymers against solar radiation. Also, significant differences have been shown among various types of exposures in the ability of HALS to protect against photooxidation of acrylic melamine coatings.

Owing to variation in the wavelengths primarily responsible for damage to a specific polymeric material with differences in the SPD of the radiation source, the screening requirements and thus the type of UV absorber required will differ. For example, activation spectra data showed that yellowing of a polyarylate film is caused mainly by 310- to 340-nm radiation when it is exposed to fluorescent UVB lamps, but by 335- to 365-nm radiation when it is exposed to solar radiation. Thus, this artificial test source cannot provide valid data on the protective effectiveness of an additive against solar radiation.

Irradiance. The solar irradiance levels to which materials are exposed under use conditions vary widely, depending on the geographic location, season, time of day, and exposure angle. Outdoor weathering tests are commonly carried out in geographic locations in which the materials are exposed to the most intense irradiance. In North America, these are South Florida and central Arizona where at solar noon on a clear day the UV irradiance at 340 nm reaches a maximum of about 0.68 W/(m^2·nm). During the 2–3 h before and after solar noon, the irradiance at 340 nm is approximately 0.50 W/(m^2·nm). In laboratory-accelerated xenon arc tests, the irradiance level is rarely higher than this and, historically, most ASTM standard xenon arc test methods have specified an irradiance of 0.35 W/(m^2.nm) at 340 nm. Acceleration of degradation is achieved by the 24-h exposure to the radiation in contrast to the few hours of solar irradiance at levels of about 0.50 W/(m^2.nm) at 340 nm. Solar irradiance is considerably lower in the early morning and late afternoon hours and does not exist during the nighttime periods. The xenon arc dose rate is three to eight times the rate in Miami, Florida.

One of the most obvious ways to shorten test time is to increase the irradiance level. However, use of high irradiance weathering tests requires an understanding of the effect of the increase in irradiance on predicting the performance of materials under environmental conditions. Simulation of the effects of natural weathering would be compromised if high irradiance levels alter the mechanism of degradation. Also, because all materials are not affected equally by an increase in irradiance, higher levels of irradiance than materials are exposed to under environmental conditions can alter the stability ranking of the materials. The dependence of the rate of degradation on the irradiance level is complex. It varies with the type of material, the formulation, including type of stabilizer, and wavelengths responsible for the degradation. For many polymeric materials, the degradation rate is not a linear function of irradiance. For example, rates of photooxidation of polypropylene have been shown to be proportional to various fractional powers of the light intensity ranging from the square root to the first power (75). The quantum yield of degradation, that is, the amount of degradation for a specific number of photons absorbed, often decreases with increasing irradiance. In a free radical process, this is partly explained by the "cage effect." Because of the higher concentrations of free radicals formed at higher irradiance levels, the likelihood of recombination is increased and reaction with oxygen and other

molecules is reduced. Owing to more rapid oxygen depletion at the higher irradiance levels, oxygen diffusion from the surface inward becomes the rate-limiting factor at some distance from the surface in photooxidation reactions. In addition, an increase in temperature accompanies an increase in irradiance of solar and solar-simulated radiation with its consequences on weathering tests of polymeric materials discussed in the next section of this article. Thus, the reciprocity law does not necessarily apply in many weathering tests, that is, doubling the intensity may not double the rate of degradation. A method to determine the effect of increased intensity of solar radiation at several temperature levels has been reported (76)

Temperature. Temperature can have a significant influence on the degradation of polymeric materials through increase in the rate and type of secondary reactions following bond breakage by the absorbed actinic radiation. In the geographic locations in which outdoor exposure tests are commonly carried out, atmospheric temperature as well as solar irradiance are highest. The temperature of the materials is higher than that of the atmosphere since a large portion of the absorbed visible and NIR solar radiation is converted to heat. Temperatures of polymeric materials as high as 120°C have been reported inside a closed automobile exposed to solar radiation (12) but are lower when exposed to the atmosphere. Specimens mounted on a thermal insulating backing have higher temperature than unbacked specimens and dark colored specimens have a higher temperature than white specimens.

During exposure to the radiation in laboratory-accelerated tests, the temperature is generally controlled at levels between 60°C and 89°C, depending on the material tested. While degradation can be accelerated by testing at temperatures higher than materials are exposed to under use conditions, caution must be exercised to avoid altering the mechanism of degradation and/or producing unrealistic types of degradation. The photodegradation process is complex, involving many chemical reactions with different activation energies. High temperatures accelerate reactions with high activation energies more than reactions with low activation energies. Since the latter may predominate under in use exposure conditions, high temperatures can alter the normal degradation processes. Often, a different degradation mechanism is triggered at a specific temperature, particularly if the temperature exceeds the glass transition temperature of the polymer. With an increase in the temperature, the rate of decomposition of hydroperoxides or of diffusion of oxygen or free radicals formed in primary processes increases allowing secondary reactions to take place that only occur at high temperatures. Change in the degradation mechanism from that produced under natural weathering conditions precludes simulation of the effects of environmental exposures and thus the potential of predicting lifetimes under in use conditions based on laboratory-accelerated tests. Since the effect of temperature varies with the type of polymer and its formulations, temperatures higher than those encountered in enduse environments can distort the stability rankings of materials in addition to causing unrealistic aging behavior in some of the polymeric materials.

The temperature differences exhibited by differently colored specimens exposed to solar radiation can only be simulated by a laboratory-accelerated weathering device that uses a full spectrum radiation source having an SPD

representative of that of solar radiation. In the latter, the black panel used for temperature control is largely heated by the visible and NIR radiation it absorbs. Heated chamber air supplies the additional heat required to reach the specified temperature. The temperature of colored specimens varies with the amount of radiation they absorb, being highest for black and lowest for white specimens. In contrast, in devices that use fluorescent UV lamps, because they lack visible and NIR radiation, hot chamber air is the main source of heat for temperature control by the black panel. Therefore, all samples, regardless of color, are heated to the same temperature that of the chamber air, which is considerably hotter than the chamber air in devices with a full spectrum radiation source. Thus, for the same black panel temperature control, in both types of devices the black specimens will attain the same temperature during exposure, but the white specimens will be exposed at a much lower temperature in the device with the full spectrum radiation source. The difference in temperatures of colored specimens will vary with the color.

Owing to the difference in the temperature of white samples in the two types of devices, exposure of an acrylic white sealant for 2000 h in each resulted in a major difference in the effect of weathering on the surface of the material (77). The black panel temperatures were 60°C in the fluorescent UVA-340 lamp device and 63°C in the xenon arc device. In the fluorescent UV device, the exposure resulted in substantial surface erosion and melting of the material at the edges as well as formation of rigid surface layers. Exposure in the xenon arc device resulted in very little change, similar to results of outdoor tests of the sealant. The most logical explanation is the difference in sample temperature in the two types of exposure.

Moisture. Moisture is one of the critical weathering factors contributing to degradation of polymeric materials exposed to environmental conditions. The various ways in which moisture, in combination with absorbed actinic radiation, can promote degradation is described in the section Weathering Factors and Their Effect on Polymeric Materials. The processes of photoinitiated oxidation and hydrolysis are enhanced by the presence of sufficient moisture. This was shown in a study on the effect of relative humidity on the photodegradation of an acrylic melamine coating. Both the rate and magnitude of chain scission and oxidation increased with an increase in relative humidity (78). While some polymers are themselves sensitive to moisture, often due to the moisture sensitivity of formulation ingredients, moisture can have a significant effect on weathering of the polymeric materials. For example, some plasticizers in PVC can be hydrolyzed under hot, humid conditions by traces of the hydrogen chloride released on exposure of PVC to UV radiation, resulting in significant loss in elongation.

Because water absorption by polymers from a humid atmosphere or by direct wetness is a diffusion-controlled process, the frequency and duration of the exposure to moisture is often a critical parameter. Weathering processes can be accelerated by more frequent swelling and contraction than that occurring during natural exposures. The length of the required wet period depends on the water diffusion coefficient and water absorption capacity of the material as well as on its thickness. Long periods of moisture may be required for some polymeric types.

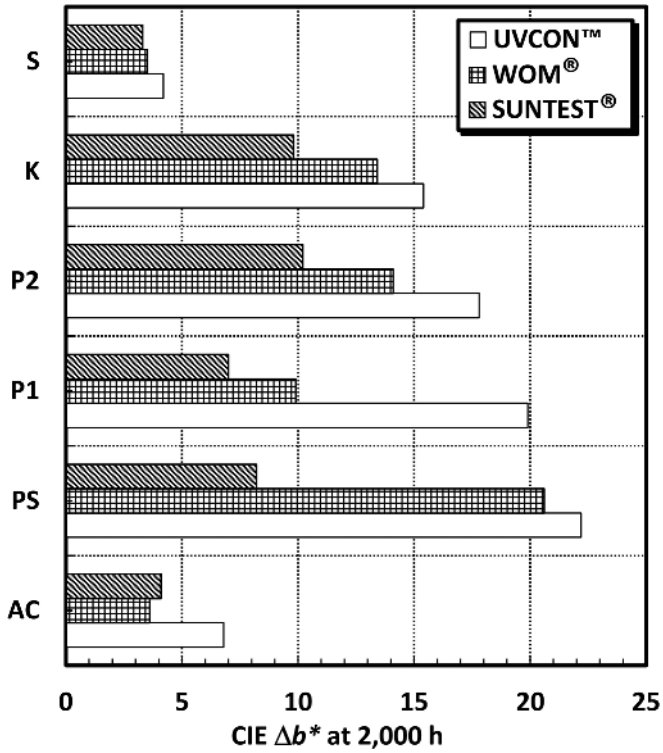

Fig. 9. Dependence of lightfastness (yellowing in terms of CIE Δb^*) of sealants (S = silicone; K = Kraton-based thermoplastic; P_2 and P_1 = one-component polyurethanes (P_2 softer than P_1); PS = polysulfide; AC = siliconized acrylic) on type of exposure (UVCON = fluorescent UVA-340; WOM = xenon arc with moisture; SUNTEST = xenon arc without moisture). Reprinted from Ref. 77, copyright 2000, with kind permission from RILEM Publications S.A.R.L.

The fact that moisture can have a significant influence on the degradation of polymeric materials initiated by absorbed actinic radiation is shown in Figure 9 (79). It compares data on the degradation of various types of sealants based on yellowing by three types of exposures (77). The WOM and SUNTEST are both xenon arc devices, but in the WOM, samples are periodically sprayed with water during exposure, whereas in the SUNTEST they are tested in the absence of added moisture. The irradiance level and black panel temperature were the same in both devices, 0.35 W/(m^2.nm) at 340 nm and 63°C, respectively. The UVCON contained fluorescent UVA-340 lamps and was operated using the cycle of 8-h radiation at 60°C followed by 4-h condensation at 50°C in the absence of UV radiation. The irradiance was estimated to be 0.7 W/(m^2.nm) at 340 nm. Although the irradiance at 340 nm is twice that in the xenon arc devices, it lacks the long wavelength UV of the xenon arc devices and exposes samples to radiation only two-thirds of the total exposure time. Exposure in all three devices was for 2000 h.

Differences in the increase in yellowness by the two xenon arc exposures varied with the type of sealant. However, for four of the six sealants, the WOM produced more severe yellowing than the SUNTEST. The difference was largest

for exposure of polysulfide, the polymer most sensitive to moisture, the weather factor that differed between the two types of xenon arc tests. The presence of moisture during exposure in the WOM also had a significant effect on the stability ranking of these sealants. Tests in the WOM ranked polysulfide as less stable than the Kraton-based thermoplastic (K) and polyurethane 2 (P_2), but tests in the SUNTEST, which lacked moisture, ranked polysulfide as more stable than K and P_2. Thus, the data demonstrate that for materials that are sensitive to moisture it is an important weathering factor

Experience has shown that the more intense yellowing of the samples exposed in the UVCON is due to the lack of long wavelength UV and visible radiation in the emission of the fluorescent UV lamps. These wavelengths are known to photobleach the yellow species produced by short wavelength UV radiation. Thus, photobleaching concurrent with the formation of yellow species on exposure to xenon arc and solar radiation is absent during exposure to fluorescent UV lamps.

Correlation. The term, "correlation," as applied to weathering tests, implies that the laboratory-accelerated weathering test produces similar weatherability rankings for a series of materials, that is, *rank correlation*, or the same types of failure modes as weathering under environmental conditions. The term has also been used when comparing tests by linear regression analysis of the weathering data or in terms of similar profiles of graphed data for change versus exposure time or radiant exposure. The term, "correlation" has often been erroneously used for the relation between tests in terms of exposure times to produce equal levels of degradation. The latter is the "acceleration factor." Ideally, the laboratory-accelerated test should satisfy all correlation criteria to provide a reliable early evaluation of the weatherability of a polymeric material. Good correlation between laboratory-accelerated and environmental weathering tests depends on simulation of the SPD of the natural source, environmental surface temperature of the materials, type and total amount of moisture, relative humidity level during exposure to the radiation, and the light/dark cycle. The reasons for the importance of closely matching the SPD of the artificial test source to the SPD of terrestrial solar radiation and the consequences of exposing materials to an abnormally high level of irradiance or temperature were described in earlier sections of Laboratory-Accelerated versus Natural Weathering. For some materials, continuous exposure to light without a dark period can preclude correlation with natural exposures due to elimination of critical dark reactions that occur during outdoor exposures. Simulation of the natural balance of all critical weathering factors by the laboratory-accelerated test is required to reproduce the degradation processes that occur under environmental conditions, that is, provide good correlation. Because of the synergistic effects of the weather factors and the complex nature of the weathering processes, acceleration by intensification of one factor alone can distort degradation mechanisms, failure modes, and stability ranking of materials. In the absence of good correlation with natural weathering degradation processes based on all the latter criteria, the laboratory-accelerated weathering test cannot be used in methodologies to predict service life of polymeric materials.

Factors that can interfere with correlation between laboratory-accelerated tests and natural exposures are described in ASTM G151 (80). Performance

rankings can vary with the duration of exposure and thus with the extent of degradation at which they are determined. Therefore, correlation should be evaluated at an optimum point in the exposures (64). The extent of correlation between two types of tests may also depend on the material property measured as the criterion of degradation. Similar to the effect of the season on the test results of some materials in which the outdoor weathering test is started, in laboratory-accelerated tests for some materials, whether they are exposed first to a dry period with radiation or first to a wet, dark period can alter their resistance to weathering (81). Some studies have claimed a high correlation between artificial and natural weathering, at least for certain performance properties. For example, in the study shown in Figure 9, very good correlation was obtained between xenon arc exposure that included water spray and humidity control and exposure in South Florida. Simulation in laboratory-accelerated weathering tests of the atmospheric acid precipitations to which materials are subjected in outdoor exposures has been shown to improve correlations based on stability ranking and type of degradation for various types of polymeric materials including sealants and automotive clearcoats (20,21,82,83). Test conditions that give good correlation with one exposure site for one type and formulation of a material do not necessarily assure good correlation to other sites or for other materials.

Acceleration Factors. The appropriate term for the relation between test times for laboratory-accelerated and outdoor weathering exposures that produce the same extent of degradation is *acceleration factor.* It is the time under natural exposure divided by the time in the accelerated test, both based on the same criterion of degradation. Acceleration over "real-time" weathering can be accomplished in several ways (1) by continuous exposure to the critical weather factors, uninterrupted by the diurnal cycle and variations in weather conditions; (2) by continuous exposure to irradiance levels that are only encountered during optimum conditions outdoors; and (3) by setting irradiance, temperatures, relative humidity, and thermal and moisture cycles to higher stress levels than materials encounter under end-use conditions. The acceleration factor is only valid if the laboratory-accelerated weathering test does not alter the degradation mechanism, cause unnatural failure modes or distort stability ranking of the test materials, that is, provides good correlation with outdoor exposure. For years, accelerated weathering test methods, both in the laboratory and outdoors, have only moderately intensified the stress factors. An acceleration factor of 10 has generally been considered the maximum for obtaining good correlation. The belief is that the greater the acceleration, the poorer the correlation. Very little attention has been given to studies on greater intensification of stress factors and its effect on correlations with weathering under in use conditions and thus on its use in predicting long-term service life of polymeric materials. However, due to the development of polymeric materials capable of 20 or more years of satisfactory service, there is a need for highly accelerated tests to evaluate new materials for this application. Therefore, techniques to further accelerate degradation by both natural and laboratory-accelerated weathering tests have been surfacing to be followed by verifications of their validities.

Acceleration factors are material dependent and can be significantly different for each material and for different formulations of the same material.

Therefore, it is not possible to establish a single acceleration factor for a laboratory-accelerated test to predict lifetimes under natural weather conditions for a variety of materials and formulations. Owing to the complexity of the effect of intensification of weather factors on a material, the acceleration factor cannot be estimated but must be determined experimentally for each material. For many polymeric materials, the rate of degradation is not simply a linear function of the level of irradiance. The relation between the increase in irradiance and rate of degradation and the effect of the increase in temperature on the degradation vary with the material. In addition, moisture and other weather factors also have a significant effect on the degradation. Therefore, there is no substitute for experimentally determining the acceleration factor for a given material.

A practical approach to determining acceleration factors for materials that are expected to have long life expectancy is to determine the acceleration factor during the early stages of weathering using a sensitive analytical technique for measuring chemical changes (84,85). These are the precursors to the macroscopic property changes that occur later in the weathering processes. The acceleration factor can then be used to extrapolate the time to failure for the macroscopic property change determined by the laboratory-accelerated test to estimate the time under natural exposure conditions. The validity of this technique is based on the reliance that both types of exposure cause the same degradation mechanism and have the same relation between chemical and macroscopic property change. Also, it requires that the acceleration factor is consistent throughout the service life of the material. A curve-fitting method to determine the "acceleration shift factor" has been developed (86) to account for change in the acceleration factor with progression of weathering. However, the technique requires that the profiles of the graphed property change versus exposure are similar for the two types of exposures.

The acceleration factor for a specific material depends not only on the type of laboratory-accelerated test, the test parameters, and the property change measured but also on the geographical environmental conditions of outdoor exposure and on the specific type of outdoor test. Furthermore, variability in the rate of the degradation in both the laboratory-accelerated and natural exposures can have a significant effect on the acceleration factor calculated. Therefore, the latter should be based on a sufficient number of exterior and laboratory-accelerated exposures and at least two, preferably three, replicate specimens in each test so that time to failure in each can be analyzed accurately. Standardizing test conditions with a reference material, such as polystyrene, in devices that provide for control of weather factors, can improve reproducibility of laboratory tests. Often, problems related to repeatability and reproducibility in test results can be traced to differences in the samples, either because of differences in polymer batches or because of nonuniformity among test specimens from a single batch. Even specimens cut from the same sheet often vary significantly. Poor reproducibility in weathering among specimens from the same production lot can be due to the nonuniform distribution of stabilizers or UV absorbing impurities that initiate the degradation. Aliphatic-type polymers are particularly prone to this problem since only the impurities in these polymers are capable of absorbing terrestrial solar radiation. In aromatic-type polymers with aliphatic moieties, UV

absorbing impurities are also largely responsible for the degradation and thus for poor reproducibility in weathering of these test specimens. Preparation of samples and their treatment during storage can have a substantial effect on the test results.

Durations of Exposure. The exposure duration is a very important consideration in testing the weatherability of materials. Outdoor exposure tests are generally carried out in a geographic location in which stress factors are more severe than they are under in use conditions. In addition, depending on the type of outdoor weathering test, one or more of the weather factors is often intensified. Therefore, the exposure duration necessary to evaluate the material's weatherability for its intended useful lifetime is shorter than the latter. The duration required varies with the geographic location, the type of outdoor test, the in use geographic location and the expected, and useful service life of the material.

The duration of the laboratory-accelerated weathering test is critical to its validity for testing the weatherability of materials. If the duration of the test is insufficient to fail a material known to have poor weathering performance in the intended application, the test is invalid as it cannot identify an unacceptable material, which is one of the major reasons for doing these tests. The exposure duration required for one type of polymeric material under specific laboratory weathering test conditions cannot be assumed to be applicable for other types of polymeric materials. Therefore, specification of the minimum exposure duration must be based on experimental determination of the time to failure of an unacceptable product for each type of polymeric material. The ultimate goal for the use of accelerated weathering tests is to be able to determine in a short time the suitability of a material for its intended lifetime. A very rough estimate of the required duration for this purpose can be obtained by extrapolation of the time to failure by the laboratory-accelerated test using the acceleration factor determined for the type of material of interest. For example, assuming an acceleration factor of 10, absence of failure after 1 year of exposure in the laboratory-accelerated test device can qualify the material for at least 10 years of service. Because the in-service environmental conditions are generally less harsh than the outdoor test conditions, the serviceability can be expected to be more than 10 years.

Generally, for quality control and specification requirements, laboratory-accelerated weathering tests are carried out for a specified test time or radiant exposure. Evaluation is based on pass/fail criteria and the statistically determined repeatability of the combined test exposure and property measurement. In the absence of statistical information, acceptance should be based on comparison of the weatherability of the test materials with the weatherability of one or more control materials of known weatherability exposed at the same time. Three replicates of the test and control specimens should be exposed to determine the significance of weatherability differences using analysis of variance. When exposing for a single period, the latter should be selected to give the largest performance difference between test materials. However, as extent of degradation is usually not a linear function of exposure, relative weatherabilites are more accurately evaluated in terms of the time or radiant exposure required to produce a defined property change in the material than in terms of property change after a specified

period of exposure. The required periodic evaluations of the changes in the test and control materials also provide information on rates and direction of property changes as a function of exposure time or radiant exposure. In some tests, for example, the AATCC Test Methods (87), timing is based on a specified change of color in a weathering reference material, such as the AATCC Blue Wool Lightfastness Standards. However, these reference materials are only applicable to tests with minimum moisture and low heat because of their sensitivity to these factors. Change in color of test specimens compared to that of the standards has also been used to rank the lightfastness of specimens.

Evaluations of Weathering. Weathering effects on all polymeric materials proceed from the irradiated surface inward. Therefore, the effects can be detected sooner by surface-oriented techniques than by methods that measure changes in bulk properties, such as mechanical changes. The latter becomes evident only after prolonged exposure when degradation has penetrated a sufficient distance into the material. Surface changes can take the form of discoloration, crazing, cracking, chalking (whitening), loss of gloss, and surface erosion. Most of these are appearance changes, some of which may be measured photometrically, and others are commonly assessed subjectively by visual inspection. The most frequently used criteria for determining the weather resistance of polymeric products that will be subjected to mechanical stress are tensile (or flexural) strength, elongation, impact strength, hardness, and elastic modulus. These techniques and others are described in several reviews on the subject (78,79). The particular test method used to evaluate weathering effects depends on the type of polymer and the appearance or mechanical property most important in its application. The specific criteria used to determine the effects of weathering can significantly influence the acceleration factor and correlation between the laboratory-accelerated weathering test and outdoor weathering.

Most of the macroscopic property changes require exposure in laboratory-accelerated devices for an impractically long length of time when evaluating weatherabilities of products designed for useful lifetimes of more than 5 years. An alternative to further intensifying exposure conditions to shorten test time is evaluation of weathering effects by sensitive analytical methods that detect molecular (chemical) changes. Infrared spectroscopy provides information on the chemical structure of a material. It is particularly useful in identifying the formation of new functional groups, as, for example, carboxyls, hydroperoxides, and free radicals resulting from photooxidation reactions. It is also useful for determining the reduction of existing functional groups caused by the breaking of chemical bonds. Other methods include UV spectroscopy and measurements of fluorescence and chemiluminescence (88–91). The value of these methods lies in the extent to which the changes measured are related to the macroscopic changes of the polymers.

Service Life Predictions. The service life of a polymeric material is the period of time after it is placed into use during which all relevant properties exceed minimum acceptable values while the material is being routinely maintained. Failure occurs when one or more critical properties required for its use falls below a predefined level. Both natural and laboratory-accelerated weathering tests, even those with enhanced stress factors, require impractically long durations for testing polymeric materials expected to have acceptable performance for more

than 5 years. Therefore, service life prediction of polymeric materials under actual use conditions is essential for the development of new materials. Although a need has existed for many years for a methodology capable of providing reliable service life predictions based on short-term accelerated weathering tests, there is currently no commonly accepted predictive method. The prediction of service life based on accelerated weathering test data is still largely an unsolved weathering problem because of the extensive experimental requirements and complexity of the methodologies proposed.

The apparently simplest and most direct approach to predicting lifetimes under natural weathering is extrapolation of the time to failure by laboratory-accelerated weathering using an experimentally determined acceleration factor relating exposure times in the laboratory test versus outdoor weathering for the same property change. However, determination of the acceleration factor is not a simple, direct procedure and has many limitations in addition to the requirement to determine it for each polymer type and formulation (refer to the section Acceleration Factors). Regression analysis is another technique for deducing lifetimes under natural weathering from lifetimes in laboratory-accelerated tests. It is based on measurements of property changes as a function of exposure by both types of tests and depends on good linear relations over the period measured or on finding the mathematical expression between property change and exposure that gives a linear relationship (92). However, the same limitations exist as those inherent in using acceleration factors. Recently, a simple empirical method of estimating lifetimes of polymeric materials by comparison with control materials was reported (93). It consists of exposing test materials in the laboratory-accelerated test device simultaneously with several control materials having similar composition and construction to the test materials and a range of known failure times outdoors. As for all service life methods, it requires that the accelerated tests produce the same failure modes as natural exposure. In addition, it requires that the rank correlation among materials exposed in the two types of exposures is very high. If these conditions prevail and the service life of the control materials is well defined, the service life of the test material can be bracketed by two control materials.

Various forms of exponential expressions have been used to quantitatively describe the kinetic relations between weather factors and change in properties of polymeric materials (94–96). An approach referred to as the concept of "exposure parameters" was able to successfully predict 2–3 years of outdoor performance of a large number of materials based on several months of accelerated testing (95,96). It has the potential for predicting long-term outdoor weatherability at any location on the basis of accelerated indoor tests using appropriate local weather factors. Investigations have also included mathematical modeling of the effects of weather factors on the degradation process based on data obtained by varying stress levels in laboratory-accelerated tests. One proposed method (97). is based on the "cumulative damage theory," which assumes, among other things, that the deterioration of a material is a cumulative effect of individual deteriorating stresses, and their effects on physical properties can be represented by a general form of a kinetic equation. The cumulative effect during service life aging is then estimated for various levels and types of natural stress conditions by

computer simulation. The mathematical treatment includes determination of the survival distribution function to account for the fact that all specimens do not fail at the same time. In another study (98), a service life prediction model was developed based on tests of four aircraft coatings using three stress factors in the laboratory-accelerated test, UV, temperature, and sulfuric acid aerosols. Probability density functions obtained at the high stress levels were extrapolated to in-service conditions by assuming an Arrhenius life-stress relationship for temperature and an inverse power life-stress relationship with a power coefficient of 0.46 for UV irradiance. The aerosol effect was treated as an indicator variable using the value of zero without aerosol and the value of one when aerosol was included. The service life predictions of times to failure compared favorably with times to failure determined from experimental tests under in-service conditions that lasted for more than 60 months. Mathematical modeling in an ongoing study (99) of other types of coatings and polymeric materials also uses reliability-based analyses of laboratory-accelerated data in which weathering is characterized by frequency of failures.

The validity of the estimates of service life depends on the validity of a number of assumptions including the assumption that the failure mechanism at the higher stress levels of the accelerated tests is the same as the failure mechanism under in use conditions. Accurate service life predictions also depend on reliable laboratory test data requiring precise control of the variables in the laboratory-accelerated test device, the appropriate number of replicate specimens so that life distribution information can be extracted and translated to service life predictions, accurate quantitative data on environmental factors, and considerable experimental effort.

BIBLIOGRAPHY

"Weathering" in *EPST* 1st ed., Vol. 14, pp. 779–795, by J. E. Clark, National Bureau of Standards; "Weathering" in *EPSE* 2nd ed., Vol. 17, pp. 796–827, by N. D. Searle, Consultant, Plastics and Chemicals; "Weathering" in *EPST* 3rd ed., Vol. 4, pp. 629–659, by N. D. Searle, Chemical Consultant.

CITED PUBLICATIONS

1. N. Robinson, *Solar Radiation*, Elsevier Science Publishing Co(Inc.), New York, 1966, Chapt. 5, pp. 161–195.
2. ASTM G173-08, in *Annual Book of ASTM Standards*, Vol. **14.04**, American Society for Testing and Materials, West Conshohocken, Pa., 2010.
3. ASTM D1435-05, in *Annual Book of ASTM Standards*, Vol. **8.01**, American Society for Testing and Materials, West Conshohocken, Pa., 2010.
4. J. E. Pickett, D. A. Gibson, and M. M. Gardner, *Polym. Degad. Stab.* **93**, 1597–1606 (2008).
5. N. D. Searle, in S. H. Hamid, ed., *Handbook of Polymer Degradation*, 2nd ed, Marcel Dekker, Inc., New York, 2000, Chapt. 16, pp. 605–643.
6. ASTM G178-09, in *Annual Book of ASTM Standards*, Vol. **14.04**, American Society for Testing and Materials, West Conshohocken, Pa., 2010.

7. N. D. Searle, in A. V. Patsis, ed., *International Conference on Advances in the Stability and Controlled Degradation of Polymers*, Vol. 1, Technomic Publishing Co., Lancaster, Pa., 1989, pp. 62–74.
8. N. D. Searle, in D. Kockott, ed., *International Symposium on Natural and Accelerated Weathering of Organic Materials, Part B, Atlas SFTS BV*, Essen, Germany, Sept. 28–29, 1987, Lochem, The Netherlands, 1988, pp. 1–15.
9. L. D. Johnson, W. C. Tincher, and H. C. Bach, *J. Appl. Polym. Sci.* **13**, 1825–1832 (1969).
10. R. M. Fischer and co-workers, *Polym. Mater. Sci. Eng.* **83**, 136–139 (2000).
11. ACS National Meeting, Aug. 20–24, 2000.
12. B. L. Garner and P. J. Papillo, *Ind. Eng. Chem. Prod. Res. Dev.* **1**, 249–253 (1962).
13. D. Clauson, in *75th Annual IFAI Convention*, Nov. 1987, Industrial Fabrics Assoc. Int'l, St. Paul, Minn., 1988, pp. 96–110 (Preprint).
14. M. E. Nichols and C. A. Darr, *ACS Symp. Ser.* **722**, 333–353 (1999).
15. G. C. Furneaux, K. J. Ledbury, and A. Davis, *Polym. Degrad. Stab.* **3**, 441–432 (1980–1981).
16. A. V. Cunliffe and A. Davis, *Polym. Degrad. Stab.* **4**, 17–37 (1982).
17. G. E. Schoolenberg, J. C. M. deBruijn, and H. D. F. Meijer, in *Proc. 14th Int. Conf. on Advances in Stabilization and Degradation of Polymers*, Lucerne, Switzerland, 1992, p. 25.
18. G. Yanai, A. Ram, and J. Miltz, *J. Appl. Polym. Sci.* **59**, 1145–1149 (1996).
19. D. Patil, R. D. Gilbert, and R. E. Fornes, *J. Appl. Polym. Sci.* **41**, 1641–1650 (1990).
20. U. Schulz and P. Trubiroha, in R. J. Herling, ed., *Durability Testing of Nonmetallic Materials*, American Society for Testing and Materials, West Conshohocken, Pa., 1996, pp. 106–120. ASTM STP 1294.
21. P. Trubiroha and U. Schulz, *Polym. Polym. Compos.* **5**, 359–367 (1997).
22. ASTM D4364-05, in *Annual Book of ASTM Standards*, Vol. **8.03**, American Society for Testing and Materials, West Conshohocken, Pa., 2010.
23. ISO 877:1994 International Organization for Standardization, Geneva, Switzerland, 1994.
24. ASTM G7-05, in *Annual Book of ASTM Standards*, Vol. **14.04**, American Society for Testing and Materials, West Conshohocken, Pa., 2010.
25. ASTM G24-05, in *Annual Book of ASTM Standards*, Vol. **14.04**, American Society for Testing and Materials, West Conshohocken, Pa., 2010.
26. M. M. Quayyum and A. Davis, *Polym. Degrad. Stab.* **6**, 201–209 (1984).
27. H. H. G. Jellinek, *Aspects of Degradation and Stabilization of Polymers*, Elsevier, Amsterdam, The Netherlands, 1978, Chapt. 3.
28. G. C. Newland, R. M. Schulken Jr., and J. W. Tamblyn, *Mater. Res. Stand.* **3**, 487–488 (1963).
29. T. G. B. Jones and M. A. Lacasse, in A. T. Wolf, ed., *Durability of Building Sealants*, RILEM Report 21, RILEM Publications, Cachan, France, 1999, pp. 73–105.
30. K. K. Karpati, *Adhes. Age* **31**(5), 20–23 (1988).
31. Data supplied by South Florida Test Services, Inc., Miami, Fla.
32. M. P. Morse, in G. G. Schurr, ed., *Permanence of Organic Materials*, American Society for Testing and Materials, West Conshohocken, Pa., 1982, pp. 43–66. ASTM STP 781.
33. ASTM D4141-07, in *Annual Book of ASTM Standards*, Vol. **6.01**, American Society for Testing and Materials, West Conshohocken, Pa., 2010.
34. SAE J 1976, 2002, SAE International, Warrendale, Pa., 2002.
35. Atlas Material Testing Technology LLC, Chicago, IL. 60613.
36. ASTM G90-10, in *Annual Book of ASTM Standards*, Vol. **14.04**, American Society for Testing and Materials, West Conshohocken, Pa., 2010.

37. U.S. Pat. 6,659,638 B1 (2003), H. K. Hardcastle (to Atlas Material Testing Technology, LLC).
38. H. K. Hardcastke, G. J. Jorgensen and C. E. Bingham, in *4th European Weathering Symposium EWS*, Budapest, Hungary, Sept. 16–18, 2009.
39. G. A. Zerlaut and M. L. Ellinger, *J. Oil Col. Chem. Assoc.* **64**, 387–397 (1981).
40. G. A. Zerlaut, in W. E. Brown, ed., *Testing of Polymers*, Wiley-Interscience, New York, 1969, Vol. 4, pp. 10–34.
41. R. J. Martinovich and G. R. Hill, in M. R. Kamal, ed., *Weatherability of Plastic Materials*, Wiley- Interscience, New York, 1967, pp. 141–154. Appl. Polym. Symp. No. 4.
42. J. B. Howard and H. M. Gilroy, *Polym. Eng. Sci.* **9**, 286–294 (1969).
43. C. R. Caryl, in W. E. Brown, ed., *Testing of Polymers*, Wiley-Interscience, New York, 1969, Vol. 4, pp. 379–397.
44. G. A. Zerlaut, in W. D. Ketola and D. Grossman, eds., *Accelerated and Outdoor Durability Testing of Organic Materials*, American Society for Testing and Materials, West Conchohocken, Pa., 1994, pp. 3–26. ASTM STP 1202.
45. G. A. Zerlaut, M. W. Rupp, and T. E. Anderson, in *Proceedings of SAE International Congress, Detroit, Mich.*, Feb. 1985, paper 850378.
46. R. W. Singleton, R. K. Kunkel, and B. S. Sprague, *Text. Res. J.* **35**, 228–237 (1965).
47. R. W. Singleton and P. A. C. Cook, *Text. Res. J.* **39**, 43–49 (1969).
48. G. A. Zerlaut, in Ref. 31, pp. 10–34.
49. B. Zahradnik and B. Juriaanse, in *ANTEC '84, 42nd Annual Technical Conference*, 1984, pp. 397–400 (preprint).
50. Atlas Material Testing Technology LLC, Chicago, IL 60613.
51. ASTM D2565-99 (2008), in *Annual Book of ASTM Standards*, Vol. **8.02**, American Society for Testing and Materials, West Conshohocken, Pa., 2010.
52. ASTM D4459-06, in *Annual Book of ASTM Standards*, Vol. **8.03**, American Society for Testing and Materials, West Conshohocken, Pa., 2010.
53. ASTM G155-05a, in *Annual Book of ASTM Standards*, Vol. **14.04**, American Society for Testing and Materials, West Conshohocken, Pa., 2010.
54. ISO 4892-2:2006, International Organization for Standardization, Geneva, Switzerland, 2006.
55. Atlas Material Testing Technology LLC, Chicago, IL 60613.
56. Atlas Material Testing Technology LLC, Chicago, IL 60613.
57. K. P. Scott, in J. W. Martin, R. A. Ryntz, and R. A. Dickie, eds., *Service Life Prediction, Challenging the Status Quo*, Federation of Societies for Coatings Technology, Blue Bell, Pa. 2005, Chapt. 19, pp. 259–271.
58. Atlas Material Testing Technology LLC, Chicago, IL 60613.
59. ASTM D4329-05, in *Annual Book of ASTM Standards*, Vol. **8.03**, American Society for Testing and Materials, West Conshohocken, Pa., 2010.
60. ASTM D4587-05, in *Annual Book of ASTM Standards*, Vol. **6.01**, American Society for Testing and Materials, West Conshohocken, Pa., 2010.
61. ASTM G154-06, in *Annual Book of ASTM Standards*, Vol. **14.04**, American Society for Testing and Materials, West Conshohocken, Pa., 2010.
62. ISO 4892-3:2007, International Organization for Standardization, Geneva, Switzerland, 2007.
63. N. D. Searle, in Ref. 43, pp. 52–67.
64. R. M. Fischer, SAE Tech. Paper Ser. No. 841022, In *West Coast Int'l Mtg. & Expos.*, San Diego, Calif., 1984, Society of Automotive Engineers, Warrendale, Pa., 1984, pp. 1–9.
65. H. H. McEwan and L. A. Simpson, *Tech. Serv. Rept*. D9187GC, Tioxide Group, Plc., London, 1985.

66. D. R. Bauer, M. C. Paputa Peck, and R. O. Carter III, *J. Coat. Technol.* **59**(755), 103–109 (1987).
67. Atlas Material Testing Technology LLC, Chicago, IL 60613.
68. Atlas Material Testing Technology LLC, Chicago, IL 60613.
69. ASTM D5031-01(2006), in *Annual Book of ASTM Standards*, Vol. **6.01**, American Society for Testing and Materials, West Conshohocken, Pa., 2010.
70. ASTM D6360-07, in *Annual Book of ASTM Standards*, Vol. **8.03**, American Society for Testing and Materials, West Conshohocken, Pa., 2010.
71. ASTM G153-04, in *Annual Book of ASTM Standards*, Vol. **14.04**, American Society for Testing and Materials, West Conshohocken, Pa., 2010.
72. ASTM D822-01(2006), in *Annual Book of ASTM Standards*, Vol. **6.01**, American Society for Testing and Materials, West Conshohocken, Pa., 2010.
73. ASTM D1499-05, in *Annual Book of ASTM Standards*, Vol. **8.01**, American Society for Testing and Materials, West Conshohocken, Pa., 2010.
74. ASTM G152-06, in *Annual Book of ASTM Standards*, Vol. **14.04**, American Society for Testing and Materials, West Conshohocken, Pa., 2010.
75. T. M. Kollmann and D. G. M. Wood, *Polym. Eng. Sci.* **20**, 684–687 (1980).
76. H. K. Hardcastle, in *2nd European Weathering Symposium EWS*, Confederation of European Environmental Engineering Societies, June 16–17, 2005.
77. G. Wypych, F. Lee, and B. Pourdeyhimi, in A. T. Wolf, ed., *Durability of Building and Construction Sealants*, RILEM Publications S.A.R.L., Cachan, France, 2000, pp. 173–197.
78. T. Nguyen, J. W. Martin, E. Byrd, and N. Embree, *Polym. Mater. Sci. Eng.* **83**, 118–119 (Aug. 2000).
79. RILEM Publications S.A.R.L., Cachan, France, in Ref. 76.
80. ASTM G151-10, in *Annual Book of ASTM Standards*, Vol. **14.04**, American Society for Testing and Materials, West Conshohocken, Pa., 2010.
81. L. E. Pimental Real, A. M. Ferraria, and A. M. Botelho do Rego, *Polym. Test.* **26**, 77–87 (2007).
82. U. Schulz, P. Trubiroha, T. Boettger, and H. Bolte, in *8th Int. Conf. on Durability of Building Materials and Components*, May 30–June 3, 1999.
83. K. M. Wernstahl and B. Carlsson, *J. Coat. Technol.* **69**(865), 69–75 (1997).
84. D. R. Bauer, J. L. Gerlock, and R. A. Dickie, *Prog. Org. Coat.* **15**, 209–221 (1987).
85. J. L. Gerlock, D. F. Mielewski, and D. R. Bauer, *Polym. Degrad. Stab.* **20**, 123–134 (1988).
86. J. A. Simms, *J. Coat. Technol.* **59**(748), 45–53 (1987).
87. *AATCC Technical Manual*, Vol. 85, American Association of Textile Chemists and Colorists, Research Triangle Park, N.C., 2010, Method 16, pp. 25–36.
88. N. D. Searle, in J. M. Fitzgerald, ed., *Analytical Photochemistry and Photochemical Analysis: Solids, Solutions and Polymers*, Marcel Dekker, Inc., New York, 1971, Chapt. 9, pp. 249–336.
89. J. L. Gerlock, D. Bauer, L. M. Briggs, and R. A. Dickie, *J. Coat. Technol.* **57**, 37–46 (1985).
90. G. A. George and M. Ghaemy, *Polym. Degrad. Stab.* **33**, 411–428 (1991).
91. V. Dudler, Th. Bolle, and G. Rytz, *Polym. Degrad. Stab.* **60**, 351–365 (1998).
92. F. Gugumus, in *Symposium on Polymer Stabilization and Degradation: Problems, Techniques and Applications*, Manchester, UK, Sept. 1985 (preprint).
93. R. M. Fischer and W. D. Ketola, in S. H. Hamid, ed., in Ref. 5, 2000, Chapt. 17, pp. 645–669.
94. J. E. Clarke and J. A. Slater, *NBS Technical Report No*. 10116, National Bureau of Standards, Washington, D.C., Oct. 1969.
95. M. R. Kamal, *Polym. Eng. Sci.* **6**, 333–340 (1966).

96. M. R. Kamal and R. Saxon, in M. R. Kamal, ed., in Ref. 40, 1967, pp. 1–28.
97. C. S. Shah and M. J. Patni, *Polym. Test.* **13**(4), 295–322 (1994).
98. O. Guseva, S. Brunner and P. Richner, *Polym. Degrad. Stab.* **82**(1), 1–13 (2003).
99. J. W. Martin, S. C. Saunders, F. L. Floyd, and J. P. Wineburg, *Federation Series on Coatings Technology*, Federation of Societies for Coating Technology, Blue Bell, Pa., 1996, pp. 1–34.

NORMA D. SEARLE
Consultant in Weathering of Materials
MATTHEW MCGREER
ALLEN ZIELNIK
Atlas Material Testing Technology, LLC
Chicago, Illinois

WOOD COMPOSITES

Introduction

Wood composites can be defined as materials made by gluing together small pieces of wood, residue materials from wood processing operations, or other elements into larger materials to produce products with specific definable mechanical and physical properties. Wood composite products continue to be among the most widely utilized building materials throughout the world. They are commonly manufactured as lumber, flooring, roofing, paneling, palettes, decking, fencing, cabinets, furniture, millwork, structural beams, etc.

The increased number and importance of wood composite products are directly related to the decreased supply of high quality large timber, and as the quality and variety of wood composite products increases, and new applications for them are found, the trend toward increased use and importance of wood composites should continue. Wood composites offer numerous advantages over lumber. They can be produced from waste wood, agricultural residues, little used and low commercial value wood species, as well as smaller and fast growing trees, which can relieve stress on old growth forests that are increasingly unavailable for use. Also, the increased homogeneity of the raw material obtained by combining small wood elements allows a wide variety of composite products to be produced that have consistent, high quality properties. The properties can often surpass those of lumber (eg, have stronger and more uniform properties throughout the product, and be completely free of growth characteristics, weak spots, or defects such as knots), and often, the product can be produced with customized engineered properties, dimensions, and complex shapes (eg, complex roof shapes, cathedral ceilings, cantilevered supports).

The exact properties and the appropriate end use for a composite depend on the wood species and wood adhesive, and are very dependent on the size, shape, and arrangement of the wood in the composite. In fact, the names of the composite products are mostly based on the wood geometry (wood shape and size) and their

arrangement in the product, without involving the name of the wood species or adhesive. These elements (species and adhesive) can be changed with far less effect on properties than changing wood geometry or arrangement.

The procedure for making a wood composite begins with the raw wood being processed by removal of leaves and bark, then being cut into pieces of the desired size and shape, followed by drying to the desired moisture content, and then going through a sorting process to ensure the wood pieces meet the selection criteria. This process is followed regardless of wood species or wood geometry. Some composite processes allow more than 90% of the tree stem to be utilized with either small or large diameter trees, while lumber can only be produced from large diameter trees and even then typically less than 50% of the tree can be converted to the intended product.

A large number of product types having quite different properties can be prepared using the same wood element. Processing conditions to convert the wood element into a composite product will depend on the type of adhesive selected and/or if the product being produced is pressed, impregnated, extruded, etc. Therefore, wood composites can be classified into two major types: (*1*) wood bonded with thermoset adhesives and (*2*) wood combined with other materials such as cement and thermoplastics.

This article outlines some of the features and components of wood composites, describes some major wood composite products and properties, and describes some future directions in the wood composites industry. For additional information the reader is referred to some recent reviews (1–7).

Wood Bonded with Thermoset Adhesives

Wood composite products are conventionally manufactured from wood materials having various geometries (eg, fibers, particles, strands, flakes, veneers, and lumber) combined with a thermoset resin and bonded in a press (4). The press applies heat (if needed) and pressure to activate (cross-link) the adhesive resin and bond the wood material into a solid panel, lumber, or beam having good mechanical (strength and stiffness) and physical (form, dimensional stability, etc) properties.

Types of Wood Elements. A wide range of wood elements are employed to produce an increasing number of wood composite products. These elements can be broadly divided into two categories: "long grain" and "short grain" elements based on their size and shape (Table 1). The largest of the commonly used long grain wood elements, excluding lumber itself, is veneer. Shorter grain elements include strands, flakes, wafers, particles, and fibers. It should also be noted that increasing numbers of wood composite products are employing recycled wood such as sawdust and wood flour, which can be considered to be a separate wood type. Agrofibers are increasingly being employed as a raw material to produce commercial products similar to wood composites but with varying degrees of success. Some of the reasons for the rising interest in agrofibers include their low density and low abrasion, the potential to improve some properties such as stiffness, and potential cost savings when used as a filler for thermoplastics, and because many of these materials are the by-products of annual crops (8). In the United States and Canada wheat straw is currently the most important

Table 1. Types of Wood Elements Used In Wood Composites[a]

	Length		Width		Thickness	
Elements	cm	in.	cm	in.	cm	in.
Lumber	120–600	48–240	10–30	4–12	12.5–50	0.5–2
Veneer	120–240	48–96	10–120	4–48	0.5–12.5	0.02–0.5
Strands	1.27–7.5	0.5–3	0.63–2.5	0.25–1	0.25–0.625	0.010–0.025
Flakes	1.25–7.5	0.5–3	0.125–7.5	0.5–3	dito	0.010–0.025
Wafers	3.3	1.3	2.5–7.5	1–3	0.625–1.25	0.025–0.05
Particles	0.125–1.25	0.05–0.5	0.0125–0.125	0.005–0.05	0.125–1.25	0.005–0.050
Fibers	0.1–0.63	0.04–0.25	0.0025–0.0075	0.001–0.003	0.025–0.075	0.001–0.003

[a]Adapted from Ref. 7.

agrofiber furnish but many other agrofibers are of interest. Agrofiber preferences vary with availability and geographical region of the world (9). Soybean and cotton stalks, kenaf, flax, coffee and rice husk, hemp, fescue straw, ramie, and sugarcane bagasse are just some of the agrofiber raw materials being used or studied. Composites made from various agrofibers include low density insulating board, medium density fiberboard, hardboard, and particleboard (9,10). The mechanical properties for some agrofiber composites are reported in the literature, but additional research is needed, particularly on the long-term durability and weathering properties of these composites (10).

Thermoset Wood Adhesives

A wide range of adhesive types and chemistries are used to bond wood elements to one another (Table 2), but relatively few adhesive types are utilized to form the composites themselves. The vast majority of pressed-wood products use synthetic thermosetting adhesives. In North America the most important wood adhesives are the amino resins (qv), eg, urea–formaldehyde (UF) and melamine–formaldehyde (MF), which account for 60% by volume of adhesives used in wood composite products, followed by the phenolic resins (qv) eg, phenol–formaldehyde (PF) and resorcinol–formaldehyde (RF), which account for 32% of wood composite adhesives (12,13). The remaining 9% consists of cross-linked vinyl (X-PVAc) compounds, thermoplastic poly(vinyl acetates) (PVA), soy-modified casein, and polymeric diphenylmethylene diisocyanate (pMDI). Some products may use various combinations of these adhesives to balance cost with performance.

The thermosetting amino and phenolic adhesives are by far the predominant adhesives used in making wood composites. These adhesives are described below, but more detailed information is available elsewhere (4,7,16–21) (see ADHESIVE COMPOUNDS).

Urea–Formaldehyde (UF) Adhesives. UF resins are produced in a two-stage condensation polymerization process through the reaction of urea with excess formaldehyde. In the first stage of the polymerization process, urea and formaldehyde are heated under slightly alkaline conditions (pH 7–8) to produce methylolurea resins (Fig. 1). Depending on the synthesis conditions (eg, the

Table 2. Characteristics of Major Wood Composites Bonded with Thermoset Adhesives

Types of composites	Raw materials[a]	Adhesives used	Structural (S) vs nonstructural (NS)	Applications	Typical thickness, mm (in.)	Typical density, kg/m^3 (lb/ft^3)
Particleboard	Particles	UF, MF, MDI	Mostly NS	Furniture, cabinetry, floor underlay, stair treads,	6–57 ($\frac{1}{4}$–2$\frac{1}{4}$)	640–800 (40–50)
Medium density fiberboard (MDF)	Fibers	UF, pMDI	NS	Furniture, kitchen and bath cabinet, fixtures, molding, millwork, laminate flooring	5–38, max. 76 (3/16–1$\frac{1}{2}$, max. 3)	640–800 (40–50)
Construction and industrial plywood	Softwood veneer, some hardwood	PF	S	Roof, floor, wall sheathing, single-layer floor, siding, floor underlayment, preserved wood foundations, laminated veneer lumber	6–31.5 ($\frac{1}{4}$–1$\frac{1}{4}$)	450–500 (28–31)
Decorative plywood	Hardwood veneer, some softwoods	UF, MF, RF, PVAc	Mostly NS	Decorative wall paneling, furniture, cabinetry, decorative flooring	6–19 ($\frac{1}{4}$–$\frac{3}{4}$)	400–880 (25–55)
Oriented strandboard (OSB)	Strand, flake, wafer	PF, pMDI	S	Roof, floor, wall sheathing, floor underlayment, siding, I-beams web stock, hybrid products	6–32 ($\frac{1}{4}$–11/8)	580–700 (36–44)
Laminated veneer lumber (LVL)	Softwood veneer	PF, pMDI	S	Floor and roof joists, roof ridge beams, roof truss chords, window and doorheaders, wood I-joist flanges, concrete form, scaffold planking, window and door joinery	19–75 ($\frac{3}{4}$–3 in.), 27–50 in. wide, up to 24.4 m (80 ft) long	
Wood I-joist	Lumber, LVL, OSB, plywood	Cold setting glue (eg, RF, PRF), pMDI	S	Floor and roof construction	Flange sizes (1.5–3 in. in depth, 2.5–3.5 in. in width), Joist depths range from 9$\frac{1}{2}$ to 50 in. and lengths up to 50 ft	
Glulam beams	Lumber, some LVL	RF, PRF, MF		Headers, girders, purlins, beams, arches, bridges, marinas, power transmission structures	Up to 50 m long	
Parallel strand lumber (PSL)	Strands from softwood veneer	PF	S	Headers, beams, columns and posts; industrial uses such as bridge structures and power poles; and with CCA pressure treatment, post, beams and columns for decks, balconies, car-ports	280 by 430 cross section (11 by 17), length up to 66 ft	
Laminated strand lumber (LSL)	Strand	pMDI	S	Industrial and light structural applications	140 mm (5.5 in.) thick, 2.4 m wide, 10–15 m long	

[a]Refer to Table 1. The data in this table are adapted from various references 3–6,11–16.

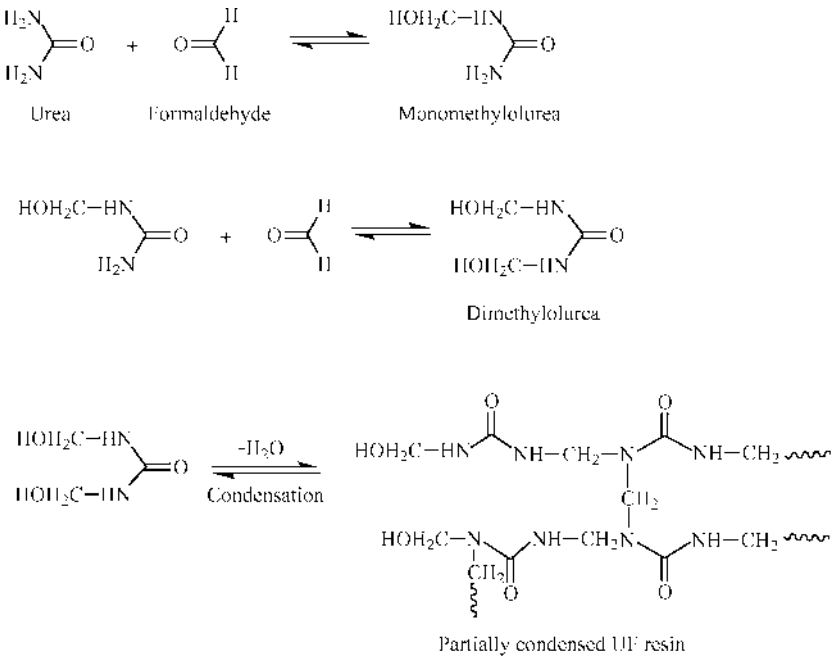

Fig. 1. Polymerization reaction of UF resin.

relative urea-to-formaldehyde molar ratios, the reaction temperature, and pH), up to four molecules of formaldehyde can bond to urea owing to the four replaceable hydrogen atoms of urea. The methylolureas produced at this stage are low molecular weight prepolymer solutions that have no adhesive properties. During the second stage, these prepolymer solutions are slightly acidified, which causes the methylolureas produced in the first stage to condense with one another. As this occurs the prepolymer molecular weight increases, and as the polymerization of the UF resin advances further the growing chains begin to cross-link through the formation of methylene–ether links. At the desired point in this polymerization process the aqueous suspension of UF adhesive is neutralized, which stops the reaction before the resin precipitates, and cooled. Water is removed under reduced pressure (vacuum) to produce a final resin content of about 65% nonvolatile resin solids. The final stage of the condensation polymerization, which produces a solid cross-linked thermoset, is completed during production of the wood composite. It is accomplished by the addition of a small amount of acid catalyst to the UF suspension immediately prior to its application to the wood element and occurs during the pressing cycle to produce the wood composite.

UF resin is applied to wood furnish as an aqueous suspension. With the addition of a catalyst such as an acid, the curing can occur at room temperature in a few days, but most industrial processes employ high temperatures and ammonium salts to shorten the bonding cycle (7). In the presence of heat and catalyst, UF condenses into a cross-linked three-dimensional network of macromolecules that provide bonding. UF resin cures rapidly, provides strong adhesion in a permanently dry environment, and is the least expensive of the major wood

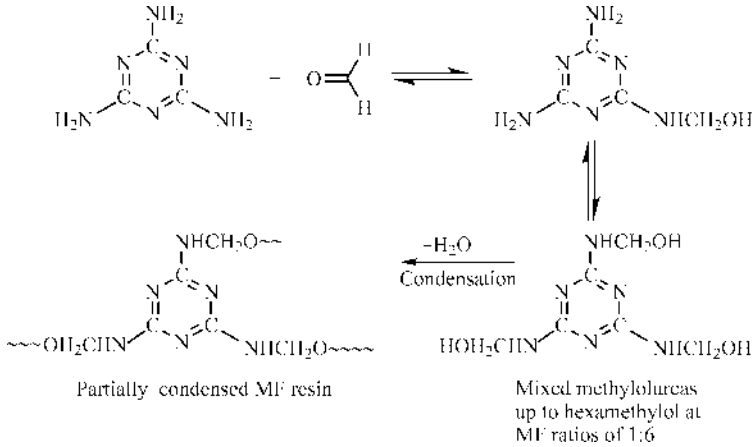

Fig. 2. Formation of MF resin.

adhesives. For these reasons, UF resin is by far the dominant commercial adhesive and is widely used throughout the world for bonding wood and wood-based composites. Despite these attributes, UF resins have three major drawbacks: (*1*) their brittleness once cured, (*2*) their limited resistance to moisture in the cross-linked state (limiting their use to interior products), and (*3*) the potential for formaldehyde emission from UF-bonded wood composites.

Although the urea (U) to formaldehyde (F) molar ratios can be in the range of 1:1.2 to 1:2, governmental regulations on the permissible level of free formaldehyde have forced resin producers and wood-composite manufacturers to lower the molar ratio, and so today resins with a U:F ratio as low as 1:1.1 are not uncommon. The potential for formaldehyde release from UF resin-bonded wood composites is caused by two factors: (*1*) release of a portion of the excess formaldehyde that did not react and (*2*) hydrolysis of susceptible bonds in the UF resin producing the urea and formaldehyde reactants (hydrolytic degradation), which can occur in the presence of moisture and heat during the pressing operation or subsequent installation (18,19). The low moisture resistance of UF resins limits their application to interior products, but if greater moisture resistance is required various urea derivatives or melamine are included in the UF formulation.

Melamine–Formaldehyde (MF) Adhesives. MF resins are produced by a condensation process by reacting melamine with excess formaldehyde (Fig. 2). The reaction proceeds in a manner similar to that between formaldehyde and urea but progresses to a greater extent (see MELAMINE–FORMALDEHYDE RESINS).

Cured MF resins are considerably more water-resistant than UF resins. This is attributed to the lower solubility of melamine in cold water compared to urea (18,19), and the overall greater hydrophobicity of the MF. These resins also have superior heat resistance and shorter curing times than UF resins because of the higher functionality of melamine compared to urea (up to six molecules of formaldehyde can react with melamine). Therefore, MF-bonded composites can be employed in both interior and in some exterior applications.

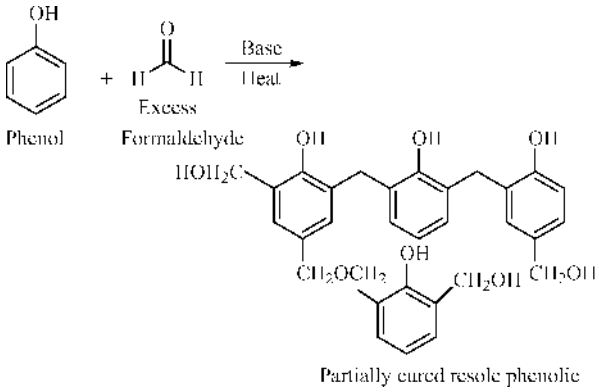

Fig. 3. Formation of resole PF resins.

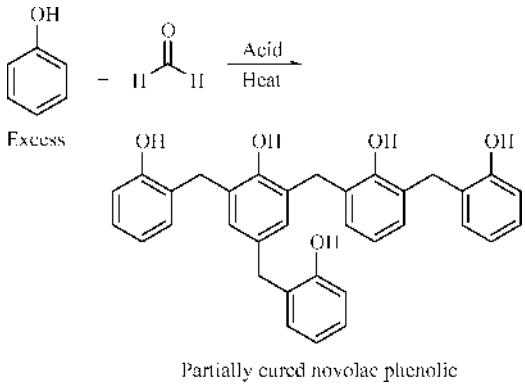

Fig. 4. Formation of novolac PF resins.

However, MF resins are costly (about 3.5 times the price of UF based on 100% resin solids), and can only be cured properly at high temperature, which adds to the cost. This is a serious commercial drawback.

As previously mentioned, MF and UF resins are often combined. In the case of UF resins it is done to improve their moisture resistance, to accelerate their cure rate, and to reduce formaldehyde emission from UF-bonded wood composites, while in the case of MF resins it is done to reduce the cost. However, because of the differences in reactivity between urea and melamine mixing these components can complicate the curing. The conditions needed to cure the MF can overcure the UF, and conditions designed to properly cure the UF can leave the MF component undercured. However, when a suitable cure cycle is found for the blended resin, a good combination of properties can be achieved.

Phenol–Formaldehyde (PF) Adhesives. PF resins are produced by the reaction of a phenol and formaldehyde. Depending upon the phenol-to-formaldehyde (P:F) molar ratios and the type of catalyst, two types of PF resins can be produced: resole and novolac PF resins (Figs. 3 and 4).

Resole PF resins are produced by the reaction of phenol with excess formaldehyde (P:F molar ratio 1:1.8 to 1:2.2) in the presence of an alkali

catalyst (Fig. 3). Because resole resins contain reactive methylol groups, they are self-curing resins that can condense with active sites on the phenol rings to form a cross-linked network in the presence of heat even without additional hardener. Resole resins have a very branched structure (Fig. 3) and are by far the more important of the two types of PF resins for wood composites.

Conversely, novolac PF resins are produced by the reaction of excess phenol with formaldehyde (P:F molar ratio 1:0.8 to 1:1) in the presence of an acid catalyst. Unlike resole resins, novolac PF resins have a more linear structure (Fig. 4) and do not self-cure because they lack the residual reactive methylol groups of resoles. Therefore, an external curing agent such as hexamethylenetetraamine must be added to novolac resins to yield a cross-linked structure. Novalac PF resins cured under acidic conditions are not recommended for wood composites for long-term structural applications.

In the presence of heat and on the addition of sodium hydroxide (NaOH) or other catalyst, resole PF resins condense into a three-dimensional cross-linked network having reactive sites suitable for wood bonding. While too much heat accelerates the degradation of UF resins, use of heat is desirable in PF-bonded composites to achieve a high degree of cross-linking. It should also be mentioned that the curing rate of PF resins is strongly influenced by the amount of NaOH added to the resins, with the higher NaOH content affording a faster cure up to a point. However, use of an excessive amount of NaOH in PF resins has adverse effects, including increasing the affinity of the composite for absorbing moisture from the air, which in turn results in PF-bonded composites having a higher thickness swell. As is the case with UF bonding, the adhesion to the wood surfaces in PF-bonded wood composites is achieved through secondary and/or physical bonding. PF resins have greater moisture resistance and greater strength retention when exposed to a high moisture environment than UF resins, and so are employed extensively in the manufacture of wood composites slated for exterior applications. Long-term aging studies in which plywood specimens prepared using various adhesives bonds were exposed to natural weathering confirmed the superior moisture resistance of PF. The PF-bonded specimens retained up to 90% of their original strength even after 8 years, while the UF-bonded specimens lost 100% of their original strength after only 4 years in service (7).

Resorcinol–Formaldehyde (RF) Adhesives. RF resins are a type of phenolic adhesive that are distinguished by a very high reactivity relative to PF resins. This greater reactivity is due to the two phenolic hydroxyl groups on resole. The groups *activate* one another by making each other more electron-rich. Therefore, the first hydroxyl group is much more reactive than the phenol hydroxyl group, and following its reaction the remaining hydroxyl group is still highly reactive. Consequently, although RF adhesives are generally prepared using excess resorcinol to produce a novolac-type resin, in contrast to PF novalacs, these resins set rapidly *with the addition of hardener* even at low temperatures (eg, anywhere from 5 to 70°C). This is termed *cold curing*. The high reactivity between resorcinol and formaldehyde with additional hardener, eg paraformaldehyde, allows the cure to proceed rapidly to completion. The reaction can be further accelerated by applying heat. Attempts to produce a resole RF resin typically result in an unusable gel (18–20). Despite the ability to cure at room or elevated temperatures and give composite products having good moisture resistance, RF

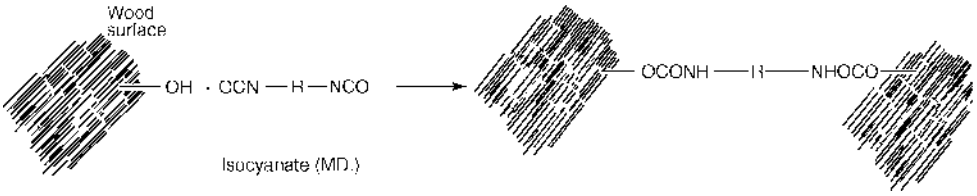

Fig. 5. Reaction of wood with MDI resin.

adhesives are not used extensively because they are among the most expensive of the thermoset adhesives, being second only to the isocyanates in cost. Nevertheless, RF adhesives are used as binders for selected wood products.

Isocyanates. Polymeric diphenylmethane diisocyanate (pMDI) is the most commonly used isocyanate wood adhesive mainly because of its lower volatility and toxicity when compared to other isocyanates such as toluene diisocyanate and dicylcohexylmethane diisocyanate. Some of the advantages enjoyed by pMDI include the fact that it is a liquid polymer, and so it does not require a solvent carrier for application, it is free of formaldehyde, and also it does not require acidic (the case with UF) or alkaline catalysts (the case with PF). It is an effective wood adhesive because the high reactivity of the isocyanate (—N=C=O) groups allows the resin to cure rapidly, and it has the potential to covalently bond directly to the wood by reacting with the hydroxyl groups on the wood surface (Fig. 5) (7,18–20).

The ability of pMDI to cure rapidly is due to the high reactivity of isocyanate (—N=C=O) groups that react rapidly with active hydrogen atoms. Wood possesses active hydrogens from hydroxyl groups on wood surfaces and from moisture in the wood. When the isocyanates react several reactions occur simultaneously but at different rates. The —N=C=O groups first add water to form unstable carbamic acid groups that then dissociate into an amine and carbon dioxide. The resulting amine is more reactive than water and reacts rapidly with another isocyanate to form a polyurea (22). The —N=C=O groups can also add cellulosic hydroxyl groups on the wood surface to form covalent bonds via urethane linkages (Fig. 5). pMDI can cure at ambient temperature in the presence of moisture and so it can also be used in cold pressing of wood-based composites, but hot pressing is usually preferred to shorten the press cycle.

pMDI forms covalent bonds and polar interactions with wood and tolerates both high moisture content in the wood and lower press temperatures during composite manufacture. When wood composites are prepared with equal amounts of adhesive and the bond strength and the dimensional stability of wood composites are compared it is found that pMDI's bond strength and dimensional stability of composites prepared with it are generally superior to those of amino and phenolic resins in both dry and moist environments. Despite these advantages, pMDI adhesives also have some disadvantages. There are some perceived health hazards associated with the manufacturing process, and it can bond to the metal surfaces of a hot press, which is undesirable, although this can be prevented by applying release agents to the surfaces of the press. However, the primary drawback is cost. pMDI is the most expensive of the wood adhesives.

Other Wood Adhesives. There is considerable interest in developing adhesives from renewable resources that can be used as a primary adhesive or as an adhesive component (an "extender") to replace a portion of petroleum-based adhesives. These natural and renewable resources include lignin, tannins, and natural oils such as soy bean and proteins.

Lignin. Lignin is a waste product produced in large quantities by the pulp and paper industry that is often burned as fuel. Lignin-modified PF resins have been formulated to bond fiberboards, strandboards, and structural plywood (14,15,23–29). Lignin (qv) is employed in this manner primarily to reduce the consumption of oil-based products and to a lesser extent for cost savings since lignin can be less expensive than phenols. The lignin is usually methylolated *in situ* during the PF resin formulation, replacing anywhere from 15 to 35% of the phenol (12,13). Some lignins (eg, lignosulfonates) have also been added directly into the adhesive formulation as a PF resin extender (24–26). Although lignin-based adhesives are used in bonding wood composites, these adhesives require longer press times, produce darker coloration of the panel, and potentially have lower strength relative to PF without lignin (19,25). However, composites having good dimensional stability and good performance under conditions of high moisture have been reported for boards produced with lignin-extended resins, so interest in developing these adhesives continues (4).

Tannin. Tannin is an inexpensive naturally occurring polyphenol found mostly in the bark of trees but also as a component of the wood of some species. Tannin, like lignin, has also been used as a substitute for phenol in the manufacture of PF resins (4,30,31). Although using tannin-based adhesives in the manufacture of wood composites is thought to have potential, some reports indicate that these resins have lower cohesive strength and lower moisture resistance compared to common exterior wood adhesives (30). The poor performance of tannin-based adhesives is attributed to their limited ability to cross-link into a three-dimensional network, their high initial viscosity, and a short pot life owing to the high reactivity of tannin with formaldehyde. However, extensive research has been conducted in recent years to improve the performance of tannin-based adhesives. For example, the addition of small amounts of amino or phenolic resins (4) or metallic ion catalysts (18) has been shown to effectively increase the degree of cross-linking, thereby improving the strength and moisture resistance of tannin adhesives. Reducing the pH or adding hardeners such as hexamethylenetetramine during resin formulation has been shown to decrease the initial viscosity of some tannin-based adhesives (19) thus extending their pot life. These breakthroughs have allowed tannin-based glues to be used in the manufacture of wood composites in South Africa, New Zealand, India, South America, and to some extent in North America.

Other adhesives such as hot melt adhesives (HMA), poly(vinyl acetate) (PVA, catalyzed or uncatalyzed), pressure-sensitive adhesives (PSA), or elastomeric adhesives (based on natural or synthetic rubbers) are also used in wood bonding (7). However, their use is mostly limited to nonstructural applications (eg, secondary manufacturing processes such as kitchen furniture, interior joinery, decorative paper, and packaging) where strength and water resistance are of limited concern.

Advances in Wood Composite Adhesives

Improvements in wood composite properties can be achieved in three areas: (*1*) improvements in wood properties, (*2*) improvement in adhesive properties, and (*3*) improvement in the overall wood composite design. Most advances in wood composites witnessed over the last 10–15 years have been brought about by improved manufacturing equipment and improved composite design (eg, oriented strandboard, I-joist, parallel strand lumber, and laminated strand lumber), while significant advances in future wood composites seem likely to involve changes in wood properties (eg, genetic modification to produce species with some desired property such as improved resistance to decay). However, given the importance of developing alternatives to petroleum-based materials, development of new adhesives may yield the next generation of significant advances in wood composite products.

Some of the more recent research efforts that may lead to new adhesive types are categorized as follows: (*1*) adhesives from natural products, (*2*) adhesives generated *in situ* in the wood, (*3*) adhesive modifications to facilitate processing, and (*4*) adhesive modification for improved properties. Examples of these approaches are given below.

Prior to the 1930s all adhesives were based on natural products (eg, proteins such as animal blood, casein, soy protein). Use of adhesives from natural products steadily decreased thereafter with the development of synthetic polymers that had superior properties. Recently, renewed interest has been shown in using natural products to replace, entirely or in part, petroleum-based adhesive components with natural products, without sacrificing the performance levels achieved with modern petroleum-based adhesives. The purposes are often to reduce cost and dependence on petrochemicals, to reduce formaldehyde emissions, and improve selected properties (eg, biodegradability).

For example, there is renewed interest in using soy-based adhesives for fiber-based composites. New research is underway to develop soy-based adhesives that have improved properties and durability, and that have low volatile emissions (32).

Lignin-modified PF has been utilized for more than 20 years in a variety of different wood products (fiberboards, strandboards, structural plywood, etc.) where the lignin extender has lowered the cost. More recently lignosulfonates have been utilized as extenders to replace up to 35% of phenol in PF formulations (15). It has also been evaluated as an extender for other resins such as epoxy and polyurethane. Considerable research has recently been directed toward incorporating lignin into copolymers or grafting reactive monomers onto lignin allowing it to be copolymerized (33). One recent example of this approach describes using enzymes to copolymerize lignin with alkenes to produce well-defined lignin acrylate copolymers within fibers and pressing those fibers into medium density fiberboard (MDF) (34).

Work in South Africa and in South America has resulted in development of adhesives based largely or entirely on tannins. Tannins, which like lignins are renewable natural products, have the advantage of affording adhesives with low or no formaldehyde emissions, but tannin-based adhesives tend to be brittle.

A useful tannin-based particleboard adhesive was reported using tannin extract from radiata pine bark that was formulated with 5% isocyanate and 5% urea (13). Another report described a tannin-based adhesive in which a significant number of the phenolic groups of the tannin had been esterified to produce a less brittle adhesive (35). The partially esterified tannin was blended with paraformaldehyde and the resulting resin afforded a less brittle adhesive that had better properties than those of the unmodified tannin adhesive.

Because lignin and tannin are phenolic species they have both been evaluated as extenders for PF and UF adhesives. It was subsequently shown that they could be used as primary adhesives. Because these natural phenolics can function as primary adhesives, and because these and other phenolics are components of wood and bark, researchers are investigating reactions of wood's natural phenolic components *in situ* to form a composite without added adhesives. Bark contains not only high amounts of tannins, but also carbohydrates and various other reactive phenolic components. Composites have been prepared by subjecting bark particles to high temperature and pressure to react the phenolic components within the bark so that these components cross-link *in situ* to serve as the sole binder for composites (13). A 1999 publication reported a similar approach for binding wood (36). In that work, birch wood was heated for 1–15 min at 170–230°C under 2 MPa pressure from hot steam. These conditions were used to hydrolyze the polysaccharides within the wood. Under the acidic conditions (formic and acetic acid from hemicellulose and sugars) the resulting sugars reacted with phenolic fragments originating from hydrolyzed lignin. These reactions yield a polymeric binder *in situ*, and have several advantages over adding adhesives to wood. These advantages include eliminating the need for equipment to apply adhesive to wood, no formaldehyde emissions from added synthetic adhesive, and this approach accommodates a high moisture content in wood, which is a major processing advantage. Nevertheless, the long processing time required at high temperature is expensive and additional research is required to evaluate the composite properties, so it is not yet known if this approach will be cost-effective.

Research efforts have been directed towards developing new adhesives that address some disadvantages associated with the processing of pressed wood composites. Pressed wood composites using thermosetting adhesives typically employ a high temperature press cycle. This process requires that the wood furnish be dried to a moisture content typically below 5%. Pressing wood with higher moisture content at higher temperatures can produce a poor product because of "blows," delaminated wood produced when water vapor generated within the mat during the hot-press cycle is rapidly released. Development of effective adhesives that tolerate high moisture content wood has been a goal for many years because drying the wood furnish to a low moisture level is time-consuming and costly, and the potential exists for overdrying some of the wood furnish. Moisture-tolerant isocyanate and PF adhesives are currently available that can tolerate high moisture content furnish (above 15%). Isocyanate adhesives have been used for many years with composites that use higher moisture-content conditions such as "wet wood." Under these conditions isocyanate adhesives have less tendency to delaminate than other adhesives (37). This is probably because of several characteristics of isocyanate-bonded wood composites, including that they can be pressed at a lower temperature than is usual for UF and PF adhesives, isocyanates can

chemically bond to the wood rather than rely only on mechanical adhesion, and the cured adhesive retains greater flexibility than UF and PF adhesives. PF adhesives that can be used with wet wood are also available, but their exact composition and method of function is not clear, although these adhesives may make use of higher formaldehyde content, a coupling agent to promote wood bonding, and/or be a PF/isocyanate blend.

Approaches have been developed that allow some other adhesives to be used with wet wood. The simplest of these approaches uses foamed adhesives. Foaming allows the adhesive to be applied at a higher solid content, often having only 15–20% water, and so higher moisture content in wood can be tolerated, and the composite cures faster since less moisture needs to be removed during cure. A recent investigation reported use of a soy protein-modified PF as a foamed adhesive for plywood production (38). The soy replaced animal blood in the formulation, which not only improves durability but can alleviate health concerns.

Another major difficulty with hot-pressed wood composites is adequate thermal transfer across the thickness of the composite. Heat is transferred through the press platens, sometimes with the aid of steam. However, wood is a low thermal transfer medium and so there is risk of overcuring resin nearer the surfaces of the composite, while undercuring resin in the interior. This is particularly true with thicker composites. Also the pressing step is probably the most expensive of the processing steps so any adhesive modification that reduces the press time and facilitates a more uniform cure is a significant advantage for cost and properties. Matuana (39) reported using thermally conductive filler material such as synthetic graphite (carbon filler) in the mat or adhesive to facilitate thermal transfer. Use of the carbon filler not only reduced the required cure time but also significantly increased the internal bond strength of the wood composites.

Wood composites are now being considered for use under increasingly demanding conditions and so adhesive modifications to improve specific composite properties, such as improved strength, durability, and dimensional stability, are needed. These types of modifications which usually increase adhesive cost were previously considered not cost-effective, but now might find markets. Early efforts to improve properties included adding thermoplastic polymers to the reactive adhesive prepolymer and applying the thermoplastic-modified prepolymer to the wood furnish and pressing. Examples of this approach include adding poly(furfural alcohol), a water-soluble polymer, to a UF prepolymer (40) and using chlorinated natural rubber to modify PF (41). The poly(furfural alcohol) did not improve properties, while the chlorinated natural rubber did improve properties but required processing conditions that were not industrially viable. These efforts highlight issues that must be addressed for an industrially useful modification. Any modifications must allow the processing conditions to be similar to those used now. Therefore, solvent should not be required, and prepolymer viscosity, stability, and cure conditions should be similar to those used now, and the resulting properties must be improved sufficiently so that an increased resin cost is worthwhile. A series of publications by Ebewele and coworkers (42–45) described modifying UF resins with di- and trifunctional amines and ureas without excessive increases in viscosity or processing difficulty. Particleboard made with the modified UF resins had an internal bond (IB) strength that was significantly greater than the IB strength of the control particleboards

before and after exposure to moisture. Recently a method was reported that yielded thermoplastic-modified UF adhesives that could be processed in the same way as unmodified control UF and gave wood flour composites with improved mechanical properties and moisture resistance. A premade thermoplastic polymer suspension (46–48), or aqueous slurry of acrylic and vinylic monomers, and a radical polymerization initiator (49) were combined with the UF prepolymer. The modified UF was used to prepare hot-pressed wood flour composites with significant improvements in notched Izod impact strengths. Further development simplified the method and modified UF resins were employed for hot pressing of particleboards (50) that, depending on the choice of thermoplastic monomers employed, also gave a higher IB strength and the neat resin showed lower moisture uptake than unmodified UF neat resin. Zanetti and co-workers (51) recently reported substantial increases in the IB strength of melamine–urea–formaldehyde (MUF) resins by the addition of small amounts (10%) of acetals to MUF resins. The authors reported that the acetals worked by improving the solubility of melamine and higher molecular weight reactive oligomers in the MUF resin and also appeared to disrupt the clustering of colloidal particles of MUF. This modification afforded 25–50% increases in IB strength and yet required no additional modification of the MUF formulation or the processing conditions.

Wood Composites Bonded with Thermoset Adhesives

The principal wood composite products currently in use in the United States and Canada, based on volume, are plywood (17.5 million cubic meters), oriented strandboard (16.8 million cubic meters), particleboard (10.3 million cubic meters), medium density fiberboard (3.4 million cubic meters), hardboard (2.0 million cubic meters), hardwood plywood (1.0 million cubic meters), and laminated veneer lumber (1.2 million cubic meters) (13). These products are described below. While all of these composites occupy an important place in the market now, some of these products are gaining in importance while others appear to be losing market share to other composite products.

Wood composites for structural and nonstructural applications that are bonded with thermosetting glues can be produced in many different geometries, including panels (3 ft or more in width by 3/8 to 1 in. thick), lumber (2 in. or more in width by 2–4 in. thick), or beams ($3\frac{1}{8}$ in. wide by 9 in. or more in depth) (Table 2). The exact procedure for making wood composites depends on the type of wood furnish (wood geometry), the desired arrangement of the particles in the final product, and the adhesive to be used, as well as the cure cycle if the adhesive needs to be reacted during the process step. These processing variables determine the characteristics of the final products, including mechanical properties, water resistance, dimensional stability, surface quality, and workability. Regardless of the increasing number of wood composite products being introduced into the market, the different sizes and shapes of these products, and the different volumes of these products that are produced, the fabrication process is a highly automated one, and once the adhesive mixture is applied to the wood furnish the general manufacturing method for preparing these composites is similar (Fig. 6).

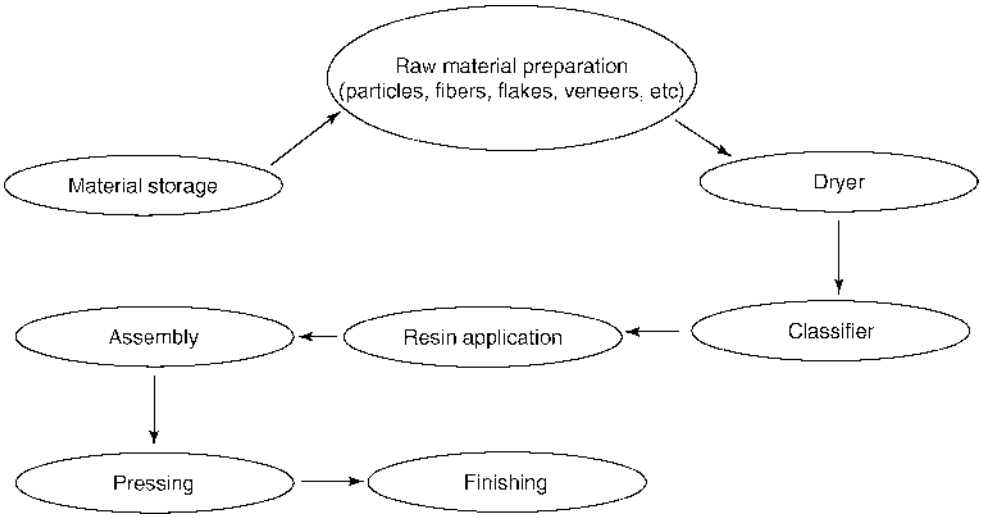

Fig. 6. A typical wood composites manufacturing process.

The composite fabrication process begins once the trees have been processed into a dried furnish and the furnish is transported to a device such as rotating drum (as is the case for flakes, particles, and fibers). Here, the adhesive and other additives are applied to the furnish by air spray, airless spray, or a high shear atomizer. The rotating drum possesses nozzles that are fed by hose lines connected to resin storage drums. Adhesive resin mixtures are applied to veneer-based wood products (plywood, laminated veneer lumber) by a roll coater, curtain coater, spray coater, or liquid or foam extrusion. The amount of adhesive applied to the furnish varies with the product and adhesive type. Common additives are also applied during this step and include wax (to improve dimensional stability by reducing moisture absorption), wood preservatives (for protection against insect and fungal attack), and fire retardants.

After resin application, the coated wood furnish moves to a forming apparatus. The forming apparatus arranges the furnish appropriately into a mat having the specified dimensions and orientation of wood raw material to give the desired product type with the desired dimensions and density after pressing. This mat is then prepressed to remove much of the air, ie, consolidate a loosely formed mat into a rigid mat which has a certain degree of cohesion to reduce its thickness. The formed mat then goes to a hot press where it is subjected to a selected press cycle. Here it is heated and pressed at the desired temperature and pressure for specified periods of time to bond the wood into a composite part of the desired thickness. The pressed wood composite finally goes on to the finishing steps where the panel is sized, sanded, trimmed to the desired thickness and dimensions, edge sealed, and packaged for shipment. In some cases the hot composite product is stacked to help retain heat and continue the cure out of the hot press, as is the case with phenolic resins.

The biggest differences in processing for each type of wood composite reside in the geometry and arrangement of wood furnish, the adhesive type and amount

applied, and the cure cycle. The following sections describe the main characteristics of the major wood composite products made with thermoset adhesives.

Plywood. Plywood panels have been produced and marketed in the United States for more than five decades. They are considered a material of choice in the building industry because of outstanding structural performance as defined by a high strength-to-weight ratio, excellent dimensional stability, and durability compared to other building material (6). Plywood typically consists of an uneven number of thin layers of wood veneers, called plies, that are glued together into a panel. The individual plies are typically arranged in the panel so that their grains are perpendicular to one another (right angles of 90°). The plies are arranged at 90° to one another to improve the dimensional stability and make the properties of the plywood more uniform along both the vertical and horizontal axes. The anisotropic nature of wood results in a tendency to swell less parallel to the grain than perpendicular to the grain and simultaneously gives wood greater strength parallel to the grain than perpendicular to the grain. Therefore, arranging individual plies at 90° to one another affords greater dimensional stability, decreases the tendency to split, and generally evens out the strength properties in all directions. If the grain angles were not varied then the plywood would have less dimensional stability and be much stronger along the grain axis but weaker perpendicular to the axis. The appearance of the final product can be improved if desired by applying a decorative surface veneer to give the final plywood a desired appearance. The final overall properties of the plywood depend on many factors, including the wood species, the quality of wood veneers, the order of placement of the veneer plies in the panel, the type and amount of adhesive applied, and the curing or pressing conditions.

Both hardwood and softwood species are utilized in the manufacture of plywood. Softwoods (Douglas-fir, western hemlock, larch, white fir, ponderosa pine, redwood, and southern pine are examples) are generally preferred in construction applications where strength and stiffness are required. Hardwood plywood is generally preferred for decorative applications where appearance is most important and strength is a limited criterion, although hardwood plywood can also be designed for structural applications. In decorative applications, hardwood plywood often competes with thin MDF which can be given a high quality overlay giving it an appearance similar to that of hardwood plywood.

Oriented Strandboard (OSB). Oriented strandboard (OSB) panels have been developed as an alternative to plywood in building construction. The emergence of OSB was driven in part by a decreased supply of large diameter logs suitable for veneer production, and by innovation and productivity changes in the North American wood products industry over the past few decades as well as the structural performance of OSB products, which are suitable for use in most plywood applications but at a much lower cost. In addition, OSB manufacture allows small, low grade timber resources to be processed into a marketable product. This effectively saves raw materials that are in short supply and promotes efficient utilization of wood (3,5,6).

OSB panels are made up of rectangular strands (wafers or flakes) of wood approximately 0.030 in. thick, bonded together with exterior-grade adhesive under extreme heat and pressure to develop adequate strength properties in the panel. During this process, long grain strands are compressed and mechanically

oriented more or less parallel to each other and arranged into three to five distinct layers. These layers are oriented at ca 90° to one another, ie, strands are aligned lengthwise in layers perpendicular to each other similar to veneer plywood. The strands near the surface are typically ≥ 3 in. long but shorter strands are sometimes used in core layers. The core layers are also sometimes randomly arranged rather than oriented. The strands for the faces are typically oriented parallel with the long direction of the panel, whereas the core layers are oriented perpendicular to the length of the panel. Hardwood species, alone or in combinations with softwood species, can be used in the manufacture of OSB panels, but preferably lower density wood species (eg, aspen poplar in the northern part of North America and southern yellow pine in the south) are employed because strands of these woods can be compressed into medium density boards with sufficient contact between strands during pressing for good bonding (4).

The alignment of strands and the use of long strands give OSB panels improved mechanical (strength and stiffness) and physical (dimensional stability) properties in the direction of alignment, which make them acceptable in a wide range of industrial, residential, and commercial applications (Table 2). Even though OSB panels are being used as a substitute for plywood, their potential for use in some structural applications has been limited because of poor dimensional stability and durability compared to that of plywood. OSB panels will swell in thickness, and like all wood products decay when they come into extended contact with water. Since most of the thickness swelling is not reversed when the panels are re-dried, the products are regarded as unacceptable for some applications where high moisture contact is expected (52–54).

Particleboard. Particleboard is prepared using small dried-particles combined with a thermally curable adhesive or other suitable binder and bonded together under high heat and pressure into panels of the desired thickness. The raw materials used to produce particleboard consist of wood wastes from sawmills, primarily from milled or ground wood chips, sawdust, and planer shaving. In some cases recycled cellulosic materials and plant residues such as wheat straw and bagasse are utilized as furnish to make particleboard. Most particleboard is formed into flat panels. However, molded and extruded particleboard products such as furniture parts, molded door skins, and molded pallets are also produced.

Particleboard usually consists of a three-layered panel with two surface layers (outer layers) and one core layer (inner layer). The face furnish is usually thinner than that in the core. This permits the strength and stiffness of the panel to be tailored and the faces to be produced with smooth surfaces. The American National Standard for Particleboard, ANSI A208.1, classifies particleboard by density, properties, and class, and is the voluntary particleboard standard for the North American industry (Table 3).

Medium Density Fiberboard (MDF). MDF is manufactured from refined wood chips or other fine cellulosic materials combined with a synthetic resin. The adhesive coated furnish is joined together under heat and pressure to form a versatile material having varying characteristics depending on the composition and processing conditions (Tables 2 and 3).

The surface of MDF can be controlled so that it is smooth, flat, and uniform in appearance and free of wood growth features such as knots and grain patterns. MDF panels are highly valued by woodworkers because they machine well and

Table 3. Selected Properties of Wood-Based Composite Panels

Physical properties	Plywood[a]	OSB[b]	Particleboard[c]	MDF[a]
Density, lb/ft^3[d]	28–31	36–44	40–48	<40 to >50
Thickness, in.	1/4–$1\frac{1}{4}$	1/4–3/4	1/2–$1\frac{1}{4}$	3/4 or higher
Internal bond (IB), psi[e]	Species specific	50	15–145	44–131
Modulus of rupture (MOR), psi[e]	3000–7000	3394–4206 (‖) 1392–1799 (⊥)	435–3408	2030–5003
Modulus of elasticity (MOE), 10^3 psi[e]	1000–1900	653–798 (‖) 189–218 (⊥)	79.8–449.6	203–500
Screw holding capacity—face, lb	Species specific	100–300	90–450	172–342
Screw holding capacity—edge, lbs	Species specific	100–300	180–348	147–294
Hardness, lb	Species specific	—	500–1,500	—
Linear expansion (max. avg. percent)	0.15	0.20–0.40	0.35	—

[a]Properties for various plywood grades or MDF (55).
[b]Properties obtained from the Canadian Standards Association, standard CAN3–0437.0-M85, Waferboard and Strandboard/Test Methods for Waferboard and Strandboard (June 1985). ‖ means parallel to the indicated direction of face alignment; ⊥ means perpendicular to the indicated direction of face alignment. The Wood Handbook (55) shows OSB having MOR values of 3000–4000 psi and MOE values of (700–1200) × 10^3 psi.
[c]Properties obtained from ANSI standard (ANSI A208.1–1999) for various grades of particleboard.
[d]To convert lb/ft^3 to kg/m^3, multiply by 16.
[e]To convert psi to MPa, divide by 145.

are suitable for finishing operations such as direct printing (eg, wood grains), thin laminating (eg, paper, decorative foil laminates), and painting (eg, custom colors). These attributes allow MDF panels to serve as excellent substitutes for solid wood in many interior applications such as kitchen cabinets, furniture, door parts, and moldings (Table 2).

Composite Lumbers and Beams. Composite lumbers and beams comprise a large and diverse family of products known as engineered wood products (EWPs). EWPs include laminated veneer lumber (LVL), laminated strand lumber (LSL), parallel strand lumber (PSL), glulam, and I-joists, among others.

LVL [also known as structural composite lumber (SCL)] technology was developed in Finland. Trus Joist became the first U.S. producer of LVL in 1970 (3,6). LVL is a structural building material manufactured by layering dried and graded wood veneers with waterproof adhesive into billets of various thicknesses and widths. Generally, high quality laminates are used at the faces and low quality laminates in the center of the lumber. This specific arrangement gives LVL greater strength (by a factor of 2 or more) than conventional solid lumber having equivalent dimensions. In LVL billets, all veneers are laminated with the grain angle parallel to the longitudinal axis of the wood (one-grain direction) rather than arranging the veneer grains perpendicular to one another as in plywood. PF and pMDI are the resins that are typically employed to produce LVL and so the billets are hot-pressed or radio-frequency-pressed to consolidate the laminates. Common wood species used for LVL include Douglas fir, larch, southern yellow pine, and poplar, but other wood species can be used as the raw

material. As an engineered wood product, LVL is an ideal structural building material for applications in housing, commercial, and industrial construction. Typical applications include floor and roof joists, roof beams, roof truss chords, flanges for prefabricated wood I-joists, concrete form, and scaffolding plank, among others (Table 2).

Wood I-joists are hybrid beam elements that are made by gluing together lumber and panel composites to produce a dimensionally stable lightweight member having specified engineering properties. The product utilizes the geometry of the I-shaped cross section composed of two flanges (top and bottom) of various widths linked by a web (or two webs) of various depths (Table 2). The flanges are typically LVL, or finger-jointed sawn lumber of various machine stress-rated grades, while the webs are either structural grade OSB or structural plywood. The flanges are designed to resist bending strength and provide stiffness, while the web is designed to resist shear forces in the beam. Thus, the I-shaped geometry of these products gives a high strength-to-weight ratio. I-joists are marketed as building products that do not warp, twist, or shrink, and their dimensions are more uniform than those of conventional sawn lumber joists. The wood I-joists performs much better than solid lumber because greater joist spacing can be used and their frames are lighter and more dimensionally stable than lumber, making their installation less costly for the builders. Wood I-joists are used in residential and light commercial construction in applications such as floor and roof joists, rafters, and purloins, among others (Table 2). Wood I-joists are certified by the APA-Engineered Wood Association as the APA-Engineered Wood System (APA-EWS), and are manufactured in compliance with Performance Rated I-Joists (PRI-400), Performance Standard for APA-EWS I-Joists.

Glued laminated timber, or glulam, is a structural beam element manufactured by gluing laminates of solid wood lumber, finger-jointed lumber, or LVL. The individual lumber elements are oriented parallel to the longitudinal axis of the beam and laminated flat-wise to bond along the entire length and width of the lumber elements. Based on the stiffness rating of the individual laminations high quality laminates are generally applied at the beam faces, while low quality laminates are placed in the middle of the beam. This combination is preferred since the load is carried by the beam in the top and bottom faces, while the middle only has to resist shear. A cold curing resin adhesive such as resorcinol or phenol–resorcinol is usually used to produce the beam by applying the adhesive and clamping or cold-pressing the laminates. Since little or no heat is required for the cure, curved glulam members and other customized shapes can easily be produced. Glulams are manufactured in accordance with the American National Standards Institute (ANSI) ANSI standard A190.1 for structural glued laminated timber. The strength values (bending and shear) for glulam are higher than for lumber. Glulam members are typically used as headers, beams, arches, etc (Table 2). The production of glulam is not expected to grow significantly in North America because of the scarcity and high cost of laminating grade lumber, combined with stiff competition from LVL and other engineered wood products such as LSL and PSL, which are expected to grow because they have excellent structural properties and they employ more readily available raw materials (5,6).

PSL is an engineered wood product developed by MacMillan Bloedel, Ltd., of Canada and was first commercialized in 1988 (3,6). PSL is made in a similar

manner to glulam beams with the difference being that strands of broken-up veneer (about $\frac{1}{2}$ in. wide and up to about 37 in. long) are employed instead of solid lumber laminates. The strands are oriented and laid-up into a mat in a lengthwise direction, ie, aligned parallel to one another. The strands are glued with a water-resistant adhesive (PF) and are consolidated in a continuous microwave press. PSL is stronger, stiffer, and more stable than sawn lumber having the same cross section and is free of splits, knots, and warp. PSL is employed in various applications such as head beams, trusses, and other structural frames (Table 2).

LSL is another type of engineered wood product in which all the strands are aligned in one direction, ie, LSL is an oriented strand lumber. The strands in LSL are shorter than in PSL and produced from strand wood rather than veneer. The strands are typically longer than strands utilized in oriented strandboard. Pressing includes steam injection rather than radio-frequency heating, and isocyanate resin is typically used rather than PF adhesive. LSL is used in industrial and light structural applications (Table 2).

Wood Thermoplastic Composites

Wood-based composites continue to be among the most widely used building materials throughout the world. While thermoset wood composites date back to the early 1900s (a wood flour/PF composite called Bakelite®), wood combined with thermoplastic composites have become of major commercial importance only since the 1980s in the United States, although they have been in use longer in Europe (2). Wood-plastic composites (WPCs) represent a rapidly growing industry in the United States in both the plastic processors and forest products industries (56–58).

To plastic processors wood and other lignocellulosic fibers (eg, agrofibers) represent a vast supply of readily available raw materials for all types of WPCs. Statistics show that 2.5 million tons of fillers were used in North America in 2001 with the most important fillers being inorganic materials (2.3 million tons) such as calcium carbonate (1 million tons), glass fiber (0.77 million tons), and other mineral fillers such as clay, talc, mica (0.55 million tons). Only 182,000 t was natural fibers (57). The inorganic materials enhance some composite properties (eg, strength and modulus) and are extensively employed as fillers, but have several drawbacks. They are produced from nonrenewable sources and they have high density, so products prepared with inorganic fillers tend to be heavy. Furthermore, these inorganic fillers cause equipment wear during processing (59). Therefore, on a volumetric basis, their use may not be very cost-effective. During the past two decades, wood fibers and other lignocellulosic materials have begun to penetrate the filled thermoplastic markets because they possess many advantages relative to the common inorganic fillers. These advantages include high specific stiffness and strength, easy availability, lower density, lower cost on a unit-volume basis, low hardness which minimizes wear of the processing equipment, renewability, recyclability, safety, and biodegradability (60,61). The replacement of inorganic fillers with lignocellulosic fibers also provides an opportunity to increase processing productivity rates (56).

Table 4. Some Physicomechanical Properties of WPCs and Comparative Performance of WPCs with (Oak) and Softwood (Pine) Solid Wood

Tests	Test methods	HDPE/WF[a]	PVC/WF[a]	Northern oak[b]	Ponderosa pine[b]
Specific gravity	ASTM D143	0.96–1.1	1.36	0.56–0.63[b]	0.38–0.40[b]
MOR, psi[c]	ASTM D790	790–1423	2100–4500	14300[b]	9400[b]
MOE, 10^3 psi[c]	ASTM D790	160–510	700–980	1820[b]	1290[b]
Water absorption, %	ASTM D1037	0.7–4.3	1.2	—	17.2
Thickness swell, %	ASTM D1037	0.2	—	—	2.6
Nail withdrawal, lb	ASTM 1761	90–170	—	—	50
Screw withdrawal, lb	ASTM 1761	430–600	—	—	165
Hardness, lb	ASTM 143	1290	—	1290[b]	460[b]
Linear coefficient of expansion (per °F)	ASTM 696	16×10^{-6}	17×10^{-6}	—	25×10^{-6}

[a]HDPE/WF and PVC/WF contained 50–70% wood fiber.
[b]MOE and MOR values measured at 12% moisture content (7).
[c]To convert psi to MPa, divide by 145.

The forest products companies, on the other hand, see plastics as a way to expand sustainable forest resource utilization through the use of wood waste, fibers from underutilized species, and reclamation and recycling of wood, other agricultural species and waste, and paper materials from municipal solid waste streams (62), as well as a way to make new construction materials with attributes that wood does not have (56).

WPCs are typically manufactured by first mixing dried cellulosic materials (in powder or fibrous form) with various plastics and other processing ingredients (eg, lubricants, fusion promoters, coupling agents, flame and smoke retardants, ultraviolet stabilizers). Cellulosic materials that are used in the production of WPCs include wood flour or particle, flax, jute, or other agricultural waste. The most commonly employed plastics are polyethylene (PE), polypropylene (PP), polystyrene (PS), and poly(vinyl chloride) (PVC). These thermoplastics are selected mainly because they can be processed at lower temperatures (150–220°C) to prevent the degradation of cellulosic materials (2). Generally, wood flour and other coarse particles (10–100 mesh size) are easier to handle during processing than long fibers which tend to agglomerate and cause dispersion problems during mixing. However, because of their higher aspect ratio, long fibers provide greater reinforcing effects in WPCs than particles. The fiber can be difficult to disperse but the dispersion problems can be offset by using compatibilizers during processing (60,63,64). Once mixed, the blended material is processed into the desired shape by conventional plastic processing equipment such as an extruder, injection molder, and a hot press (compression molding). Most of the WPCs used in construction applications are extruded to a profile of uniform cross section (solid or hollow) and any practical length, whereas products having more complex shapes such as those used in the automotive industry or other consumer products are injection- or compression-molded.

WPCs comprise an emerging class of materials that combine the favorable performance and cost attributes of both wood and plastics (Table 4). Because

WPCs are true hybrid materials, they have strength and stiffness properties that are somewhere between both materials. They have outstanding bolt, drill, screw, and nail retention and they machine similarly to wood. Generally, WPCs are stiffer than neat plastics and have attributes that solid wood does not have. If properly manufactured, WPCs are more resistant to moisture (water absorption and thickness swell) than wood and resist attack by insects and fungi better than other wood products. This outstanding performance is due to the fact that the plastic matrix encapsulates the individual wood fibers, thus interfering with moisture uptake by the wood element. Moisture can only be absorbed into the exposed sections of the wood. WPCs can be sanded, stained, painted, and finished just like natural solid wood. However, sealants and paints are not required for protection because WPCs resist moisture better than wood, and WPC products can be prepared with colorants and other additives during the processing phase, which eliminates the need for additional finishing.

Because of their performance, easy installation, and cost-effectiveness, WPC products are being selected by homebuilders over other materials such as solid wood, concrete, clay, and aluminum, especially as building materials for applications like decking, siding, and window and door frames. WPCs are also used as molded panel components for automotive interiors. The market for these composites continues to expand in the United States and other parts of the world. In 1999, 460 million pounds of WPCs were produced in North America (56). In 2000, production of these composites increased to 760 million pounds and experts believe that the production of WPCs will continue to grow particularly because of their acceptance as a substitute for chromated copper arsenate pressure-treated lumber (57,58).

Although a variety of WPC products have been commercialized, some drawbacks in their properties may limit the market potential of these products. For example, WPCs are more brittle and have lower impact resistance than neat plastic products (61,65). In addition, their high density (62–85 lb/ft^3), which is almost twice that of solid lumber (22–40 lb/ft^3 for various pine species), may hinder their acceptance in the conventional structural lumber market (66). In general, unfilled plastics are more ductile than WPCs because the incorporated brittle wood fibers alter the ductile mode of failure of the matrix making the composites more brittle (61,65,67). The higher density of WPCs compared to the unfilled plastic and solid wood is mainly due to the compression of wood cell walls during processing. The final specific gravity of WPCs manufactured by injection molding, extrusion, and compression molding, even when made with a 0.9 specific gravity thermoplastic resin, is over 1 because the wood cell walls are crushed or compressed nearly to the specific gravity of solid wood without air spaces (approximately 1.5), and voids between and within the wood fiber structure are completely filled with resin (68,69).

Several attempts have been made to overcome the drawbacks of dense WPCs (65,70–72). Significant improvements in the impact strength of WPCs are achieved by incorporating impact modifiers into the formulation (65). However, impact modification of WPCs does not enhance their ductility or reduce the density of the products (65). The creation of a microcellular void structure (wood-like structure) in WPCs through foaming has recently been found appropriate to reduce the weight of the composites (70–73). The lightweight WPCs, as a result of the presence of microcells, exhibit enhanced ductility and impact resistance.

Table 5. Mechanical Properties of Microcellular Pure Plastic and WPC Foams

	Mechanical properties[b]							
	Strength at break, MPa[c]		Tensile modulus (stiffness), GPa[d]		Elongation at break, %		Notched Izod impact strength, J/m[e]	
Samples[a]	Unfoamed	Foamed	Unfoamed	Foamed	Unfoamed	Foamed	Unfoamed	Foamed
Pure plastic (PVC)	17	14	0.06	0.07	84	126	72	206
WPC	14	13	0.37	0.20	28	63	31	87

[a]The density of pure PVC was 1.35 g/cm^3 whereas the densities of the composites with 30% wood fibers were in the range of 1.35–1.45 g/cm^3. The densities of foamed PVC and WPC samples were 0.60 g/cm^3.
[b]Properties are expressed as specific properties, ie, property divided by the specific density of the sample (72).
[c]To convert MPa to psi, multiply by 145.
[d]To convert GPa to psi, multiply by 145,000.
[e]To convert J/m to ft·lbf/in., divide by 53.38.

However, the reduced density can be achieved at the expense of other mechanical properties such as strength and stiffness (72,74) (Table 5).

There currently are no manufacturing standards for WPCs and the standard test methods for evaluating the mechanical and physical properties of WPC products are under development by the American Society for Testing and Materials (ASTM), committee D7 on Wood. The lack of manufacturing standards combined with the increased use of WPCs by the construction industry have also resulted in concern about the durability of these products exposed to outdoor environments. In applications such as decks and docks, landscaping timber, fencing, signposts, playground equipment, window frames, etc, the products can be in ground contact and/or are in an above-ground environment where there often are risks of material deterioration. When WPCs are in ground contact, biological agents such as fungi and subterranean termites may be the main cause of degradation (75,76). On the other hand, exposure to sunlight and moisture can cause degradation in an above-ground environment (77,78). Freeze-thaw durability may also be of significant importance in colder regions where freeze-thaw action is prevalent. These climatic environments may cause millions of dollars of material damage and high material cost may be involved to replace damaged products. Therefore, the durability of these composites is of special concern for their use in outdoor applications and is currently being extensively studied.

BIBLIOGRAPHY

"Composition Board" in *EPST* 1st ed., Vol. 4, pp. 75–118, by M. N. Carroll, Washington State University; "Composition Board" in *EPSE* 2nd ed., Vol. 4, pp. 47–66, by T. M. Maloney, Washington State University; "Wood, Polymer-Impregnated" in *EPSE* 2nd ed., Vol. 17, pp. 887–900, by J. A. Meyer. SUNY College of Environmental Science and Forestry; "Wood Composites" in *EPST* 3rd ed., Vol. 12, pp. 521–546, by L. M. Matuana, Michigan State University, and P. A. Heiden, Michigan Technological University.

CITED PUBLICATIONS

1. J. L. Bowyer, R. Shmulsky, and J. G. Haygreen, *Forest Products and Wood Science: An Introduction*, 4th ed., Iowa Press, Ames, Iowa, 2003, p. 554.
2. C. Clemons, *Forest Products J.* **52**(6), 10–19 (2002).
3. T. M. Maloney, *Forest Products J.* **46**(2), 19–22 (1996).
4. T. M. Maloney, *Modern Particleboard and Dry-Process Fiberboard Manufacturing* (updated edition), Miller Freeman Publications, Inc., San Francisco, 1993, p. 681.
5. L. M. Guss, *Forest Products J.* **45**(7/8), 17–24 (1995).
6. D. A. Pease in J. A. Sowle, ed., *Panels: Products, Applications and Production Trends, A Special Report from Wood Technology*, Miller Freeman Publications, Inc., San Francisco, 1994, p. 272.
7. A. A. Marra, *Technology of Wood Bonding: Principles in Practice*, Van Nostrand Reinhold, New York, 1992.
8. R. M. Rowell, A. R. Sanadi, D. F. Caulfield, R. E. Jacobson, in A. L. Leao, F. X. Carvalho, E. Frollini, eds., *Proceedings of the First International Lignocellulosics-Plastics Composites, Mar. 13–15, 1996*, Sao Paulo, Brazil, 1997, pp. 23–51.
9. J. A. Youngquist, A. M. Krzysik, B. W. English, H. N. Spelter, and P. Chow, *The Use of Recycled Wood and Paper in Building Applications* (Proceedings of a 1996 symposium sponsored by the U. S. Department of Agriculture Forest Service, Forest Products Laboratory and the Forest Products Society, in cooperation with the National Association of Home Builders Research Center, the American Forest & Paper Association, the center for Resourceful Building Technology, and Environmental Building News), Proc. 7286, Forest Products Society, Madison, Wis., 1996, pp. 123–134.
10. J. A. Youngquist, A. M. Krzysik, P. Chow, and R. Meimban, in R. M. Rowell, R. A. Young, J. K. Rowell, eds., in *Paper and Composites from Agro-Based Resources*, CRC Lewis Publishers, Boca Raton, Fla., 1997, Chapt. 9, pp. 301–336.
11. Anonymous, Wood-based Panel Products: Technology roadmap (Canadian Cataloguing in Publication Data), 1998, http://strategis.ic.gc.ca/trm.
12. T. Sellers Jr., *Wood Technol.* **127**(3), 40–43 (2000).
13. T. Sellers Jr., *Forest Products J.* **51**(6), 12–22 (2001).
14. T. Sellers Jr., *Panel World* **35**(3), 22–26 (1994).
15. T. Sellers Jr., *Panel World* **31**(5), 26–29, 44 (1990).
16. T. Sellers Jr., *Plywood and Adhesive Technology*, Marcel Dekker, Inc., New York, 1985, p. 661.
17. A. Gardziella, L. A. Pilato, and A. Knop, *Phenolic Resins*, 2nd ed., Springer, New York, 2000, p. 560.
18. A. Pizzi, *Advanced Wood Adhesives Technology*, Marcel Dekker, Inc., New York, 1994, p. 89.
19. A. Pizzi and A. Pizzi, eds., in *Wood Adhesives: Chemistry and Technology*, Vols. 1 and 2, Marcel Dekker, Inc., New York, 1983, 1989.
20. A. Pizzi and K. L. Mittal, eds., *Handbook of Adhesive Technology*, Marcel Dekker, Inc., New York, 1994, p. 680.
21. A. V. Pocius, *Adhesion and Adhesives Technology: An Introduction*, Hanser–Gardner Publications, Inc., Cincinnati, Ohio, 1997.
22. Z. W. Wicks, F. N. Jones, and S. P. Pappas, *Organic Coatings, Vol. 1: Film Formation, Components, and Appearance*, Wiley-Interscience, New York, 1992, p. 190.
23. M. Turunen, L. Alvila, T. T. Pakkanen, and J. Rainio, *J. Appl. Polym. Sci.* **88**, 582–588 (2003).
24. J.-S. Kazayawoko, B. Riedl, and J. Poliquin, *Holzforschung* **46**, 349–354 (1992).
25. J. S. M. Kazayawoko, B. Riedl, J. Poliquin, A. O. Barry, and L. M. Matuana, *Holzforschung* **46**, 257–261 (1992).

26. L. M. Matuana, B. Riedl, and A. O. Barry, *Eur. Polym. J.* **29**, 483–490 (1993).
27. W. Peng and B. Riedl, *Polymer* **35**, 1280–1286 (1994).
28. A. O. Barry, W. Peng, and B. Riedl, *Holzforschung* **47**, 247–252 (1993).
29. D. J. Gardner and G. D. McGinnis, *J. Wood Chem. Technol.* **8**, 261–288 (1988).
30. M. Fechtal and B. Riedl, *Holzforschung* **47**, 349–357 (1993).
31. M. Fechtal, B. Riedl, and L. Calvé, *Holzforschung* **47**, 419–424 (1993).
32. United Soybean Board 2002. Market Opportunity Summary, Soy-Based Wood Adhesives, Feb. 2002, and Soy-Based Wood Adhesives and the Environment, Feb. 2002, www.unitedsoybean.org.
33. J. J. Meister, Presented at the *2nd Annual Partnerships for Environmental Improvement and Economic Development Conference on Wood and Cellulose, Building Blocks for Chemicals, Fuels and Advanced Materials*, Syracuse, New York, Apr. 9–11, 2000.
34. A. Huttermann, C. Mai, and A. Kharazipour, *Appl. Microbiol. Biotechnol.* **55**, 387–394 (2001).
35. A. P. Barbosa, E. B. Mano, and C. T. Andrade, *Forest Products J.* **50**, 89–92 (2000).
36. O. V. Startsev, B. N. Salin, Yu. G. Skuridin, R. M. Utemesov, and A. D. Nasonov, *Wood Sci. Technol.* **33**, 73–83 (1999).
37. R. D. Palardy, B. A. Haataja, S. M. Shaler, A. D. Williams, and T. L. Laufenberg, *Forest Products J.* **39**, 27–32 (1989).
38. Anonymous, Soy-Based Foaming Adhesive May Change Plywood Industry, http:://www.unitedsoybean.org/feedstocks.pdf/fs9803.pdf, accessed May 26, 2003.
39. L. M. Matuana, *Forest Products J.* **53**(3), 40–42 (2003).
40. M. H. Schneider, Y. H. Chui, and S. B. Ganev, *Forest Products J.* **46**(9), 79–83 (1996).
41. J. Neetha and J. Rani, *J. Appl. Polym. Sci.* **68**, 1185–1189 (1998).
42. R. O. Ebewele, G. E. Myers, B. H. River, and J. A. Koutsky, *J. Appl. Polym. Sci.* **42**, 2997–3012 (1991).
43. R. O. Ebewele, G. E. Myers, B. H. River, and J. A. Koutsky, *J. Appl. Polym. Sci.* **43**, 1483–1490 (1991).
44. R. O. Ebewele, B. H. River, and G. E. Myers, *J. Appl. Polym. Sci.* **52**, 689–700 (1994).
45. R. O. Ebewele, B. H. River, and G. E. Myers, *J. Appl. Polym. Sci.* **49**, 229–245 (1993).
46. P. Rachtanapun, M.S. thesis, Michigan Technological University, 1999, p. 171
47. P. Rachtanapun and P. Heiden, *J. Appl. Polym. Sci.* **87**, 890–897 (2003).
48. P. Rachtanapun and P. Heiden, *J. Appl. Polym. Sci.* **87**, 898–907 (2003).
49. S. Das, M.S. thesis, Michigan Technological University, 2000, p. 169.
50. K. Carlborn, M.S. thesis, Michigan Technological University, 2002, p. 131.
51. M. Zanetti, A. Pizzi, M. Beaujean, H. Pasch, K. Rode, and P. Dalet, *J. Appl. Polym. Sci.* **86**, 1855–1862 (2002).
52. Can. Pat. 1,215,510 (1986), W. E. Hsu.
53. R. L. Geimer, and J. H. Kwon, *Wood Fiber Sci.* **31**(1), 15–27 (1999).
54. R. L. Geimer, J. H. Kwon and J. Bolton, *Wood Fiber Sci.* **30**, 326–338 (1998).
55. Wood Handbook: Wood as an Engineering Material, Forest Products Laboratory General Technical Report FPL-GTR-113, U.S. Department of Agriculture, Forest Service, Forest Products Laboratory, Madison, Wis., 1999.
56. J. Patterson, *J. Vinyl Additive Technol.* **7**(3), 138–141 (2001).
57. M. Defosse, *Mod. Plast.* 25–30 (Jan. 2003).
58. R. Donnell, *Timber Processing* 28–30 (Nov. 2000).
59. L. C. Czarnecki and J. L. White, *J. Appl. Polym. Sci.* **25**, 1217 (1980).
60. R. T. Woodhams, G. Thomas, and D. K. Rodgers, *Polym. Eng. Sci.* **24**, 1166–1177 (1984).
61. L. M. Matuana, C. B. Park, and J. J. Balatinecz, *J. Vinyl Additive Technol.* **3**, 265–273 (1997).
62. J. J. Balatinecz and R. T. Woodhams, *J. of Forestry* **91**(11), 22–26 (1993).

63. L. M. Matuana, R. T. Woodhams, J. J. Balatinecz, and C. B. Park, *Polym. Comp.* **19**, 446–455 (1998).
64. M. Kazayawoko, J. J. Balatinecz, and L. M. Matuana, *J. Mater. Sci.* **34**, 6189–6199 (1999).
65. F. Mengeloglu, L. M. Matuana, and J. A. King, *J. Vinyl Additive Technol.* **6**(3), 153–157 (2000).
66. F. Mengeloglu and L. M. Matuana, *J. Vinyl Additive Technol.* **7**(2), 142–148 (2001).
67. C. M. Clemons, A. J. Giacomin, and J. A. Koutsky, *Polym. Eng. Sci.* **37**, 1012–1018 (1997).
68. B. D. Park and J. J. Balatinecz, *J. Thermoplast. Comp. Mater.* **9**, 342–364 (1996).
69. R. L. Geimer, C. M. Clemons, and J. E. Wood Jr., *Wood Fiber Sci.* **25**(2), 163–169 (1993).
70. L. Matuana-Malanda, C. B. Park, and J. J. Balatinecz, *J. Cell. Plast.* **32**, 449–467 (1996).
71. L. M. Matuana, C. B. Park, and J. J. Balatinecz, *Polym. Eng. Sci.* **37**, 1137–1147 (1997).
72. L. M. Matuana, C. B. Park, and J. J. Balatinecz, *Polym. Eng. Sci.* **38**, 1862–1872 (1998).
73. L. M. Matuana and F. Mengeloglu, *J. Vinyl Additive Technol.* **7**(2), 67–75 (2001).
74. F. Mengeloglu and L. M. Matuana, *J. Vinyl Additive Technol.* **9**(1), 26–31 (2003).
75. P. I. Morris and P. Cooper, *Forest Products J.* **48**(1), 86–88 (1998).
76. W. Chetanachan, D. Sookkho, W. Sutthitavil, N. Chantasatrasamy, and R. Sinsermsuksakul, PVC/Wood: A New Look in Construction, in *Proceedings of Vinylitec 2000: Rigid PVC in the New Millennium: Innovations, Applications, Properties*, Sponsored by Vynil Division-SPE and Philadelphia Section, Philadelphia, Pa., Oct. 11–12, 2000, pp. 15–18.
77. L. M. Matuana and D. P. Kamdem, *Polym. Eng. Sci.* **42**, 1657–1666 (2002).
78. L. M. Matuana, D. P. Kamdem, and J. Zhang, *J. Appl. Polym. Sci.* **80**, 1943–1950 (2001).

LAURENT M. MATUANA
Michigan State University
PATRICIA A. HEIDEN
Michigan Technological University

WOOL

Raw Wool Specification

Wool is the fibrous covering from sheep (1) and is by far the most important animal fiber used in textiles. It appears to have been the earliest fiber to be spun and woven into cloth. In 2000–2001, world greasy wool production was 2.3×10^9 kg from 1×10^9 sheep, which is equivalent to 1.4×10^9 kg of clean wool (2) (Tables 1 and 2). This is down from a peak of 2.0×10^9 kg in 1989–1990.

Wool belongs to a family of proteins, the keratins, that also includes hair and other types of animal protective tissues such as horn, nails, feathers, beaks, and outer skin layers. The relative importance of wool as a textile fiber has declined over the past decades with the increasing use of synthetic fibers for textile products. Wool, however, is still an important fiber in the middle and upper price ranges of the textile market. It is also an extremely important export commodity

Table 1. World Production (10^6 kg) of Wool (2000/2001)[a]

Source	Fiber diameter, μm	Greasy	Clean
Merino	<24.5	932	572
Crossbred	24.6–32.5	540	308
Other (carpet)	>32.5	852	494
Total		*2324*	*1374*

[a]From Ref. 2.

Table 2. Wool Production and Numbers of Sheep in Principal Wool-Producing Countries (2000/2001)[a]

	Wool production (greasy)		
Country/region	10^6 kg	%	No. of sheep, (10^6)
Australia	652	28.1	113
China	291	12.5	135
New Zealand	258	11.1	45.3
South Africa	50	2.2	17.5
Argentina	62	2.7	13.4
Uruguay	57	2.5	13.0
United Kingdom	62	2.7	27.6
Turkey	70	3.0	30.2
Iran	74	3.2	53.9
Former USSR	128	5.5	49.2
Others	620	26.5	508
Total	*2324*	*100*	*1006*

[a]From Ref. 2.

for several nations, notably Australia, New Zealand, South Africa, and Argentina, and commands a price premium over most other fibers because of its outstanding natural properties. These include soft handle (the feel of the fabric), water absorption (and hence comfort), and superior drape (the way the fabric hangs). Table 2 shows wool production and sheep numbers in the world's principal wool-producing countries.

The principal characteristics of clean wool types are average diameter, measured in micrometers (referred to as microns), and average length, measured in millimeters. Essentially all fine diameter wool is produced by merino sheep or merino crossbreeds. Over 75% of the sheep in Australia (the world's largest wool producer) are merino sheep, which are also bred in large numbers in South Africa, Argentina, and the former USSR. The softness, fineness, and lightness of fabrics is determined primarily by fiber diameter, and so the price is very sensitive to the mean diameter (3) (Fig. 1).

Medium diameter wool includes sheep breeds of English origin, eg, southdown, hampshire, dorset, and cheviot, as well as crossbreds, eg, columbia, targhee, corriedale, and polwarth, from interbreeding with merinos. Coarse diameter wool comes from sheep chiefly bred for meat, eg, lincoln, cotswold, and leicester.

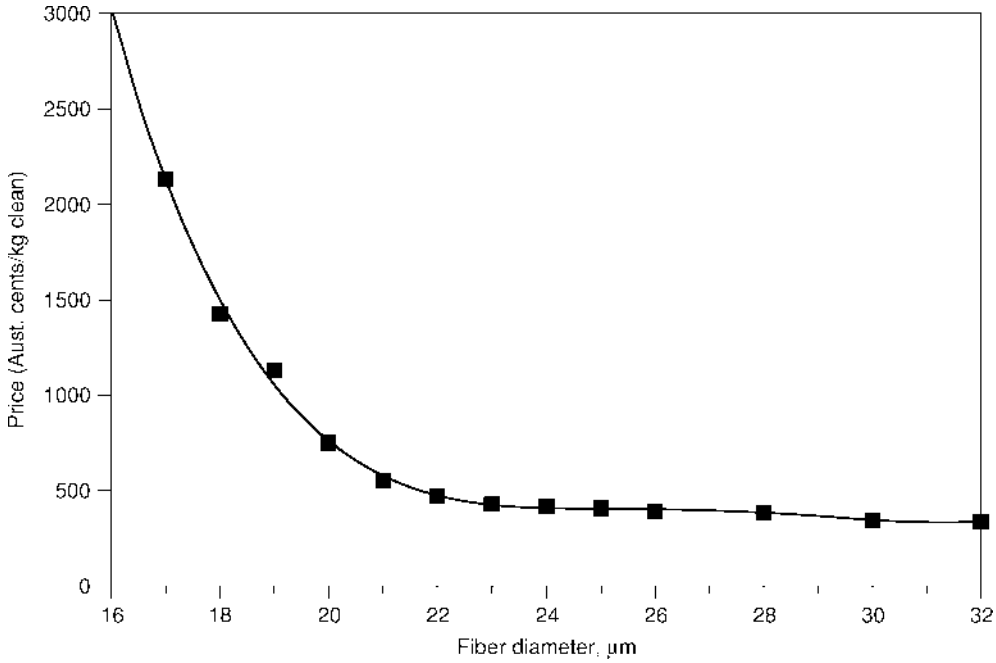

Fig. 1. Dependence of Australian wool prices on fiber diameter (1999/2000) (3).

Raw wool from sheep contains other constituents considered contaminants by wool processors. These can vary in content according to breed, nutrition, environment, and position of the wool on the sheep. The main contaminants are a solvent-soluble fraction (wool grease), protein material, a water-soluble fraction (largely perspiration salts, collectively termed *suint*), dirt, and vegetable matter (VM) (eg, burrs and seeds from pastures).

In buying raw wool, wool processors are concerned about its quality, the quantity of pure fiber present, and its freedom from contamination (4). For the fine and medium wools used for apparel, the major characteristics are average fiber diameter, yield (ie, the percentage content of pure fiber), content and type of VM, average fiber length, strength of fiber staples, and the position of any weak spot along the fibers. For very fine wools, the frequency and clarity of waves (crimp) in the staples has a significant effect on price. The range of fiber diameters, color of the clean wool, and the number (if any) of naturally colored fibers present can also be important. For carpet-type wools (long wools), the important properties (5) are yield, fiber diameter, fiber length, color, bulk (the volume occupied by the fibers in a yarn), and VM content. Also important for coarse wools is the degree of medullation. This is associated with cells containing air, arranged along the fiber axis. The presence of medulla cells increase light scattering by the fibers, restricting the use of these wools for some purposes.

Until the early 1970s, the characteristics of different wools were largely evaluated visually by wool classers and valuers. With the development of sampling techniques and equipment capable of rapid and economical measurement of yield, diameter, and VM (6,7), objective measurement and the sale of wool by

sample became dominant in major wool-exporting countries. In sale by sample, cores are drawn from each lot and tested for yield, diameter, and VM content in accordance with international standards (8,9). Measurements of staple length, strength, and position of weakness are also now in routine commercial use. In addition, a full-length display sample, representative of each lot and obtained by standard procedure (10), is available for buyers to appraise other characteristics. Sale by sample decreased costs by reducing the handling of bulk wool in wool-brokers' stores and selling operations. It also enabled the processing performance of wool to be predicted in topmaking (11) and spinning (12).

Fiber Characteristics

New instrumentation for measuring fiber diameter (13,14) has meant that data on the range of diameters present (CV_D) and fiber curvature (related to crimp frequency) are now available. The impact of these is fairly well established (15). These instruments have also been introduced on-farm so that the fleece quality of each animal can be assessed from a mid-side (16) or whole-fleece (17) sample. In some cases it is possible to gain increased returns from separating out the finest fleeces but bigger gains are possible from accelerating the rate of genetic progress. A remaining objective of research is to facilitate the introduction of a system of sale of raw wool by description in which a sale sample will not be required for inspection.

Fiber Growth. Wool fibers are produced from multicellular tube-like structures known as follicles. These follicles are located in the skin layers (dermis and epidermis) of sheep, and two types of follicles, primary and secondary, are usually identified. Primary and secondary follicles are described from the order of their initiation and development in foetal skin. The primary follicles develop first, in the unborn lamb. Secondary follicles develop later and in finer wooled sheep derived secondary follicles subsequently form by branching from the original secondaries, with which they share a common orifice (18). Each primary follicle has a sebaceous gland and a sweat gland together with an arrector muscle, whereas secondary follicles usually have only an associated sebaceous gland (19).

Fiber Morphology. Wool fibers consist of cells, where flattened overlapping cuticle cells form a protective sheath around cortical cells. A scanning electron micrograph of a clean merino wool fiber is shown in Figure 2. In some coarser fibers, a central vacuolated medullary cell type may be present.

In fine wool, such as that obtained from merino sheep, the cuticle is normally one cell thick (approximately $20 \times 30 \times 0.5$ μm) and usually constitutes about 10% by weight of the total fiber. Sections of cuticle cells show an internal series of laminations (Fig. 3), comprising outer sulfur-rich bands known as the exocuticle and inner regions of lower sulfur content called the endocuticle (20). On the exposed surface of cuticle cells, a membrane-like proteinaceous band (epicuticle) and a unique lipid component form a hydrophobic-resistant barrier (21). These lipid and protein components are the functional moieties of the fiber surface and are important in fiber protection and textile processing (22).

The cortex comprises the main bulk and determines many mechanical properties of wool fibers (Fig. 3). Cortical cells are polyhedral, spindle-shaped, and

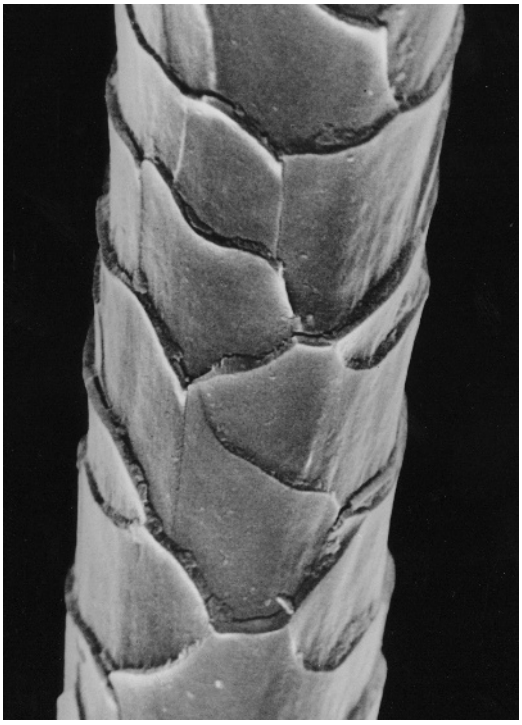

Fig. 2. Scanning electron micrograph of merino fiber, showing overlapping cuticle cells.

approximately 100 μm long. They consist of a class of biological filaments known as intermediate filaments (23) embedded in a sulfur-rich matrix. The intermediate filaments (originally termed microfibrils), together with the matrix, are organized into large macrofibrillar units and these are often observed in sections of cortical cells. In fine merino wool, two main types of cortical cell, known as ortho- and para-, are arranged bilaterally. Orthocortical cells show different intermediate filament/matrix packing arrangements from those of paracortical cells (24). The arrangement of ortho- and paracortical cells differs among wool types. For example, in lincoln wool an annular (orthocortical core surrounded by paracortex) cellular arrangement is present. Merino fibers possess a characteristic crimp and in these fibers the orthocortex is located on the outer side of the crimp curvature.

A continuous intercellular material is present between cuticle and cortical cells which, despite being a relatively minor fraction of the total fiber weight, is of increasing interest because of its presumed role in the penetration of water and chemical reagents into wool fibers. This region, called the cell membrane complex, is approximately 25 nm wide (25). It comprises a continuous phase of intercellular material, together with the apposing cellular membranes of the cuticle and cortical cells.

Over the past decade, major advances have been made in our knowledge of the cellular and molecular processes in wool follicles that lead to the formation of the wool fiber cuticle, fiber surface, and fiber cortex. In the wool follicle, presumptive cuticle cells undergo flattening during their passage up the follicle and

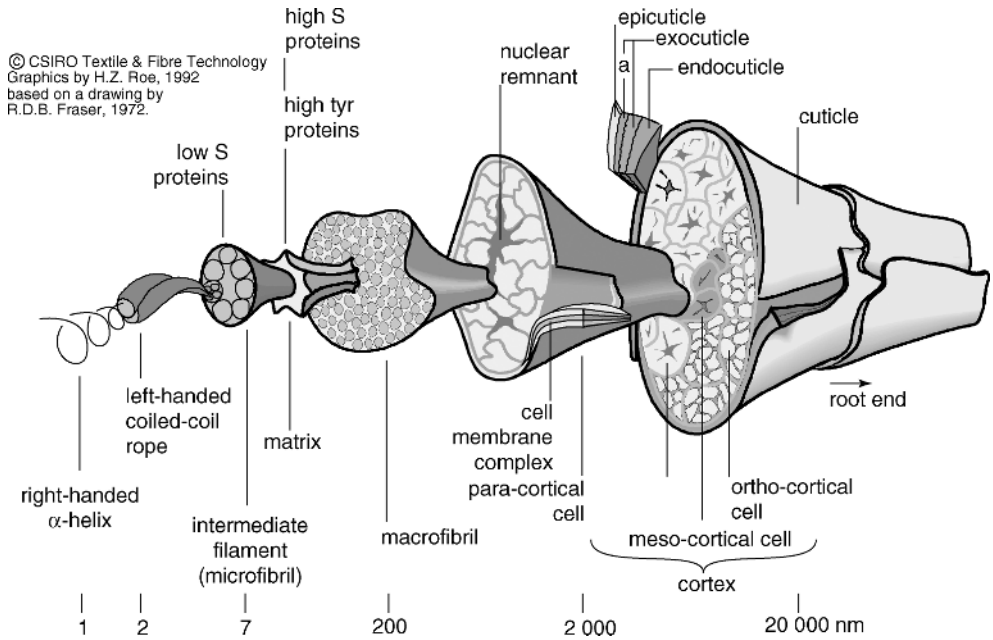

Fig. 3. Schematic of the structure of a fine merino wool fiber.

are interlocked with the cuticle cells of the inner root sheath (IRS). When examined by transmission electron microscopy (TEM), the developing fiber cuticle cells demonstrate densely stained intracellular laminae forming in the outer regions of the cells. As the laminae develop, they separate to form an outermost layer, the a-layer, and an underlying layer. Together, these layers comprise the exocuticle.

The remaining cellular volume contains an innermost lightly stained endocuticle (20). In the final stages of cuticle differentiation, proteolipid complexes are formed on the presumptive fiber surface. Unusual mixtures of fatty acids are present in these complexes, which lead to the formation of a hydrophobic surface on the emergent wool fiber (26).

During their upward growth in the follicle, fiber cuticle cells remain adhered to the IRS cuticle by intercellular laminae that develop between two cell types (20). This produces a membrane complex that is different in appearance to that formed between differentiated cortical cells. The main differences exist in the presumptive surface of fiber cuticle cells, where the original plasma membrane appears to be disrupted. This process has been observed by using energy-filtered TEM (21), where it appears that the intercellular laminae are precursors to the formation of a new fiber cuticle surface membrane. It seems reasonable to conclude that a specialized hydrophobic membrane must be synthesized, because a plasma membrane is designed to exist only in a physiological environment and could not perform the protective and other specialist functions of the fiber surface membrane. The mechanism involving separation of inner root sheath cuticle and fiber cuticle cells is essentially unknown, but the cleavage plane appears to occur

along a densely stained ultrafine band located in the center of the intercellular laminae (21).

Cortical cells form from a central or annular stream of germinal epithelia. During their early differentiation they undergo elongation and alignment processes. The initial sites for the formation of keratin structural components (arising concurrently with cell elongation) are at the outer boundaries (plasma membranes) of cortical cells, often in association with desmosomes (27,28). At high magnification, these initial keratin structures appear to consist of intermediate filaments (IFs) of 7–8 nm in diameter. These show appreciable staining when viewed after application of the heavy-metal preparations commonly used for contrast enhancement in TEM studies (28). After the formation and packing of IFs into lattice structures, a densely stained proteinaceous material appears to occupy the interfilamentous spaces. This proteinaceous material forms a matrix that is generally considered to be composed of high sulfur and high tyrosine proteins. The formation of these various structural components from their constituent proteins follows this two-stage sequential differentiation (29). As differentiation proceeds, the IF matrix aggregates to form structures, often known as macrofibrils, which increase in size and eventually occupy the bulk of presumptive cortical cells (30).

Chemical Structure

Wool belongs to the family of proteins called α-keratins, which also include materials such as hooves, horns, claws, and beaks (31). A characteristic feature of these "hard" keratins is a higher concentration of sulfur than "soft" keratins, such as those in skin. Although clean wool consists mainly of proteins, wool also contains approximately 1% by mass of nonproteinaceous material. This consists mainly of lipids plus very small amounts of polysaccharide material, trace elements, and, in colored fibers, pigments called melanin. The lipids are both structural and free.

Protein Composition. Proteins, or polypeptides, are formed by multiple condensation of α-amino acids via their amino and carboxyl groups to form secondary amide (ie peptide) bonds (—CONH—). The general structure of all proteins or polypeptides may be represented as (—NHCHRCO—), where R represents the side chain of the amino acid. The peptide grouping is also known as an amino acid residue, because it is the part of the amino acid that remains after the condensation reaction. Complete acid hydrolysis of wool yields 18 amino acids, the relative amounts of which vary considerably between fibers from different sheep breeds, from different individuals of the same species, and sometimes along the length of single fibers from the same animal (31). These differences are the result of several factors, including genetic origin and nutrition. Studies on the chemical structure of wool have been largely confined to fine merino fibers, although aspects treated herein are relevant to all wool types. Typical figures for two different samples of wool are given in Table 3.

The side groups of the amino acids derived from wool vary markedly in size and chemical nature and play an important role in the physical and chemical properties of the fiber. Those containing nonpolar, hydrocarbon groups are hydrophobic and of low chemical reactivity. The polar, aliphatic hydroxyl groups of

Table 3. Amino Acid Composition of Merino Wool

	Amino acid content, residues/100 residues		
Amino acid[a]	Sample 1[b]	Sample 2[c]	Nature of R group
Glycine	8.6	8.2	Aliphatic hydrocarbon
Alanine	5.3	5.4	Aliphatic hydrocarbon
Valine	5.5	5.7	Aliphatic hydrocarbon
Leucine	7.7	7.7	Aliphatic hydrocarbon
Isoleucine	3.1	3.1	Aliphatic hydrocarbon
Phenylalanine	2.9	2.8	Aromatic hydrocarbon
Tyrosine	4.0	3.7	Aromatic hydrocarbon
Serine	10.3	10.5	Hydroxyl
Threonine	6.5	6.3	Hydroxyl
Aspartic acid[d]	6.4	6.6	Acidic
Glutamic acid[e]	11.9	11.9	Acidic
Histidine	0.9	0.8	Basic
Arginine	6.8	6.9	Basic
Lysine	3.1	2.8	Basic
Methionine	0.5	0.4	Sulfur containing
Cystine[f]	10.5	10.0	Sulfur containing
Tryptophan	[g]	[g]	Heterocyclic
Proline	5.9	7.2	Heterolytic

[a]($+H_3N—C(R)—COO^-$)
[b]Ref. 32.
[c]Ref. 33.
[d]Includes asparagine.
[e]Includes glutamine.
[f]The amount of cystine is shown as the concentration of its reduction product, cysteine (also termed "half-cystine"). This includes any of the oxidation by-product, cysteic acid, that is present).
[g]Tryptophan is destroyed under the conditions used for these analysis; values of about 0.5 residues % have been obtained by alternative techniques (Refs. 34–36).

serine and threonine are chemically more reactive than the hydrocarbon residues. The side chains that have the most overall influence on the properties of wool are, however, the acidic groups of aspartic and glutamic acids and the basic groups of hystidine, arginine, and lysine. These acidic and basic groups give wool an amphoteric character and play an important role in wool dyeing. They are also responsible for wool's ability to combine with large amounts of acids or bases. The individual polypeptide chains of wool are held together and stabilized by both covalent and noncovalent bonds and interactions.

The most important of these is the disulfide bond (Fig. 4). This occurs by reaction of pairs of cysteine residues to form cystine (disulfide) linkages (—S—S—) between different polypeptide molecules, or between segments of the same molecules, as shown. The disulfide interchain cross-links have been compared with the rungs of a ladder. They are important because they prevent movement of chains and chain segments and, thus, are responsible for the higher stability and lower solubility of wool fibers compared with most proteins. The disulfide cross-links are readily rearranged through a thiol/disulfide interchange reaction under the influence of heat and water, or more rapidly on treatment with

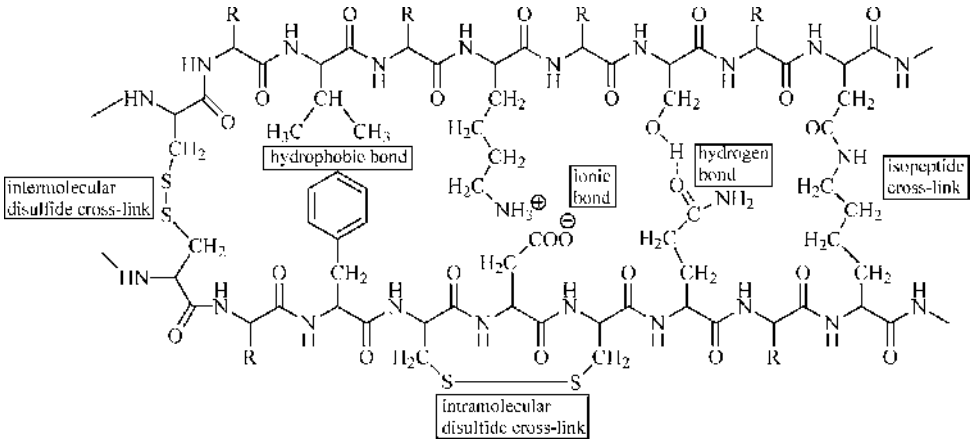

Fig. 4. Types of covalent and noncovalent bonds in wool.

alkaline-reducing agents (eq. 1 where W = Wool).

$$WS_1{-}S_2W \; - \; {-}S_3^- \rightleftharpoons {-}S_1^- \; - \; WS_2{-}S_3W \tag{1}$$

Thiol/disulfide interchange facilitates conformational rearrangement of the wool proteins, leading to relaxation of molecular stress in the fiber. This property is employed in the permanent setting of wool fabrics. Another type of covalent cross-link present in wool is the isopeptide bond, formed between the side chains of lysine and either aspartic or glutamic acid (Fig. 4). Noncovalent bonds or interactions also make an important contribution to the properties of wool. These secondary bonds can occur within a single protein chain, or between different chains. They include hydrogen bonds between —CO and —NH groups in the polypeptide chains and the amino and carboxyl groups in the side chains, and also between suitable donor and acceptor groups in the amino acid side chains. Strong electrostatic interactions (ionic bonds, or "salt linkages") also occur between ionized carboxyl and amino groups in some of the side chains. Ionic bonds contribute to the dry mechanical properties of wool fibers. Hydrophobic interactions can occur between nonpolar groups in some of the side chains and these contribute to the mechanical properties of keratin fibers, particularly when wet. They are also important in wool setting.

Structure of Wool Proteins. The structure of wool proteins has been the subject of much research. Methods to solubilize, separate, and determine the amino acid sequence of these proteins have been reviewed (31,37). It is estimated that wool contains about 170 different types of polypeptides varying in relative molecular mass from below 10,000 to greater than 50,000 (37,38). Morphologically, wool fibers are biological composites, with each component having a different physical and chemical composition (Fig. 3). The groups of proteins that constitute wool are not uniformly distributed throughout the fiber, but are aggregated within the various regions.

Except for a small amount of the amino acid methionine, the sulfur in wool occurs in the form of the amino acid cystine. Only approximately 82% of clean

wool consists of keratinous proteins, which are characterized by a high concentration of cystine. Approximately 17% of the fiber is protein material of relatively low cystine content (<3%); this has been termed nonkeratinous. As a result of the lower cystine content, the nonkeratinous proteins have a lower concentration of disulfide cross-links compared with the keratinous proteins in the fiber. The nonkeratinous material is, therefore, more labile and less resistant to chemical attack than the keratinous proteins. The nonkeratinous proteins are located primarily in the cell membrane complex between the cortical cells and in the endocuticle (Fig. 3). Approximately 13% of the total nonkeratinous material is also located within the cortical cells, where its distribution differs between the cells of the ortho- and paracortex.

The keratinous proteins of wool belong to three groups:

(1) low sulfur proteins, rich in amino acids that contribute to α-helix formation (glutamic acid, aspartic acid, leucine, lysine, arginine)
(2) high sulfur proteins, rich in cystine, proline, serine, and threonine
(3) high glycine, high tyrosine proteins which are also rich in serine.

The proteins derived from the rod-like intermediate filaments (microfibrils) of the cortical cells contain the helical segments of low sulfur proteins. These are surrounded by a relatively amorphous, nonfilamentous matrix, which consists principally of high sulfur and high glycine/high tyrosine proteins. It has been shown that the amino acid sequences of the helical portions are highly homologous with those of intermediate filament proteins derived from skin and other tissues. For this reason the microfibrils of wool are now generally referred to as intermediate filaments (37). Although the filament proteins of the ortho- and paracortex are similar, the orthocortex contains a higher proportion of intermediate filaments than the paracortex. The orthocortex is, therefore, richer in the low sulfur proteins that favor α-helix formation. The intermediate filaments contain a rod-like central helical domain in which the sequences show a heptad repeat, interrupted at three positions by short nonhelical segments. The ends of the polypeptides consist of nonhelical domains terminated in carboxyl and *N*-acetyl groups, respectively (37,39). The proportion of matrix (and hence of the high sulfur proteins) is greater in the paracortex than in the cells of the orthocortex (40). Furthermore, the proteins of highest sulfur content (ultrahigh sulfur proteins) are concentrated in the paracortex (41).

Wool Lipids. The lipids of wool are located mainly in the cell membrane complex. They constitute less than 1% of the fiber mass but play an important role in many properties, such as the intercellular diffusion of dyes and reagents (25,31). The free lipids are extractable with organic solvents and consist of fatty acids, fatty alcohols, sterols, sterol esters, and trace amounts of glycerides, sphinolipids, and glycolipids (26). Although phospholipid is present in the wool follicle membranes, only trace amounts of phospholipid are found in the keratinized fiber (42,43). Cholesterol and its biosynthetic precursor, desmosterol, are the main sterol components of the free lipids. In addition to the free lipids, wool contains some lipids that are believed to be covalently bound to proteins. These components are not readily removed by organic solvents, but those at the fiber surface

can be released by alkaline hydrolysis under conditions where damage or modification of the fiber interior cannot occur (44). Covalently bound surface lipids represent approximately 0.025% of the fiber mass and are a distinct component of the fiber that has been termed the F-layer (44,45). This component is very important because it is responsible for the hydrophobicity of the fiber surface. The major component of the F-layer is an unusual branched-chain fatty acid (18-methyleicosanoic acid), which accounts for approximately 60% of the surface lipid material. Removal of the bound surface lipids generates a clean protein surface, which is more wettable, and has higher friction and better adhesion properties than the surface of clean untreated wool (44).

Physical Properties

Fiber Size and Shape. Wool is usually harvested from sheep by annual shearing. The fiber length is, therefore, determined largely by the rate of growth, which in turn depends on both genetic and environmental factors. Typical merino fibers are 50–125 mm long. They have irregular crimp (curvature), with the finer fiber generally showing lower growth rates and higher crimp. The fiber surface is rough as a consequence of the outer layer of overlapping cuticle cells. By far the most important dimension is the fiber diameter. Wool fibers exhibit a range of diameters, which like fiber length is dependent on both genetics and environment. Coarse wool fibers (25–70 μm diameter) are used in carpets, while fine merino fibers (10–25 μm) are used in apparel because of their soft handle. Fibers from an individual sheep also exhibit a range of diameters. The mean diameter is the prime dictator of price; however, the distribution of diameters is also important. When worn next to the skin, the number of coarse fibers affects comfort as these fibers, rather than buckling, indent the skin and activate nerve receptors (46,47). This gives rise to a sensation of prickle and itch that has been incorrectly assumed, by some consumers, to be an allergic reaction. True allergies are rare, if they exist at all, and the irritation is mechanical and not immunological. Instruments that measure the full diameter distribution as well as fiber curvature have been developed recently (13,14). Individual fibers exhibit curvature in three dimensions; however, by measuring the circular curvature of short segments, a two-dimensional value can be obtained that correlates with the crimp frequency measured in staples. Crimp contributes to the excellent insulating properties of wool fabrics by improving their bulkiness and, hence, the amount of entrapped air.

Water Sorption. Wool is hygroscopic and able to absorb and desorb large amounts of water as the relative humidity surrounding the fiber changes. The water is believed to be associated with specific chemical groups in the amorphous regions, with polar side groups and peptide groups of the protein chains considered to be the most important (48). Debate continues, however, on the exact location of this water, its state, and the mechanism by which it enters the fiber (49–51). As a consequence of the lipid outer layer, the surface of wool is hydrophobic. It is dry to touch and not readily wet-out by liquid water. In line with other polymers having functional surfaces, the surface of wool is believed to rearrange in different environments (52). In textiles, the amount of water absorbed is generally expressed as a percentage of the dry weight. This is referred to as "regain" and

Table 4. Effect of Moisture Sorption on the Physical Properties of Wool Fibers at 25°C[a]

	Regain, %							
Property	0	5	10	15	20	25	30	33
Relative humidity, % (absorption)	0	15	42	68	85	94	99	100
Relative humidity, % (desorption)	0	8	32	58	79	92	98	100
Specific gravity, kg/m^3	1.304	1.314	1.315	1.313	1.304	1.292	1.277	1.268
Volume swelling, %	0	4.24	9.07	14.25	20.0	26.2	32.8	36.8
Length swelling, %	0	0.55	0.93	1.08	1.15	1.17	1.18	1.19
Radial swelling, %	0	1.82	4.00	6.32	8.88	11.69	14.57	16.26
Heat of wetting[b], kJ/kg wool	101	64.4	38.1	20.5	10.0	4.2	1.13	0
Young's modulus, relative[c]	2.69	2.54	2.36	2.02	1.59	1.27	1.05	1.00
Torsional rigidity modulus, GPa[d]	1.76	1.60	1.26	0.90	0.50	0.28	0.16	0.11
Electrical resistivity, MΩ · m	—	3×10^4	400	8	0.40	0.06	—	—

[a]Unless otherwise stated, data from Ref. 55.
[b]Heat evolves when wool, dry mass of 1 kg, at a particular regain is immersed in water.
[c]Ref. 56.
[d]To convert GPa to psi, multiply by 145,000.

is different to "water content", which is the mass of water in the fiber expressed as a percentage of the total mass of fiber plus water. A pronounced hysteresis is observed in the water sorption isotherm of wool. This is 2% higher on desorption than on absorption, at most relative humidities (53). The saturated regain of wool is about 33%, which is higher than that of most other fibers (54).

Heat is liberated when wool absorbs water; this increases comfort by helping to buffer the wearer against sudden environmental changes. The absorption of water by wool also results in other improvements to comfort during wear. At a given relative humidity, wool has similar water sorption to skin. Wool garments, therefore, act as an excellent buffer during physical activity by transporting perspiration away from the skin, thereby keeping its moisture content close to the comfort level. A new wool-containing product designed for active sportswear (SportWool™) utilizes the moisture-buffering properties of wool (CSIRO Textile and Fibre Technology Web site: http://www.tft.csiro.au; Sportwool Web site: http://www.sportwool.com). As can be seen from Table 4, most physical properties of the fiber are affected by (water) regain.

Table 4 Effect of Water Sorption on the Physical Properties of Wool Fibers at 25°C

Wool is sold by weight; thus, allowance for uptake of water must be made. A premium is paid for fine wools and because the diameter changes with regain, diameter measurements must be made under standard conditions of temperature and humidity.

Thermal Properties. The regular packing of α-helical polypeptide chains within the intermediate filaments forms a crystalline phase that occupies about 70% of the dry volume of the fiber (57). This phase melts irreversibly at a temperature that is both time- and regain-dependent (58). During the dyeing and finishing of wool, no melting of the fiber occurs. Care should be taken, however, when processing blends of wool and synthetic fibers that require higher

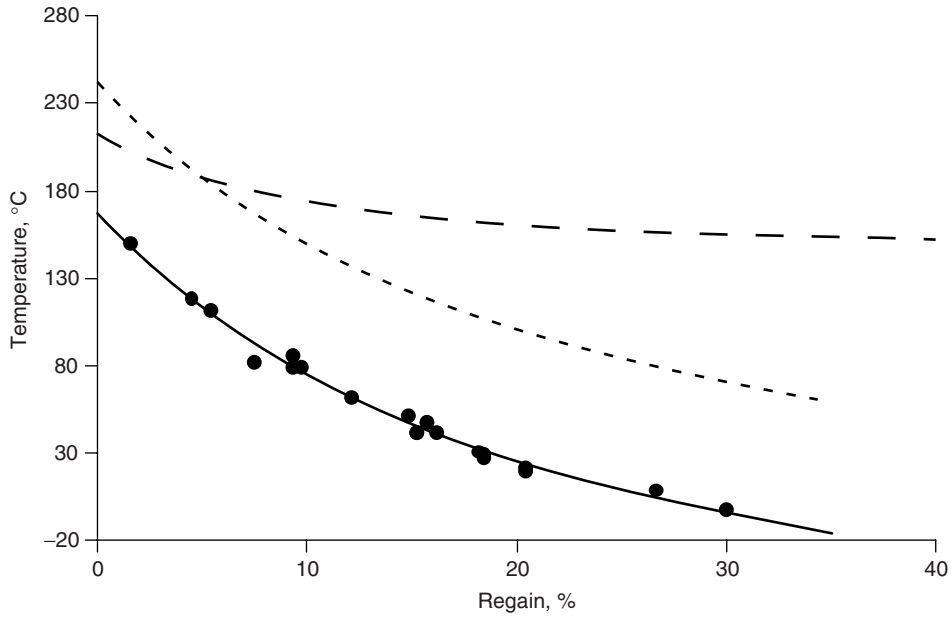

Fig. 5. Glass-transition (—) (60), indicative permanent setting temperature (----), and melting temperature (– – – –) (58) of wool as a function of regain.

temperatures. The amorphous matrix phase contains a high concentration of the amino acid cystine and is, therefore, highly cross-linked. As with other amorphous materials, a glass transition T_g has been detected in the wool fiber (59,60) which is sensitive to physical aging (61). Water acts as a plasticizer, lowering the glass-transition temperature of the dry fiber from 170°C to below zero when saturated (Fig. 5).

The glass-transition temperature is an important parameter, as the properties and performance of wool are influenced by the environmental conditions (temperature and humidity) relative to the glass transition. The insertion of temporarily set creases or pleats in wool fabric (equivalent to thermally set creases in synthetic polymer fabrics) is achieved by subjecting wool to bending strain above T_g and fixed by transition to conditions below T_g. This can be done by heating and cooling, wetting and drying, or a combination of both, eg, steam pressing. Wrinkle recovery is poorer when wrinkles are inserted above T_g and recovery is below T_g. This is likely to occur under hot and humid conditions where local wetting (perspiration) and wrinkle insertion occurs simultaneously. When the fabric moves away from the skin, the wrinkle has insufficient time for complete recovery before the fabric dries. This causes the T_g of the fabric to rise to a temperature above that of the environment. The viscoelastic properties (59), physical aging (59), felting (62), and the water absorption isotherm of wool (50) are also influenced by the glass transition.

Tensile Properties. The tensile properties of wool are quite variable but, typically, at 65% RH and 20°C individual fibers have a tenacity of 110–140 N/ktex (140–180 MPa), a breaking elongation of 30–40%, and an initial

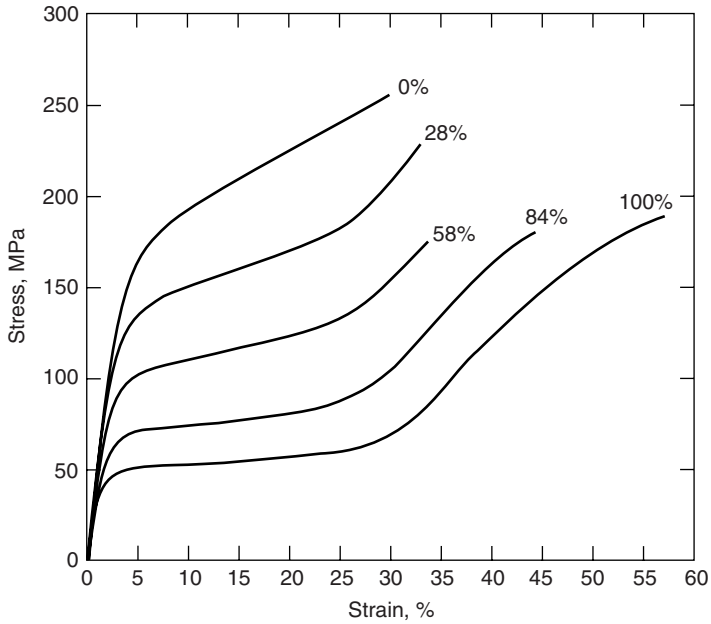

Fig. 6. Stress–strain curves of typical wool fibers at different relative humidities.

modulus of 2100–3000 N/ktex (2.7–3.9 GPa) (54). Although wool has a complicated hierarchical structure (see Fig. 3), the tensile properties of the fiber are largely understood in terms of a two-phase composite model (63–65). In these models, water-impenetrable crystalline regions (generally associated with the intermediate filaments) oriented parallel to the fiber axis are embedded in a water-sensitive matrix to form a semicrystalline biopolymer. The parallel arrangement of these filaments produces a fiber that is highly anisotropic. While the longitudinal modulus of the fiber decreases by a factor of 3 from dry to wet (56), the torsional modulus (a measure of the matrix stiffness) decreases by a factor greater than 10 (Table 4 and Reference 66). The longitudinal stress–strain curves for a wool fiber at different relative humidities are shown in Fig. 6 (54).

Three distinct regions can be discerned, especially for fibers at higher relative humidity. Once the fiber crimp is removed, a near-linear region up to about 2% strain is obtained (pre-yield region). For the wet fiber, this is generally associated with stretching of the α-helices within the intermediate filaments. At lower (water) regain, the matrix phase plays an increasingly dominant role. Between 2 and 25% strain (yield-region) progressive unfolding of zones of α-helices to form a β-pleat configuration occurs. Very little increase in stress is observed during this stage and complete recovery is still possible, provided the fiber is allowed to relax in water. Beyond 25% strain (post-yield region), the fiber stiffens and breaks. At a molecular level, the reasons for this are still a matter of debate but include resistance to the unfolding of a stabilized region of the intermediate filaments (63,65) and the rubber-like response of the matrix (64). A recent review looks critically at the different models (67).

For a fiber immersed in water, the ratio of the slopes of the stress–strain curve in these three regions is about 100:1:10. While the apparent modulus of the fiber in the pre-yield region is both time- and water-dependent, the equilibrium modulus (1.4 GPa) is independent of water content and corresponds to the modulus of the crystalline phase (68). The time-, temperature-, and water-dependence can be attributed to the viscoelastic properties of the matrix phase.

Wool Processing

The conversion of raw wool into a textile fabric or garment involves a long series of separate processes. There are two main processing systems, worsted and woolen. A significant volume of wool is also processed on the semiworsted system, for carpet use. Some wool is processed on the short-staple (cotton) system. Details of the principal stages in the woolen and worsted systems and discussion of more recent developments can be found elsewhere (69,70).

The majority of the world's apparel wool clip is combing wool and this is processed on the worsted system. This process was so named because the combed wool spinning industry in England developed in the English town of Worsted in the fourteenth century (70). Fine, smooth yarns were produced by "spinsters" who placed the combed parallel array of fibers on top of a distaff (combed wool even today is known as top), drew the strand down to the required linear density, and inserted the twist using a spindle. Prior to the development of worsted spinning, and coexisting ever since with it, the traditional system produced yarns in which the fibers were much more disorientated. Although the texture was not as smooth, there was a high degree of bulk, and the finished woven fabrics produced coatings, blankets, and distinctive products such as tweeds and flannels. Woolen spinning is the mechanized form of the traditional system.

Besides scoured (cleaned) wool, the next saleable commodity in worsted processing is top, or combed wool. Generally the combing plant combines the processes of scouring and combing. Most often, a separate commercial enterprise which buys top from the topmaker carries out spinning. Although there are woolen sales-to-yarn spinners, particularly in the knitwear area, the production of woven woolen products in the one enterprise from raw wool is more common. The woolen process is characterized by a much higher degree of vertical integration than the worsted system.

Scouring. The first stage in wool processing is to remove the fleece impurities by scouring. The impurities consist principally of wool wax, dirt, proteinaceous contaminants, and suint. The latter is a water-soluble component, consisting mainly of potassium and other inorganic salts arising from perspiration. Scouring is carried out by washing the raw wool in an aqueous medium, a solvent medium, or a combination of the two. Aqueous scouring is used to process 99% of the world's wool. This involves washing the raw wool in aqueous solutions (neutral or slightly alkaline) of nonionic detergent or, less frequently, soap and alkali. This is followed by rinsing in water.

The process is carried out in a series of between four and seven tanks (called bowls), in which the wool is transported through the wash liquor by mechanical rakes, or by passing it around perforated drums (71,72). At the end of each bowl,

the wool passes through a roller squeeze. Agitation of wool in anhydrous solvents does not cause felting, and several systems (71,73,74) have been operated to take advantage of this property, but none are still in commercial operation.

There are two broad categories of contaminants on raw wool: those that are easily removed and those that are hard to remove. The different rates of removal of these contaminants in the scouring process has led to the development by CSIRO of a new scouring technology, known as Siroscour™. This uses the principles of multistage scouring, rather than severe mechanical action, to optimize the removal of contaminants during aqueous scouring. The three separate stages which comprise the Siroscour process are a modified desuinting bowl, designed to remove as much dirt as possible; a hot scouring stage that removes the easy-to-remove contaminants; and a third stage, designed to remove the hard-to-remove contaminants. To achieve optimum performance, separate dirt and grease contaminant recovery loops are incorporated into the Siroscour process, as well as specific bowl designs for optimum scouring efficiency of Australian wools. Comparative trials have shown Siroscour to consistently produce wool of superior whiteness and lower residual content of mineral contaminents (ash content) than other scouring systems (75).

In most situations, wastewater discharged from a scouring machine contains large quantities of wool wax and both water-soluble and water-insoluble material (organic and inorganic). The pollution load of a single modern scouring machine is equivalent to a population of 50,000 people. Disposal or treatment of the wastes to comply with environmental requirements is expensive. In the past, the least expensive approach involved biological treatment by irrigation of large land areas, or maturation in very large, shallow lagoons. The high levels of potassium present in scour effluent require 1000 ha of land for sustainable irrigation. These factors have forced scourers to install large evaporation ponds that cover many hectares. Technology has been developed that enables scourers to recover a large amount of the potassium from the scour liquor. This can be used as a potassium supplement in fertilizer.

Physicochemical methods of wastewater treatment have been investigated. These include flocculation with inorganic or polymeric flocculants, or with sulfuric acid, and also physical techniques, eg, membrane processes and solvent extraction. Few of these processes have proceeded beyond pilot-scale evaluation, however. One of the most recent processes that has proved to be commercially viable is the Sirolan CF™ technology developed by CSIRO (76). This is a chemical flocculation process that removes more than 75% biological oxygen demand, 80% chemical oxygen demand, and 99% of the suspended solids and wool wax. This is a simpler process with lower operating costs than other methods involving chemical flocculation. Sludge disposal technologies have been developed that can be used in conjunction with the Sirolan CF process. These include composting, incineration, and pelletizing (77). The centrate from the Sirolan CF process contains mainly suint salts. Plant growth trials, carried out by Agriculture Victoria and CSIRO, demonstrated that suint salts, which contain about 27% potassium, are equal or better than inorganic sources of potassium (78).

Carbonizing. Carbonizing is a process used to remove excessive amounts of cellulosic impurities, eg burrs and VM, from wool. It is carried out on loose wool, rags (79), and fabric (80). With loose wool and fabric, the wool is treated with

aqueous sulfuric acid and then baked. The cellulosic matter is rapidly destroyed by the hot concentrated acid, by conversion into friable hydrocellulose, whereas wool is scarcely affected by the treatment. For dyed rags, hydrogen chloride gas is preferred as the mineral acid, because it has less effect on the colors. After acid treatment, the carbonized VM is crushed to facilitate its removal. The wool is then normally neutralized in alkali, although some mills omit this stage to facilitate subsequent dyeing under acid conditions.

Most industrial carbonizing is done on loose wool, the technology having changed little over the past 40 years. Australian carbonizers use surface-active agents to reduce fiber damage in the carbonizing process (81,82). The improved results depend on the use of high acid concentrations and rapid throughput (81).

Processing on the Worsted and Woolen Systems. The wool is dried after scouring and blended before carding. Carding individualizes the entangled fibers and reassembles them into a "sliver" weighing about 25 g/m. At the same time, up to 90% of the VM is removed. Lubrication (83) is used to minimize fiber breakage. After carding, there are three stages of gilling, to align fibers and remove hooked fiber ends before combing. Here, the advancing beard of fibers is inserted into a circular comb, and the leading fibers are then gripped and pulled through a top comb before being reassembled, like overlapping tiles, in the output sliver. The process removes short and entangled fibers and almost all remaining VM. The waste (noil) can be carbonized and fed into the woolen system. The sliver is then given two more gillings and consolidated into top. Some combing plants also produce shrink-resist treated wool top. The current process incorporates chlorination followed by application of a polymer.

The worsted spinner converts top of about 25 g/m linear density into roving of between 200 and 2000 g/km, depending on the linear density of the yarn to be spun. The sequence of processes incorporates four or five drawing stages. The first three or four usually employ gills, whereas the last is commonly carried out on a roving frame in which the attenuated strands are rubbed or twisted to impart cohesion. For finer wool, dyed tops or after blending with synthetic fibers, it is normal to recomb the wool before the above drawing stages.

Long-staple ring spinning is similar to short-staple (cotton) ring spinning, except that the components are increased in approximate proportion to the length of the fibers. On the spinning frame, the rovings are drafted by a factor of about 20, twist is inserted, and at the same time the yarn is wound onto bobbins. The yarn on the bobbins is usually steam-set in an autoclave to reduce its twist liveliness, then wound onto packages or cones. Detection and removal of thick, thin, and colored faults can occur during winding. Following twisting into a twofold yarn and further setting, the yarns are ready for knitting or weaving. Open-end (rotor) spinning is rarely used for wool, and spinning and twisting are very costly operations, because of their low productivity: typically 40 spindles produce 1 kg/h of yarn.

In woolen processing, there are no highly efficient mechanical methods to remove VM. Generally, very clean scoured wool, combed wools, or carbonized wool must be used as inputs. Alternatively, fabrics must be carbonized. A much longer card than in worsted processing and shorter fibers are used. The web of fibers at the card delivery is split longitudinally into about 120 ends, rubbed to impart cohesion, and wound into cylindrical packages called slubbing. Twisting of these

slubbings occurs on the woolen spinning frame with a draft of 1.3–1.5, to produce woolen singles yarn. This yarn can be woven without any further processing, other than a winding and clearing operation similar to that used in the worsted sequence. Woolen spinning is, thus, a very short sequence of operations compared to worsted processing. Woolen yarns, however, become economically uncompetitive with worsted yarns at relatively coarse yarn counts, because production is tied to the number of ends times their weight.

Woolen yarns cannot be spun as fine as worsted yarns, even when using the same fiber diameter. The fabric weights are greater and they have a harsher feel. For these reasons, woolen products have not been able to follow the modern trend to smoother lightweight clothing as easily as their worsted counterparts.

Setting

Setting operations form an important part of the processing of wool yarn, fabric, and garments. Yarn is set in steam to stabilize twist and prevent snarling during winding and warping, while fabrics may be set after weaving to prevent the formation of distortions during wet processes, such as scouring and dyeing. Normally, fabrics are flat-set near the end of the finishing routine to impart dimensional stability and to confer the required handle. Finally, garments are set by steam pressing to form their desired shape, for example, to insert pleats and creases.

Two forms of set may be conferred to the wool fiber and these two forms can be distinguished on the basis of stability. Temporary set (or cohesive set as it is generally referred to in the wool industry) is imparted when wool fibers are dried, or steamed for a short time and then cooled while under strain. This set is readily lost when the fibers are gently steamed or allowed to relax in water at room temperature (84). Permanent set, as the name implies, is set that has a considerable degree of permanency. Set that remains after relaxation in water at 70°C for approximately 15 min is generally considered permanent, ie, the set is permanent to conditions in excess of those that a wool garment would normally encounter during use, eg machine washing.

At the molecular level, setting is a process of stress relaxation which results from the rearrangement of the protein macromolecules that form the fiber. Under ambient conditions of water content and temperature, the matrix regions of wool are glass-like (ie below the glass-transition temperature, see Fig. 5). When fibers are deformed under these conditions, stress relaxation is slow.

If wool is heated or becomes wet, the matrix regions become rubber-like and stress relaxation occurs much more rapidly. Cohesive or temporary setting occurs whenever the fibers are deformed under conditions where stress relaxation is high (rubbery state), and then cooled or dried to a glassy state before they are released. In the glassy state the relaxation rate is slow, so that the fiber will essentially maintain its new shape indefinitely, or until it is again wetted-out or heated to make it rubber-like.

The protein molecules, particularly those of the cuticle and matrix regions of the fiber, are stabilized by a number of covalent bonds and noncovalent interactions. The most important of these are disulfide bonds, which cross-link the

peptide chains (Fig. 4). A unique feature of the wool fiber is the ability, under suitable conditions, for these disulfide bonds to rearrange and form a new cross-linked polymer network. This occurs via a mechanism involving thiol/disulfide interchange (eq. 1). Permanent setting will occur if this rearranged network, cross-linked by reformed disulfide bonds, is at equilibrium with the new shape of the fiber. The rate of disulfide rearrangement is "catalyzed" by the concentration of thiol anions in the fiber (85), as well as by the macromolecular mobility of the protein chains. Hence, the rate of disulfide rearrangement can be increased by increasing the pH, breaking disulfide bonds with a reducing agent to form additional thiol anions, or by increasing the regain or temperature to facilitate molecular mobility. In addition to the rearrangement of disulfide cross-links via thiol/disulfide interchange, other mechanisms are also involved. These include rearrangement of hydrogen bonds and the formation of new types of covalent cross-links that are formed from residues produced by breaking disulfide bonds. The new bonds include lanthionine and lysinoalanine cross-links (86). These cross-links are more stable than the disulfide bonds from which they were produced and make a significant contribution to the stability of permanently set wool fibers. In some circumstances, hydrophobic bonds between suitably located nonpolar side chains can also contribute to the stabilization of permanent set (87). Figure 5 depicts a curve above which the temperature and regain are sufficient for imparting permanent set to wool within a few minutes. This curve is indicative only, as its actual position can vary between different wool types, previous treatments, and process conditions, because it is influenced by the thiol content and pH of the wool fiber, and also the definition of "permanent set."

During wool processing, the regain and temperature are carefully selected and controlled in order to impart either permanent or temporary set. As indicated in Figure 5, permanent setting can be achieved under wet or dry conditions (less than saturation, ie <33% regain). The most common form of wet permanent setting is continuous crabbing. This is an operation in which a wet fabric, sandwiched between a hot (up to 160°C) roller and an impermeable belt, is heated to temperatures above 100°C for up to 1 min, before being rapidly quenched in cold water. The amount of permanent set imparted in a continuous crab is less than that conferred by a traditional batch crabbing operation. The continuous method has greater productivity, however. The effectiveness depends on the pH of the wool and the treatment time and temperature. The rate of permanent setting can be increased by increasing the number of thiol groups within the fiber by impregnating the fabric with a reducing agent. Some dyeing operations can impart large amounts of permanent set to wool. This can be minimized by including in the dyebath a chemical that reacts with the thiol anions. Minimizing permanent set during dyeing is beneficial in maintaining fiber strength (88) and for maintaining yarn bulk (89).

Dry setting operations usually involve the use of steam. As is the case for wet setting, the amount of permanent set imparted in steam-setting depends on the wool pH, water content, and the time and temperature of setting. Fabrics are steam-set by decatizing. In this process, the wool fabric, interleaved with a cotton wrapper cloth, is wound onto a perforated drum, through which steam is forced. In continuous machines, the conditions are mild and little permanent set is imparted. In a batch process, in which the fabric roll is placed in a pressure

vessel (autoclave), setting temperatures up to 130°C for 3–5 min are used. These conditions impart a higher degree of permanent set than continuous methods. The amount of temporary or cohesive set imparted in both batch and continuous machines depends on the temperature of the fibers when the fabric is released from the wrapper cloth. The cooler the fabric, the higher the level of cohesive set. Yarns on packages are normally cohesively set in an autoclave at temperatures up to 90°C, in order to reduce twist liveliness. A vacuum pump is used to remove air from the packages, which ensures even penetration of steam and, thus, a uniform level of set.

Normal pressing operations carried out during garment making impart only temporary set to the fibers. A number of commercial processes are used, however, to set permanent creases into wool garments (90–92). These include autoclave setting and wet or dry pressing in the presence of chemical assistants. Permanent pleats are fixed into skirts by autoclave setting at around 110°C. In the SIROSET™ process of CSIRO, for inserting permanent creases into trousers, a chemical assistant (monoethanolamine sulfite) is sprayed onto the trousers before steam-pressing.

A New Textile Fiber from Wool. The most recent application of wool setting is in the manufacture of OPTIM™ (CSIRO Textile and Fibre Technology Web site: http://www.tft.csiro.au), a new textile fiber produced from wool (93). The production process involves stretching and setting wool to create two new fiber types; Optim fine and Optim max (94). A key aspect of the continuous process is the use of false twist to maintain cohesion within a large fiber assembly during the whole operation.

In the Optim fine manufacturing process a chemical setting agent, such as sodium bisulphite, is applied to wool. A twisted assembly of the treated fibers is stretched by around 40–50% and then permanently set in the extended state. This procedure gives longer fibers of decreased diameter. Stretching and setting the fibers converts ordered intermediate filaments in the wool from an α-crystallite helical form to a β-pleated sheet structure that more closely resembles silk (95). Typically, the diameter is reduced by about 3–4 μm for a 19-μm parent wool fiber. The use of false twist to control fiber movement applies a large transverse force to the twisted assembly that changes the cross-sectional shape of the fibers so that common measures of diameter that assume a mostly circular cross section are no longer valid (Fig. 7).

Optim fine fibers are stronger and softer than the parent wool and exhibit an attractive lustre. They are used to produce fabrics with many of the aesthetic properties of silk. The modified wool is ideal for spinning into fine yarns, especially with other high value natural fibers, eg, silk, cashmere, and alpaca, where softness, lightness, and sheen are desirable attributes.

Optim max utilizes a key benefit of the manufacturing process that allows the extent of set in the fiber to be manipulated in a controlled manner. Optim max fiber is wool that has been temporarily set while stretched, so that the fiber retracts when released in hot moist conditions by about 25% in length. This fiber offers scope for innovation in yarn and fabric design. For example, when Optim max is blended with normal wool, spun into yarn, and relaxed in hank form in hot water, the Optim max fibers retract and force the normal wool fibers to buckle. The yarn has an increased volume and this property produces increased "cover"

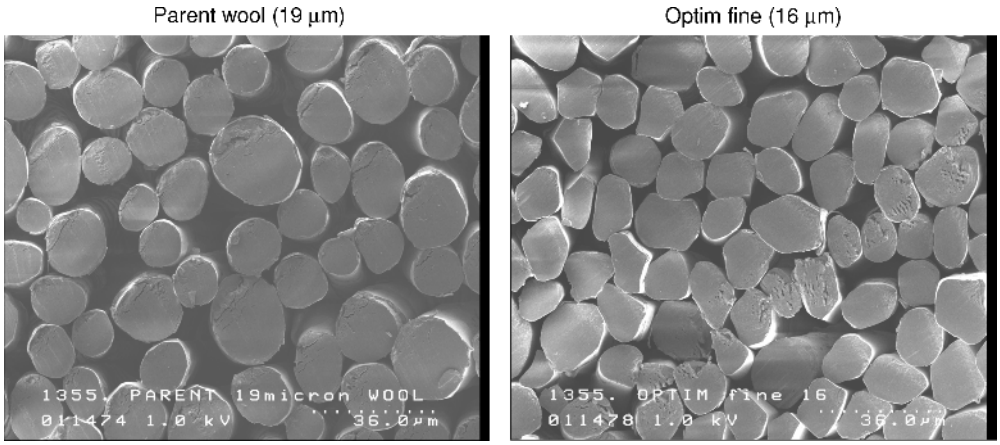

Fig. 7. Scanning electron micrograph of cross sections of normal wool and Optim fine fibers.

in knitted fabric and decreased weight. When knitted to the same cover factor, a weight saving of 20–30% is possible compared with fabrics made from normal wool yarns.

Shrinkage of Wool Textiles

Two mechanisms of fabric shrinkage are observed for wool: relaxation shrinkage and felting shrinkage (22,96). Relaxation shrinkage occurs when a fabric or yarn made from any textile fiber is first immersed in water. It results from the release of temporarily set strains imparted during previous processing operations such as spinning, knitting, and fabric finishing. Relaxation shrinkage also occurs when a knitted garment or fabric is immersed in water after it has been dried while in a stretched state (for example by line drying). Felting results from the presence of cuticle cells (scales) on the wool fiber surface that point away from the fiber root and overlap like tiles on a roof (Fig. 2). The protruding scale edges result in differential friction between the with-scale and against-scale direction, which under some conditions results in irreversible migration of individual fibers toward their root ends. Felting is exploited in the "milling" of wool. This is a process of controlled, mild felting used to close up the structure of fabrics and garments. Milling is also used to produce wool felts, which are composed of a very dense matting of fibers. Felts are used for products as diverse as hats, polishing pads, table covers, and piano hammers.

Felting in garments and fabrics that leads to excessive shrinkage is, however, undesirable. It occurs when the wet material is subjected to severe mechanical action, for example, in laundering or tumble drying (22). Shrink-resist treatments are directed at preventing felting shrinkage, whereas minimization of relaxation shrinkage requires careful control during fabric finishing. Felting of loose fibers results in entanglement, whereas in fabrics fiber migration inside and between yarns reduces the fabric area, ie, shrinkage occurs. The

mechanisms of felting shrinkage and its prevention have been discussed comprehensively (22). Many factors influence felting shrinkage; these include (*1*) yarn and fabric structure (woolen or worsted, knitted or woven, yarn twist level); (*2*) the method of wash-testing (pH, temperature of wash liquor, presence of detergents, electrolytes, or lubricants, and the severity of the mechanical action of the washing machine); (*3*) the properties of the fiber (elasticity, diameter, length). Recently, felting shrinkage has been related to the glass-transition temperature of wool (97). Important points to note are that products made from fine diameter wools felt more readily than those from coarse fibers, and that if a small amount of untreated wool is added to shrink-resist treated wool, the blend will felt as readily as the untreated material.

Shrink-Resistent Terminology and Testing. The term shrink-resistant is preferred to "shrinkproofed," although in recent years emphasis has switched to performance-related terms, such as hand-washable and machine-washable. A recent trend is to use the term easy-care, which for knitwear means resistance to felting shrinkage under severe conditions, including tumble drying. It also includes assessment of the fabric appearance after testing. For woven garments, this includes retention of pleats or creases as well as smooth drying performance. All these terms are meaningless unless related to some standard testing sequence and criteria for passing the test.

Relaxation shrinkage tests usually involve mild agitation in water. Felting shrinkage is then determined after more severe agitation. Hence, in practice it may be difficult to say when relaxation ceases and felting starts. The most commonly used methods to test for felting shrinkage is to use multiple wash-test cycles in domestic-type washing machines (front loading in Europe, or top loading in the United States). The Woolmark Company (formally the International Wool Secretariat) has developed test methods for machine washability, together with performance criteria for different garment types and end uses. Woolmark test methods are widely used around the world, although in the United States AATCC methods predominate.

Development of Shrink-Resist Science and Technology. Felting of wool and its use in fabric finishing has been known for a very long time. Monge observed the differential friction effect in wool fibers in 1790 and Mercer chlorinated wool to improve dye affinity in printing in 1839, but chlorination was soon found to impart shrink-resistance (22). Chlorination was widely used during World War II to produce shrink-resistant wool socks and blankets for the military. From then on, two distinct trends in shrink-resist research and technology emerged. Firstly, better control of the reaction of chlorine or other oxidants with wool, and secondly, the use of synthetic polymers to bond adjacent wool fibers together. The reader is directed to Reference 98, which gives a good summary up to the early 1950s, and to Reference 22, which continues to the late 1970s and discusses the mechanism of felting. Recent research has been directed toward environmental aspects of the shrink-resist treatment of wool, particularly the reduction or elimination of organochlorine compounds in effluents from treatment plants. In future years, replacements for chlorination processes are likely to emerge.

Figures published by The Woolmark Company in 2002 show that approximately 40×10^6 kg of wool is shrink-resist-treated each year. This figure may include some low level chlorination treatments of fine wools, designed to

prevent felting during wet processing or to improve garment appearance or dyeability. The products of these low level treatments are generally not claimed to be machine-washable. The fact that only 5–10% of all wool is shrink-resist-treated indicates that many end uses do not require an antifelting treatment. More than 90–95% of the treated wool is used in knitwear. The amount treated, however, varies markedly from country to country and also with the type of product, with those worn next to the skin, eg, underwear, being most likely to be treated. Wool can be shrink-resist-treated at various stages, from loose wool to garments. Approximately 5% is treated at the loose wool stage, mainly for use in bedding products such as futons; 80% at the top stage; very little as yarn; 10% as knitted garments; and about 5% as woven fabrics. The chlorine-Hercosett process for treating loose wool or top is by far the most important method used. In 2002 this method accounted for at least 80% of shrink-resist-treated wool.

Industrial Shrink-Resist Treatments. Mechanistically, shrink-resist treatments can be divided into degradative and additive types. Degradative treatments use an oxidizing agent to eliminate or reduce the differential friction effect of the fiber surface by modifying or removing the scales. In some cases, a polymer is also applied to the surface to mask the modified scales. The additive approach prevents fiber migration by bonding fibers together with elastomeric polymers. Some polymer deposition processes involve a degradative chemical pretreatment, to improve the adhesion of the polymer to the fiber surface. Additive treatments must be applied after spinning (usually at the fabric stage), whereas degradative treatments can be used at any stage from loose wool through to garments.

Chlorine-Based Shrink-Resist Treatments. The principal oxidizing agent used in degradative shrink-resist treatments is chlorine. Free chlorine reacts very rapidly with wool; hence, it is difficult to treat a mass of wool fibers evenly. Two different types of chlorination methods are used commercially: continuous treatment and batch treatment. In the continuous method, top or loose wool is reacted with an aqueous solution of chlorine gas for a short time (<30 s). The batch treatment method involves a longer treatment time (5–30 min) with a less reactive chlorinating agent, such as DCCA (*N*,*N*′-dichloroisocyanuric acid). Batch treatments are mainly used on garments and fabrics but can also be applied to loose wool or tops. Generally, in both continuous and batch treatments a reactive polymer, usually cationic, is applied after the chlorination step.

The features and chemistry of chlorination shrink-resist treatments are best illustrated by consideration of the chlorine-Hercosett process for wool top (99). This process uses a dedicated plant, of which there are about 40 around the world. A web of parallel slivers is treated with water and chemicals in a series of bowls (tanks), separated by squeeze rollers. The wool is then dried. Usually, 30–40 slivers (20–30 g/m) are treated simultaneously at a speed of 5–10 m/min. Overall production rates range from 200 to 500 kg/h.

The first stage involves chlorination, either with chlorine gas dissolved in water or with sodium hypochlorite acidified with sulfuric acid. Chlorination is the most critical step of the process and modern plants incorporate features designed to achieve uniform treatment of the web. These include cooling the chlorine solution to 10–12°C, to slow down the rate of reaction with wool, and special application devices, eg, those produced by the Kroy or Fleissner companies, to rapidly contact the web with a large volume of dilute chlorine solution. The second stage

of the process is a neutralization, or anti-chlor, treatment with sodium sulfite. In the third stage, the wool is treated with a cationic polyamide/epichlorohydrin polymer, usually Hercosett 57 (Hercules, Inc.). The final stage consists of treatment with a cationic softener and a lubricant to facilitate further processing, followed by drying to cross-link the polymer on the fiber surface. The reaction of chlorine with wool is complex, but the principal effect of the combination of the chlorination and neutralization stages is to remove surface lipid from the fiber. This increases the surface energy and shifts the isoelectric point of the fiber to a lower pH, by converting cystine disulfide residues to cysteic acid (sulfonic acid) groups. Some of the surface protein is also solubilized and removed, which softens the fiber cuticle. These changes allow the cationic Hercosett polymer to spread on the fiber surface. Virtually all the shrink-resistance is imparted by the chlorination step. The function of the Hercosett is to compensate for any weight loss arising from chlorination, prevent further loss of soluble protein during subsequent dyeing, and improve the shrink-resistance of any insufficiently chlorinated fibers.

Chlorine-Free Shrink-Resist Treatments. Commercially, the only other oxidizing agent used to any extent is permonosulfuric acid (PMS; $HOOSO_3H$). This is used in the form of its potassium triple salt, containing potassium sulfate and bisulfate. It is employed in batch processes at elevated temperatures, because it reacts more slowly with wool than chlorine (100). The process sequence is similar to that used for chlorine-based treatments. It involves degradative oxidation with PMS, followed by neutralization with sodium sulfite and then application of a resin. Unlike chlorine, however, PMS does not remove the bound lipid or oxidize cystine to cysteic acid. The main product of the reaction is cystine sulfonic acid or Bunte salt groups.

Other chlorine-free shrink-resist technologies under development include plasma and ozone treatments for sliver and enzyme treatments for garments and fabrics.

Additive Shrink-Resist Treatments. The principal additive shrink-resist treatment for wool fabrics uses the polymer Synthappret BAP (Bayer AG). This is a poly(propylene oxide) polyurethane, containing reactive carbamoyl sulfonate (bisulfite adducts of isocyanate) groups, ie $-NHCOSO_3^-\ Na^+$. An aqueous solution of this polymer is padded onto woven fabrics. The polymer cross-links on drying to form flexible linkages between fibers and yarns (101). Other polymers may be applied at the same time to modify the handle.

Easy-Care Wovens

Dry-clean-only garments are increasingly becoming a turnoff to the modern consumer. Consumers now demand "total easy-care" garments that can withstand repeated machine washing and tumble drying, while maintaining their "just pressed" appearance with no more than minimal ironing. In addition to dimensional stability, wool-containing fabrics and garments must be specifically engineered so that, after laundering, seams remain flat and without pucker, the fabric remains wrinkle-free without the development of fuzz or pills, and the creases or pleats stay sharp.

To produce total easy-care garments from a blend, of wool and polyester, heat-setting the polyester component using a hot head press will generally impart sufficient set to the creases and pleats to make them stable to repeated laundering. A minimum of 20–30% polyester is needed for adequate stability. An alternative procedure that sets the entire garment is to impart temporary set to the wool component of the blend by steam-pressing the garment, followed by baking the entire garment in an oven to permanently set the polyester. The wool dries out in the oven and maintains the garment shape during setting of the polyester (102). A fabric-based treatment to prevent felting may be unnecessary, provided the polyester content is above 50% and a suitable fabric construction is used.

It is more difficult to produce pure wool total easy-care garments. The challenge is to obtain adequate permanent set rather than obtaining shrink resistance, because some wool setting processes are not stable to machine washing. The problem of set stability is further exacerbated when the garments are tumble-dried, because the tumbling action tends to flatten the creases and they become temporarily set in a distorted configuration, even if a high level of permanent set has been imparted to the garment. The application of a delay-cure polymer to the fabric, followed by curing in an oven after the garment has been made and pressed, appears to be the latest approach to producing total easy-care wool garments.

Dyeing

Commercially, wool is dyed from aqueous solutions, usually under acidic conditions. In the past, methods have been proposed for dyeing wool from organic solvents, in particular concentrated formic acid. More recently, the use of supercritical carbon dioxide has also been investigated. These solvent systems are, however, very unlikely to replace water as the preferred dyeing medium for wool, because of the relative cost of the solvent compared with water and also the specialized, expensive equipment required.

The majority of dyes used on wool are sodium salts of aromatic anions. Water solubility is usually provided by sulfonic acid groups, but in a few cases carboxyl or hydrophilic, nonionic substituents are used. In a typical wool dyeing operation, the ratio of the mass of dyestuff solution to the mass of wool ranges from approximately 10:1 to as high as 60:1, depending on the type of wool substrate and the equipment used. Wool is dyed as loose fiber, sliver, yarn, fabric, or in garment form by batch methods (103,104). In the case of fiber, sliver or yarn, the process involves pumping dye solution through the stationary substrate, whereas in fabric dyeing the material may be transported through the dye liquor or, alternatively, both liquor and fabric may be moved through the machine. Simultaneous circulation of liquor and wool substrate is also used in garment dyeing techniques. In a typical operation, the liquor is heated from around 40°C to a temperature of 98–100°C, where it is held for a period that can range from around 30 min to over 2 h. The actual time depends on the type of dye and depth of shade. Procedures have also been developed for continuously dyeing wool in loose, or sliver form and wool fabric can be dyed by a pad-batch method (105). These techniques

have found only limited use, however, because they are uneconomic unless a large quantity of substrate is dyed to a single color, which is uncommon in the wool industry.

Dyeing Theory. Wool is composed mainly of a large number of different proteins, the fundamental structural units of which are α-amino acids (31). It is amphoteric in character because of the presence of basic amino groups in the side chains of lysine, hystidine, and arginine, and acidic carboxyl groups in the side chains of aspartic and glutamic acids. In an aqueous, acidic dyebath protonation of the amino and carboxyl groups results in a net positive charge on the fiber. Early workers explained the mechanism of wool dyeing in terms of electrostatic interactions between the positively charged amino groups and anionic dye molecules. The two most popular theories were the Gilbert–Rideal theory and the Donnan theory (106–108). Later studies, however, showed that the affinity and wetfastness properties of dyes on wool are largely determined by other types of interactions, namely, van der Waals' forces and interactions between hydrophobic regions in the fiber and hydrophobic parts of the dye molecules (109,110). Dyes differ markedly in their hydrophilic–hydrophobic character (105,110,111). Ionic forces are of greatest importance for dyes of relatively low molecular weight. With increasing molecular weight, van der Waals' and hydrophobic interactions become increasingly important, which is reflected in a higher affinity for the fiber and better wetfastness properties. Ionic interactions are important, however, for all wool dyes in determining the rate at which the dye is taken up by the fiber from the dye liquor. The dyeing rate can be controlled by varying the amount of acid added to the dyebath, because this determines the size of the net positive charge on the wool, produced by protonation of amino groups.

In early studies on the uptake of dyes by wool, the fiber was treated as a cylinder of uniform composition. The main focus was on the thermodynamics of the dyeing process, in particular the situation applying when equilibrium had been attained. These studies provided little information, however, on the mechanism of the dyeing process itself. Recent work has clarified the relationship between fiber structure and the mechanism of wool dyeing (112,113).

Dyeing Mechanism. Wool fibers have a very complex morphological structure (Fig. 3). They can be considered as biological composite materials, in which the various regions are both chemically and physically different (31). Fine wool fibers contain two types of cell: those of the internal cortex and those of the external cuticle. Cortical cells, which constitute around 90% of the fiber, are spindle-shaped and are arranged in an overlapping pattern, parallel to the fiber axis. They are separated and held together by a continuous network, the cell membrane complex. This region of the fiber contains protein and also lipid material. The proteinaceous material in the cell membrane complex is relatively lightly cross-linked compared with the proteins in other regions of wool. The external cuticle cells are rectangular in shape and overlap, rather like tiles on a roof (Fig. 2). Dyes enter wool fibers at the junctions where the cuticle cells overlap and in the early stages of the dyeing process they diffuse into the interior along the lightly cross-linked network of the cell membrane complex (31,112,113). Later in the cycle, the dyes transfer, progressively, from the cell membrane complex into the cortical cells. The affinity of the dyes for wool is largely the result of their interaction with hydrophobic proteins located within the matrix of cortical cells.

Wool Dyes. The dyes used on wool can be divided into the following groups: acid dyes, chrome dyes, premetallized dyes, and reactive dyes (103,105, 107,110,111,114–116). Strictly speaking, all types of wool dyestuffs can be described as acid dyes, but in practice this term is confined to leveling acid dyes, half-milling dyes, milling dyes, and supermilling dyes (111,114). This subclassification of acid dyes arises out of the methods used for their application and their fastness properties on wool.

Levelling acid dyes (sometimes called level-dyeing or equalizing dyes) are the simplest type of dyes used on wool. They are of relatively low molecular weights (300–600) and have a comparatively low affinity for the fiber, because they interact largely by ionic attraction. They are applied at around pH 3, obtained with sulfuric acid. Under these conditions, the initial uptake of dye is usually uneven because the exhaustion rate is very rapid. As their name implies, levelling acid dyes have good migration properties and levelling occurs during the stage of the dyeing cycle when the dye liquor is held at the boil, thus producing a very even result. Levelling of the dyes is assisted by the presence of sodium sulfate in the dye bath, because the anionic sulfate ions compete with dye anions for the positively charged amino groups in the fiber. In general, these dyes are not particularly resistant to wet treatments, but are used when level dyeing is critically important.

Milling acid dyes are so named because they are more resistant than levelling acid dyes to extraction from wool during the milling process. They are of higher molecular weight (600–900) and are more hydrophobic than levelling acid dyes, which gives them a higher affinity for wool. The higher molecular weight and lower dependence on ionic attraction means that they diffuse out of the fiber more slowly than levelling dyes, which is responsible for their higher fastness to wet treatments such as milling and laundering. Their migration properties, and hence their ability to level during application, is not as good as that of acid dyes. To obtain level results it is important to ensure that the rate of exhaustion is uniform and not too rapid. This is achieved by setting the dyebath at a higher pH (ca pH 4.5–6.0) with a weak acid, such as acetic acid, and also by the addition of a surfactant-type levelling agent, which promotes even uptake on wool. Half-milling dyes fall between levelling acid and milling dyes in molecular weight (500–600), migration properties, and wetfastness. They are applied at a pH in the range pH 4.0–4.5.

Supermilling acid dyes are similar in molecular weight to milling dyes, but contain long alkyl groups that make them more hydrophobic in character. This gives them a high affinity for wool that is virtually independent of ionic interactions with the fiber; consequently, they have very good wetfastness properties. They show good exhaustion under almost neutral (pH 5.5–7.0) dyeing conditions, but their high affinity means that they have poor migration and relatively poor levelling properties. Auxiliary products are often used to assist level application of these dyes.

Chrome dyes are acid dyes (mol. wt. 300–600) that contain groups capable of forming complexes by reaction with a metal salt, usually sodium or potassium dichromate (111,114). The chrome/dye complex has lower solubility, and hence better wetfastness, than the parent dyestuff. Reaction between the dye molecule and chromium salt can be carried out before, during or after application of the

dye to the wool. Modern practice is to carry out the chroming step after dyeing. Chrome dyes are relatively cheap, and have good migration and level dyeing behavior and excellent wetfastness properties. Their popularity, except for black and navy blue shades, has declined in recent years. This is because of the need for prolonged dyeing cycles, fiber damage associated with oxidation of the fiber in the chroming step, and environmental concerns about the use of chromium salts in the textile industry.

In many applications, chrome dyes have been replaced by metal-complex dyes, which have a very high affinity for wool (111,115). In these dyes, the metal complex is preformed during manufacture of the dye, by reaction of one metal atom with either one (1:1 metal-complex dyes) or two (1:2 metal-complex dyes) dyestuff molecules that contain groups capable of coordinating with chromium or, occasionally, cobalt atoms. In general, metal-complex dyes produce duller shades than acid or milling dyes. The 1:1 metal-complex dyes are applied to wool from strongly acidic dyebaths at around pH 2. They are almost all monosulfonates (mol. wt. 400–500) and have good levelling behavior and wetfastness properties. Some degradation of the fiber can be caused by the low dyeing pH. The earliest type of 1:2 metal-complex dyes were unsulfonated; solubility was provided by nonionic polar groups, such as sulfonamide or methylsulfone. More recently, monosulfonated, disulfonated, and some carboxyl-containing types have become available. These dyes range in molecular weight from 700 to around 1000. They are applied at pH values ranging from pH 4.5 to 7.0, depending on the degree of sulfonation and molecular size of the dye.

Reactive dyes have molecular weights in the range 500–900 and usually contain two or three sulfonic acid groups (105,116). These dyes also contain groups that react covalently with wool, which gives them outstanding wetfastness properties. They are characterized by bright colors and moderate migration and levelling properties, provided careful attention is given to ensuring that the exhaustion rate is not too rapid. This is achieved by careful control of the dyebath pH and by using special amphoteric levelling agents. Their ability to react with the fiber means that uneven uptake of these dyes is very difficult to rectify. Reactive dyes are relatively expensive and, currently, their most important application is on wools that have been treated to withstand shrinkage in machine washing. They are, however, becoming increasingly important as alternatives to chrome dyes for dyeing all types of wool. At present, reactive dyes offer the only viable alternative to chrome dyes for products where very high wetfastness properties are required.

Fiber Damage in Dyeing. When wool is dyed for prolonged times at the boil, the fiber can be damaged as a result of hydrolysis of the component proteins. Methods of dyeing wool substrates at temperatures below the boil (85–90°C) have been developed. One such method, the CSIRO Sirolan-LTD™ process employs a special chemical (Valsol LTA-N, APS Chemicals) that increases the rate of exhaustion and diffusion of dye into the fiber, thus enabling satisfactory dyeings to be obtained at temperatures below the boil (117). Wool dyed by this method suffers less degradation than wool dyed for a similar time at the boil. This leads to benefits in the processing performance of the dyed fiber and in improved quality of end products (118). Permanent setting of wool fibers during dyeing has been identified as a major factor that also contributes to deterioration of the quality of

dyed wool (117). This effect is separate from hydrolytic degradation. Setting occurs via a mechanism involving thiol/disulfide interchange (eq. 1). Methods of inhibiting the permanent setting of wool fibers during dyeing have been developed (89). These involve addition to the dyebath of auxiliaries (antisetting agents such as Basolan AS, BASF) that block thiol groups and, thus, prevent thiol/disulfide interchange. Improvements in the properties of a range of products made from wool are obtained by reducing the amount of permanent set that occurs during dyeing.

Printing

Printing provides the means of transferring bright multicolor designs onto textiles. The amount of wool fabric printed is very small compared to cotton and synthetics. This is partly because the pigment printing systems widely used for cotton and synthetics have a severe adverse effect on the natural handle of wool. Furthermore, although the printing of wool using dyes maintains the natural qualities of the fiber, it requires a more complex processing sequence involving several stages, some of which are technically challenging.

The usual route for printing wool with dyestuffs is fabric preparation/print/dry/steam at 100°C (to fix dye to fabric)/wash off (to remove thickener and unfixed dye)/dry. Globally, an estimated 20 million meters per annum of high quality printed wool fabric is produced, with the center of excellence being in Northern Italy.

Fabric preparation is considered to be the most important stage for obtaining good color yields, levelness, and brightness on wool fabric (119,120). Currently, this is done almost exclusively by an oxidative chlorination process. The most popular commercial methods use either a batch treatment with DCCA or a continuous fabric treatment with gaseous chlorine (the Kroy process). Chlorination has a profound effect on wool, especially near the fiber surface. The number of anionic groups is increased, with cystine residues oxidized to cysteic acid and accessible peptide bonds cleaved to form carboxyl groups. These reactions increase the wettability of the surface of wool, which facilitates spreading of the dye formulations. Chlorination also reduces the degree of cross-linking of wool, which increases the rate of dye diffusion into the fiber. Chlorination can have several adverse effects, however. At higher levels (4% on mass fabric of DCCA), there are problems in obtaining level treatments. Yellowing, especially after steaming, can also occur. These problems can be minimized by treating fabrics continuously in open width in a machine such as the Kroy chlorinator. With all chlorination processes, soluble protein and free oxidation products must be removed from the wool before drying. This is done by neutralization with a reducing agent, such as sodium bisulphite or sodium dithionite.

The effluent from the chlorination of wool contains adsorbable organohalogen compounds (AOX), which are now regarded as undesirable products to release into the environment, particularly in Europe. Several AOX-free methods for preparing wool for printing are currently being investigated. Plasma (121) and corona discharge (122) treatments have been investigated as potential prepare-for-print methods for wool, as they oxidize the surface of wool fibers and have the

advantage of being dry processes. Although the wettability of fabrics prepared using these methods is high, the color yields of prints are significantly less than prints on chlorinated fabric and the fabric handle is inferior. An alternative approach is the CSIRO "Siroflash" process. This method involves continuous ultraviolet (UV) irradiation of dry wool fabric with the type of commercial UV source used for curing polymer films. This is followed by a conventional oxidative bleaching treatment with hydrogen peroxide (123). This process is surface-specific, giving a white fabric with good handle properties and similar color yields to DCCA treatment.

Most wool is printed directly onto the prepared fabric. Automatic flat-screen printing remains the most popular method over the rotary screen process used for most cotton printing, because of the shorter run lengths normally processed for wool fabrics. The dyestuffs most commonly used for wool printing are acid milling, metal complex, and reactive dyes. A simple dye paste is prepared using a suitable thickener, urea (to swell wool fibers during steaming), and the dyestuffs. Various additives may be included in the paste recipe, such as antifoam, glycerol to prevent screen blocking, an acid donor (to maintain a low pH), wetting agent, and a dye solvent such as thiodiglycol (120).

During the steaming stage, large aggregates of dye molecules break down into smaller entities which can then penetrate the swollen wool fibers, allowing fixation to take place. Typical steaming times are 10–15 min for reactive dyes and 30 min for acid milling and metal complex dyes. Saturated steam is essential for optimum penetration and fixation of dyes, especially for dyes of high molecular weight such as those based on copper phthalocyanine derivatives. Both continuous and batch steamers are used commercially. Chlorinated fabrics are highly prone to yellowing during steaming, which can be detrimental to printed pale shades.

The aim of washing off is to remove the thickener and any residual chemicals and unfixed dye from the fabric, without causing staining of any pale or unprinted areas. Fabrics printed with metal complex or acid milling dyes are usually washed off in water at 30–40°C, whereas reactive dyes require higher temperatures (60–80°C), with addition of ammonium hydroxide (120).

Discharge printing of wool remains popular, despite its technical difficulties (119,120). In this style of printing, a predyed fabric is printed with a reducing agent that destroys the background shade. Included in the print paste is a dye which is resistant to the discharge agent. The result is bleaching of the color in the printed areas and replacement with the illuminating color. It is often impossible to reproduce the designs and effects of discharge printing with direct printing. The reducing agents used in discharge printing are zinc, calcium or sodium formaldehyde sulfoxylate, or thiourea dioxide. The technique is limited by the choice of dyes that are resistant to the reducing agent.

Other techniques, such as resist printing, cold batch printing, and transfer printing have been applied to wool with some success, but these now occupy only a small share of the current wool printing market (119,120).

Digital inkjet printing is a recent development for printing textiles (124). It has the advantage that any design can be transferred rapidly from a personal computer onto a fabric, without the requirements to perform a color separation and make a separate screen to print each color. It is also more cost-effective for

producing the short runs of printed fabric designs that are typical for wool compared with other methods. The wool fabric is prepared for printing using a conventional method, padded with a mixture of a thickening agent and urea and dried before digital printing. The padding process assists penetration of the dye into the wool fabric and avoids flushing of the prints during steaming.

Yellowing

In common with many other polymeric materials, yellowing of wool is an undesirable property that can be caused by several different mechanisms (see DEGRADATION). For wool, the most important of these are exposure to sunlight and heat.

The rate and extent of photoyellowing of wool exposed to direct sunlight is a serious shortcoming when compared with fibers such as cotton and synthetics. Photoyellowing is caused by the UV components of natural sunlight (285–380 nm), whereas exposure of wool to sunlight filtered through window glass, which absorbs most of the UV, causes photobleaching (125). Photoyellowing of wool by sunlight only occurs in the presence of oxygen and it has been proposed that it is a photo-oxidative process involving the formation of singlet oxygen (126,127). More recent work, however, has shown that in common with cotton, polyester, and nylon, wool in the wet state is capable of producing hydroxyl radicals ($OH^{\bullet}$) on irradiation with UV light at 366 nm and blue light at 430 nm (128). This reaction appears to be catalyzed by trace metals such as iron and copper. It has been proposed that the photoyellowing mechanism for wool may involve a free-radical chain reaction involving formation of hydroperoxide intermediates (as is the case for most other polymers), rather than a singlet oxygen mechanism (128). There is now general agreement in the literature that yellow chromophores formed in irradiated wool are derived (at least in part) from tryptophan residues (129,130).

The use of some water-soluble benzotriazoles (a well-known class of UV absorber) can be effective against both photoyellowing and phototendering (see UV STABILIZERS). The effectiveness of these reagents relies on intramolecular hydrogen bonding and proton transfer, and intermolecular bonding of the compounds to wool fibers was found to be highly detrimental to their performance. Optimization of the photochemical properties of soluble benzotriazoles has resulted in a suitable formulation (Cibafast W) for use on both bleached and unbleached wool (131). Unfortunately, UV absorbers cannot be used on wool together with a fluorescent whitening agent (FWA) because they absorb the UV wavelengths necessary to excite fluorescence. FWA treatment is essential to achieve a high level of whiteness on wool, because even wool that has been bleached retains some of its natural cream color. An important problem for wool is the very rapid photoyellowing that occurs following treatment with FWAs (132). The poor light-fastness of bright white and pastel colors severely limits the range of possible shades for wool products. This is reflected in wool's limited market share in fashion and summer knitwear, sportswear, hosiery, and baby wear. Wet photoyellowing of whitened (FWA-treated) wool is extremely rapid and can cause unacceptable yellowing after a single laundering and drying cycle in direct sunlight. When wet FWA-treated wool is exposed to sunlight, hydrogen peroxide is formed (133). The rate

of photoyellowing of FWA-treated wool is significantly increased by doping with hydrogen peroxide. This indicates that blocking the formation of peroxide (via the superoxide radical anion) could improve the photostability of whitened wools.

Treatment of wool with a FWA, followed by post-treatment with thiourea/formaldehyde by a pad/cure method, confers a high level of protection against photoyellowing and also improves the initial fabric whiteness (134). Unfortunately, this process is not commercially viable, partly because of environmental concerns about thiourea and formaldehyde and also because much of the benefit is lost after laundering. An alternative approach is to physically separate the FWA from the wool fiber by incorporating the whitener into a suitable polymer that can be applied as a surface treatment to wool fabrics (135). The photostability of the treated fabrics is somewhat better than for conventional FWA treatments (being similar to bleached wool) but the initial whiteness is significantly lower than that of FWA-treated wool.

Two comprehensive reviews on the photodegradation of wool keratin have been published recently by Smith (129) and by Davidson (136). There is also an excellent review dealing specifically with the problem of sunlight yellowing of wool treated with FWAs (126).

Thermal yellowing of wool can be a problem during wool processing, in particular during extended dyeing at the boil, in setting with superheated steam (decatizing), and in drying for extended times, particularly under alkaline conditions (137). The thermal yellowing of wet wool is far more rapid than for dry wool, which is similar to the behavior observed for photoyellowing. Thermal yellowing of wool during dyeing is influenced by pH, temperature, and time, chlorinated wools being especially sensitive. Yellowing during dyeing can be counteracted by adding a bleaching agent, based on sodium bisulfite or hydroxylamine sulphate, to the dyebath (138). Addition of hydrogen peroxide to the dyebath after exhaustion of the dyestuffs can also be effective.

Bleaching and Fluorescent Whitening

The natural pale cream color of wool is due to absorption of light above 320 nm. This is the result of natural pigments and also photodecomposition products in the fiber. Reduction of the natural cream-yellow color of wool is sometimes necessary for improving the brightness of dyed shades, particularly pastel colors, and also for improving the whiteness of undyed wool fabrics. Commercially, wool bleaching is carried out using either an oxidative or a reductive system, or a combined oxidation/reduction process. Oxidative bleaching in the dyebath is also possible (138). In general, oxidative bleaching with hydrogen peroxide gives superior whiteness over reductive methods.

A batch treatment with hydrogen peroxide is used for most bleaching applications. An activator (eg an alkali) is normally added to increase the rate of bleaching. Typically, wool is bleached at pH 8–9 for 1 h at 60°C with a stabilized solution of hydrogen peroxide (0.75% w/w). It is generally accepted that, under alkaline conditions, the active bleaching species is the perhydroxy anion (OOH^-), the formation of which is encouraged by higher pH (139). Peroxide bleaching of wool under mild acidic conditions (pH 5–6) can also be carried out using a peracid

activator such as Prestogen W (BASF) or citric acid (140). As wool sustains some damage in the presence of alkali, this method is useful for bleaching delicate fabrics. An undesirable side effect is the rapid decomposition of hydrogen peroxide to water and oxygen, a reaction catalyzed by transition-metal ions. A stabilizer, which sequesters these ions, is used to prevent this side reaction occurring. The most common stabilizers for alkaline wool bleaching are phosphates, particularly tetrasodium pyrophosphate. However, recent concerns over phosphates in effluents from textile treatment have led to the development of alternative stabilizers based on silicates (141). An alkaline peroxide bleaching process using the silicate-based product Stabicol BAC (Allied Colloids) has been developed (138).

Heavily pigmented fibers, such as Karakul wools, require a more severe approach known as mordant bleaching. In this method, the wool is treated with a metal salt and then with hydrogen peroxide. In the first step, the melanin pigment in the wool preferentially absorbs the metal cations; and in the second step, the cations catalytically decompose the peroxide to produce highly aggressive hydroxyl free radicals, which selectively attack and bleach the melanin (142).

The two most popular chemicals used for reductive bleaching of wool are stabilized sodium dithionite and thiourea dioxide. Most reductive bleaching of wool is carried out using stabilized dithionite (2–5g/L) at pH 5.5–6 and 45–65°C for 1 h. Thiourea dioxide is more expensive than sodium dithionite, but is an effective bleach when applied (1–3 g/L) at 80°C and pH 7 for 1 h. Whiter fabrics are produced when oxidative bleaching is followed by a reductive process—this is often referred to as "full bleaching."

To obtain a high level of whiteness, comparable to white cotton and synthetics, wool must be treated with a FWA after bleaching. The normal procedure is to carry out a full bleaching process and include the FWA in the reductive bleaching bath. FWA-treated wool absorbs UV light and emits blue fluorescence, which makes it appear much whiter than bleached wool. Commercial FWAs for wool are usually based on a sulfonated stilbene, distyrylbiphenyl, or pyrazoline derivative.

Wool fabrics that have been bleached or treated with FWAs yellow rapidly when exposed to sunlight, especially when wet. This is a major problem when bright whites and pastel shades are required. Despite a significant amount of research into the chemistry of photoyellowing processes progress in this area has been limited (126).

Insect-Resist Treatment

Wool is a protein fiber but, because it is insoluble and highly cross–linked, it is not widely available as a food resource. Only a few keratin-digesting animals have developed specialized digestive systems that allow them to derive nutrition from the potential protein resource. These animals, principally the larvae of clothes moths and carpet beetles, perform a useful function in nature by scavenging the keratinous parts of dead animals (fur, skin, beak, claw, feathers) that are unavailable to other animals.

The principal insects that attack wool are the common clothes moth (*Tineola bisselliella*), the case-bearing clothes moths (*Tinea metonella, T. dubiella,*

T. translucens, and *T. pellionella*), the brown house moth (*Hofmannophila pseudospretella*), the variegated carpet beetle (*Anthrenus verbasci*), the black carpet beetle (Attagenus piceus), and a few others. The taxonomy of the Tineid species has been comprehensively reviewed (143). These insects have different temperature sensitivities and tend to be found in different climates. Studies in Australia have shown that the native Tineids are rarely involved in domestic infestations. The introduced species, such as *T. translucens*, are the major textile pests and these are often associated with the nests of introduced urban bird species such as sparrows and swallows (144), while *T. bisselliella* is widely distributed and is common in domestic infestations.

All keratinous materials stored for long periods, including stored greasy wool in bales, animal skins, furs, and horns, are liable to attack. Strategies for protecting goods vary with the product type. Buildings used to store wool may be fumigated or sprayed periodically. Small articles of clothing may be isolated from the environment in sealed bags, often with the use of heat (sunlight), cold (refrigerated storage), or volatile repellent agents (mothballs), with varying degrees of success.

The most practical means of protecting wool textile products is treatment with an insecticide during manufacture (145). Wool products most commonly treated are carpets, furnishings, and insulation. Except for insulation, the most convenient point for treating wool goods is during dyeing, which is attractive because it avoids the needs for an additional wet processing step. Under ideal application conditions the pesticide will be adsorbed inside the highly swollen fiber. This ensures that the pesticide will have maximum resistance to desorption from the dry fiber, and also have optimum fastness to washing, dry-cleaning, and skin contact. An additional benefit of locating the pesticide inside the fiber is that there is little contact action against nontarget pests, as the active agent is released only in the insect gut when the fiber is completely degraded.

Unfortunately, it is impossible under practical dyebath conditions to ensure 100% transfer of pesticide from dyebath to fiber. It is also extremely difficult and expensive to remove residual insect-resist agent from dyehouse effluents (146). Even if the pesticide is removed by absorption or flocculation, the fate of the adsorbed material also needs to be considered (147). As a result, there is inevitably some environmental contamination. With the current generation of insect-resist agents, discharge of residual pesticide from dyebaths is a cause of significant environmental concern in large processing centers. Insect-resist agents must have a broad spectrum of activity because of the variety of moth and beetle species that must be controlled. They must also be reasonably stable to the dyeing conditions used in their application and be durable on wool for long periods. It is also essential that the agent is relatively hydrophobic so that it exhausts effectively from the dyebath onto wool. Unfortunately, this combination of properties is likely to lead to adverse effects on aquatic insects and invertebrates. To minimize environmental damage an allowable environmental concentration for permethrin of 10 ng/L has been set in the United Kingdom (148,149). To meet this requirement, the U.K. carpet dyeing industry has introduced a range of "best practice" operational procedures. These include dyeing at low pH and high temperature, avoiding dyes and dyeing assistants that may decrease the efficiency of application of the insecticide, containing spillages, and avoiding the discharge of effluents from

tape scouring machines. Additionally, a number of manufacturers are using alternative application procedures, where little or no aqueous effluent is produced (147,150–152).

Prior to the introduction of synthetic pyrethroids, insect-resist agents were based mainly on speciality materials, such as polychloro chloromethyl sulfonamido diphenyl ether (PSCDs) (Eulan U33, Eulan WA New). The production of these compounds has been discontinued, however, because of a combination of environmental toxicity (149) and cost. One speciality insect-resist agent based on sulcofuron (Mitin FF), released in 1939 (153), retains a small market share for specific applications where cost is less important and where high resistance to wet conditions is required. It has also been used on wool insulation where it also has low volatility and provides resistance to rotting (154).

The principal active agent used for insect-resist treatments since the late 1970s has been permethrin. Although other broad-spectrum agricultural insecticides (including other synthetic pyrethroids) have been examined, permethrin remains dominant as it is a nonirritant with a good human health profile, especially when strongly adsorbed into the wool fiber. Pyrethroids with a safer environmental profile, such as cycloprothrin, have also been examined (155). These, however, require higher application levels, which increases the cost of the treatment. Newer commercial insect-resist agents under development are based on lufenuron (an insect growth regulator) (147,156) and on bifenthrin (a synthetic pyrethroid). The latter agent includes a synergist to counter the resistance to synthetic pyrethroids that is being observed in Australia (147). Resistance is an inevitable result of using a single protective agent for more than two decades. Resistance to pyrethroids is common among other agricultural pests, and pyrethroid-resistant strains of the Australian carpet beetle and the case-bearing clothes moth have been found in domestic infestations in northern Australia (157). In the future, it is unlikely that speciality insect-resist agents for the protection of wool will be developed, as the market is too small to support the testing required to demonstrate the safety of modern, biologically active agents. The focus remains, therefore, on the use of commercial insecticides for protecting wool against insect damage.

A diverse range of nonpesticidal approaches has also been studied (144). Attempts to find triggers for such behaviors as egg-laying and recognition of food were inconclusive. Although it has been long known that otherwise unrelated clothes moths and carpet beetles have developed unique reducing systems in the gut that allow them to digest wool, specific inhibitors of these systems have not yet been identified.

Flame-Resist Treatment

Wool is regarded as a naturally flame-resistant fiber, which is partly due to its high nitrogen content, high sulfur content, and high (water) regain under ambient conditions. It has a high ignition temperature (570–600°C), high limiting oxygen index (25–26%), and a low heat of combustion (4.9 kcal/g) (158). In most cases, when wool fabrics are ignited they will rapidly self-extinguish, because of the formation of a high volume, insulating ash, or char. Unlike thermoplastic

materials, wool does not melt or drip when ignited. In many end uses, no additional fire-retardant treatment is needed.

If higher standards of flammability are needed, such as in aviation, furnishing fabrics, or protective clothing, durable protective treatments are available. These treatments evolved from the observation that wool treated with a chrome mordant, such as that used in chrome dyeing, has a markedly improved flame resistance (159). The chrome mordant, however, discolors undyed wool. It was shown, subsequently, that titanium or zirconium compounds give similar improvements in fire retardancy (160), with reduced discoloration of the wool. The Zirpro Process, developed by IWS (now, The Woolmark Company) has been used extensively for wool in aircraft interiors to meet FAA requirements. It is also used for protective clothing and for stage curtains and carpets in public buildings and similar areas, where high flame resistance is required by legislation (161,162). Other wool finishes (dyeing, insect-resist, shrink-resist) have been developed that are compatible with the Zirpro Process.

BIBLIOGRAPHY

"Keratin" in *EPST* 1st ed., Vol. 8, pp. 1–44, by E. G. Bendit and M. Feughelman, CSIRO Wool Research Laboratories; "Wool" in *EPST* 1st ed., Vol. 15, pp. 41–79, by K. R. Makinson, CSIRO Wool Research Laboratories; "Keratin" in *EPSE* 2nd ed., Vol. 8, pp. 566–600, by Max Feughelman, University of New South Wales; "Wool" in *EPST* 3rd ed., Vol. 12, pp. 546–586, by J. R. Christoe, R. J. Denning, D. J. Evans, M. G. Huson, L. N. Jones, P. R. Lamb, K. R. Millington, D. G. Phillips, A. P. Pierlot, J. A. Rippon, and I. M. Russell, CSIRO Textile and Fibre Technology.

CITED PUBLICATIONS

1. *Textile Terms and Definitions*, 10th ed., Textile Institute, Manchester, England, 1996.
2. *Wool Statistics*, International Wool Textile Organisation (IWTO), London, 2000–2001.
3. *Australian Wool Statistics Yearbook*, 1999–2000, Australian Wool Exchange, 2000, p. 57.
4. *Seminar Proceedings CSIRO Woolspec 94*, CSIRO, Sydney, Australia, 1994.
5. G. A. Carnaby and A. J. McKinnon, *Aus. Text.* **2**, 11 (1982).
6. *Objective Measurement of Wool in Australia*, Australian Wool Corp., Melbourne, Australia, 1973.
7. B. H. Mackay, In *Proc. 6th Int. Wool Text. Res. Conf.*, South African Wool and Textile Research Institute (SAWTRI), Pretoria, South Africa, 1980, Vol. I, p. 59.
8. Core Test Regulations Test Methods IWTO 19–76.28–75, 3–73, 20–69, International Wool Textile Organisation (IWTO), London, 1968.
9. B. P. Baxter, In *Proc. Inaugural Wool Ind. Sci. Technol. Conf.*, Hamilton, Australia, 2002.
10. *Australian Standard 1363–1976*, Standards Association of Australia, Melbourne, Australia, 1976.
11. *Report on Trials Evaluating Additional Measurement, 1981–1988*, Australian Wool Corp., Melbourne, Australia, 1988.
12. P. R. Lamb and S. Yang, In *Proc. 9th Int. Wool Text. Res. Conf.*, Città degli Studi Biella and International Wool Secretariat (IWS), Biella, Italy, 1995, Vol. V, p. 159.
13. A. R. Edmunds, *Wool Tech. Sheep Breeding* **45**(3, 27 (1997).

14. B. P. Baxter, *Wool Tech. Sheep Breeding* **45**, 267 (1997).
15. P. R. Lamb, In *Proc. Inaugaural Wool Ind. Sci. Technol. Conf.*, Hamilton, Australia, 2002.
16. A. D. Peterson and S. G. Gherardi, *Wool Tech. Sheep Breed.* **49**(2), 110 (2001).
17. K. A. Hansford, *Wool Tech. Sheep Breed.* **47**(1, 19 (1999).
18. M. H. Hardy and A. G. Lyne, *Aust. J. Biol. Sci.* **9**, 423 (1965).
19. R. E. Chapman and K. A. Ward, in J. L. Black and P. J. Reis, eds., *Physiological and Environmental Limitations to Wool Growth*, University of New England Publishing Unit, Armidale, Australia, 1979, p. 193.
20. R. D. B. Fraser, T. P. MacRae, and G. E. Rogers, *Keratins, Their Composition, Structure and Biosynthesis*, Charles C. Thomas, Springfield, Ill., 1972.
21. L. N. Jones, T. J. Horr, and I. J. Kaplin, *Micron* **25**, 589 (1994).
22. K. R. Makinson, *Shrinkproofing of Wool*, Marcel Dekker, Inc., New York, 1979.
23. R. C. Marshall, D. F. G. Orwin, and J. M. Gillespie, *Electron Microsc. Rev.* **4**, 47 (1991).
24. I. J. Kaplin and K. J. Whiteley, In *Proc. 7th Int. Wool Text. Res. Conf.*, Society of Fiber Science and Technology, Tokyo, Japan, 1985, Vol. 1, p. 95.
25. J. D. Leeder, *Wool Sci. Rev.* **63**, 35 (1986).
26. D. E. Rivett, *Wool Sci. Rev.* **67**, 1 (1991).
27. M. S. C. Birbeck and E. H. J. Mercer, *Biophys. Biochem. Cytol.* **3**, 203 (1957).
28. R. E. Chapman and R. T. J. Gemmell, *Ultrastruct. Res.* **36**, 342 (1971).
29. K. M. Rudall, In *Proc. 1st Int. Wool Text. Res. Conf.*, Commonwealth Scientific and Industrial Research Organisation (CSIRO), Melbourne, Australia, 1955 Vol. F, p. 176.
30. D. F. G. Orwin, in D. A. D. Parry and L. K. Creamer, eds., *Fibrous Proteins: Scientific, Industrial and Mechanical Aspects*, Academic Press, New York, 1979, pp. 271–297.
31. J. A. Rippon, in D. M. Lewis, ed., *Wool Dyeing*, Society of Dyers and Colourists, Bradford, U.K., 1992, Chapt. 1.
32. J. H. Bradbury, G. V. Chapman and N. L. R. King, in W. G. Crewther, ed., *Symposium on Fibrous Proteins*, Butterworths, Australia, 1967, p. 368.
33. J. D. Leeder and R. C. Marshall, *Text. Res. J.* **52**, 245 (1982).
34. B. Milligan, L. A. Holt, and J. B. Caldwell, *Appl. Polym. Symp.* **18**, 113 (1971).
35. M. Cole, J. C. Fletcher, K. L. Gardner, and M. C. Corfield, *Appl. Polym. Symp.* **18**, 147 (1971).
36. L. A. Holt, B. Milligan, and L. J. Wolfram, *Text. Res. J.* **44**, 846 (1974).
37. J. M. Gillespie, in R. D. Goldman and P. M. Steinert, eds., *Cellular and Molecular Biology of Intermediate Filaments*, Plenum Press, New York, 1990, Chapt. 4.
38. H. Zahn and P. Kusch, *Melliand Textilber. (Eng. Ed.)* **10**, 75 (1981).
39. J. F. Conway, R. D. B. Fraser, T. P. Macrae and D. A. D. Parry, in G. E. Rogers, P. J. Reis, K. A. Ward, and R. C. Marshall, eds., *The Biology of Wool and Hair*, Chapman and Hall, London, 1988, p. 127.
40. I. J. Kaplin and K. J. Whiteley, *Aust. J. Biol. Sci.* **31**, 231 (1978).
41. L. M. Dowling, K. F. Ley, and A. M. Pearce, In *Proc. 8th Int. Wool Text. Res. Conf.*, Wool Research Organisation of New Zealand (WRONZ), Christchurch, New Zealand, 1990, Vol. I, p. 205.
42. J. Herrling and H. Zahn, In *Proc. 7th Int. Wool Text. Res. Conf.*, Society of Fiber Science and Technology, Tokyo, Japan, 1985, Vol. 1 p. 181.
43. A. Schwan, J. Herrling and H. Zahn, *Colloid Polym. Sci.* **264**, 171 (1986).
44. J. D. Leeder and J. A. Rippon, *J. Soc. Dyers Colour.* **101**, 11 (1985).
45. D. E. Evans, J. D. Leeder, J. A. Rippon, and D. E. Rivett, In *Proc. 7th Int. Wool Text. Res. Conf.*, Society of Fiber Science and Technology, Tokyo, Japan, 1985, Vol. 1, p. 135.
46. G. R. S. Naylor, D. G. Phillips, C. J. Veitch, M. Dolling, and D. J. Marland, *Text. Res. J.* **67**, 288 (1997).

47. G. R. S. Naylor and D. G. Phillips, In *Proc. 9th. Int. Wool Text. Res. Conf.*, Città degli Studi Biella and International Wool Secretariat (IWS), Biella, Italy, 1995, Vol. II, p. 203.
48. I. C. Watt, *J. Macromol. Sci.-Rev. Macromol. Chem., C* **18**(2), 169 (1980).
49. H. Sakabe, H. Ito, T. Miyamoto, and H. Inagaki, *Text. Res. J.* **57**, 66 (1987).
50. A. P. Pierlot, *Text. Res. J.* **69**, 97 (1999).
51. C. Popescu and F.-J. Wortmann, *Wool Tech. Sheep Breed.* **50**(1), 52 (2002).
52. D. J. Evans, R. J. Denning, and J. S. Church, *Encyclopedia of Surface and Colloid Science*, Marcel Dekker, Inc., 2002, p. 2628.
53. I. C. Watt and R. L. D'Arcy, *J. Text. Inst.* **70**, 298 (1978).
54. W. E. Morton and J. W. S. Hearle, *Physical Properties of Textile Fibres*, 3rd ed., The Textile Institute, Manchester, U.K., 1993.
55. *Wool Research*, Wool Industries Research Association, Leeds, U.K., 1955, Vol. 2.
56. M. G. Huson, *Text. Res. J.* **68**, 595 (1998).
57. M. Feughelman, *Text. Res. J.* **59**, 739 (1989).
58. A. R. Haly and J. W. Snaith, *Text. Res. J.* **37**, 898 (1967).
59. F.-J. Wortmann, B. J. Rigby, and D. G. Phillips, *Text. Res. J* **54**, 6 (1984).
60. J. M. Kure, A. P. Pierlot, I. M. Russell, and R. A. Shanks, *Text. Res. J.* **67**, 18 (1997).
61. M. G. Huson, *Polym. Int.* **26**(3), 157 (1991).
62. A. P. Pierlot, *Text. Res. J.* **67**, 616 (1997).
63. M. Feughelman, in J. I. Kroschwitz, ed., *Encyclopedia of Polymer Science and Engineering*, Vol. 8, 1987, p. 566.
64. J. W. S. Hearle and M. Susutoglu, In *Proc. 7th Int. Wool Text. Res. Conf.*, Society of Fiber Science and Technology, Tokyo, Japan, 1985, Vol. 1, 214.
65. F.-J. Wortmann and H. Zahn, *Text. Res. J.* **64**, 737 (1994).
66. T. W. Mitchell and M. Feughelman, *Text. Res. J.* **30**, 662 (1960).
67. J. W. S. Hearle, *Int. J. Biol. Macromol.* **27**, 123 (2000).
68. M. Feughelman and M. S. Robinson, *Text. Res. J.* **41**, 469 (1971).
69. A. Brearley and J. A. Iredale, *The Worsted Industry: An Account of the Worsted Industry and Its Processes from Fibre to Fabric*, Wira, Leeds, U.K. (1980).
70. R. G. Stewart and R. G. Jamieson, *Wool Sci. Rev.* **64**, 16 (Dec. 1987); J. R. Christoe, *Wool Sci. Rev.* **64**, 25 (Dec. 1987); B. V. Harrowfield, *Wool Sci. Rev.* **64**, 44 (Dec. 1987).
71. G. F. Wood, *Text. Prog.* **12**(1), 1 (1982).
72. *Text. Recorder* **81**, 69 (Jan. 1964).
73. CSIRO Division of Textile Industry Report No. G. 10, CSIRO Division of Textile Industry, Geelong, Australia, 1960.
74. J. Brach, *Wool Sci. Rev.* **36**, 38 (May 1969).
75. B. Robinson, C. P. S. Lee, and T. Shaw, Technical Information Letter, TIL/ET-14, International Wool Secretariat, Jan. 1993; J. R. Christoe and B. O. Bateup, CSIRO Division of Wool Technology Report, G70, CSIRO Division of Wool Technology, Geelong, Australia, 1992.
76. J. R. Christoe and B. O. Bateup, In *Proceedings of Third Asian Textile Conference*, Hong Kong Polytechnic University, Hong Kong, 1995.
77. B. O. Bateup, J. R. Christoe, F. W. Jones, A. J. Poole, C. Skourtis, and D. J. Westmoreland, *Enviro. 2000*, Sydney, Australia, 2000; B. O. Bateup, J. R. Christoe, F. W. Jones, A. J. Poole, C. Skourtis, and D. J. Westmoreland, *In 80th Textile Institute Conference*, Melbourne, Australia, 2001.
78. A. Elice-Invaso, J. Maheswaran, K. I. Peveril, J. R. Christoe, and C. Skourtis, *Wool Scour Effluent as a Potassic Fertiliser. ASSI & NZSS National Soils Conference, Aural Papers*, Melbourne, Australia, July 1996, p. 75.
79. N. C. Gee, *Shoddy and Mungo Manufacture*, Emmott & Co., Bradford, U.K., 1950.

80. H. K. Rouette and G. K. Kittan, *Text. Praxis Int.* **36**, 784 (1981).
81. W. G. Crewther, In *Proc. 1st Int. Wool Text. Res. Conf.*, Commonwealth Scientific and Industrial Research Organisation (CSIRO), Melbourne, Australia, 1955, Vol. E, p. 408.
82. W. G. Crewther and T. A. Pressley, *Text. Res. J.* **28**, 67 (1958).
83. Lubrication for Improved Worsted Top, CSIRO, Division of Textile Industry Report No. G.65, CSIRO Geelong, Australia, Oct. 1989.
84. D. G. Phillips, *Text. Res. J.* **55**, 171 (1985).
85. J. A. Maclaren and B. Milligan, *Wool Science: The Chemical Reactivity of the Wool Fibre*, Science Press, Marrickville, NSW, Australia, 1981.
86. K. Ziegler, In *Proc. 3rd Int. Wool Text. Res Conf.*, Institut Textile de France, Paris, 1965, Vol. II, p. 403.
87. R. S. Asquith and A. K. Puri, *J. Soc. Dyers Colour.* **84**, 461 (1968).
88. M. G. Huson, *Text. Res. J.* **62**, 9 (1992).
89. P. G. Cookson, P. R. Brady, K. W. Fincher, P. A. Duffield, S. S. Smith, K. Reincke, and J. Schreiber, *J. Soc. Dyers Colour.* **111**, 228 (1995).
90. M. A. White, CSIRO Division of Textile Industry Report No. G 44, CSIRO, Geelong, Australia, 1982.
91. A. J. Farnworth, *Am. Dyest. Rep.* **49**, 996 (1960).
92. J. R. Cook and J. Delmenico, In *Proc. 3rd Int. Wool Text. Res. Conf.*, Institut Textile de France, Paris, 1965, Vol. III, p. 619.
93. Aust. Pat. 645026 (May 20, 1994), D. G. Phillips and J. J. Warner (to CSIRO).
94. A. Y. Bhoyro, J. S. Church, D. G. King, G. J. O'Loughlin, D. G. Phillips, and J. A. Rippon, In *Proc. Text. Inst. 81st World Conf.*, Melbourne, Australia, 2001.
95. E. G. Bendit, *Text. Res. J.* **30**, 547 (1960).
96. P. Alexander, R. F. Hudson, and C. Earland, *Wool Its Chemistry and Physics*, 2nd ed., Chapman and Hall, London, 1963, Chapt. 2.
97. A. P. Pierlot, *Text. Res. J.* **67**, 616 (1997).
98. R. W. Moncrieff, *Wool Shrinkage and Its Prevention*, National Trade Press, London, 1953.
99. J. Lewis, *Wool Sci. Rev.* **55**, 23 (1978).
100. R. J. Denning, G. N. Freeland, G. B. Guise, and A. H. Hudson, *Textile Res. J.* **64**, 413 (1994).
101. J. A. Rippon and M. A. Rushforth, *Textilver.* **11**, 224 (1976).
102. A. G. De Boos, K. W. Fincher, and A. M. Wemyss, *Text. Chem. Colorist* **29**(10), 28 (1997).
103. C. L. Bird, *The Theory and Practice of Wool Dyeing*, Society of Dyers and Colourists, Bradford, U. K., 1972.
104. F. W. Marriott, in D. M. Lewis, ed., *Wool Dyeing*, Society of Dyers and Colourists, Bradford, U.K., 1992, Chapt. 5.
105. D. M. Lewis, *Rev. Prog. Colorat.* **8**, 10 (1977).
106. P. Alexander, R. F. Hudson, and C. Earland, *Wool Its Chemistry and Physics*, 2nd ed., Chapman and Hall, London, 1963, Chapts. 6 and 7.
107. L. Peters, in C. L. Bird and W. S. Boston, eds., *The Theory of Coloration of Textiles*, Dyers' Company Publications Trust, Bradford, U.K., 1975, p. 163.
108. R. H. Peters, *Textiles Chemistry*, Vol. III, Elsevier Publishing, Amsterdam, 1975, p. 203.
109. J. Meybeck and P. Galafassi, *Appl. Polym. Symp.* **1**, 463 (1971).
110. M. T. Pailthorpe, in D. M. Lewis, ed., *Wool Dyeing*, Society of Dyers and Colourists, Bradford, U.K., 1992, Chapt. 2.
111. J. A. Bone, J. Shore, and J. Park, *J. Soc. Dyers Colour.* **104**, 12 (1988).

112. J. D. Leeder, J. A. Rippon, F. E. Rothery, and I. W. Stapleton, In *Proc. 7th Int. Wool Text. Res. Conf.*, Society of Fiber Science and Technology, Tokyo, Japan, 1985, Vol. V, p. 14.
113. J. D. Leeder, L. A. Holt, J. A. Rippon, and I. W. Stapleton, In *Proc. 8th Int. Wool Text. Res. Conf.*, Wool Research Organisation of New Zealand (WRONZ), Christchurch, New Zealand, 1990, Vol. IV, p. 227.
114. P. A. Duffield, in D. M. Lewis, ed., *Wool Dyeing*, Society of Dyers and Colourists, Bradford, U.K., 1992, Chapt. 6.
115. S. M. Burkinshaw, in D. M. Lewis, ed., *Wool Dyeing*, Society of Dyers and Colourists, Bradford, U.K., 1992, Chapt. 7.
116. D. M. Lewis, in D. M. Lewis, ed., *Wool Dyeing*, Society of Dyers and Colourists, Bradford, U.K., 1992, Chapt. 8.
117. P. R. Brady and J. A. Rippon, *J. Soc. Dyers Colour.* **108**, 114 (1992).
118. J. A. Rippon, F. J. Harrigan, and A. R. Tilson, In *Proc. 9th Int. Wool Text. Res. Conf.*, Città degli Studi Biella and International Wool Secretariat (IWS), Biella, Italy, 1995, Vol. III p. 122.
119. V. A. Bell, *J. Soc. Dyers Colour.* **104**, 159 (1989).
120. V. A. Bell, in in D. M. Lewis, ed., *Wool Dyeing*, Society of Dyers and Colourists, Bradford, U.K., 1992, Chapt. 10.
121. D. Radetic, D. Josic, P. Jovancic, and R. Trajkovic, *Text. Chem. Colorist* **32**(4), 55 (2000).
122. J. Ryu, T. Wakida, and T. Takagishi, *Text. Res. J.* **61**, 595 (1991).
123. K. R. Millington, *J. Soc. Dyers Colour.* **114**, 286 (1998).
124. T. L. Dawson, *J. Soc. Dyers Colour.* **116**, 52 (2000).
125. M. G. King, *J. Text. Inst.* **62**, 251 (1971).
126. B. Milligan, In *Proc. 6th Int. Wool Text. Res. Conf.*, South African Wool and Textile Research Institute (SAWTRI), Pretoria, South Africa, 1980, Vol. V, p. 167.
127. C. H. Nicholls and M. T. Pailthorpe *J. Text. Inst.* **67**, 397 (1976).
128. K. R. Millington and L. J. Kirschenbaum, *Coloration Technol.* **118**, 6 (2002).
129. G. J. Smith, *J. Photochem. Photobiol., B: Biol.* **27**, 187 (1995).
130. S. Collins, R. S. Davidson, P. H. Greaves, M. Healy, and D. M. Lewis, *J. Soc. Dyers Colour.* **104**, 348 (1988).
131. I. H. Leaver and J. F. K. Wilshire, *Chem. Aust.* 174 (1990).
132. D. R. Graham and K. W. Statham, *J. Soc. Dyers Colour.* **72**, 434 (1956).
133. K. R. Millington, In *Proc. 9th Int. Wool Text. Res. Conf.*, Città degli Studi Biella and International Wool Secretariat (IWS), Biella, Italy, 1995, Vol. III, p. 174.
134. B. Milligan and D. J. Tucker, *Text. Res. J.* **34**, 681 (1964).
135. R. Levene, *Text. Res. J.* **57**, 298 (1987).
136. R. S. Davidson, *J. Photochem. Photobiol., B: Biol.* **33**, 3 (1996).
137. J. A. Maclaren and B. Milligan, *Wool Science: The Chemical Reactivity of the Wool Fibre*, Science Press, Marrickville, NSW, Australia, 1981, p. 85.
138. P. A. Duffield, IWS Review of Wool Bleaching Processes, International Wool Secretariat, Ilkley, U.K., 1996.
139. K. M. Thompson, W. P. Griffith, and M. Spiro, *J. Chem. Soc., Chem. Commun.* 1600 (1992).
140. A. W. Karunditu, C. M. Carr, K. Dodd, P. Mallinson, I. A. Fleet, and L. W. Tetler, *Text. Res. J.* **64**, 570 (1994).
141. J. Cegarra, J. Gacen, D. Cayuela, and M. C. Riva, *J. Soc. Dyers Colour.* **110**, 308 (1994).
142. A. Bereck, *Rev. Prog. Colorat.* **24**, 17 (1994).
143. G. Robinson and E. Nielsen, *Tineid Genera of Australia: Lepidoptera*, CSIRO Publications, Canberra, Australia, 1993.

144. D. E. Rivett, S. Ciccotosto, R. I. Logan, E. S. Nielsen, C. P. Robinson, L. G. Sparrow, and R. M. Traynier, In *Proc. 8th Int. Wool Text. Res. Conf.*, Wool Research Organisation of New Zealand (WRONZ), Christchurch, New Zealand, 1990, Vol. IV, p. 548.
145. R. J. Mayfield, *Text. Progress* **11**(4, 1 (1982); D. M. Lewis and T. Shaw, *Rev. Prog. Colorat.* **17**, 86 (1987).
146. P. I. Norman and R. Seddon, *J. Soc. Dyers Colour.* **107**, 215 (1991).
147. J. Barton, *Intern. Dyer*, 14 (Sept. 2000).
148. T. Zabel, J. Seager, and S. D. Oakley, Proposed Environmental Quality Standards For List 2 Substances in Water-Mothproofing Agents, Report TR261, Water Research Center, U.K., 1988.
149. T. Shaw, In *Proc. 8th Int. Wool Text. Res. Conf.*, Wool Research Organisation of New Zealand (WRONZ), Christchurch, New Zealand, 1990, Vol. IV, p. 533.
150. *Anon, Wool Rec.* **154**, 25 (Mar. 1995).
151. D. Allenach, In *Proc. 8th Int. Wool Text. Res. Conf.*, Wool Research Organisation of New Zealand (WRONZ), Christchurch, New Zealand, 1990, Vol. IV p. 568.
152. D. Allenach, *Wool Rec.* **151**, 35 (Mar. 1992).
153. R. W. Moncrieff, *Mothproofing*, Billing and Sons, Ltd., London, U.K., 1950, p. 70.
154. I. M. Russell, Combined Insect Resist and Rot-Resist Treatments for Wool Insulation, CSIRO Division of Wool Technology Report G69, CSIRO, Geelong, Australia, May 1992.
155. I. M. Russell, In *Proc. 8th Int. Wool Text. Res. Conf.*, Wool Research Organisation of New Zealand (WRONZ), Christchurch, New Zealand, 1990, Vol. IV, p. 606.
156. *Anon, WRONZ News* **44**, 2 (2001).
157. Specification of Insect Resistance. E 10, The Woolmark Co., Australia, 2001.
158. T. Shaw and M. A. White, in M. Lewin and S. B. Sello, eds., *Handbook of Fiber Science and Technology, Vol. II: Chemical Processing of Fibers and Fabrics*, Part B, Marcel Dekker, Inc., New York, 1984, Chapt. 5.
159. M. J. Koroskys, *Am. Dyes. Rept.* **60**(5), 48 (1971).
160. L. Benisek, *Text. Manuf.* **99**, 36 (Jan.–Feb. 1972); *Melliand Textilber.* **53**, 931 (1972).
161. L. Benisek, *J. Text. Inst.* **65**, 102 and 140 (1974).
162. P. Gordon and L. Stephen, *J. Soc. Dyers Colour.* **90**, 239 (1974).

GENERAL READING

Textile Terms and Definitions, 10th ed., Textile Institute, Manchester, England, 1996.
W. E. Morton and J. W. S. Hearle, *Physical Properties of Textile Fibres*, 3rd ed., The Textile Institute, Manchester, U.K., 1993.
P. Alexander, R. F. Hudson, and C. Earland, *Wool Its Chemistry and Physics*, 2nd ed., Chapman and Hall, London, 1963.
J. A. Maclaren and B. Milligan, *Wool Science: The Chemical Reactivity of the Wool Fibre*, Science Press, Marrickville, NSW, Australia, 1981.
R. S. Asquith, ed., *Chemistry of Natural Protein Fibers*, Plenum Press, New York, 1977.
A. Brearley and J. A. Iredale, *The Worsted Industry: An Account of the Worsted Industry and Its Processes from Fibre to Fabric*, Wira, Leeds, U.K., 1980.
D. M. Lewis, ed., *Wool Dyeing*, Society of Dyers and Colourists, Bradford, U.K., 1992.
K. R. Makinson, *Shrinkproofing of Wool*, Marcel Dekker, Inc., New York, 1979.
P. R. Brady, ed., *Finishing and Wool Fabric Properties: A Guide to the Theory and Practice of Finishing Woven Wool Fabrics*, CSIRO Division of Wool Technology, Victoria, Australia, 1997.
Proc. 1st Int. Wool Text. Res. Conf., Melbourne, Australia, 1955.
Proc. 2nd Int. Wool Text. Res. Conf., Harrogate, U. K., 1960.
Proc. 3rd Int. Wool Text. Res. Conf., Paris, 1965.

Proc. 4th Int. Wool Text. Res. Conf., San Francisco, 1970; Published in *Appl. Polym. Symp., No. 18*, Interscience Publishers, a Division of John Wiley & Sons, Inc., New York, 1971.
Proc. 5th Int. Wool Text. Res. Conf., Aachen, Germany, 1975.
Proc. 6th Int. Wool Text. Res. Conf., Pretoria, South Africa, 1980.
Proc. 7th Int. Wool Text. Res. Conf., Tokyo, 1985.
Proc. 8th Int. Wool Text. Res. Conf., Christchurch, NZ, 1990.
Proc. 9th Int. Wool Text. Res. Conf., Biella, Italy, 1995.

JOHN R. CHRISTOE
RON J. DENNING
DAVID J. EVANS
MICKEY G. HUSON
LESLIE N. JONES
PETER R. LAMB
KEITH R. MILLINGTON
DAVID G. PHILLIPS
ANTHONY P. PIERLOT
JOHN A. RIPPON
IAN M. RUSSELL
CSIRO Textile and Fibre Technology

X

XANTHAN

Introduction

Industrial polysaccharides are useful because they thicken or stabilize aqueous systems. These polysaccharides, or gums as they are also called, can produce gels or act as emulsion stabilizers, flocculants, binders, film formers, lubricants, and friction reducers. Thus, industrially useful polysaccharides modify and control the rheological properties of aqueous systems.

Traditionally, industrially useful polysaccharides have been derived from botanical sources, but more recently several microbial polysaccharides have achieved commercial status. These include dextran, gellan gum, xanthan gum, and welan gum, the generic name for polysaccharide S-130, which was commercialized in 1985.

Xanthan gum has found significant commercial success in food, industrial, and oilfield applications and has provided the springboard for the development of a new generation of microbial polysaccharides (1). Several excellent reviews have been written on the structure, properties, and uses of xanthan gum (2–5).

Manufacture

An appropriate medium for xanthan production comprises carbohydrate and other nutrients. As shown in Figure 1, a pure *Xanthomonas campestris* culture (after inoculum buildup) is grown in a seed vessel, which is then used to inoculate a large fermentor. The additional nutrients required by this organism include ammonium ion, a phosphate buffer, magnesium ion, and trace elements (6). Broth pH decreases during the fermentation, because anionic groups are formed as part of the polysaccharide molecules, and it is necessary to add caustic to maintain the pH within the range of 6.0–7.5. A suitable fermentation temperature is about 28°C (7). Glucose, sucrose, and starch are similar with respect to polysaccharide production efficiency.

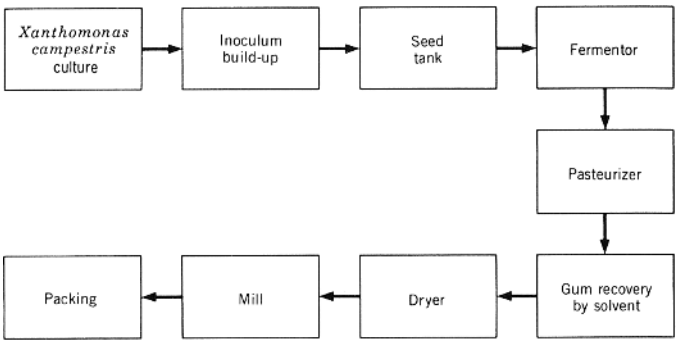

Fig. 1. Diagram of production process.

At completion, that is, when the carbohydrate source is exhausted, the fermentation broth is heat-treated at near-boiling temperature. Xanthan gum is recovered by precipitation with isopropyl alcohol, and the polysaccharide is dried and milled to the desired particle size distribution.

In another commercial process, pasteurization, alcohol precipitation, and drying are omitted, biocide is added to the fermentor and the liquid broth is hipped as the final product. Alternatively, the broth is ultrafiltered and shipped as a liquid concentrate.

Alternative methods have been suggested for the recovery of xanthan gum. Each process starts with pasteurization of the broth to kill bacterial cells. Because xanthomonads are nonspore-forming organisms and vegetative cells are sensitive to elevated temperatures, complete pasteurization can readily be accomplished. Drum drying or spray drying of fermentation broth yields a crude grade of polysaccharide (8). Also, high molecular-weight quaternary ammonium salts have been proposed as precipitants (9).

Xanthan gum can also be recovered by precipitation with aluminum at low pH (10) or calcium ion at high pH (11). Washing the insoluble aluminum or calcium complex with acid or salt generates the soluble gum.

Structure

Xanthan gum is a high-molecular-weight heteropolysaccharide comprising three different monosaccharides: mannose, glucose, and glucuronic acid (as a mixed potassium, sodium, and calcium salt) (12). The repeating-unit structure of xanthan gum is shown in Figure 2 (13,14).

Numerous studies have indicated a molecular weight of approximately 2 million, but values as high as 13–50 million have been reported (15). These differences probably reflect different degrees of association of the polymer chains.

An ordered conformation of the xanthan gum molecule was proposed as a result of x-ray-diffraction studies using oriented fibers (16). A molecular conformation of a right-handed, fivefold helix with a rise per backbone disaccharide residue of 0.94 nm, that is, a fivefold helix with a pitch of 4.7 nm (Fig. 3), was postulated. In this conformation, the trisaccharide side chains are believed to align

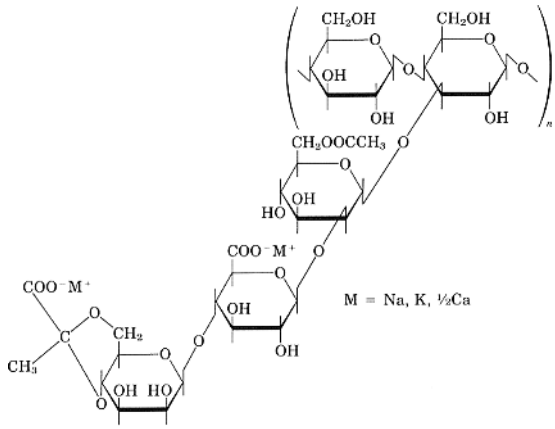

Fig. 2. Structure of xanthan gum.

with the backbone and presumably stabilize the overall conformation by various noncovalent interactions. Multistranded structures are consistent with the x-ray data and represent alternative conformations.

Solution studies on the conformation of xanthan gum suggest that the molecule is rodlike with some degree of flexibility (17) and is related to the solid-state conformation. The nature of the association between chains and the role of the side chain in the overall conformation have yet to be determined, and current data do not clearly define the nature of the xanthan molecule in solution.

In 1977, Holzwarth and Prestridge (18) suggested a double or multistranded assembly, whereas later studies (19) argue for a single helical entity in solution. Other studies based on intrinsic viscosity and molecular weight measurements have presented evidence for both single (20) and double (21),(22) helical structures; the question of whether the xanthan gum molecule is a single or double strand in an aqueous solution is still not resolved. Electron micrographs (23) obtained for xanthan gum samples, vacuum dried from high and low ionic strength solutions, show double- and single- stranded structures, respectively. Xanthan solutions at low ionic strength undergo a thermal transition that has been detected by a variety of physical methods. This transition was first detected (24) as a sigmoidal change in viscosity of 1% salt-free solutions ($t_m \sim 5$ to 5°C). Subsequent work (25) demonstrated that optical rotation and circular dichroic transitions are coincident with the viscosity change, indicating a conformation transition of the molecule. These data are consistent with the unwinding of an ordered conformation such as a helix into a random coil with a consequent decrease in effective hydrodynamic volume and, therefore, viscosity.

Intermolecular association among polymer chains results in the formation of a complex network of entangled, rodlike molecules. These weakly bound aggregates are progressively disrupted under the influence of applied shear. Upon heating above the transition temperature, there is a progressive melting of the ordered structure, which is partly or totally reversible upon cooling, depending on the salt environment. All these features are summarized schematically in Figure 4 (19). Atomic force microscopy studies of single molecules revealed a

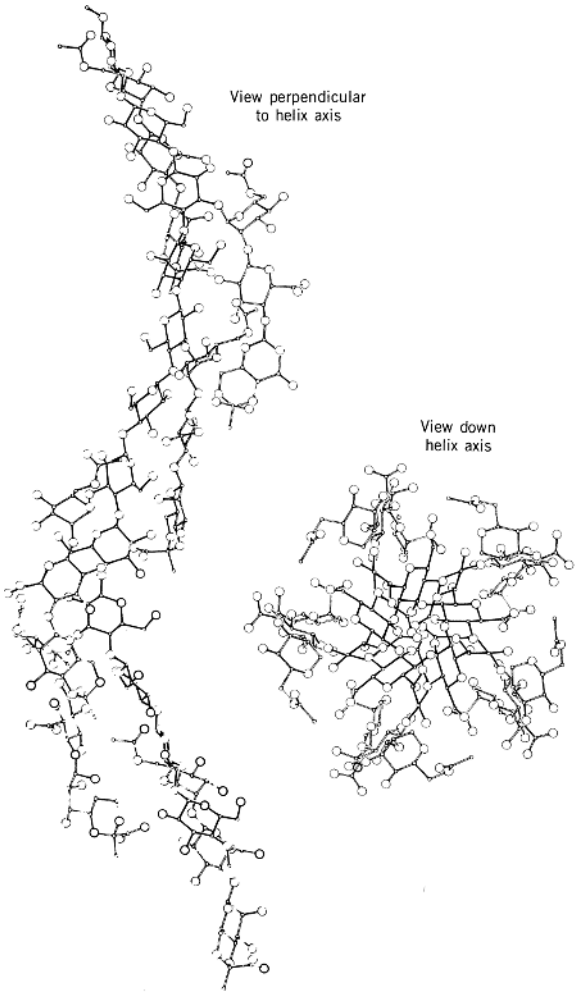

Fig. 3. Helical conformation of xanthan gum viewed parallel and perpendicular to helix axis. [Reprinted with permission from (16). Copyright (1977) American Chemical Society.]

double helical structure in the presence of salt for renaturated xanthan and a single helix in the absence of salt; see Figure 5.(26).

Pyruvate and Acetate Content. The pyruvate content of xanthan gum varies and is dependent on the strain (27), fermentation conditions (28),(29), and recovery conditions employed (30). Pyruvate content influences the viscosity in salt solutions (31–33) and the thermal stability (34) of xanthan gum. Recent studies (35) indicate that pyruvate has a strong destabilizing effect on the ordered conformation, which is ascribed to an unfavorable electrostatic contribution. These data indicate that xanthan gum with increased pyruvate may be characterized by increased viscosity. However, the pyruvate content of the commercial product demonstrates minimal variability by using a defined strain and carefully controlled fermentation and recovery conditions.

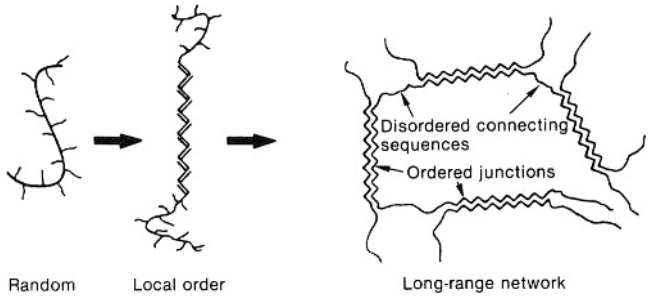

Fig. 4. Conformation ordering in xanthan polysaccharide. [Reprinted from (19), Copyright (1984), with permission from Elsevier.]

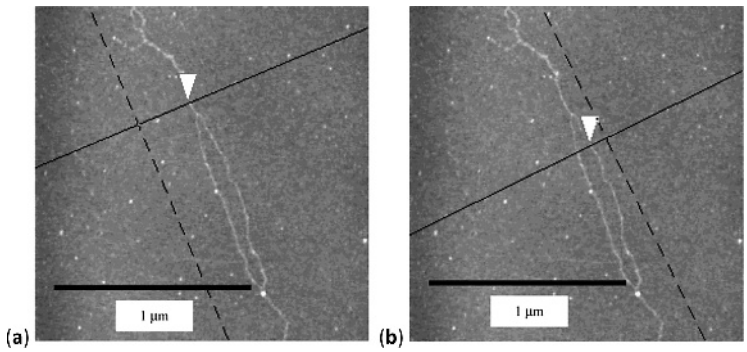

Fig. 5. Incomplete renaturation of xanthan chain in pure water. (**a**) Where renaturation has occurred, there is a double helix with a height of 0.86 nm. (**b**) Where renaturation has not occurred, there is a single helix with a height of 0.48 nm. Arrows point to regions where strands are very thin or a loop has formed. [Reprinted with permission from (26). Copyright (2001) American Chemical Society.]

Although no variability in the *O*-acetyl content of xanthan gum has been noted, these ester groups can be removed by the use of mild alkali. An increased synergism between deacetylated xanthan gum and galactomannans has been reported (36).

Properties

The commercial importance of xanthan gum results from several unique rheological properties, and its stability and compatibility over a wide range of solution conditions, including ionic strength variations, heat, pH changes, shear, enzymes, and additions of salts, acids, or bases (Table 1). Xanthan solutions display high viscosity at low concentration, high viscosity at low shear rates, a high degree of pseudoplasticity, and high elastic modulus.

Pseudoplasticity. Xanthan gum solutions are pseudoplastic. When shear stress is applied, viscosity is reduced in proportion to the amount of shear. Upon the release of shear, total viscosity recovery occurs instantaneously. This

Table 1. Structure—Property Relationships

Structural Features	Properties
Complex aggregates, with weak intermolecular forces	High viscosity at low shear rates (suspension stabilizing properties) pseudoplasticity
Rigid helical conformation, hydrogen-bonded complexes, anionic charge on side chains	Temperature insensitivity and salt compatibility
$\beta - 1 \rightarrow 4$-linked backbone protected by large overlapping side chains	Stability to acids, alkali, and enzymes

behavior of xanthan gum solutions can be explained on the basis of the high-molecular weight, rodlike molecule, which forms complex molecular aggregates through hydrogen bonds and polymer entanglement see Figure 6 (37). Also, this highly ordered network of entangled, stiff molecules accounts for the high viscosity at low shear rates, which translates, in practical terms, into the gum's outstanding suspending properties. The shear thinning results from further dissociation of this network by the continued application of shear. However, when the shearing force is removed, the aggregates (junction zones) reassociate to produce high viscosity. This is the basis of pseudoplastic behavior.

The ordered conformation is stabilized by hydrogen bonding but destabilized by the repulsion between the negatively charged groups on the overlapping side chains. This is also suggested by an oscillatory behavior of aggregation and dissociation of xanthan gum hydrogels (37) with stable homogeneous networks observed only after annealing. A low concentration of electrolyte stabilizes the ordered conformation of xanthan gum by reducing the electrostatic repulsion between carboxylate anions on the trisaccharide side chains. This stabilized helical conformation is maintained with an increase in temperature and explains the insensitivity of the viscosity of xanthan gum solutions to temperature changes below the transition temperatures. Xanthan polyelectrolyte complexes with low polycationic strength and also generates a variety of nonaggregated stable and metastable morphologies, including rods and toroids; see Figure 7 (38). Subsequent kinetic studies show that only the compacted toroidal morphologies are stable (39).

The rigidity of the helical conformation is also responsible for the relative insensitivity of xanthan gum viscosity to differences in ionic strength and pH. In contrast, other polysaccharides that are polyelectrolytes usually have a random coil conformation, a state in which increasing or decreasing electrolyte levels inversely affect solution viscosities. Finally, protection of the backbone by the side chains results in the extraordinary stability of xanthan gum when exposed to acid, alkali, and enzymes.

Solution Viscosity. Solutions of xanthan gum have high apparent viscosity at low concentration and exhibit pseudoplastic rheology. The decreased apparent viscosity at high shear rates facilitates mixing, pumping, and pouring; high apparent viscosity at low shear rates stabilizes foams, emulsions, and suspensions.

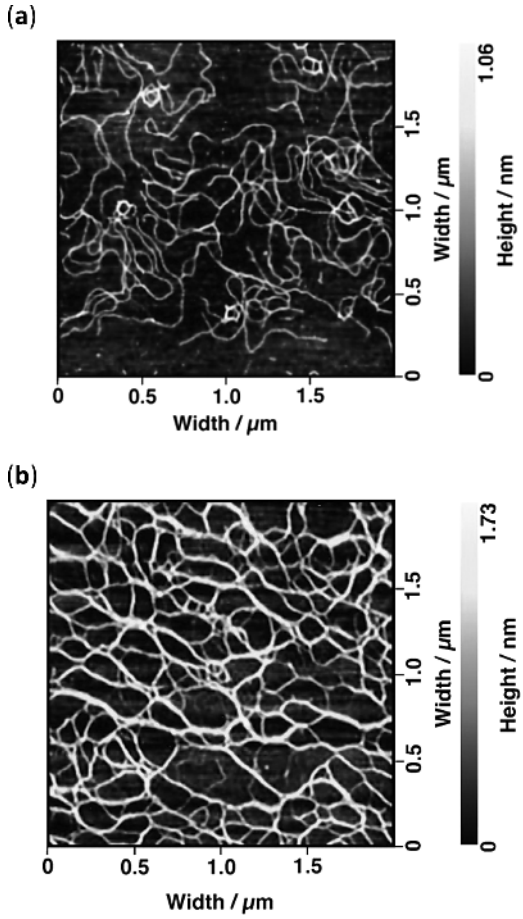

Fig. 6. AFM images of xanthan gum: without annealing (**a**), and after 24 h annealing of hydrogel (**b**). [Reprinted from (37), Copyright (2007), with permission from Elsevier.]

The effect of salts on viscosity depends on the concentration of xanthan gum in solution. At low gum concentrations (below approximately 0.3%), monovalent salts such as sodium chloride cause a slight decrease in viscosity. At higher gum concentrations, viscosity increases. At a monovalent salt level of about 0.1%, the peak viscosity is reached and further addition of salt has no effect on the viscosity.

The same effects occur with salts of most divalent metals (eg, calcium and magnesium). The degree of change in viscosity that occurs in formulated systems depends on pH and on other ingredients in the system. To develop optimal rheology and uniform solution properties, some type of salt should be present. Usually, the salts naturally present in tap water are sufficient.

Although the magnitude of the change increases at low shear rates and concentrations, pH generally has very little effect on the viscosity of xanthan gum solutions. Xanthan gum solutions maintain high viscosity over the pH range 2–12 with some reduction at extreme pH values. Also, solutions have excellent stability over time; actual stability depends on the temperature.

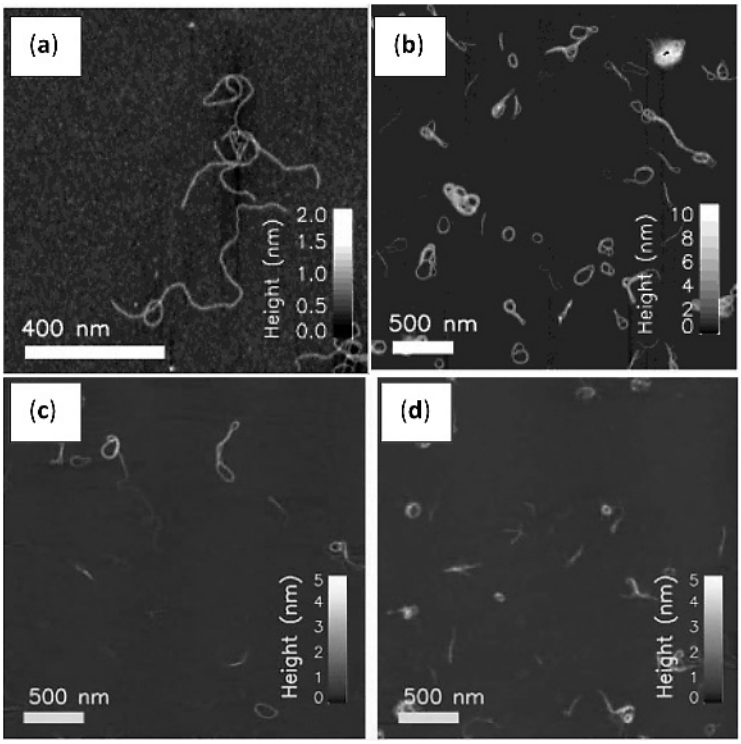

Fig. 7. AFM images of xanthan polyelectrolyte complexes: xanthan (**a**), xanthan-chitosan (**b**), xanthan-Cr^{3+} (**c**), and xanthan – poly-L-lysine (**d**). The complexes form metastable morphologies (eg, rods, coiled, or folded toroids) and stable toroidal structures (see b–d). [(a, b): reprinted with permission from (38), Copyright (2003) American Chemical Society. (c, d): reprinted with permission from (39), Copyright (2004) Wiley.]

The change in viscosity with increasing temperature depends on the concentration, pH, and shear rate. However, when salts are present, only a small change in viscosity occurs at temperatures up to 80°C. At higher temperatures, viscosity is reduced but even at elevated temperatures xanthan gum solutions have excellent stability and, upon cooling, essentially all viscosity returns. In other words, xanthan gum solutions have excellent heat stability in the presence of salts and viscosity reductions at high temperatures are reversible upon cooling.

Rheology. Viscosity and shear rate curves of xanthan gum at different gum concentrations are shown in Figure 8 (40). The relatively higher viscosity of xanthan gum at low shear rates and lower viscosity at high shear rates is indicated. This illustrates the potential for the use of xanthan gum at low concentrations to produce solutions with high viscosity at low shear rates and therefore excellent suspension and emulsion stabilizing properties; low viscosity at high shear rates facilitates pumping.

Figure 9 is a plot of "zero shear" viscosity versus the concentration of xanthan gum, hydroxyethylcellulose (HEC), and guar gum. Although data were obtained from different literature sources, they illustrate the potential to use

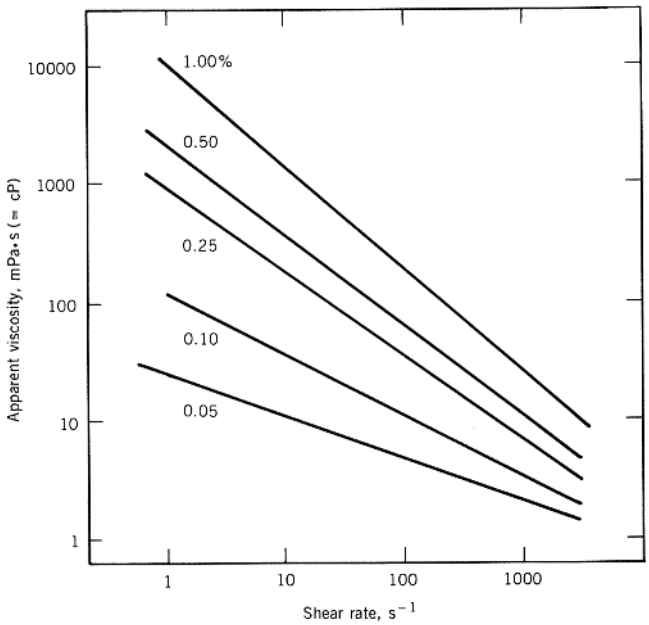

Fig. 8. Effect of the shear rate on apparent viscosity (at 100 s^{-1}) at 25°C for 0.05–1.00% (w/w) xanthan gum dispersions (40). Courtesy of the Institute of Food Technologists.

Xanthan gum at one-half to one-third of the concentration of guar and HEC to produce equivalent zero shear viscosity, which in turn relates to suspension ability.

In the evaluation of polysaccharides as stabilizing agents for suspensions or emulsions, it is important to determine viscosity under relevant conditions, that is, at low concentrations, low shear rates, and in the presence of salts, or at elevated temperature. Under these conditions, the superior functionality of Xanthan gum compared with other thickeners is evident. Although in some applications, this advantage can be compensated for by the use of higher concentrations of lower cost competitive gums such as starch, guar, and carboxymethylcellulose (CMC); this often leads to formulations with unacceptably high viscosity at higher shear rates and inferior stability to changes in pH and salt. The superiority of xanthan has led to its emergence as the stabilizer of choice in many food, industrial, and oilfield applications.

The viscoelastic response, at 25% strain level, of 0.25% Xanthan gum prepared in 0.1% NaCl is shown in Figure 10 (41). At low frequencies, G'' (viscous modulus) predominates over G' (elastic modulus). The point at which G' becomes greater than G'' is known as the crossover frequency; above this point G' predominates, indicating increased structure in the fluid. The lower the frequency at which G' becomes $>G''$, the more solid-like the rheology and the more structure is present. Behavior of this type is characteristic of xanthan gum solutions at low concentrations and exemplifies a solution with good suspending properties. The quantity labeled eta star (η^*) is the complex viscosity and is calculated by dividing the vector sum of G' and G'' by the deformation frequency in radians per second. For most materials η^* correlates with the steady shear viscosity, eta (η).

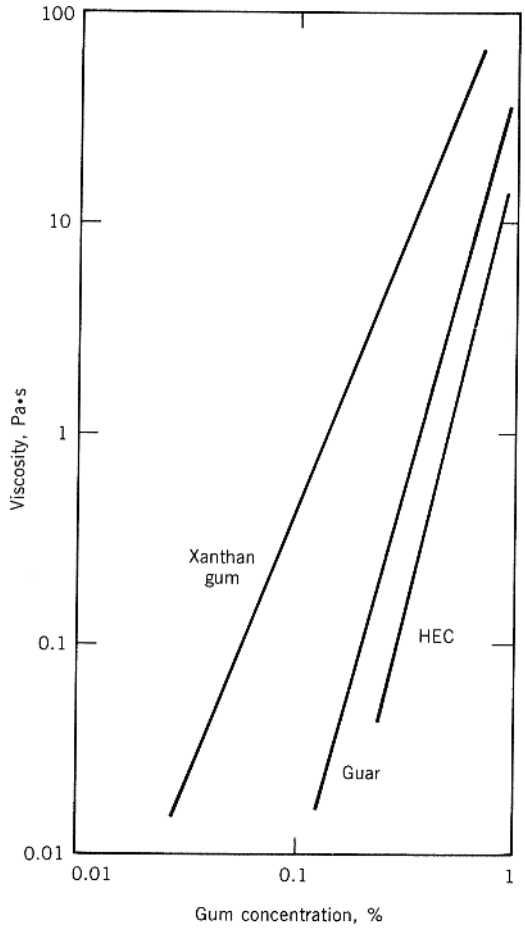

Fig. 9. Zero shear rate viscosity versus gum concentration. To convert Pa·s to P, multiply by 10.

However, in the case of highly elastic fluids such as xanthan gum solutions, η^* can be several percentage points larger, especially at low imposed strain levels. This increase in η^* is thought to be due to the large amount of structure or association that exists between chains in xanthan gum solutions. Taken in sum, these data confirm what is well known about xanthan gum solutions. They are gel-like in nature and have a pseudoplastic (or "shear thinning") rheological flow profile.

Compatibility. Xanthan gum solutions have excellent compatibility and stability in the presence of many other chemicals.

Acids. Xanthan gum dissolves directly in many acidic solutions. The best results are obtained, however, when acid is added to a xanthan gum solution, rather than adding the gum to the acid solution. Xanthan gum stability is excellent in the presence of most organic acids. The compatibility with mineral acids depends on the type of acid and its concentration in the solution. However, at elevated temperatures acid hydrolysis of the polysaccharide is accelerated and lower viscosities may result.

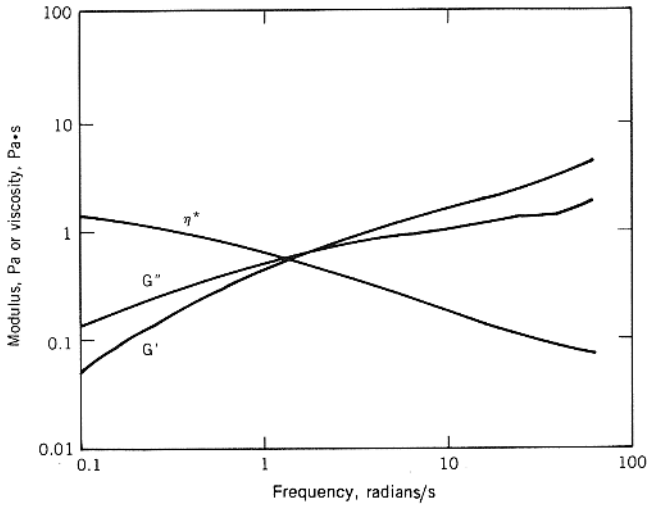

Fig. 10. Rheological properties 0.25% xanthan gum in 0.1 *M* NaCl. η^* = complex viscosity; G' = elastic modulus; G'' = viscous modulus. To convert Pa to dyn/cm^2 or Pa·s to P, multiply by 10.

Bases. Xanthan gum is compatible with many basic compounds, including concentrated ammonium hydroxide. Sodium hydroxide concentrations greater than 12.0% cause gelation or precipitation of xanthan gum in the solution. Basic salts, such as sodium carbonate, phosphate, or metasilicate, may also produce gelation after prolonged storage of xanthan gum solutions, if their concentrations in the solutions are greater than 5%.

Salts. Xanthan gum solutions are unusually stable in the presence of many salts. In some cases, compatibility is limited only by the solubility of the salt. However, xanthan gum is incompatible with polyvalent metal ions in solutions with high pH. This incompatibility often can be controlled or prevented by the addition of sequestrants, such as polyphosphates.

Very low concentrations of borates, generally less than 300 ppm as boron, can cause gelation when other soluble salts are present in xanthan gum solutions. Usually, this gelation can be avoided by increasing the boron ion concentration to greater than 300 ppm or by lowering the pH to ~5.0 or less.

Substances that contain vicinal hydroxyl groups also prevent gelation by forming soluble complexes with the borate ion. Ethylene glycol and mannitol are useful for this purpose.

Oxidizing Agents. Persulfates, peroxides, hypochlorites, and other strong oxidizers degrade xanthan gum. High temperature and alkaline pH accelerate this reaction.

Reducing Agents. In the presence of reducing agents, xanthan gum is generally stable. Even so, care is needed to prevent the formation of free radicals that may cause degradation of long-chain polymers. Such degradation can also occur if oxidizers are present.

Thickeners. Xanthan gum shows good compatibility with sodium alginate and the starches. With dextrin, guar, and locust bean gum, xanthan gum exhibits synergistic increases in viscosity.

Compatibility is good with the synthetic, water-soluble resins. Gum arabic forms complexes with xanthan gum at medium to high concentrations. It is generally not recommended that xanthan gum be used along with cellulose derivatives.

Enzymes. Those enzymes that are commonly encountered as microbial byproducts or as commercially available products, for example, protease, cellulase, pectinase, and amylase, have no effect on xanthan gum.

Surfactants. The compatibility of xanthan gum solutions with nonionic surfactants is quite good for surfactant concentrations of 20% or lower. At surfactant concentrations of about 15% or higher, anionic and amphoteric surfactants tend to salt out the xanthan gum. Below this concentration, stability is good.

Preservatives. Although xanthan gum is compatible with most of the commonly used preservatives, quaternary ammonium compounds should not be used as preservatives unless there is a suitable salt present to serve as a shielding agent. As is true for other polysaccharides, xanthan gum solutions support microbial growth, even though xanthan is a poorer supporter of growth than most other polysaccharides. Therefore, an antimicrobial preservative is recommended if xanthan gum solutions are to be stored for periods of 24 h or longer.

Latex Emulsions. For the manufacture of paints, foams, coatings, or adhesives, xanthan gum is compatible with the common types of latex emulsions, making it effective as a stabilizer, thickener, and rheological properties modifier.

Cationic Dyes. Although xanthan gum is incompatible with cationic dyes, it may be stabilized to prevent reaction by lowering the solution pH to 1.5 or by adding a shielding agent (eg, a soluble monovalent or divalent salt). The salt needed depends on the type of dye and the cation that must be shielded, but the salt concentration used is generally in the 2.0–3.0% range.

Combination and Modification

Interaction between Xanthan and Galactomannans. When xanthan gum is combined at ambient temperature with galactomannans such as guar and locust bean gum, a synergistic viscosity increase occurs (42). In addition, the xanthan gum/locust bean gum combinations form a thermal reversible gel when solutions of these polymers are heated above 54°C and subsequently cooled (43). Mixtures of xanthan and Konjac glucomannan were also shown to form reversible hydrogels (44).

Guar gum and locust bean gum are galactomannans, that is, polysaccharides composed solely of mannose and galactose. The backbone of both polymers is made up of a linear chain of $\beta - 1 \rightarrow 4$-linked D-mannose units, and attached to the backbone by $\alpha - 1 \rightarrow 6$ links are single-unit D-galactose side chains. For guar gum, the mannose-to-galactose ratio is 1.8:1 and for locust bean gum the ratio is 4:1.

In guar galactomannan, the galactose side chains occur on alternate mannose units, but, in locust bean galactomannan, the galactose side chains occur in blocks. Since the galactomannans that are most reactive with xanthan gum have

higher proportions of mannose units, it is assumed that the smooth regions are involved in the interaction. As mentioned earlier, it has been suggested that xanthan gum contains helical regions and that the xanthan gum/locust bean gum gel arises from the interaction between these helices and the "smooth" regions of the locust bean gum to form a cross-linked, three-dimensional network.

Xanthan gum/locust bean gum solutions and gel properties are influenced by a number of variables, such as colloid concentration, colloid ratio, and hydrogen ion concentration.

Although guar gum and locust bean gum are galactomannans and are structurally similar, the difference in structure is sufficient to prevent the same type of gelation with guar gum that occurs with locust bean gum. A viscosity synergism does occur with guar gum; however, the magnitude depends on many factors, such as pH, ionic environment, and so on.

In addition to increased viscosity, the addition of xanthan gum to solutions of guar gum or modified guar gum permits modification of flow properties and can be a useful development tool in a number of applications.

Xanthan and Proteins. Interactions between polysaccharides and proteins are critically dependent on hydrocolloid concentrations, ionic strength, pH, other ingredients, and processing conditions (45). Consequently, it is inadvisable, as is sometimes done, to generalize on the so-called reactivity of a particular polysaccharide with proteins. For the same reason, it is often misleading to extrapolate the results from model studies on protein/polysaccharide combinations to more complex food systems. The most reliable information is usually obtained by observing the end result of combining a particular polysaccharide with the desired protein(s), and processing under the conditions of interest. This empirical approach has successfully identified combinations in which the interaction between xanthan gum and proteins must either be prevented or, alternatively, used to best advantage.

Xanthan and Starch. Several years ago, studies on the effect of heating and cooling starches in the presence of xanthan gum (46) suggested that xanthan gum lowered the gelatinization temperature, thereby offering a means of reducing energy input during starch processing. Although the initial increase in viscosity does indeed occur at a lower temperature, this viscosity is generated, not by lowering the gelatinization temperature, but by interaction between the rodlike xanthan gum molecules and the slightly swollen but essentially ungelatinized starch granules. Later studies (47) using differentiated scanning calorimetry (DSC) to monitor starch gelatinization more accurately have confirmed these findings. They show that xanthan gum has no influence on gelatinization of cornstarch and does not change the energy required for gelatinization. However, a very small but statistically significant drop in the onset temperature of gelatinization was observed.

Upon storage, many starch-containing foods exhibit a phenomenon known as retrogradation. Retrogradation refers to the tendency for the linear amylose molecules to associate, progressively building up additional structure within the food, and leading to excessive thickening or gelation. Retrogradation is a major factor in bread staling and, in frozen foods, can reduce freeze—thaw stability. Xanthan gum has been successfully used in a number of foods to reduce the adverse effects of retrogradation. For example, xanthan gum can reduce the rate of bread staling to some extent.

Table 2. Food and Industrial Applications of Xanthan Gum

Food	Oilfield
Pourable salad dressing (high oil, low oil, no oil)	Drilling fluids (muds)
Relishes and sauces	Work over and completion fluids
Syrups and toppings	Stimulation
Starch-based products (canned desserts, sauces, puddings, and fillings, and retort pouches)	Hydraulic fluids
Dry mix products (desserts, gravies, beverages, sauces, and dressings)	Acidizing
Farinaceous foods (cakes)	Enhanced oil recovery-polymer flooding
Beverages	
Dairy products (ice cream, shakes, processed cheese spread, and cottage cheese)	*Industrial*
Confectionery	flowable pesticides
	Liquid feed supplements
Personal Care	Cleaners, abrasives, and polishes
Lotions	Metalworking
Creams	Ceramics
Toothpaste	Foundry coatings
	textures coatings
	Slurry explosives
	Dye and pigment suspensions

Differentiation. Over the past few years, further improvements have been made in modifying the functionality of xanthan gum to increase its value in various applications.

In 1985, a high clarity food-grade xanthan gum, KELTROL-T, was introduced in the United States by the Kelco Division of Merck & Co., Inc. for applications that demand high clarity, for example, beverages, syrups, and personal care products (48). Xanthan gums with improved dispersibility have been developed for industrial or oilfield applications where large volumes are required quickly, or mixing equipment is limited. Also, a xanthan gum with altered rheology (more Newtonian rheology at low shear rates) and improved compatibility to alkali is finding application in alkaline cleaners.

Applications

The unique physical and rheological properties of xanthan gum make it one of the most versatile hydrocolloids for use in a host of food, pharmaceutical, and personal care products (Table 2; (49–51)). These properties result in products with longer shelf life, improved flow, consistent viscosity, better texture, and a pleasing appearance.

Food Applications. Xanthan gum's stability to acid and salt, effectiveness at low concentrations and highly pseudoplastic rheology make it an ideal choice for stabilization of pourable no-oil, low oil, and regular oil dressings (52),(53). Long-term emulsion stability is readily obtained, and the dressings,

which pour easily from the bottle but cling well to the salad, have excellent flavor release and a nongummy mouthfeel.

Xanthan gum at low levels provides high viscosity, which is stable to changes in temperature, in sauces and gravies at both acid and neutral pH. Relishes stabilized with xanthan gum have excellent sheen and improved cling.

In syrups and toppings, the rheological properties of xanthan gum provide ease of pouring and excellent cling to ice cream, fruits, and pancakes. In chocolate syrups, the cocoa powder remains uniformly suspended, eliminating settling and ensuring consistency.

In starch-based desserts, such as puddings, mousses, and flans, inclusion of xanthan gum provides additional body or structure, improved mouthfeel and reduced syneresis upon storage. In reduced and low calorie foods, xanthan can be used as a partial or total replacement for starch.

Baked goods containing xanthan gum often show increased volume and have improved eating quality. In reduced-calorie baked goods and gluten-free breads, xanthan gum provides improved volume, texture, and moisture retention (54).

The addition of xanthan gum to bakery and pie fillings improves texture, mouthfeel, and flavor release, with the added benefits of extended shelf stability, freeze-thaw stability, and syneresis control (55).

Inclusion of xanthan gum in dry mix bases for beverages provides a pleasant body and mouthfeel to the reconstituted drink. Xanthan gum keeps particulate materials, such as fruit pulp, uniformly suspended in prepared drinks to improve product appearance and provides improved mouthfeel without impairing flavor release. The potential interaction of xanthan gum with the protein in the citrus pulp can be eliminated by the addition of small amounts of highly substituted carboxymethylcellulose (56). Xanthan gum, in combination with gum arabic or modified starch, can be used to stabilize orange oil emulsions, traditionally stabilized with gum arabic alone (57),(58).

Blends of xanthan gum, carrageenan, and galactomannans are excellent stabilizers for frozen and chilled dairy products, including ice cream, sherbet, and sour cream (59). Blends are formulated to take advantage of xanthan gum's unique rheological properties and its synergistic interaction with galactomannans and proteins. Xanthan gum can be used to control viscosity of purees (60),(61).

Addition of low concentrations of xanthan gum extends the shelf life of marshmallows while allowing for a reduction in the gelatin content. The synergistic gelling reaction between xanthan gum and locust bean gum can be utilized to improve the efficiency of manufacturing starch jelly candies by accelerating the set time and to improve storage stability.

Xanthan gum and various galactomannan polysaccharides such as guar gum, locust bean gum, tara gum, and the like, can interact in a "synergistic" manner. This interaction is important for the food industry as it is used commercially in a number of situations that require lower cost or a lower level of stability than that provided by unblended xanthan gum (62). Such applications can include dairy stabilizers, sauces, soups, frozen foods, and certain salad dressings (creams).

Personal Care Products. Xanthan gum provides excellent stability to creams and lotions. The high-at-rest viscosity effectively stabilizes the dispersed

oil phase, whereas the shear thinning properties provide good lubricity and skin-feel during application. Xanthan gum improves the flow properties of shampoos and liquid soaps, suspends insoluble pigments and medicants, and provides a stable, rich, and creamy lather.

Xanthan gum is an excellent binder for all types of toothpastes. Its ease of hydration, excellent enzyme stability, and consistent viscosity produce a uniform stable product and improve extrusion.

Industrial Applications. The excellent suspension properties at low concentration and compatibility with salts, acid, and alkali have resulted in the use of xanthan gum in a variety of industrial applications (Table 1).

Xanthan gum is an excellent suspending agent for flowable herbicides and fungicides and suspension fertilizers (63),(64). Owing to its pseudoplastic property, it can also be used to produce excellent drift control agents. A dispersible-grade xanthan gum is particularly advantageous in these systems.

Xanthan gum prevents separations of insolubles, such as minerals and fats, and maintains a homogeneous concentration of vitamins throughout animal feeds. It is particularly effective in feeds containing magnesium oxide or calcium carbonate and is also used in feeds where molasses is partly replaced by other carriers.

Xanthan gums are used as suspending agents in electrode coatings, as well as in glazes and frits for tiles and sanitary ware. In these products, it is also used because it prevents sagging and pinholing.

Xanthan gum's rheological properties and its outstanding stability at pH extremes make it the thickener of choice in products such as highly alkaline drain, tile, and grout cleaners; acidic descalers for rust and metal oxide removal; graffiti removers; aerosol oven cleaners; toilet bowl cleaners; and metal-cleaning compounds. In these products, xanthan gum also provides cling to vertical surfaces combined with ease of washing off.

The pseudoplastic property of xanthan gum provides excellent texturing in high-build paints and ceiling tile coatings, ensuring in-can stability, ease of application to the wall, and retention of the textured finish. It thickens latex emulsions and dispersions and maintains uniform suspension of zinc, copper, and other metal additives in corrosion coatings. It is also used to suspend particles of refractory materials used in products such as foundry mold and core washes.

Xanthan gum stabilizes highly loaded coal—water fuels, prevents settling, and maintains a stable viscosity during the atomization and combustion cycle. Its low viscosity under conditions of high applied shear as well as its low extensional viscosity enables the fuel to be atomized into a fine spray.

Xanthan gum suspends solids in leather and silver polish, provides lubricity to lotions and heavy creams, and stabilizes emulsions and polishes. It provides excellent print definition in space printing, forms temperature-stable foams for printing and finishing, and acts as a flow modifier for dyeing heavy fabrics and inkjet printing (65). Its rheological properties and temperature stability make it ideal for carpet jet printing where it ensures sharp print definition, the absence of frosting, and trouble-free operation.

Oilfield Application. The shear thinning viscosity provided by xanthan gum allows optimal hydraulic efficiency of drilling fluids (66),(67). It reduces pressure losses within the drill strings, enabling maximum hydraulic horsepower to be delivered to the bit. As a result, penetration rates can be increased, Other

benefits from drilling fluids formulated with xanthan gum include improved bottom-hole cleaning, increased cutting—carrying capacity under annular shear rate conditions, and better separation efficiency in mechanical solids control equipment.

Because of its compatibility with most drilling fluid additives, xanthan gum can be used in a wide variety of drilling fluids. These fluids include those with high pH, fresh water, seawater, and electrolyte-inhibited systems containing dissolved electrolytes such as calcium, potassium, and sodium (68). For special drilling applications, xanthan gum is also used to formulate stiff foams to improve stability and carrying capacity for drilled cuttings.

The pseudoplastic properties of fluids formulated with xanthan gum make it a highly functional additive for work over and completion operations (69). Other key features include its compatibility with most field-formulated brines and its temperature stability, pH stability, and lack of shear degradation. It provides superior hole cleaning, sand suspension, and friction reduction, and purified xanthan gum produces minimal formation damage.

Carrier fluids, formulated with xanthan gum, help improve the competency and durability of gravel packs. In addition, they allow efficient gravel placement in deviated wells, improved slurry transport at high gravel concentrations, and superior suspension at low polymer concentrations.

Xanthan gum provides the ideal viscosity requirements for water- or acid-based hydraulic fracturing fluids. The unique pseudoplastic properties offer improved proppant suspension and maximum viscosity within the fracture.

Xanthan gum forms viscous, pseudoplastic fluids that offer superior mobility control for increased fluid displacement efficiency in secondary and tertiary oil recovery processes. In profile modification applications, xanthan gum provides unique functionality in high salinity formations when cross-linked with chromium and/or other metal ions (70),(71).

Regulatory Status

Food-grade xanthan gum products meet the following requirements: (*i*) U.S. Food and Drug Administration (FDA) food additive order for xanthan gum, 21 CFR 172.695; (*ii*) Food Chemicals Codex (FCC) requirements (72) and the National Formulary (73); (*iii*) EEC purity criteria for xanthan gum, laid down in EEC Directive 82/504/EEC.

Xanthan gum appears as E-415 on Annex I to Directive 74/329/EEC authorizing emulsifiers, stabilizers, thickeners, and gelling agents for use in EEC foodstuffs, amended by Directive 80/597/EEC.

In addition to the food-grade products named above, food-grade xanthan gum has been formulated for use as an additive for liquid feed supplements for ruminant animals and calf milk replacers (21 CFR 573.1010). Xanthan gum is particularly useful in agricultural applications. It is exempted from tolerance requirements when used as a thickener in pesticide formulations applied to growing crops or to raw agricultural commodities after harvest under 40 CFR 180.1001(c). It is also exempted when used in formulations applied to animals under 40 CFR 180.1001(e).

Food-grade products can be used in specified meat products under Department of Agriculture regulation 9 CFR 318.7, and in most poultry products under 9 CFR 381.147. They also meet the FDA requirements for components of paper and paperboard in contact with aqueous and fatty foods under 21 CFR 176.170, and are included in many FDA food standards. It is recommended that current regulations be consulted before any additive is included in new food formulations.

Analytical and Test Methods

Methods for moisture content, ash, pyruvate, trace elements, residual isopropyl alcohol, and so on may be found in the monographs for xanthan gum in the current editions of both the FCC (72) and NF (73). Because of the wide variety of products in which these biogums are used, it would be impossible to give a general method that would not be subject to interference from some other material present.

BIBLIOGRAPHY

"Xanthan" in *EPSE* 2nd ed., Vol. 17, pp. 901–918, by John K. Baird, Kelco Division of Merck & Co., Inc.

CITED PUBLICATIONS

1. (a) J. K. Baird, P. A. Sandford, and I. W. Cottrell, *Bio. Technol.* **9**, 778–783 (1983); (b) I. W. Sutherland, *Int. Dairy J.* **11**, 663 (2001).
2. H. McNeely and K. S. Kang, in R. L. Whistler, ed., *Industrial Gums*, 2nd ed., Academic Press, New York, 1973, pp. 473–497.
3. I. W. Cottrell and K. S. Kang, *Dev. Ind. Microbiol.* **19**, 117 (1978).
4. B. Katzbauer, *Polym. Degrad. Stabil.* **59**, 81 (1998).
5. A. Becker, F. Katzen, A. Puhler, and L. Ielpi, *Appl. Microbiol. Biotechnol.* **50**, 145 (1998).
6. M. P. Starr, *J. Bacteriol.* **51**, 131 (1946).
7. F. Garcia-Ochoa, V. E. Santos, J. A. Casas, and E. Gomez, *Biotechnol. Adv.* **18**, 549 (2000).
8. S. P. Rogovin, W. J. Albrecht, and V. Sohns, *Biotechnol. Bioeng.* **7**, 161 (1965).
9. U.S. Pat. 3,119,812 (Jan. 28, 1964), S. P. Rogovin and W. J. Albrecht (to U.S. Agriculture Secretary).
10. U.S. Pat. 4,051,317 (Sept. 27, 1977), G. A. Towle (to Hercules, Inc.).
11. U.S. Pat. 3,232,929 (Feb. 1, 1966), W. H. McNeely and J. J. O'Connell.
12. J. H. Sloneker and A. R. Jeanes, *Can. J. Chem.* **40**, 2066 (1962).
13. P. Jansson, L. Kenne, and B. Lindberg, *Carbohydr. Res.* **45**, 275 (1975).
14. L. D. Melton, L. Mindt, D. A. Rees, and G. R. Sanderson, *Carbohydr. Res.* **46**, 245 (1976).
15. F. R. Dintzis, G. E. Babcock, and R. Tobin, *Carbohydr. Res.* **13**, 257 (1970).
16. R. Moorehouse, M. D. Walkinshaw, and S. Arnott, in P. A. Sandford and A. Laskin, eds., *Extracellular Microbial Polysaccharides*, ACS Symposium Ser. 45, American Chemical Society, Washington, D.C., 1977, pp. 90–102.
17. P. J. Whitcomb and C. W. Macosko, *Rheology* **22**, 493 (1978).

18. G. Holzwarth and E. G. Prestridge, *Science* **197**, 757 (1977).
19. I. T. Norton, D. M. Goodall, S. A. Frangou, E. R. Morris, and D. A. Rees, *J. Mol. Biol.* **175**, 371 (1984).
20. G. Muller, J. Lecourtier, G. Chauveteau, and C. Allain, *Makrom. Chem. Rap. Commun.* **5**, 203 (1984).
21. T. Sato, S. Kojima, T. Norisuye, and H. Fujita, *Polym. J.* **16**, 423 (1984).
22. T. Sato, T. Norisuye, and H. Fujita, *Polym. J.* **16**, 341 (1984).
23. B. T. Stokke and A. Elgsaeter, *Carbohydr. Res.* **160**, 13 (1987).
24. A. Jeanes, J. E. Pittsley, and F. R. Senti, *J. Appl. Polym. Sci.* **5**, 519 (1961).
25. E. R. Morris, D. A. Rees, G. Young, M. D. Walkinshaw, and A. Darke, *J. Mol. Biol.* **110**, 1 (1977).
26. T. A. Camesano and K. J. Wilkinson, *Biomacromolecules* **2**, 1184 (2001).
27. G. Danute, J. H. Orentas, J. H. Sloneker, and A. Jeanes, *Can. J. Microbiol.* **9**, 427 (1963).
28. I. W. Davidson, *FEMS Microbiol. Lett.* **3**, 347 (1978).
29. B. Seeger, *Nahrung* **25**, 655 (1981).
30. M. Rinaudo, M. Milas, F. Lambert, and M. Vincendon, *Macromolecules* **16**, 816 (1983).
31. P. A. Sandford, P. R. Watson, and C. A. Knutson, *Carbohydr. Res.* **63**, 253 (1978).
32. K. C. Symes, *Food Chem.* **6**, 63-76 (1980).
33. I. H. Smith, K. C. Symes, C. J. Lawson, and E. R. Morris, *Int. J. Biol. Macromol.* **3**, 129 (1981).
34. S. G. Ash, A. J. Clarke-Sturman, R. Calvert, and T. M. Nisbet, *Soc. Pet. Eng. AIME Pap.*, 12085 (1983).
35. M. Dentini, V. Crescenzi, and D. Blasi, *Int. J. Biol. Macromol.* **6**, 93 (1984).
36. U.S. Pat. 4,369,125 (Jan. 18, 1985), H. Kragen and G. Brigand (to Ceca SA FR).
37. M. Iijima, M. Shinozaki, T. Hatakeyama, M. Takahashi, and H. Hatakeyama, *Carbohydr. Polym.* **68**, 701 (2007).
38. G. Maurstad, S. Danielsen, and B. T. Stokke, *J. Phys. Chem. B* **107**, 8172 (2003).
39. G. Maurstad and B. T. Stokke, *Biopolymers* **74**, 199 (2004).
40. R. A. Speers and M. A. Tung, *J. Food Sci.* **51**(1), 96 (1986).
41. R. Moorhouse, Kelco Div. of Merck & Co., Inc., 1987, personal communication.
42. J. K. Rocks, *Food Technol. Chicago* **25**(5), 22 (1971).
43. P. Kovacs, *Food Technol. Chicago* **27**(3), 26 (1973).
44. G. Paradossi, E. Chiessi, A. Barbiroli, and D. Fessas, *Biomacromolecules* **3**, 498 (2002).
45. J. M. R. Patino and A. M. R. Pilosof, *Food Hydrocolloids* **25**, 1925 (2011).
46. Brit. Pat. 1,562,275 (Mar. 12, 1980), D. D. Christian and H. W. Gardner, US Commerce.
47. R. C. Clark, *Poster session, presented at the 27th Annual Conference of the Canadian Institute of Food Science and Technology*, Vancouver, Canada, 1984.
48. C. Andres, *Food Process. Chicago* **46**(12), 66 (1985).
49. G. R. Sanderson, *Food Technol. Chicago* **35**(7), 50 (1981).
50. (a) H. B. Chen, X. L. Chang, D. R. Du, J. Li, H. B. Xu, and X. L. Yang, *Int. J. Pharm.* **315**, 52 (2006); (b) J. Ceulemans, I. Vinckier, and A. Ludwig, *J. Pharm. Sci.* **91**, 1117 (2002); (c) C. W. Vendruscolo, I. F. Andreazza, J. Ganter, C. Ferrero, and T. M. B. Bresolin, *Int. J. Pharm.* **296**, 1 (2005).
51. P. A. Sandford, I. W. Cottrell, and D. J. Pettitt, *Pure Appl. Chem.* **56** (7), 879 (1984).
52. K. A. Coia and K. R. Stauffer, *J. Food Sci.* **52** (1), 166–172 (1987).
53. A. Parker, P. A. Gunning, K. Ng, and M. M. Robins, *Food Hydrocolloids* **9**, 333 (1995).
54. A. Lazaridou, D. Duta, M. Papageorgiou, N. Belc, and C. G. Biliaderis, *J. Food Eng.* **79**, 1033 (2007).
55. M. Gomez, F. Ronda, P. A. Caballero, C. A. Blanco, and C. M. Rosell, *Food Hydrocolloids* **21**, 167 (2007).
56. U.S. Pat. 4,163,807 (Aug. 7, 1979), K. R. Jackman (to Merck & Co., Inc.).

57. C. Andres, *Food Process. Chicago* **43**(6), 85 (1982).
58. H. Mirhosseini, C. P. Tan, N. S. A. Hamid, S. Yusof, and B. H. Chern, *Food Hydrocolloids* **23**, 271 (2009).
59. G. Downey, *Int. J. Food Sci. Technol.* **37**, 869 (2002).
60. C. P. Kechinski, A. B. Schumacher, L. D. F. Marczak, I. C. Tessaro, and N. S. M. Cardozo, *Food Hydrocolloids* **25**, 299 (2011).
61. C. M. Rosell, W. Yokoyama, and C. Shoemaker, *Carbohydr. Polym.* **84**, 373 (2011).
62. S. G. Collyer, in G. O. Phillips, D. J. Wedlock, and P. A. Williams, eds., *Gums and Stabilizers for the Food Industry, Vol. 2: Applications of Hydrocolloids*, Pergamon Press, Oxford, UK, 1984, pp. 349–355.
63. G. T. Colegrove, *Ind. Eng. Chem. Prod. Res. Dev.* **22**, 456 (1983).
64. G. T. Colegrove, *Ind. Eng. Chem. Prod. Res. Dev.* **25**, 108 (1986).
65. M. I. H. Panhuis, A. Heurtematte, W. R. Small, and V. N. Paunov, *Soft Matter* **3**, 840 (2007).
66. R. Caenn, *Soc. Pet. Eng. AIME Pap.*, 5870 (1976).
67. R. Caenn and F. R. Bagshaw, *Soc. Pet. Eng. AIME Pap.*, 7747 (1978).
68. D. E. O'Brien and M. E. Chenevert, *J. Pet. Technol.* **25**, 1089 (1973).
69. U.S. Pat. 3,625,889 (Dec. 7, 1971), C. D. Branscum (to Phillips Petroleum Co.).
70. U.S. Pat. 4,606,772 (Aug. 19, 1986), S. W. Almond and D. J. Hanion (to Halliburton Co.).
71. U.S. Pat. 4,606,407 (Aug. 19, 1986), P. Shu (to Mobil Oil Corp.).
72. *Food Chemicals Codex*, 3rd ed., National Academy Press, Washington, D.C., 1981.
73. *The National Formulary*, 16th ed., U.S. Pharmacopeia Convention, Rockville, Md., 1985.

JOHN K. BAIRD
Kelco Division of Merck & Co., Inc.

X-RAY MICROSCOPY

Introduction

Various types of microscopy have played a crucial role throughout the history of Polymer Science by elucidating the underlying organization and morphology of multiphasic polymeric materials and systems in real space. In many applications, there is often the need to not only visualize the morphology of a multicomponent system or material, but to also quantify the composition of the various phases in detail. Typically, techniques providing very high quantitative chemical information, such as infra red (ir), Raman, and nuclear magnetic resonance (nmr) spectroscopy, would be ideal for these tasks, but these techniques have very limited spatial resolution and achieve at best a resolution of the order of a micron. In contrast to this, electron microscopy has very high spatial resolution, but relies generally on heavy metal staining or only elemental contrast to provide qualitative compositional information. On surfaces, scanning force microscopy (sfm) has proven to be a very versatile characterization tool, but the compositional information obtained is only qualitative in nature. X-ray microscopy bridges this gap between ir, nmr on the one hand and electron and scanning force microscopy on

the other, and fills a need by providing quantitative compositional information at a spatial resolution of presently 40 nm.

This article reviews Near Edge X-ray Absorption Fine Structure (nexafs) spectroscopy, which underlies the ability for quantitation of sample composition in x-ray microscopy. Also covered are state-of-the-art x-ray microscopy instrumentation techniques and a relatively complete overview of nexafs microscopy applications.

Near Edge X-ray Absorption Fine Structure Spectroscopy

The utility of x-ray microscopy is based on the range and subtlety of the spectroscopic and hence compositional information content of nexafs spectroscopy. As is true for all spectroscopies, the higher the chemical speciation capability that can be achieved, the better the compositional quantitation. In nexafs spectroscopy, the photoabsorption cross section for the excitation or photoionization of tightly bound core electrons is measured. NEXAFS spectra are necessarily element specific, as each element has a characteristic core binding energy (ie, carbon 1*s*: ~290 eV, nitrogen 1*s*: ~400 eV, oxygen 1*s*: ~530 eV, etc). The spectral features observed in nexafs spectra correspond to transitions from the ground state to a core excited state. Figure 1 presents a schematic of the x-ray photoabsorption process for the carbon 1*s* nexafs spectrum of poly(styrene-*r*-acrylonitrile) (SAN). The most pronounced spectral features are intense and narrow peaks at the lowest energies in the spectrum. The first transition at ~285 eV is a C 1*s* $\rightarrow \pi^*$ transition corresponding to carbon atoms of the phenyl functional group. The second transition at ~287 eV is a C 1*s* $\rightarrow \pi^*$ electronic transition corresponding to the carbon atoms of the acrylonitrile functional groups. The energy of these features is dictated by the combination of initial state effects (core binding energies) and final state effects (energy of the optical orbital in the presence of the core hole). The relative magnitude of initial and final state effects in SAN can be gleamed from the energy diagram on the right-hand side of Figure 1. At higher photon energies in the spectrum, broad C 1*s* $\rightarrow \sigma^*$ transitions are superimposed on the photoionization continuum.

A more broadly based illustration of the compositional sensitivity of nexafs spectroscopy can be seen in Figure 2 (1), displaying spectra from a number of unsaturated polymers that consist primarily of various aromatic functional groups, C=C bonds in the polymer chain backbone, as well as amide, ester, and carbonyl groups. It is readily apparent that the shape and intensity of the spectral features observed are unique for each polymer. Most nexafs spectra of these polymers are dominated by low energy C 1*s* $\rightarrow \pi^*_{C=C}$ transitions at 285–287 eV. The shape and intensity of this $\pi^*_{C=C}$ band varies with the chemical and hence electronic structure. An example of this chemical sensitivity can be observed in the C 1*s* nexafs spectra of polystyrene (PS) and poly(bromo styrene) (PBrS) (right panel of Fig. 2). In the PBrS spectrum, the core $\rightarrow \pi^*_{C=C}$ (LUMO) transition has two major components, a C 1*s*(C—H) $\rightarrow \pi^*_{C=C}$ component at ~285 eV and a C 1*s*(C—Br) $\rightarrow \pi^*_{C=C}$ component at ~286.2 eV, whereas PS has only one major component at ~285 eV. Note that in this notation, the core level is indicated parenthetically before the arrow (eg C—H), and the nature of the upper level of a given transition

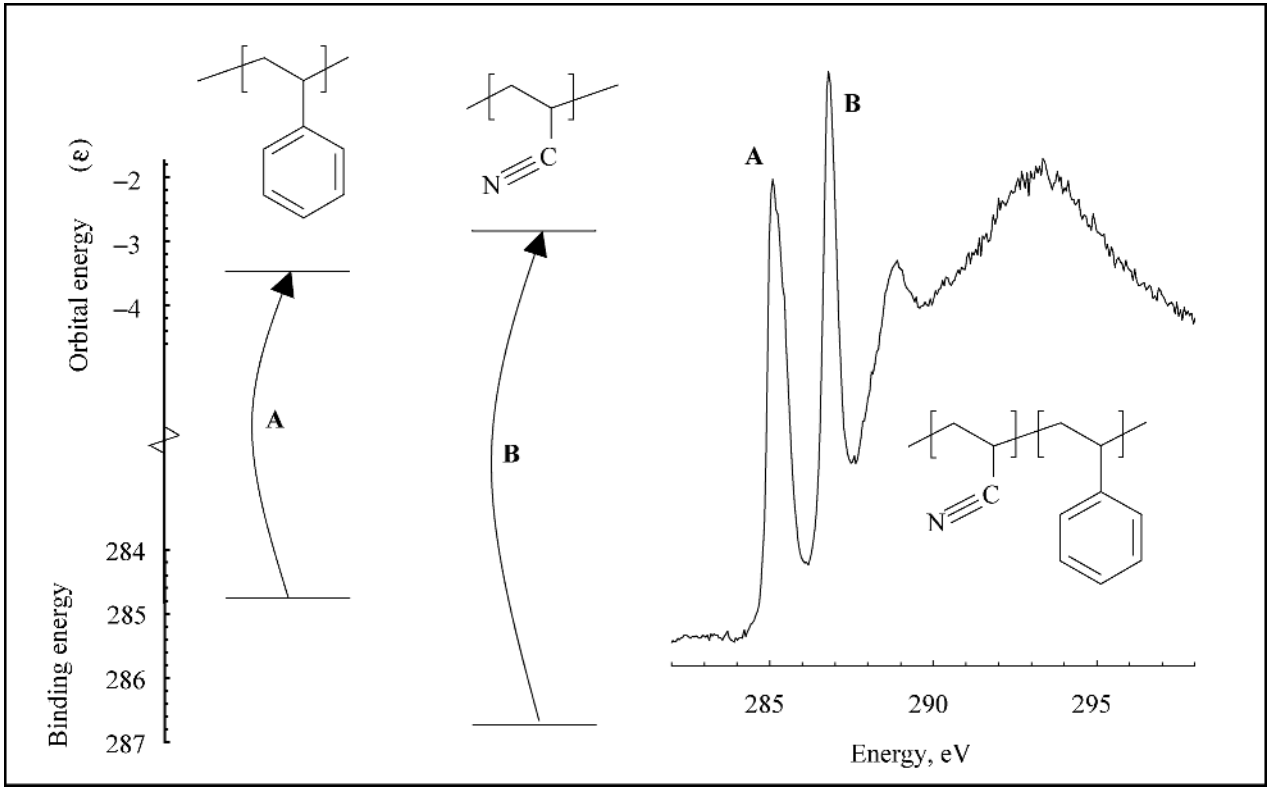

Fig. 1. Electronic schematic for the nexafs photoabsorption spectrum of poly(styrene-*r*-acrylonitrile). The C 1*s* binding energies were obtained from xps. Orbital energies of the C 1*s* → LUMO(π^*) transition of the phenyl (A) and acrylonitrile (B) functional groups were obtained from ab initio calculations. Reproduced from Ref. 1.

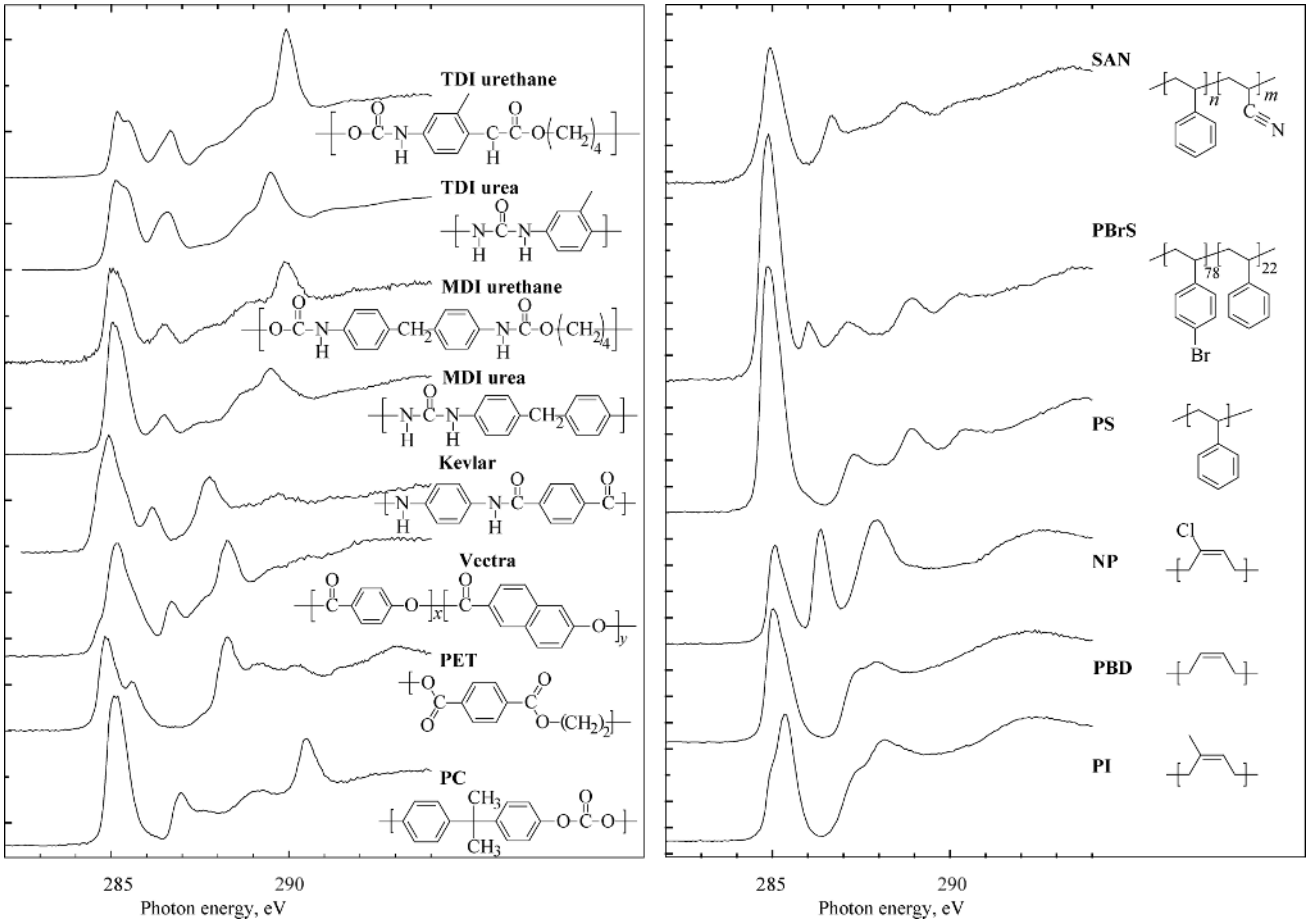

Fig. 2. C 1*s* nexafs spectra for a series of unsaturated polymers, recorded with the Stony Brook STXM. Reproduced from Ref. 1.

is indicated by the final subscript (eg C=C for phenyl). The inductive effect of the bromine shifts the C 1*s* ionization potential of the C—Br carbon atom to lower energy, increasing the energy of the C 1*s*(C—Br) $\rightarrow \pi^*_{C=C}$ transition to the common manifold of π^*(LUMO) states.

A similar situation applies to 4,4′-methylene di-*p*-phenylene isocyanate (MDI) and toluene diisocyanate (TDI) polyurea and polyurethane spectra, where the core $\rightarrow \pi^*_{C=C}$ (LUMO) transition has two major components: a C 1*s*(C—H) $\rightarrow \pi^*_{C=C}$ component at ~285 eV and a C 1*s*(C—R) $\rightarrow \pi^*_{C=C}$ component at ~286.5 eV. In TDI, the main, low energy π^* peak itself is furthermore split into two components. The inductive effect of a heteroatom can also be clearly observed by comparing the spectra of neoprene (NP) and polyisoprene (PI). A complementary series of nexafs spectra is shown in Figure 3, which presents the evolutionary trend of the spectral signature of carbonyl functional groups as the nearest neighbor environment is changed progressively and systematically from a keton to a carbonate (2).

Unfortunately, peaks attributable to different functional groups and specific carbon atoms have the tendency to overlap in a nexafs spectrum. Most of the spectroscopic information is compressed into a 6-eV wide energy window, while lineshapes are about 100 meV wide. Most notably, π^* spectral features corresponding to carbonyl, ester, and carbonate groups generally sit on top of C 1*s* (C—H) $\rightarrow \sigma^*$ transitions or the vacuum continuum.

Sometimes the shifts of slightly inequivalent carbon atoms are small and of the order of the intrinsic line width of a spectral feature (about 80–100 meV) that arises from the finite core-hole lifetime. Small chemical shifts can be found, for example, for the six inequivalent carbon atoms of the phenyl ring of PS. Further complicating matters, these small chemical energy shifts overlap with vibrational effects that have also similar energy shifts. The chemical shifts can thus not be observed in isolation from vibration and are furthermore convolved with the natural line width. The relative contributions of chemical and vibrational effects to the spectrum of PS has been explored (3). The magnitude of the shifts of these six carbon atoms based on calculations ranges from 50 to 400 meV. Figure 4 shows the lowest energy spectral features of PS and deuterated PS (d-PS). Difference of up to 15% in intensity can be observed that can be clearly attributed to vibrations.

NEXAFS spectroscopy is also sensitive to differences in the chemical structure of saturated polymers (polyolefins and polyethers). The nexafs features in spectra of these materials are predominantly core $\rightarrow \sigma^*$ electronic transitions with some Rydberg character (4–6). In general, the spectral differences and variations observed for σ^* transitions as a function of chemical structure are not as great as those for π^* transitions. Only slight, although noticeable, differences in the nexafs spectra of polyethylene (PE), polypropylene (PP), polyisobutylene (PIB), and ethylene propylene rubber (EPR) have been observed (1). The main chemical structural differences between these polymers are the number and distribution of methyl groups to the $(CH_2)_x$ backbone. The small spectroscopic differences are not surprising, since the structural differences involve bonds of the same C—C and C—H σ-bonded character. Nevertheless, spectroscopic differences have even been observed for PE of different density. These differences have been attributed to a matrix effect that varies between amorphous and crystalline regions of the semicrystalline PE materials (6). The largest spectral differences

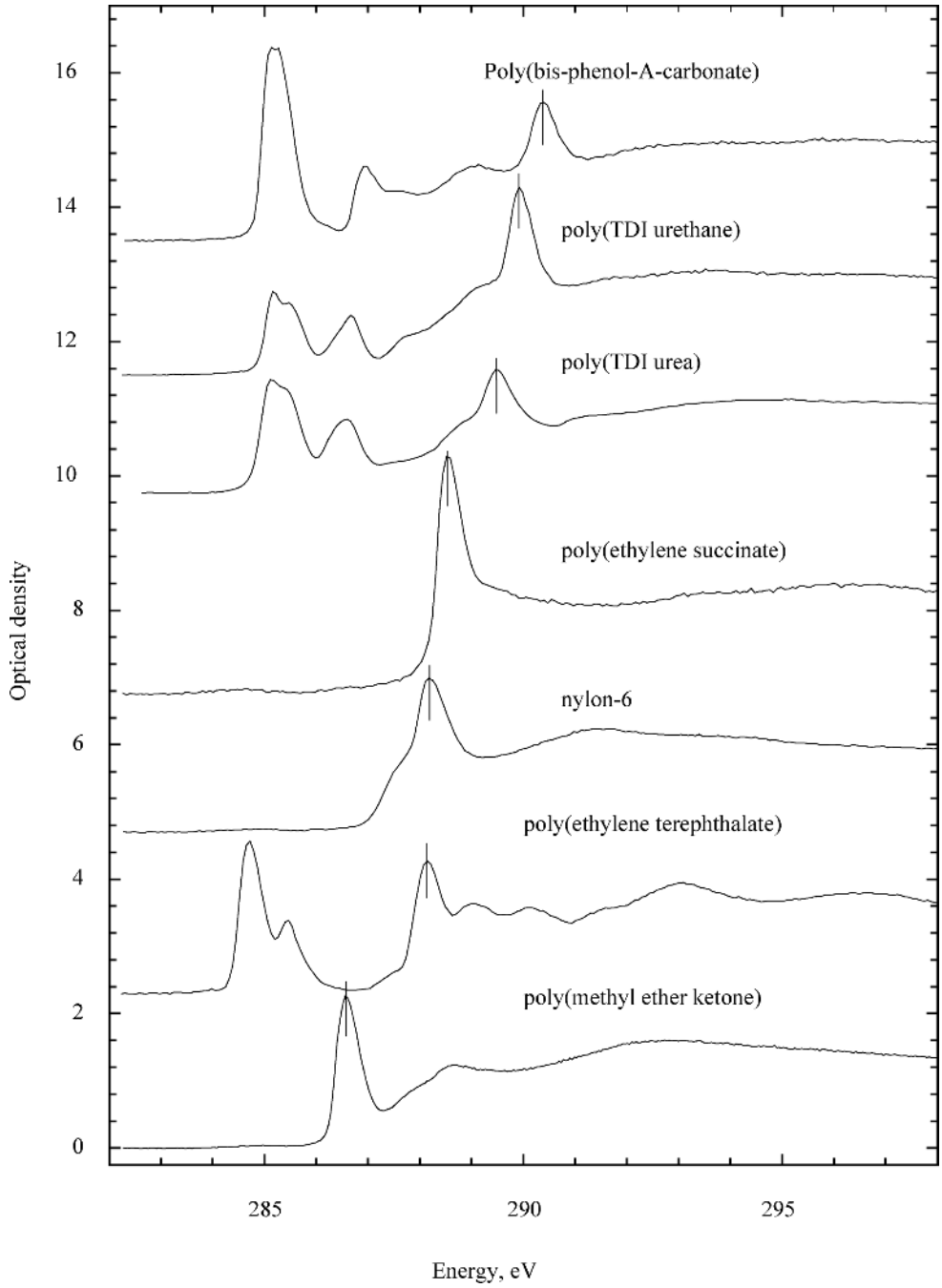

Fig. 3. C 1*s* nexafs spectra for a series of polymers that have carbonyl functional groups in different local electronic environments. (Data recorded with the Stony Brook STXM.) Reproduced from Ref. 2.

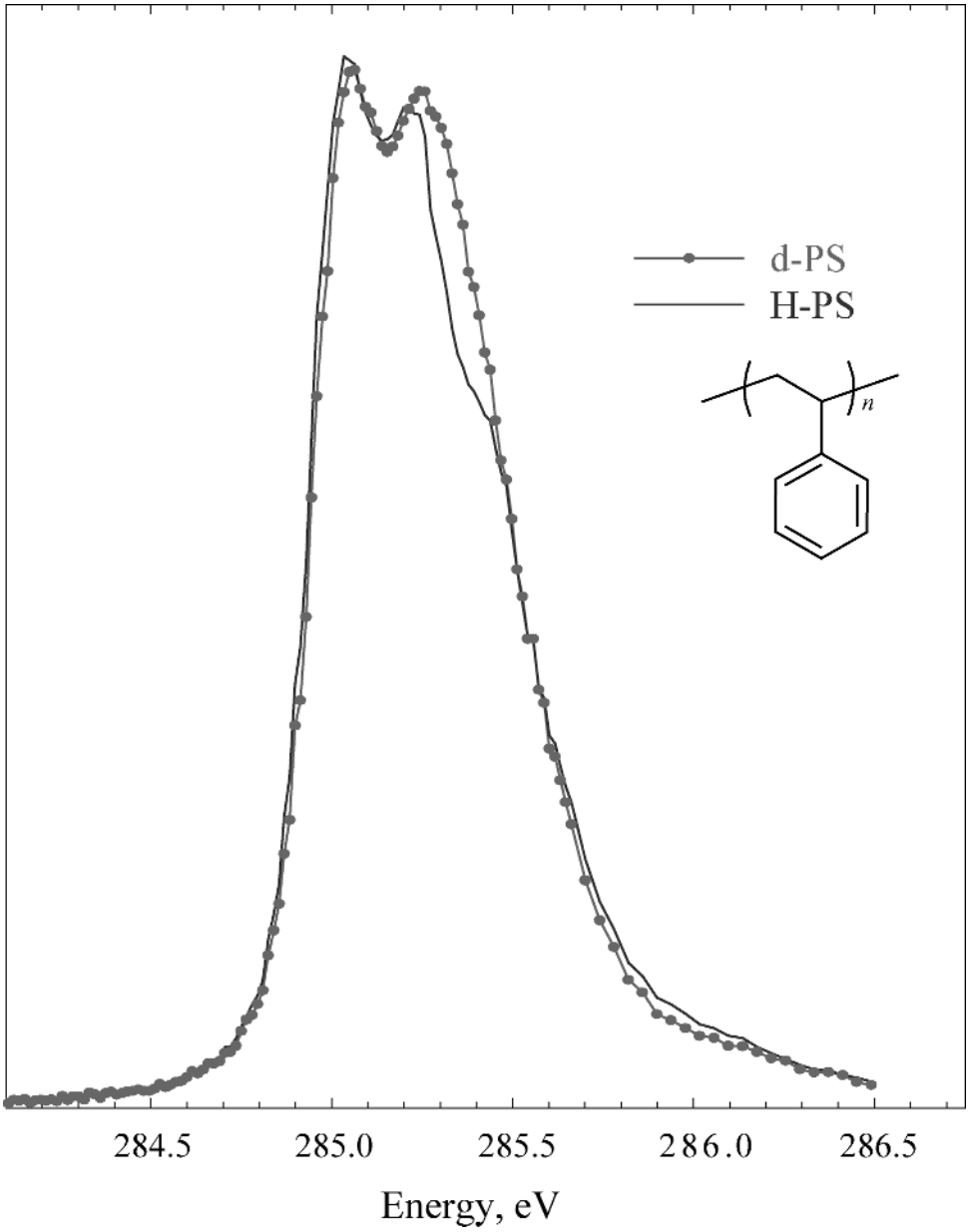

Fig. 4. C 1*s* nexafs spectra of polystyrene (gray line) and deuterated polystyrene (light gray line) recorded with a resolving power of about 6100. The area of the C 1*s* $\rightarrow \pi^*$ transition is normalized so that absolute differences in the spectral intensity are chemically meaningful. (Data acquired with ALS BL7.0 STXM.) Reproduced from Ref. 3.

between the nexafs spectra of saturated polymers are observed when heteroatoms such as oxygen, chlorine, or fluorine are present. Substantial shifts of the corresponding features of PE toward higher energy are observed in poly(ethylene

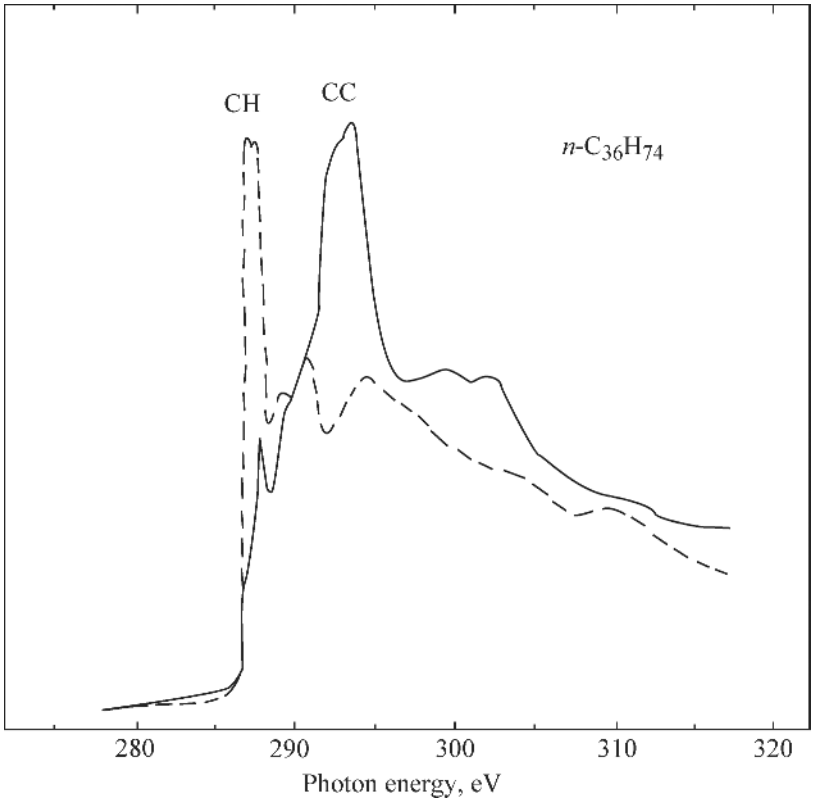

Fig. 5. Angle-dependent C 1*s* nexafs spectra of evaporated hexatriacontane-$CH_3(CH_2)_{34}CH_3$. Although this is not a polymeric substance, it provides a good illustration how large the linear dichroic signal can be even for fully saturated materials. The solid line data has the polarization vector aligned along the molecular axis of the oriented materials, while the dashed line data is for polarization perpendicular to the molecular axis. Reproduced from Ref. 7.

oxide), polytetrafluoroethylene, polyvinylidine, or poly(vinyl chloride), primarily on account of shifts in the ionization potential because of the heteroatom.

NEXAFS experiments are almost exclusively performed with linearly polarized light from synchrotron radiation facilities. Since the discrete nexafs transitions obey dipole selection rules, oriented samples exhibit linear x-ray dichroism. This can be utilized to explore and measure orientation in polymeric materials. As an example, Figure 5 displays two nexafs spectra of an oriented long-chain hydrocarbon molecule (8). The orientation of the electric field vector with respect to the sample can be changed by rotating the sample relative to the x-ray beam. The spectra shown in Figure 5 correspond to glancing and normal incident radiation. Large spectral differences are observed, even though saturated molecules with only σ bonds tend to give less well-defined spectral features than polymers with π bonds.

The principles and underlying physics of nexafs spectroscopy and x-ray linear dichroism and their applications to small molecules and some polymers

have been reviewed in a monograph (9). Complementary, but somewhat limited, overviews of polymer nexafs spectra have been presented (10–13). A more detailed "primer" of nexafs spectroscopy of polymers has also been provided (1). A carefully energy-calibrated library of nexafs spectra is presently being compiled by the North Carolina State University nexafs microscopy research group. Energy calibration is accomplished by leaking a small amount of CO_2 gas into the experimental chamber and by recording characteristic polymer features and characteristic features of the CO_2 gas simultaneously, thus reducing any ambiguity about the energy scale (14).

The chemical and orientational sensitivity of nexafs spectroscopy has been used for analysis in a variety of applications. Examples of studies involving nexafs spectroscopy are given below:

(1) Photoactive polymers: poly(phenylene vinylene) (15), poly-*p*-phenylenes and polyacenes (16), photo-oxidation of electroluminescent polymers (17), and uv-polymerized diacetylene (8)
(2) Polyurethanes and model compounds (18,19)
(3) Plasma and radiation damaged polymers: oxygen plasma damaged polypropylene (20) and argon plasma damaged polycarbonate (21). Electron and x-ray beam damaged or decomposing polymers: poly(methy methacrylate) (PMMA) (22–24), several polymers with carbonyl functionality (25).
(4) Metal polymer interfaces: chromium coated poly(ethylene terephthalate) (PET) (26) and metalized polycarbonate (PC)(27)
(5) Surface relaxation of PS (28)
(6) Surface structure of polyimides (29–34)
(7) Surface orientation and grafting density of semifluorinated polymers (35–39)
(8) Organic geochemical polymers: petroleum asphaltenes and coals (40,41) and kerogens and bitumens (42)
(9) Inorganic polymers: polydimethylsilane films (43,44) and poly(di-*N*-hexyldisiloxane) (45).

Additional studies comprise various forms of polyethylene $(CH_2)_x$, such as oriented homopolymer (7,46). Other examples include polytetrafluoroethylene homopolymer and models (7,47–50); poly(ethylene terephthalate) and the related polymers poly(butylene terephthalate) and poly(ethylene naphthalate) (51–53); and electrochemically polymerized thin films such as poly(3-methyl thiophene) (54) and polypyrrole (55). This is not intended to be a comprehensive list, but only an indication of the wide range of applications possible with nexafs spectroscopy.

Energy electron loss spectroscopy (eels) used under dipole approximation conditions is a closely related tool to nexafs spectroscopy as it measures the same electronic transitions (56,57). Indeed, most of the early polymer core excitation spectroscopy, work particularly at the C 1*s* core edge, was performed by eels (58–61). EELS can be performed in a scanning transmission electron microscope (stem) at high spatial resolution (62–64), or by energy filtered tem

imaging (65). The relatively poor energy resolution in commercial instruments and higher beam damage (66) limits the use of these eels methods for compositional analysis of complex polymeric materials. EELS is best used for elemental analysis or semiquantitative low loss spectroscopy (67–69). Specialized tem–eels instruments have demonstrated 0.2–0.4 eV FWHM energy resolution for semiconductors (70) and nickel aluminum intermetallics (71). The development of tem-monochromators capable of reaching 50 meV resolution is in progress (72–74).

NEXAFS Microscopy: Instrumentation and Analysis Tools

Having seen the power (and limitation) of nexafs spectroscopy in the preceding sections, one can readily envision the enhanced utility of nexafs spectroscopy as a characterization tool that would result from the addition of high spatial resolution capabilities. Since the spectroscopic sensitivity to specific moieties and functional groups can in many or even most cases be exceeded by ir, nmr, and Raman spectroscopies, nexafs microscopy will have to exceed the spatial resolution of these other spectroscopy techniques in order to be truly useful. To date, nexafs microscopy has surpassed a spatial resolution of 50 nm both in transmission to measure bulk properties (75–77) and in a reflection geometry to study surfaces (78,79). This level of spatial resolution is at least an order of magnitude better than what can be accomplished with complementary compositional analysis techniques. Future developments in nexafs microscopy might achieve a spatial resolution of a few nanometers (80,81). In addition, nexafs microscopy has exceptional surface sensitivity of about 10 nm, a sensitivity that could be improved to about 1 nm with photoemission electron microscopes (peem's) that incorporate a bandpass filter (80–82).

High spatial resolution nexafs microscopy is generally accomplished in two ways: (*1*) instruments for transmission experiments typically employ high resolution zone plate optics (83), whereas (*2*) surfaces are characterized with peem's (78,79,82). Zone-plate-based microscopes are true x-ray microscopes. PEEM's are essentially electron microscopies in which high spatial resolution is achieved with electrostatic or electromagnetic electron optics. The quality of the optics system is essential in both cases.

For zone-plate-based microscopes, the accuracy of the zone placement and the width of the outermost zone determines the spatial resolution achievable with these elements. The Rayleigh resolution of a perfect zone plate is 1.22 times the outermost zone width. Zone plates with outermost zone widths between 20 and 40 nm are presently in use with experimental spatial resolution in the range of 25–50 nm (77). Two types of instruments have been developed and are being continually refined and improved: (*1*) scanning transmission x-ray microscopes (stxm) and (*2*) full-field conventional transmission x-ray microscopes (txm) (see schematics in Fig. 6). Present stxm's generate a microprobe of about 40–50 nm in size, and the sample is raster scanned through the focus of the x-ray microprobe by mechanical means (84,85). In a txm, a zone plate downstream of the stationary sample magnifies the sample onto a 2-D detector (86–88). NEXAFS microscopy with good chemical sensitivity requires good energy resolution. For a stxm that

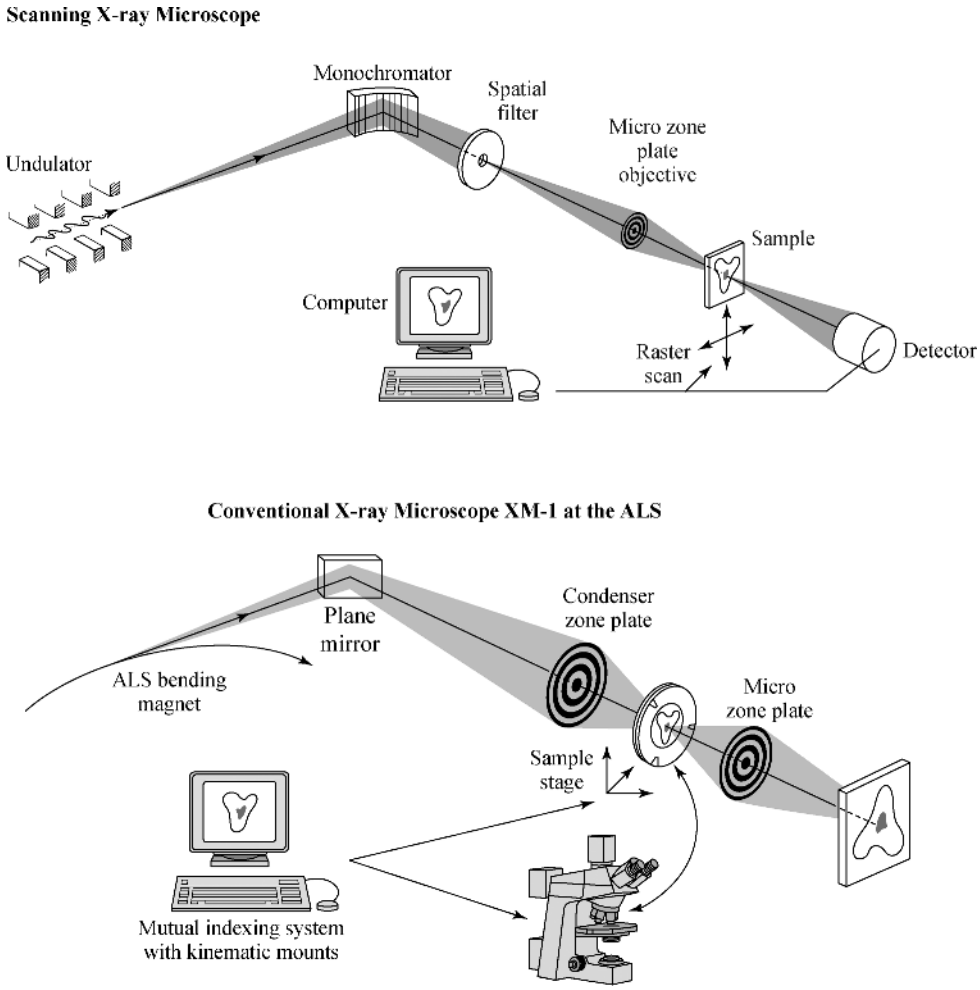

Fig. 6. Schematic of a scanning transmission x-ray microscope (stxm) and a conventional transmission x-ray microscope (txm). Courtesy of W. Meyer-Ilse, CXRO.

is operated in the 200–900 eV energy range, this is achieved with a grazing incidence monochromator upstream of the microscope. Near the carbon edge, the most widely used edge for polymeric materials, a resolving power of 2000–5000 is routinely available (85,89,90). TXM's presently employ zone plate monochromators in order to match the numerical aperture of the illumination at the sample to the numerical aperture of the objective. Present zone plate monochromators used in a txm have relatively low energy resolution (~0.5 eV), limiting the utility of txm for nexafs microscopy of polymers. Efforts are underway to improve this shortcoming of txm's.

Zone plates are highly chromatic, with a focal length proportional to the photon energy. As a result, continual refocusing is required during the photon energy change necessary for spectroscopy. This is accomplished by changing the sample to zone plate distance. If a high spatial resolution point spectrum is to be

acquired, care and effort must be exercised to control the transverse motion of the scanned element (sample or zone plate) during refocusing to avoid blurring of the region from which the spectrum is acquired. Controlling this "run-out" is a technological challenge, and places severe constraints on the accuracy of the mechanical apparatus. An accuracy, stability, and repeatability consistent with the spatial resolution of the zone plate has not yet been routinely achieved in existing stxms. One way to work around these problems, at least partially, is to acquire image sequences at each photon energy in the spectrum (91). The images in these sequences can then be correlated to each other and shifted to provide the proper alignment. If one is only interested in spectra from a few locations, the image sequence approach results in a time penalty: image sequences typically require between 0.5 and 3 h, while a few point spectra require a few minutes. Refocusing after a change in energy is also necessary in a txm, with similar requirements to an stxm regarding stability and alignment. In a txm, one has to translate both the zone plate objective and the detector in order to keep the magnification the same.

The first stxm had been operated at a relatively low brightness bending magnet beamline at the National Synchrotron Light Source (NSLS) uv ring (92), but was moved to an undulator beamline as these high brightness sources became available (93). This was motivated by the requirement to illuminate the zone plate coherently to achieve the highest spatial resolution possible. High intensity at high spatial resolution is thus most easily accomplished at the brightest sources available, ie, undulator sources at synchrotron radiation facilities (83,85,90). In order to increase stxm capacity at relatively low cost, an effort is underway to build an stxm at a bending magnet beamline at the Advanced Light Source (ALS) in Berkeley that is about two orders of magnitude brighter than a bending magnet at the NSLS uv ring. In order to achieve the best data rates for the majority of polymer experiments, the ALS bending magnet stxm and beamline has been optimized for C-nexafs (94). The brightness requirement for a txm is less severe than for an stxm. TXM's can be successfully operated with short exposure times at bending magnet beamlines even at second generation synchrotron facilities. Since most laboratory based x-ray sources do not have a continuous and stable emission spectrum, laboratory based nexafs microscopy, with its requirement for photon energy tunability, is an unlikely development in the near future.

To study surfaces, secondary processes, such as fluorescent photons and secondary or primary photoelectrons, that track the absorption cross section as a function of photon energy are utilized. All three of these secondary processes are already extensively employed in nexafs spectroscopy without spatial resolution, in what is called the fluorescent yield (FY), total- (TEY) or partial electron yield (PEY) mode, respectively (9). PEY traditionally refers to experiments that utilize a bias voltage on the channel plate or channeltron detector or an energy window set with an energy analyzer. Both methods strive to accept primarily electrons with kinetic energy in the 100–300 eV range near the minimum of the secondary electron mean free path in order to achieve high surface sensitivity of about 1 nm. In nexafs microscopy, only a modified version of PEY mode is presently available. In a peem, the photoelectrons emitted from the sample surface are accelerated in a cathode lens to high energies, and subsequent electrostatic or electromagnetic

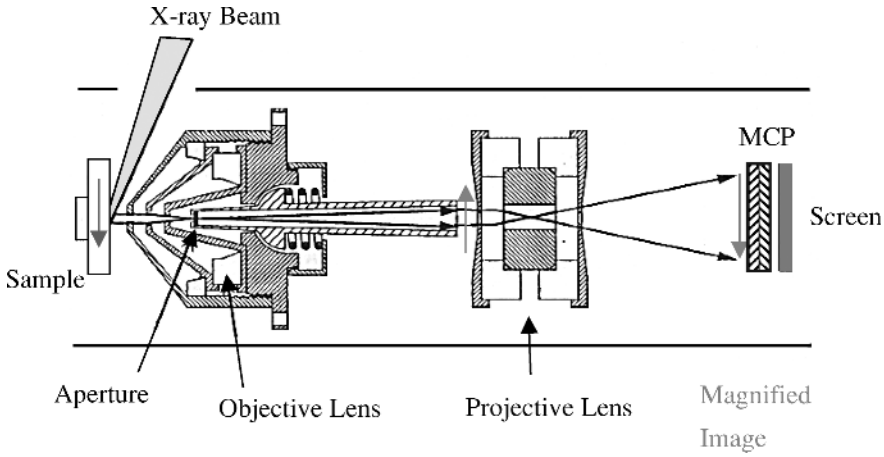

Fig. 7. Schematic of a photoemission electron microscope (peem). Courtesy of S. Anders, ALS, and B. Tonner, University of Central Florida.

lenses magnify the image onto a 2-D detector (see Fig. 7 as an example). The peem instrument itself acts as a low pass energy filter with a bandwidth of a few electro volts near the photoelectron threshold. This energy window is not near the mean free path minimum and has a large sampling depth of about 10 nm associated with it. True energy filtering in a peem would allow operation near the mean free path minimum. However, the one instrument presently available with an energy filter, the spectroscopic low energy electron microscope (SPLEEM) developed by the group of E. Bauer, has not yet been utilized for nexafs experiments (95).

Several contrast mechanisms assert themselves simultaneously in a peem instrument: (*1*) composition, ie, the cross section difference between different materials at a given photon energy, (*2*) topography and (*3*) illumination effects. Topographic contrast arises from the modified collection efficiency in the peem from sample locations that are not perpendicular to the optical axis. Concave round features tend to have reduced collection efficiency, while convex features are enhanced. Illumination effects arise because the sample is illuminated at a shallow angle of 30° or less. The local photon intensity of the sample depends thus on the topography. Even complete shadowing is possible. Typically, one is interested primarily in the compositional information, and analysis procedures are presently developed to disentangle the spectroscopic, ie, compositional, information from topography and illumination effects. Generally, these methods use pre- and post-edge normalization of the nexafs spectra acquired with the peem and reference spectra acquired with the same instrument (see, for example, Ref. 96)

Since peem's acquire information in parallel from all pixels in the image, and incoherent illumination of the sample is possible, the source requirements are generally not extreme. peem's can be successfully operated at any bending magnet beamline that provides sufficient energy resolution (78,79,97,98). PEEM's also do not require any refocusing during photon energy changes. However, for future ultrahigh spatial resolution (<10 nm) instruments, the necessary flux densities on the sample can only be provided with undulator beamlines.

Quantitative Microanalysis. In transmission nexafs spectroscopy, quantitative analysis can be achieved by inverting Lambert–Beer's law of x-ray absorption:

$$\mathrm{OD} = \mu\rho t = \alpha t = -\ln(I/I_0)$$

where OD is the optical density, μ is the energy-dependent mass absorption coefficient, ρ is the density, t is the sample thickness, and an energy scan from the sample (I) is normalized to another energy scan recorded without a sample (I_0). The product of μ and ρ is the linear absorption coefficient α.

For accurate quantitation, well-characterized nexafs spectra of carefully chosen analytical models of the polymer components are required. The basic and well-founded assumption is that nexafs spectra of *non-interacting* moieties or components are additive. For a blend of two or more homopolymers, such as PS/PMMA, the analytical models can simply be the individual homopolymers. Even for quantitation of components in a random block copolymer, eg poly(styrene-*r*-acrylonitrile) (SAN), the spectra of the homopolymers PS and polyacrylonitrile (PAN) can be used, provided that the blocks do not interact electronically. Accuracy of a few per cent can presently be obtained for a variety of polymers including polyurethanes (19). In general, care must be exercised to choose models and reference spectra that indeed reflect noninteracting moieties (1). The utility and limitations of quantitative nexafs analysis for polymeric materials has recently been discussed (1).

Quantitative Image Analysis. Two methods are available if the composition of large sample areas is to be analyzed quantitatively: (*1*) singular value decomposition (SVD) of a few images at carefully chosen photon energies (98–101), or (*2*) acquisition of image sequences at many energies that provide nexafs spectra at each point (91). SVD requires prior knowledge about the sample and works only if the overall composition of the sample is known. In addition, the linear absorption coefficients of the components must be accurately known in order to minimize systematic errors in the analysis. The nexafs spectra used as standards must be free of spectral distortions caused by absorption saturation because of the presence of higher order spectral contamination and detector nonlinearity.

The SVD procedure requires a series of images acquired at a number of energies that equal or exceed the number of compositional components. The reference spectra provide crucial guidance for the selection of the photon energy. Usually energy values for images are chosen that correspond to large spectral differences between the constituent components. An example of raw transmission images is shown in Figure 8. Each transmission image is converted to an optical density (OD) image by computing $\mathrm{OD} = -\ln(I/I_0)$, where I is the transmitted intensity and I_0 is the incident intensity. The normalization with I_0 can be most readily and accurately accomplished if the image itself contains an open area (see Fig. 9), but recording a separate I_0 spectrum is also possible. Since $\mathrm{OD} = \alpha t = \mu\rho t$, each pixel in an OD image can be described by a linear combination of the product of the linear absorption coefficient α and the thickness t for each component respectively. This results in a set of linear equations that can be solved for the thickness of each component. Since SVD utilizes only a limited and small number of images,

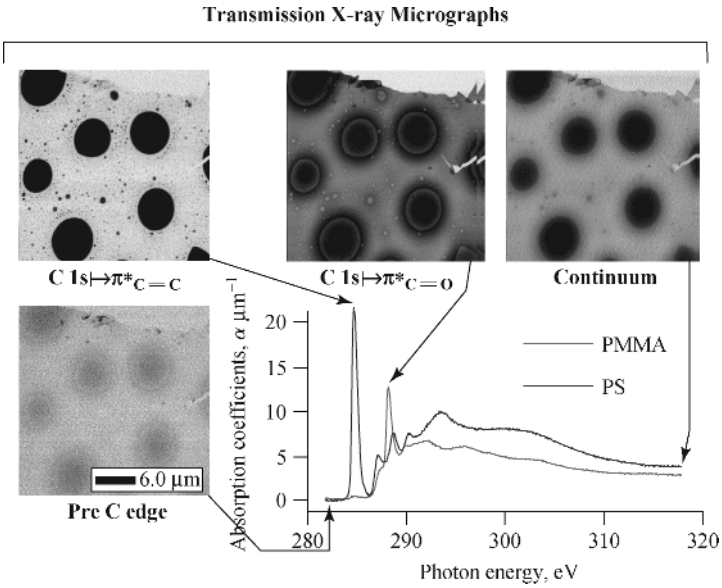

Fig. 8. Basic data set for SVD analysis, with reference spectra of PS and PMMA and transmission images of a PS/PMMA sample at the four energies indicated. Generally, each image has a weighted absorption for each substance present, based on the cross sections at the particular photon energy and the abundance of the substance, even though the absorption in some x-ray micrographs can be dominated by one or the other chemical substance, eg 285.2 eV is dominated by PS absorption. (Data acquired with the Stony Brook STXM.) Courtesy of D. A. Winesett, NCSU.

it results in the smallest (and minimum) dose to the sample to extract the desired information. Since $\alpha t = \mu \rho t$, one could alternatively use the mass absorption coefficient as the known quantity and calculate the mass-thickness ρt, rather than the thickness itself. The latter is advantageous if the same component might be present in the sample with different densities, ie, a polymer in an amorphous and crystalline form. The relative contrast and intensities of the images derived from the SVD analysis are not affected by this change in perspective, only their interpretation.

Acquisition of image sequences has the advantage that complete spectroscopic information is acquired from all sample areas (91). Hence the spectra extracted from image sequences can be compared *post facto* to a large number of possible reference spectra, and the existence and identification of unknown species can be more readily accomplished than with SVD (see, for example, Ref. 96).

For C-NEXAFS transmission, optimum signal-to-noise ratios are achieved with sample thicknesses of 50–200 nm. For bulk materials, these sample requirements can usually be met using well-developed electron microscopy (em) preparation techniques such as ultramicrotomy or cryomicrotomy. Alternatively, thin films can be spun-cast to the right thickness and transferred to em grid for x-ray microscopy inspection. Thin samples and section of samples can also be examined in a completely hydrated/solvated state sandwiched between two very thin Si_3N_4

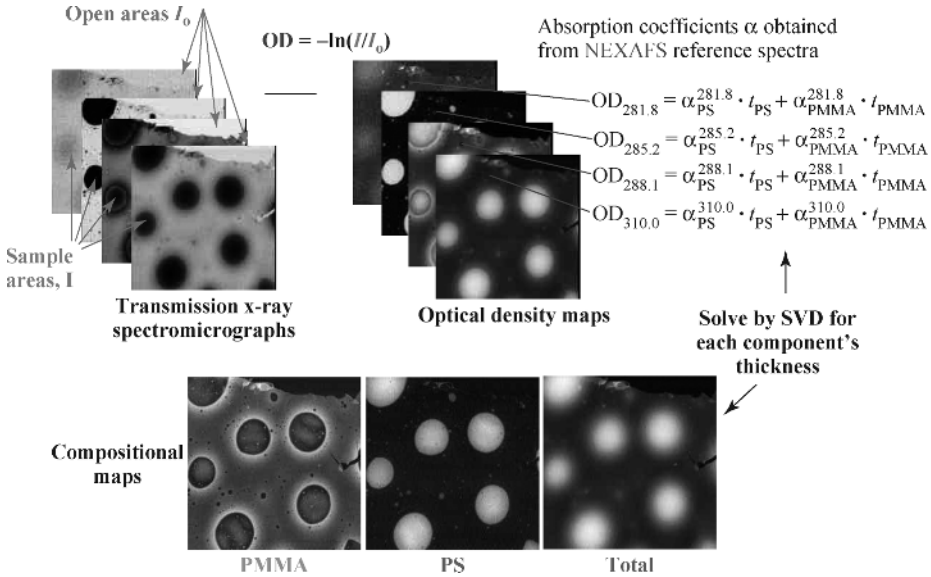

Fig. 9. The transmission images shown in Figure 8 are normalized to optical density (OD) images by inversion of Lambert–Beer's Law. These OD images are now linear in the absorption coefficients α and thickness t. A set of OD images can subsequently be processed via a singular value decomposition (SVD) procedure to yield quantitative composition maps in terms of the thickness t. (Data acquired with the Stony Brook STXM.) Courtesy of D. A. Winesett, NCSU.

membranes (102). For surface analysis in a peem, polymer thin films typically show the propensity to charge. Generally, only thin polymer films with a thickness of less than 200 nm on top of a conducting substrate can be investigated. Precise temperature control in an stxm and txm is not yet routinely available. PE samples have been melted near 120°C (6), and biological materials have been examined in the frozen state (103). Temperature range in a peem can be from −70 to >1200°C. However, accuracy for near room temperatures is not very good.

NEXAFS Microscopy: Applications

NEXAFS spectroscopy and microscopy provide a new approach to study carbon-based materials. During the last couple of years, nexafs microscopy has been successfully applied to materials characterization in a variety of fields ranging from polymer science and biology to meteoritics (1,83,99). Here, the discussion is focused on synthetic polymeric materials. Organizing the presentation by separating it into compositional and orientational analysis does not work well, as several studies of one material combine both aspects of nexafs spectroscopy. The discussion progresses thus from the "simple" to the apparently or supposedly "more complex" without regards as to whether compositional or orientational information is sought. The discussion starts with homopolymer surfaces, then progresses to single or multicomponent thin polymer films and structured spheres,

followed by bulk properties of multicomponent polymers. The latter might involve formation of "unknown" compounds during processing, presenting a challenge that necessitates careful selection of nexafs reference spectra. These applications will be complemented by a short discussion of research on polymer fibers.

Homopolymer and Polymer Blend Surfaces and Ultrathin Films. Because of the various technological applications of polymer thin films, ranging from multicolor photographic printing to flat panel and liquid crystal displays, it is important to understand thin film and polymer surface characteristics in order to improve performance or to develop entirely new applications or processing methodologies. Polymer and block copolymer thin films and surfaces thus enjoy continued research interest from both a technological and fundamental perspective.

NEXAFS spectroscopy, on account of its excellent surface sensitivity (about 1–10 nm) and its polarization dependence, can and has been utilized to study a variety of surface properties. Some recent, nonexhaustive examples of nexafs spectroscopy applications are the investigation of the alignment and orientation of polymers and its functional groups in polyimide surfaces after rubbing with a buffing cloth (29–34), the surface relaxation of PS (28), and the orientation of semifluorinated polymers and block copolymers (35–38,104,105). The potential for nexafs characterization of polymer surfaces even without spatial resolution is in fact enormous. A large number of polymer surface characterizations, eg in adhesion science, are currently performed with laboratory x-ray photoemission spectroscopy (xps), even though nexafs spectroscopy might be much more suitable to the task because of increased chemical and surface sensitivity. NEXAFS microscopy has been utilized to investigate the stability and dewetting behavior of bilayers, the phase separation in polymer thin films, and the orientation produced by buffing and rubbing polyimide films. Several examples are provided below.

Polyimide Films and Surfaces. In flat panel displays, polyimide films typically about 0.2-μm thick are coated onto the electrode surfaces. To prepare a surface that aids the alignment of the liquid crystal (LC) molecules in the final device, the polyimide surface is buffed with a velour cloth. Valuable information about the function and the possible improvement of flat panel displays is provided by understanding the conditions and factors that cause LC alignment. Numerous nexafs studies without spatial resolution have investigated the effect of the buffing (29–34). In addition, nexafs microscopy in a peem was utilized to characterize the inhomogeneity of the surface orientation produced by buffing (106). Stripes several microns in width were observed with contrast based entirely on differences in local orientation of polymer chains, chain segments, or moieties. While it was clearly observed that buffing does not orient the surface homogeneously, polyimide films produced under the same rubbing conditions than the samples observed in the peem resulted in LC films with the liquid crystal oriented uniformly over the entire sample surface. The separation distance between the oriented stripes of polymers was less than the correlation length of the liquid crystal and the heterogeneous distribution of the pinning centers is sufficient to align the liquid crystal.

Local stress during buffing is an important parameter that might cause the polymer to orient. However, the local stress cannot be estimated well for

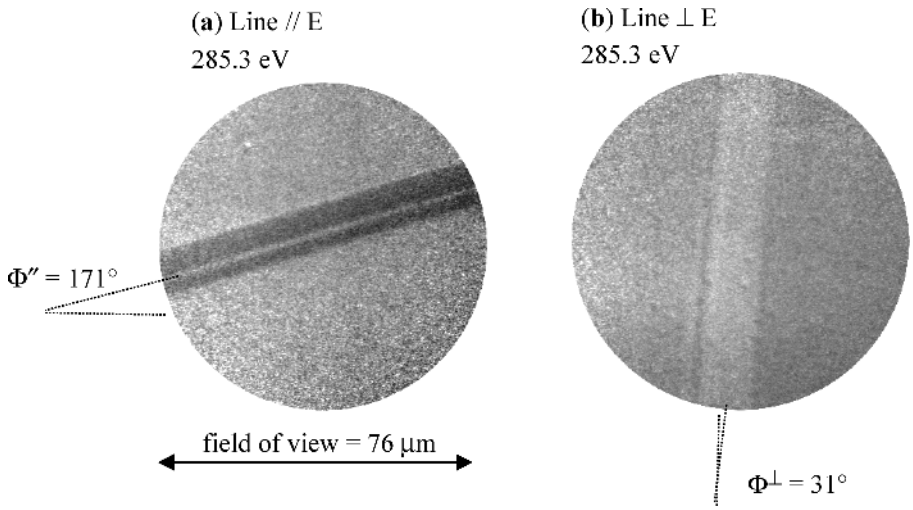

Fig. 10. PEEM images of a stylus track on a polyimide surface at a photon energy of 285.3 eV and two different orientations as indicated. Contrast is based on differences in functional group alignment between the stylus track and the virgin surface. The uniform gray outside the track corresponds to isotropic chains (106). (Data acquired with ALS PEEM-I.) Courtesy of A. Cossey-Favre.

buffing with a cloth. Hence, BPDA-PDA polyimide surfaces rubbed with a stylus of well-defined shape and with a known load were also investigated with nexafs microscopy. Stylizing with a radial tip is an ideal model case that produces an ellipsoidal stress profile on the polymer surface. The nexafs micrographs of a track from the stylus are shown in Figure 10, acquired at two different sample orientations relative to the polarization orientation of 285.3 eV x-rays. Spectra from inside the track from the two different sample orientations relative to the polarization orientation of the x-rays are displayed in Figure 11 and clearly demonstrate the dichroic nature of the contrast in Figure 10. By measuring the width of the track that resulted in alignment and comparing it to the expected stress profile, the minimum stress necessary to cause alignment of the BPDA-PDA film was determined to be 45 MPa. This stress is much lower than the bulk yield stress of 200–300 MPa. The low surface value was attributed to a reduction of polymer entanglement at the surface.

Confined Free-Standing Homopolymer Thin Films. Free standing thin polymer films (eg of PS) can form holes when annealed, driven by dispersion forces that amplify structural instabilities at the film surface. Mechanical confinement offers the possibility to control these instabilities, and raises the possibility to generate unique self-assembled structures. While thin (~50 nm) PS films confined between continuous layers of silicon oxide (SiO_x) are prevented from hole formation, aggressive annealing at temperatures well above the PS glass-transition temperature generates an in-plane microstructure (107). The formation of the microstructure is driven by the attractive dispersion force between the SiO_x–air surface. To properly model the mechanisms for this spontaneously generated lateral morphology, it is important to measure the thickness of

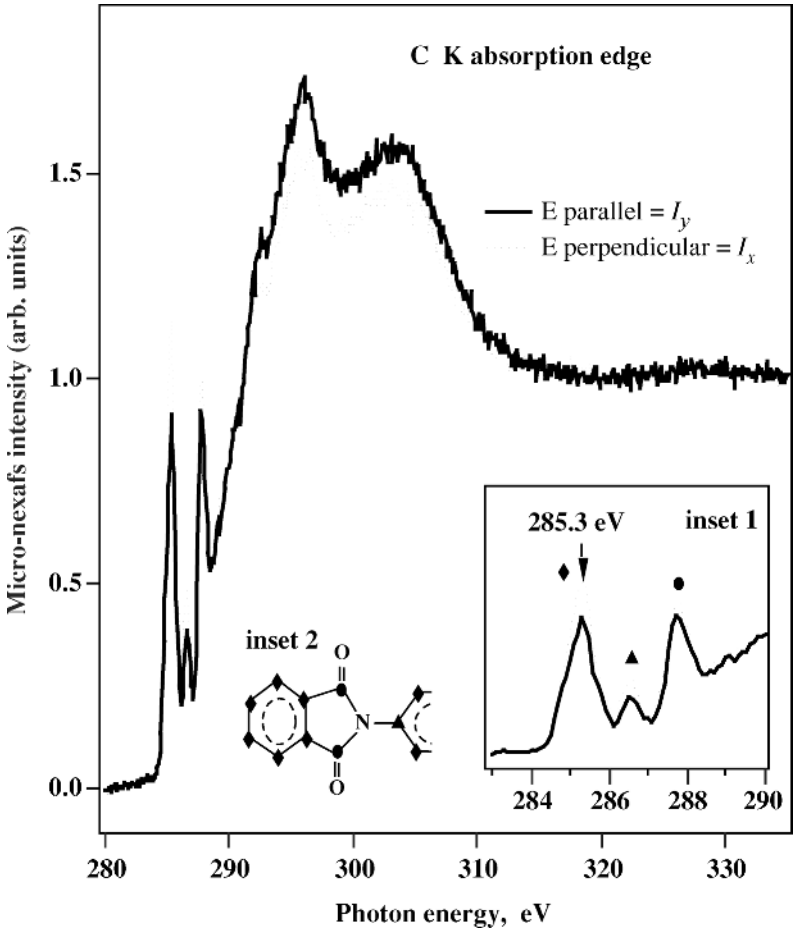

Fig. 11. Linear dichroic nexafs spectra from within the stylus track in Figure 10 at two orientations. Spectral differences are due to differences in orientation and alignment of the polymer functional groups (106). Primary peak assignment is indicated by the symbols. (Data acquired with ALS PEEM-I.) Courtesy of A. Cossey-Favre.

the trapped polymer film throughout the structure. This requires a quantitative tool that can measure the thickness of the polymer inside the trilayer system. While it might be a reasonable assumption that there is almost a complete exclusion of the PS in the thin regions of the pattern, nexafs microscopy indicated ~30% residual PS in the thinnest parts of the sample (see Fig. 12) (108). This fact can now be incorporated into models of the structure formation.

Superabsorbent Polymers: Lightly Cross-Linked Homopolymers. Third generation superabsorbent polymers (SAP) are a class of highly engineered cross-linked polymers widely used as gels in a variety of fields. SAPs are designed to simultaneously provide high fluid absorption capability, retain the fluid in a weight bearing mode with high gel strength, provide attrition resistance during manufacture, be compatible with other manufacturing materials, and remain safe for hygienic uses (109–111). SAPs are made from partially neutralized

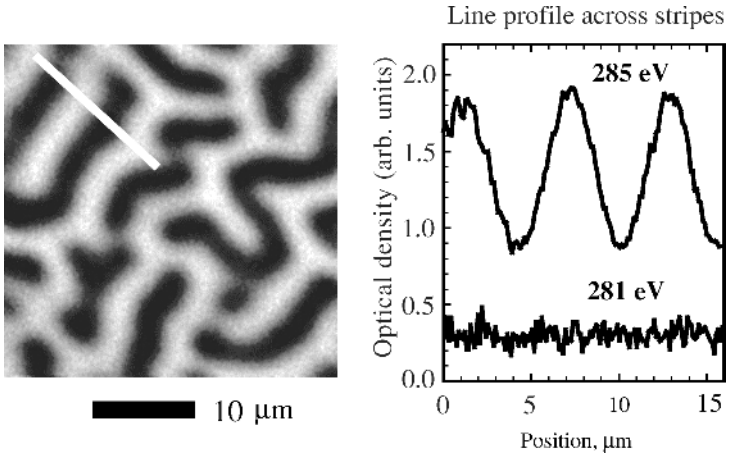

Fig. 12. Image acquired at 285.2 eV of a trilayer structure consisting of a 60-nm thick film of polystyrene (PS) coated on each side with 30 nm of SiO_x. Annealing above the glass-transition temperature of PS results in the observed morphology. Profiles that emphasize PS (top profile labeled 285 eV) and spectra show that significant amounts of PS remain in the thin regions. Note that the preabsorption edge profile at 281 eV is essentially flat. (Data acquired with the ALS BL7.0 STXM.) Courtesy of A. P. Hitchcock, McMaster University, and J. Dutcher, Guelph University.

polyacrylic acid which is lightly cross-linked throughout small (<0.5 mm) beads to form an insoluble, hydrophilic gel. Several different methods have been developed for surface cross-linking SAP gels as means to improve materials properties (112,113). Until now, however, the outcome of these different surface cross-link processes, and the resulting core/shell structure and cross-link density gradient could not be directly visualized and quantitatively assessed.

Crosslinking involves the change in only a very small number of bonds and cannot be monitored directly via spectroscopic differences. A more indirect method, that nonetheless can provide quantitative cross-link density, has to be used. The swelling of SAP beads (polyacrylic acid, sodium salt) and particularly of the more highly cross-linked surface shell depends on the cross-link density of the polymer. Regions or beads with a high cross-link density will expand less in water and therefore will have a higher carbon density when examined in the swollen state. A wet cell was developed and used to characterize cross-link density in thin sections from SAP beads (102,114). NEXAFS resonances were used to provide the highest image contrast possible: The π^* spectral feature of the carboxylic acid increased the signal by a factor of 2 with respect to the core edge jump. Core/shell structures in SAP beads prepared by chemically cross-linking the surface of SAP beads were directly visualized, and variations in surface cross-link density resulting from different cross-link protocols were observed and compared on a common, quantitative cross-link density basis. Figures 13 and 14 compare the results of two different processes that resulted in a gradient and abrupt surface cross-link density profile, respectively. The direct observation of these cross-link density profiles can now be used to optimize the manufacturing and development process of these polymers.

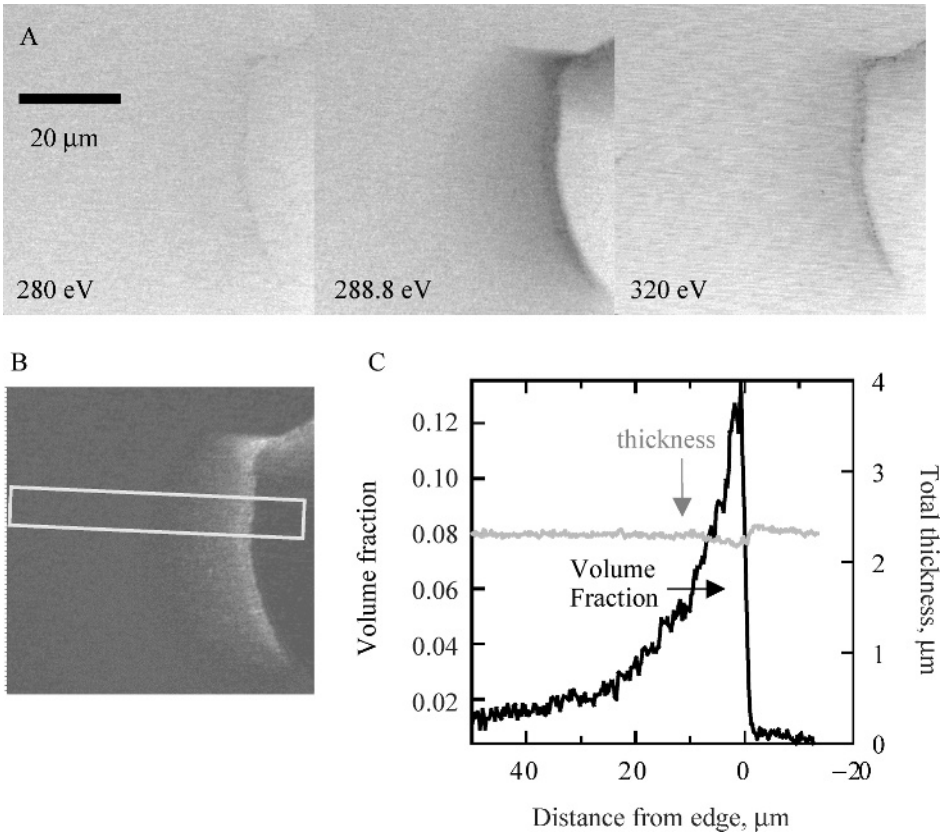

Fig. 13. (**A**) Transmission nexafs images of a saline-swollen microtomed thin section of an SAP bead that was surface cross-linked with ethylene glycol diglycidyl ether. The images were recorded at 280, 288.8, and 320 eV, as indicated; (**B**) Quantitative map of the polymer volume fraction derived via SVD from the three images; (**C**) Profiles of the polymer volume fraction and the total sample thickness (water and polymer) across the edge of the SAP bead, derived from the SVD analysis in the indicated region. (Data acquired with the ALS BL7.0 STXM.) Courtesy of G. Mitchell (102).

Thin-Film Blends and Bilayers. Generally, the properties of polymer blends when they are processed into thin films are not as well understood as those of bulk polymer blends. The constraints imposed by the two close-by interfaces alter the equilibrium morphology as well as the polymer mobility and phase separation dynamics. Numerous studies (115–124) have elucidated some aspects of these effects. Interfacial energies are important since they determine thermodynamic equilibrium structures. The viscosity and diffusion near surfaces and attractive interfaces can be substantially modified (125), which will influence the dynamics, and possibly cause the formation of kinetically trapped morphologies. A number of morphologies that evolve during the phase separation process in polymer thin films have been previously observed (117–123,126). NEXAFS microscopy provides an additional tool to study such systems (100,127–129). The two primary beneficial aspects of nexafs microscopy for these applications

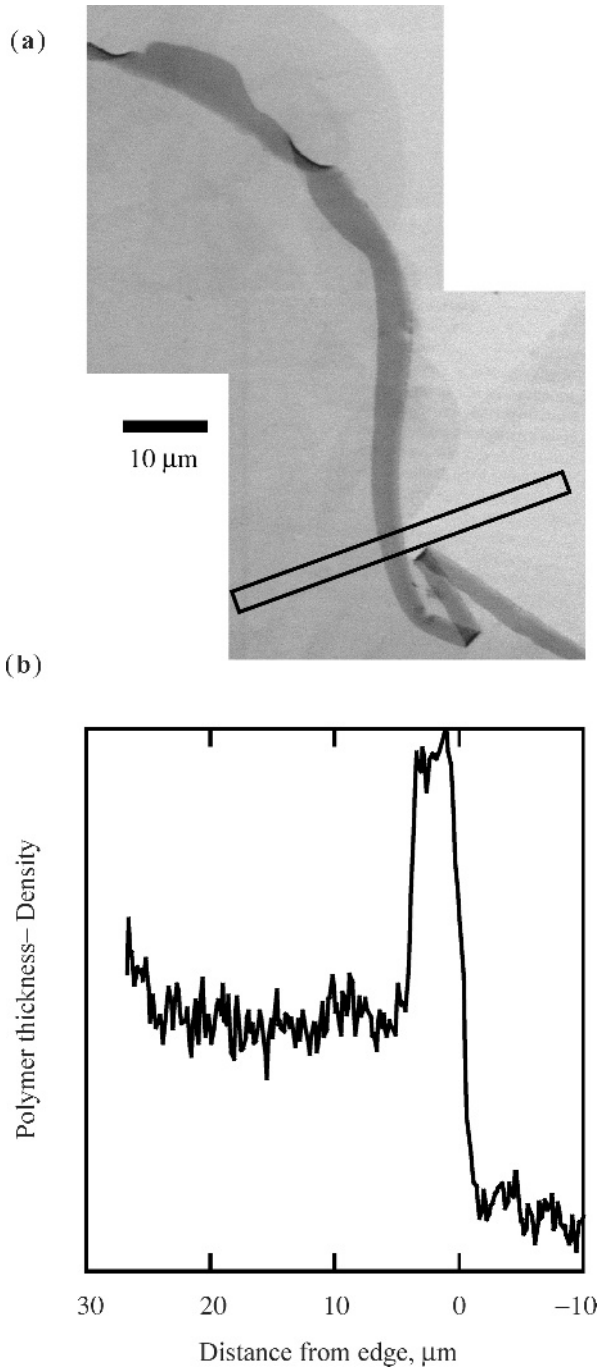

Fig. 14. (**a**) Transmission nexafs image acquired at 288.8 eV of the microstructured shell of an SAP bead surface cross-linked with glycerol. A 5-μm wide band of uniform cross-link density that is twisting back and forth can be observed; (**b**) Profile of polymer density–thickness across the edge of the cross-linked shell in the region indicated on the image. (Data acquired with the ALS BL7.0 STXM.) Courtesy of G. Mitchell (102).

are (*1*) quantitative mapping that can be translated into thickness profiles, and (*2*) compositional analysis of surfaces.

The first nexafs microscopy characterization of phase-separated thin-film blends was performed by two groups (127,130,131). The first group observed good chemical contrast between PS and PBrS phases in phase-separating PS/PBrS blends, and made a strong suggestion that the PS encapsulates the PBrS after sufficient annealing (130,131). The second group used a peem to observe chemical surface contrast in annealed, phase-separated PS/PVME (PVME – poly(vinyl methyl ether)) and PS/SAN thin-film blends (127). Additional peem observations concluded that the formation of protrusions in the PS/PVME film are not accompanied by a total dewetting of the polymers from the Si substrate.

PS/PBrS Thin-Film Blends and Bilayers. Initial nexafs microscopy investigations explicitly exploring the time evolution and composition of domains in thin films focused on morphology formation during spin-casting and annealing of PS and PBrS blends. Emphasis was placed on elucidating the late stage morphology after annealing above the glass-transition temperature of both components for samples with different PS/PBrS composition ratios (128). Quantitative nexafs maps derived via SVD composition procedures were compared to atomic force afm topographs and complemented with secondary ion mass spectroscopy (sims) depth profiling. NEXAFS microscopy of annealed samples showed directly that the morphology changes from "PS droplets" to "PS surface holes" in a continuous PBrS matrix layer as PBrS becomes the majority phase. SIMS data indicated a continuous PS layer at the substrate and the surface interface. The observed continuous PS layer for all blend compositions explained the observed "droplet" and "hole" structures formed for different PBrS fractions. Although the interfacial energy could have been minimized in the bulk if the PS formed spheroidal domains in the PBrS-rich phases, the continuity constraint of the PS at the interfaces requires the formation of the hole morphologies at high PBrS volume fraction. From the morphologies formed, constraints for the values of the various interfacial energies could be deduced.

PEEM from surfaces can provide a much more direct and unambiguous means of showing PS encapsulation of PBrS than the combination of area averaged sims, surface afm (atomic force microscopy), and bulk stxm measurements. Direct evidence for encapsulation was observed during the dewetting of a PS/PBrS bilayer consisting of a 50-nm thick PBrS film on top of a 30-nm thick PS film (98). These investigations were the first combination of surface (peem) and quantitative bulk (stxm) characterization of a polymeric system to assess and reconstruct the 3-D morphology. As the PBrS is dewetting the PS sublayer, holes form randomly in the PBrS top layer and subsequently grow to form Veronoi tesselation patterns. These patterns consist of an interconnected network of spines that eventually break up to form droplets. The mass thickness maps of the constituent polymers PBrS and PS, as well as the total thickness maps of the bilayer annealed for 1 week, reveal that these "spines" consist of sharply delineated PBrS, which are at least partially wetted, if not encapsulated, by PS walls. PEEM studies of the same type of sample provided surface nexafs spectra from the top 10 nm of the surface from sample areas that included the spines and droplets. Since the PBrS C 1*s* to π^* characteristic spectral feature at 286 eV was not observed from any sample areas (see Fig. 15), one can conclude

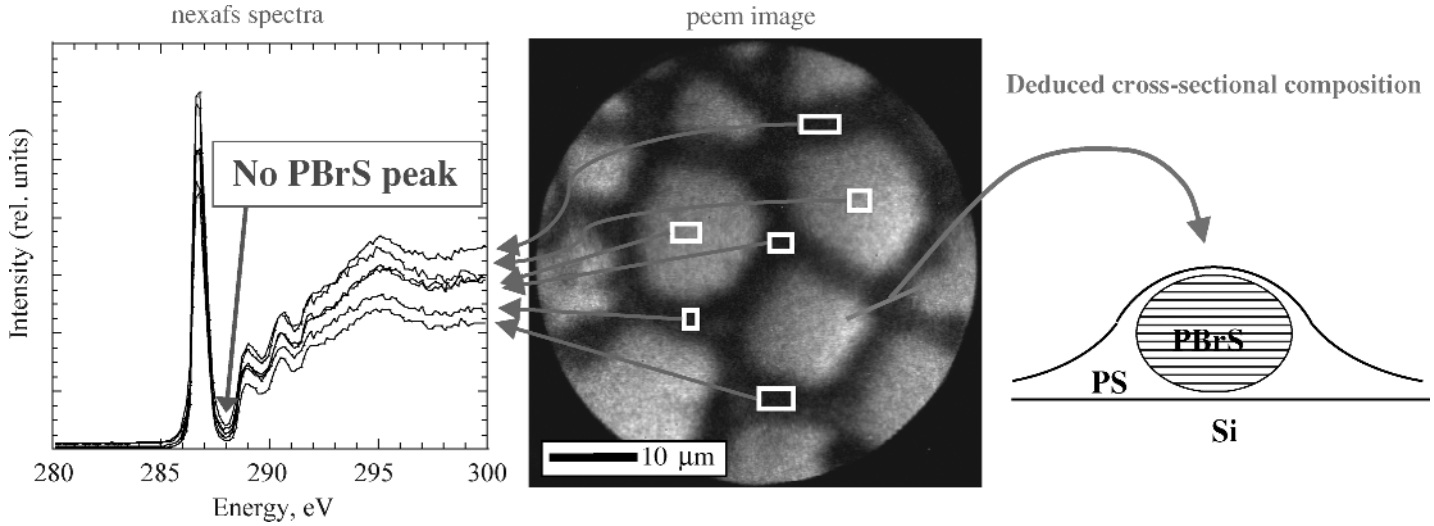

Fig. 15. PEEM images and spectra from a dewetting PBrS/PS bilayer after one week of annealing at 180°C. Spectra from the sample locations are indicated. The combination of stxm and peem characterization allowed the deduction of the 3-D morphology with certainty. (Data acquired with the ALS PEEM-I.) Adapted from Ref. 98.

that the PBrS spines are completely encapsulated. The time taken for evolution (from 0 to 11 days of annealing) of the dewetting process furthermore revealed the encapsulation pathway and also allowed one to know whether polymer diffusion or viscous flow was the dominant encapsulation process: A sufficient number of holes have to form in the PBrS layer through which the PS can penetrate the PBrS film and subsequently flow along the PBrS/air and PBrS/PS interfaces.

Related studies showed that the apparent contact angle at the polymer/air interface decreases exponentially with the PS film thickness, with a constant that depend upon the radius of gyration R_g. The droplets consist of a PBrS core fully encapsulated by PS for substrates thicker than R_g while only partial encapsulation is seen with nexafs for substrates with a thickness less than R_g (132).

PS/PMMA Thin-Film Blends. Another excellent model system to investigate the dynamics and the morphologies formed during phase separation in thin films are PS/PMMA blends. A variety of interesting morphologies during both the early and late stages of the phase separation process in PS/PMMA blends have been observed and characterized by a combination of quantitative nexafs mapping and lateral force microscopy (100). Films (143 nm thick) of monodisperse, 50/50 (w/w) PS/PMMA blends spun cast out of toluene solution onto Si substrates were annealed in a vacuum, quenched to room temperature, and subsequently characterized. The composition of the mixed phases resulting from solvent spin casting were determined with quantitative nexafs microscopy. After very short annealing times at 180°, a sudden rearrangement into domains smaller than those originally formed was observed. Subsequently, unique, jagged patterns formed during the early stages of coarsening. These patterns resemble turbulent hydrodynamic mass flow, although they might have an entirely different physical origin. A 50-nm thick 50/50 (w/w) blend of PS/PMMA 27K/27K film on Si annealed at 165°C, and a 50-nm thick 50/50 (w/w) blend of 90k PS and 27K PMMA on Au showed the same kind of ragged morphology, while a 50-nm layer of the 90K/27K blends on Si did not (129). Complicated polymer/polymer interface morphologies persisted in several cases even after extended annealing. These were explained by the dependence of polymer viscosity on film thickness and the constraints imposed by the substrate (100). An example is shown in Figure 16 that shows trapped PMMA spikes inside the PS droplets.

As shown by numerous studies, the initial morphologies from spin casting as well as the final morphologies after annealing depend on the substrate utilized. The dependence of PS/PMMA morphologies and phase separation dynamics on Si, Au, and Co surfaces has been investigated (129). Clearly phase-separated domains are observed on Si and Au surfaces. The morphologies on Co surfaces, however, are more complex. They have a layered appearance and do not evolve much during annealing, presumably because of a lack of either a PS or PMMA wetting layer on the substrate.

PS/PMMA blends spun to different film thickness onto SiO_x surfaces showed that time-temperature superposition is observed. Indirectly, this indicates that the influence of the film thickness on the dynamics is relatively small (133).

While most work on annealed PS/PMMA blends support the formation of phase-separated domains right to the surface, a recent study (134) reports that an encapsulating layer of PS-skin forms over the PMMA domains. The stxm and peem might be a good complementary tool to afm, xps, and nexafs spectroscopy to

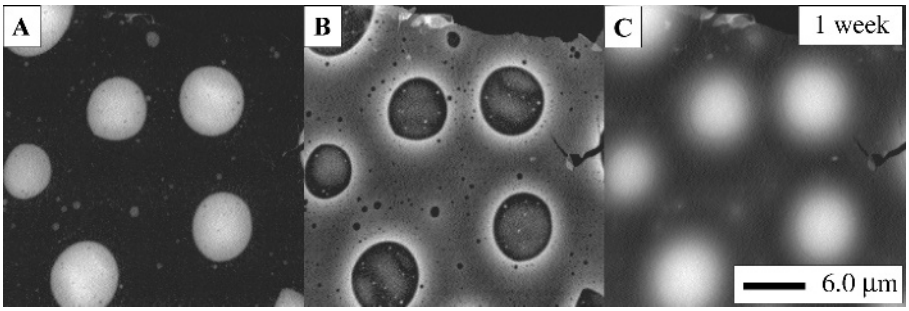

Fig. 16. Quantitative compositional maps derived via an SVD procedure of a nominally 143-nm thick 50/50 (w/w) PS/PMMA blend annealed for 1 week: (**A**) PS mass thickness, (**B**) PMMA mass thickness, and (**C**) total thickness maps, ie, PS plus PMMA maps. All images are individually scaled for good contrast, with Black = 0 and White = maximum mass-thickness. The maximum total thickness of the films increases from the initial 143 nm to 460 nm in Figure 16C due to surface roughening. (Data acquired with the Stony Brook STXM at the National Synchrotron Light Source.) Adapted from Ref. 100.

further elucidate PS/PMMA thin-film blends, their phase separation dynamics, and their surface composition (96).

PS/PMMA with PS-*b*-PMMA Copolymer Thin-Film-Blends and Bilayers. Polymer blends when processed into thin films are typically rough when produced by spin casting on a substrate and roughen even further when annealed. The surface modulation amplitudes of certain spatial frequencies might actually get much larger than the original film thickness. This is due to the phase separation between immiscible polymers, and the effect can be readily observed from Figure 16. This roughening would be a serious problem in many applications and limits the use of polymer blends as materials in ultrathin films. A common strategy to improve miscibility of polymer blends is to add copolymer compatibilizers. The compatibilizer will reduce the interfacial tension if located at the polymer/polymer interface. The tendency of the compatibilizer to form micelles in one of the phases often limits the amount of copolymer that locates at the interface. For relatively strongly segregating systems, formation of a microemulsion has never been achieved. Relying on entropy as a driving mechanism, rather than interfacial energies, it was shown that PS/PMMA thin films can be compatibilized with a PS-*b*-PMMA diblock copolymer (135). Samples of a bottom PMMA layer and a top layer of a blend of PS and 30% of a PS-*b*-PMMA diblock copolymer were annealed. When the top PS/PS-*b*-PMMA layer thickness was comparable to or less than the size of bulk micelles, the film evolves toward a stable 2-D microemulsion. The two-dimensionality of the film was established by showing with nexafs microscopy that the microemulsion phases extended throughout the thin film. It was observed (135) that the loss in configurational entropy as a result of confinement can change the micellar transition for copolymers. Mixing in thin films in the presence of block copolymers can thus be achieved independently of the specific polymer chemistry by making the films thin enough.

The dynamics of the formation of the microemulsion has been assessed (136). The initial growth of the domain size had a growth exponent of 1/3, using the inverse of the wave-vector with maximum amplitude $q_{\max}$ derived from

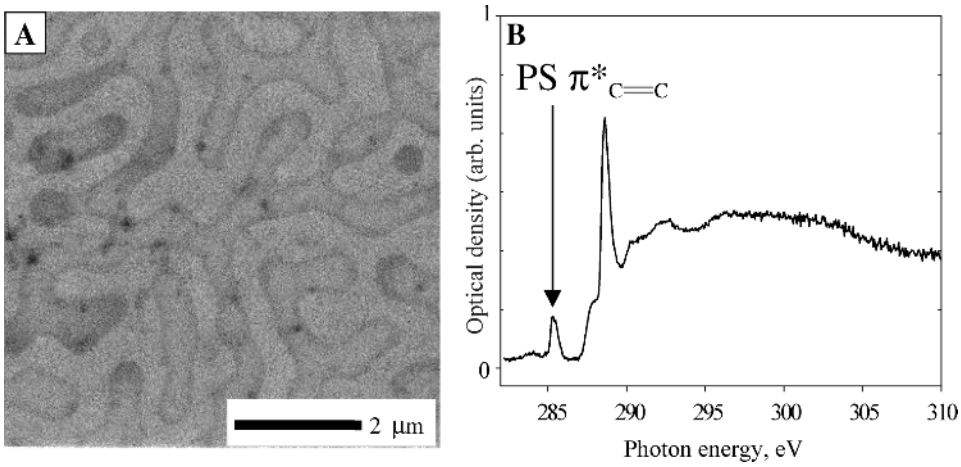

Fig. 17. (**A**) PS $\pi^*_{C=C}$ image acquired at 285.3 eV from a 168-h annealed PS/PMMA/PS-*b*-PMMA microemulsion thin film washed with cyclohexane to remove all PS. At this photon energy, only the aromatic content of styrene will appear dark. Enhanced absorption, although at low contrast, can be detected at the domain interfaces that directly shows that the highest PS-*b*-PMMA block copolymer concentration is located at the PS/PMMA domain interface; (**B**) The nexafs spectrum acquired from 10 μm^2 area of this sample. The PS and PMMA intensities reveal that cyclohexane washing is removing essentially all PS. The remnant 285 eV signal is consistent with expected signal from the PS-*b*-PMMA block copolymer. (Data acquired with the Stony Brook STXM.)

Fourier transform analysis as the measure of the domain size. At long annealing times, domain growth slowed dramatically as the block copolymer was forced to the interface, lowering the interfacial energy and thus reducing the driving force for further phase separation. NEXAFS microscopy of the microemulsion thin films that had the PS preferentially washed with cyclohexane revealed directly that the PS-*b*-PMMA diblock copolymer is located at the PS/PMMA interface (see Fig. 17).

Polystyrene/Poly(*n*-butyl methacrylate) Thin-Film Blends. The morphology of polystyrene/poly(*n*-butyl methacrylate) (PS/PnBMA) thin-film blends, and whether encapsulation occurs in this system has been assessed by using SFM, txm, and peem (137). The same droplet-to-hole transition found in the earlier studies by Slep and co-workers (128) with PS/PBrS blends as a function of composition was observed in the PS/PnBMA blends. This strongly suggests that one of the two polymers preferentially segregates to both the substrate and air interface. Investigations of the PS/PnBMA thin films with peem were indeed interpreted to have preferential PnBMA segregation to the surface. Based on the surface composition and morphology observation, one would expect PnBMA to also segregate to the substrate, although no direct measurement regarding preferential segregation to the substrate has been made (137).

Block Copolymer Thin Films. NEXAFS microscopy is also a tool that can provide complementary and unique information for block copolymer organization, which traditionally has been investigated using a wide variety of analytical techniques, including electron microscopy, x-ray scattering, and optical

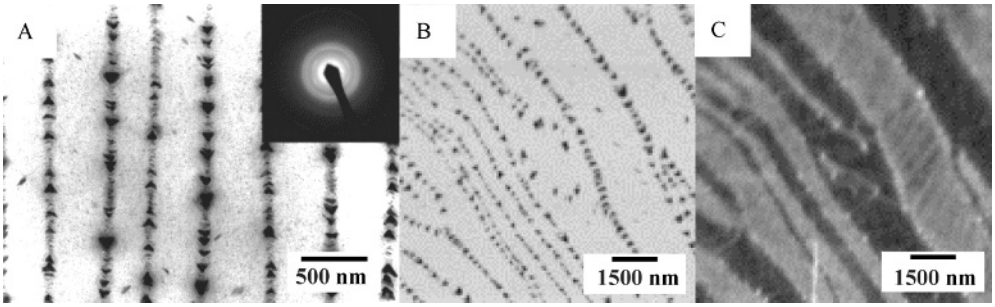

Fig. 18. (**A**) tem image of PS-*b*-PHIC diblock copolymer and small area electron diffraction pattern averaged over several lamellae; (**B**) nexafs image at 285.2 eV (PS dark); and (**C**) nexafs image at 288.5 eV, where the PHIC layers have altering contrast because of differences in orientation. (Data acquired with the Stony Brook STXM.) Courtesy of C. Zimba, NIST, and E. Thomas, MIT.

microscopy. These traditional techniques yield considerable information about the morphology and organization of block copolymer materials, but occasionally the information provided is incomplete and provides only "circumstantial" evidence for a conclusion. For example, the novel molecular organization of a high molecular weight rod-coil block copolymer has been investigated (138). This block copolymer has a PS coil block of 9K molecular weight and a main-chain poly(hexyl isocyanate) (PHIC) rod block of 245K molecular weight. Homopolymer PHIC is known to behave as a lyotropic nematic liquid crystal in a wide range of solvents with a persistence length of 50–60 nm. Rotational motion along the backbone of the PHIC is limited by short-range interactions, leading to inherent chain stiffness. The PS behaves as a typical coil polymer with a low persistence length. Combined as a block copolymer, there is competition between the microphase separation of the PS and PHIC blocks into periodic structures and the tendency of the PHIC block to form anisotropically ordered structures, giving rise to new morphologies. A typical tem image from solution cast thin films is shown in Figure 18A and clearly shows a microphase-separated morphology with long-range order over tens of microns. The PS domains, stained with RuO_4, appear as dark regions shaped somewhat like arrowheads while the PHIC regions appear as largely featureless light regions between rows of PS domains. An interesting feature in this image is the orientation of the PS arrowheads which changes direction between adjacent PS-rich layers. On account of radiation damage, the small area electron diffraction (SAED) pattern had to be obtained from a sample area of 10–20 lamellae. The SAED pattern (inset of Fig. 18A) shows a superposition of two distinct single crystal-like PHIC patterns rotated relative to each other by approximately 90°, indicating that the PHIC chain axis alternates between +45° and −45° with respect to the geometric normal of the lamellae layers. While the evidence for the alternating 45° PHIC oriented layers is quite strong, it is only indirect, and the orientation could not be observed directly with tem.

To directly investigate the orientation of the PHIC lamella, thin film samples cast from 0.05% solutions in toluene onto uncoated tem grids were examined with nexafs microscopy (139). Using an x-ray energy corresponding to the phenyl

carbon resonance of the PS (285.2 eV), nexafs imaging clearly shows a similar arrowhead morphology as the tem image, albeit at lower spatial resolution (see Fig. 18B). At the carbonyl resonance of the PHIC at 288.5 eV, nexafs images reveal the structure of the PHIC layers in ways not available with tem (Fig. 18C). The PHIC domains appear as layers of alternating intensity separated by the PS domains that appear as white pearls. The intensity variation of the PHIC layers arises from differences in dichroic absorbance of the polarized synchrotron radiation because of orientation of the carbonyl moiety, and thus also the backbone, of the PHIC. In contrast to the average SAED pattern, the nexafs image is able to give detailed information about the orientation of individual PHIC domains. NEXAFS microscopy furthermore reveals previously unsuspected microstructure within the PHIC domains that are clearly not entirely homogeneous, but show striations in a direction across the lamellae.

Multicomponent, Multiphasic Polymers

Many polymeric materials of academic and industrial interest are multicomponent polymers that have multiple phases in the bulk. Control over the composition and size distribution of the domains and their interface properties is often very important in determining the materials properties. A variety of blends and multiphasic polymers have already been investigated with nexafs microscopy. These include studies of

(1) the morphology of PET/PC (140), low density PE/PET/Kraton (141), and PC/(acrylonitrile butadiene styrene) blends (141,142), and macrophase-separated random block copolymer/homopolymer blends (143);
(2) the morphology and composition of mechanically alloyed PET/poly(oxybenzoate-*r*-oxynaphthoate) [Vectra (Celanese Corp.)] blends (144), mechanically alloyed and rubber-toughened PMMA (145), mechanically alloyed poly(ethylene-*alt*-propylene) (PEP)/PMMA and PI/PMMA blends (146–150), and the assessment of recycling of tires by mechanical alloying (151);
(3) the characterization of phase separation during processing, such as the formation of precipitates in polyurethanes (13,19,152) and multiphase liquid crystalline polyesters (141);
(4) single- and multistep synthesized latexes and structured microspheres (153–155); and
(5) various multilayers (156,157).

Included here as examples is a discussion of the characterization of PET/Vectra blends, blends produced by cryogenic mechanical alloying, various polyurethane polymers, multilayers and structured spheres, as well as rubber composites. The discussion of the PET/Vectra blends is particularly instructive, as this study combined chemical and orientational analysis.

NEXAFS Microscopy of Mechanically Alloyed Blends. Mechanical alloying of polymers has the potential of becoming an alternative, novel means of producing and recycling polymer blends (144,146–148,150,151,158). The efficacy

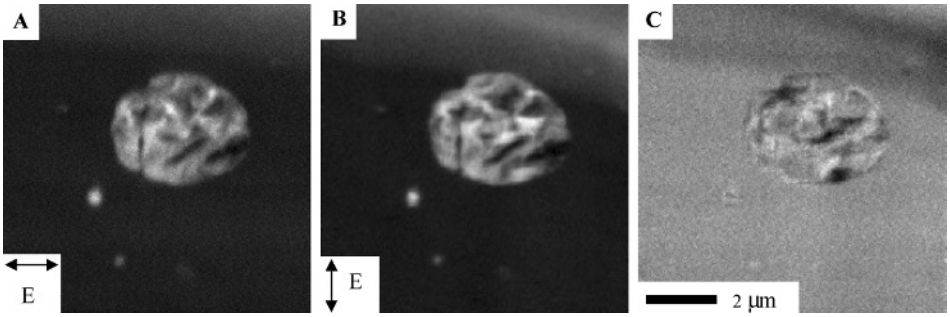

Fig. 19. NEXAFS images acquired at 286.7 eV of a 99/1 (w/w) PET/Vectra blend subjected to post-milling melt pressing. Images (**A**) and (**B**) have been converted to optical density. In images (**A**) and (**B**), the electric polarization vector ($\vec{E}$) is rotated by 90° with respect to each other, as indicated. Changes in the relative intensity in these images are primarily due to anisotropic molecular orientation. The ratio of these images (**C**) reveals the linear dichroism of the specimen. Small Vectra domains appear gray and possess no discernible orientation, whereas the large dispersion exhibits a measurable degree of molecular orientation (black and white areas) because of the nematic nature of this liquid crystalline polymer. (Data acquired with the Stony Brook STXM.) Reproduced from Ref. 144.

of such a new method is best assessed by direct visualization of the morphology of the generated materials.

Since incorporation of liquid crystalline polymers (LCPs) into commodity thermoplastic polymers remains an ongoing challenge in the design of new high performance, low cost polymeric blends, the feasibility of blending of PET and Vectra A950 [73/27 (mol/mol) oxybenzoate/2,6-oxynaphthoate] with mechanical alloying was investigated (144). The morphology and composition of dispersions in PET and Vectra blends are difficult to assess with conventional microscopies, because of a lack of staining agents for electron microscopy, and spatial resolution limitations of optical and ir microscopy. Despite the presence of similar functional groups in each polymer, such as aromatic and carbonyl groups, nexafs microscopy can readily delineate the morphology. After mechanical alloying, the resulting powders were melt-pressed at 285°C (above the melting points of PET and Vectra) for 5 min and cryomicrotomed at −100°C to obtain sufficiently thin sections for nexafs microscopy. Melt-pressed films of PET/Vectra alloyed blends varying in composition from 75/25 to 99/1 by weight percent were investigated. The frequency and size of the Vectra dispersions increased with increasing Vectra concentration (144). The distribution in size ranged from 100 nm to about 20 μm in diameter. The presence of these small, 100-nm Vectra domains demonstrated that mechanical alloying is capable of pulverizing Vectra. The PET/Vectra blends retained much of the initial degree of mixing during post-processing in the molten state. Point nexafs spectroscopy showed that the Vectra domains contained little, if any PET. Molecular orientation in the Vectra domains was characterized with linear dichroism microscopy. Figure 19 shows x-ray micrographs of the 99/1 (w/w) PET/Vectra blends acquired at 286.7 eV. The image contrast between Vectra dispersions and the PET matrix is based on differences in the nexafs spectra of the two polymers (see Fig. 2). Some of the contrast within the larger Vectra domains arises from molecular orientation and thickness variations. The dichroic ratio

image (Fig. 19C), derived from the two orientations displayed in Figures 19A and 19B, cancels thickness and compositional effects: anisotropic orientation inside Vectra domains was only observable in domains larger than about 2 μm.

Other blends produced by mechanical alloying and investigated with nexafs microscopy included blends of poly(ethylene-*alt*-propylene) (PEP), polyisoprene (PI), and PMMA (146–150). PI can be readily differentiated from PMMA with electron microscopy by heavy metal staining of the PI, but PEP and PMMA cannot be differentiated. In the blends investigated, intimate mixing at the nanoscale was accomplished. Since mechanical alloying is a highly nonequilibrium, high energy method with effects that resemble those of high energy radiation (159), it seems likely that bonds are breaking, and radicals, and maybe even new bonds in new chemical configuration, are forming during alloying. It is the detection of these chemical modifications where nexafs microscopy might be particularly useful. However, the extent of any chemical changes occurring has been below the sensitivity limit of nexafs microscopy.

In the PEP/PMMA blends an anomalous phase inversion was observed (148). Phase inversion in polymer blends is typically encountered under conditions of melt flow. However, the unexpected phase inversion occurred upon quiescent annealing in an asymmetric blend of PMMA and PEP prepared by cryogenic mechanical alloying, where there is very little flow. For short milling times, consolidation of the cryomilled powders at temperatures above the glass-transition temperature of PMMA exhibited dispersions of PEP in 75/25 (w/w) PMMA/PEP blends. However, as the milling time increased to 10 h, the consistency of the blends changed from rigid to pliable. nexafs microscopy revealed that for the long milling times the PMMA becomes the dispersed phase upon consolidation, and it directly confirmed that phase inversion occurs during consolidation. The transition from PEP dispersions to a continuous PEP phase as observed with nexafs microscopy is shown in Figure 20.

The strategy of producing highly dispersed blends of thermoplastics and tires was also investigated in an effort to provide a potentially new route by which to recycle discarded tires (151). NEXAFS microscopy showed that cryogenic mechanically alloyed tires can be dispersed in PET and PMMA matrices with submicron domains. The tire and thermoplastic did not appear to interact chemically. For the milling conditions employed, there was also no significant chemical interaction between constituent polymers in PI/tire/PMMA ternary blends. Based on the ability to produce good dispersion of the tire material, the results indicated that cryogenic mechanical alloying constitutes a viable alternative for recycling elastomeric materials.

Engineered Polyurethane and Polyurea Polymers. Polyurethane polymers constitute a versatile class of engineered polymers of great economic value. Despite the ubiquitous utilization and considerable past research, several fundamental aspects of these polymers are not well understood because of the complex chemical reactions and physical processes during production. Over the past few years it has become clear that x-ray spectromicroscopy can uniquely address some complex issues in polyurethane research (19,66,160–163).

The urea distribution in polyurethanes is presumed to have a major influence on the mechanical properties of polyurethane foam (modulus, compression set, load bearing, etc), yet relatively little is known beyond the average size and

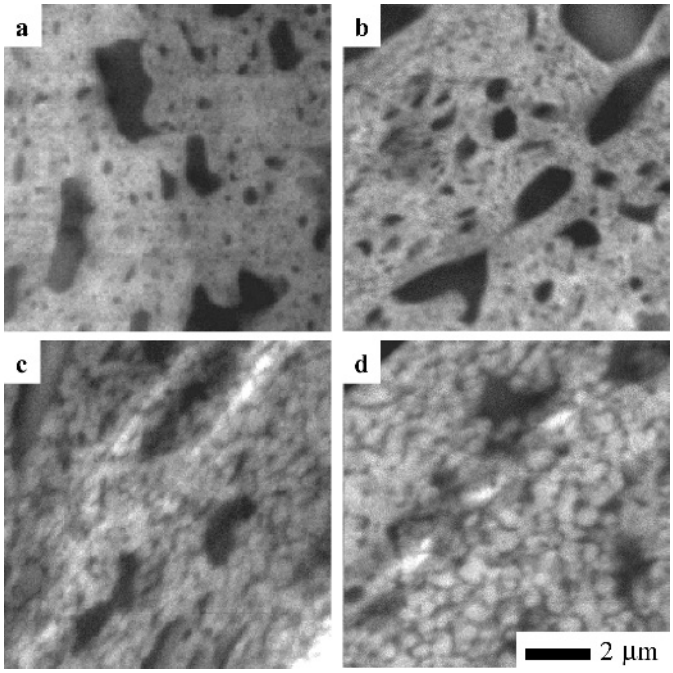

Fig. 20. NEXAFS images at 288 eV (PEP appears dark) of a 25/75 PEP/PMMA blend cryomilled for 10 h and annealed at 150°C for different times (in min): (**a**) 1, (**b**) 2, (**c**) 5, and (**d**) 30. (Data acquired with the Stony Brook STXM.) Adapted from Ref. 148.

nanoscale distribution of the so-called hard-segment urea as measured with x-ray and neutron scattering techniques. The mesoscale hard-segment urea distribution in polyurethane materials might be connected to physical properties and is strongly influenced by the relative amounts of urea and carbamate (urethane) present, which in turn is closely linked to formulation and processing. The urea/urethane ratio and its distribution through the material is thus an important quantity. In certain formulations, macrophase separation occurs. Using polymer reference standards with known chemical composition, the spectral signal corresponding to the urea and urethane components (typically only ~20% in systems of interest) can be isolated and quantified (18,19). Based on similar quantitation, the composition and sharpness of precipitates in two high water TDI polyurethane plaques made with different polyols have been assessed at the submicron level (164). The precipitates in both materials were highly enriched in urea. One of the materials had a fuzzy interface to the polyether-rich matrix, while the second material had a more sharply delineated interface. The fuzzy precipitates were more isolated, while the sharper "precipitates" appear to have formed a network of urea-rich domains. These observations will lead to an improved understanding of structure–property–processing relationships in polyurethane polymers.

Another key parameter influencing physical properties in polyurethane foams is the distribution of additive or modifier phases. These modifier phases are typically smaller than a few microns in size. Two compositionally

different, common modifier particles, polyurethane-rich, polyisocyanate polyaddition (PIPA) based and styrene-acrylonitrile (SAN) based particles, were dispersed in a TDI-based, polyether-rich polyurethane matrix. Both particles have the same contrast in tem and cannot be distinguished. In contrast, nexafs micrographs of this material show clear differences: at 285 eV, both types of particles are dark dispersions, while at 287 eV, only the SAN particles are highly absorbing relative to the matrix. The uniformity of their composition and the size distribution could thus be determined (165). Discrimination between the two types of particles has also been achieved at the nitrogen absorption edge and, to a lesser extent, the oxygen edge. The chemical composition of the largest SAN particles was found to be independent of particle size. It was furthermore determined that the SAN particles contain about 12 wt% polyether.

Structured walls of complex capsules based on polyurea chemistry have been investigated (166). Polymer capsules are frequently used to encapsulate other chemicals for a variety of purposes, including controlled release of drugs, nutrients, or pesticides. In these applications, the structure and composition of the capsule wall is of paramount importance. The capsules investigated were produced by a polymerization reaction between amine- and isocyanate-based chemicals at the interface of organic and aqueous phases. In addition to the amine–isocyanate reaction that produces an asymmetric aromatic urea, a competing reaction between the isocyanate and water produces a symmetric diaromatic urea. These competing reactions can lead to the formation of compositional gradients in the submicrometer thick capsule wall. Figure 21 shows reference spectra of model urea compounds, compositional maps, and line profiles of two capsule walls produced by different protocols. The asymmetry of the urea and diurea functionalities can be clearly observed. Comparison of these compositional profiles with diffusion and reaction kinetics will allow the detailed modeling of the capsule wall formation.

Multilayers and Structured Spheres. Multilayer structures are used extensively in photographic applications, such as optical and x-ray photography and xerographic processes, as well as in packaging materials. Several such materials were so far investigated with nexafs microscopy.

The degree of spatial uniformity of a nitrogen containing charge transfer compound present in a protective polycarbonate (PC) capping layer above the image sensing layer of a test photoconductive thin-film structure from Xerox Research Center of Canada has been determined with nexafs microscopy. A simple, 5-min measurement consisting of an image at 407 eV of the film and a nitrogen 1*s* linescan energy sequence showed that the (~10%) nitrogen content of the PC layer was distributed throughout the PC layer with a relatively uniform (±20%) distribution, but with some gradient in density toward the exterior of the thin film. By comparison, it was barely possible to detect any nitrogen, and thus impossible to analyze the spatial distribution of the charge transfer component, by either energy loss or x-ray fluorescence spectroscopy in a state-of-the-art JEOL 2010 analytical tem (168).

Several multilayer polymer films used in photography have been characterized with nexafs microscopy. In one structure, consisting of four layers of 0.7–3 μm in thickness coated on a base layer, nexafs images clearly showed each of the layers. The nexafs spectra from closely spaced points showed no significant

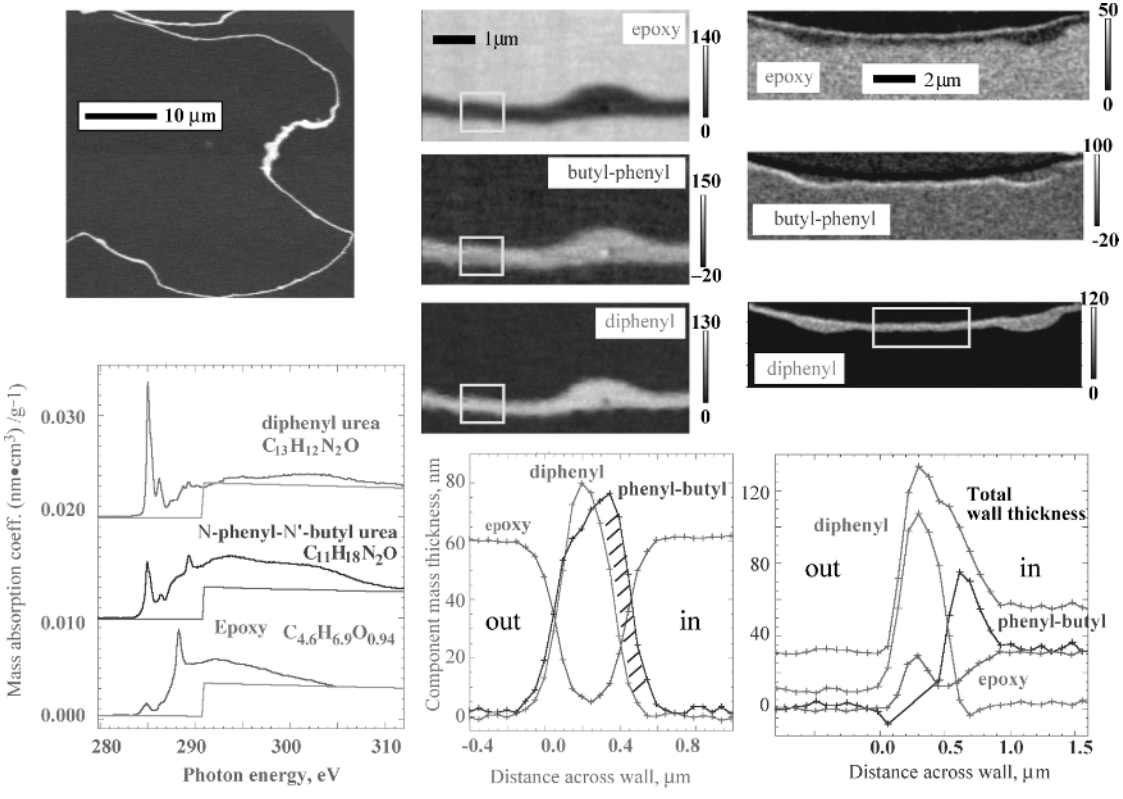

Fig. 21. NEXAFS characterization of polyurea capsules. The upper left shows a low resolution image acquired at 285 eV of a microtomed section containing a nearly complete capsule embedded in epoxy. The lower right shows the C 1*s* spectra of the epoxy, butylphenylurea (asymmetric model) and diphenylurea (symmetric model). The center panel displays (top) component maps derived from image sequences and (bottom) average line profiles of each component across the capsule wall in the indicated region. The right panel shows the corresponding signals for a capsule wall prepared with a longer emulsification step. This process leads to a thick outer skin of symmetric urea. (Data acquired with the ALS BL 7.0 STXM.) Courtesy of A. P. Hitchcock. Adapted from Ref. 166 and 167.

interpenetration between two layers of interest, poly(styrene acrylonitrile) and a porous carbon black (156). The nexafs microscopy of another laminate consisting of nine layers on a base layer revealed a microstructure of undetermined origin dispersed throughout the fourth layer (169,170). The domains of these microstructures are elongated in the direction parallel to the layer boundary. This microstructure is not observed in the tem, and is likely due to a compositional microphase separation or a preferential orientation of the aromatic groups present in some of the compounds.

A commercially available multilayer used as food container provided a suitable test structure for nexafs microscopy, particularly since this multilayer had been previously characterized with ir microscopy. Because of the spatial resolution limitations of ir microscopy, a special procedure had to be used to analyze the thinnest of the nine layers, about 4 μm thick. The objective of an x-ray microscopy study of this multilayer was to further elucidate the chemical composition of the thinnest layers within the sample, and to provide a basic comparison between ir and nexafs microscopy (157). NEXAFS microscopy could acquire spectra from all layers without interference from adjacent layers. It established that several of the thin layers had virtually the same composition, a result not obtained from the ir measurements. Unfortunately, the present lack of a comprehensive and accurate nexafs spectroscopy database of polymers prevented the positive identification of some of the layers.

Structured polymer microspheres are attractive for a wide number of applications, including biomedical devices and controlled release reservoirs. Particular morphologies desired for different applications require control over internal porosity and core–shell structures. In order to optimize the internal or core–shell morphologies of such composite materials for particular applications, quantitative compositional analysis is often required. Structured latex spheres have first been analyzed using nexafs microscopy (153). More recently, core–shell microspheres have been investigated (155). In the latter experiment, a two-step precipitation polymerization resulted in 3.2 μm polydivinylbenzene-55 (DVB55) cores coated with $\sim$0.4–0.9 μm wide shells composed of poly(DVB55-*co*-EDMA), a copolymer of DVB55 and ethylene glycol dimethylacrylate (EDMA). Singular value decomposition of images recorded at selected photon energies yielded quantitative maps of the DVB55 and EDMA components. The EDMA concentration in the shell as determined by nexafs microscopy was in good agreement with that predicted from the comonomer composition. It was shown that the precision of compositional quantitation is adequate to be useful in guiding the development of structured polymeric systems for particular applications.

Elastomeric Composites. Blends and composites based on styrene–butadiene rubber (SBR) and butadiene rubber (BR) are widely used throughout the rubber industry in order to get a balance of properties that cannot be achieved through the use of a single elastomer. Typically blends are formed using immiscible elastomers. The vast majority of these blends are heterogeneous on some length scale (171,172), and their mechanical properties are determined, in part, by their phase morphology. Many blends are further complicated by the addition of both fillers and curatives. In addition to determining the polymer phase structure itself, it is desirable to determine the distribution of fillers and curatives in each of the elastomer phases.

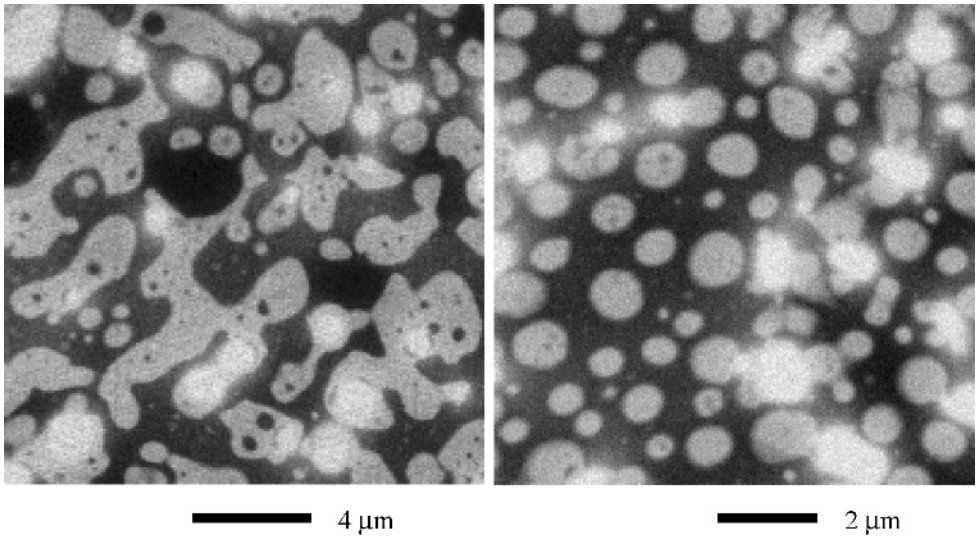

Fig. 22. NEXAFS micrographs of (**A**) d-PB/BIMS-1 [50/50 (w/w)] and (**B**) d-PB/BIMS-1/hSBR [45/45/10 (w/w)] blend supported by a Si_3N_4 membrane. The film was annealed in a vacuum oven for 18 h at 150°C. The dark areas correspond to the dPB phase. (Data acquired with the Stony Brook STXM.) Adapted from Ref. 174.

Most present automobile and truck tires are made from SBR and BR mixtures. These application requirements are severe and tires are constantly being improved. For example, poly(isobutylene-*co*-4-bromomethylstyrene) can be blended with highly unsaturated general-purpose rubbers to impart unique barrier or dynamic properties and enhanced oxidative stability. The final properties of such a blend are the result of a complex series of compounding, mixing, and curing stages. These stages profoundly impact the homogeneity of the mixed components, which include the polymers, the filler, and the curatives. The characterization of the phase morphology of blends of commercial rubbers like polybutadiene (PB), polyisoprene (PI), poly(butadiene-*co*-styrene), and brominated poly(isobutylene-*co*-4-methylstyrene) (BIMS) continues to represent a problem for conventional techniques, especially in the case of filled rubbers. The utility of nexafs microscopy for these applications have thus been explored and it was found that the phase morphology of various blends and the distribution of silica and carbon black fillers can be determined based on spectroscopic differences (173). However, the size of most filler particles is still below the present spatial resolution of nexafs microscopy. These kinds of applications will greatly benefit from future technical advances and improvements in spatial resolution.

Similar elastomer blends were also studied (174). The interfacial properties of PB and BIMS blends were determined with a variety of tools including neutron scattering and microscopy. The interfacial width decreased with increasing bromine functionality. The effects of a styrene butadiene random copolymer (SBR) on the miscibility were also investigated. The results show that SBR enhances the compatibilization of the PD/BIMS blends. NEXAFS micrographs of annealed PB/BIMS and PB/BIMS/SBR blends are shown in Figure 22.

The smaller BIMS domains in the PB/BIMS/SBR blends indicate that SBR indeed compatibilizes PB/BIMS blends, which is consistent with the observations and conclusions drawn from neutron reflectivity and afm measurements. The effects of carbon black and silica on the interfacial properties of PB/BIMS blends have been investigated with neutron reflectivity, ultra-small angle neutron scattering, spm, and nexafs microscopy (175).

Fibers

NEXAFS microscopy is also well suited to study the composition and structure of fibers. The qualitative orientation of functional groups in poly(*p*-phenylene terephthalamide) [Kevlar (DuPont)] fibers has been investigated and it was found that aromatic groups are, on average, pointing radially outwards (176). Subsequently, the relative quantitative orientational order was characterized in three different grades of Kevlar fibers and it was found that Kevlar 149 is 2.3 and 1.6 times as radially orientated as Kevlar 29 and Kevlar 49, respectively (177). This variation in orientation is relatively large, given that the crystallinity of all fiber grades is above 85%. More recent work on these fibers combined absorption spectroscopy at the carbon, nitrogen, and oxygen edges. This combination, in conjunction with theoretical calculations, can estimate the absolute degree of radial orientation in these fibers. Preliminary analysis indicated that Kevlar 149 is about 50% radially orientated (178,179).

NEXAFS microscopy has been used to study the effect of heat treatment on polyacrylonitrile fibers (180). In heat-treated fibers, a clear core-rim structure was observed in images at several photon energies. A decrease in the nitrile group concentration was measured in the core of these fibers when compared to the untreated fibers.

Conclusion and Future Outlook

NEXAFS microscopy has moved well beyond proof-of-principle experiments and has evolved into a tool that has been used in a variety of polymer science and technology projects. It is particularly noteworthy to remark that numerous industrial partners have participated over the last few years in nexafs microscopy experiments. Some of these industrial experiments performed, some with high industry internal impact, will remain unpublished, because of proprietary concerns.

While nexafs microscopy capabilities are continually improving, the field has not yet reached any fundamental performance limits. For example, the far-field wavelength-limited spatial resolution for zone-plate-based microscopes is about 3 nm for carbon K-edge energies, about an order of magnitude better than the resolution presently achieved. Similarly, several aberration corrected peem's with a projected spatial resolution of about 2 nm are planned or under construction (80,81), while the best peem's to date have a spatial resolution of 20 nm. Significant technical challenges have to be overcome for both peem and, in particular, zone-plate-based microscopes to achieve these substantial improvements in spatial resolution. Nonetheless, improvements and further technological developments can be confidently anticipated in the next few years.

Several new operating modalities such as tomography (181,182), cryomicroscopy (103,182), and dark-field microscopy (183) have already been implemented in transmission. Because of their limited routine availability, they have not been discussed in detail in this review. These operating modes should prove very beneficial for certain applications in polymer science and technology. In particular, the radiation dose will have to increase as the spatial resolution improves. This might evolve into a relatively serious issue for the study of the more sensitive polymeric materials. Procedural improvements, more efficient detector development, and use of cryomicroscopy might have to be used extensively to minimize damage.

Applications beyond those possible today might be enabled through the use of higher energy resolution that reveals subtle spectral features. Studies on PS and deuterated PS have shown, for example, that nexafs of polymers can be sensitive to vibrations (3). This might serve as an additional contrast mechanism in several applications. The establishment of a nexafs spectroscopy database similar to the spectroscopy database available in the ir community would greatly facilitate quantitation and analysis of materials for which prior knowledge is very limited. In parallel to the development of a spectroscopic database, improved theoretical modeling would expand the ability to interpret nexafs spectra and the chemical structural information that they provide.

Improved and more dedicated facilities are about to be commissioned at the ALS in Berkeley and BESSY-II in Berlin, and are under development at the Canadian Light Source in Saskatoon. While there remain many scientific questions that can be addressed with the present performance of existing nexafs microscopes, improved capabilities and the increasing availability of nexafs microscopy will result in significant growth of applications in polymer science and related fields.

Based on the progress made to date and the improvements that can still be achieved, we are confidently looking forward to continuing growth of the nexafs spectroscopy and microscopy community and to exciting applications that have not yet been conceived.

BIBLIOGRAPHY

In *EPST* 3rd ed., Vol. 8, pp. 477–516, by H. Ade, North Carolina State University.

CITED PUBLICATIONS

1. H. Ade and S. Urquhart, in T. K. Sham, eds., *Chemical Applications of Synchrotron Radiation*, World Scientific Publishing, Singapore, 2002.
2. S. G. Urquhart and H. Ade, *J. Phys. Chem. B* **106**, 8531 (2002).
3. S. G. Urquhart and co-workers, *Chem. Phys. Lett.* **322**, 412 (2000).
4. P. S. Bagus and co-workers, *Chem. Phys. Lett.* **248**, 129 (1996).
5. K. Weiss, P. S. Bagus, and C. Wöll, *J. Chem. Phys.* **111**, 6834 (1999).
6. A. Schöll, R. Fink, E. Umbach, G. Mitchell, S. G. Urquhart, and H. Ade, *Chem. Phys. Lett.* **370**, 834 (2003).
7. T. Ohta, and co-workers, *Phys. Scr.* **41**, 150 (1990).
8. K. Seki and co-workers, *Phys. Scr.* **41**, 172 (1990).

9. J. Stöhr, *NEXAFS Spectroscopy*, Springer-Verlag, Berlin, 1992.
10. J. Kikuma and B. P. Tonner, *J. Electron Spectrocs. Relat. Phenom.* **82**, 53 (1996).
11. W. E. S. Unger and co-workers, *Fresenius' J. Anal. Chem.* **358**, 89 (1997).
12. H. Ade, in J. A. R. Samson and D. L. Ederer, eds., *Experimental Methods in the Physical Science*, Vol. **32**, Academic Press, New York, 1998, p. 225.
13. H. Ade, *Trends Polym. Sci.* **5**, 58 (1997).
14. H. Ade and co-workers, *J. Electron Spectrosc. Relat. Phenom.* **84**, 53 (1997).
15. J.-H. Guo and co-workers, *J. Chem. Phys.* **108**, 5990 (1998).
16. T. Yokoyama, and co-workers, *Phys. Scr.* **41**, 189 (1990).
17. D. G. J. Sutherland and co-workers, *Appl. Phys. Lett.* **68**, 2046 (1996).
18. S. G. Urquhart and co-workers, *J. Phys. Chem. B* **103**, 4603 (1999).
19. S. G. Urquhart and co-workers, *J. Electron Spectrosc. Relat. Phenom.* **100**, 119 (1999).
20. T. Gross and co-workers, *Polymer* **35**, 5590 (1994).
21. M. Keil and co-workers, *Appl. Surf. Sci.* **125**, 273 (1998).
22. M. C. K. Tinone and co-workers, *J. Chem. Phys.* **100**, 5988 (1994).
23. M. C. K. Tinone and co-workers, *Appl. Surf. Sci.* **80**, 89 (1994).
24. X. Zhang and co-workers, *J. Vac. Sci. Technol., B* **13**, 1477 (1995).
25. T. Coffey, S. G. Urquhart, and H. Ade, *J. Electron Spectrosc. Relat. Phenom.* **122**, 65 (2002).
26. I. Koprinarov and co-workers, *Polymer* **38**, 2005 (1997).
27. A. Lippitz and co-workers, *Polymer* **37**, 3157 (1996).
28. Y. Liu and co-workers, *Macromolecules* **30**, 7768 (1997).
29. J. Stöhr and co-workers, *Macromolecules* **31**, 1942 (1998).
30. J. Stöhr and M. G. Samant, *J. Electron Spectrosc. Relat. Phenom.* **99**, 189 (1999).
31. M. G. Samant and co-workers, *Macromolecules* **29**, 8334 (1996).
32. K. Weiss and co-workers, *Macromolecules* **31**, 1930 (1998).
33. K. Weiss, C. Wöll, and D. Johannsmann, *J. Chem. Phys.* **113**, 11297 (2000).
34. I. Mori and co-workers, *J. Electron Spectrosc. Relat. Phenom.* **78**, 371 (1996).
35. J. Genzer and co-workers, *Mater. Res. Soc. Symp. Proc.* **524**, 365 (1998).
36. J. Genzer and co-workers, *Macromolecules* **33**, 1882 (2000).
37. J. Genzer and co-workers, *Langmuir* **16**, 1993 (2000).
38. J. Genzer and co-workers, *Macromolecules* **33**, 6068 (2000).
39. M. L. Xiang and co-workers, *Macromolecules* **33**, 6106 (2000).
40. S. M. Kirtley and co-workers, *Fuel* **72**, 133 (1993).
41. O. C. Mullins and co-workers, *Appl. Spectrocs.* **47**, 1268 (1993).
42. S. Mitra-Kirtley and co-workers, *Energy Fuels* **7**, 1128 (1993).
43. S. Furukawa and T. K., *Solid State Commun.* **87**, 931 (1993).
44. K. Seki and co-workers, *J. Electron Spectrosc. Relat. Phenom.* **78**, 403 (1996).
45. V. R. McCrary and co-workers, *J. Chem. Phys.* **88**, 5925 (1988).
46. J. Stöhr and co-workers, *Phys. Rev. B* **36**, 2976 (1987).
47. H. Ågren and co-workers, *Phys. Rev. B* **51**, 17848 (1995).
48. D. G. Castner and co-workers, *Langmuir* **9**, 537 (1993).
49. K. Nagayama and co-workers, *J. Electron Spectrosc. Relat. Phenom.* **78**, 375 (1996).
50. C. Ziegler and co-workers, *Langmuir* **10**, 4399 (1994).
51. A. Lippitz and co-workers, *Polymer* **37**, 3151 (1996).
52. I. Ouchi and co-workers, *J. Electron Spectrosc. Relat. Phenom.* **78**, 363 (1996).
53. T. Okajima and co-workers, *J. Phys. Chem. A* **102**, 7093 (1998).
54. X. Q. Yang and co-workers, *Synth. Met.* **28**, C329 (1989).
55. G. Appel and co-workers, *Chem. Phys. Lett.* **313**, 411 (1999).
56. A. P. Hitchcock, *Phys. Scr. T* **31**, 159 (1990).
57. P. Rez, in Ref. 62, p. 107.
58. J. Fink and co-workers, *Phys. Rev. B* **34**, 1101 (1986).

59. J. Fink and co-workers, *Synth. Met.* **18**, 163 (1987).
60. J. J. Ritsko and co-workers, *J. Chem. Phys.* **69**, 3931 (1978).
61. J. J. Ritsko and R. W. Bigelow, *J. Chem. Phys.* **69**, 4162 (1978).
62. M. M. Disko, C. C. Ahn, and B. Fultz, eds., *Transmission Electron Energy Loss Spectrometry in Materials Science Minerals*, Metals and Materials Society, Warrendale, Pa. 1992.
63. R. F. Egerton, *Electron Energy Loss Spectroscopy in the Electron Microscope*, Plenum Press, New York, 1986.
64. D. A. Muller and co-workers, *Nature* **366**, 725 (1993).
65. F. P. Ottensmeyer, *J. Ultrastruct. Res.* **88**, 121 (1984).
66. E. G. Rightor and co-workers, *J. Phys. Chem. B* **101**, 1950 (1997).
67. K. Siangchaew and M. Libera, *Macromolecules* **32**, 3051 (1999).
68. G. Kim and M. Libera, *Macromolecules* **31**, 2569 (1998).
69. Y. C. Wang and co-workers, *Microsc. Microanal.* **4**, 146 (1998).
70. P. E. Batson, in Ref. 62, p. 217.
71. D. A. Muller, P. E. Batson, and J. Silcox, *Phys. Rev. B.* **58**, 11970 (1998).
72. H. W. Mook and P. Kruit, *Electron Microsc. Anal.* **153**, 81 (1997).
73. P. Kruit, *Electron Microsc. Anal.* **153**, 269 (1997).
74. P. E. Batson, H. W. Mook, and P. Kruit, *Inst. Phys. Conf. Ser.* **165**, 213 (2000).
75. H. Ade and co-workers, *Science* **258**, 972 (1992).
76. M. Feser and co-workers, *Proc., SPIE.* **3449**, 19 (1998).
77. E. H. Anderson and co-workers, *J. Vac. Sci. Technol. B* **18**, 2970 (2000).
78. S. Anders and co-workers, *Rev. Sci. Instrum.* **70**, 3973 (1999).
79. G. De Stasio and co-workers, *Rev. Sci. Instrum.* **70**, 1740 (1999).
80. R. Fink and co-workers, *J. Electron Spectrosc. Relat. Phenom.* **84**, 231 (1997).
81. R. Wichtendahl and co-workers, *Surf. Rev. Lett.* **5**, 1249 (1998).
82. E. Bauer and co-workers, *J. Electron Spectrosc. Relat. Phenom.* **84**, 201 (1997).
83. J. Kirz, C. Jacobsen, and M. Howells, *Q. Rev. Biophys.* **28**, 33 (1995).
84. C. Jacobsen and co-workers, *Opt. Commun.* **86**, 351 (1991).
85. T. Warwick and co-workers, *Rev. Sci. Instrum.* **69**, 2964 (1998).
86. W. Meyer-Ilse, D. Attwood, and M. Koike, in B. Chance and co-workers, *Synchrotron Radiation in Biosciences*, Clarendon Press, Oxford, 1994, p. 624.
87. B. Nieman, D. Rudolph, and G. Schmahl, *Appl. Opti.* **15**, 1883 (1976).
88. G. Schmahl and co-workers, *Q. Rev. Biophys.* **13**, 297 (1980).
89. B. Winn and co-workers, *Rev. Sci. Instrum.* **67**, A31 (1996).
90. B. Winn and co-workers, *Proc. SPIE* **2856**, 100 (1996).
91. C. Jacobsen and co-workers, *J. Microsco.—Oxford* **197**, 173 (2000).
92. J. Kirz and H. Rarback, *Rev. Sci. Instrum.* **56**, 1 (1985).
93. H. Rarback and co-workers, *J. X-Ray Sci. Technol.* **2**, 274 (1990).
94. T. Warwick, H. W. Padmore, and H. Ade *Proc. SPIE* **3449**, 12 (1998).
95. T. Schmidt and co-workers, *Surf. Rev. Lett.* **5**, 1287 (1998).
96. C. Morin and co-workers, *J. Electron Spectrosc. Relat. Phenom.* **121**, 203 (2001).
97. B. P. Tonner and co-workers, *J. Electron Spectrocs. Relat. Phenom.* **75**, 309 (1995).
98. H. Ade and co-workers, *Appl. Phys. Lett.* **73**, 3775 (1998).
99. X. Zhang and co-workers, *J. Struct. Biol.* **116**, 335 (1996).
100. H. Ade and co-workers, *Europhys. Lett.* **45**, 526 (1999).
101. C. J. Buckley, N. Khaleque, S. J. Bellamy, M. Robbins, and X. Zhang, in J. Thieme, G. Schmahl, E. Umbach, and D. Rudolph, eds., *X-ray Microscopy and Spectromicroscopy*, Springer-Verlag, Berlin, 1997.
102. G. E. Mitchell and co-workers, *Macromolecules* **35**, 1336 (2002).
103. J. Maser and co-workers, *J. Microsc.* **197**, 68 (2000).
104. J. Genzer and K. Efimenko, *Science* **290**, 2130 (2000).

105. T. Hayakawa and co-workers, *Macromolecules* **33**, 8012 (2000).
106. A. Cossy-Favre and co-workers, *Macromolecules* **31**, 4957 (1998).
107. K. Dalnoki-Veress, B. G. Nickel, and J. R. Dutcher, *Phys. Rev. Lett.* **82**, 1486 (1999).
108. A. P. Hitchcock, T. Tyliszczak, I. Koprinarov, H. Stöver, W.-H. Li, Y.-M. Heng, H. W. Ade, J. Dutcher, and K. Dalnoki, *Advanced Light Source Compendium of User Abstracts*, 1999.
109. F. L. Buchholz, in F. L. Buchholz and A. T. Graham, eds., *Modern Superabsorbent Polymer Technology*, Wiley-VCH, New York, 1998, p. 251.
110. T. Shimomura and T. Namba, in F. L. Buchholz and N. A. Peppas, eds., *Superabsorbent Polymers: Science and Technology*, American Chemical Society, Washington, D.C., 1994 p. 112.
111. K. Hogari and F. Ashiya, in Ref. 110, p. 128.
112. T. L. Staples, D. E. Henton, and F. L. Buchholz, in Ref. 109, p. 55.
113. F. L. Buchholz, in Ref. 109, p. 190.
114. G. Mitchell and co-workers, *Inst. Phys. Conf. Ser.* **165**, 113 (2000).
115. S. Reich and Y. Cohen, *J. Polym. Sci. Part B: Polym. Phys.* **19**, 1255 (1981).
116. F. Bruder and R. Brenn, *Phys. Rev. Lett.* **69**, 624 (1992).
117. J. Genzer and E. J. Kramer, *Phys. Rev. Lett.* **78**, 4946 (1997).
118. S. Affrossman and co-workers, *Macromolecules* **29**, 5010 (1996).
119. E. Kumacheva and co-workers, *Langmuir* **13**, 2483 (1997).
120. G. Krausch and co-workers, *Appl. Phys. Lett.* **64**, 2655 (1994).
121. W. Straub and co-workers, *Europhys. Lett.* **29**, 353 (1995).
122. K. Tanaka, A. Takahara, and T. Kajiyama, *Macromolecules* **29**, 3232 (1996).
123. S. Walheim and co-workers, *Macromolecules* **30**, 4995 (1997).
124. A. Karim and co-workers, *Macromolecules* **31**, 857 (1998).
125. X. Zheng and co-workers, *Phys. Rev. Lett.* **74**, 407 (1995).
126. P. Müller-Buschbaum and co-workers, *Macromolecules* **31**, 5003 (1998).
127. A. Cossy-Favre and co-workers, *Acta Phys. Pol. A* **91**, 923 (1997).
128. D. Slep and co-workers, *Langmuir* **14**, 4860 (1998).
129. D. A. Winesett and co-workers, *Polym. Int.* **49**, 458 (2000).
130. A. P. Smith, H. Ade, D. Slep, S. Qu, M. Rafailovich, J. Sokolov, G. Halada, S. A. Schwarz, and Y. Strzhemechny, *Abstracts, MRS 1996 Fall Meeting*, 1996.
131. A. P. Smith, H. Ade, D. Slep, S. Qu, M. Rafailovich, and J. Sokolov, NSLS Activity Report for 1996, Brookhaven National Laboratory, 1997.
132. D. Slep and co-workers, *Langmuir* **16**, 2369 (2000).
133. D. A. Winesett and co-workers, *High Perform. Polym.* **12**, 599 (2000).
134. C. Ton-That and co-workers, *Macromolecules* **33**, 8453 (2000).
135. S. Zhu and co-workers, *Nature* **400**, 49 (1999).
136. D. A. Winesett, H. Ade, D. Gersappe, M. H. Rafailovich, J. Sokolov, and S. Zhu, in preparation.
137. T. Schmitt, P. Guttmann, O. Schmidt, P. Müller-Buschbaum, M. Stamm, G. Schönhense, and G. Schmahl, *X-ray Microscopy, AIP Conf. Proc.* **507**, 245 (1999).
138. J. T. Chen and co-workers, *Science* **273**, 343 (1996).
139. C. Zimba, E. Thomas, and C. Ober, unpublished.
140. H. Ade and co-workers, *Polymer* **36**, 1843 (1995).
141. H. Ade and co-workers, *Mater. Res. Soc. Symp. Proc.* **437**, 99 (1996).
142. C. C. Sloop and co-workers, *J. Polym. Sci. Part B: Polym. Phys.* **39**, 531 (2001).
143. A. P. Smith and co-workers, *Macromolecules* **30**, 663 (1997).
144. A. P. Smith and co-workers, *Macromol. Rapid Commun.* **19**, 557 (1998).
145. A. P. Smith and co-workers, *Microsc. Microanal.* **4 S-2**, 142 (1998).
146. A. P. Smith and co-workers, *Macromolecules* **33**, 2595 (2000).
147. A. P. Smith and co-workers, *Macromolecules* **33**, 1163 (2000).

148. A. P. Smith and co-workers, *Macromolecules* **34**, 1536 (2001).
149. A. P. Smith and co-workers, *Macromol. Mater. Eng.* **274**, 1 (2000).
150. A. P. Smith and co-workers, *Adv. Mater.* **11**, 1277 (1999).
151. A. P. Smith and co-workers, *Polymer* **42**, 4453 (2001).
152. A. P. Hitchcock and co-workers, *Microsc. Microanal.* **4 S-2**, 808 (1998).
153. G. Mitchell, M. Cheatham, Y. Chonde, J. Marshall, H. Ade, and V. Zhuang, 1995 National Synchrotron Light Source Activity Report, 1996.
154. A. P. Hitchcock and co-workers, *AIP Conf. Proc. Ser.* **507**, 235 (2000).
155. I. Koprinarov and co-workers, *Macromolecules* **34**, 4424 (2001).
156. C. G. Zimba, H. W. Ade, and A. P. Smith, "*Characterization of the Interfacial Regions in Multilayer Coatings by nexafs Microscopy*," presented at the Society of Plastics Engineers, Brookfield, Conn., 2000 (unpublished).
157. A. P. Smith and co-workers, *Appl. Spectrosc.* **55**, 1676 (2001).
158. A. P. Smith and co-workers, *Polymer* **41**, 6271 (2000).
159. A. P. Smith, R. J. Spontak, and H. Ade, *Polym. Degrad. Stab.* **72**, 519 (2001).
160. S. G. Urquhart and co-workers, *J. Polym. Sci., Part B: Polym. Phys.* **33**, 1593 (1995).
161. S. G. Urquhart and co-workers, *J. Polym. Sci., B: Polym. Phys.* **33**, 1603 (1995).
162. S. G. Urquhart and co-workers, *J. Phys. Chem. B* **101**, 2267 (1997).
163. S. G. Urquhart and co-workers, *Mater. Res. Soc. Symp. Proc.* **437**, 243 (1996).
164. E. G. Rightor, S. Urquhart, A. Hitchcock, H. Ade, A. P. Smith, G. Mitchell, R. Priester, and W. Lidy, *Macromolecules*, **35**, 5873 (2002).
165. A. P. Hitchcock and co-workers, *Ultramicroscopy* **88**, 33 (2001).
166. A. P. Hitchcock, *J. Synchr. Radiat.* **8**, 66 (2001).
167. A. P. Hitchcock, I. N. Koprinarov, H. P. Stöver, L. Croll, and E. Kneedler, in preparation.
168. I. N. Koprinarov, A. P. Hitchcock, C. McCrory, and R. F. Childs, *J. Phys. Chem. B* **106**, 5358 (2002).
169. C. Zimba, A. P. Smith, and H. Ade, unpublished.
170. C. Zimba, A. P. Smith, and H. Ade, NSLS Activity Report for 1996, Brookhaven National Laboratory, 1997.
171. C. M. Roland, *Rubber Chem. Technol.* **62**, 456 (1989).
172. W. M. Hess, C. R. Herd, and P. C. Vegvari, *Rubber Chem. Technol.* **66**, 329 (1993).
173. J. Dias, S. G. Urquhart, H. Ade, and P. Stevens, *155th Meeting of the Rubber Division (Paper no. 30)*, American Chemical Society, Chicago, 1999.
174. Y. Zhang and co-workers, *Polymer* **42**, 9133 (2001).
175. Y. M. Zhang and co-workers, *Macromolecules* **34**, 7056 (2001).
176. H. Ade and B. Hsiao, *Science* **262**, 1427 (1993).
177. A. P. Smith and H. Ade, *Appl. Phys. Lett.* **69**, 3833 (1996).
178. H. Ade and co-workers, *Bull. Am. Phys. Soc.* **42**, 47 (1997).
179. A. P. Smith, A. Garcia, and H. Ade, *Microsc. Microanal.* **4 S-2**, 812 (1998).
180. J. Kikuma and co-workers, *J. Electron. Spectrosc. Relat. Phenom.* **94**, 271 (1998).
181. Y. Wang and co-workers, *J. Microsc.* **197**, 80 (2000).
182. D. Weiss and co-workers, *Ultramicroscopy* **84**, 185 (2000).
183. H. N. Chapman, C. Jacobsen, and S. Williams, *Ultramicroscopy* **62**, 191 (1996).

H. ADE
North Carolina State University

XYLYLENE POLYMERS

Introduction

In a process capable of producing pinhole-free coatings of outstanding conformality and thickness uniformity through the unique chemistry of *p*-xylylene (PX) [502-86-3] (1), a substrate is simply exposed to a controlled atmosphere of pure gaseous monomer. The coating process is best described as a *vapor deposition polymerization* (VDP). The monomer molecule is thermally stable, but kinetically very reactive toward polymerization with other molecules of its kind. Although it is stable as a rarified gas, upon condensation it polymerizes spontaneously to produce a coating of high molecular weight, linear poly(*p*-xylylene) (PPX) [25722-33-2] (2). This article emphasizes recent VDP developments. There have been several reviews of the subject (1,2), which offer a more thorough treatment of early developments in the field.

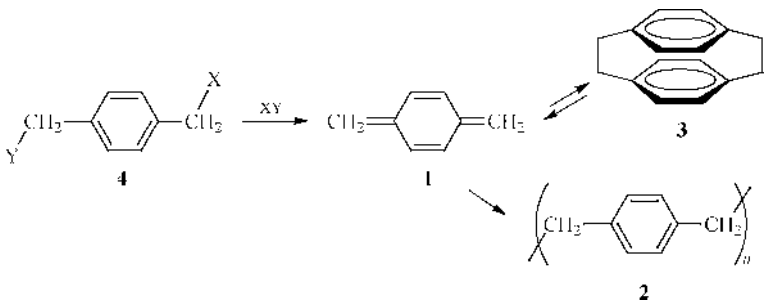

In the commercial Gorham process (3), the extremely reactive PX is conveniently generated by the thermal cleavage of its stable dimer, *cyclo*-di-*p*-xylylene (DPX), a [2.2]paracyclophane [1633-22-3] (3). In many instances, substituents attached to the paracyclophane framework are carried through the process unchanged, ultimately becoming substituents of the polymer in the coating.

The process takes place in two stages that must be physically separate but temporally adjacent. Figure 1 presents a schematic of a typical parylene deposition process, also indicating the approximate operating conditions.

The PPXs formed as coatings in the Gorham process are referred to generically as the parylenes. The terms Parylene N [25722-33-2], Parylene C [9052-19-1], and Parylene D [52261-45-7] refer specifically to polymers produced as coatings by the Gorham process using the dimers DPXN, DPXC [28804-46-8], and DPXD [30501-29-2], respectively, originally marketed by Union Carbide Corp.

The parylene process has certain similarities with vacuum metallizing. The principal distinction is that truly conformal parylene coatings are deposited even on complex, three-dimensional substrates, including on sharp points and in hidden or recessed areas. Vacuum metallizing, on the other hand, is a line-of-sight coating technology. Whatever areas of the substrate cannot be "seen" by the evaporation source are "shadowed" and remain uncoated.

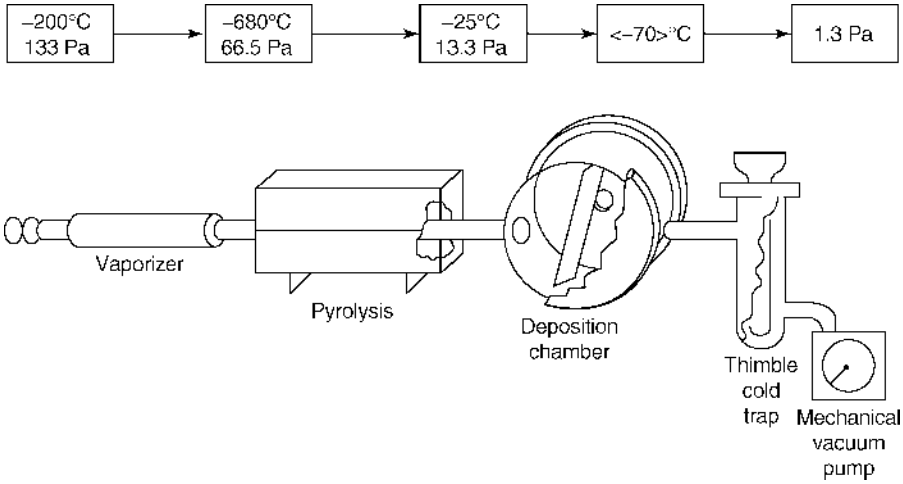

Fig. 1. Parylene deposition apparatus. To convert Pa to torr, multiply by 0.0075.

The *p*-xylylene species plays a central role in the coating process itself as well as in the making of the dimers which are used as feedstocks for the coating process. Polymers and dimers have both been made from precursor *p*-xylene compounds (4) featuring a variety of X and Y leaving groups. The conditions of the reaction determine the relative amounts of the resulting dimeric or polymeric products. Dilution is of course the key element in any procedure which offers a high yield of dimer.

The modest commercial success the *p*-xylylene dimer based Gorham process has achieved to date is readily attributed to the fact that thermal cleavage of cyclic dimer produces the *p*-xylylene monomer in essentially quantitative yield, while at the same time producing no gaseous by-products. In a gas-to-solid coating process, any gaseous entities generated from the leaving groups X and Y, necessarily formed in volumes comparable to the volume of the monomeric *p*-xylylene generated, would at the very least need to be exhausted through the pumping system, thereby slowing the process down. Moreover, certain of the most effective leaving groups XY, such as halogens or halogenide acids, would create a corrosion hazard both for any sensitive substrates to be coated and for the deposition equipment itself.

Gorham Process Monomers

The eight-carbon monomer PX is generated in the first stage of the parylene process by heating gaseous dimer as it passes through a high temperature zone. Its intermediacy in the process was deduced by the earliest investigators. Apprehending the unusual properties of PX is an important aid to understanding the unique features of the coating process.

Chemical Evidence for PX Monomer. Establishing early on that PX is indeed the pyrolysis product, rather than the molecule formed by breaking only one of the original dibenzyl bonds, the dimer diradical (5), would prove to be an important development.

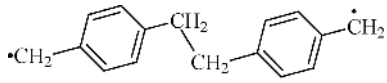

5

When the pyrolysis gases are quenched with a molar excess of iodine vapor, a yield of greater than 50% *p*-xylylene diiodide is recovered. The observation of this effect offered the first direct chemical support for the idea that DPX pyrolysis results in PX (1) (4).

Moreover, where *ar*-acetyldi-*p*-xylylene [10029-00-2] (6) is pyrolyzed, by adjusting temperatures in the deposition region, it is possible to isolate two different polymeric products, ie, poly(acetyl-*p*-xylylene) [67076-72-6] (8) and poly(*p*-xylylene) (PPX) (2). This of course requires the cleavage of the original dimer into two fragments.

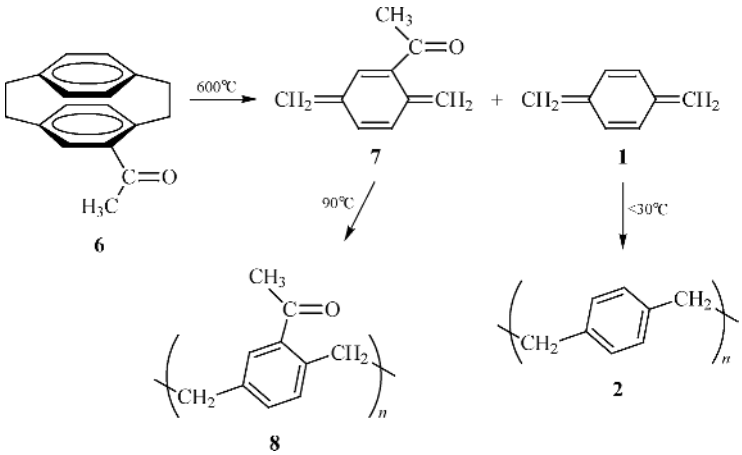

Experiments with monoethyl and monocarbomethoxy di-*p*-xylylene (5) gave similar results. These experiments do not, however, shed any light on whether the rupture of the methylene–methylene bonds in the dimer upon pyrolysis is simultaneous or sequential.

Only one exception to the clean production of two monomer molecules from the pyrolysis of dimer has been noted. When α-hydroxydi-*p*-xylylene (9) is subjected to the Gorham process, no polymer is formed, and the 16-carbon aldehyde (10) is the principal product in its stead, isolated in greater than 90% yield. This transformation indicates that, at least in this case, the cleavage of dimer proceeds in stepwise fashion rather than by a concerted process in which both methylene–methylene bonds are broken at the same time. This is consistent with the

predictions of Woodward and Hoffmann from orbital symmetry considerations for such [6 + 6] cycloreversion reactions in the ground state (6).

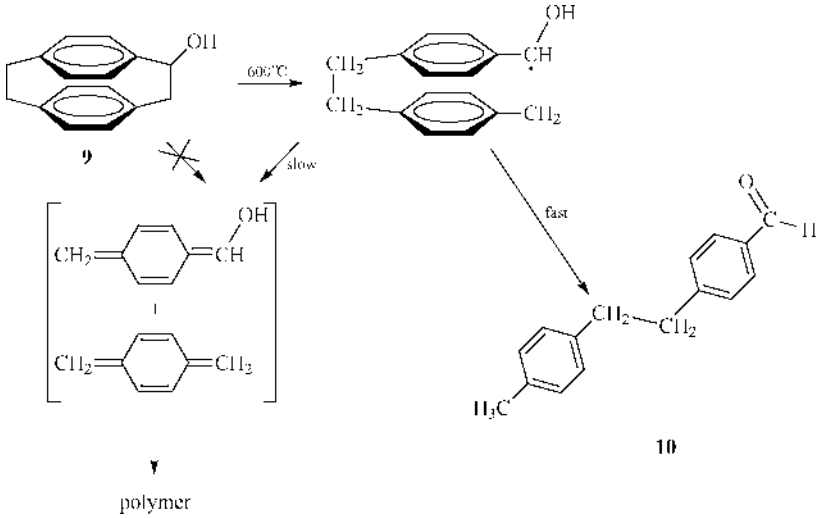

Monomer Properties. Despite difficulties involved in studying it owing to its great reactivity, a great deal is known about the structure of the parylene process monomer PX: the eight-carbon framework is planar (7); The molecule is diamagnetic, ie, all electron spins are paired in the ground state (spectroscopically, a singlet). Although many have ascribed its reactivity to its so-called biradical nature, the true biradical (triplet) form (11) of the molecule, an electronically excited state, is substantially more energetic, estimated at ca 50 kJ/mol (12 kcal/mol), and therefore cannot contribute to the monomer at equilibrium to any appreciable extent, even at pyrolysis temperatures. The PX molecule is instead a conjugated tetraolefin whose particular arrangement gives it extreme reactivity at its end carbons.

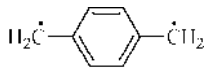

11

This extreme reactivity of PX has precluded many experimental approaches that otherwise would have been useful in studying it. Most of the present structural knowledge has been gleaned from spectroscopic studies and molecular orbital calculations. A noteworthy exception is an electron diffraction study (8) in which an electron beam was directed at a stream of gaseous PX, generated much as it is in the parylene process, issuing from a nozzle in a specially constructed apparatus. The results of the study are shown in Figure 2. Although the study was unable to resolve the lengths of the two different C=C and C—H bonds, it clearly distinguished between the C—C and C=C bond lengths. Thus *p*-xylylene is experimentally demonstrated to have an olefinic geometry rather than that of an aromatic biradical.

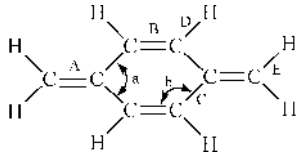

Fig. 2. Structure of PX monomer molecule from electron diffraction (9). Bond lengths: C=C A = B + 0.1381 ± 0.008; C—C, C = 0.1451 ± 0.0007 nm; C—H, D = E = 0.1116 ± 0.0035 nm. Bond angles: a = 122.2 ± 3.7°, b = 118.9 ± 1.9°.

By trapping PX at liquid nitrogen temperature and transferring it to THF at −80°C, the ^{1}H NMR spectrum could be observed (10). It consists of two sharp peaks of equal area at chemical shifts of 5.10 and 6.49 ppm downfield from tetramethylsilane (TMS). The fact that any sharp peaks are observed at all attests to the absence of any significant concentration of unpaired electron spins, such as those that would be contributed by the biradical (11). Furthermore, the chemical shift of the ring protons, 6.49 ppm, is well upfield from the typical aromatic range and more characteristic of an olefinic proton. Thus the olefin structure (1) for PX is also supported by NMR.

A particularly useful property of the PX monomer is its enthalpy of formation. Conventional means of obtaining this value, such as through its heat of combustion, are, of course, excluded by its reactivity. An experimental attempt was made to obtain this measure of chemical reactivity with the help of ion cyclotron resonance; a value of 209 ± 17 kJ/mol (50 ± 4 kcal/mol) was obtained (11). Unfortunately, the technique suffers from lack of resolution in addition to experimental imprecision. It is perhaps better to rely on molecular orbital calculations for the formation enthalpy. Using a semiempirical molecular orbital technique, which is tuned to give good values for heat of formation on experimentally accessible compounds, the heat of formation of *p*-xylylene has been computed to be 234.8 kJ/mol (56.1 kcal/mol) (12).

Successful *p*-Xylylene VDP Monomers. Within the limits mentioned above, it is frequently possible, and often desirable, to modify the *p*-xylylene monomer by attaching to it certain substituents. Limitations on such modifications lie in three areas: reactivity, performance in the coater, and cost.

Reactivity. Although the reactivity which enables the gas–solid polymerization to proceed is a characteristic of the eight-carbon *p*-xylylene tetraolefin system, it is possible to subdue that reactivity. For example, by attaching electron-withdrawing substituents to the alpha positions and thereby further delocalizing the π-electrons of the highly reactive *p*-xylylene nucleus, it is in several instances possible to prepare *p*-xylylenes that are so stable that they can be isolated and handled as normal organic compounds (Fig. 3). These sorts of substitutions must of course be avoided if the goal is to make polymer.

It is also possible to interfere with the polymerization by attaching at the alpha positions either too many groups, or groups which are too bulky. Four chlorine atoms (13) or four methyl groups (14) seem to be sufficient to hinder the production of polymer. These crowded *p*-xylylene monomers can be polymerized, but not through a VDP process.

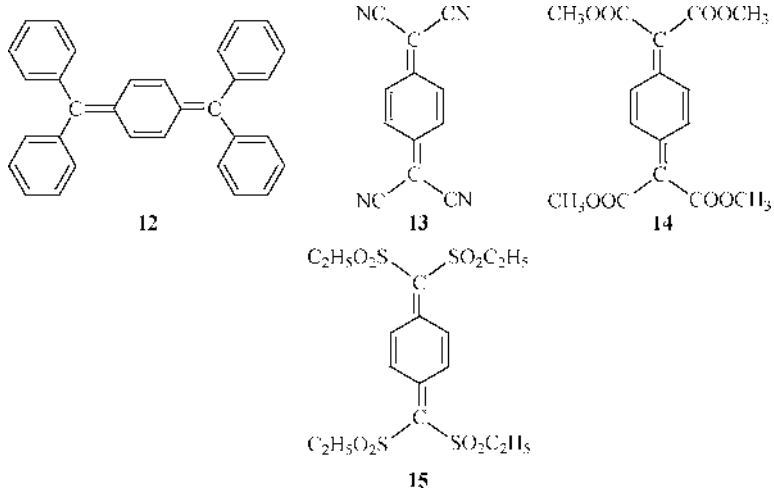

Fig. 3. Isolatable *p*-xylylene derivatives: 12, Thiele's hydrocarbon—1904 [26392-12-1]; 13, tetracyanoquinodimethane [1518-16-7] (TCNQ); 14, tetrakis(methoxycarbonyl)-quinodimethan [65649-20-9]; 15, tetrakis(ethylsulfonyl)quinodimethan [84928-90-5].

Thus, except for electron-withdrawing or bulky substituents, at least from the standpoint of reactivity toward polymerization, modification by most other substituents is possible.

Performance in Coater. The modified monomer should perform well in commercial deposition equipment. Performance considerations include the growth rate of the coating, the uniformity of thickness of the coating over the chamber volume, and the efficiency with which the dimer is converted to useful coatings on the substrates.

An important further constraint is the fact that economic considerations in the construction of deposition equipment normally lead to a preference for an ambient-temperature deposition chamber. Control of deposition temperature is possible, but it adds to both equipment expense and operational complexity.

The vapor pressure of a parylene monomer is a prime factor in determining how rapidly a coating grows when exposed to an atmosphere of monomer at a given pressure. Vapor pressure is reduced as molecular weight increases, thereby increasing the monomer's tendency to condense and, along with it, increasing the VDP growth rate. The presence of polar functionality in the molecule further depresses vapor pressure. But too low a vapor pressure makes it difficult to transport gaseous monomer from point to point in the deposition chamber. Hence, some optimum value of monomer volatility is expected.

The widely used Parylene C owes its popularity principally to the room-temperature volatility of its monomer. The Parylene C monomer, chloro-*p*-xylylene, has become the de facto performance standard. By comparison, the Parylene N monomer, *p*-xylylene itself, is too volatile and would perform better in a sub-ambient-temperature deposition system. The Parylene D monomer, dichloro-*p*-xylylene [85586-88-5] is too heavy, and causes distribution problems in larger deposition systems.

Cost. It is necessary to produce the feedstock from which the monomer is generated, viz, the dimer, at a cost which can be supported by the commercial application, and yet allow it to be economically competitive with all other alternative ways to achieve the same end result. This factor often, but not always, seriously limits the amount of effort that can be put into dimer synthesis and purification.

Other, Related Processes

VDP processes using means other than the pyrolytic cleavage of DPX (Gorham process) to generate the reactive monomer are also known, although none are practiced commercially at the time of this writing (ca 1997).

Photopolymerization and Plasma Polymerization. The use of ultraviolet light alone (15,16) as well as the use of electrically excited plasmas or glow discharges to generate monomers capable of undergoing VDP have been explored. The products of these two processes, called plasma polymers, continue to receive considerable scientific attention. Interest in these approaches is enhanced by the fact that the feedstock material from which the monomer capable of VDP is generated is often inexpensive and readily available. In spite of these widespread scientific efforts, however, commercial use of the technologies is quite limited.

When *p*-xylene is used as the monomer feed in a plasma polymer process, PX may play an important role in the formation of the plasma polymer. The plasma polymer from *p*-xylene closely resembles the Gorham process polymer in the infrared, although its spectrum contains evidence for minor amounts of nonlinear, branched, and cross-linked chains as well. Furthermore, its solubility and low softening temperature suggest a material of very low molecular weight (17).

VDP Polyimides. Polyimide films have also been prepared by a kind of VDP (18). The poly(amic acid) layer is first formed by the coevaporation and condensation of two monomers, followed by copolymerization on the substrate. The imidization is carried out in a separate baking step (see POLYIMIDES).

***o*-Xylylene/BCB.** Thermosetting resins based on benzocyclobutene (BCB)

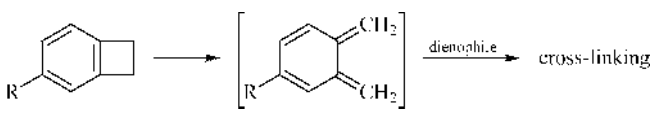

chemistry have been reported (19,20). In these condensed phase cures, the *o*-xylylene isomer is the key reactive intermediate. From the behavior of this energetically similar ortho isomer, the value of the para configuration's rendering any ring closure reaction—analogous to cyclobutene formation from the ortho isomer—geometrically forbidden can be appreciated.

Dimer

In contrast to the extreme reactivity of the monomeric PX (1) generated from it, the dimer DPX (3) feedstock for the parylene process is an exceptionally stable

compound. Because of their chemical inertness, dimers in general do not exhibit shelf-life limitations. Although a variety of substituted dimers are known in the literature, at present only three are commercially available: DPXN, DPXC, and DPXD, which give rise to Parylene N, Parylene C, and Parylene D, respectively.

The unsubstituted C-16 hydrocarbon, [2.2]paracyclophane (3), is DPXN. Both DPXC and DPXD are prepared from DPXN by aromatic chlorination and differ only in the extent of chlorination; DPXC has an average of one chlorine atom per aromatic ring and DPXD has an average of two.

Manufacture. For the commercial production of DPXN (di-*p*-xylylene) (3), two principal synthetic routes have been used: the direct pyrolysis of *p*-xylene (4, X = Y = H) and the 1,6-Hofmann elimination of ammonium (HNR_3^+) from a quaternary ammonium hydroxide (4, X = H, Y = NR_3^+). Most of the routes to DPX share a common strategy: PX is generated at a controlled rate in a dilute medium, so that its conversion to dimer is favored over the conversion to polymer. The polymer by-product is of no value because it can neither be recycled nor processed into a commercially useful form. Its formation is minimized by careful attention to process engineering. The chemistry of the direct pyrolysis route is shown in equation 1:

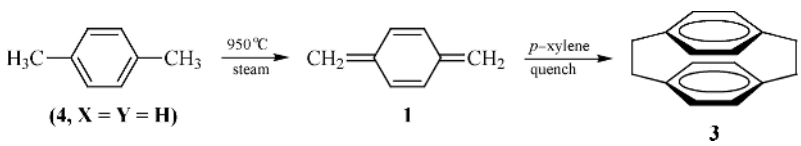

(1)

First, *p*-xylene is dehydrogenated pyrolytically in the presence of steam at about 950°C to give *p*-xylylene (PX), which in turn forms di-*p*-xylylene (DPX) when quenched in liquid xylene. The xylene is recycled to the pyrolysis vessel. Yields and conversion efficiency are satisfactory. However, several engineering challenges need to be overcome, including the choice of a suitable diluent; establishing optimal residence time, vapor velocity, and operating pressure during pyrolysis; and the design and construction of novel equipment to withstand the highly corrosive reaction environment.

The Hofmann elimination route, of which many versions exist, can be carried out at much lower temperatures in conventional equipment. The PX is generated by a 1,6-Hofmann elimination of amine from a quaternary ammonium hydroxide in the presence of a base. This route gives yields of 17–19%. Undesired polymeric products can be as high as 80% of the product. In the presence of a polymerization inhibitor, such as phenothiazine, DPXN yields can be increased to 50%.

In the 1,6-elimination of *p*-trimethylsilylmethylbenzyltrimethylammonium iodide with tetrabutylammonium fluoride, yields as high as 56% have been reported (21). The starting materials are not readily accessible, however, and are costly.

The yield can be raised to 28% if the Hofmann elimination is conducted in the presence of a water-soluble copper or iron compound (22). Further improvements up to 50% were reported when the elimination was carried out in the

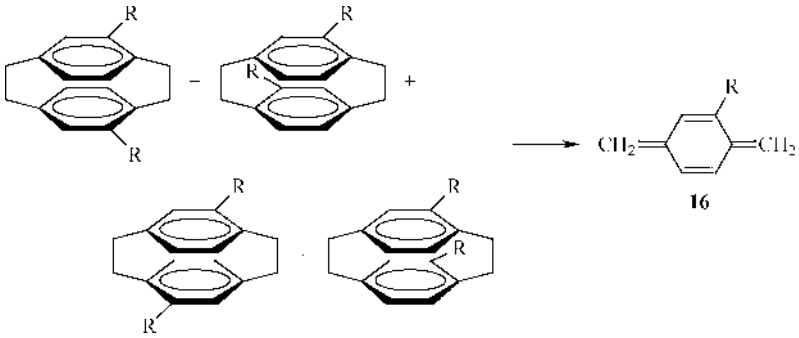

Fig. 4. Isomeric dichloro[2.2]paracyclophanes produce the same xylylene.

presence of ketone compounds (23). Further beneficial effects have been found with certain cosolvents, with reported yields of greater than 70% (9).

DPXC and DPXD. The economic pressure to control dimer costs has had an important effect on what is in use today (ca 1997). Attaching substituents to the ring positions of a [2.2]paracyclophane does not proceed with isomeric exclusivity. Indeed, isomeric purity in the dimer is not an essential requirement for obtaining isomeric purity, eg, monosubstituted monomer, in the pyrolysis. Any mixture of the four possible heteronuclearly disubstituted dichloro[2.2]paracyclophanes, will, after all, if pyrolyzed produce the same monomer molecule, chloro-*p*-xylylene [10366-09-3] (16) (Fig. 4).

Although DPXC and DPXD prepared by the chlorination of DPXN are relatively complex mixtures, after pyrolytic cleavage the resulting mixture of monomers is considerably simpler. Thus DPXC, when pyrolyzed, gives predominantly monochloro PX, which is accompanied by small but significant amounts of PX and dichloro PX. The resulting polymer, Parylene C, consequently has an average of about one chlorine atom per repeat unit. However, it contains significant amounts of unchlorinated, as well as dichlorinated, repeat units.

DPXC and DPXD are prepared from DPXN by chlorinating to different extents. The conditions are controlled to favor aromatic ring chlorination to the exclusion of the free-radical chlorination of the ethylene bridges. However, the chlorination products are complex mixtures of the homologues DPXN, monochloro DPX, dichloro DPX, trichloro DPX, and tetrachloro DPX, and even higher homologues, as well as the several possible isomers of each.

New synthetic routes for the preparation of homologously pure dichloro DPX and tetrachloro DPX have been reported through the 1,6-Hofmann elimination of chlorinated *p*-methylbenzyltrimethylammonium hydroxide. In the case of dichloro DPX, yields of 30% were reported (24). In the presence of ketone compounds, yields were increased to 50% (23).

Purification. Unsubstituted di-*p*-xylylene (DPXN) is readily purified by recrystallization from xylene. It is a colorless, highly crystalline solid. The principal impurity is polymer, which fortunately is insoluble in the recrystallization solvent and easily removed by hot filtration.

In purifying DPXC and DPXD, care must be taken not to disturb the homologue composition, so that product uniformity is maintained. For example, a

Table 1. Properties of Parylene Dimers

Dimer	Melting point, °C	Density, g/cm^3
DPXN	284[a]	1.22
DPXC	140–160[b]	1.30
DPXD	170–195[b]	1.45

[a]Decomposes.
[b]Mixture of homologues and their isomers.

recrystallization of DPXC from ethanol would give a higher melting, more crystalline dimer material, at the expense of a decrease in yield owing to the removal of otherwise useful isomers, but the polymer made from it would not be identical to the historical Parylene C, as defined by its preparation from the chlorination mixture. The real purification issues are the removal of insoluble residues and any components that contain aliphatic side-chain chlorine. Although ring-substituted chlorine is stable, side-chain chlorine can give rise to hydrogen chloride gas under the conditions of the parylene process, or subsequent to it, which in certain applications could initiate substrate corrosion. Fortunately, the aliphatic chlorine problem can be minimized by proper attention to process detail.

Properties. The DPXs are all crystalline solids; melting points and densities are given in Table 1. Their solubility in aromatic hydrocarbons is limited. At 140°C, the solubility of DPXN in xylene is only about 10%. DPXC is more readily soluble in chlorinated solvents, eg, in methylene chloride at 25°C its solubility is 10%. In contrast, the corresponding figure for DPXN is 1.5%.

The structure of DPXN was determined in 1953 from X-ray diffraction studies (25). There is considerable strain energy in the buckled aromatic rings and distorted bond angles. The strain has been experimentally quantified at 130 kJ/mol (31 kcal/mol) by careful determination of the formation enthalpy through heat of combustion measurements (26). The release of this strain energy is doubtless the principal reason for success in the particularly convenient preparation of monomer in the parylene process.

Polymer

The linear polymer of PX, poly(*p*-xylylene) (PPX) (2), is formed as a VDP coating in the parylene process. The energetics of the polymerization set it apart from all other known polymerizations and enable it to proceed as a vapor deposition polymerization.

Thermodynamic Considerations. On the basis of the value for the enthalpy of formation of *p*-xylylene, ΔH_f^0 (PX), the enthalpy of polymerization, $\Delta H^0_{polym} = \Delta H_f^0(PPX)\ \Delta H_f^0(PX)$, can be estimated. No experimental combustion data are available for high molecular weight poly(*p*-xylylene) as it is formed in the parylene process, ΔH_f^0 (PPX).

For crystalline [2.2]paracyclophane [(1,2), DPXN], a ΔH_f^0 of +154.4 kJ/mol (+36.9 kcal/mol) is reported (26). The hypothetical transformation of crystalline DPXN into polymer is accompanied by the release of 129.7 kJ/mol (31.0 kcal/mol)

of paracyclophane strain energy per mole of paracyclophane, and 12.6 kJ/mol (3.0 kcal/mol) per polymer repeat unit as a result of the bibenzyl hyperconjugative stabilization, which is permitted in the polymer but excluded by geometry in the dimer. Thus the standard enthalpy of formation for the hypothetical 100% crystalline poly(*p*-xylylene) is estimated to be −0.3 kJ/mol (−0.05 kcal/mol), assuming that the energies associated with crystallinity are the same in both cases. Although it might be acceptable to assume that such energies per repeat unit are similar in the crystalline polymer and crystalline dimer, Parylene N, as produced by the parylene process, is typically only about 57% crystalline. Using a value of 14.1 kJ/mol (3.37 kcal/mol) for the heat of fusion for poly(*p*-xylylene) (27), the standard formation enthalpy for Parylene N, as it is typically deposited in the parylene process, ΔH_f^0 (Parylene N), is +5.7 kJ/mol (+1.4 kcal/mol).

In estimating the enthalpy of polymerization, the physical state of both starting monomer and polymer must be specified. Changes in state are accompanied by ethalpy changes. Therefore, they also affect the level of the polymerization enthalpy. The ΔH_f^0 for *p*-xylylene previously mentioned is applicable to the monomer as an ideal gas. To make comparisons with other polymerization processes, most of which start with condensed monomer, a heat of vaporization for *p*-xylylene is needed. It is assumed herein that it is the same as that for *p*-xylene, 42.4 kJ/mol (10.1 kcal/mol). Thus the ΔH_f^0 of the liquid monomer *p*-xylylene is 192.3 kJ/mol (46.0 kcal/mol).

The enthalpy of polymerization of unannealed (57% crystalline) Parylene N, as it is deposited, starting with liquid monomer, $\Delta H^0_{\text{polym(lu)}}$, is −186.6 kJ/mol (−44.6 kcal/mol). This is an exceptionally high value compared with those of other addition polymers, which generally fall in the −60 to −100 kJ/mol (−14.3 to −23.8 kcal/mol) range. It quantifies the vigor of the polymerization. Because the source of polymerization enthalpy is within the *p*-xylylene system, substituents affect it only to a minor extent. All parylenes are expected to have a similar molar enthalpy of polymerization. An experimental value for the heat of polymerization of Parylene C has appeared. Using the gas evolution from the liquid nitrogen cold trap to measure thermal input from the polymer, and taking advantage of a peculiarity of Parylene C at −196°C to polymerize abruptly, perhaps owing to the arrival of a free radical, a $\Delta H^0_{\text{polym}}$ of −152 ± 8 kJ/mol (−36.4 ± 2.0 kcal/mol) at −196°C was reported (28). The correction from −196°C to room temperature is estimated at −17 kJ/mol, bringing this experimental value for Parylene C closer to the calculated value for Parylene N. It is assumed that S_{polym} is 0 at 0 K (third law), 125 J/(mol · K) [30 cal/(mol · K)] at 298 K, and proportional to T in between—a crude assumption, but appropriate to the current level of knowledge. Thus experiment and calculation are in harmony in quantifying the exceptional exothermicity of parylene polymerization (see THERMODYNAMIC PROPERTIES OF POLYMERS).

The thermodynamic ceiling temperature (29) T_c for a polymerization is computed by dividing the $\Delta H^0_{\text{polym}}$ by the standard entropy of polymerization, $\Delta S^0_{\text{polym}}$. The T_c is the temperature at which monomer and polymer are in equilibrium in their standard states at 25°C (298.15 K) and 101.3 kPa (1 atm). (In the case of *p*-xylylene, such a state is, of course, purely hypothetical.) The T_c quantifies the binding forces between monomer units in a polymer and measures the tendency of the polymer to revert back to monomer. In other systems, the T_c indicates a

Table 2. Entropies, Enthalpies, and Ceiling Temperatures for the Polymerization of Various Monomers at 25°C (298.15 K) and 101.3 kPa (1 atm)[a]

	Liquid			Gas		
Monomer	$-\Delta H^0$, kJ/mol[b]	$-\Delta S^0$, J/(mol · K)[b]	T_c, °C	$-\Delta H^0$, kJ/mol[b]	$-\Delta S^0$ J/(mol · K)[b]	T_c, °C
Ethylene	108.4	173.6	351			
Propylene	81.6	116.3	429			
Isoprene	74.9	101.3	467	101.3	187.0	268
Styrene	69.9	104.6	395	113.4	212.1	262
Methyl methacrylate	55.2	117.2	198			
α-Methylstyrene	35.1	103.8	65			
p-Xylylene	186.6	56.4	3035	229.1	161.1	1149

[a]Ref. 26.
[b]To convert J to cal, divide by 4.184.

temperature above which the polymer is unstable with respect to its monomer, but in the case of parylene it serves rather as a means of comparing the relative stability of the polymer with respect to its reversion to monomer. For computing the T_c, however, the standard entropies of polymerization are required.

The standard polymerization entropies can be estimated from the following. The standard entropy S^0 for PX as an ideal gas is computed by a group-contribution method (30) to be 310.6 J/(mol · K) [74.24 cal/(mol · K)]. The entropy of vaporization for PX is assumed to be the same as that of *p*-xylene, 104.7 J/(mol · K) [25.03 cal/(mol · K)] (31). Therefore, the S^0 for liquid PX is 205.9 J/(mol · K) [49.21 cal/(mol·K)]. Noting that the experimental specific heat C_p of PPX follows that of polystyrene over the range of 160 to 340 K (32), it can be assumed that the proportionality continues down to 0 K and that the factor 135/116 at 298 K can be applied to the known S^0 for polystyrene [S = 128.5 J/(mol · K) or 30.70 cal/(mol · K) (33). It follows that the S^0 for as-deposited 57% crystalline Parylene N is 149.5 J/(mol · K) [35.73 cal/(mol · K)]. Therefore, $\Delta S^0_{\text{polym(g)}} = -161.1$ J/(mol · K) [−38.50 cal/(mol · K)] and $\Delta S^0_{\text{polym(l)}} = -56.4$ J/(mol · K) [−13.4 8cal/(mol · K)].

The results of the above polymerization thermodynamics calculations for parylene are compared to similar data for typical addition polymers in Table 2. The T_c quantifies the stability of the polymer only with respect to reversion to monomer. When PPX is thermally degraded (ca 500°C), a mixture of degradation products including hydrogen gas, *p*-xylene, toluene, and *p*-methylstyrene is observed (34), suggesting that the path taken in thermal degradation requires the cleavage of bonds other than those formed in the polymerization, very likely starting with the methylene C—H bond. Complete replacement of the methylene hydrogens in PPX with fluorine gives a polymer with substantially better stability at elevated temperatures (35).

The enthalpy liberated on the VDP of parylene is real and in an adiabatic situation causes a rise in temperature of the coated substrate. For Parylene C, 229.1 kJ/mol (54.7 cal/mol) corresponds to 1654 J/g (395 cal/g) whereas its specific heat at 25°C is only 1.00J/(g · K) [0.239 cal/(g · K)] (36). In most practical

situations, however, the mass of parylene deposited is dwarfed by the substrate mass, and the heat of polymerization is dissipated within the coated substrate over the time required to deposit the coating with minimal actual temperature rise.

Polymerization Mechanism. The physical processes of condensation and diffusion must be considered along with the *p*-xylylene polymerization chemistry for a proper understanding of what happens microscopically during vapor deposition polymerization (37). These processes point to an important distinction between VDP and vacuum metallization, ie, that in the latter, adsorption is followed by a surface reorganization of the existing deposited material, and diffusion of incoming species through the bulk is nonexistent. In most parylene depositions, a coating forms from gaseous monomer under steady-state conditions.

Gaseous monomer is transported to the location within the coating where it is to be consumed to produce polymer by an initial condensation, followed by diffusion. The net flux of monomer molecules through the growth interface, ie, the outer boundary of the coating, between the gaseous and condensed phases, needed to sustain growth at a given rate can be readily calculated [for Parylene C, 10 μm/h requires $1.55 \times 10^{15}/(\mathrm{cm}^2 \cdot \mathrm{s})$]. Comparing a net flux so obtained with the flux of molecules that according to the kinetic theory of gases are striking the growth surface ($Z = PN_0/\sqrt{2\pi MRT}$) for the conditions typical of parylene deposition, a large difference (two or three orders of magnitude) is observed. For Parylene C monomer at a pressure of 1.3 Pa (10 μm Hg) and 25°C, $Z = 6.7 \times 10^{17}/(\mathrm{cm}^2 \cdot \mathrm{s})$. For each molecule that eventually enters the coating, some hundred or thousand molecules strike the growth interface. Those that condense and do not react must, of course, evaporate. The term "sticking coefficient" has sometimes been borrowed from vacuum metallization to describe this ratio of incident molecules to consumed molecules. However, the VDP situation is not adequately described by hard spheres bouncing off a growth interface. Every incident molecule spends at least some time in the polymeric coating phase beyond the growth interface before it is lost again to the gas phase.

Because most of the condensing molecules evaporate, condensation equilibrium at the growth surface can be assumed, to a good approximation. The concentration of monomer dissolved in the coating near the growth interface is, therefore, governed by Henry's law, and monomer concentration in polymer solution increases proportionately to the partial pressure of monomer in the gas phase. Furthermore, as the temperature is lowered, or as higher molecular weight monomers of lower volatility are selected, monomer concentration at the growth interface increases. In most practical situations, these Henry's law effects dominate in determining growth rates for VDP coatings by regulating monomer concentration within the coating. For each monomer, there exists a threshold condensation temperature, T_{tc}, above which the rate of growth of coating is, for all practical purposes, zero (Table 3), but this phenomenon is governed by the competition between initiation and propagation chemistries, discussed herein.

Once it is in "solution" in the coating, the monomer moves about in random directions by diffusion until it evaporates or is consumed by chemical reaction. The polymer molecules that have already grown to higher molecular weight cannot relocate appreciably owing to entanglement with their neighbors. The rate of diffusion of monomer through the polymer bulk is adequate for the

Table 3. Threshold Condensation Temperatures T_{tc} for Substituted *p*-Xylylene Monomers

Monomer	T_{tc}, °C
p-Xylylene	30
2-Methyl-*p*-xylylene	60
2-Ethyl-*p*-xylylene	90
2-Chloro-*p*-xylylene	90
2-Acetyl-*p*-xylylene	130
2-Cyano-*p*-xylylene	130
2-Bromo-*p*-xylylene	130
Dichloro-*p*-xylylene	130

participation of diffusive transport in the mechanism of VDP (ca 10^{-10} cm^2/s at room temperature). This can be confirmed in swelling-rate experiments with solvents having similar physical properties, such as *p*-xylene.

The monomer is consumed by two chemical reactions: initiation, in which new polymer molecules are generated, and propagation, in which existing polymer molecules are extended to higher molecular weight. In steady-state VDP, both reactions proceed continuously inside polymeric coating, in the reaction zone just behind the growth interface.

The first step of the initiation reaction is the coupling of two monomer molecules to form the dimer diradical (5). The formation of this diradical is energetically uphill, ie, the energy of two benzyl radicals is greater than that of two starting *p*-xylylene systems. The rate of destruction greatly exceeds the rate of formation. Only a trace concentration of the dimer diradical species exists at equilibrium. Further reaction of the dimer diradical with monomer gives more stable diradicals. In these subsequent transformations, a *p*-xylylene is converted into a benzene with a net stabilizing effect. At some stage of oligomerization, the resulting n-mer diradical becomes more stable than the n *p*-xylylene molecules from which it was constructed. At this point, the new polymer molecule is formed. Thus the overall order of the initiation reaction, the reaction in which new polymer molecules are generated, is some $n > 2$. Initiation chemistry requires no species other than monomer, another unusual aspect of the polymerization chemistry of *p*-xylylene.

The order n of the initiation reaction has an important influence on the manner in which the VDP occurs. Because monomer molecules, even in solution at low concentration, are closer together in the condensed phase than they are in the gaseous phase, the rate of initiation is greater in the condensed phase than in the gaseous phase. The higher the order n, the more the condensed phase is favored. The order n, according to the mathematical model (37) of *p*-xylylene VDP, at the same time governs the effect of monomer pressure on growth rate at a given deposition temperature. The model predicts that growth rate should vary with the pressure raised to the power $(n + 3)/4$. Thus, if $n = 3$, the growth rate should be proportional to $p^{1.5}$. In an early attempt to determine the pressure dependence of parylene growth rate γ, an expression of $\gamma = kp^2$ was reported (38). A pressure exponent of 2 would be interpreted as an initiation order of $n = 5$. Although such a high order would favorably deemphasize "snow," consideration

of the energetics of oligomeric *p*-xylylene diradicals would seem to place the order nearer to 3. Perhaps the early investigators did not anticipate a nonintegral order for pressure dependence. A more recent report (39) places n at 3 for Parylenes N and C, and 4 for Parylene D. Thus, with $n \geq 3$, the parylenes are more likely to form a continuous coating than a dust or a snow, the physical form of the product of a gas-phase polymerization. To the extent that snow is included in the formation of a coating (ie, dual-phase polymerization), haze develops.

In the propagation reaction, the monomer molecule reacts with an existing free-radical polymer chain end to make the chain one repeat unit longer. The polymer chains have two active ends, and they grow from both ends at the same time. Under normal coating conditions, the consumption of monomer by propagation must be much higher than its consumption by initiation to obtain high molecular weight polymer. In fact, the number-average molecular weight is determined by the proportion of monomer consumed by the two reactions, and is diminished by increases in deposition temperature or monomer partial pressure.

The concentration of monomer within the coating decreases approximately exponentially with distance from the growth interface. With this decrease in monomer concentration, the rates of initiation and propagation reactions also decrease. Moving back into the polymer from the growth interface, through the reaction zone where polymer is being manufactured, a region in which the polymer formation is essentially complete is gradually entered. Because initiation is of higher order in monomer concentration, it tends to occur closer to the growth interface than does propagation. Under conditions prevailing during a typical deposition, the characteristic depth of the reaction zone is a few hundred nanometers, and the maximum concentration of monomer, ie, the concentration at the growth interface, is of the order of a few tenths percent by weight. Thus the parylene polymerization takes place just behind the growth interface in a medium that is best described as a slightly swollen, solid polymer.

During the vapor deposition process, the polymer chain ends remain truly alive, ceasing to grow only when they are so far from the growth interface that fresh monomer can no longer reach them. No specific termination chemistry is needed, although subsequent to the deposition, reaction with atmospheric oxygen, as well as other chemical conversions that alter the nature of the free-radical chain ends, is clearly supported experimentally.

Polymer Properties. The single most important feature of the parylenes, that feature which dominates the decision for their use in any specific situation, is the VDP process by which they are applied. VDP provides the room-temperature coating process and produces the films of uniform thickness, having excellent thickness control, conformality, and purity. The engineering properties of commercial parylenes once they have been formed are given in Table 4. As crystalline polymers, the parylenes retain useful physical integrity up to temperatures approaching their crystalline melting points. However, their glass-transition temperatures, T_g, the temperature spans over which the continuous amorphous phase, usually the minority phase, changes from a rigid, vitreous condition to a more flexible, rubbery condition, are probably in the vicinity of ambient temperature. In the case of PPX (Parylene N), careful measurements have established the T_g to be centered at 13°C, the range over which T affects heat capacity measurements extending from 240 to 330 K (−33 to + 57°C) (27). Because they

Table 4. Typical Engineering Properties of Commercial Parylenes

Property	Parylene N	Parylene C	Parylene D	ASTM method
General				
Density, g/cm^3	1.110	1.289	1.418	D1505
Refractive index, n_D^{23}	1.661	1.639	1.669	
Mechanical				
Tensile modulus, GPa[a]	2.4	3.2	2.8	D882
Tensile strength, MPa[b]	45	70	75	D882
Yield strength, MPa[b]	42	55	60	D882
Elongation to break, %	30	200	10	D882
Yield elongation, %	2.5	2.9	3	D882
Rockwell hardness	R85	R80		D785
Coefficient of friction				D1894
Static	0.25	0.29	0.35	
Dynamic	0.25	0.29	0.31	
Thermal				
Melting point, °C	420	290	380	
Linear coefficient of expansion to 25°C × 10^5, K^{-1}	6.9	3.5		
Heat capacity at 25°C, J/(g · K)[c]	1.3[d]	1.0[e]		
Thermal conductivity at 25°C, W/(m · K)	0.12	0.082		
Electrical				
Dielectric constant				D150
60 Hz	2.65	3.15	2.84	
1 kHz	2.65	3.10	2.82	
1 MHz	2.65	2.95	2.80	
Dissipation factor				D150
60 Hz	0.0002	0.020	0.004	
1 kHz	0.0002	0.019	0.003	
1 MHz	0.0006	0.013	0.002	
Dielectric strength at 25 μm, MV/m				D149
Short time	275	220	215	
Step-by-step	235	185		
Volume resistivity at 23°C, 50% RH, Ω	1.4×10^{17}	8.8×10^{16}	2×10^{16}	D257

(*Continued*)

have similar backbone structures, other parylenes are expected to have similar T_gs, although no measurements taken with equal care exist. Earlier reports have quoted a somewhat higher (60–90°C) range for the entire family (5). In either case, the parylenes as prepared by their VDP process are further distinguished from conventional polymers in having been generated in a medium that is at least to some extent vitreous.

During formation, the motions of the parylene polymer chains in the vitreous medium are restricted. The properties of freshly deposited parylenes,

Table 4. (Continued)

Property	Parylene N	Parylene C	Parylene D	ASTM method
Surface resistivity at 23°C, 50% RH, Ω	1×10^{13}	1×10^{14}	5×10^{16}	D257
Barrier				
Water absorption, %	< 0.1	< 0.1	<0.1	D570
Water vapor transmission at 37°C, ng/(Pa · s · m) [f]	0.0012	0.0004	0.0002	E96
Gas permeability at 25°C, amol/(Pa · s · m) [g]				D1434
N_2	15.4	2.0	9.0	
O_2	78.4	14.4	64.0	
CO_2	429	15.4	26.0	
H_2S	1590	26.0	2.9	
SO_2	3790	22.0	9.53	
Cl_2	148	0.7	1.1	

[a] To convert GPa to psi, multiply by 145,000.
[b] To convert MPa to psi, multiply by 145.
[c] To convert J to cal, divide by 4.184.
[d] Refs. 25 and 30.
[e] Ref. 34.
[f] To convernt ng/(Pa · s · m) to g·mil/(100 in^2 · day) at 90% RH, 37°C, multiply by 1240.
[g] To convert amol/(Pa · s · m) to cm^3 (STP) mil/(100 in^2 · day · atm), multiply by 0.498.

therefore, generally differ from those that have been aged or annealed. Restricted polymer chain motion during VDP severely limits their ability to organize into crystallites, and consequently freshly deposited parylenes are metastable. With the passage of time, and sooner if heated, they will reorganize into a thermodynamically more satisfactory configuration, increasing crystallinity. Certain physical properties of freshly deposited parylenes therefore can be expected to change upon aging or annealing. Of the commercial materials, Parylene C, perhaps as a result of the asymmetry of its repeat unit, is particularly subject to modifications subsequent to its initial formation.

Mechanical Properties. Many of the mechanical properties of the parylenes are similar to those of other conventional plastics. The values in Table 4 are typical of those quoted for the parylenes, but in any particular case can vary with aging or annealing. In an outstanding instance of this effect, the 200% elongation quoted for Parylene C is the value commonly observed on the freshly deposited material. It drops dramatically as crystallinity builds. In general, an increase in crystallinity with aging or annealing results in a lowering of elongation to break and an increase in modulus and strength. The variation in mechanical rigidity of the parylenes as temperature increases is shown in Figure 5, which plots the logarithm of the secant modulus, a measure of stiffness, vs temperature. Generally, a small decrease in rigidity occurs near ambient temperature as the glass transition is traversed. Significant rigidity is then retained up to the point where the crystallites begin to melt.

It has been reported that Parylene N is deposited in a state of compressive stress (40). The inherent stress is 18 MPa (2300 psi) and is invariant with

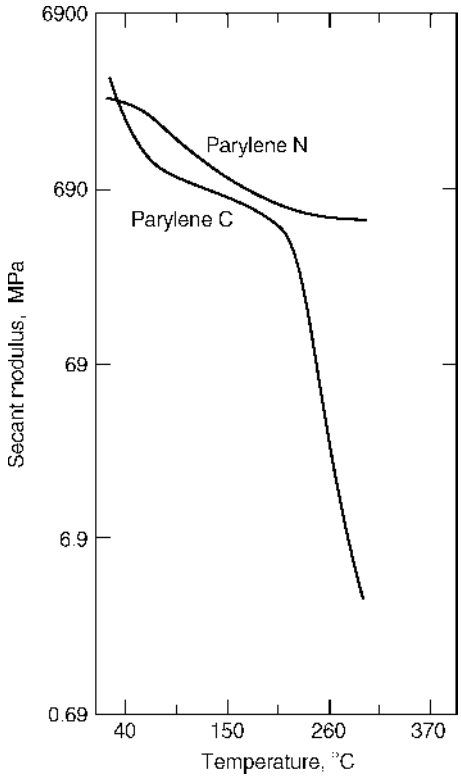

Fig. 5. Stiffness–temperature behavior of Parylenes N and C. To convert MPa to psi, multiply by 145.

thickness. This congenital compressive stress can be removed and rendered tensile by a thermal cycle.

Electrical Properties. The bulk electrical properties of the parylenes make them excellent candidates for use in electronic construction. The dielectric constants and dielectric losses are low and unaffected by absorption of atmospheric water. The dielectric strength is quoted for specimens of 25 μm thickness because substantially thicker specimens cannot be prepared by VDP. If the value appears to be high in comparison with other materials, however, it should be noted that the usual thickness for such a measurement is 3.18 mm. Dielectric strength declines with the square root of increasing thickness. Viewed in this light, the dielectric strength of the parylenes is good, but not outstandingly high. The bulk resistivities are advantageously high because of the purity of the parylenes, their low moisture absorption, and in particular their freedom from the trace ionic impurities present in conventional polymers as residues. Such impurities might be the residues of the catalysts necessary for their formation. The surface resistivities are advantageously high in part because of their low affinity for atmospheric water. The experimental dependence of the electrical properties on temperature is shown in Figure 6.

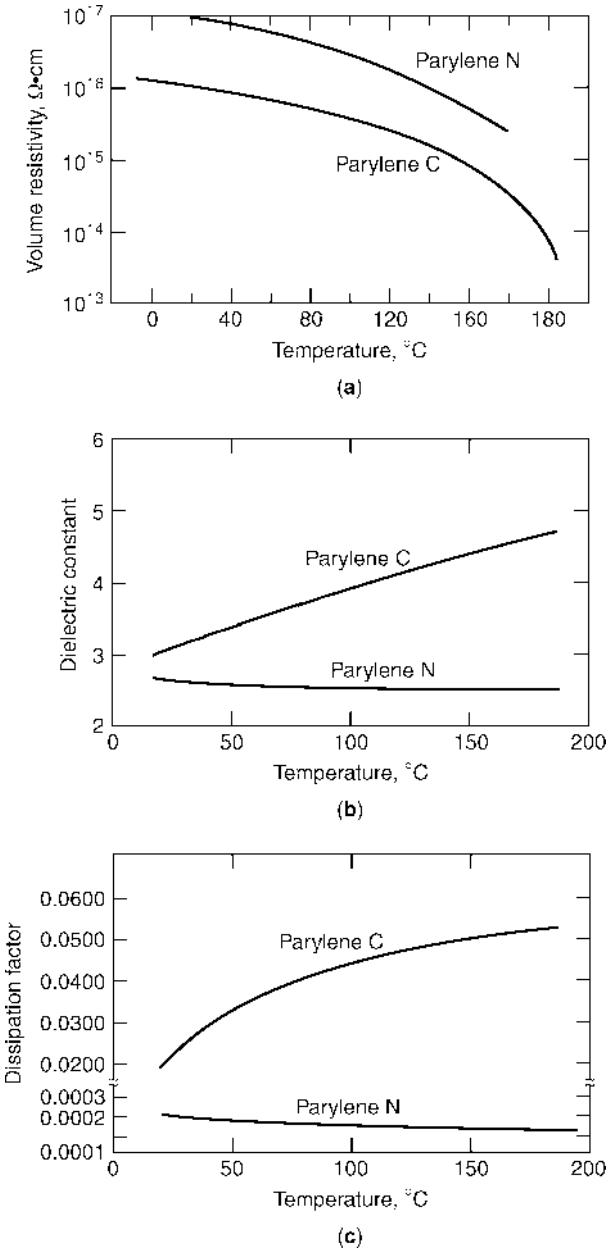

Fig. 6. Variation of electrical properties of Parylenes N and C with temperature.

The question of the value of the dielectric constant of the parylenes in the gigahertz range of frequencies is often of interest to designers of high frequency circuitry. Making such measurements on low loss, low dielectric constant, thin films is experimentally difficult, and no reliable data exist as of this writing (ca 1997). Fortunately, however, an indicator is available. For nonabsorbing,

Table 5. Dielectric Constants and Refractive Indexes of Parylenes

Parameter	Parylene N	Parylene C	Parylene D
Dielectric constant			
60 Hz	2.65	3.15	2.84
1 kHz	2.65	3.10	2.84
1 MHz	2.65	2.95	2.80
Refractive index			
n_D line	1.661	1.639	1.669
Squared	2.76	2.69	2.79

nonmagnetic materials such as the parylenes, the well-known Maxwell relation applies: at any particular frequency, the square of the index of refraction equals the relative permittivity, or dielectric constant (41). The refractive indices for the parylenes at the sodium D line (589 nm), a visible wavelength that corresponds to a frequency of 510 THz (5.1×10^{14} Hz), are shown in Table 5, along with their squares and the lower frequency measurement of dielectric constant. Because by virtue of the Maxwell relation the dielectric constants of the parylenes at the much higher frequency of visible light are close to those observed by conventional means, it seems likely that when reliable gigahertz dielectric constant measurements on the parylenes become available, similar values will be obtained.

Thermal Properties and Endurance. The heat capacity or specific heat, C_p is a quantity of theoretical thermodynamic significance as well as of practical importance. It has been determined for Parylene N over the temperature range of 220 to 620 K (−53 to + 347°C) (27,32).

Figure 7 gives the results of an experiment in which free-standing films were exposed to constant elevated temperatures in air-circulating ovens for periods of weeks to months; the failure criterion was a 50% loss in tensile strength. Because the test is destructive, each data point (failure time at a given temperature) required many specimens. In the degradation of many polymers, including the parylenes, tensile strength is maintained until chain scission has reduced molecular weight to the point at which entanglement is no longer a factor in determining physical properties. Beyond that point it drops abruptly. Thus despite the relatively large variance in tensile strength measurements, the 50% loss criterion allows a reasonably precise location of end of useful life on a log time scale (Fig. 8). The data of Figure 7 suggest that Parylenes N, C, and D perform in air without significant loss of physical properties for 10 years at 60, 80, and 100°C, respectively. Clearly, these data can justifiably be made to serve only as a guide for considering the parylenes for a specific application. Questions of thermal endurance tend to have no clear-cut answers. In situations where performance may be marginal, there is no substitute for retesting under conditions more directly relatable to the application.

Degradation. The most important mode of degradation for parylenes is oxidative chain scission. Significantly, hydrolytic degradation is chemically impossible. Oxidative degradation limits the use of parylenes at elevated temperatures in many common applications. Figure 9 shows the effect of exposure to elevated

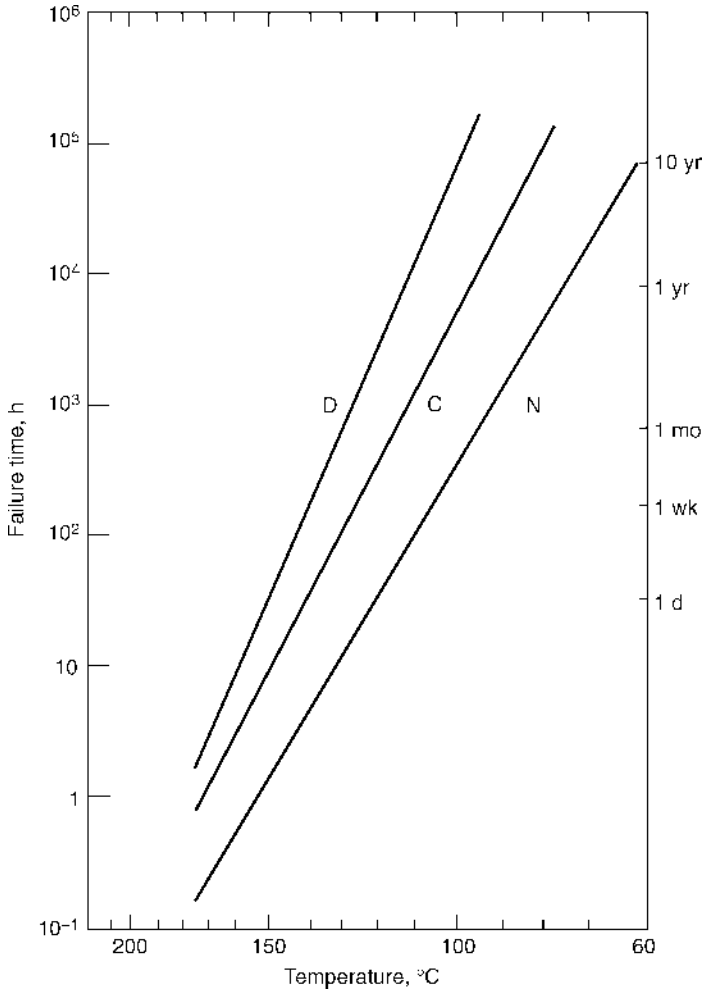

Fig. 7. Useful lifetime of Parylenes N, C, and D as a function of temperature in air. Failure = 50% loss in tensile strength.

temperature in air or in vacuum on elongation to break, an indicator of toughness or lack of brittleness. The data are given for Parylene C, which suffers substantial change in mechanical properties as the freshly deposited material is annealed. Aging in air at 150°C for ca 100 h causes the elongation to break to drop from its initially very high value to 0, at which point the specimen is mechanically useless. Aging in vacuum at yet higher temperatures (265°C) for a similar length of time gives a stronger, more rigid, stabilized material with 15% elongation at break, the result of annealing.

For applications where oxygen can be excluded, eg, in outer space, Figure 10 shows that 10-year-use projections exceed 200°C for Parylenes N, C, and D. Conventional antioxidants, incorporated during or after VDP, can extend the life of the parylenes at elevated temperatures (42,43).

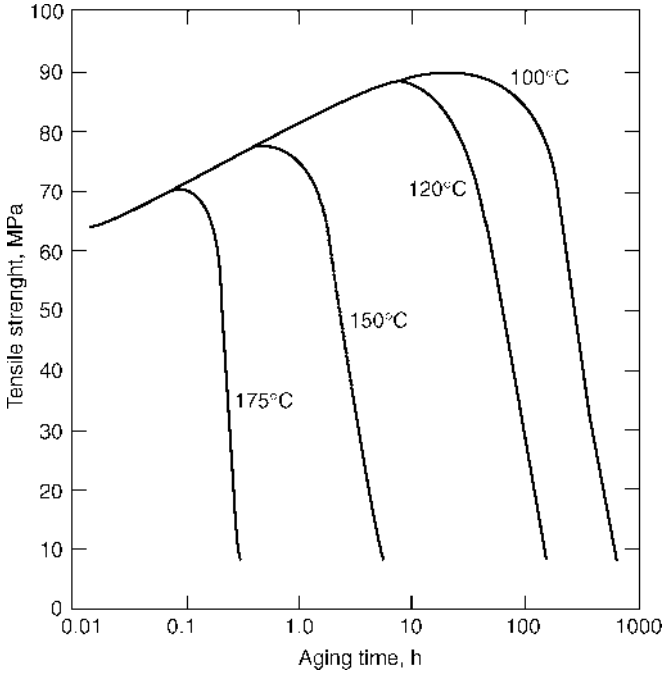

Fig. 8. Tensile strength of Parylene C on aging at elevated temperature. To convert Pa to psi, multiply by 0.145×10^3.

Another factor in oxidative degradation is ultraviolet radiation, of which sunlight is a rich source. The oxidation of parylene appears to be enhanced by ultraviolet radiation. Ozone may play a mechanistic role in the ambient-temperature exposure of parylenes to ultraviolet radiation in the presence of oxygen. For the best physical endurance, exposure of the parylenes to ultraviolet light must be minimized.

Barrier Properties. The bulk barrier properties of parylenes are among the best of organic polymeric coatings. The data in Table 4 are the results of tests conducted some time ago, and certain entries seem unaccountably high, particularly the values for the permeability of Parylene N by SO_2 and H_2S. Because film damage might have been the cause of these high test values, experimental confirmation is advisable. More recent values for water transport rates in Parylene C films are available over the temperature range of 20–55°C in a comparative study which includes Mylar A and Kapton H (44). Similar information is provided for Parylene D in a study over the temperature range of 30–80°C (45).

Spectral and Optical Properties. The parylenes do not absorb visible light, and absorb only at the shorter wavelength, high energy end of the ultraviolet range (Fig. 11). Such absorption is expected for the electronic system of the parylenes' benzene ring. Films and coatings are colorless in the visible, becoming opaque to sufficiently short wavelength uv light.

The infrared transmission spectra of Parylenes N, C, and D are compared in Figure 12. Infrared spectra can be used to distinguish among sample films of

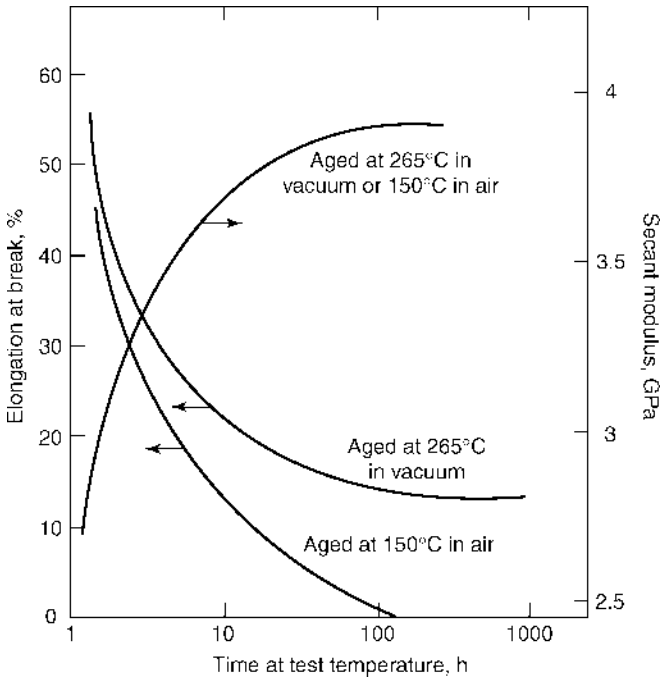

Fig. 9. Effect of temperature on the flexibility of Parylene C in air and vacuum. To convert GPa to psi, multiply by 145,000.

the three commercial materials should a practical question of identity arise. The spectra in Figure 12 are taken on films of ca 18 μm thickness, which gives a good picture of a typical organic film in the standard infrared presentation format. It is, however, thicker than normally encountered in a typical parylene application. The amount of incident light absorbed at any given wavelength is predictably less than that indicated by the ordinate of Figure 12.

Interference effects, which arise because of the extraordinary uniformity of thickness of the film over the spectrometer sample beam, superimposed on the absorption of incident light by parylene films, can be observed. Experimentally, a sinusoidal undulation of the baseline of the spectrum is seen, particularly in the spectral regions where there is little absorption by the sample. These so-called "interference fringe" excursions can amount to some 15–20% transmission and are uniformly spaced in frequency. Larger excursions indicate greater uniformity in thickness. Such fringes are seen toward the left side of the experimental spectra of Figure 12. Although interference phenomena are also encountered experimentally in the visible and ultraviolet regions, their effects have been removed in the consolidation and replotting of the data of Figure 11. In transmission spectra, at the top of the interference fringes (the wavelengths of the sinusoidal maxima), constructive interference occurs in which all incident light that is not absorbed appears for detection. At the fringe troughs (the wavelengths of the sinusoidal minima), a condition of destructive interference exists, at which a portion of the incident beam is reflected back toward the source, thereby escaping detection

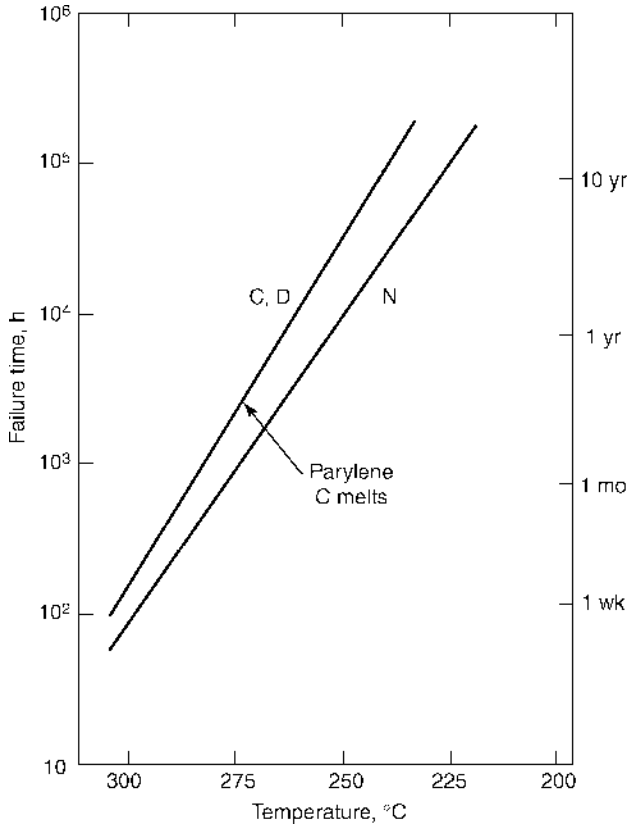

Fig. 10. Long-term effect of aging in vacuum on flexibility of Parylenes C, D, and N at elevated temperature. Failure = 50% loss in tensile strength.

even though it is not absorbed by the sample. By observing the wavelengths at which constructive interference occurs, the approximate thickness of the sample can be determined by using the expression

$$d = \frac{m\lambda_1\lambda_2}{2\,R(\lambda_1 - \lambda_2)}$$

where λ_1 and λ_2 are any two wavelengths at which interference transmission maxima (ie, constructive fringes) exist, separated by m-1 intervening constructive fringes; R is the refractive index of the sample film. The thickness d takes the units of wavelength used for λ. At any condition of constructive interference (fringe), twice the thickness times the refractive index equals an integral number of wavelengths of the incident light. That integer is known as the order of the fringe. Much more precise and accurate thicknesses may be computed from the experimental optical spectra if the order of the fringe is known and if any variation of refractive index with wavelength is taken into consideration.

Unstretched PPX films exhibit an inherent negative birefringence, the optical axis of which is perpendicular to the plane of the film. The refractive index

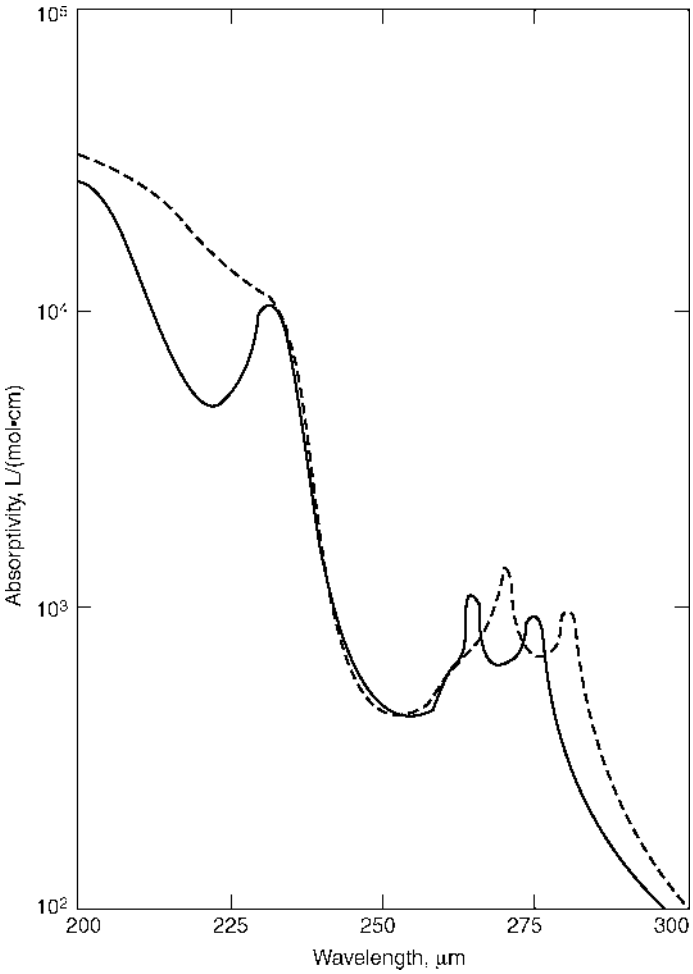

Fig. 11. Ultraviolet absorption spectra of Parylenes N (——) and C (– – –).

along the optical axis is lower than the refractive index observed in the plane of the film, the difference being $n_e - n_0 = -0.075 \pm 0.001$ (46). Where they are observed from the direction normal to the film plane, the films appear to be isotropic. Birefringence is observable only when the films are tilted, or observed in cross section. When stretched, PPX films exhibit a much greater birefringence. The stretch birefringence has an optical axis in the direction of stretch and is positive: $n_z - n_0 = +0.2$.

Surface Energy. The surface energies of Parylenes N, C, and D were measured by observing the contact angles for several standard probe liquids. All three have surface energies of approximately 45 mJ/m^2 (= dyn/cm), ie, all test liquids having less than 45 mJ/m^2 surface tension completely wet the as-deposited parylene surfaces (47).

Plasma treatments using reactive gases (N_2, O_2) as well as inert gases (Ar, He) seemed universally to lower the contact angle for water, an observation that

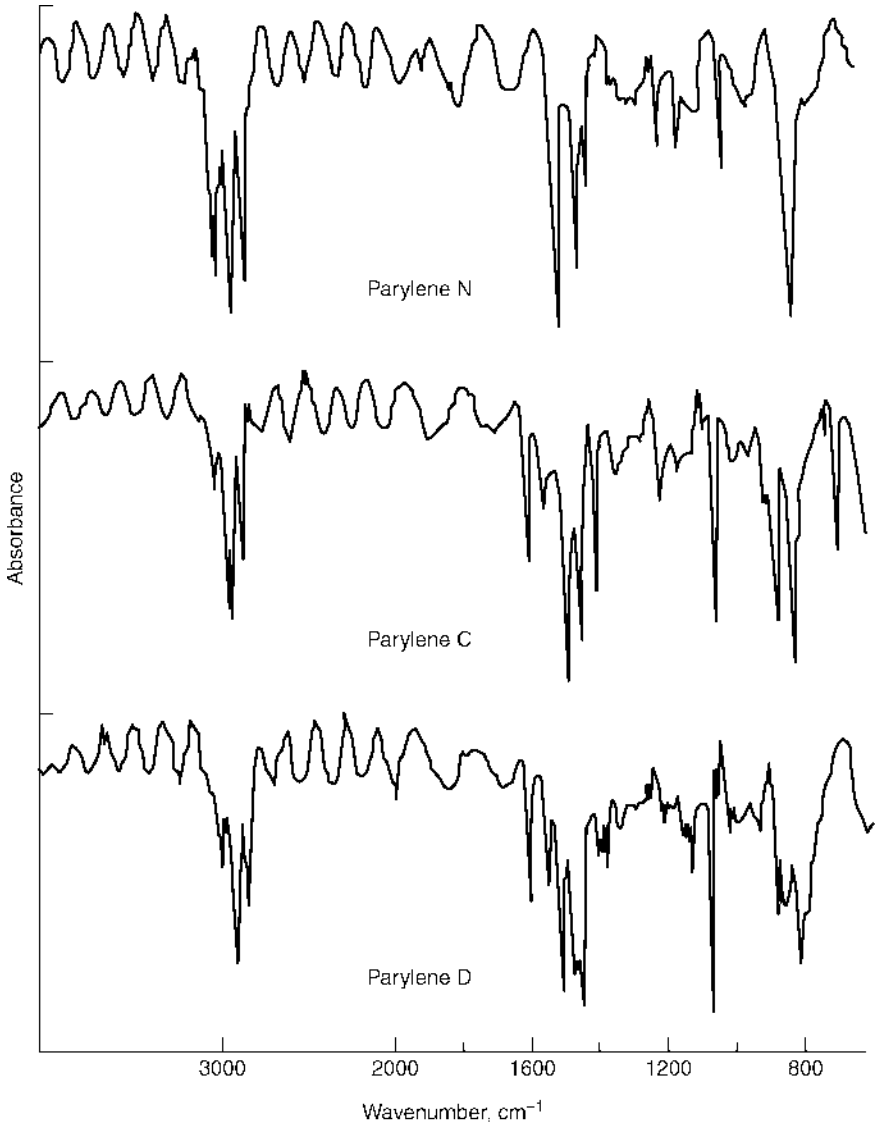

Fig. 12. Infrared absorption spectra of Parylenes N, C, and D films of 18-μm thickness.

would imply that all such treatments raise the surface energy. Reflectance spectroscopy confirmed the presence of carbonyl in all plasma-treated specimens. Surprisingly, the inert-gas-plasma treatments affected the surface energies of the parylenes more than the reactive gas plasmas did, as indicated by a water contact angle. However, the surface energies of the plasma-treated specimens universally dropped toward the original value on standing in air, but stabilized in about 1 day, without recovering the original value. Plasma treatment of parylene surfaces markedly improves the adhesion of polyurethanes, a result that could be in part, at least, the result of the surface energy change.

Crystallinity. The crystallinity of the parylenes determines two of their most important practical characteristics: mechanical strength at elevated temperatures (see Fig. 5) and solvent resistance.

In a manner typical of crystalline polymers, the crystallinity of parylenes is confined to small-submicrometer domains that are randomly dispersed throughout an amorphous continuum. Adjacent polymer chains, in order to acquire greater overall system stability, exhibit a preference to be close to one another, but the extent to which they actually can be is limited by the tangles already present. Because a given polymer chain is long enough to participate successively in several crystallites, these crystallites function as cross-links to strengthen the bulk polymer. This structural role of the crystallites is retained as temperature rises, giving the bulk polymer physical strength even above its glass-transition temperature, where the amorphous phase is changed to a low modulus, rubbery consistency. Because the crystalline domains are much more resistant to permeation than the amorphous phase, they retain their reinforcing structural role even in the presence of permeants in the amorphous phase, thus giving the parylenes their resistance to solvent attack. The crystalline content increases in freshly deposited polymer as it ages, particularly when it is heated.

Parylene N (PPX) possesses a singularly complex crystalline morphology in which two distinct crystalline modifications are recognized. When deposited in the usual VDP fashion, the crystallites tend to be mostly of the α modification. On annealing at a temperature of about 220°C, the α form is converted to the β modification. This transition was originally thought to be irreversible, but studies have demonstrated that it can be made reversible (48). The crystalline phase undergoes further modifications at higher temperatures before reaching its melting point of 420°C; these modifications have not been fully explored. The detailed crystal structures of the α ($a = 592$ pm, $b = 1060$ pm, $c = 655$ pm, $\beta = 134.7°$ for two monomer repeat units per cell) (49) and β ($a = b = 2052$ pm, $c = 655$ pm, $\gamma = 120°$, for 16 monomer repeat units per cell) (50) modifications have been determined.

In Parylene C, the single crystalline form observed is very similar to the α form of Parylene N. Its detailed crystal structure has been determined [$a = 596$ pm, $b = 1269$ pm, c (chain axis) $= 666$ pm, $\beta = 135.2°$] (51). X-ray studies on the crystal structure of Parylene D have not been reported.

The diffraction pattern produced where X-rays or electrons are directed perpendicularly at the film is the familiar pattern of concentric rings (a powder pattern) produced where the crystallites within the sample are randomly oriented. When the incident beam is directed at an angle to the plane, however, the uniform rings break up into bands or spots, indicative of a preferred orientation of unit cells. Tilted electron diffraction results (52) demonstrate that in Parylene N there is a preference for the ⟨100⟩ face of the unit cell to lie in the film plane. Because the polymer chain is oriented along the c axis of the unit cell with the benzene rings lying approximately in the plane of the ⟨100⟩ face, it follows that, at least among molecules within crystallites, there is a preference for the polymer chains and benzene rings to be oriented in the film plane. Within the film plane, however, the direction of the chains is random. That benzene rings are preferentially oriented in the plane of the film is supported by negative birefringence and by the Raman spectrum of the polymer (53).

Table 6. Swelling on Immersion in Various Solvents for the Commercial Parylenes at Room Temperature

	Volume change, %		
Solvent	Parylene N	Parylene C	Parylene D
Dichlorobenzene	0.2	3.0	1.8
Mixed xylenes	1.4	2.3	1.1
Monochlorobenzene	1.1	1.5	1.5
2,4-Pentanedione	0.6	1.2	1.4
Trichloroethylene	0.5	0.8	0.8
Acetone	0.3	0.9	0.4
Pyridine	0.2	0.5	0.5
Isopropyl alcohol	0.3	0.1	0.1
Freon	0.2	0.2	0.2
Water, deionized	0.0	0.0	0.0

Solvent Resistance. At temperatures below the melting of the crystallites, the parylenes resist all attempts to dissolve them. Although the solvents permeate the continuous amorphous phase, they are virtually excluded from the crystalline domains. Consequently, when a parylene film is exposed to a solvent a slight swelling is observed as the solvent invades the amorphous phase. In the thin films commonly encountered, equilibrium is reached fairly quickly, within minutes to hours. The change in thickness is conveniently and precisely measured by an interference technique. As indicated in Table 6, the best solvents, specifically those chemically most like the polymer (eg, aromatics such as xylene), cause a swelling of no more than 3%.

Applications

Although there is ample evidence in the literature that several industrial groups had a research interest in the PPXs during the 1950s, industrial exploitation was for the most part prevented by the obstacle the parylenes present to conventional fabrication technologies. Because they are generally insoluble in most solvents, even at elevated temperatures, they cannot be used as solvent-based coatings; neither can they be cast as films nor spun as fibers from solution. Because of their high crystalline melting points, melt-working (molding, extrusion, calendering, etc) is also difficult. Yet it is often just these features of solvent resistance and high temperature mechanical strength that constitute the advantages of PPX materials.

It had been recognized from the outset that polymer forms spontaneously on surfaces exposed to the gaseous monomer PX, but the recognition of VDP as an industrially viable process was not immediate. The public announcement, in 1965, of the convenient generation of pure monomer by the Gorham process from the dimer marked the beginning of a period of a gradually increased understanding and acceptance of the unique features of the parylenes.

As a coating technique, VDP offers certain advantages over other coating techniques such as brushing, dipping, or spraying. These advantages stem principally from the fact that the solid coating is formed from the gaseous monomer directly, without an intermediate liquid stage. As a result, the forces of surface tension, which would cause a pulling away from sharp edges and a filling in of troughs in conventional methods, are not operative and therefore do not affect the cross-sectional profile of VDP coatings. Coatings of PPX grow from the substrate surface outward, producing a conformal layer of uniform thickness. Extensive tests (54) demonstrate that the coating so formed is pinhole-free at thicknesses well below those achievable with conventional coating techniques (see COATINGS).

The PPX coatings are formed spontaneously on substrates at or near room temperature; a cure cycle at elevated temperature is not necessary to complete the polymerization chemistry. The substrate need not be subjected to any temperatures above ambient, and no further time is required beyond that needed for the growth of the film. Because the polymerization is spontaneous, no catalyst is necessary. Catalysts that promote other polymerizations are often ionic or ionogenic and, to the extent that they remain in the coating after cure, their residues are capable of participating in charge mobilization, with resulting detrimental effects in electrical properties. Because the coating is formed at room temperature, stresses that might be induced by differential thermal expansion between the temperature of cure and room temperature are avoided. Because PPX coatings are generally much thinner than conventional coatings, any stress that they impart on the substrate is proportionately less.

Circuit Boards. The most important application of parylenes is as a conformal coating for printed wiring assemblies. The parylene VDP process has the ability to produce a continuous, thin, truly conformal coating on geometrically complex, delicate articles. These coatings provide excellent chemical resistance, especially to solvent attack, and resistance to fungal attack. In addition, they exhibit stable dielectric properties over the wide range of temperatures in which military boards are expected to perform, as well as low dielectric constants, which together with thinness minimize the undesirable loading of high frequency tuned circuits. The reliability with which the process operates substantially reduces labor-intensive touch-up and inspection operations otherwise required for conventional coatings.

Parylene C was included among the earliest MIL-I-46058 (55) qualified coatings (as type XY) and has since enjoyed a reputation for superior performance in protecting and preserving the operation of electronic circuits against the detrimental effects of their operating environments. Environmental water is, of course, chief among these adverse factors. Although the rate of water transport through a parylene coating is finite and well documented, the hydrophobic nature of the parylenes makes them excellent barriers to penetration by ionic species. Once the circuit board is clean to the extent that surface ionic contamination is minimized and weak surface layers are eliminated, the parylene coating adheres well to the organic substrate material between the conductors. Ionic conduction along the coating–substrate interface, which would otherwise impair electrical performance in the short run and promote galvanic corrosion and dendritic growths in the long term, is minimized.

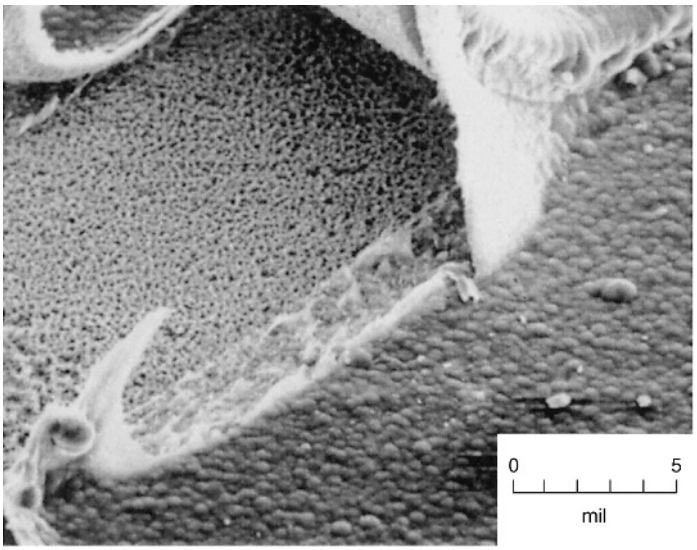

(a)

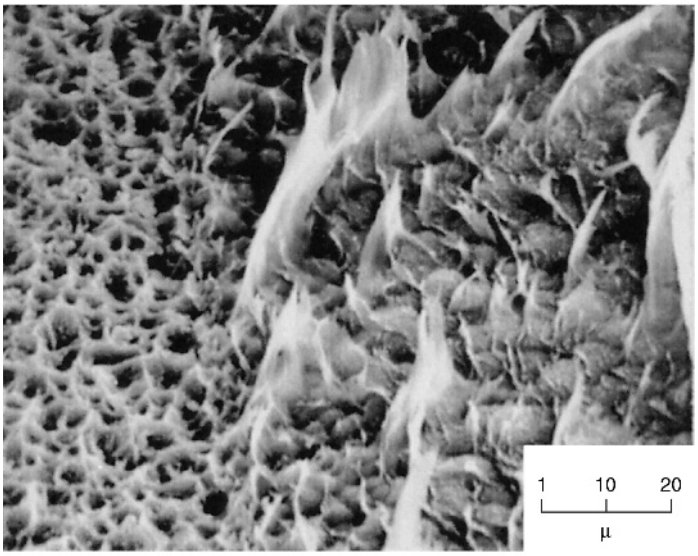

(b)

Fig. 13. Scanning electron microscope (SEM) photographs of Parylene C-coated printed circuit conductor peeled to demonstrate the adhesion of the coating to the substrate. To convert mil to meters, multiply by 2.54×10^{-5}.

The SEM photographs of Figure 13 show a conventional FR-4 printed wiring board, coated with an 8-μm film of Parylene C, on which the copper conductor trace has been peeled back. The peeling reveals the rough texture of the epoxy gel coat produced during the original lamination against etched copper in order to achieve maximum laminate peel strength. The region covered with Parylene

C in Figure 13 was of the same texture before coating, a fact that, along with parylene's conformality, accounts for much of the texture in the upper surface. Of particular interest is the mode of Parylene C failure as the conductor is peeled. There is evidence of substantial yield prior to failure in the filamentous nature of the failed regions and the web of stretched Parylene C at the apex of the peel. Furthermore, all tensile failure is cohesive, ie, the adhesion of Parylene C to the underlying epoxy gel coat is greater than the cohesive strength within the coating material. The higher magnification (Fig. 13b) shows the line of demarcation between the regions covered with copper and with Parylene C prior to the peel, revealing that the breadth of the failed Parylene C exceeded by far its original thickness.

The circuit board with all its components attached presents a variety of surface types for the conformal coating, ranging from plastics through ceramics and glass to metals, in particular aluminum and tin–lead solder. No single mechanism for adhesion can serve all sites effectively. Of particular importance for the epoxy board are the surfaces between conductor traces. Because epoxy is an organic material that is permeable to PX monomer, the growth mechanism of the parylene coating provides adhesion by the interpenetrating network it produces. Care must be taken in cleaning the board surface before coating of leakage-producing ionic contamination as well as organic soils, which interfere with a secure xylylene interpenetration lock. In the cases of ceramic and metal surfaces, monomer penetration is impossible, and other adhesion mechanisms must be engaged. Adhesion to metals is often not essential to the performance of the board, but it is usually desirable. Adhesion to ceramics or glasses is vital in situations where electrical leakage across their surfaces is to be minimized, and is particularly necessary in hybrids. Because the outside surface of common metals is an adherent coating of native oxide, adhesion to metals, ceramics, and glasses can often be achieved using the same approach, ie, treatment with a compatibilizing layer of an organosilane (56). γ-Methacryloxypropyltrimethoxysilane (A-174) is the organosilane most commonly used for the purpose. In action, the trialkoxysilane end of the molecule hydrolyzes and bonds covalently with the oxide on the substrate surface. The methacrylic end of the molecule provides a hydrophobic surface to accommodate parylene deposition, as well as the opportunity to form covalent bonds with the *p*-xylylene polymer through its double bond. It is, of course, essential to provide no more than a monolayer of the organosilane. Water plays an important role in the bonding chemistry between the organosilane and the oxide, and the treatment is often applied from aqueous solution. An alternative treatment is by exposure of the substrate circuit boards to pure gaseous organosilane (57), a process which often takes several days to develop optimum adhesion.

Fluorescence is frequently required in a circuit-board coating to assist inspection of the board after it is coated. Fluorescent parylene coatings can be prepared by admixing a fluorescent agent into the dimer charge. The agent must have just the right volatility to pass through the process and deposit with the polymer, yet it must be sufficiently stable that it survives the conditions it encounters during the process. Agents that have been used in this manner are anthracene and certain fluorescent whiteners of the Calcofluor family, the 7-dialkylamino-4-methylcoumarins.

Hybrid Circuits. The use of parylenes as a hybrid circuit coating is based on much the same rationale as its use in circuit boards. A significant distinction lies in obtaining adhesion to the ceramic substrate material, the success of which determines the eventual performance of the coated part. Adhesion to the ceramic must be achieved using adhesion promoters, such as the organosilanes.

In the coating of hybrid circuits, parylene provides certain other advantages. In certain technologies, chips are mounted with substrate clearances of as little as 10 μm. The parylene VDP process penetrates this narrow space, coating the underside of the chip as well as the substrate opposite it. Conventional coatings cannot flow into such a narrow space and must rely on simply sealing it off, leaving an air pocket under the chip. Where the fabrication technology uses wire bonds to connect the chips with substrate conductor patterns electrically, the fine (25-μm dia) wires are coated by the parylene VDP process to the same thickness as all other surfaces. A marked increase in wire-bond strength in pull tests on coated hybrids is observed. The increase in strength can be attributed to the strengthening effect of the coating on the wire (which typically exceeds in cross section the amount of metal in the wire) or to a reinforcement of the welded junction to the chip pad or substrate conductor.

A hybrid solid-state relay needed for a NASA space experiment underwent redesign to provide 2500-V dc isolation, input-to-output, while undergoing temperature cycling from -120 to $+180^\circ$C, as detailed in an instructive published case history (58). The electrical isolation requirement was met only by using a conformal coating, although several conventional coatings were evaluated along with parylene. These stresses in the thicker conventional coatings associated with temperature excursions resulted, in all cases other than parylene, in the rupture of the circuitry and the functional failure of the relay.

During the manufacture of hybrid circuits, it is possible to generate small metallic fragments such as wire chips and solder balls. If they are not removed before hermetic packaging, they can disrupt performance of the unit at some future time. In certain aerospace or military applications where no physical replacement of the unit is possible, such a failure could mean the loss of a mission. A program intended to improve the reliability of hermetic packages in critical systems concluded by finding a solution to this problem by applying a parylene coating to the inside of the hybrids. The coating confers electrical insulation to all surfaces and tends to anchor any loose particles; it also confers nonconductance should they break loose from their moorings. From the standpoint of coating technology, the most interesting part of this solution to the particle-immobilization problem is the throwing power, demonstrated by the fact that the entire internal surface of the hybrid is coated through a 0.5–1.0-mm hole in the lid of the hermetic package (59).

Semiconductors. The distinctive conformality of parylene is often regarded as a handicap for meeting the requirements of an interlayer dielectric (ILD) in large-scale integration (LSI) multilevel interconnection systems. After many layers of successive patterning, a planarizing procedure is very much needed, not a procedure that would replicate the existing lumpiness. A polyimide, the first organic compound to be used in a commercial semiconductor structure, was selected for this application (60), because of the planarization inherent in its spinning application procedure. However, because parylene offers distinct advantages in purity and thickness control and low moisture absorption (particularly

in comparison to the polyimides), it receives continued attention in the search for new fabrication techniques (61–63). Recognition of the need to lower the dielectric constant of ILD insulating materials as a means of improving device performance has generated a renewed interest in organics in general, and the parylenes in particular. To meet this opportunity, the intent to produce the dimer of the per-α-fluorinated version known as Parylene AF4, poly(α,α,α',α'-tetrafluoro-*p*-xylylene) [74952-03-7], has been announced (64). In addition to offering a dielectric constant in the vicinity of 2.35, its thermal stability is such that it can withstand back-end-of-line processing steps at temperatures up to 450°C without perceptible weight loss.

In an interesting extension of the conventional solid-state device concept, where a thin film covers the channel of a field-effect transistor (FET), the electron current in the channel may be made to respond to changes in the chemical environment on the opposite side of the film. Thus a silicon nitride film on a channel gives an ion-selective FET (ISFET) that responds to the pH of a solution with which it is in contact. The hydrophobic nature of parylene, on the other hand, enables the channel it covers to be independent of solution composition, and such a channel can be used as a reference electrode. An important advantage of parylene in this context is the thinness with which it can be deposited as a continuous film. The gate coatings are 0.1 μm thick, a thinness required if the sensor is to have a speedy response. An experimental probe-type all-solid-state pH sensor has been demonstrated (65). It was also demonstrated that chemically modifying the parylene surface with crown ether compounds can give an ISFET (known as a CHEMFET) that responds to potassium ion concentration.

Sensors for physical effects are also fabricated using standard semiconductor technology. A notable example is a silicon membrane pressure transducer, which, among its many other uses, is currently employed as a manifold pressure transducer in automobiles (66). The thin membrane of single-crystal silicon was prepared by etching most of the wafer thickness away, into which a resistive Wheatstone Bridge network that enables an electrical readout of the membrane's physical strain while flexing had previously been diffused. Although it is desirable to insulate the membrane electrically from the medium it measures, it is also desirable to do so without affecting the elasticity of the membrane, so that it retains its calibration of electrical output vs input pressure. A thin coating of Parylene C easily accomplishes both. In an inversion of roles, these same pressure transducers were used to sense the stresses imparted to coated substrates by a variety of MIL-I-46058C qualified coating materials (67). Whereas all other coatings, as a result of their cure shrinkages acting through their greater thicknesses modified by their assorted elastic moduli, affected sensor calibration in all cases, the presence of 13 μm of Parylene C was barely detectable.

Capacitors. The outstandingly low dielectric loss of parylenes make them superior candidates for dielectrics in high quality capacitors. Furthermore, their dielectric constant and loss remain constant over a wide temperature range. In addition, they can be easily formed as thin, pinhole-free films. Kemet Flatkaps are fabricated by coating thin aluminum foil with Parylene N on both sides and winding the coated foils in pairs (68).

Parylenes are also used to coat the rotor and stator plates of miniature variable-air-gap tuning capacitors (69). Coating the plate raises the voltage that must be applied between two parallel plates for a discharge to occur in the air

gap. Thus, a closer plate spacing is permitted, and a smaller unit having the same electrical function can be built. This is also beneficial in improving design capacitance per unit volume. Compared to the alternative of interleaving dielectric films between the plates, the coated-plate technique offers the advantages of simplicity in assembly as well as reliability of the unit. Uniformity and thickness control are of paramount importance in this case.

The Bathythermograph. The thermistor sensing probe of a disposable bathythermograph is coated with parylene. This instrument is used to chart the ocean water temperature as a function of depth. Parylene provides the needed insulation resistance and is thin and uniform enough to permit a rapid and accurate response to the temperature of the surrounding salt water (70).

Miniature Electrical Components. In the manufacture of miniature transformers and motor armatures, it is often necessary that the winding be electrically isolated from the bobbin. The insulating varnish of fine copper wire often does not survive the rigors of the winding operation, and, particularly in the case of the smaller devices, the bobbin requires insulation. However, a thicker insulation than is absolutely necessary takes up space that otherwise could be used for more turns of wire. Thus, thickness control in the coating of the bobbin means better performance of the finished device. Parylene is used in the manufacture of high quality miniature stepping motors, such as those used in wristwatches, and as a coating for the ferrite cores of pulse transformers, magnetic tape-recording heads, and miniature inductors, where the abrasiveness of the ferrite is particularly damaging. In the coating of complex, tiny objects such as these, the VDP process has an extra labor-saving advantage. It is possible to coat thousands of such articles simultaneously by tumbling them during the VDP operation (71).

Medical Uses. Under the auspices of the National Institutes of Health Artificial Heart program (72), Parylene C received considerable attention as a component of a novel scheme for achieving blood compatibility in a flexible pump chamber wall by anchoring the endothelial tissue of the host to it. A microfiber nonwoven fabric anchored to the flexible wall by an overcoating of Parylene C provides scaffolding for cellular ingrowth (73). Although the scheme is not used today, the program contributed a significant amount of favorable biocompatibility data on Parylene C, particularly in the area of cytotoxicity (74). Parylene's minimal perturbance of cells growing in its vicinity can be ascribed to its high purity and its ability to slow down impurity species that might otherwise diffuse out of a substrate material. The corrosive biological environment does not affect parylene, which cannot be hydrolytically degraded.

Parylene's use in the medical field is linked to electronics. Certain pacemaker manufacturers use it as a protective conformal coating on pacemaker circuitry (75). The coated circuitry is sealed in a metal can, so that the parylene coating serves only as a backup should the primary barrier leak. There is also interest in its use as an electrode insulation in the fabrication of miniature electrodes for long-term implantation to record or to stimulate neurons in the central or peripheral nervous system, as the "front end" of experimental neural prostheses (76). One report describes the 3-year survival of functioning parylene-coated electrodes in the brain of a monkey (77).

Artifact Conservation. As books age, the paper of their pages becomes brittle. A relatively thin coating of parylene can make these embrittled pages

stronger (78). Parylene coats the fibers conformally and welds them together at crossing points, providing added structural strength. Although parylene does little to retard the chemical processes that make the paper brittle, it restores some physical strength. Furthermore, the parylene coating can be applied to the existing book without disturbing the binding, thus saving the labor of disassembly. The concept has been extended to other fragile artifacts, such as fabrics.

Laser Fusion Targets. In the search for new energy sources, some research is directed toward the thermonuclear fusion of deuterium–tritium (DT) mixtures. In laser-driven inertial confinement fusion, a single laser pulse crushes a target containing the DT fuel to one thousandth of its normal volume and achieves a temperature of 10^8 K. The energy per pulse in current lasers is small, which limits the experimental targets to a diameter of about 100 μm. The outer layer of the spherical target absorbs the omnidirectionally incident laser energy and ablates as it is thermally destroyed, imparting a reactive compressive force on the inner portions of the target, thus compressing it. The dimensions of the outer layer are central to achieving hydrodynamic stability during the implosion process. Concentricity, sphericity, and thickness (ca 10 μm) must be better than 5%, and surface roughness must be no greater than 0.1 μm. Parylene is a leading contender for the outer layer, and considerable ingenuity has been applied in several methods for experimental target fabrication (79,80).

Contamination Control. In a number of developing technologies, contamination by small particles is a serious problem. To the extent that the generation of freely mobile particles is reduced by securing them to their initial locations, parylene coating of critical system components can be useful. In the manufacture of Winchester disk drive units, large magnesium castings are coated with parylene. This increases system reliability (81), presumably because the large surface within the sealed unit, if not coated, is capable of producing particles of the same destructive potential that the system seal is supposed to prevent from entering.

Barrier Coating. The bulk permeabilities of parylenes, although finite, are generally lower than those of most other types of plastic materials. The further advantage of coating continuity inherent in the VDP process allows the parylenes to realize the benefits of their low permeabilities to the fullest, without leakage of the permeant through coating defects such as cracks or pinholes. Thus the parylenes are uniquely suited as protective encapsulants or barrier coatings (see BARRIER POLYMERS).

Where pieces of lithium metal are coated with Parylene C, and their subsequent reaction to water vapor follows, the steady-state generation of hydrogen can be controlled exactly by the rate of water transport through the coating (82). Pellets of nitronium perchlorate, a potent oxidizer useful as a solid-rocket propellant component, can be rendered less moisture-sensitive and compatible with organic binders by applying a coating of Parylene C (83). The absorption of water by particulate ammonium nitrate could be reduced tenfold by as little as a 0.7% coating of Parylene C (84). Particles of ammonium nitrate remain free-flowing after long exposures to ambient conditions of temperature and moisture when coated with as little as 0.2% Parylene C. The thermal sensitivity of Parylene C–coated ammonium nitrate (time to explosion) is unaffected by the coating. On the other hand, the 1.5–8% coating of particulate military-grade RDX explosive,

cyclotrimethylene trinitramine, produced significant changes in physical and explosive properties. The changes were attributed to the chemical properties of the protective Parylene C coating and to the virtual absence of encapsulated agglomerates of RDX crystals (85).

In a recent report (86), a 150–200 mg/cm^2 Parylene C coating provided protection against moisture uptake by three-phase—polyimide, microballoons, and air—syntactic foams. In a previously reported coating of a similar foam, the stated purpose was strengthening (87).

Corrosion Control. The oxygen and water permeability and thinness of the parylene coatings notwithstanding, the rate of corrosion of a coated surface is often significantly reduced. In one case, the corrosion of a plated wire memory was reduced to the point where no bits were lost during 30 cycles of a MIL STD 202D-106C test by overcoating the permalloy plating, which had been previously coated with a Ni–P anticorrosive layer, with Parylene N (88).

Dry Lubricant. The static and dynamic coefficients of friction for the parylenes are low and virtually the same. This feature is an advantage in the use of a parylene coating as a dry lubricant on the bearing surfaces of miniature stepping motors. Coating a threaded ferrite core significantly reduces the abrasion to coil forms (89).

Pellicles and Membranes. By separating the coating from the substrate after deposition, the unique coating features of parylenes, especially continuity and thickness control and uniformity, can be imparted to a free-standing film. In practice, a sheet of smooth glass is coated with a layer of a hygroscopic substance before being coated with parylene. The film is then lifted from the glass by water immersion to activate the release agent. In this manner, uniform, continuous, free-standing parylene films with thicknesses of less than 0.1 μm can be prepared. Applications of such films include optical beam splitters (90), a window for a micrometeoroid detector (91), a detector cathode for an X-ray streak camera (92), windows for X-ray proportional counters (93), a charge stripper for converting a portion of the H-output beam of a 50 MV LINAC to neutral H^0 for diagnostic purposes (94), and a massless support for projectile abrasion testing (95); proposals have included the membrane structure for a solar sail (96).

Health and Safety

In a world increasingly conscious of the dangers of contact with chemicals, a process that is conducted within the walls of a vacuum chamber, such as the VDP process for parylene coatings, offers great advantages. Provided the vacuum pump exhaust is appropriately vented and suitable caution is observed in cleaning out the cold trap (trace products of the pyrolysis, which may possibly be dangerous, would collect here), the VDP parylene process has an inherently low potential for operator contact with hazardous chemicals.

To an experienced operator trained in the handling of industrial chemicals, the dimers present little cause for concern in handling or storage. The finished polymer coating presents even less of a health problem; contact with the reactive monomer is unlikely. In the ancillary operations, such as cleaning or adhesion promotion, the operator must observe suitable precautions. Before using the

process chemicals, operators must read and understand the current Material Safety Data Sheets, which are available from the manufacturers.

BIBLIOGRAPHY

"Xylylene Polymers" in *EPST* 1st ed., Vol. 15, pp. 98–124, by William F. Gorham and W. D. Niegisch, Union Carbide Corporation; in *EPSE* 2nd ed., Vol. 17, pp. 990–1025, by W. F. Beach, C. Lee, D. R. Bassett, and T. M. Austin, Union Carbide Corporation, and R. Olson, Nova Tran Corporation; in *EPST* 3rd ed., Vol. 12, pp. 587–626, by W. F. Beach, Alpha Metals.

CITED PUBLICATIONS

1. L. A. Errede and M. Szwarc, *Q. Rev. Chem. Soc.* **12**, 301 (1958); M. Szwarc, *Polym. Eng. Sci.* **16**(7), 473 (1976).
2. W. F. Gorham and W. D. Niegisch, in N. M. Bikales, ed., *Encyclopedia of Polymer Science and Technology*, Vol. 15, Wiley-Interscience, New York 1989, 98–124.
3. U. S. Pat. 3,342, 754 (Sept. 19, 1967), W. F. Gorham (to Union Carbide Corp.).
4. W. F. Gorham, *J. Polym. Sci. A-1* **4**, 3030 (1966).
5. W. F. Gorham, *J. Polym. Sci. A-1* **4**, 3027 (1966).
6. R. B. Woodward and R. Hoffmann, *The Conservation of Orbital Symmetry*, John Wiley & Sons, Inc., Hoboken, N.J., Chapt. 6, pp. 70, 85, and reference 96 therein.
7. L. K. Montgomery and co-workers, *J. Am. Chem. Soc.* **108**, 6004 (1986).
8. P. G. Mahaffy, J. D. Wieser, and L. K. Montgomery, *J. Am. Chem. Soc.* **99**, 4514 (1977).
9. U. S. Pat. 4,532,369 (July 30, 1985), H. Hartner (to Merck); U. S. Pat. 4,769,505 (Sept. 6, 1988), C. Lee and D. R. Bassett (to Union Carbide Corp.).
10. D. J. Williams, J. M. Pearson, and M. Levy, *J. Am. Chem. Soc.* **92**, 1436 (1970).
11. S. K. Pollak, B. C. Raine, and W. J. Hehre, *J. Am. Chem. Soc.* **103**, 6308 (1981).
12. M. J. S. Dewar, *J. Am. Chem. Soc.* **104**, 1449 (1982).
13. H. G. Gilch, *J. Polym. Sci. A-1* **4**, 438–439 (1966).
14. V. V. Korshak and S. L. Sosin, *Vysokomol. Soyed.* **7**, 232–238 (1965).
15. U. S. Pat. 3,787,382 (Jan. 22, 1974), A. N. Wright, W. R. Burgess, and E. V. Wilkus (to General Electric Co.).
16. M. Inoue, H. Fujioka, T. Sorita, and T. Tanaka, *ACS Polym. Prepr.* **28**, 332 (1987).
17. Y. Takai, Y. Hayase, T. Mizutani, and M. Ieda, *J. Phys. D.* **17**, 399 (1984).
18. J. R. Salem, F. O. Sequeda, J. Duran, W. Y. Lee, and R. M. Yang, *J. Vac. Sci. Technol.* **A4**, 369 (1986); Y. Takahashi, M. Iijima, K. Inagawa, and A. Itoh, *J. Vac. Sci. Technol.* **A5**, 2253 (1987).
19. F. E. Arnold and L. S. Tan, *31st Int. SAMPE Symp.* **31**, 1185 (1986).
20. U. S. Pat. 4,711,964 (Dec. 8, 1987), L. S. Tan and F. E. Arnold (to University of Dayton).
21. Y. Ito, S. Miyata, M. Nakatsuka, and T. Saegusa, *J. Org. Chem.* **46**, 1043 (1981).
22. Eur. Pat. 220,743 (May 6, 1987), R. Ungarelli, M. A. Baretta, and L. Sogli (to Montedison SpA).
23. Eur. Pat. 226,255 (June 24, 1987), R. Ungarelli, M. A. Baretta, and A. Malacrida (to Montedison SpA).
24. Eur. Pat. 220,744 (May 6, 1987), G. F. Pregaglia, M. A. Baretta, and A. Malacrida (to Montedison SpA).
25. C. J. Brown, *J. Chem. Soc*. 3265 (1953).
26. R. H. Boyd, *Tetrahedron* **22**, 119 (1966); D. L. Rodgers, E. F. Westrum, Jr., and J. T. S. Andrews, *J. Chem. Thermodyn.* **5**, 733–739 (1973).

27. D. E. Kirkpatrick, Ph.D. dissertation, Rensselaer Polytechnic Institute, Troy, N.Y., 1984.
28. M. Gazicki, G. Surendran, W. James, and H. Yasuda, *J. Polym. Sci., Polym. Chem. Ed.* **23**, 2255 (1985).
29. H. Sawada, *Thermodynamics of Polymerization*, Marcel Dekker, Inc., New York, 1976.
30. M. Souders and co-workers, *Ind. Eng. Chem.* **41**, 1048 (1949).
31. D. R. Stull, E. F. Westrum Jr., and G. C. Sinke, *The Chemical Thermodynamics of Organic Compounds*, Krieger, Malabar, Fla., 1987, p. 699.
32. D. E. Kirkpatrick, L. Judovits, and B. Wunderlich, *J. Polym. Sci., Polym. Phys. Ed.* **24**, 45 (1986).
33. R. W. Warfield and M. C. Petree, *J. Polym. Sci.* **55**, 497 (1961).
34. S. Y. Lazareva, *Vysokomol. Soedin.* **A21**, 1509 (1979).
35. B. L. Joesten, *J. Appl. Polym. Sci.* **18**, 439 (1974).
36. W. A. Alpaugh and D. R. Morrow, *Thermochim. Acta* **9**, 171 (1974).
37. W. F. Beach, *Macromolecules* **11**(1), 72 (1978).
38. F. E. Cariou, D. J. Vally, and W. E. Loeb, *IEEE Trans. Parts Mater. Packag.* **PMP-1**(1), 54 (1965).
39. J. F. Gaynor, S. B. Desu, and J. J. Senkevich, *Macromolecules* **28**, 7343–7348 (1996).
40. B. J. Bachman, in *Proceedings of the 1st International SAMPE Electronics Conference*, Santa Clara, Calif., June 23–25, 1987, 431–440.
41. A. von Hippel, in E. U. Condon and H. Odishaw, eds., *Handbook of Physics*, 2nd ed., McGraw-Hill Book Co., Inc., New York, 1968, Part 4, p. 104.
42. U. S. Pats. 4,163,828 (Aug. 7, 1979); 4,173,664 (Nov. 6, 1979), both to G. S. Cieloszyk (to Union Carbide Corp.); and U. S. Pat. 4,176,209 (Nov. 27, 1979), T. E. Baker, G. L. Fix, and J. S. Judge (to Raytheon).
43. T. E. Nowlin, D. F. Smith, and G. S. Cieloszyk, *J. Polym. Sci., Polym. Chem. Ed.* **18**(7), 2103 (1980). T. E. Baker, G. L. Fix, and J. S. Judge, *J. Electrochem. Soc.* **127**, 1851 (1980).
44. W. H. Hubbel Jr., H. Brandt, and Z. A. Munir, *J. Polym. Sci., Polym. Phys. Ed.* **13**, 493 (1975).
45. E. Sacher, *J. Appl. Polym. Sci.* **28**, 1535 (1983).
46. R. S. Corley, H. C. Haas, M. W. Kane, and D. I. Livingston, *J. Polym. Sci.* **13**, 137 (1954).
47. T. E. Nowlin and D. F. Smith, *J. Appl. Polym. Sci.* **25**, 1619 (1980).
48. D. E. Kirkpatrick and B. Wunderlich, *J. Polym. Sci., Polym. Phys. Ed.* **24**, 931 (1986).
49. R. Iwamoto and B. Wunderlich, *J. Polym. Sci., Polym. Phys. Ed.* **11**, 2403 (1973).
50. S. Isoda, M. Tsuji, M. Ohara, A. Kawaguchi, and K. Katayama, *Polymer* **24**, 1155 (1983).
51. S. Isoda, T. Ichida, A. Kawaguchi, and K. Katayama, *Bull. Inst. Chem. Res. Kyoto Univ.* **61**, 222 (1983).
52. W. D. Niegisch, *J. Appl. Phys.* **38**, 4110 (1967).
53. M. S. Mathur and G. C. Tabisz, *J. Cryst. Mol. Struct.* **4**, 23 (1973).
54. M. A. Spivack and G. Ferrante, *J. Electrochem. Soc.* **119**, 1592 (1969).
55. *MIL-I-46058C(6): Insulating Compound, Electrical (for Coating Printed Circuit-Assemblies)*, U.S. Dept. of Defense, Washington, D.C., Nov. 8, 1982.
56. U. S. Pat. 3,600,216 (Aug. 17, 1971), D. D. Stewart (to Union Carbide Corp.).
57. Ger. Pat. 2,737,792 (Mar. 2, 1978), D. M. Mahoney and W. F. Beach (to Union Carbide Corp.).
58. B. L. Slater, T. J. Riley, and W. Janssen, *Proceedings of the IEEE Power Electronics Specialists Conference*, Pasadena, Calif., June 11–13, 1973, 163–169.

59. V. S. Kale and T. J. Riley, *IEEE Trans. Parts Hybrids Packag.* **PHP-1**(3), 273 (1977).
60. D. L. Bergeron, J. P. Kent, and K. E. Morrett, *22nd Proceedings of the International Reliability Physics Symposium*, Las Vegas, Nev., 1984, 229–233.
61. J. M. Baker, J. H. Magerlein, and M. J. Palmer, *IBM Tech. Disel. Bull.* **27**, 4382 (Dec. 1984).
62. Jpn. Pat. 62 106456 (Nov. 1, 1986), M. Kanazawa and S. Kawanako (to Fujitsu, Ltd.).
63. W. F. Beach and T. M. Austin, *Hybrid Circ. Technol.*, 33–36 (Jan. 1990).
64. J. Wary, R. A. Olson, and W. F. Beach, in *2nd International Dielectrics for VLSI/ULSI Multilevel Insulation Conference (DUMIC)*, Santa Clara, Calif., Feb. 20–21, 1996, 207–213.
65. T. Matsuo, H. Nakajima, T. Osa, and J. Anzai, *Sens. Actuat.* **9**(2), 115 (1986).
66. R. Olson, *Electron. Packag. Prod.*, 213 (May 1980).
67. R. Olson, *Circuits Mfg*. 57 (Jan. 1986).
68. U. S. Pat. 3,327,184 (June 20,1967), D. J. Valley (to Union Carbide Corp.); U. S. Pat. 3,319,141 (May 9, 1967), F. E. Cariou, W. E. Loeb, and D. J. Valley (to Union Carbide Corp.).
69. U. S. Pat. 3,949,280 (Apr. 6, 1976), S. Odagiri, M. Nuka, N. Shinba, M. Baba, and Y. Iizuka (to Mitsumi Electric Co., Ltd.); Ger. Pat. 2,546,332 (Apr. 29, 1976), J. Lefeber and J. deJonge (to N. V. Philips Gloeilampenfabriken).
70. U. S. Pat. 3,389,604 (June 25, 1968), G. B. Williams (to Buzzards Corp.).
71. Ger. Pat. 2,329,186 (Jan. 3, 1974), F. R. Tittmann (to Union Carbide Corp.); U. S. Pat. 3,300,332 (Jan. 27, 1967), W. F. Gorham and H. L. Willard (to Union Carbide Corp.).
72. *Contract No. N01-HV-8-1388*, National Heart, Lung and Blood Institute, Division of Heart and Vascular Diseases, Bethesda, Md.
73. F. R. Tittmann and W. F. Beach, in M. Szycher and W. J. Robinson, eds., *Synthetic Biomedical Polymers: Concepts and Applications*, Technomic Publishing Co., Inc., Westport, Conn., 1980, 117–132.
74. R. H. Kahn and W. E. Burkel, *In Vitro* **8**, 451 (1973).
75. R. Olson, *Electron. Packag. Prod.*, 213 (May 1980).
76. E. M. Stemmed, *J. Electrophysiol. Tech. Eng.* **10**(1), 19 (1983); G. E. Loeb, M. Salcman, and E. M. Schmidt, *IEEE Trans. Bionwd. Eng.* **BME-24**(2), 121 (1977).
77. E. M. Schmidt, J. S. McIntosh, and M. J. Bak, *Med. Biolog. Eng. Comput.*, 96 (Jan. 1988).
78. B. J. Humphrey, *J. Am. Inst. Conserv.* **25**, 15 (1986); C. J. Shahani and W. K. Wilson, *Am. Sci.* **75**, 240 (1987).
79. D. F. Peiffer, T. J. Corley, G. M. Halpern, and B. A. Brinker, *Polymer* **22**, 450 (1981); R. Q. Gram, H. Kim, J. F. Mason, and M. Wittman, *J. Vac. Sci. Technol.* **A4**(3), 1145 (1986); K. W. Beig, *J. Vac. Sci. Technol.* **18**, 1231 (1981).
80. U. S. Pat. 4,381,963 (May 3, 1983), I. S. Goldstein, F. D. Kalk, and H. W. Deckman (to The University of Rochester).
81. R. Olson and R. Veague, *Microcontamination*, 57 (Jan. 1985).
82. M. A. Spivack, *Corrosion (Houston)* **26**, 371 (1970).
83. U. S. Pat. 3,523,839 (Aug. 11, 1970), L. Shechter and W. E. Loeb (to Union Carbide Corp.); U. S. Pat. 3,556,881 (Jan. 19, 1971), W. F. Gorham and W. E. Loeb (to Union Carbide Corp.).
84. T. C. Castorina and A. F. Smetana, *J. Appl. Polym. Sci.* **18**, 1373 (1974).
85. A. F. Smetana and T. C. Castorina, in *Proceedings of the Propellants, Explosives and Pyrotechnics Conference*, Dec. 3–4, 1974, Picatinny Arsenal, Dover, N.J.
86. A. Calahorra, O. Gara, and S. Kenig, *J. Cell. Plast.* **23**, 383 (1987).
87. R. J. McWhirter, *Report from Bendix Corp., BDX-613-2358*, Bendix Corp., Kansas City, Mo., Sept. 1980.

88. K. Makino, S. Kawakami, and S. Orihara, *Fujitsu Sci. Tech. J.* **9**(4), 153 (1973).
89. R. Olson, *Electron. Packag. Prod.*, 213 (May 1980).
90. M. A. Spivack, J. N. Pike, and W. M. Jayne, in *Proceedings of the Electro-Optical Systems Design Conference*, New York, Sept. 18–20, 1973, 362–371.
91. N. Pailer and E. Grun, *Planet. Space Sci.* **28**, 321 (1980).
92. P. L. Tassano, *J. Vac. Sci. Technol.* **A3**, 2036 (1980).
93. P. H. Sheather, *J. Physics E.* **6**, 319 (1973).
94. S. L. Kramer and D. R. Moffett, *IEEE Trans. Nucl. Sci.* **NS-28**, 2174 (1981).
95. U. S. Pat. 3,940,530 (Feb. 24, 1976), W. E. Loeb and M. A. Spivack (to Union Carbide Corp.); U. S. Pat. 3,864,202 (Feb. 4, 1975), W. E. Loeb and M. A. Spivack (to Union Carbide Corp.).
96. U. S. Pat. 4,321,299 (Mar. 23, 1982), R. A. Frosch and R. A. Frazer (to NASA).

W. F. BEACH
Alpha Metals

Y

YIELD AND CRAZING IN POLYMERS

Introduction

Polymers serve increasingly in structural applications as lightweight replacements for more traditional materials such as metals and wood. In light of this it is important to understand and be able to characterize the engineering or mechanical properties over the likely service conditions. Typically when a material fails in service it is thought of in terms of a catastrophic brittle failure and these modes have been partially discussed elsewhere (see FRACTURE; FATIGUE). However, polymers (both thermoplastics and thermosets) can also fail by yielding, and while generally this is not necessarily a catastrophic event (ie the material remains intact) it does mean the material retains a degree of permanent deformation and is usually considered a failure criterion in terms of structural integrity. Furthermore, the yield response of polymers affects the plastic zone at the crack tip and this is important in fracture events.

Another deformation mechanism common to many polymers is that of crazing. Crazes are generally a precursor to brittle failure, though on the local scale they are the result of highly localized yielding phenomena. As such they provide a significant source of energy absorption and, further, since the crazes remain load bearing, the time for their initiation and growth can be a significant portion of the overall lifetime of the material.

The present article focuses on yield and crazing in polymers and does not deal directly with the viscoelastic response, though it is recognized that yield and viscoelasticity share many of the same features—strain rate and temperature dependence (1) and even concepts such as time–temperature superposition (2) (see VISCOELASTICITY; AGING, PHYSICAL). We first present a summary of conventional yield criteria, these being methods to quantify the yield stress as a function of the applied stress field, ie uniaxial vs biaxial. Following this the phenomenology of yield is addressed by considering a number of models of the yield process in polymers, including the observation of strain softening and strain hardening. A brief overview of craze structure and morphology is

given and several criteria for the initiation, growth, and failure of crazes are described.

Yield

A general definition of yield is the point at which a material ceases to deform elastically in a recoverable manner and undergoes permanent (irreversible) plastic deformation. Historically, the study of yield and the theories describing it were developed for metals (3) and, there, this definition works well, with elastic deformation arising from lattice distortions and plastic deformation from the motion of dislocations. In polymers the molecular processes involved in deformation cannot be so easily split into such distinct mechanisms. Further, it has long been recognized that polymers exhibit a viscoelastic response to deformation (4–7) and consequently the general mechanical properties are both rate and temperature dependent. Such a viscoelastic response is evidenced not only on deformation but also on recovery. The time-dependent nature of the recovery means that for polymers the determination of permanent (plastic) deformation can depend on how long one is prepared to conduct the relevant measurements. That said, general aspects of the large deformation behavior of amorphous glassy and semi-crystalline polymers can be usefully discussed in terms of conventional yield criteria.

We begin by examining general stress (load per unit area)–strain (fractional change in length) responses for polymers under uniaxial tensile loading and develop what is essentially an elastic–plastic analysis of the material behavior. Loading under compressive and shear forces is then considered. This is followed by general yield criteria: these can be considered macroscopic criteria relating the applied stress to some critical value for yielding (generally a critical shear stress) and their modification to introduce pressure dependence. While such criteria are useful engineering concepts, it is perhaps more satisfying to be able to describe yielding from a microscopic perspective, and this is addressed in the section on yield theories. Subsequent to the discussion of yield phenomena we present a section on another important aspect of polymer mechanical behavior, that of crazing. Crazing is a localized yielding process that may be dilatational in nature. It results in essentially load-bearing cracks that are generally a precursor to macroscopically brittle failure when the craze density is low.

Before describing the yield response of polymers in the next section, we remark here that polymer mechanical behavior depends strongly not only on the time (rate) and temperature, but also on the morphology of the material (8,9). Hence the yield phenomenology described below will approximately describe the behavior, but the details of the behavior will depend strongly on the morphology and where one is relative to the glass-transition temperature, T_g. For example, above the T_g, an amorphous polymer such as polystyrene does not yield but undergoes viscous flow. On the other hand, a material such as polyethylene, which is semi-crystalline, will undergo a yield process above the glass transition. Below T_g, both glassy amorphous and glassy semi-crystalline polymers can undergo yielding, though the processes may differ between the two types of materials. Much of the development of the present article deals with yield of glassy

amorphous polymers, though some discussion of yielding in semi-crystalline materials is also presented.

General Stress–Strain Curves under Uniaxial Tensile Loading. In uniaxial extension or compression, the true axial stress, σ_T, is given by the current load (P) divided by the current cross sectional area (A):

$$\sigma_T = P/A \tag{1}$$

If it is assumed that the deformation takes place at constant volume (a reasonable assumption under most conditions of plastic deformation where the volume changes are small compared to the total strain), then the instantaneous area (A) and length (l) are related to the original cross sectional area and length (A_0, l_0 respectively) by

$$Al = A_0 l_0 \tag{2}$$

We now define the engineering (or nominal) stress, σ_E, as

$$\sigma_E = P/A_0 \tag{3}$$

and the engineering strain, ε, as

$$\varepsilon = (l - l_0)/l_0 \tag{4}$$

so that

$$l/l_0 = (l + \varepsilon) \tag{5}$$

From equations 1–5 we find that

$$\sigma_E = \sigma_T/(l + \varepsilon) \quad \sigma_T = \sigma_E(l + \varepsilon) \tag{6}$$

The deformation response of a material to a given loading regime is described by generalized equations known as constitutive relations. For uniaxial loading in the limit of small strains, the simplest of these is known as Hooke's Law and linearly relates the stress to the strain:

$$E = \frac{\sigma}{\varepsilon} \tag{7}$$

where E is Young's modulus.

The extreme temperature and rate sensitivity of polymers means that they can display a wide range of mechanical behaviors depending on the precise conditions under which they are tested. Figure 1 shows a set of typical engineering stress–strain curves that an amorphous polymer might be expected to exhibit as a function of rate or temperature in a uniaxial tensile test (10,11). At low temperatures or high rates polymers tend to fail in a brittle manner (Curve A)—the strain to failure is low (of the order of a few percent) and the modulus high (of the order

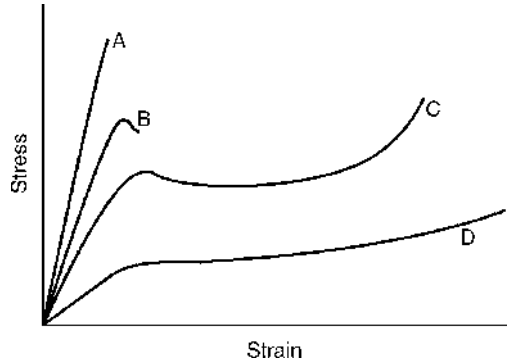

Fig. 1. Typical engineering stress–strain curves for an amorphous polymer as a function of temperature or strain rate.

of a few GPa). As the temperature increases (or the strain rate decreases) the curves progress such that the material passes through a softening regime (Curve D), characterized by low moduli, an indistinct (or nonexistent) yield point, and large strains to failure (>100 percent). Ultimately, at a sufficiently high temperature (or low enough strain rate), the material may show a pure rubbery response with a modulus some orders of magnitude lower than those indicated in Figure 1 (curve omitted for clarity).

Of particular interest in this discourse is the behavior shown in Curves B and C. At small strains (typically <1%), the stress rises approximately linearly with increasing strain, ie the material displays Hookean-like behavior (note that this is not strictly true for polymers because of viscoelastic effects; however if the applied strain rate is faster than the relaxation time for the material then little relaxation will occur and it is a reasonable approximation). At larger strains (above the proportional limit) the engineering stress will continue to rise with strain, though less rapidly. Eventually, at a certain strain, the stress reaches a maximum and then falls with increasing strain. It is this peak stress which is generally taken to be the yield stress, σ_y, and the strain at which it occurs as the yield strain, ε_y. The nature of the load drop and the postyield behavior are discussed subsequently. Here it is sufficient to note that the peak in engineering stress is normally accompanied by macroscopic changes to the sample geometry. The plastic deformation is concentrated locally to a small portion of the specimen. This section is seen to reduce in width and to form what is called a "neck." Because of the change in cross-sectional area, the local stresses in the neck region can be significantly higher than the engineering stress and indeed may be rising while the load or engineering stress is falling (12,13). Accordingly it is instructive to look at the true stress–strain behavior. This is important because while strain localization is often associated with yield behavior, such localization is not necessary for yielding to occur.

Considère Construction (14). Referring back to equation 6 for the true and engineering stresses,

$$\sigma_E = \sigma_T/(1+\varepsilon); \quad \sigma_T = \sigma_E(1+\varepsilon)$$

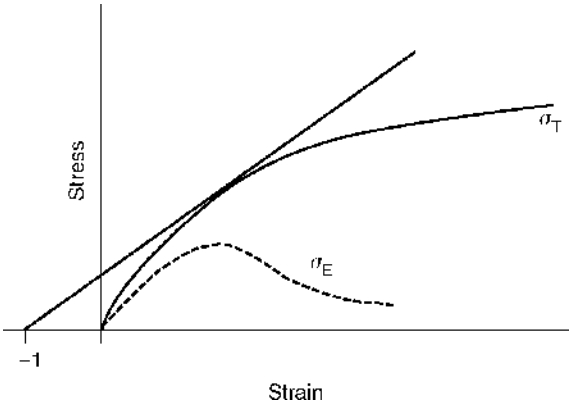

Fig. 2. Engineering (σ_E) and true stress (σ_T) as a function of strain in uniaxial tension. The Considère criterion for necking, that is the ability to draw a tangent to the true stress curve from $\varepsilon = -1$, is also shown.

we see that for all finite strains under uniaxial tensile loading, the true stress is greater than the engineering stress (for uniaxial compressive loading, the true stress is always lower than the engineering stress).

Figure 2 compares the engineering stress, σ_E, and true stress, σ_T, as a function of engineering strain for uniaxial tensile loading. As noted above, the neck is seen to form at the point where the load (or engineering stress) ceases to rise, ie where

$$\frac{d\sigma_E}{d\varepsilon} = 0 = \frac{1}{(1+\varepsilon)}\frac{d\sigma_T}{d\varepsilon} - \frac{\sigma_T}{(1+\varepsilon)^2} \tag{8a}$$

or

$$\frac{d\sigma_T}{d\varepsilon} = \frac{\sigma_T}{(1+\varepsilon)} \tag{8b}$$

In practice then, the point at which a polymer will form a neck is given by drawing a tangent to the true stress–strain curve from the point $\varepsilon = -1$, as illustrated in Figure 2. [We note here that in this condition, yielding is a localization phenomenon. It is also possible that yielding can be a material property unrelated to localization and this is touched upon in a subsequent section.]

Necking and Cold Drawing. Before further discussion of the Considère construction it would be useful to discuss the phenomenology of the yield and necking processes. As discussed above, yield in a material under uniaxial tensile loading is characterized by highly localized plastic deformation within the specimen and a corresponding decrease in the engineering stress. The exact position at which yield occurs on a nominally isotropic and uniform sample is impossible to predict. However, a small change in the local properties at some segment in the sample can lower the local yield stress such that yield will initiate there first. Alternatively, a flaw or inclusion can cause a stress concentration such that the

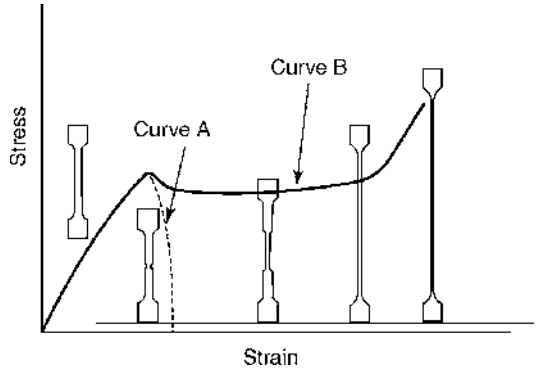

Fig. 3. Engineering stress–strain curves for a material showing, with increasing strain, strain localization(necking), cold drawing, and strain hardening. Also shown are schematics of the sample geometry at each stage.

local stress is higher than the yield stress. After this point one of two things may happen (refer to Fig. 3).

(1) The material in the neck may continue to draw down. As it does so, the true stress continues to rise in the segment, which leads rapidly to failure. This is the case shown in Curve A in Figure 3.
(2) The yielded material can undergo strain hardening. As the material yields and draws down, the polymer chains align along the stress direction, increasing the local stiffness (hence strain hardening is also known as orientation hardening). If the rate of strain hardening is greater than linear, this is sufficient to offset the increase in local stress due to area reduction, and the neck can stabilize. This is the case shown in Curve B in Figure 3. Also shown in Figure 3 are sketches of the deformation that would be seen in a typical tensile specimen as a function of cross-head displacement. Once the yielded material has hardened sufficiently to offset the increase in local stress, the stress (load) stabilizes to a constant value (the draw stress, σ_D) and the neck is seen to propagate along the remaining gage length of the sample until the whole sample has yielded. This process is known as cold drawing.

The oriented material in the strain-hardened section draws down to a characteristic extent under any given conditions and is known as the natural draw ratio, λ_D, and is given by the ratio of the length of the drawn section to its length before deformation. Further deformation can cause additional extension and hence further orientation and strain hardening, and the stress is seen to once again rise until eventually it exceeds the ultimate strength of the material and failure occurs.

In terms of the Considère construction, the criterion for a material to neck and cold draw is indicated by the ability to draw a second tangent to the true stress–strain curve from the point $\varepsilon = -1$ (Fig. 4). Another important aspect of yielding is that, while there is a clear drop in the engineering stress at (or near)

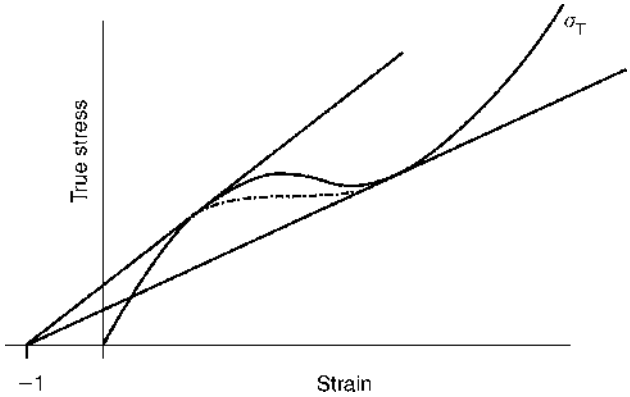

Fig. 4. True stress (σ_T) as a function of strain in uniaxial tension. The Considère criterion for cold drawing, that is the ability to draw a second tangent to the true stress curve from $\varepsilon = -1$, is also shown.

the yield point, there may also, though not necessarily, be a drop in the true stress after yield (Fig. 4). This drop in true stress is commonly referred to as strain softening. At the point of the second tangent, molecular orientation is sufficient to stiffen the material and strain hardening occurs.

Compressive Loading. The discussion above has been developed specifically for uniaxial tensile loading conditions, and this is still the most widely used method for testing of polymers. However, the formation of a localized neck means that it is difficult to measure the true strain at any given point and hence determine the true stress–true strain behavior. Moreover, because tests are generally carried out at a constant cross-head displacement rate, the spatially varying strain means the strain rate is poorly defined. G'Sell and co-workers (15,16) have gone some way to resolving this difficulty by using an optical system to monitor the local strain and a feedback mechanism to adjust the imposed deformation rate to perform constant true strain rate experiments. Alternatively, others (17,18) have used a video system to monitor the neck profile and so back-calculate the true stress–true strain rate profile in the neck region.

Some of the shortcomings of tensile testing are mitigated by the use of compressive loading, typically performed on cylindrical specimens. Since the localization seen when the sample necks is suppressed in this geometry it is experimentally easier to ensure a more uniform strain field; however, some care needs to be exercised to prevent buckling or barreling of the specimens. Barreling is caused by lateral constraint on the cylinder ends due to friction with the loading plates. A suitable (inert) lubricant or a thin PTFE film applied to the cylinder ends is often sufficient to prevent barreling. Buckling will occur if the aspect ratio of the cylinder (height-to-diameter) is too large—aspect ratios of 0.5 to 1 are typically used.

From tests conducted on polymer glasses under both tension and compression (19–23) the true stress versus true strain rate response can be determined and typical plots are shown in Figure 5 (19). As can be seen, qualitatively the true stress–true strain behaviors are similar for both deformation modes.

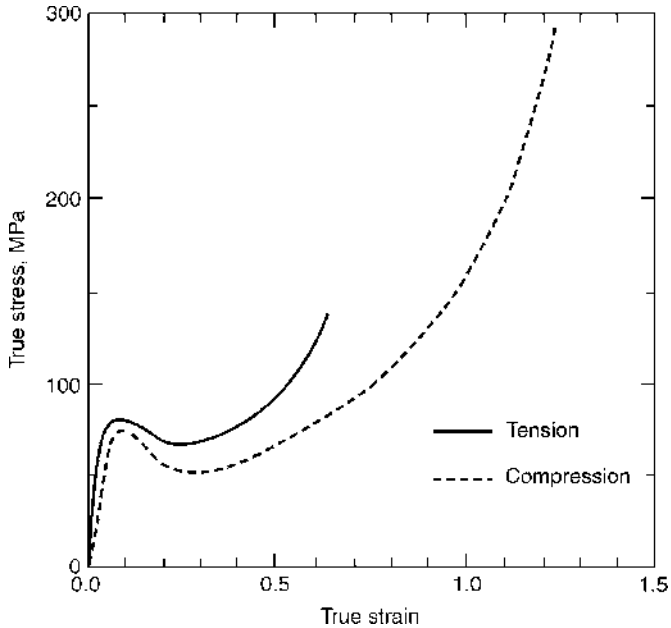

Fig. 5. True stress–strain curves for a polycarbonate under tension and compression. After Boyce and Arruda (19) with permission.

Importantly they both show a drop in true stress at the yield point. The observation of a drop in true stress without the localization (necking) seen in tensile tests confirms that the material is undergoing intrinsic strain softening. Importantly this shows that localization is not a necessary requirement for yield and further that the load drop seen in tensile tests is not necessarily simply the result of geometric changes.

While the true stress–true strain response is qualitatively similar in both compression and tension, the resulting deformation states are very different. Tensile loading leads to uniaxial molecular orientation along the loading axis. Compression on the other hand results in a biaxial orientation state in a plane perpendicular to the loading direction and so it is expected that quantitatively different stress–strain curves are seen. In addition, as discussed below, the hydrostatic pressure difference between tension and compression leads to differences in yield strength because yield in polymers is pressure dependent.

The preceding is a general overview of the main features of yield in polymers. From a practical point of view, structures are rarely subjected to simple uniaxial or shear loads and it is instructive to be able to determine when a material might yield under more complicated stress states. The following yield criteria attempt to do this from a phenomenological point of view, that is they do not address the fundamental mechanisms of yield but rather provide yield criteria for multiaxial loading conditions.

Yield Criteria. A practical yield criterion needs to describe the conditions under which yield will occur for a general stress state (eg tension, compression, shear, or some combination). Before we consider the various yield criteria which

have been proposed, it is useful to very briefly recap the definition of the principal stress components as these are generally the terms which are used to define the yield criteria (see VISCOELASTICITY for a more thorough introduction to the generalized stress and strain definitions).

If we take a small representative cube within a body, then the general stress state is given by the stress tensor of the forces acting on the faces of the cube:

$$\sigma_{ij} = \begin{bmatrix} \sigma_{11} & \sigma_{12} & \sigma_{13} \\ \sigma_{21} & \sigma_{22} & \sigma_{23} \\ \sigma_{31} & \sigma_{32} & \sigma_{33} \end{bmatrix} \tag{9}$$

and the generalized strain tensor as

$$\varepsilon_{ij} = \begin{bmatrix} \varepsilon_{11} & \varepsilon_{12} & \varepsilon_{13} \\ \varepsilon_{21} & \varepsilon_{22} & \varepsilon_{23} \\ \varepsilon_{31} & \varepsilon_{32} & \varepsilon_{33} \end{bmatrix} \tag{10}$$

where i refers to the axis normal to the plane on which the stress is acting and j the direction in which the stress acts.

For an isotropic, elastic material two elastic constants are sufficient to describe the material response, the elastic modulus E (eq. 7) and the Poisson's Ratio (ν), defined as the ratio of the axial to the (negative) transverse strain ($-\varepsilon_{11}/\varepsilon_{22}$).

Other mechanical functions such as the bulk modulus, K, and the shear modulus, G are interrelated by the following expressions:

$$\begin{aligned} G &= \frac{E}{2(1+\nu)} \\ K &= \frac{E}{(1-2\nu)} \\ E &= \frac{9KG}{3K+G} \end{aligned} \tag{11}$$

From equation 9, it is seen that the general stress state is described by nine independent components. However, if we assume that the sample is not undergoing rigid body rotation, then the shear components must give a net torque of zero, that is,

$$\sigma_{12} = \sigma_{21} : \sigma_{13} = \sigma_{31} : \sigma_{23} = \sigma_{32} : \tag{12}$$

Thus the stress state is defined by six independent components. Further, if the body is in equilibrium, then it is possible to define a set of orthogonal axes such that the shear components are zero. Such axes are termed the "principal axes"

and the resulting stress components the "principal stresses":

$$\sigma_i = \begin{bmatrix} \sigma_1 & 0 & 0 \\ 0 & \sigma_2 & 0 \\ 0 & 0 & \sigma_3 \end{bmatrix} \tag{13}$$

The sum of the three principle stresses is known as the first stress invariant (or trace), I_1,

$$\sigma_1 + \sigma_2 + \sigma_3 = \text{constant}$$

and the related quantity, the mean stress, σ_M

$$\sigma_M = \frac{\sigma_1 + \sigma_2 + \sigma_3}{3}$$

Tresca Yield Criterion. The earliest proposal for a yield criterion in metals is due to Tresca (24), and it stated that yield occurs when the maximum shear stress reaches a critical value. With $\sigma_1 > \sigma_2 > \sigma_3$ the criterion can be written as

$$1/2(\sigma_1 - \sigma_3) = \tau_s \tag{14}$$

For the simplest loading situation of a tensile test at a stress level of σ_1, with $\sigma_2 = \sigma_3 = 0$ we have

$$\tau_s = \sigma_1/2 \tag{15}$$

so that yield occurs when the applied tensile stress reaches twice the shear yield stress.

Von Mises Yield Criterion. The Von Mises yield criterion (also known as the maximum distortional energy criterion or the octahedral stress theory) (25) states that yield will occur when the elastic shear-strain energy density reaches a critical value. There are a number of ways of expressing this in terms of the principal stresses, a common one being

$$(\sigma_1 - \sigma_2)^2 + (\sigma_2 - \sigma_3)^2 + (\sigma_3 - \sigma_1)^2 = \text{constant} \tag{16}$$

If we again look at the case of simple tension, then we have $\sigma_2 = \sigma_3 = 0$. Defining the tensile yield stress as σ_Y, we see that the constant in equation 16 is $2\sigma_Y^2$.

If we look now at the case of pure shear, where we have $\sigma_1 = -\sigma_2 = \tau$ and $\sigma_3 = 0$, we find that

$$4\sigma_1^2 + \sigma_1^2 + \sigma_1^2 = 6\sigma_1^2 = 6\tau^2 = \text{constant} = 2\sigma_Y^2$$

ie

$$\tau = \frac{\sigma_Y}{\sqrt{3}} \tag{17}$$

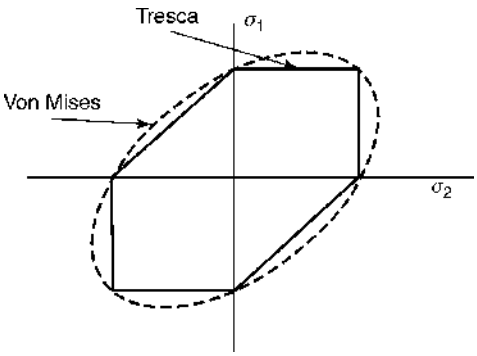

Fig. 6. The Tresca and von Mises yield criteria for plane strain conditions ($\sigma_3 = 0$).

Compare this to the prediction of $\sigma_Y/2$ from the Tresca criterion. The yield criteria for both the Tresca and Von Mises theories are shown graphically in Figure 6. For simplicity, the plots are shown for conditions of plane stress (ie $\sigma_3 = 0$). We can see that the Von Mises criterion describes an ellipse in stress space, with the Tresca criterion consisting of a series of straight lines bounded by the Von Mises limits.

Coulomb Yield Criterion. In 1773, Coulomb (26) identified two components important in the strength of building stone—cohesion and friction. He observed that the shear stress, τ, necessary to cause shear failure across a plane is resisted by the cohesion of the material S_0 and by the product, $\mu\sigma_N$, across that plane, where the constant μ is called the coefficient of internal friction and σ_N is the force normal to the shear plane:

$$\tau = S_0 + \mu\sigma_N \tag{18}$$

This criteria is often expressed in the form

$$\tau = \tau_c + \sigma_N \tan\phi \tag{19}$$

where τ_c is now the critical shear stress for yield and

$$\phi = 2\theta - \frac{\pi}{2} \tag{20}$$

and θ is the angle between the normal to the shear plane and the direction of the applied stress. Data from tensile, compressive, and torsional tests on a range of polymers under imposed hydrostatic pressure (20,27) have been successfully described by the Coulomb criterion, though it should be noted that the modified Von Mises criteria (see below) was equally successful.

Pressure-Modified Criteria. One major shortcoming of the criteria described above is that they predict that the yield stresses in tension and compression are the same. However, in practice it is generally found for polymers that the yield stress in compression is higher than that in tension. This effect is usually considered to be a consequence of the fact that the yield stress depends on

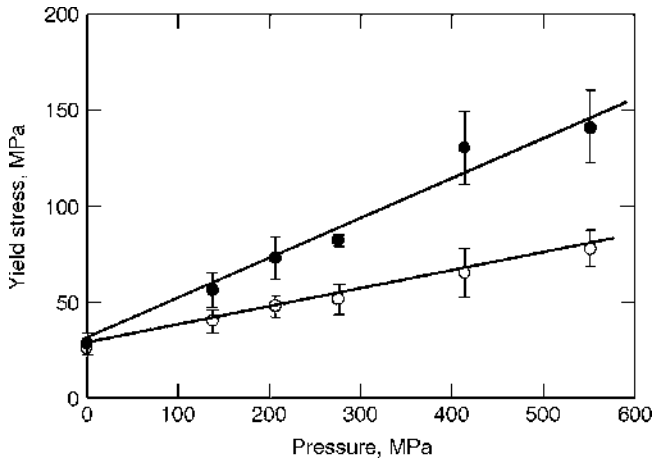

Fig. 7. Yield stress as a function of imposed hydrostatic pressure for polyethylene and polypropylene. Data from Ref. 28. ○, polyethylene, ●, Polypropylene.

the hydrostatic pressure that develops under load. The hydrostatic pressure component of the load in tension is negative, while in compression it is positive. In fact, experiments in which measurements were made under imposed hydrostatic pressures exhibit a strong pressure dependence of the yield stress in polymers (27–29 see also the extensive review in Reference 30). In general it was seen that the yield stress increased linearly with imposed hydrostatic compression (Fig. 7).

Modified Tresca Criterion. A simple way to modify the Tresca criterion to allow for a pressure dependence is to make the critical shear yield stress a linear function of hydrostatic pressure:

$$\tau_T = \tau_T^0 + \mu_T P \tag{21}$$

where τ_T^0 is the critical shear stress with no hydrostatic pressure, P is the hydrostatic pressure, given by $P = -(\sigma_1 + \sigma_2 + \sigma_3)/3$ and μ is a constant. Substituting into equations 14 and 15, we find that the yield stresses in tension σ_{Yt} and compression σ_{Yc} are given by

$$\sigma_{Yt} = 2\tau_T^0/(1 + 2\mu/3) \tag{22}$$

$$\sigma_{Yc} = 2\tau_T^0/(1 - 2\mu/3) \tag{23}$$

Modified Von Mises Criterion. In the same manner as the modification to the Tresca yield criterion one can modify the Von Mises criterion by introducing a linear dependence of the critical shear stress on the hydrostatic pressure:

$$\tau_M = \tau_M^0 + \mu_M P \tag{24}$$

where τ_M^0 is the critical shear stress with no hydrostatic component, P is the hydrostatic pressure, and μ_M is a material constant.

It can be seen from the above criteria that for polymers under uniaxial loading, yield is essentially characterized as a shear-controlled process. There is good experimental evidence for this being the case, and is shown most clearly by the observation of the formation of shear bands on uniaxially loaded specimens. These are regions of locally strained material running at an angle to the applied load, typically at approximately 45°. For isochoric deformation in an isotropic material the angle is precisely 45°, which corresponds to the angle of maximum shear stress. Any preorientation in the material (which introduces an anisotropy to the material) or dilatation during deformation can cause the angle to change. Dilatation generally causes the angle to decrease in the loading direction, while the change due to preorientation depends on the direction of the applied load to the orientation direction.

The criteria discussed above are certainly useful from an engineering point of view and offer a method to estimate the likelihood of failure for a given loading situation. However, from a fundamental viewpoint, they are lacking as they provide no insight into the microscopic or molecular mechanisms that give rise to yield. The following section examines a number of theories that seek to explain yield to varying degrees of complexity.

Theories of Yield

Adiabatic Heating. As far back as 1949 (31–33) it was postulated that local adiabatic heating in polymers causes a temperature rise in the neck region, thereby lowering the local yield stress. While this may be a factor at high rates of deformation where the heat generated cannot be dissipated, experiments using, for example, thermal imaging techniques have shown that the temperature rise is not sufficient to account for yielding. In addition, experiments conducted at rates low enough such that the system is essentially under quasi-isothermal conditions still show yield behavior (34) and therefore simple heating is not an adequate explanation for polymer yield.

Strain-Induced Dilatation. An alternative view of yield in polymers comes from the fact that a tensile strain induces a hydrostatic tension in the material and a corresponding increase in the sample volume. This in turn translates to an increase in the free volume, which increases the polymer mobility and effectively lowers the glass-transition temperature (T_g) of the polymer (alternatively it can be looked upon as increasing the free volume to the value it would have at the normal measured T_g). The increased mobility results in a lowering of the yield stress. Knauss and Emri (35) used an integral representation of nonlinear viscoelasticity with a state-dependent variable related to free volume to model the yield behavior, with the free volume a function of temperature, time, and stress history. This model uses the concept of reduced time (see VISCOELASTICITY), where application of a tensile stress causes a volume dilatation and consequently causes the material time scale to change by a shift factor related to the magnitude of the applied stress. Yield occurs because the free-volume shift factor causes the molecular mobility to increase in such a way that yield can occur.

However yield and plastic deformation are also observed in uniaxial compression and shear (19–23). In the former case the hydrostatic component of

stress is compressive and this leads to a reduction in free volume. Further, as was shown above when discussing the yield criteria, yielding in either tension or compression seems, for polymers, to be associated with the deviatoric (shear) component of the stress tensor, and this intrinsically involves no volume change. Thus, it seems unlikely that strain-induced changes in volume are the underlying cause of yield.

Models of Yield Based on Activated Processes

Models put forward in the in the late 1960s and early 1970s (eg Robertson (36), Haward and Thackray (37), Argon (38)) suggested that for yield and large-strain plastic deformation to occur two distinct sources of resistance must be overcome. First, yield is thought to occur when the polymer is stressed sufficiently to be able to overcome intermolecular resistance to segmental motion. Once the material has started to flow, molecular alignment occurs and changes the configurational entropy of the system. This change in entropy of the system causes the second resistance and is seen physically as a strain-hardening effect.

Yield is generally taken to be an activated process, and the first three of the following theories address this aspect. Models are then presented which address not only the yield of the material but the subsequent strain-softening and strain-hardening events that are observed. The first of these is the Haward and Thackray (37) one-dimensional model, which, while not physically realistic, laid the groundwork for many of the theories that followed it. This is followed in some detail by the BPA model of Boyce, Parks, and Argon (39), which addresses the rate, temperature, and pressure dependence of the intermolecular resistance and also the temperature dependence of entropic hardening. The model proposed by Tervoort and co-workers (40) is then discussed as this addresses some of the shortcomings of the BPA model, specifically the omission of a spectrum of relaxation times to describe the material behavior. The section is finished by examining the model of Caruthers and co-workers (41,42), which approaches yield from the framework of Rational Thermodynamics and seeks to explain a range of behaviors using a set of unified constitutive equations.

Internal Viscosity Model (Eyring Model). If we think of amorphous polymers as essentially viscous fluids then it is reasonable to think of yield and plastic deformation as viscous flow. Eyring (43) in 1936 developed a theory for flow in viscous fluids based on transition-state theory and it is instructive to look at this in more detail as it shows the temperature and rate dependency of the flow process. The Eyring model treats segmental motion as an activated process in which for a given segment to "jump" to an alternative position it needs to cross an energy barrier of height E^*. In the unstrained state the likelihood of either a forward jump or backward jump is equal, ie the stable states on either side of the barrier are at the same energy level (Fig. 8). The rate at which the segments cross the barrier is given by the Arrhenius equation:

$$\nu_0 = A \exp\left[-\frac{E^*}{kT}\right] \tag{25}$$

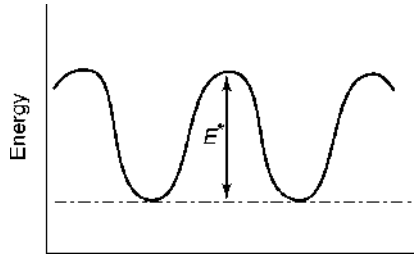

Fig. 8. Schematic of the energy landscape for an unstrained polymer for Eyring's model of viscous flow.

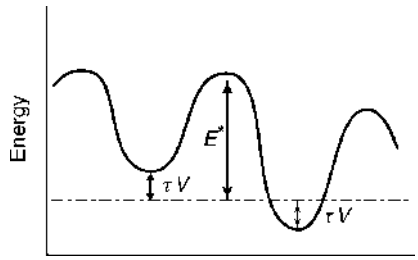

Fig. 9. Schematic of the energy landscape for a strained polymer for Eyring's model of viscous flow.

where A is a constant, E^* is the energy barrier height, k is Boltzmann's constant, and T the absolute temperature. According to the theory, application of a stress causes an asymmetric change in the stable energies on either side of the barrier of $+\tau V$ and $-\tau V$ for the forward and backward motions, respectively (Fig. 9). V is the Eyring activation volume and τ the applied shear stress. It is difficult to relate the activation volume V to a physical volume in the polymer, though the term τV in the model notionally represents the work required to move a polymer segment during flow. Under applied stress then, the frequency with which the segments jump in the forward direction is given by

$$\nu_{\mathrm{f}} = A \exp\left(-\frac{E^* - \tau V}{kT}\right) \tag{26}$$

and the frequency they jump in the reverse direction is given by

$$\nu_b = A \exp\left(-\frac{E^* + \tau V}{kT}\right) \tag{27}$$

So, the net rate at which the segments jump is simply the difference in the forward and backward rates:

$$\nu_{\mathrm{f}} - \nu_{\mathrm{b}} = A \exp\left(-\frac{E^*}{kT}\right)\left[\exp\left(\frac{\tau V}{kT}\right) - \exp\left(-\frac{\tau V}{kT}\right)\right] \tag{28}$$

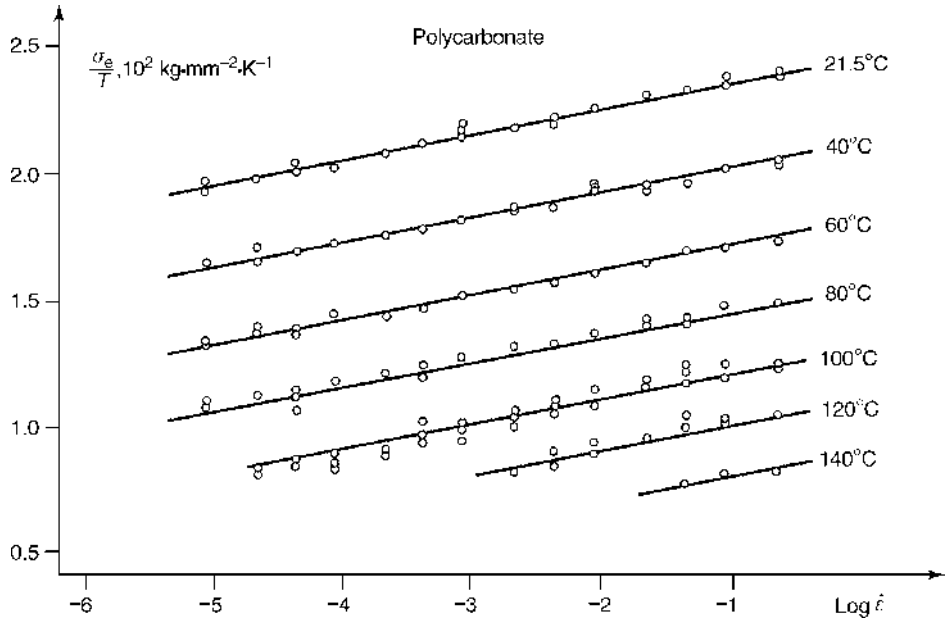

Fig. 10. Yield stress normalized to temperature as a function of logarithmic strain rate for polycarbonate. After Bauwens-Crowet and co-workers (44) with permission.

In a solid, the backward jump rate is negligible in comparison to the forward jump rate (the term τV being sufficiently large such that the term $e^{-\tau V/kT}$ becomes small), and taking the net jump rate ($\nu_f - \nu_b$) to be proportional to the strain rate, $\dot{\varepsilon}$, then

$$\dot{\varepsilon} = A^* \exp\left(-\frac{E^*}{kT}\right) \exp\left(\frac{\tau V}{kT}\right) \tag{29}$$

As shown earlier, a simple criterion for yield is that the maximum shear stress reaches a critical value given by $\tau = \sigma_y/2$, where σ_y is the tensile yield stress (ie the Tresca yield criterion). Substituting and rearranging equation 29 gives

$$\sigma_Y = \left[k \ln\left(\frac{\dot{\varepsilon}}{A^*}\right) + \frac{E^*}{T}\right] \frac{2T}{V} \tag{30}$$

Equation 30 shows that the yield stress is both rate and temperature dependent, hence it captures some important features of yield in polymers. For example, Figure 10 (44) shows a plot of σ_Y/T (or σ_e/T in the notation of Reference (44)) as a function of log strain rate and, as predicted by equation 30, a linear relationship is seen at each temperature. It is worth noting that the Eyring equation (typically in the form of two activated processes acting in parallel) has been successfully applied not only to the yield behavior of polymers but also to the creep rupture behavior of isotropic and oriented polymers (45–48).

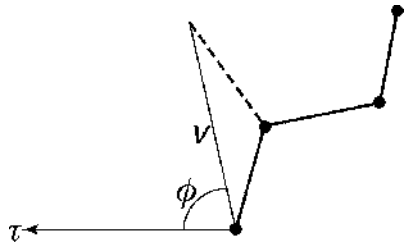

Fig. 11. Schematic of the Robertson (36) model for a shear-induced conformation change.

Robertson Model. The model developed by Robertson in 1966 (36) is also based on an activated process. He stated that the rigidity of a glass is a result of the intermolecular forces between adjacent chains, though for polymer glasses they suppose that the intramolecular forces are also important. Thus, to cause a glassy polymer to move into the liquid state it is necessary to reduce the effect of either the intramolecular or intermolecular forces. Robertson posited that a shear stress alone could achieve this and so induce Newtonian flow in the material. A shear stress field set up in the material can increase the number of flexed bonds (conformations) to a level above the preferred level of the equilibrium glass and may increase to the level that would be typically seen in a polymer liquid.

The model introduces the strain energy as a bias on the energy difference between bonds in the preferred (trans) and flexed (cis) conformations, with the simplifying assumption that the bonds can only exist in one of these two stable states. A polymer below the glass-transition temperature has a fixed, or "frozen-in," distribution of bond conformations in either the high energy (cis) or low energy (trans) states, with the difference in energy between the two states denoted as ΔE. Application of a stress causes conformations to shift from the trans to the cis state, effectively increasing the mobility to liquid-like levels. At sufficiently high stress levels the mobility is sufficiently increased such that yield can occur. More specifically the shear component of the stress (τ) causes a change in the energy difference between the two states by an amount $\tau v \cos \phi$, where v is the "flex volume" and is approximately the average volume of chain segments containing two bonds, and ϕ is the angle between the applied stress and vector displacement of the flexed bond (Fig. 11). The resulting energy difference between the two states (ΔE^*) is now given by

$$\Delta E^* = \Delta E - \tau \mathrm{v} \cos \phi \tag{31}$$

An assumption is then made that the material can be described by a term θ_g, which is the temperature at which the polymer structure in the glass would be an equilibrium structure and can be conveniently set to T_g. By performing a statistical average, the maximum number of flexed bonds for a given applied stress can be calculated and the current structure related to an "equivalent temperature," θ_1.

Using the WLF (49) equation to model the effect of temperature on the material viscosity Robertson went on derive an equation for the maximum shear

strain rate, $\dot{\gamma}_{\mathrm{MAX}}$, induced by the shear stress, τ, as

$$\dot{\gamma}_{\mathrm{MAX}} = \frac{\tau}{\eta_{\mathrm{g}}} \exp\left\{ -2.303 \left[\left(\frac{c_1^{\mathrm{g}} c_2^{\mathrm{g}}}{\theta_1 - T_{\mathrm{g}} + c_2^{\mathrm{g}}} \right) \left(\frac{\theta_1}{T} \right) - c_1^{\mathrm{g}} \right] \right\} \tag{32}$$

where c_1^{g} and c_2^{g} are the "universal" constants from the WLF equation, η_{g} is the "universal viscosity" at T_{g}, and θ_1 is as discussed above.

The model can be used to predict the shear rate as a function of shear stress for a range of temperatures. In the original paper a lack of shear stress data meant that the predictions were compared to tensile stress–strain data by decomposing the tensile data into shear and biaxial components. The point on the tensile stress–strain data that Robertson took to be the most appropriate stress to compare with the computed strain rate was the yield point. The model gives values for the yield stress and the temperature dependence of the yield stress that agree well with experiment for a number of polymers.

The model is attractive since the six parameters required above can be obtained independently and thus no fitting to the data is required. Of these six parameters, only two relate directly to the individual polymer, namely the glass-transition temperature, T_{g}, and the parameter v, the average volume of chain segments containing two bonds (though in practice Robertson took this to be the volume of a monomer unit in the glassy state at room temperature).

The Robertson model was extended by Duckett and co-workers in 1970 (29) to account for the pressure dependence of the yield stress. By their argument, if the two states are trans and cis and the effect of stress is to increase the number of cis conformations, then this implies a lower resulting density since the packing is less efficient. This in turn implies the change in conformations has an impact on the hydrostatic component of the applied stress. They further suggest that the hydrostatic component of the stress, p, will do work during the activation process leading to an overall energy difference between the two states of

$$\Delta E - \tau v + p\Omega \tag{33}$$

where p is positive in compressive loading and negative in tensile loading. The term Ω has units of volume. Using this modification they successfully correlated the torsional yield stress dependence of PMMA under hydrostatic pressure with the variation in the yield stress under compressive and tensile stresses as a function of temperature and strain rate.

Argon Model. Argon in 1973 (38) developed a molecular model for the initial yield based on the Gibbs free energy of the system. Again it considers that yield does not occur until the resistance to segmental rotation can be overcome by the application of stress. Strain in the sample is proposed to occur by the rotation of small molecular segments from an initially random orientation to a preferential orientation along the load axis. Such a process is modeled by introducing a "kink pair" into the molecule. The resistance to this kink formation is primarily from the surrounding molecular chains, and is modeled as an equivalent elastic medium. Argon derived an expression for the change in free energy, $\mathrm{d}G^*$, required

to produce segmental rotation:

$$dG^* = \frac{3\pi G\omega^2\alpha^3}{16(1-\nu)}\left[1-\left(\frac{\tau}{\frac{0.077G}{1-\nu}}\right)^{5/6}\right] \tag{34}$$

where G is the temperature-dependent shear modulus, ν is Poisson's ratio, ω is the net angle of rotation between the two configurations, α is the mean molecular radius, and τ is the applied shear stress. This leads to an energy maximum as a function of the distance between molecular kinks and defines an energy barrier for kink formation. The rate of transfer between the ground and activated states is then modeled in a manner similar to that of a thermally activated Arrhenius process.

This leads to a plastic strain rate given by

$$\dot{\gamma}_{\mathrm{P}} = \dot{\gamma}_0 \exp\left(\frac{-\mathrm{d}G^*}{kT}\right) \tag{35}$$

where $\dot{\gamma}_0$ is a pre-exponential factor having the units of s^{-1}, k is Boltzmann's constant, and T the absolute temperature.

Equation 35 can be rewritten as

$$\dot{\gamma}_{\mathrm{p}} = \dot{\gamma}_0 \exp\left\{-\frac{As_0}{T}\left(1-\left(\frac{\tau}{s_0}\right)^{5/6}\right)\right\} \tag{36}$$

where

$$A = 39\pi\omega^2\alpha^3/16\kappa$$

and

$$s_0 = 0.077G/(1-\nu)$$

s_0 is termed the athermal shear yield strength and is the value of the shear yield strength as the temperature approaches absolute zero (and assuming finite strain rates). The above equation can be rearranged to give

$$\tau = s_0\left[1-\frac{T}{As_0}ln\left(\frac{\dot{\gamma}_0}{\dot{\gamma}_{\mathrm{P}}}\right)\right]^{6/5} \tag{37}$$

Equation 37 thus captures both rate and temperature dependencies of the shear yield stress.

Haward and Thackray Model. In 1968 Haward and Thackray (37) developed a one-dimensional model for yield using a spring in series with a parallel arrangement of a spring and dashpot (Fig. 12). The dashpot, rather than being Newtonian as with the standard Maxwell/Kelvin models, was instead an Eyring

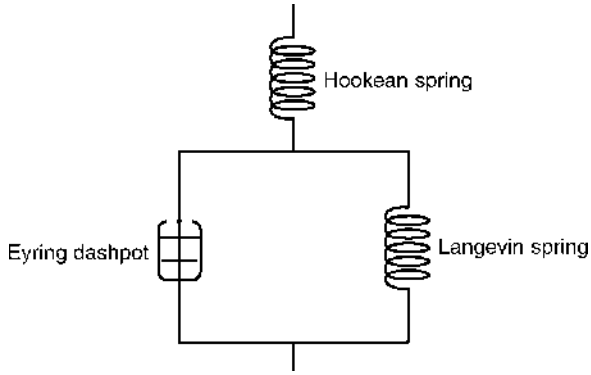

Fig. 12. Schematic of the one-dimensional model of Haward and Thackray.

dashpot. The standard Hookean-type spring was replaced with a Langevin (finite extensible) spring to account for the strain hardening (entropic resistance) observed at larger strains. The initial elastic response remains modeled with a Hookean spring in series. While the model correctly gives the dependence of the yield stress on strain rate it gives only a somewhat simple approximation to the realistic stress–strain response. Also, in common with all the previous models (Eyring, Robertson, and Argon), it does not address the issue of strain softening. However, the general principle of the model has been widely accepted and has been further refined and extended to address some of the shortcomings as discussed in the following sections.

Boyce, Parks, and Argon model (BPA Model). In a fashion that is conceptually the same as the Haward and Thackray (37) model, the BPA (39) model assumes that after an initial elastic response, the plastic resistance can be separated into a resistance to flow due to an activated process and an entropic resistance due to molecular alignment. The model builds on the Argon model to describe the initial yield in terms of the resistance to segmental motion and extends it to include pressure and strain-softening effects. It then goes on to model the second component of resistance to (large-strain) deformation, that of entropic resistance, in terms the "three chain" non-Gaussian (inverse Langevin) statistical model of Wang and Guth (50).

In the BPA model, it is the athermal shear strength given in the Argon model, s_0, which is modified to explain the observed strain-softening behavior. The reasoning behind this is that as the material undergoes the initial stages of plastic flow some restructuring of the molecular chains is assumed to occur and these changes are in turn assumed to cause a reduction in the athermal shear resistance. The evidence for this is discussed in detail in the paper by Boyce and co-workers (39). Briefly, tests carried out on polycarbonate after different thermal treatments and tested under identical conditions give different peak yield stress levels. However, the post-yield strain softening generally brings the stress levels down to the same value and this is interpreted as the material achieving a "preferred structure" during plastic flow. The decrease in the athermal shear resistance with strain is modeled phenomenologically by the following

expression:

$$\dot{s} = h\left(1 - \frac{s}{s_{ss}}\right)\dot{\gamma}_P \tag{38}$$

where s is the current value for the athermal shear resistance and is a function of the instantaneous structure, s_{ss} is the value s reaches at steady state, ie in the preferred structure, and $\dot{\gamma}_P$ is the plastic strain rate. Note that s_{ss} can itself be temperature and rate dependent. h is the slope of the yield drop with respect to strain, with the yield drop defined as the difference in the maximum stress before softening and the lowest stress level after plastic flow. The yield drop depends on temperature and strain rate and varies with strain as a function of structure and strain rate.

As noted above in discussing yield criteria, the shear yield strength generally increases linearly with applied hydrostatic pressure. Similar to the modified Tresca or von Mises yield criteria, where the shear yield stress is modified by a term linearly dependent on pressure, the BPA model introduces a term to modify the current athermal shear yield strength, s:

$$\tilde{s} = s + \alpha P \tag{39}$$

where α is the pressure coefficient, P the hydrostatic pressure, and s the athermal shear resistance modified for strain softening.

Thus the term s_0 in the original Argon model for yield (eq. 36) is replaced by $\tilde{s}$ to give

$$\dot{\gamma}_P = \dot{\gamma}_0 \exp\left\{-\frac{A\tilde{s}}{T}\left[1 - \left(\frac{\tau}{\tilde{s}}\right)^{5/6}\right]\right\} \tag{40}$$

where the pressure and strain-softening effects are contained in the $\tilde{s}$ term.

The second part of the BPA model concerns the entropic resistance resulting from molecular orientation and which leads ultimately to strain-hardening behavior. This is strictly a postyield phenomenon and indeed the physics of the development of chain orientation and subsequent material behavior alone is the subject of books (eg Ward I.M. (51)). The BPA model uses the development of three-dimensional entropic resistance as first modeled by Parks and co-workers (52). Consider an amorphous polymer that is plastically deformed below its glass-transition temperature (T_g). If this material is then heated to above T_g it will recover to its original undeformed state. In order to prevent the material returning to the undeformed state at temperatures above T_g, it would be necessary to impose a stress on the sample. This restraining force then acts to counteract the shrinkage force or 'back stress' B_i. For the plastically deformed material below T_g, this back stress can be considered to be frozen-in to the deformed polymer at temperatures below T_g and is the source of resistance to further deformation. The recovery of the material deformation above T_g clearly has parallels with rubber elasticity and the orientation hardening is modeled using the statistical mechanics theories of rubber elasticity (Treloar 1975 (53)). For low stretch ratios, the standard Gaussian statistical model of Treloar (53) is sufficient. However, the BPA model as originally developed used the non-Gausssian statistical mechanics

network (Three-chain model) of Wang and Guth (50). This gave an expression for the back stress, B_i, as a function of the number of statistical segments between entanglements, the plateau rubber modulus (through which the temperature effects are taken into account) and the change in entropy as a function of the principal plastic stretches. The reader is referred to the original paper (39) for the specific details and development of this aspect of the model. The model has since been incorporated into commercial finite element codes (ABAQUS).

The model has been subsequently refined (Arruda and co-workers (54)) to more accurately describe the three-dimensional spatial orientation of the stretched molecular network using the eight-chain model (though comparison of the predictions from the eight-chain model with experimental results from natural rubber and polydimethylsiloxane has called into question the physics of that model (55)). The BPA model has been further developed (56) to account for aging effects (see, eg Reference 57). A model using the same underlying concepts, but again developed to improve the description of the strain hardening (entropic resistance), has been given by Wu and van der Giessen (58) using a "full chain" model.

Tervoort and co-workers Model. While the above models make reasonable predictions of the stress–strain behavior in monotonic loading conditions, a main drawback to them is that they use only a single stress-dependent characteristic (relaxation) time. As a consequence, the predicted behavior tends to show a sharp transition between elastic (solid-like) and plastic (fluid-like) behavior. However, it is found in practice that all polymers exhibit behavior consistent with a spectrum of relaxation times and this is clearly going to affect the stress–strain response at constant strain rate. In an effort to address this inconsistency Tervoort and co-workers (40) have developed a "modified compressible Leonov model."

The model is based on an earlier one by the same authors, the "compressible Leonov model" (59). In this, the behavior is modeled with a single Maxwell element where the dashpot and spring now have a relaxation time that is a function of the applied shear stress. This is similar in principle to the change seen in the relaxation time with a change in temperature (time–temperature superposition, (see VISCOELASTICITY), leading to the concept of time-stress superposition and a "stress clock" within the material. The model is developed with thermodynamically consistent constitutive equations by assuming that the free energy of the system (a measure of the stored energy) is given by two state variables, the relative volume deformation and the isochoric strain tensor. The volume deformation is coupled to the hydrostatic component of stress while the isochoric strain is determined by the deviatoric stress. It is assumed that the volume deformation remains elastic, whereas the accumulated isochoric elastic strain is reduced over time because of a plastic strain rate. This plastic strain rate is described by a three-dimensional Eyring equation. The single-element model is essentially an elastic–plastic model and still exhibits a sharp transition between the two behaviors. To make the model more realistic, it was extended (40) to include a discrete relaxation spectrum by using an array of 18 Leonov modes, each with a unique relaxation time.

Tervoort and co-workers tested the multimode model using polycarbonate since it could be described with a single relaxation mechanism having a distribution of relaxation times at the temperature of interest. The model parameters for

the Eyring term were determined from plateau creep rates and the linear Leonov parameters from a linear shear relaxation curve (obtained from inversion of the creep compliance curves). The resulting model predictions agreed excellently with stress–strain curves over a range of strain rates up to approximately 8% strain. However, the model lacks any term to account for the entropic resistance (strain hardening) and so is valid only up to the yield point.

In subsequent work, Govaert and co-workers (60,61) specifically address the postyield large-strain phenomenon of strain hardening, again for a polycarbonate. In an effort to minimize the effects of a localized, inhomogeneous strain deformation (neck), they adopted a technique of mechanical preconditioning. This technique aims to reduce the strain-softening characteristics of the material by conditioning the material through plastic deformation (61,62). The resulting true stress–true strain curves show a markedly reduced yield drop, while maintaining the same large-strain response. Interestingly, the authors found that the large-strain data could be modeled as simple neo-Hookean behavior and this was true up to the failure point (at a draw ratio of approximately 3). As the authors observed, this is in contrast with the results of eg Arruda and co-workers (63) for a different grade of polycarbonate where there was a deviation from neo-Hookean behavior indicating finite extensibility effects (ie a rapid upturn in the true stress–true strain response).

Caruthers and co-workers Model. The group of J.M. Caruthers at the Chemical Engineering Department of Purdue University has, over the last decade or so, been developing a set of unified constitutive equations that aim to realistically model a wide range of rheological and mechanical properties (41,42). A detailed description of the model is beyond the scope of this article and we mention here only the main ideas behind the development of the model (see also VISCOELASTICITY). The model addresses the time, temperature, and history (thermal and mechanical) dependence of the material behavior using a set of thermoviscoelastic constitutive equations based on Rational Thermodynamics (64,65). The model introduces a material (or reduced) time, where the material timescale is determined by the instantaneous thermodynamic state of the material, using the Adam–Gibbs (66) model, which relates the relaxation time to configurational entropy. This is a potentially important development in the context of this article, as it allows the prediction of nonlinear mechanical behavior including yield. The model is still in development, but has successfully predicted a range of behaviors including specifically isobaric volume relaxation, yielding under uniaxial extension, shear thinning, and stress overshoot in transient shear (42).

A particularly appealing aspect of the model is that all the model parameters can be determined from independent experiments and further that they are relatively few in number. Thus a material can be characterized in a relatively short period of time, though the mathematical framework of the model is somewhat intensive.

Dislocation Plasticity

The observation of microscopic shear bands in polymeric materials, coupled with the highly successful application of dislocation theory to plasticity in ductile

metals, has led to the concept of dislocation plasticity in polymeric materials. The first application of dislocation mechanisms was, not surprisingly, to semicrystalline polymers (67). Predeki and Statton (68,69) looked at the effect of chain ends on crystalline regions and introduced the idea of screw and edge dislocations occurring in nylon-6,6 (68). They further examined the effect of shear stress on such dislocations in polyethylene (69). Direct evidence for the presence of dislocations in polymer crystals was obtained by Petermann and Gleiter (70) from the electron microscopy of single crystals of polyethylene. Gilman (71,72) further suggested that dislocation mechanisms can be applied to amorphous solids such as glasses and polymers. Bowden and Raha (73) developed a model of yield in which micro–shear bands are created by the formation and growth of dislocation loops, the energetics of which are influenced by the shear stress and the thermal energy. Unlike metals, where the dislocations or defects are inherent, the dislocations in polymers are formed under the action of an applied stress. Once formed, they may grow with the aid of thermal activation, ultimately leading to yield. The authors emphasize that the dislocation process they envision as occurring in an amorphous solid is not the same as in the classic concept of crystal plasticity, though it is a close analogy.

The energy U of a dislocation loop of radius R is

$$U = (2\pi R)\frac{Gb^2}{4\pi}\ln\left(\frac{2R}{r_0}\right) - (\pi R^2)\tau b \tag{41}$$

where r_0 is the radius of the dislocation core, τ the applied shear stress, G the shear modulus and b the Burgers vector (essentially equal to the magnitude of the shear displacement). The first term in equation 41 is the elastic strain energy associated with a loop of length $2\pi R$ and the second term the work done by the applied stress to expand the loop to radius R (of the order of 1 nm). As the loop expands the energy at first increases then reaches a maximum at some critical radius (R_c), then will monotonically decrease. As expected, the height of this energy barrier decreases with increasing shear stress. The Bowden and Raha model is thus a thermally activated model whereby both the rate and temperature dependence are captured in the term U/kT. Interestingly, the model also implicitly accounts for strain softening—as the dislocation loop overcomes the peak in the energy barrier, further growth leads to a lower energetic state with the implication of reduced resistance to further extension. As the model is presented, the reduction in resistance (and hence the degree of strain softening) is monotonic, that is there is no limit to the extent to which the material will strain soften. This is clearly a major limitation of the model, though the authors have suggested a number of mechanisms that may limit the degree of strain softening.

The above model based on dislocation-type defects in polymer glasses is attractive in that it allows one to put some order and physical interpretation to the (obviously complicated) processes occurring during deformation. Care must be exercised though in taking the analogy with dislocations in metals too far—the ordered structure of metals is not seen in polymers, hence the meaning of a defect such as a dislocation is unclear.

Ultimate Shear Strength

The maximum theoretical strength of a crystal had been estimated by Frenkel as far back as 1926 (74), and the same general ideas have been applied to amorphous polymers (73,75,76). Briefly, if an equilibrium crystal lattice is sheared to a strain of 1, each atom will have moved to a new equilibrium position. At a strain of 0.5, the atoms will be between one equilibrium position and the next and the shear stress required to hold it in position will be zero (albeit in an unstable state). Consequently, the maximum shear stress is assumed to occur at a shear strain of approximately 0.25. Since the initial slope of the stress–strain curve is the shear modulus G, this gives an estimate of the maximum shear stress to be approximately $G/6$. While the structure of an amorphous polymer is far from that of an ideal crystal it is reasonable to suppose that the molecular segments are at some equilibrium position and at a high enough shear stress most, if not all, will fall into a new equilibrium position (though the energy landscape, and hence equilibrium potentials, will not be as uniform as those in a crystal). The model as proposed did not allow for thermal fluctuations (ie it was effectively for a material at 0 K) and it is expected that taking account of such fluctuations would reduce the theoretical strength.

Other estimates of the ultimate shear strength of amorphous polymers have been made by a number of authors and generally all fall within a factor of 2 of each other (38,77,78). Stachurski (79) has expressed doubt as to the validity of the concept of an intrinsic shear strength based on the value of the shear modulus, G, for an amorphous solid. He questions which modulus is the correct value to use—the initial small strain value or the value at higher strain (the yield point or the ultimate extension). Further, the temperature and strain-rate dependence of both the yield strength and modulus (however defined) suggests that perhaps the ratio of yield strength to modulus is not a true intrinsic material property. We remark however that the temperature and strain-rate dependence of both the yield stress and the shear modulus are often similar.

A related issue is that the modulus is a viscoelastic property, as evidenced by the temperature/strain-rate dependence, and that for most polymers (at least those without a large beta transition near the alpha transition) time–temperature superposition of, for example, the shear relaxation modulus is valid (80). Further, G'Sell and McKenna (81) have shown that the yield stress vs strain rate also seems to obey time–temperature superposition. Hence there is a correlation between the viscoelastic properties and the yield response of polymers, though one that is not generally stated explicitly. We note that some of the models mentioned previously, such as those of Caruthers' group (41,42), Tervoort and coworkers (40), and Knauss and Emri (35), are (nonlinear) viscoelastic models that have yield arising due to the nonlinear response induced by the material clock (see VISCOELASTICITY).

Calorimetry and Dilatometry

When a polymer is deformed, work is necessarily done in the material. On subsequent unloading, the stress–strain curve does not generally follow the loading

curve and the difference in the areas under the two curves gives the net work done on the material (W). This work can be subdivided into work done in changing the internal energy of the material ($\mathrm{d}U$) and heat liberated (Q):

$$W = \mathrm{d}U + Q \tag{42}$$

By measuring both the heat flow generated during deformation (Q) and the engineering stress–strain data (and from this the quantity W) it is possible to estimate the change in the internal energy of the sample. A pioneer in this field of study is Oleinik (also spelled Oleynik) (82). In a series of experiments, samples of polystyrene placed in a calorimeter were compressed to varying levels of strain (up to approximately 40%) and unloaded, and the W and Q were calculated. The total work (W) rises somewhat linearly with applied stress while the amount of heat liberated (Q) rises at an initially slower rate then increases to become parallel to the W curve at a strain of approximately 25%. This means that the stored internal energy ($\mathrm{d}U$) rises at lower strains then plateaus out at strains above 25%, with an inflection point at or near the yield strain of 12%.

The same effect can be observed by performing DSC tests on previously strained samples. Hasan and Boyce (83) subjected annealed polystyrene to compressive strains up to 170% followed by DSC scans up to and through the glass-transition temperature (T_g). Comparing the results to freshly annealed samples, it was seen that for samples that had been strained, a pre-T_g exotherm appeared that increased with increasing compressive strain. This pre-T_g exotherm increases in magnitude up to a strain of 25% and remains constant thereafter up to the maximum strain of 170%, in excellent agreement with the data of Oleinik. They also note that the exotherm is spread over a wide temperature range (starting at approximately $T_g - 35^\circ$C), which they attribute to the distributed nature of the structural state. In addition, there appears to be a similar inflection point at a strain near the yield strain (within the range 10–15%).

The exact nature of the storage mechanism that is reflected in the increase in internal energy remains unclear. Indeed it is not clear that the energy term $\mathrm{d}U$ can be considered simply as a storage term, especially at the higher strains where energy could be expended on chain scission or processes akin to phase changes occurring at and above yield.

Polymers are inherently viscoelastic, compressible materials and under conditions of dilatational deformation (eg uniaxial tension or compression) a full description of their behavior needs to take into account the volume changes due to, at least, the hydrostatic component of the stress (84). One of the earliest works on volume effects on yielding in glassy polymers was by Whitney and Andrews (85), who examined a range of polymers under uniaxial compression. In the study, the authors observed a volume contraction upon loading up to the yield point, after which the volume remained approximately constant. More recently (86), subyield tension and compression tests were performed on two commercial grades of polycarbonate (PC). These tests were performed under stress relaxation conditions and showed that under tension the volume increased somewhat monotonically with strain while under compression the reverse was true, ie the volume decreased monotonically. While the volume at a small strain was found to recover toward the initial state, at strains approaching yield and in tension the material

actually densified to a state of higher density than the undeformed polymer. It was postulated that the mobility that allowed the material to densify was related to its propensity to yield rather than fail in a brittle manner. A number of studies have been performed on the volume evolution during mechanical deformation [eg (87–89)]. Also studies on the changes in "free volume" with deformation using positron annihilation spectroscopy (PALS) (90–92), have been carried out. The reader is referred to the texts for further details.

Computer Modeling

With the advent in recent years of increasingly powerful and cheap computing power, molecular modeling of the deformation response of polymers has come to be of increasing importance (76). Molecular mechanics uses the Newtonian equations of motion to calculate the step-wise displacement of individual atoms within a molecule in small time intervals (typically of the order of femtoseconds). On each step, the atom's position is modified with reference to its previous state (position, velocity, etc) and taking into consideration, for example, its bond length and bond angle (bonded interactions) and Van der Waals forces (nonbonded interactions) with its nearest neighbor. The system as a whole is then optimized using potential energy functions to determine the equilibrium conformation. Molecular mechanics calculations are performed on systems that are generally considered to have little, if any, thermal energy (ie at low temperature). As such, the optimization procedure may only find the conformation representing the *local* minimum in the energy landscape and this will not necessarily (indeed rarely) be the lowest possible energy. Molecular dynamics, on the other hand, considers not only the force interactions but also the thermal motions of the molecule. By doing so, the molecule is allowed to overcome energy barriers and so explore its surroundings more effectively, assisting in finding the *global* energy minimum. Importantly, in molecular dynamics the thermal motion is always active and the molecules tend to oscillate about the energy minimum, giving additional information about the time-dependent motion of the molecules.

As noted, the field of molecular simulation is relatively new, and a detailed review of it is beyond the scope of this text and we introduce here a few of the more relevant references. One of the first applications of molecular mechanics to polymers was by Theodorou and Suter (93,94), who modeled atactic polypropylene as an amorphous cell subjected to a range of stress conditions (hydrostatic pressure, pure strain, and uniaxial strain). Such modeling generally gives reasonable estimates of the elastic constants of a material [within 15% (79)], providing the density of the glass is correctly modeled.

Argon and co-workers (95,96) have developed an atomistic mechanics model of polypropylene and related it to experiments performed at a temperature of 10°C below the glass-transition temperature. Stress–strain curves calculated after small strain increments showed a series of generally monotonically increasing stress versus applied strain sections (elastic response), interspersed with sudden step-wise drops in the load (plastic events). Significantly, the authors note that the plastic events are not associated with any deformation process invoked by many of the molecular theories discussed above (ie a sudden conformation or

configuration change, a dislocation motion or kink propagation). However, because this was an athermal model, the meaning of these events for a real viscoelastic or viscoplastic polymer is unclear.

Computer modeling can clearly help in the understanding of the deformation and yield behavior of polymeric systems by giving an insight into the individual molecular, indeed atomic, movements that occur. However, the simulations are typically run over a few tens of picoseconds at most and in a volume of a few cubic nanometers—such scales of time and dimensions cannot fully capture the processes involved in yield at the present state of development.

Semicrystalline Materials

The propensity of a polymer to crystallize is chiefly determined by its molecular architecture, specifically the regularity of the polymer chain. Polymers consisting of the same repeat unit, the simplest example being linear polyethylene, can fit together neatly to form the ordered crystalline phase and typically have 70–80% crystallinity. For polymers where a hydrogen from the ethylene monomer is replaced by a bulky side group [for example the methyl group ($-CH_3-$) in polypropylene or the phenyl group ($-C_6H_5$) in polystyrene], the polymer chain can exist in one of three forms of handedness, or tacticity. If all the side groups lie on the same side of the main chain the material is called isotactic; if they lie in a regularly alternating fashion left and right of the main chain the material is termed syndiotactic; and finally, if they occur randomly positioned along the main chain they are termed atactic. The least regular, atactic form generally does not crystallize to any degree, while both the isotactic and syndiotactic forms can crystallize, though the degree to which either form does so depends on the structure, polarity of the side group, etc.

Early X-ray studies on the structure of Semicrystalline Polymers (qv) showed that the longest dimension of the crystallites was typically of the order of a few tens of nanometers. This is a small fraction of the length of a typical polymer chain, which may be of the order of several thousands of nanometers, and it was originally thought that the polymer chain moved successively between different regions of amorphous and ordered crystalline phases in what is termed the "fringed micelle model." However, later work on single crystals grown from dilute solutions revealed that the polymer backbone was perpendicular to the longest dimensions of the crystal. Such a structure could only be produced if the polymer chains were folding back upon themselves.

The current prevailing view is that the crystalline regions in semicrystalline polymers are made up of plate-like structures formed from mostly chain-folded molecules. These plate-like structures are termed lamella and are typically some 10–20 nm thick. As the molecules forming the lamella chain fold, they may either reenter adjacent to the current position, reenter at some position farther along the lamella, or stay in the amorphous region. Ultimately, farther along the molecular chain, such molecules may enter another lamella thus forming "tie molecules," akin to entanglements in amorphous polymers. These lamellae may in turn form supramolecular structures called spherulites—aggregations of lamellae forming and growing from a central nucleation point.

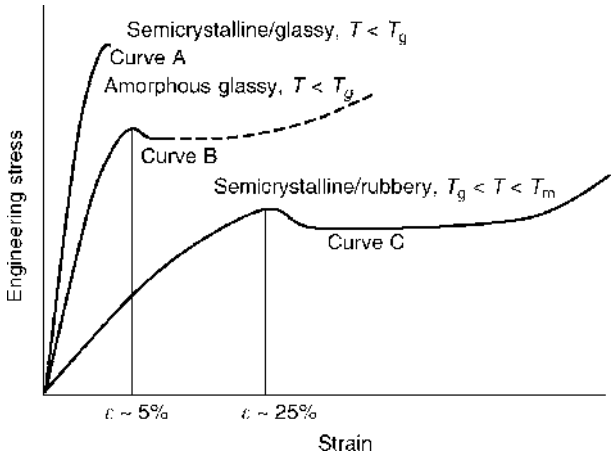

Fig. 13. Representative engineering stress–strain curves for a semicrystalline polymer as a function of temperature.

Below the crystalline melting point, semi-crystalline polymers are then essentially two-phase systems consisting of a stiff, rigid crystal phase embedded in a more flexible amorphous phase. The amorphous phase may be either above its glass-transition temperature (semi-crystalline/rubber) or below it (semi-crystalline/glass). The yield behavior of semi-crystalline polymers depends critically on a number of factors, eg the degree of crystallinity, the lamellar thickness and interlamellar spacing, spherulite size, the number of tie molecules and, of course, temperature. That said, however, they still show the same general behavior as depicted in Figure 1: brittle at low temperatures, yield and possible strain hardening at intermediate temperatures, and rubbery or viscous flow behavior at higher temperatures.

At temperatures below the T_g of the amorphous phase, the crystallites and associated tie molecules can severely reduce the mobility of the polymer chains and thus tend to embrittle the material. This generally leads to a brittle-like failure (Fig. 13, curve A) though at slow enough rates yielding and drawing may be observed (Fig. 13, curve B).

At temperatures above the T_g of the amorphous phase, the crystallite regions still act to prevent the free movement of the amorphous region and the material does not behave in a rubber-like fashion as would be expected for a pure amorphous polymer. Under these conditions, where the amorphous fraction would not be expected to show a yield point, yield is associated purely with the crystallites. On initial deformation, the crystallites act as hard inclusions, and the strain in the material is carried predominantly within the amorphous fraction. Given that the yield strain in these materials is typically of the order of 0.25 it is unlikely that the (rubbery) network has been sufficiently stretched and strain hardened to load the crystallites to yield. However, it is expected that the network has been sufficiently stretched, such that the tie molecules associated with the lamellae have become taut and so are able to transfer the load to the crystallites. The precise mechanisms associated with the subsequent yield of the

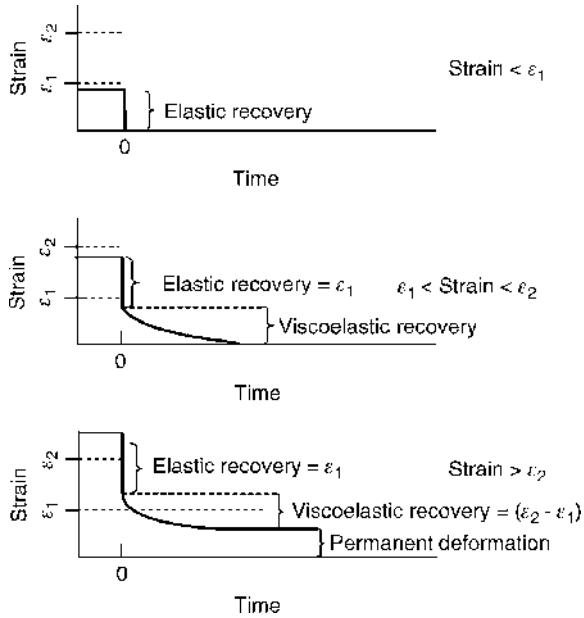

Fig. 14. Schematic of the strain recovery with respect to the double yield point observed in some semicrystalline materials (stress removed at time 0).

crystallites are still not well understood. However, the observation of two yield points (double yield) in polyethylene (97–99) has provided some insight into the molecular processes at work. Up to the first yield point, the material is elastic and deformations are fully recoverable (Fig. 14). The first yield point occurs at low strains (~5%) and marks the onset of recoverable deformation. This process has been associated with an interlamellar shear process or martensitic transformation within the lamellae and leads to a reorientation of the lamellae, with little or no destruction of the lamellae themselves. The second yield point occurs at a higher strain (20–50%) and marks the onset of permanent plastic deformation and is generally associated with the formation of a neck. At this point coarse slip occurs within the lamellae leading to fragmentation and destruction of the lamellae themselves. The post-yield behavior is largely associated with the amorphous regions and, like a pure amorphous polymer, is controlled by the entangled network. As such, phenomena such as strain hardening and cold drawing are commonly observed as discussed previously (Fig. 13, curve C).

Phenomenologically, the rate and temperature dependence of the yield stress of semi-crystalline polymers can be described by the Eyring activated state model, as discussed earlier, with either one (100,101) or two (46,102) activated processes. However, developing a theory for the yield of semi-crystalline polymers is clearly complicated by the presence of two distinct phases. It is unclear at present whether the models discussed above are even applicable to the amorphous phase present in semi-crystalline polymers because of the topological constraints that the crystalline regions impose. Nevertheless, in light of the fact that above the T_g of the amorphous region, it is the crystallites that dominate the yield behavior the ideas of classical crystal plasticity are obviously attractive.

Young (103) developed a theory along such lines in which the energy required to initiate a screw dislocation in the crystal lamellae determines the yield stress. The model correctly predicts the observed linear relation between yield stress and lamellar thickness, though the quantitative agreement with experiment is controversial (104–107). A model has been recently developed (108) wherein the driving force for the screw dislocations are thermally activated "chain twist" defects that transfer along the chain backbone.

In the early 1990s Bartczak, Argon, and Cohen conducted a series of tests on what they termed "single-crystal textured high density polyethylene" (109,110). These were samples that had been compressed under plain strain conditions, producing an axisymmetric texture that approximated to a macroscopic single crystal. X-ray scattering studies were conducted on the material at various stages of deformation (up to a strain of 1.86, after recovery) to monitor the structural evolution. The resulting material showed distinct crystallographic features indicating unique crystallographic planes, with the *c*-axis of the crystallites aligned along the flow direction (indicating that the lamellae are, broadly speaking, oriented perpendicular to the flow direction). Samples were then cut from the textured samples at particular orientations in order to investigate specific deformation mechanisms. Significant differences in the stress–strain response of samples tested at differing angles to the chain axis were observed under both tension and compression. The papers offer considerable insight into the contribution from different crystallographic deformation mechanisms. Interestingly, when such mechanisms could be isolated, it was found that the Coulomb criterion was an adequate description of the yield surface. The specifics of the various deformation mechanisms and their relation to the specific crystallographic planes is beyond the scope of this article, and the reader is referred to the original papers (109,110) for details.

Crazing

The previous section was concerned with what may be termed "macroscopic yield," which is the shear yield over an entire sample ligament area (albeit localized in the case of neck formation). Another mode of deformation that is commonly observed in thermoplastics is that of crazing. Unlike the shear yielding discussed above, crazing is a microscopically localized phenomenon. The crazes that result from the localized process can be looked upon as load-bearing cracks, where the load-bearing capacity is provided by highly drawn fibrils of material spanning the two interfaces. This is a unique aspect of crazing in polymers as the fibrils can support the crack and help prevent or delay failure.

Crazing generally occurs where the stress on the sample has become highly concentrated owing to, for example, surface defects such as flaws, scratches, or inclusions within the material such as dust or other contaminants. Crazes can also occur in homogenous polymers, ie those without any contaminants or additives and which are flaw-free. An elegant series of experiments by Argon and co-workers (111) using samples carefully prepared from single pellets has shown that crazing can still occur without any tell tale origins relating to contaminants, a behavior denoted as "intrinsic crazing." While no obvious cause for the craze

nucleation may be evident, it must nevertheless originate at a particular point because of an intrinsic local heterogeneity in the molecular structure, such as a local density variation. The stress required to craze such samples is higher than that observed in bulk (and implicitly contaminated) samples and indicates that while flaws or inclusions are not a necessary condition for crazing, they do lead to premature crazing.

The appearance of crazes in a material is generally a precursor to brittle failure. While such a mode is normally to be avoided, the presence of crazes can provide some beneficial effects. Because the crazes contain highly drawn fibrils of material, considerable plastic deformation and hence energy goes in to their formation and this can be a major source of fracture toughness. Indeed, the deliberate inclusion of small, typically rubber, particles into inherently brittle polymers is commonly undertaken to produce tough materials (112–115), because the presence of the particles dramatically increases the craze density.

The following is a brief overview of the subject matter which introduces the reader to the main features of craze morphology and current theories on their initiation, growth, and failure. The reader is pointed in particular to excellent reviews on many aspects of crazing by Kramer (116), Kramer and Berger (117), Kambour (118), and Donald (119,120), and much of the subsequent discussion follows the development in those reviews.

Crazing in polymers follows three distinct stages: craze initiation where the craze is nucleated, craze growth where the craze continues to grow in a direction perpendicular to the applied stress, and finally craze failure, the precursor to ultimate failure. Before discussing these three aspects of crazing, a general overview of craze morphology is given to familiarize the reader with the structure of the craze and the salient features involved in craze growth. The specific details and evolution of the structures are discussed in the relevant subsequent sections.

Craze Morphology. Figure 15 shows a schematic of craze nucleation and growth. The presence of an intrinsic or extrinsic heterogeneity causes the bulk stress to be locally modified. This results in an increase in the local triaxial stress field and forms a localized plastic zone (Fig. 15a). Small voids form in this plastic zone and, as the voids grow, they eventually coalesce with the original material between the voids forming the fibrils (Fig. 15b). The final craze structure (Fig. 15c) consists of the two surfaces bridged by a network of fibrils of drawn (highly anisotropic) polymer with a voided region at the craze tip from which craze growth may continue. Such fibrils typically have a diameter of a few tens of nanometers and a length (craze thickness) of the order of a micron. As the craze continues to grow, the fibrils extend by either a creep mechanism or by drawing in additional material from the bulk–fibril interface (Fig. 16) under the influence of the local stress at the craze boundary (σ_{CR}), which is typically slightly lower ($\sim$5%) than the applied bulk stress (σ_B) (Fig. 17, after Reference 121—the data shown is for an isolated craze in an "infinite" sheet, points on the x-axis denoting the distance from the centerline of the craze and is of course symmetrical about that line). Eventually a failure criterion is reached and the fibrils fail. The loss of the load-bearing capacity of the failed fibrils means the neighboring fibrils are subjected to an additional load and this can, under certain circumstances, lead to a runaway failure of the fibrils, true crack formation, and ultimately brittle failure.

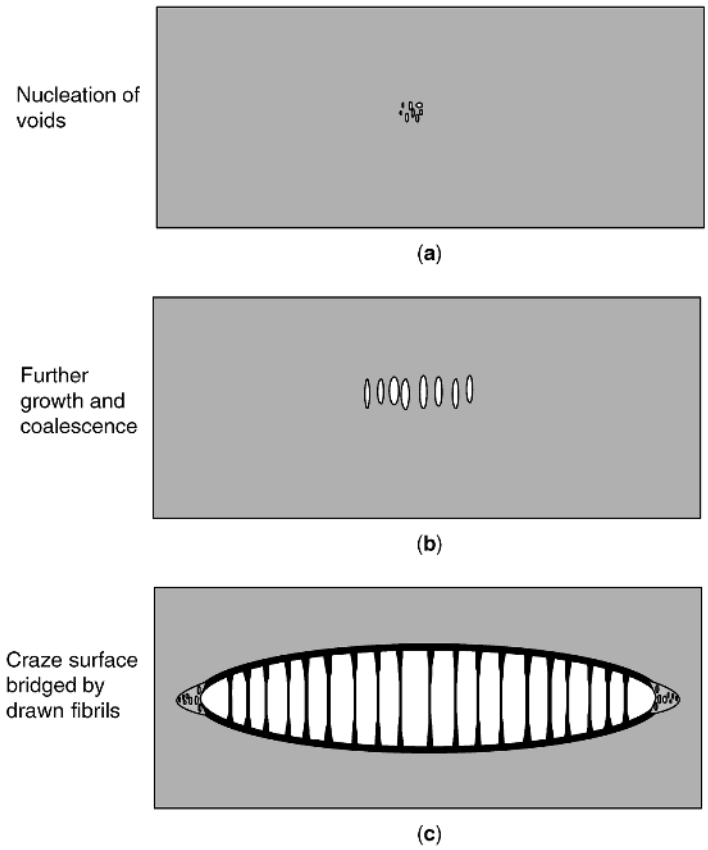

Fig. 15. Schematic of (**a**) void formation, (**b**) craze initiation, and (**c**) craze growth.

Crazes also normally occur at surface crack tips. The presence of a crack causes a geometrically imposed increase in the local stress (stress concentration), which results in a dilatational stress field. This in turn leads to the formation of a local plastic zone and, in a manner similar to the above, to cavitation and the formation of a craze. The general features of a surface craze are the same as those of an internal craze (Fig. 15), though with the obvious lack of symmetry owing to the presence of the crack. Such crazes tend to stabilize a crack by blunting the crack tip, reducing the stress concentration while retaining a load-bearing capacity.

We now look in more detail at the individual stages of craze formation and subsequent growth.

Craze Initiation

Unlike the shear yield process, crazing is an inherently non-isovolume event. Cavitation of the material requires a dilatational component of the stress tensor, such as occurs in triaxial stress systems that may be found in samples subjected to plane strain conditions. In addition, it is found in practice that there is a time

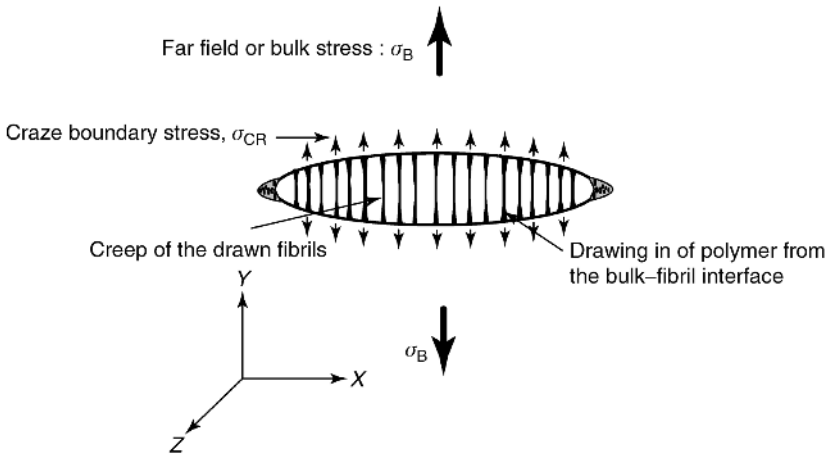

Fig. 16. Craze morphology and possible growth mechanisms.

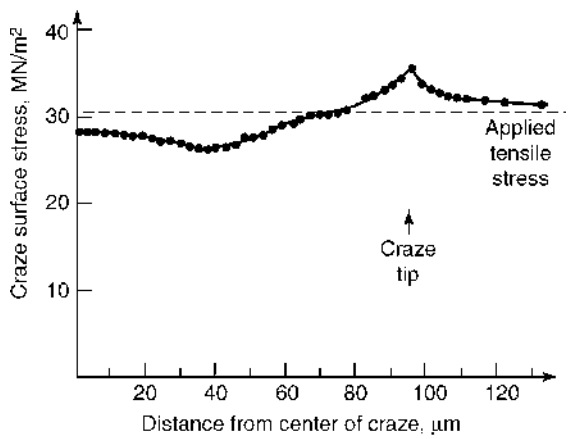

Fig. 17. Craze surface stress as a function of position from the craze centre for polystyrene. After Lauterwasser and Kramer (121), with permission of Taylor and Francis Ltd., http://www.tandf.cp.uk/journals.

dependency on the appearance of crazing. That is, there is generally a time delay between application of the load and the first visible appearance of a craze. A number of models have been proposed which require either a critical cavitation stress, a critical strain, or the presence of inherent microvoids, which can grow under the applied local stress or strain.

Sternstein and Ongchin (1969). Considering that cavitation was required for craze nucleation, Sternstein and Ongchin (122) postulated that it is the dilatational component of the stress tensor along with a stress bias σ_b (flow stress) that controls craze initiation:

$$\sigma_b = A + \frac{B}{I_1} \tag{43a}$$

where for plane stress, $\sigma_b = \sigma_1 - \sigma_2$, and

$$I_1 = \sigma_1 + \sigma_1 + \sigma_1 = 3p > 0 \tag{43b}$$

where I_1 is the first stress invariant ie the dilatational component of the stress tensor. A and B are temperature-dependent constants. We note that under this criterion, crazing will not occur under pure hydrostatic tension ($\sigma_1 = \sigma_2 = \sigma_3$), pure shear stress [$(\sigma_1 + \sigma_2 + \sigma_3)/3 = 0$, $I_1 = 0$], or compressive stress states ($I_1 < 0$). The model was extended beyond the specific case of plane (or biaxial) stress conditions to a general three-dimensional case by Sternstein and Meyers (123). Because they are essentially empirical, the Sternstein et al models have several shortcomings: (*1*) the stress bias, $\sigma_1 - \sigma_2$, is related to the shear stress and it is difficult to reconcile a shear stress component controlling initiation of a craze in a direction perpendicular to the principal stress component σ_1, (*2*) the parameters A and B have no direct or obvious physical interpretation, (*3*) no time dependency for the initiation of crazes.

Gent (1970). Gent (124) proposed a model in which the hydrostatic tensile stress at an inclusion or local heterogeneity increases the free volume and therefore effectively reduces the T_g of the material. At a sufficiently high stress concentration, the reduction in T_g is sufficient to reduce the local T_g to the test temperature. The reduced yield stress of the material in this rubber-like phase and the hydrostatic tensile stress then leads to cavitation and craze initiation. Implicit in this free-volume approach is that an imposed hydrostatic pressure will tend to prevent the formation of crazes in accordance with experimental observation. The criterion is summarized in the equation for the critical applied stress for initiation, σ_c:

$$\sigma_c = \frac{\beta(T_g - T) + P}{k} \tag{44}$$

where T_g is the glass temperature of the material, T is the test temperature, P is the bulk hydrostatic pressure, k is the stress concentration, and β is a constant related to the pressure dependence of T_g, and has a value of approximately 5 MPa/K. However, the inferred stress concentrations, k, required to induce crazing at room temperature were unrealistically large (of the order of 20) and the authors acknowledge it is a factor not easily accessible to experimental techniques. In addition, Lauterwasser and Kramer (121) calculated the reduction in T_g at the crack tip due to the imposed hydrostatic stress. Using the data in Figure 15 they calculated the hydrostatic pressure term to be one third of the bulk stress (σ_{bulk} = approximately 30 MPa) plus the additional surface stress at the craze tip of approximately 5 MPa, giving a total of 15 MPa. Using a value of 1°C/5 MPa for the pressure dependence of T_g, they estimated the reduction in T_g at the crack tip to be a modest 3°C, certainly not enough to reduce the local T_g to the test temperature.

Oxborough and Bowden (1973). Addressing the lack of generality in terms of the usable stress states in the original Sternstein and Ongchin paper (122), which was limited to plane stress conditions, and concerns as to the physical interpretation of the critical stress (stress bias $\sigma_b = \sigma_1 - \sigma_2$) Oxborough and

Bowden (125) proposed a criterion for craze initiation based on a critical strain. The form of the criterion is identical to that in the Sternstein and Ongchin paper, with the critical stress σ_b replaced by a critical strain ε_c:

$$\varepsilon_c = X' + \frac{Y'}{I_1} \tag{45}$$

where I_1 is again the first stress invariant and X' and Y' are time- and temperature-dependent variables. Noting that under a general stress state the maximum strain is in the direction of the principal stress and is given by

$$\varepsilon_1 = \frac{1}{E}(\sigma_1 - \nu\sigma_2 - \nu\sigma_3) \tag{46}$$

ν is the Poisson's ratio and assuming that crazing occurs at the critical strain given by equation 45, they derived a criterion for crazing that is written in terms of the principal stresses:

$$\sigma_1 - \nu\sigma_2 - \nu\sigma_3 = \frac{X}{\sigma_1 + \sigma_2 + \sigma_3} + Y \tag{47}$$

where $X = EX'$ and $Y = EY'$.

Using this criterion, Bowden and Oxborough could successfully fit the crazing data of Sternstein and Ongchin as well as their own data on four grades of polystyrene. Further, their data showed that the critical strain for crazing decreased with an increasing component of tensile hydrostatic stress and also decreased with increasing load time. Both the X and Y fitting parameters were shown to decrease with increasing temperature. The Y parameter also decreased with increasing load time, though the X parameter appeared to be relatively insensitive to loading time. Ultimately however, the X and Y parameters remain curve-fitting variables and offer little insight into the mechanisms or underlying structural parameters controlling craze initiation/growth.

Argon and Hannoosh (1977). The apparent time dependence for craze initiation after initial loading suggests the possibility that a thermally activated process may control initiation. Argon and co-workers (111,126,127) suggested a mechanism which considered that craze initiation occurs when a critical porosity is reached. The initial microscopic pores are formed when thermally activated micro-shear bands are blocked, the resulting local strain energy being sufficient to provide the surface energy for the formation of a microcrack. Allowing for additional free energy to form a stable pore, Argon and co-workers (111,126) derived the following expression for the free energy required for pore formation:

$$\Delta G^*_{\text{pore}} = (0.15)^2 \pi (G/\tau)(\mu\phi^3) + \alpha L^3 \sigma_Y \tag{48}$$

where G is the shear modulus at the test temperature, τ the shear stress, φ a dimension related to the size of the sheared region (typically of the order of a molecular diameter), σ_Y the yield strength, L a length scale related to the

spacing of molecular inhomogeneities, and α a factor of the order of 0.1. By considering the local stress field at an inclusion or groove and by taking the deviatoric stress, s, to be largest for a groove perpendicular to the maximum principal tensile stress, an expression was derived for the increase in the local porosity β as a function of time t, given by

$$\beta = \dot{\beta}_0 \, t \, \exp(-\Delta G^*_{\text{pore}}(s)/kT) \tag{49}$$

where $\dot{\beta}_0$ is a pre-factor characteristic of the vibrational frequency of the sheared region. Following these arguments, two criteria for the negative pressure p and the critical initial porosity β_{i} required for the expansion of the pores was determined (126):

$$p = \left(\frac{2\sigma_Y}{3}\right) \ln\left(\frac{1}{\beta}\right) Q \tag{50a}$$

$$\beta_{\text{i}} < \frac{1}{(1+2G/\sigma_Y)} \tag{50b}$$

where σ_{Y} is the yield stress, and Q a normalization factor. By further considering the negative pressure required to expand the porous region, an expression was derived for the initiation time, t_{in}, of craze nucleus formation (111):

$$t_{\text{in}} = \frac{1}{\dot{\beta}_0} \exp\left(\frac{\Delta G^*_{\text{pore}}}{kT} - \frac{\xi}{Q}\right) \tag{51}$$

where ξ is $(\sigma_1+\sigma_2)/2\,\sigma_{\text{Y}}$, with σ_1 and σ_2 the principal stresses and σ_{Y} and Q are as before. The authors also recognized that while the craze may have initiated, it requires additional time for the craze to grow before it becomes visible (this is an inherent problem when discussing initiation times for crazes as it almost inevitably includes a period of craze growth for the crazes to be detectable). An estimate for the growth time, Δt_{growth} was derived based on a power law relationship between effective strain rate, $\dot{\varepsilon}_e$, and effective stress, σ_{e}:

$$\left(\frac{\dot{\varepsilon}_{\text{e}}}{\dot{\varepsilon}_{\text{eo}}}\right) = \left(\frac{\sigma_e}{\sigma_{e0}}\right)^m \tag{52}$$

where $\dot{\varepsilon}_{\text{e0}}$, σ_{e0}, and m are temperature-dependent material constants.

Thus, the total time for craze nucleation is the sum of the time to initiation and the growth time to the point where the crazes are visible:

$$t_{\text{craze nucleation}} = t_{\text{in}} + \Delta t_{\text{growth}}$$

For small negative pressures, the growth time can be a significant proportion of the total time for nucleation. The model also predicts that under pure shear stress (an isovolume deformation), though considerable pore formation is present, no craze nucleation will occur because of the lack of a dilatational component of

the stress. The authors went on to derive expressions to model the time dependence of the density of pore formation and subsequent craze saturation density (where the crazes have relieved the stress sufficiently that further craze nucleation is stopped) and expressions for biaxial craze nucleation. A set of such data from reference (111) is shown in Figure 18, where the surface density of crazes is plotted as a function of initiation time for polystyrene samples subjected to a combination of deviatoric stresses and negative pressures. The general features under each set of conditions are the same, with an increase in the craze density with time followed by saturation. It is also seen that the saturation density increases with increasing deviatoric stress and also with increasing negative pressure. The solid lines are the results from the model developed in reference (111). While the model captures the broad features of the material response, it should be noted that a number of parameters in the model cannot be easily determined from independent experiments. Consequently, a number of the parameters have been determined by optimizing the fit to experimental data such as that shown in Figure 18. These parameters, however, compare favorably with the expected ranges for such values. The reader is referred to the original paper for further discussions (111).

Kambour [1978]. Kambour, one of the pioneers in the area of crazing from as early as the mid-60's, has made significant contributions to the field and his thorough review article has already been mentioned (118). In 1978 Kambour and Gruner (128) reported a set of data for eight resins which showed a correlation between the critical strain for crazing in air, ε_c, and a combination of three factors, σ_y, the yield stress in tension, ΔT, the difference in the glass-transition temperature and the test temperature (T_g-T_{test}), and the solubility parameter (δ_p), [reported here in terms of the cohesive energy density, CED ($=\delta_p^2$)]:

$$e_c \propto \left[\frac{\text{CED}\cdot\Delta T}{\sigma_Y}\right] \tag{53}$$

In a follow-up paper in 1983 (129) it was shown that the correlation held for a further 29 polymers and copolymers, though in this case an additional correlation was used:

$$e_c \propto \left[\frac{\text{CED}\ \cdot\ \Delta T}{E}\right] \tag{54}$$

where E is the elastic modulus, and an implicit correlation between E and σ_Y is assumed. Figure 19 shows the data from the 1983 paper (129) and, while the correlations are shown to be satisfactory, the author acknowledges that the underlying source of the correlation is open to interpretation. [Note: In the 1983 paper (129), it appears that the abscissa labels have been inadvertently swapped between Figures 1 and 2, though the captions are correct. The abscissa has been corrected here.] Experimental craze growth studies as a function of temperature and aging time are compared with the general predictions of this and two of the models discussed above (Sternstein et al and Argon et al) in Reference (130).

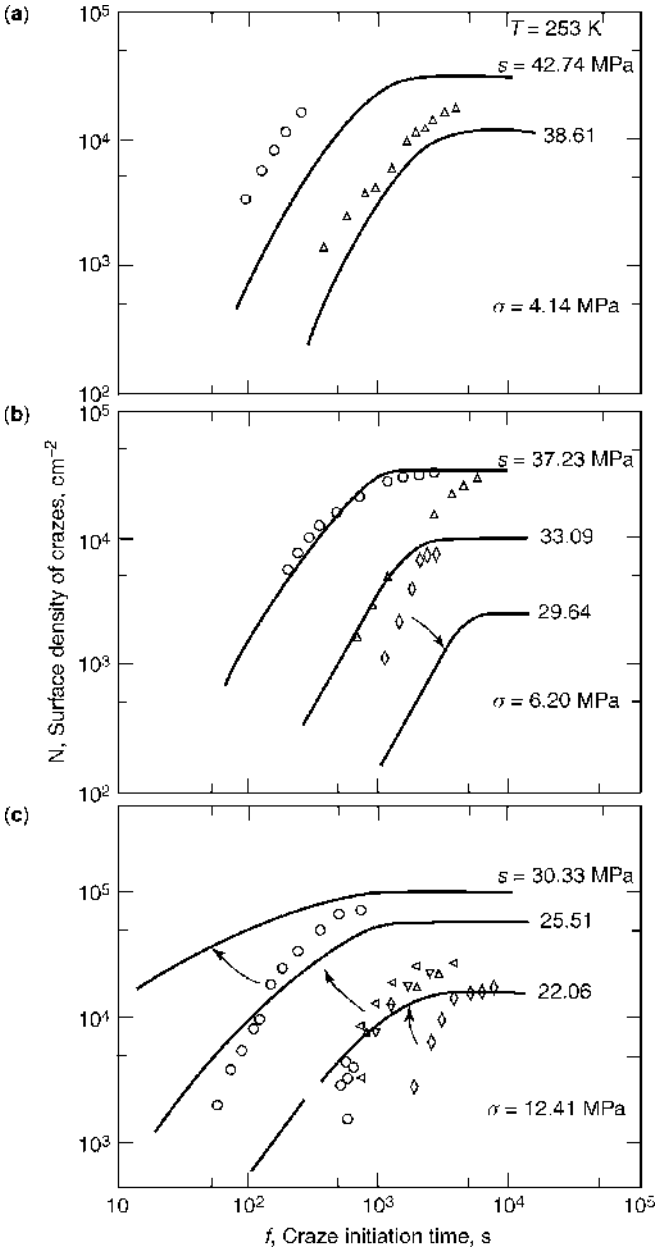

Fig. 18. Craze density as a function of initiation time for polystyrene subjected to a combination of deviatoric stresses (s) and negative pressures (σ). After Argon and Hannoosh (111), with permission of Taylor and Francis Ltd., http://www.tandf.cp.uk/journals.

Craze Growth

After initiation the craze starts to grow. There are two aspects to consider when considering craze growth:

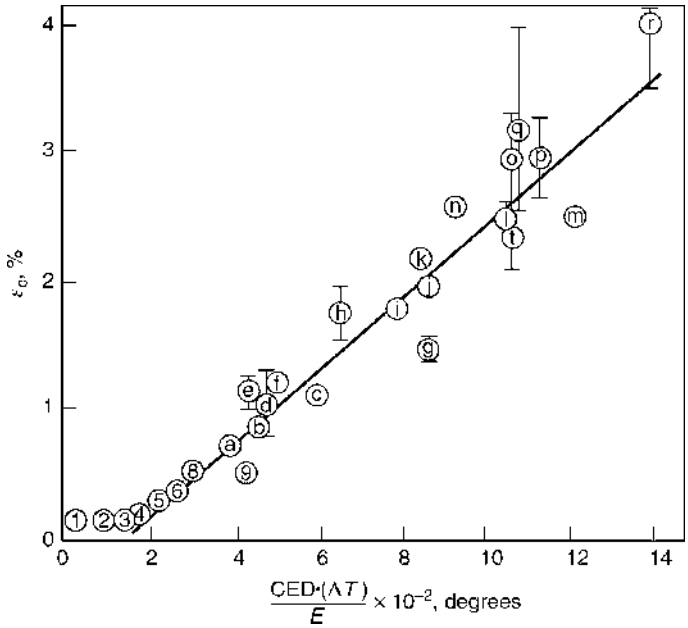

Fig. 19. Correlation between the critical strain for crazing, ε_c, and the product of the cohesive energy density (CED), the difference between the test temperature and the glass-transition temperature ΔT, and the elastic modulus E. Reprinted from Ref. 129, with permission from Elsevier.

(1) Growth of the craze in the plane perpendicular to the load direction and in the direction of the craze tip (direction X in Fig. 16).

(2) Craze thickening, ie opening of the craze–bulk interfaces and extension of the fibrils in the Y direction (Fig. 16).

Craze Tip Advance. The earliest explanation for the advance of the craze tip was the continued nucleation of isolated voids ahead of the craze tip and their subsequent expansion (127).

However, experimentally it has been observed that craze growth occurs faster than craze initiation and so it is difficult to explain growth with such a model as it is essentially the same mechanism as initiation. Also, some of the features of the craze predicted from such a mechanism, such as a closed cell structure formed from the formation of isolated voids, are inconsistent with experiments that clearly show that the craze has an open structure.

The currently accepted model for craze tip advance is that proposed by Argon and Salama (131) and based on the Taylor meniscus instability mechanism (132,133). This is the same phenomenon that is observed when two wetted plates are pulled apart and is shown schematically in Figure 20. In this scenario, the craze–bulk interface is treated as the solid boundary, and the plastically deformed, strain-softened matter at the craze tip is the liquid. As the boundary layers separate an instability is set up owing to a negative pressure gradient in the "fluid." Small fingers propagate into the craze tip at a characteristic spacing

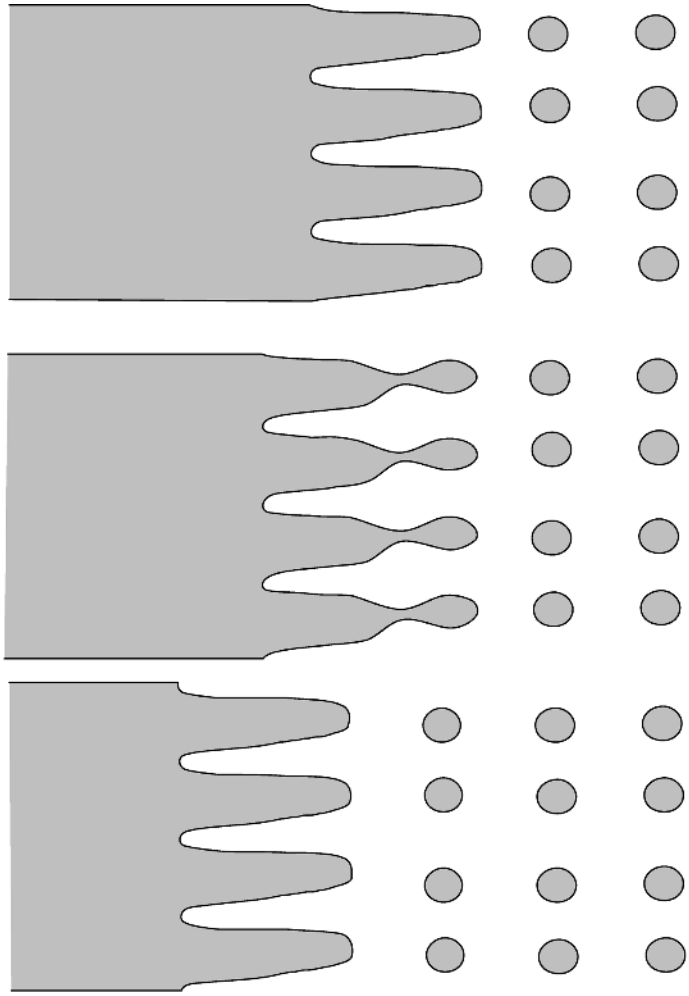

Fig. 20. Schematic for the Taylor meniscus instability mechanism for craze front advance. After Argon and Salama (131)

of λ_c. The fingers expand as shown in Figure 20, eventually joining up to leave isolated columns of polymer. It is possible to calculate the minimum spacing, λ_M, necessary for the instability to grow (116):

$$\lambda_M = 2\pi\sqrt{\frac{\Gamma}{d\sigma_0/dx}} \tag{55}$$

where $d\sigma_0/dx$ is the hydrostatic stress gradient ahead of the craze and Γ is the surface energy. The fastest growing wavelength, λ_c, is given by (131,134)

$$\lambda_c = \sqrt{3}\lambda_M \tag{56}$$

Though a somewhat idealized picture of craze growth, the basic premise of the Taylor meniscus instability model has been verified by Donald and Kramer (135), who measured a critical wavelength in polystyrene crazes that was in close agreement with the interfibrillar distance. Further, following the procedure of Fields and Ashby (134) a steady-state craze tip velocity may be estimated by assuming a non-Newtonian fluid of the form

$$\left(\frac{\dot{\varepsilon}}{\dot{\varepsilon}_{\mathrm{F}}}\right) = \left(\frac{\sigma}{\sigma_{\mathrm{F}}}\right)^{n} \tag{57}$$

where $\dot{\varepsilon}_{\mathrm{F}}$, σ_{F}, and n are material constants, leading to the expression for the tip velocity V_0:

$$V_0 = \frac{\sqrt{3}}{2}\frac{\dot{\varepsilon}_{\mathrm{F}}\, h}{(n+2)}\left[\frac{\sqrt{3}h(\beta^{*}S_{\mathrm{t}})^{2}}{8\sigma_{\mathrm{F}}\Gamma}\right]^{n}\left(1-\frac{2\Gamma}{\beta^{*}S_{\mathrm{t}}h}\right)^{2n} \tag{58}$$

where h is the thickness of the craze at the crack front and $\beta^{*}S_{\mathrm{t}}$ is the hydrostatic pressure between the void fingers.

The (relatively) simple form of equation 58 leading to a constant craze growth rate belies the complicated nature of craze growth in practice. While a linear growth in the craze length has been observed (136), equally a linear growth of the craze has been observed with logarithmic time (137–139). Undoubtedly the complicated, and possibly changing, nature of the stress field at the craze tip and even subtle differences in the morphology of the polymer can dramatically affect craze growth.

Craze Thickening. As indicated in Figure 16, two mechanisms exist for craze thickening:

(1) Drawing in of isotropic material from the bulk–craze interface
(2) Creep of the fibrillar material

Both processes can of course occur simultaneously, though it is generally accepted that it is the drawing in of fresh material that dominates the thickening of the craze in amorphous polymers. Evidence for this comes from a number of experiments aimed at examining either the volume fraction of craze material or the draw ratio of the fibrils as a function of position in the craze. If fibril creep occurred to any significant extent, then the fibrils farther from the craze tip, which are naturally older and hence have been subjected to the interface stress for longer, would have a higher draw ratio. Evidence from crazes in PS (121) and poly-*tert*-butylstyrene (140) show an essentially constant draw ratio along the craze length, rising slightly at the craze tip owing to the locally high craze stresses present when they form (117)—this actually leads to a narrow band along the center line of the craze where the draw ratio is higher and volume fraction lower (127). Hence, the main mechanism of craze thickening is from material drawing in at the craze–fibril interface in a manner analogous with that of cold drawing under tensile loading. The material that is drawn in comes from what is termed the "active zone," a thin layer of material at the bulk–craze interface

consisting of strain-softened material and which is typically of the order of a fibril diameter in size.

As noted, once the material has been drawn into the craze it appears to stabilize, and little, if any, further extension takes place. As with cold drawing, the fibrillar material is seen to take on a natural draw ratio, λ_N, the value of which is characteristic of the individual polymer. Kramer (116,141) found that the natural draw ratio correlated well with the maximum theoretical extension expected for an entangled network, λ_{max}:

$$\lambda_{max} = \frac{L_c}{k(M_e)^{1/2}} \text{ and } L_c = \frac{L_M M_e}{M_{m0}} \tag{59}$$

where M_e is the molecular weight between entanglements, L_M the monomer unit length, M_{m0} the monomer molecular weight, and k a constant. The molecular weight between entanglements, M_e, is a characteristic of any given polymer and can be determined experimentally from

$$M_e = \rho RT / G_N \tag{60}$$

where G_N is the measured rubbery plateau shear modulus, ρ the density, T the temperature, and R the gas constant. It is interesting to note that in polymers with a molecular weight less than approximately half the entanglement molecular weight, stable crazes are not seen to form and it seems then that entanglements are a necessary feature for stabilizing the craze–fibril structure.

During the surface drawing process in the active zone, it is inevitable that material that is destined to go into two neighboring fibrils can share a common molecule. Thus, as the fibrils form, the molecule must either disentangle such that the molecule flows into only one fibril or the chain must break. As we noted above, entanglements appear to be necessary for the formation of stable fibrils and, if the molecule is unable to disentangle, then it is inevitable that chain scission must occur during craze growth. On this basis Kramer (116,117) suggests that the energy required to create new surface (Γ) is given by the standard surface energy plus a component due to the energy required for chain scission:

$$\Gamma = \gamma + \frac{U v d}{4} \tag{61}$$

where γ is the Van der Waals surface energy, U the polymer backbone bond energy, v the network strand density, and d is the root mean square end-to-end distance between entanglements. Kramer also estimated the force required to break a molecule, f_b, given approximately by

$$f_b = \frac{U}{2a} \tag{62}$$

where a is the bond length. If, during the fibril formation, the force should rise above this level breakage will obviously occur. If the force remains below this level then fibril formation can proceed via disentanglement.

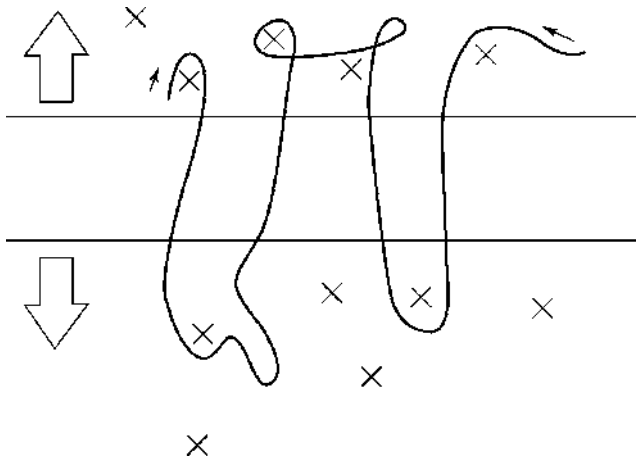

Fig. 21. Block-and-tackle arrangement for disentanglement at the craze boundary as proposed by McLeish and co-workers. Reprinted from Ref. 142, and 144, with permission from Elsevier.

Disentanglement of the polymer chains is generally accepted to occur by the mechanism of reptation as proposed by Doi and Edwards (142) and by deGennes (143). In this model, the movement of the chain is taken to be confined to a tube, the confinement coming from neighboring chains. The molecule moves through this tube in a snake-like motion by a series of cooperative steps. McLeish (144) has introduced the concept of "forced reptation" with regards to craze formation. Here, one end of the molecule is locked into a formed fibril and as material continues to be drawn in to the fibril, the molecule is pulled through its confining tube at a velocity v_f. From such considerations they determined that the maximum force acting on the molecule, f_d, is given by

$$f_d = v_f \xi \frac{M}{M_0} \tag{63}$$

where ξ is a monomeric friction coefficient, M the molecular weight, and M_0 the monomer molecular weight. Thus, if $f_d < f_b$ disentanglement will occur in preference to chain scission. It is worth noting also that if we assume that the velocity of the chain through the confining tube, v_f, is proportional to the applied strain rate and further that the monomeric friction coefficient is a thermally activated process (proportional to $e^{(1/T)}$) then equation 63 indicates that disentanglement is favored by low molecular weights, low strain rates, and high temperatures. However, while this approach correctly accounts for the dependence of craze growth on these parameters, in practice the majority of polymers are of a sufficiently high molecular weight (and hence chain length) that a single molecule will cross between the prefibril regions several times. Again, following the argument of McLeish this results in the polymer chain being pinned at several points along its length in what has been described as a 'block and tackle' arrangement (Fig. 21). This has the effect of increasing the velocity the chain must move at through the confining tube for a given macroscopic strain rate. On the basis of

these concepts, Kramer (117) derived an expression for the maximum force on the chain (at its center) of

$$f_{\max} = \xi v_{\mathrm{f}} \frac{M^2}{16 M_0 M_{\mathrm{e}}} \tag{64}$$

where M_{e} is the average molecular weight between the entanglements. It is seen then that the maximum force on the chain is proportional to the square of the molecular weight. During the formation of the fibril the chain is assumed to break randomly along its length, thereby reducing M, until the maximum force in the chain falls below the level required for scission. The concept of entangled molecules and the competition between chain scission and disentanglement is important not only for the growth kinetics but also, as we will see in the following section, for the ultimate failure of the fibrils/craze.

Craze Failure

Craze breakdown is obviously of fundamental importance since it is the mechanism by which the crack grows and so leads ultimately to failure. However, the mechanism of craze failure is still unclear. The two main mechanisms that have been proposed are

(1) Failure in the fibril, or
(2) Failure at the active zone

It is likely that both occur depending on the conditions and morphology of the material. The first step in considering the likelihood of fibril failure is to look at the stress levels within the fibril. Because of the reduced cross-sectional area in the craze region, the true stress on the fibrils (σ_{CT}) can be considerably higher than the stress at the craze boundary (σ_{CR}) by a factor given by the draw ratio of the fibril (λ):

$$\sigma_{\mathrm{CT}} = \lambda \sigma_{\mathrm{CR}} \tag{65}$$

λ is typically of the order of 2 to 4 for amorphous polymers and as noted above can be somewhat higher at the midrib of the fibril. Though at these stresses the creep contribution to the fibril length is minor, any small inhomogeneities in the local structure can lead to localized creep. Further, as discussed above, the material which forms the fibril has passed through the active zone at the craze–bulk boundary and has undergone chain scission. This results in the fibrillar material having a lower molecular weight and a reduced entanglement density. These conditions can then lead to chain disentanglement by essentially plastic flow. Such a mechanism can be facilitated by the small diameter of the fibrils leading to a reduction in the constraints that a polymer chain might otherwise see in the bulk. However, if fibril failure were the dominant mechanism in the breakdown of the craze, then it would be reasonable to expect failure to occur at the fibril midpoint where the fibril is oldest and has been subjected to the highest stresses

for the longest length of time. While this has indeed been observed (145,146), it is more generally seen that the point of failure is at the craze–bulk interface, ie at the active zone. This in turn would imply that, for the majority of polymers, the reduction in entanglement density on traversing the active zone during fibril formation is not sufficient to destabilize the fibril.

We saw above that the material that flows into the active zone, and which may go on to form fibrils, has to undergo a degree of disentanglement or chain scission. This results in the material within the active zone having a lower entanglement density than the bulk material. Further the material in the active zone is in a strain-softened state, characterized by more liquid-like dynamics. If the entanglement density is low enough and the polymer strands dwell within the active zone for a sufficiently long period of time then the strands may fully disentangle. The material then loses its load-bearing capacity, and that particular fibril element will fail. In practice, because polymers generally have a broad distribution of molecular weights, there is a chance that the material destined to form a fibril will consist of relatively short chains with a low entanglement density. Thus, the likelihood of a given fibril failing is ultimately governed by a statistical distribution (note that, although not included in this analysis, the presence of inhomogeneities, inclusions, flaws etc can also lead to a breakdown in the active zone owing to a decreased load-bearing capacity). Kramer and Berger (117) developed such a statistical model and the reader is referred to the original paper for the full mathematical development. In brief, they based their calculations on the number of effectively entangled strands, n_e, that survive during the formation of the active zone, ie those which do not undergo chain scission. From this they formulated an expression for the probability that a given fibril would fail, P_F, given by the product of the probability that a strand survives fibril formation, $P_{survive}$, and the probability that it then disentangles, P_{dis}, summed over the total number of chains which go into fibril formation. The probability of a chain i surviving, $P_{survive}(i)$, is given by a normal distribution:

$$P_{survive}(i) = \frac{1}{\sqrt{2\pi n_e(1-q)}} \exp\left(\frac{(i-n_e)^2}{2(1-q)n_e}\right) \tag{66}$$

and where q is the fraction of originally entangled strands which do not undergo chain scission. The probability of disentanglement P_{dis} is given by

$$P_{dis}(i) \approx \exp\left(\frac{-t_{dis}(i)}{\tau_{res}}\right) \tag{67}$$

τ_{res} is a measure of the time the strand spends within the active zone and t_{dis} is the time for disentanglement, and is a function of strand molecular weight, the molecular weight between entanglements, the force on the strand, and the monomeric friction coefficient. Though the τ_{res} term is a fitting parameter, the model captures many of the features observed with craze stability such as the molecular weight dependence (117).

Other Considerations for Crazing

The preceding sections only touch upon the main characteristics of crazing and many of the additional factors that go into determining the initiation, growth, and failure of the craze have been omitted. Without elaboration, we mention several such factors and refer the reader to the relevant references.

The structure of the craze as discussed above has been idealized as a uniform array of isolated fibrils bridging the boundaries of the craze. In reality it is found that the main fibrils are connected to their neighbors by small "cross-tie" fibrils (117,147). The formation of these cross-tie fibrils has been modeled by Tijssens and van der Giessen (148), interestingly using many of the concepts presented in the section on yield. The presence of such cross-tie fibrils gives the craze some tangential load-bearing capacity, and a modeling of such a structure shows that their presence can lead to an increase in the stress on the main fibril, at times sufficient to cause failure of the polymer backbone (149,150).

A common, and potentially serious, drawback of polymers is their susceptibility to environmental factors, causing a greater likelihood to form crazes. Indeed, it has been estimated that environmental-stress cracking is responsible for as much as 30% of failures in engineering polymers in service (151). Environmental stress cracking (ESC), as the phenomenon is known, occurs predominately (though not exclusively) in amorphous polymers in contact with organic solvents. The other prerequisite for ESC is the presence of a stress since ESC is a result of the *physical* interaction of the polymer and solvent and is not due to a *chemical* interaction (ie no chemical degradation occurs).

One view of how the ESC agents act on the polymer is that they can diffuse into the polymer and cause it to swell. This in turn will increase the polymer chain mobility and so cause an effective decrease in the local T_g, leading to an increase in the propensity to craze ie crazing occurs at lower stresses or strain. An alternative view is that the liquid can wet the surface, reducing the energy required to create new surfaces and so aiding the formation of voids. This latter effect may be important in the early stages of craze initiation. The reviews by Kambour (118), Volynskii (152), Wright (153), and the work of, for example, Arnold (154–156) cover this area in detail and are briefly discussed in the chapter Fracture (qv)Fracture in this encyclopedia.

Just as crazing tends to be a precursor to failure under static loading, it is also seen to develop under cyclic loading conditions. The area of cyclic or fatigue failure of polymers has been extensively investigated, with much of the early work carried out by Hertzberg and co-workers (157–160) and Döll and co-workers (161–163). The reader is referred to the chapter Fatigue (qv)Fatigue in this encyclopedia for a detailed review.

BIBLIOGRAPHY

"Crazing" in *EPST* 1st ed., Vol. 4, pp. 294–307, by R. W. Raetz, Catalin Corp.; in *EPSE* 2nd ed., Vol. 4, pp. 299–323, by R. P. Kambour, General Electric Co.; "Mechanical Properties" in *EPST* 1st ed., Vol. 8, pp. 445–516, by V. A. Kargin and G. L. Slonimsky; Akademii Nauk

SSSR; in *EPSE* 2nd ed., Vol. 9, pp. 379–466, by D. W. Hadley, University of Reading, U.K., and I. M. Ward, University of Leeds, U.K.; in *EPST* 3rd ed., Vol. 12, pp. 627–681, by P. A. O'Connell and G. B. McKenna, Texas Tech University.

CITED PUBLICATIONS

1. G. Langford, W. Whitney, and R. D. Andrews, *Materials Research Laboratory Research Report No. R63-49*, MIT School of Engineering, Cambridge, 1963.
2. J. D. Ferry, *Viscoelastic Properties of Polymers*, 3rd ed., John Wiley & Sons, Inc., New York, 1980.
3. R. A. Hill, "A Theory of the Yielding and Plastic Flow of Anisotropic Materials", *Proc. R. Soc. London, Ser. A* **193**, 281–297 (1948).
4. W. Weber, "Über die Elastizität der Seidenfäden", *Pogg. Ann. Phys.* **4**, 247–257 (1835).
5. L. Boltzmann, "Zur Theorie der Elastischen Nachwirkung", *Sitzungsber Akad. Wiss. Wien. Mathem-Naturwiss Kl.* **70**, 275–300 (1874).
6. B. Bernstein, E. A. Kearsley, and L. J. Zapas, "A Study of Stress Relaxation with Finite Strains", *Trans. Soc. Rheol.* **7**, 391–410 (1963).
7. R. A. Schapery, "On the Characterization of Nonlinear Viscoelastic Materials", *Polym. Eng. Sci.* **9**, 295–310 (1969).
8. N. W. Brooks, M. Ghazli, R. A. Duckett, R. A. Unwin, and I. M. Ward, "Effects of Morphology on the Yield Stress of Polyethylene", *Polymer* **40**, 821–825 (1999).
9. R. O. Sirotkin and N. W. Brooks, "The Effects of Morphology on the Yield Behaviour of Polyethylene Copolymers", *Polymer* **42**, 3791–3797 (2001).
10. I. M. Ward, *Mechanical Properties of Solid Polymers* 2rd ed., John Wiley & Sons, Inc., Chichester, U.K., 1983.
11. I. M. Ward and D. W. Hadley, *An Introduction to the Mechanical Properties of Solid Polymers*, John Wiley & Sons, Inc., New York, 1993.
12. A. Nadai, *Theory of Flow and Fracture of Solids*, McGraw-Hill, New York, 1950.
13. E. Orowan, "Fracture and Strength of Solids", *Rep. Prog. Phys.* **12**, 185–232 (1949).
14. A. Considère, "Memoire sur l'Emploi du Fer et de l'Acier dans les Constructions", *Ann. Ponts et Chaussées* **9**, 574–775 (1885).
15. C. G'Sell and J. J. Jonas, "Yield and Transient Effects During the Plastic Deformation of Solid Polymers", *J. Mater. Sci.* **16**, 1956–1974 (1981).
16. C. G'Sell, J. M. Hiver, A. Dahouin, and A. Souahi, "Video-Controlled Tensile Testing of Polymers and Metals beyond the Necking Point", *J. Mater. Sci.* **27**, 5031–5039 (1992).
17. A. R. Haynes and P. D. Coates, "Semi-automated image analysis of the true tensile drawing behavior of polymers to large strains", *J. Mater. Sci.* **31**, 1843–1855 (1996).
18. S. Nazarenko, S. Bensason, A. Hiltner, and E. Baer, "The Effect of Temperature and Pressure on Necking of Polycarbonate", *Polymer* **35**, 3883–3892 (1994).
19. M. C. Boyce and E. M. Arruda, "An Experimental and Analytical Investigation of the Large Strain Compressive and Tensile Response of Glassy Polymers", *Polym. Eng. Sci.* **30**, 1288–1298 (1990).
20. W. Whitney and R. D. Andrews, "Yielding of Glassy Polymers: Volume Effects", *J. Polym. Sci., Part C* **16**, 2981–2990 (1967).
21. N. Brown and I. M. Ward, "Load Drop at the Upper Yield Point of a Polymer", *J. Polym. Sci., Part A* **2**, 607–620 (1968).
22. M. C. Boyce, E. M. Arruda, and R. Jayachandran, "The Large Strain Compression, Tension and Simple Shear of Polycarbonate", *Polym. Eng. Sci.* **34**, 716–725 (1994).
23. M. Kitagawa, D. X. Zhou, and J. H. Qiu, "Stress–Strain Curves for Solid Polymers", *Polym. Eng. Sci.* **35**, 1725–1732 (1995).
24. H. Tresca, "Sur l'écoulement des corps solids soumis ´ des fortes pression" *C. R. Acad. Sci. (Paris)* **59**, 754–758 (1864).

25. R. von Mises, "Die Mechanik der festen Körper im plastischen deformablen Zustand", *Göttinger Nachricten, Math-Phys. Klasse* 582–592 (1913).
26. C. A. Coulomb, "Sur une application des regles de Maximis et Minimis à quelques Problèmes de Statique, relatifs à l'Architecture", *Mem. Math et Phys.* **7**, 343–382 (1773).
27. S. Rabinowitz, I. M. Ward, and J. S. C. Parry, "The Effect of Hydrostatic Pressure on the Shear Yield Behavior of Polymers", *J. Mater. Sci.* **5**, 29–39 (1970).
28. D. R. Mears, K. D. Pae, and J. A. Sauer, "Effects of Hydrostatic Pressure on the Mechanical Behavior of Polyethylene and Polypropylene", *J. Appl. Phys.* **40**, 4229–4237 (1969).
29. R. A. Duckett, S. Rabinowitz, and I. M. Ward, "The Strain-rate, Temperature and Pressure Dependence of Yield of Isotropic Poly(Methyl Methacrylate) and Poly(Ethylene Terephthalate)", *J. Mater. Sci.* **5**, 909–915 (1970).
30. K. D. Pae and Bhateja, "The Effects of Hydrostatic Pressure on the Mechanical Behavior of Polymers", *J. Macromol. Sci., Chem.* **13**(1), 1–75 (1975).
31. F. H. Muller, "Zum Problem der Kaltverstreckung hochpolymerer Substanzen", *Kolloid Zeitschrift* **114**, 59–61 (1949).
32. F. H. Muller, "Zur Kaltverstreckung hochmolekularer Stoffe", *Kolloid Zeitschrift* **115**, 118–123 (1949).
33. F. H. Muller, "Weitere Versuche und Betrachtungen zur Kaltverstreckung", *Kolloid Zeitschrift* **126**, 65–72 (1956).
34. P. I. Vincent, "Necking and cold-drawing of rigid plastics", *Polymer* **1**, 7–19 (1960).
35. W. G. Knauss and I. Emri, "Volume Change and the Nonlinearly Thermoviscoelastic Constitution of Polymers", *Polym. Eng. Sci.* **27**(1), 86–100 (1987).
36. R. E. Robertson, "Theory of the Plasticity of Glassy Polymers", *J. Chem. Phys.* **44**, 3950–3956 (1966).
37. R. N. Haward and G. Thackray, "The Use of a Mathematical Model to Describe Isothermal Stress–Strain Curves in Glassy Polymers", *Proc. R. Soc., London, Ser. A* **302**, 453–472 (1968).
38. A. S. Argon, "A Theory for the Low-Temperature Plastic Deformation of Glassy Polymers", *Philos. Mag.* **28**, 839–865 (1973).
39. M. C. Boyce, D. M. Parks, and A. S. Argon, "Large Inelastic Deformation of Glassy Polymers. Part I: Rate Dependent Constitutive Model", *Mech. Mater.* **7**, 15–33 (1988).
40. T. A. Tervoort, E. T. J. Klompen, and L. E. Govaert, "A Multi-Mode Approach to Finite, Three-Dimensional, Nonlinear Viscoelastic Behavior of Polymer Glasses", *J. Rheol.* **40**, 779–797 (1996).
41. R. M. Shay and J. M. Caruthers, "A New Nonlinear Viscoelastic Constitutive Equation for Predicting Yield in Amorphous Solid Polymers", *J. Rheol.* **30**, 871–827 (1986).
42. S. R. Lustig, R. M. Shay, and J. M. Caruthers, "Thermodynamic Constitutive Equations for Materials with Memory on a Material Time Scale", *J. Rheol.* **40**, 69–106 (1996).
43. H. Eyring, "Viscosity, Plasticity and Diffusion as Examples of Absolute Reaction Rates", *J. Chem. Phys.* **4**, 283–291 (1936).
44. C. Bauwens-Crowet, J. C. Bauwens, and G. Homes, "Tensile Yield-Stress Behavior of Glassy Polymers", *J. Polym. Sci., Part A* **2**, 735–742 (1969).
45. J. S. Foot, R. W. Truss, I. M. Ward, and R. A. Duckett, "The Yield Behavior of Amorphous Polyethylene-teraphthalate—An Activated Rate Theory Approach", *J. Mater. Sci.* **22**, 1437–1442 (1987).
46. Y. Liu and R. W. Truss, "A Study of Tensile Yielding of Isotactic Polypropylene", *J. Polym. Sci, Part B: Polym. Phys.* **32**, 2037–2047 (1994).
47. M. Bonner, R. A. Duckett, and I. M. Ward, "The Creep Behaviour of Isotropic Polyethylene", *J. Mater. Sci.* **34**, 1885–1897 (1999).

48. I. M. Ward, "Creep and Yield Behavior of Polyethylene", *Macromol. Symp.* **98**, 1029–1041 (1995).
49. M. L. Williams, R. F. Landel, and J. D. Ferry, "The Temperature Dependence of Relaxation Mechanisms in Amorphous Polymers and Other Glass-Forming Liquids", *J. Am. Chem. Soc.* **77**, 3701–3706 (1955).
50. M. C. Wang and E. J. Guth, "Statistical Theory of Networks of Non-Gaussian Flexible Chains", *J. Chem. Phys.* **20**, 1144–1157 (1952).
51. I. M. Ward, *Structure and Properties of Oriented Polymers*, 2nd ed. Chapman and Hall, London, 1997.
52. D. M. Parks, A. S. Argon, and B. Bagepalli, "Large Elastic–Plastic Deformation of Glassy Polymers", *Program in Polymer Science and Technology*, Technical Report, MIT, 1984.
53. L. R. G. Treloar, *The Physics of Rubber Elasticity*, 3rd ed., Clarendon Press, Oxford, 1975.
54. E. M. Arruda and M. C. Boyce, "A 3-Dimensional Constitutive Model for the Large Stretch Behavior of Rubber Elastic Materials", *J. Mech. Phys. Solids* **41**, 389–412 (1993).
55. W. H. Han, F. Horkay, and G. B. McKenna, "Mechanical and Swelling Behaviors of Rubber: A Comparison of Some Molecular Models with Experiment", *Math. Mech. Solids* **4**(2), 139–167 (1999).
56. O. A. Hasan, M. C. Boyce, X. S. Li, and S. Berko, "An Investigation of the Yield and Post-Yield Behavior and Corresponding Structure of Poly(Methylmethacrylate)", *J. Polym. Sci., Part B: Polym. Phys.* **31**(2), 185–197 (1993).
57. C. G'Sell and G. B. McKenna, "Influence of Physical Ageing on the Yield Response of Model DGEBA/Poly(Propylene Oxide) Epoxy Glasses", *Polymer* **33**, 2103–2113 (1992).
58. P. D. Wu and E. van der Giessen, "On Improved Network Models for Rubber Elasticity and Their Applications to Orientation Hardening in Glassy Polymers", *J. Mech. Phys. Solids* **41**, 427–456 (1993).
59. A. Leonov, "Nonequilibrium Thermodynamics and Rheology of Viscoelastic Polymer Media", *Rheol. Acta* **15**, 85–98 (1976).
60. T. A. Tervoort and L. E. Govaert, "Strain Hardening Behavior of Polycarbonate in the Glassy State", *J. Rheol.* **44**, 1263–1277 (2000).
61. L. E. Govaert, P. H. M. Timmermans, and W. A. M. Brekelmans, "The Influence of Intrinsic Strain Softening Localization in Polycarbonate: Modeling and Experimental Validation", *J. Eng. Mater. Tech., Trans ASME* **122**(2), 177–185 (2000).
62. M. Aboulfaraj, C. G'Sell, D. Mangelinck, and G. B. McKenna, "Physical Aging of Epoxy Networks after Quenching and/or Plastic Cycling", *J. Non-Cryst. Solids* **172–174**, 615–621 (1994).
63. E. M. Arruda and M. C. Boyce, "Evolution of Plastic Anisotropy in Amorphous Polymers during Finite Straining", *Int. J. Plast.* **9**, 697–720 (1993).
64. B. D. Coleman, "Thermodynamics of Materials with Memory", *Arch. Ration. Mech. Anal.* **17**, 230–254 (1964).
65. W. Noll, "Mathematical Theory of the Mechanical Behavior of Continuous Media", *Arch. Ration. Mech. Anal.* **2**, 197–226 (1958).
66. G. Adam and J. H. Gibbs, "On the Temperature Dependence of Cooperative Relaxation Properties in Glass Forming Liquids" *J. Chem. Phys.* **43**, 139–146 (1965).
67. D. A. Zaukelies, "Observation of Slip in Nylon 66 and 610 and Its Interpretation in Terms of a New Model", *J. Appl. Phys.* **33**, 2797–2803 (1962).
68. P. Predecki and W. O. Statton, "Dislocations Caused by Chain Ends in Crystalline Polymers", *J. Appl. Phys.* **37**, 4053–4059 (1966).
69. P. Predecki and W. O. Statton, "A Dislocation Mechanism for Deformation of Polyethylene", *J. Appl. Phys.* **38**, 4140–4144 (1967).

70. J. Petermann and H. Gleiter, "Direct Observation of Dislocations in Polyethylene Crystals", *Philos. Mag.* **25**, 813–816 (1972).
71. J. J. Gilman, in A. R. Rosenfield, G. T. Hahn, A. L. Bement and R. I. Jaffee, eds., *Dislocation Dynamics*, John Wiley & Sons, Inc., New York, 1968.
72. J. J. Gilman, in A. S. Argon, ed., *Physics of Strength and Plasticity*, MIT, 1969.
73. P. B. Bowden and S. Raha, "A Molecular Model for Yield and Flow in Amorphous Glassy Polymers Making Use of a Dislocation Analogue", *Philos. Mag.* **29**, 149–166 (1974).
74. J. Frenkel, "Zur Theorie der Elastizitätsgrenze und der Festigkeit Kristallinischer Körper ", *Z. Physik* **37**, 572–609 (1926).
75. P. B. Bowden in R. N. Haward, ed. *The Physics of Glassy Polymers*, 1st ed., John Wiley & Sons, Inc., New York, 1973.
76. B. Crist, in R. N. Haward and R. J. Young, eds., *The Physics of Glassy Polymers*, 2nd ed., Chapman and Hall, London 1997.
77. A. Kelly and N. H. MacMillen, *Strong Solids*, 3rd ed., Oxford University Press, New York, 1986.
78. N. Brown, "A Theory of Yielding of Amorphous Polymers at Low Temperature–A Molecular Viewpoint" *J. Mater. Sci.* **18**, 2241–2254 (1983).
79. Z. H. Stachurski, "Deformation Mechanisms and Yield Strength of Amorphous Polymers", *Prog. Polym. Sci.* **22**, 407–474 (1997).
80. P. A. O'Connell and G. B. McKenna, "Large Deformation Response of Polycarbonate: Time–Temperature, Time–Aging Time and Time–Strain Superposition", *Polym. Eng. Sci.* **37**, 1485–1495 (1997).
81. C G'Sell and G. B. McKenna, "Influence of Physical Ageing on the Yield Response of Model DGEBA/Poly(Propylene Oxide) Epoxy Glasses", *Polymer* **33**, 2103–2113 (1992).
82. E. Oleynik, "Plastic Deformation and Mobility in Glassy Polymers", *Prog. Colloid Polym. Sci.* **80**, 140–150 (1989).
83. O. A. Hasan and M. C. Boyce, "Energy Storage During Inelastic Deformation of Glassy Polymers", *Polymer* **34**, 5085–5092 (1993).
84. Y. C. Yung, *Foundations of Solid Mechanics*, Prentice-Hall, Inc., Englewood Cliffs, N.J., 1965.
85. W. C. Whitney and R. D. Andrews, "Yielding of Glassy Polymers: Volume Effects", *J. Polym. Sci., Part B* **16**, 2981–2990 (1967).
86. D. M. Colucci, P. A. O'Connell, and G. B. McKenna, "Stress Relaxation Experiments in Polycarbonate: A Comparison of Volume Changes for Two Commercial Grades", *Polym. Eng. Sci.* **37**, 1469–1474 (1997).
87. W. G. Knauss and I. Emri, "Volume Change and Nonlinearly Thermo-Viscoelastic Constitution of Polymers", *Polym. Eng. Sci.* **27**(1), 86–100 (1987).
88. C. G'Sell, J. M. Hiver, and A. Dahoun, "Experimental Characterization of Deformation Damage in Solid Polymers under Tension, and Its Interrelation with Necking", *Int. J. Solids. Struct.* **39**, 3857–3872 (2002).
89. R. S. Duran and McKenna, "A Torsional Dilatometer for Volume Change Measurements on Deformed Glasses: Instrument Description and Measurements on Equilibrated Glasses", *J. Rheol.* **34**, 813–839 (1990).
90. L. Xie, D. W. Gidley, H. A. Hristov, and A. F. Yee, "Evolution of Nanometer Voids in Polycarbonate under Mechanical Stress and Thermal Expansion using Positron Spectroscopy", *J. Polym. Sci., Part B* **33**(1), 77–84 (1995).
91. O. A. Hasan, M. C. Boyce, X. S. Li, and S. Derko, "An Investigation of the Yield and Post-Yield Behavior and Corresponding Structure of Poly(Methyl Methacrylate)", *J. Polym. Sci., Part B* **31**, 185–197 (1993).

92. M. Y. Ruan, H. Moaddel, A. M. Jamieson, R. Simha, and J. D. McGervey, "Positron Annihilation Lifetime Studies of Free Volume Changes in Polycarbonate under Static Tensile Deformation", *Macromolecules* **25**, 2407–2411 (1992).
93. D. N. Theodorou and U. W. Suter, "Detailed Molecular Structure of a Vinyl Polymer Glass", *Macromolecules* **18**, 1467–1478 (1986).
94. D. N. Theodorou and U. W. Suter, "Atomistic Modeling of Mechanical Properties of Polymeric Glasses", *Macromolecules* **19**(1), 139–154 (1986).
95. P. H. Mott, A. S. Argon, and U. W. Suter, "Atomistic Modeling Cavitation of Glassy Polymers", *Philos. Mag.* **67**, 931–978 (1993).
96. P. H. Mott, A. S. Argon, and U. W. Suter, "Atomistic Modeling of Plastic Deformation of Glassy Polymers", *Philos. Mag.* **68**, 537–564 (1993).
97. N. W. Brooks, R. A. Duckett, and I. M. Ward, "Investigation into Double Yield Points in Polyethylene", *Polymer* **33**, 1872–1880 (1992).
98. N. W. Brooks, A. P. Unwin, R. A. Duckett, and I. M. Ward, "Double Yield Points in Polyethylene—Structural Changes under Tensile Deformation", *J. Macromol. Sci., Phys.* **B34**(1–2), 29–54 (1995).
99. R. Seguela and O. Darras, "Phenomenological Aspects of the Double Yield of Polyethylene and Related Copolymers under Tensile Loading", *J. Mat. Sci.* **29**, 5342–5352 (1994).
100. P. A. Botto, R. A. Duckett, and I. M. Ward, "The Yield and Thermoelastic Properties of Oriented Poly(Methyl-Methacrylate)", *Polymer* **28**, 257–262 (1987).
101. J. P. Chen, A. F. Yee, and E. J. Moskala, "The Molecular Basis for the Relationship between the Secondary Relaxation and Mechanical Properties of a Series of Polyester Copolymer Glasses", *Macromolecules* **32**, 5944–5955 (1999).
102. R. W. Truss, P. L. Clarke, and R. A. Duckett, "The Dependence of Yield Behavior on Temperature, Pressure and Strain Rate for Linear Polyethylenes of Different Molecular Weight and Morphology", *J. Polym. Sci., Polym. Phys.* **22**, 191–209 (1984).
103. R. J. Young, "A Dislocation Model for Yield in Polyethylene", *Philos. Mag.* **30**, 85–94 (1974).
104. M. A. Kennedy, A. J. Peacock, M. D. Failla, J. C. Lucas, and L. Mandelkern, "Tensile Properties of Crystalline Polymers—Random Copolymers of Ethylene", *Macromolecules* **28**, 1407–1421 (1995).
105. B. Crist, C. J. Fisher, and P. R. Howard, "Mechanical Properties of Model Polyethylenes—Tensile Elastic Modulus and Yield Stress", *Macromolecules* **22**, 1709–1718 (1989).
106. O. Darras, and R. Seguela, "Tensile Yield of Polyethylene in Relation to Crystal Thickness", *J. Polym. Sci., Part B: Polym. Phys.* **31**, 759–766 (1993).
107. N. W. J. Brooks and M. Mukhtar, "Temperature and Stem Length Dependence of the Yield Stress of Polyethylene", *Polymer* **41**, 1475–1480 (2000).
108. R. Seguela, "Dislocation Approach to the Plastic Deformation of Semicrystalline Polymers: Kinetic Aspects for Polyethylene and Polypropylene", *J. Polym. Sci., Part B: Polym. Phys.* **40**, 593–601 (2002).
109. Z. Bartczak, R. E. Cohen, and A. S. Argon, "Evolution of the Crystalline Texture of High-Density Polyethylene during Uniaxial Compression", *Macromolecules* **25**, 4692–4704 (1992).
110. Z. Bartczak, A. S. Argon, and R. E. Cohen, "Deformation Mechanisms and Plastic Resistance in Single Crystal Textured High Density Polyethylene", *Macromolecules* **25**, 5036–5053 (1992).
111. A. S. Argon and J. G. Hannoosh, "Initiation of Crazes in Polystyrene", *Philos. Mag.* **36**, 1195–1216 (1977).
112. A. Lazzeri and C. B. Bucknall, "Dilatational Bands in Rubber Toughened Polymers", *J. Mater. Sci.* **28**, 6799–6808 (1989).

113. C. B. Bucknall and A. Lazzeri, "Rubber Toughening of Plastics. Part XIII: Dilatational Yielding in PA6.6/EPR Blends", *J. Mater. Sci.* **35**, 427–435 (2000).
114. M. Todo, K. Takahasi, P. Y. B. Jar, and P. Beguelin, "Toughening Mechanisms of Rubber Toughened PMMA", *JSME Int. J., Ser. A: Solid. Mech. Mater. Eng.* **42**, 585–591 (1999).
115. Y. Huang and A. J. Kinloch, "Modeling of the Toughening Mechanisms in Rubber Modified Epoxy Polymers. Part I: Finite Element Analysis Studies", *J. Mater. Sci.* **27**, 2753–2762 (1992).
116. E. J. Kramer, "Microscopic and Molecular Fundamentals of Crazing" in *Adv. Polym. Sci.* **52/53**, 1–56 (1983).
117. E. J. Kramer and L. L. Berger, "Fundamental Processes of Craze Growth and Fracture" in *Adv. Polym. Sci.* **91/92**, 1–68 (1990).
118. R. P. Kambour, "A Review of Crazing and Fracture in Thermoplastics", *J. Polym. Sci., Macromol. Rev.* **7**, 1–154 (1973).
119. A. M. Donald, in W. Brostow, ed., *Performance of Plastics*, Hanser Publishers, Munich, pp. 283–296, 2000.
120. A. M. Donald, in R. N. Haward and R. J. Young, eds., *The Physics of Glassy Polymer*, Chapman and Hall, London, 1997.
121. B. D. Lauterwasser and E. J. Kramer, "Microscopic Mechanisms and Mechanics of Craze Growth and Fracture", *Philos. Mag. A* **39**, 469–495 (1979).
122. S. S. Sternstein and L. Ongchin, "Yield Criteria for Plastic Deformation of Glassy High Polymers in General Stress Fields", *Polym. Prepr.* **10**, 1117–1124 (1969).
123. S. S. Sternstein and F. A. Myers, "Yielding of Glassy Polymers in the Second Quadrant of Principal Stress Space", *J. Macromol. Sci., Phys.* **B8**, 539–571 (1973).
124. A. N. Gent, "Hypothetical Mechanism of Crazing in Glassy Plastics", *J. Mater. Sci.* **5**, 925–932 (1970).
125. R. J. Oxborough and P. B. Bowden, "A General Critical–Strain Criterion for Crazing in Amorphous Glassy Polymers", *Philos. Mag.* **28**, 547–559 (1973).
126. A. S. Argon, "Role of Heterogeneities in the Crazing of Glassy Polymers", *Pure Appl. Chem.* **43**, 247–272 (1975).
127. A. S. Argon, "Physical Basis of Distortional and Dilatational Plastic Flow in Glassy Polymers", *J. Macromol. Sci., Phys.* **B8**, 573–596 (1973).
128. R. P. Kambour and C. L. Gruner, "Effects of Polar Group Incorporation on Crazing of Glassy Polymers: Styrene–Acrylonitrile Copolymer and a dicyano Bisphenol Polycarbonate", *J. Polym. Sci., Polym. Phys.* **16**, 703–716 (1978).
129. R. P. Kambour, "Correlations of the Dry Crazing Resistance of Glassy Polymers with Other Physical Properties", *Polym. Commun.* **24**, 292–296 (1983).
130. G. M. Gusler and G. B. McKenna, "The Craze Initiation Response of a Polystyrene and a Styrene–Acrylonitrile Copolymer during Physical Aging", *Polym. Eng. Sci.* **37**, 1442–1448 (1997).
131. A. S. Argon and M. M. Salama, "The Mechanics of Fracture in Glassy Materials Capable of Some Inelastic Deformation", *Mater. Sci. Eng.* **23**, 219–230 (1977).
132. G. I. Taylor, "The Instability of Liquid Surfaces When Accelerated in the Direction Perpendicular to Their Planes", *Proc. R. Soc. London, Ser. A* **201**, 192–196 (1950).
133. P. G. Saffman and G. I. Taylor, "The Penetration of Liquid into Porous Medium or Hele–Shaw Cell Containing a More Viscous Liquid", *Proc. R. Soc. London, Ser. A* **245**, 312–329 (1958).
134. R. J. Fields and M. F. Ashby, "Finger-Like Crack Growth in Solids and Liquids", *Philos. Mag.* **33**, 33–48 (1976).
135. A. M. Donald and E. J. Kramer, "The Mechanisms for Craze Tip Advance in Glassy Polymers", *Philos. Mag. A* **43**, 857–870 (1981).

136. A. S. Argon and M. M. Salama, "Growth of Crazes in Glassy Polymers", *Philos. Mag. B* **36**, 1217–1234 (1977).
137. N. Verheulpen-Heymans, and J. C. Bauwens, "Effect of Stress and Temperature on Dry Craze Growth Kinetics during Low-Stress Creep of Polycarbonate", *J. Mater. Sci.* **11**, 1–6 (1976).
138. J. L. S. Wales, "Surface Crazing in PVC and Other Polymers", *Polymer* **21**, 684–690 (1980).
139. M. Delin and G. B. McKenna, "The Craze Growth Response in Stress Relaxation Conditions for a Styrene–Acrylonitrile Copolymer during Physical Aging", *Mech. Time Dep. Mater.* **4**, 231–255 (2000).
140. A. M. Donald, E. J. Kramer, and R. A. Bubeck, "The Entanglement Network and Craze Micromechanics in Glassy Polymers", *J. Polym. Sci., Polym. Phys.* **20**, 1129–1141 (1982).
141. A. M. Donald and E. J. Kramer, "Effect of Molecular Entanglements on Craze Microstructure in Glassy Polymers", *J. Polym. Sci., Polym. Phys.* **20**, 899–909 (1982).
142. M. Doi and S. F. Edwards, "Dynamics of Concentrated Polymer Systems. Part I: Brownian Motion in the Equilibrium State", *J. Chem. Soc., Faraday Trans. 2* **74**, 1789–1801 (1978).
143. P. G. deGennes, "Reptation of a Polymer Chain in the Presence of Fixed Obstacles", *J. Chem. Phys.* **55**, 572–579 (1971).
144. T. C. B. McLeish, C. J. G. Plummer, and A. M. Donald, "Crazing by Disentanglement–Non-Diffusive Reptation", *Polymer* **30**, 1651–1655 (1989).
145. R. Schirrer, J. Le Masson, and B. Tomatis, "The Disentanglement Time of the Craze Fibrils under Cyclic Load", *Polym. Eng. Sci.* **24**, 820–824 (1984).
146. W. Doll, "Optical Interference Measurements and Fracture Mechanics Analysis of Crack Tip Craze Zones", *Adv. Polym. Sci.* **52/53**, 105–168 (1983).
147. P. Behan, M. Bevis and D. Hull, "Fracture Processes in Polystyrene", *Proc. R. Soc.London, Ser. A* **343**, 525–535 (1975).
148. M. G. A. Tijssens and E. van der Giessen, "A Possible Mechanism for Cross-Tie Fibril Generation in Crazing of Amorphous Polymers", *Polymer* **43**, 831–838 (2002).
149. H. R. Brown, "A Molecular Interpretation of the Toughness of Glassy Polymers", *Macromolecules* **24**, 2752–2756 (1991).
150. Y. Sha, C. Y. Hui, A. Ruina, and E. J. Kramer, "Detailed Simulation of Craze Fibril Failure at a Crack Tip in a Glassy Polymer", *Acta. Mater.* **45**, 3555–3563 (1997).
151. D. C. Wright, *Environmental Stress Cracking of Plastics*, ChemTec, Ontario, 1996.
152. A. L. Volynskii and N. F. Bakeev, *Solvent Crazing of Polymers*, Elsevier, New York, 1995.
153. W. A. Woishnis and D. C. Wright, "Select Plastics to Avoid Product Failure", *Adv. Mater. and Proc.* **12**, 39–40 (1994).
154. J. C. Arnold, "Environmental Stress Crack Initiation in Glassy Polymers", *Trends Polym. Sci.* **4**, 403–408 (1996).
155. J. C. Arnold, "Craze Initiation during the Environmental Stress Cracking of Polymers", *J. Mater. Sci.* **30**, 655–660 (1995).
156. J. C. Arnold, "Environmental Stress Cracking Behavior of Urethane Methacrylate Based Resins. Part I: Environmental Crazing and Cracking under Bending Conditions", *J. Mater. Sci.* **29**, 3095–3101 (1994).
157. R. W. Hertzberg and J. A. Manson, *Fatigue in Engineering Plastics*, Academic Press, New York, 1980.
158. C. Rimnac, R. W. Hertzberg and J. A. Manson, "On the Nature of Craze Development and Breakdown During Fatigue", *J. Mater. Sci. Lett.* **2**, 325–328 (1983).
159. C. Rimnac, R. W. Hertzberg, and J. A. Manson, "Craze Development and Breakdown in PVC during Cyclic Loading", *J. Mater. Sci.* **19**, 1116–1124 (1984).

160. R. W. Lang, J. A. Manson, and R. W. Hertzberg, "Craze Development in Poly(Methyl-Methacrylate) during Stable Fatigue Crack Propagation", *Polym. Eng. Sci.* **24**, 833–842 (1984).
161. W. Döll and L. Könczöl, "Micromechanics of Fracture under Static and Fatigue Loading: Optical Interferometry of Crack Tip Craze Zones" *Adv. Polym. Sci.* **91/92**, 137–214 (1990).
162. R. Schirrer, M. G. Schinker, L. Konczol, and W. Döll, "Interference Optical Studies on Crack Propagation during Cyclic Loading in PMMA", *Colloid Polym. Sci.* **259**, 812–817 (1981).
163. W. Döll, L. Kinczol, and M. G. Schinker, "Size and Mechanical Properties of Craze Zones at Propagating Crack Tips in Poly(Methyl Methacrylate) during Fatigue Loading", *Polymer* **24**, 1213–1219 (1983).

PAUL A. O'CONNELL
GREGORY B. MCKENNA
Texas Tech University

Z

ZIEGLER–NATTA CATALYSTS

Introduction

Ziegler–Natta catalysts have had enormous impact on the polymer industry in the past 50 years, with current world production of polyolefins using Ziegler–Natta catalysis amounting to more than 50 million tons per annum. The vast advances made during the past decades stem from breakthrough discoveries made by Karl Ziegler and Giulio Natta in the early 1950s. It was in 1953 that Ziegler and co-workers, at the Max Planck Institute in Mülheim, were investigating the "Aufbau" reaction in which triethylaluminum reacts with ethylene to give higher aluminum trialkyls (1). Unexpectedly, one experiment led not to the oligomerization of ethylene via the Aufbau reaction, but to the formation of 1-butene. It turned out that this dimerization reaction had been catalyzed by traces of nickel present as a contaminant in the reactor. Soon afterwards, a revolutionary breakthrough was achieved when combinations of transition-metal compounds and aluminum alkyls were found that could polymerize ethylene under mild conditions, yielding high density polyethylene (2,3). In 1954 Giulio Natta and co-workers at Milan Polytechnic succeeded not only in polymerizing propylene with the Ziegler catalyst combination $TiCl_4/Al(C_2H_5)_3$, but also in fractionating the resulting polymer to obtain and characterize isotactic polypropylene (4–6). This demonstration of stereoregular polymerization led to an explosive growth of new polymers and industrial applications as the full scope of Ziegler–Natta catalysis was realized (7–9); Ziegler and Natta were jointly awarded the Nobel Prize for Chemistry in 1963.

Ziegler–Natta catalysts for polyethylene and polypropylene have progressed from first-generation titanium trichloride catalysts, used in the manufacturing processes of the late 1950s and the 1960s, to the high activity magnesium chloride supported catalysts used today. Improvements in catalyst performance have facilitated the development of efficient gas-phase and bulk processes for polyethylene and polypropylene, and at the same time have led to ever-increasing control over polymer composition and properties.

Early Catalysts

Titanium Trichloride. One of the first catalysts found by Ziegler to be effective in ethylene polymerization was the product of the reaction of titanium tetrachloride with triethylaluminum. At low Al/Ti ratios, this reaction yields titanium trichloride as a solid precipitate. $TiCl_3$ exists in four crystalline modifications, the α, β, δ, and γ forms, of which the β-modification has a linear (chain-like) structure and the α, δ, and γ forms have a layered structure (10,11). The reaction product of $TiCl_4$ and AlR_3 is β-$TiCl_3$, which can be converted to the γ form by heating. The latter catalyst has much higher stereoregulating ability in propylene polymerization, while β-$TiCl_3$ is an effective catalyst for the production of *cis*-1,4-polyisoprene. α-$TiCl_3$ can be prepared by reduction of $TiCl_4$ with hydrogen or with aluminum powder. The δ form can be prepared by prolonged grinding of γ- or α-$TiCl_3$ and has a more disordered structure as a result of sliding of Cl–Ti–Cl triple layers during mechanical activation (12).

The first-generation Ziegler–Natta catalysts used in early manufacturing processes for polypropylene (PP) comprised $TiCl_3$ and cocrystallized $AlCl_3$, resulting from reduction of $TiCl_4$ with Al or an aluminum alkyl. The cocatalyst used in the polymerization process was $Al(C_2H_5)_2Cl$ (DEAC). Catalyst activity was relatively low, giving polymer yields of around 1 kg PP/g cat., necessitating removal (deashing) of catalyst residues from the polymer. In many cases, extractive removal of atactic polymer was also required.

Other Early Developments. In addition to the breakthrough by Ziegler, two other discoveries of ethylene polymerization catalysts were made in the early 1950s. A patent by Standard Oil of Indiana, filed in 1951, disclosed reduced molybdenum oxide or cobalt molybdate on alumina (13). At the same time, Phillips discovered supported chromium oxide catalysts, prepared by impregnation of a silica–alumina support with CrO_3 (14–16). Both the Phillips catalyst and titanium chloride based Ziegler catalysts are widely used in the production of high density polyethylene (HDPE).

The various discoveries made independently by different industrial research groups in the early 1950s resulted in intensive patent litigations (8,17,18), which in the case of PP continued up to the 1980s, when a composition of matter patent on PP was awarded in the United States to Phillips, because a fraction of crystalline PP was found to be present in a polymer prepared using a $CrO_3/Al_2O_3/SiO_2$ catalyst (19). However, despite the importance of the Phillips catalyst for HDPE, it was unsuitable for PP, which is produced entirely using Ziegler–Natta catalysts and (to a much smaller extent) metallocene-based catalysts.

Second-Generation Catalysts. In the 1970s, an improved $TiCl_3$ catalyst for PP was developed by Solvay (20). Catalyst preparation involved reduction of $TiCl_4$ using DEAC, followed by treatment with an ether and $TiCl_4$. The ether treatment results in removal of $AlCl_3$ from $TiCl_3 \cdot nAlCl_3$, while treatment with $TiCl_4$ effects a phase transformation from β- to δ-$TiCl_3$ at a relatively mild temperature ($<100^\circ C$) (21). Using catalysts of this type, it was possible to obtain PP yields in the range 5–20 kg/g cat. in 1–4 h of polymerization in liquid monomer (22). Commercial implementation of second-generation catalysts was, however,

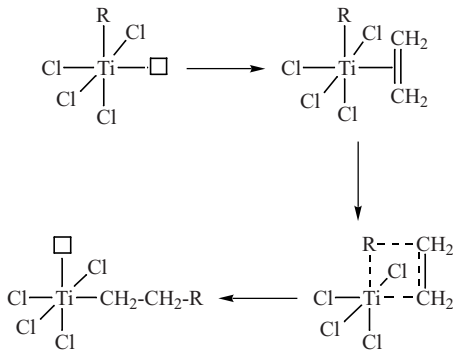

Fig. 1. Cossee–Arlman mechanism for polymerization.

$$\text{Ti-CH}_2\text{-CH}_2\text{-Polymer} + \text{H}_2 \longrightarrow \text{Ti-H} + \text{CH}_3\text{-CH}_2\text{-Polymer}$$

$$\text{Ti-CH}_2\text{-CH}_2\text{-Polymer} + \text{CH}_2{=}\text{CH}_2 \longrightarrow \text{Ti-CH}_2\text{-CH}_3 + \text{CH}_2{=}\text{CH-Polymer}$$

$$\text{Ti-CH}_2\text{-CH}_2\text{-Polymer} + \text{AlR}_3 \longrightarrow \text{Ti-R} + \text{AlR}_2\text{-CH}_2\text{-CH}_2\text{-Polymer}$$

Fig. 2. Chain transfer in ethylene polymerization.

overshadowed by the advent of third- and later-generation magnesium chloride supported catalysts (discussed under Ziegler–Natta Catalysts for Polypropylene).

Polymerization and Particle Growth

Polymer Chain Growth. The essential characteristic of Ziegler–Natta catalysis is the polymerization of an olefin or diene using a combination of a transition-metal compound and a base-metal alkyl cocatalyst, normally an aluminum alkyl. The function of the cocatalyst is to alkylate the transition metal, generating a transition-metal–carbon bond. It is also essential that the active center contains a coordination vacancy. Chain propagation takes place via the Cossee–Arlman mechanism (23), in which coordination of the olefin at the vacant coordination site is followed by chain migratory insertion into the metal–carbon bond, as illustrated in Figure 1.

Regulation of polyolefin molecular weight is effected by the use of hydrogen as chain-transfer agent. Chain transfer can also occur via β-hydrogen transfer from the growing chain to the transition metal or to the monomer, and to a lesser extent via alkyl exchange with the cocatalyst (Fig. 2).

In propylene polymerization using titanium chloride catalysts, chain propagation takes place via primary (1,2-) insertion of the monomer. For isospecific propagation, there must be only one coordination vacancy and the active site must be chiral. Corradini and co-workers have demonstrated that the asymmetric environment of the active site forces the growing chain to adopt a particular orientation so as to minimize steric interactions with (chlorine) ligands present on the catalyst surface (24). This in turn leads to one particular prochiral face of the

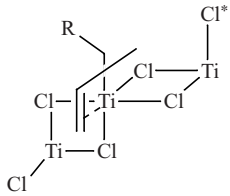

Fig. 3. Model for stereospecific polymerization of propylene. The orientation of the growing chain is influenced by the chlorine atom marked with an asterisk.

incoming monomer being preferred, as illustrated in Figure 3, leading to isotactic polymer.

An elegant demonstration of the above mechanism has been provided by Zambelli and co-workers (25), who showed that the first insertion of propylene into a Ti—CH_3 bond generated by chain transfer with Al alkyl using the system $TiCl_3/Al(CH_3)_3$ is *not* stereospecific, whereas the second insertion (ie into Ti–isobutyl) *is* stereospecific. The importance of the combined effects of the steric bulk of the Ti–alkyl group and the halide ligand is apparent from the very high stereospecificity observed using TiI_3 (26). Particularly high stereospecificity (but low activity) was also found by Natta when $TiCl_3$ was used in combination with $Al(C_2H_5)_2I$ (27).

In contrast to the isospecific titanium-based catalysts, vanadium-based catalysts give predominantly syndiotactic PP. At very low polymerization temperature (−78°C), living polymerization can be obtained using homogeneous catalysts obtained by reaction of a vanadium compound (eg VCl_4 or a V(III) β-diketonate) with R_2AlCl (28,29). With these catalysts, syndiospecific propagation occurs via secondary (2,1-) insertion of the monomer. The overall stereo- and regioregularity of the polymer is poor, comprising not only syndiotactic blocks resulting from secondary insertions but also short, atactic blocks arising from sequences of primary insertions. This polymer has not been developed commercially, but vanadium catalysts are used in ethylene (co)polymerization (outlined under Ziegler–Natta Catalysts for Ethylene (Co)polymerization). C_s-symmetric metallocene catalysts (30) have been developed for the production of syndiotactic polypropylene having significantly higher chain regularity.

Polymer Particle Growth. A very important feature of any heterogeneous catalyst used in slurry and gas-phase processes for polyolefin production is particle morphology. Heterogeneous Ziegler–Natta catalysts are microporous solids, with particle sizes typically in the range 10–100 μm. Each particle comprises millions of primary crystallites with sizes of up to about 15 nm. On contacting the catalyst components, at the start of polymerization, cocatalyst and monomer diffuse through the catalyst particle and polymerization takes place on the surface of each primary crystallite within the particle. As solid, crystalline polymer is formed, the primary crystallites are pushed apart as the particle grows, analogous to the expanding universe. The particle shape is retained, and this phenomenon is therefore referred to as replication (Fig. 4). Ideally, the catalyst particle should have spherical morphology and controllable porosity. It is important that the mechanical strength of the catalyst is high enough to prevent

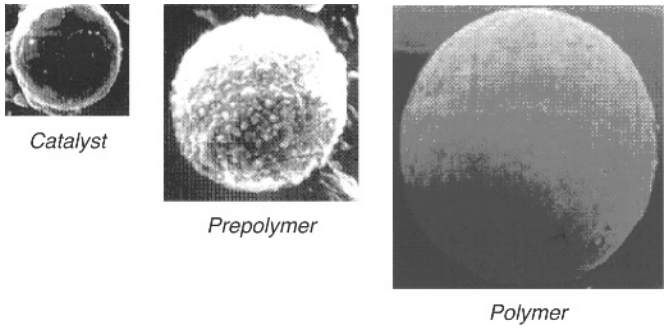

Fig. 4. "Replication" phenomenon during polymerization.

disintegration but low enough to allow progressive expansion as polymerization proceeds (31). Further implications of particle morphology and porosity are discussed under Ziegler–Natta Catalysts for Ethylene (Co)polymerization and also under Reactor Granule Technology.

Ziegler–Natta Catalysts for Ethylene (Co)polymerization

Ziegler–Natta catalysts are widely used in the production of high density and linear low density polyethylene (HDPE and LLDPE). More than half the world production of HDPE is based on Ziegler–Natta catalysts, chromium catalysts also being widely used. Less than 1% of HDPE production utilizes metallocene or other single-site catalysts. In LLDPE production, Ziegler–Natta catalysts occupy a dominant position, accounting for more than 90% of the total production. Single-site catalysts currently account for less than 10% of this market, but increased use of such catalysts is expected throughout the next decade.

The most important titanium-based catalysts for HDPE and LLDPE are those comprising a titanium component on magnesium chloride or on a magnesium chloride containing support. Toward the end of the 1960s, catalysts obtained by reaction of $TiCl_4$ or a derivative thereof with a magnesium compound such as $Mg(OH)Cl$, $Mg(OH)_2$, or $MgCl_2$ were found to give very high activity in ethylene polymerization, eliminating the need for deashing of the polymer (31,32). The most effective support was found to be active magnesium chloride, prepared by co-milling of $MgCl_2$ and titanium halides or by chlorination of organomagnesium compounds (32). Numerous catalyst systems and methods of preparation have been disclosed (33), and the characteristics of magnesium chloride as a support for Ziegler–Natta catalysts are discussed in depth under Ziegler–Natta Catalysts for Polypropylene. Magnesium chloride can also be used in combination with a silica support, for example by impregnation of the porous support with a solution of $MgCl_2$ and $TiCl_4$ in tetrahydrofuran (34).

An important manufacturing process for HDPE that makes use of high mileage catalysts is the cascade process, in which polymerization reactors in series are used to give reactor blends with improved properties for film and

pipe applications (35). Broad molecular weight distribution (MWD) can be obtained by the use of different hydrogen concentrations in each reactor. In addition, the process can be designed to give low molecular weight homopolymer in the first reactor and a high molecular weight copolymer in the second. The high molecular weight copolymer chains function as tie molecules linking the crystalline, homopolymer domains, thereby leading to high stress crack resistance of the polymer. This process allows an "inverse" comonomer distribution to be obtained, in the sense that the comonomer is in the high molecular weight fraction, counteracting the general tendency of Ziegler–Natta catalysts to incorporate the comonomer mainly in the low molecular weight chains. The latter feature is an important consideration in Ziegler–Natta catalyst design for LLDPE. Comonomer incorporation is highest at the most open catalytic centers, whereas sterically hindered centers will tend to give polyethylene chains with little or no comonomer. The best catalysts for LLDPE are therefore those that have relatively uniform active center distribution, lacking excessively hindered or unhindered active sites.

Vanadium catalysts have also been developed for polyethylene and ethylene-based copolymers, particularly ethylene–propylene–diene rubbers (EPDM). Homogeneous (soluble) vanadium catalysts produce relatively narrow MWD polyethylene, whereas supported vandium catalysts give broad MWD (36). Polymerization activity is strongly enhanced by the use of a halogenated hydrocarbon as promoter in combination with a vanadium catalyst and aluminum alkyl cocatalyst (36,37).

Ethylene polymerization, in contrast to the polymerization of propylene and other alpha-olefins, is often affected by diffusion limitations, which occur if the monomer reactivity in polymerization is high relative to diffusivity through the catalyst particle. This can result in the formation of an "onion" particle structure as polymerization first takes place at the external surface of the particle, particle growth occurring step by step as the monomer reaches the inner parts of the catalyst particle. This mechanism of particle growth is associated with a kinetic profile in which an initial induction period is followed by an acceleration period, after which, in the absence of chemical deactivation, a stationary rate is obtained.

Ziegler–Natta Catalysts for Polypropylene

Worldwide manufacture of PP, currently around 30 million tons per annum, is dominated by high activity $MgCl_2$-supported Ziegler–Natta catalysts. The first- and second-generation $TiCl_3$ catalysts have all but disappeared, and the recently developed metallocene catalysts still account for less than 1% of all PP produced, although they are likely to grow in importance. The development and implementation of $MgCl_2$-supported catalysts in bulk (liquid monomer) and gas-phase processes has led to the advent of simple, low-cost (nondeashing, nonextracting) manufacturing processes for PP (18).

The basis for the development of the high activity supported catalysts lay in the discovery, in the late 1960s, of "activated" $MgCl_2$ able to support $TiCl_4$ and give high catalyst activity, and the subsequent discovery, in the mid-1970s, of electron donors (Lewis bases) capable of increasing the stereospecificity of the

catalyst so that (highly) isotactic PP could be obtained (32,38,39). A further feature that has contributed greatly to the commercial success of $MgCl_2$-supported catalysts is the development of spherical catalysts with controlled particle size and porosity (40), which not only replicate their morphology during polymerization as the polymer particle grows, but which have now opened the way to a broad range of homo- and copolymers and multiphase polymer alloys via what has been termed Reactor Granule Technology (41).

Catalyst Structure and Composition. In the early stages of $MgCl_2$-supported catalyst development, activated magnesium chloride was prepared by ball milling in the presence of ethyl benzoate, leading to the formation of very small ($\leq$3 nm thick) primary crystallites within each particle (21). Nowadays, however, the activated support is prepared by chemical means such as complex formation of $MgCl_2$ and an alcohol or by reaction of a magnesium alkyl or alkoxide with a chlorinating agent or $TiCl_4$. Many of these approaches are also effective for the preparation of catalysts having controlled particle size and morphology. For example, the cooling of emulsions of molten $MgCl_2 \cdot nC_2H_5OH$ in paraffin oil gives almost perfectly spherical supports, which are then converted into the catalysts (18). A typical catalyst preparation involves reaction of the $MgCl_2 \cdot nC_2H_5OH$ support with excess $TiCl_4$ in the presence of an "internal" electron donor. Temperatures of at least 80°C and at least two $TiCl_4$ treatment steps are normally used, in order to obtain high performance catalysts in which the titanium is mainly present as $TiCl_4$ rather than the $TiCl_3OC_2H_5$ generated in the initial reaction with the support. Catalysts obtained via chemical routes generally have a BET surface area of around 300 m^2/g and pore volumes in the range 0.3–0.4 cm^3/g (18).

High activity Ziegler–Natta catalysts comprising $MgCl_2$, $TiCl_4$, and an internal donor are typically used in combination with an aluminum alkyl cocatalyst such as $Al(C_2H_5)_3$ and an "external" electron donor added in polymerization. The first catalyst systems containing ethyl benzoate as internal donor were used in combination with a second aromatic ester such as methyl *p*-toluate as external donor (39). These were followed by catalysts containing a diester (eg diisobutyl phthalate) as internal donor, used in combination with an alkoxysilane external donor of type $RR'Si(OCH_3)_2$ or $RSi(OCH_3)_3$ (42). The combination $MgCl_2/TiCl_4$/phthalate ester–AlR_3–alkoxysilane is currently the most widely used catalyst system in PP manufacture. The most effective alkoxysilane donors for high isospecificity are methoxysilanes containing relatively bulky alkyl groups branched at the position alpha to the silicon atom (43–46). Typical examples include cyclohexyl(methyl)dimethoxysilane and dicyclopentyldimethoxysilane (47). Of these, the latter gives particularly high stereospecificity (48) and broader MWD (49). High PP stereoregularity and broad MWD have also been obtained by the use of dimethoxysilanes containing polycyclic amino groups (50,51).

The function of the internal donor in $MgCl_2$-supported catalysts is twofold. One function is to stabilize small primary crystallites of magnesium chloride; the other is to control the amount and distribution of $TiCl_4$ in the final catalyst. Activated magnesium chloride has a disordered structure comprising very small lamellae. Giannini (32) has indicated that, on preferential lateral cleavage surfaces, the magnesium atoms are coordinated with four or five chlorine atoms, as opposed to six chlorine atoms in the bulk of the crystal. These lateral cuts correspond to (110) and (100) faces of $MgCl_2$, as shown in Figure 5.

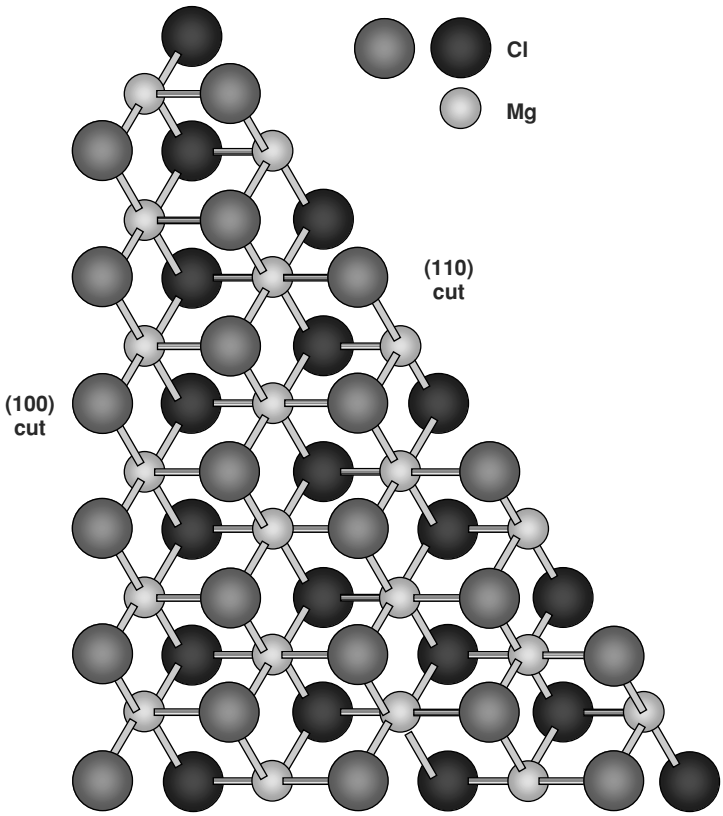

Fig. 5. Model of a $MgCl_2$ layer showing the (100) and (110) lateral cuts. Based on Ref. 31.

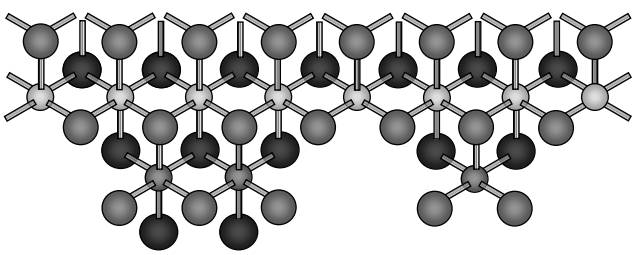

Fig. 6. Model showing dimeric and monomeric Ti species on a (100) lateral cut of $MgCl_2$. Based on Ref. 31.

It has been proposed that bridged, dinuclear Ti_2Cl_8 species can coordinate to the (100) face of $MgCl_2$ and give rise to the formation of chiral, isospecific active species (Fig. 6), it being pointed out that Ti_2Cl_6 species formed by reduction on contact with $Al(C_2H_5)_3$ would resemble analogous species in $TiCl_3$ catalysts (52, 53). Accordingly, it has been suggested (18) that a possible function of the internal donor is preferential coordination on the more acidic (110) face of $MgCl_2$, such

that this face is prevailingly occupied by donor and the (100) face is prevailingly occupied by Ti_2Cl_8 dimers.

Analytical studies (54) have indicated that a monoester internal donor such as ethyl benzoate is coordinated to $MgCl_2$ and not to $TiCl_4$. In the search for donors giving catalysts having improved performance, it was considered (55) that bidentate donors should be able to form strong chelating complexes with tetracoordinate Mg atoms on the (110) face of $MgCl_2$, or binuclear complexes with two pentacoordinate Mg atoms on the (100) face. This led to the development of the $MgCl_2/TiCl_4$/phthalate ester catalysts, used as indicated above in combination with an alkoxysilane as external donor. The requirement for an external donor when using catalysts containing a benzoate or phthalate ester is due to the fact that, when the catalyst is brought into contact with the cocatalyst, a large proportion of the internal donor is lost as a result of alkylation and/or complexation reactions. In the absence of an external donor, this leads to poor stereospecificity because of increased mobility of the titanium species on the catalyst surface. When the external donor is present, contact of the catalyst components leads to replacement of the internal donor by the external donor, as has been shown (56,57) with $MgCl_2/TiCl_4$/ethyl benzoate–$Al(C_2H_5)_3$–methyl *p*-toluate and with $MgCl_2/TiCl_4$/dibutyl phthalate–$Al(C_2H_5)_3$–$C_6H_5Si(OC_2H_5)_3$. The most active and stereospecific systems were those which allowed the highest incorporation of external donor (58), the effectiveness of a catalyst system depending more on the combination of donors rather than on the individual internal or external donor. For example, the use of a monoester rather than an alkoxysilane as external donor with a phthalate-containing system is ineffective (59), as in this case very little of the external donor is adsorbed (58). Further studies (60,61) showed that a phthalate-containing catalyst adsorbed alkoxysilanes to a greater extent than a catalyst without internal donor.

Recently, research on $MgCl_2$-supported catalysts has led to systems not requiring the use of an external donor. This required the identification of bidentate internal donors that not only had the right oxygen–oxygen distance for effective coordination with $MgCl_2$ but that, unlike phthalate esters, were not removed from the support on contact with $Al(C_2H_5)_3$ and that were unreactive with $TiCl_4$ during catalyst preparation. It was found (55,62–64) that certain 2,2-disubstituted 1,3-dimethoxypropanes met all these criteria. The best performance was obtained when bulky substituents in the 2-position resulted in the diether having a most probable conformation (65) with an oxygen–oxygen distance in the range 2.8–3.2 Å. The successive "generations" of high activity $MgCl_2$-supported catalyst systems for PP are summarized below:

(1) $MgCl_2/TiCl_4$/ethyl benzoate–AlR_3–aromatic ester
(2) $MgCl_2/TiCl_4$/phthalate ester–AlR_3–alkoxysilane
(3) $MgCl_2/TiCl_4$/diether–AlR_3

Catalyst performance has improved considerably with each generation. The PP yield obtained under typical polymerization conditions (liquid monomer, in the presence of hydrogen, 70°C, 1–2 h) has increased from 15–30 kg/g cat. for the third-generation ethyl benzoate containing catalysts to 30–80 kg/g cat. for

the fourth-generation phthalate-based catalysts. With the recently developed fifth-generation catalysts containing a diether as internal donor, yields of 80–160 kg/g cat. can be achieved. These different catalysts also display different kinetic profiles in propylene polymerization. The catalysts containing a diether as internal donor exhibit very stable activities during polymerization. A low rate of catalyst decay during polymerization is also obtained with the catalyst system $MgCl_2/TiCl_4$/phthalate ester–AlR_3–alkoxysilane, whereas the system $MgCl_2/TiCl_4$/ethyl benzoate–AlR_3–aromatic ester has a very high initial polymerization activity but also a high decay rate, limiting the final polymer yield. The rapid decay in activity can at least partially be ascribed to the use of an ester as external as well as internal donor, the ester being able to react with titanium–hydrogen bonds formed in chain transfer with hydrogen, generating Ti—O bonds inactive for chain propagation (66).

Most recently, a further family of $MgCl_2$-supported catalysts has been developed (67,68), in which the internal donor is a succinate rather than a phthalate ester. As is the case with the phthalate-based catalysts, an alkoxysilane is used as external donor. The essential difference between these catalysts is that the succinate-based systems produce PP having much broader MWD (discussed under Catalyst/Polymer Relationship).

Mechanistic Aspects. It is well established that effective external donors not only increase the isotactic index of the polymer (the proportion of polymer insoluble in boiling heptane or in xylene at 25°C), but can also increase in absolute terms the amount of isotactic polymer formed. This has been demonstrated by Kashiwa (69) for the catalyst system $MgCl_2/TiCl_4$–$Al(C_2H_5)_3$. An increase in the molecular weight and stereoregularity of the isotactic fraction was also noted. Similar trends are apparent with catalyst systems of type $MgCl_2/TiCl_4$/phthalate ester–AlR_3–alkoxysilane (70). Kakugo (71) has used elution fractionation to demonstrate that the external donor not only decreases "atactics" formation but also increases the degree of steric control at isospecific sites. Soga has reported that an almost aspecific $MgCl_2/TiCl_3$ catalyst, with a very low content of (probably isolated, monomeric) Ti species, could be rendered isospecific by the addition of ethyl benzoate as external donor (72) or by using $Cp_2Ti(CH_3)_2$ as cocatalyst (73). It was suggested (74) that in both cases aspecific sites having two coordination vacancies could be converted to isospecific sites by blocking one of the two vacancies.

A powerful technique to study the effects of electron donors on site selectivity in Ziegler–Natta catalysts is the determination of the stereoregularity of the first insertion step in propylene polymerization. Sacchi and co-workers (60,75) have investigated the effect of Lewis bases on the first-step stereoregularity resulting from propylene insertion into a Ti—C_2H_5 bond formed via chain transfer with ^{13}C-enriched $Al(C_2H_5)_3$. First-step stereoregularity is particularly sensitive to the steric environment of the active center, because the stereospecificity of the first monomer insertion is always lower than that of the following propagation steps. For example, with a $MgCl_2/TiCl_4$/diisobutyl phthalate catalyst it was found (60) that the mole fraction of erythro (isotactic) placement in the isotactic polymer fraction was 0.67 with no external donor, 0.82 with $CH_3Si(OC_2H_5)_3$, and 0.92 with $C_6H_5(OC_2H_5)_3$. It could be concluded that the alkoxysilane external donor was present in the environment of at least part of the isospecific centers (Fig. 7).

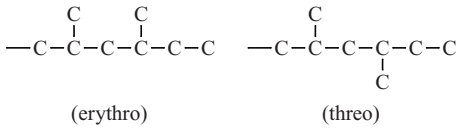

Fig. 7. Erythro (isotactic) and threo (syndiotactic) placement resulting from insertion into a Ti–ethyl unit.

Subsequent studies (76,77) indicated that similar considerations apply to diether donors.

Recently, significant advances have been made in understanding the fundamental factors determining the performance of state-of-the-art $MgCl_2$-supported catalysts. Studies by Busico and co-workers (78) have shown that the chain irregularities in isotactic PP prepared using heterogeneous catalysts are not randomly distributed along the chain but are clustered. The chain can therefore contain, in addition to highly isotactic blocks, sequences that can be attributed to weakly isotactic (isotactoid) and to syndiotactic (syndiotactoid) blocks. This implies that the active site can isomerize very rapidly (during the growth time of a single polymer chain, ie in less than a second) between three different propagating species. The same sequences are present, but in different amounts, in both the soluble and the insoluble fractions. The polymer can therefore be considered to have a stereoblock structure in which highly isotactic sequences alternate with defective isotactoid and with syndiotactoid sequences. A mechanistic model has been formulated in which the relative contributions of these sequences can be related to site transformations involving the presence or absence of steric hindrance in the vicinity of the active species. ^{13}C NMR studies have indicated (79) the presence of C_1-symmetric active species in $MgCl_2$-supported catalysts, with a mechanism of isotactic propagation which is analogous to that for certain C_1-symmetric metallocenes, in the sense that propylene insertion at a highly enantioselective site tends to be followed by chain "back-skip" rather than a less regio- and stereoselective insertion when the chain is in the coordination position previously occupied by the monomer. The probability of chain "back-skip" will increase with decreasing monomer concentration, and it has indeed been confirmed that increased polymer isotacticity is obtained at low monomer concentration. It is proposed (78) that a (temporary) loss of steric hindrance from one side of an active species with local C_2-symmetry, giving a C_1-symmetric species, may result in a transition from highly isospecific to moderately isospecific propagation. Loss of steric hindrance on both sides can lead to syndiospecific propagation in which chain-end control becomes operative. The model is illustrated in Figure 8.

If it is considered that the steric hindrance in the vicinity of the active species can result from the presence of a donor molecule, and that the coordination of such a donor is reversible, the above model provides us with an explanation for the fact that strongly coordinating, stereorigid donors typically give stereoregular polymers in which the highly isotactic sequences predominate. Several types of active species in which the presence of a donor in the vicinity of the active Ti atom is necessary for high isospecificity have been proposed (80), although the exact structure of the active species is still by no means resolved. Isospecific

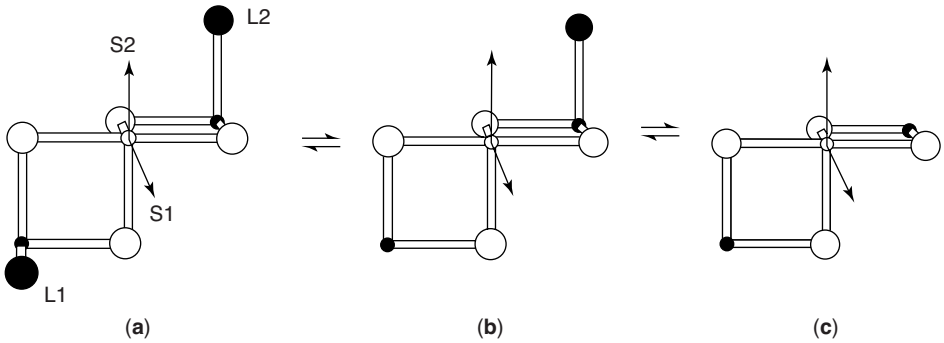

Fig. 8. Model of possible active species for (**a**) highly isotactic, (**b**) isotactoid, and (**c**) syndiotactic propagation (78).

active species not requiring the presence of a donor for high stereospecificity have also been proposed (81).

In PP production, hydrogen is used as a chain-transfer agent for polymer molecular weight (melt-flow rate) control. The effect of hydrogen (concentration) on polymer molecular weight is dependent on the catalyst system. An advantage of catalysts containing a diether donor, in addition to very high activity, is high sensitivity to hydrogen, so that relatively little hydrogen is required for molecular weight control. This effect can be ascribed to chain transfer after the occasional secondary (2,1-) rather than the usual primary (1,2-) insertion, a 2,1-insertion slowing down a subsequent monomer insertion and therefore increasing the probability of chain transfer (82). Reactivation of "dormant" (2,1-inserted) species via chain transfer with hydrogen also explains the frequently observed activating effect of hydrogen in propylene polymerization, giving yields which may be around three times those observed in the complete absence of hydrogen. These conclusions have been based on the ^{13}C NMR determination of the relative proportions of i-C_4H_9 and n-C_4H_9 terminated chains, resulting from chain transfer with hydrogen after primary and secondary insertion respectively:

$$\mathrm{Ti{-}CH_2{-}CH(CH_3){-}[CH_2{-}CH(CH_3)]}_n\mathrm{Pr} + \mathrm{H_2} \rightarrow \mathrm{Ti{-}H} + i\mathrm{{-}C_4H_9{-}CH(CH_3)[CH_2(CH_3)]}_{n-1}\mathrm{Pr}$$

$$\mathrm{Ti{-}CH(CH_3){-}CH_2{-}[CH_2{-}CH(CH_3)]}_n\mathrm{Pr} + \mathrm{H_2} \rightarrow \mathrm{Ti{-}H} + n\mathrm{{-}C_4H_9{-}CH(CH_3)[CH_2(CH_3)]}_{n-1}\mathrm{Pr}$$

Other studies have demonstrated that chain transfer is dependent not only on regio- but also on stereoselectivity (48). This is in keeping with the tendency that, with catalyst systems of type $MgCl_2/TiCl_4$/phthalate ester–AlR_3–alkoxysilane, the silanes that give the most stereoregular isotactic polymer also give relatively low hydrogen response.

Catalyst/Polymer Relationship. By varying the catalyst composition, and in particular the nature of the electron donors (esters, silanes, diethers) present in the catalyst system, it is possible to control the PP tacticity, molecular weight, and MWD to produce a range of polymers having the processing and end-use properties required for very different applications. Ziegler–Natta catalysts typically give broader MWDs than are obtained with homogeneous

(metallocene) catalysts. This is because Ziegler–Natta catalysts contain a range of different active centers, each center giving different relative rates of chain propagation and chain transfer. Each individual site produces a Schulz–Flory distribution with $M_w/M_n = 2$ and $M_z/M_w = 1.5$, and the overall polymer MWD represents a combination of these individual distributions. The dominant effect of active center distribution has been demonstrated by the use of stopped-flow polymerization (83), where the polymer MWD was shown to be unaffected by the polymerization time. Stopped-flow polymerization has also been used to determine active site concentration ($C*$) and propagation rate constants, k_p. For $MgCl_2$-supported catalysts, $C*$ values of around 4% (of total Ti present) have been obtained from stopped-flow experiments (84). $C*$ values obtained by other techniques, notably ^{14}CO quenching of propylene polymerization, have ranged from 1% or less (85) to more than 20% (86). Clearly, there are large differences in $C*$ values obtained by different groups, but it is consistently found that the major proportion of the Ti present in Ziegler–Natta catalysts is inactive. The k_p values for isospecific active sites are around an order of magnitude greater than those for weakly specific sites (85,86). The value of k_p increases significantly in the presence of hydrogen (87), in accordance with the reactivation of "dormant" (2,1-inserted) centers by chain transfer.

Recent work by Terano and co-workers (88) has shown that, under stopped-flow conditions, hydrogen is only effective as chain-transfer agent when catalyst and cocatalyst have been precontacted. These and subsequent (89,90) results indicated that effective chain transfer with hydrogen requires the presence of species able to promote the dissociation of H_2 to atomic hydrogen.

The donors present in the catalyst system play an active role in the formation or modification of isospecific sites, and the polymer MWD depends on the relative contribution and hydrogen response (ie sensitivity to chain transfer with hydrogen) of each type of active site. The incorporation of an external donor into the catalyst system generally leads to an increase in molecular weight, the magnitude of the MW increase depending on the nature of the donor. The characteristics of different catalyst systems with regard to PP MWD are as follows (68):

Internal donor	External donor	M_w/M_n
Diether	—	5–5.5
Phthalate	Alkoxysilane	6.5–8
Succinate	Alkoxysilane	10–15

It can be seen that the diether-based catalysts give relatively narrow MWD. A narrow MWD, and relatively low molecular weight, is advantageous in fiber spinning applications. In contrast, extrusion of pipes and thick sheets requires high melt strength, and therefore relatively high molecular weight and broad MWD. A broad MWD, along with high isotactic stereoregularity, is also beneficial for high crystallinity and therefore high rigidity. The new succinate-based catalysts enable very broad MWD PP homopolymers to be produced in a single reactor and are also of interest for the production of heterophasic copolymers having an improved balance of stiffness and impact strength, taking into account that the incorporation of a rubbery (ethylene/propylene) copolymer phase into a

PP homopolymer matrix increases impact strength but leads at the same time to decreased stiffness.

The relatively narrow PP molecular weight distributions obtained using diether-based catalysts can be attributed to the fact that in these systems even the most highly stereospecific active sites are not totally regiospecific. A proportion of approximately one secondary insertion for every 2000 primary insertions at highly isospecific sites has been noted for the system $MgCl_2/TiCl_4$/diether–AlR_3 (82). The probability of chain transfer with hydrogen after a secondary insertion is such that this is sufficient to prevent the formation of very high molecular weight chains, taking into account that the highest molecular weight fraction of the polymer is formed on the active species having the highest isospecificity. The broader MWDs obtained with catalysts containing ester internal donors are likely to be due to the presence of (some) isospecific active sites having very high regiospecificity and therefore lower hydrogen sensitivity. Such results illustrate the profound effect of catalyst regio- and stereospecificity distribution on both molecular weight control and polymer MWD and properties.

Reactor Granule Technology. As indicated in the section Polymer Particle Growth, particle morphology and porosity are very important features of a Ziegler–Natta catalyst used in modern bulk (liquid monomer or gas-phase) polymerization processes. Under appropriate polymerization conditions, polymer particles can be obtained that have an internal morphology that can range from a compact to a porous structure (91). In what is termed Reactor Granule Technology (RGT), porous polymer particles can be produced, which can then function as a microreactor for the polymerization of other monomers within the solid matrix. A polypropylene skin encloses the second polymer phase, thereby preventing coalescence of particles in which the second phase is an amorphous, low-melting material (92). RGT has been defined as "controlled, reproducible polymerization of olefinic monomers on an active $MgCl_2$-supported catalyst, to give a growing, spherical granule that provides a porous reaction bed within which other monomers can be introduced and polymerized to form a polyolefin alloy" (93).

Today, RGT is able to provide products ranging from superstiff, high fluidity PP homopolymers to stiff/impact or clear/impact heterophasic copolymers and supersoft alloys, produced using the *Cataloy* process (31,68). The feasibility of producing heterophasic alloys containing up to 70% of multimonomer copolymers arises from the use of a controlled porosity catalyst and the ability to control the porosity of the growing polymer particle during the early stages of polymerization. Prepolymerization is applied to give the particles sufficient heat capacity to withstand injection into a gas-phase polymerization step.

Several models have been put forward to explain the mechanism of particle growth during polymerization. One of the most popular models is the "multigrain model," put forward by Ray and co-workers (94), in which the monomer diffuses into the catalyst macroparticle and polymerizes on the surface of the microparticles within, causing the macroparticle to expand progressively as polymerization proceeds. An investigation by Kakugo and co-workers (95) of nascent polymer morphology obtained using a $TiCl_3$ catalyst showed that the polymer particle comprised numerous globules, each of which contained some tens of much smaller primary particles. Recently, a model for particle growth with $MgCl_2$-supported catalysts has been proposed by Cecchin (68,96), who has also provided evidence for polymer "subglobule" formation within the growing particle. Again,

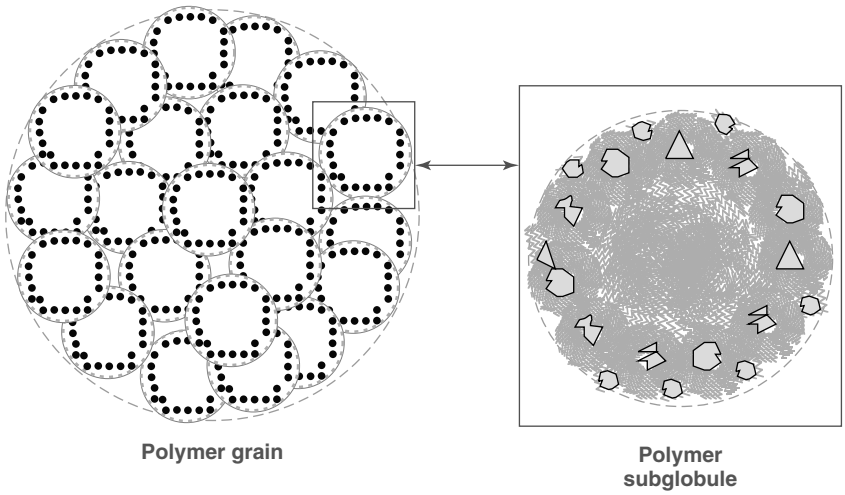

Fig. 9. Particle growth model for propylene polymerization with a $MgCl_2$-supported catalyst (96).

these subglobules originate from clusters of primary crystallites, but the crystallites themselves are pushed to the surface of each subglobule as the polymer forms. This model, illustrated in Figure 9, explains the fact that, in the preparation of heterophasic copolymers via propylene homopolymerization followed by ethylene/propylene copolymerization, the rubbery ethylene/propylene copolymer is formed at the surface of the homopolymer subglobules, gradually filling up the pores within the particle. Clearly, the higher the porosity of the homopolymer matrix, the greater the proportion of (rubbery) copolymer that can be incorporated into the particle without running into problems of stickiness if the rubber phase blooms to the surface. Evidence for drifting of catalyst microparticles to the surface of polymer (sub)globules has been provided by scanning electron microscopy studies of prepolymerized catalyst particles (97).

Polymerization of Other Monomers Using Ziegler–Natta Catalysts

In addition to their widespread use in the production of polyethylene and polypropylene, Ziegler–Natta catalysts play an important role in the production of poly-1-butene and are also widely used in the manufacture of synthetic rubbers such as *cis*-1,4-polybutadiene and *cis*-1,4-polyisoprene, the synthetic equivalent of natural rubber. Ziegler–Natta catalysts for the manufacture of butadiene rubber, based on titanium, cobalt, nickel, or neodymium systems, are described elsewhere (see BUTADIENE POLYMERS). Isoprene rubber is produced using β-$TiCl_3$ (98), typically prepared by reaction of approximately equimolar quantities of $TiCl_4$ and Al-*i*-$(C_4H_9)_3$ in the presence of a small quantity of an ether. Increased catalyst activity can be obtained by incorporation of a sterically hindered phenoxyaluminum cocatalyst component (99). The latter component also gives increased activity in propene polymerization using $TiCl_3$ (100); in both cases the improvement in catalyst performance can be attributed to selective complexation of the catalyst

poison $RAlCl_2$. In addition to aluminum alkyls, poly(*N*-alkylaluminoxanes) have been found to be effective cocatalysts in isoprene polymerization (101). These components have cage structures (eg $[HAlN\text{-}i\text{-}C_3H_7]_6$) in which both Al and N atoms are tetracoordinated (102).

Cis-1,4-polymerization of conjugated dienes requires the presence of two coordination vacancies on the transition-metal atom, allowing bidentate coordination of the diene. β-$TiCl_3$ has a fiber-like structure in which the titanium atoms in the lattice are octahedrally coordinated to six chlorine atoms. The terminal titanium atoms are, however, incompletely coordinated and are linked to four or five chlorine atoms. Alkylation of the tetracoordinated titanium atoms will generate the double-vacancy species active in isoprene polymerization. Stereospecificity in diene polymerization can change dramatically if one of the coordination vacancies is blocked by a Lewis base. An interesting illustration of this (103) is that the addition of an external donor in isoprene polymerization with $TiCl_4$–$Al(C_2H_5)_3$ or $MgCl_2/TiCl_4$–$Al(C_2H_5)_3$ changes the catalyst stereospecificity to give mainly *trans*-1,4- rather than *cis*-1,4-polyisoprene. At the same time, a notable increase in isospecificity in propylene polymerization is observed.

$TiCl_3$-based and $MgCl_2$-supported catalysts have been developed for the production of poly-1-butene. $TiCl_3$ catalysts are used with dialkylaluminum halide cocatalysts, $Al(C_2H_5)_2I$ giving higher isotacticity than $Al(C_2H_5)_2Cl$ (104). Very high isotacticity has been obtained using $TiCl_3$ in combination with $Cp_2Ti(CH_3)_2$ (105). Much higher polymerization activity, as well as high isotacticity and broad MWD, is obtained using $MgCl_2$-supported catalysts, for example the catalyst system $MgCl_2/TiCl_4$/diisobutyl phthalate–$Al(C_2H_5)_3$–alkoxysilane (106).

Ziegler–Natta catalysts have also been developed for the polymerization of 4-methyl-1-pentene (107) and higher alpha-olefins. Polymerization activity decreases with increasing steric bulk of the monomer. For example, with the catalyst system $MgCl_2/TiCl_4$/ethyl benzoate–$Al(C_2H_5)_3$–ethyl benzoate the relative activities in propylene, 1-butene, and 4-methyl-1-pentene polymerization were 100:80:15 (108). For catalyst systems of type $MgCl_2/TiCl_4$/phthalate ester–AlR_3–alkoxysilane, the type of silane required is dependent on the steric bulk of the monomer. An active center having high stereospecificity in propylene polymerization may be too sterically hindered for effective polymerization of a bulkier monomer, propylene/1-butene copolymerization studies having shown (109) that the incorporation of 1-butene into the polymer chain decreases with increasing site stereospecificity. This phenomenon is also illustrated by the fact that nonbulky alkoxysilanes such as $(CH_3)_3SiOCH_3$ are effective donors in 4-methyl-1-pentene polymerization (110), whereas such donors are relatively ineffective in propylene polymerization.

Concluding Remarks

The dominant position of Ziegler–Natta catalysts in the manufacture of polyolefins, in particular PP, is likely to continue for a considerable length of time, despite the many developments taking place in the field of metallocene and other single-site catalysis. Indeed, the range of polymer types and grades is so varied that there is ample scope for further development and implementation of both Ziegler–Natta and single-site catalysts.

It will be clear that the composition and characteristics of a Ziegler–Natta catalyst must be tailored such that the required polymer molecular structure and properties are obtained. Different catalysts are required for different polymer applications, and the recent development and implementation of $MgCl_2$-supported catalysts containing diether and succinate donors, for the production of narrow and broad MWD PP respectively, illustrates the ongoing activity in Ziegler–Natta catalyst research. The ability to control catalyst particle size, morphology, and porosity has allowed the development of advanced and versatile polymerization process technologies, so that the characteristics of the catalyst can be tuned to both process and product requirements.

Ziegler–Natta catalysts are complex systems and are still by no means fully understood, but significant advances in basic understanding have recently been made. This will continue, with both experimental and molecular modeling studies providing additional mechanistic insight, which in turn can be applied in the further development and implementation of these catalysts.

BIBLIOGRAPHY

In *EPST* 3rd ed., Vol. 8, pp. 517–536, by J. C. Chadwick, Eindhoven University of Technology.

CITED PUBLICATIONS

1. G. Wilke, in G. Fink, R. Mülhaupt, and H. H. Brintzinger, eds., *Ziegler Catalysts. Recent Scientific Innovations and Technological Improvements*, Springer-Verlag, Berlin, 1995, p. 1.
2. Ger. Pat. 973626 (Filed Nov. 17, 1953), K. Ziegler, H. Breil, E. Holzkamp, and H. Martin; *Chem. Abstr.* **54**, 14794b (1960).
3. K. Ziegler, E. Holzkamp, H. Breil, and H. Martin, *Angew. Chem.* **67**, 541 (1955).
4. Ital. Pat. 535712 (Filed June 8, 1954), G. Natta (to Montecatini).
5. G. Natta, *J. Polym. Sci.* **16**, 143 (1955).
6. G. Natta, P. Pino, P. Corradini, F. Danusso, E. Mantica, E. Mazzanti, and G. Moraglio, *J. Am. Chem. Soc.* **77**, 1708 (1955).
7. P. Pino and R. Mülhaupt, *Angew. Chem., Int. Ed. Engl.* **19**, 857 (1980).
8. P. Pino and G. Moretti, *Polymer* **28**, 683 (1987).
9. P. Corradini, *Macromol. Symp.* **89**, 1 (1995).
10. G. Natta, P. Corradini, and G. Allegra, *J. Polym. Sci.* **51**, 399 (1961).
11. J. Boor, *Ziegler–Natta Catalysts and Polymerizations*, Academic Press, Inc., New York, 1979.
12. G. Guidetti, R. Zannetti, D. Ajo, A. Marigo, and M. Vidali, *Eur. Polym. J.* **16**, 1007 (1980).
13. U. S. Pat. 2692257 (Filed Apr. 28, 1951), A. Zletz (to Standard Oil of Indiana).
14. Belg. Pat. 530617 (Filed Jan. 27, 1953), J. P. Hogan and R. L. Banks (to Phillips Petroleum Co.).
15. H. R. Sailors and J. P. Hogan, *J. Macromol. Sci., Chem. A* **15**, 1377 (1981).
16. M. P. McDaniel, in D. D. Eley, H. Pines, and P. B. Weisz, eds., *Advances in Catalysis*, Vol. **33**, Academic Press, Inc., New York, 1985, p. 47.
17. H. Martin, in G. Fink, R. Mülhaupt, and H. H. Brintzinger, eds., *Ziegler Catalysts. Recent Scientific Innovations and Technological Improvements*, Springer-Verlag, Berlin, 1995, p. 15.

18. E. P. Moore, *Polypropylene Handbook. Polymerization, Characterization, Properties, Processing, Applications*, Hanser Publishers, Munich, 1996.
19. U.S. Pat. 4376851 (Filed Jan. 11, 1956), J. P. Hogan and R. L. Banks (to Phillips Petroleum Co.).
20. U.S. Pat. 4210738 (Filed Mar. 21, 1972), J. P. Hermans and P. Henrioulle (to Solvay).
21. B. L. Goodall and S. van der Vens, *Polypropylene and Other Polyolefins. Polymerization and Characterization*, Elsevier, Amsterdam, 1990, Chapt. "1".
22. A. Bernard and P. Fiasse, in T. Keii and K. Soga, eds., *Catalytic Olefin Polymerization*, Elsevier, Amsterdam, 1990, p. 405.
23. E. J. Arlman and P. Cossee, *J. Catal.* **3**, 99 (1964).
24. P. Corradini, V. Busico, and G. Guerra, *Comprehensive Polymer Science*, Vol. **4**, Pergamon Press, Oxford, U.K., 1988, p. 29.
25. A. Zambelli, M. C. Sacchi, P. Locatelli, and G. Zannoni, *Macromolecules* **15**, 211 (1982).
26. I. Tritto, M. C. Sacchi, and P. Locatelli, *Makromol. Chem.* **187**, 2145 (1986).
27. G. Natta, I. Pasquon, A. Zambelli, and G. Gatti, *J. Polym. Sci.* **51**, 387 (1961).
28. Y. Doi, S. Suzuki, and K. Soga, *Makromol. Chem., Rapid Commun.* **6**, 639 (1985).
29. A. Zambelli, I. Sessa, F. Grisi, R. Fusco, and P. Accomazzi, *Macromol. Rapid Commun.* **22**, 297 (2001).
30. J. A. Ewen, R. L. Jones, A. Razavi, and J. D. Ferrara, *J. Am. Chem. Soc.* **110**, 6255 (1988).
31. T. Simonazzi and U. Giannini, *Gazz. Chim. Ital.* **124**, 533 (1994).
32. U. Giannini, *Makromol. Chem., Suppl.* **5**, 216 (1981).
33. K.-Y. Choi and W. H. Ray, *J. Macromol. Sci., Rev. Macromol. Chem. Phys. C* **25**, 1 (1985).
34. Eur. Pat. 4647 (Filed Mar. 30, 1979), G. L. Goerke, B. E. Wagner, and F. J. Karol (to Union Carbide Corp.).
35. L. L. Böhm, D. Bilda, W. Breuers, H. F. Enderle, and R. Lecht, in G. Fink, R. Mülhaupt, and H. H. Brintzinger, eds., *Ziegler Catalysts. Recent Scientific Innovations and Technological Improvements*, Springer-Verlag, Berlin, 1995, p. 387.
36. F. J. Karol, K. J. Cann, and B. E. Wagner, in W. Kaminsky and H. Sinn, eds., *Transition Metals and Organometallics as Catalysts for Olefin Polymerization*, Springer-Verlag, Berlin, 1988, p. 149.
37. H. L. Hsieh, M. P. McDaniel, J. L. Martin, P. D. Smith, and D. R. Fahey, in R. B. Seymour and T. Cheng, eds., *Advances in Polyolefins*, Plenum Press, New York, 1985, p. 153.
38. P. Galli, L. Luciani, and G. Cecchin, *Angew. Makromol. Chem.* **94**, 63 (1981).
39. P. C. Barbè, G. Cecchin, and L. Noristi, *Adv. Polym. Sci.* **81**, 1 (1987).
40. P. Galli, P. C. Barbè, and L. Noristi, *Angew. Makromol. Chem.* **120**, 73 (1984).
41. P. Galli, *Macromol. Symp.* **78**, 269 (1994); *Macromol. Symp.* **112**, 1 (1996).
42. Eur. Pat 45977 (Filed Aug. 13, 1981), S. Parodi, R. Nocci, U. Giannini, P. C. Barbè, and U. Scatà (to Montedison).
43. J. V. Seppälä, M. Härkönen and L. Luciani, *Makromol. Chem.* **190**, 2535 (1989).
44. M. Härkönen, J. V. Seppälä, and T. Väänänen, in T. Keii and K. Soga, eds., *Catalytic Olefin Polymerization*, Elsevier, Amsterdam, 1990, p. 87.
45. A. Proto, L. Oliva, C. Pellecchia, A. J. Sivak, and L. A. Cullo, *Macromolecules* **23**, 2904 (1990).
46. T. Okano, K. Chida, H. Furuhashi, A. Nakano, and S. Ukei, in T. Keii and K. Soga, eds., *Catalytic Olefin Polymerization*, Elsevier, Amsterdam, 1990, p. 177.
47. Eur. Pat. 350170 (Filed June 13, 1989), N. Ishimaru, M. Kioka, and A. Toyota (to Mitsui).
48. J. C. Chadwick, G. M. M. van Kessel, and O. Sudmeijer, *Macromol. Chem. Phys.* **196**, 1431 (1995).

49. J. C. Chadwick, *Macromol. Symp.* **173**, 21 (2001).
50. Eur. Pat. 841348 (Filed Nov. 3, 1997), S. Ikai, H. Ikeuchi, H. Satoh, T. Inoue, and H. Sano (to Grand Polymer).
51. S. Yao and Y. Tanaka, *Macromol. Theory Simul.* **10**, 850 (2001).
52. P. Corradini, V. Busico, and G. Guerra, in W. Kaminsky and H. Sinn, eds., *Transition Metals and Organometallics as Catalysts for Olefin Polymerization*, Springer-Verlag, Berlin, 1988, p. 337.
53. V. Busico, P. Corradini, L. De Martino, A. Proto, V. Savino, and E. Albizzati, *Makromol. Chem.* **186**, 1279 (1985).
54. M. Terano, T. Kataoka, and T. Keii, *Makromol. Chem.* **188**, 1477 (1987).
55. E. Albizzati, U. Giannini, G. Morini, C. A. Smith, and R. C. Zeigler, in G. Fink, R. Mülhaupt, and H. H. Brintzinger, eds., *Ziegler Catalysts. Recent Scientific Innovations and Technological Improvements*, Springer-Verlag, Berlin, 1995, p. 413.
56. V. Busico, P. Corradini, L. De Martino, A. Proto, and E. Albizzati, *Makromol. Chem.* **187**, 1115 (1986).
57. L. Noristi, P. C. Barbè, and G. Baruzzi, *Makromol. Chem.* **192**, 1115 (1991).
58. M. C. Sacchi, I. Tritto, C. Shan, R. Mendichi, G. Zannoni, and L. Noristi, *Macromolecules* **24**, 6823 (1991).
59. R. Spitz, C. Bobichon, and A. Guyot, *Makromol. Chem.* **190**, 707 (1989).
60. M. C. Sacchi, F. Forlini, I. Tritto, R. Mendichi, G. Zannoni, and L. Noristi, *Macromolecules* **25**, 5914 (1992).
61. M. Kioka and N. Kashiwa, *J. Mol. Catal.* **82**, 11 (1993).
62. Eur. Pat. 361494 (Filed Sept. 29, 1989), E. Albizzati, P. C. Barbè, L. Noristi, R. Scordamaglia, L. Barino, U. Giannini, and G. Morini (to Himont).
63. Eur. Pat. 728724 (Filed Feb. 21, 1996), G. Morini and A. Cristofori (to Montell).
64. E. Albizzati, U. Giannini, G. Morini, M. Galimberti, L. Barino, and R. Scordamaglia, *Macromol. Symp.* **89**, 73 (1995).
65. L. Barino and R. Scordamaglia, *Macromol. Symp.* **89**, 101 (1995).
66. E. Albizzati, M. Galimberti, U. Giannini, and G. Morini, *Makromol. Chem., Macromol. Suppl.* **48/49**, 223 (1991).
67. Int. Pat. WO 00/63261 (Filed Apr. 12, 2000), G. Morini, G. Balbontin, Y. Gulevich, H. Duijghuisen, R. Kelder, P. A. Klusener, and F. Korndorffer (to Basell).
68. G. Cecchin, G. Morini, and A. Pelliconi, *Macromol. Symp.* **173**, 195 (2001).
69. N. Kashiwa, J. Yoshitake, and A. Toyota, *Polym. Bull. (Berlin)* **19**, 333 (1988).
70. J. C. Chadwick, in G. Fink, R. Mülhaupt, and H. H. Brintzinger, eds., *Ziegler Catalysts. Recent Scientific Innovations and Technological Improvements*, Springer-Verlag, Berlin, 1995, p. 427.
71. M. Kakugo, T. Miyatake, Y. Naito, and K. Mizunuma, *Macromolecules* **21**, 314 (1988).
72. K. Soga, J. R. Park, T. Shoino, and N. Kashiwa, *Macromol. Chem., Rapid Commun.* **11**, 117 (1990).
73. K. Soga, J. R. Park, H. Uchino, T. Uozumi, and T. Shiono, *Macromolecules* **22**, 3824 (1989).
74. K. Soga, *Makromol. Chem., Macromol. Symp.* **66**, 43 (1993).
75. M. C. Sacchi, C. Shan, P. Locatelli, and I. Tritto, *Macromolecules* **23**, 383 (1990).
76. M. C. Sacchi, F. Forlini, I. Tritto, P. Locatelli, G. Morini, G. Baruzzi, and E. Albizzati, *Macromol. Symp.* **89**, 91 (1995).
77. G. Morini, E. Albizzati, G. Balbontin, I. Mingozzi, M. C. Sacchi, F. Forlini, and I. Tritto, *Macromolecules* **29**, 5770 (1996).
78. V. Busico, R. Cipullo, G. Monaco, G. Talarico, M. Vacatello, J. C. Chadwick, A. L. Segre, and O. Sudmeijer, *Macromolecules* **32**, 4173 (1999).
79. V. Busico, R. Cipullo, G. Talarico, A. L. Segre, and J. C. Chadwick, *Macromolecules* **30**, 4786 (1997).

80. L. Barino and R. Scordamaglia, *Makromol. Theory Simul.* **7**, 407 (1998).
81. M. Boero, M. Parrinello, S. Hüffer, and H. Weiss, *J. Am. Chem. Soc.* **122**, 501 (2000).
82. J. C. Chadwick, G. Morini, E. Albizzati, G. Balbontin, I. Mingozzi, A. Cristofori, O. Sudmeijer, and G. M. M. van Kessel, *Macromol. Chem. Phys.* **197**, 2501 (1996).
83. T. Keii, M. Terano, K. Kimura, and K. Ishii, *Makromol. Chem., Rapid Commun.* **8**, 583 (1987).
84. B. Liu, H. Matsuoka, and M. Terano, *Macromol. Rapid Commun.* **22**, 1 (2001).
85. G. D. Bukatov and V. A. Zakharov, *Macromol. Chem. Phys.* **202**, 2003 (2001).
86. P. J. Tait, G. H. Zohuri, A. M. Kells, and I. D. McKenzie, in G. Fink, R. Mülhaupt, and H. H. Brintzinger, eds., *Ziegler Catalysts. Recent Scientific Innovations and Technological Improvements*, Springer-Verlag, Berlin, 1995, p. 343.
87. G. D. Bukatov, V. S. Goncharov, and V. A. Zakharov, *Macromol. Chem. Phys.* **196**, 1751 (1995).
88. H. Mori, K. Tashino, and M. Terano, *Macromol. Rapid Commun.* **16**, 651 (1995).
89. H. Mori, K. Tashino, and M. Terano, *Macromol. Chem. Phys.* **197**, 895 (1996).
90. H. Mori, T. Iizuka, K. Tashino, and M. Terano, *Macromol. Chem. Phys.* **198**, 2499 (1997).
91. P. Galli, *Prog. Polym. Sci.* **19**, 959 (1994).
92. J. C. Chadwick, *Encyclopedia of Materials: Science and Technology*, Elsevier, 2001, p. 7703.
93. P. Galli and J. C. Haylock, *Makromol. Chem., Macromol. Symp.* **63**, 19 (1992).
94. R. A. Hutchinson, C. M. Chen, and W. H. Ray, *J. Appl. Polym. Sci.* **44**, 1389 (1992).
95. M. Kakugo, H. Sadatoshi, M. Yokoyama, and K. Kojima, *Macromolecules* **22**, 547 (1989).
96. G. Cecchin, E. Marchetti, and G. Baruzzi, *Macromol. Chem. Phys.* **202**, 1987 (2001).
97. J. T. M. Pater, G. Weickert, J. Loos, and W. P. M. van Swaaij, *Chem. Eng. Sci.* **56**, 1 (2001).
98. E. Schoenberg, H. A. Marsh, S. J. Walters, and W. M. Saltman, *Rubber Chem. Technol.* **52**, 526 (1979).
99. Eur. Pat. 107871 (Filed Sept. 30, 1983), J. C. Chadwick and B. L. Goodall (to Shell).
100. B. L. Goodall, in W. Kaminsky and H. Sinn, eds., *Transition Metals and Organometallics as Catalysts for Olefin Polymerization*, Springer-Verlag, Berlin, 1988, p. 361.
101. A. Mazzei, S. Cucinella, and W. Marconi, *Makromol. Chem.* **122**, 168 (1969).
102. A. Balducci, M. Bruzzone, S. Cucinella, and A. Mazzei, *Rubber Chem. Technol.* **48**, 736 (1975).
103. K. Soga, T. Sano, K. Yamamoto, and T. Shiono, *Chem. Lett. (Japan)* 425 (1982).
104. S. van der Ven, *Polypropylene and other Polyolefins. Polymerization and Characterization*, Elsevier, Amsterdam, 1990, Chapt. 11.
105. K. Soga and H. Yanagihara, *Makromol. Chem.* **189**, 2839 (1988).
106. U. S. Pat. 6306996 (Filed Mar. 4, 1999), G. Cecchin, G. Collina, and M. Covezzi (to Basell).
107. L. C. Lopez, G. L. Wilkes, P. M. Stricklen, and S. A. White, *J. Macromol. Sci., Rev. Macromol. Chem. Phys. C* **32**, 301 (1992).
108. N. Kashiwa and J. Yoshitake, *Polym. Bull. (Berlin)* **11**, 485 (1984).
109. M. C. Sacchi, Z.-Q. Fan, F. Forlini, I. Tritto, and P. Locatelli, *Macromol. Chem. Phys.* **195**, 2805 (1994).
110. U. S. Pat. 4659792 (Filed Dec. 23, 1985), N. Kashiwa and K. Fukui (to Mitsui).

JOHN C. CHADWICK
Dutch Polymer Institute,
Eindhoven University of Technology

ZWITTERIONIC POLYMERIZATION

Introduction

Zwitterionic polymerization is defined (1–4) as an ionic polymerization (or copolymerization) in which both cationic and anionic sites are located at each of the two chain ends of one propagating species (**1**).

Zwitterionic propagating species

1

It is assumed that the zwitterionic propagating species in the reaction mixture takes an intramolecular cyc1ic form (**2**) or a form of intermolecular association (**3**).

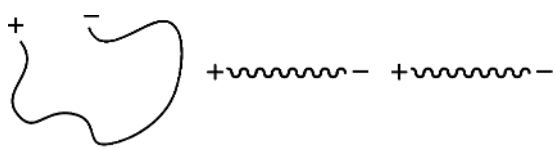

2 **3**

There are two possibilities for the propagating reactivities of the cationic and anionic sites. In the first case, propagation takes place at only one site, either cationic or anionic. In the second case, propagation is achieved by the cation–anion reaction between two zwitterions. It is often that these two patters take place simultaneously. There is an additional pattern that zwitterion is formed to activate a monomer successively. The types of monomers involved in zwitterionic polymerization include polar olefinic, heterocyclic, and divalent carbon group element compounds.

The category of spontaneous polymerization covers the wider range of combinations of donor and acceptor monomers, since it involves not only the zwitterion but also the biradical mechanisms (5). It is sometimes difficult to distinguish between these two mechanisms.

Propagation via One Site

An initiating zwitterion, (**4**) or (**5**), is generated by the reaction between the initiator and monomer (eqs. 1 and 2). In the zwitterion (**4**) (eq. 1), only the anionic

site is directly involved in causing anionic propagation (eq. 3). The zwitterion (**5**) (eq. 2), on the other hand, causes cationic propagation (eq. 4).

Generation of zwitterion (initiation)

$$X + M \longrightarrow \underset{\mathbf{4}}{{}^{+}XM^{-}} \tag{1}$$

$$Y + M \longrightarrow \underset{\mathbf{5}}{{}^{-}YM^{+}} \tag{2}$$

Propagation

$${}^{+}XM_nM^{-} + M \longrightarrow {}^{+}XM_{n+1}M^{-} \tag{3}$$

$${}^{-}YM_nM^{+} + M \longrightarrow {}^{-}YM_{n+1}M^{+} \tag{4}$$

Propagation via the Anionic Site. Vinyl monomers having electron-withdrawing substituents, such as acrylonitrile (6–10), methacylonitrile (11),(12), nitroethylene (13),(14), 2,4,6-trinitrostyrene (15), methylenemalonate (16),(17), and α-cyanoacrylate (18–21), have been polymerized by phosphine, phosphite, and tertiaryamine initiators; for example

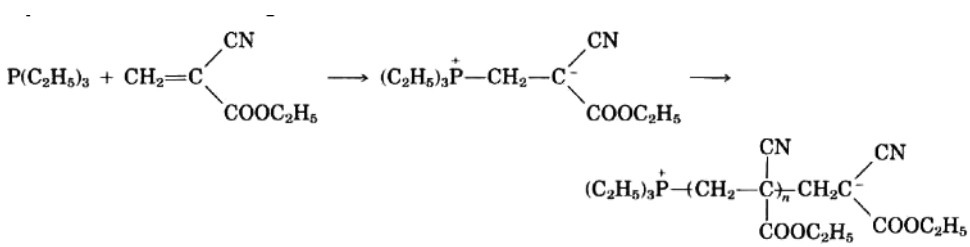

In some of these polymerization systems, mechanisms of propagation via the anionic site of zwitterions have been established. The cationic sites of these zwitterions are phosphonium or quaternary ammonium structures that do not add to the monomer. Poly(ethylene oxide) end-functionalized with a triphenylphosphine group acts as the macroinitiator for the polymerization of α-cyanoacrylate to yield the block copolymer (M_n = 10,000–20,000) (22).

The polymerization of the less electron-deficient olefin, that is, methyl methacrylate (MMA), requires sterically hindered aluminum Lewis acid as the monomer activator in the combination with enamine (M_n < 16,000, M_w/M_n = 1.2–1.9) or phosphine (M_n < 40,000, M_w/M_n = 1.4–2.3) as the initiator (23,24a). *N*-Heterocyclic carbene (NHC) initiates the anionic addition polymerization of not only exomethylene lactone (M_n < 90,000, M_w/M_n = 1.5–2.1), which is more reactive, but also MMA in dimethylformamide as the crucial solvent (M_n = 33,000, M_w/M_n = 2.0) (24b). Equation 5 shows the polymerization mechanism involving

the zwitterion.

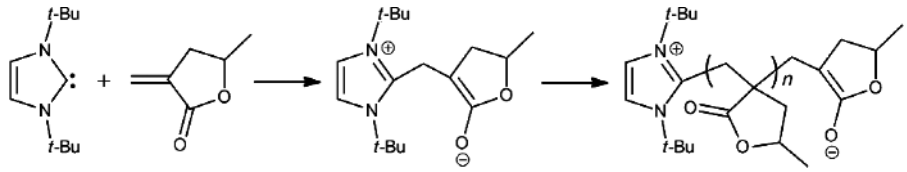

(5)

Ring-opening polymerizations also take place via zwitterion mechanisms. For the lactone monomer, tertiary amines are used as an initiator (25–27). An ammonium carboxylate zwitterion (**6**) is the growing species (eq. 6).

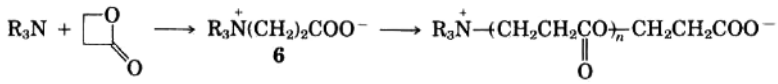

(6)

When the initiator is a cyclic tertiary amine such as quinuclidine (**7**), *N*-alkylaziridine, and *N*-methylazetidine, the ammonium site is no longer inactive; that is, it participates in the ring-opening polymerization with the lactone monomer to produce a copolymer. For example, a zwitterion (**9**) from (**7**) and pivalolactone (**8**) is responsible for the copolymerization (eq. 7) (28).

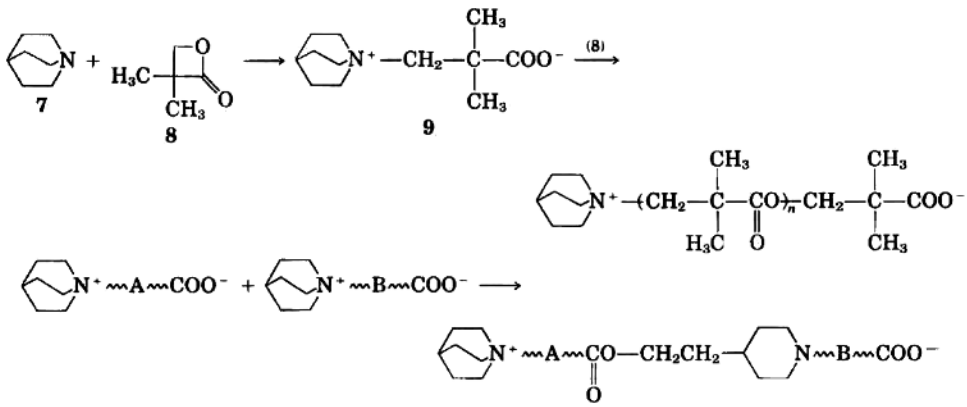

(7)

The reaction of equation 7 corresponds to the key step of "No Catalyst Copolymerization via Zwitterion Intermediates" to be described later. As mentioned below in the section of Polymerization of Isolated Zwitterions, analogous zwitterions having the quinuclidinium cation are isolated and polymerized.

Amino acid *N*-carboxyanhydride (NCA) shows various kinds of polymerization mechanisms depending on the initiator. Sarcosine NCA with pyridine forms the zwitterion, and there are two ways for the polymer formation (eq. 8) (29). One is the chain growth where the anionic site attacks the NCA for the propagation along with CO_2 liberation, and the other is the step growth where the reaction between the zwitterions takes place liberating pyridine and CO_2. Under the appropriate conditions, cyclic polysarcosine is almost exclusively produced by the backbiting attack of the anionic site to the carbonyl group adjacent to the

pyridinium cation in the macro zwitterion.

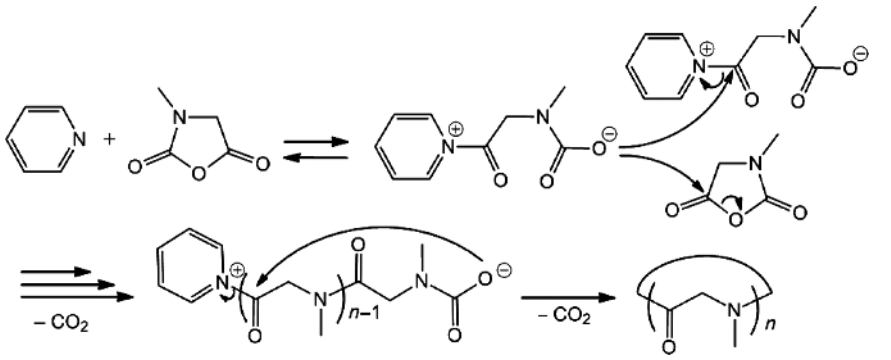

(8)

Analogous reactions are also proposed for the spontaneous polymerization of sarcosine NCA without any additive in DMF, which promotes the zwitterionic dissociation of NCA (29). Also in the thermal polymerizations of NCA as well as dithiolane-2,4-dione, there are proposed the zwitterion intermediates generated by the reactions between two monomer molecules (29).

N-Heterocyclic carbenes (NHCs) initiate the ring-opening polymerizations of ethylene oxide (30), propylene oxide (31), lactide (32), ε-caprolactone (33), and *N*-alkylglycine *N*-carboxyanhydride (*N*-RNCA) (34). The polymerizations of ethylene and propylene oxides show the living nature, producing α,ω-heterodifunctionalized polymers ($M_n < 13{,}000$, $M_w/M_n = 1.02$–1.18) by the *in situ* treatment with Nu-E (eq. 9) as well as forming the block copolymer with ε-caprolactone by the sequential addition.

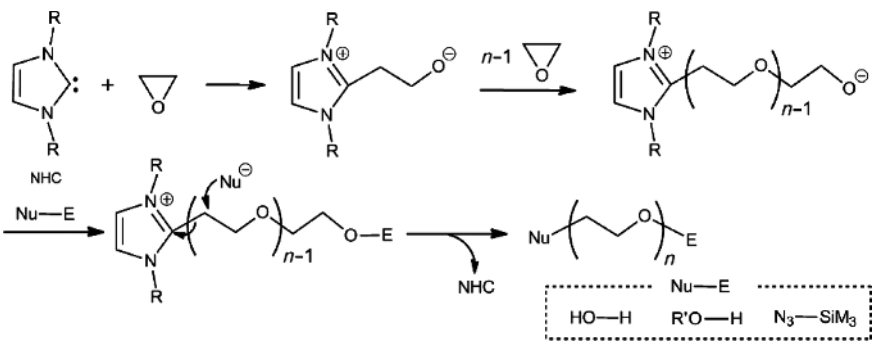

(9)

The cyclic polymers are exclusively obtained by the NHC-initiated polymerizations of lactide, ε-caprolactone, and *N*-RNCA. In a similar manner with a scheme presented in equation 8, the propagation end of the alkoxy anion backbites the carbonyl group of the initiating end, giving high molecular weight cyclic polylactide ($M_n = 4200$–$15{,}000$, $M_w/M_n = 1.15$–1.35) or poly(ε-caprolactone) ($M_n = 41{,}000$–$114{,}000$, $M_w/M_n = 1.4$–2.2) and simultaneously releasing NHC. On the other hand, the backbiting reaction in the polymerization of the cyclic *N*-RNCA does not liberate NHC but produces cyclic poly(α-peptoide) incorporating the NHC residue ($M_n = 3000$–$27{,}000$, $M_w/M_n = 1.04$–1.12) (eq. 10). The

treatment of this cyclic polymer with acetyl chloride gives the linear polymer, whereas NHC residue is excluded from the cyclic polymer by the reaction with sodium hexamethyldisilazide (34e). In addition, the living nature allows the preparation of cyclic block copoly(α-peptoide) (34c, f).

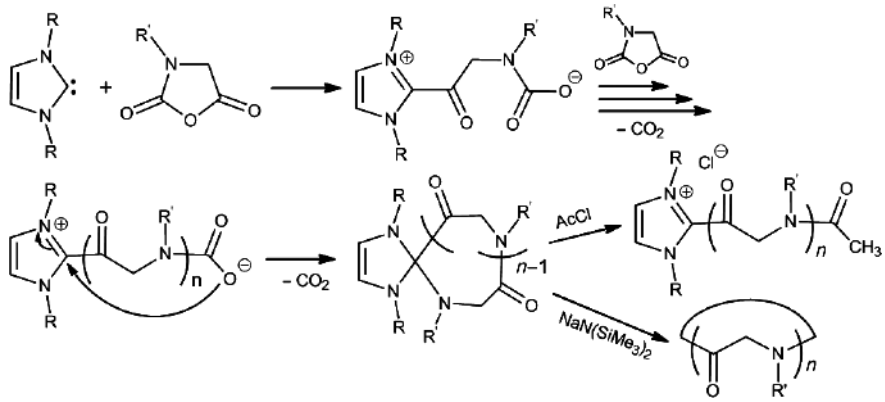

(10)

DBU (1,8-diazabicyclo[5.4.0]undec-7-ene) is also an effective initiator to produce cyclic polylactide (M_n = 32,000–53,000, M_w/M_n < 1.6) by the ring-opening polymerization and the subsequent backbiting reaction (35). As mentioned above from the old literature (eq. 6), amines are known to initiate the ring-opening polymerization of lactone. Cyclic polyester may also be produced in these cases. Recent progress in polymer structure analyses can make it possible to study that. The one site propagation process from the zwitterion, which is generated by the reaction of an initiator with a monomer, would be generally an effective tool to prepare cyclic polymers.

Propagation via the Cationic Site. An example for a zwitterion mechanism where a cationic site works for the propagation (eq. 4) is the polymerization of trioxane with BF_3 initiation, which may be shown as equation 11. The cation produced by ring opening is stabilized by the resonance between two canonical forms. The propagation is not simple, however, because the polyoxymethylene cation at the growing end is in equilibrium with the significant concentration of formaldehyde; that is, a formaldehyde monomer splits from the cationic growing end (36).

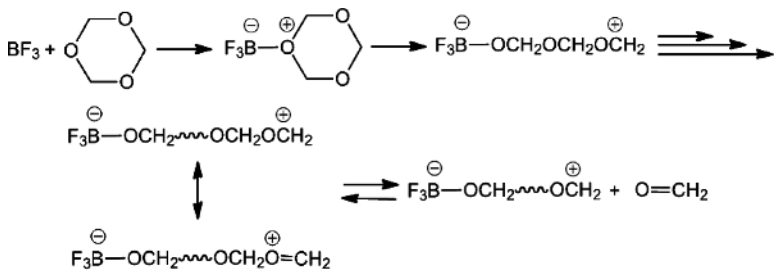

(11)

Highly electron-deficient olefins such as tetracyanoethylene, dimethyl 2,2-dicyanoethylene-1,l-dicarboxylate, and tetracyanoquinodimethane initiate the

cationic polymerization of cyclohexene oxide (M_n < 17,000) (37) or of electron-rich olefins such as *N*-vinylcarbazole and alkyl vinyl ether (38) by forming the zwitterionic species (eq. 12). This topic is discussed again in the section No Catalyst Copolymerization.

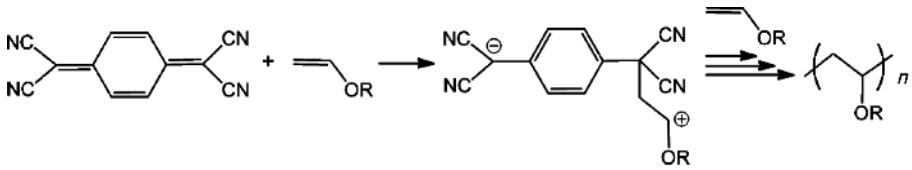

(12)

Monomer Activation

Some of ionic polymerizations proceed via the reaction of a neutral propagating end with an ionic species generated from monomer, that is, a monomer activation mechanism. Zwitterion is one of such species (29,39). The typical example is the ring-opening polymerization of lactide (LA) in the presence of 4-(dimethylamino)pyridine (DMAP) and alcohol (eq. 13) (40). LA is activated by forming 4-(dimethylamino)pyridinium alkoxide in equilibrium and reacts with alcohol to give the insertion product into the RO—H bond, releasing DMAP, which activates another LA. The successive reactions of the zwitterion with the hydroxyl group at the polymer end give poly-LA (DP_n < 120, M_w/M_n = 1.06–1.19).

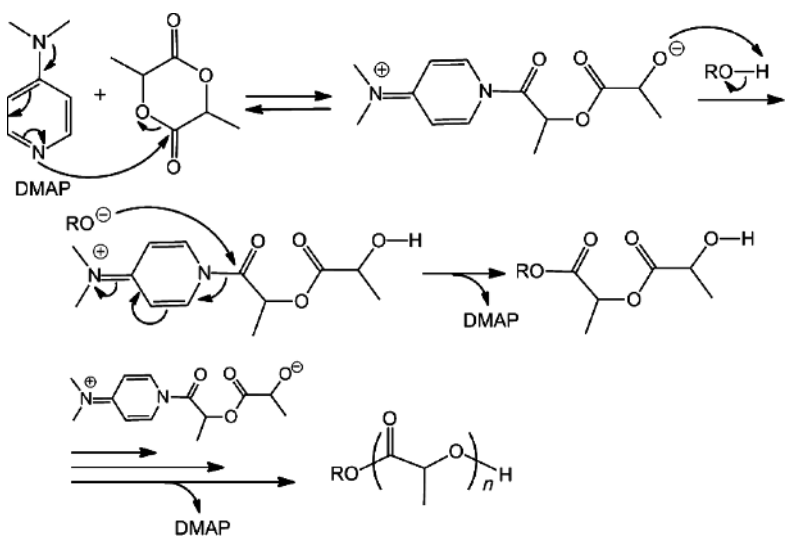

(13)

Phosphine and NHC also conduct similar mechanisms for the polymerization of LA and produce the well-defined linear polymer. In contrast, as mentioned in the above section for NHC, cyclic poly-LA is obtained in the absence of alcohol. In addition, it is noteworthy that NHC with alcohol performs the stereoselective polymerizations of racemic and meso LA, respectively, at low temperatures.

Racemic LA yields the stereoblock copolymer of *L*- and *D*-LA, whereas meso LA yields heterotactic poly-LA (39). An analogous monomer activation mechanism is also proposed for the NHC-catalyzed polymerizations of propylene oxide, cyclic carbonate, and cyclic siloxane in the presence of alcohol or trimethylsilyl ether (31,39).

Propagation by Cation–Anion Reactions

Polymerization of Isolated Zwitterions. A group of polymerizable zwitterions consisting of cyclic sulfonium cations and arene oxide anions has been prepared and isolated; they polymerize on heating (M_n = 6300–46,000) (41–44). For example,

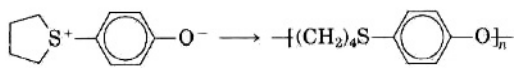

The isolation of the above zwitterion is possible due to the decreased reactivities (stabilization) of both cyclic sulfonium and phenoxide anions.

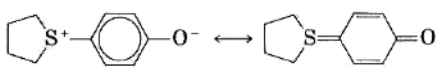

Several substituted phenoxides (41–43) and 4-naphthoxide (44) have been employed as arene oxide anions.

A reaction similar to the above polymerization is the alternating copolymerization between benzene-1,4-diazo-oxide (**10**) and tetrahydrofuran (45,46), although the zwitterion (**11**) directly involved in propagation is not isolated.

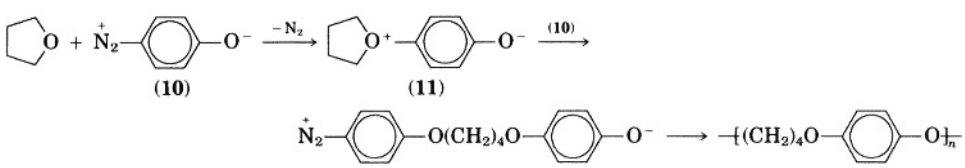

The combination of sulfonium naphthoxide with quinuclidine affords the new zwitterion, quinuclidinium naphthoxide, which is isolable (eq. 14) (47). The thermal polymerization yields the three-component polymer (M_n = 8,500–13,000).

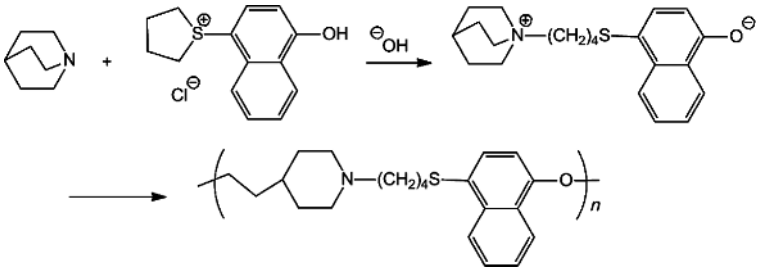

(14)

Quinuclidinium carboxylate is also isolable, and its thermal polymerization involves not only ring opening but also elimination reactions of the quinuclidine moiety (M_n = 4,000–17,000) (48).

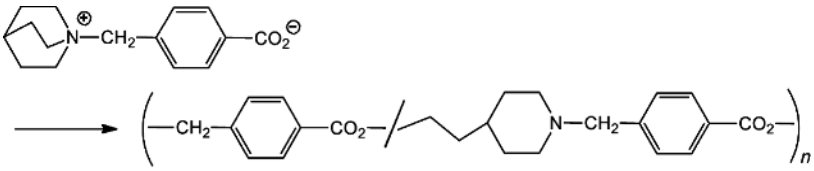

No Catalyst Copolymerization via Zwitterion Intermediates. A large number of zwitterionic copolymerizations that proceed without any added catalyst have been explored (1,4,49–57). A monomer having nucleophilic reactivity M_N is mixed with another monomer electrophilic reactivity M_E to generate a zwitterion $^{+}M_N - M_E^{-}$ (**12**) called a genetic zwitterion, "Two molecules of (**12**) react with each other to produce the first propagating zwitterion ("macrozwitterion") (**13**) that grows by successive reactions with (**12**).

$$\mathbf{M_N + M_E \longrightarrow \underset{\mathbf{12}}{{}^{+}M_N{-}M_E^{-}}} \tag{15}$$

$$\mathbf{(12) + (12) \longrightarrow \underset{\mathbf{13}}{{}^{+}M_N{-}M_EM_N{-}M_E^{-}}} \tag{16}$$

$$\mathbf{(13) + \mathit{n}(12) \longrightarrow \underset{\mathbf{14}}{{}^{+}M_N{-}(M_EM_N)_{n+1}M_E^{-}}} \tag{17}$$

As the reaction proceeds, the concentration of macrozwitterions of various sizes (**13**) and (**14**) is increased and reactions among macrozwitterions take place to increase the molecular weight sharply.

$$\mathbf{{}^{+}M_N{-}(M_EM_N)_m M_E^{-} + {}^{+}M_N{-}(M_EM_N)_n M_E^{-} \longrightarrow {}^{+}M_N{-}(M_EM_N)_{m+n+1} M_E^{-}} \tag{18}$$

Intramolecular cation–anion reactions in a single zwitterion sometimes occur to produce "macrocycles," although this contribution is small or at least minor. A series of the consecutive reactions, equations 15–18, leads to the formation of so-called "1:1 alternating copolymers". In addition to the above elementary reactions, the reaction of a free monomer, M_N or M_E, with the ionic growing site of a zwitterion may sometimes occur, disturbing the alternating arrangement of the two monomeric units.

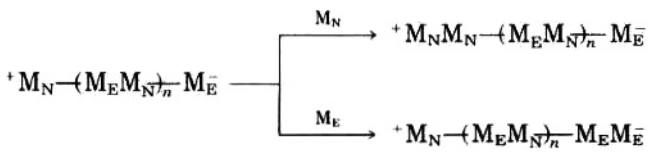

When the functional groups of the monomers are highly polarizable, dipole–dipole reactions between two monomers occur, in preference to the ion–dipole reactions between monomers and zwitterions, producing 1:1 alternating copolymerization.

On the basis of the above concept, many combinations of copolymerizations have been explored. A typical example is the copolymerization between 2-oxazoline (**15**) and β-propiolactone (**16**) (M_n = 1100–4000) (58), which proceeds at room temperature to produce an alternating copolymer (**18**) in an almost quantitative yield. A zwitterion (**17**) is the key intermediate (eq. 19). Opening of the oxazolinium ring by the nucleophilic attack of the carboxylate anion in the reaction between zwitterion molecules is the elementary step of propagation (eq. 20).

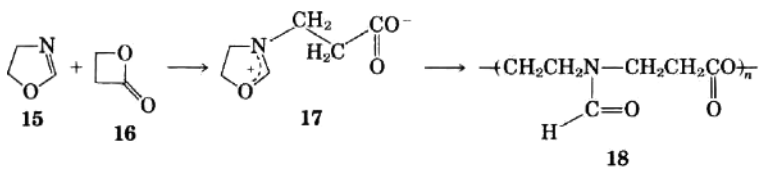

(19)

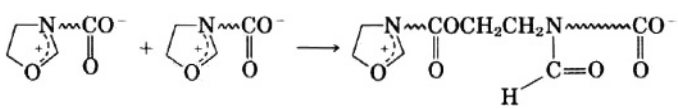

(20)

When the **15**:**16** feed ratio is less than 1.0, the composition of the product copolymer is not 1:1. Homopropagation of **16** at the anionic site takes place to produce a **16**-rich copolymer. Copolymerizations of 2-oxazoline (M_N) with other substituted β-propiolactones have been found to proceed in a similar way (59,60).

Table 1 shows combinations between representative M_N and M_E. The characteristics and scope of this copolymerization may be taken from the table.

Copolymerization of M_E monomers of acrylic acid and acrylamide with some M_N monomers presented in Table 1 is of vital interest. Copolymerization (M_n < 13,000) between acrylic acid (**19**) and 2-oxazoline (**15**) proceeds through a genetic

Table 1. M_N and M_E monomers and results of copolymerization[a–c]

M_N \ M_E		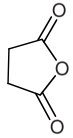		$CH_2{=}CHCOOH$	$CH_2{=}CHCONH_2$	$CH_2{=}CHCOOCH_2CH_2OH$	$CH_2{=}CHSO_2NH_2$
	R=H[b] R=CH_3[c] Ref. 58	R=H[c] R=CH_3[c] Ref. 61-65	R=H[c] R=CH_3[b] Ref. 66	R=H[a] R=CH_3[a] Ref. 67-69	R=H[a] R=CH_3[a] Ref. 70	R=CH_3[a] Ref. 71	R=CH_3[b] Ref. 72
	R=H[b] R=CH_3[c] R=C_6H_5[c] Ref. 73			R=H[a] R=CH_3[a] R=C_6H_5[a] Ref. 73	R=H[a] Ref. 70	R=H[a] Ref. 71	
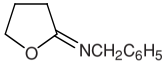	b Ref. 74				a Ref. 74		
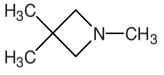	c Ref. 75				a Ref. 75		
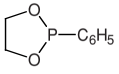	a Ref. 77		a Ref. 78	a Ref. 77	a Ref. 77		a Ref. 79
$C_6H_5CH{=}NC_6H_5$	c Ref. 80	a Ref. 80		b Ref. 80			

[a]Alternating copolymerization under a wide range of reaction conditions.

[b]Alternating copolymerization under certain conditions.

[c]Copolymerization occurred, but conditions for alternating copolymerization were not found.

zwitterion (**20**) that is a tautomer of excluded **17** in the copolymerization between 2-oxazoline and β-propiolactone (see eq. 19). The addition of **15** to the electron-deficient olefinic bond of acrylic acid produces a transient species that is quickly converted by hydrogen transfer into a zwitterion (**17**). Since the key intermediate is common to both copolymerizations of **15** + **16** and **15** + **19**, the structures of the product copolymers are identical.

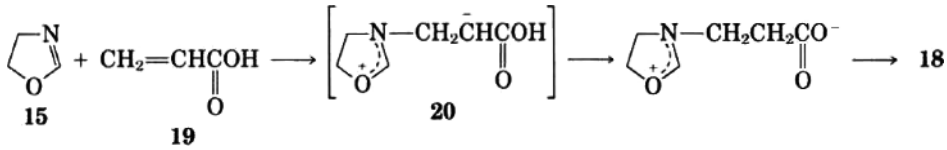

The above scheme showing **15** + **19** copolymerization is supported by the successful isolation of a zwitterion (**21**) in a related system of copolymerization.

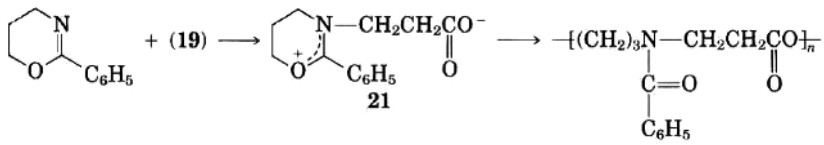

Copolymerization ($M_n < 1500$) of acrylamide (**22**) with 2-oxazoline (**15**) takes place similarly (70), that is, by the addition of **15** to the electron-deficient olefinic bond of **22** followed by hydrogen transfer to form a transient species of **23**. The anionic site of **24** is of ambident character: The oxygen atom reacts.

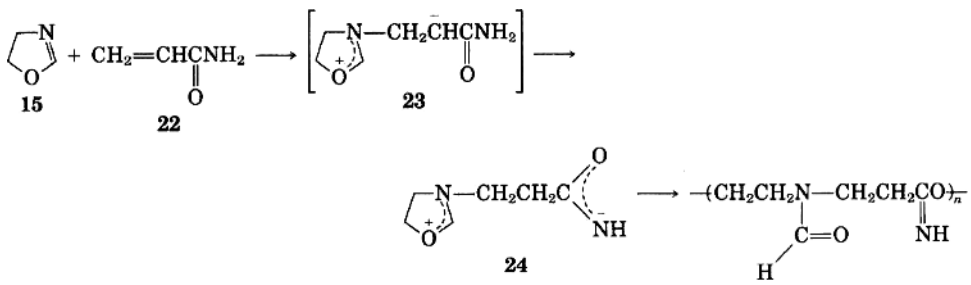

Similar behavior of β-hydroxyethyl acrylate (**25**) as the M_E monomer in the copolymerization with 2-oxazoline (**15**) has been observed ($M_n < 2400$), that is the addition of **15** to **25** followed by hydrogen transfer from the hydroxy group to the enolate anion (71). An oxazolinium-alkoxide zwitterion (**27**) is the key intermediate of copolymerization.

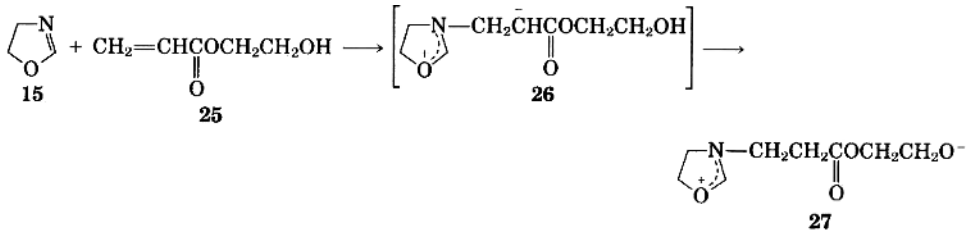

Spontaneous copolymerization (M_n = 30,000, M_w/M_n = 3.0) between 2-methyl-2-oxazoline and methyl maleate takes place, involving the proton transfer process, at room temperature in DMF, whereas the zwitterion intermediate is isolable in the reaction in acetone and characterized well (eq. 21) (76).

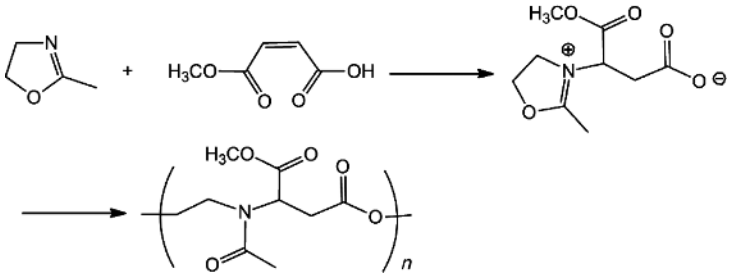

(21)

The cyclic trivalent phosphorus compound, 2-phenyl-1,3,2-dioxaphospholane (**28**), has been successfully copolymerized with several M_E monomers such as β-propiolactone (**16**) (77), propanesulfolactone (78,79), acrylic acid (**19**) (77), acrylamide (77), ethylenesulfonamide (79), alkyl acrylates (81), vinyl ketones (81), β-hydroxyethyl acrylate (82), *o*- and *p*-formylbenzoic acids (83,84), and vinylphosphonic acid (85) to give the corresponding 1:1 alternating copolymers (M_n < 4400). Copolymerization of **28** with **16** and with **19** gives copolymers of an identical structure (**30**), as explained in the following by the common zwitterion (**29**).

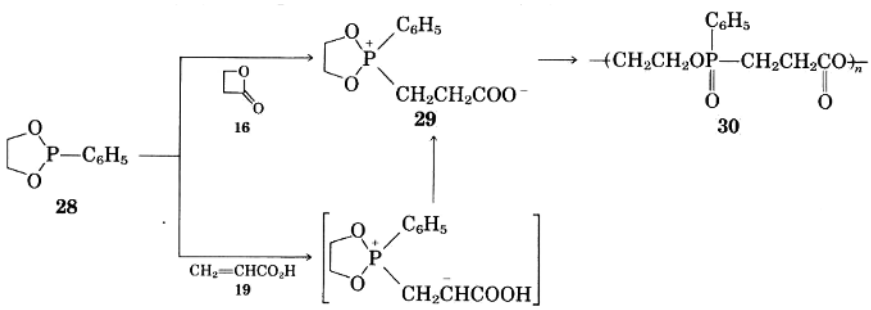

Propagation proceeds by the nucleophilic attack of the carboxylate anion of one zwitterion on the phosphonium ring of another zwitterion according to the pattern of the Arbusov reaction.

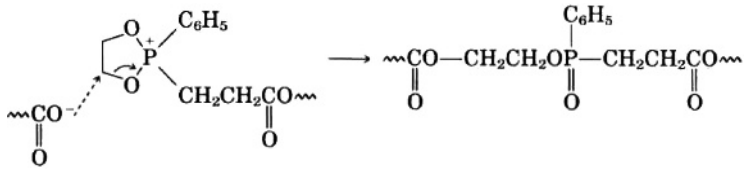

The trivalent phosphorus atom in the monomer (**28**) is converted into the pentavalent state during the above examples of copolymerization. This is also the case when the monomer (**28**) is copolymerized with other M_E monomers.

The copolymerization of **28** with **19** takes place only at temperatures higher than 100°C (77). At room temperature, these two monomers yield a pentavalent phosphorus compound of the spiro-ring structure (**31**) in an almost quantitative yield (86). On heating, **31** polymerizes to **30**. This result has been taken to support the above scheme involving a zwitterion (**29**).

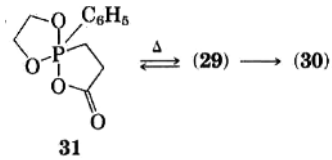

In the cases of combinations of **28** with the M_E monomers acrylate and vinyl ketone, the corresponding spiro-ring compounds (**32**) are formed instead of linear polymers at lower temperatures (room temperature to 50°C) (81).

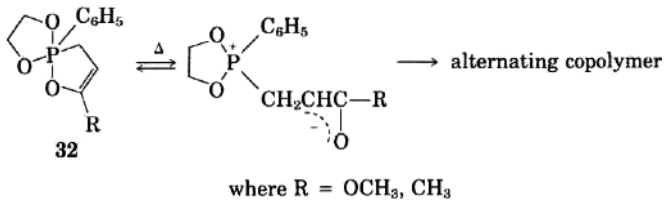

When the copolymerization of **28** with methyl acrylate (**33**) is carried out under CO_2, a 1:1:1 periodic terpolymer (**35**) ($M_n < 2800$) is produced (87). The following scheme explains this sequence-regulated terpolymerization, in which a zwitterion of a 1:1:1 three-component adduct is the key intermediate. Two outstanding points should be mentioned concerning the periodic terpolymerization: Copolymerization of carbon dioxide and the sequence regulation of three different monomeric units occur. An isolated sample of a spiro-ring compound (**32**) (R = OCH_3) dissolved in acetonitrile has been copolymerized with CO_2 at room temperature to produce **35**.

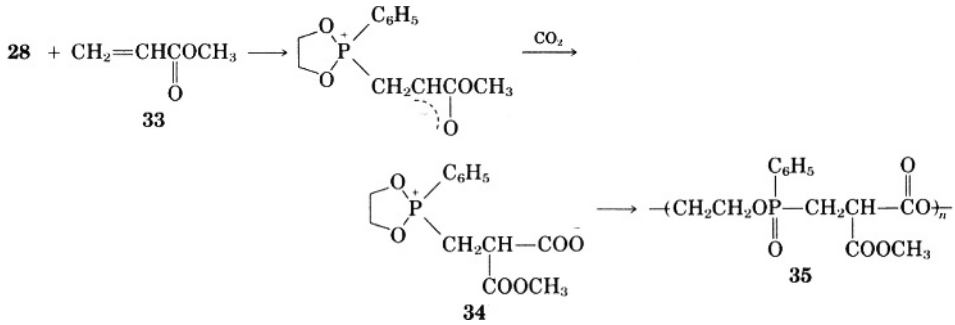

The cyclic phosphite of 2-phenoxy-1,3,2-dioxaphospholane (**36**), not included in Table 1, has exhibited an interesting polymerization behavior; that is, it readily copolymerized with ketoacid (**37**) at temperatures above 120°C without any added catalyst ($M_n < 7500$) (88).

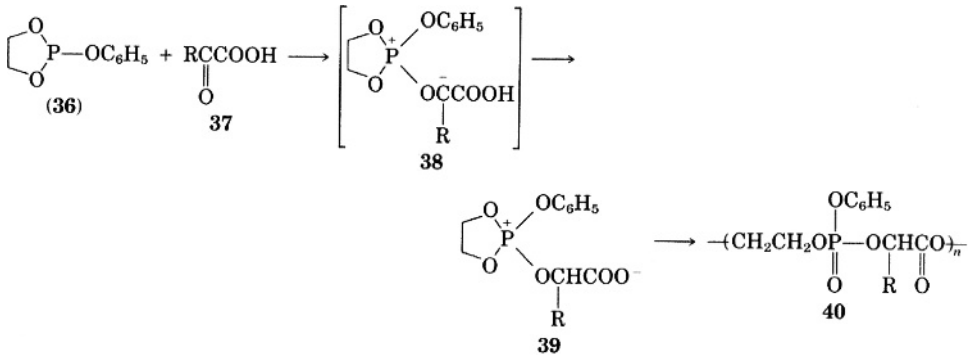

The trivalent phosphorus in **36** has been oxidized to the pentavalent state in the unit of copolymer (**40**), and correspondingly the ketoacid has been reduced to an ester of a hydroxyacid in the copolymer. The term "redox copolymerization" has been proposed to express this copolymerization in which one monomer is reduced, and the other is oxidized. In the binary mixture of **36** and **37** at a lower temperature, for example, –20°C, a pentaoxyphosphorane (**41**) has been isolated as a crystalline material, which is polymerized to **40** at a higher temperature, for example, 120°C (89). Thus, the intermediacy of a zwitterion (**39**) has been supported.

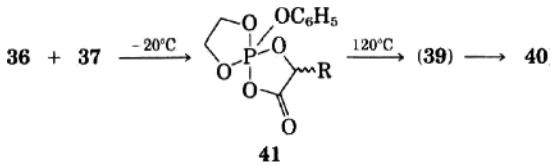

Cyclic acylphosphonite (**42**) (R = C_6H_5) and acylphosphite (**43**) (R = OC_6H_5) have been found to copolymerize with electron-deficient olefinic monomers such as vinyl ketone (90), acrylate (90), and acrolein (90), benzoquinone (**44**) (91), and

4,4′-diphenoquinone (92) (M_n < 8600). One of their reactions is shown in equation 22, which affords another example of redox copolymerization.

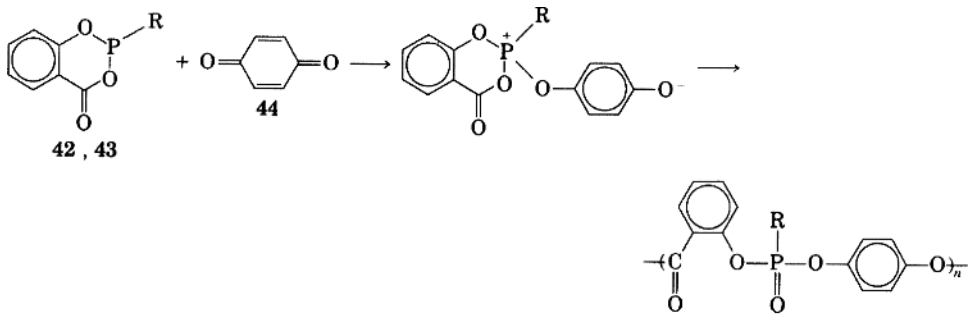

(22)

A patent (93) describes the alternating copolymerization of a cyclic phosphorus compound (**45**) with benzoquinone that is well explained by the intermediate zwitterion (**46**).

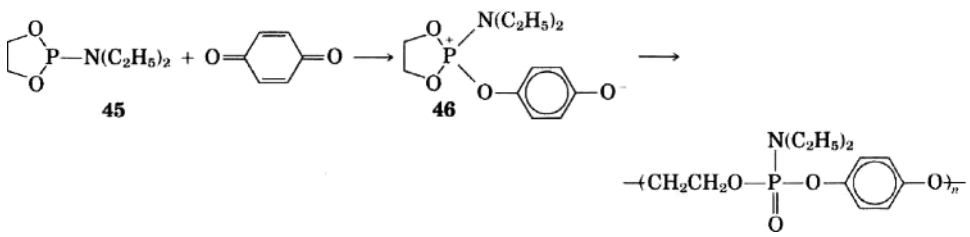

The combination of a cyclic trivalent phosphorus compound as M_N with M_E possessing two electrophilic sites performs ring-opening–closing alternating copolymerization (M_n < 6500). *Cis, trans-* and *cis,cis*-muconic acids (94), α,ω-dialdehydes (95), and methacrylic and acrylic anhydrides (96) are such as M_Es.

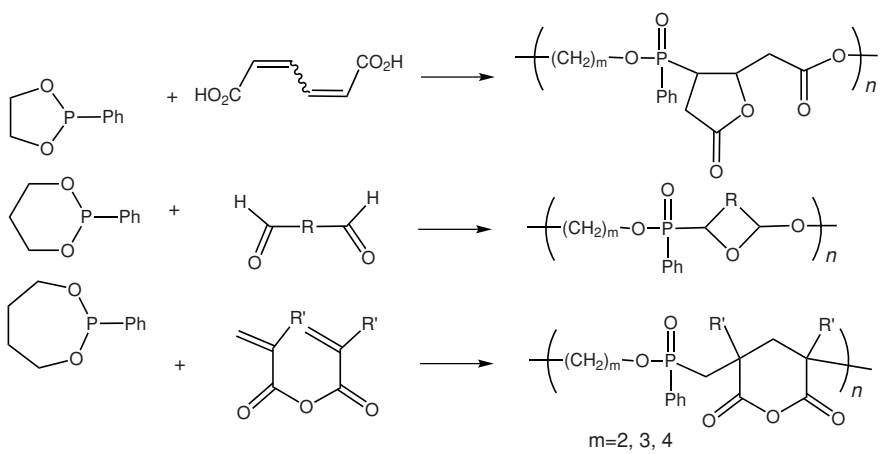

From divalent tin or germanium compounds, that is, stannylene (97) or germylene (98,99), with benzoquinone (97,98) or thietane (99) are formed the alternating copolymers (M_n < 780,000), involving redox processes. The copolymerization with benzoquinone is proved to proceed via the biradical intermediate (98), whereas two kinds of zwitterion mechanisms are proposed for the copolymerization of germylene with thietane (99).

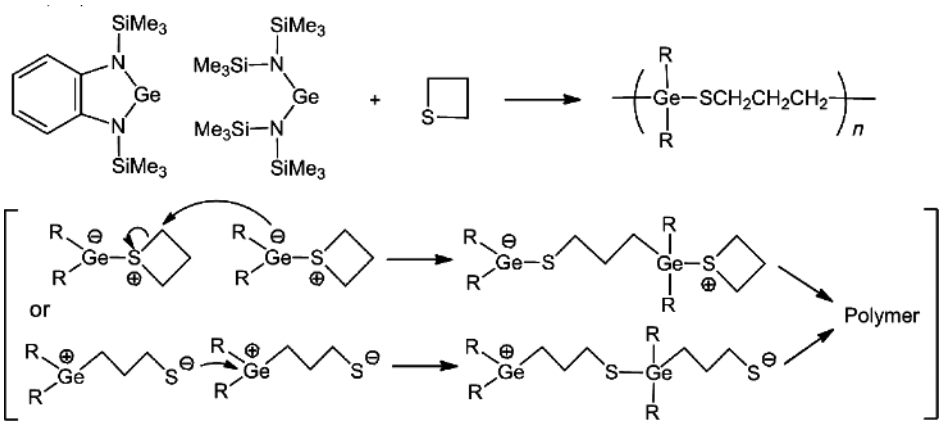

There are only two examples for cyclic ether, which is less nucleophilic than nitrogen or phosphorus compounds, to act as M_N (eq 23). Ethylene oxide or oxetane with 2,4-bis(4′-methoxyphenyl)-1,3,2,4-dithiadiphosphetane-2,4-disulfide (Lawesson's reagent) produces the copolymer (M_n = 5,000–20,000) having the 1:1/2 (cyclic ether : Lawesson's reagent) composition in the alternating arrangement, regardless of the feed ratio (100). The combinations of oxiranes with 1,1,2,2-tetracyano-3-ethoxycyclobutane give the copolymers (M_n < 70,000) having the alternating structure or the higher content of the unit from the cyclobutane, depending on the oxirane employed and the reaction conditions (101).

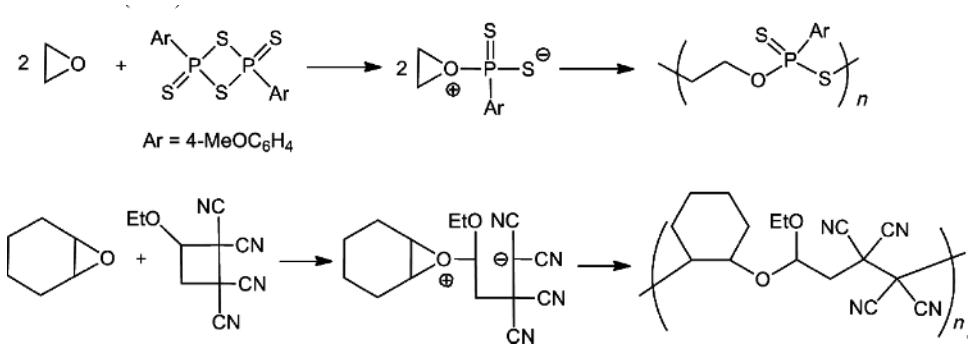

(23)

There are reported other interesting copolymerization reactions that proceed through zwitterion intermediates, for example, triazoline (**47**) with vinyl ethers (**48**) (X = OR) and with vinyl carbamates (**49**) (X = NHCOOR) (M_n < 4400) (102–104). Therein electron-rich olefins behave as M_N.

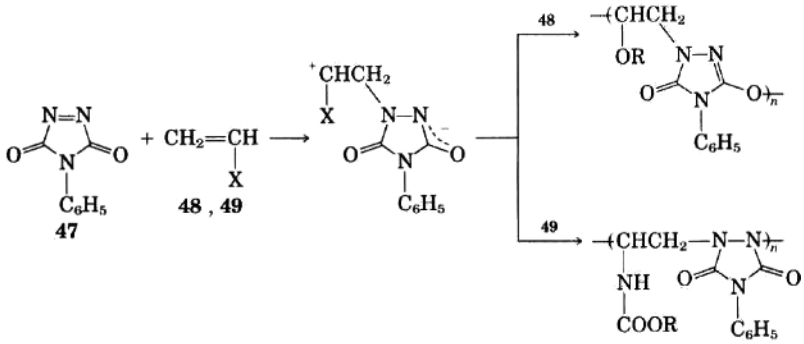

Similarly, the combinations of electron-rich olefins with highly electron-deficient olefins conduct spontaneous polymerization (5). It is proposed that polymerization mechanisms are governed by electron disparity between the donor and acceptor monomers; the very small electron disparity conducts a biradical mechanism for alternating copolymerization, and the enlarging electron disparity promotes a zwitterionic initiation of homopolymerization (see the section "Propagation via One Site"), finally leading the zwitterionic alternating copolymerization. The combination of *p*-methoxystyrene with 7,7-dicyanobenzoquinone methide produces the alternating copolymer (M_n = 7200–9500) via the zwitterion intermediate (105) (eq. 24). On the other hand, the biradical mechanism is proposed for the alternating copolymerization, when cyclohexadiene is the partner for 7,7-dicyanobenzoquinone methide (106).

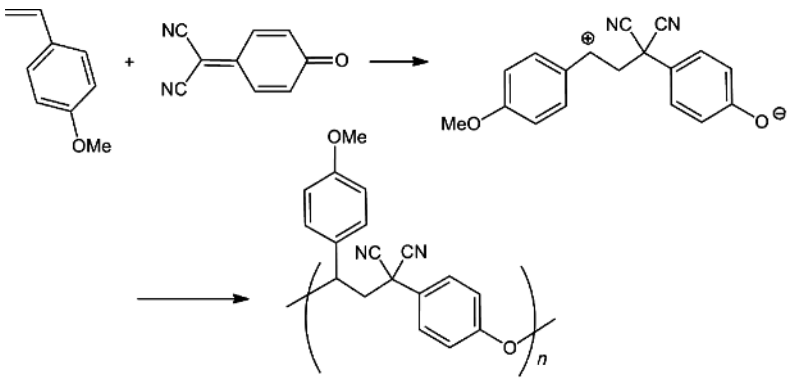

(24)

A more electron-rich olefin, cyclic ketene acetal, has enough nucleophilicity for generating the zwitterion intermediate with carbon disulfide and producing the alternating copolymer, which reacts further with cyclic ketene acetal (107).

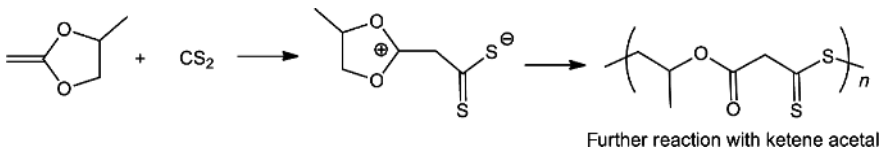

Aziridine and carbonyl sulfide also gives the alternating copolymer (108).

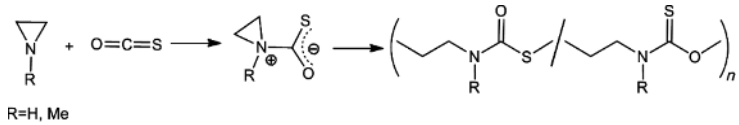

Electron-rich and electron -deficient allenes work as M_N and M_E, respectively. The zwitterion intermediate, which is detected as the methanol adduct, is formed by the reaction between methoxy- and cyano-allenes, and the alternating copolymer ($M_n = 50{,}000$) composed of four isomeric units is obtained (109). It is noteworthy that an excess amount of one of two monomers remains to be unreacted.

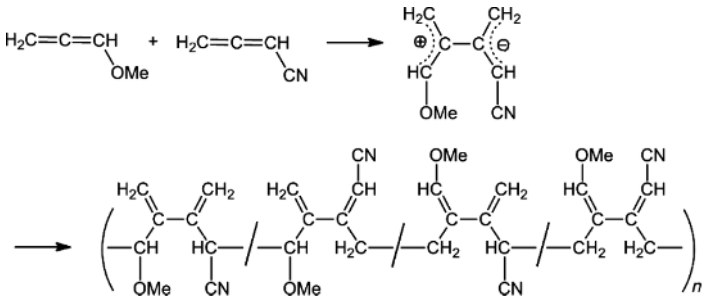

The combination of methoxyallene with aryl isocyanates gives the copolymer via the zwitterion intermediate (110). The copolymer compositions are dependent on the reaction conditions; 4-chlorophenyl isocyanate produces the alternating copolymer with methoxyallene ($M_n < 1300$) (eq. 25). In contrast, the reactions in DMF promote the formation of the cyclic trimers of aryl isocyanates, which are given by the backbiting of the homopropagating terminals of aryl isocyanates from the anionic sites of the zwitterions (111).

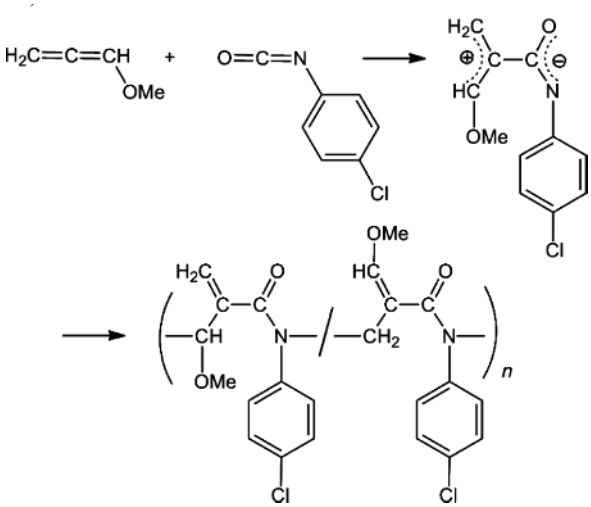

(25)

There is the report that these zwitterionic polymerizations are applied for the cross-liking reactions. When polystyrene having allenyl ether groups as the pendants is treated with cyanoallene or 4-chlorophenyl isocyanate, the cross-linking polymers are spontaneously obtained (112)

BIBLIOGRAPHY

"Zwitterionic polymerization" in *EPSE* 2nd ed., Vol. 17, pp. 1028–1039, by Takeo Saegusa and Masato Suzuki, Kyoto University, Japan.

CITED PUBLICATIONS

1. T. Saegusa, *Angew. Chem., Int. Ed.* **16**, 826 (1977).
2. D. S. Johnston, *Adv. Polym. Sci.* **42**, 51 (1982).
3. H. K. Hall, Jr., *Angew. Chem., Int. Ed.* **22**, 44 0 (1983).
4. I. J. McEwen, *Prog. Polym. Sci.* **10**, 317 (1984).
5. H. K. Hall, Jr. and A. B. Padias, *J. Polym. Sci., Polym. Chem.* **47**, 6735 (2009).
6. T. Ogawa and T. Tanikawa, *J. Polym. Sci., Part A-1: Polym. Chem.* **10**, 2005 (1972).
7. T. Ogawa and J. Romero, *Eur. Polym. J.* **13**, 419 (1977).
8. Ye. V. Kotchetov, A. A. Berlin, and N. S. Enikolopyan, *Polym. Sci. USSR* **8**, 1122, 1127 (1966).
9. Ye. V. Kotchetov, A. A. Berlin, Ye. M. Masal'skaya, and N. S. Enikolopyan, *Polym. Sci. USSR* **12**, 1264 (1970).
10. M. A. Markevich, Ye. V. Kolchetov, and N. S. Enikolopyan, *Polym. Sci. USSR* **13**, 1163 (1970).
11. H. Klippert and H. Ringsdorf, *Makromol. Chem.* **153**, 289 (1972).
12. F. Ranogayets, Ye. V. Kotchetov, M. A. Markovich, and N. S. Enikolopyan, *J. Polym. Sci. Polym. Symp.* **42**, 531 (1973).
13. D. Vofsi and A. Katchalsky, *J. Polym. Sci.* **26**, 127 (1957).
14. J. Grodzinsky, A. Katchalsky, and D. Volsi, *Makromol. Chem.* **44–46**, 591 (1961).
15. G. B. Butler and K. N. Sivaramakrishnan, *Polym. Prepr. Am. Chem. Soc. Div., Polym. Chem.* **17** (2), 608 (1976).
16. H. Hopf, H. Lussi, and S. Allison, *Makromol. Chem.* **44–46**, 95 (1961).
17. V. Jaacks and G. Franzmann, *Makromol. Chem.* **143**, 283 (1971).
18. E. F. Donnelly, D. S. Johnston, D. C. Pepper, and D. J. Dunn, *J. Polym. Sci., Polym. Lett. Ed.* **15**, 399 (1977).
19. D. C. Pepper, *J. Polym. Sci., Polym. Symp.* **62**, 65 (1978).
20. D. S. Johnston and D. C. Pepper, *Makromol. Chem.* **182**, 393, 407, 421 (1981).
21. J. P. Cronin and D. C. Pepper, *Makromol. Chem.* **189**, 85 (1988).
22. Y. K. Choi, Y. H. Bae, and S. W. Kim, *Macromolecules* **28**, 8419 (1995).
23. M. Miyamoto and S. Kanetaka, *J. Polym. Sci., Polym. Chem.* **37**, 3671 (1999).
24. (a) Y. Zhang, G. M. Miyake, and E. Y.-X. Chen, *Angew. Chem., Int. Ed.* **49**, 10158 (2010); (b) Y. Zhang and E. Y.-X. Chen, *Angew. Chem., Int. Ed.* **51**, 2465 (2012).
25. Y. Etienne and R. Soulas, *J. Polym. Sci., Part C: Polym. Symp.* **4**, 1061 (1963).
26. V. Jaacks and N. Mathes, *Makromol. Chem.* **131**, 295 (1970).
27. N. Mathes and V. Jaacks, *Makromol. Chem.* **142**, 209 (1971).
28. D. R. Wilson and R. G. Beaman, *J. Polym. Sci., Part A-1: Polym. Chem.* **8**, 216 (1970).
29. H. R. Kricheldorf, *Macromol. Rapid Commun.* **30**, 1371 (2009).
30. J. Raynaud, C. Absalon, Y. Gnanou, and D. Taton, *J. Am. Chem. Soc.* **131**, 3201 (2009).
31. J. Raynaud, W. N. Ottou, Y. Gnanou, and D. Taton, *Chem. Commun.* **46**, 3203 (2010).

32. (a) D. A. Culkin, W. Jeong, S. Csihony, E. D. Gomez, N. P. Balsara, J. L. Hedrick, and R. M. Waymouth, *Angew. Chem., Int. Ed.* **46**, 2627 (2007); (b) W. Jeong, E. J. Shin, D. A. Culkin, J. L. Hedrick, and R. M. Waymouth, *J. Am. Chem. Soc.* **131**, 4884 (2009).
33. E. J. Shin, W. Jeong, H. A. Brown, B. J. Koo, J. L. Hedrick, and R. M. Waymouth, *Macromolecules* **44**, 2773 (2011).
34. (a) L. Guo and D. Zhang, *J. Am. Chem. Soc.* **131**, 18072 (2009); (b) S. H. Lahasky, W. K. Serem, L. Guo, J. C. Garno, and D. Zhang, *Macromolecules* **44**, 9063 (2011); (c) C.-U. Lee, T. P. Smart, L. Guo, T. H. Epps, III, and D. Zhang, *Macromolecules* **44**, 9574 (2011); (d) L. Guo, J. Li, Z. Brown, K. Ghale, and D. Zhang, *Biopolym.: Peptide Sci.* **96**, 596 (2011); (e) L. Guo, S. H. Lahasky, K. Ghale, and D. Zhang, *J. Am. Chem. Soc.* **134**, 9163 (2012); (f) S. H. Lahasky, X. Hu, and D. Zhang, *ACS Macro Lett.* **1**, 580 (2012).
35. H. A. Brown, A. G. De Crisci, J. L. Hedrick, and R. M. Waymouth, *ACS Macro Lett.* **1**, 1113 (2012).
36. W. Kern and V. Jaacks, *J. Polym. Sci.* **48**, 399 (1960).
37. M. Abdelkader, A. B. Padias, and H. K. Hall, Jr., *Macromolecules* **20**, 949 (1987).
38. (a) T. Gotoh, A. B. Padias, and H. K. Hall, Jr., *J. Am. Chem. Soc.* **108**, 4920 (1986); (b) H. K. Hall, Jr., T. Itoh, S. Iwatsuki, A. B. Padias, and J. E. Mulvaney, *Macromolecules* **23**, 913 (1990).
39. N. E. Kamber, W. Jeong, and R. M. Waymouth, *Chem. Rev.* **107**, 5813 (2007).
40. F. Nederberg, E. F. Connor, M. Moller, T. Glauser, J. L. Hedrick, *Angew. Chem., Int. Ed.* **40**, 2712 (2001).
41. M. J. Hatch, M. Yoshimine, D. L. Schmidt, and H. B. Smith, *J. Am. Chem. Soc.* **93**, 4617 (1971).
42. M. J. Hatch, M. Yoshimine, D. L. Schmidt, and H. B. Smith, *J. Polym. Sci., Part A-1: Polym. Chem.* **10**, 2951 (1972).
43. D. L. Schmidt, Ring-Opening Polymerization, in T. Saegusa and E. Goethals, eds., *Am. Chem. Soc. Symp. Ser*. **59**, 318–331 (1977).
44. P. Gunatillake, G. Odian, and D. L. Schmidt, *Macromolecules* **19**, 1779 (1986).
45. T. Kunitake and C. C. Price, *J. Am. Chem. Soc.* **85**, 761 (1963).
46. J. K. Stille and P. Cassidy, *J. Polym. Sci., Polym. Lett.* **1**, 565 (1963).
47. D. L. Cangiano, G. Odian, and D. L. Schmidt, *J. Polym. Sci., Polym. Chem.*, **34**, 801 (1996).
48. C. Lu, P. Gunatillake, and G. Odian, *Macromolecules* **25**, 4464 (1992).
49. T. Saegusa, *Chem. Technol.* **5**, 295 (1975).
50. T. Saegusa, S. Kobayashi, Y. Kimura, and H. Ikeda, *J. Macromol. Sci. Chem.* **9**, 641 (1975).
51. T. Saegusa, S. Kobayashi, and Y. Kimura, *Pure Appl. Chem.* **48**, 307 (1976)
52. T. Saegusa. S. Kobayashi, Y. Kimura, and T. Yokoyama, in T. Saegusa and E. Goethals, eds., *Am. Chem. Soc. Symp. Ser*. **59**, 332–343 (1977).
53. T. Saegusa and S. Kobayashi, *Pure Appl. Chem.* **50**, 281 (1978).
54. T. Saegusa and S. Kobayashi, *J. Polym. Sci., Polym. Symp.* **62**, 79 (1978).
55. T. Saegusa, *Makromol. Chem. Suppl.* **3**, 157 (1979).
56. T. Saegusa, *Pure Appl. Chem.* **53**, 691 (1981).
57. T. Saegusa, *Top. Curr. Chem.* **100**, 75 (1981).
58. T. Saegusa, H. Ikeda, and H. Fujii, *Macromolecules* **5**, 354 (1972).
59. T. Saegusa, S. Kobayashi, and Y. Kimura, *Macromolecules* **7**, 1 (1974).
60. B. L. Rivas, G. S. Canessa, and S. A. Pooley, *Makromol. Chem.* **187**, 71 (1986).
61. S. Kobayashi, M. Isobe, and T. Saegusa, *Macromolecules* **15703** (1982).
62. B. L. Rivas, G. S. Canessa, and S. A. Pooley, *Polym. Bull.* **9**, 417 (1983).
63. G. S. Canessa, S. A. Pooley, M. Parra, and B. L. Rivas, *Polym. Bull.* **11**, 465 (1984).
64. B. L. Rivas, G. S. Canessa, and S. A. Pooley, *Polym. Bull.* **13**, 65 (1985).

65. B. L. Rivas, G. S. Canessa, and S. A. Pooley, *Polym. Bull.* **13**, 519 (1985).
66. T. Saegusa, H. lkeda, S. Hirayanagi, Y. Kimura, and S. Kobayashi, *Macromolecules* **8**, 259 (1975).
67. T. Saegusa, S. Kobayashi, and Y. Kimura, *Macromolecules* **7139** (1974).
68. G. Odian and P. A. Gunatillake, *Macromolecules* **17**, 1297, 2236 (1984); **18**, 605 (1985).
69. S. Kobayashi, M. Miyamoto, and T. Saegusa, *Macromolecules* **14**, 1582 (1981).
70. T. Saegusa. S. Kobayashi, and Y. Kimura. *Macromolecules* **8**, 374 (1975).
71. T. Saegusa, Y. Kimura, and S. Kobayashi, *Macromolecules* **10**, 239 (1977).
72. T. Saegusa, S. Kobayashi, and J. Furukawa, *Macromolecules* **9**, 728 (1976).
73. T. Saegusa, Y. Kimura, and S. Kobayashi, *Macromolecules* **10**, 236 (1977).
74. T. Saegusa, Y. Kimura, K. Sano, and S. Kobayashi, *Macromolecules* **7**, 546 (1974).
75. T. Saegusa, Y. Kimura, S. Sawada, and S. Kobayashi, *Macromolecules* **7**, 956 (1974).
76. K. I. Lee and M.-H. Lee, *Polymer* **34**, 650 (1993).
77. T. Saegusa, Y. Kimura, N. Ishikawa, and S. Kobayashi, *Macromolecules* **9**, 724 (1976).
78. T. Saegusa, S. Kobayashi, and J. Furukawa, *Macromolecules* **10**, 73 (1977).
79. T. Saegusa, S. Kobayashi, and J. Furukawa, *Macromolecules* **11**, 1027 (1978).
80. T. Saegusa, S. Kobayashi, and J. Furukawa, *Macromolecules* **8**, 703 (1975).
81. T. Saegusa, S. Kobayashi, and Y. Kimura, *Macromolecules* **10**, 64 (1977).
82. T. Saegusa, M. Niwano, and S. Kobayashi, *Polym. Bull.* **2**, 249 (1980).
83. T. Saegusa, T. Kobayashi, and S. Kobayashi, *Polym. Bull.* **1**, 259 (1979).
84. T. Saegusa, T. Yokoyama, Y. Kimura, and S. Kobayashi, *Polym. Bull.* **1**, 91 (1978).
85. J. Kadokawa, I.-F. Yen, S. Shoda, H. Uyama, and S. Kobayashi, *Polym. J.* **11**, 1205 (1992).
86. T. Saegusa, S. Kobayashi, and Y. Kimura, *J. Chem. Soc., Chem. Commun.* 443 (1976).
87. T. Saegusa, S. Kobayashi, and Y. Kimura, *Macromolecules* **10**, 68 (1977).
88. T. Saegusa, T. Yokoyama, Y. Kimura, and S. Kobayashi, *Macromolecules* **10**, 791 (1977).
89. T. Saegusa, S. Kobayashi, Y. Kimura, and T. Yokoyama, *J. Am. Chem. Soc.* **98**, 7843 (1976).
90. T. Saegusa, T. Kobayashi, and S. Kobayashi, *Polym. Bull.* **1**, 535 (1979).
91. T. Saegusa, T. Kobayashi, T. Y. Chow, and S. Kobayashi, *Macromolecules* **12**, 533 (1979).
92. S. Kobayashi, M. Okawa, M. Niwano, and T. Saegusa, *Polym. Bull.* **5**, 331 (1981).
93. Jpn. Pat. 71 02352 (1971), Asahi Chem. Ind. H. Kobayashi. H. Ohama and Y. Kodaira.
94. S. Kobayashi, J. Kadokawa, H. Uyama, S. Shoda, and S. Lundmark, *Macromolecules* **25** 5862 (1992).
95. S. Kobayashi, S. Lundmark, J. Kadokawa, and A.-C. Albertsson *Macromolecules* **25**, 5867 (1992).
96. S. Lundmark, J. Kadokawa, and S. Kobayashi, *Macromolecules* **25**, 5873 (1992).
97. S. Kobayashi, S. Iwata, and S. Shoda, *Acta Polym.* **46**, 471 (1995).
98. S. Kobayashi, S. Iwata, M. Abe, and S. Shoda, *J. Am. Chem. Soc* **117**, 2187 (1995).
99. S. Shoda, S. Iwata, H J. Kim, M. Hiraishi, and S. Kobayashi, *Macromol. Chem. Phys.* **197**, 2437 (1996).
100. S. Kobayashi, T. Y. Chow, and T. Saegusa, *Polym. Bull.* **10**, 491 (1983).
101. T. Yokozawa and T. Suzuki, *Macromolecules* **29**, 22 (1992).
102. G. B. Butler, L. J. Guilbault, and S. R. Turner, *J. Polym. Sci., Part B: Polym. Lett.* **9115** (1971).
103. L. J. Guilbaut, S. R. Turner, and G. B. Butler, *J. Polym. Sci., Part B: Polym. Lett.* **10**, 1 (1972).
104. K. B. Wagener and G. B. Butler, *J. Org. Chem.* **38**, 3070 (1973).

105. Y. Mitsuda, S. Kawaguchi, T. Uno, M. Kubo, and T. Itoh, *Macromolecules* **37**, 1251 (2004).
106. S. Kawaguchi, Y. Mitsuda, T. Uno, M. Kubo, and T. Itoh, *Kobunshi Ronbunshu* **61**, 263 (2004).
107. T. Endo. H. Fukuda, and M. Hirota, *J. Am. Chem. Soc.* **106**, 4035 (1984).
108. H. Yokota and M. Kondo, *J. Polym. Sci., Part A-I: Polym. Chem.* **9**, 13 (1971).
109. J. Mizuya, T. Yokozawa, and T. Endo, *J. Am. Chem. Soc.* **111**, 743 (1989).
110. (a) J. Mizuya, T. Yokozawa, and T. Endo, *Chem. Lett.* 479 (1989); (b) J. Mizuya, T. Yokozawa, and T. Endo, *Macromolecules* **24**, 2299 (1991).
111. J. Mizuya, T. Yokozawa, and T. Endo, *J. Polym. Sci., Polym. Chem.* **29**, 1545 (1991)
112. J. Mizuya, T. Yokozawa, and T. Endo, *Macromolecules* **23**, 4724 (1990).

MASATO SUZUKI
Nagoya Institute of Technology
Nagoya, Japan

CONTENTS OF VOLUMES 1–15 OF THE ENCYCLOPEDIA

VOLUME 1

VOLUME 2

VOLUME 3

VOLUME 4

VOLUME 5

VOLUME 6

VOLUME 7

VOLUME 8

VOLUME 9

VOLUME 10

VOLUME 11

VOLUME 12

VOLUME 13

VOLUME 14

VOLUME 15

CONTRIBUTORS TO VOLUMES 1–15 OF THE ENCYCLOPEDIA

Alaa S. Abd-El-Aziz, *University of Prince Edward Island, Charlottetown, Canada; University of British Columbia Okanagan, Kelowna, Canada,* Metal-Containing Polymers

W. Wade Adams, *Rice University, Houston, Texas,* Rigid-Rod Polymers

H. Ade, *North Carolina State University, Raleigh, North Carolina,* X-Ray Microscopy

Josh C. Agar, *School of Materials Science and Engineering, Georgia Institute of Technology, Atlanta, Georgia,* Conductive Polymer Composites

Suk-kyun Ahn, *Institute of Material Science, University of Connecticut, Storrs, Connecticut,* Liquid Crystalline Block Copolymers

Fadi Aldeek, *Florida State University, Tallahassee, Florida,* Nanocrystals Surface Functionalization

Michael W. Allsopp, *Independent PVC Technology Consultant, Heswall, Wirral, England,* Vinyl Chloride Polymers

S. Al-Malaika, *Aston University, Birmingham, England, United Kingdom,* Stabilization

Bruno Ameduri, *Institut Charles Gerhardt, Montpellier, France,* Fluorinated Copolymers

R. Amin-Sanayei, *Atofina Chemicals Inc., King of Prussia, Pennsylvania,* Vinylidene Fluoride Polymers (PVDF)

H. Magnus Andersson, *Autonomic Materials, Inc, Champaign, Illinois,* Self-Healing Polymers

James H. Andrews, *Youngstown State University, Youngstown, Ohio,* Nonlinear Optical Properties; Photorefraction

Stephen M. Andrews, *BASF Corporation,* Additives

Steve Andrzejewski, *Ashland Distribution, Parkway Dublin, Ohio,* Rotational Molding

Anthony Anton, *E. I. du Pont de Nemours & Company, Inc., Wilmington, Delaware,* Polyamides, Fibers

Nicolas Anton, *Laboratory of Design and Application of Bioactive Molecules (CAMB), Faculty of Pharmacy, University of Strasbourg, France,* Microfluidic Production of Micro- and Nanoparticles

Fátima Aparicio, *Universidad Complutense de Madrid, Madrid, Spain,* Supramolecular Polymers

Valeria Arrighi, *Heriot-Watt University, Edinburgh, United Kingdom,* Miscibility

Ayse Asatekin, *Massachusetts Institute of Technology, Cambridge, Massachusetts,* Filtration Membranes

Rafael Auras, *Michigan State University, East Lansing, Michigan,* Poly(lactic acid)

Neil Ayres, *Department of Polymer Science, University of Southern Mississippi, Hattiesburg, Mississippi,* Water-Soluble Polymers

Darlene M. Back, *The Dow Chemical Company, Piscataway, New Jersey,* Ethylene Oxide Polymers

David G. Bailey, *Eastern Regional Research Center, U.S. Department of Agriculture,* Leather

Bennett R. Baird, *E. I. du Pont de Nemours & Company, Inc., Wilmington, Delaware,* Polyamides, Fibers

John K. Baird, *Kelco Division of Merck & Co., Inc.,* Xanthan

Madhab P. Bajgai, *Centre for Blood Research, University of British Columbia, Vancouver, Canada; Department of Pathology & Laboratory Medicine, University of British Columbia, Vancouver, Canada,* Polymer Brushes

Richard W. Baker, *Membrane Technology & Research, Inc., Menlo Park, California,* Membrane Technology

Edward Balizer, *U.S. Naval Surface Warfare Center, West Bethesda, Maryland,* Acoustic Properties

Florence Bally, *ICPEES, University of Strasbourg, Strasbourg, France,* Microdevices

George Barany, *The University of Minnesota, Minneapolis, Minnesota,* Polypeptide Synthesis, Solid-Phase Method

Christopher Barner-Kowollik, *The University of New South Wales, Sydney, New South Wales, Australia,* Copolymerization; Radical Polymerization

Edward G. Bartick, *Counterterrrorism and Forensic Science Research Unit, FBI Academy, Quantico, Virginia,* Forensic Analysis

D. C. Bassett, *University of Reading, Reading, United Kingdom,* Morphology

Catia Bastioli, *Novamont SpA, Novara, Piedmont, Italy,* Starch

Subhadeep Basu, *University of Massachusetts, Amherst, Massachusetts,* Dendrimers, Molecular Recognition

Giuseppe Battaglia, *Department of Engineering Materials, University of Sheffield, Sheffield, United Kingdom; The Kroto Research Institute, Sheffield, United Kingdom,* Bioinspired Polymers

W. F. Beach, *Alpha Metals, Bridgewater, New Jersey,* Xylylene Polymers

Sam Belcher, *Consultant, Moscow, Ohio,* Blow Molding

V. A. Beloshenko, *Donetsk Physics and Technology, Institute of the National Academy of Sciences of Ukraine, Donetsk, Ukraine,* Solid State Extrusion

James N. BeMiller, *Purdue University,* Glycogen

Elizabeth Benham, *Chevron Phillips Chemical Company, Kingwood, Texas,* Ethylene Polymers, HDPE

Noelie R. Bertoniere, *Southern Regional Research Center, USDA,* Cellulose

D. E. Beyer, *The Dow Chemical Company,* Vinylidene Chloride Polymers (PVDC)

Y. E. Beygelzimer, *Donetsk Physics and Technology, Institute of the National Academy of Sciences of Ukraine, Donetsk, Ukraine,* Solid State Extrusion

Jozef Bicerano, *Bicerano & Associates Consulting, Inc., Midland, Michigan,* Glass Transition

N. C. Billingham, *University of Sussex, Brighton, United Kingdom,* Degradation

Kurt Binder, *Institut für Physik, Johannes Gutenberg Universität, Mainz, Germany,* Phase Transformation

Wolfgang H. Binder, *Institute of Applied Synthetic Chemistry, Technical University of Vienna, Vienna, Austria; Martin-Luther University Halle-Wittenberg, Halle (Saale), Germany,* "Click" Chemistry in Macromolecular Synthesis; Melamine-Formaldehyde Resins

J. D. Birchall, *Imperial Chemical Industries,* Cement Additives

Frank D. Blum, *University of Missouri-Rolla, Rolla, Missouri,* Silane Coupling Agents

B. Blümich, *Institut für Technische Chemie und Makromolekulare Chemie, Rheinisch-Westfälische Technische Hochschule, Worringerweg, Aachen, Germany,* Nuclear Magnetic Resonance

Christophe Boisson, *Université de Lyon, Laboratoire de Chimie Catalyse Polymères et Procédés, Villeurbanne, France,* Single-Site Catalysts

John E. Boliek, *E. I. du Pont de Nemours & Co., Inc., Wilmington, Delaware,* Fibers, Elastomeric

Armen Boranian, *Consultant,* Flooring Materials

Uwe Borchert, *University of Hamburg, Hamburg, Germany,* Vesicles

Sara C. Bourke, *University of Toronto, Toronto, Ontario,* Inorganic Polymers

John W. Bozzelli, *Injection Molding Solutions, Midland, Michigan,* Injection Molding

Mark Bradley, *University of Southampton, Southampton, United Kingdom,* Polymer-Supported Reagents

D. G. Brady, *Phillips Petroleum Company,* Poly(arylene suflide)s

Paul V. Braun, *University of Illinois at Urbana-Champaign, Urbana, Illinois,* Self-Healing Polymers

Martin Brehmer, *Institute of Organic Chemistry, University of Mainz, Mainz, Germany,* Ferroelectric Liquid Crystalline Elastomers

David S. Breslow, *D. S. Breslow Associates,* Ethylenesulfonic Acid Polymers

Victoria A. Briand, *University of Connecticut,* Protein-Polymer Conjugates

David Briggs, *University of Nottingham, University Park, Nottingham, United Kingdom,* Surface Analysis

B. J. Briscoe, *Imperial College, London, UK,* Surface Mechanical Damage and Wear

Donald E. Brooks, *Centre for Blood Research; Department of Chemistry; Department of Pathology & Laboratory Medicine, University of British Columbia, Vancouver, Canada,* Polymer Brushes

Paul D. Brothers, *E. I. du Pont de Nemours & Co., Inc., Wilmington, Delaware,* Perfluorinated Polymers, Tetrafluoroethylene–Ethylene Copolymers; Perfluorinated Polymers, Tetrafluoroethylene–Perfluorodioxole Copolymers; Perfluorinated Polymers, Tetrafluoroethylene–Perfluorovinyl Ether Copolymers; Perfluorinated Polymers, Perfluorinated Ethylene–Propylene Copolymers; Perfluorinated Polymers, Polytetrafluoroethylene

R. Malcolm Brown, *The University of Texas at Austin,* Cellulose

Yefim Brun, *Waters Corporation, Milford, Massachusetts,* Chromatography, HPLC

Daniel J. Brunelle, *GE Corporate R&D, Niskayuna, New York,* Macrocyclic Polymers; Polycarbonates

Andreas J. Brunner, *Center for Nondestructive Testing, EMPA, Swiss Federal Laboratories for Materials Testing and Research, Dübendorf, Switzerland,* Nondestructive Testing

Robert G. Bryant, *NASA Langley Research Center, Hampton, Virginia,* Polyimides

Fredric L. Buchholz, *The Dow Chemical Company, Midland, Michigan,* Superabsorbent Polymers

Peter M. Budd, *University of Manchester, Manchester, United Kingdom,* Polymers of Intrinsic Microporosity

Matthew Butts, *GE Global Research Center, Niskayuna, New York,* Silicones

Israel Cabasso, *Polymer Research Institute, State University of New York-ESF,* Radiopaque Polymers

Joao Cabral, *Imperial College London, London,* Miscibility

Ying Cai, *University of Iowa, Iowa City, Iowa,* Photopolymerization, Free Radical

F. J. Baltá Calleja, *Instituto de Estructura de la Materia, CSIC, Madrid, Spain,* Hardness

Neil R. Cameron, *Durham University, Durham, United Kingdom,* PolyHIPEs

Frank A. Cangelosi, *Cytec Industries, Stamford, Connecticut,* UV Stabilizers

Adam S. Cantor, *3M Drug Delivery Systems Division, St. Paul, Minnesota,* Pressure-Sensitive Adhesives

Gary J. Capone, *Solutia, Inc., Decatur, Alabama,* Acrylic Fibers

G. Carotenuto, *Institute for the Composite Material Technology, National Research Council, Piazzale Tecchio, Napoli, Italy,* Nanocomposites, Metal-Filled

James Cella, *GE Global Research Center, Niskayuna, New York,* Silicones

John C. Chadwick, *Dutch Polymer Institute, Eindhoven University of Technology, The Netherlands,* Ziegler-Natta Catalysts

Ling Chang, *National Cheng Kung University, Tainan, Taiwan,* Tacticity in Vinyl Polymers

Henri Chanzy, *CNRS-CERMAV, Grenoble, France,* Cellulose

Sung-Hsuen Chao, *Dow Corning Europe S.A., Seneffe, Belgium,* Antifoaming Agents

Roger Chapman, *Texon UK Limited, Leicester, United Kingdom,* Nonwoven Fabrics, Staple Fibers

Richard P. Chartoff, *University of Arizona, Tucson, Arizona,* Thermal Analysis of Polymers

Ananda M. Chatterjee, *Shell Development Company,* Butene Polymers

M. Chatzichristidi, *University of Athens, Athens, Greece,* Graft Copolymers

Mahesh Chaubal, *Drugdel.com, Columbia, Maryland,* Controlled Release Technology

K. K. Chawla, *University of Alabama at Birmingham, Birmingham, Alabama,* Composite Foams

Eugene Y.-X. Chen, *Colorado State University, Fort Collins, Colorado,* Methylene Butyrolactone Polymers

Si-Xue Cheng, *Institute of Materials Research and Engineering, Singapore; National University of*

Singapore, Singapore, Liquid Crystalline Polymers, Main-Chain

Stephen Z. D. Cheng, *The University of Akron, Akron, Ohio,* Semicrystalline Polymers

Chorng-Shyan Chern, *National Taiwan University of Science and Technology, Taipei, Taiwan,* Microemulsion Polymerization

T. T. Peter Cheung, *Phillips Petroleum Company, Bartlesville, Oklahoma,* Cyclopentadiene and Dicyclopentadiene

Y. Wilson Cheung, *Polyolefins R&D, The Dow Chemical Company, Freeport, Texas,* Ethylene Copolymers

John R. Christoe, *CSIRO Textile and Fibre Technology, Belmount, Victoria, Australia,* Wool

Hoe H. Chuah, *Shell Chemical Company, Houston, Texas,* Poly(trimethylene terephthalate)

Tai-Shung Chung, *Institute of Materials Research and Engineering, Singapore; National University of Singapore, Singapore,* Liquid Crystalline Polymers, Main-Chain; Membranes for Energy Applications

A. William M. Coaker, *Consultant,* Calendering

Edward D. Cohen, *Technical Consultant, Fountain Hills, Arizona,* Coating Methods, Survey

Martin P. Cohen, *The Goodyear Tire & Rubber Company, Akron, Ohio,* Rubber Chemicals

Brian Condon, *U.S. Department of Agriculture, ARS, New Orleans, Louisiana,* Cotton

Robert P. Conger, *Consultant,* Flooring Materials

Kay Cooksey, *Clemson University Clemson, South Carolina, East Lansing, Michigan,* Oxygen Scavenging Systems

Anthony R. Cooper, *Lockheed Martin Space Systems, Los Altos, California,* Molecular Weight Determination

Michelle L. Coote, *Australian National University, Canberra ACT, Australia,* Computational Quantum Chemistry for Free-Radical Polymerization; Copolymerization

Cajetan F. Cordeiro, *Air Products and Chemicals, Inc.,* Vinyl Acetate Polymers

Katrina Cornish, *United States Department of Agriculture, Agricultural Research Service, Western Regional Research Center, Albany, California,* Rubber, Guayule

Bruno Cortese, *Micro Flow Chemistry/Chemical Reaction Engineering Groups, Eindhoven University of Technology, Eindhoven, The Netherlands,* Microfluidic Production of Micro- and Nanoparticles

John M.G. Cowie, *Heriot-Watt University, Edinburgh, United Kingdom,* Miscibility

Henri Cramail, *Université de Bordeaux; CNRS, Laboratoire de Chimie des Polymères Organiques, Pessac Cedex, France,* Single-Site Catalysts

Bill M. Culbertson, *Ashland Chemical Co.; The Ohio State University, Columbus, Ohio,* Dental Applications; Aminimide Polymers

Mark D. Dadmun, *University of Tennessee, Knoxville, Tennessee,* Neutron Scattering

Larry R. Dalton, *University of Washington, Seattle, Washington,* Electrooptical Applications

Alberto D'Amore, *The Second University of Naples—SUN, Aversa, Italy,* Composite Materials

Daniel Ayuk Mbi Egbe, *Linz Institute for Organic Solar Cells (LIOS), Johannes Kepler University Linz, Linz, Austria,* Solar Cells

Thierry Darmanin, *Laboratoire de Physique de la Matière Condensée, Université de Nice–Sophia Antipolis, Nice, France,* Superhydrophobic Polymers

Leonard H. Davis, *Cytec Industries, Stamford, Connecticut,* UV Stabilizers

Thomas P. Davis, *The University of New South Wales, Sydney, New South Wales, Australia,* Radical Polymerization; Copolymerization

John V. Dawkins, *Loughborough University, Loughborough, United Kingdom,* Chromatography, Size Exclusion

Mart H. J. M. de Croon, *Micro Flow Chemistry/Chemical Reaction Engineering Groups, Eindhoven University of Technology, Eindhoven, The Netherlands,* Microfluidic Production of Micro- and Nanoparticles

D. E. Demco, *Institut für Technische Chemie und Makromolekulare Chemie, Rheinisch-Westfälische Technische Hochschule, Worringerweg, Aachen, Germany,* Nuclear Magnetic Resonance

Mehmet Demirors, *The Dow Chemical Company, Midland, Michigan,* Styrene–Butadiene Copolymers

Stacy A. Denney, *E. I. du Pont de Nemours & Co., Inc., Waynesboro, Virginia,* Fibers, Elastomeric

Ron J. Denning, *CSIRO Textile and Fibre Technology, Belmount, Victoria, Australia,* Wool

Prashant Deshmukh, *University of Connecticut, Storrs, Connecticut,* Liquid Crystalline Block Copolymers

Joseph M. DeSimone, *University of North Carolina at Chapel Hill, Chapel Hill, North Carolina,* Critical Phase Polymerization

Martin Dexter, *Ciba Specialty Chemicals, Tarrytown, New York,* Antioxidants

Pradeep K. Dhal, *GelTex Pharmaceuticals, Inc., A Genzyme General Business, Waltham, Massachusetts,* Polymeric Drugs

Sushil N. Dhoot, *University of Texas at Austin, Austin, Texas,* Barrier Polymers

Günter Dlubek, *ITA Institute Köthen/Halle, Lieskau (bei Halle/S.), Germany,* Positron Annihilation Spectroscopy

Phillip T. Dodge, *Lyondell Chemical Company's Cincinnati Technology Center, Cincinnati, Ohio,* Rotational Molding

Thomas J. Dolce, *Celanese Engineering Resins Company,* Acetal Resins

Abraham J. Domb, *The Hebrew University of Jerusalem, Jerusalem, Israel,* Polyanhydrides; Controlled Release Technology; Biodegradable Polymers, Medical Applications

E. Drent, *Shell International Chemicals B.V., Amsterdam, Netherlands,* Polyketones

M. P. Dreyfuss, *Michigan Molecular Institute,* Oxetane Polymers

P. Dreyfuss, *Michigan Molecular Institute,* Oxetane Polymers

P. Driva, *University of Athens, Athens, Greece,* Graft Copolymers

Jianzhong Du, *Tongji University, Shanghai, People's Republic of China,* Micelles

Etienne Duguet, *Institut de Chimie de la Matière Condensée de Bordeaux, CNRS & Université des Sciences et Technologies de Bordeaux, Pessac, France,* Intercalation Polymerization

Manfred Dunky, *Dynea Austria GmbH, Krems an der Donau, Austria,* Melamine-Formaldehyde Resins

Kenneth L. Dunlap, *Bayer Corporation, New Martinsville, West Virginia,* Phosgene

William R. Dunnavant, *Ashland Chemical Company,* Foundry Resins

Anthony J. East, *Consultant, Madison, New Jersey,* Polyesters, Thermoplastic

Sina Ebnesajjad, *FluoroConsultants Group, LLC,* Vinyl Fluoride Polymers (PVF)

Anja Eckelt, *University of Mainz—Institute of Physical Chemistry, Mainz, Germany,* Solubility of Polymers

John Eckelt, *University of Mainz—Institute of Physical Chemistry, Mainz, Germany; WEE-Solve GmbH, Mainz, Germany,* Solubility of Polymers

Kevin J. Edgar, *Eastman Chemical Company, Kingsport, Tennessee,* Cellulose Esters, Organic

Christoph Edlinger, *Department of Chemistry, University of Basel, Basel, Switzerland,* Nanoreactors

Tirtsa Ehrenfroind, *The Hebrew University of Jerusalem, Jerusalem, Israel,* Biodegradable Polymers, Medical Applications

G. W. Ehrenstein, *University of Erlangen – Nuremberg, Erlangen, Germany,* Fractography

B. E. Eichinger, *Accelrys, Inc., San Diego, California,* Molecular Modeling

M. Jamal El-Hibri, *BP Amoco Polymers, Inc., Alpharetta, Georgia,* Polysulfones

Royce Ennis, *Consultant, Silsbee, Texas,* Ethylene Polymers, Chlorosulfonated

Paquita E. Erazo-Majewicz, *Hercules Inc., Wilmington, Delaware,* Cellulose Ethers

B. Erman, *Department of Chemical and Biological Engineering, Koc University, Sariyer, Istanbul, Turkey,* Networks, Elastomeric

David J. Evans, *CSIRO Textile and Fibre Technology, Belmount, Victoria, Australia,* Wool

Aviva Ezra, *The Hebrew University of Jerusalem, Jerusalem, Israel,* Biodegradable Polymers, Medical Applications

Raymond S. Farinato, *Cytec Industries Inc., Stamford, Connecticut,* Acrylamide Polymers

Jeffry J. Fedderly, *U.S. Naval Surface Warfare Center, West Bethesda, Maryland,* Acoustic Properties

Ozana Fischer-Onaca, *Department of Chemistry, University of Basel, Basel, Switzerland,* Nanoreactors

Cynthia Flanigan, *Materials & Processes R&A, Ford Motor Company, Dearborn, Michigan,* Automotive Plastics and Composites

A. Flores, *Instituto de Estructura de la Materia, CSIC, Madrid, Spain,* Hardness

G. Floudas, *University of Ioannina, Ioannina, Greece; Foundation for Research and Technology-Hellas, Institute of Electronic Structure and Laser, Heraklion, Crete, Greece,* Amorphous Polymers

Stephan Förster, *University of Hamburg, Hamburg, Germany,* Vesicles

Ivan Fortelný, *Institute of Macromolecular Chemistry, Academy of Sciences of the Czech Republic, Prague, Czech Republic,* Polymer Blends

Frank Fowler, *SUNY, Stony Brook, New York,* Diacetylene and Triacetylene Polymers

Benny D. Freeman, *University of Texas at Austin, Austin, Texas,* Barrier Polymers

Alfred D. French, *Southern Regional Research Center, USDA,* Cellulose

Ulrich Frenzel, *Lanxess Elastomers B.V., Geleen, The Netherlands,* Metathesis Polymerization

Barbara J. Furches, *The Dow Chemical Company, Midland, Michigan,* Test Methods

S. K. Gaggar, *GE Plastics, Technology Center, Washington, West Virginia,* Acrylonitrile-Butadiene-Styrene Polymers

Steven D. Gagnon, *BASF Corporation,* Propylene Oxide and Higher 1,2-Epoxide Polymers

I. Yu. Galaev, *DSM Food Specialties B.V., Delft, The Netherlands,* Smart Polymers, Biotechnological and Biomedical Applications

Nicola Galaffu, *University of Southampton, Southampton, United Kingdom,* Polymer-Supported Reagents

Vassilios Galiatsatos, *Equistar Chemicals, L.P., Cincinnati, Ohio,* Optical Properties

J. Gallini, *E. I. du Pont de Nemours, & Company, Inc., Richmond, Virginia,* Polyamides, Aromatic

Erik Grann Gammelgaard, *FiberVisions, Varde, Denmark,* Olefin Fibers

Subhash V. Gangal, *E. I. du Pont de Nemours & Co., Inc., Wilmington, Delaware,* Perfluorinated Polymers, Tetrafluoroethylene–Ethylene Copolymers; Perfluorinated Polymers, Tetrafluoroethylene–Perfluorodioxole Copolymers; Perfluorinated Polymers, Tetrafluoroethylene–Perfluorovinyl Ether Copolymers; Perfluorinated Polymers, Perfluorinated Ethylene–Propylene Copolymers; Perfluorinated Polymers, Polytetrafluoroethylene

Guang Hui Gao, *Department of Polymer Science and Engineering, Theranostic Macromolecules Research Center, Sungkyunkwan University, Suwon, Korea,* Block Copolymer Hydrogels

Fabio Garbassi, *EniChem SpA Research Center, Novara, Italy,* Engineering Thermoplastics, Overview

Fátima García, *Universidad Complutense de Madrid, Madrid, Spain,* Supramolecular Polymers

Dhiraj K. Garg, *ICUBE, University of Strasbourg, Strasbourg, France,* Microdevices

Jerry D. Gargulak, *LignoTech USA, Inc., Rothchild, Wisconsin,* Lignin

A. N. Gent, *The University of Akron, Akron, Ohio,* Adhesion

Francesco Giacalone, *Università degli Studi di Palermo, Palermo, Italy,* Fullerene Polymers

Gregory Gillette, *GE Global Research Center, Niskayuna, New York,* Silicones

Ray Giornelli, *Shell Chemical Company,* Furniture

Gary M. Gladysz, *Los Alamos National Laboratory, Los Alamos, New Mexico,* Composite Foams

Wolfgang Glasser, *Virginia Polytechnic Institute and State University,* Cellulose

Furman E. Glenn, *DuPont Dow Elastomers L.L.C., Louisville, Kentucky,* Chloroprene Polymers

Keith A. Mesch, *The Dow Chemical Company, Cincinnati, Ohio,* Heat Stabilizers

Thierry Meyer, *École Polytechnique Fédérale de Lausanne, Lausanne, Switzerland,* Supercritical Fluids

Goerg H. Michler, *Martin-Luther-Universität, Halle-Wittenberg, Merseburg, Germany,* Micromechanical Properties

A. Milella, *Department of Chemistry, University of Bari, Bari, Italy,* Plasma Processing

Keith R. Millington, *CSIRO Textile and Fibre Technology, Belmount, Victoria, Australia,* Wool

Graeme Moad, *CSIRO Molecular and Health Technologies, Clayton, Victoria, Australia,* Reversible Addition–Fragmentation Chain Transfer Polymerization

Mónica Pérez, *ICTP-CSIC,* Plasticizers

Jeffrey S. Moore, *University of Illinois at Urbana-Champaign, Urbana, Illinois,* Self-Healing Polymers

Paul W. Morgan, *Consultant,* Interfacial Polymerization

Hiroshi Moriyama, *Department of Chemistry, Toho University, Funabashi, Japan,* Solid State Circular Dichroism Spectroscopy

Roger J. Mortimer, *Department of Chemistry, Loughborough University, Loughborough, Leicestershire, United Kingdom,* Electrochromic Polymers

Eldridge M. Mount III, *EMMOUNT Technologies, Fairport, New York,* Films, Manufacture

Laura A. Mueller, *Carnegie Mellon University, Pittsburgh, Pennsylvania,* Atom Transfer Radical Polymerization

W. P. Mul, *Shell International Chemicals B.V., Amsterdam, Netherlands,* Polyketones

Daniel G. Mullen, *The University of Minnesota, Minneapolis, Minnesota,* Polypeptide Synthesis, Solid-Phase Method

Marcus Müller, *Institut für Physik, Johannes Gutenberg Universität, Mainz, Germany,* Phase Transformation

Liubov P. Myasnikova, *Ioffe Physical Technical Institute of Russian Academy of Science, St. Petersburg, Russia,* Transitions and Relaxations

Terry N. Myers, *Atofina Chemicals, Inc., King of Prussia, Pennsylvania,* Initiators, Free-Radical

K. Nagoshi, *Kuraray Company, Ltd.,* Leatherlike Materials

E. Bruce Nauman, *Rensselaer Polytechnic Institute, Troy, New York,* Bulk and Solution Polymerizations Reactors; Flash Devolatilization

Rodrigo Navarro, *ICTP-CSIC,* Plasticizers

Thomas X. Neenan, *GelTex Pharmaceuticals, Inc., A Genzyme General Business, Waltham, Massachusetts,* Polymeric Drugs

K.G. Neoh, *National University of Singapore, Singapore,* Surface Modification of Polymers

Jürg Neuenschwander, *Center for Nondestructive Testing, EMPA, Swiss Federal Laboratories for Materials Testing and Research, Dübendorf, Switzerland,* Nondestructive Testing

James A. Newell, *Rowan University, Glassboro, New Jersey,* Carbon Fibers

K. L. Ngai, *Naval Research Laboratory, Washington, DC,* Amorphous Polymers

L. Nicolais, *Institute for the Composite Material Technology, National Research Council, Piazzale Tecchio, Napoli, Italy,* Nanocomposites, Metal-Filled

Hiroyuki Nishide, *Waseda University,* Magnetic Polymers

Jacobus W. M. Noordermeer, *DSM Elastomers, R&D, Geleen, the Netherlands,* Ethylene-Propylene Elastomers

Oskar Nuyken, *Wacker-Lehrstuhl für Makromolekulare Chemie, Technische Universität München, München, Germany; Technische Universität München, Garching, Germany,* Telechelic Polymers; Metathesis Polymerization

George Odian, *The College of Staten Island, The City University of New York,* Chain-Reaction Polymerization

Fumio Ohama, *Unitika Corporation Ltd., Japan,* Polyarylates

Kunio Oka, *Osaka Prefecture University, Osaka, Japan,* Polysilanes

Tsutomu Ono, *Department of Applied Chemistry, Graduate School of Natural Science and Technology, Okayama University, Okayama, Japan,* Microfluidic Production of Micro- and Nanoparticles

Yoshitsugu Oono, *University of Illinois, Urbana-Champaign,* Statistical Thermodynamics

Z. Ounaies, *Virginia Commonwealth University, Richmond, Virginia,* Piezoelectric Polymers

Michael J. Owen, *Dow Corning Corporation, Midland, Michigan,* Release Agents

Skip Palenik, *Microtrace, Elgin, Illinois,* Forensic Analysis

Cornelia G. Palivan, *Department of Chemistry, University of Basel, Basel, Switzerland,* Nanoreactors

Robert J. Palmer, *Du Pont de Nemours International S.A., Geneva, Switzerland,* Polyamides, Plastics

Goutam Palui, *Florida State University, Tallahassee, Florida,* Nanocrystals Surface Functionalization

C. D. Papaspyrides, *National Technical University of Athens, Athens, Greece,* Solid-State Polymerization

Dambarudhar Parida, *ICPEES, University of Strasbourg, Strasbourg, France,* Microdevices

Costas S. Patrickios, *University of Cyprus, Nicosia, Cyprus,* Group-Transfer Polymerization

Paul A. O'Connell, *Texas Tech University, Lubbock, Texas,* Yield and Crazing in Polymers

Svetlana Pavlukhina, *Stevens Institute of Technology, Hoboken, New Jersey,* Adsorption

Warren J. Peascoe, *Uniroyal Chemical Group,* Blowing Agents

Richard A. Pethrick, *University of Strathclyde, Glasgow, Scotland, United Kingdom,* Characterization of Polymers; Diffusion

Francis P. Petrocelli, *Air Products and Chemicals, Inc.,* Vinyl Acetate Polymers

Ha Q. Pham, *Dow Chemical, Freeport, Texas,* Epoxy Resins

David G. Phillips, *CSIRO Textile and Fibre Technology, Belmount, Victoria, Australia,* Wool

George E. Pickering, *Arthur D. Little, Inc.,* Toys

Gregory C. Rutledge, *Massachusetts Institute of Technology, Cambridge, Massachusetts,* Electrospinning

Ryosuke Sakai, *Hokkaido University, Sapporo, Japan,* Chiral Polymers

S. L. Sakellarides, *BP Amoco Chemical Company, Naperville, Illinois,* Poly(ethylene naphthalate) (PEN)

G. Sakellariou, *University of Athens, Athens, Greece,* Graft Copolymers

Luis Sánchez, *Universidad Complutense de Madrid, Madrid, Spain,* Supramolecular Polymers

Britto S. Sandanaraj, *University of Massachusetts, Amherst, Massachusetts,* Dendrimers, Molecular Recognition

Jorge G. F. Santos Jr., *Universidade Federal do Rio de Janeiro, Rio de Janeiro, Brazil,* Suspension Polymerization Processes

A. Sezai Sarac, *Istanbul Technical University, Istanbul, Turkey,* Electropolymerization

Niyazi Serdar Sariciftci, *Linz Institute for Organic Solar Cells (LIOS), Johannes Kepler University Linz, Linz, Austria,* Solar Cells

Hideo Sawada, *Biodegradable Plastics Society, Tokyo, Japan,* Depolymerization

Florian Schattenmann, *GE Global Research Center, Niskayuna, New York,* Silicones

D. A. Schiraldi, *KoSa, Spartanburg, South Carolina,* Atomic Force Microscopy

Shulamith Schlick, *University of Detroit Mercy, Detroit, Michigan,* Electron Spin Resonance

William W. Schloman Jr., *Department of Chemistry, University of Akron, Akron, Ohio,* Rubber, Guayule

Claude J. Schmidle, *Congoleum Corporation,* Flooring Materials

Robert L. Schmitt, *The Dow Chemical Company, Piscataway, New Jersey,* Ethylene Oxide Polymers

Martin Schneider, *Lanxess Deutschland GmbH, Dormagen, Germany,* Metathesis Polymerization

Volker Schöppner, *Institute of Polymer Engineering, University of Paderborn, Paderborn, Germany,* Compounding

Laurier L. Schramm, *Saskatchewan Research Council, Saskatoon, Saskatchewan, Canada,* Colloids

R. R. Schrieke, *Ballarat C.A.E., Victoria,* Casein

John L. Schultz, *E.I. Du Pont de Nemours, Wilmington, Delaware,* Structural Representation of Polymers; Nomenclature of Polymers

Rolf Christian Schulz, *University of Mainz, FRG,* Acrolein Polymers

Alec B. Scranton, *University of Iowa, Iowa City, Iowa,* Photopolymerization, Cationic

Norma D. Searle, *Consultant in Weathering of Materials,* Weathering of Polymeric Materials

Arno Seeboth, *Fraunhofer-Institut für Angewandte Polymerforschung, Berlin-Adlershof, Germany,* Thermochromic Polymers

Scott Seidel, *Mork Family Department of Chemical Engineering and Materials Science, University of Southern California, Los Angeles, California,* Chemical Vapor Deposition of Polymer Films

Arup K. SenGupta, *Lehigh University, Bethlehem, Pennsylvania,* Ion-Exchange Technology

Michael L. Senyek, *The Goodyear Tire and Rubber Co.,* Isoprene Polymers

Mike Sepe, *Michael P. Sepe, LLC, Sedona, Arizona,* Injection Molding

Christophe A. Serra, *Group for the Intensification and Integration of Polymer Processes (G2IP), Institute of Chemistry and Processes for Energy Environment and Health (ICPEES), Ecole de Chimie Polymères et Matériaux (ECPM), University of Strasbourg, France,* Microdevices; Microfluidic Production of Micro- and Nanoparticles

Robert W. Seymour, *Eastman Chemical Company, Kingsport, Tennesse,* Cyclohexanedimethanol Polyesters

Timothy D. Shaffer, *ExxonMobil, Baytown, Texas,* Butyl Rubber

Kenneth J. Shea, *University of California, Irvine, California,* Molecularly Imprinted Polymers

Michael C. Shelton, *Eastman Chemical Company, Kingsport, Tennessee,* Cellulose Esters, Inorganic

C. S. Sheppard, *Pennwalt Corporation,* Azo Compounds

Yutaka Shirahama, *Unitika America Corporation, Georgetown, Kentucky,* Polyarylates

Antonín Sikora, *Institute of Macromolecular Chemistry, Academy of Sciences of the Czech Republic, Prague, Czech Republic,* Polymer Blends

Michael S. Silverstein, *Technion, Israel Institute of Technology, Haifa, Israel,* PolyHIPEs

D. H. Silvey, *BFGoodrich Co.,* Belting

Sindee L. Simon, *Texas Tech University, Lubbock, Texas,* Aging, Physical

D. M. Simpson, *Exxon Mobil Chemical Company, Baytown, Texas,* Ethylene Polymers, LLDPE

Ram Prakash Singh, *Indian Institute of Technology, Kharagpur, West Bengal, India,* Drag Reduction

S. K. Sinha, *National University of Singapore, Singapore,* Surface Mechanical Damage and Wear

Vishal Sipani, *University of Iowa, Iowa City, Iowa,* Photopolymerization, Cationic

Anil K. Sircar, *University of Dayton, Dayton, Ohio,* Thermal Analysis of Polymers

Wanda Sliwa, *Institute of Chemistry, Environment Protection and Biotechnology, Jan Dlugosz University of Czestochowa, Czestochowa, Poland,* Cyclodextrin Polymers, Applications

Robert V. Slone, *The Dow Chemical Company,* Methacrylic Ester Polymers; Acrylic Ester Polymers

A. A. Smaardijk, *Shell International Chemicals B.V., Amsterdam, Netherlands,* Polyketones

Thomas W. Smith, *Eastman Chemical Company, Kingsport, Tennesse,* Cyclohexanedimethanol Polyesters

Ronald S. Smorada, *Versacore Industrial Corporation, Kennett Square, Pennsylvania,* Nonwoven Fabrics, Spunbonded

Joao B. P. Soares, *University of Waterloo, Waterloo, Ontario, Canada,* Fractionation

Ju-Myung Song, *Korea Atomic Energy Research Institute, Jeollabuk-do, Korea,* Ionomers

Mark F. Sonnenschein, *Fellow, The Dow Chemical Company, Corporate Research and Development,* Polyurethanes

Nancy R. Sottos, *University of Illinois at Urbana-Champaign, Urbana, Illinois,* Self-Healing Polymers

CUMULATIVE INDEX, VOLUMES 1–15